PROGRESS IN EXPLORATION, DEVELOPMENT AND UTILIZATION OF GEOTHERMAL ENERGY

EDITED BY: Yinhui Zuo, Shu Jiang, Yanlong Kong, Haibing Shao and Haiyan Zhu

PUBLISHED IN: Frontiers in Earth Science

frontiers Research Topics

ISSN 1664-8714
ISBN 978-2-83250-016-3
DOI 10.3389/978-2-83250-016-3

About Frontiers

Frontiers is more than just an open-access publisher of scholarly articles: it is a pioneering approach to the world of academia, radically improving the way scholarly research is managed. The grand vision of Frontiers is a world where all people have an equal opportunity to seek, share and generate knowledge. Frontiers provides immediate and permanent online open access to all its publications, but this alone is not enough to realize our grand goals.

Frontiers Journal Series

The Frontiers Journal Series is a multi-tier and interdisciplinary set of open-access, online journals, promising a paradigm shift from the current review, selection and dissemination processes in academic publishing. All Frontiers journals are driven by researchers for researchers; therefore, they constitute a service to the scholarly community. At the same time, the Frontiers Journal Series operates on a revolutionary invention, the tiered publishing system, initially addressing specific communities of scholars, and gradually climbing up to broader public understanding, thus serving the interests of the lay society, too.

Dedication to Quality

Each Frontiers article is a landmark of the highest quality, thanks to genuinely collaborative interactions between authors and review editors, who include some of the world's best academicians. Research must be certified by peers before entering a stream of knowledge that may eventually reach the public - and shape society; therefore, Frontiers only applies the most rigorous and unbiased reviews.
Frontiers revolutionizes research publishing by freely delivering the most outstanding research, evaluated with no bias from both the academic and social point of view. By applying the most advanced information technologies, Frontiers is catapulting scholarly publishing into a new generation.

What are Frontiers Research Topics?

Frontiers Research Topics are very popular trademarks of the Frontiers Journals Series: they are collections of at least ten articles, all centered on a particular subject. With their unique mix of varied contributions from Original Research to Review Articles, Frontiers Research Topics unify the most influential researchers, the latest key findings and historical advances in a hot research area! Find out more on how to host your own Frontiers Research Topic or contribute to one as an author by contacting the Frontiers Editorial Office: frontiersin.org/about/contact

PROGRESS IN EXPLORATION, DEVELOPMENT AND UTILIZATION OF GEOTHERMAL ENERGY

Topic Editors:
Yinhui Zuo, Chengdu University of Technology, China
Shu Jiang, The University of Utah, United States
Yanlong Kong, Institute of Geology and Geophysics, Chinese Academy of Sciences (CAS), China
Haibing Shao, Helmholtz Centre for Environmental Research, Helmholtz Association of German Research Centres (HZ), Germany
Haiyan Zhu, Chengdu University of Technology, China

Citation: Zuo, Y., Jiang, S., Kong, Y., Shao, H., Zhu, H., eds. (2022). Progress in Exploration, Development and Utilization of Geothermal Energy. Lausanne: Frontiers Media SA. doi: 10.3389/978-2-83250-016-3

Table of Contents

frontiers | Frontiers in Earth Science

EDITORIAL
published: 10 August 2022
doi: 10.3389/feart.2022.911376

Editorial: Progress in Exploration, Development and Utilization of Geothermal Energy

Yinhui Zuo[1,2*†], *Yanlong Kong*[3,4,5*†], *Shu Jiang*[6,7], *Haibing Shao*[8,9], *Haiyan Zhu*[1,2] *and MeiHua Yang*[1,2]

[1]State Key Laboratory of Oil and Gas Reservoir Geology and Exploitation, Chengdu University of Technology, Chengdu, China, [2]Geothermal Research Center, Chengdu University of Technology, Chengdu, China, [3]Key Laboratory of Shale Gas and Geoengineering, Institute of Geology and Geophysics, Chinese Academy of Sciences, Beijing, China, [4]Innovation Academy for Earth Science, Chinese Academy of Sciences, Beijing, China, [5]University of Chinese Academy of Sciences, Beijing, China, [6]Key Laboratory of Tectonics and Petroleum Resources of Ministry of Education, China University of Geosciences, Wuhan, China, [7]Energy & Geoscience Institute, University of Utah, Salt Lake City, UT, United States, [8]Department Environmental Informatics, UFZ-Helmholtz Centre for Environmental Research, Leipzig, Germany, [9]Applied Environmental System Analysis TU Dresden, Dresden, Germany

Keywords: geothermal geology, geothermal system conceptual model, geothermal resources assessment, geothermal energy, hydrothermal energy, enhanced geothermal system (EGS), geothermal energy exploration, geothermal energy development and utilization

OPEN ACCESS

Edited by:
Guanglong Sheng,
Yangtze University, China

Reviewed by:
Chuanqing Zhu,
China University of Petroleum, Beijing, China
Wei Xu,
Xi'an Jiaotong University, China

****Correspondence:***
Yinhui Zuo
zuoyinhui@tom.com
Yanlong Kong
ylkong@mail.iggcas.ac.cn

†These authors have contributed equally to this work and share first authorship

Specialty section:
This article was submitted to Economic Geology, a section of the journal Frontiers in Earth Science

Received: *02 April 2022*
Accepted: *06 June 2022*
Published: *10 August 2022*

Citation:
Zuo Y, Kong Y, Jiang S, Shao H, Zhu H and Yang M (2022) Editorial: Progress in Exploration, Development and Utilization of Geothermal Energy. Front. Earth Sci. 10:911376. doi: 10.3389/feart.2022.911376

Editorial on the Research Topic

Progress in Exploration, Development and Utilization of Geothermal Energy

1 INTRODUCTION

This Research Topic includes 27 papers, grouped under the Research Topic "*Progress in Exploration, Development and Utilization of Geothermal Energy.*" This editorial highlights each of the papers, which relate to two major aspects and six sub-aspects, including geothermal energy exploration including geothermal geology, geothermal system conceptual model and geothermal resource assessment, and geothermal development and utilization including shallow geothermal energy, hydrothermal energy, and enhanced geothermal systems (EGSs).

2 GEOTHERMAL ENERGY EXPLORATION

2.1 Geothermal Fields

Geothermal fields include a geological description of the present geothermal fields and paleo geothermal fields. Thermal history is a significant constraint in accurately restoring the characteristics of the paleo geothermal fields (Jiang et al., 2021). Gao and Li studied the thermal history of the Fuyang sag for the first time based on their geophysical exploration and drilling results.

The present geothermal fields represented in this Research Topic mainly include terrestrial heat flow and thermal structure research, rock thermal conductivity and heat production rate researches, and remote sensing data in geothermal applications (Zuo et al., 2020).

2.1.1 Terrestrial Heat Flow and Thermal Structure Research

Based on the surface heat flow and rock thermal properties, Zhu et al. evaluated the temperature distribution characteristics and discussed the primary influencing factors on the geothermal state of the Sichuan Basin. Xu et al. calculated the geothermal gradient and terrestrial heat flow in the Xi'an Depression of the Weihe Basin and indicated a high thermal background in the area. Lithospheric thermal structure refers to the ratio of the heat flow between the crust and the mantle in a region and its fabric relationship (Zuo et al., 2020). The distribution of heat flow of crust and mantle affects the distribution of deep temperature and the activity of crust and upper mantle. Liu et al. selected the Yanheying Basin, a typical intermountain basin located in the eastern foothills of the Yanshan Mountain, to undertake a comprehensive analysis of heat flow and lithospheric thermal structure, to have a better understanding of the geothermal background and resource utilization potential of the area.

2.1.2 Rock Thermal Conductivity and Heat Production Rate Research

Rock thermal properties include the thermal conductivity and radioactive heat production of rocks. Zeng et al. proposed a novel fractal model with variation pore diameter relating to effective thermal conductivity and the microstructural parameters and fluid properties. This model improved the accuracy of predicting effective thermal conductivity. Cui et al. calculated the radioactive heat production of sedimentary layers and igneous rocks using the logging curve and analyzed the influence of igneous rock distribution, residual heat, and its thermal increment on the crust.

2.1.3 Remote Sensing Data in Geothermal Applications

The inversion of surface temperature is particularly important for the present geothermal field. Dong et al. systematically reviewed the characteristics of surface temperature retrieval methods. Based on Landsat 8 remote sensing data, the differences among these three algorithms (Radiative Transfer Equation, Mono-Window Algorithm, and Split window Algorithm) were researched by adopting them to detect the surface temperature in Kangding County, Sichuan Province, China.

2.2 Geothermal System Conceptual Model

The geothermal system mainly includes five elements, namely a heat source, a fluid source, a flow path, a thermal reservoir, and cap rock.

The heat sources of sedimentary basins mainly come from two parts, one is the heat generated by the decay of radioactive elements in the crust and the other is the heat flow in the deep mantle. Wang et al. reviewed the exploration process of deep geothermal resources in the North Jiangsu Basin and outlined that the geothermal genesis mechanism has been influenced by mantle-source heat and the upper crustal-scale heat control, which was mainly caused by thermal refraction. Chemical composition and the isotopes of fluids are often used to trace fluid source and path. Xing et al. used the Piper trigram and Na-K-Mg software to explore the genesis of underground hot water. They revealed the genesis of the Gaoyang geothermal field based on the water chemistry and isotopic in the geothermal fluid. Wang et al. performed a comprehensive investigation using multiple chemical and isotopic tracers (δ^2H, δ^{18}O, ^{87}Sr/^{86}Sr, δ^{13}C, and ^{14}C) to reconcile the anomalies and examine both the recharging water source and the circulation dynamics of these geothermal systems.

Zhang et al. systematically collected indicators including ^{14}C dating, ^{18}O, and ^{2}H to identify the dominant flow path of regional carbonate geothermal water. They indicated that the geothermal water in areas with young ^{14}C age, a high value of D, and weak ^{18}O drift phenomenon had good flow conditions. Tian et al. reported new data on chemical compositions and He–Ne–C isotopes for gas samples from representative hot springs and wells in the Guangdong and Fujian provinces to identify the origin of hydrothermal volatiles and provided insight into geothermal tectonic affinities. They revealed that the NE-trending faults were heat-control tectonic structures and that their intersections with the NW-trending faults provided expedite channels for geothermal fluid rising to the surface. Baoqing et al. observed that the microtremor survey method is often adopted for geothermal exploration in urban areas. Using this method, the Rayleigh wave dispersion curve was extracted using spatial autocorrelation based on the vertical component signal at the observation station. A genetic algorithm was then used to invert the dispersion curve of one survey point to obtain strata parameters such as layer thickness, S-wave velocity, and density. This approach provided critical parameters for the cap layers and reservoirs for geothermal exploration. On the cause and overall evaluation of the geothermal system, Zheng et al. studied the geological conditions of the deep granite reservoir and discussed the genesis of the deep granite geothermal system based on rock geochemistry and zircon U-Pb chronology. They proved that there is a huge amount of deep granite geothermal resources in the southeastern coastal area in China. Li et al. systematically analyzed the nature and forming mechanisms of the Xifeng low-temperature geothermal field using element geochemical (ions, rare Earth elements) and stable isotopic (D, O) composition. They assigned the geothermal field as a faults-controlling and deeply circulating meteoric water of low-temperature category.

2.3 Geothermal Resources Assessment

Geothermal resource assessment involves calculating and evaluating verified, proven, controlled, and inferred geothermal resources, which are based on a comprehensive analysis of the exploration results of geothermal resources and using reasonable methods. Yuan et al. analyzed the mechanism and prediction of geothermal resources controlled by neotectonics in mountainous areas and established a conceptual model of geothermal resources in southeastern Zhangjiakou City, China. This conceptual model is verified by the geothermal fields already discovered in the study area and has been proven to be reasonable. A potential drilling site was also predicted and showed success. Huang et al. proposed a revised volumetric approach for evaluating the deep geothermal potential in an active oil field by integrating a 3D geological model into a hydrothermal (HT)-coupled numerical model. Integrating the 3D geological modeling and HT numerical model into the

geothermal resource assessment improved its accuracy and helped to identify the distribution map of the available geothermal resources, which indicated optimal locations for further development and utilization of the geothermal resources.

3 GEOTHERMAL DEVELOPMENT AND UTILIZATION

3.1 Shallow Geothermal Energy

Shallow geothermal energy refers to the low-temperature geothermal energy stored in water, soil, and rocks at depths of 200 m between the surface and the underground. They contribute most to the utilization of geothermal energy with help from heat pump technology. Two papers in this issue shed light on advances in this area. Zhu et al. simulated the heat transferring process of the groundwater heat pump system in terms of a single well. They found the major reasons leading to the cold accumulation and then optimized single-well technology to improve the coefficient of performance (COP). They also introduced the concept of borehole thermal energy storage (BTES), which is paper's other main theme. Meng et al. discussed the thermal impact of the long-term utilization of BTES. The environmental impact of the interaction with hydrocarbon contaminants was also investigated using OpenGeoSys software. They concluded that the change of subsurface temperature will lead to the alteration of hydrocarbon contaminants. For example, they found that over 70% of the trichloroethylene mass was removed from a discontinuous contaminant plume after 5 years of operation of a small BTES installation in their modeled scenarios.

3.2 Hydrothermal Energy

Hydrothermal energy is geothermal energy utilized in terms of extracting groundwater fluids generally without help from a heat pump (Kong et al., 2014). Six papers in this Research Topic address this issue. To extract the geothermal fluid, the primary approach is to perform the borehole. Zhang and Li examined the affecting factors on the thermal insulation cement of a geothermal borehole, as they show, porosity, with Skeleton ingredients, curing temperature, and test temperature being vital factors.

Three papers focus on the optimization of hydrothermal energy. Yuan et al. carried out a numerical simulation based on the monitoring data in a small geothermal reservoir. They found an optimized strategy for a multi-well layout to prevent fast water level drawdown through reinjection. They also checked the factors of openhole length, production rate, and reinjection water temperature on the heat performance. Such a strategy is of course useful for geothermal energy utilization of hydrothermal energy. Sun et al. considered the sustainable utilization of hydrothermal energy in complex geological layers with faults. Both 2D and 3D numerical models were employed to establish that groundwater reinjection strategies should be carried out in advance. They emphasized the detailed geological parameters of the fracture zone, which should be examined further for better utilization of hydrothermal energy. These results can be compared with those of Kong et al. (2017a), who developed a model to couple numerical simulation and economic analysis. In the follow-up work included here, Fan et al. developed a model to estimate the recovery ratio, which is useful for assessing geothermal energy during the production process at a geothermal field.

Different from the three geological papers mentioned above, Zhao et al. focused on the power generation method to utilize hydrothermal energy. Two systems, including binary flashing cycle (BFC) and organic Rankine cycle (ORC), are compared in terms of thermodynamic and economic performance. They described the effects on the performance of several indicators including thermal efficiency, exergy efficiency, net power output per ton of geothermal water, heat exchanger area, and heat recovery efficiency. Their results showed that the BFC can realize the full utilization of low-grade energy.

One paper in this Research Topic utilized geothermal energy without extracting geothermal fluid. Such technology is called the deep borehole heat exchanger (DBHE). Following the heat exchange model developed by Kong et al. (2017b), Cai et al. performed a comprehensive economic analysis of DBHE in 15 heating seasons. They found the minimum COP is 4.74 in their study area of the Weihe Basin in Northwest China. They also undertook an optimal analysis and concluded that a depth of 2,600 m has the lowest Levelized cost of total heating amount (LCOH) for the Weihe Basin, which could support geothermal energy in this region.

3.3 EGS

The EGS is a major way of utilizing hot dry rock geothermal energy, although it is also used for hydrothermal energy (Kong et al., 2021). Two papers in this issue are included in this Research Topic.

The key technology for developing an EGS reservoir is hydraulic fracturing. Xu et al. studied the characteristics of damage zone porosity for stimulation in a sandstone reservoir. A simulation experiment was carried out to locate the damage zone. Meanwhile, the effects of high temperature and pressure were also examined in this paper. Another important aspect of extracting geothermal energy using EGS is the working fluid. Lei compared CO_2 and H_2O using the data in the Songliao Basin, Northeast China. Considering the temperature drop limitation at the downhole of the production well, he concluded that the heat extraction performance was better using H_2O than that using CO_2 as the working fluid. However, there were also disadvantages to using CO_2, because the CO_2 based EGS had a low-power consumption for maintaining fluid circulation.

AUTHOR CONTRIBUTIONS

YZ, SJ, and MY summarized the geothermal energy exploration; YK, HS, and HZ summarized the geothermal development and utilization.

FUNDING

This work was financially supported by the National Natural Science Foundation of China (Grant no. 41972144, 52192623, 52192625) and the National Key Research and Development Program of China (Grant no. 2019YFB1504101).

REFERENCES

Jiang, S., Zuo, Y., Yang, M., and Feng, R. (2021). Reconstruction of the Cenozoic Tectono-Thermal History of the Dongpu Depression, Bohai Bay Basin, China: Constraints from Apatite Fission Track and Vitrinite Reflectance Data. *J. Pet. Sci. Eng.* 205, 108809. doi:10.1016/j.petrol.2021.108809

Kong, Y., Chen, C., Shao, H., Pang, Z., Xiong, L., and Wang, J. (2017b). Principle and Capacity Quantification of Deep-Borehole Heat Exchangers. *Chin. J. Geophys.* 60 (12), 4741–4752. doi:10.6038/cjg20171216

Kong, Y., Pan, S., Ren, Y., Zhang, W., Wang, K., Jiang, G., et al. (2021). Catalog of Enhanced Geothermal Systems Based on Heat Sources. *Acta Geol. Sin. Engl. Ed.* 95 (6), 1882–1891. doi:10.1111/1755-6724.14876

Kong, Y., Pang, Z., Shao, H., Hu, S., and Kolditz, O. (2014). Recent Studies on Hydrothermal Systems in China: A Review. *Geotherm. Energy* 2, 19. doi:10.1186/s40517-014-0019-8

Kong, Y., Pang, Z., Shao, H., and Kolditz, O. (2017a). Optimization of Well-Doublet Placement in Geothermal Reservoirs Using Numerical Simulation and Economic Analysis. *Environ. Earth Sci.* 76, 118. doi:10.1007/s12665-017-6404-4

Zuo, Y., Jiang, S., Wu, S., Xu, W., Zhang, J., Feng, R., et al. (2020). Terrestrial Heat Flow and Lithospheric Thermal Structure in the Chagan Depression of the Yingen-Ejinaqi Basin, North Central China. *Basin Res.* 32 (6), 1328–1346. doi:10.1111/bre.12430

Conflict of Interest: The authors declare that the research was conducted in the absence of any commercial or financial relationships that could be construed as a potential conflict of interest.

Publisher's Note: All claims expressed in this article are solely those of the authors and do not necessarily represent those of their affiliated organizations, or those of the publisher, the editors and the reviewers. Any product that may be evaluated in this article, or claim that may be made by its manufacturer, is not guaranteed or endorsed by the publisher.

frontiers in Earth Science

ORIGINAL RESEARCH
published: 13 August 2021
doi: 10.3389/feart.2021.683696

Geological Characteristics and Distribution of Granite Geothermal Reservoir in Southeast Coastal Areas in China

Herong Zheng, Jun Luo, Ying Zhang, Jianyun Feng, Yan Zeng and Mingchuan Wang*

Sinopec Petroleum Exploration and Production Research Institute, Beijing, China

The southeast coastal areas in China have distributed lots of granite outcrops of different periods. Previous research has shown that granite geothermal reservoirs are also distributed under sedimentary basins in these areas, such as in Zhangzhou basin. Therefore, granites with fractures buried in deep can be used as a potential deep geothermal reservoir in these areas. In order to study geological conditions of the deep granite reservoir and discuss the genesis of the deep granite geothermal system, rock geochemistry and zircon U-Pb chronology from outcrop and parts of the drilling cores of granitic rocks have been analyzed, combined with the anatomy of the deep seismic data and electromagnetic detection data in selected area. Based on the results of geochemistry and zircon U-Pb chronology, most granites in this area are of Yanshanian periods. Based on the seismic data, the thickness of the overlying strata on granite in Huangshadong area of Huizhou City is up to 1.5 km. According to the regional geological survey, multi-stage joints are developed in the granite, and most of hot springs rise from intersection of fracture with different directions to the surface. The heat source in the study area mainly comes from the mantle carried up by the deep NNE-trending faults. There are a large number of thermal springs at the intersection of the surface and the NW-trending fault, and the NW-trending fault provides the drainage conditions for the upwelling of underground thermal springs. There is a huge amount of deep granite geothermal resources in the southeast coastal area. The analysis of deep granite geological conditions and genetic models can provide guidance for the evaluation of deep granite geothermal resources and the further optimization of favorable zones in these areas.

Keywords: southeast coastal areas, granite geothermal reservoir, geothermal resources, geochemistry, geochrohology

OPEN ACCESS

Edited by:
Shu Jiang,
The University of Utah, United States

Reviewed by:
Tianfu Xu,
Jilin University, China
Cao Rui,
Chengdu University of Technology, China

****Correspondence:***
Jun Luo
luojun.syky@sinopec.com

Specialty section:
This article was submitted to Economic Geology, a section of the journal Frontiers in Earth Science

Received: *22 March 2021*
Accepted: *30 July 2021*
Published: *13 August 2021*

Citation:
Zheng H, Luo J, Zhang Y, Feng J, Zeng Y and Wang M (2021) Geological Characteristics and Distribution of Granite Geothermal Reservoir in Southeast Coastal Areas in China. Front. Earth Sci. 9:683696. doi: 10.3389/feart.2021.683696

INTRODUCTION

Geothermal resources, as a renewable and clean energy, have been widely used globally in recent years, and the utilization has been increasing year by year (Bertani, 2012; Bertani, 2016; Lund and Boyd, 2016). Recently, most of the geothermal resources under exploitation and utilization are hydrothermal geothermal resource, which is widely distributed in southeastern areas of China (Li Dewei and Wang Yanxin, 2015). Deep geothermal resources are considered as an important part of future energy supply due to their huge thermal energy storage and reserves.

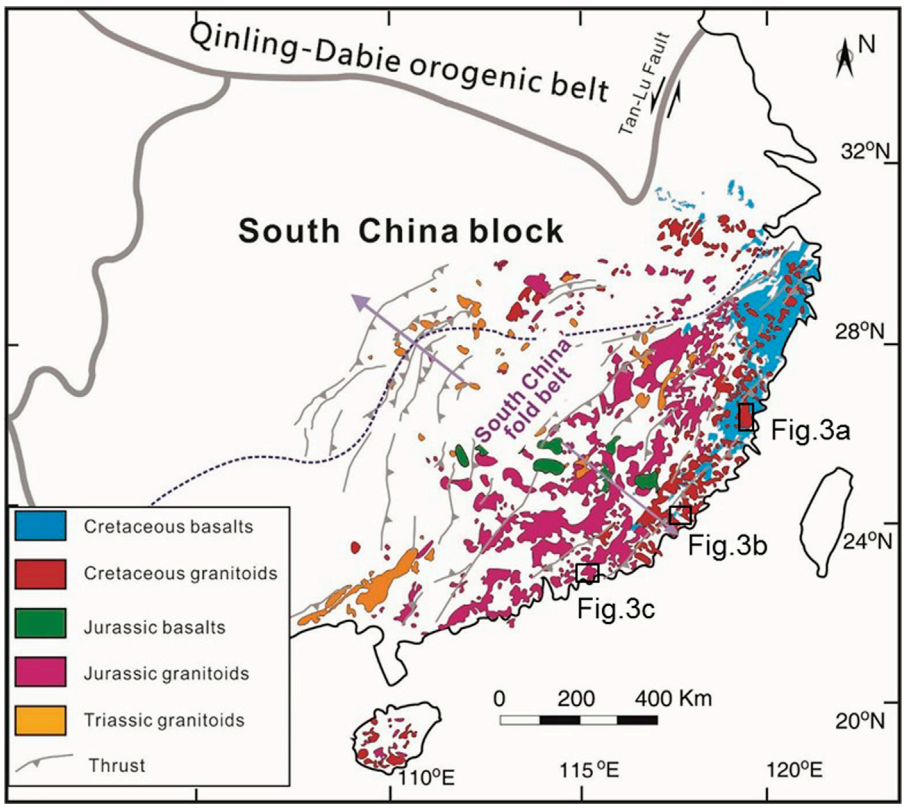

FIGURE 1 | The granite distribution map of the study area (Modified after Zhang et al., 2020).

Most of the deep geothermal reservoir are granite (Brown et al., 2012), and Metamorphic rocks (Li et al., 2019) beneath the sedimentary basins and numerous studies have shown that the granite radioactive heat production has significant contribution to the heat source, such as Australia Cooper basin geothermal field caused by granites with intrusion age less than 0.5 Ma (Goldstein et al., 2008), Rose-manowes geothermal field in England due to Early Permian granite heat generation (Richards et al., 1992), the Soultz geothermal field in France due to Late Paleozoic granite heat generation (Genter et al., 1995).

In the southeast coastal area of China, ground or near surface geothermal manifestations are widely distributed, such as hot springs and other surface heat. They are mainly located in the fractures within igneous rock, such granites. Granites in South China are widely distributed, with an outcropping area of 20,000 km^2, accounting for about 1/5 of the area, and it is considered to be formed in three phases, i.e., Caledonian, Indosinian and Yanshanian period (Zhou et al., 2006) (**Figure 1**). Radioactive elements from those granites such as U, Th, K, are important radioactive elements to generate heat by atom decaying. Meanwhile, Southeast coastal areas in China is the second largest region with high heat flow value (Hu et al., 2000). Xi et al. (2018) analyzed the gravity anomaly in Guangdong province and concluded that the decay of thermal elements in granite may be an important part of the geothermal heat sources in the southeast coastal areas. The region is rich in geothermal resources, covering medium-low temperature, medium-high temperature and high-temperature geothermal resources.

In order to further study geological conditions of the deep granite reservoir and discuss the genesis model of the deep granite geothermal system, this paper adopted rock samples from outcrops and parts of the drilling core rocks to analyze the formation background of granite and discuss its geothermal significance to the southeast region in China.

GEOLOGICAL SETTING

Geologically, the southeast coastal region of China is part of the Cathaysia block (Wang et al., 2013; Deng et al., 2019). These areas have experienced multiple periods of intense magmatic events since the Paleozoic, mainly manifested as a large number of Paleozoic and Mesozoic granitic rocks (Wang et al., 2013) and Cenozoic mafic magmatism (Gong and John, 2014). Large-scale structural deformation caused by emplacements are very strong to the stratum reconstruction, forming a series of faults with different scales and directions.

Granite reservoirs are distributed among the southeastern coastal areas, such as in Zhangzhou, Fuzhou, Fengshun, Yangjiang, and southern Hainan Province. In these areas, the distribution of reservoir is mainly controlled by NE-trending

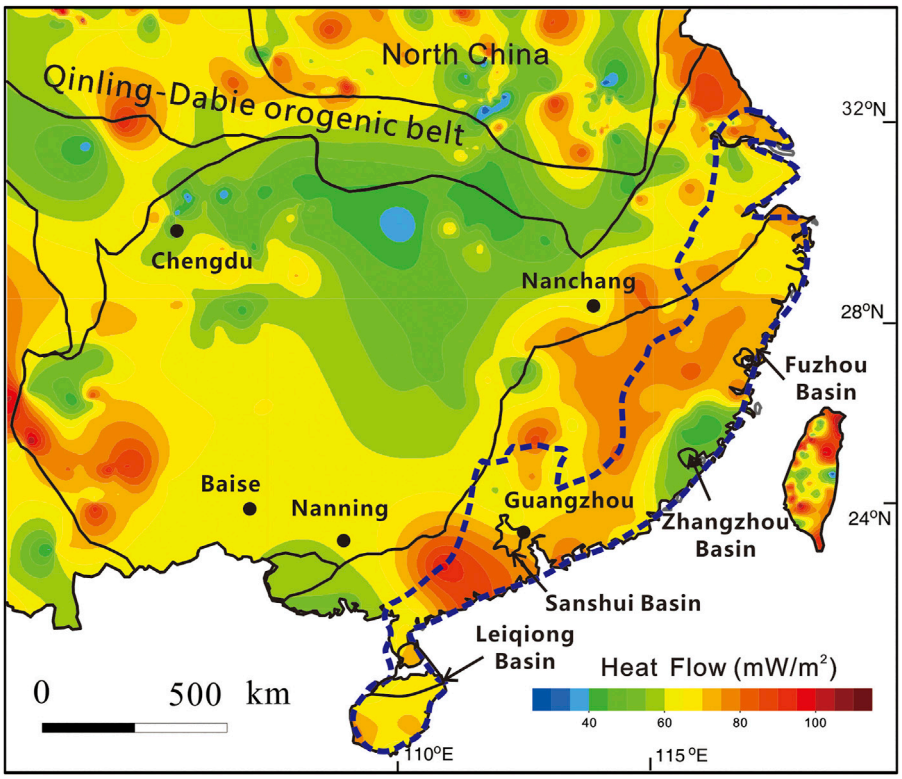

FIGURE 2 | The Heat flow map distribution of the study area (Modified after Zhang et al., 2020).

faults. Most of these granites were formed during the Yanshanian period. There are two types of heat source: Crust source originating from radiogenic heat from K-, Th- and U-bearing minerals of granites and mantle source connecting to the nearby ground by the deep faults. In the Quaternary, most of the radiogenic heat of granite was lost along the fault zone and could not constitute a source of geothermal heat in the fault. Therefore, it is easy to form deep fracture zone and become the channel for hot water to migrate from the deep mantle. In southeast coastal area, 74% of hot springs are located in fault zone or lithological contact zone in magmatic plutons.

The distribution of most granite geothermal fields are mainly located in basins, such as Fuzhou basin, Zhangzhou basin, Sanshui basin (**Figure 1**). They are mainly controlled by the deep and large fault in NE direction, and most of them are along the Neo-Cathaysian faults. The zone has experienced many strong tectonic movements and multiple periods of magma intrusion, resulting in secondary faults, rock mass fragmentation and joint fractures near the fault zone, providing space and channels for the storage and migration of geothermal fluids. At the same time, the tectonic activities of deep and large faults not only promote the formation of heat storage space, but also communicate the spatial connection between deep geothermal fluids and shallow geothermal reservoirs, becoming an important heat transfer channel in geothermal fields. From the regional analysis, most of the geothermal fields are linear distribution along the fault zone, mainly exposed on the deep fault axis. The rest are mostly distributed among the deep and large faults, which are locally influenced by the secondary NW tensioned water-conducting faults or pinnate faults. The distribution of heat flow in South China is shown in **Figure 2**. It contains three obvious thermal structure divisions: Eastern, central and southwestern regions. The eastern and southwestern regions are characterized by high heat flow, while the heat flow in the central region is relatively lower. The heat flow in the eastern and southwestern regions are generally higher than 70 mW/m^2, while that in the central region is lower than 60 mW/m^2. In the eastern region, there are 2 NE-trending high value abnormal belts along the Fuzhou-Zhangzhou zone. These two anomaly zones are characterized by high heat flow values (>80 mW/m^2, locally up to 220 mW/m^2). The average heat flow in northern Jiangsu Basin is 71.2 mW/m^2, while that in southern Jiangsu and southern Anhui areas is 62.7 mW/m^2. In the central region, from Baise to Dabie Mountains, lower heat flow is distributed along the NE-direction. In the southwestern region, the higher heat flow is concentrated only in southwestern Yunnan. The average of heat flow in the north of Sichuan Basin is 53.6 mW/m^2, while that in southern Yunnan is 76.7 mW/m^2. In the middle of northern Jianghan Basin, the heat flow is lower in the north and higher in the south. The average heat flow in the north of the fault is 47.8 mW/m^2, and that in the south is 61.6 mW/m^2. The average heat flow value of 64.2 mW/m^2 in southern China is higher than that of 61 mW/m^2 in other mainland parts in China (Wang et al., 1990), which is close with that of the globe for 65 mW/m^2 (Yuan, 2006). The

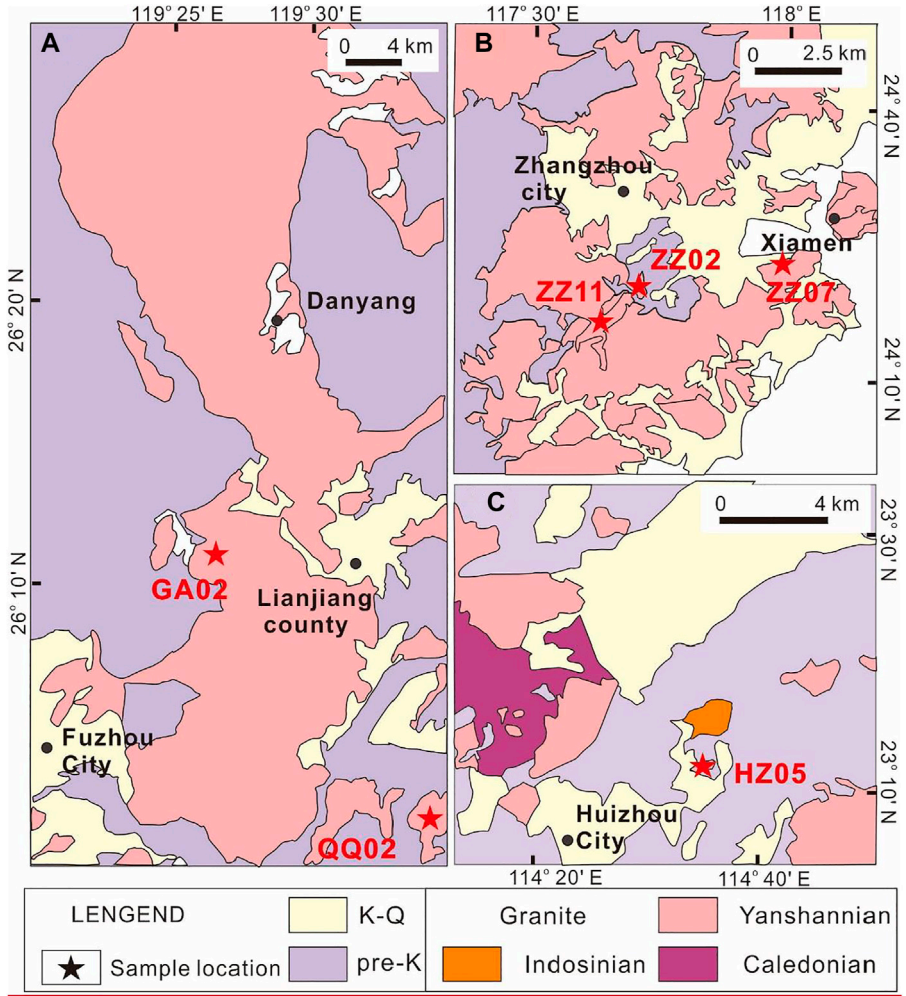

FIGURE 3 | Simplified geological map of selected regions in Southeast Coastal Area: **(A)** Fuzhou area; **(B)** Zhangzhou area; **(C)** Huizhou area (Modified after Zhu 2015; Yang 2016; Zhang et al., 2021).

abnormally high value areas in South China are mainly distributed in the suture zone or regional deep fault zone. Some granite geothermal reservoirs in typical areas in South China have been studied by previous researchers, including Fuzhou, Zhangzhou, Huizhou, Yangjiang areas (Zhu 2015; Yang 2016; Zhang et al., 2021; Zhou, 2015). The Fujian granite geothermal reservoir is located around Fuzhou basin (**Figure 3A**). Most of them are Yanshanian granites. Early detailed geothermal resource exploration shows that the geothermal reservoir is an area of 9 km^2 with a north-south length of about 5 km and an east-west width of about 2 km. The basement consists of Yanshanian granodiorite, intrusions of medium-coarse biotite granite and fine-grained granite, as well as a large number of intermediate-acid and intermediate-basic dike rocks (Zhu 2015). Zhangzhou granite geothermal reservoir is located around Zhangzhou Basin (**Figure 3B**). The Quaternary sediments on granite are a set of Marine and continental deposits with a thickness of 20 m–30 m. There are several granite rock masses, such as Zhangzhou granite, Chengxi granite and Maping granite, which are around Zhangzhou geothermal field (Yang, 2016). In Huizhou area, Huangshadong geothermal field is located in the northeast of Huizhou city (**Figure 3C**). This area has experienced several periods of intense magmatic events since the Paleozoic. The granites include Caledonian granodiorite, Indo-Chinese granites, Yanshanian granites and Neogene tholeiitic basaltic dikes (Zhang et al., 2021). Xinzhou complex granite is located in the coastal area of west Guangdong, Yunkai block geologically, on the southwest Cathaysia block, with a total outcropping area of 350 km^2. The rock is composed of medium-coarse-grained macro porphyritic biotite monzonite and fine-grained porphyritic biotite quartz syenite, surrounded by the Proterozoic Yunkai Group plagioclase gneiss. The latest outcropped strata around this area are Late Cretaceous sandstone and conglomerate, distributed with NE direction. Xinzhou complex granite mainly includes Xinzhou granite, Dongping granite and Naqin rock granite (Zhou, 2015).

Favorable granite geothermal reservoir is distributed in the exposed magmatic rock mass, near the late intrusive dike or the

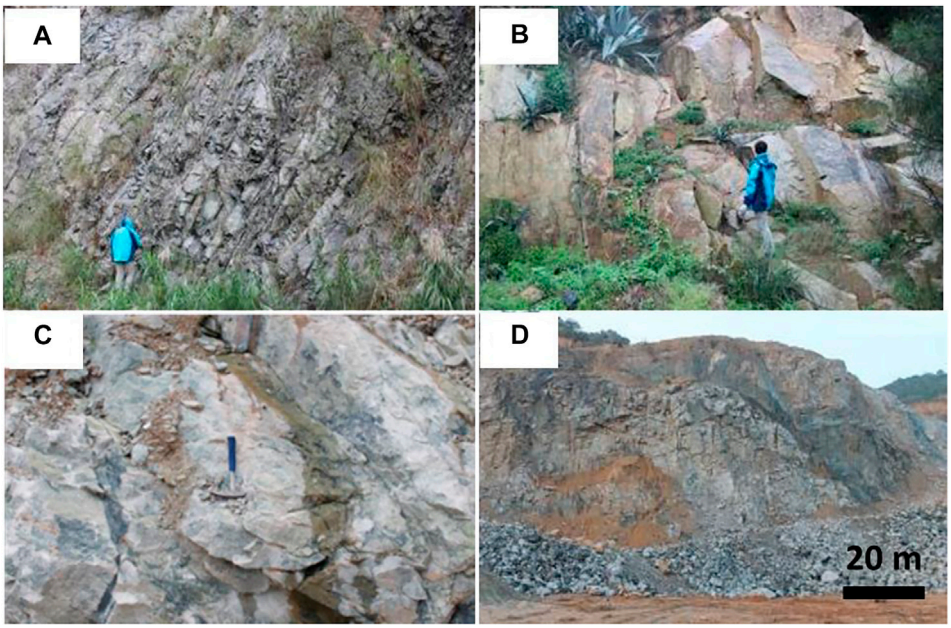

FIGURE 4 | Photograph showing outcrops of granites in different areas, **(A)** granite outcrop with fractures in Minhou, Fuzhou area; **(B)** granite outcrops in Qinqian, Fuzhou area; **(C)** granites with fractures in Huizhou; **(D)** granites in Zhangzhou.

contact zone between rock mass and surrounding rock mass. The distribution of geothermal field is not only related to the fracture and fracture development of primary rock mass and contact zone rock due to the multi-stage intrusion of magma or the influence of deep fault structure, but also related to the geological age of intrusive rock.

SAMPLE DESCRIPTION AND ANALITICAL METHODS

In order to interpret magmatism in the study area of granite, a total of 20 samples of magmatic rocks were collected in the selected areas, such as Fuzhou, Zhangzhou and Huizhou area (**Figure 3**).and they were measured by principal trace element analysis, and zircon U-Pb dating analysis was conducted for six granite samples.

The granite samples collected were mainly distributed along a line of about 1,300 km with an exposed area of about 10–784 square kilometers. These granites are mainly granitic (**Figure 4**), with a few being orthogonality, quartz dimorphism and granitic diorite, with granular structure of different thickness and fineness (**Figure 5**). The mineralogy of these samples is relatively simple, consisting mainly of plagioclase (30–42%), potash feldspar (30–8%), quartz (20–30%), biotite (5%), and a small amount of amphibole (2–10%). Accessory minerals include sphere, zircon, and titanium-iron oxides.

U-Pb dating and trace element analyses of zircon were conducted synchronously by LA-ICP-MS at the State Key Laboratory of Geological Processes and Mineral Resources, China University of Geosciences, Wuhan. Detailed operating conditions for the laser ablation system and the ICP-MS instrument and data reduction are the same as description by Liu et al. (2010). Laser sampling was performed using a GeoLas 2005. An Agilent 7500a ICP-MS instrument was used to acquire ion-signal intensities. A "wire" signal smoothing device is included in this laser ablation system, by which smooth signals are produced even at very low laser repetition rates down to 1 Hz (Hu et al., 2012b). Helium was applied as a carrier gas. Argon was used as the make-up gas and mixed with the carrier gas via a T-connector before entering the ICP. Nitrogen was added into the central gas flow (Ar + He) of the Ar plasma to decrease the detection limit and improve precision (Hu et al., 2008a; Liu et al., 2010). Each analysis incorporated a background acquisition of approximately 20–30 s (gas blank) followed by 50 s of data acquisition from the sample. The Agilent Chemstation was utilized for the acquisition of each individual analysis. Off-line selection and integration of background and analyze signals, and time-drift correction and quantitative calibration for trace element analyses and U-Pb dating were performed by ICPMS DataCal (Liu et al., 2008).

Zircon 91,500 was used as external standard for U-Pb dating, and was analyzed twice every five analyses. Time-dependent drifts of U-Th-Pb isotopic ratios were corrected using a linear interpolation (with time) for every five analyses according to the variations of 91,500 (i.e., two zircon 91,500 + 5 samples +2 zircon 91,500) (Liu et al., 2010). Preferred U-Th-Pb isotopic ratios used for 91,500 are from Wiedenbeck et al. (1995). Uncertainty of preferred values for the external standard 91,500 was propagated to the ultimate results of the samples. Concordia diagrams and weighted mean calculations were made using Isoplot/Exver3 (Ludwig, 2003). Trace element compositions

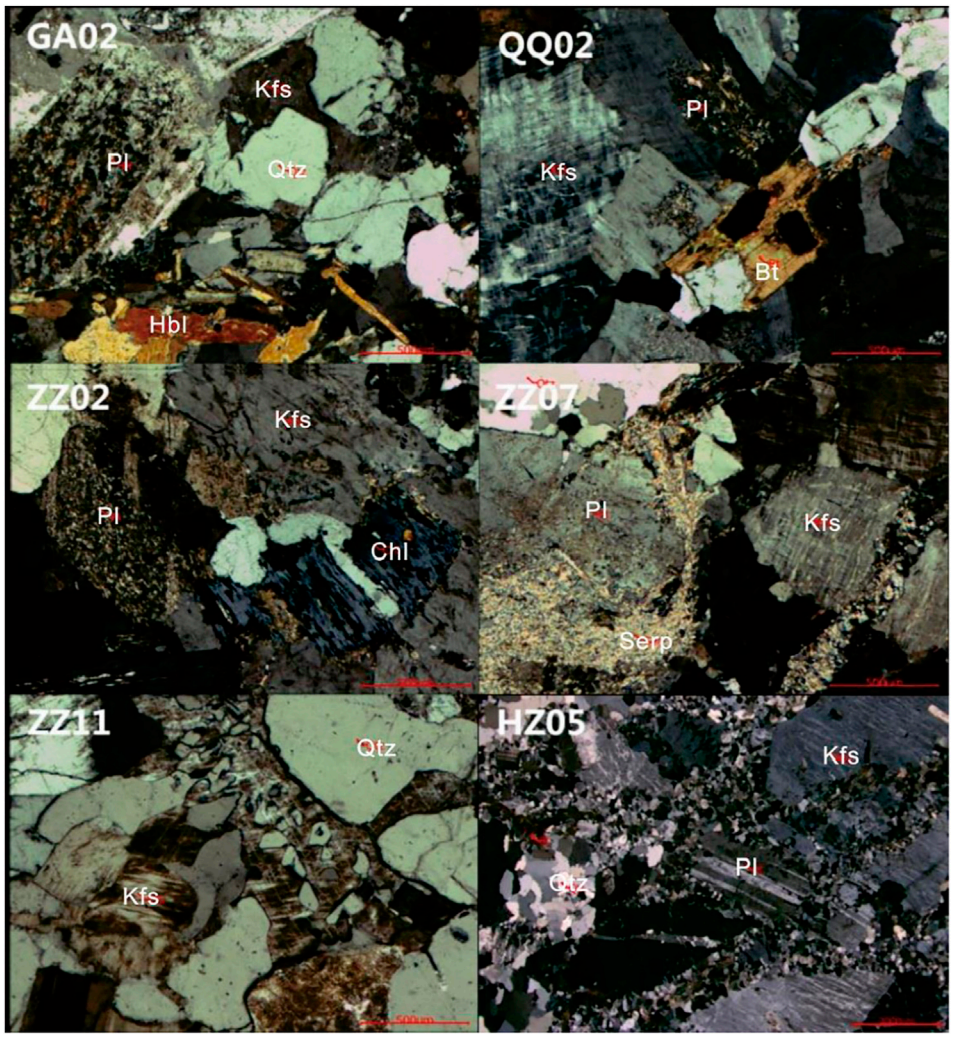

FIGURE 5 | Microphotographs showing mineral assemblage of representative granites. The abbreviations are: Pl-plagioclase, Qz-quartz, Bt-biotite, Kfs-K-feldspar, Amp-amphibole.

of zircons were calibrated against multiple-reference materials (BCR-2G and BIR-1G) combined with internal standardization (Liu et al., 2010). The preferred values of element concentrations for the USGS reference glasses are from the GeoReM database.

RESULTS

U-Pb Dating

The concordance ages and analysis results of typical zircons of six samples are shown in **Figure 5**. They are collected from different areas, such as Fuzhou area (GA02, QQ02) (**Figure 3A**), Zhangzhou area (ZZ02, ZZ07, ZZ11) (**Figure 3B**) and Huizhou area (HZ05) (**Figure 3C**). It can be seen from the CL image that the zircons generally have good autogenesis (**Figure 6**). Most of them are columnar or long-column-cone shaped with a length of 50–360 m. The aspect ratio of most of them is about 1.5:1–3:1, which is similar to the characteristics of magmatic zircons (Wu Yuanbao and Zheng Yongfei, 2004). The dating results of six samples show that the rock mass in the study area has a wide age distribution, ranging from 94.7 to 138.4 Ma. The LA-ICP-MS U-Pb zircon analysis spots are presented in **Table 1**, and the results are illustrated in **Figure 6**.

A total of 26 valid data were obtained from GA02. These zircon grains have moderate and variable concentrations of Th (102–200 ppm) and U (125–318 ppm), corresponding Th/U ratios of 0.8–1.14, showing the characteristic of magmatic zircon (Hoskin and Black, 2000; Sun and McDonough, 1989). These data yield a weighted mean $^{206}Pb/^{238}U$ age of 117.95 ± 0.47 Ma (MSWD = 0.45), representing the formation age of the granite. A total of 28 valid data were obtained from QQ02. These zircon grains have moderate and variable concentrations of Th (127–291 ppm) and U (287–606 ppm), corresponding Th/U ratios of 0.37–0.85, showing the characteristic of magmatic zircon. These data yield a weighted mean $^{206}Pb/^{238}U$ age of 112.92 ± 0.85 Ma (MSWD = 1.6), representing the formation

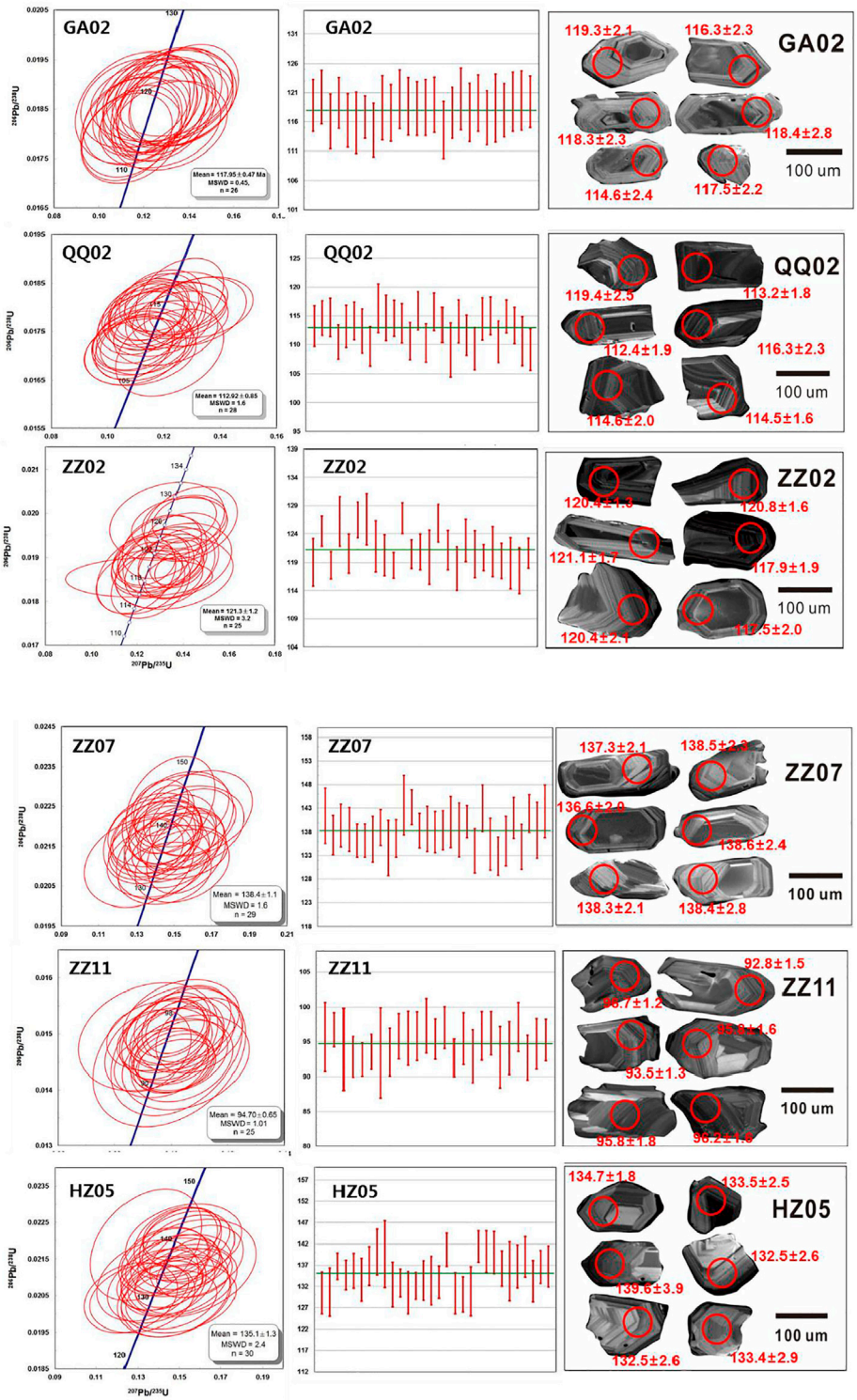

FIGURE 6 | The $^{206}Pb/^{238}U$-$^{207}Pb/^{235}U$ concordia plot and the weighted mean age of representative zircons of the granites.

age of the granite. A total of 25 valid data were obtained from ZZ02. These zircon grains have moderate and variable concentrations of Th (108–535 ppm) and U (154–1,090 ppm), corresponding Th/U ratios of 0.3–0.99, showing the characteristic of magmatic zircon. These data yield a weighted mean $^{206}Pb/^{238}U$ age of 121.3 ± 1.2 Ma (MSWD = 3.2), representing the formation age of the granite. A total of 29 valid data were obtained from ZZ07. These zircon grains have moderate and variable

TABLE 1 | Zircon U-Pb data of granites in the study area.

Spot	Element content			Isotope ratio						Age (Ma)					
	^{232}Th	^{238}U	Th/U	$^{207}Pb/^{206}Pb$	1sigma	$^{207}Pb/^{235}U$	1sigma	$^{206}Pb/^{238}U$	1sigma	$^{207}Pb/^{206}Pb$	1sigma	$^{207}Pb/^{235}U$	1sigma	$^{206}Pb/^{238}U$	1sigma
GA02-01	200	175	1.14	0.0537	0.0042	0.1365	0.0095	0.0186	0.0004	366.72	177.76	129.95	8.46	118.81	2.23
GA02-02	131	150	0.87	0.0528	0.0049	0.1334	0.0106	0.0188	0.0004	320.43	212.94	127.11	9.49	120.27	2.29
GA02-03	114	142	0.80	0.0530	0.0047	0.1313	0.0105	0.0182	0.0004	327.84	197.20	125.29	9.44	116.08	2.33
GA02-04	114	134	0.85	0.0494	0.0053	0.1269	0.0125	0.0187	0.0003	164.90	301.81	121.30	11.23	119.25	2.17
GA02-07	147	170	0.86	0.0521	0.0052	0.1271	0.0110	0.0182	0.0004	300.06	223.12	121.51	9.94	116.25	2.30
GA02-08	112	124	0.90	0.0465	0.0045	0.1144	0.0092	0.0181	0.0004	20.47	218.49	109.96	8.39	115.86	2.61
GA02-10	370	318	1.16	0.0467	0.0032	0.1182	0.0071	0.0183	0.0003	31.58	155.54	113.40	6.45	116.81	1.81
GA02-11	128	149	0.86	0.0476	0.0048	0.1126	0.0083	0.0179	0.0004	76.02	225.89	108.33	7.53	114.63	2.29
GA02-12	125	138	0.91	0.0491	0.0039	0.1237	0.0076	0.0185	0.0004	153.79	174.05	118.47	6.83	118.41	2.76
GA02-13	164	183	0.90	0.0513	0.0044	0.1271	0.0084	0.0184	0.0004	253.77	199.98	121.49	7.59	117.54	2.44
GA02-14	119	135	0.88	0.0515	0.0050	0.1316	0.0115	0.0188	0.0004	261.18	225.90	125.50	10.33	119.89	2.51
GA02-15	121	143	0.84	0.0492	0.0043	0.1254	0.0095	0.0186	0.0004	166.75	187.01	119.93	8.61	118.66	2.46
GA02-16	142	157	0.90	0.0486	0.0041	0.1228	0.0086	0.0185	0.0004	127.87	188.86	117.58	7.80	118.29	2.31
GA02-17	164	172	0.96	0.0520	0.0042	0.1280	0.0082	0.0185	0.0004	283.40	185.16	122.33	7.39	118.47	2.39
GA02-18	106	125	0.85	0.0465	0.0048	0.1162	0.0099	0.0186	0.0004	33.43	224.04	111.59	9.02	118.91	2.36
GA02-19	108	128	0.85	0.0475	0.0045	0.1144	0.0092	0.0179	0.0004	76.02	211.08	109.99	8.35	114.62	2.44
GA02-20	225	226	0.99	0.0480	0.0041	0.1188	0.0088	0.0184	0.0003	98.24	201.82	114.02	8.00	117.53	2.18
GA02-22	144	159	0.90	0.0545	0.0048	0.1380	0.0099	0.0188	0.0004	394.50	202.75	131.25	8.79	119.92	2.65
GA02-23	219	225	0.98	0.0526	0.0040	0.1296	0.0086	0.0184	0.0004	309.32	174.05	123.74	7.73	117.63	2.50
GA02-24	134	148	0.90	0.0482	0.0045	0.1223	0.0096	0.0187	0.0004	109.35	207.38	117.15	8.70	119.21	2.42
GA02-25	146	161	0.91	0.0467	0.0043	0.1160	0.0094	0.0183	0.0004	35.28	207.38	111.39	8.56	116.70	2.30
GA02-26	118	132	0.89	0.0481	0.0056	0.1165	0.0110	0.0185	0.0005	105.65	261.08	111.88	10.03	118.35	2.92
GA02-27	191	204	0.94	0.0527	0.0044	0.1299	0.0090	0.0185	0.0004	322.28	186.09	124.02	8.13	117.97	2.29
GA02-28	102	126	0.81	0.0532	0.0056	0.1314	0.0121	0.0187	0.0004	344.50	243.49	125.34	10.89	119.43	2.54
GA02-29	139	157	0.88	0.0523	0.0042	0.1322	0.0092	0.0187	0.0004	298.21	183.31	126.04	8.22	119.65	2.53
GA02-30	181	182	0.99	0.0514	0.0043	0.1288	0.0093	0.0187	0.0003	257.47	190.72	123.04	8.40	119.45	2.21
QQ02-02	246	439	0.56	0.0467	0.0028	0.1122	0.0063	0.0177	0.0003	35.28	137.03	107.98	5.77	113.18	1.76
QQ02-03	261	552	0.47	0.0505	0.0028	0.1249	0.0071	0.0179	0.0002	216.74	129.61	119.54	6.39	114.57	1.51
QQ02-04	261	501	0.52	0.0469	0.0025	0.1146	0.0058	0.0180	0.0003	42.69	122.21	110.18	5.31	114.70	1.68
QQ02-05	291	495	0.59	0.0465	0.0025	0.1099	0.0057	0.0173	0.0002	33.43	112.95	105.87	5.23	110.46	1.46
QQ02-06	210	388	0.54	0.0485	0.0031	0.1186	0.0075	0.0177	0.0003	124.16	140.72	113.76	6.81	113.13	1.84
QQ02-07	317	530	0.60	0.0465	0.0024	0.1137	0.0054	0.0179	0.0003	33.43	112.95	109.37	4.96	114.10	1.65
QQ02-08	251	433	0.58	0.0472	0.0031	0.1124	0.0067	0.0176	0.0003	61.21	148.13	108.20	6.10	112.40	1.90
QQ02-09	265	532	0.50	0.0461	0.0025	0.1094	0.0056	0.0172	0.0003	400.05	272.19	105.40	5.15	109.75	1.68
QQ02-10	176	469	0.38	0.0503	0.0026	0.1256	0.0064	0.0182	0.0003	209.33	120.35	120.11	5.75	116.29	2.11
QQ02-11	254	386	0.66	0.0481	0.0031	0.1166	0.0064	0.0179	0.0003	105.65	148.13	111.97	5.82	114.61	1.97
QQ02-12	236	542	0.44	0.0470	0.0023	0.1154	0.0053	0.0179	0.0002	55.65	105.55	110.92	4.80	114.54	1.58
QQ02-13	373	516	0.72	0.0495	0.0025	0.1206	0.0058	0.0178	0.0003	172.31	118.50	115.62	5.23	113.68	1.71
QQ02-14	250	530	0.47	0.0467	0.0028	0.1106	0.0064	0.0173	0.0003	35.28	140.73	106.50	5.88	110.62	1.59
QQ02-15	233	506	0.46	0.0480	0.0026	0.1189	0.0060	0.0181	0.0003	98.24	122.20	114.06	5.41	115.87	1.65
QQ02-16	151	310	0.49	0.0480	0.0035	0.1139	0.0067	0.0173	0.0003	101.94	159.24	109.52	6.12	110.31	1.65
QQ02-17	153	363	0.42	0.0491	0.0030	0.1244	0.0074	0.0181	0.0003	153.79	56.48	119.04	6.72	115.67	1.63
QQ02-18	167	455	0.37	0.0515	0.0030	0.1258	0.0069	0.0177	0.0002	264.88	135.17	120.35	6.23	113.39	1.53
QQ02-19	168	297	0.57	0.0532	0.0041	0.1220	0.0078	0.0171	0.0004	338.95	175.90	116.92	7.06	109.09	2.33
QQ02-20	208	294	0.71	0.0467	0.0032	0.1158	0.0073	0.0178	0.0003	35.28	155.54	111.29	6.61	114.03	1.87
QQ02-21	146	367	0.40	0.0505	0.0034	0.1206	0.0075	0.0175	0.0003	216.74	155.54	115.62	6.82	111.66	1.73
QQ02-22	225	289	0.78	0.0466	0.0032	0.1098	0.0073	0.0171	0.0003	27.88	155.54	105.82	6.72	109.31	1.81
QQ02-23	268	419	0.64	0.0525	0.0040	0.1311	0.0074	0.0179	0.0003	305.62	176.83	125.11	6.63	114.43	1.85
QQ02-25	192	395	0.49	0.0539	0.0032	0.1332	0.0075	0.0180	0.0003	364.87	130.54	127.01	6.73	114.97	1.65
QQ02-26	189	368	0.51	0.0473	0.0032	0.1120	0.0072	0.0173	0.0003	64.91	151.83	107.76	6.54	110.54	1.78
QQ02-27	281	574	0.49	0.0500	0.0030	0.1238	0.0073	0.0180	0.0002	194.53	136.09	118.54	6.61	114.89	1.43
QQ02-28	517	606	0.85	0.0472	0.0027	0.1149	0.0066	0.0177	0.0002	61.21	129.62	110.42	5.98	113.30	1.58
QQ02-29	127	287	0.44	0.0481	0.0035	0.1133	0.0077	0.0173	0.0003	105.65	166.64	109.01	6.98	110.62	2.11
QQ02-30	152	351	0.43	0.0476	0.0036	0.1115	0.0081	0.0171	0.0003	79.72	170.35	107.34	7.41	109.16	1.78
ZZ02-01	108	154	0.70	0.0546	0.0050	0.1361	0.0105	0.0186	0.0003	394.50	205.53	129.56	9.35	118.98	2.08
ZZ02-02	418	846	0.49	0.0522	0.0025	0.1402	0.0065	0.0195	0.0002	300.06	104.62	133.21	5.80	124.45	1.34
ZZ02-03	429	888	0.48	0.0528	0.0021	0.1357	0.0052	0.0186	0.0002	320.43	88.88	129.23	4.62	118.52	1.22
ZZ02-04	123	216	0.57	0.0527	0.0031	0.1433	0.0083	0.0198	0.0003	316.73	139.80	135.99	7.34	126.17	2.19
ZZ02-05	209	336	0.62	0.0484	0.0030	0.1257	0.0069	0.0189	0.0003	120.46	140.72	120.19	6.20	120.55	1.72
ZZ02-07	206	373	0.55	0.0511	0.0027	0.1405	0.0075	0.0198	0.0002	242.66	122.21	133.51	6.65	126.43	1.57

(Continued on following page)

TABLE 1 | (*Continued*) Zircon U-Pb data of granites in the study area.

Spot	Element content			Isotope ratio						Age (Ma)					
	^{232}Th	^{238}U	Th/U	^{207}Pb/^{206}Pb	1sigma	^{207}Pb/^{235}U	1sigma	^{206}Pb/^{238}U	1sigma	^{207}Pb/^{206}Pb	1sigma	^{207}Pb/^{235}U	1sigma	^{206}Pb/^{238}U	1sigma
ZZ02-08	204	207	0.99	0.0499	0.0042	0.1330	0.0102	0.0198	0.0004	187.12	188.86	126.75	9.13	126.56	2.28
ZZ02-09	135	185	0.73	0.0507	0.0036	0.1308	0.0079	0.0191	0.0004	233.40	164.79	124.80	7.07	121.82	2.24
ZZ02-13	136	247	0.55	0.0497	0.0033	0.1266	0.0073	0.0188	0.0003	188.97	153.68	121.08	6.61	120.23	1.79
ZZ02-14	535	1090	0.49	0.0474	0.0051	0.1208	0.0131	0.0186	0.0002	77.87	231.45	115.76	11.85	118.49	1.15
ZZ02-15	426	933	0.46	0.0513	0.0024	0.1406	0.0057	0.0199	0.0002	253.77	112.02	133.57	5.03	126.74	1.36
ZZ02-16	512	786	0.65	0.0480	0.0020	0.1244	0.0051	0.0189	0.0002	98.24	96.29	119.01	4.58	120.42	1.25
ZZ02-17	263	673	0.39	0.0520	0.0033	0.1354	0.0061	0.0189	0.0002	287.10	116.65	128.94	5.44	120.84	1.57
ZZ02-18	110	163	0.68	0.0535	0.0044	0.1321	0.0088	0.0188	0.0004	350.06	187.01	126.02	7.93	119.89	2.37
ZZ02-19	148	283	0.52	0.0505	0.0033	0.1384	0.0085	0.0197	0.0003	220.44	151.83	131.64	7.59	125.86	1.66
ZZ02-20	189	311	0.61	0.0492	0.0031	0.1288	0.0079	0.0190	0.0003	166.75	146.28	123.00	7.12	121.13	1.71
ZZ02-21	179	218	0.82	0.0479	0.0037	0.1213	0.0079	0.0184	0.0003	94.54	238.86	116.27	7.13	117.85	1.91
ZZ02-22	176	278	0.63	0.0504	0.0032	0.1307	0.0070	0.0192	0.0003	213.04	144.43	124.77	6.30	122.89	1.86
ZZ02-23	237	416	0.57	0.0534	0.0034	0.1380	0.0071	0.0189	0.0003	342.65	142.57	131.23	6.37	120.42	2.06
ZZ02-24	504	1001	0.50	0.0535	0.0017	0.1384	0.0043	0.0188	0.0002	350.06	78.70	131.62	3.88	119.78	1.13
ZZ02-26	201	223	0.90	0.0527	0.0045	0.1375	0.0096	0.0189	0.0003	316.73	196.27	130.79	8.61	120.86	2.19
ZZ02-27	183	604	0.30	0.0497	0.0024	0.1271	0.0051	0.0187	0.0002	188.97	119.43	121.52	4.58	119.21	1.54
ZZ02-28	125	184	0.68	0.0480	0.0036	0.1197	0.0071	0.0186	0.0004	101.94	231.45	114.78	6.40	118.78	2.25
ZZ02-29	255	261	0.98	0.0509	0.0036	0.1258	0.0070	0.0184	0.0003	235.25	164.79	120.28	6.31	117.50	2.01
ZZ02-30	248	720	0.34	0.0526	0.0020	0.1372	0.0047	0.0189	0.0002	309.32	88.88	130.57	4.24	120.59	1.30
ZZ07-01	74.8	156	0.48	0.0519	0.0046	0.1521	0.0121	0.0222	0.0005	283.40	203.68	143.79	10.62	141.40	2.91
ZZ07-02	165	272	0.61	0.0463	0.0032	0.1384	0.0090	0.0215	0.0003	13.06	159.25	131.61	8.05	137.29	2.06
ZZ07-03	99.4	234	0.43	0.0461	0.0035	0.1399	0.0102	0.0219	0.0004	400.05	224.04	132.97	9.08	139.37	2.24
ZZ07-04	137	232	0.59	0.0463	0.0032	0.1390	0.0092	0.0217	0.0004	13.06	159.25	132.12	8.21	138.51	2.30
ZZ07-05	219	355	0.62	0.0524	0.0039	0.1530	0.0104	0.0214	0.0003	301.91	168.50	144.54	9.18	136.21	1.76
ZZ07-05	219	355	0.62	0.0524	0.0039	0.1530	0.0104	0.0214	0.0003	301.91	168.50	144.54	9.18	136.21	1.76
ZZ07-06	118	201	0.59	0.0526	0.0045	0.1486	0.0102	0.0214	0.0004	322.28	196.27	140.72	9.06	136.44	2.42
ZZ07-07	178	361	0.49	0.0478	0.0025	0.1445	0.0077	0.0218	0.0003	87.13	118.50	137.07	6.80	138.94	1.88
ZZ07-08	50.5	93.8	0.54	0.0480	0.0058	0.1314	0.0119	0.0211	0.0005	98.24	262.93	125.33	10.65	134.59	2.91
ZZ07-10	118	324	0.36	0.0464	0.0031	0.1351	0.0081	0.0214	0.0003	20.47	155.54	128.69	7.23	136.61	1.97
ZZ07-11	145	201	0.72	0.0491	0.0037	0.1481	0.0097	0.0225	0.0005	150.09	170.35	140.23	8.60	143.69	3.15
ZZ07-12	318	609	0.52	0.0464	0.0022	0.1424	0.0062	0.0225	0.0003	16.77	111.10	135.20	5.55	143.25	1.81
ZZ07-13	166	419	0.40	0.0526	0.0027	0.1576	0.0078	0.0217	0.0003	309.32	114.80	148.62	6.86	138.26	1.82
ZZ07-14	113	244	0.46	0.0480	0.0038	0.1414	0.0098	0.0217	0.0004	98.24	177.75	134.27	8.70	138.61	2.37
ZZ07-15	182	323	0.56	0.0525	0.0033	0.1542	0.0091	0.0216	0.0003	309.32	144.43	145.62	8.05	137.93	2.17
ZZ07-16	242	367	0.66	0.0511	0.0031	0.1514	0.0085	0.0217	0.0003	242.66	138.87	143.15	7.53	138.34	2.06
ZZ07-17	88.5	209	0.42	0.0534	0.0051	0.1563	0.0125	0.0220	0.0004	346.35	212.01	147.42	11.01	140.11	2.70
ZZ07-18	90.7	178	0.51	0.0505	0.0039	0.1481	0.0100	0.0217	0.0004	216.74	176.83	140.24	8.83	138.40	2.84
ZZ07-19	446	865	0.52	0.0481	0.0024	0.1469	0.0071	0.0220	0.0003	105.65	111.10	139.14	6.30	140.17	1.69
ZZ07-20	228	325	0.70	0.0542	0.0038	0.1543	0.0103	0.0210	0.0004	388.94	159.24	145.74	9.05	134.03	2.38
ZZ07-21	82.3	179	0.46	0.0500	0.0037	0.1538	0.0104	0.0224	0.0004	194.53	176.83	145.25	9.17	143.03	2.43
ZZ07-22	76.1	159	0.48	0.0510	0.0042	0.1441	0.0101	0.0212	0.0004	242.66	197.20	136.72	8.95	135.37	2.72
ZZ07-23	133	269	0.49	0.0510	0.0038	0.1453	0.0101	0.0208	0.0003	238.96	204.61	137.76	8.93	132.85	2.02
ZZ07-24	99.6	224	0.45	0.0546	0.0038	0.1565	0.0086	0.0213	0.0004	398.20	155.54	147.66	7.59	136.01	2.61
ZZ07-26	245	428	0.57	0.0528	0.0031	0.1599	0.0093	0.0221	0.0003	320.43	130.54	150.58	8.17	140.97	2.15
ZZ07-27	78.9	175	0.45	0.0492	0.0045	0.1419	0.0111	0.0211	0.0004	166.75	199.97	134.72	9.91	134.88	2.39
ZZ07-28	209	623	0.34	0.0470	0.0021	0.1448	0.0065	0.0223	0.0003	50.10	99.99	137.31	5.76	141.91	2.00
ZZ07-29	65.8	149	0.44	0.0478	0.0044	0.1384	0.0106	0.0217	0.0005	100.09	199.97	131.64	9.42	138.37	2.95
ZZ07-30	90.9	168	0.54	0.0535	0.0043	0.1626	0.0118	0.0223	0.0004	350.06	178.68	152.95	10.30	142.34	2.78
ZZ11-01	144	94.5	1.53	0.0469	0.0065	0.0919	0.0101	0.0150	0.0004	55.65	294.41	89.24	9.38	95.68	2.50
ZZ11-02	837	1124	0.75	0.0482	0.0020	0.1014	0.0043	0.0151	0.0002	109.35	98.14	98.03	3.93	96.73	1.22
ZZ11-03	105	104	1.01	0.0540	0.0074	0.1019	0.0094	0.0147	0.0005	372.28	311.07	98.48	8.69	93.92	2.95
ZZ11-04	268	352	0.76	0.0499	0.0032	0.1007	0.0058	0.0145	0.0002	190.82	148.13	97.39	5.40	92.83	1.45
ZZ11-05	343	407	0.84	0.0507	0.0030	0.1017	0.0058	0.0144	0.0002	227.85	141.65	98.31	5.33	92.46	1.18
ZZ11-06	480	532	0.90	0.0493	0.0029	0.0998	0.0054	0.0146	0.0002	166.75	143.50	96.59	4.98	93.53	1.27
ZZ11-07	58.7	61.0	0.96	0.0546	0.0083	0.0993	0.0110	0.0146	0.0005	394.50	344.40	96.11	10.16	93.41	3.25
ZZ11-08	178	228	0.78	0.0518	0.0045	0.1025	0.0072	0.0146	0.0003	275.99	201.83	99.10	6.59	93.55	1.71
ZZ11-10	187	290	0.65	0.0471	0.0041	0.0954	0.0074	0.0150	0.0003	53.80	196.27	92.49	6.86	95.78	1.63
ZZ11-11	169	266	0.63	0.0499	0.0043	0.1003	0.0075	0.0149	0.0003	190.82	198.12	97.03	6.95	95.51	1.95
ZZ11-12	281	308	0.91	0.0529	0.0031	0.1099	0.0063	0.0150	0.0003	324.13	135.17	105.86	5.74	95.81	1.75
ZZ11-13	187	222	0.84	0.0501	0.0044	0.1034	0.0084	0.0152	0.0003	198.23	192.56	99.95	7.69	97.31	1.97

(Continued on following page)

TABLE 1 | (*Continued*) Zircon U-Pb data of granites in the study area.

Spot	Element content			Isotope ratio						Age (Ma)					
	^{232}Th	^{238}U	Th/U	$^{207}Pb/^{206}Pb$	1sigma	$^{207}Pb/^{235}U$	1sigma	$^{206}Pb/^{238}U$	1sigma	$^{207}Pb/^{206}Pb$	1sigma	$^{207}Pb/^{235}U$	1sigma	$^{206}Pb/^{238}U$	1sigma
ZZ11-14	406	378	1.07	0.0501	0.0038	0.1021	0.0069	0.0149	0.0002	198.23	175.91	98.68	6.33	95.39	1.45
ZZ11-18	436	422	1.03	0.0483	0.0028	0.1003	0.0055	0.0152	0.0002	122.31	133.31	97.09	5.11	97.01	1.51
ZZ11-19	306	368	0.83	0.0517	0.0033	0.1018	0.0056	0.0145	0.0002	272.29	146.28	98.48	5.13	92.67	1.35
ZZ11-20	211	199	1.06	0.0490	0.0043	0.0976	0.0061	0.0149	0.0003	146.38	192.57	94.60	5.68	95.46	1.87
ZZ11-21	180	179	1.01	0.0542	0.0051	0.1038	0.0074	0.0145	0.0003	375.98	212.94	100.25	6.82	92.92	1.90
ZZ11-22	204	277	0.74	0.0522	0.0040	0.1051	0.0070	0.0150	0.0003	294.51	169.42	101.50	6.45	95.88	1.75
ZZ11-23	212	308	0.69	0.0482	0.0033	0.0988	0.0061	0.0150	0.0002	109.35	151.83	95.62	5.60	96.23	1.56
ZZ11-24	152	140	1.09	0.0563	0.0065	0.1051	0.0091	0.0145	0.0003	464.86	259.22	101.50	8.39	92.76	2.20
ZZ11-26	179	187	0.96	0.0463	0.0040	0.0918	0.0062	0.0147	0.0003	13.06	196.27	89.20	5.79	94.08	1.90
ZZ11-27	149	239	0.62	0.0503	0.0035	0.1054	0.0065	0.0152	0.0003	209.33	161.09	101.71	5.95	97.12	1.77
ZZ11-28	152	218	0.70	0.0504	0.0043	0.0966	0.0068	0.0145	0.0003	213.04	0.92	93.66	6.31	92.71	1.61
ZZ11-29	253	374	0.68	0.0510	0.0038	0.1020	0.0067	0.0148	0.0003	238.96	204.61	98.66	6.17	94.69	1.82
ZZ11-30	222	333	0.67	0.0492	0.0041	0.0978	0.0069	0.0149	0.0002	166.75	172.20	94.71	6.35	95.25	1.50
HZ05-01	128	186	0.69	0.0475	0.0041	0.1323	0.0104	0.0204	0.0004	76.02	257.37	126.12	9.29	130.46	2.45
HZ05-02	114	146	0.78	0.0522	0.0048	0.1477	0.0112	0.0205	0.0004	294.51	213.86	139.85	9.89	130.66	2.82
HZ05-03	534	913	0.59	0.0526	0.0019	0.1558	0.0056	0.0214	0.0002	322.28	80.55	147.01	4.90	136.72	1.56
HZ05-04	227	548	0.41	0.0540	0.0032	0.1574	0.0075	0.0211	0.0003	368.57	133.32	148.40	6.56	134.69	1.75
HZ05-05	159	306	0.52	0.0505	0.0036	0.1474	0.0096	0.0213	0.0003	220.44	160.17	139.61	8.46	135.68	2.06
HZ05-06	205	246	0.83	0.0536	0.0045	0.1513	0.0108	0.0209	0.0004	366.72	216.64	143.06	9.49	133.53	2.53
HZ05-07	159	347	0.46	0.0493	0.0033	0.1435	0.0087	0.0214	0.0004	164.90	157.38	136.17	7.71	136.80	2.28
HZ05-08	107	260	0.41	0.0514	0.0047	0.1519	0.0114	0.0220	0.0004	257.47	209.24	143.57	10.08	140.06	2.69
HZ05-09	65.9	88.3	0.75	0.0501	0.0068	0.1340	0.0110	0.0219	0.0006	198.23	288.85	127.69	9.82	139.58	3.94
HZ05-10	152	243	0.62	0.0493	0.0038	0.1392	0.0097	0.0208	0.0004	161.20	183.31	132.35	8.63	132.47	2.62
HZ05-11	328	732	0.45	0.0505	0.0024	0.1448	0.0067	0.0208	0.0003	216.74	111.10	137.29	5.93	132.80	1.65
HZ05-12	125	217	0.58	0.0461	0.0036	0.1267	0.0092	0.0204	0.0004	400.05	211.08	121.12	8.28	130.49	2.48
HZ05-13	228	582	0.39	0.0484	0.0024	0.1384	0.0066	0.0207	0.0003	120.46	86.10	131.61	5.89	132.15	1.59
HZ05-14	108	243	0.45	0.0526	0.0035	0.1510	0.0092	0.0209	0.0004	322.28	151.83	142.79	8.16	133.36	2.32
HZ05-15	158	202	0.78	0.0483	0.0043	0.1348	0.0100	0.0209	0.0005	122.31	199.97	128.42	8.96	133.37	2.85
HZ05-16	195	390	0.50	0.0486	0.0029	0.1408	0.0085	0.0208	0.0003	127.87	137.02	133.75	7.55	132.97	1.90
HZ05-17	245	594	0.41	0.0512	0.0032	0.1535	0.0086	0.0221	0.0003	250.07	144.43	144.96	7.56	140.60	1.95
HZ05-18	157	259	0.61	0.0538	0.0042	0.1498	0.0113	0.0204	0.0004	364.87	177.76	141.74	9.94	130.37	2.43
HZ05-19	114	303	0.38	0.0530	0.0036	0.1461	0.0090	0.0204	0.0003	327.84	153.68	138.49	7.99	130.10	2.06
HZ05-20	102	167	0.61	0.0553	0.0053	0.1483	0.0107	0.0205	0.0005	433.38	219.41	140.44	9.45	130.83	2.90
HZ05-21	448	570	0.79	0.0495	0.0026	0.1512	0.0077	0.0222	0.0003	172.31	115.73	142.94	6.79	141.37	1.85
HZ05-22	140	260	0.54	0.0486	0.0030	0.1483	0.0083	0.0220	0.0004	127.87	137.02	140.41	7.31	140.18	2.42
HZ05-23	154	308	0.50	0.0512	0.0032	0.1506	0.0081	0.0219	0.0004	250.07	142.58	142.43	7.16	139.94	2.48
HZ05-24	139	282	0.49	0.0517	0.0035	0.1483	0.0089	0.0214	0.0003	272.29	149.06	140.37	7.89	136.21	2.08
HZ05-25	56.2	90.4	0.62	0.0534	0.0057	0.1544	0.0133	0.0212	0.0005	342.65	244.42	145.80	11.66	135.52	3.46
HZ05-26	174	176	0.99	0.0552	0.0040	0.1582	0.0092	0.0214	0.0004	420.42	160.17	149.16	8.04	136.71	2.54
HZ05-27	105	201	0.53	0.0513	0.0035	0.1544	0.0091	0.0218	0.0004	253.77	183.31	145.77	7.99	138.92	2.36
HZ05-28	127	214	0.60	0.0512	0.0037	0.1446	0.0092	0.0209	0.0004	255.62	164.79	137.15	8.20	133.20	2.43
HZ05-29	129	386	0.33	0.0520	0.0032	0.1525	0.0092	0.0214	0.0003	283.40	110.17	144.12	8.13	136.59	1.93
HZ05-30	97.9	184	0.53	0.0490	0.0038	0.1425	0.0088	0.0214	0.0004	150.09	174.05	135.27	7.82	136.71	2.40

concentrations of Th (50.5–318 ppm) and U (149–865 ppm), corresponding Th/U ratios of 0.34–0.72, showing the characteristic of magmatic zircon. These data yield a weighted mean $^{206}Pb/^{238}U$ age of 138.4 ± 1.1 Ma (MSWD = 1.6), representing the formation age of the granite. A total of 25 valid data were obtained from ZZ11. These zircon grains have moderate and variable concentrations of Th (58.7–837 ppm) and U (61–1,124 ppm), corresponding Th/U ratios of 0.62–1.53, showing the characteristic of magmatic zircon. These data yield a weighted mean $^{206}Pb/^{238}U$ age of 94.7 ± 0.25 Ma (MSWD = 1.01), representing the formation age of the granite. A total of 30 valid data were obtained from HZ05. These zircon grains have moderate and variable concentrations of Th (56.2–448 ppm) and U (88.3–548 ppm), corresponding Th/U ratios of 0.33–0.99, showing the characteristic of magmatic zircon. These data yield a weighted mean $^{206}Pb/^{238}U$ age of 135.1 ± 1.3 Ma (MSWD = 2.4), representing the formation age of the granite.

There is no obvious pattern of age distribution of such samples in the region. In general, the age of all samples in the study area shows that they are formed in Cretaceous age, indicating that Yanshanian tectonic thermal events are the dominant thermal events in the area. According to the U-Pb dating results, at least three acidic magmatic events occurred during Cretaceous: early stage of Early Cretaceous (about 138–135.1 Ma), late stage of Early Cretaceous (110–121 Ma) and the early stage of Late Cretaceous (about 93–96 Ma).

Geochemistry

20 fresh granite samples are obtained for major and trace element analyses. The results are listed in **Table 2**. The samples have very low loss on ignition (~0.85 wt%), indicating little or no modification by weathering. Rock geochemical test results show that the rock mass geochemical composition analyses are as follows: SiO_2 content ranged from 65.86 to 83.83% with an average of 73.64%; TiO_2 content ranged from 0.08 to 0.55% with an average of 0.23%; Al_2O_3 content ranged from 7.38 to 15.8% with an average of 13.53%; MgO content ranged from 0.12 to 1.73% with an average of 0.48%; and (K_2O + Na_2O) content ranged from 4.76 to 8.87% with an average of 7.66%, belonging to high-K calc-alkaline series. The granites are characterized by weakly peraluminous (A/CNK = 1.03). At the diagram of SiO_2 (Na_2O + K_2O) (**Figure 7**), sample dots fell within the granite region. The aluminum saturation index (A/CNK) ranges from 0.88 to 1.33 and ranges mainly from 1.0 to 1.1 on the diagram of A/NK–A/CNK (**Figure 7**).

On the primitive mantle normalized trace element spider diagram (**Figure 8**), Large ionic Lithophile Elements (LILE) such as K and Rb, Th, and U are enriched, and there is a strong loss of Ba, Sr, and High Field Strong Elements (HFSE) such as Nb, Ti, Ta, and P, which are similar to the geochemical characteristics of rocks in the subduction zone (Kelemen et al., 2003). On the Chondrite Normalized REE distribution diagram (**Figure 8**), the pattern is smooth and show light rare Earth element (LREE) concentration and heavy rare Earth element (HREE) losses. Eu in the pattern shows negative anomaly, indicating that the magma evolution of plagioclase crystallization separation. The value of ΣREE is between 50.50 $\times 10^{-6}$–401.02 $\times 10^{-6}$, with a mean of 183.31 $\times 10^{-6}$. The value of LREE/HREE is 0.84–12.46, with an average of 6.44, showing that obvious fractionation between light and heavy rare Earth. The value of $(La/Yb)_N$ is 0.67–19.24, while the average value is 7.18. The value of Eu is between 0.03 and 0.71, and the average value is 0.32. In primitive mantle normalized trace element spider diagram, most of the sample elements distribution features are similar, indicating that most of the samples have the same or similar formation patterns.

DISCUSSION

Genetic Mechanism of Yanshannian Granite

Large-scale Yanshanian granites constitute the main part of southeastern China, and were formed related to the subduction of the Pacific plate, large-scale basaltic magma invasion, crust-mantle mixing, and extensive melting of crustal rocks (Liu et al., 2016; Pan et al., 2017). Meanwhile, other researchers have proposed the relationship between the lithospheric thinning in eastern China and the subduction of the Pacific plate (Wang and Shen, 2003; Wu et al., 2007). Li et al. (2017) discussed the starting time of palaeo-Pacific subduction. Through the study of Mesozoic tectonic transition and transformation in South China, they found that the palaeo-Pacific plate subduction had already started in the Late Triassic. It is considered that the crustal thickness of the South China Block gradually thinning from west to east is caused by two crustal mantle interactions, which resulted in two lithospheric delamination and subsidence, and both of them are related to the subduction of the palaeo-Pacific Plate, which were caused by plate tearing, subduction retraction and high Angle subduction respectively.

According to the results of this paper, at least three acidic magmatic events occurred during Cretaceous: early stage of Early Cretaceous (about 138–135.1 Ma), late stage of Early Cretaceous (about 112–121 Ma) and the early stage of Late Cretaceous (about 93–96 Ma).

The age of the granite sample (ZZ07) in Zhangzhou area and the granite sample (HZ05) in the south of Huangshadong geothermal field in Huizhou are 138.4 ± 1.1 Ma and 135.1 ± 1.3 Ma, indicating that the granite body is the product of magmatic activity in the early stage of early Cretaceous. At the diagram of SiO_2/(Na_2O + K_2O) (**Figure 7A**), sample dots fell within the granite region. The granites are characterized by weakly peraluminous (A/CNK = 1.02–1.08) (**Figure 7B**). The aluminum saturation index (A/CNK) ranges from 1.14 to 1.33. On the SiO_2 – FeO_T/(FeO_T + MgO) and SiO_2 – Al_2O_3 diagram (**Figures 9A,B**), most samples are plotted in the POG (post-Orogenic Grabite) zone (Frost et al., 2001). On the Nb-Y and (Y + Nb)–Rb diagram (**Figures 9C,D**), samples are plotted within the scope of the volcanic island arc granite (VAG), within plate granite (WPG) and sys-collision granite (syn-COLG). Combined with the trace element characteristics of the samples, it can be inferred that the samples have dual characteristics of volcanic arc and within plate environment. The ages of the granite rock (GA02, QQ02) and the granite rock (ZZ02) around the Fuzhou geothermal field and Zhangzhou geothermal field are 117.9 ± 0.47 Ma, 112.9 ± 0.85 Ma and 121.3 ± 1.2 Ma, respectively, which are the products of magmatic activity in the late Early Cretaceous. It is the product of the same magmatism as most of the granites along the Fujian coast area in Fujian Province. At the diagram of SiO_2/(Na_2O + K_2O), sample dots fell within the granodiorite region (**Figure 7A**). They are characterized by Metaluminous - peraluminous (A/CNK = 0.95–1.05) (**Figure 7B**). The aluminum saturation index (A/CNK) ranges from 1.42 to 1.68. On the SiO_2 – FeO_T/(FeO_T + MgO) and SiO_2 – Al_2O_3 diagram (**Figures 9A,B**), most samples are plotted out of the POG (post-Orogenic Grabite) zone (Frost et al., 2001). On the Nb-Y and (Y + Nb) – Rb diagram (**Figures 9C,D**), samples are plotted within the scope of the volcanic island arc granite (VAG), indicating rocks in this periods are mainly influenced by subduction related environment. The age of the sample granite rock mass (Z11) in coastal Zhangzhou is 94.7 ± 0.65 Ma, which is similar to the age of the rock mass (93 Ma, 95 Ma) in the south of Fuzhou geothermal field. It is the product of magmatic activity in the early stage of Late Cretaceous. At the diagram of SiO_2/(Na_2O + K_2O), sample dots fell within the granite region (**Figure 7A**). They are characterized by also weakly peraluminous (A/CNK = 1.03–1.34) (**Figure 7B**). The aluminum saturation index (A/CNK) ranges from 1.06 to 1.38. On the SiO_2 – FeO_T/(FeO_T + MgO) and SiO_2 – Al_2O_3 diagram (**Figures 9A,B**), most samples are plotted in the POG (post-Orogenic Grabite) zone (Frost et al., 2001). On the Nb-Y and

TABLE 2 | Analytical data of major (%) and trace element(ppm) of granites in the study area.

Sample	GA02	GA05	GM01	GM02	QQ02	ZZ01	ZZ02	ZZ03	ZZ04	ZZ07	ZZ09	ZZ11	ZZ12	ZZ13	ZZ14	ZZ15	ZZ17	HZ05	HZ06	HZ18
SiO2	66.74	65.86	73.18	74.69	75.27	68.43	69.24	69.89	69.62	73.05	83.83	73.59	77.34	75.35	76.67	75.66	76.34	75.50	75.03	77.56
TiO2	0.51	0.55	0.26	0.24	0.14	0.39	0.35	0.31	0.35	0.13	0.08	0.31	0.08	0.12	0.11	0.13	0.17	0.11	0.11	0.09
Al2O3	15.16	15.25	14.68	13.65	13.41	15.80	15.21	14.49	14.65	13.70	7.38	13.71	12.83	13.28	12.45	13.58	12.71	12.93	13.37	12.60
Fe2O3T	4.26	4.80	1.60	1.63	1.54	3.06	2.62	2.61	2.72	1.66	0.47	2.05	0.58	0.81	0.79	0.95	1.05	1.57	1.36	0.67
FeOT	3.83	4.32	1.44	1.47	1.39	2.75	2.36	2.34	2.45	1.50	0.43	1.84	0.52	0.73	0.71	0.85	0.95	1.42	1.22	0.60
MnO	0.11	0.11	0.07	0.06	0.04	0.05	0.07	0.09	0.08	0.04	0.03	0.09	0.07	0.05	0.04	0.09	0.04	0.04	0.03	0.03
MgO	1.52	1.73	0.44	0.37	0.22	0.92	0.77	0.79	0.85	0.15	0.21	0.51	0.06	0.15	0.15	0.17	0.20	0.14	0.19	0.12
CaO	3.84	3.92	1.53	1.07	1.17	3.35	2.86	2.06	2.66	1.08	1.75	0.88	0.28	0.70	0.66	0.89	0.79	0.76	0.79	0.13
Na2O	3.48	3.46	3.96	3.69	4.17	3.49	3.21	3.20	3.19	3.20	2.52	3.57	4.52	3.29	3.20	3.99	3.53	3.74	3.75	2.09
K2O	3.05	3.21	4.17	4.29	3.73	3.62	3.76	4.57	4.07	5.28	2.25	4.47	4.35	4.78	4.53	4.19	4.60	4.71	5.13	5.28
P2O5	0.16	0.18	0.05	0.05	0.04	0.14	0.10	0.10	0.11	0.03	0.02	0.08	0.01	0.03	0.02	0.03	0.03	0.03	0.02	0.01
LOI	1.01	0.65	0.38	0.41	0.43	0.54	1.35	1.42	1.41	1.38	1.66	1.01	0.28	1.48	1.00	0.44	0.14	0.45	0.43	1.10
SUM	99.83	99.72	100.31	100.15	100.17	99.80	99.53	99.51	99.70	99.70	100.18	100.26	100.39	100.02	99.62	100.11	99.61	99.97	100.20	99.68
Li	7.48	14.16	22.27	14.90	12.87	5.82	7.87	6.14	8.05	7.67	3.06	12.72	29.82	6.51	6.66	32.62	10.45	31.40	27.34	11.30
Be	1.90	1.70	2.48	2.95	2.07	2.27	2.36	2.41	2.46	3.92	0.87	3.81	5.38	2.94	2.13	1.96	4.70	6.43	4.17	4.27
Sc	8.44	10.11	4.55	4.18	5.24	4.27	5.20	4.99	7.47	2.50	0.80	4.57	1.58	2.69	2.48	3.32	1.71	5.21	5.34	2.50
V	68.35	75.21	15.12	13.15	6.29	42.70	26.92	21.09	33.17	5.87	4.73	24.17	2.00	4.21	6.10	6.10	8.91	5.19	4.20	1.53
Cr	1.50	1.61	1.06	0.92	0.42	1.51	0.87	0.96	1.00	0.49	0.89	0.98	0.33	0.38	0.34	0.32	0.88	0.91	0.83	0.26
Co	6.84	8.07	1.26	1.31	0.90	4.98	3.77	3.31	3.41	1.03	0.77	2.13	0.07	0.54	0.39	0.53	0.68	0.56	0.41	0.10
Ni	2.07	2.15	1.12	1.01	0.89	2.41	1.27	1.28	1.28	0.82	1.05	1.43	0.58	0.74	0.63	0.59	1.17	0.71	0.87	0.55
Cu	3.06	3.45	1.33	1.81	0.40	2.91	58.72	16.73	60.52	0.45	0.64	1.24	0.32	0.46	0.36	0.45	0.98	0.34	0.44	0.71
Zn	52.38	47.76	36.14	40.53	35.11	76.11	48.94	49.04	33.91	25.69	6.19	50.24	39.48	21.08	17.89	26.62	14.54	17.29	22.26	36.71
Ga	15.30	15.76	16.70	16.03	15.85	18.90	15.10	12.72	15.65	17.38	7.16	17.65	19.23	27.27	25.91	15.10	15.77	17.97	17.56	16.93
Rb	90.99	112.01	170.09	155.20	133.37	133.14	116.49	144.05	131.38	174.51	62.06	210.19	267.52	191.46	179.68	189.25	233.26	262.13	263.46	324.54
Sr	431.06	415.98	212.04	209.11	156.40	527.36	392.22	303.69	383.07	150.88	76.96	154.73	5.22	1378.40	934.19	132.30	75.50	55.80	62.44	30.99
Y	15.98	21.59	27.60	29.06	29.35	13.29	21.35	24.63	31.65	36.83	18.59	30.76	29.91	19.15	20.32	25.91	27.96	49.38	26.70	37.10
Zr	169.31	183.67	189.84	174.22	144.86	162.57	183.96	168.97	186.27	125.39	74.57	186.87	79.85	82.43	66.27	86.58	129.71	140.49	120.91	83.32
Nb	9.12	9.97	15.77	16.33	13.59	9.25	12.02	11.56	15.66	11.47	5.77	22.01	37.09	15.50	13.71	21.89	23.34	26.17	17.96	25.55
Sn	1.08	1.36	2.07	2.20	2.02	1.19	1.73	1.78	2.72	2.53	1.03	2.89	2.98	1.95	1.82	2.58	1.36	2.93	2.82	1.56
Cs	2.87	2.57	5.56	3.72	2.04	5.10	2.29	2.28	2.15	1.24	0.52	3.42	6.92	15.89	11.50	3.65	2.93	7.34	6.28	4.07
Ba	987.77	975.04	1207.11	1068.56	838.01	844.17	558.96	678.02	580.46	647.35	375.27	418.07	16.66	1479.56	1122.94	694.20	203.27	140.57	167.22	97.67
La	34.94	42.64	55.29	52.86	30.36	34.59	36.67	39.59	45.19	49.08	19.65	47.87	21.88	24.55	22.60	29.54	39.57	42.38	25.79	115.84
Ce	63.02	77.08	105.87	101.44	58.86	65.44	69.14	75.19	87.19	98.22	40.22	89.59	44.37	48.88	46.18	58.76	72.62	87.62	52.83	57.85
Pr	6.52	8.02	11.58	10.92	6.80	7.24	7.44	8.00	9.53	10.92	4.43	9.69	4.55	5.30	4.92	6.34	7.47	10.11	6.21	20.79
Nd	23.18	28.76	41.92	39.51	25.69	26.41	26.03	28.10	33.39	38.05	15.85	32.19	13.42	18.01	16.49	21.34	23.20	36.99	22.86	60.89
Sm	4.07	5.19	7.10	7.01	5.11	4.76	4.84	5.45	6.81	7.32	3.15	6.08	3.05	3.75	3.53	4.54	4.33	8.85	5.47	10.89
Eu	1.11	1.09	1.26	1.19	0.87	1.05	1.11	1.21	1.07	0.74	0.37	0.81	0.15	0.48	0.47	0.53	0.36	0.38	0.30	1.01
Gd	3.55	4.24	5.45	5.52	4.66	3.39	3.73	4.24	5.21	5.65	2.52	4.87	2.64	2.82	2.71	3.59	3.27	7.38	4.43	8.18
Tb	0.53	0.59	0.80	0.80	0.74	0.47	0.57	0.68	0.86	0.97	0.46	0.81	0.57	0.52	0.51	0.66	0.60	1.33	0.75	1.08
Dy	2.99	3.52	4.60	4.78	4.48	2.54	3.59	4.12	5.13	5.75	2.93	4.86	4.01	3.14	3.19	4.08	3.75	8.19	4.57	6.00
Ho	0.61	0.71	0.92	0.95	0.94	0.47	0.66	0.81	1.01	1.20	0.62	0.98	0.89	0.61	0.64	0.82	0.83	1.63	0.88	1.14
Er	1.78	2.10	2.82	2.86	2.85	1.33	2.16	2.41	3.03	3.52	1.82	2.94	2.97	1.86	1.87	2.44	2.67	4.74	2.43	3.44
Tm	0.27	0.32	0.39	0.43	0.45	0.17	0.32	0.38	0.46	0.54	0.29	0.44	0.47	0.30	0.30	0.38	0.45	0.71	0.37	0.54
Yb	1.88	2.27	2.70	2.78	3.15	1.23	2.18	2.49	3.19	3.70	2.00	3.22	3.39	2.04	2.08	2.73	3.37	4.89	2.45	3.81
Lu	0.30	0.34	0.40	0.42	0.47	0.17	0.32	0.38	0.47	0.57	0.36	0.47	0.51	0.32	0.32	0.43	0.53	0.75	0.38	0.60
Hf	4.39	4.56	5.42	5.11	4.47	4.44	4.89	4.52	5.03	4.33	2.36	5.71	4.05	2.96	2.38	3.26	4.40	5.14	4.04	3.72
Ta	0.66	0.70	1.08	1.08	1.00	0.65	0.82	0.85	1.22	1.58	0.46	1.51	2.07	1.39	1.21	2.22	1.93	2.25	1.45	1.53
Tl	0.52	0.73	1.05	0.87	0.62	0.61	0.83	1.30	0.96	0.99	0.39	1.44	1.46	1.37	1.35	1.08	1.17	1.46	1.41	2.48
Pb	22.31	17.76	34.83	33.99	16.54	23.25	25.30	19.93	16.29	21.95	3.88	32.90	36.59	26.41	26.40	26.24	28.24	19.91	21.00	14.85
Th	17.38	19.36	23.75	24.02	13.98	20.82	12.79	14.31	21.04	20.57	9.22	27.36	29.67	15.78	14.46	17.44	32.61	27.06	16.77	26.36
U	3.04	3.31	3.63	4.96	2.71	4.29	3.01	2.89	3.63	4.48	1.56	4.82	8.33	3.48	3.27	7.70	4.30	7.11	4.61	3.17

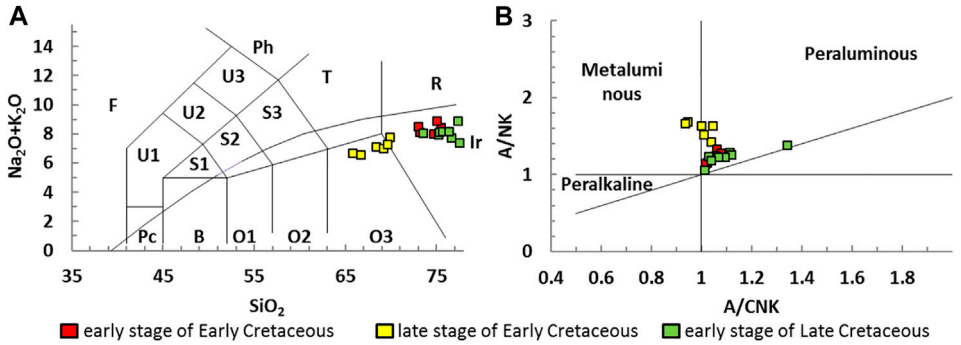

FIGURE 7 | TAS **(A)** and A/CNK **(B)** diagrams of magmatic rocks.

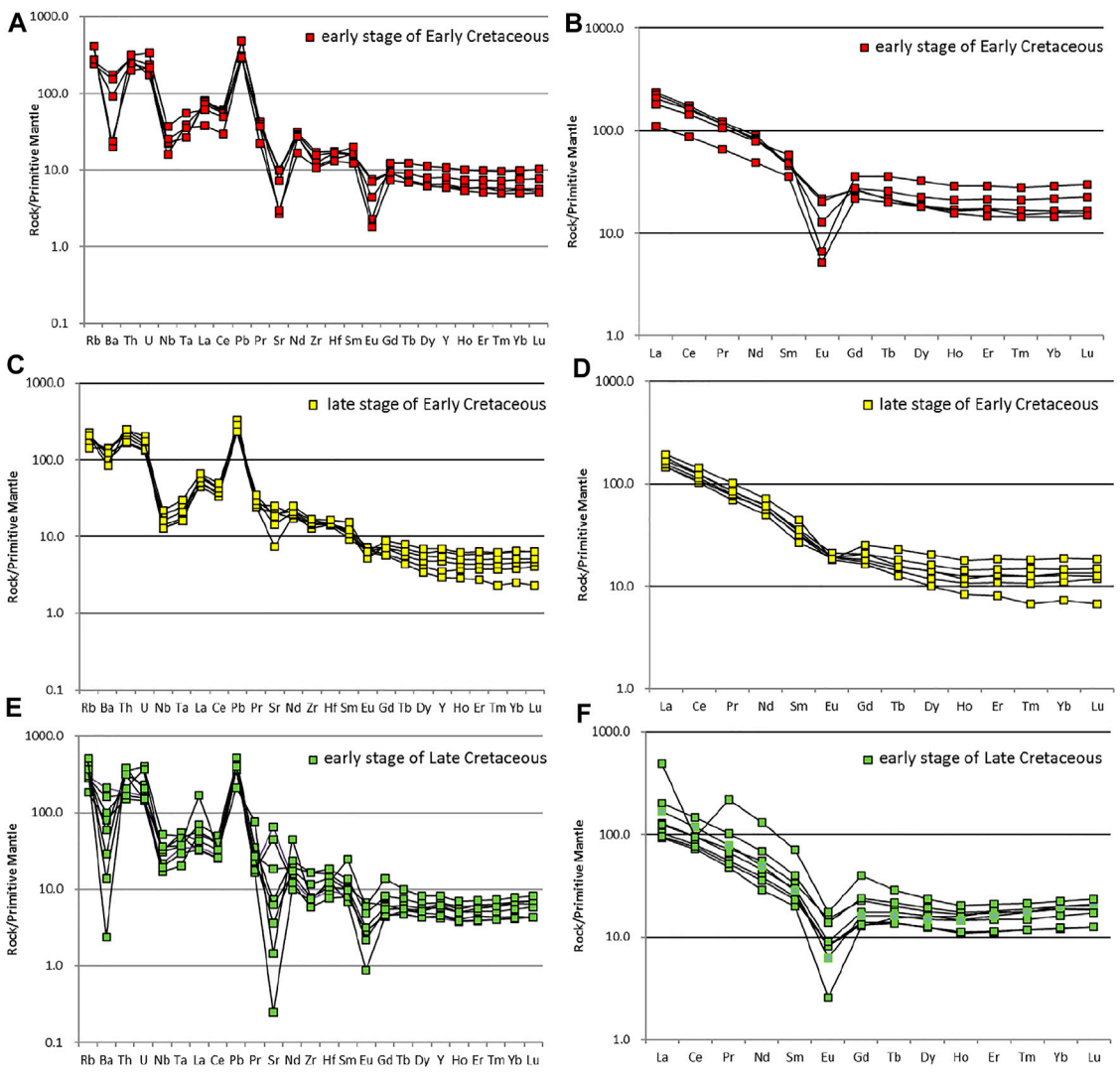

FIGURE 8 | Chondrite Normalized REE distribution patterns **(A), (C), (E)** and primitive mantle normalized trace element spider diagram **(B), (D), (F)** of granitic rocks.

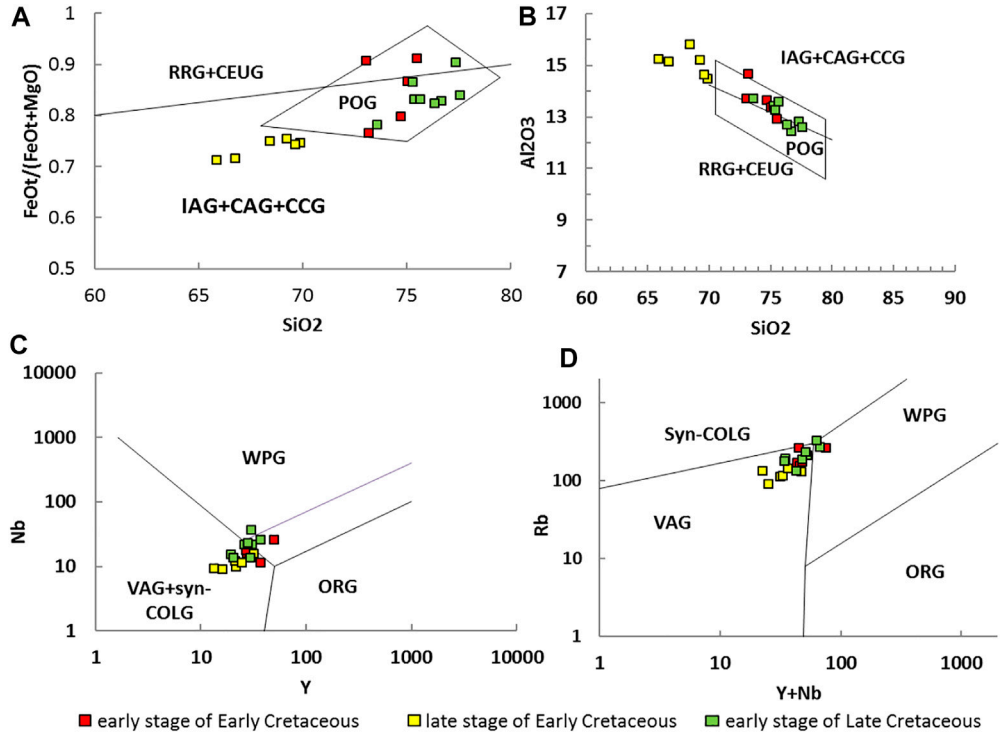

FIGURE 9 | SiO_2-FeOT/(FeOT + MgO), **(A)** SiO_2 – Al_2O_3, **(B)** Y – Nb, **(C)** and (Yb +Nb) – Rb, **(D)** diagrams of granites.

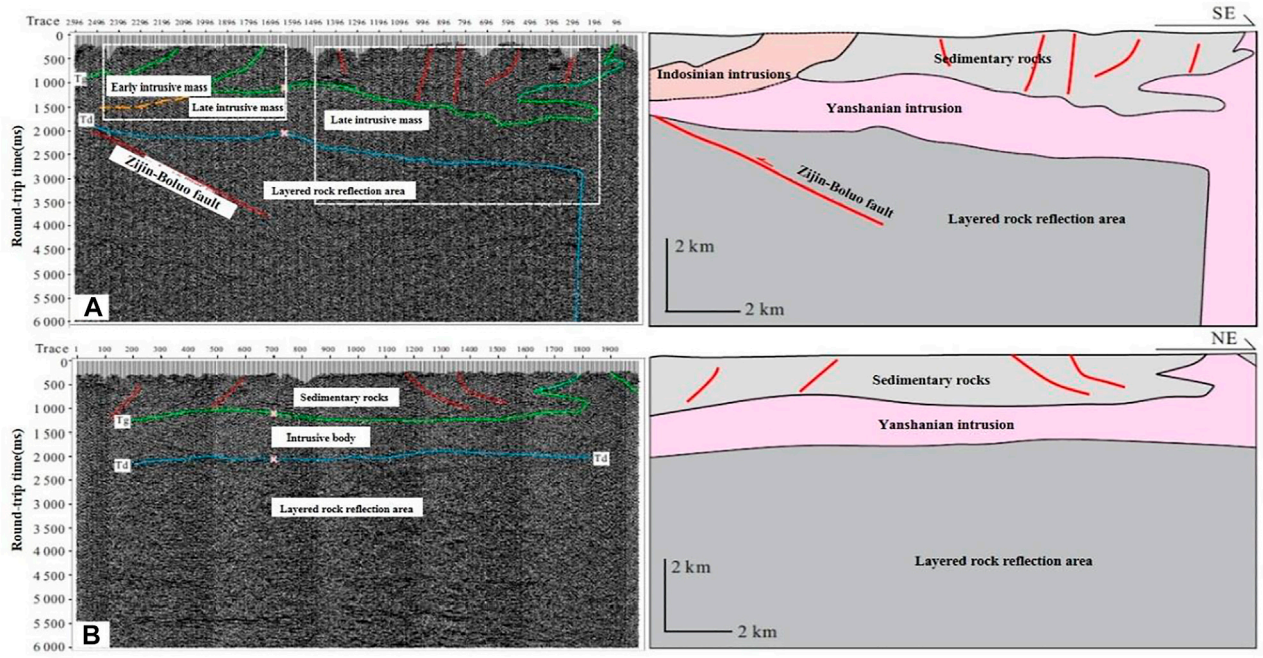

FIGURE 10 | Profiles of seismic inversion, **(A), (B)** and its geological interpretation in Huangshadong area (Kuang et al., 2020).

(Y + Nb)–Rb diagram (**Figures 9C,D**), samples are plotted within the scope of the volcanic island arc granite (VAG), within plate granite (WPG) and sys-collision granite (syn-COLG). Combined with the trace element characteristics of the samples, it can be inferred that the samples of this period is similar to the granite formed in ~135 Ma. Li Jianhua (2013) divided the acidic magmatic rocks of the Cretaceous into three periods: Adakite and gneis-like granite at 145–137 Ma, calc-alkaline granite at 136-118 Ma and related volcanic rocks, bimodal volcanic rocks at 107–90 Ma and A-type granite at 145–137 Ma. This is similar to what we found in this study.

Discussion on the Burial Depth of Deep Granite

Seismic Profiles in Huangshadong Area of Guangdong Province

The two seismic profiles in Huangshadong area of Guangdong Province (**Figures 10A,B**) (Kuang et al., 2020) reflect the sedimentary strata overlying granites. The sedimentary strata in the study area have undergone complex tectonic evolution, repeated tectonic uplifting, compression folding and fault processes have caused the sedimentary strata to have dramatic occurrence changes in a small range, and multiple periods of magmatic intrusion and eruption have complicated the contact relationship strata and rock mass. Therefore, the spatial continuity of stratigraphic interface and the stability of fault characteristics in seismic profile are poor in different ages.

According to the profiles of seismic inversion (**Figure 10**), the buried depth of Tg (interface between sedimentary strata and granites) is generally located between 1,000–1,900 ms (corresponding depth of 1,400–2,200 m), and the seismic phase characteristics of Tg interface are significantly different from each other. The granite core sample from Well Huire one is similar to Yanshanian granite, indicating that seismic facies unit may correspond to the intrusive body in Yanshanian period, emplaced from the deep crust upward into shallow rock bed. 2050–2,900 ms (corresponding to the depth of 3,600–4,800 m) for the bedrock under the bottom of the interface (Td), reflection of geological units in phase axis continuity better, different from the adjacent granite rock mass. It may be older sedimentary rocks or metamorphic rocks with certain stratification.

Apparent Resistivity Inversion Profiles in North Hainan Province

In the area outside the east of Fushan Depression of Hainan Province, wide field electromagnetic detection has been conducted (**Figure 11**) (Tan et al., 2020). From the resistivity

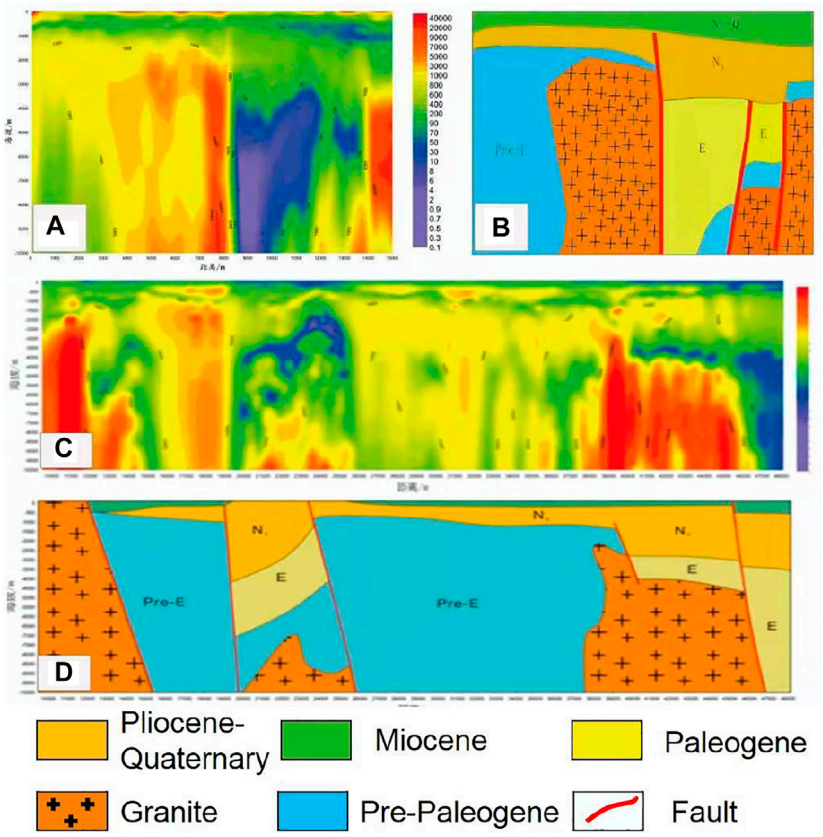

FIGURE 11 | Profiles of apparent resistivity inversion based on wide field electromagnetic method and corresponding geological interpretation in North Hainan Province (Tan et al., 2020).

profile of the final inversion processing, a set of high resistance developed in the west of the L1 line and a set of low resistance developed in the east (**Figure 11A**). The two parts were clearly bounded and featured with great difference. Based on regional geological analysis, the corresponding geological model is established (**Figure 11B**), and it is preliminarily considered that the high resistivity in the east is a set of intrusive concealed granite, and the low resistivity in the west is a paleoproximal sedimentary stratum, and the middle fault controls its scale. According to the analysis of geological model, the basement of North Hainan area is composed of pre-Mesozoic sedimentary rocks and granite intrusive bodies, and the rock strains develop. The fault-block-graben-barrier is developed in this area, and the structure is complex. The fault-block-graben-barrier structure is developed in the east, which is similar to Fushan Depression. Moreover, the distribution of Paleogene strata is obviously controlled by the size of the fault depression. The L4 line extends southward to the granite outflowing area. According to the resistivity result diagram (**Figure 11C**), the electrical characteristics of the outflowing granite are similar to those of the latent granite (**Figure 11D**). By comparing the two survey lines, the latent high-resistivity stability exists. In the intersection area where survey line L1 and survey line L4 meet, the granite has a large scale, a buried depth of about 3000 m, and an overburden, which is a potential favorable area for deep high-temperature geothermal exploration.

The Significance of Granite to the Geothermal Energy

The heat source of geothermal energy mainly include heat transfer in the mantle, local anomalous heat transfers in the crust (magma chamber), and radioactive heat generation from granitic rocks. Surface heat flow, as a direct reflection of deep heat, usually accounts for 40–60% of the heat flow from the mantle. The heat flow caused by radioactive heat generation in the crust is slightly less than that from the mantle, accounting for about 40% and up to 50% in some areas (Wang Shejiao et al., 1999). The terrestrial heat flow value in the study area is about 70 mW/m^2, which is higher than the average terrestrial heat flow value of 64.2 mW/m^2 in South China (Yuan et al., 2006). The Yanshannian granite in the Southeast Coastal region has a high thermal conductivity, with an average thermal conductivity of 3.15 W/mK. This means that the granite in the deep part with a thickness of up to 3.5 km can better conduct the heat in the deeper part to the near surface. Consequently, the mantle heat gets better performance on the surface, which promotes the formation of the geothermal energy in the area.

Former research suggested that the heat generated by radioactive element decay in rocks is one of the main sources of Earth heat (Huang Shaopeng, 1992), and it is also a major factor controlling the temperature field distribution in the lithosphere (Sclater et al., 1980). Previous scholars proposed that the lower crust has little influence on the surface heat flow value (Hasterok and Chapman, 2007), and the research on the lower crust inclusion also shows that the radioactive heat generation rate of rocks in the lower crust is very low (Rudnick and Fountain, 1995). Thus, the heat source in the area mainly comes from the decay of radioactive elements in the middle and upper crust, and depends on the abundance of thermogenic elements, such as ^{238}U, ^{232}Th, and ^{40}K (Rybach and Buntebarth, 1984).

Previous studies have analyzed the overall heat generation rate of radioactive elements in the study area shown as low heat generation rate of strata and high heat generation rate of granitic rocks (Kuang et al., 2020). The value of heat generation rate from Yanshanian rocks is far higher than the average global continental upper crust rock, with the average value of 5.50 $\mu W/m^3$ and the maximum value up to 9.15 $\mu W/m^3$. It is also much higher than the average measured value of the radioactive heat generation rate of granitic rocks in other regions, which was about 2.5 $\mu W/m^3$ (Rybach, 1988), 3.3–3.8 $\mu W/m^3$ (Wollenberg and Smith, 1987) and 3.0 $\mu W/m^3$ (Rybach and Buntebarth, 1984).

This is mainly attributed to Yanshanian granites formed from remelting of pre-Cambian rocks in this region (Xu et al., 2007), The rocks have been experienced the redistribution process, and enriched large ion lithophile elements (LILE) of rocks, lead to extreme enrichment of LILE (including Th, U, K element), and then forming high value of heat generation rate in granites. Consequently, the high thermal conductivity and high radioactive thermogenic elements of Yanshanian granites are the reasons for the formation of high-temperature geothermal in this area.

The Significance of Granite to Deep Geothermal in Southeast China

Large-scale granite events occurred in the coastal area of southeast China during Mesozoic, especially Yanshannian (Li, et al., 2014; Gao et al., 2014; Deng et al., 2016). The Yanshannian granitoids magmatism in the southeast coastal area has a general trend from west to east, and the emplacement age of the rocks from old to young. Due to the high radioactive heat generation rate of granitoids, granitoids provide a direct heat source for crustal heat generation. Therefore, the widespread occurrence of granitoids magmatic activity in Mesozoic provides a significant condition for the formation of geothermal resources. The terrestrial heat flow value is one of the important geothermal geological indexes for the occurrence and distribution of geothermal resources. The terrestrial heat flow value in the southeast coastal area of China is obviously affected by the tectonic background (Hu and Wang, 1994; Zhang et al., 2020): The overall tectonic activity in the northwestern basin is relatively stable, showing a lower terrestrial heat flow value, while the southeastern coast shows a higher terrestrial heat flow value. As the overall heat flow value gradually increases from west to east, the local deep thermal structure controls the ground heat flow value. As shown in **Figure 2**, Fujian and Yangjiang-Maoming reached the highest ground heat flow value, reaching more than 95 $\mu W/m^3$. Radiogenic heat is one of the main sources of heat in the lithosphere. U, Th and natural radio isotope ^{40}K are the main thermal elements. According to the Zhao Ping et al. (1995), most of the southeast coastal areas are in the range of high heat generation rate, basically higher than 2.1 $\mu W/m^3$. Especially in the whole province of Guangdong,

southern Jiangxi and southern Fujian, the large area of granite outcrops, the heat generation rate background is more than 2.8 $\mu W/m^3$, such a large area of high heat generation rate area is rare. Radioactive heat generation is the main source of crustal heat generation, which is of great significance to the occurrence of dry hot rock resources. The southeast coastal area, especially Huizhou and Sanhui of Guangdong Province, has a good prospect of exploration and development of geothermal resources.

Based on produced heat rate of typical magmatic rocks in Guangdong, Jiangxi and southeast of Fujian, previous scholars indicated that the radioactive heat production rate of most granitic rocks is greater than the average heat production rate of the Earth's crust, signifying that the Yanshanian granite radioactive heat production have great contribution to regional heat (Zhao et al., 1995). Meanwhile, the southeastern coastal area has basically the same tectonic evolution pattern in Mesozoic (Wang et al., 2013), which is controlled by Paleo-Pacific plate subduction during the Yanshanian period and experienced large-scale magmatic events.

Based on seismic inversion in the area, it is clear that in this area and the surrounding granite areas, based on P wave inversion of deep seismic profiles, shows 5–10 km depth of granite. A reasonable speculation in the area is that Yashaninan granites have great potential for the geothermal reservoirs. Moreover, the Moho surface in the whole southeast region is relatively shallow and the temperature of the Moho surface is relatively high (Zhang et al., 2018). The deep granite can promote the heat transfer of the mantle to the surface. In summary, Yanshaninan granite in the southeast coastal area is of great significance to the geothermal energy system.

CONCLUSION

1) The age of granite reservoirs are mainly 94.7–138.4 Ma, mainly late Yanshanian period. The geochemical characteristics of rocks show they are formed in the subduction zone signature, indicating they are formed related to the extensional environment formed by retractable subduction of the ancient Pacific plate.
2) Deep Yanshanian granites promote mantle heat transfer to the surface and increase the proportion of mantle heat flow in the heat flow value. Yanshanian granite has high content of Th, U, and K, and its radioactive decay heat generation provides heat source for the high-temperature geothermal in the study area. The combined action of the two forms the high-temperature geothermal energy in the study area.
3) The deep granite in the study area has huge potential for geothermal resources. The geothermal genesis model in the study area has reference significance for the understanding of geothermal in the southeast region or the calculation of geothermal reserves.

DATA AVAILABILITY STATEMENT

The original contributions presented in the study are included in the article/supplementary material, further inquiries can be directed to the corresponding author.

AUTHOR CONTRIBUTIONS

JL is responsible for experimental design, HZ and YZ are responsible for providing overall ideas, JF is responsible for data analysis, YZ and MW is responsible for instrument operation.

FUNDING

This study was financially supported by National Key Research and Development Project (No. 2019YFC0604903), National Natural Science Foundation of China (Grant No. U20B6001) and consultation research project of Chinese Academy of Engineering (No. 2019-XZ-35-04 and No. 2021-XZ-16-01).

REFERENCES

Bertani, R. (2012). Geothermal Power Generation in the World 2005-2010 Update Report. *Geothermics* 41, 1–29. doi:10.1016/j.geothermics.2011.10.001

Bertani, R. (2016). Geothermal Power Generation in the World 2010–2014 Update Report. *Geothermics* 60, 31–43. doi:10.1016/j.geothermics.2015.11.003

Brown, D. W., Duchane, D. V., Heiken, G., and Hriscu, V. (2012). *Mining the Earth's Heat: Hot Dry Rock Geothermal Energy*. Heidelberg: Springer Science & Business Media. doi:10.1007/978-3-540-68910-2

Deng, J., Feng, Y., Di, Y., Cui, L., Xiao, Q., and Guo, S. S. (2016). The Instrusive Spatial Temporal Evolutional Framework in the Southeast China. *Geol. Rev.* 62 (1), 3–16.

Deng, Y. F., Li, J. T., and Peng, T. P. (2019). Lithospheric Structure in the Cathaysia Block (South China) and its Implication for the Late Mesozoic Magmatism. *Physics of the Earth and Planetary Interiors*, 24–34.

Frost, B. R., Barnes, C. G., Collins, W. J., Arculus, R. J., Ellis, D. J., and Frost, C. D. (2001). A Geochemical Classification for Granitic Rocks. *J. Pet.* 42 (11), 2033–2048. doi:10.1093/petrology/42.11.2033

Gao, W., Wang, Z., Li, C., and Wang, D. (2014). Zircon U-Pb Geochronological, Geochemistry and Tectonic Implication of Lndosinian Granite from southeastern Zhejiang, South China. *Acta Geologica Sinica* 88 (6), 1055~1067.

Genter, A., Traineau, H., Dezayes, C., Elsass, P., and Villemin, T. (1995). Fracture Analysis and Reservoir Characterization of the Granitic Basement in the HDR Soultz Project (France). *Geothermal Sci. Tech.* 4 (3), 189–214.

Goldstein, B. A., Hill, A. J., and Long, A. (2008). Hot Rocks in Australia National Overview. *ASEG Extended Abstr.* 1, 1.

Gong, J., and John Chen, Y. (2014). Evidence of Lateral Asthenosphere Flow beneath the South China Craton Driven by Both Pacific Plate Subduction and the India-Eurasia continental Collisin. *Terra Nova* 26 (1), 55–63. doi:10.1111/ter.12069

Hasterok, D., and Chapman, D. S. (2007). Continental Thermal Isostasy: 2. Application to North America. *J. Geophys. Res. Solid Earth* 112 (B6). doi:10.1029/2006jb004664

Hu, S., He, L., and Wang, J. (2000). Heat Flow in the Continental Area of China: A New Data Set. *Earth Planet. Sci. Lett.* 179 (2), 407–419. doi:10.1016/s0012-821x(00)00126-6

Hu, S., and Wang, J. (1994). Heat Flow Characteristics of Orogenic Belts in southeastern China. *Geol. Rev.* 40 (5), 387-394.

Huang, S. P. (1992). Variations of Heat Flow and Crustal Thickness in the Continental Area of China. *Chin. J. Geophys.* 35 (4), 441–450.

Kelemen, P. B., Hanghøj, K., and Greene, A. R. (2003). One View of the Geochemistry of Subduction - Related Magmatic Arcs, with an Emphasis on Primitive Andesite and Lower Crust. *Treatise Geochem.* 3, 659.

Kuang, J., Qi, S., and Wang, S. (2020). Granite Intrusion in Huizhou, Guangdong Province and its Geothermal Implications. *Earth Sci.* 45 (2020), 1466–1480.

Li, D. W., and Wang, Y. X. (2015). Major Issues of Research and Development of Hot Dry Rock Geothermal Energy. *Earth Sci.* 40 (11), 1858–1869.

Li, J., Zhang, Y., Dong, S., and Johnston, S. T. (2014). Cretaceous Tectonic Evolution of South China: a Preliminary Synthesis. *Earth-Science Rev.* 134, 98–136. doi:10.1016/j.earscirev.2014.03.008

Li, L., Luo, J., Chen, Q., Shi, D., Yun, J., and Li, T. (2019). Discovery of Silurian schist from Well J6 in Chagan Sag, Yin'e Basin: Evidence from Zircon U-Pb Geochronology. *Geology in China* 46 (1), 209–201

Li, Sanzhong., Zang, Yibo., and Wang, P. (2017). *Earth Sci. Front.* 24 (4), 213–225.

Li, X. H., Li, Z. X., Li, W., Ying, L., Yuan, C., Wei, G., et al. (2007). U– Pb Zircon, Geochemical and Sr-Nd-Hf Isotopic Constraints on Age and Origin of Jurassic I- and A-Type Granites from Central Guangdong, SE China: A Major Igneous Event in Response to Foundering of a Subducted Flat-Slab? *Lithos* 96 (1-2), 186–204. doi:10.1016/j.lithos.2006.09.018

Li, Z.-X., and Li, X.-H. (2007). Formation of the 1300-km-wide Intracontinental Orogen and Postorogenic Magmatic Province in Mesozoic South China: A Flat-Slab Subduction Model. *Geol.* 35 (2), 179. doi:10.1130/g23193a.1

Liu, K., Li, Z., Xu, W., Ye, H., Zhao, X., Hu, Y., et al. (2016). Geochemical Characteristics and Metallogenic Regularity of Mesozoic Magmatic Rocks in South China [J]. *J. Mineralogy, Pet. Geochem.* 35 (6), 1141–1155.

Liu, Y. S., Hu, Z. C., Gao, S., Günther, D., Xu, J., Gao, C. G., et al. (2008). *In Situ* analysis of Major and Trace Elements of Anhydrous Minerals by LA-ICP-MS without Applying an Internal Standard. *Chem. Geology* 257 (1-2), 34–43. doi:10.1016/j.chemgeo.2008.08.004

Ludwig, K. R. (2003). *Isoplot 3.00: A Geochronological Toolkit for Microsoft Excel*. Berkeley: Berkeley Geochronology Center Special Publication, 4–70.

Lund, J. W., and Boyd, T. L. (2016). Direct Utilization of Geothermal Energy 2015 Worldwide Review. *Geothermics* 60, 66–93. doi:10.1016/j.geothermics.2015.11.004

Pan, Z., Zhang, Q., Chen, G., Jiao, S., Du, X., Miao, X., et al. (2017). The Relationship between the Mesozoic Magmatic Activity and Plate Subduction in Eastern China: The Relation between the Zhe-Fujian and the Japanese Arc and the Andean Arc and its Significance [J]. *Acta Petrologica Sinica* 33 (5), 1507–1523.

Pearce, J. A., Harris, N. B. W., and Tindle, A. G. (1984). Trace Element Discrimination Diagrams for the Tectonic Interpretation of Granitic Rocks. *J. Pet.* 25 (4), 956–983. doi:10.1093/petrology/25.4.956

Richards, H. G., Savage, D., and Andrews, J. N. (1992). Granite-water Reactions in an Experimental Hot Dry Rock Geothermal Reservoir, Rosemanowes Test Site, Cornwall, U.K. *Appl. Geochem.* 7 (3), 193–222. doi:10.1016/0883-2927(92)90038-5

Rudnick, R. L., and Fountain, D. M. (1995). Nature and Composition of the Continental Crust: A Lower Crustal Perspective. *Rev. Geophys.* 33 (3), 267. doi:10.1029/95rg01302

Rybach, L., and Buntebarth, G. (1984). The Variation of Heat Generation, Density and Seismic Velocity with Rock Type in the Continental Lithosphere. *Tectonophysics* 103 (1-4), 335–344. doi:10.1016/0040-1951(84)90095-7

Rybach, L., 1988. Determination of Heat Production Rate. Handbook of Terrestrial Heat Flow Density Determinations.

Sclater, J. G., Jaupart, C., and Galson, D. (1980). The Heat Flow through Oceanic and Continental Crust and the Heat Loss of the Earth. *Rev. Geophys.* 18 (1), 269–311. doi:10.1029/rg018i001p00269

Sun, S.-s., and McDonough, W. F. (1989). Chemical and Isotopic Systematics of Oceanic Basalts: Implications for Mantle Composition and Processes. *Geol. Soc. Lond. Spec. Publications* 42 (1), 313–345. doi:10.1144/gsl.sp.1989.042.01.19

Tan, H., Lin, F., Wen, J., Li, J., and Fan, Y. (2020). Application of Wide Field Electromagnetic Method in the Exploration of Deep Dry Hot Rocks in Hainan Province. *China Pet. Chem. Stand. Qual.* (4), 150–152.

Wang, D., and Shen, W. (2003). Granite Genesis and Crustal Evolution in southeastern China. *Earth Sci. Front.* 10 (3), 209–220.

Wang, S. J., Hu, S. B., and Wang, S. J. (1999). The Geothermal Effect of Radioactive Heat Generation and its Signif-icance to Hydrocarbon Maturation in Tarim Basin. *Pet. Exploration Dev.* 26 (5), 36–38.

Wang, Y., Fan, W., Zhang, G., and Zhang, Y. (2013). Phanerozoic Tectonics of the South China Block: Key Observations and Controversies. *Gondwana Res.* 23 (4), 1273–1305. doi:10.1016/j.gr.2012.02.019

Wollenberg, H. A., and Smith, A. R. (1987). Radiogenic Heat Production of Crustal Rocks: An Assessment Based on Geochemical Data. *Geophys. Res. Lett.* 14 (3), 295–298. doi:10.1029/gl014i003p00295

Wu, F., Li, X., Yang, J., and Zheng, Y. (2007). Discussions on the Petrogenesis of Granites [J]. *Acta Petrologica Sinica* 23 (6), 1217–1238.

Xi, Y., Wang, G., Liu, S., Zhao, Y., and Hu, X. (2018). The Formation of a Geothermal Anomaly and Extensional Structures in Guangdong, China: Evidence from Gravity Analyses. *Geothermics* 72, 225–231. doi:10.1016/j.geothermics.2017.11.009

Xu, X. S., O'Reilly, S. Y., Griffin, W. L., Wang, X., Pearson, N., and He, Z. (2007). The Crust of Cathaysia: Age, Assembly and Reworking of Two Terranes. *Precambrian Res.* 158 (1-2), 51–78. doi:10.1016/j.precamres.2007.04.010

Yuan, Y. S., Ma, Y. S., Hu, S. B., Guo, T., and Fu, X. (2006). Present - Day Geothermal Characteristics in South China. *Chin. J. Geophys.* 49 (4), 1118–1126. doi:10.1002/cjg2.922

Zhang, J., Wang, B. Y., Tang, X. C., and Dong, M. (2018). Temperature Structure and Dynamic Background of Crust and Mantle beneath the High Heat Flow Area of the South China Continental Margin. *Chin. J. Geophys.* 61 (10), 3917–3932.

Zhang, Y., Luo, J., and Feng, J. (2020). Characteristics of Geothermal Reservoirs and Utilization of Geothermal Resources in the Southeastern Coastal Areas of China. *Journal of Groundwater Science and Engineering* 8 (2), 134–142.

Zhao, P., Wang, J., and Wang, J. A. (1995). Characteristics of Heat Production Distribution in SE China. *Acta Petrologica Sinica* 11 (3), 292–305.

Zhou, X., Sun, T., Shen, W., Shu, L., and Niu, Y. (2006). Petrogenesis of Mesozoic Granitoids and Volcanic Rocks in South China: A Response to Tectonic Evolution. *Episodes* 29 (1), 26–33. doi:10.18814/epiiugs/2006/v29i1/004

Conflict of Interest: The authors declare that the research was conducted in the absence of any commercial or financial relationships that could be construed as a potential conflict of interest.

Publisher's Note: All claims expressed in this article are solely those of the authors and do not necessarily represent those of their affiliated organizations, or those of the publisher, the editors and the reviewers. Any product that may be evaluated in this article, or claim that may be made by its manufacturer, is not guaranteed or endorsed by the publisher.

frontiers in Earth Science

ORIGINAL RESEARCH
published: 07 October 2021
doi: 10.3389/feart.2021.759872

Thermo-Economic Comparison Between Organic Rankine Cycle and Binary-Flashing Cycle for Geothermal Energy

*Yuan Zhao[1,2], Bowen Du[1], Shunyi Chen[1], Jun Zhao[2], Yulie Gong[3], Xianbiao Bu[3], Huashan Li[3] and Lingbao Wang[3]**

[1]Powerchina HuaDong Engineering Corporation Limited, Hangzhou, China, [2]Key Laboratory of Efficient Utilization of Low and Medium Grade Energy, MOE, Tianjin University, Tianjin, China, [3]Guangzhou Institute of Energy Conversion, Chinese Academy of Sciences, Guangzhou, China

Geothermal energy is a characteristic of widely distributed, high capacity factor, high reliability, and lower environmental impact potential values. And it will play an important role in achieving the goal of carbon neutral carbon peak. Nonetheless, geothermal energy presents its own particular challenges, i.e., the high investment cost and long payback period. The binary flashing cycle (BFC) system is proved to be a promising power generation technology due to the efficient and full utilization of a low-grade heat source. While the economic performance still needs further evaluation, in the present study, the thermo-economic comparison between organic Rankine cycle (ORC) and the BFC for geothermal energy has been investigated. R245fa has been chosen as the working fluid. Considering the thermodynamic and economic performance simutaneously, several evaluation indicators were selected including thermal efficiency, exergy efficiency, net power output per ton geothermal water, heat exchanger area, and heat recovery efficiency, and the system modeling and comparison were presented. The simulation results reveal that the BFC system obtains 32% more net power output than the ORC system under the working conditions investigated. The heat recovery efficiency of the BFC is 1.96 times as much as that of the ORC, which indicates that the BFC can realize the full utilization of low-grade energy. And more heat exchanger areas are required in the BFC system. What is more, the preliminary discussion of the economic feasibility of BFC system applied in the FengShun geothermal power plant is presented. The payback period of the BFC is just 6.0 years under the generation pressure of 600 kPa. It is indicated that the BFC system has obvious economic benefits, especially in a nonflowing geothermal well.

Keywords: geothermal energy, organic Rankine cycle, binary flashing cycle, thermo-economic, payback period

OPEN ACCESS

Edited by:
Yanlong Kong,
Institute of Geology and Geophysics (CAS), China

Reviewed by:
Tailu Li,
Hebei University of Technology, China
Tiantian Zhang,
Harbin Institute of Technology, China

****Correspondence:***
Lingbao Wang
wanglb@ms.giec.ac.cn

Specialty section:
This article was submitted to Economic Geology, a section of the journal Frontiers in Earth Science

Received: *17 August 2021*
Accepted: *15 September 2021*
Published: *07 October 2021*

Citation:
Zhao Y, Du B, Chen S, Zhao J, Gong Y, Bu X, Li H and Wang L (2021) Thermo-Economic Comparison Between Organic Rankine Cycle and Binary-Flashing Cycle for Geothermal Energy. Front. Earth Sci. 9:759872. doi: 10.3389/feart.2021.759872

1 INTRODUCTION

At the 75th sessions of the UN General Assembly in September 2020, China announced her pledge to reach peak emission by 2030 and carbon neutrality by 2060 (Mallapaty, 2020). On the path to carbon peak and carbon neutralization, the development and utilization of renewable energy will play a vital role. And renewable energy may be the main driving force of carbon reduction for a long time (Yu et al., 2020). Compared with other renewable energies, geothermal energy has the highest capacity

factor. Geothermal energy power generation has attracted great attention all over the world. The world geothermal energy reserve available is abundant, but the widely distributed hydrothermal geothermal accounts for 70% with the temperature below 150°C (Franco and Vaccaro, 2014; Kong et al., 2014). Organic Rankine Cycle (ORC) has been proved to be one of the most efficient ways to utilize low-grade geothermal energy, owing to compact structure, stable operation, and easy maintenance (Cao and Dai, 2017). Extensive studies on the ORC have been carried out, including working fluid selection, operating parameters optimization, system modification, ORC-based cogeneration system research, experimental study, and thermo-economic investigation (Astolfi et al., 2014; Li et al., 2016; Miao et al., 2017; LiHungWuSuXi and Wang, 2021; Sun et al., 2021).

Although great efforts were made to boost the ORC performance, the ORC thermal efficiency is generally less than 12%, which limits the commercial application (Basaran and Ozgener, 2013). It is not well optimized from the viewpoint of thermodynamics. At the outlet of the evaporator in the ORC system, the working fluid stays in saturated state or superheated state. The input total heat in the evaporator includes two parts, one is used to improve the latent heat of the working fluid, the other is used to lift the sensible heat. Obviously, the latent heat is much larger than the sensible heat. That is to say, most of the input heat is not beneficial to the evaporation temperature improvement. Consequently, the evaporation pressure and temperature have to be restricted relatively low due to the working fluid complete evaporation, resulting in smaller net power output. The phase state of the working fluid at the evaporator outlet is modified to address such an issue, followed by the system organization process. The modified ORC system, named binary flashing cycle (BFC) technology, is demonstrated to be an efficient solution to improve the system thermodynamics performance (Michaelides and Scott, 1984; Shi and Michaelides, 1989; Yuan and Michaelides, 1993; Edrisi and Michaelides, 2013; Michaelides, 2016; Wang et al., 2016; Liu et al., 2018; Wang et al., 2018; Wang et al., 2019). The working fluid in the evaporator of the BFC system is heated into gas-liquid state; as a consequence, smaller proportion of the total input heat is required to heat the latent heat of the working fluid. Therefore, the evaporation pressure and temperature have been improved. The liquid working fluid from the separator flows into the flashing tank, where relative lower pressure working fluid vapor is obtained to push the turbine to produce more work.

Recently, few researchers conducted investigations on the BFC. As early as in 1984, Michaelides and Scott (1984) proposed the BFC system and conducted the performance comparison between the ORC and the BFC. It is revealed that 20% more power can be produced in the BFC system than that of the ORC system under the same operating conditions. Shi and Michaelides (1989) established the BFC system using ammonia, freon-12, and isobutene as working fluid. Because the ORC and the BFC have different operation characteristics, their respective optimum performances were compared. The BFC yields superior thermodynamics performance. Yuan and Michaelides (1993) also conducted a comparative study, and indicated that, under the optimum design conditions, the BFC may provide up to 25% more power than the ORC. The conclusion is consistent with the reports by Michaelides and Scott (1984). Edrisi and Michaelides (2013) conducted pure working fluid selection, and 6 refrigerants were selected as the working fluid candidates. The results revealed that the hexane and pentane yield better thermodynamics performance among the working fluids candidates. Michaelides (2016) found the BFC has less total entropy production compared with the ORC system. And it is deemed as a future cycle to make the geothermal plants economically competitive. Wang et al. (2018) presented a regenerative type BFC system to improve the thermodynamic performance. Wang et al. (2016) conducted the ORC and BFC system performance comparison. At the respective optimal evaporation temperature, the net power outputs per ton geothermal water of the ORC and BFC are 8.77 and 10.09 kWh/t. Liu et al. (2018) optimized the operating parameters and conducted working fluid selection for the BFC. There exist optimal evaporation and flashing temperatures at which the system possesses the best thermodynamics performance. Among the working fluid candidates, R601 is supposed to be the most suitable working fluid. Wang et al. (2019) presented R245fa/R600 zeotropic mixtures mass concentration optimization for the BFC. The results indicated that it is favorable to employ the zeotropic mixtures to improve the exergy efficiency and reduce the irreversible loss.

As can be seen from the literature review, the studies on the BFC system were carried out considering the thermodynamic performance. It has been proved that the BFC yields better thermodynamic performance than the ORC; nevertheless, the BFC system requires a larger heat exchanger area, which indicates more investment cost. None of the previous investigations compared the ORC and the BFC from the viewpoint of both thermodynamic and economics. To fill up this research gap, thermo-economic comparison between the ORC and the BFC driven by geothermal energy is conducted. Furthermore, a case study in the Fengshun geothermal field is presented. The preliminary economic feasibility of the BFC system is discussed. R245fa is selected as the working fluid due to excellent thermal performance and environmental friendly characteristic. The thermophysical properties are presented in **Table 1**.

2 SYSTEM MODELING

2.1 System Description

The ORC flow diagram is illustrated in **Figure 1**. It mainly includes evaporator, expander, condenser, and working fluid pump. And the system description and the thermodynamic model can be referred in Basaran and Ozgener, (2013). The BFC flow diagram is shown in **Figure 2**. It is composed of preheater, vapor generator, gas-liquid separator, expander, flash drum, condenser, working fluid pump. The geothermal brine from the production well enters into the vapor generator and heats the R245fa. It should be noted that the R245fa is heated to a gas-liquid state, which is the largest difference with the ORC

TABLE 1 | R245fa thermo-physical properties.

Fluid	Fluid type	Molecular mass (kg/kmol)	Critical temperature (°C)	Critical pressure (kPa)	Normal boiling point (°C)	Ozone depletion potential	Global warming potential
R245fa	Dry	134.05	154.01	3651.00	15.14	0	1030

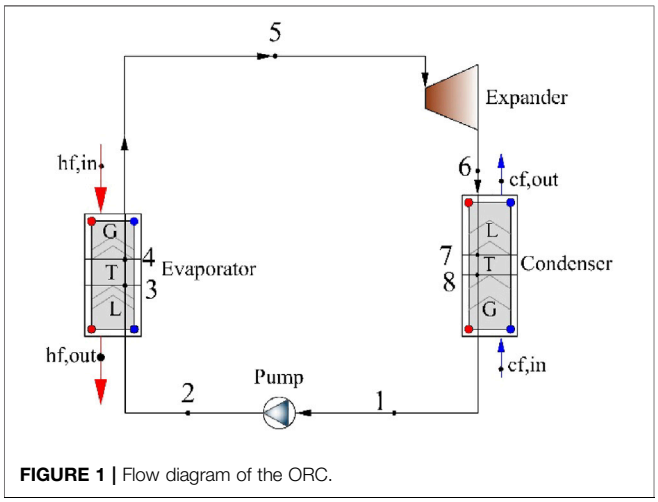

FIGURE 1 | Flow diagram of the ORC.

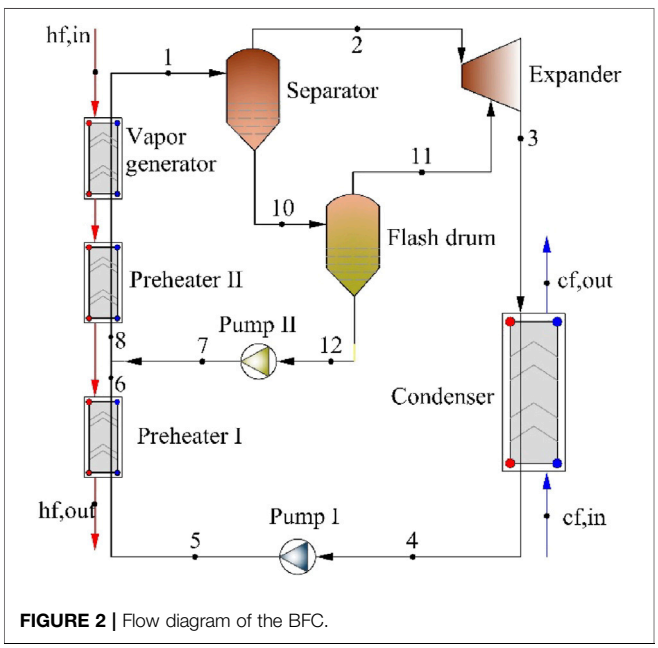

FIGURE 2 | Flow diagram of the BFC.

system. The gas-liquid two-phase R245fa is fed into the separator. The gas-phase R245fa from the separator is sent to the high-pressure-stage expander to produce power. The remaining liquid-phase R245fa from the separator flows into the flash drum through the throttle value. The flashed gas-phase R245fa flows into the low-pressure-stage expander to produce work again. The liquid R245fa released from the flash drum is pressurized into preheater II to absorb the heat of the geothermal brine from the vapor generator. The R245fa from the expander is driven toward the condenser, at which it is condensed to liquid state by rejecting heat to the cooling water. And then R245fa is pressurized into preheater I, where it absorbs the heat of the geothermal brine from preheater II. The left geothermal water is reinjected to the injection well. Finally, R245fa from preheater II flows into the vapor generator.

2.2 Thermo-Economic Model

To simplify the ORC and BFC system model, the following assumptions are listed as follows (Van et al., 2014).

1) Both the ORC and the BFC are modeled under steady state;
2) Pressure loss of each component is neglected except for the turbine and the pump;
3) Friction losses, heat dissipation, kinetic energy, and potential energy are ignored;
4) The irreversibility related to the separator is ignored;
5) Plate-type heat exchangers are adopted;
6) The geothermal water is assumed to be pure water;
7) The pinch point temperature differences of the evaporator and the condenser are set to be 10 and 5°C, respectively.

2.2.1 Thermodynamic Model

The heat balance in the preheater I, preheater II, and vapor evaporator yields the following expression:

The heat transferred in preheater I is given by

$$Q_{\mathrm{Pre1}} = m_{\mathrm{hf}} c_{\mathrm{p,hf}} \left(T_{\mathrm{p,2}} - T_{\mathrm{hf,out}}\right) = m_5 \left(h_6 - h_5\right) \tag{1}$$

The heat transferred in preheater II is given by

$$Q_{\mathrm{Pre2}} = m_{\mathrm{hf}} c_{\mathrm{p,hf}} \left(T_{\mathrm{p,1}} - T_{\mathrm{p,2}}\right) = m_{\mathrm{wf}} \left(h_9 - h_8\right) \tag{2}$$

The heat transferred in vapor evaporator is given by

$$Q_{\mathrm{gen}} = m_{\mathrm{hf}} c_{\mathrm{p,hf}} \left(T_{\mathrm{hf,in}} - T_{\mathrm{p,1}}\right) = m_2 \left(h_1 - h_9\right) \tag{3}$$

The total input heat into the BFC is given by

$$Q_{\mathrm{tot}} = Q_{\mathrm{Pre1}} + Q_{\mathrm{Pre2}} + Q_{\mathrm{gen}} \tag{4}$$

where Q denotes heat transfer rate, kW; c_p denotes specific heat capacity, kJ/(kg·K); T represents temperature, °C; h denotes the specific enthalpy, kJ/kg; the subscripts "hf," "wf," "Pre1," "Pre2," "in," "out," "gen," and "tot" denote geothermal brine, R245fa, preheater I, preheater II, inlet, outlet, vapor generator, and total, respectively. The subscript numbers represent the BFC working state points shown in **Figure 2**.

The heat transferred in the condenser is given by

$$Q_{\mathrm{con}} = m_{\mathrm{cf}} c_{\mathrm{p,cf}} \left(T_{\mathrm{cf,out}} - T_{\mathrm{cf,in}}\right) = m_3 \left(h_3 - h_4\right) \tag{5}$$

where the subscripts "con" and "cf" denote the condenser and cooling water, respectively.

Mass balance equations of BFC are given by

$$m_5 = m_1\left(qu_{\mathrm{gen}} + \left(1 - qu_{\mathrm{gen}}\right)qu_{\mathrm{fsh}}\right) \tag{6}$$

$$m_2 = m_1 qu_{\mathrm{gen}} \tag{7}$$

$$m_1 = m_2 + m_{10} \tag{8}$$

$$m_{10} = m_{11} + m_{12} \tag{9}$$

$$m_{11} = m_{10} qu_{\mathrm{fsh}} + m_{12} \tag{10}$$

$$m_3 = m_2 + m_{11} = m_{\mathrm{wf}} qu_{\mathrm{gen}} + m_{\mathrm{wf}}\left(1 - x_{\mathrm{gen}}\right)x_{\mathrm{fsh}} \tag{11}$$

$$m_5 = m_4 = m_3 \tag{12}$$

where m is the mass flow rate, kg/s; qu is the dryness degree of the working fluid at the evaporator outlet. The subscript "fsh" is the flash drum.

The power output in the high-pressure stage of the expander is given by:

$$\begin{aligned} W_{\mathrm{exp}} &= m_2 \left(h_2 - h_3\right) + m_{11} \left(h_{11} - h_3\right) \\ &= m_2 \left(h_2 - h_{2,s}\right)\eta_{\mathrm{exp}} + m_{11} \left(h_{11} - h_{11,s}\right)\eta_{\mathrm{exp}} \end{aligned} \tag{13}$$

where the subscripts "exp" and "s" denote expander and isentropic, respectively.

The consumed power of the working fluid pump I is given by:

$$W_{\mathrm{pp1}} = m_5 \left(h_5 - h_4\right) = m_5 \left(h_{4,s} - h_4\right)/\eta_{\mathrm{pp}} \tag{14}$$

$$m_5 = m_4 = m_3 \tag{15}$$

The consumed power of the working fluid pump II is given by:

$$W_{\mathrm{pp2}} = m_{12} \left(h_7 - h_{12}\right) = m_{12} \left(h_{12,s} - h_{12}\right)/\eta_{\mathrm{pp}} \tag{16}$$

where the subscript "pp" denotes the working fluid pump.

The net power output of the BFC is given by

$$W_{\mathrm{net}} = W_{\mathrm{exp}} - W_{\mathrm{pp1}} - W_{\mathrm{pp2}} \tag{17}$$

where the subscript "net" denotes net power output.

The thermal efficiency is expressed by:

$$\eta_{\mathrm{th}} = W_{\mathrm{net}}/Q_{\mathrm{tot}} \tag{18}$$

The input exergy is defined as:

$$E_{\mathrm{in}} = m_{\mathrm{hf}} c_{\mathrm{p,hf}} \left[\left(T_{\mathrm{hf,in}} - T_{\mathrm{hf,out}}\right) - T_0 \ln\left(\frac{T_{\mathrm{hf,in}}}{T_{\mathrm{hf,out}}}\right)\right] \tag{19}$$

Considering the inherent qualitative difference between heat and mechanical power, the exergy analysis is applied to analyze the quality of energy or the potential of thermal energy. The exergy efficiency is given by:

$$\eta_{\mathrm{ex}} = W_{\mathrm{net}}/E_{\mathrm{in}}$$

The heat recovery rate is used to indicate the utilization degree of geothermal water, as given by:

$$UR = \frac{T_{\mathrm{hf,in}} - T_{\mathrm{hf,out}}}{T_{\mathrm{hf,in}} - \left(\frac{m_5 T_5 + m_7 T_7}{m_5 + m_7} + pp_{\mathrm{eva}}\right)} \tag{20}$$

where UR is the heat recovery rate; pp_{eva} is pinch point temperature difference, ˚C.

2.2.2 Plate-Type Heat Exchanger Model

The plate-type heat exchangers are applied as the evaporator and the condenser due to the compactness, flexibility, higher heat transfer coefficient, and lower refrigerator charge. And the heat transfer area of the evaporator is calculated sectionalized.

The heat transfer rate of the evaporator is given by:

$$Q = UA\Delta T_m \tag{21}$$

where U is the overall heat transfer coefficient, W/(m^2·˚C); A is the heat transfer area, m^2; ΔT_{m} is the log mean temperature difference between the geothermal brine and R245fa, ˚C.

$$\Delta T_m = \frac{\Delta T_{\max} - \Delta T_{\min}}{\ln\left(\Delta T_{\max}/\Delta T_{\min}\right)} \tag{22}$$

The heat transfer coefficient of the plate-type heat exchanger can be calculated by:

$$\frac{1}{U_i} = \frac{1}{\alpha_{i,\mathrm{hs}}} + \frac{\delta}{\lambda} + \frac{1}{\alpha_{i,\mathrm{cs}}} \tag{23}$$

where $\alpha_{\mathrm{i,hs}}$ is the heat transfer coefficient on the geothermal brine side, W/(m^2·˚C); δ is the plate-type heat exchanger fin thickness, m; λ is heat conductivity coefficient, W/(m·˚C); $\alpha_{\mathrm{i,cs}}$ is the heat transfer coefficient on the R245fa side, W/(m^2˚C).

The heat transfer coefficient of the single-phase flow section is obtained by the following equation (Chisholm and Wanniarachchi, 1992).

$$Nu = \frac{\alpha_{i,\mathrm{hs/cs}} d_{\mathrm{h}}}{\lambda} = 0.724\left(\frac{6\beta}{\pi}\right)^{0.646} Re^{0.583} Pr^{1/3} \tag{24}$$

where d_{h} is hydraulic diameter, m; β is plate-type heat exchanger corrugation angle, ˚; Nu is Nusselt number; Re is Reynolds number; Pr is Prandtl number.

$$Re = Gd_h/\mu \tag{25}$$

where G is R245fa mass velocity, kg/(m^2·s); μ is viscosity, Pa·s.

$$Pr = \frac{C_p \eta}{\lambda} \tag{26}$$

The convection heat transfer coefficient of the gas-liquid two-phase fluid is calculated by the correlation presented by Yan and Lin (1999).

$$Nu = \frac{\alpha_{\mathrm{i,cs}} d_{\mathrm{h}}}{\lambda} = 1.926 \mathrm{Pr}^{1/3} \mathrm{Re}_{\mathrm{eq}}^{0.5}\, \mathrm{Bo}_{\mathrm{eq}}^{0.3}\left[1 - x_{\mathrm{m}} + x_{\mathrm{m}}\left(\frac{\rho_{\mathrm{l}}}{\rho_{\mathrm{v}}}\right)^{0.5}\right] \tag{27}$$

where x_{m} denotes the R245fa vapor quality, the subscript "eq" denotes equivalent.

The heat transfer area of the condenser is also calculated sectionalized.

The heat transfer coefficient of the single-phase flow region is obtained by **Eq. 24**. The convection heat transfer coefficient of the condenser two-phase flow region is given by

$$Nu = \frac{\alpha_{i,\mathrm{hs}} d_{\mathrm{h}}}{\lambda} = 4.118\mathrm{Re}^{0.4}\mathrm{Pr}^{1/3} \tag{28}$$

2.2.3 Economic Model

The chemical engineering plant cost (CEPCI) model is used to conduct economic analysis. The investment cost of the heat exchangers is given by (Hou et al., 2018):

$$C_{\mathrm{hx}} = \frac{\mathrm{CEPCI}_{2019}}{\mathrm{CEPCI}_{2001}} F_{\mathrm{s}} C_{\mathrm{hx}}^{0} \left(B_{1,\mathrm{hx}} + B_{2,\mathrm{hx}} F_{\mathrm{m,hx}} F_{\mathrm{p,hx}}\right) \tag{29}$$

where C_{hx} is the heat exchanger investment cost, \$; CEPCI_{2001} and CEPCI_{2019} are 2001 and 2019 chemical engineering plant cost index, respectively; *Fs* is an additional factor; $C_{\mathrm{hx}}{}^{0}$ is the basic investment cost, \$; $B_{1,\mathrm{hx}}$, $B_{2,\mathrm{hx}}$ are the constants; $F_{\mathrm{m,hx}}$ is the material factor; $F_{\mathrm{p,hx}}$ is the pressure factor.

$$\log C_{\mathrm{hx}}^{0} = K_{1,\mathrm{hx}} + K_{2,\mathrm{hx}} \log A_{\mathrm{hx}} + K_{3,\mathrm{hx}} \left(\log A_{\mathrm{hx}}\right)^{2} \tag{30}$$

$$\log F_{\mathrm{p,hx}} = C_{1,\mathrm{hx}} + C_{2,\mathrm{hx}} \log P_{\mathrm{hx}} + C_{3,\mathrm{hx}} \left(\log P_{\mathrm{hx}}\right)^{2} \tag{31}$$

where $K_{1,\mathrm{hx}}$, $K_{2,\mathrm{hx}}$, $C_{1,\mathrm{hx}}$, $C_{2,\mathrm{hx}}$, and $C_{3,\mathrm{hx}}$ are the constants; A_{hx} is the plate-type heat exchanger heat transfer area, m^2; P_{hx} is the plate-type heat exchanger design pressure, bar.

The working fluid pump investment cost is given by:

$$C_{\mathrm{pp}} = \frac{\mathrm{CEPCI}_{2019}}{\mathrm{CEPCI}_{2001}} F_{\mathrm{s}} C_{\mathrm{pp}}^{0} \left(B_{1,\mathrm{pp}} + B_{2,\mathrm{pp}} F_{\mathrm{m,pp}} F_{\mathrm{p,pp}}\right) \tag{32}$$

where C_{pp} is working fluid pump capitalized cost, \$; $F_{\mathrm{m,pp}}$ is an additional factor; $F_{\mathrm{p,pp}}$ is pressure factor, which is calculated as follows; $C_{\mathrm{pp}}{}^{0}$ is the basic cost that is calculated as follows, \$;

$$\log C_{\mathrm{pp}}^{0} = K_{1,\mathrm{pp}} + K_{2,\mathrm{pp}} \log W_{\mathrm{pp}} + K_{3,\mathrm{pp}} \left(\log W_{\mathrm{pp}}\right)^{2} \tag{33}$$

$$\log F_{\mathrm{p,pp}} = C_{1,\mathrm{pp}} + C_{2,\mathrm{pp}} \log P_{\mathrm{pp}} + C_{3,\mathrm{pp}} \left(\log W_{\mathrm{pp}}\right)^{2} \tag{34}$$

where $B_{1,\mathrm{pp}}$, $B_{2,\mathrm{pp}}$, $K_{1,\mathrm{pp}}$, $K_{2,\mathrm{pp}}$, $K_{3,\mathrm{pp}}$, $C_{1,\mathrm{pp}}$, $C_{2,\mathrm{pp}}$, and $C_{3,\mathrm{pp}}$ are the constants; P_{pp} is the pressure, bar; W_{pp} is the consumed power, kW.

The expander investment cost is given by:

$$C_{\mathrm{exp}} = \frac{\mathrm{CEPCI}_{2019}}{\mathrm{CEPCI}_{2001}} F_{\mathrm{s}} C_{\mathrm{exp}}^{0} F_{\mathrm{m,exp}} \tag{35}$$

$$\log C_{\mathrm{exp}}^{0} = K_{1,\mathrm{exp}} + K_{2,\mathrm{exp}} \log W_{\mathrm{exp}} + K_{3,\mathrm{pp}} \left(\log W_{\mathrm{exp}}\right)^{2} \tag{36}$$

where C_{exp} is investment cost of expander, \$; $F_{\mathrm{m,exp}}$ is pressure factor; $C_{\mathrm{exp}}{}^{0}$ is the basic cost; $K_{1,\mathrm{exp}}$, $K_{2,\mathrm{exp}}$, $K_{3,\mathrm{exp}}$ are the constants.

The investment cost of the separator and the flashing tank is given by (Chisholm and Wanniarachchi, 1992):

$$C_{\mathrm{sep}}\left(C_{\mathrm{fsh}}\right) = \left(2.25 + 1.82 \times 3.2\right) \times 10^{\mathrm{sf}} \tag{37}$$

$$sf = 3.4974 + 0.4483 \log V + 0.1074 \log V \tag{38}$$

where C_{sep} and C_{fsh} are investment costs of the separator and the flashing tank, respectively, \$; *V* is the volume, m^3.

TABLE 2 | Input parameters of CEPCI model (Imran et al., 2014; Hou et al., 2018).

Parameter	Value	Parameter	Value
CEPCI_{2001}	394	$F_{\mathrm{m,pp}}$	2.20
CEPCI_{2019}	607.5	$K_{1,\mathrm{pp}}$	3.389
F_{s}	1.70	$K_{2,\mathrm{pp}}$	0.536
$B_{1,\mathrm{hx}}$	0.96	$B_{1,\mathrm{pp}}$	1.89
$B_{2,\mathrm{hx}}$	1.21	$B_{2,\mathrm{pp}}$	1.35
$F_{\mathrm{m,hx}}$	2.40	$C_{1,\mathrm{pp}}$	−0.3935
$K_{1,\mathrm{hx}}$	4.66	$C_{2,\mathrm{pp}}$	0.3957
$K_{2,\mathrm{hx}}$	−0.1557	$C_{3,\mathrm{pp}}$	−0.00226
$K_{3,\mathrm{hx}}$	0.1547	$F_{\mathrm{m,exp}}$	3.50
$C_{1,\mathrm{hx}}$	0.00	$K_{1,\mathrm{exp}}$	2.2659
$C_{2,\mathrm{hx}}$	0.00	$K_{2,\mathrm{exp}}$	1.4398
$C_{3,\mathrm{hx}}$	0.00	$K_{3,\mathrm{exp}}$	−0.1776
		$K_{3,\mathrm{pp}}$	0.1538

The investment cost of the circulating water pump is given by (Yan and Lin, 1999):

$$C_{\mathrm{watpp}} = 630 W_{\mathrm{watpp}}^{0.4} \tag{39}$$

$$W_{\mathrm{watpp}} = m_{\mathrm{wat}} g H_{\mathrm{watpp}} / \left(1000 \eta_{\mathrm{watpp}}\right) \tag{40}$$

where W_{watpp} is the consumed mechanical power, kW; *g* is the acceleration of gravity, $\mathrm{m/s}^2$; H_{watpp} is the hydraulic head, m; η_{watpp} is the efficiency of the water pump.

The total investment cost is given by:

$$C_{\mathrm{tot}} = C_{\mathrm{hex}} + C_{\mathrm{exp}} + C_{\mathrm{pp}} + C_{\mathrm{sep}} + C_{\mathrm{fsh}} + C_{\mathrm{watpp}} + C_{\mathrm{well}} \tag{41}$$

where C_{well} is the mining rights cost, \$.

The operation and maintenance cost is given by (Hou et al., 2018):

$$C_{\mathrm{om}} = 6\% * C_{\mathrm{tot}} \tag{42}$$

The operation cost of the circulating water pump is given by:

$$C_{\mathrm{OPR}} = W_{\mathrm{watpp}} C_{\mathrm{ele}} TPY \tag{43}$$

where C_{ele} is unitary cost of the electricity, \$/kW; *TPY* is the annual operating time, h.

In consideration of time value of money, the payback period is calculated by:

$$W_{\mathrm{net}} TPY C_{\mathrm{ele}} - C_{\mathrm{om}} - C_{\mathrm{OPR}}\left(\left(1+i\right)^{pb} - 1/i\right) = C_{\mathrm{tot}} \left(1+i\right)^{\left(pb-1\right)} \tag{44}$$

where *pb* is payback period, year; *i* is interest rate, assumed to be 5%.

The input parameters of CEPCI model are listed in **Table 2**.

Based on the established thermo-economic model above, all the codes were developed. The R245fa thermo-properties are obtained by NIST REFPROP 9.0 (Lemmon et al., 2013).

3 MODEL VALIDATION

Based on the present and Wang et al. (2016) thermodynamic model, the variations of thermal efficiency (η_{th}) and net power

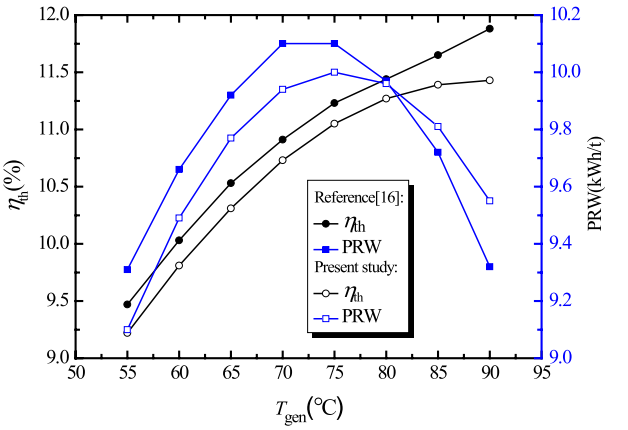

FIGURE 3 | Validation of the present model.

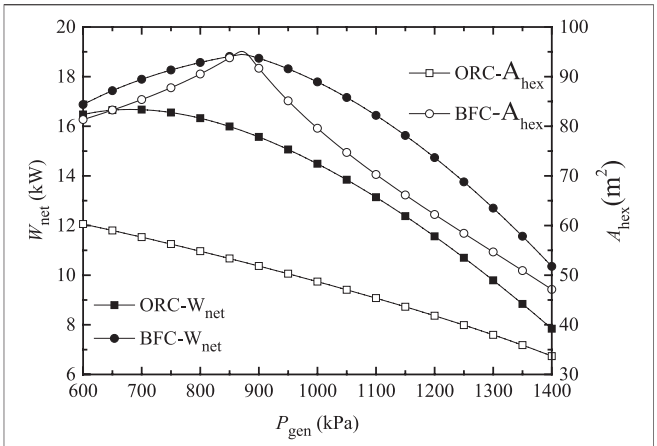

FIGURE 4 | Variations of W_{net} and A_{hex} for the ORC and BFC with P_{gen}.

TABLE 3 | Input parameters of thermo-economic comparison.

Parameters	Value
Geothermal water inlet temperature (°C)	120°C
Geothermal water mass flow rate (kg/s)	1.0
Cooling water inlet temperature (°C)	20°C
Expander efficiency	65%
Work fluid pump efficiency	50%
Ambient temperature (°C)	20°C
Generation pressure (kPa)	1000
Dryness degree	0.3
Condensation temperature (°C)	30°C
Flashing temperature (°C)	$(T_{eva} + T_{con})/2$
Plate thickness (mm)	0.6
Plate spacing (mm)	2
Corrugation pitch (mm)	7.2
Chevron angle (°)	45

output per ton of geothermal water (*PRW*) against generation temperature (T_{gen}) under the same operating conditions are illustrated in **Figure 3**. As can be seen, the maximum deviations of η_{th} and *PRW* between the results of the present model and Wang et al. (2016). are less than 3.8 and 2.5%, respectively. The comparison shows a good agreement between the present model and Wang et al. (2016). That is to say the present model can be used to simulate the system performance within an acceptable error range.

4 RESULTS AND DISCUSSION

4.1 Thermo-Economic Comparison Between ORC and BFC

Based on the model developed above, the thermo-economic comparison between ORC and BFC is conducted. The typical input parameters and boundary conditions investigated are listed in **Table 3**. Note that the given efficiencies of the expander and the pump are far lower than those set in literatures (Meng et al., 2017; Yang et al., 2017), which will be more closer to reality. The

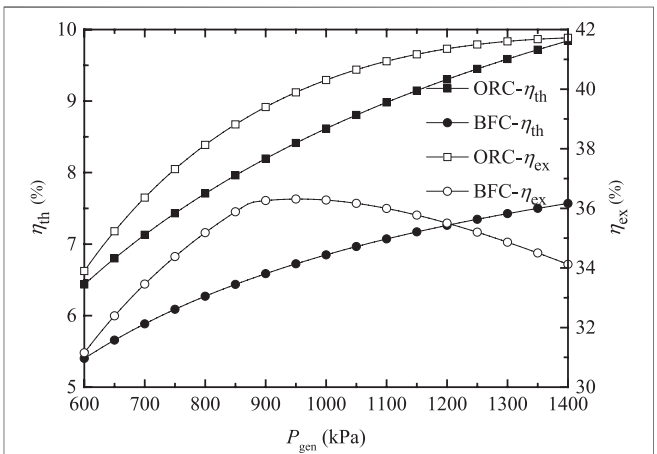

FIGURE 5 | Variations of η_{th} and η_{ex} for the ORC and BFC with P_{gen}.

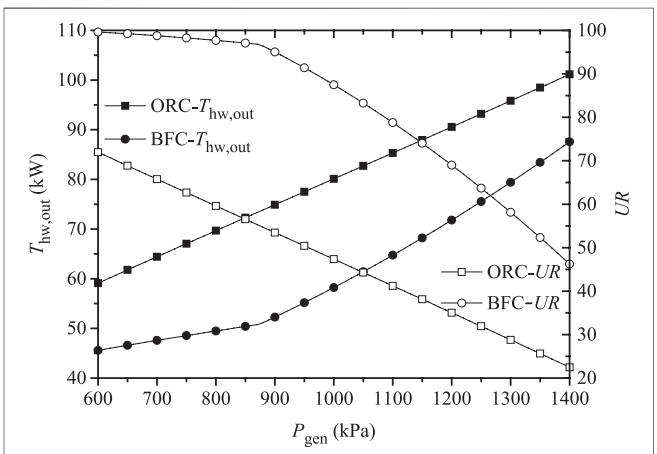

FIGURE 6 | Variations of $T_{th,out}$ and *UR* for the ORC and BFC with P_{gen}.

TABLE 4 | Input parameters of case study.

Parameter	Value
Geothermal water inlet temperature (°C)	91
Geothermal water mass flow rate (kg/s)	63.4
Cooling water inlet temperature (°C)	14.4
Condensation temperature (°C)	30
Expander efficiency	0.65
Working fluid pump efficiency	0.5
Circulating water pump efficiency	0.8
Interest rate	0.1
Annual operation time (h)	8000
Life time (year)	30

variations of W_{net} and A_{hex} for the ORC and BFC with generation pressure (P_{gen}) are displayed in **Figure 4**. As can be seen, with the rising of P_{gen}, both the W_{net}, and A_{hex} of the ORC are decreased, while the W_{net} and A_{hex} of the BFC first increase and then decrease. The ORC and BFC have different operating characteristics. The variation of W_{net} for the BFC is mainly due to that for a specific condensation temperature, an increase in P_{gen} leads to rising of the specific enthalpy drop across the expander, but meanwhile it will drop the working fluid mass flow rate. With the interaction between the two influences, an optimal P_{gen} exists and maximizes W_{net}, which is well in conformity with the results reported by Edrisi and Michaelides (2013). The optimal P_{gen} is 870 kPa, at which W_{net} and A_{hex} achieve the maximum. As can be seen the W_{net} and A_{hex} of the BFC are always higher than those of the ORC. With the rising of P_{gen}, the ratio of W_{net} of BFC to that of ORC increases basically linearly. The W_{net} of BFC is 32% larger than that of ORC with P_{gen} of 1400 kPa. Nevertheless, the ratio of A_{hex} of the BFC to that of the ORC first rises then declines, after reaching the peak value (1.8) at 870 kPa. To sum up, the BFC produces more work compared with the ORC. In the meantime, the heat exchangers investment cost of the BFC is much larger.

The variations of η_{th} and η_{ex} for the ORC and BFC with P_{gen} are depicted in **Figure 5**. As expected, the η_{th} of the ORC and the BFC increase with the rising P_{gen}, presenting the same behavior. The η_{ex} of the ORC is increased as P_{gen} increases. While the η_{ex} of the BFC first rises and subsequently decreases, and an optimum P_{gen} (950 kPa) occurs, at which the η_{ex} obtains the maximum value. The dryness degree of the working fluid at the evaporator exit is a fixed constant in the present study. The heat transfer temperature difference between the working fluid and the geothermal water is decreased with the increasing P_{gen}, leading to the rising of the reinjection temperature of geothermal water. As a consequence, the input exergy is decreased. The variation of W_{net} with P_{gen} has been already shown in **Figure 4**. With the interaction between the two effects, there exists an optimum P_{gen} at which the η_{ex} obtains the maximum value. It is obvious that the η_{th} and η_{ex} of the ORC are higher than those of the BFC. When P_{gen} is 1100 kPa, the η_{th} and η_{ex} of the ORC are 1.26 and 1.14 times as large as those of the BFC.

The heat recovery efficiency is an important indicator for the low-grade waste heat utilization system. For the nonflowing geothermal energy, the acquiring of geothermal water requires a lot of power consumption for the geothermal water pump. Full use of the geothermal water is beneficial. It is of practical significance to evaluate the system performance with the heat recovery efficiency as criteria. The variations of geothermal water injection temperature ($T\text{th}_{,out}$) and heat recovery rate (UR) for the ORC and BFC with P_{gen} are depicted in **Figure 6**. As can be discovered, the $T\text{th}_{,out}$ of the BFC is 15–20°C lower than that of the ORC. And the UR of BFC is always much larger than that of ORC. The UR of BFC is 1.96 times as much as that of ORC. As can be seen, the BFC can achieve the full use of low-grade energy. After comprehensive consideration, the BFC system obtains the larger net power output, sacrificing its efficiency.

4.2 Case Study of the ORC and BFC in Fengshun Geothermal Plant

The first geothermal power generation station with a capacity of 300 kW was established in 1970 in Dengwu village of Fengshun county, Guangdong province, which was established by the Guangzhou Institute of Energy Conversion. The establishment of Fengshun power plant marked that China became the 8th country owning the geothermal energy power generation technology for realistic operation. The geothermal well is approximately 800 m deep and produces geothermal water at 91°C. The geothermal water is pumped to the flashing tank with the mass flow rate of 63.4 kg/s. The cooling water from the river nearby is used to cool the turbine exhaust. The power station had retired since the last year and finished the historical mission. From the above-mentioned investigation, the BFC has the advantage of higher utilization rate of geothermal water

TABLE 5 | Economic comparison of the ORC and BFC.

Parameters	ORC			BFC		
Generation pressure (kPa)	660	700	740	660	700	740
Condensation temperature (°C)	30	30	30	30	30	30
Pinch point temperature difference (°C)	5	5	5	5	5	5
Mining rights cost (million yuan)	8	8	8	8	8	8
Total investment cost (million yuan)	1.55	1.53	1.50	2.12	2.36	2.93
Maintenance cost (thousand yuan)	93	92	90	127	141	176
Electric charge of water pump (million yuan)	0.29	0.28	0.28	0.32	0.32	0.33
Net power output (kW)	372	328	281	470	461	473
Power output per unit geothermal water (kWh/t)	1.63	1.44	1.23	2.06	2.02	2.07
Payback period (year)	7.9	10.0	14.3	6.0	6.5	6.9

compared with the ORC due to lower reinjection temperature. The preliminary economic feasibility study of BFC will be investigated based on working condition in Fengshun power plant. The input parameters of the economic simulation are listed in **Table 4**. The economic comparison of the ORC and BFC is presented in **Table 5**. As can be seen, the total investment cost, maintenance cost, and electric charge of circulating water pump for the BFC are all higher than those of the ORC. Meanwhile, with the P_{gen} of 600, 700, and 740 kPa, the W_{net} of the BFC is 1.26, 1.41, and 1.68 times as large as those of ORC, and compared with the ORC, the payback period of the BFC is shortened by 1.9, 3.5, and 7.4 years, respectively. The payback period of BFC is just 6.0 years under the P_{gen} of 600 kPa. It is indicated that the BFC exhibits better economic benefits.

5 CONCLUSION

In the present article, the thermo-economic comparison between the ORC and BFC for geothermal energy is conducted. The main contribution is the performance contrast from the viewpoint of thermodynamic and economic, simutaneously. And the preliminary discussion of the economic feasibility of BFC system applying in FengShun geothermal field. According to the investigation, several conclusions can be drawn as follows:

1) With the rising generation pressure, the net power output and the heat exchanger area of the BFC first increase and then decrease. There exists the optimum generation pressure for the BFC. The BFC has larger net power output and heat exchanger area than ORC.
2) The ORC and BFC yield different operating characteristics. The thermal efficiency and exergy efficiency of ORC are 1.26 and 1.14 times as large as those of the BFC with the generation pressure of 1,100 kPa.
3) The geothermal tail water temperature of the BFC is much lower than that of the ORC, approximately 15–20°C. The heat recovery rate of the BFC is always much larger than that of the ORC. The heat recovery rate of BFC is 1.96 times as much as that of the ORC.
4) With the Fengshun power plant as a case study, under the generation pressure of 600, 700, and 740 kPa, the net power output of the BFC is 1.26, 1.41, and 1.68 times as large as those of the ORC, and compared with the ORC, the payback period of the BFC is shortened by 1.9, 3.5, and 7.4 years, respectively. The payback period of BFC is only 6.0 years under the generation pressure of 600 kPa. It is indicated that the BFC exhibits excellent economic benefits, especially in the nonflowing geothermal well (Berhane et al., 2009; Mosaffa et al., 2016; Zhao and Wang, 2016; Rayegan and Tao, 2011).

DATA AVAILABILITY STATEMENT

The raw data supporting the conclusions of this article will be made available by the authors, without undue reservation.

AUTHOR CONTRIBUTIONS

YZ: Conceptualization. BD: Formal analysis. SC: Methodology. JZ: Investigation. YG: Writing—review and editing. XB: Supervision. HL: Software, Writing—review and editing. LW: Methodology, Writing—original draft.

ACKNOWLEDGMENTS

The authors gratefully acknowledge the financial supports provided by the Natural Science Foundation of Guangdong Province (No. 2021A1515011763), Science and Technology Plan Project of Guangzhou (No. 202102020301) and China Postdoctoral Science Foundation (No. 2020M681799).

REFERENCES

Astolfi, M., Romano, M. C., Bombarda, P., and Macchi, E. (2014). Binary ORC (Organic Rankine Cycles) Power Plants for the Exploitation of Medium-Low Temperature Geothermal Sources - Part B: Techno-Economic Optimization. *Energy* 66, 435–446. doi:10.1016/j.energy.2013.11.057

Basaran, A., and Ozgener, L. (2013). Investigation of the Effect of Different Refrigerants on Performances of Binary Geothermal Power Plants. *Energ. Convers. Manage.* 76, 483–498. doi:10.1016/j.enconman.2013.07.058

Berhane, H. G., Gonzalo, G. G., Laureano, J., and Dieter, B. (2009). Design of Environmentally Conscious Absorption Cooling Systems via Multi-Objective Optimization and Life Cycle Assessment. *Appl. Energ.* 86, 1712–1722. doi:10.1016/j.apenergy.2008.11.019

Cao, Y., and Dai, Y. (2017). Comparative Analysis on Off-Design Performance of a Gas Turbine and ORC Combined Cycle under Different Operation Approaches. *Energ. Convers. Manage.* 135, 84–100. doi:10.1016/j.enconman.2016.12.072

Chisholm, D., and Wanniarachchi, A. S. (1992). Maldistribution in Single-Pass Mixed- Channel Plate Heat Exchangers. *Compact Heat Exchangers Power Process. Industries, Htd-asme* 201, 95–99.

Edrisi, B. H., and Michaelides, E. E. (2013). Effect of the Working Fluid on the Optimum Work of Binary-Flashing Geothermal Power Plants. *Energy* 50, 389–394. doi:10.1016/j.energy.2012.10.025

Franco, A., and Vaccaro, M. (2014). Numerical Simulation of Geothermal Reservoirs for the Sustainable Design of Energy Plants: a Review. *Renew. Sustain. Energ. Rev.* 30, 987–1002. doi:10.1016/j.rser.2013.11.041

Hou, S., Zhou, Y., Yu, L., Zhang, F., and Cao, S. (2018). Optimization of the Combined Supercritical CO2 Cycle and Organic Rankine Cycle Using Zeotropic Mixtures for Gas Turbine Waste Heat Recovery. *Energ. Convers. Manage.* 160, 313–325. doi:10.1016/j.enconman.2018.01.051

Imran, M., Park, B. S., Kim, H. J., Lee, D. H., Usman, M., and Heo, M. (2014). Thermo-economic Optimization of Regenerative Organic Rankine Cycle for Waste Heat Recovery Applications. *Energ. Convers. Manage.* 87, 107–118. doi:10.1016/j.enconman.2014.06.091

Kong, Y., Pang, Z., Shao, H., Hu, S., and Kolditz, O. (2014). Recent Studies on Hydrothermal Systems in China: a Review. *Geotherm Energy* 2, 19. doi:10.1186/s40517-014-0019-8

Lemmon, E. W., Huber, M. H., and McLinden, M. O. (2013). *REFPROP, NIST Standard Reference Database 23*. USA: National Institute of Standards and Technology. Version 9.1.

Li, T., Yuan, Z., Li, W., Yang, J., and Zhu, J. (2016). Strengthening Mechanisms of Two-Stage Evaporation Strategy on System Performance for Organic Rankine Cycle. *Energy* 101, 532–540. doi:10.1016/j.energy.2016.02.068

Li, Y.-M., Hung, T.-C., Wu, C.-J., Su, T.-Y., Xi, H., and Wang, C.-C. (2021). Experimental Investigation of 3-kW Organic Rankine Cycle (ORC) System Subject to Heat Source Conditions: A New Appraisal for Assessment. *Energy*, 2021, 217:119342. doi:10.1016/j.energy.2020.119342

Liu, X., Li, H., Bu, X., Wang, L., Xie, N., and Zeng, J. (2018). Performance Characteristics and Working Fluid Selection for Low-Temperature Binary-Flashing Cycle. *Appl. Therm. Eng.* 141, 51–60. doi:10.1016/j.applthermaleng.2018.05.106

Mallapaty, S. (2020). How China Could Be Carbon Neutral by Mid-century. *Nature* 586, 482–483. doi:10.1038/d41586-020-02927-9

Meng, F., Zhang, H., Yang, F., Hou, X., Lei, B., Zhang, L., et al. (2017). Study of Efficiency of a Multistage Centrifugal Pump Used in Engine Waste Heat Recovery Application. *Appl. Therm. Eng.* 110, 779–786. doi:10.1016/j.applthermaleng.2016.08.226

Miao, Z., Xu, J., and Zhang, K. (2017). Experimental and Modeling Investigation of an Organic Rankine Cycle System Based on the Scroll Expander. *Energy* 134, 35–49. doi:10.1016/j.energy.2017.06.001

Michaelides, E. E. (2016). Future Directions and Cycles for Electricity Production from Geothermal Resources. *Energ. Convers. Manage.* 107, 3–9. doi:10.1016/j.enconman.2015.07.057

Michaelides, E. E., and Scott, G. J. (1984). A Binary-Flashing Geothermal Power Plant. *Energy* 9, 323–331. doi:10.1016/0360-5442(84)90103-8

Mosaffa, A. H., Garousi Farshi, L., and Farshi, L. G. (2016). Exergoeconomic and Environmental Analyses of an Air Conditioning System Using thermal Energy Storage. *Appl. Energ.* 162, 515–526. doi:10.1016/j.apenergy.2015.10.122

Rayegan, R., and Tao, Y. X. (2011). A Procedure to Select Working Fluids for Solar Organic Rankine Cycles (ORCs). *Renew. Energ.* 36, 659–670. doi:10.1016/j.renene.2010.07.010

Shi, H., and Michaelides, E. E. (1989). Binary Dual-Flashing Geothermal Power Plants. *Int. J. Energ. Res.* 13, 127–135. doi:10.1002/er.4440130202

Sun, X., Liu, L., Dong, Y., Zhuang, Y., Li, J., Du, J., et al. (2021). Multi-objective Optimization and Thermo-Economic Analysis of an Enhanced Compression-Absorption cascade Refrigeration System and ORC Integrated System for Cooling and Power Cogeneration. *Energ. Convers. Manage.* 236, 114068. doi:10.1016/j.enconman.2021.114068

Van, L. L., Michel, F., Abdelhamid, K., and Sandrine, P. P. (2014). Performance Optimization of Low-Temperature Power Generation by Supercritical ORCs (Organic Rankine Cycles) Using Low GWP (Global Warming Potential) Working Fluids. *Energy* 67, 513–526. doi:10.1016/j.energy.2013.12.027

Wang, L., Bu, X., and Li, H. (2019). Investigation on Geothermal Binary-Flashing Cycle Employing Zeotropic Mixtures as Working Fluids. *Geotherm Energy* 7 (1), 36. doi:10.1186/s40517-019-0153-4

Wang, L., Bu, X., Li, H., Wang, H., and Ma, W. (2018). Working Fluids Selection for Flashing Organic Rankine Regeneration Cycle Driven by Low-Medium Heat Source. *Environ. Prog. Sustain. Energ.* 37, 1201–1209. doi:10.1002/ep.12774

Wang, Y. X., Wang, L. B., Li, H. S., and Bu, X. B. (2016). Thermodynamic Calculation and Optimization of Geothermal Power Generation in Ganzi. *J. Harbin Eng. Univ.* 37, 873–877. doi:10.11990/jheu.201504026

Yan, Y.-Y., and Lin, T.-F. (1999). Evaporation Heat Transfer and Pressure Drop of Refrigerant R-134a in a Plate Heat Exchanger. *J. Heat Transfer* 121, 118–127. doi:10.1115/1.2825924

Yang, M.-H., Yeh, R.-H., and Hung, T.-C. (2017). Thermo-economic Analysis of the Transcritical Organic Rankine Cycle Using R1234yf/R32 Mixtures as the Working Fluids for Lower-Grade Waste Heat Recovery. *Energy* 140, 818–836. doi:10.1016/j.energy.2017.08.059

Yu, S., Hu, X., Li, L., and Chen, H. (2020). Does the Development of Renewable Energy Promote Carbon Reduction? Evidence from Chinese Provinces. *J. Environ. Manage.* 268, 110634. doi:10.1016/j.jenvman.2020.110634

Yuan, Z., and Michaelides, E. E. (1993). Binary-flashing Geothermal Power Plants. *J. Energ. Resour. Tech.* 115, 232–236. doi:10.1115/1.2905999

Zhao, Y., and Wang, J. (2016). Exergoeconomic Analysis and Optimization of a Flash-Binary Geothermal Power System. *Appl. Energ.* 179, 159–170. doi:10.1016/j.apenergy.2016.06.108

Conflict of Interest: YZ, BD, and SC were employed by the company Powerchina HuaDong Engineering Corporation Limited.

The remaining authors declare that the research was conducted in the absence of any commercial or financial relationships that could be construed as a potential conflict of interest.

Publisher's Note: All claims expressed in this article are solely those of the authors and do not necessarily represent those of their affiliated organizations, or those of the publisher, the editors and the reviewers. Any product that may be evaluated in this article, or claim that may be made by its manufacturer, is not guaranteed or endorsed by the publisher.

NOMENCLATURE

Symbols

A area (m^2)

Bo boiling number

C investment cost ($)

c_p specific heat capacity ($kJ/kg{\cdot}K^{-1}$)

D_h hydraulic diameter (m)

E available solar exergy (kW)

g acceleration of gravity (m/s^2)

G mass velocity ($kg/(m^2\ s)$)

h specific enthalpy (kJ/kg), convection heat transfer coefficient ($W/m^2{\cdot}K^{-1}$)

H hydraulic head (m)

i interest rate

m mass flow rate (kg/s)

Nu Nusselt number

P pressure (kPa)

pb payback period (year)

pp pinch point temperature difference (°C)working fluid pump

Pr Prandtl number

Q heat transfer rate (kW)

qu dryness degree of the working fluid

R thermal resistance

Re Reynolds number

T temperature (°C)

TPY annual operating time (h)

U overall heat transfer coefficient ($W/(m^2{\cdot}K)$)

UR heat recovery rate

V volume

W work (kW)

x quality of the working fluid

ΔT logarithmic temperature difference (°C)

Greek

η efficiency

α heat transfer coefficient ($W/(m^2{\cdot}K)$)

λ coefficient of thermal conductivity ($W/(m{\cdot}K)$)

β corrugation anlge (°)

ρ density (kg/m^3)

μ viscosity (Pa·s)

ε isotropic efficiency

Φ enlargement factor of the corrugated plates

Subscripts

1, 2,. . ., 4 state points

cf cooling water

cs cold fluid side

con condenser

ele electriciy

eq equivalent

eva evaporator

ex exergy

exp expander

fsh flash drum

gen vapor generator

hs hot fluid side

hx heat exchanger

in inlet

net net power output

om operation and maintenance

out outlet

pp working fluid pump

s isentropic process

sep separator

tot total

th thermal

watpp water pump

well well

wf working fluid

Acronyms

BFC binary flashing cycle

CEPCI chemical engineering plant cost index

GWP global warming potential

ORC Organic Rankine Cycle

ODP ozone depletion potential

frontiers in Earth Science

ORIGINAL RESEARCH
published: 03 November 2021
doi: 10.3389/feart.2021.758605

Characteristics of Terrestrial Heat Flow and Lithospheric Thermal Structure in Typical Intermountain Basin at the Eastern Foot of Yanshan Mountain, North China

Feng Liu[1,2,3], *Andong Wang*[4], *Guiling Wang*[1,3]*, *Wei Zhang*[1,3], *Yuzhong Liao*[1,3] *and Jue Tong*[5]

[1]Institute of Hydrogeology and Environmental Geology, Chinese Academy of Geological Sciences, Shijiazhuang, China, [2]China University of Geosciences, Beijing, China, [3]Technology Innovation Center of Geothermal and Hot Dry Rock Exploration and Development, Ministry of Natural Resources, Shijiazhuang, China, [4]State Key Laboratory of Nuclear Resources and Environment, East China University of Technology, Nanchang, China, [5]Group 901, Jiangxi Provincial Bureau of Geology, Pingxiang, China

OPEN ACCESS

Edited by:
Yanlong Kong,
Institute of Geology and Geophysics (CAS), China

Reviewed by:
Jian Chang,
China University of Petroleum, China
Xiaoyin Tang,
Chinese Academy of Geological Sciences (CAGS), China
Zhuting Wang,
China University of Mining and Technology, China

***Correspondence:**
Guiling Wang
guilingw@163.com

Specialty section:
This article was submitted to Economic Geology, a section of the journal Frontiers in Earth Science

Received: 14 August 2021
Accepted: 07 October 2021
Published: 03 November 2021

Citation:
Liu F, Wang A, Wang G, Zhang W, Liao Y and Tong J (2021) Characteristics of Terrestrial Heat Flow and Lithospheric Thermal Structure in Typical Intermountain Basin at the Eastern Foot of Yanshan Mountain, North China. Front. Earth Sci. 9:758605. doi: 10.3389/feart.2021.758605

The Yanshan area is rich in geothermal resources. However, limited research has been done on the geothermal resources of intermountain basins in the area, which restrict the exploration and development of geothermal resources. In this study, the Yanheying Basin, a typical intermountain basin located in the eastern foothills of Yanshan Mountain, is selected to perform a comprehensive analysis regarding heat flow and lithospheric thermal structure, to have a better understanding of the geothermal background and resource utilization potential of the area. The methods of deep borehole temperature logging, and rock sampling and testing were applied. With geological and geophysical data collected in the surrounding basins, the thermophysical parameters of rock formations, terrestrial heat flow and temperature distribution on a crustal-scale around the basin were analyzed. Results show that the ratio of crust heat flow to that of the mantle in the Yanheying Basin is 0.68, which falls in the range of that of the North China Plain (0.6–0.8), showing an obvious result of lithospheric thinning. The results also show that both crust and mantle heat flows in the Yanheying Basin are far lower than those of the North China Plain. it indicates that the crust of the Yanheying Basin and the entire Yanshan area has experienced a low degree of damage. That provides a piece of good thermodynamic evidence for the spatial variation of North China Craton destruction. The depth of the Curie surface in the study area is estimated to be about 24 km, which is consistent with the results of aeromagnetic data analysis. It confirms the results of lithospheric thermal structure and deep temperature distribution in the Yanheying Basin. The Yanheying Basin has certain potential for geothermal resources utilization in the depth of 2–6 km, where probably exist several carbonate thermal reservoirs with medium-temperature geothermal water. The above results can provide new insights into the geothermal research and exploration of intermountain basins in the Yanshan area.

Keywords: terrestrial heat flow, lithospheric thermal structure, thermal conductivity, radioactive heat production, intermountain basin, Yanshan mountain

INTRODUCTION

In the research of geothermal resources, it is of practical significance to study terrestrial heat flow and lithospheric thermal structure (Jiang et al., 2019). Terrestrial heat flow is a surficial manifestation of the Earth's internal thermal dynamic process (Davies and Davies, 2010). It (q_0) is a combination of crust heat flow (q_c) and mantle heat flow (q_m) (Birch et al., 1968). Briefly, the lithospheric thermal structure includes the distribution of heat flow and temperature at different depths of the lithosphere. It represents the deep thermal state of the region and forms the basis for researches of the formation mechanism of regional geothermal resources (Lachenbruch et al., 1970).

The Yanshan area is located in the northern part of the Beijing-Tianjin-Hebei region and has been a green ecological shelter in the north of Beijing City. The research and utilization of geothermal resources is of great theoretical and practical significance in this area. However, existing geothermal studies there have mainly focused on hot springs (Liu, 2006; Zhang, 2012; Shen, 2017). Limited studies have been conducted to address the deep thermal status of intermountain basins in the Yanshan area. Furthermore, there are only 21 terrestrial heat flow data (Jiang et al., 2016 and references therein; Sun et al., 2019; Liu et al., 2020) within the Yanshan area and all of them are located in the central and western parts (**Figure 1**). The eastern part of the Yanshan area is still a blank area of heat flow measurement. As a result, subsequent research om the lithospheric thermal structure, deep temperature distribution, and utilization of this area are also limited.

Therefore, to fill the blank area of terrestrial heat flow measurement in the Yanshan area and to improve the research degree of geothermal resources in intermountain basins, the Yanheying Basin is selected as a typical area in this paper to analyze thermophysical parameters of shallow and deep strata, the terrestrial heat flow and temperature distribution of the crust around it. The reasons are as follows: First is the location advantage. The Yanheying Basin is located at the Eastern Foot of Yanshan Mountain, which is rich in geothermal resources but lacks basic geothermal research, especially in the intermountain basins. Secondly, the stratigraphic distribution in this basin is the same as that of Zhangjiakou Basin, Chengde Basin in the central and west, respectively, with the lithospheric structure close to the average of the Yanshan area (Jia et al., 2009; Liu et al., 2020). Thirdly, its geothermal condition is well represented. Hot springs are developed around the basin and carbonate geothermal reservoirs are developed inside the basin, which is consistent with the general characteristics of geothermal resources distribution of intermountain basins in the Yanshan area (Liu, 2006; Zhang, 2012; Shen, 2017).

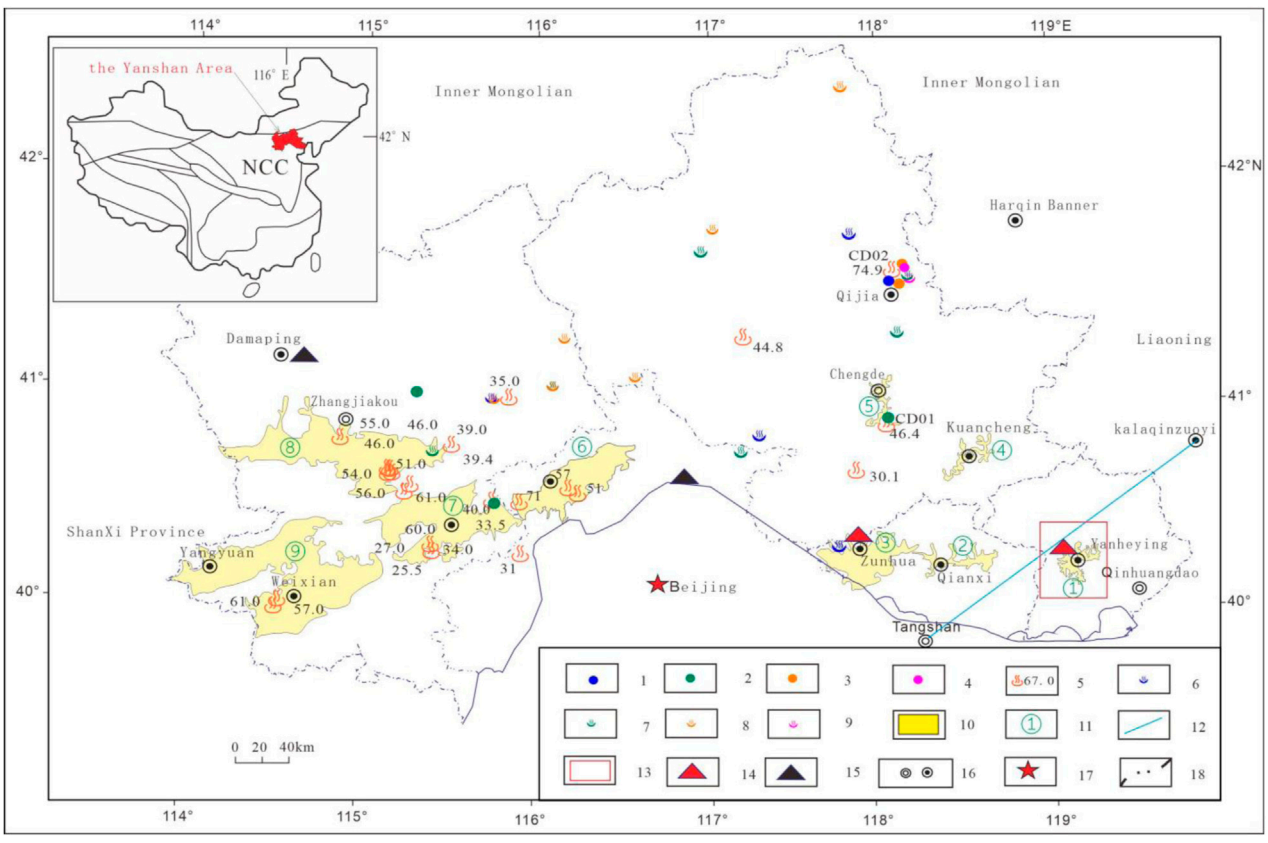

FIGURE 1 | Terrestrial heat flow observations and surface geothermal manifestations in the Yanshan area.

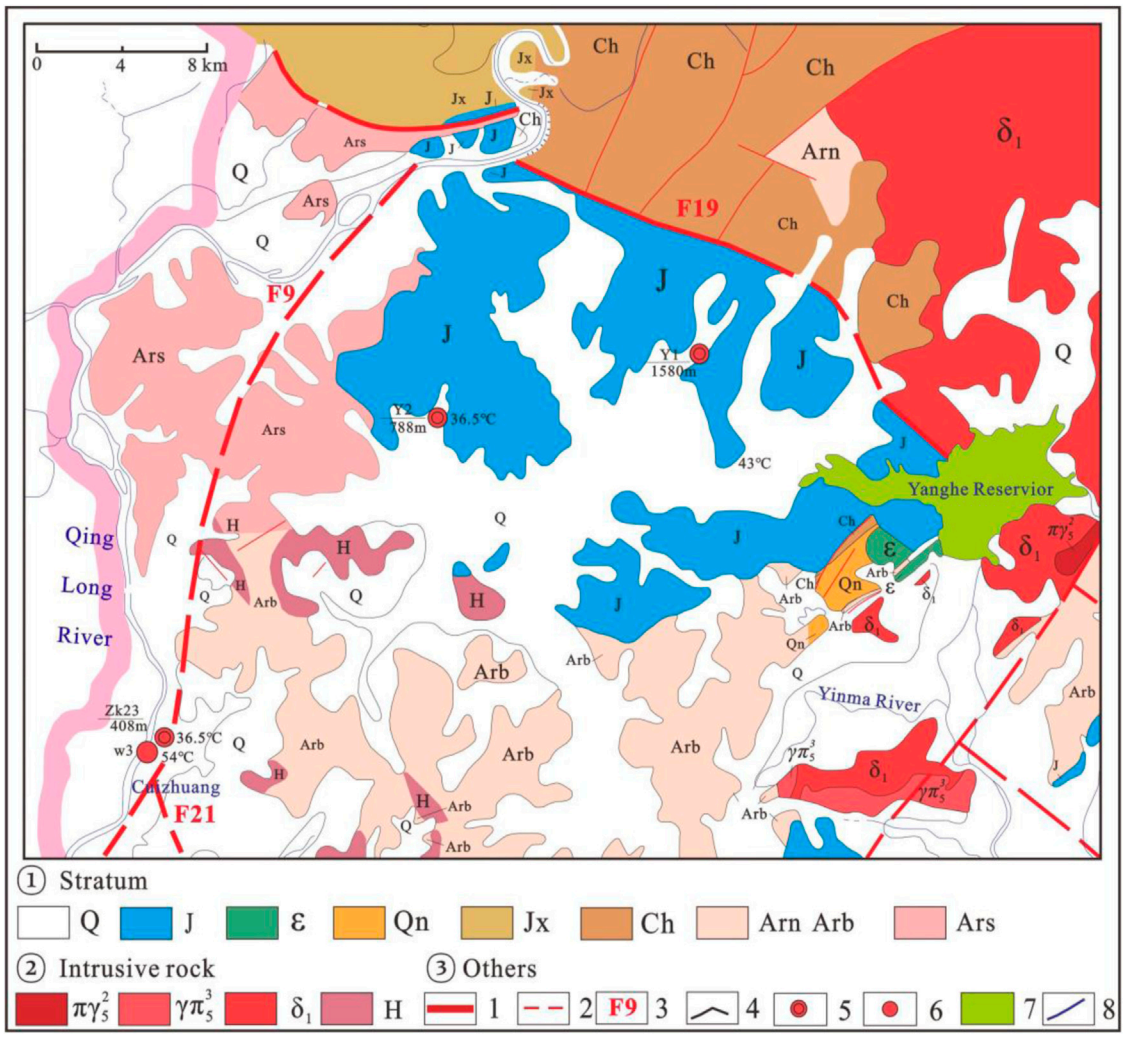

FIGURE 2 | Simplified geothermal geology of the Yanheying Basin (the location of the study area is defined in **Figure 1**).

GEOLOGICAL SETTING

Geologically, the Yanshan area is located in the northeastern part of the North China Craton (**Figure 1**), adjacent to the North China Plain to the south and the Taihang Mountains to the southwest. Since the Mesozoic era, the Yanshan structural belt has undergone multiple stages of tectonic activities, leading to the formation of intermountain basins (Liu et al., 2013), such as Yanheying Basin, Qianxi Basin, Zunhua Basin, Kuanchegn Basin, Chengde Basin, Yanqing Basin, Huailai Basin, Yangyuan-Yuxian Basin, Zhangjiakou Basin from east to west in the Yanshan area (**Figure 1**). Although these basins are sparsely located, they can still be correlated due to similar sedimentary facies (Liu et al., 2004). Firstly, these intermountain basins mainly comprise a series of sedimentary strata from the Archaean, through the Proterozoic to Cambrian (Cope et al., 2007; Liu et al., 2013). Among the strata, the sedimentary rocks of Gaoyuzhuang Formation of the Changcheng System, Wumishan Formation of the Jixian System, and the Changping Formation of the Cambrian have been identified as good geothermal reservoirs, where the geothermal resources are accumulated *via* rock thermal conduction (Wang et al., 2019). Secondly, affected by the tectonic uplift and subsidence in the Yanshan area, the strata between the Late Middle Cambrian and the Late Permian, as well as the Neogene and Paleogene are missing across the basins, replaced by a wide presence of well-developed and thick-layered Cretaceous sedimentary rocks and Jurassic volcanic rocks underlain by Yanshanian granites of various thicknesses. Additionlly, the shallow layers such as the Minghuazhen Formation and the Guantao Formation are not developed in these basins, showing a completely different character from that of the North China Plain (Liu et al., 2004; Zhang, 2018). The Yanheying Basin selected in this paper accords with the general stratigraphic characteristics of intermountain basins described above.

As shown in **Figure 2**, the Yanheying Basin, extending from Taiying in Funing County to Yanheying in Lulong County and spatially appearing as an irregular oval shape, is a Mesozoic

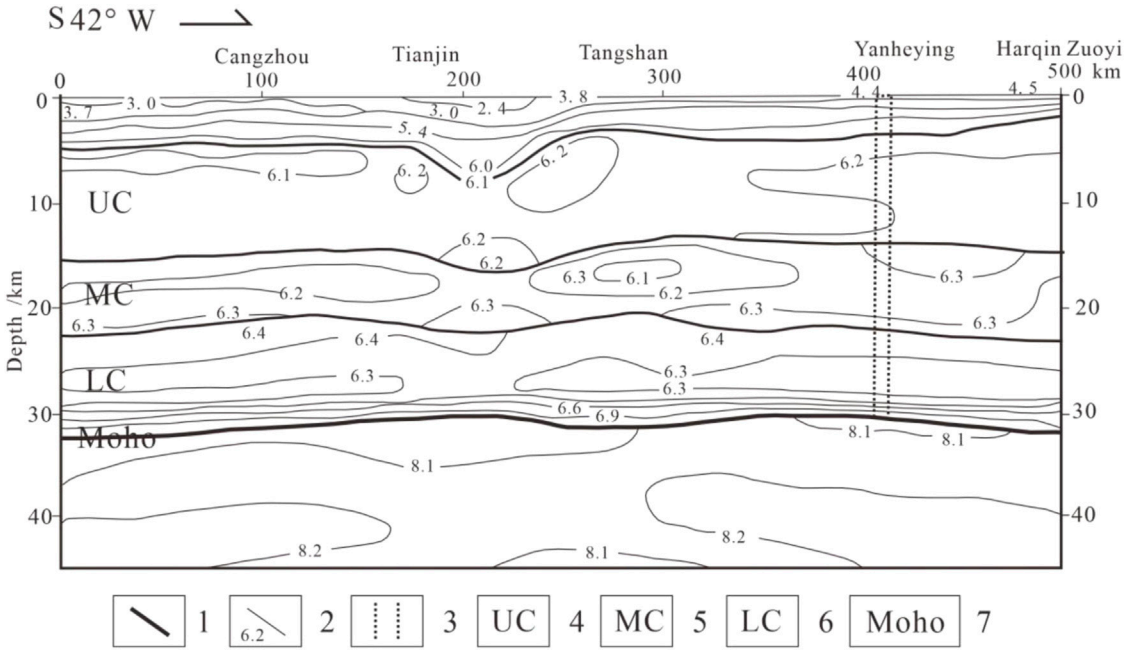

FIGURE 3 | Distribution of P-wave velocity in the geological transect from Cangzhou to Harqin Zuoyi (modified from Shao et al., 1989; the location of the section line is defined in **Figure 1**).

continental volcanic-sedimentary basin to the east of the Yanshan Mountain, with an aerial size of 230 km^2. The surface of the basin is covered by the Quaternary deposits, underlain by Cretaceous sedimentary rocks and Jurassic volcanic rocks. Below the volcanic rocks are the strata of the Cambrian, the Qingbaikou System, the Jixian System, and the Changcheng System of the Proterozoic (Zhang, 2018), respectively. At the bottom, the crystalline basement is composed of the Luanxian System and the Lulong rock suite of the Archean, forming the top layer of the region's upper crust.

The Yanheying Basin is located southeast of the Yanshan area (**Figure 1**). Its north and northeast are bounded by the Lengkou fault (F19 in **Figure2**) and its western boundary is controlled by the Qinglonghe fault (F9 in **Figure2**), while in the south the basin is angularly unconfirmed with the metamorphic basement of the Neoarchean (**Figure 2**).

In terms of geothermal conditions, there is a hot spring issuing at the junction of Fault F9 and the Leidianzi tensile basement Fault F21 (**Figure 2**). It outcrops in the vicinity of the Cuizhuang area, the southwestern margin of the basin, with a surface temperature of 36.5°C. Similar hot springs with a surface temperature of 30–60°C are also exposed in the Zhangjiakou Basin, the Huailai Basin, the Zunhua Basin, the Qianxi Basin, and so on, showing relatively consistent characteristics in the Yanshan area (Liu, 2006; Zhang, 2012; Shen, 2017). The borehole Y1 and Y2 are located in the basin, with a bottom hole temperature of 43.0°C and 26.4°C, respectively (**Figure 2**).

Figure 3 shows the result of seismic exploration along the Harqin Zuoyi - Cangzhou cross-section that transects the northern side of the Yanheying Basin (**Figure 1**) (Shao et al., 1989). The P-wave velocity (Vp) in the section provides important information about the stratification of the crust for analyzing the lithospheric thermal structure.

METHODOLOGY

Terrestrial Heat Flow Measurement

The terrestrial heat flow value can be attributed to the product of two parameters, i.e., geothermal gradient and rock thermal conductivity.

Geothermal Gradient

In this study, we used the well temperature probe ANTS-3S, with a working range of 0–150°C and an accuracy of 0.01°C, to measure the well temperature at depth. The measurement was performed in accordance with the national guideline titled Coal Geophysical Logging Specification (DZ/T0080-2010). During this process, the temperatures were repeatedly logged untill their difference at a well depth section was less than 0.5°C in 24 h, to ensure that the recorded well temperature was in a steady-state or a quasi-steady heat flow state (He et al., 2008). After that, the influence of groundwater on the temperature and lithological data was analyzed, the well sections with a relative straight-line feature of temperature against depth were selected to calculate the well thermal gradient $\Delta T/\Delta h$.

Thermal Conductivity

The thermal conductivity automatic scanner TCS (Thermal Conductivity Scanning), with a working range of 0.2–25 W/m

K and an accuracy of ±3%, was applied in this study, to perform the rock conductivity analysis. The thermal conductivity of the rock decrease with increasing temperature (Anand et al., 1973). In the current research, the thermal conductivity test was done at a temperature of 25°C. As the lab temperature was different from that of the well, the thermal conductivity of borehole cores was corrected according to the *in situ* temperature of the borehole (Liu et al., 2017), by employing the empirical formula developed by Sass et al. (1992), which has been proved to be suitable for calibrating the conductivity within a depth of several kilometers in the continental areas (He et al., 2008).

$$K(0) = K(25)(1.007 + 25(0.0037 - 0.0074/K(25))) \quad (1)$$

$$K(T) = K(0)/(1.007 + T(0.0036 - 0.0072/K(0))) \quad (2)$$

Where T is the *in situ* temperature of the core in borehole (°C), K (0) and K (25) are the thermal conductivity values of the rock at 0 and 25°C (W/m K), respectively.

Pressure, porosity, and water saturation are also key factors in thermal conductivity (Pribnow et al., 1996). The effect of pressure is insignificant within a buried depth of 1–2 km (Abdulagatova et al., 2009). The effects of porosity and water saturation depend on the degree of porosity. Some researchers suggest that only when the porosity is greater than 6% does its effect have practical significance for thermal conductivity (Yang et al., 1993). The effects on mudstone and metamorphic rocks in some areas are ignored because of their low porosity (He et al., 2008; Zhang et al., 2020). In general, for rocks with a porosity of more than 5%, water saturation correction for the thermal conductivity can be made using equations raised by Abdulagatova (2009) and Guo et al. (2017).

For the strata under the basin basement, the following formula is frequently used for correction (Cermak et al., 1982; Artemieva et al., 2001).

$$K = K_0/(1 + cT) \quad (3)$$

Where, c is the temperature coefficient determined by the experiment and K_0 is the initial value of the thermal conductivity at the top of each structural layer, which is given by experimental or empirical parameters of different cases. Here, according to previous studies, the c values are 0.001, 0 for the middle crust and −0.00025 for the lower crust and mantle, respectively, while the K_0 values are 2.3 and 2.5 W/m K for the middle and lower crusts, and the mantle, respectively (Cermak et al., 1982; Gong et al., 2011).

Lithospheric Thermal Structure

Demarcation of the Lithosphere

As discussed in the Geological Setting, the bottom of the Yanheying Basin in the study region is the Archaean crystalline basement and above the basement are sedimentary and intrusive rocks, while the space below that boundary is the upper crust and then downwards are the middle crust, lower crust and upper mantle, respectively. In general, the lithology and thickness of the sedimentary and intrusive rocks can be identified *via* core drilling and the bedrock exposed on the surface. The data of the structural layers below the crystalline basement can only be obtained through geophysical methods, of which the artificial seismic exploration can reflect the structure above the upper mantle briefly (**Figure 3**). According to a previous study of the interfaces determined by compressional wave (P wave) velocity (Vp), the structure of the lithosphere can be demarcated (Fullea et al., 2014).

There are two ways to obtain the lithospheric structure of the Yanheying Basin. The first one is to query from the Vp profile map like **Figure 3**. Data from that are more accurate but lack the validation of data from surrounding areas. For the area with no artificial seismic exploration done, the regional structure of the lithosphere can be obtained from the model Crust1.0 developed by Laske et al. (2013). This model facilitates the collection of global artificial seismic data and the establishment of a global lithospheric structure model with a resolution of 1° × 1°. In addition, the model can provide parameters such as the depth of the upper, middle, and lower crust interfaces in various regions of the world, the density of each structural layer and Vp. The resulting data is a better representation of the whole area but has a lower resolution.

In this study, the crustal structure was demarcated using the average data derived from the application of the above two methods. For the strata above the upper crust, the geothermal structure was demarcated through the interpretation of deep borehole core-logging data and typical geological profiles in the vicinity of the study area.

Crust—Mantle Heat Flow Distribution

The crustal heat flow q_c is referred to as cumulative heat resulting from the decay of radioactive elements in all layers of the Earth crust in the study region. Taking the thickness of each layer and associated radioactive heat production rate into account, the layer-stripping method is used to calculate the heat flow generated in all layers, which can be represented by the **Eqs 4**, **5**.

$$q_i = D_i \cdot A_i \quad (4)$$

$$q_c = \sum q_i \quad (5)$$

Where D_i is the thickness of the structural layer i, A_i is its heat production rate, q_i is the heat flow generated in the layer and q_c is the crust heat flow. Furthermore, the mantle heat flow value can be calculated as $q_m = q_0 - q_c$.

The radioactive heat production rate of the rock is determined by measuring the concentrations of radioactive elements such as uranium (as U), thorium (as Th) and potassium (as K) in the rocks. At present, **Eq. 6** proposed by Rybach (1976) is widely used to calculate the rate.

$$A = 0.01\rho(9.52C_U + 2.56C_{Th} + 3.48C_K) \quad (6)$$

In this formula, A (μW/m^3) is the radioactive heat production rate, ρ is the rock density (g/cm^3), C_U, C_{Th}, and C_K are the concentrations of U (μg/g), Th (μg/g) and K (%), respectively. The contents of U and Th are analyzed by the ICP-MS method with an uncertainty of ±1–±10%, and the weight percentage of K can be determined by the XRF method with an analytical uncertainty of ±1~±2%.

For deep rock formations in the crust, there have been so far two commonly used methods for calculating the heat production rate. One is the geophysical method proposed by Lachenbruch (1970) and Rybach (1984) who separately established the relationship between V*p* and *A*. However, due to the lack of theoretical basis of the empirical method and limited satisfactory application effects in many cases, an increasing number of researchers have questioned the mothod (Kern and Siegesmund, 1989; Zhao, 1995). Another method is to identify the lithologies in the crustal layers based on existing geological information and to test the representative rocks of each layer via outcrop or borehole sampling. The advantage of this method is that it effectively gains the heat production data of deep crustal rock formations to the greatest extent. However, it is extremely difficult to obtain the rock samples from the deep portions of the crust, because deep rock sampling requires a lot of effort toward deep drilling or deep rock inclusion detection (Liu et al., 2001). In this study, we used the second approach to assessing the heat production rate. Through rock sampling and data collection in the study area and even over the entire Yanshan area, relevant data associated with deep rock formations were acquired (**Tables 2, 4**), which enabled us to analyze regional lithospheric thermal structure more accurately.

Deep Geothermal Distribution

The temperature of the shallow strata can be accessed by well logging, while in the deep portion of the crust, it can only be explored by applying indirect methods. The linear relationship between temperature and depth in Y1 and Y2 (**Figure 4**) shows that the ground temperature rising in Yanheying Basin is mainly attributed to deep heat conduction. Thus, the temperature of deep strata can be calculated using the one-dimensional steady-state heat conduction formula as follows (Lachenbruch et al., 1970).

$$T_Z = T_0 + \frac{qD}{k} - \frac{AD^2}{2k} \tag{7}$$

Where *Tz* is the temperature (°C) at the depth z (m), T_0 and *q* are the temperature (°C) and heat flow (mW/m^2) at the top of the layer, respectively, *D* is the thickness of the layer (km), *k* the thermal conductivity of rock (W/m K) in the layer calculated, and *A* heat production rate of the rock (μW/m^3).

RESULTS AND DISCUSSION

Terrestrial Heat Flow Measurement

The temperature logs done in the boreholes Y1 and Y2 installed in the Yanheying Basin show a good trend of heat conduction and temperature increase at a depth below the Quaternary deposits (**Figure 4**), which is suitable for calculating the terrestrial heat flow of the study area.

The logging depth is 1,580 m with a maximum temperature of 43.0°C in the borehole Y1 and the geothermal gradient from 200 to 1,500 m deep is 17.9°C/km with a fit goodness of 0.997. The lithologies in this depth range are sandstone, mudstone and conglomerate of the Cretaceous. Their average rock thermal conductivity is 2.50 W/m K estimated from 15 samples. The logging depth of the borehole Y2 is 788 m with a maximum temperature of 26.4°C. The temperature gradient in 300–700 m below the surface is 15.1°C/km, and the fitting goodness with the temperature against depth is 0.999. The lithology in this depth range is dominated by Jurassic volcanic rock with an average rock thermal conductivity of 2.34 W/m K (5 samples). Giving that the average porosity of sandstone, mudstone, conglomerate, and volcanic rock samples mentioned above are 1.4, 2.8, 3.6, and 2.3% respectively, with an average value of 2.8%. The effect of water saturation is about 0.7% according to our estimates from the Abdulagatova (2009) and Guo et al. (2017) equations, which is far less than the test accuracy of ±3%. Thus, only temperature correction is made for the heat flow measurement. The calibrated thermal conductivity is shown in **Table 1**.

Based on the above data, the calibrated terrestrial heat flow of the Y1 is 44.57 mW/m^2 and that of the Y2 is 35.33 mW/m^2, with an average of 39.95 mW/m^2. The quality of the two data fulfills the criteria for Category A (Jiang et al., 2016). It can be seen that the average terrestrial heat flow in Yanheying Basin is much lower than the average value of 62.5 mW/m^2 in continental China (Jiang et al., 2019) and that of the North China Plain (63.6 mW/m^2) (Gong et al., 2011) but is close to the value of the Zhangjiakou Basin (45 mW/m^2) and Chengde Basin (40.4 mW/m^2) (Jiang et al., 2016; Sun et al., 2019). As the more frequent and intense the tectonic motion, the greater the terrestrial heat flow value is (Liu et al., 2016; Zhang et al., 2016). The low value of geothermal background in the study area and Yanshan area proves that the crust within the Yanshan area is relatively stable. The Yanshan area experienced a low degree of damage in the North China Craton destruction (Zhang et al., 2016). It also suggests that hot springs in the Yanshan area are mainly controlled by fault systems. The effect of terrestrial heat flow is non-significant.

Lithospheric Thermal Structure

The strata exposed in Y1 and Y2 (**Figure 4**) show that the thicknesses of the Cretaceous and Jurassic strata in Yanheying Basin are about 1.2 and 0.5 km, respectively. As these two boreholes do not penetrate in the strata below the Jurassic, the thicknesses of the rock formations below the Jurassic were hence determined by analyzing the typical geological cross-section that transects the Luanxian area in the vicinity of the study area (Zhang et al., 2017). As a result, the Changcheng System is about 1.2 km and the Jixian System 1.4 km in thickness. The Qingbaikou and the Cambrian strata are respectively 0.2 and 0.8 km thick. Thus, the total thickness of the sedimentary layers in the basin is around 5.3 km, underlain by the basement consists of crystalline rock. Previous studies show that the top of the upper crust crystalline rock, i.e. G interface in this area is 6.5 km deep, while the Vp = 6.1 km/s velocity interface (**Figure 3**) as the top of the upper crust is 4.2 km deep in this area. The depth of this interface can hence be averaged from the two depth values, which is 5.35 km below the surface.

Figure 3 shows the interfaces of P wave velocity of 6.2, 6.4, and 8.05 km/s, standing for bottoms of the upper crust, middle crust and the Moho surface, respectively, with depths of 14.2, 22.4 and 30.7 km (Sun et al., 1991). Simultaneously, depths of the above

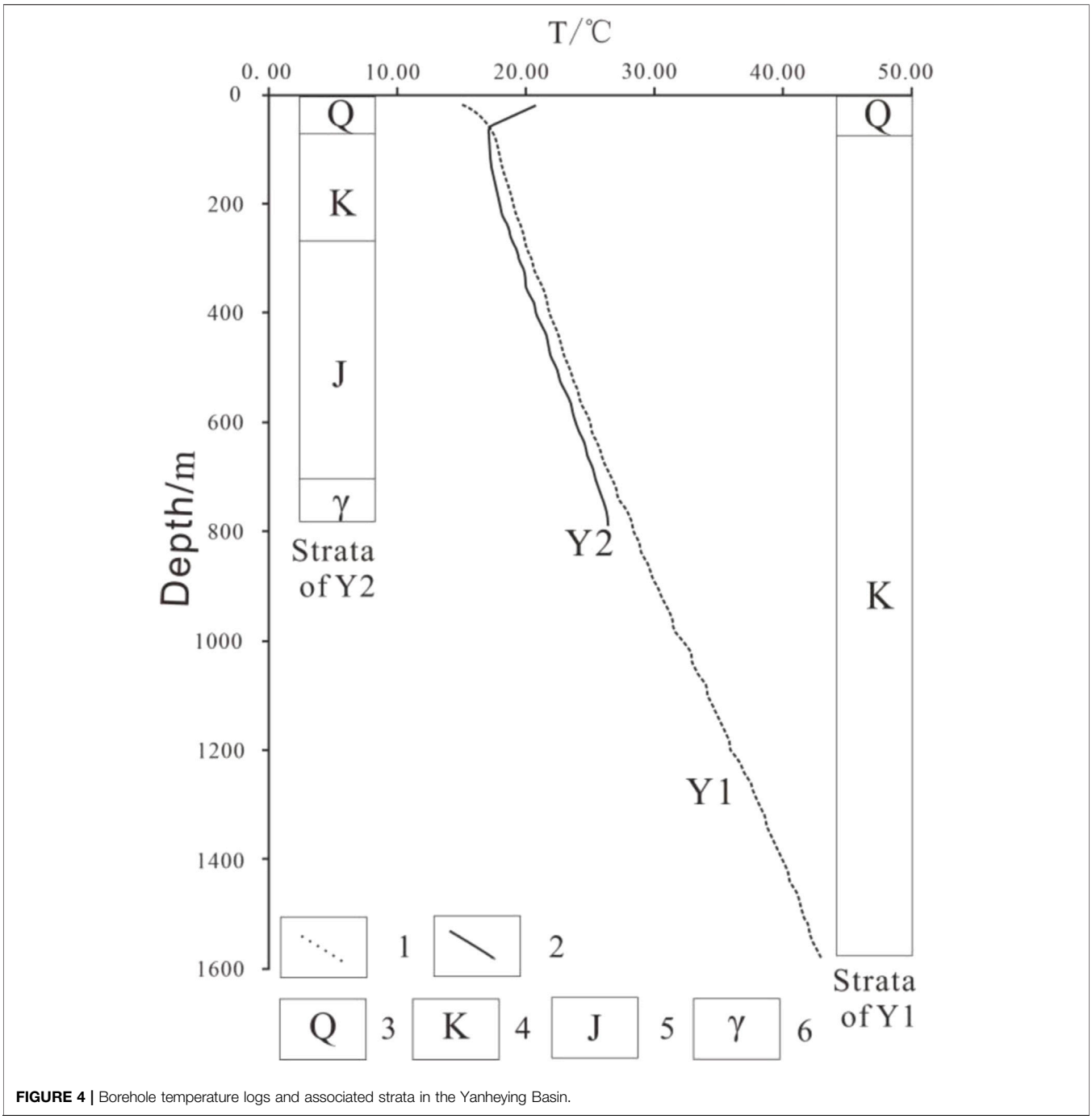

FIGURE 4 | Borehole temperature logs and associated strata in the Yanheying Basin.

TABLE 1 | Calculated result of terrestrial heat flow in the Yanheying Basin.

Borehole	Coordinate	Geothermal gradient (°C/km)	Measured depth (m)	Calibrated average thermal conductivity	Sample number	Calibrated terrestrial heat flow (mW /m^2)	Data quality
Y1	119.10°E, 40.05°N	17.9	200–1,500	2.49	16	44.57	A
Y2	119.01°E, 40.02°N	15.1	300–700	2.34	5	35.33	A

TABLE 2 | Radioactive heat production rates in the Yanheying Basin and surrounding pre-Cenozoic strata.

Stratum code	Lithology	Number of samples	Radioactive heat production rate range ($\mu W/m^3$)	Average heat production rate ($\mu W/m^3$)	Sampling location	Data source
K	Sandy conglomerate, mudstone, sandstone	14	0.83–1.77	1.33	Borehole Y2	Current study
J	Coarse andesite, tuff, basalt	9	0.68–1.53	1.14	Borehole Y1	Current study
Є	Dolomite, shale	10	0.2–2.69	1.11	Yanheying and Beijing	Current study and Lei et al. (2020)
Qn	Sandstone, conglomerate, shale	4	1.91–2.02	2.01	Beijing	Lei et al. (2020)
Jx	Dolomite, shale	23	0.2–0.86	0.53	Beijing	Lei et al. (2020)
Ch	Dolomite, limestone, quartz sandstone	8	0.12–1.92	0.67	Yanheying	Current study
UC	Archean granodiorite and gneiss	8	0.15–1.24	0.66	Yanheying	Current study
MC	Zunhua group of Archean: amphibolitic schist, granodioritic gneiss	6	0.15–0.63	0.41	Zunhua	Current study
LC	Granulite	10	0.1–0.45	0.24	Damaping	Liu et al. (2020)

TABLE 3 | Calculation result of lithospheric thermal structure in the Yanheying Basin.

Code of the structural layer	The average depth of layer bottom (km)	Di (km)	Ai ($\mu W/m^3$)	Qi (mW/m^2)	Heat flow at bottom of each layer (mW/m^2)
—	0	—	—	—	39.95
K	1.2	1.2	1.33	1.60	38.35
J	1.7	0.5	1.14	0.57	37.78
Є	2.5	0.8	1.11	0.89	36.90
Qn	2.7	0.2	2.01	0.40	36.49
Jx	4.1	1.4	0.53	0.74	35.75
Ch	5.3	1.2	0.67	0.80	34.95
UC	12.3	7.05	0.66	4.65	30.30
MC	21.6	9.30	0.41	3.81	26.49
LC	31.0	9.34	0.24	2.24	24.25

interfaces are 10.5, 20.9, and 31.3 km, respectively, by referring to Crust1.0 (Laske et al., 2013). Taking their average values into account, the depths are respectively 12.3, 21.6, and 31.0 km (**Table 4**).

Lithologically, the upper crust is formed by granodiorite and gneiss, which are exposed around the Yanheying Basin border (**Figure 2**) and the northern part of Chengde City. The middle crust is largely composed of amphibolitic schists and granodioritic gneisses, which are similar in lithology to the Zunhua Group of the Archaean; they widely expose in Luanxian and Zunhua. The lower crust is formed by intermediate-acid and basic granulite, the deep-derived xenoliths of which are exposed in Shangmaping, Zhangjiakou (**Figure 1**). Rock sampling and data collection of A and K focused on these regions, mainly on the study area (Liu et al., 2001; Lei et al., 2018). Radioactive heat production rates of different layers and data sources are shown in **Table 2**.

The analytical results with data derived from rock sample testing and data collection collectively show that the heat production rate (A) in the Yanheying Basin gradually decreases from shallow to the deep portion of the crust, which is consistent with the general trend of lithospheric heat production (Xu et al., 2018). The average value of the layers' heat production rate below the Qn formation is less than 1 $\mu W/m^3$, which is similar to the results of previous studies conducted in North China (Zang et al., 2002; Wu et al., 2005).

Based on the above data and **Eqs 4**, **5**, the lithospheric crust-mantle heat flow distribution in the study area is hence calculated with results listed in **Table 3**, from which the mantle heat flow q_m is about 24.3 mW/m^2 and the ratio of crustal heat flow to that of the mantle q_c/q_m is 0.65. Moreover, the results indicate a hot-mantle- cold-crust type of heat flow in the study area and in the Yanshan area (Liu et al., 2020), which conforms to results from the studies of the thermal structure in the North Craton done by Wang et al. (1996) and Qiu et al. (1998), indicating that terrestrial heat flow is mainly composed of mantle heat flow in these regions. That phenomenon provides good thermodynamic evidence for overall lithospheric thinning in the North China Craton destruction.

Based on **Table 3**, a conceptual model is established for the crustal heat production rate and lithospheric thermal structure in the study area (**Figure 5**). The heat flow values of each layer can be directly identified from the figure. Among them, the mantle heat flow is 24.3 mW/m^2, which is lower than the global average of 48.0 mW/m^2 and the North China Plain average value of

TABLE 4 | Thermal conductivity of the Yanheying Basin and surrounding pre-Cenozoic strata.

Stratum code	Lithology	Number of samples	Thermal conductivity range (W/m·K)	Average value (W/m·K)	Sampling location	Data source
K	Sandy conglomerate, mudstone, sandstone	16	1.96–3.01	2.45	Yanheying	Current study
J	Coarse-grained andesite, tuff, basalt	6	1.96–2.99	2.41	Yanheying	Current study
Є	Dolomite, shale	43	1.84–4.71	2.95	Yanheying and Beijing	Current study and Lei et al. (2020)
Qn	Sandstone, conglomerate, shale	30	1.93–5.84	3.34	Beijing	Lei et al. (2020)
Jx	Dolomite, shale	50	1.53–6.33	5.06	Beijing	Lei et al. (2020)
Ch	Dolomite, limestone, quartz sandstone	8	2.36–6.03	4.44	Yanheying	Current study
Basement and UC	Archean granodiorite and gneiss	15	1.80–3.46	2.28	Yanheying	Current study

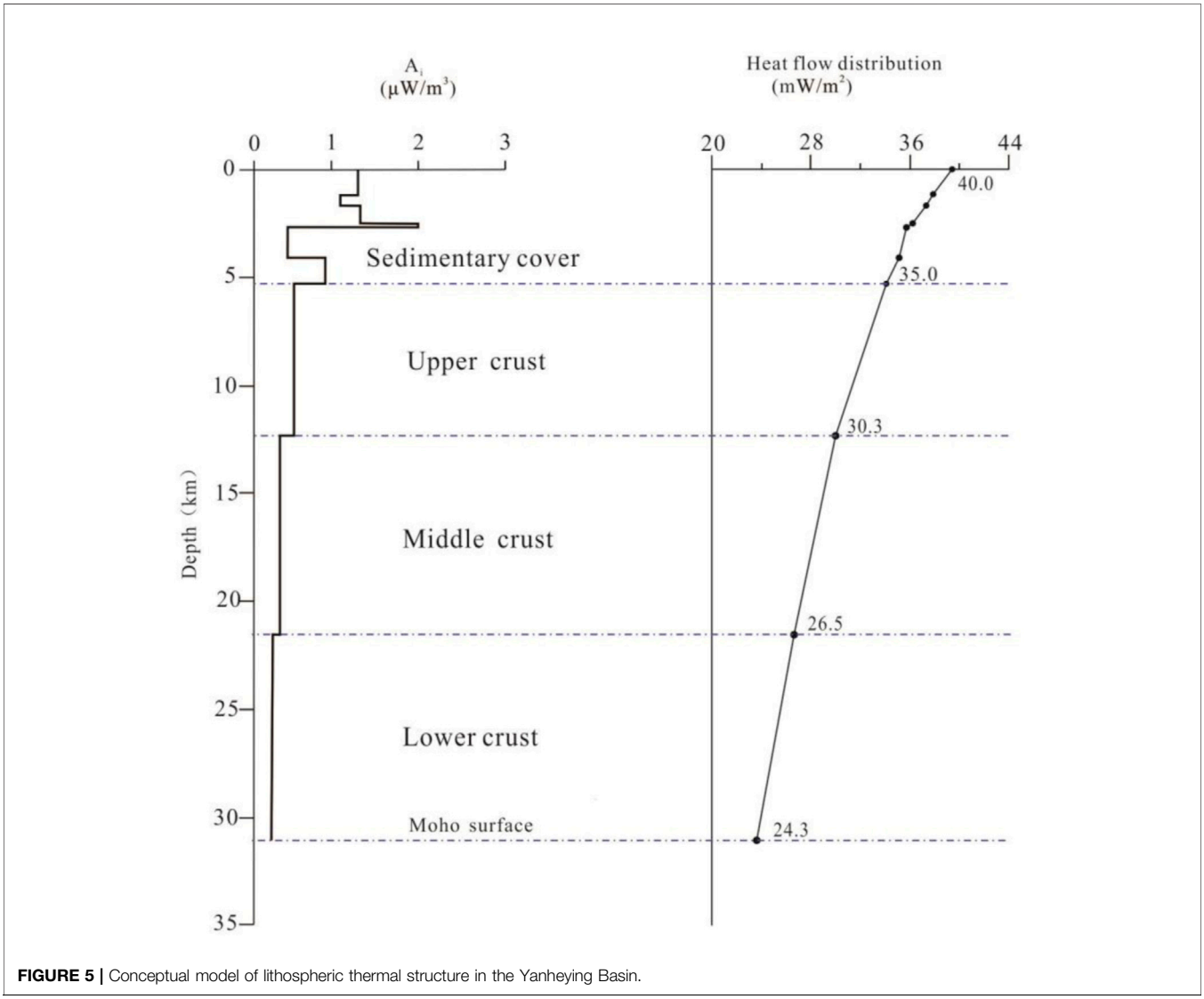

FIGURE 5 | Conceptual model of lithospheric thermal structure in the Yanheying Basin.

30.0 mW/m^2 (Chi and Yan, 1998). The low mantle heat flow and terrestrial heat flow of the study area indicate that compared with the North China Plain, the Yanshan area experienced a low degree of damage in the North China Craton destruction. It also provides good thermodynamic evidence for the spatial variation of that tectonic motion.

TABLE 5 | Deep temperature distribution in the Yanheying Basin.

Thermal layer	Depth (km)	Thickness (km)	Initial thermal conductivity K0 (W/m·K)	Calibrated thermal conductivity K (W/m·K)	Average heat production rater A ($\mu W/m^3$)	Surficial heat flow q (mW/m^2)	Ground temperature T (°C)	Geothermal gradient dT/dH (°C/km)
—	0	—	—	—	—	39.95	15.0	—
K	1.2	1.2	2.45	2.43	—	38.4	34.3	16.1
J	1.7	0.5	2.41	2.38	1.14	37.8	42.3	16.0
Є	2.5	0.8	2.95	2.85	1.11	36.9	52.8	13.1
Qn	2.7	0.2	3.34	3.19	2.01	36.5	55.1	11.5
Jx	4.1	1.4	5.06	4.65	0.53	35.8	66.0	7.8
Ch	5.3	1.2	4.44	4.03	0.67	34.9	76.5	8.8
UC	12.3	7.0	2.28	2.11	0.66	30.3	185.3	15.4
MC	21.6	9.3	2.3	2.30	0.41	26.5	300.1	12.3
LC	31.0	9.3	2.5	2.55	0.24	24.2	392.9	9.9

Deep Temperature Distribution

Based on the lithospheric thermal structure in the Yanheying Basin, the deep temperature distribution of the area can be assessed. In this study, the starting point for the calculation was set at the constant temperature zone with a temperature of 15°C and a depth of 20 m (Zhang et al., 2013). The thermal conductivity of the layers above the middle crust is shown in **Table 4**, as the samples of these formations can be obtained via borehole sampling or surface sampling. Below the upper crust, the thermal conductivity cannot be directly measured. These thermal conductivity values are set and calibrated by **Eq. 4**.

As shown in **Table 5**, the rock formations above the Moho surface are divided into 9 layers for calculating the temperature distribution at depth. In the 0–31 km deep range, the temperature distribution and geothermal gradient of the Yanheying Basin were calculated through an iterative calculation by using **Eq. 7**. The results show that the temperature at the Moho surface is about 393°C, and the geothermal gradient gently decreases from 15.9°C/km to 9.8°C/km by depth generally. The geothermal gradient of the Jx and Ch formations is the lowest at 7.6°C/km, while their thermal conductivity is highest.

The Curie point of rocks containing iron minerals is the temperature at which highly magnetic minerals are converted to paramagnetic minerals (Ramotoroko et al., 2021). The depth of the Curie point in a certain region is the Curie isothermal surface or Curie surface. The demagnetized temperature of ilmenite and pyrrhotite is 300–350°C, and; that of magnetite is 585°C. For the minerals containing cobalt, nickel and iron, their demagnetized temperature is 760–800°C (Yang, 2015). Thus, the depth of the Curie isothermal surface can provide an effective clue to the study of the deep thermal state as well as material composition in the lithosphere (Trifonova et al., 2009; Bansal et al., 2013).

Based on the continental Curie surface map of China with data derived from aeromagnetic data (Xiong et al., 2016), the depth of the Curie surface around the Yanheying Basin is 22–25 km. In our research, the Curie surface depth is estimated to be 21.6–26.6 km with a temperature of 300–350°C. This consistency verifies the lithospheric thermal structure and deep temperature distribution in the Yanheying Basin. It also suggests that the lower crust of the Yanheying Basin is composed of rocks containing ilmenite and pyrrhotite.

CONCLUSION

In this paper, a comprehensive analysis of heat flow and lithospheric thermal structure was performed, with the case study area in the Yanheying Basin, to have a better understanding of the geothermal background and resource utilization potential of the typical intermountain basin in the eastern foothills of Yanshan Mountain. According to these analyses, some conclusions are drawn as follows:

1) The Yanheying Basin is a typical intermountain basin in the Yanshan area, North China due to the uniqueness of its location, lithospheric structure, thermal reservoirs distribution and research degree of geothermal background. The average terrestrial heat flow here is close to that of the Zhangjiakou Basin and the Chengde Basin but far lower than that of the China Mainland and the North China Plain. It indicates a relatively low value of geothermal background in the whole Yanshan area. It can be inferred that hot springs around the basins are mainly controlled by geological structures such as faulting systems. In addition, the ratio of q_c/q_m in the study area is 0.65. It indicates a hot-mantle-cold-crust type of lithospheric thermal structure, which is consistent with that in the North China Plain. The mantle heat is the main source of terrestrial heat flow in this area. These results provide good thermodynamic evidence for lithospheric thinning in the North China Craton and the crust of the Yanshan area.
2) The distribution of temperatures below the surface was analyzed using the one-dimensional steady-state equation. The temperature at the Moho surface is approximately 400°C, located at the low limit of the global Moho temperature. The low temperature at the deeper portion is attributed to the less thickness (31 km) of the lithosphere and low heat production (less than 1.4 $\mu W/m^3$) of rocks. The depth of the Curie interface is estimated at 21.6–26.6 km, which is close to the analyzed result on the basis of aeromagnetic data. The consistency verified the regional lithospheric thermal structure and thermophysical parameters in our paper.
3) The calculation results show that the rock temperature in the Yanheying Basin is about 40–70°C at a depth of 2–6 km, where

the rock formations such as Є, Qn, Jx, and Ch distribute. As karst fissures in these strata are well developed, the groundwater in the karst aquifers is heated, leading to the presence of several thermal reservoirs formed by dolomite and limestone with mid-temperature geothermal resources. These geothermal reservoirs have a potential for geothermal resources utilization in the future.

DATA AVAILABILITY STATEMENT

The original contributions presented in the study are included in the article/Supplementary Material, further inquiries can be directed to the corresponding author.

AUTHOR CONTRIBUTIONS

FL, writing and revising the manuscript; AW, revising the manuscript; GW, providing the scienctific idea and revising the manuscript; WZ, revising the manuscript; YL, field investigation and resiving the manuscript; JT, revising the manuscript.

FUNDING

This study was financially supported by the National Key Research and Development Program of China (Grant No. 2018YFA0404104), Key Research and Development Program of Jiangxi Province (Grant No. 20203BBG72W011)and grants from the geothermal survey project of the China Geological Survey (Grant No. DD20190128).

REFERENCES

Abdulagatova, Z., Abdulagatov, I. M., and Emirov, V. N. (2009). Effect of Temperature and Pressure on the thermal Conductivity of sandstone. *Int. J. Rock Mech. Mining Sci.* 46 (6), 1055–1071. doi:10.1016/j.ijrmms.2009.04.011

Anand, J., Somerton, W. H., and Gomaa, E. (1973). Predicting thermal Conductivities of Formations from Other Known Properties. *Soc. Petrol. Eng. J.* 13 (5), 267–273. doi:10.2118/4171-pa

Artemieva, I. M., and Mooney, W. D. (2001). Thermal Thickness and Evolution of Precambrian Lithosphere: a Global Study. *J. Geophys. Res.* 106 (B8), 16387–16414. doi:10.1029/2000jb900439

Bansal, A. R., Anand, S. P., Rajaram, M., Rao, V. K., and Dimri, V. P. (2013). Depth to the Bottom of Magnetic Sources (DBMS) from Aeromagnetic Data of Central India Using Modified Centroid Method for Fractal Distribution of Sources. *Tectonophysics* 603, 155–161. doi:10.1016/j.tecto.2013.05.024

Cermak, V., and Rybach, L. (1982). "Thermal Conductivity and Specific Heat of Minerals and Rocks," in *Physical Properties of Rocks*. Editor G. Angenheister (Berlin: Springer), 305–343.

Chi, Q. H., and Yan, M. C. (1998). Radioactive Elements of Rocks in North China Platform and the thermal Structure and Temperature Distribution of the Modern continental Lithosphere. *J. Chin. J. Geophys.* 41 (1), 38–48. (in Chinese).

Cope, T. D., Shultz, M. R., and Graham, S. A. (2007). Detrital Record of Mesozoic Shortening in the Yanshan Belt, NE China: Testing Structural Interpretations with basin Analysis. *Basin Res.* 19 (2), 253–272. doi:10.1111/j.1365-2117.2007.00321.x

Davies, J. H., and Davies, D. R. (2010). Earth's Surface Heat Flux. *Solid Earth* 1 (1), 5–24. doi:10.5194/se-1-5-2010

Fullea, J., Muller, M. R., Jones, A. G., and Afonso, J. C. (2014). The Lithosphere-Asthenosphere System beneath Ireland from Integrated Geophysical-Petrological Modeling Ii: 3d thermal and Compositional Structure. *Lithos* 189 (3), 49–64. doi:10.1016/j.lithos.2013.09.014

Gong, Y. L., Wang, L. S., and Liu, S. W. (2011). *The thermal Structure and thermal Evolution of Bohai Bay Basin in East China*. Beijing: Atomic Energy Press. (in Chinese).

Guo, P. Y., Zhang, N., He, M. C., and Bai, B. H. (2017). Effect of Water Saturation and Temperature in the Range of 193 to 373k on the thermal Conductivity of sandstone. *Tectonophysics* 699, 121–128. doi:10.1016/j.tecto.2017.01.024

He, L., Hu, S., Huang, S., Yang, W., Wang, J., Yuan, Y., et al. (2008). Heat Flow Study at the Chinese Continental Scientific Drilling Site: Borehole Temperature, thermal Conductivity, and Radiogenic Heat Production. *J. Geophys. Res.* 113, B02404. doi:10.1029/2007jb004958

Jia, S. X., Zhang, C. K., Zhao, J. R., Fang, S. M., Liu, Z., and Zhao, J. M. (2009). Crustal Structure of the Rift-Depression basin and Uplift in the Northeast Part of North China. *Chin. J. Geophys.* 52 (1), 99–110. (in Chinese). doi:10.1002/cjg2.1326

Jiang, G., Hu, S., Shi, Y., Zhang, C., Wang, Z., and Hu, D. (2019). Terrestrial Heat Flow of continental China: Updated Dataset and Tectonic Implications. *Tectonophysics* 753 (20), 36–48. doi:10.1016/j.tecto.2019.01.006

Jiang, G. Z., Gao, P., Rao, S., Zhang, Y. L., Tang, X. Y., Huang, F., et al. (2016). Compilation of Heat Flow Data in the continental Area of China (4th Edition). *J. Chin. J. Geophys.* 59 (8), 2892–2910. (in Chinese).

Kern, H., and Siegesmund, S. (1989). A Test of the Relationship between Seismic Velocity and Heat Production for Crustal Rocks. *Earth Planet. Sci. Lett.* 92 (1), 89–94. doi:10.1016/0012-821x(89)90023-x

Lachenbruch, A. H. (1970). Crustal Temperature and Heat Production: Implications of the Linear Heat-Flow Relation. *J. Geophys. Res.* 75 (17), 3291–3300. doi:10.1029/jb075i017p03291

Laske, G., Masters, G., Ma, Z., and Pasyanos, M. (2013). *Update on CRUST1.0 - A 1-degree Global Model of Earth's Crust: EGU General Assembly.*

Lei, X. D., Hu, S. B., Li, J., Jiang, G. Z., Yang, Q. H., and Li, Q. L. (2018). Characteristics of Heat Flow and Geothermal Distribution in the Northwest Beijing Plain. *J. Chin. J. Geophys.* 61 (9), 3735–3748. (in Chinese with English abstract).

Liu, C. H. (2006). *A Study of Hydrochemistry and Isotopes of Baimiao Hot spring, Chicheng Hot spring and Tangzimiao Hot spring*. [dissertation]. Beijing: China University of Geosciences (Beijing. (in Chinese).

Liu, F., Lang, X., Lu, C., Lin, W., Tong, J., and Wang, G. (2017). Thermophysical Parameters and Lithospheric thermal Structure in Guide Basin, Northeast Qinghai-Tibet Plateau. *Environ. Earth Sci.* 76 (5), 199. doi:10.1007/s12665-017-6503-2

Liu, Q., Zhang, L., Zhang, C., and He, L. (2016). Lithospheric thermal Structure of the North China Craton and its Geodynamic Implications. *J. Geodynamics* 102, 139–150. doi:10.1016/j.jog.2016.09.005

Liu, S. F., Li, Z., and Zhang, J. F. (2004). Evolution and Tectonic System of Mesozoic Basins in Yanshan Area. *J. Scientia Sinica (Terrae)* 34 (0z1), 19–31. (in Chinese).

Liu, S., Su, S., and Zhang, G. (2013). Early Mesozoic basin Development in North China: Indications of Cratonic Deformation. *J. Asian Earth Sci.* 62, 221–236. doi:10.1016/j.jseaes.2012.09.011

Liu, Y.-S., Gao, S., Jin, S.-Y., Hu, S.-H., Sun, M., Zhao, Z.-B., et al. (2001). Geochemistry of Lower Crustal Xenoliths from Neogene Hannuoba basalt, north china Craton: Implications for Petrogenesis and Lower Crustal Composition. *Geochimica et Cosmochimica Acta* 65 (15), 2589–2604. doi:10.1016/s0016-7037(01)00609-3

Qiu, N. S. (1998). Thermal Status Profile in Terrestrial Sedimentary Basins in China. *J. Adv. Earth Sci.* 13 (5), 447–451. (in Chinese).

Rybach, L., and Buntebarth, G. (1984). The Variation of Heat Generation, Density and Seismic Velocity with Rock Type in the continental Lithosphere. *J. Tectonophysics* 103 (1-4), 335–344. doi:10.1016/0040-1951(84)90095-7

Sass, J. H., Lachenbruch, A. H., Moses, T. H., and Morgan, P. (1992). Heat Flow from a Scientific Research Well at Cajon Pass, California. *J. Geophys. Res.* 97 (B4), 5017–5030. doi:10.1029/91jb01504

Shao, X. Z., and Zhang, J. R. (1989), Structure of the Lithosphere in the Northern Part of North China. *Atlas of Lithospheric Dynamics in China*. Beijing: Map Publishing House. (in Chinese).

Shen, X. W. (2017). *Characteristics of Some hot springs in the north of Hebei and Beijing*. [dissertation]. Beijing: China University of Geosciences (Beijing. (in Chinese).

Sun, M., Liu, F., Lu, C., and Yue, C. (2020). Terrestrial Heat Flow in Chengde, Hebei Province. *J. Sci. Technology Eng.* 20 (25), 10144–10150. (in Chinese).

Sun, W. C., Liu, C. Q., Zhu, Z. P., Zhang, L., Song, S. Y., and Zhang, X. K. (1991). Velocity Structure of the Crust and Upper Mantle in the Northern Part of North China," in *Atlas of Lithospheric Dynamics of China*, G. Y. Ding. Beijing: China Cartographic Publishing House), 251–154.

Trifonova, P., Zhelev, Z., Petrova, T., and Bojadgievaet, K. (2009). Curie point Depths of Bulgarian Territory Inferred from Geomagnetic Observations and its Correlation with Regional thermal Structure and Seismicity. *J. Tectonophysics.* 473 (3-4), 362–374. doi:10.1016/j.tecto.2009.03.014

Wang, J. Y. (1996). *Geothermics in China*. Beijing: Seismological Press.

Wang, J. Y., Pang, Z. H., Hu, S. B., Wang, S. J., Xu, P. F., and Wang, G. J. (2015). *Geothermics and its Applications*. Beijing: Science Press. (in Chinese).

Wang, Z., Jiang, G., Zhang, C., Hu, J., Shi, Y., Wang, Y., et al. (2019). Thermal Regime of the Lithosphere and Geothermal Potential in Xiong'an New Area. *Energy Exploration & Exploitation* 37 (2), 787–810. doi:10.1177/0144598718778163

Wu, Y., Jin, Z. M., Ou, X. G., Xu, H, J., and Wang, L. (2005). The Lithospheric thermal Structure beneath the Area of the Chinese Continental Scientific Drilling Site (CCSD). *J. Acta Petrologica Sinica.* 21 (2), 440–450. (in Chinese).

Xiong, S. Q., Yang, H., Ding, Y. Y., and Li, Z. K. (2016). Characteristics of Chinese Continent Curie point Isothermal. *J. Chin. J. Geophys.* 59 (10), 3604–3617. (in Chinese).

Xu, W., Qiu, N., Wang, Y., and Chang, J. (2018). Evolution of Meso-Cenozoic Lithospheric thermal-rheological Structure in the Jiyang sub-basin, Bohai Bay Basin, Eastern North China Craton. *Int. J. Earth Sci. (Geol Rundsch)* 107 (1), 153–166. doi:10.1007/s00531-016-1360-x

Yang, H. (2015). *Characteristics of Chinese continental Curie point Isotherm*. [dissertation]. Chengdu: Chengdu University of Technology. (in Chinese).

Yang, S. Z., Zhang, W. R., Li, G. H., and Shen, X. (1993). Experimental Research on the thermal Conductivity of Water-Saturated Rocks and Correction to the Heat Flow Observed in Qaidam Basin. *ACTA petrologica sinca* 9 (2), 199–204.

Zang, S. X., Liu, Y. G., and Ning, J. Y. (2002). Thermal Structure of the Lithosphere in North China. *J. Chin. J. Geophys*. 45(1), 56–66. (in Chinese) doi:10.1002/cjg2.216

Zhang, D. Z., Liu, Z. G., and Lu, H. L. (2013). *Hebei Geothermal*. Beijing: Geological Publishing House. (In Chinese).

Zhang, J., Huang, S., Zuo, Y., Zhou, Y., Liu, Z., Duan, W., et al. (2020). Terrestrial Heat Flow in the Baiyinchagan Sag, Erlian Basin, Northern China. *Geothermics* 86, 101799. doi:10.1016/j.geothermics.2019.101799

Zhang, L. Y., Liu, Q. Y., and He, L. J. (2016). The Different Lithospheric thermal Structure of North China Craton and its Implications. *Chin. J. Geophys.* 59 (10), 3618–3626. (in Chinese).

Zhang, X. (2012). *A Study of the Characteristics of hot springs of Low to Moderate Temperature in Chengde District of Northern Hebei*. [dissertation]. [Beijing]: China University of Geosciences (Beijing. (in Chinese).

Zhang, X. (2018). The Evolutionary Process of Yanheying Basin and Understanding of Mine Exploration. *J. China Well Rock Salt* 49 (1), 21–24. (in Chinese).

Zhang, Y. Q., Zhang, Z. L., Liu, Z. X., Jv, Z. Y., Li, Q., and Zhang, Y. H. (2017). *Regional Geology of Hebei Province*. Beijing: Geological Publishing House. (in Chinese).

Zhao, P. (1995). Studies of the Relationship between Seismic Velocity and Heat Production in the Rocks of the Crust. *J. Prog. Geophys.* 1, 114–124. (in Chinese).

Conflict of Interest: The authors declare that the research was conducted in the absence of any commercial or financial relationships that could be construed as a potential conflict of interest.

Publisher's Note: All claims expressed in this article are solely those of the authors and do not necessarily represent those of their affiliated organizations, or those of the publisher, the editors and the reviewers. Any product that may be evaluated in this article, or claim that may be made by its manufacturer, is not guaranteed or endorsed by the publisher.

frontiers in Earth Science

ORIGINAL RESEARCH
published: 26 November 2021
doi: 10.3389/feart.2021.772977

Study on the Long-Term Performance and Efficiency of Single-Well Circulation Coupled Groundwater Heat Pump System Based on Field Test

Ke Zhu[1,2], *Yifan Zeng*[1,2]*, *Qiang Wu*[1,2], *Shengheng Xu*[1,2], *Kun Tu*[1,2] *and Xiaoxiu Liu*[1,2]

[1]College of Geoscience and Surveying Engineering, China University of Mining and Technology (Beijing), Beijing, China, [2]National Engineering Research Center of Coal Mine Water Hazard Controlling, Beijing, China

Although buildings are often heated and cooled by single-well circulation coupled groundwater heat pump systems, few studies have evaluated the long-term performance of these systems. Therefore, the present study investigated the performance of these systems by analyzing the efficiency and energy consumption using 4 years of operating data. The results indicate that the coefficient of performance (*COP*) of the system gradually decreases because of thermal breakthrough or an accumulation of cold. In addition, the sealing clapboards could effectively slow down thermal breakthrough. In addition, compared with the heating period, the *COP* of the heat pump unit (HPU) and system increases, and its energy consumption decreases in the cooling period. It was also found that partial heat loss occurs when water from the single-well circulation outlet penetrates the main pipeline. Moreover, the heat-exchange efficiency of a single HPU exceeds that of multiple HPUs, and the *COP* of a HPU decreases during operation with increasing indoor temperature. Accordingly, we improved the performance of system by increasing the underground heat storage. Herein, we focus on optimizing the system design during long-term operation, which includes taking steps such as lengthening the sealing clapboards, using insulated pipes, discharging the remaining water and adding intelligent control devices.

Keywords: single-well circulation, groundwater heat pump, efficiency, energy consumption, coefficient of performance

OPEN ACCESS

Edited by:
Yanlong Kong,
Institute of Geology and Geophysics (CAS), China

Reviewed by:
Xiaoming Tian,
Delft University of Technology, Netherlands
Xianbiao Bu,
Guangzhou Institute of Energy Conversion (CAS), China

***Correspondence:**
Yifan Zeng
48279214@qq.com

Specialty section:
This article was submitted to Economic Geology, a section of the journal Frontiers in Earth Science

Received: *09 September 2021*
Accepted: *04 November 2021*
Published: *26 November 2021*

Citation:
Zhu K, Zeng Y, Wu Q, Xu S, Tu K and Liu X (2021) Study on the Long-Term Performance and Efficiency of Single-Well Circulation Coupled Groundwater Heat Pump System Based on Field Test. Front. Earth Sci. 9:772977. doi: 10.3389/feart.2021.772977

INTRODUCTION

In the context of the global energy and environmental crisis, groundwater heat-pump (GWHP) systems have been extensively implemented to use shallow geothermal energy sources for heating or cooling of residential and commercial buildings (Li et al., 2013). In winter, groundwater is extracted and used as a heat source to heat to residential or commercial buildings; in summer, groundwater is extracted as a cold source to cool buildings by reversing the heat-pump system. Furthermore, surplus heat is injected underground, which is serves as a heat storage medium for thermal energy. Compared with other types of traditional heating, ventilation, and air conditioning (HVAC) systems, GWHP systems consume less electric power and generate more heat energy without

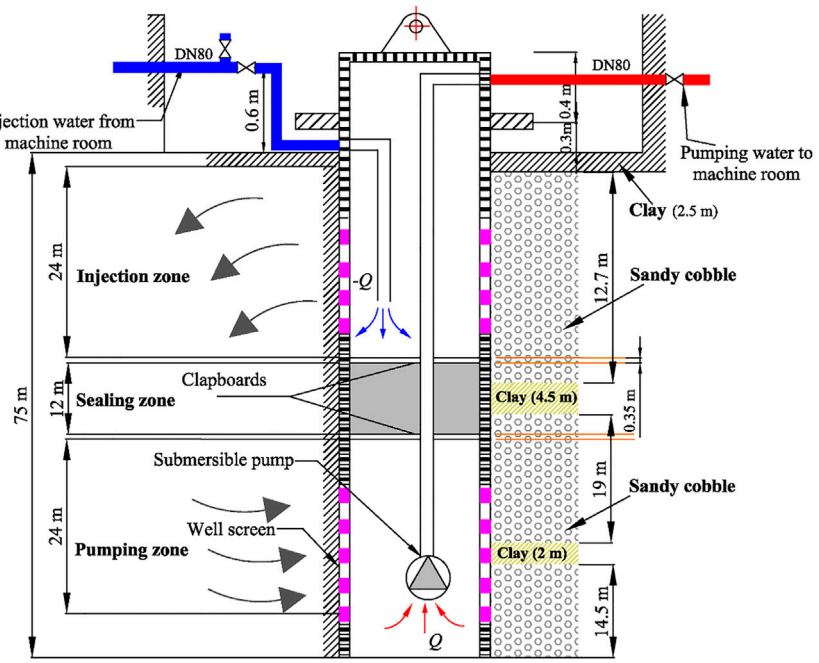

FIGURE 1 | Schematic diagram of the SWC system.

producing polluting gas and without the consumption of groundwater (Luo et al., 2018; Blázquez et al., 2019; Fang and Zhang, 2020; Luo et al., 2020; Qiu et al., 2021; Zhang et al., 2021).

With the development of GWHP systems, many different GWHP systems have been applied in practical engineering. The single-well circulation (SWC) coupled GWHP system, as a new technology that has attracted extensive attention. As shown in **Figure 1**, the SWC system consists of three parts: a lower pumping zone, a middle sealing zone and an upper injection zone. First, the lower pumping zone is filled with groundwater into which is placed a submersible pump connected to a suction pipe. Groundwater is pumped by the submersible pump through a suction pipe into the machine room. Pumping groundwater exchanges heat via the heat-pump units (HPUs). Next, the upper injection zone is filled with heat-exchanged groundwater, which is injected through the discharge tube into the upper injection zone. Third, the middle sealing zone contains clapboards to prevent the heat-exchanged groundwater from entering the pumping well. Gravity-induced pressure causes the heat-exchanged water to exchange heat with surrounding rock and soil before it flows back to the pumping area. In the whole process, the system extracts heat without consuming groundwater by completely recharging in the same layer (Sun et al., 2015). The system also offers the advantages of lower initial investment and operational costs, a smaller footprint, and a diminished on groundwater quality (Song et al., 2019a), which has led to the wide use of these systems in practical engineering.

As far as we known, the performance and efficiency of other forms of heat-pump systems decrease over long-term operation (Sommer et al., 2015; Hein et al., 2016). Significant research efforts have sought to avoid the phenomenon and promote the efficient and sustainable operation of SWC coupled GWHP systems in practical engineering. First, in terms of system design, Yuill and Mikler (1995) and Mikler (1993) found that the equivalent thermal conductivity coefficient can be used to calculate the depth of the thermal well by using a model involving coupled thermohydraulic energy transfer in an aquifer surrounding a thermal well. By investigating successful commercial cases of SWC systems, Orio *et al.* showed that the key parameter of an SWC system design must be "bleed" (Orio, 1994; Orio et al., 2005). They also reported that bleeding can keep the SWC system sustainable when the system design assumes suitable hydrological and geological conditions. In other work, Wu et al. (2015) found that the aquifer properties should be determined and considered in the system design to maximize efficiency, reduce installation costs, and minimize environmental impact. Through field and numerical studies, Park et al. (2015) verified that thermal dispersion significantly affects the heat transfer of SWC systems with high flow rate, which is important for system design. Deng et al. (2005) established a computationally efficient numerical model of groundwater flow and heat transfer in and around SWC systems, which serves as a design tool.

Site conditions including seepage field, temperature field, groundwater level, and surface temperature, are also relatively important to maintain the efficiency and stability of SWC systems. In an extreme cold-climate experiment, Minea (2013) found that the residential SWC systems in Canada are not suitable for extreme cold weather without seepage, whereas Nguyen et al. (2020) reported that SWC systems can be used in cold climates. By simulating a seepage field, it has been found that groundwater seepage and fluid flow improves thermal

conductivity and enhances the heat-transfer capacity of the heat exchanger (Deng et al., 2006; Al-Sarkhi et al., 2008). However, Kastrinos et al. (2019) found that heat transfer caused by horizontal groundwater flow is very small by injecting tracer bromide into an SWC system. Using a thermal-response experiment, Chang et al. (2017); Chang et al., 2019) investigated how hydrogeology affects the thermal characteristics of an SWC system and found that groundwater flow has negligible impact on the thermal conductivity of an SWC system. Finally, three-dimensional numerical models of the seepage field and temperature field were developed by Lee (2011) and Song et al. (2019b), and these showed that groundwater flow improves thermal transport and heat transfer. By modeling groundwater seepage and heat transfer, Ni et al. (2011) derived an analytic seepage solution to show that SWC systems can accommodate large space heating and cooling loads with a thermal effective radius exceeding 40 m. To investigate SWC seepage fields, Tu et al. (2018); Tu et al., 2020a; Tu et al., 2020b) developed a mathematical model and derived an analytical solution for groundwater flow and an approximate analytical solution for non-Darcian flow. The results reveal how the flow field varies as a function of SWC. By using numerical simulations, Wu et al. (2018) and Choe and Ko (2017) studied how hydrogeology and thermogeological affect thermal performance, sustainability, and efficiency of SWC systems.

Researchers also considered operational strategies to analyze the sustainability of SWC systems and found that heat storage should be increased to maintain the efficient and sustainable operation of SWC systems in practical operation (Song et al., 2019a; Lee et al., 2019). Zeng et al. (2017) found that the groundwater quality in areas where SWC strongly effects system operation and can reduce equipment efficiency and lifetime. Léo et al., (2020) found that excess calcium concentration in groundwater can degrade system efficiency, requiring the calcium concentration to be decreased by operating a groundwater treatment unit, using suitable flowmeters, and purging the above-ground piping network, which requires a prolonged downtime period.

These studies show the significant research that has been conducted on the sustainable use of SWC systems, and have focused on system design, site conditions and operational strategies through both simulations and experiments. However, relatively few studies have considered the repercussions of the long-term operation of SWC coupled GWHP systems. In particular, little information is available on the relevant parameters for practical engineering experimentation, despite these parameters affecting the long-term operation of SWC systems. Researchers and designers would thus like to know the parameters and factors influencing SWC systems in practical operation so that the SWC can be better promoted and applied.

Given these difficulties, we report herein on a 4 year field test of an SWC coupled GWHP system conducted in Beijing, China. Based on data measured over 4 years, we studied the factors that reduce the SWC system efficiency and increase energy consumption to evaluate the long-term performance of this SWC system. In addition, we suggest ways to optimize SWC systems, including suggestions on operational strategies and system design. The results are significant for practical engineering and related research.

EXPERIMENTAL APPARATUS AND METHODS

Description of Building

The SWC system was installed in a school building in the Haidian District of, Beijing. The building has four floors above ground and two floors underground, is 18 m high, and has a total floor area of 45,952 m^2. The main functional areas of the building are classrooms, gymnasiums and other teaching rooms. The total heating and cooling loads of the building are 3,450 and 3,600 kW, respectively. In addition, the hot-water heating and swimming-pool heating loads sum to 514 kW. The heating period lasts 120 days (from November 15 to March 15), and the SWC system operates daily from 7:00 to 16:00. The cooling period is 122 days (from May 15 to September 15), and the system operating time is from 8:00 to 16:00. For this paper, 4 years of monitoring data were collected (2016–2019), with the academic year 2016-2017 serving as the system trial operation stage. During the monitoring period, the groundwater level was recorded for all 4 years. The total energy consumption was also collected from May 2016 to Dec 2019, while the system was shut down in the transition period without data. Data relating to the practical operation of the system was collected from May 2016 to July 2018.

Site Conditions

According to a geological survey of the project site, a quaternary system is widely distributed over the working area. The stratum lithology consists mainly of gravel, sand gravel and coarse sand gravel with a thin cohesive-soil layer between the gravel and sand gravel. The quaternary system is about 150 m thick, and the cumulative thickness of the aquifer is 80–120 m. When the groundwater level drops by 1 m, the water yield of a single well is more than 5,000 m^3/d. The heat-exchange capacity of the SWC system was designed to be 300 kW in winter and 420 kW in summer. Finally, the circulating water flow was about 60 m^3/h, and the well was 70–80 m deep.

System Configuration

Figure 2 shows a schematic diagram of the monitoring system of the SWC coupled GWHP system. The SWC system is composed essentially of four parts: energy collection, energy boost, energy release and monitoring well area. In **Figure 2**, the energy collection area contains the 12 sets of SWCs devices that enter the theoretical calculation. Non-storage particle geothermal energy collection wells were used. The energy boost area is divided into two parts: the heating-cooling part and the part for heating water. The machine room contains four sets of HPUs. Two YSSR-1300A/2 and one YSSR-700A/2 geothermal HPUs are selected to meet the building heating and cooling requirements, and one YSSR-600B/2 heats the swimming pool and provides domestic hot water. The energy release area consists of a

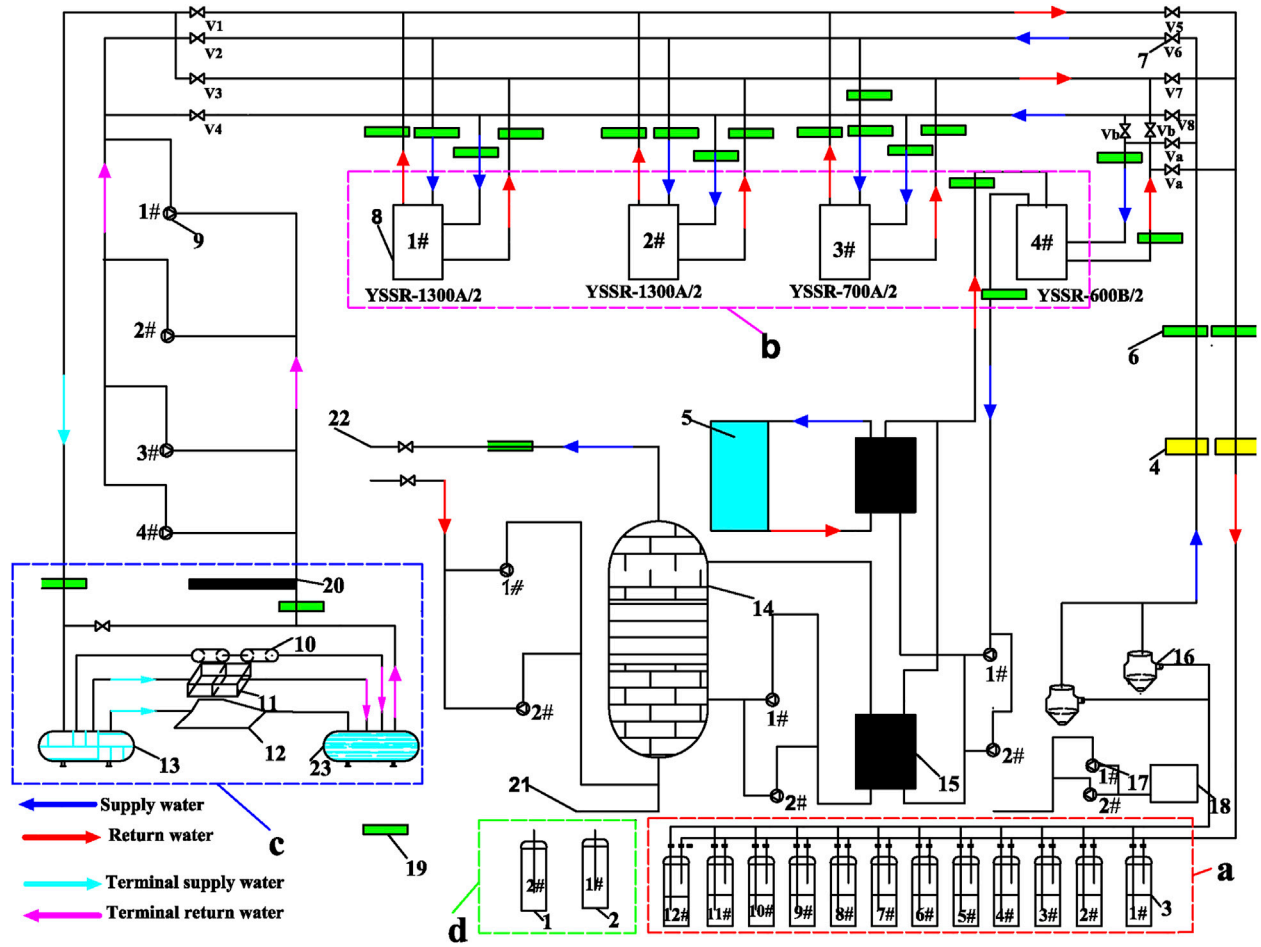

FIGURE 2 | Monitoring schematic for SWC coupled GWHP system.

circulating pump, a water divider, and a water collector. The air conditioning units mainly use fan coils and floor radiators to meet the cooling and heating requirements of the building. The monitoring well area consists of a well for monitoring the groundwater level and a well for monitoring the underground temperature.

(a) energy collection area, (b) energy boost area (machine room), (c) energy release area (terminal), (d) monitoring well area.

1: water level monitoring well, 2: underground temperature monitoring well, 3: 1#-12# SWCs, 4: circulating water flowmeter, 5: swimming pool, 6: thermoreceptor, 7: Valve, 8: 1#-4# HPUs, 9: terminal system circulating pump, 10: fan coil, 11: air condition unit, 12: floor heating, 13: water segregator, 14: water storage tank, 15: hot water heat pump, 16: heat source circulating pump, 17: terminal feed pump, 18: softened water tank, 19: outdoor temperature recorder, 20: connect the make-up pump area, 21: tap water connection, 22: hot water area, 23:mainfold.

Monitoring Methods

The monitoring data from the of SWC system monitoring part and from the two monitoring wells were collected to analyze the system's performance. The monitoring methods are introduced below.

Temperature Monitoring

The water temperature of each key pipeline was monitored during the operation of the SWC system for the cooling period and heating period. The minimum monitoring frequency was four times per day generally and once per day during intermittent periods. The system temperature data include the outlet and inlet water temperature of the SWC systems, the supply and return water temperature of the single well-side main pipe, the supply and return water temperature of the terminal main pipe of the SWC system and the exterior temperature. The temperature parameters were measured by using a one-piece temperature transmitter.

The 1# monitoring well was 70–80 m deep and separated by 10 m from the nearest SWC. The cable for measuring the

temperature was 80 m long and held 100 temperature sensors at 0.8 m intervals. The temperature measuring cables buried in the monitoring well were used to monitor the soil temperature.

Monitoring Groundwater-Level

The groundwater level is monitored by the 2# monitoring well, which is 6 m from the nearest SWC. The groundwater-level monitoring terminal automatically measures groundwater-level, and the data are saved automatically in memory and exported regularly to the computer.

Monitoring Groundwater Circulation

During the operation of the SWC system, the following flow rates are monitored: 12 sets of SWCs inlet-outlet pipe flows, the well-side main pipeline supply-return water flow, the circulating pump supply-return water flow, and other parameters. The minimum monitoring frequency was once per month during the operation period.

Power Consumption Record

The main operating cost of the SWC system is electricity charge, which is required to monitor the SWC system's operational costs and to analyze its power consumption. During the operation of the SWC system, electric meters were set up to monitor the electric consumption of the submersible pump of the single well, the circulating pump and the HPUs. There were two compressors for the 1# and 2# HPUs, respectively, and each compressor was equipped with an electric meter. The 3# and 4# HPUs were also equipped with electric meter, respectively. The 4# HPU and 12 branches of the submersible pumps used the same electric meter. The following automatic calculations occurred in the background: cumulative total power of submersible pump equals the cumulative power of the 4# unit and the 12 submersible pump branches minus the cumulative power of the 4# unit.

Monitoring Platform

The monitoring software had a modular structure consisting of two main modules: a communication unit and a human-machine interface. Each module was composed of several small modules. The communication unit was mainly responsible for communication between the monitoring center and the field equipment. It supported the coexistence of multiple communication methods in a system. The human-machine interface included dynamic system diagrams, a basic data display, manual input, data management and many other functions. The data-collection cycle could be set as required. The specifications of the monitoring system are shown as **Table 1**.

RESULTS AND DISCUSSIONS

Operation Characteristics of SWC System

To analyze the operating characteristics of the SWC coupled GWHP system, we collected the parameters of the well-side supply-return water temperature, the inlet-outlet temperature of 12 SWC systems, the terminal supply-return water temperature, the fluid flow rate in each link, and the exterior temperature. In addition, two typical days were selected, January 26, 2017 and July 6, 2017, to analyze the operating performance of the SWC system. The typical days were in the middle of the heating and cooling periods when the SWC system had been operating for a long time. Moreover, the SWC system operated in the steady state on the two typical days, which ensured more representative data.

Well-Side Supply-Return Water Temperature

The well-side supply-return water temperature reflects the stability of the SWC system during operation. As shown in **Figure 3**, the well-side supply-return water temperatures vary with time. Changes in the supply-return water temperature show a similar trend in **Figure 3A**. The temperature difference in the supply-return water falls in the range 1.7–4.2°C, which decreases with increasing exterior temperature. An increase in exterior temperature reduces the indoor heat load, which in turn reduces the heat exchanged in the HPU. As indicated in **Figure 3A**, the temperature difference is about 0.5°C between the temperature of the 7# SWC and the main pipeline. This is because the 7# SWC outlet water dissipates heat into the environment and reduces the outlet water temperature at the point where the outlet water enters the main pipeline. Therefore, the temperature of the water supply for the main pipeline is 0.5°C lower than the outlet water temperature of the 7# SWC. We further improve the efficiency by wrapping the main pipeline in insulated pipe to reduce heat loss.

The temperature of the well-side supply-return water for the SWC system during the heating period appear in **Figure 3B**. The temperature difference between the supply and return water is maintained at 5°C in the main pipeline, which indicates that the pumping temperature is relatively stable and not affected by the return water in the pumping area of the wells. During the cooling period, the 10# SWC outlet water temperature is higher than the temperature of the main pipeline supply water for a reason, which is similar to that of the heating period. **Figures 3A,B** show that the temperature difference between the supply and return water during the cooling period is greater than that during the heating period, which reveals that the cooling capacity exceeds the heating capacity given the same time and flow conditions. In addition, the efficiency of the cooling period is relatively high, and the SWC system operates stably with large thermal reserves. Furthermore, heat loss from the main pipeline significantly degrades the performance of the SWC system, therefore, we must consider heat loss when designing a SWC system.

Fluid Circulation

Figure 4 shows the mean fluid temperature (right axis) and the flow rate (left axis) as functions of time during the heating and cooling periods. The flow rate is 5.62 m^3/min in the steady state, as shown in **Figure 4A**. The mean fluid temperature fluctuates between 10.0 and 11.5°C, giving a fluctuation range of 1.5°C. **Figure 4A** shows that the mean fluid temperature rises with increasing pumping capacity. The system was initially operated with a low supply-water temperature because the well supply water was mixed with return water from the previous day's thermal breakthrough and incomplete heat exchange. With the system in operation, part of the supply water came from the aquifer, so the water temperature was higher, which explains the phenomenon. This means that the aquifer stores abundant energy, and this is beneficial for long-term operation of the system.

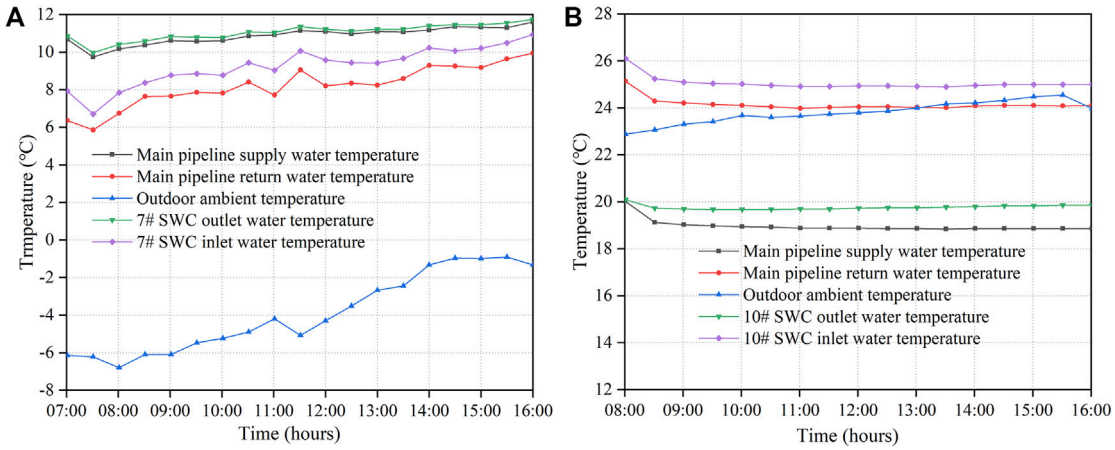

FIGURE 3 | Well-side supply-return water temperature as a function of time during **(A)** heating period (January 26, 2017) and **(B)** cooling period (July 6, 2017).

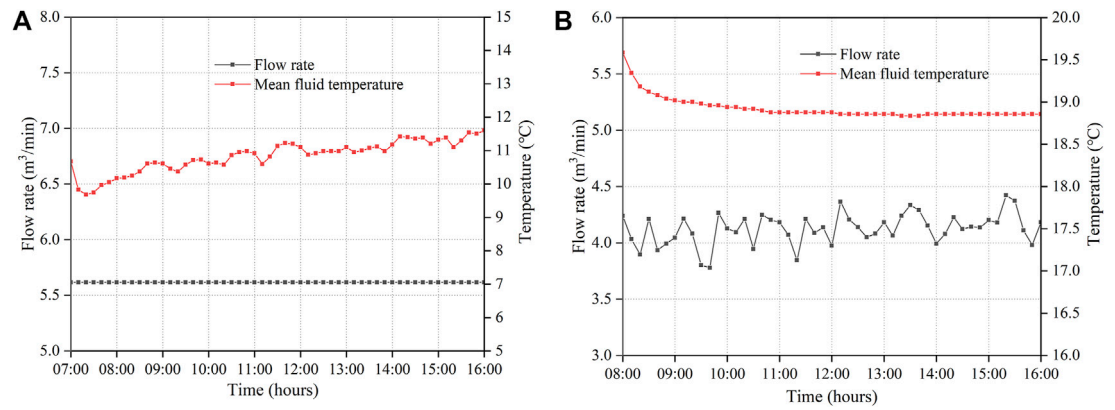

FIGURE 4 | Mean fluid temperature and flow rate as functions of time during **(A)** heating period (January 26, 2017) and **(B)** cooling period (July 6, 2017).

Figure 4B shows that, during the cooling period, the flow rate and mean fluid temperature different from those during the heating period. After 30 min of operation, the flow temperature drops from 19.5 to 18.8°C and then remains stable. This evolution is attributed to the temperature monitoring device, which is affected by the surrounding environment-in this case, cooling water that flowed over in the pipe, causing a period of temperature fluctuation. The flow rate fluctuates in the range 3.7–4.4 m^3/min (a fluctuation range of 0.7 m^3/min). Given the essentially constant fluid temperature in **Figure 4B**, the SWC system is in normal operation.

Temperature of Terminal Supply-Return Water

Figure 5 shows the temperature and flow rate as functions of time of the terminal supply-return water. In the first 25 min, the temperature of the terminal supply-return water increases as the system starts operation, as shown in **Figure 5A**. This is because that the temperature of the water remaining in the pipe is lowered by the lower exterior temperature. Thus, the remaining water should be discharged.

The two curves also mirror each other in **Figure 5B**. The supply-return water of the terminal main pipe is supplied by different HPUs, so the variation indicates that the other HPUs are operating stably and properly. At 13:30, both curves rise by about 1°C because the operator adjusted the set temperature according to the actual load requirements. To meet the cooling load, the energy savings of the system are about 5% in actual operation when the supply-water temperature increase by 1°C to meet the building load, the temperature of the supply water it should be adjusted to save energy.

Geo-Temperature Field of SWC System Under Long-Term Operation

The operating performance of the SWC system is closely related to the geo-temperature field, making it necessary to monitor and analyze the underground temperature. We monitored the

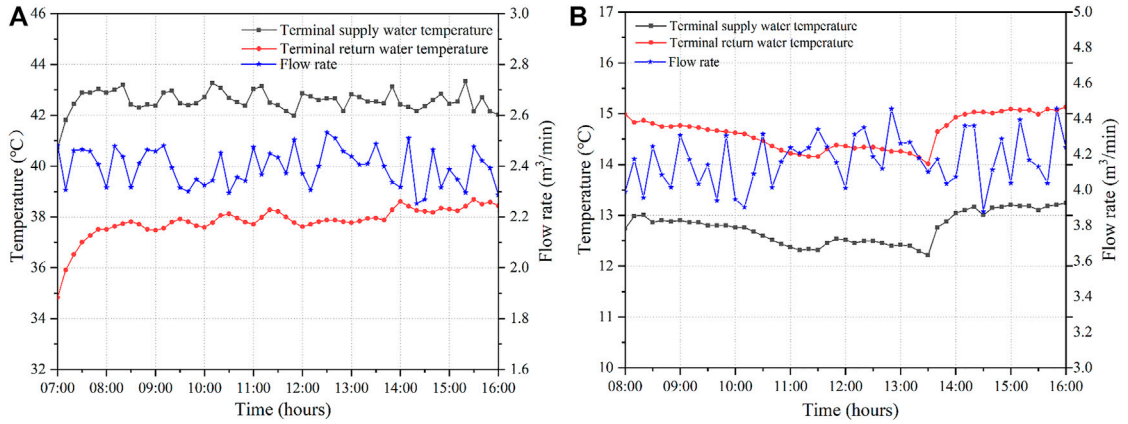

FIGURE 5 | Temperature and flow rate of terminal supply-return water as a function of time during **(A)** operation in heating period (January 26, 2017) and **(B)** operation in cooling period (July 6, 2017).

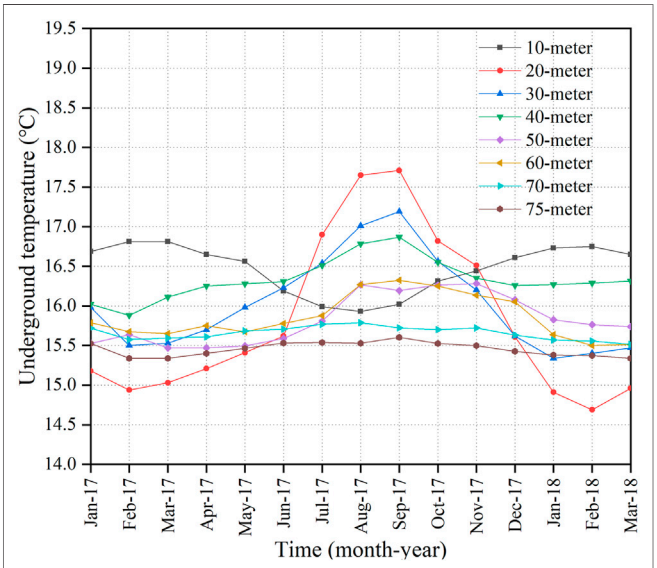

FIGURE 6 | Underground temperature at different depths from January 17, 2017 to March 18, 2018.

underground temperature of the 1# monitoring well (see **Figure 6**). The monthly mean underground temperatures for different depths around the SWC were recorded from January 2017 to March 2018. The underground temperatures at 10 m intervals underground (see **Figure 1**) serve to investigate the temperature variations.

The temperature variations at 10-m depth are opposite those of the other depths shown in **Figure 6** (concave versus convex). The 10-m depth is thus within the variable-temperature part, where the temperature basically follows the annual average surface temperature. The temperature varies the most at 20-m depth, and where the curve is convex. The maximum temperature difference is about 3°C. Because the 20-m depth is near the injection zone, its temperature is significantly influenced by recharge water. During the transition period, the temperature recovers slowly, producing a natural heat exchange. During the cooling period, the surplus heat is injected underground through the injection area, and in cooling period, the temperature recovers quickly. Using the underground as a heat-storage medium is an effective way to slow the accumulation of heat or cold.

A depth of 30-m falls in the sealing partition zone and is adjacent to the injection zone. The temperature variation resembles that of the 20-m depth, but the maximum temperature difference is 2°C, and the temperature essentially returns to its original value. The 40-m depth is close to the lower part of the sealing partition zone. The temperature varies relatively slowly and weakly here, with a maximum difference of 1°C. The recharge water partially exchanges heat with the surrounding rock and soil, which has a relatively small impact on the underground temperature near 40-m depth. This result shows that the sealing partition is necessary for the SWC system to weaken or avoid thermal breakthrough.

At 50- and 60-m depth, the temperature is relatively stable, which reveals that the recharge water exchanges significant thermal energy with the surrounding rock and soil. However, the recharge water enters into the pumping area, so the temperature at 60-m depth drops by 0.35°C. The SWC system appears to suffer a thermal breakthrough, except that the temperatures at 70- and 75-m depth remain stable. However, the temperature at 70- and 75-m depth drops by 0.1°C, which reflects cold accumulation.

Analyzing the eight curves in **Figure 6** shows that the temperature of each curve is periodic with a period of 15 months. However, the temperature drops over long periods at 60-,70-, and 75-m depth. In particular, the temperature drops by 0.35°C at 60-m depth, which indicates cold accumulation. This is attributed to the imbalance of the cooling and heating loads of the buildings.

To summarize, operating of the SWC system affects the underground temperature, and changes the temperature of the supply-water, and the performance of the SWC system. Therefore, the operating strategy of the SWC system must be

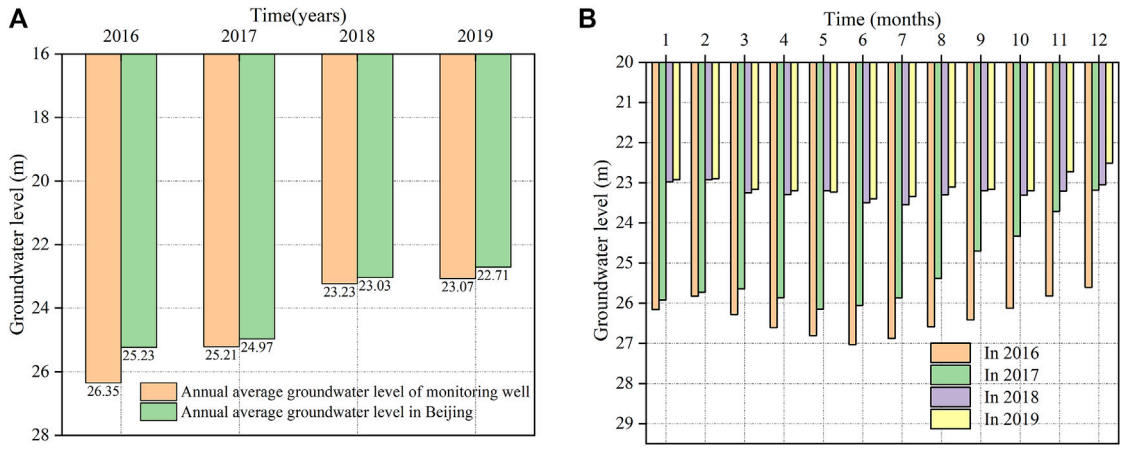

FIGURE 7 | (A) Annual average groundwater level from 2016 to 2019, **(B)** monthly average groundwater level from 2016 to 2019.

adjusted to compensate for increasing heat storage and lengthening of the sealing clapboards.

Monitoring Groundwater Level

Monitoring the groundwater level involves investigating how a system's operation affects the groundwater level and evaluating the sustainability of SWC systems. It is closely related to the long-term operating performance of the system. **Figure 7** shows the annual average groundwater level and the monthly average groundwater level of the monitoring well from 2016 to 2019. In this study, the South-to-North Water-Diversion Project in Beijing caused a huge recharge of groundwater and a concomitant increase in groundwater level. As shown in **Figure 7A**, the groundwater level in Beijing increased 3 m from 2016 to 2019. Compared with the year 2017, the groundwater level in Beijing, rose by 1.94 m in 2018 and, the monitoring-well groundwater level rose by 1.98 m. From 2017 to 2019, the groundwater level fluctuated by 0.2–0.3 m between the groundwater monitoring wells and that of Beijing. Unfortunately, because of the groundwater recharge of the South-to-North Water-Diversion Project, **Figure 7A** does not show whether the SWC system consumes groundwater.

The variations in groundwater level are basically repeated each year (see **Figure 7B**). The groundwater level dropped from January to June in the 4 years studied, reaching the lowest point in May or June, following which they rose from July to December. Although the groundwater level rose every year, it underwent periodic changes, except in 2017 (which is due to the recharge of the South-to-North Water- Diversion Project). Compared with the groundwater level in January, the groundwater level in December varied little from year to year (except for 2017), which indicates that the system operates without consuming groundwater.

To summarize, the operation cycle of a SWC system has a negligible impact on groundwater level, which means that SWC systems do not consume groundwater but only extract heat for building heating and cooling.

Energy Distribution of SWC Coupled GWHP System

Heat Exchange of SWC System

To determine the actual performance of SWC systems, we analyze and evaluate the heat exchange capacity (*HEC*) of the HPUs on the well side. The heat exchanged is expressed as:

$$Q = \rho\, c\, (T_{inlet} - T_{outlet})\, q\, t \tag{1}$$

where Q is the heat exchanged [J], ρ is the density of water [kg/m^3], c is the specific heat capacity of water [J/Kg°C], T_{inlet} and T_{outlet} are the inlet and outlet temperatures of the well side, respectively [°C], q is the flow rate of sidewall water [m^3/h], and t is time [h].

The data recorded on a typical day are used in **Eq. 1**. **Figure 8A** shows that the *HEC* average is 247 kW h, and the average energy consumption is 42.7 kW h. In **Figure 8A**, the ratio of the two averages is 1:5.88. During the cooling period, the *HEC* of the 2# HPU compressor is relatively high, reflecting the high efficiency and stability of the system operation. **Figure 8B** shows the *HEC* of 2# HPU for the heating period. The two curves basically mirror each other, with similar ranges of variation. The maximum *HEC* and energy consumption reaches 180 and 41 kW h, respectively. In **Figure 8B**, the ratio of energy consumption and average *HEC* is 1:4.5. Compared with the cooling period in **Figure 8A**, the heat exchange efficiency (*HEE*) is lower than that during the cooling period. **Figure 3** shows that the difference in temperature of the supply water during the cooling period exceeds that during the heating period. Thus, according to **Eq. 1**, the *HEE* is higher under the same conditions.

Figure 9 shows the *HEC* of the 1# and 2# HPUs operating together versus time during the heating period. The *HEC* of the HPUs gradually increases with increasing energy consumption. However, when the energy consumption reaches a threshold, the *HEE* begins to decrease or is even limited. As indicated in **Figure 9**, the total energy consumption of compressor is about 115 kW h, and the maximum *HEC* is 320 kW h, so the *HEC* decreases. The *HEC* of the system is not positively proportional to

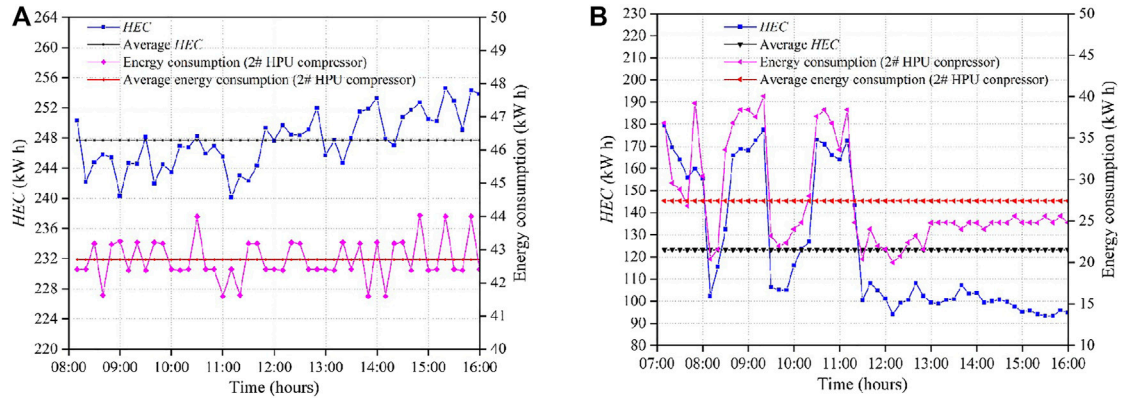

FIGURE 8 | *HEC* of SWC system and energy consumption as a function of time during **(A)** cooling period (July 6, 2017) and **(B)** heating period (January 20, 2017).

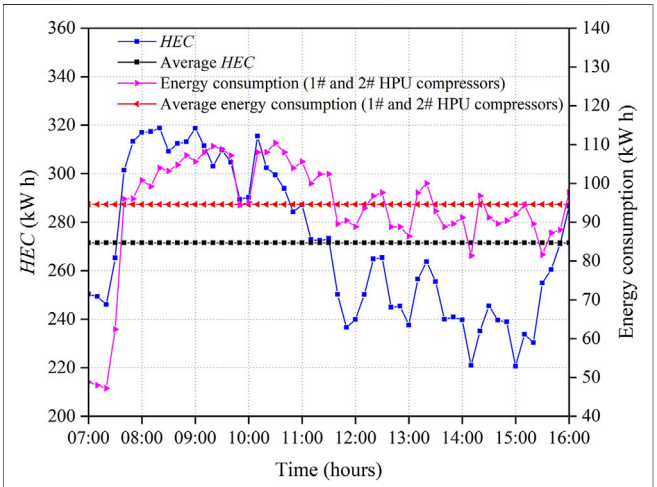

FIGURE 9 | *HEC* of system and energy consumption as a function of time during heating period (January 17, 2018).

the energy consumption of the compressor, therefore the *HEE* decreases after reaching a threshold. To maintain a high the HPU efficiency, the HPU should be equipped with complete control equipment.

The ratio of the two average lines in **Figure 9** is 1:2.87. Compared with the analogous ratio during the heating period (**Figure 8B**), the *HEE* is lower than that of a single HPU during the heating period. The *HEE* of a single HPU is thus stronger than that of multiple-HPUs over a heating period. In addition, the ratio of the two average values during the cooling period (**Figure 8A**) also exceeds that in **Figure 9**. A comprehensive comparison shows that the *HEE* of the system during the cooling period is greater than that during the heating period. Therefore, energy consumption should be reduced by optimizing the operation strategy.

Energy Consumption of Each Part of the SWC System

The economy and efficiency were investigated over the long-term operation of the SWC system. **Figure 10** shows the total energy consumption (*TEC*) and monthly energy consumption of each part. The *TEC* of the system varies periodically, therefore the energy consumption is basically the same each year, except from May 2016 to March 2017 (**Figure 10A**), which is because the system was in the trial operation and commissioning stage and thus consumed more energy in this period. The school schedule includes holidays in February and August each year, so some buildings are not heated or cooled at these times. In addition, only 15 days of heating are provided in November and March. Therefore, the system consumes relatively little energy during these periods.

The *TEC* during the heating period exceeded that during the cooling period (**Figure 10A**). The ratio of *TEC* during the heating period to that during the cooling period falls in the ranges 2.70–2.79, which may be explained by two main reasons. The first reason is that the 4# HPU was turned on to supply hot water and therefore consumed a larger amount of energy. The second reason is that the system is less efficient during the heating period than during the cooling period, resulting in increased of energy consumption. The average temperature difference of the main pipeline supply-return water during the cooling period is 2.15°C higher than that of in heating period, as shown in **Figure 3**. Therefore, the system can extract more heat during the heating period. To further investigate the composition of the system *TEC* and the difference in energy consumption between the heating period and the cooling period, we plot each part of the energy consumption of the system, **Figure 10B**, and the data are listed in **Table 2**.

Each part of the energy consumption from May 2016 to June 2018 is recorded, and the ratio of 4 # HPU energy consumption is displayed in **Figure 10B**. Using **Table 2**, the ratio of the 4# HPU energy consumption to the energy consumption of the system was 0.24 and 0.13 during the two heating periods. Therefore, the 4# HPU was one of the reasons for the large energy consumption in the heating period. Excluding the energy consumption of the 4# HPU in the system, the ratio of the *TEC* of the heating period and that of the cooling period was 2.43:1. Compared with the ratio of the *TEC* above, the maximum difference between the

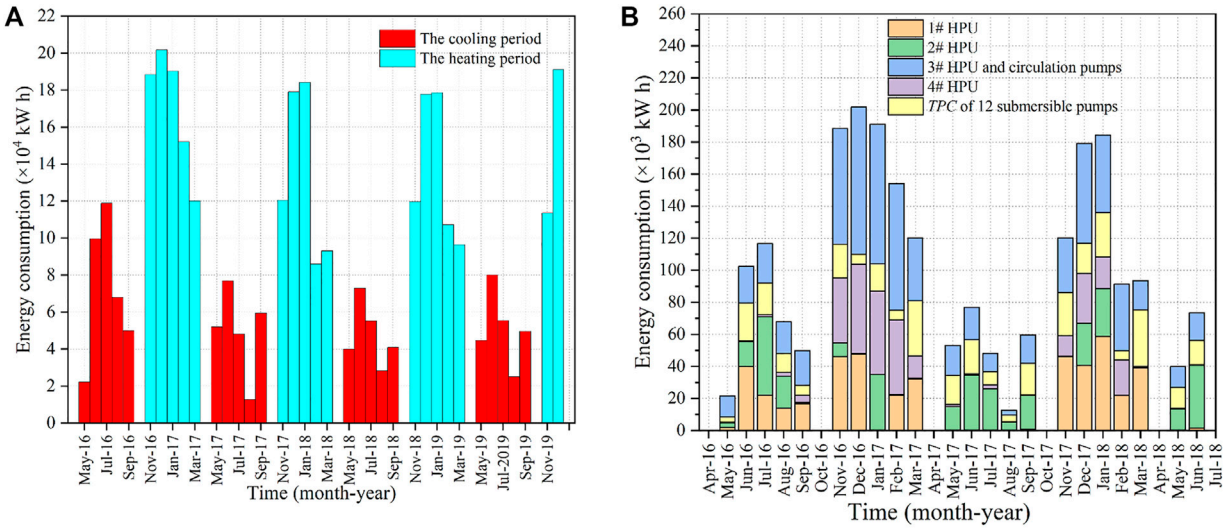

FIGURE 10 | (A) Total energy consumption of the SWC system from 2016 to 2019 and **(B)** each part the energy consumption of the SWC system from 2016 to 2018.

TABLE 1 | Specification of the monitoring system.

Parameter	Specification
Fluid temperature	One-piece temperature transmitter: PT-1000 platinum resistance, Measuring range: 25–85°C, monitoring accuracy ≥0.3%, pressure bearing ≥0.6 MP. Support remote signal output and communication protocol
Flow rate	Integrated pipe section ultrasonic flowmeter: monitoring accuracy ≥±1%; pressure bearing≥0.6 MP: DC2V power supply, power ≤1.6 W Instantaneous flow and velocity, cumulative flow and running time measured; supports time data storage, remote signal output and communication protocol
Underground temperature	Temperature monitoring cable: accuracy of ±0.01°C

ratios was only 0.36. Thus, the *TEC* was greater during the heating period than the during the in cooling period.

As shown as **Figure 10B**, the HPU consumed the most energy in the system, followed by the submersible pump and then the circulating pump (during the cooling period). According to this analysis, the energy consumption of the HPU compressor accounted for about 60–70% of the energy consumption of the system during the heating period. During the cooling period, the energy consumption of the HPU compressor accounted for about 50% of the energy consumption of the system. Therefore, to meet the load, the reduced of the energy consumption of the HPU can improve the system energy efficiency, thereby saving and reducing emissions.

TABLE 2 | 4# HPU energy consumption in the SWC system.

Date	4#HPU energy consumption (kW h)	*TEC* of system (kW h)	Ratio
Nov-2016	40703.2	188533.1	0.22
Dec-2016	55812.8	201718.1	0.28
Jan-2017	52162.5	190280.6	0.27
Feb-2017	46420.5	152041.8	0.32
Mar-2017	13762.4	120092.5	0.13
Nov-2017	12766.4	120510.3	0.11
Dec-2017	30841.6	179089	0.17
Jan-2018	19732.8	184201.8	0.11
Feb-2018	21871.0	85937.8	0.25
Mar-2018	544.0	93027.0	0.01

Energy Efficiency of SWC System

Coefficient of Performance of HPU

The coefficient of performance (*COP*) is an important indicator of the energy efficiency of a heat pump and this is defined as the ratio of the cooling capacity (heating capacity) to the input power.

The cooling capacity (heating capacity) Q of the HPU is given by:

$$Q = V \rho c \Delta t/3600 \quad (2)$$

where V is the average flow on the user side of the HPU [m^3/h], Δt is the temperature difference between the inlet and the outlet on the user side of the HPU [°C], ρ is the density of water [kg/m^3], and c is the specific heat capacity of water [kJ/(kg °C)].

The *COP* of a heat pump during the cooling period can be expressed as:

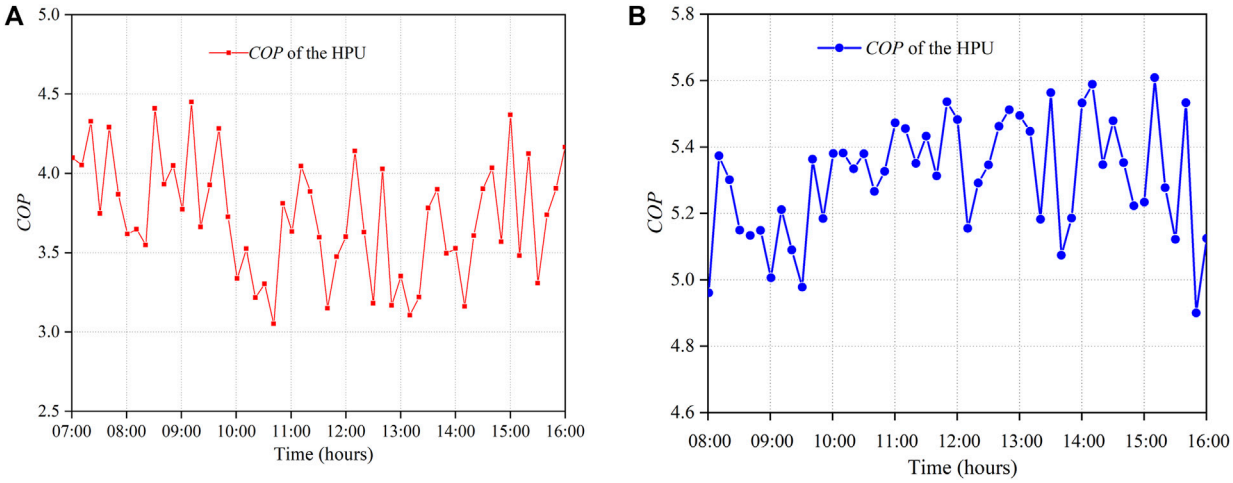

FIGURE 11 | *COP* of an HPU as a function of time for a typical day during **(A)** heating period (January 26, 2018) and **(B)** cooling period (July 4, 2017).

$$COP = \frac{Q}{Ni} \tag{3}$$

where *COP* is the cooling (heating) coefficient of the unit, *Q* is the average cooling (heating) capacity of the unit [kW h], *Ni* is the average input power of the unit [kW h].

The *COP* of the system is the ratio of the cooling capacity (heating capacity) to the total energy input into the system.

The energy sufficiency ratio of the system can be written as follows:

$$COP_s = \frac{Q}{N_i + \Sigma N_j} \tag{4}$$

where COP_s is the cooling (heating) energy efficiency ratio of the system, *Q* is the total cooling capacity (heating capacity) [kW h], N_i is the energy consumption of the HPU [kW h], $\sum N_j$is the sum of electricity consumption of the submersible pumps and circulating pumps [kW h].

COP of HPU During Operation

Figure 11 plots the *COP* for HPU as a function of time during operation with time intervals of 10 min. During heating (cooling) period, the average *COP* was 3.7 (5.3), which meets the design requirements for the normal operation of the system. The average *COP* for an HPU during the cooling period exceeded that during the heating period. The difference in the average *COP* between cooling and hearing periods was 1.6. Although the heat-pump reverse Carnot cycle predicts a greater *COP* during the heating period, the opposite occurs in practical engineering because the temperature difference of the supply-return at the well side and the operating power differ between the cooling period and the heating period in actual operation.

In **Figure 11A**, it can be seen that the *COP* fluctuates during the heating period. The overall trend of the *COP* is decreasing, and the *COP* decreases to a minimum at 10:00-11:00 because the indoor temperature increases gradually as the SWC system operates and peaks at 10:00-11:00 in practical operation. Combined with the relation in **Figure 9** between *HEE* and energy consumption, the variation in the *COP* is similar in **Figure 11A**. In addition, the heat pump reverse Carnot cycle predicts that, the heating coefficient of a heat pump decreases with increasing temperature of the high-temperature object. It also verifies that the *COP* varies with indoor temperature in **Figure 11A**. Therefore, the *COP* of an HPU may be increased by optimizing the system operation.

COP_s of SWC System

Figure 12 plots *COPs* as a function of time with a time interval of 10 min for the SWC system operating during the heating and cooling periods. As shown in **Figure 12A**, the value of COP_s fell in the range 2.5-3.5 with an average of 3.0 during the heating period. As shown in **Figure 12B**, COP_s fell in the range 3.1-4.2 with an average of 3.6 during the cooling period. The difference between the average COP_s of the heating and cooling periods was 0.6. The lower average *COPs* in the heating period is due to the significant power consumption of the submersible pumps and circulating pumps. To improve efficiency, the energy consumption of the submersible pumps and circulating pumps should be decreased. During the heating period, the operating efficiency of the SWC system is less than that during the cooling period. The SWC system is thus more efficient during the cooling period.

Long-Term Operation Performance of SWC System and HPUs

Figure 13 shows that the monthly average *COP* and *COPs* from May 2016 to Jul 2018, which show similar fluctuations. COP_s and *COP* reach their lowest levels in January. One reason for this phenomenon is that the system has been running for a long time and experiences a slight thermal breakthrough (Tu et al., 2018), which decreases its energy efficiency. In addition, the decrease in exterior temperature increases the indoor load, which indirectly reduces the energy efficiency. However, during the cooling

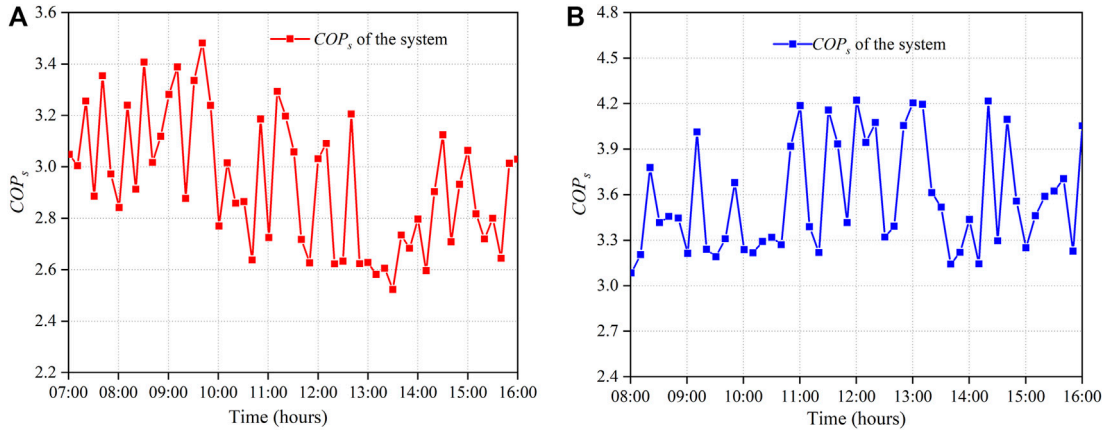

FIGURE 12 | COP_s of the SWC system as a function of time for a typical day during **(A)** heating period (January 26, 2018) and **(B)** cooling period (July 4, 2017).

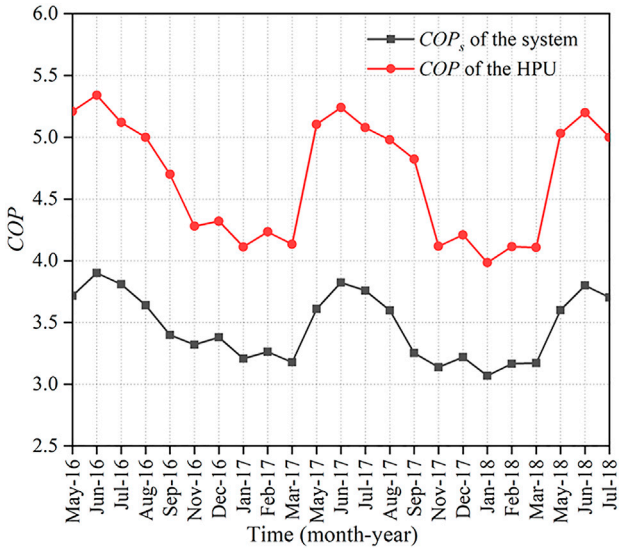

FIGURE 13 | *COP* as a function of time of SWC system and HPU from May 2016 to Jul 2018.

period, the COP_s and *COP* decrease. As shown in **Figure 3**, the temperature difference between the supply and return water is 5°C during the cooling period. The lower temperature return water affects the temperature of the pumping area in long-term operation (Tu et al., 2018).

Under the long-term operation of system, COP_s varies slightly during the long-term operation of the system. The average COP_s value was 3.25 from November 2016 to March 2017, and the average COP_s was 3.19 from November 2017 to March 2018. The difference between the two periods is 0.06. The COP_s of SWC system thus varied by 0.06. In addition, the *COP* of the HPU varied by 0.036. Meanwhile, two curves have a downward trend as whole in **Figure 13**. This phenomenon is caused by thermal breakthroughs during the long-term operation and attenuation of the system (Tu et al., 2020b). According to **Figure 6**, the phenomenon of cold accumulation is also a reason to make the system COP_s change. Therefore, thermal breakthrough and the cold accumulation should be considered in system design. In practical engineering, thermal breakthrough should be avoided by lengthening the sealing zone (Song et al., 2019a). Furthermore, the variations in the system *COPs* and the HPU *COP* curves verify the high efficiency and energy savings of the SWC system.

CONCLUSION

We investigate the operating performance of an SWC coupled GWHP system by monitoring 4 years of data. The SWC system was designed for an HVAC system for a middle school in the Haidian District of Beijing, China. The data were analyzed to determine the system performance, including the supply-return water temperature of the well and user sides, the underground temperature, the groundwater level, and the energy consumption of the HPUs. In addition, suggestions have been made to optimize the system. Overall, the system operates in a stable and efficient state. The results lead to the following main conclusions.

1) The SWC system operation has a periodic effect on the underground temperature. The return water basically completes heat exchange with the surrounding rock and soil, and enters the pumping water area. However, part of the low-temperature recharge water enters the pumping area and causes thermal breakthrough. In addition, cold accumulates underground due to the imbalance of the cold and hot load.
2) The *HEE* of the cooling period is greater than that of the heating period, and the ratio of the two *HEEs* approaches two. Also, the *HEE* of a single HPU is greater than that of multiple units during the heating period, and the *HEE* of the two approaches 1.6.
3) The energy consumption of the SWC system during the heating period exceeds that during cooling period. The ratio of energy consumption during the heating period to

that during the cooling period is 2.4:1. For the SWC system, the HPUs consume the most power, accounting for 60–70% of the *TEC* during the heating period, and about 50% of the *TEC* during the cooling period.

4) The *COP* of an HPU decreases with the increase of indoor temperature when the indoor temperature (heated object) reaches a certain temperature.
5) The COP_s and *COP* values during the cooling period exceed those during the heating period, and the *COP* and COP_s values vary periodically during the long-term operation of the SWC system, when the COP_s (COP) of the SWC system decreases by 0.06 (0.036). This phenomenon is caused by thermal breakthrough and the accumulation of cold during the long-term operation of the system. This topic should be studied further in future work.

DATA AVAILABILITY STATEMENT

The original contributions presented in the study are included in the article/supplementary material, further inquiries can be directed to the corresponding author.

AUTHOR CONTRIBUTIONS

KZ, YFZ, and QW contributed to conception and design of the study. KZ wrote the first draft of the manuscript and performed the statistical analysis. SHX, KT, and XXL wrote sections of the manuscript. All authors contributed to manuscript revision, read, and approved the submitted version.

FUNDING

This research was financially supported by the China National Natural Science Foundation (41430318, 41572222, 41877186, 41602262, 41702261), the National Key R&D Program of China (2016YFC0801800), the Beijing Natural Science Foundation (8162036), and the Fundamental Research Funds for the Central Universities (2010YD02).

ACKNOWLEDGMENTS

The authors would like to thank the editor and reviewers for their constructive suggestions.

REFERENCES

Al-Sarkhi, A., Abu-Nada, E., Nijmeh, S., and Akash, B. (2008). Performance Evaluation of Standing Column Well for Potential Application of Ground Source Heat Pump in Jordan. *Energ. Convers. Management* 49, 863–872. doi:10.1016/j.enconman.2007.06.028

Blázquez, C. S., Verda, V., Nieto, I. M., Martín, A. F., and González-Aguilera, D. (2019). Analysis and Optimization of the Design Parameters of a District Groundwater Heat Pump System in Turin. *Italy. Renew. Energ.* 149, 374–383.doi:10.1016/j.renene.2019.12.074

Chang, K. S., Kim, M. J., and Kim, Y. J. (2017). An Experimental Study on the Thermal Performance Evaluation of SCW Ground Heat Exchanger. *Int. J. Air-Conditioning Refrigeration* 25 (1), 1750006. doi:10.1142/s2010132517500067

Chang, K. S., Kim, Y. J., and Kim, M. J. (2019). An Investigation of Hydrological Effects on the thermal Performance of Standing Column Well Using the *In-Situ* thermal Response Test. *Int. J. Air-Conditioning Refrigeration* 27 (2). doi:10.1142/s2010132519500159

Choe, T. C., and Ko, L. J. (2017). Method of Simulation and Estimation of SCW System Considering Hydrogeological Conditions of Aquifer. *Energy & Buildings* 163, 140–148. MAR. doi:10.1016/j.enbuild.2017.10.058

Deng, Z., Rees, S. J., and Spitler, J. D. (2005). A Model for Annual Simulation of Standing Column Well Ground Heat Exchangers. *Hvac&r Res.* 11 (4), 637–655. doi:10.1080/10789669.2005.10391159

Deng, Z., Spitler, J. D., and Rees, S. J. (2006). Performance Analysis of Standing Column Well Ground Heat Exchanger Systems. *ASHRAE Trans.* 112 (2), 633–643.

Fang, Q., and Zhang, Y. (2020). Evaluation of the Performance of a Hybrid Cooling/heating System Combining Groundwater Direct Cooling with Groundwater Heat Pump for Rural Buildings. *IOP Conf. Ser. Earth Environ. Sci.* 467, 012049. doi:10.1088/1755-1315/467/1/012049

Hein, P., Kolditz, O., Görke, U.-J., Bucher, A., and Shao, H. (2016). A Numerical Study on the Sustainability and Efficiency of Borehole Heat Exchanger Coupled Ground Source Heat Pump Systems. *Appl. Therm. Eng.* 100, 421–433. doi:10.1016/j.applthermaleng.2016.02.039

Kastrinos, J. R., Chiasson, A., and Ormond, P. (2019). Estimating Groundwater Heat Exchange in a Standing-Column Well by Injection of a Bromide Tracer. *Geothermics* 82, 121–127. doi:10.1016/j.geothermics.2019.06.006

Lee, D. Y., Seo, B. M., Hong, S. H., Choi, J. M., and Lee, K. H. (2019). Part Load Ratio Characteristics and Energy Saving Performance of Standing Column Well Geothermal Heat Pump System Assisted with Storage Tank in an Apartment. *Energy* 174, 1060–1078. MAY 1. doi:10.1016/j.energy.2019.03.029

Lee, K. S. (2011). Modeling on the Performance of Standing Column Wells during Continuous Operation under Regional Groundwater Flow. *Int. J. Green Energ.* 8 (1-4), 474–485. doi:10.1080/15435075.2011.576290

Léo, C., Courcelles, B., and Pasquier, P. (2020). Impact of Standing Column Well Operation on Carbonate Scaling. *Water* 12 (8), 2222. doi:10.3390/w12082222

Li, H., Yang, L., and Dong, H. Q. (2013). Groundwater Source Heat Pump Technology Use for Heating and Air-Conditioning of a Commercial Building. *Adv. Mater. Res.*, 608–609. doi:10.4028/www.scientific.net/AMR.608-609.994

Luo, J., Luo, Z., Xie, J., Xia, D., Huang, W., Shao, H., et al. (2018). Investigation of Shallow Geothermal Potentials for Different Types of Ground Source Heat Pump Systems (GSHP) of Wuhan City in China. *Renew. Energ.* 118, 230–244. doi:10.1016/j.renene.2017.11.017

Luo, J., Xue, W., and Shao, H. B. (2020). Thermo-economic Comparison of Coal-Fired Boiler-Based and Groundwater-Heat-Pump Based Heating and Cooling Solution – A Case Study on a Greenhouse in Hubei, China. *Energy and Buildings* 223, 110214. doi:10.1016/j.enbuild.2020.110214

Mikler, V. (1993). A Theoretical and Experimental Study of the Energy Well Performance, Master Thesis. Tarragona: Pennsylvania State University.

Minea, V. (2013). Experimental Investigation of the Reliability of Residential Standing Column Heat Pump Systems without Bleed in Cold Climates. *Appl. Therm. Eng.* 52, 230–243. doi:10.1016/j.applthermaleng.2012.11.031

Nguyen, A., Beaudry, G., and Pasquier, P. (2020). Experimental Assessment of a Standing Column Well Performance in Cold Climates. *Energy and Buildings* 226, 110391. doi:10.1016/j.enbuild.2020.110391

Ni, L., Li, H., Jiang, Y., Yao, Y., and Ma, Z. (2011). A Model of Groundwater Seepage and Heat Transfer for Single-Well Ground Source Heat Pump Systems. *Appl. Therm. Eng.* 31, 2622–2630. doi:10.1016/j.applthermaleng.2011.04.030

Orio, C. D. (1994). Geothermal Heat Pumps and Standing Column wells. *Geothermal Resour. Counc. Trans.* 18, 375–379.

Orio, C. D., Johnson, C. N., Rees, S. J., Chiasson, A., Deng, Z., and Spitler, J. D. (2005). A Survey of Standing Column Well Installations in North America. *ASHRAE Trans.* 111 (2), 109–121.

Park, B.-H., Bae, G.-O., and Lee, K.-K. (2015). Importance of thermal Dispersivity in Designing Groundwater Heat Pump (GWHP) System: Field and Numerical Study. *Renew. Energ.* 83, 270–279. doi:10.1016/j.renene.2015.04.036

Qiu, H., Gui, H., Fang, P., and Li, G. (2021). Groundwater Pollution and Human Health Risk Based on Monte Carlo Simulation in a Typical Mining Area in Northern Anhui Province, China. *Int. J. Coal. Sci. Technol.*

Sommer, W., Valstar, J., Leusbrock, I., Grotenhuis, T., and Rijnaarts, H. (2015). Optimization and Spatial Pattern of Large-Scale Aquifer thermal Energy Storage. *Appl. Energ.* 137, 322–337. doi:10.1016/j.apenergy.2014.10.019

Song, W., Ni, L., and Yao, Y. (2019). Experimental Research on the Characteristics of Single-Well Groundwater Heat Pump Systems. *Energy and Buildings* 191, 9062. doi:10.1016/j.enbuild.2019.02.039

Song, X., Wang, G., Shi, Y., Zheng, R., and Li, J. (2019). Numerical Analysis on Thermal Characteristics of an Open Loop Geothermal System in a Single Well. *Energ. Proced.* 158, 6112–6117. doi:10.1016/j.egypro.2019.01.501

Sun, H. Z., Wu, Q., Xu, S. H., Zeng, Y. F., and Liu, S. H. (2015). Research on Thermophysical Characteristics with SWGECCHE Coupled by Stokes-Darcy Flow. *Acta Energiae Solaris Sinica* 31, 2571–2577.

Tu, K., Wu, Q., and Sun, H. Z. (2018). A Mathematical Model and thermal Performance Analysis of Single-Well Circulation (SWC) Coupled Ground Source Heat Pump (GSHP) Systems. *Appl. Therm. Eng.* 147, S1359431117366747. doi:10.1016/j.applthermaleng.2018.09.029

Tu, K., Wu, Q., Simunek, J., Chen, C. F., Zhu, K., Zeng, Y. F., et al. (2020). An Analytical Solution of Groundwater Flow in a Confined Aquifer with a Single-Well Circulation System. *Water Resour. Res.* 56, e2020WR027529. doi:10.1029/2020WR027529

Tu, K., Wu, Q., Simunek, J., and Zhu, K. (2020). An Approximate Analytical Solution for Non-darcian Flow in a Confined Aquifer with a Single Well Circulation Groundwater Heat Pump System. *Adv. Water Resour.* 145, 103740. doi:10.1016/j.advwatres.2020.103740

Wu, Q., Tu, K., Sun, H., and Chen, C. F. (2018). Investigation on the Sustainability and Efficiency of Single-Well Circulation Groundwater Heat Pump Systems. *Renew. Energ.* 130, 656–666. JAN. doi:10.1016/j.renene.2018.06.107

Wu, Q., Xu, S., Zhou, W., and LaMoreaux, J. (2015). Hydrogeology and Design of Groundwater Heat Pump Systems. *Environ. Earth Sci.* 73 (7), 3683–3695. doi:10.1007/s12665-014-3654-2

Yuill, G. K., and Mikler, V. (1995). Analysis of the Effect of Induced Groundwater Flow on Heat Transfer from a Vertical Open-Hole Concentric-Tube thermal Well. *ASHRAE Trans.* 101 (1), 173–185.

Zeng, Y. F., Zhou, W. F., and Lamoreaux, J. (2017). Single-well Circulation Systems for Geothermal Energy Transfer. *Environ. Earth Sci.* 76, 296. doi:10.1007/s12665-017-6621-x

Zhang, K., Li, H., Han, J., Jiang, B., and Gao, J. (2021). Understanding of Mineral Change Mechanisms in Coal Mine Groundwater Reservoir and their Influences on Effluent Water Quality: A Experimental Study. *Int. J. Coal. Sci. Technol.* 8 (1), 154–167.

Conflict of Interest: The authors declare that the research was conducted in the absence of any commercial or financial relationships that could be construed as a potential conflict of interest.

Publisher's Note: All claims expressed in this article are solely those of the authors and do not necessarily represent those of their affiliated organizations, or those of the publisher, the editors and the reviewers. Any product that may be evaluated in this article, or claim that may be made by its manufacturer, is not guaranteed or endorsed by the publisher.

frontiers in Earth Science

ORIGINAL RESEARCH
published: 30 November 2021
doi: 10.3389/feart.2021.786051

Geochemical Characteristics of Hydrothermal Volatiles From Southeast China and Their Implications on the Tectonic Structure Controlling Heat Convection

Jiao Tian[1,2,3], *Yiman Li*[2,3], *Xiaocheng Zhou*[1]*, *Zhonghe Pang*[2,3], *Liwu Li*[4], *Lantian Xing*[4] and *Zhongping Li*[4]

[1]Institute of Earthquake Forecasting, China Earthquake Administration, Beijing, China, [2]Institute of Geology and Geophysics, Chinese Academy of Sciences (CAS), Beijing, China, [3]Key Laboratory of Shale Gas and Geological Engineering, Institute of Geology and Geophysics (CAS), Beijing, China, [4]Key Laboratory of Petroleum Resources Research, Northwest Institute of Eco-environment and Resources, Chinese Academy of Science, Lanzhou, China

OPEN ACCESS

Edited by:
Haibing Shao,
Helmholtz Centre for Environmental Research (UFZ), Germany

Reviewed by:
Wenjing Lin,
Chinese Academy of Geological Sciences, China
Nevzat Özgür,
Süleyman Demirel University, Turkey

***Correspondence:**
Xiaocheng Zhou
zhouxiaocheng188@163.com

Specialty section:
This article was submitted to Economic Geology, a section of the journal Frontiers in Earth Science

Received: *29 September 2021*
Accepted: *01 November 2021*
Published: *30 November 2021*

Citation:
Tian J, Li Y, Zhou X, Pang Z, Li L, Xing L and Li Z (2021) Geochemical Characteristics of Hydrothermal Volatiles From Southeast China and Their Implications on the Tectonic Structure Controlling Heat Convection. Front. Earth Sci. 9:786051. doi: 10.3389/feart.2021.786051

Hot springs and igneous rocks are present widely in southeast China, influenced by the subduction of the Western Pacific and Philippine Sea Plates. This study reports on new data of chemical compositions and He–Ne–C isotopes for gas samples from representative hot springs and wells in the Guangdong and Fujian provinces to identify the origin of hydrothermal volatiles and provide insight into geothermal tectonic affinities. The primary hydrothermal volatile component from southeast China is atmospheric N2, with a volumetric percentage of 82.19%–98.29%. It indicates medium-low temperature geothermal systems where geothermal fluids suffered a shallow circulation in closed fracture systems. Low CO_2 and CH4 contents and their depleted δ13C values confirmed the small number of deep-derived components in the study area. However, spatially discernible geochemical characteristics imply enhanced hydrothermal fluid convection in the adjacent area of the two provinces, including the Fengshun, Zhangzhou, Longyan, and Sanming geothermal fields. Specifically, the He–Ne isotopes from this area exhibit mantle He contribution of more than 10% and mantle heat flow accounts for more than half of the total heat flow. Moreover, according to the thermal background calculations, the highest heat flow value of 77.7 mW/m^2 is indicated for the Zhangzhou geothermal area and the lowest value of 54.7 mW/m^2 is indicated for the Maoming geothermal area. Given the epicenter distributions and the corresponding earthquake magnitudes, the NE-trending faults are heat-control tectonic structures and their intersections with the NW-trending faults provided expedite channels for geothermal fluids rising to the surface. Therefore, the preferred development potential of geothermal resources can be expected in the adjacent area of the two provinces where two sets of active faults crossed. This study provides critical information on understanding the geothermal distribution controlled by the tectonic structure in southeast China.

Keywords: Southeast China, geothermal gas, heat-control structure, thermal background, hot springs

1 INTRODUCTION

Convective geothermal systems, also called fracture-controlled geothermal systems, are formed *via* deep-water circulation in tectonically active areas (Santilano et al., 2015). Regional tectonic structures, where extensional channels formed by crossed faults provide channels for geothermal fluid rising to the surface (Jolie et al., 2015), control the formation of this type of system. This type of geothermal system is prominent in nonvolcanic areas with high-temperature backgrounds. The depth of the faults

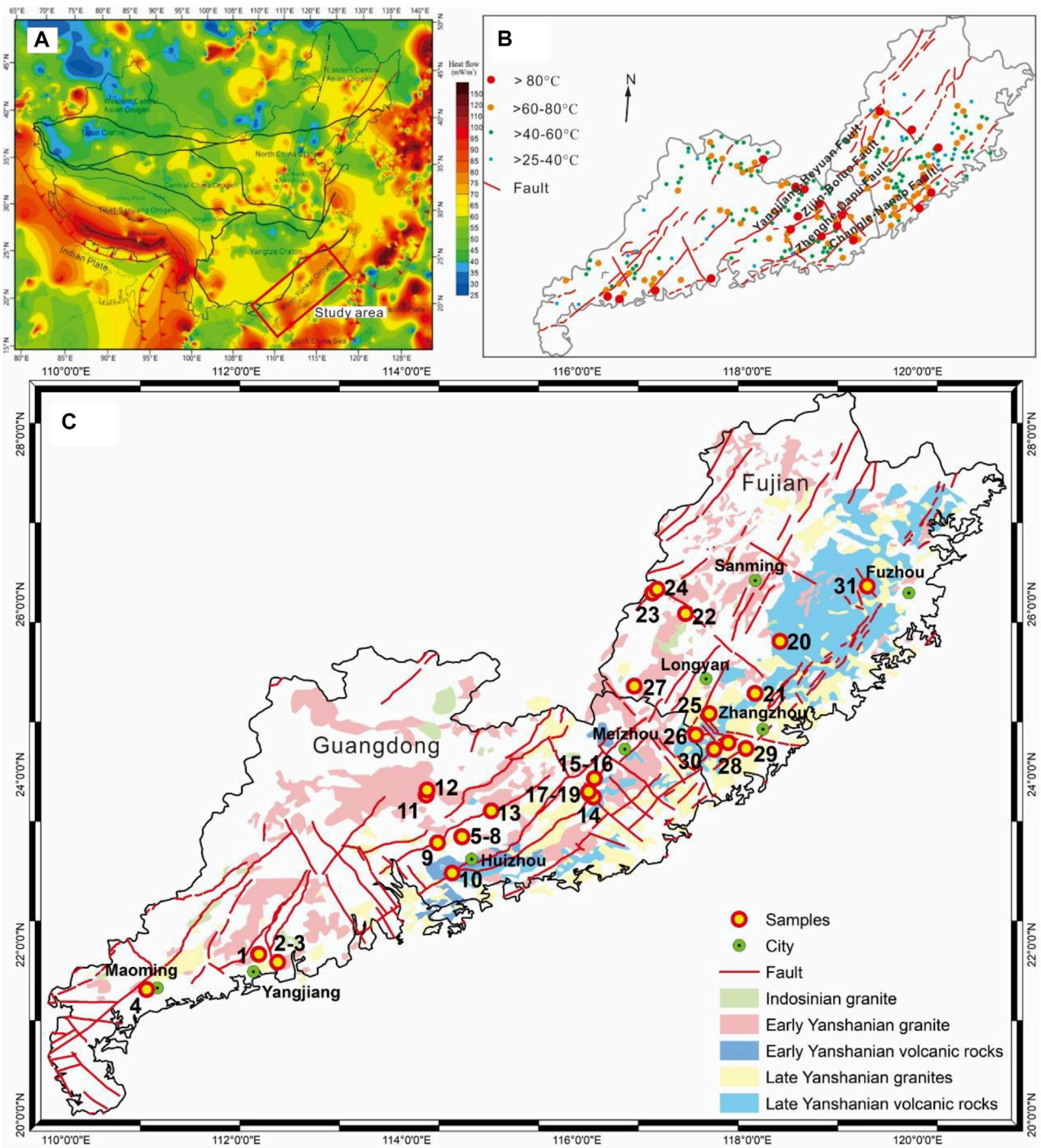

FIGURE 1 | (A) Heat flow map of continental China (Jiang et al., 2019). **(B)** Hot spring and active faults in the study area (Guangdong and Fujian provinces). **(C)** Igneous rocks (Li et al., 2012) and sampling sites in this study (the sampling points are labeled with numbers, which are consistent with those listed in the "No." column in **Table 1**. For the samples located tightly in the study area, they are labeled as a range, for example, "5–8" represents sample number range from 5 to 8).

significantly influences the reservoir temperature. For example, in the eastern edge of the Qinghai–Tibet Plateau, the Xianshuihe fault, an active lithospheric-scale strike-slip fault, functions as a conduit for deep-derived geothermal volatiles, and enhances the heat convection process down to a depth of 8 km, forming high-temperature geothermal systems with reservoir temperatures as high as 260°C. However, in the Longmenshan Thrust fault zone, the shallow groundwater circulation in relatively closed fracture systems accounts for its low reservoir temperature (<150°C), with a circulation depth of less than 4 km (Tian et al., 2021). Thus, extensional deep faults in convective geothermal systems are typically the focus of geothermal exploration as preferential targets for high-temperature geothermal resources.

Located in the coupled domain between the two global geothermal belts, southwest China is a segment of the Mediterranean–Himalayas geothermal belt and southeast China belongs to the Circum–Pacific geothermal belt. These two geothermal belts are marked with high heat flow values (**Figure 1A**). For the southwest part, the Qinghai–Tibet Plateau has attracted the attention of many researchers to conduct studies on how tectonic structures control hot spring distributions (Guo, 2012; Hochstein and Regenauer-Lieb, 1998; Liao and Zhao, 1999). Studies on hydrothermal volatiles were critical in identifying the influence of tectonic structures on geothermal exhibitions (Tian et al., 2021; Zhang et al., 2021; Zhou et al., 2017). The southeast Chinese mainland is characterized by widespread Jurassic–Cretaceous granitic magmatism (**Figures 1B,C**) associated with more than 500 hot springs exposed along a series of NE-trending faults, with temperatures of 50°C–100°C (Pei and Hong, 1995; Jiang et al., 2019). According to recent broadband magnetotelluric (MT) results, no magma chamber or partial melt exists beneath the geothermal systems, and radiogenic heat produced from decaying radioactive elements in the crust is the heat source of southeastern China (Cheng et al., 2021). Therefore, the depth of circulation controlled by active faults could be a critical factor affecting reservoir temperatures. However, only a few hydrothermal studies have focused on the flow path of geothermal water in limited or individual regions in this area (Mao et al., 2015; Qiu et al., 2018; Mao et al., 2020). Genetic models for geothermal volatile origins have not been fully integrated into the geodynamic setting, and a comprehensive understanding of the mechanism of fault controlling hot spring distributions remains deficient for southeast China.

Geothermal gas studies allow tracing deep mass and energy inputs from shallow, meteoric-dominated, and geothermal reservoirs (Lowenstern et al., 2015). Specifically, isotopic and elemental compositions of He, CO_2, and N_2 in the gases are sensitive tracers of crustal and mantle components in the overall volatile inventory (Hilton et al., 2002; Smith et al., 2005; Sano et al., 2017). Furthermore, the melting and stress-induced dilatancy of deep-seated rocks can cause detectable changes in volatile geochemistry (Zhang et al., 2021). Thus, geothermal volatiles have been used as an effective tool for understanding tectonic structures (Hoke et al., 2000; Newell et al., 2008). They provide significant information on active structures and upflow conduit distributions for geothermal fluids in a specific region. In this study, we report chemical compositions and He–Ne–C isotopes for geothermal gas samples from representative hot springs and drilled wells in the Guangdong and Fujian provinces, southeast China, to identify the origin and evolution of hydrothermal volatiles. Finally, this study provides insight into the tectonic affinities with a geothermal distribution in such granite–hosted area.

2 GEOLOGICAL SETTING

As shown in **Figure 1A**, southeast China is a high-heat flow area in the Chinese mainland. Belonging to Wuyi–Yunkai Orogen and located at the junction of the three tectonic systems of the Pacific, Paleo–Asian, and Tethys Oceans, southeast China mostly comprises the Cathaysia Block, Jiangnan Orogen, and Yangtze Block. The interaction among these energetic tectonic domains aerated widespread intracontinental deformation in South China, including intracontinental rifting, a large-scale strike-slip fault with transtension and transpression properties, and an extensional basin (Tannock et al., 2020). Pre-Neoproterozoic crystalline basement rock outcrops are scarce in South China. The Middle–Late Neoproterozoic geology of the South China Block was characterized by continental rifting and widespread anorogenic magmatism since 850 Ma (Wang and Li, 2003; Carter and Clift, 2008). The change in regional tectonic stress from Mesozoic extension to Cenozoic compression in South China is accompanied by the mid-crustal quartz-reef formation in the former to a strike-slip-associated upper-crustal hydrological fault-hosted permeability network (Tannock et al., 2020). The Cenozoic South China tectonic deformation is complex, including coupled rifting and intraplate volcanism faults, uplifting events, a large-scale termination of basin development, and volcanism. The deformation was originally considered to be because of the impact of the Pacific Plate subduction; however, an increasing number of multidisciplinary studies propose that the India–Eurasia collision has a tremendous or decisive effect on the tectonic evolution of South China and even East Asia (Yin, 2010; Gong and Chen, 2014; Wu et al., 2018; Tannock et al., 2020).

The South China Block experienced multistage tectonomagmatic events from the Proterozoic to the Late Mesozoic, contemporaneous with the Indosinian tectonic event in the Indochina Block, forming an intracontinental orogenic belt with a width of approximately 1,300 km and exposing a large area of Mesozoic igneous rocks (Li et al., 2012; Li, 2000). Early Paleozoic granites are widespread in the eastern South China Block. These rocks were mostly dated at 450–420 Ma (Li et al., 2010). Late Paleozoic igneous rocks are exposed only in 290–260 Ma potassic to calc-alkaline intrusive rocks in the Hainan Island and 250 Ma syenites in the Wuyishan Mountains. Mesozoic igneous rocks occur over a vast area in the Fujian and Guangdong provinces. Among these rocks, granites and rhyolites account for nearly 50% each, whereas gabbros and basalts are rare, and diorite and andesites are even less common (Zhou and Li, 2000). They are subdivided into the Triassic (Indosinian-aged), Jurassic (Early Yanshanian),

and Cretaceous (Late Yanshanian) (**Figure 1C**) (Zhou et al., 2006; Li et al., 2012). Indosinian magmatic rocks dominated by plutonic bodies account for only 6.6% of the Mesozoic magmatic rocks. Crustal uplift and subsidence control the Early Yanshanian granites, mostly comprising plutonic intrusive rocks. This is related to crustal thickening caused by the horizontal compression stress field. Since the late Yanshanian, many crust-mantle mixed-source alkaline granite belts and Cenozoic alkaline basalts have appeared, following crustal thinning of the lithosphere of the South China Block (Li et al., 2010; X. et al., 2000).

The multiple tectonic events are characterized by crust shortening deformation and form a tectonic framework of an interpenetrative fault system with dominant NE-trending, concomitant NW-trending and supplementary EW-trending faults. Here, the Yanshannian deformation is characterized by wide NNE-trending thrust-and-fold belts (Li et al., 2019). NNE- and NE-trending faults and NW-trending faults interweave to form a complex fault system controlling tectonic evolution, magmatic activity, geothermal activity, and mineralization. From the north to the south, lithospheric scale faults include the Yangjiang–Heyuan normal fault, the Zijin–Boluo thrust, the Zhenghe–Dapu normal, and the Changle–Nanao normal-dextral strike-slip faults (**Figure 1B**) (Tong and Tobisch, 1996; Shu et al., 2009). As recorded, the thicknesses of the continental crust and the lithosphere of East China are 30–35 and 70 km, respectively. The upwelling asthenosphere heats the thinned lithosphere, developing basin and mountain systems. Consequently, the mantle heat flow significantly increases, accompanying widespread low-medium temperature springs, Cenozoic magmatism, active faults, and earthquakes. Thus, the high heat flow (65–100 Mw m^{-2}) of southeast China corresponds to the thinning of the lithosphere (Zhao G. et al., 1998; Jiang et al., 2019).

3 SAMPLING AND METHODS

In this study, geothermal gas samples were collected from 31 sites, including natural springs and drilled wells. For the bubbling springs, a Teflon funnel that was invertedly submerged into the geothermal spring was used. For drilling wells, a copper cooling coil was connected to the sampling valve on the wellhead. By sinking the cooling coil into cold water, the geothermal fluid was cooled to a temperature lower than 20°C to enhance the degassing process. After the pipe-flushing step, the gas drainage method using a lead glass bottle connected by a silicone tube to the funnel or the cooling coil gathered gaseous samples. After the gas filled approximately two-thirds of the glass bottle volume, the bottle was sealed with a rubber cap. Subsequently, the bottle was encapsulated in a 500-ml brown polyethylene bottle filled with the *in situ* geothermal water to avoid atmospheric contamination (Tian et al., 2021). For each sampling site, three parallel samples are collected and used for determining the gas composition, $^{3}He/^{4}He$ and $^{4}He/^{20}Ne$ ratios, and $\delta^{13}C_{V\text{-}PDB}$ (CO_2 and CH_4) values, respectively. Unfortunately, two samples (HZ12 and HZ13) were destroyed during transit, and their $\delta^{13}C_{V\text{-}PDB}$ values could not be determined.

All samples were analyzed within 1 month after the fieldtrip in the Key Laboratory of Petroleum Resources in the Northwest Institute of Eco-Environment and Resources, Chinese Academy of Sciences. Gas compositions were determined using a mass spectrometer MAT 271 with relative standard deviations of less than 5%. The detection limit is 0.0001%. The $^{3}He/^{4}He$ and $^{4}He/^{20}Ne$ ratios were analyzed using a Noblesse noble gas mass spectrometer produced by Nu Instruments, United Kingdom. Air from the Gaolan Hill south of Lanzhou calibrated the instrument. The $\delta^{13}C_{V\text{-}PDB}$ (CO_2 and CH_4) values were determined using the GC-IRMS analytical system gas chromatography (Agilent 6,890) stable isotope ratio mass spectrometer (Thermo-Fisher Scientific Delta Plus XP), coupled with an online sample preprocessor (Zhou et al., 2017). The conventional delta notation per mil (‰) expressed the C isotopic ratios following the Pee Dee Belemnite (PDB) from South Carolina. The measurement errors for carbon isotopic ratios were ±0.2‰, and the analytical precision of $\delta^{13}C$ was 0.3‰.

4 RESULTS

As shown in **Table 1**, the primary component of hydrothermal volatiles from the southeastern China mainland is N_2, with a volumetric percentage range of 82.19%–98.29%. It is followed by variable amounts of CO_2, CH_4, H_2, He, O_2, Ar and other trace gases, such as CO and C_2H_6. The H_2S, SO_2, C_2H_4, and C_3H_8 contents in these samples are lower than the detection limit (0.0001%). O_2 in the gas components indicates that air contamination occurred during either the sampling or measurement.

Except for SM22 which has CO_2 (75.65 vol%) as a major component, the CO_2 content in the study area is lower (0.02%–10.27%) than typical high-temperature geothermal areas with volumetric percentages higher than 80%. For example, the CO_2 content in the Yangbajing, Tengchong, and Batang geothermal systems from the Himalayan geothermal belt is as high as 95.2% (Zhao P. et al., 1998), 86% (Zhang et al., 2016), and 98.75% (Tian et al., 2018), respectively. In the Mud Volcano from the Yellowstone geothermal system, US, CO_2 accounts for 99.5% of noncondensable gas (Lowenstern et al., 2015). CO_2 is also the main gaseous component in Icelandic geothermal areas and represents 80%–99% (Ármannsson, 2016).

The volumetric contents of H_2 and CH_4 are lower than 0.22 and 2.21%, respectively. The He content ranges between 10 and 7,098 ppmv, which is less than 1%. No abnormally high content for these constituents was shown in this area. However, these constituents could indicate specific geological conditions. For instance, high H_2 concentrations (2.4%–99%) were recognized in the Jimo geothermal system on China's eastern coast, indicating its underlying basaltic bedrock where the oxidation of Fe^{II}-rich pyroxene and olivine occurred (Hao et al., 2020). He contents as high as 2.52% were identified in Guanzhong Basin geothermal system in northwestern China, and it is attributed to the million-year circulation of groundwater and the corresponding

TABLE 1 | Chemical composition of hydrothermal volatiles from Southeast China in this study ("-" represents the content lower than the detection limit 0.0001%).

Location	No	T (°C)	Latitude (°)	Longitude (°)	He (ppm)	N_2 (%)	CO_2 (%)	CH_4 (%)	H_2 (%)	O_2 (%)	Ar (%)	CO (%)	C_2H_6 (%)
Yangjiang	YJ1	89	21.889056	112.261786	2,336	96.21	1.11	0.58	—	0.34	1.56	—	—
	YJ2	86	21.889111	112.265767	1,684	96.33	0.46	0.53	0.0260	0.92	1.54	—	—
	YJ3	80	21.795881	112.485256	2,221	94.34	0.89	0.31	0.2200	2.45	1.54	—	—
Maoming	MM4	80	21.473411	110.946908	1,771	95.44	1.82	0.15	0.0003	0.90	1.50	—	—
Huizhou	HZ5	55	23.268756	114.649539	3,714	82.19	10.27	1.58	0.1700	4.28	0.92	—	—
	HZ6	52	23.270883	114.647947	3,081	83.89	9.12	1.14	0.1300	4.26	0.99	—	0.0015
	HZ7	50	23.270633	114.648361	1,313	94.13	0.89	0.64	0.0002	3.10	1.06	—	—
	HZ8	50	23.268542	114.650747	5,587	90.46	7.13	0.32	0.0003	0.24	1.02	0.0017	—
	HZ9	56	23.200103	114.363697	3,716	95.8	0.44	1.23	0.0005	0.90	1.16	0.0052	—
	HZ10	41	22.841883	114.534281	10	95.23	0.042	2.21	0.0003	1.24	1.27	—	—
	HZ11	54	23.759094	114.231308	2,486	95.36	1.24	0.29	0.0005	1.61	1.19	—	—
	HZ12	54	23.820247	114.239425	702	91.04	0.1	0.10	0.0330	7.50	1.16	0.0110	—
	HZ13	42	23.573350	114.994322	178	98.29	0.22	0.01	0.0001	0.38	1.09	—	—
Fengshun	FS14	89	23.736031	116.192108	967	91.37	3.97	0.32	0.0350	2.67	1.56	—	—
	FS15	96	23.953317	116.206367	1,816	95.68	0.2	0.37	0.1400	1.99	1.48	—	—
	FS16	82	23.954178	116.205147	2,501	95.97	0.83	1.03	0.0008	0.31	1.60	—	—
	FS17	94	23.775528	116.144239	1,184	90.28	0.36	0.17	0.0025	7.70	1.39	—	—
	FS18	54	23.737144	116.194658	617	96.51	0.28	0.78	0.0001	1.11	1.26	—	—
	FS19	60	23.797300	116.137594	759	89.11	0.11	0.24	0.0270	9.34	1.09	—	—
Zhangzhou	ZZ20	90	25.567022	118.384899	3,761	94.27	1.20	1.59	0.0040	0.54	1.77	—	—
	ZZ21	82	24.953542	118.091856	2,512	94.32	0.02	0.04	0.0063	1.97	1.28	—	—
	ZZ25	58	24.716668	117.554358	1,433	96.32	0.37	0.06	0.0001	1.45	1.32	—	—
	ZZ26	75	24.463856	117.395976	2,826	96.71	0.92	0.08	0.0028	0.42	1.35	—	—
	ZZ28	66	24.374366	117.777054	1,274	96.67	1.79	0.18	0.0005	0.30	1.39	—	—
	ZZ29	65	24.307501	117.984466	1,249	95.06	0.23	0.06	0.0151	0.77	1.13	—	—
	ZZ30	70	24.297266	117.611400	1,523	97.28	0.15	0.03	0.0012	0.64	1.44	—	—
Sanming	SM22	72	25.892461	117.274494	484	19.22	75.65	0.04	0.0001	1.69	0.21	—	—
	SM23	54	26.130642	116.886600	7,098	92.59	4.90	0.34	0.0001	0.52	1.22	—	—
	SM24	76	26.176875	116.941361	6,863	92.29	3.41	0.74	0.0006	0.65	1.42	—	—
Longyan	LY27	68	25.040260	116.673924	4,599	94.30	2.28	0.04	0.0001	1.14	1.14	—	—
Fuzhou	FZ31	81	26.214173	119.410192	2,491	95.77	0.13	0.08	0.0018	0.53	1.72	—	—

accumulation of gaseous components in the reservoir (Li et al., 2017). Furthermore, the high CH_4 content (up to 60.95%) in the Niutuozhen geothermal field, North China, indicates organic sediments existing in the reservoir rocks (Pang et al., 2018). Therefore, low H_2, CH_4, and He concentrations indicate that the abovementioned geologic conditions could not occur in the study area.

As shown in **Table 2**, the measured $^3He/^4He$ ratios of samples range from 1.07×10^{-7} to 1.95×10^{-6}, 0.08 Ra–1.39 Ra (where Ra denotes the atmospheric $^3He/^4He = 1.39 \times 10^{-6}$). The $^4H/^{20}Ne$ ratio is 2.8–646. Because ^{20}Ne is assumed to originate from the atmosphere (Craig et al., 1978), $^4H/^{20}Ne$ ratios are used to evaluate air contamination levels in samples. All $^4H/^{20}Ne$ ratios are more than two orders of magnitude larger than the atmospheric value of 0.318 (Sano and Wakita, 1985), indicating that minimum atmospheric contamination occurred during sampling and He/Ne isotope measurements. As summarized in **Table 2**, the measured $^3He/^4He$ ratios were corrected (R_c) for air contamination using the method proposed by Craig (1978), and only slight differences occurred for samples with relatively lower $^4H/^{20}Ne$ ratios, such as HZ10, HZ12, and HZ13.

As reported in **Table 2**, the $\delta^{13}C$ values (versus PBD) for CO_2 and CH_4 of the samples ranged from −19.6‰ to −6.7‰ and from −65.4‰ to −8.8‰, respectively. These carbonic isotopic ratios exhibit values lower than those from the high-temperature geothermal systems in the Chinese mainland. In the Batang geothermal system, the eastern edge of the Qinghai-Tibet Plateau, the $\delta^{13}C$ contents of CO_2 and CH_4 were −7.7‰ to −0.5‰ and −40.2‰ to −21.1‰, respectively (Tian et al., 2018). In the Yangbajing geothermal system, $\delta^{13}C_{CO2}$ values were −11.3‰ and −7.7‰ (Zhao P. et al., 1998). In Tengchong volcanic geothermal area, the range of $\delta^{13}C$ values for CO_2 and CH_4 are −9.0‰ to −2.1‰ and −25.5‰ to −9.7‰, respectively (Zhao et al., 2011; Zhang et al., 2016). This comparison shows that the evolution process of hydrothermal volatiles from the southeast China is different from the abovementioned areas and the probability of feeding high-temperature geothermal reservoirs in such geological settings remains to be studied.

5 DISCUSSION

5.1 Origin of Essential Gaseous Components

5.1.1 Nitrogen and Argon

As mentioned in the **Section 4**, CO_2, a prominent component of mantle volatiles, is the major component in high-temperature geothermal systems in magmatic areas (Lowenstern et al., 2015; Ármannsson, 2016). However, N_2 domination is a typical characteristic for medium-low temperature geothermal

TABLE 2 | Isotopic composition of hydrothermal volatiles in this study area ("n.a." represents no analysis).

No	$\delta^{13}C_{CH4}$ (‰)	$\delta^{13}C_{CO2}$ (‰)	$^{4}He/^{20}Ne$	R	R/Ra	Rc	Rc/Ra	q (mW/m^2)	qc (mW/m^2)	qm (mW/m^2)	T–40 km (°C)	T–50 km (°C)
YJ1	−45.4	−17.5	131	5.00E−07	0.36	4.98E−07	0.36	67	35	32	821	935
YJ2	−47.1	−17.1	91	6.53E−07	0.47	6.51E−07	0.47	69	35	34	855	975
YJ3	−45.3	−16.9	132	6.12E−07	0.44	6.10E−07	0.44	69	35	33	848	966
MM4	−40.9	−14.5	109	1.11E−07	0.08	1.07E−07	0.08	55	34	21	631	715
HZ5	−46.5	−11.4	492	7.09E−07	0.51	7.08E−07	0.51	70	35	35	867	988
HZ6	−56.8	−13.4	265	6.95E−07	0.50	6.94E−07	0.50	70	35	34	863	984
HZ7	−61.9	−17.0	70	7.51E−07	0.54	7.48E−07	0.54	70	35	35	873	995
HZ8	−51.3	−14.6	646	6.67E−07	0.48	6.67E−07	0.48	69	35	34	859	979
HZ9	−62.0	−16.3	303	5.84E−07	0.42	5.83E−07	0.42	68	35	33	842	959
HZ10	−50.2	−19.6	3	6.26E−07	0.45	5.28E−07	0.38	69	36	33	850	968
HZ11	−48.8	−16.5	166	4.17E−07	0.30	4.15E−07	0.30	65	35	30	798	909
HZ12	n.a	n.a	33	2.22E−07	0.16	2.11E−07	0.15	61	35	25	723	822
HZ13	n.a	n.a	7	5.14E−07	0.37	4.74E−07	0.34	67	36	31	825	939
FS14	−62.1	−15.6	53	1.35E−06	0.97	1.35E−06	0.97	75	34	41	946	1,079
FS15	−58.0	−16.7	78	1.04E−06	0.75	1.04E−06	0.75	73	35	38	914	1,042
FS16	−58.4	−15.8	182	1.32E−06	0.95	1.32E−06	0.95	75	34	41	943	1,076
FS17	−55.6	−17.1	57	6.39E−07	0.46	6.35E−07	0.46	69	35	34	855	974
FS18	−34.6	−19.4	31	8.62E−07	0.62	8.56E−07	0.62	71	35	36	889	1,014
FS19	−54.9	−16.6	43	1.11E−06	0.80	1.11E−06	0.80	73	34	39	923	1,053
ZZ20	−65.4	−11.1	211	4.03E−07	0.29	4.02E−07	0.29	65	35	30	797	907
ZZ21	n.a	−8.3	96	2.92E−07	0.21	2.88E−07	0.21	63	35	28	759	863
ZZ25	−8.8	−7.4	69	5.98E−07	0.43	5.94E−07	0.43	68	35	33	845	963
ZZ26	−44.5	−15.9	130	1.40E−06	1.01	1.40E−06	1.01	75	34	42	951	1,086
ZZ28	−58.2	−18.8	61	4.03E−07	0.29	3.98E−07	0.29	65	36	30	798	908
ZZ29	n.a	−16.9	51	8.20E−07	0.59	8.17E−07	0.59	71	35	36	884	1,007
ZZ30	n.a	−15.4	73	1.93E−06	1.39	1.93E−06	1.39	78	32	45	990	1,131
SM22	−57.6	−6.7	162	1.78E−06	1.28	1.78E−06	1.28	77	33	44	980	1,119
SM23	−49.1	−12.1	408	5.70E−07	0.41	5.69E−07	0.41	68	35	33	840	956
SM24	−52.2	−13.7	386	4.45E−07	0.32	4.44E−07	0.32	66	35	31	807	919
LY27	−13.2	n.a	265	1.53E−06	1.10	1.53E−06	1.10	76	33	42	961	1,097
FZ31	−19.1	n.a	109	4.87E−07	0.35	4.84E−07	0.35	67	35	31	820	933

systems, indicating that the geothermal fluid suffered a relatively shallow circulation depth through limited contact with deep-derived volatiles (Tian et al., 2021). The N_2 accumulation is due to the inert activity of nitrogen, whereas during the long-term interaction between air-saturated water and wall rocks in the reduced runoff, the oxidizing components (such as O_2) were consumed. In the comparison of the Ar/He and N_2/CO_2 ratios (**Figure 2**), the volatiles from the study area exhibit a mixing relationship between atmospheric and the geological endmembers (mantle or crustal). The shift toward high N_2/CO_2 ratios indicates the accumulation process of N_2 during the circulation path which has limited supplementary CO_2. For example, the point for ZZ21 exhibits the strongest shift of N_2 accumulation, indicating that the geothermal fluid in this area underwent long-term circulation in a relatively closed shallow fracture system. However, SM22 exhibits an opposite shift, indicating that an additional CO_2 source exists in this geothermal field. Samples from the Huizhou, Sanming, Longyan, and Zhangzhou geothermal areas exhibit more geologically derived contributions than others, indicating that either deep faults or a specific lithology affect the supplementary sources. However, it is challenging to further identify which of the two possibilities is the main factor because the excessive He could come from either the radiogenic process in the crust or the mantle volatile. Simultaneously, the metamorphic process of crustal materials and mantle–derived volatile could contribute to the CO_2. Their origins remain to be determined based on the isotopic analysis in the following sections. For the triangle plot of N_2-He-Ar in **Figure 3**, the mixing process is depicted. Since N_2 and Ar are chemically inert or only minimally reactive and have limited sources in geological environments, they are inferred to be of largely atmospheric origin in southeast China in this study. However, many samples are close to the mixing line between the endmembers of the mantle/crust and air rather than the line between the mantle/crust and air-saturated water, indicating that air contaminants affect the N_2/Ar ratios. This phenomenon is consistent with that shown by O_2. Combined with the He/Ne isotopic ratios, this air contamination is due to the measurement process of the gas composition rather than the sampling procedure because they have the same sampling method.

5.1.2 Helium

He is a critical geothermal volatile providing information on the geological setting and the regional thermal background (Polyak et al., 2000; Gautheron and Moreira, 2002). ^{3}He mainly escapes from the mantle. The predominant source is primordial He that has been trapped within the Earth from the time of its formation, whereas the reaction of ^{6}Li (n, α) ^{3}H ($^{-1}$ β) ^{3}He accounts for a negligible portion. Typically, the upper mantle sampled by the mid-ocean ridge basalts (MORB) with an R/Ra ratio of eight is

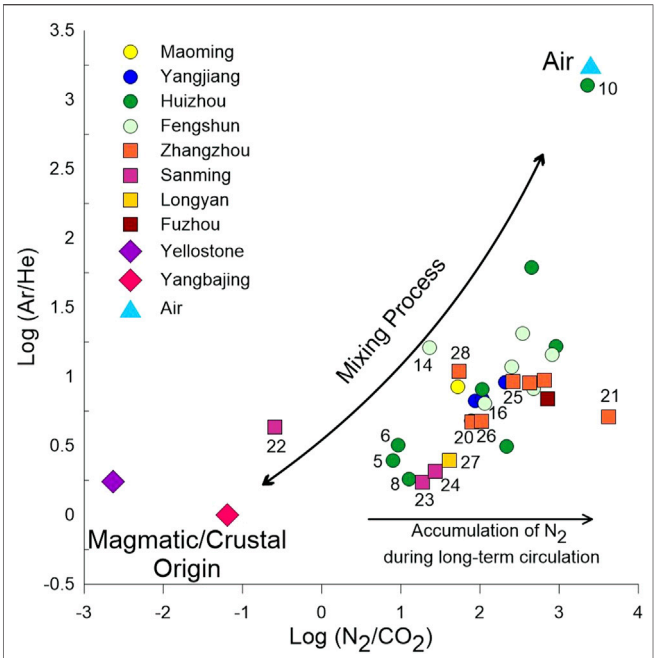

FIGURE 2 | Plot of results from gas collected from Southeast China with Log(N_2/CO_2) vs. Log(Ar/He). Samples from the Yellowstone geothermal system in the US and Yangbajing geothermal system in China represent magmatic-and crustal-derived geothermal gaseous compositions, respectively (Zhao et al., 2002; Lowenstern et al., 2015). Samples from Guangdong Province are represented by circle symbols, and those from Fujian Province are represented by rectangle symbols.

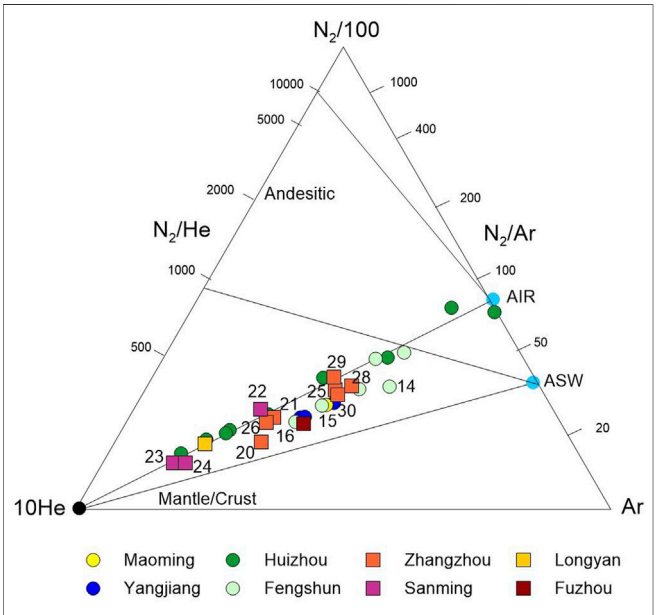

FIGURE 3 | Triangle plot of N_2-He-Ar for hydrothermal volatiles from Southeast China. The AIR represents the atmospheric component, and the ASW represents air-saturated water.

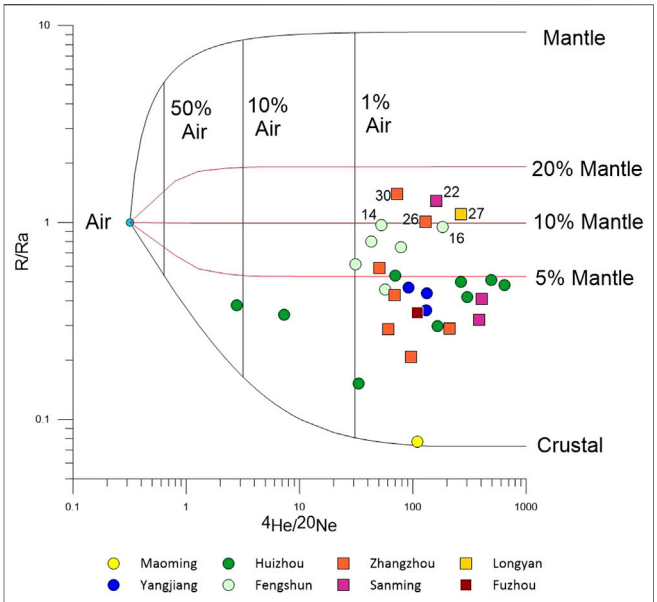

FIGURE 4 | $^4He/^{20}Ne$ ratios versus $^3He/^4He$ ratios. The $^3He/^4He$ ratios are expressed as R/Ra where R is the corrected measured ratio.

recognized as the typical asthenosphere endmember (Gautheron and Moreira, 2002). Decaying crustal U and Th predominantly produce ^4He (O'nions and Oxburgh, 1988). The conventional $^3He/^4He$ ratio of the continental crust is 0.02 Ra with a range of 0.01 Ra to 0.1 Ra (Lupton, 1983). In a specific area, the location-dependent variation of $^3He/^4He$ ratios can indicate the depth variation of fault extensions. According to the method proposed by Sano and Wakita (1985), mantle He proportions can be recognized when taking $^3He/^4He$ ratios of eight Ra and 0.02 Ra for the mantle and crustal He, respectively. From **Figure 4**, the typical crustal He isotopic ratio (0.08 Ra) is shown for the sample from the Maoming geothermal field in the south of the study area. For most of the other samples, the mantle He proportions are lower than 5%. This phenomenon indicates that radiogenic products in crustal materials mostly account for the He component. In other words, the deep-seated endmember for the geothermal volatile in the Yangjiang, Maoming, and Huizhou geothermal areas is largely crustal metamorphic rather than mantle-derived volatile. However, FS14, FS16, SM22, ZZ26, LY27, and ZZ30 exhibit mantle He contributions exceeding 10%. Because these samples are from North Guangdong and South Fujian provinces, it indicates that relative deep fault extensions and fluent uprising channels occurred in these areas. Furthermore, enhanced convection of geothermal fluids could be expected in the adjacent area of the two provinces. As illustrated in the **Section 2**, a series of NE-trending lithospheric faults in southeast China dominantly control the magmatic and geothermal activity, acting as a heat controller. However, the temperatures, chemical compositions, and isotopic compositions of geothermal volatiles exhibit distinct characteristics. According to the He isotopic ratios, a conclusion could be drawn that the NW-trending faults considerably influence constructing regional extensional conduits for fluid

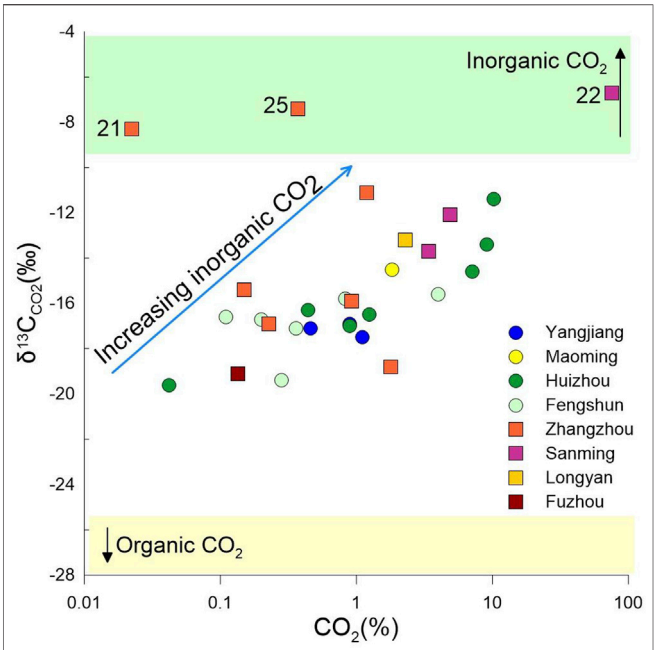

FIGURE 5 | $\delta^{13}C$ (‰) versus CO_2 for hydrothermal volatiles from Southeast China.

and heat conventions. Furthermore, **Figure 4** confirmed that air contamination during sampling is less than 1% except for two samples contaminated by 1–10%.

5.1.3 Carbon Dioxide

Biotic CO_2 is typically marked by low $\delta^{13}C$ values from −70 to −25‰ (Faure et al., 1965). Abiotic CO_2 contains a large number of heavy carbon isotopes, for example, the $\delta^{13}C$ value of carbonate metamorphic CO_2 is close to 0‰ (Sano and Marty, 1995). For the mantle-derived CO_2, the MORB ratio (−8 to −5‰) represents its isotopic ratio (Javoy et al., 1986). As shown in **Figure 5**, the CO_2 content increase is accompanied by ^{13}C isotope enrichment. For example, SM22 has the highest CO_2 content, with a volumetric percentage as high as 75.65% and a $\delta^{13}C_{CO2}$ value of −6.7‰. This CO_2-rich sample with a high $\delta^{13}C_{CO2}$ value could result from the involvement of carbonate rocks ($\delta^{13}C$). By combining its inorganic carbon composition with the He and Ne isotopic signature, a deep developed fracture system could be expected in this area. Therefore, the deep-derived volatile functions as the additional CO_2 source for the SM22. Considering the above discussion that mantle-derived volatile accounted for more than 10% in SM22, the mantle CO_2 contributes to a larger ratio in this area than those of other sampling sites. Nevertheless, the major source of inorganic CO_2 could still be attributed to carbonate metamorphic processes deep within the crust rather than mantle volatiles. Although enriched carbonic isotopes also occurred at ZZ21 and ZZ25 in the Zhangzhou geothermal area, the low CO_2 contents and low $^3He/^4He$ ratios of these sampling sites indicate that the fractures in these areas could not provide sufficiently deep volatiles. Carbonate metamorphism in the shallow crust could be the major source of geothermal volatiles. For other samples, the depleted $\delta^{13}C_{CO2}$ values can be attributed to either the organic metamorphic or degassing processes in the geothermal fluid. In the first case, hydrothermal volatiles have pervasively received contributions from inorganic and organic carbon endmembers with different mixing ratios. In the second case, the strong isotopic fractionation during the degassing process of the dissolved CO_2 results in ^{13}C depletion in the gaseous component, which occurred in areas with carbonate formations, such as the Huizhou geothermal field (Yan et al., 2019). Although it is challenging to identify the controlling mechanism, both these cases indicate trace amount of mantle CO_2 in the closed fracture systems.

5.1.4 Methane Component

Irrespective of the sample locations and CH_4 contents (**Figure 6A**), most hydrothermal CH_4 contents from southeast China exhibit depleted carbon isotopic compositions, with $\delta^{13}C_{CH4}$ values lower than −30‰. As recorded, the typical ranges for thermogenic and microbial CH_4 are −30‰ to −50‰ and −50‰ to −120‰, respectively, whereas the $\delta^{13}C_{CH4}$ values higher than −30‰ indicate abiogenic CH_4 or microbial consumption residue (Etiope and Schoell, 2014; Wilson et al., 2014; Sano et al., 2017). According to these threshold values, CH_4 from the study area is largely biogenic in the shallow crust or near the surface rather than the magmatic volatile. Furthermore, no coordinated variation occurs between $\delta^{13}C_{CH4}$ and $\delta^{13}C_{CO2}$ (**Figure 6B**), indicating that the CH_4 is not sourced from CO_2 by stoichiometrically inorganic reactions, and the carbon isotopic exchange equilibrium has not been achieved before surface exposure. This phenomenon could be linked to the lack of an underlying magma chamber or deep-extended fault where high-affinity binding exists between CH_4 and CO_2. Notably, ZZ25 ($\delta^{13}C_{CH4}$ = −8.8‰) exhibits heavy carbon isotopic compositions in both CH_4 and CO_2, whereas its He isotopic ratio is lower than 1 Ra. It could be attributed to some inorganic contribution from the specific lithology.

5.2 Heat Flow and Lithospheric Thermal Structure

The terrestrial heat flow (q, mW/m^2) indicates the magnitude of conductive heat transfer and has been commonly measured where conductive heat transfer dominates. It expresses an integral energetic effect of all processes occurring at depths (Polyak et al., 2000). For estimating the heat flow in areas with hot springs, convective heat transfer must be considered because the hydrothermal system provides a heat transfer mechanism in the crust based on geothermal fluid transport (Umeda et al., 2006; Tang et al., 2017). In continental areas, three nuclides (^{232}Th and $^{235,\ 238}U$) are the principal sources of radiogenic heat in the Earth, yielding ^4He as decay products. Furthermore, ^3He produced by the radiogenic process accounts for a negligible portion of the ^3He escaping from the mantle. Therefore, ^3He flux is in proportion to mantle heat flux, whereas the ^4He flux is linear with crustal heat flux. The rough estimation of crustal and mantle heat flow according to He isotopic ratios is given by (O'nions and Oxburgh, 1983, 1988; Polyak et al., 1979):

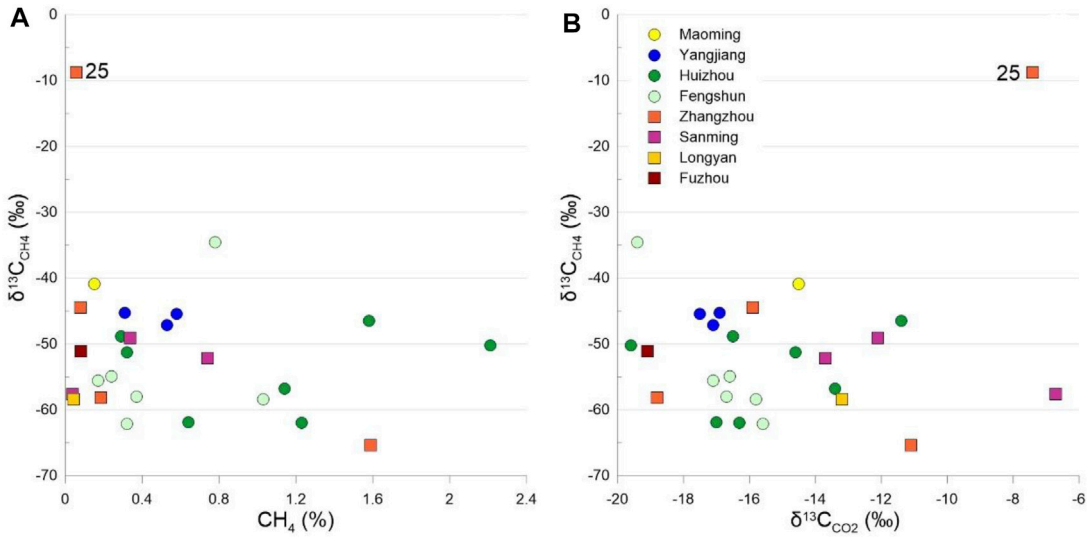

FIGURE 6 | (A) $\delta^{13}C_{CH4}$ value versus CH_4 content. **(B)** $\delta^{13}C_{CH4}$ value versus $\delta^{13}C_{CO2}$ value for hydrothermal volatiles from southeast China.

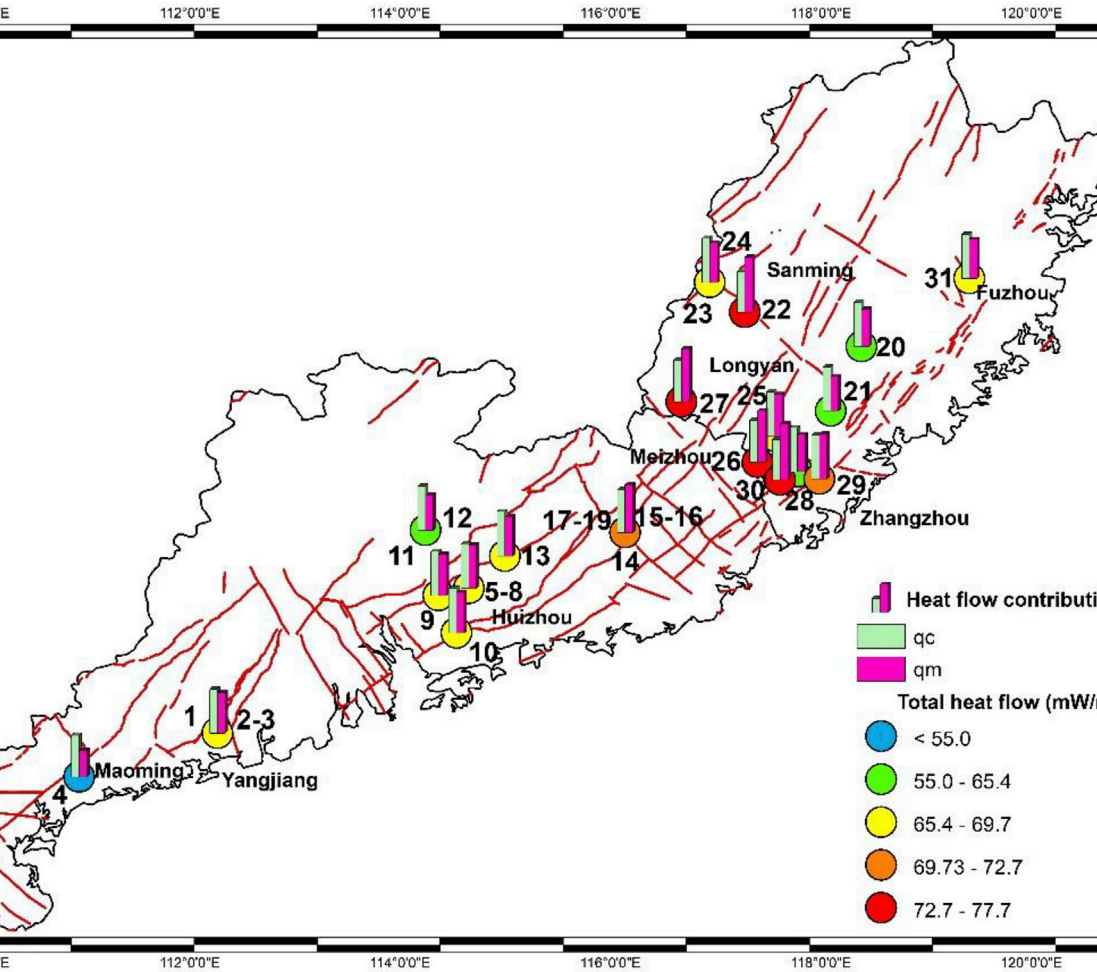

FIGURE 7 | Calculated heat flow and its contribution of crust and mantle according to He isotopic ratios of hydrothermal volatile.

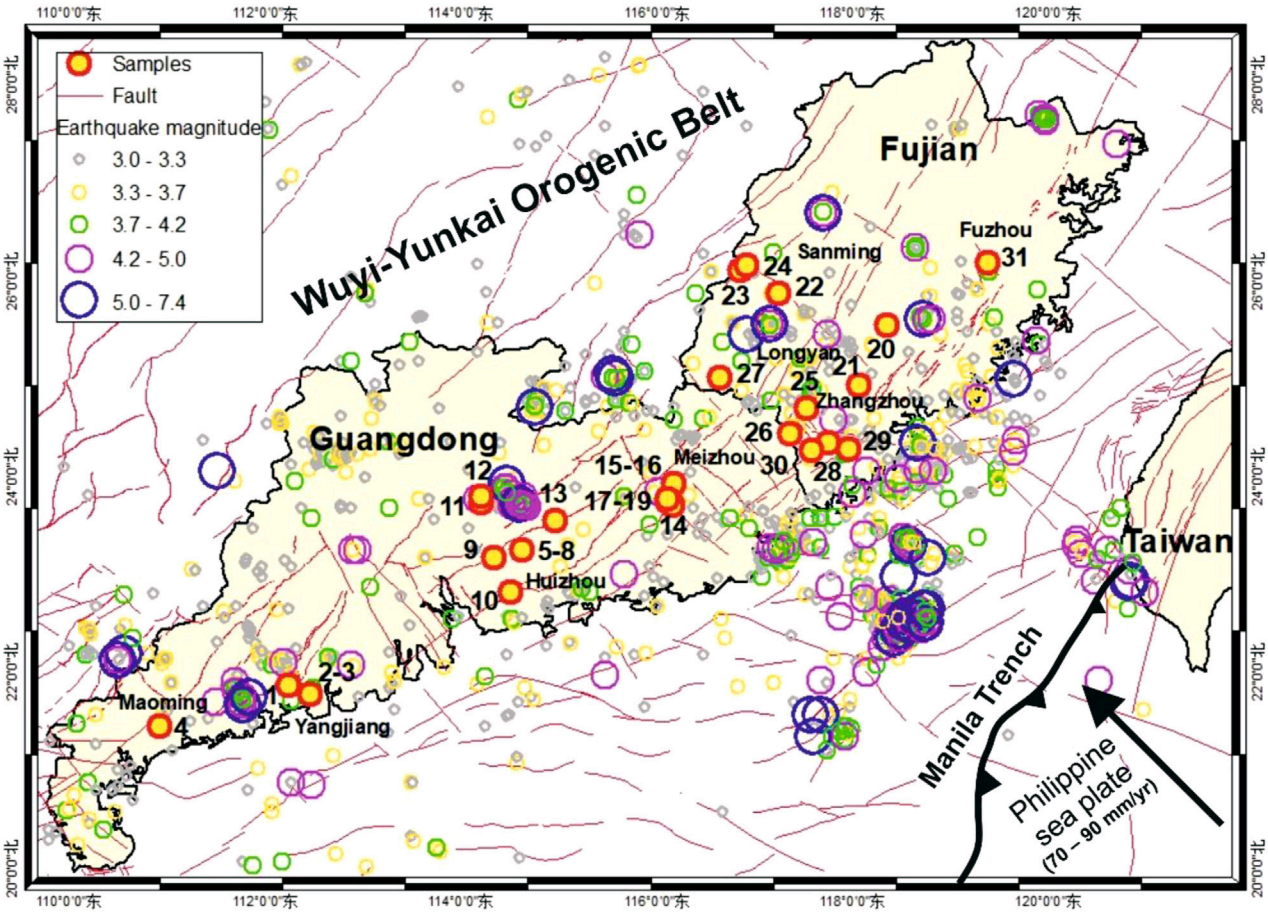

FIGURE 8 | Epicenters of Ml >3.0 earthquakes recorded during 1972–2021. Data of earthquake are from the China Earthquake Networks Center (CENC) (Ai et al., 2019).

$$q = 18.231 \log R_c + 181.82 \quad (1)$$

$$\frac{q_c}{q_m} = 0.815 - 0.3 Ln\, R \quad (2)$$

where R_c is the corrected He isotopic ratios, qc (mW/m^2) is the crustal heat flow, and qm (mW/m^2) is the mantle heat flow. Furthermore, the He isotopic data were also used to estimate the ratio between the crust and mantle heat flow components (Wang, 1999) according to **Eq. 2**. At specific depths, the heat flow q and calculated temperature T (°C) are linearly dependent with a correlation coefficient of 0.9 and higher. For depths of 40 km (the bottom of the Earth's crust) and 50 km, these dependencies are as follows (Duchkov et al., 2010):

$$T_{40} = 15.61q - 223\,(accuracy \sim \pm 40°C) \quad (3)$$

$$T_{50} = 18.09q - 275\,(accuracy \sim \pm 50°C) \quad (4)$$

These equations were used to calculate the thermal background of the study area. As shown in **Table 2**, most heat flow values are higher than the average heat flow value of continental China (63 mW/m^2) (Hu et al., 2000) and equal to the average heat flow value of South China (69.4 ± 11.0 mW/m^2) (Jiang et al., 2019). In the Zhangzhou geothermal area, the highest heat flow of 77.7 mW/m^2 (ZZ30) is indicated; however, in the Maoming geothermal area, the lowest heat flow is 54.7 mW/m^2 (MM4). The results correlate well with the heat flow values previously reported for the adjacent areas (**Figure 1A**) (Hu et al., 2000; Jiang et al., 2019). To present the heat flow distribution in **Figure 7**, we calculated the average values of hot springs crowed together, such as the average values of the following five groups: 1) YJ1, YJ2, and YJ3; 2) HZ5, HZ6, HZ7, and HZ8; 3) HZ11 and HZ12; 4) FS14, FS15, FS16, FS17, FS18, and FS19; and 5) SM23 and SM24. Notably, calculated heat flows exhibit high values in the Zhangzhou, Longyan, and Sanming geothermal areas, which are adjacent area to the two provinces and are characterized by crossed faults of the NE and NW groups. In these areas, mantle heat flow accounts for more than half of the total heat flow. Moreover, the high heat flow values are accompanied by high temperatures deep within the Earth (>900°C at 40 km and >1,000°C at 50 km). This is consistent with the above conclusion that the crossed faults function as conduits for deep-derived geothermal volatiles, but also enhance

the heat convection within the Earth. Therefore, hydrothermal systems near the boundary of the two provinces should have the highest potential for geothermal exploitation. Additionally, heat flow values for the Fengshun and Huizhou (69.0 –74.9 and 60.6–70.2 mW/m^2, respectively) also indicate their geothermal potential. Although the accuracy of these estimations remains to be further studied, the results could provide useful information about the regional variation of the lithospheric thermal structure.

5.3 Heat–Control Structure and Up–Flow Conduit

Active faults formed in the Neotectonic movement provide preferential channels for heat and mass convection in high-temperature geothermal backgrounds. To identify the activities of faults in the study area, epicenters of Ml >3.0 earthquakes that occurred from January 1972 to September 2021 were compiled in **Figure 8**. Two prominent phenomena are worth examining. On the one hand, to the southeast of the study area, the Taiwan province and its surrounding areas are earthquake–prone, where earthquakes with magnitudes higher than Ml 4.2 are concentrated. These tectonic movements are triggered by the northward subduction of the Philippine Sea Plate to the Eurasia Plate (Ai et al., 2019). Consequently, the adjacent area of the two provinces is influenced by the tectonic movements, which is proven by the high density of earthquake occurrences near Meizhou, Zhangzhou, Longyan, and Sanming. Therefore, fault activity is a controlling factor of high mantle-derived hydrothermal volatile contributions in these areas. However, the depth and permeability of faults are also significant factors for hydrothermal system formation. **Figure 8** shows the epicenters of earthquakes, especially those with high magnitudes, distributed along the NE direction. This phenomenon indicates that major tectonic movements in this area are expressed by NE-trending faults. These faults extend deeply toward the crust, where strong earthquakes originate. Simultaneously, the NE faults can provide convection conduits for heat and mass from deep within the Earth. In other words, the NE-trending faults are recognized as heat-control structures in the study area. However, the permeability of the NE faults varies. Specifically, the intersection with active NW-trending faults enhances the amount of geothermal fluid rising to the surface as verified by the discussion in the **Section 5.2**. Thus, the NW-trending faults profoundly affect the formation of upflow conduits for geothermal fluids.

6 CONCLUSION

In granite-hosted southeast China, the active faults formed during the Neotectonic movement constrain the convection of mass and heat in geothermal fluids. Based on the chemical compositions and He-Ne-C isotopes of hydrothermal volatiles, the thermal controlling structures are identified. In the geothermal volatiles, the CO_2 and CH_4 contents are low and the corresponding carbon isotopic compositions are depleted. N_2 dominates volatiles, indicating medium–low temperature geothermal systems with limited contact with deep-derived CO_2, CH_4, etc. Most He isotopic ratios exhibit typical crustal metamorphic properties; however, samples from the Longyan, Sanming, Zhanghzou, and Fengshun geothermal fields have more than 10% of mantle contribution. As calculated, the mantle heat flow accounts for more than half of the total heat flow in these geothermal fields, which is accompanied by high deep-level temperatures (>900°C at 40 km and >1,000°C at 50 km). Considering the fault system formed by the northward subduction of the Philippine Sea Plate and the eastward subduction of the Pacific Plate, it could be deduced that the deep-extended faults enhanced geothermal fluid convection in the adjacent area of the two provinces. Additionally, spatially discernible geochemical characteristics of the hydrothermal volatiles have close affinities with earthquakes that occurred in the study area. This study demonstrates that although the NE-trending faults are heat-controlling structures, the heterogeneity of geothermal volatiles is largely affected by the intersections with NW-trending faults, which provided regional expedite channels for geothermal fluid rising to the surface. Deep circulated hydrothermal systems in southeast China could be expected in the adjacent of the Guangdong and Fujian provinces.

DATA AVAILABILITY STATEMENT

The original contributions presented in the study are included in the article/supplementary material. Further inquiries can be directed to the corresponding author.

AUTHOR CONTRIBUTIONS

JT is the first author. XZ is the corresponding author. The other coauthors contributed to the sampling, determination, and analysis.

FUNDING

The study has been financially supported by the National Key R&D Program of China (Nos. 2019YFC0604901) and by the National Natural Science Foundation of China (Grant No. 41902252, 41673106, 42073063, 4193000170) and The Special Fund of the Institute of Earthquake Forecasting, China Earthquake Administration (2018IEF010104, 2019CSES0104, 2020IEF0604, 2020IEF0703, 2021IEF0602, 2021IEF0101).

REFERENCES

Ai, S., Zheng, Y., and Xiong, C. (2019). Ambient Noise Tomography across the Taiwan Strait, Taiwan Island, and Southwestern Ryukyu Arc: Implications for Subsurface Slab Interactions. *Tectonics* 38 (2), 579–594. doi:10.1029/2018TC005355

Ármannsson, H. (2016). The Fluid Geochemistry of Icelandic High Temperature Geothermal Areas. *Appl. Geochem.* 66, 14–64. doi:10.1016/j.apgeochem.2015.10.008

Carter, A., and Clift, P. D. (2008). Was the Indosinian Orogeny a Triassic Mountain Building or a Thermotectonic Reactivation Event. *Comptes Rendus Geosci.* 340 (2–3), 83–93. doi:10.1016/j.crte.2007.08.011

Cheng, Y., Han, B., Li, Y., Guo, J., and Hu, X. (2021). Lithospheric Electrical Structure beneath the Cathaysia Block in South China and its Tectonic Implications. *Tectonophysics* 814, 228981. doi:10.1016/j.tecto.2021.228981

Craig, H., Lupton, J. E., Welhan, J. A., and Poreda, R. (1978). Helium Isotope Ratios in Yellowstone and Lassen Park Volcanic Gases. *Geophys. Res. Lett.* 5 (11), 897–900. doi:10.1029/GL005i011p00897

Duchkov, A. D., Rychkova, K. M., Lebedev, V. I., Kamenskii, I. L., and Sokolova, L. S. (2010). Estimation of Heat Flow in Tuva from Data on Helium Isotopes in thermal mineral Springs. *Russ. Geol. Geophys.* 51 (2), 209–219. doi:10.1016/j.rgg.2009.12.023

Etiope, G., and Schoell, M. (2014). Abiotic Gas: Atypical, but Not Rare. *Elements* 10 (4), 291–296. doi:10.2113/gselements.10.4.291

Faure, G., Hurley, P. M., and Powell, J. L. (1965). The Isotopic Composition of Strontium in Surface Water from the North Atlantic Ocean. *Geochim. Cosmochim. Acta* 29 (4), 209–220. doi:10.1016/0016–7037(65)90018–9

Gautheron, C., and Moreira, M. (2002). Helium Signature of the Subcontinental Lithospheric Mantle. *Earth Planet. Sci. Lett.* 199 (1–2), 39–47. doi:10.1016/s0012-821x(02)00563-0

Gong, J., and John Chen, Y. (2014). Evidence of Lateral Asthenosphere Flow beneath the South China Craton Driven by Both Pacific Plate Subduction and the India-Eurasia continental Collision. *Terra Nova* 26 (1), 55–63. doi:10.1111/ter.12069

Guo, Q. (2012). Hydrogeochemistry of High-Temperature Geothermal Systems in China: A Review. *Appl. Geochem.* 27 (10), 1887–1898. doi:10.1016/j.apgeochem.2012.07.006

Hao, Y., Pang, Z., Tian, J., Wang, Y., Li, Z., Li, L., et al. (2020). Origin and Evolution of Hydrogen-Rich Gas Discharges from a Hot spring in the Eastern Coastal Area of China. *Chem. Geol.* 538, 119477. doi:10.1016/j.chemgeo.2020.119477

Hilton, D. R., Fischer, T. P., and Marty, B. (2002). Noble Gases and Volatile Recycling at Subduction Zones. *Rev. Mineralogy Geochem.* 47 (1), 319–370. doi:10.2138/rmg.2002.47.9

Hochstein, M. P., and Regenauer–Lieb, K. (1998). Heat Generation Associated with Collision of Two Plates: the Himalayan Geothermal belt. *J. Volcanol. Geoth. Res.* 83 (1–2), 75–92. doi:10.1016/S0377–0273(98)00018–3

Hoke, L., Lamb, S., Hilton, D. R., and Poreda, R. J. (2000). Southern Limit of Mantle–Derived Geothermal Helium Emissions in Tibet: Implications for Lithospheric Structure. *Earth Planet. Sci. Lett.* 180 (3–4), 297–308. doi:10.1016/S0012–821X(00)00174–6

Hu, S., He, L., and Wang, J. (2000). Heat Flow in the continental Area of China: a New Data Set. *Earth Planet. Sci. Lett.* 179 (2), 407–419. doi:10.1016/s0012-821x(00)00126-6

Javoy, M., Pineau, F., and Delorme, H. (1986). Carbon and Nitrogen Isotopes in the Mantle. *Chem. Geol.* 57 (1–2), 41–62. doi:10.1016/0009-2541(86)90093-8

Jiang, G., Hu, S., Shi, Y., Zhang, C., Wang, Z., and Hu, D. (2019). Terrestrial Heat Flow of continental China: Updated Dataset and Tectonic Implications. *Tectonophysics* 753, 36–48. doi:10.1016/j.tecto.2019.01.006

Jolie, E., Moeck, I., and Faulds, J. E. (2015). Quantitative Structural-Geological Exploration of Fault-Controlled Geothermal Systems-A Case Study from the Basin-and-Range Province, Nevada (USA). *Geothermics* 54, 54–67. doi:10.1016/j.geothermics.2014.10.003

Li, Z. X., Li, X. H., Wartho, J. A., Clark, C., Li, W. X., Zhang, C. L., et al. (2010). Magmatic and Metamorphic Events during the Early Paleozoic Wuyi-Yunkai Orogeny, southeastern South China: New Age Constraints and Pressure-Temperature Conditions. *Geol. Soc. Am. Bull.* 122 (5–6), 772–793. doi:10.1130/B30021.1

Li, X.-H., Li, Z.-X., He, B., Li, W.-X., Li, Q.-L., Gao, Y., et al. (2012). The Early Permian Active continental Margin and Crustal Growth of the Cathaysia Block: *In Situ* U-Pb, Lu-Hf and O Isotope Analyses of Detrital Zircons. *Chem. Geol.* 328, 195–207. doi:10.1016/j.chemgeo.2011.10.027

Li, J., Pang, Z., Yang, G.-M., Tian, J., Tong, A. L., Zhang, X.-Y., et al. (2017). Million-year-old Groundwater Revealed by Krypton-81 Dating in Guanzhong Basin, China. *Sci. Bull.* 62 (17), 1181–1184. doi:10.1016/j.scib.2017.08.009

Li, S., Suo, Y., Li, X., Zhou, J., Santosh, M., Wang, P., et al. (2019). Mesozoic Tectono-Magmatic Response in the East Asian Ocean-Continent Connection Zone to Subduction of the Paleo-Pacific Plate. *Earth-Sci. Rev.* 192, 91–137. doi:10.1016/j.earscirev.2019.03.003

Li, X.-h. (2000). Cretaceous Magmatism and Lithospheric Extension in Southeast China. *J. Asian Earth Sci.* 18 (3), 293–305. doi:10.1016/s1367-9120(99)00060-7

Liao, Z., and Zhao, P. (1999). *Yunnan–Tibet Geothermal belt–geothermal Resources and Case Histories*. Beijing: Science. (in Chinese with English abstract).

Lowenstern, J. B., Bergfeld, D., Evans, W. C., and Hunt, A. G. (2015). Origins of Geothermal Gases at Yellowstone. *J. Volcanol. Geotherm. Res.* 302, 87–101. doi:10.1016/j.jvolgeores.2015.06.010

Lupton, J. E. (1983). TERRESTRIAL INERT GASES: Isotope Tracer Studies and Clues to Primordial Components in the Mantle. *Annu. Rev. Earth Planet. Sci.* 11, 371–414. doi:10.1146/annurev.ea.11.050183.002103

Mao, X., Wang, Y., Zhan, H., and Feng, L. (2015). Geochemical and Isotopic Characteristics of Geothermal Springs Hosted by Deep-Seated Faults in Dongguan Basin, Southern China. *J. Geochem. Explor.* 158, 112–121. doi:10.1016/j.gexplo.2015.07.008

Mao, X., Zhu, D., Ndikubwimana, I., He, Y., and Shi, Z. (2021). The Mechanism of High-Salinity thermal Groundwater in Xinzhou Geothermal Field, South China: Insight from Water Chemistry and Stable Isotopes. *J. Hydrol.* 593, 125889. doi:10.1016/j.jhydrol.2020.125889

Newell, D. L., Jessup, M. J., Cottle, J. M., Hilton, D. R., Sharp, Z. D., and Fischer, T. P. (2008). Aqueous and Isotope Geochemistry of Mineral Springs along the Southern Margin of the Tibetan Plateau: Implications for Fluid Sources and Regional Degassing of CO_2. *Geochem. Geophys. Geosyst.* 9 (8). doi:10.1029/2008GC002021

O'nions, R. K., and Oxburgh, E. R. (1988). Helium, Volatile Fluxes and the Development of continental Crust. *Earth Planet. Sci. Lett.* 90 (3), 331–347. doi:10.1016/0012–821X(88)90134–3

O'nions, R. K., and Oxburgh, E. R. (1983). Heat and Helium in the Earth. *Nature* 306 (5942), 429–431. doi:10.1038/306429a0

Pang, J., Pang, Z., Lv, M., Tian, J., and Kong, Y. (2018). Geochemical and Isotopic Characteristics of Fluids in the Niutuozhen Geothermal Field, North China. *Environ. Earth Sci.* 77 (1), 12. doi:10.1007/s12665-017-7171-y

Pei, R., and Hong, D. (1995). The Granites of South China and Their Metallogeny. *Episodes* 18, 77–82. doi:10.18814/epiiugs/1995/v18i1.2/017

Polyak, B. G., Tolstikhin, I. N., and Yakutseni, V. P. (1979). The Isotopic Composition of Helium and Heat–Flow–Geochemical and Geophysical Aspects of Tectogenesis. *Geotectonics* 13 (5), 339–351.

Polyak, B. G., Tolstikhin, I. N., Kamensky, I. L., Yakovlev, L. E., Cheshko, A. L., and Marty, B. (2000). Helium Isotopes, Tectonics and Heat Flow in the Northern Caucasus. *Geochim. Cosmochim. Acta* 64 (11), 1925–1944. doi:10.1016/s0016-7037(00)00342-2

Qiu, X., Wang, Y., Wang, Z., Regenauer-Lieb, K., Zhang, K., and Liu, J. (2018). Determining the Origin, Circulation Path and Residence Time of Geothermal Groundwater Using Multiple Isotopic Techniques in the Heyuan Fault Zone of Southern China. *J. Hydrol.* 567, 339–350. doi:10.1016/j.jhydrol.2018.10.010

Sano, Y., and Marty, B. (1995). Origin of Carbon from Fumarolic Gas in Island Arc. *Chem. Geol.* 119 (1), 265–274. doi:10.1016/0009-2541(94)00097-r

Sano, Y., and Wakita, H. (1985). Geographical Distribution of3He/4He Ratios in Japan: Implications for Arc Tectonics and Incipient Magmatism. *J. Geophys. Res.* 90 (B10), 8729–8741. doi:10.1029/JB090iB10p08729

Sano, Y., Kinoshita, N., Kagoshima, T., Takahata, N., Sakata, S., Toki, T., et al. (2017). Origin of Methane-Rich Natural Gas at the West Pacific Convergent Plate Boundary. *Sci. Rep.* 7 (1), 15646. doi:10.1038/s41598-017-15959-5

Santilano, A., Manzella, A., Gianelli, G., Donato, A., Gola, G., Nardini, I., et al. (2015). Convective, Intrusive Geothermal Plays: what about Tectonics. *Geoth. Energ. Sci.* 3 (1), 51–59. doi:10.5194/gtes–3–51–201510.5194/gtes-3-51-2015

Shu, L. S., Zhou, X. M., Deng, P., Wang, B., Jiang, S. Y., Yu, J. H., et al. (2009). Mesozoic Tectonic Evolution of the Southeast China Block: New Insights from

basin Analysis. *J. Asian Earth Sci.* 34 (3), 376–391. doi:10.1016/j.jseaes.2008.06.004

Smith, N. J. P., Shepherd, T. J., Styles, M. T., and Williams, G. M. (2005). Hydrogen Exploration: A Review of Global Hydrogen Accumulations and Implications for Prospective Areas in NW Europe. *Pet. Geology. Conf. Ser.* 6 (2), 349–358. doi:10.1144/0060349

Tang, X., Zhang, J., Pang, Z., Hu, S., Tian, J., and Bao, S. (2017). The Eastern Tibetan Plateau Geothermal belt, Western China: Geology, Geophysics, Genesis, and Hydrothermal System. *Tectonophysics* 717, 433–448. doi:10.1016/j.tecto.2017.08.035

Tannock, L., Herwegh, M., Berger, A., Liu, J., and Regenauer-Lieb, K. (2020). The Effects of a Tectonic Stress Regime Change on Crustal-Scale Fluid Flow at the Heyuan Geothermal Fault System, South China. *Tectonophysics* 781, 228399. doi:10.1016/j.tecto.2020.228399

Tian, J., Pang, Z., Guo, Q., Wang, Y., Li, J., Huang, T., et al. (2018). Geochemistry of Geothermal Fluids with Implications on the Sources of Water and Heat Recharge to the Rekeng High-Temperature Geothermal System in the Eastern Himalayan Syntax. *Geothermics* 74, 92–105. doi:10.1016/j.geothermics.2018.02.006

Tian, J., Pang, Z., Liao, D., and Zhou, X. (2021). Fluid Geochemistry and its Implications on the Role of Deep Faults in the Genesis of High Temperature Systems in the Eastern Edge of the Qinghai Tibet Plateau. *Appl. Geochem.* 131, 105036. doi:10.1016/j.apgeochem.2021.105036

Tong, W., and Tobisch, O. (1996). Deformation of Granitoid Plutons in the Dongshan Area, Southeast China: Constraints on the Physical Conditions and Timing of Movement along the Changle–Nanao Shear Zone. *Tectonophysics* 267 (1–4), 303–316. doi:10.1016/s0040-1951(96)00107-2

Umeda, K., Kanazawa, S., Kakuta, C., Asamori, K., and Oikawa, T. (2006). Variations in the 3 He/4 He Ratios of hot springs on Shikoku Island, Southwest Japan. *Geochem. Geophys. Geosyst.* 7 (4). doi:10.1029/2005GC001210

Wang, J., and Li, Z. (2003). History of Neoproterozoic Rift Basins in South China: Implications for Rodinia Break–Up. *Precambrian Res.* 122 (1–4), 141–158. doi:10.1016/s0301-9268(02)00209-7

Wang, Y. (1999). A Study on Mantle Heat Flow of continental Area of China by Helium Isotope Ratio of the Underground Fluid. *Acta Geoscientia Sinica* 20, 48–50. (in Chinese with English abstract).

Wilson, R. M., Macelloni, L., Simonetti, A., Lapham, L., Lutken, C., Sleeper, K., et al. (2014). Subsurface Methane Sources and Migration Pathways within a Gas Hydrate mound System, Gulf of Mexico. *Geochem. Geophys. Geosyst.* 15 (1), 89–107. doi:10.1002/2013gc004888

Wu, L., Mei, L., Paton, D. A., Guo, P., Liu, Y., Luo, J., et al. (2018). Deciphering the Origin of the Cenozoic Intracontinental Rifting and Volcanism in Eastern China Using Integrated Evidence from the Jianghan Basin. *Gondwana Res.* 64, 67–83. doi:10.1016/j.gr.2018.07.004

Yan, X., Gan, H., and Yue, G. (2019). Hydrogeochemical Characteristics and Genesis of Typical Geothermal fields from Huangshadong to Conghua in Guangdong. *Geol. Rev.* 65 (3), 743–754. CNKI:SUN:DZLP.0.2019-03-020 (in Chinese with English abstract).

Yin, A. (2010). Cenozoic Tectonic Evolution of Asia: A Preliminary Synthesis. *Tectonophysics* 488 (1–4), 293–325. doi:10.1016/j.tecto.2009.06.002

Zhang, M., Guo, Z., Sano, Y., Zhang, L., Sun, Y., Cheng, Z., et al. (2016). Magma-derived CO_2 Emissions in the Tengchong Volcanic Field, SE Tibet: Implications for Deep Carbon Cycle at Intra-continent Subduction Zone. *J. Asian Earth Sci.* 127, 76–90. doi:10.1016/j.jseaes.2016.06.009

Zhang, M., Guo, Z., Xu, S., Barry, P. H., Sano, Y., Zhang, L., et al. (2021). Linking Deeply–Sourced Volatile Emissions to Plateau Growth Dynamics in southeastern Tibetan Plateau. *Nat. Commun.* 12 (1), 1–10. doi:10.1038/s41467-021-24415-y

Zhao, G., Wilde, S. A., Cawood, P. A., and Lu, L. (1998a). Thermal Evolution of Archean Basement Rocks from the Eastern Part of the North China Craton and its Bearing on Tectonic Setting. *Int. Geology. Rev.* 40 (8), 706–721. doi:10.1080/00206819809465233

Zhao, P., Dor, J., Liang, T., Jin, J., and Zhang, H. (1998b). Characteristics of Gas Geochemistry in Yangbajing Geothermal Field, Tibet. *Chin. Sci. Bull.* 43 (21), 1770–1777. doi:10.1007/BF02883369

Zhao, P., Xie, E., Duo, J., Jin, J., Hu, X., Du, S., et al. (2002). Geochemical Characteristics of Geothermal Gases and Their Geological Implications in Tibet. *Acta Petrol. Sin.* 18 (4), 539–550. doi:10.1002/poc.1772

Zhao, C., Ran, H., and Chen, K. (2011). Presen–Day Temperatures of Magma chambers in the Crust beneath Tengchong Volcanic Field: Estimation from Carbon Isotopic Fractionation between CO_2 and CH_4 of Free Gases Escaped from thermal Springs. *Acta Petrol. Sin.* 27 (10), 2883–2897. (in Chinese with English abstract). CNKI:SUN:YSXB.0.2011–10–009.

Zhou, X., and Li, W. (2000). Origin of Late Mesozoic Igneous Rocks in Southeastern China: Implications for Lithosphere Subduction and Underplating of Mafic Magmas. *Tectonophysics* 326 (3–4), 269–287. doi:10.1016/s0040-1951(00)00120-7

Zhou, X., Sun, T., Shen, W., Shu, L., and Niu, Y. (2006). Petrogenesis of Mesozoic Granitoids and Volcanic Rocks in South China: A Response to Tectonic Evolution. *Episodes* 29 (1), 26–33. doi:10.18814/epiiugs/2006/v29i1/004

Zhou, X., Liu, L., Chen, Z., Cui, Y., and Du, J. (2017). Gas Geochemistry of the Hot spring in the Litang Fault Zone, Southeast Tibetan Plateau. *Appl. Geochem.* 79, 17–26. doi:10.1016/j.apgeochem.2017.01.022

Conflict of Interest: The authors declare that the research was conducted in the absence of any commercial or financial relationships that could be construed as a potential conflict of interest.

Publisher's Note: All claims expressed in this article are solely those of the authors and do not necessarily represent those of their affiliated organizations, or those of the publisher, the editors, and the reviewers. Any product that may be evaluated in this article, or claim that may be made by its manufacturer, is not guaranteed or endorsed by the publisher.

frontiers in Earth Science

ORIGINAL RESEARCH
published: 13 December 2021
doi: 10.3389/feart.2021.784600

Exploration Process and Genesis Mechanism of Deep Geothermal Resources in the North Jiangsu Basin, East China: From Nothing to Something

Yibo Wang[1,2], Yang Bai[3], Lijuan Wang[4], Junpeng Guan[4], Yaqi Wang[1,2,5], Zhuting Wang[6], Jie Hu[7] and Shengbiao Hu[1,2,5]*

[1]State Key Laboratory of Lithospheric Evolution, Institute of Geology and Geophysics, Chinese Academy of Sciences, Beijing, China, [2]Innovation Academy for Earth Science, Chinese Academy of Sciences, Beijing, China, [3]College of Mining Engineering, Taiyuan University of Technology, Taiyuan, China, [4]Key Laboratory of Earth Fissures Geological Disaster, Ministry of Land and Resources, Geological Survey of Jiangsu, Nanjing, China, [5]College of Earth and Planetary Sciences, University of Chinese Academy of Sciences, Beijing, China, [6]School of Mines, China University of Mining and Technology, Xuzhou, China, [7]State Key Laboratory of Oil and Gas Reservoir Geology and Exploitation, Chengdu University of Technology, Chengdu, China

OPEN ACCESS

Edited by:
Yinhui Zuo, Chengdu University of Technology, China

Reviewed by:
Jian Chang, China University of Petroleum, China
Yiduo Liu, University of Houston, United States
Zongxing Li, Chinese Academy of Geologi-cal Sciences (CAGS), China

***Correspondence:**
Yaqi Wang
wangyaqi@mail.iggcas.ac.cn

Specialty section:
This article was submitted to Economic Geology, a section of the journal Frontiers in Earth Science

Received: *28 September 2021*
Accepted: *25 November 2021*
Published: *13 December 2021*

Citation:
Wang Y, Bai Y, Wang L, Guan J, Wang Y, Wang Z, Hu J and Hu S (2021) Exploration Process and Genesis Mechanism of Deep Geothermal Resources in the North Jiangsu Basin, East China: From Nothing to Something. Front. Earth Sci. 9:784600. doi: 10.3389/feart.2021.784600

Geothermal resources, as an important member of clean renewable energy, of which the exploration, development, and utilization of geothermal resources, especially deep geothermal resources, are of great significance for achieving carbon peaking and carbon neutrality. Taking the North Jiangsu Basin (NJB) as an example, this paper reviews the exploration process of deep geothermal resources in the basin and presents the latest results. The study shows that the NJB is a typical "hot basin" with an average heat flow value of 68 mW/m^2. In this region, the deep geothermal resource favorable areas in the NJB are mainly distributed in the depressions, in particular those near the Jianhu uplift, i.e., the Yanfu depression and the Dongtai depression. In addition, the genesis mechanism of the deep geothermal resource favorable area in the NJB is best explained by the "two stages, two sources" thermal concentration, that is, "two stages" means that the transformation of the lithospheric thermal regime are caused by the late Mesozoic craton destruction in East China, and the Cenozoic lithospheric extension; these two tectono-thermal events together lead to the deep anomalous mantle-source heat (the first source), and the upper crustal-scale heat control is mainly caused by thermal refraction (the second source). Overall, this case study underlines new ideas of understanding the geothermal genesis mechanism in East China, which can guide for the exploration and development of deep geothermal resources at the basin scale.

Keywords: The North Jiangsu Basin, genesis mechanism, heat flow, geothermal resources, thermal refraction, East China

INTRODUCTION

The deepening energy crisis and increasing environmental pollution force humans to focus more on new energy sources. Solar and wind energy have made great progress in recent years, while the more widely distributed, low-carbon, and sustainable geothermal energy has lagged, accounting for a small proportion of the total new energy. Geothermal energy that can be used around the clock is more

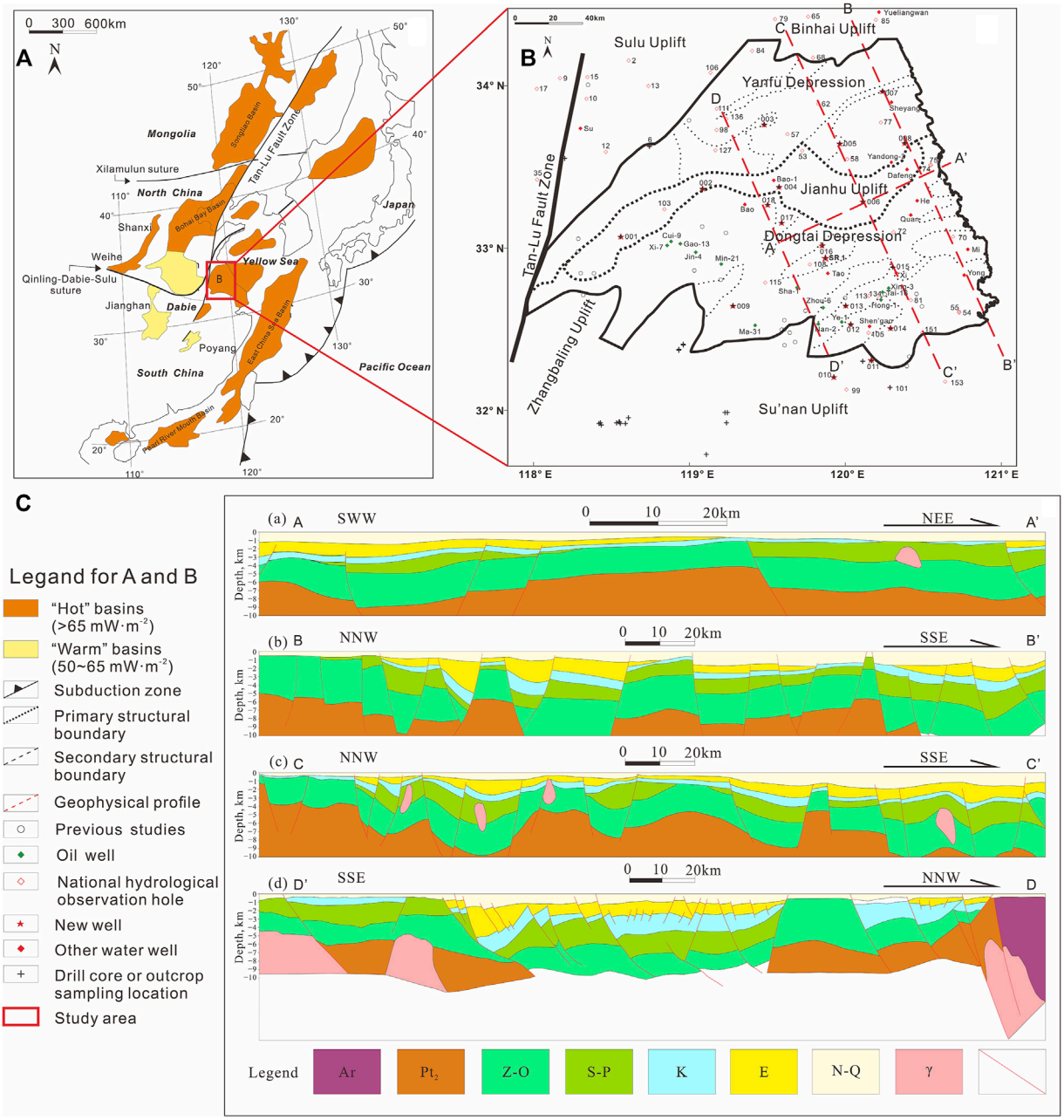

FIGURE 1 | Tectonic, geological interpretation sections and geothermal information of the North Jiangsu Basin. **(A)** is modified after Grimmer et al. (2002); **(B)** is modified after Wang et al. (2020), Wang et al. (2021a); **(C)** (a, b, c) are integrated geological profiles with joint inversion of resistivity, gravity, and magnetic data, and **(C)** (d) is depth-converted seismic interpretation, **(C)** (a, c) are modified from Wang et al. (2020), (b) is from Wang et al. (2021a), (d) is integrated from Chen (2010) and Qiao et al. (2012).

stable and universal than wind and solar energyin addition, it is cleaner and safer than nuclear energy (Lund and Toth, 2020; Tester et al., 2006). The widespread use of geothermal energy can fill the gap left by wind and solar energy subject to weather changes, so that clean renewable energy, including geothermal energy, wind, and solar energy, can play a more substantial role in a country's energy structure and effectively promote the development of low-carbon economy (Hou et al., 2018; Zhu et al., 2015). The Chinese government has committed to adopt strong policies and measures to peak CO_2 emissions by 2030 (emission peak) and strive to achieve carbon neutrality by 2060. Undoubtedly, geothermal utilization will contribute enormously to this process.

North Jiangsu Basin (NJB) that located in Jiangsu Province is a very favorable area to carry out geothermal development and utilization in China at present for the following reasons: 1) The

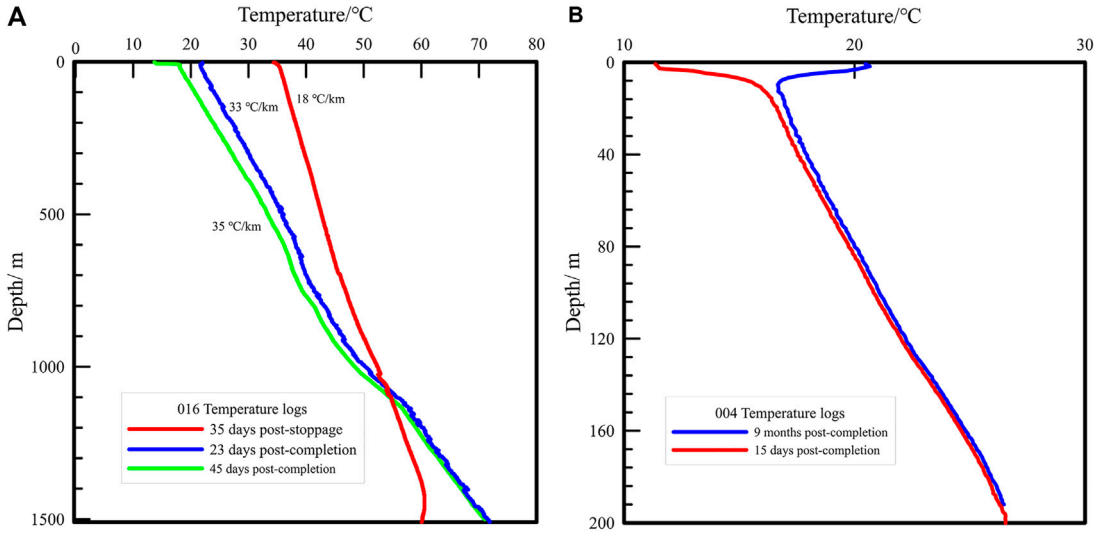

FIGURE 2 | The difference between unsteady temperature measurement and steady-state temperature measurement.

NJB is a typical "hot summer and cold winter" area with a strong heating demand market, and the high population density and energy consumption in the area enhance the feasibility of adopting geothermal heating; 2) detailed geological information guarantee for the development and utilization of geothermal resources; 3) a strong economic base is an important driving force for the efficient utilization of geothermal resources in the NJB, and 4) it also provides an possible model for the future utilization of geothermal resources in the Yangtze River Delta region. Overall, this case study guides the exploration and development of deep geothermal resources in the basin, as well as enrich the genesis mechanism of geothermal characteristics in the Lower Yangtze from the spatio-temporal perspective.

This paper updates and summarizes high-quality temperature profiles from representative wells drilled in the NJB, establishes columns of thermal conductivity, density, and porosity throughout the NJB formations (or rocks) of different geological ages. In this study, characteristics of the deep temperature field distribution in the NJB are analyzed to reveal the geothermal resource potential, in combining with geological and geophysical data, to comprehensively discuss the genesis mechanism and dynamical background of the present-day thermal state of the NJB.

GEOLOGIC SETTING

The NJB generally trends NE-SW, covering an area of about 35,000 km^2. The main body of the NJB is located in the northern part of Jiangsu province, adjacent to the Binhai uplift in the north, connected to the Lusu uplift in the northwest, adjacent to the Su'nan uplift in the south, and deep into the South Yellow Sea in the east, belonging to the onshore part of the North Jiangsu-South Yellow Sea Basin (**Figure 1**). Tectonically, the NJB belongs to the back-arc area of the Meso-Cenozoic West Pacific tectonic domain and is part of the Lower Yangtze Craton. The tectonic pattern of "one uplift (Jianhu uplift in the middle) and two depressions (the northern Yanfu depression, and the southern Dongtai depression)" in the NJB can be further subdivided into 22 highs and sags (**Figure 1**).

The NJB is a Middle Cenozoic fracture-depression type sedimentary basin which dominated by the Tertiary formation, and the Late Cretaceous Taizhou Formation to Tertiary lacustrine-riverine strata are developed, with the maximum sedimentary thickness of about 7 km (**Figure 2**). The Pre-Jurassic formations form the basement of the NJB, where the Pre-Permian strata are buried (Shu et al., 2005). The Late Cretaceous-Tertiary strata of the NJB is divided into the Taizhou Formation (K_2t), the Fu'ning Formation (E_1f), the Dai'nan Formation (E_2d), the Sanduo Formation (E_2s), the Yancheng Formation (Ny), and the Dongtai Formation (Qd) from the bottom up (Shu et al., 2005). The lithology and characteristics of strata in the NJB are shown in **Table 1**.

During the Triassic, the NJB was uplifted by the collision of the North China Craton and the Yangtze Craton, and possible southward extrusion of the Siberian plate (Guo et al., 2012; Yin and Nie, 1993). Since then, the NJB is primarily characterized by four main stages of tectonic evolution: 1) Yizheng movement (ca. 83 Ma), which is marked by the Taizhou Formation unconformity overlying the Chishan or Pukou Formations, forming the tectonic pattern of "two uplifts and one depression"; 2) Wubao movement (ca. 55 Ma), the low-angle unconformity of the Dai'nan Formation overlies the Fu'ning Formation; 3) Zhenwu movement (about 50 Ma), the Dai'nan Formation is unconformably overlain by the Sanduo Formation; 4) Sanduo movement (ca. 38–25 Ma), the Yancheng Formation unconformably overlies the Sanduo Formation, with Neocene-Quaternary fluvial facies (Qian, 2001; Shu et al., 2005; Qiu et al., 2006).

TABLE 1 | Representative strata of the North Jiangsu Basin (Revised from Wang (2020) and oil company reports).

Time stratigraphy			Formation	Abbreviation	Thickness (m)	Main rock types
Era	Period	Epoch				
Cenozoic	Q	Pleistocene-Holocene		Q	0–200	Clay, sand
	N	Miocene-Pliocene	Yancheng	$N_{1\text{-}2}yn$	0–463	Sandstone, conglomerate, mudstone interlayer
	E	Oligocene	Sanduo	E_3s	0–160	Mudstone, sandstone, locally interspersed with basalt
		Eocene	Dai'nan	E_2d	0–312	Mudstone, sandstone
		Paleocene	Fu'ning	E_1fn	0–1100	Sandstone, mudstone
Mesozoic	K	Upper	Taizhou	K_2t	0–621	Sandstone, mudstone
			Chishan	K_2c	0–1425	Siltstone, sandstone, mudstone
			Pukou	K_2p	0–1425	Siltstone, sandstone, mudstone
	J			J	0->287	Mudstone interspersed with clay
	T			T	0–22.5	Sandy mudstone, marl, limestone, conglomerate
Upper Paleozoic	P	Upper	Dalong	P_2d	0–12	Limestone, with shale in the upper part
			Longtan	P_2l	0–70	Sandstone and mudstone, topped with limestone
		Lower	Qixia	P_1q	>168	Limestone interspersed with shale
	C	Upper	Chuanshan	C_3c	28	Limestone
		Middle	Huanglong	C_2h	75	Limestone interspersed with shale
		Lower	Laohudong	C_1l	0–98	Dolomite
			Gaolishan	C1g	>194	Sandstone interspersed with mudstone, sandstone
			Jinling	C_1j	47–87	Mudstone, siltstone, topped by chert
	D	Upper	Wutong	D_3w	>199	Sandstone, mudstone, siltstone
Lower Paleozoic	S	Middle	Fentou	S_2f	52	Sandstone, mudstone, siltstone
		Lower	Gaojiabian	S_1g	287	Siltstone interspersed with chert, sandstone, and mudstone
	O	Upper	Wufeng	O_3 w	164	Siliceous mudstone
			Tangtou	O_3t	>51	Interbedded calcareous mudstone and muddy tuff
		Lower	Dawan	O_1d	>84	Limestone
			Honghuayuan	O_1h	161	Limestone
			Lunshan	O_1l	86.5	Limestone, dolomite, limestone with shale
	Є	Upper	Guanyintai	$Є_3g$	378	Dolomite, dolomite intercalated with flint nodules
		Middle	Paotaishan	$Є_3$ p	>87	Limestone, dolomite
		Lower	Mufushan	$Є_3m$	>111	Limestone with conglomerate, shale, limestone
			Hetang	$Є_3h$	81	Limestone, shale, sandstone
Upper Proterozoic	Z	Upper	Dengying	Z_2d	>930	Dolomite, limestone
			Huangxu	Z_2h	>579	Limestone, siltstone
		Lower	Nantuo	Z_1n	>257	Phyllite
			Liantuo	Z_1l	>77	Metamorphic quartz sandstone interspersed with phyllite

Proposed geothermal study of the NJB include two main parts before 2005: 1) the deep temperature field study based on the existing test oil temperature (Wang, 1989; Wang et al., 1995); 2) the thermal history inversion work based on the present-day geothermal field, and the exploration of the relationship between heat and oil and gas (Wang, 1987; Wang, 1989; Zeng, 2005). Since 2018, the Geological Survey of Jiangsu Province and the Institute of Geology and Geosciences of the Chinese Academy of Sciences have carried out a lot of drilling, coring, steady-state temperature measurement, thermal property testing, and numerical simulation. The process of above work is as follows: 1) laying and drilling of boreholes; 2) census of the NJB geothermal field; 3) identification of key target areas; 4) detailed investigation of target areas; 5) laying and drilling of pilot holes; 6) numerical simulation study; 7) finalization of deep hole points. Besides, steady-state temperature monitoring, fracturing, and pumping tests are steadily being planned and advanced.

STEADY-STATE TEMPERATURE LOGS

From November 2018 to January 2019, we designed and constructed fifteen 200-m-deep boreholes with full well coring, numbered 001–015 in **Figure 1**. In 2019, we constructed three geothermal wells (800–1500 m) in the preliminary target area, numbered 016–018 (Figure (B)). Finally, in 2020–2021, a 4700 m deep well (SR1 in **Figure 1B**) was drilled to validate previous studies and provide the basis for further work. During this period, we carried out steady-state temperature measurements on 104 wells in the NJB and its adjacent area and calculated 78 high-quality heat flow values, based on which heat flow maps of the NJB (**Figure 1A**).

Steady-State Temperature Measurement

Borehole temperature measurement is the most effective and direct means of obtaining the present-day temperature field. Systematic steady-state temperature measurement refers to temperature measurement performed after the temperature in the borehole has reached the *in-situ* temperature of the formation. The drilling process severely affects the borehole temperature, mainly in the circulation of drilling fluid and frictional heat generation. Therefore, a considerable period is needed to recover the formation temperature from the end of drilling to the time of temperature measurement. Yu (1991) estimated the time required for recovery of drilling

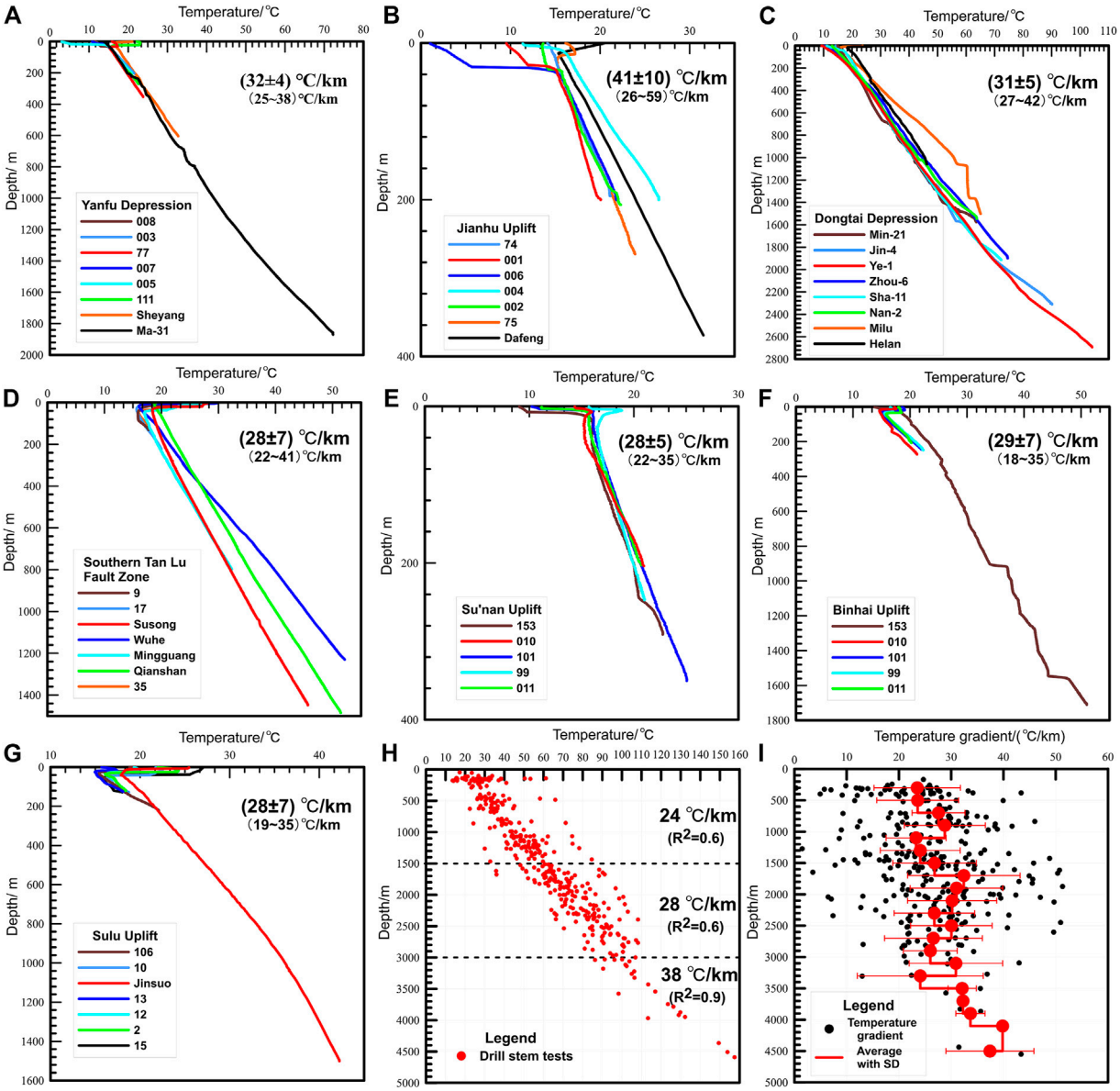

FIGURE 3 | The new drill stem tests data, temperature gradient, and temperature-depth profiles for the measured boreholes in each sub-structural unit of the North Jiangsu Basin and its adjacent areas.

disturbance temperature: 0.5–1.5 times and 10–20 times of drilling time is required to recover 90 and 99% of formation temperature, respectively.

Although temperature measurements are required in most completion reports of a borehole, the vast majority of tests are conducted within 2 days of completion and cannot meet the requirements for the regional thermal regime studies. The temperature measurement curves of Borehole 016 (1500 m; drilling time, 37 days; mud circulation time, 2 days) in the NJB at 35 days post-stoppage, 23 days post-completion, and 45 days post-completion shows that the temperature at the neutral point gradually decreases at the shallow end and increases at the deep end as the time of static well progresses (**Figure 2A**). The ground temperature gradient at 45 days post-completion is about twice the initial measured ground temperature gradient and combined with the drilling time, the temperature data is usually considered as steady-state temperature measurement data. More recently, the steady-state temperature measurement conditions can be achieved after tens of days of static wells. As shown in **Figure 2B**, the deep temperature measurement curves of Borehole 004 (200 m; drilling time, 7 days; no mud circulation) do not differ much between 15 days and 9 months after completion, as such, the temperature measurement after 15 days of completion has reached the steady-state temperature measurement condition. In summary, drilling depth, drilling time, mud circulation time, and completion process closely

affect the judgment of the steady-state condition of drilling temperature.

Temperature Logging

Geothermal work in the NJB began in the 1970s when oil companies conducted systematic temperature measurements on several exploration wells located in the southern NJB. Wang (1989) and Wang et al. (1995) collected steady-state temperature data from 21 wells and studied the geothermal field in the NJB in conjunction with the hydrostatic reservoir temperatures of 161 wells. The distribution of heat flow measurement points in the NJB and adjacent areas is generally uneven and very sparse (**Figure 1**).

From 2018 to 2020, temperature logs of 104 boreholes in the NJB and its adjacent areas were acquired, and the representative temperature profiles are shown in **Figures 3A–G**. Additionally, in this study, we collected 385 drill stem tests (DST) data from 58 boreholes in the NJB (**Figure 3H**). Temperature records below the water level of the borehole better reflect the true temperature of the formation, which exclude the effect of the thermal conductivity difference between air and water. We determine the water level of the borehole which is usually less than 40 m in the NJB (**Figure 3**) on the basis of the vertical variation of temperature, When the depth is greater than 50 m, the temperature increases linearly or nearly linearly, which is a conduction-type temperature measurement curve. Based on the temperature data, the temperature gradient of each log was calculated using the least-squares method, ranging from 22 to 59°C/km, with an average temperature of 32 ± 6°C/km for the NJB (weighted average based on the area of each tectonic unit).

Temperature Gradient

The vast majority of the DST data are from the Dongtai Depression. A large number of test oil temperatures show that the temperature gradually increases with increasing depth. Moreover, the DST data are divided into three geothermal gradient sections (**Figure 3H**): 0–1500 m, 1500–3000 m, and >3000 m. The gradient of 0–1500 m and 1500–3000 m are about 24 and 28°C/km, respectively. As for the section deeper than 3000 m, the temperature gradient is up to 38°C/km. The distribution of the temperature gradient and depth (**Figure 3I**) reveals that the gradient gradually increases with depth in the shallow part (below 1000 m), and the average value of the gradient increases from 23°C/km to about 30°C/km. From 1000 m to 1800 m, the change of the gradient approximately repeats the above trend, increasing from 23°C/km to 31°C/km. The geothermal gradient stabilizes from a depth of 1800 m to about 3500 m, with the average value fluctuating around 30°C/km. The gradient tends to increase gradually at a depth of 3500 m, and the average value of the temperature gradient reaches 40°C/km at a depth of 4100 m.

Based on the non-D quality data (heat flow can be classified into A,B,C and D categories according to the quality, where A data is the best and D data is for reference only) collected from the basin and neighboring areas (Jiang et al., 2019), we mapped the temperature gradient above the Yancheng Formation ($N_{1\text{-}2}yn$, inclusive) in the NJB by Kriging interpolation method (**Figure 4**) (Stein, 1999). The east-central NJB and the eastern edge of Dongtai depression are high gradient areas on the plane, with an average geothermal gradient value higher than 35°C/km. The average temperature gradient of the NJB, the Dongtai depression, the Yanfu depression and Jianhu uplift are 31 ± 6°C/km, 39°C/km, 30°C/km and 39°C/km, respectively. Notably, it is crucial to compare and study the temperature gradient over the region with specific layers in mind.

Vertically, there is a general trend of gradual increase from top to bottom based on the statistical results of single wells. The geothermal gradient in the NJB increases with depth, and the gradient in Ny, E_2s-E_2d is generally lower than that in the E_1f-K_2t. The Neoproterozoic and Quaternary formations are characterized by a low temperature gradient of 15–30°C/km, probably as a result of the influence of lithology and groundwater activity in the shallow formations. The high sandy content of the Ny, E_2s, and E_2d formations leads to high stratigraphic thermal conductivity and low gradient, resulting in generally lower gradient in the shallow. The Paleocene and Upper Cretaceous rocks have relatively high mud content, with gradient values between 30 and 40°C/km.

THERMAL PHYSICAL PARAMETERS MEASUREMENT

Thermal Conductivity

Rock thermal physical parameters are the basis for conducting regional geothermal field studies. Since 1986–1988, outcrop and core samples have been collected three times in the NJB to test the thermal conductivity of some strata (Wang, 1989; Wang et al., 1995). During 2018–2020, the Institute of Geology and Geophysics, Chinese Academy of Sciences and Geological Survey of Jiangsu Province systematically collected a large number of rock samples in the geothermal study of the NJB and carried out a series of thermal conductivity tests, which greatly improved the regional thermal conductivity column. Because of the large stratigraphic span and uneven distribution, the thermal conductivity values compiled in this study were combined with previous research results (Wang, 1989; Wang et al., 1995) to obtain weighted average values of thermal conductivity for different strata based on the number of test blocks. The thermal conductivity test results are shown in **Table 2** (the thermal conductivity values are those of the dry rock samples measured at room temperature).

The results show that the average rock thermal conductivity the strata in the region fluctuates widely, and the minimum value in the test results is the Quaternary clay and sand with thermal conductivity of 0.6 W/m/K; the maximum value is the Silurian S_2m^1 with thermal conductivity of 7.99 W/m/K (**Figure 5A**). In general, the thermal conductivity shows a gradual decreasing trend from old to new with the stratigraphy. The thermal conductivity of the Paleozoic strata is generally higher than 3.0 W/m/K; the Mesozoic strata have the next highest thermal conductivity, mostly 2.0–3.0 W/m/K; and the Cenozoic strata have the lowest thermal conductivity, between 1.5 and 2.5 W/m/K. The

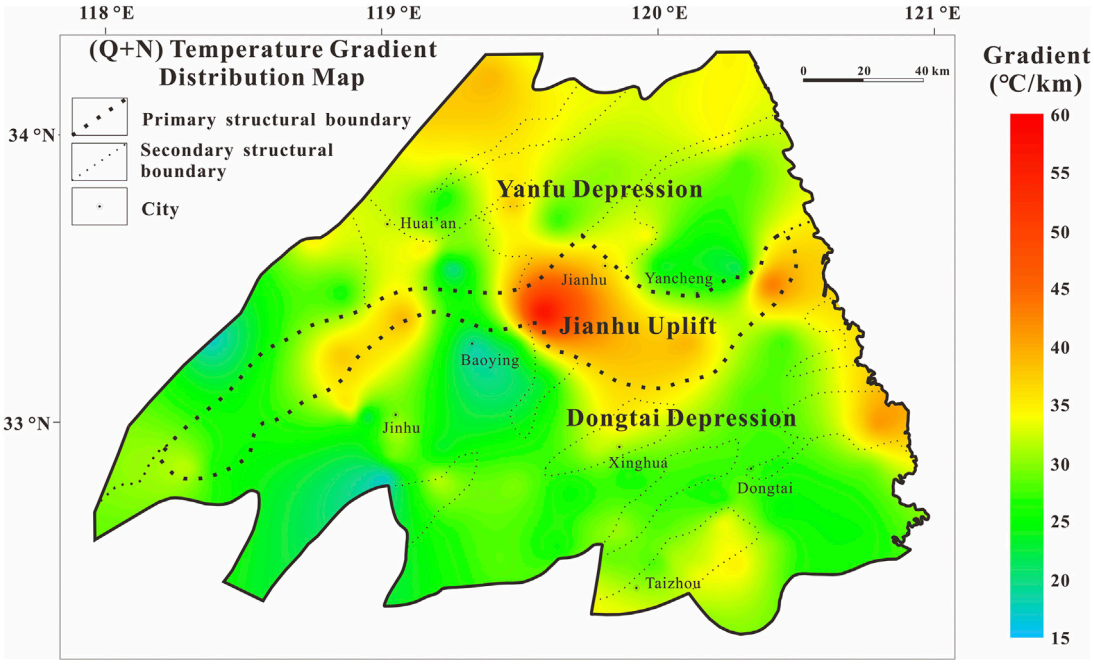

FIGURE 4 | Distribution of the (Q + N) temperature gradient in the North Jiangsu Basin.

stratigraphic thermal conductivity of the NJB can be roughly divided into two different layers, namely, the shallow low thermal conductivity layer and the deep high thermal conductivity layer. The thermal conductivity of the shallow Cretaceous-Quaternary is low (<2.7 W/m/K), especially thermal conductivity of the Late Paleogene-Quaternary is mostly less than 2.0 W/m/K, which can provide good cover for heat preservation. The thermal conductivity of the deeper Ediacaran-Jurassic is relatively high, generally greater than 3.0 W/m/K, especially the thermal conductivity of the Silurian-Devonian and Ediacaran-Cambrian can exceed 4.0 W/m/K, and the thermal conductivity of the Late Ediacaran Dengying Group can exceed 6.0 W/m/K, all of which can be used as good thermal conductivity and thermal storage layers. The thermal conductivity of magmatic rocks gradually increase with the change of composition from basic to acidic, and the thermal conductivity of medium-acidic to basic magmatic rocks is low overall, especially the thermal conductivity of Cenozoic basic volcanic rocks is comparable to that of Cenozoic sedimentary cover.

The most important factor affecting large differences in thermal conductivity is the difference in lithology, while other influencing factors such as the degree of metamorphism and porosity (**Figure 5B**) also have a large effect on thermal conductivity, and the effects of temperature, pressure, and anisotropy on thermal conductivity should not be ignored (Wang, 2020; Wang et al., 2021b).

Heat Production

In this study, the radioactive element contents of 47 samples were tested and compiled for U, Th, and K. The method proposed by Rybach (1976) was used to calculate the stratigraphic heat production. The content of U and Th was measured by ICP- MS, and the content of K was measured using atomic absorption spectroscopy. The test and summary results are shown in **Table 2**.

The results show that the average heat production of the rocks of all rock types in the varies little between 1.1 and 2.7 mW/m^3, with the lowest heat production in the Middle Proterozoic Picheng Group and the highest heat production in the fourth section of the Paleogene Fu'ning Formation. The difference in heat production is closely related to lithological changes, and rocks with more silt and mud content tend to have larger heat production. Therefore, more work on heat production test work should be carried out to obtain precise constraints on the heat flow contribution and deep temperature variation in different depths of the strata.

HEAT FLOW

The regional heat flow map is an important representation of the thermal background of a tectonic unit, and an important basis for regional geothermal resource evaluation, target area preference, and mining design. The density of heat flow measurement point distribution and the quality of heat flow data in the NJB is high in China and even in the world. In this study, we obtained seven new high-quality heat flow values in the key blank areas of the NJB (e.g., the northern margin of the Jinhu sag and the eastern margin of the Dongtai Depression) (**Table 3**). Combining the 72 geothermal heat flow data measured in 2018 (Wang et al., 2020) and 165 published

TABLE 2 | Thermal conductivity and heat production of different rock types in the North Jiangsu Basin.

Strata or igneous rocks	Formation	Abbreviation	Thermal conductivity		Heat production (previous work*)	
			Mean (W/m/K)	Mean (μW/m^3)	Mean (μW/m^3)	Number
Q	Dongtai	Q	1.56	87	1.40	10
N	Yancheng	N	1.68	16	1.25	5
E	Sanduo	E_3s	1.40	6	1.20	3
	Dai'nan	E_2d	2.38	3	1.01	2
	Fu'ning	E_4f	--	--	2.65	2
		E_3f	2.61	4	2.05	2
		E_2f	2.44	5	1.62	2
		E_1f	2.45	2	2.68	1
K	Taizhou	K_2t	2.99	1	2.21	2
	Chishan	K_2c	--	--	1.67	1
	Pukou	K_2p	2.28	8	2.08	1
		K_1	--	--	--	--
J		J	4.38	4	1.25	1
T		T	2.84	2	2.64	2
P	Dalong	P_2d	--	--	--	--
	Longtan	P_2l	2.78	10	2.71	1
	Qixia	P_1q	3.32	3	--	--
C	Chuanshan	C_3c	3.26	3	--	--
	Huanglong	C_2h	2.80	2	--	--
	Hezhou	C_1h	3.18	2	2.67	1
	Laohudong	C_1l	--	--	--	--
	Gaolishan	C_1g	3.98	3		
D	Wutong	D_3w	3.70	5	1.12	1
		D_{1+2}	--	--	--	--
S	Maoshan	S_2 m^1	7.99	1	--	--
	Fentou	S_2f	3.91	8	2.3	1
	Gaojiabian	S_1g	3.34	17		
O		O	3.85	1	2.55	2
Є	Guanyintai	Є$_3g$	3.31	2		
	Paotaishan	Є$_3p$	--	--	2.82	1
	Mufushan	Є$_3$ m	4.57	2	--	--
Z	Dengying	Z_2d	6.11	6	--	--
	Huangxu	Z_2h	2.59	4	2.07	1
	Liantuo	Z_1l	--	--	--	--
Pt_3	Jinping	Pt_3j	3.22	39	--	--
Pt_2	Picheng	Pt_2p	3.39	18	1.05	5
Cenozoic	Volcanic rock	--	1.87	3	--	--
Late Mesozoic-Cenozoic	Granite	--	2.52	5	--	--
	Gabbro	--	2.17	2	--	--
	Amphibolite	--	3.08	2	--	--

heat flow data in and around the basin, we mapped the heat flow distribution in the NJB, as shown in **Figure 6**.

The average heat flow value of the NJB is 68 mW/m^2, which is typical of "hot basin" in East China (≥65.0 mW/m^2). **Figure 6** shows that the east-central part of the Jianhu uplift, the northern part of the Jinhu sag, and the eastern margin of the Dongtai Depression in the basin are relatively high heat flow areas, with mean heat flow values above 70 mW/m^2, which is higher than the average value of 62 mW/m^2 in continental China. The Huai'an high area has the highest mean heat flow of 73 mW/m^2, followed by the Jianhu uplift, Sujiazui high, and Yuhua high. Statistical calculations of heat flow values for each sub-tectonic unit in the basin show that the heat flow in the uplift or high areas is higher than that in the depression area, but heat flow in some of the highs in the depression area is also higher, and some of them even exceed that in the uplift area, indicating that the highs in the depression may also be favorable areas for deep geothermal convergence.

CHARACTERISTICS OF THE DEEP TEMPERATURE FIELD IN THE NORTH JIANGSU BASIN

One-Dimensional Temperature Field Calculation

The characteristics of the deep temperature field are an important basis for studying both the thermal structure of the lithosphere and the deep geothermal resources. The parameters that determine the temperature distribution at different depths z include surface temperature T_0, surface heat flow q_0, rock thermal conductivity K, and rock heat generation rate A. The

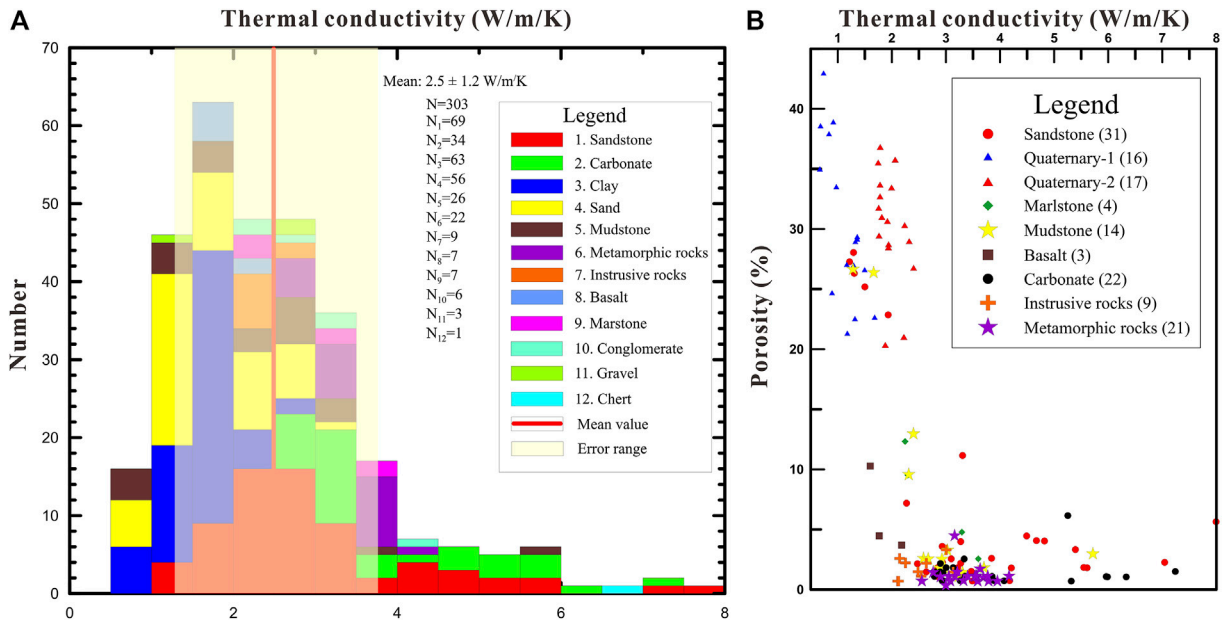

FIGURE 5 | Distribution of thermal conductivity **(A)** and its relationship with porosity **(B)** of different rock types in the North Jiangsu Basin.

TABLE 3 | Information table of new heat flow in the northern Jiangsu basin.

Borehole	Longitude	Latitude	Shut-in time	Rang of depth for heat flow calculation	Temperature gradient (°C/km)		Thermal conductivity (W/m/K)		Heat flow (mW/m^2)	
	E (°)	N (°)	D (days)	Z (m)	G	SD	λ	SD	q	SD
016	119.837	33.005	46	50–1500	35.3	4.1	2.2	0.4	77.3	15.6
017	119.586	33.131	31	50–918	23.8	1.5	2.1	0.4	49.2	10.0
018	119.488	33.241	30	50–808	24.9	0.7	2.0	0.1	50.3	3.1
Su	118.312	33.630	15	150–980	19.0	2.9	2.9	0.4	55.4	11.5
Xi	120.283	32.839	180	45–1800	31.8	3.5	2.1	0.4	66.6	15.0
He	120.432	33.247	25	50–1057	28.6	0.4	2.1	0.4	59.9	11.8
Mi	120.773	32.988	240	50–1500	35.3	5.7	2.0	0.2	70.8	12.5

surface temperature can be obtained from the multi-year surface average temperature; the surface heat flow comes from the drilling temperature and rock thermal conductivity measurements; and the thermal conductivity and heat production of the rocks come from the latest results of this update and compilation. Based on the previously published and newly added heat flow values of the NJB and its adjacent areas, the kriging interpolation method was used to interpolate the values in the whole area, with one point taken at 50 km, and a total of 480 interpolation points were taken in the study area.

Under the condition of one-dimensional steady-state heat conduction, for the distribution area of uniformly layered rocks, the thermal conductivity and heat production within a single layer can be approximated as constants (the measured averages are obtained according to different lithologies), and the corresponding deep temperature can be calculated by the following equation:

$$T_{(z)} = T_0 + (q_0 \cdot z)/K - (A \cdot z^2)/2K \quad (1)$$

Where T_0 is the temperature of the constant temperature zone, °C; q_0 denotes the surface heat flow, mW/m^2; K represent the thermal conductivity of certain crustal layer, W/m/K; A is the heat production of each layer, mW/m^3.

Based on Fourier's law, the temperature distribution at different depths of the NJB was calculated using parameters such as surface temperature, heat flow, rock thermal conductivity, and heat production, as shown in **Figure 7**. The favorable distribution area of geothermal resources in the NJB is wide, and its high temperature areas are mainly distributed in the Jinhu sag and its northern margin, the east-central part of Jianhu

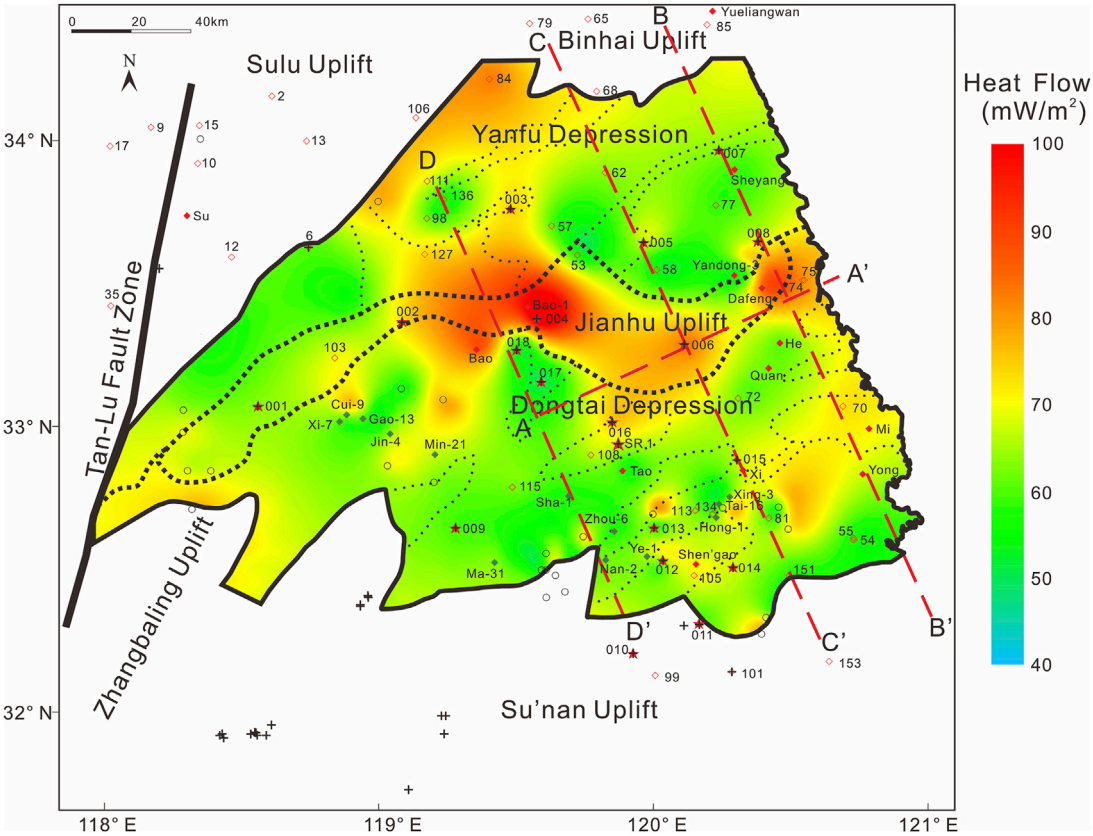

FIGURE 6 | Heat flow distribution map of the North Jiangsu Basin.

uplift, and the eastern margin of Dongtai depression, which reach 80°C at 2 km and about 200°C at 5 km.

The Two-Dimensional Temperature Field Profile

Since the "one uplift and two depressions" pattern in the NJB charactered the NEE-SWW spreading, we choose the profiles that are perpendicular to it when simulating the 2D temperature field. Accordingly, we choose three profiles, BB′, CC′, and DD' in **Figure 1**, to simulate the two-dimensional temperature field. To reduce the influence of the shallow thermal refraction and the setting of the bottom boundary heat flow on the results, we performed the simulations at a depth of 20 km.

The bottom boundary heat flow was assigned in segments based on the combination of the regional average heat flow value and the measured heat production. For each different strata or rock body, the assignment of thermal physical parameters, including the density, specific heat capacity, thermal conductivity and heat production of rocks, is also required. The initial values of the temperature in the thermostatic zone of the profile model were set regarding the annual average temperature of the province (Liu et al., 2003), and adiabatic boundaries were set at on both sides of the profile. Therefore, the temperature profiles of different profiles have certain differences in the three profiles. In order to more clearly portray the variation of the regional temperature field, we use different scale bars for the 2D temperature field profiles.

In summary, we simulated the temperature distribution at different depths on the profiles using parameters such as surface temperature, rock thermal conductivity, heat generation rate, and so on, and continuously optimized the parameters to match the observed heat flow using an interactive method. Finally, we obtained three large-scale 2D temperature field simulations (**Figure 8**).

The heat flow map of the NJB (**Figure 6**) shows that the there is a strong convergence of heat flow at the uplifts or highs, i.e., a significant thermal refraction effect occurs, with higher heat flow values relative to the depressions and sags (Xiong and Zhang, 1988; Wang et al., 2015). Two-dimensional temperature field simulations of the BB′ profile (**Figure 1**) reveal that the area where the isothermal surface uplift occurs is concentrated in the southern depressions, which does not correspond significantly to the convergence of heat flow. Heat flow distribution and two-dimensional temperature field simulation of the profiles CC′ and DD' (**Figure 1**) show that the uplifts and highs also have a strong heat flow convergence. However, the area where the isothermal surface is uplifted occurs in the Dongtai depression in the south and the Yanfu depression in the north, rather than

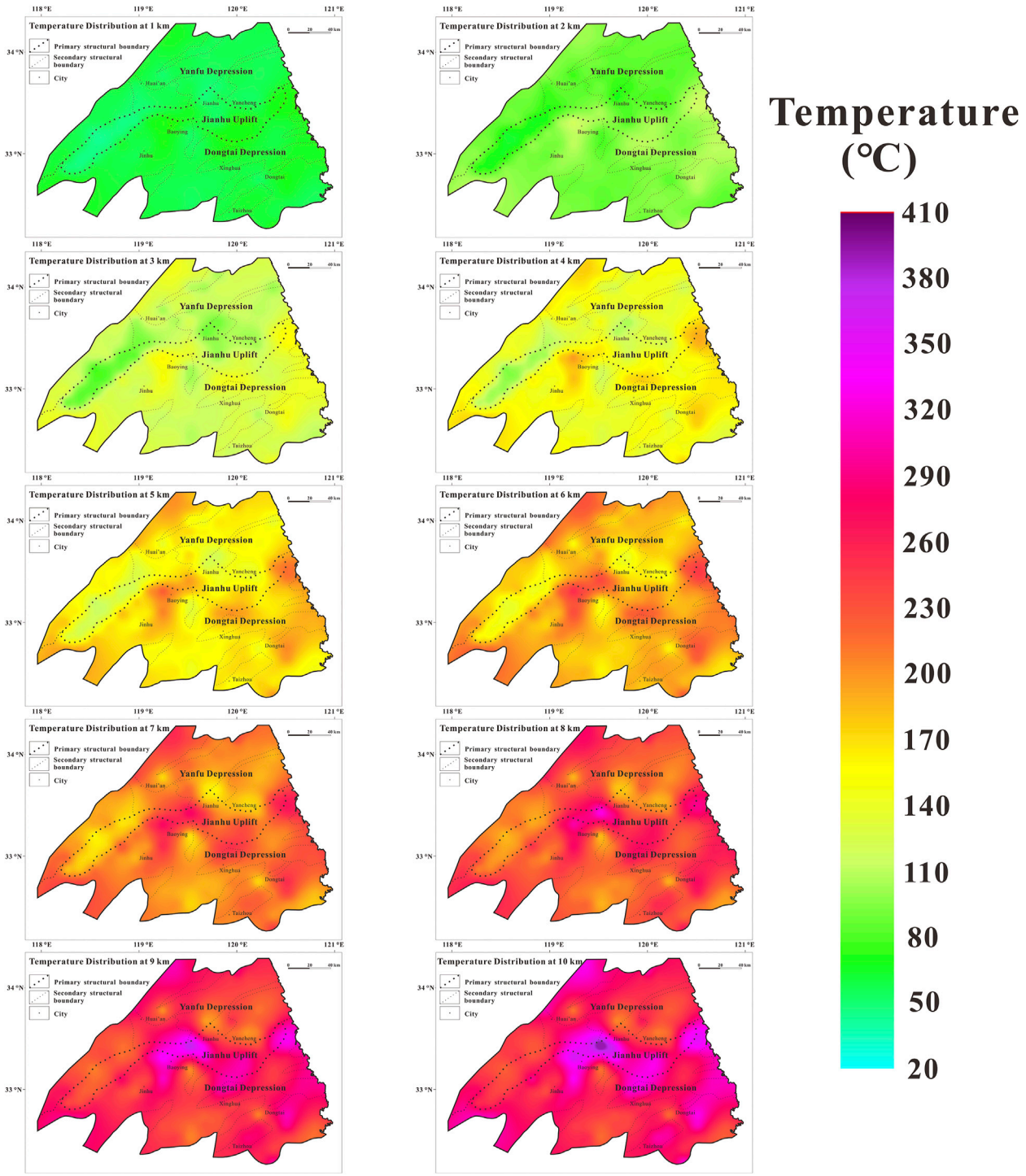

FIGURE 7 | Distribution characteristics of the geothermal field at different depths of 1–10 km in the North Jiangsu Basin.

concentrated in the Jianhu uplift. Besides, we plotted the temperature variation at 0.5 and 4.5 km depths using profile CC' as an example, as shown in **Figures 8G,H**. The trends of the two in the lateral direction indicate a very clear mirror image phenomenon, manifesting the variability of the lateral heat transfer of thermal conductivity at different depths. This aspect will be discussed in detail in the genesis mechanism section.

To check the reliability of the simulation results, we selected some boreholes adjacent to the simulated section and carried out a

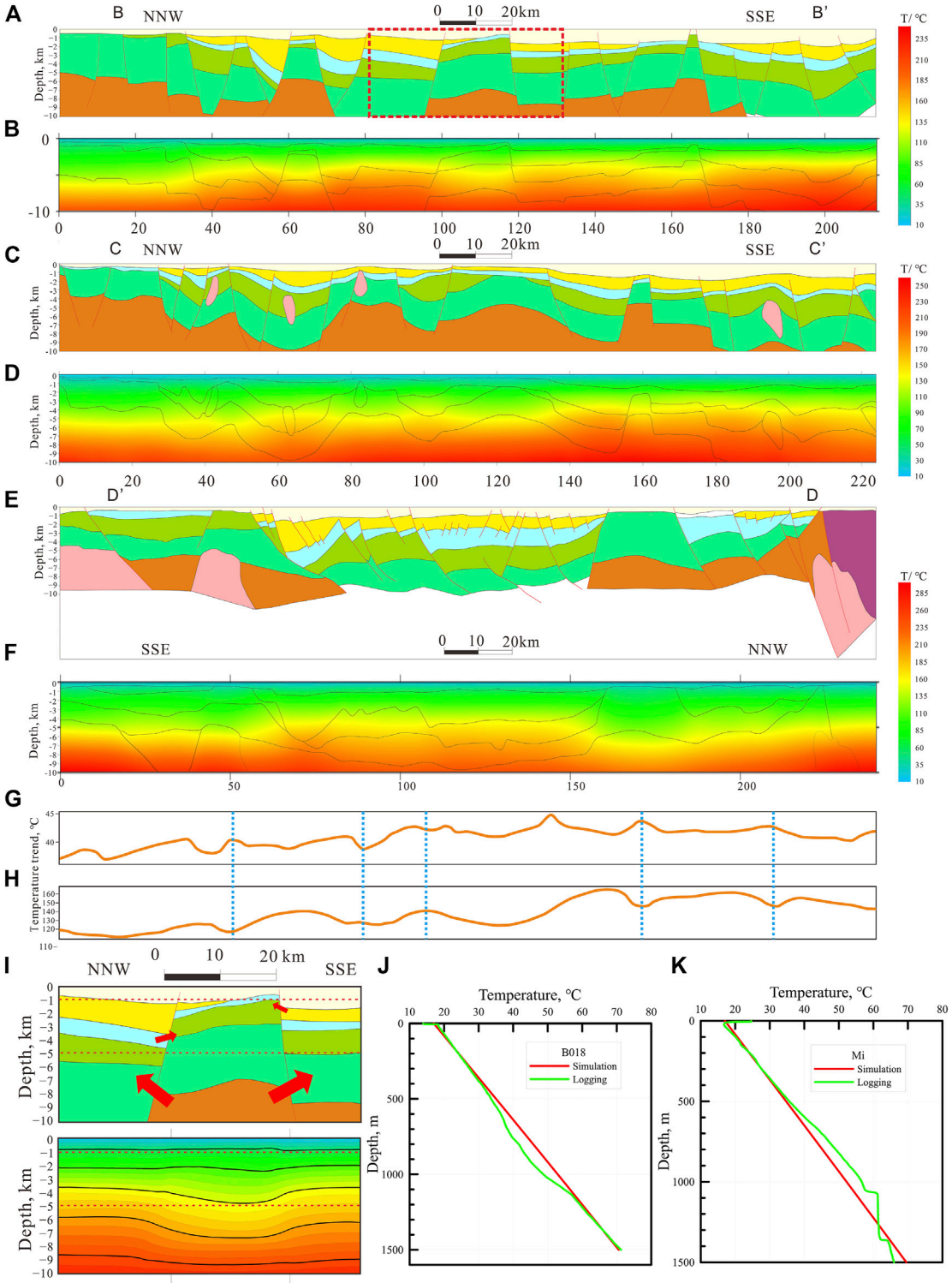

FIGURE 8 | (A–E), two-dimensional temperature field simulation of sections B-B, C-C, and D-D′ in **Figure 1C**. **(G,H)** represents the temperature variation of profile C-C′ in **Figure 1** at 0.5 and 4.5 km depth, respectively. Plot **(I)** is a zoomed-in view of the stratigraphic and simulation results in Figure a (red dashed box). **(J,K)** are comparisons of simulated and measured values of depth-temperature curves in 2 boreholes.

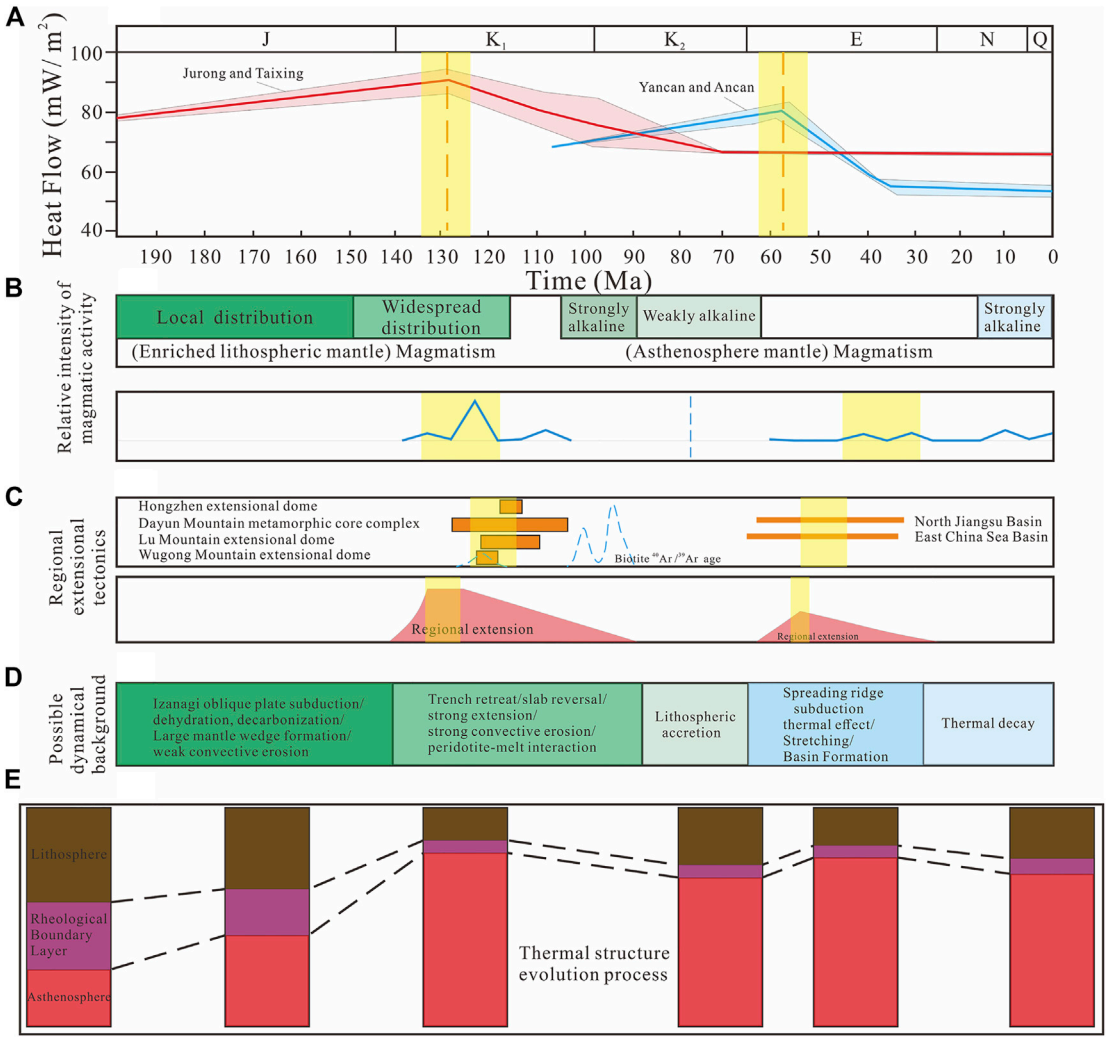

FIGURE 9 | The thermal regime transition process of the Lower Yangtze Craton in Mesozoic and Cenozoic (**(A)** thermal history evolution (modified from Zeng (2005)); **(B)** relative intensity of magmatic activity (data are from https://data.mendeley.com/datasets/yjjx5fvhvm/2 and https://github.com/Codrlocas/Oxygen); **(C)** regional extensional tectonics (modified from Lin and Li (2021)); **(D)** possible dynamical background; **(E)** schematic illustration of the evolution process of the lithospheric thermal structure of cratons in East China (revised from He and Zhang (2018))).

comparative analysis between the simulated and measured values. The analysis shows that most of the temperature profiles obtained from the simulations have a good fit with the measured data (both in the temperature gradient and the bottom-hole temperature). For example, the overall deviation of borehole B018 (**Figure 8J**) is about 1%, while this deviation is approximately 6% in Borehole Milu (**Figure 8K**). In addition, the preliminary logging work (bottom-hole temperature) on the borehole SR1 (**Figure 1**) similarly confirmed the reliability of the simulation results.

GEOTHERMAL GENESIS MECHANISM OF THE NORTH JIANGSU BASIN

The present-day temperature field of the basin is both the end of the thermal evolution process and the beginning of the thermal history recovery. The study of the present-day thermal state of the NJB confirms that the basin was not always characterized by high heat flow everywhere, which can be well explained by the theory of "thermal refraction" at the crustal scale. However, as an important part of the Lower Yangtze Craton, the "hot basin" property of the NJB should be the product of deep dynamical processes. Exploring this process from the perspective of time and deep processes can help to understand the geothermal genesis of the NJB, which consists of three main questions: 1) What are the thermal evolution processes of the Lower Yangtze Craton? 2) What are the deep mechanisms controlling the "hot basin" properties of the NJB? 3) Where are the geothermal resource "sweet spots" at different depths in the NJB? Based on the above questions, we discuss the geothermal causal mechanism in the NJB.

Thermal History and Geodynamics of the Lower Yangtze Craton

The polarization of the present-day geothermal background of the East Asian sedimentary basins (**Figure 1A**) seems to imply that they experienced different tectono-thermal events. As one of the most critical "hot" (≥65 mW/m^2) and oil-bearing basins in the Yangtze Craton, the thermal evolution and dynamical background of the NJB is a scientific issue of interest.

Since the Mesozoic, the subduction of the Izanagi plate led to dehydration/decarbonization of the overlying plate, and the strong unsteady flow of the big mantle wedge caused the craton destruction in East China, peaking at the end of the Early Cretaceous (Zhu et al., 2012; Zhu et al., 2017), accompanied by strong convective erosion and peridotite-melt interactions (He, 2014; Zhang, 2005), while the upper crust underwent large-scale extensional tectonic deformation (Lin and Li, 2021; Lin and Wei, 2018) (**Figure 9C**). Large-scale magmatism from 135–120 Ma enriched mantle sources existed in the Lower Yangzi Craton (Wu et al., 2005; Wu et al., 2019) (**Figure 9B**). Compared with the ancient craton, the lithosphere of the Lower Yangtze Craton is getting weaker and warmer. However, the dramatic increase in surface heat flow often lags behind significant erosion and magmatism (He, 2014). Thermal history studies of oil boreholes in Jurong and Taixing show that the surface heat flow reached a maximum of 85–93 mW/m^2 at about 128 Ma (**Figure 9A**). During the Late Cretaceous, trench retreat and slab reversal occurred, often accompanied by lithospheric extension and re-emergence of magmatism (Sun et al., 2008) (**Figure 9B**), as well as partial tectonic deformation (biotite ^{40}Ar-^{39}Ar age) (Lin and Li, 2021) (**Figure 9C**). Cenozoic basalts are identified as coming from a barren mantle, reflecting lithospheric thinning (Xu, 2001; Xu et al., 2009). During the Eocene and Oligocene, surface heat flow in the NJB reached 78–86 mW/m^2 (**Figure 9A**), as evidenced by apatite fission track and vitrinite reflectivity data (Ro) (Zeng, 2005). After 30–40 Ma, the thickness of the lithosphere increased to varying degrees, mainly as a result of thermal decay (Xu, 2001). Thereafter, the NJB gradually enters the thermal subsidence process in the late extensional stage, characterized by a gradual decrease in surface heat flow and lithospheric temperature. Numerical simulations by He (2015) show that the difference between the thickness of the thermal and seismic lithosphere (rheological boundary layer) gradually decreases from west to east, indicating that the viscosity coefficient of the large mantle wedge gradually decreases to the east, and suggesting that this is the result of subduction and dehydration of the western Pacific plate. Therefore, we considered the effect of this result in the schematic diagram of the evolution of the thermal structure of the NJB lithosphere (**Figure 9E**).

Lithospheric-Scale Thermal Control Mechanisms

Based on the above analysis, we suggest that the thermal control mechanism of the Lower Yangtze Craton, including the NJB, at the lithospheric scale, can be summarized as "two stages" thermal concentration (**Figure 10**).

Temporally, during the Late Mesozoic (ca. 140 Ma) (**Figure 10A**), the Izanagi plate subducted beneath the East Asian big mantle wedge, the trench retreated and the slab rollback, causing strong unstable flow in the overlying mantle, resulting massive magmatic activity and extensional tectonic deformation in the shallow (Zhu et al., 2017), and the craton destruction in East China led to a huge thinning of the lithosphere thickness of the Lower Yangtze Craton.

Since about 60 Ma (**Figure 10C**), the Pacific plate gradually succeeded the Izanagi plate and influenced the tectonic evolution of East Asia (Zhu et al., 2017). The subduction of the Pacific plate in the NW or W direction led to the previous Izanagi plate to gradually subduct into the mantle. Due to the presence of the mid-ocean ridge connecting two oceanic plates (Izanagi plate and Pacific plate), which may have caused regional extension of the lithosphere above the plate window (Zhu et al., 2017), the tectono-thermal event (45–60 Ma) of this period was recorded in the Lower Yangtze Craton under the influence of the subduction of the mid-ocean ridge. As the age of the subducted oceanic crust became older, high-angle subduction led to trench retreat and slab rollback, and regional extensional tectonics became more intense during the Oligocene-Miocene, along with large number of basaltic rocks forming in the back-arc region (Xu, 2001; Niu, 2005). Besides, it has been suggested that the Cenozoic volcanism and high heat flow in the basins of East China are mainly due to the back-arc extension caused by the subduction of the western Pacific plate (He, 2015; Liu et al., 2016; Qiu et al., 2016) (**Figure 10D**).

Most studies support that during this period, the Lower Yangtze experienced an extensional tectonic setting. Even though there was no magmatism during part of the period (46–56 Ma) (Wu and Wu, 2019; Liu et al., 2020), the high heat flow corresponding to the extensional setting has been widely accepted (Currie, 2004). Unlike central China, such as the Shanxi Rift System, which may has also been affected by subduction of the mid-ocean ridge and the Pacific plate (Liu et al., 2017; Su et al., 2021), the lithospheric thickness of the Lower Yangtze Craton has been substantially thinned due to the effects of Late Mesozoic craton destruction. Overall, the high heat flow in East China may be controlled by the combination of lithospheric extension, magmatic activity, and so on (Lei, 2012; Lei et al., 2013).

The Upper Crustal-Scale Thermal Control Mechanisms

The influence of stratigraphic relief on the crustal-scale temperature field is mainly reflected in the difference of rock thermal conductivity (similar to the fact that water always preferentially transfers to the direction of lower resistance), resulting in the redistribution of heat in the lateral direction or the thermal refraction effect.

In this study, the thermal conductivity of Paleozoic and Ediacaran rocks in the NJB is much greater than that of sedimentary layers since the Mesozoic, and even much greater than that of Neogene rocks (**Table 2**). This makes the geothermal field not all converge toward the shallow uplift area, but is related to the stratigraphic thickness and distribution scale of the

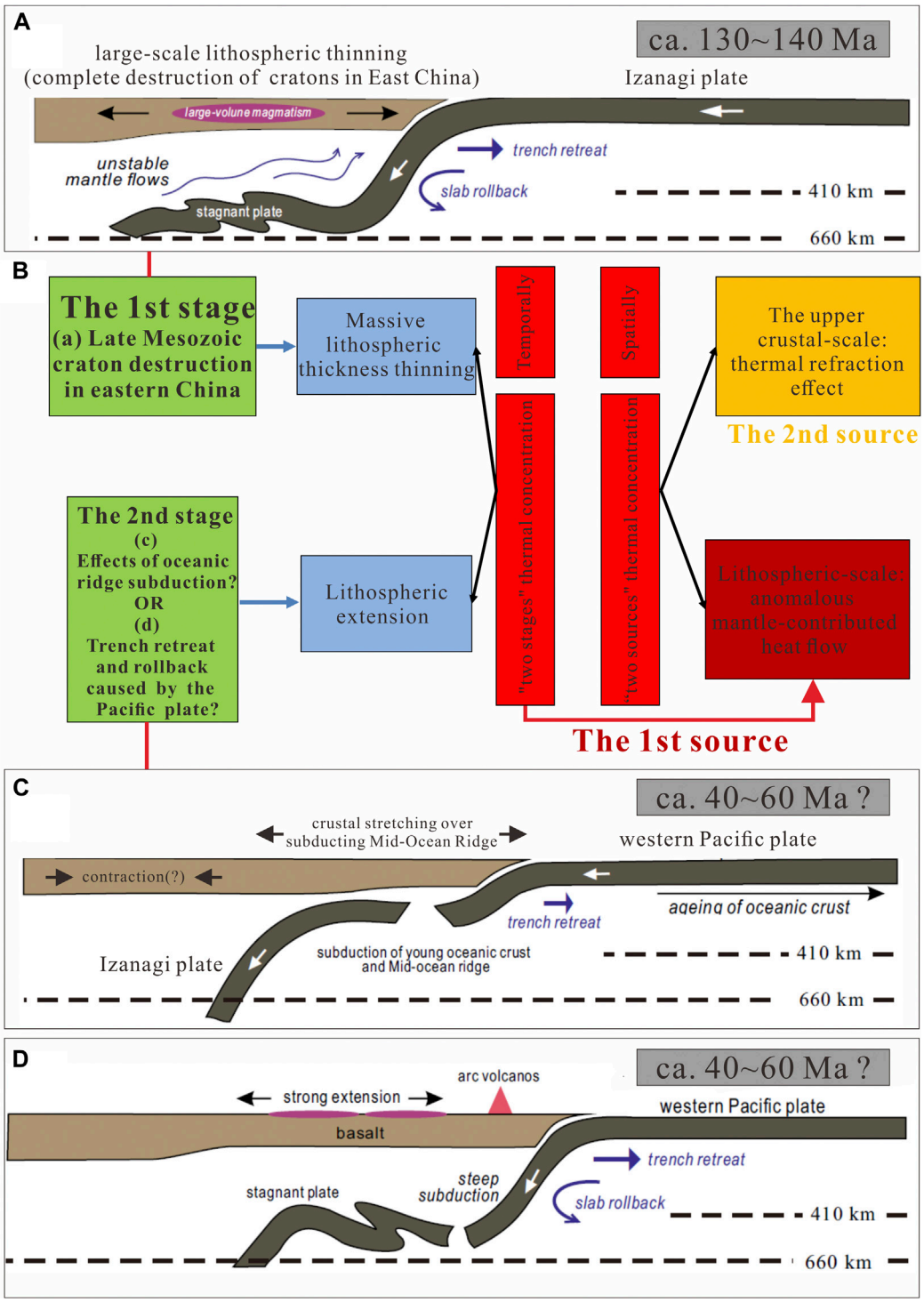

FIGURE 10 | The kinetic mechanism and model of "two stages, two sources" thermal concentration in the Lower Yangtze Craton (**(A)**, **(C)**, and **(D)** are the possible kinetic background of the thermal concentration in the Lower Yangtze Craton (**(C)** and **(D)** are the are two possible mechanisms causing lithospheric extension) (modified from Zhu et al. (2017)); **(B)** is the "two stages, two sources" thermal concentration model).

Paleozoic and Ediacaran strata. The larger the scale of the Paleozoic and Ediacaran strata with high thermal conductivity layers, the greater this control factor. Therefore, from the upper crustal scale, the Dongtai depression on the south side of Jianhu uplift has the strongest controlling effect on the regional geothermal field.

On the other hand, the control aspect of the temperature field. As shown in **Figure 8I**, high thermal conductivity rocks have higher thermal conductivity compared to nearby low thermal conductivity mudstones and sandstones, and heat will be preferentially transferred in the high thermal conductivity strata or rocks during the upward heat transfer. In the shallow section (about <3 km), heat converges from the depression to the uplift; in the deep section (about 3 km deeper), the situation is reversed, heat converges from the uplift to the depression. In detail, it can be generally divided into three parts: the first, (<1 km) uplift area with high temperature; the second, (about 2–3 km) depression area with high temperature; and the third section, (about 3.5–5 km) depression area with significantly higher temperature. Based on the above measurements and simulations, it is not difficult to derive the "sweet spots" of geothermal resources at different scales in the NJB.

CONCLUSION

We determined the thermal conditions of the NJB using the latest high-quality heat flow, thermal conductivity, and heat production of the rocks. A detailed discussion of the causal mechanisms of the present-day geothermal features in the NJB was carried out. The salient conclusions regarding the thermal state of the NJB are as follows:

1. The study of 79 heat flow points scattered in the NJB and its adjacent region shows that the average values of temperature gradient and heat flow in the NJB are 31°C/km and 68 mW/m^2, respectively.
2. The "sweet spots" of geothermal resources in the NJB are different at different study scales. Both the measured and numerical simulation results indicate that the favorable area of deep geothermal resources is mainly concentrated in the depression area near the Jianhu uplift.
3. The genesis mechanism of geothermal characteristics in the NJB is best explained by the "two stages, two sources". "Two stages" means that the transformation of the lithospheric thermal regime (such as, huge lithospheric thickness thinning) caused by the late Mesozoic craton destruction in East China, and the Cenozoic lithospheric extension; these two tectono-thermal events together determine the deep anomalous mantle-source heat, and the upper crustal-scale heat control is mainly caused by thermal refraction.

From geophysical exploration and regional drilling, census of steady-state temperature measurements, to important regional drilling and initial selection of target locations, geophysical exploration of target areas and simulation of deep temperature fields, and then to the identification of superior geothermal resources and drilling verification, geothermal research work in the North Jiangsu Basin has made great progress: from nothing to something". The exploration process and genesis mechanism of deep geothermal resources in the North Jiangsu Basin have gradually matured, laying a solid foundation for the next step of development and utilization of deep geothermal resources, and providing new ideas for the study on the genesis mechanism of geothermal characteristics in East China.

DATA AVAILABILITY STATEMENT

The raw data supporting the conclusions of this article will be made available by the authors, without undue reservation.

AUTHOR CONTRIBUTIONS

Conceptualization, YW and YB; methodology, ZW; software, JH; validation, JH and SH; formal analysis, YW and YW; investigation, YW, LW, JG, and ZW; data curation, YB, JG, and ZW; writing—original draft preparation, YW; writing—review and editing, JH; visualization, ZW; supervision, SH; project administration, YW; funding acquisition, LW. All authors have read and agreed to the published version of the article.

FUNDING

This research was accomplished under the support of National Key R&D Program of China (Grant No. 2021YFA0716003), State Key Laboratory of Lithospheric Evolution (SKL-K202104), National Natural Science Foundation of China (Grant No. 42074096), and Geological Survey of Jiangsu Province (JITC-1802AW2292; JITC-1902AW2919).

ACKNOWLEDGMENTS

We are grateful to the Geological Survey of Jiangsu Province very much, who provided help on the sample collection and borehole selection that are important for the study on the geothermal field and genesis mechanism.

REFERENCES

Chen, A. (2010). Tectonic Features of the Subei Basin and the Forming Mechanism of its Dustpan-Shaped Fault Depression. *Oil Gas Geology.* 31, 140–150.

Currie, C. A. (2004). The thermal Structure of Subduction Zones and Backarcs. *J. Geophys. Res.*

Grimmer, J. C., Jonckheere, R., Enkelmann, E., Ratschbacher, L., Hacker, B. R., Blythe, A. E., et al. (2002). Cretaceous–Cenozoic History of the Southern Tan-Lu Fault Zone: Apatite Fission-Track and Structural Constraints from the Dabie Shan (Eastern China). *Tectonophysics* 359, 225–253. doi:10.1016/s0040-1951(02)00513-9

Guo, X., Encarnacion, J., Xu, X., Deino, A., Li, Z., and Tian, X. (2012). Collision and Rotation of the South China Block and Their Role in the Formation and Exhumation of Ultrahigh Pressure Rocks in the Dabie Shan Orogen. *Terra Nova* 24, 339–350. doi:10.1111/j.1365-3121.2012.01072.x

He, L. (2014). Numerical Modeling of Convective Erosion and Peridotite-melt Interaction in Big Mantle Wedge: Implications for the Destruction of the North China Craton. *J. Geophys. Res. Solid Earth* 119, 3662–3677. doi:10.1002/2013jb010657

He, L. (2015). Thermal Regime of the North China Craton: Implications for Craton Destruction. *Earth-Science Rev.* 140, 14–26. doi:10.1016/j.earscirev.2014.10.011

He, L., and Zhang, L. (2018). Thermal Evolution of Cratons in China. *J. Asian Earth Sci.* 164, 237–247. doi:10.1016/j.jseaes.2018.06.028

Hou, J., Cao, M., and Liu, P. (2018). Development and Utilization of Geothermal Energy in China: Current Practices and Future Strategies. *Renew. Energ.* 125, 401–412. doi:10.1016/j.renene.2018.02.115

Jiang, G., Hu, S., Shi, Y., Zhang, C., Wang, Z., and Hu, D. (2019). Terrestrial Heat Flow of continental China: Updated Dataset and Tectonic Implications. *Tectonophysics* 753, 36–48. doi:10.1016/j.tecto.2019.01.006

Lei, J. (2012). Upper-mantle Tomography and Dynamics beneath the North China Craton. *J. Geophys. Res. Solid Earth* 117. doi:10.1029/2012jb009212

Lei, J., Xie, F., Fan, Q., and Santosh, M. (2013). Seismic Imaging of the Deep Structure under the Chinese Volcanoes: An Overview. *Phys. Earth Planet. Interiors* 224, 8. doi:10.1016/j.pepi.2013.08.008

Lin, W., and Li, J. (2021). Cretaceous Two Stage Extensional Tectonic in Eastern Eurasia Continent and its Geodynamics. *Acta Petrologica Sinica* 37, 2303–2323.

Lin, W., and Wei, W. (2018). Late Mesozoic Extensional Tectonics in the North China Craton and its Adjacent Regions: a Review and Synthesis. *Int. Geology. Rev.* 2018, 1–29. doi:10.1080/00206814.2018.1477073

Liu, J. Y., Zhuang, D. F., Luo, D., and Xiao, X. (2003). Land-cover Classification of China: Integrated Analysis of AVHRR Imagery and Geophysical Data. *Int. J. Remote Sensing* 24, 2485–2500. doi:10.1080/01431160110115582

Liu, K., Zhang, J., Xiao, W., Wilde, S. A., and Alexandrov, I. (2020). A Review of Magmatism and Deformation History along the NE Asian Margin from Ca. 95 to 30 Ma: Transition from the Izanagi to Pacific Plate Subduction in the Early Cenozoic. *Earth-Science Rev.* 2020, 103317. doi:10.1016/j.earscirev.2020.103317

Liu, Q., Zhang, L., Zhang, C., and He, L. (2016). Lithospheric thermal Structure of the North China Craton and its Geodynamic Implications. *J. Geodynamics* 102, 139–150. doi:10.1016/j.jog.2016.09.005

Liu, X., Zhao, D., Li, S., and Wei, W. (2017). Age of the Subducting Pacific Slab beneath East Asia and its Geodynamic Implications. *Earth Planet. Sci. Lett.* 464, 166–174. doi:10.1016/j.epsl.2017.02.024

Lund, J. W., and Toth, A. N. (2020). Direct Utilization of Geothermal Energy 2020 Worldwide Review. *Geothermics* 90, 101915. doi:10.1016/j.geothermics.2020.101915

Niu, Y. (2005). Generation and Evolution of Basaltic Magmas: Some Basic Concepts and a New View on the Origin of Mesozoic–Cenozoic Basaltic Volcanism in Eastern China. *Geol. J. China Universities* 11, 9–46.

Qian, J. (2001). Oil and Gas fields Formation and Distribution of Subei Basin-research Compared to Bohai Bay Basin. *Acta Petrolei Sinica* 22, 12–16.

Qiao, X., Li, G., Li, M., and Wang, Z. (2012). CO2 Storage Capacity Assessment of Deep saline Aquifers in the Subei Basin, East China. *Int. J. Greenhouse Gas Control.* 11, 52–63. doi:10.1016/j.ijggc.2012.07.020

Qiu, H., Xu, Z., and Qiao, D. (2006). Progress in the Study of the Tectonic Evolution of the Subei basin, Jiangsu, China (In Chinese with English Abstract). *Geol. Bull. China* 2006, 1117–1120.

Qiu, N., Zuo, Y., Xu, W., Li, W., Chang, J., and Zhu, C. (2016). Meso-Cenozoic Lithosphere Thinning in the Eastern North China Craton: Evidence from thermal History of the Bohai Bay Basin, North China. *J. Geology.* 124, 195–219. doi:10.1086/684830

Shu, L., Wang, B., Wang, L., and He, G. (2005). Analysis of Northern Jiangsu Prototype basin from Late Cretaceous to Neogene. *Geol. J. China Universities* 11, 534–543.

Stein, M. L. (1999). *Interpolation of Spatial Data: Some Theory for Kriging*. New York: Springer-Verlag New York.

Su, P., He, H., Tan, X., Liu, Y., Shi, F., and Kirby, E. (2021). Initiation and Evolution of the Shanxi Rift System in North China: Evidence from Lowmilemperature Thermochronology in a Plate Reconstruction Framework. *Tectonics* 40, 6298. doi:10.1029/2020tc006298

Sun, W., Ling, M., Wang, F., Ding, X., Hu, Y., Zhou, J., et al. (2008). Pacific Plate Subduction and Mesozoic Geological Event in Eastern China. *Bull. mineralogy, Petrol. Geochem.* 27, 218–225.

Tester, J. W., Anderson, B. J., Batchelor, A., Blackwell, D., DiPippo, R., Drake, E., et al. (2006). *The Future of Geothermal Energy*. Cambridge, Massachusetts: Massachusetts Institute of Technology, 358.

Wang, J., Pang, Z., Hu, S., He, L., and Qiu, N. (2015). *Geothermics and its Application*. Beijing: Science press.

Wang, L. (1989). *Geothermal Study on the Oil and Gas Basin (In Chinese with English Abstract)*. Nanjing: Nanjing University Press.

Wang, L., Li, C., Shi, Y., and Wang, Y. (1995). Distribution of Geotemperature and Terrestrial Heat Flow Density in Lower Yangtze Area (In Chinese with English Abstract). *Chin. J. Geophys.* 38, 469–476.

Wang, Y. (2020). *Differences of Thermal Regime of the Cratons in Eastern China and Discussion of its Deep Dynamic Mechanism*. Beijing: University of Chinese Academy of Sciences. University of Chinese Academy of Sciences.

Wang, Y. (1987). *Geothermal Characteristics of the Subei Basin and its Relationship with Oil and Gas*. Nanjing: Department of Earth Sciences. Nanjing University.

Wang, Y., Hu, D., Wang, L., Guan, J., Bai, Y., Wang, Z., et al. (2020). The Present-Day Geothermal Regime of the North Jiangsu Basin, East China. *Geothermics* 88, 101829. doi:10.1016/j.geothermics.2020.101829

Wang, Y., Wang, L., Bai, Y., Wang, Z., Hu, J., Hu, D., et al. (2021a). Assessment of Geothermal Resources in the North Jiangsu Basin, East China, Using Monte Carlo Simulation. *Energies* 14, 259. doi:10.3390/en14020259

Wang, Y., Wang, Z., Shi, L., Rong, Y., Hu, J., Jiang, G., et al. (2021b). Anisotropic Differences in the Thermal Conductivity of Rocks: A Summary from Core Measurement Data in East China. *Minerals* 11, 1135. doi:10.3390/min11101135

Wu, F.-Y., Yang, J.-H., Xu, Y.-G., Wilde, S. A., and Walker, R. J. (2019). Destruction of the North China Craton in the Mesozoic. *Annu. Rev. Earth Planet. Sci.* 47, 173–195. doi:10.1146/annurev-earth-053018-060342

Wu, F., Lin, J., Wilde, S., Zhang, X., and Yang, J. (2005). Nature and Significance of the Early Cretaceous Giant Igneous Event in Eastern China. *Earth Planet. Sci. Lett.* 233, 103–119. doi:10.1016/j.epsl.2005.02.019

Wu, T. J., and Wu, J. (2019). Izanagi-Pacific ridge Subduction Revealed by a 56 to 46 Ma Magmatic gap along the Northeast Asian Margin. *Geology* 47, 953. doi:10.1130/g46778.1

Xiong, L., and Zhang, J. (1988). Relationship between Geothermal Gradient and the Relief of Basement Rock in North China Plain. *Chin. J. Geophys.* 1988, 146–155.

Xu, Y.-G. (2001). Thermo-tectonic Destruction of the Archaean Lithospheric Keel beneath the Sino-Korean Craton in China: Evidence, Timing and Mechanism. *Phys. Chem. Earth, A: Solid Earth Geodesy* 26, 747–757. doi:10.1016/s1464-1895(01)00124-7

Xu, Y., Li, H., Pang, C., and He, B. (2009). On the Timing and Duration of the Destruction of the North China Craton. *Sci. Bull.* 54, 3379–3396. doi:10.1007/s11434-009-0346-5

Yin, A., and Nie, S. (1993). An Indentation Model for the North and South China Collision and the Development of the Tan-Lu and Honam Fault Systems, Eastern Asia. *Tectonics* 12, 801–813. doi:10.1029/93tc00313

Yu, H. (1991). *Mine Geothermal and Heat Harm Control (In Chinese with English Abstract)*. Beijing: Coal Industry Press.

Zeng, P. (2005). *The Application of the Thermometric Indicators to the Study of thermal Evolution in the Lower-Yangtze Region (In Chinese with English Abstract)*. Beijign: China University of Geosciences, 79–93.

Zhang, H.-F. (2005). Transformation of Lithospheric Mantle through Peridotite-Melt Reaction: A Case of Sino-Korean Craton. *Earth Planet. Sci. Lett.* 237, 768–780. doi:10.1016/j.epsl.2005.06.041

Zhu, J., Hu, K., Lu, X., Huang, X., Liu, K., and Wu, X. (2015). A Review of Geothermal Energy Resources, Development, and Applications in China: Current Status and Prospects. *Energy* 93, 466–483. doi:10.1016/j.energy.2015.08.098

Zhu, R.-X., Yang, J.-H., and Wu, F.-Y. (2012). Timing of Destruction of the North China Craton. *Lithos* 149, 51–60. doi:10.1016/j.lithos.2012.05.013

Zhu, R., Zhang, H., Zhu, G., Meng, Q., Fan, H., Yang, J., et al. (2017). Craton Destruction and Related Resources. *Int. J. Earth Sci. (Geol Rundsch)* 106, 2233–2257. doi:10.1007/s00531-016-1441-x

Conflict of Interest: The authors declare that the research was conducted in the absence of any commercial or financial relationships that could be construed as a potential conflict of interest.

Publisher's Note: All claims expressed in this article are solely those of the authors and do not necessarily represent those of their affiliated organizations, or those of the publisher, the editors and the reviewers. Any product that may be evaluated in this article, or claim that may be made by its manufacturer, is not guaranteed or endorsed by the publisher.

frontiers in Earth Science

ORIGINAL RESEARCH
published: 13 December 2021
doi: 10.3389/feart.2021.790315

Remediation Potential of Borehole Thermal Energy Storage for Chlorinated Hydrocarbon Plumes: Numerical Modeling in a Variably-Saturated Aquifer

Boyan Meng[1,2], Yan Yang[3], Yonghui Huang[4], Olaf Kolditz[1,2] and Haibing Shao[1]**

[1]Helmholtz Centre for Environmental Research, UFZ, Leipzig, Germany, [2]Faculty of Environmental Sciences, Dresden University of Technology, Dresden, Germany, [3]General Institute of Water Resources and Hydropower Planning and Design, MWR, Beijing, China, [4]Key Laboratory of Shale Gas and Geoengineering, Institute of Geology and Geophysics, Chinese Academy of Sciences, Beijing, China

OPEN ACCESS

Edited by:
Yinhui Zuo, Chengdu University of Technology, China

Reviewed by:
Wei Xu, Xi'an Jiaotong University, China
Chuanqing Zhu, China University of Petroleum, Beijing (CUP), China

***Correspondence:**
Yonghui Huang
yh.huang@mail.iggcas.ac.cn
Haibing Shao
haibing.shao@gmail.com

Specialty section:
This article was submitted to Hydrosphere, a section of the journal Frontiers in Earth Science

Received: *06 October 2021*
Accepted: *09 November 2021*
Published: *13 December 2021*

Citation:
Meng B, Yang Y, Huang Y, Kolditz O and Shao H (2021) Remediation Potential of Borehole Thermal Energy Storage for Chlorinated Hydrocarbon Plumes: Numerical Modeling in a Variably-Saturated Aquifer. Front. Earth Sci. 9:790315. doi: 10.3389/feart.2021.790315

Underground thermal energy storage is an efficient technique to boost the share of renewable energies. However, despite being well-established, their environmental impacts such as the interaction with hydrocarbon contaminants is not intensively investigated. This study uses *OpenGeoSys* software to simulate the heat and mass transport of a borehole thermal energy storage (BTES) system in a shallow unconfined aquifer. A high-temperature (70 C) heat storage scenario was considered which imposes long-term thermal impact on the subsurface. Moreover, the effect of temperature-dependent flow and mass transport in a two-phase system is examined for the contaminant trichloroethylene (TCE). In particular, as subsurface temperatures are raised due to BTES operation, volatilization will increase and redistribute the TCE in liquid and gas phases. These changes are inspected for different scenarios in a contaminant transport context. The results demonstrated the promising potential of BTES in facilitating the natural attenuation of hydrocarbon contaminants, particularly when buoyant flow is induced to accelerate TCE volatilization. For instance, over 70% of TCE mass was removed from a discontinuous contaminant plume after 5 years operation of a small BTES installation. The findings of this study are insightful for an increased application of subsurface heat storage facilities, especially in contaminated urban areas.

Keywords: underground thermal energy storage (UTES), contaminant transport and fate, groundwater remediation, multiphase flow modeling, opengeosys simulation, chlorinated hydrocarbon (CHC)

1 INTRODUCTION

The transition from fossil fuels to renewable energy sources is an essential step towards a sustainable energy supply of the heating and cooling sector, which currently accounts for half of the EU's final energy consumption (Heat Roadmap Europe, 2017). A key challenge for the increased share of renewables in heating and cooling is however, the seasonal mismatch between thermal energy demand and supply. To tackle this discrepancy, underground thermal energy storage (UTES) technologies have been developed. UTES is particularly suitable for large-scale seasonal storage of heat due to its high storage capacity and efficiency (Fleuchaus et al., 2018). The two most widely-used

types of UTES are aquifer thermal energy storage (ATES) and borehole thermal energy storage (BTES). In ATES systems, warm or cold water is either withdrawn or reinjected via paired doublet wells. BTES systems, on the other hand, use borehole heat exchangers (BHE) to store heat in the subsurface (Welsch et al., 2018). A heat transfer fluid is circulated within the BHEs to exchange heat with the surrounding soil by conduction. Compared to ATES, BTES is more flexible in terms of hydrogeological (e.g., permeability) and geochemical conditions (Fleuchaus et al., 2018). In addition, the storage volume of BTES can be easily expanded by adding more boreholes (Elhashmi et al., 2020).

Storage of thermal energy in the shallow subsurface can lead to temperature rises to 70°C and above, in particular for high-temperature UTES (Würdemann et al., 2014). Such significant increase in the subsurface temperature has raised concerns on the environmental impacts of UTES, specifically when its interaction with subsurface contamination comes into play. Due to the high thermal energy demand and supply, urban areas are the most favorable location of UTES. Meanwhile, many urban areas are confronted with soil or groundwater contamination, especially with chlorinated hydrocarbons (CHC) such as perchloroethene (PCE) or trichloroethylene (TCE). Commonly applied in dry cleaning and metal degreasing processes, CHCs are one of the most universal contaminants in urban groundwater as they represent more than 50% of identified aquifer contamination in Germany (Grandel and Dahmke, 2008). Known to be carcinogenic (Stroo and Ward, 2010), they are considered a threat to groundwater quality and human health. CHC plumes in groundwater are typically developed from the long-term dissolution of dense non-aqueous phase liquids (DNAPL), which tend to migrate downwards due to the higher density than water. Combined with their generally slow biodegradation rates (Ni et al., 2018), these CHC plumes can extend up to several kilometers in length (Grandel and Dahmke, 2008). In addition to the desire to remediate CHC-contaminated aquifers, currently there is also a high demand to redevelop these areas into modern residential quarters with sustainable heat production. However, due to concerns of increased contaminant release and spreading as a result of elevated temperatures, the installation of UTES is usually restricted or completely precluded at/near these sites (Casasso and Sethi, 2019; Koproch et al., 2019). Such precautionary measures largely hamper the applicability of UTES in the redevelopment of contaminated urban areas. On the other hand, positive interactions between UTES and contaminated sites, e.g., accelerating the natural attenuation of contaminants have also been suggested (Sommer et al., 2013; Ni et al., 2015a).

The impact of UTES operation on subsurface contamination have been studied by a number of researchers, mostly in the recent decade. Temperature changes induced by UTES can directly influence the physical and chemical properties of organic contaminants. It has been demonstrated that solubility (Koproch et al., 2019), dissolution kinetics (Imhoff et al., 1997), sorption equilibrium (Ngueleu et al., 2018), biodegradation (Sommer et al., 2013; Zuurbier et al., 2013), etc. are susceptible to temperature changes. Alternatively, temperature changes can also affect the transport of contaminants by altering the density and viscosity of water. Beyer et al. (Beyer et al., 2016) simulated the impact of increased temperature due to BTES on a DNAPL source zone of TCE using *OpenGeoSys* package. Their results showed a focusing of groundwater flow downgradient of the BHEs due to viscosity reduction of the heated water. Together with the increase in TCE solubility, an elevated TCE emission from the source zone was concluded. Furthermore, temperature-induced density variations may lead to the appearance of buoyant flow and change the mass transport significantly, as demonstrated in simulations of thermal remediation (Krol et al., 2014). Besides temperature changes, ATES wells can also cause dilution and spreading of contaminants (Zuurbier et al., 2013; Phernambucq, 2015) due to the displacement of groundwater.

A hotspot of research in recent years is the concept of combining UTES with subsurface remediation, mainly spurred by the demand for both renewable energy production and sustainable groundwater management. Among the various combination concepts, *in-situ* treatment of the contaminated subsurface by thermally enhanced bioremediation has received the most attention. Several studies using experimental (Ni et al., 2015a; Ni et al., 2015b), field (Pellegrini et al., 2019) and modeling (Moradi et al., 2018; Roohidehkordi and Krol, 2021) approaches have demonstrated a good potential of combining UTES and biodegradation. Nevertheless, another potential remediation strategy, which is the enhanced volatilization of contaminants from groundwater and subsequent release to the atmosphere, has received relatively little attention in combination with UTES. Many CHCs are also volatile organic contaminants with rather high Henry's law constants. Furthermore, their volatility increases strongly with temperature (Schwardt et al., 2021). Such characteristic is exploited by well-established thermal remediation technologies, e.g., steam injection and electric resistance heating (Hiester et al., 2013). Despite this fact, only until recently the concept of combining UTES and enhanced *in-situ* volatilization was proposed by Schwardt et al. (2021). These authors performed a theoretical study to estimate the potential of anthropogenic heat input (e.g., UTES or urban heat islands) for the remediation of 41 organic pollutants based on the temperature dependency of Henry constant. It was inferred that even a moderate temperature increase from 10 to 40°C would lead to a considerable mass reduction for the investigated compounds, as supported by the 2 to 4-fold increase of their Henry constants. In particular, they anticipated the highest remediation potential for chlorinated ethylenes (e.g., TCE) when combined with high-temperature UTES >70°C (Schwardt et al., 2021). On the other hand, temperature-enhanced volatilization has also been suspected to cause unintended spreading of contaminants, which could be a threat to human health due to risk of vapor intrusion into building foundations (Wang et al., 2012). Considering the increasing use of urban aquifers for subsurface heat storage and the high likelihood that these aquifers are contaminated by CHCs, an evaluation dedicated to the complex interactions between UTES and CHC-contaminated aquifers would be advantageous in underlining the remediation potential while alleviating the negative environmental impacts. Since field

monitoring data are scarce due to current restrictions on the thermal use of contaminated subsurface, numerical modeling provides an attractive means of achieving the above research goals.

The objective of this study is to investigate the impacts of periodic high-temperature heat storage through BTES on the fate and transport of CHC contaminants in a shallow unconfined aquifer. Effects of both saturated and unsaturated zones are considered to simulate the transient, non-isothermal migration of TCE in a two-phase water-air system. By analyzing the TCE flux from the saturated to unsaturated zone and eventually into the atmosphere, favorable conditions for the enhanced attenuation of CHC plumes resulting from BTES operation were delineated and discussed. Nonlinear coupled multiphase flow, mass and heat transport equations were developed and solved using the finite-element simulator *OpenGeoSys* (Kolditz et al., 2012; Huang et al., 2015). The results can improve the understanding of thermal energy storage at contaminated sites and contribute to a safe and beneficial combination of underground heat storage and groundwater remediation.

2 GOVERNING EQUATIONS

2.1 Global Conservation Equations

In this study, we extended the non-isothermal two-phase flow model of the open-source simulator *OpenGeoSys*, so that a third chemical component beyond water and air was introduced (Huang et al., 2021). As a result, the three chemical components are water (w), air (a) and the new organic contaminant (c), whereas the two fluid phases are liquid (L) and gas (G). Furthermore, we assume that water and organic contaminant can partition into either liquid or gas phases. Conversely, the air component is assumed to only exist in the gas phase, i.e. its dissolution in water is neglected for simplicity.

By summing up the contribution from both phases $\alpha \in \{L, G\}$, the component-based mass conservation equation can be written for each component $k \in \{w, a, c\}$ as (note that $x_L^a = 0$ according to our assumption)

$$\phi \frac{\partial}{\partial t}\left(\sum_{\alpha\in\{L,G\}} N_\alpha S_\alpha x_\alpha^k\right) + \mathrm{div}\left[\sum_{\alpha\in\{L,G\}} N_\alpha\left(x_\alpha^k \boldsymbol{q}_\alpha + \boldsymbol{J}_\alpha^k\right)\right] = F^k. \quad (1)$$

In the Nomenclature, a comprehensive list of the variable definitions is provided. Here, the Darcy velocity of phase α is given by the extended Darcy's law

$$\boldsymbol{q}_\alpha = -\frac{k_{r\alpha}(S_\alpha)\boldsymbol{K}}{\mu_\alpha}(\nabla P_\alpha - \rho_\alpha \boldsymbol{g}). \quad (2)$$

The dispersive flux $\boldsymbol{J}_\alpha^k$ of component k in phase α is described by the Fick's Law

$$\boldsymbol{J}_G^k = -\phi^{\frac{4}{3}} S_G^{\frac{10}{3}} D_G^k \nabla x_G^k \quad (3)$$

for the gas phase, whereas for the liquid phase the additional effect of hydrodynamic dispersion has to be accounted for

$$\boldsymbol{J}_L^k = -\left(\phi^{\frac{4}{3}} S_L^{\frac{10}{3}} D_L^k + \alpha_l \|\boldsymbol{q}_L\| \boldsymbol{I} + (\alpha_l - \alpha_t)\frac{\boldsymbol{q}_L \boldsymbol{q}_L^T}{\|\boldsymbol{q}_L\|}\right)\nabla x_L^k. \quad (4)$$

In the above equations, the classical Millington (MILLINGTON, 1959) formulation is used for the effect of tortuosity. Since we also need to consider the non-isothermal effects in this study, the energy balance equation (assuming local thermal equilibrium) for a two-phase system reads (Class and Helmig, 2002; Huang et al., 2015)

$$\begin{aligned}&\frac{\partial}{\partial t}\left\{(1-\phi)\rho_s c_{ps} T + \phi\left[\sum_{\alpha\in\{L,G\}} S_\alpha \rho_\alpha u_\alpha\right]\right\}\\ &+\mathrm{div}\left(\sum_{\alpha\in\{L,G\}} \rho_\alpha h_\alpha \boldsymbol{q}_\alpha\right) - \mathrm{div}\ (\lambda_{pm}\nabla T) = Q_T.\end{aligned} \quad (5)$$

In this work, the relationship between the specific internal energy u_α and the specific enthalpy h_α is regulated by

$$u_L = h_L \quad (6)$$

and

$$u_G = h_G - \frac{P_G}{\rho_G} \quad (7)$$

for the liquid and gas phases, respectively. Such difference is caused by the non-negligible volume-changing work of the gas phase (Class and Helmig, 2002). Finally, the effective thermal conductivity of the porous medium λ_{pm} is normally a function of the liquid saturation S_L (**Table 1** for example).

The above mass and energy balance equations **Eq. 1** (written for three components) and (**Eq. 5**) would allow us to determine four primary variables. In this study, we chose the following set of primary variables: P_G (gas pressure), P_{cap} (capillary pressure), X^c (overall molar fraction of the contaminant, **Eq. 17**) and T (temperature). Such choice of primary variables would imply that phase transition is not accounted for in our model. Instead, the model assumes that the gas phase is always present to at least some minimal saturation $S_G^{\min} = 10^{-4}$ (Yu et al., 2009). Alternatively, completely drying out of the porous medium (i.e. $S_G = 1$) can be avoided by modification of the capillary pressure model (see **Section 3.3**).

2.2 Constitutive Relationships

Apart from the four primary variables introduced above, there are ten additional unknowns in **Eqs 1–7**, i.e., P_L, S_L, S_G, N_L, N_G, x_L^w, x_L^c, x_G^w, x_G^a and x_G^c. Since these variables are dependent on the primary variables, they are known as secondary variables. In **Eqs 8–17**, the constitutive relationships describing such dependency are summarized. Together with the global conservation equations, the necessary closure is formed for the unique solution of the problem.

$$S_L + S_G = 1 \quad (8)$$

$$x_L^w + x_L^c = 1 \quad (9)$$

$$x_G^w + x_G^a + x_G^c = 1 \quad (10)$$

$$P_L = P_G - P_{cap} \quad (11)$$

TABLE 1 | Porous medium properties used in the numerical model.

Property	Value/expression	Unit	Source
Porosity, ϕ	0.373	—	(1)
Solid density, ρ_s	2,648	$kg\,m^{-3}$	(1)
Horizontal permeability, K_h	1.26×10^{-11}	m^2	(1)
Vertical permeability (excluding transport zone), K_v	1.26×10^{-13}	m^2	(2)
Solid heat capacity, c_{ps}	750	$J\,kg^{-1}.K^{-1}$	(2)
Effective thermal conductivity, λ_{pm}	$\lambda_{pm} = \lambda_{dry} + \sqrt{S_L}(\lambda_{sat} - \lambda_{dry})$		(2)
Thermal conductivity of dry porous medium, λ_{dry}	0.5	$W\,m^{-1}.K^{-1}$	(2)
Thermal conductivity of saturated porous medium, λ_{sat}	2.5	$W\,m^{-1}.K^{-1}$	(2)
van Genuchten parameter, P_{vG}	3,633	Pa	(1)
van Genuchten parameter, n_{vG}	5.459	—	(1)
Residual liquid saturation, S_{rL}	0.223	—	(1)
Longitudinal dispersivity, α_l	1.0	m	(2)
Transverse vertical dispersivity, α_v	0.05	m	(2)

(1) Measurement data; (2) model assumption

$$S_L = P_{cap}^{-1}\left(P_{cap}\right) \tag{12}$$

$$N_G = \frac{P_G}{RT} \tag{13}$$

$$N_L = \frac{\rho_L^w}{M^w} \tag{14}$$

$$\frac{x_G^w}{x_L^w} = \frac{P_{vap}\left(P_{cap}, N_L, T\right)}{P_G} \tag{15}$$

$$\frac{P_G x_G^c}{N_L x_L^c} = H(T) \tag{16}$$

$$X^c = \frac{S_L N_L x_L^c + S_G N_G x_G^c}{S_L N_L + (1 - S_L) N_G}. \tag{17}$$

Eqs 8–10 are the intrinsic constraints of a two-phase and three-component system. **Eqs 11**, **12** describes the local capillary equilibrium, in which the capillary pressure P_{cap} is a monotonically decreasing function of the liquid saturation S_L (e.g., van Genuchten model in **Eq. 18**). **Eqs 13**, **14** compute the phase molar densities. Specifically, the ideal gas law is assumed for the gas phase, while the molar density of the liquid phase can be approximated as that of the liquid water (as long as the aqueous solubility of the contaminant is small enough). Moreover, Raoult's Law (**Eq. 15**) and Henry's Law (**Eq. 16**) are applied to describe the equilibrium partitioning of water and organic contaminant between the two fluid phases. For the considered non-isothermal problem, the Henry constant $H(T)$ of the organic contaminant is a temperature-dependent parameter. Additionally the water vapor pressure P_{vap} is calculated after regulation of capillary effects (Bourgeat et al., 2008). Its detailed expression as a function of P_{cap}, N_L and T can be found in Sect. S1 of the Supplementary File. Finally, **Eq. 17** defines the contaminant overall molar fraction as the weighted mean of its phase-specific molar fractions.

The above set of governing equations was implemented as an extension of the finite-element simulator *OpenGeoSys*. The implemented model has been validated against several benchmark problems. Since the heat and mass transfer of the original two-phase two-component model was already validated (Huang et al., 2015; Huang, 2017), only the mass transport portion for the third component (organic contaminant) is validated here. To do this, the experimental data of measured gas phase TCE concentration from McCarthy and Johnson (1993) along with the semianalytical solution given by Atteia and Höhener (2010) was compared with model simulation. A very good agreement was obtained for the above comparison, for which more details are documented in Sect. S2 of the Supplementary File.

3 NUMERICAL MODEL

In this section, the numerical model of a BTES installation operating in a shallow, unconfined aquifer with CHC-contaminated groundwater is described. Here, the model configuration is intentionally kept as simple and concise, since our aim is not to represent realistic field-scale scenarios of BTES application and its interaction with subsurface contamination, but rather to highlight the fundamental mechanisms governing the fate and transport of CHC contaminants in such context.

3.1 Geometry

Figure 1 illustrates the geometrical setup of the numerical model, which represents an unconfined sandy aquifer with dimensions of 59 m × 40 m in x–and z–directions. The groundwater table is located at a depth of 5 m below surface. Currently the model is only two-dimensional (2D) to save computational resources. Due to the 2D setup, the model tends to overestimate the size of the simulated thermal plume (Piga et al., 2017) and thus the volatilization flux of TCE compared with a full 3D model.

3.2 Initial and Boundary Conditions

The initial conditions for the gas pressure and capillary pressure are hydrostatic with respect to the groundwater table. Besides, the gas pressure is fixed at 1 atm (101,325 Pa) at the ground surface. Based on the capillary pressure model applied for the sand (**Table 1**), the initial degree of saturation as a function of depth is depicted in **Figure 2A**. The regional groundwater flow is assumed from left to right, at a specific discharge of $3.07 \times 10^3\ m\,d^{-1}$. This translates to a transport velocity of 3.0 m y^{-1} given an effective porosity of 0.373 (**Table 1**). The rationale

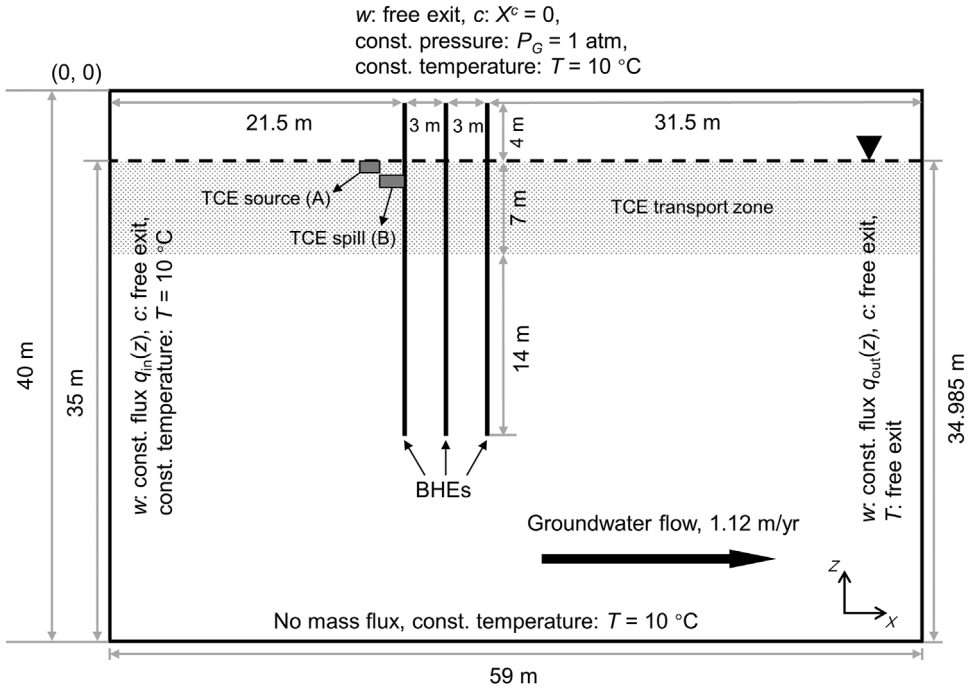

FIGURE 1 | 2D setup of the numerical model including geometry and boundary conditions. Dashed line indicates the location of water table.

for the relatively small magnitude of groundwater flow assumed here is to reduce the advective losses of the heat storage while allowing the presence of the TCE plume by groundwater advection and dispersion. For the modeling of groundwater flow in a variably-saturated aquifer, we assigned constant while depth-dependent water fluxes on the left and right boundaries (**Figure 2B**). Specifically, the boundary water fluxes are scaled by the relative permeabilities at the respective depths. This results in uniform boundary fluxes in the saturated zone and abruptly decreasing ones above the water table.

In this study, we chose TCE as the CHC contaminant of interest. The initial TCE concentration follows a Heaviside step function, i.e. the TCE molar fraction X^c is assumed to be 1×10^{-5} inside the source/spill location and null over the rest of the domain (**Figure 1**). Depending on whether the TCE is continuously released from a source (**Section 3.4**), X^c is either fixed at 1×10^{-5} within the source location (Box A) or set free. To facilitate TCE emission into the atmosphere, X^c is forced to zero at the top surface for simplicity. The contaminant TCE is set as conservative, with no sorption or biodegradation.

The initial condition for temperature is assumed uniformly at 10 °C across the entire model domain. The identical temperature was also used for Dirichlet boundary conditions on the left, top (assume to be insulated) and bottom boundaries. Seasonal heat storage and extraction is implemented with three BHEs at a 3 m spacing (**Figure 1**). In reality this could represent a 2D cross-section of a pilot-scale BTES system with 3 × 3 BHEs. The BHEs are modeled by line heat sources reaching a depth of 25 m below ground surface. For simplicity, the topmost 1 m of the BHEs are neglected assuming no heat exchange with the surrounding soil (i.e. perfectly insulated). For the annually repeating charging and discharging of heat, each year (365 days) is divided into four continuous phases of 90 (I), 90 (II), 90 (III), and 95 (IV) days (**Figure 2C**). Among them, Phase I and III are the heat injection and extraction periods, respectively. During this time, the temperature along the BHEs is assumed constant at either 70 or 30°C except for the initial 5 days of a gradual transition from 40°C. The authors are aware that the fluid temperature inside the BHEs can be very transient in real applications, nevertheless the constant temperature assumed here provides a simple boundary condition for mimicking the cyclic temperature effects of seasonal heat storage. Otherwise, the remainder of the year (Phase II and IV) are standstills of operation, i.e., no temperature boundary conditions are imposed for the BHEs. During heating, water vapor can freely escape from the subsurface by gas-phase advection. Finally, free-exit boundary condition is also applied on the right border for all components as well as heat.

3.3 Parameterization

Table 1 summarizes the porous medium properties assumed for the numerical model. The porosity, bulk density, permeability and water retention characteristics (van Genuchten model parameters) of the porous medium are taken from a set of measurement data from Kiel University (Hailemariam and Wuttke, 2017; Hailemariam and Wuttke, 2020) for a specific type of sand commonly found in Northern German Plain. The remaining properties are assumed based on typical ranges of aquifer material. Here, we assume the permeability of the sand to be anisotropic and use the measured value only for the horizontal component. Meanwhile, the vertical permeability is assumed to be 0.01 times that of the horizontal

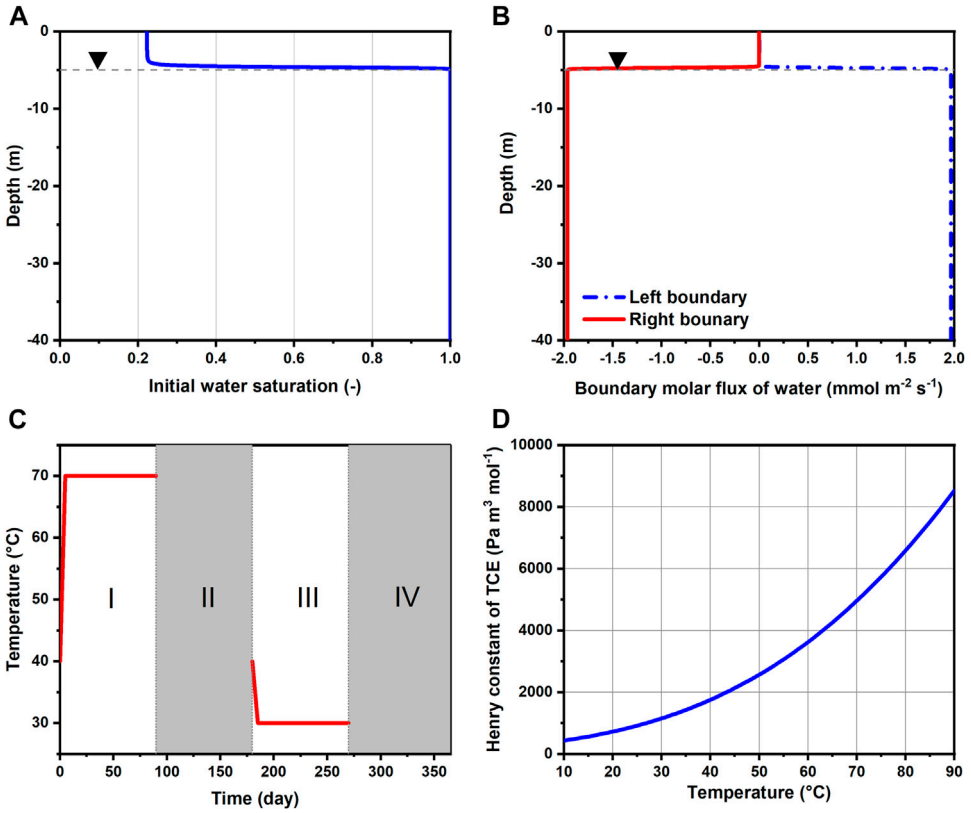

FIGURE 2 | (A) Initial water saturation along depth, **(B)** molar fluxes of water imposed as Neumann boundary conditions, **(C)** temperature Dirichlet boundary condition imposed for the BHEs annually and **(D)** change of TCE Henry constant with temperature. Horizontal dashed lines indicate the location of water table.

component except for the "TCE transport zone" (shaded area below the water table in **Figure 1**). There the vertical permeability is assigned according to scenario specifications (**Table 3**). Furthermore, the dependency of effective thermal conductivity on the liquid phase saturation is described by the Somerton model (Somerton et al., 1974), i.e., square-root increase. In lack of measurement data, thermal conductivities of dry and water-saturated soil were set to 0.5 and 2.5 $W\,m^{-1}.K^{-1}$, respectively. In addition, the capillary pressure and relative permeability functions are given by the van Genuchten (vG) model (van Genuchten, 1980)

$$P_{cap} = P_{vG}\left(S_{eL}^{-\frac{1}{m_{vG}}} - 1\right)^{\frac{1}{n_{vG}}} \tag{18}$$

$$k_{rL} = \sqrt{S_{eL}}\left(1 - \left(1 - S_{eL}^{\frac{1}{m_{vG}}}\right)^{m_{vG}}\right)^2 \tag{19}$$

$$k_{rG} = \sqrt{1 - S_{eL}}\left(1 - S_{eL}^{\frac{1}{m_{vG}}}\right)^{2m_{vG}} \tag{20}$$

where $m_{vG} = 1 - \frac{1}{n_{vG}}$ and the effective saturation S_{eL} is given by

$$S_{eL} = \frac{S_L - S_{rL}}{1 - S_{rL}}. \tag{21}$$

In **Eqs 18–20**, it is assumed that $S_L > S_{rL}$. However, to account for the possible drop of S_L below residual saturation S_{rL} due to heating of partially-saturated soil, the original capillary pressure curve is modified according to Huang et al. (2015) by linear extrapolation to the segment where $S_L \leqslant S_{rL}$. This leads to an extended vG curve with $P_{cap}^{max} = 1.46 \times 10^8$ Pa at $S_L = 0$. Likewise, a minimum relative permeability of $k_{rL}^{min} = 1 \times 10^{-8}$ was assumed for the liquid phase. Finally, mass dispersivities of TCE were assumed as $\alpha_l = 1$ m and $\alpha_t = 0.05$ m whereas thermal dispersion is neglected in all simulations.

Table 2 lists all relevant properties assigned for the chemical components and fluid phases. Of particular note is the temperature-dependency of certain parameters. Here, the water density is provided as a lookup table from the IF97 data (Kretzschmar and Wagner, 2019), while its viscosity is calculated by the empirical model of Yaws (Yaws, 2014; Beyer et al., 2016). In particular, the temperature-dependent Henry coefficient of TCE is parameterized with the recently published data by Schwardt et al. (Schwardt et al., 2021), with effective temperature ranges up to 90°C (**Figure 2D** for its increase with temperature). Additionally, all molecular diffusion coefficients are temperature-dependent. The gas phase diffusivities are given by the Fuller's extrapolation method (Tang et al., 2015) whereas the TCE diffusivity in water is computed through the Arrhenius (exponential) relation.

3.4 Numerical Simulations

In the numerical model, spatial discretization was performed with the standard Galerkin finite element method. Specifically, the 2D

TABLE 2 | Component and phase property data.

Property	Value/expression	Unit	Source
Constant			
Molar mass of water, M^w	18.02×10^{-3}	$kg\,mol^{-1}$	McNaught and Wilkinson (1997)
Molar mass of air, M^w	28.97×10^{-3}	$kg\,mol^{-1}$	McNaught and Wilkinson (1997)
Molar mass of TCE, M^w	131.4×10^{-3}	$kg\,mol^{-1}$	McNaught and Wilkinson (1997)
Specific heat capacity of water, c_p^w	4,187	$J\,kg^{-1}.K^{-1}$	Linstrom and Mallard (2001)
Specific heat capacity of air, c_p^a	1,005	$J\,kg^{-1}.K^{-1}$	Hilsenrath (1955)
Dynamic viscosity of gas phase[a], μ_G	1.8×10^{-5}	Pa s	Touloukian et al. (1970)
Latent heat of water vaporization, $h_{\Delta e}$	2.258×10^6	$J\,kg^{-1}$	Datt (2011)
Ideal gas constant, R	8.314	$J\,mol^{-1}.K^{-1}$	McNaught and Wilkinson (1997)
Temperature-dependent[b]			
Density of water, ρ^w	lookup table	$kg\,m^{-3}$	Kretzschmar and Wagner (2019)
Dynamic viscosity of water, μ^w	empirical model	Pa s	Yaws (2014)
TCE diffusivity in gas phase		$m^2.s^{-1}$	GSI Environmental (2020)
Water diffusivity in gas phase		$m^2.s^{-1}$	Cussler (2009)
TCE diffusivity in liquid phase		$m^2.s^{-1}$	Rossi et al. (2015)
Henry coefficient of TCE		$Pa\,m^3.mol^{-1}$	Schwardt et al. (2021)

[a]*The viscosity of gas phase usually changes with composition and has a much weaker dependence on temperature. For the sake of simplicity, it is assumed constant using the viscosity of air at 15 C*

[b]*Values at 10 °C:* $\rho^w = 997.8\ kg\,m^{-3}$, $\mu^w = 1.31 \times 10^{-3}\ Pa\,s$, $D_G^c = 7.22 \times 10^{-6}\ m^2.s^{-1}$, $D_G^w = 2.38 \times 10^{-5}\ m^2.s^{-1}$ $D_L^c = 6.09 \times 10^{-10}\ m^2.s^{-1}$, $H = 0.184\ Pa\,m^3.mol^{-1}$

TABLE 3 | Description of simulated scenarios.

Scenario #	Form of contamination	BTES operation	Vertical permeability of TCE transport zone (m^2)
A0 (baseline)	Continuous source	✗	1.26×10^{-13}
A1	Continuous source	✓	1.26×10^{-15}
A2	Continuous source	✓	1.26×10^{-13}
B0 (baseline)	Instantaneous spill	✗	1.26×10^{-13}
B1	Instantaneous spill	✓	1.26×10^{-15}
B2	Instantaneous spill	✓	1.26×10^{-13}

domain was discretized into 23,106 quadrilateral/triangular elements and 23,228 nodes with a minimum grid spacing of 5.5 × 4.0 cm in the x– and z– directions. In particular, mesh refinement was performed in the following key locations: 1) near the BHEs in the unsaturated zone, where high gradients of capillary pressure are expected during heat injection; 2) along the vertical direction immediately above the water table, since there will be high gradients of the overall molar fraction X^c and 3) below the water table until a depth of $z = -12$ m (TCE transport zone), so as to minimize the numerical dispersion associated with TCE transport. A mesh convergence test was conducted, and it was confirmed that further spatial discretization achieves the same simulation result. Meanwhile, temporal discretization follows the implicit Euler scheme. An automatic time-step adjustment is applied based on the number of iterations necessary for the previous time-step. The maximum time-step size was not allowed to exceed 6 days, which fulfills the Courant criteria [i.e., $v\Delta t \leqslant \Delta x$, Jang and Aral (2006)]. The resulting system of coupled residual equations was linearized with the Newton method and subsequently solved with the BiCGSTAB strategy using ILUT preconditioner.

Table 3 lists the configuration of all simulated scenarios. As aforementioned, the specific scenarios are divided into two categories distinguished by different forms of contamination, i.e. constant source (continuous plume, Group A) and instantaneous spill (discontinuous plume, Group B). In each group, a baseline scenario (A0 and B0) without BTES operation, i.e. under isothermal condition, is simulated. Among the BTES scenarios, A1 and B1 were simulated without the effect of buoyant flow. This was done by reducing the transport zone vertical permeabilities of these scenarios to 1/100th of the rest of the domain. Alternatively, the vertical permeability inside the transport zone was not reassigned for other scenarios. The simulated time period was 5 years for all scenarios.

4 RESULTS

4.1 TCE Transport Without Thermal Energy Storage

Figures 3A,B depicts the distribution of TCE molar fraction in the liquid and gas phases after 5 years in Scenario A0. Here, logarithmic scale is used for the TCE molar fractions in order to illustrate both saturated and unsaturated zones (same for below). In **Figure 3A**, a groundwater plume of dissolved TCE has formed

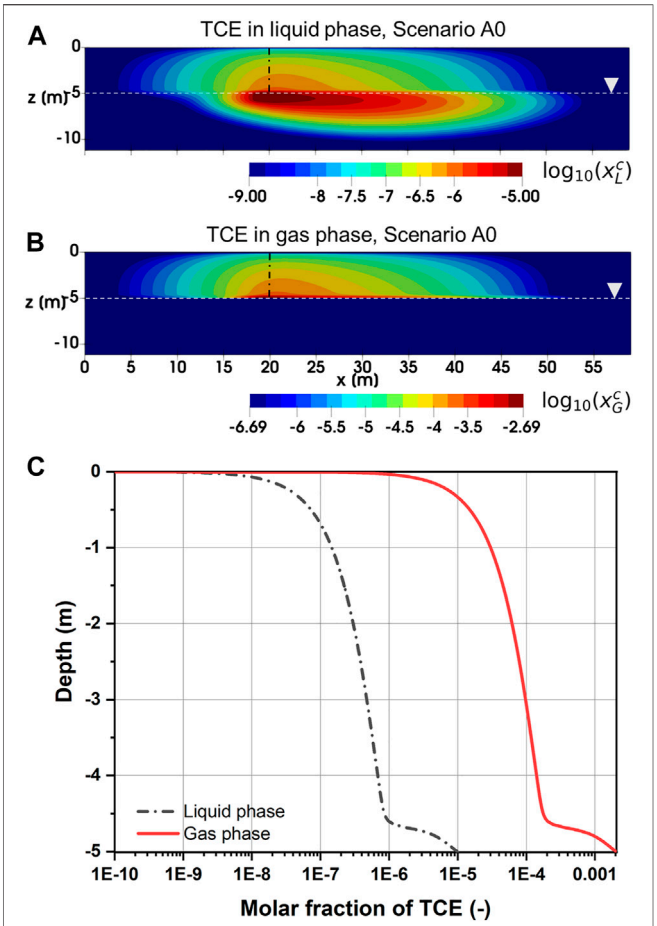

FIGURE 3 | (A) Liquid, **(B)** gas phase molar fraction of TCE after 5 years for Scenario A0 and **(C)** depth profiles in the unsaturated zone at x = 20 m [dash-dotted line in **(A)** and **(B)**].

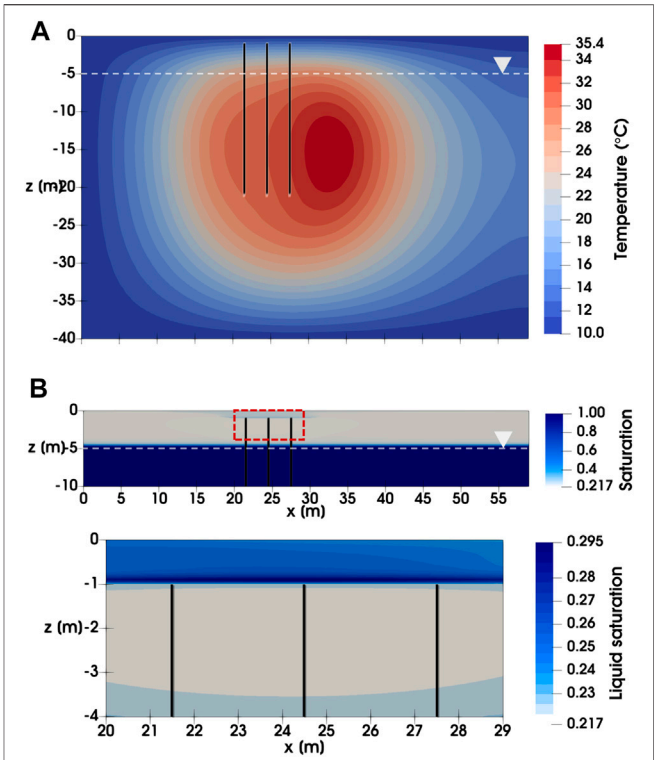

FIGURE 4 | Distribution of **(A)** temperature and **(B)** liquid saturation after 5 years of BTES operation for Scenario A1.

in the downgradient of the source due to advective-dispersive transport in the liquid phase. Besides, both aqueous and gas phase TCE plumes can also be observed in the unsaturated zone. Particularly for the liquid phase, TCE molar fraction appears to be significantly smaller above the water table than below. A further examination of the depth profiles (**Figure 3C**) reveals that both liquid and gas phase molar fractions of TCE decreased by an order of magnitude at a distance of approximately 0.4 m above the water table. Such abrupt changes are caused by the depth-dependent transport mechanisms of TCE across the capillary fringe. Here, we briefly describe the underlying physical processes as a more detailed semi-quantitative analysis is presented in Sect. S3 of the Supplementary File. As observed by McCarthy and Johnson (1993), vertical mass exchange between saturated and unsaturated zones is controlled by aqueous phase diffusion. This can be related to the fact that TCE diffusivity in the liquid phase is nearly four orders of magnitude smaller than that in the gas phase (**Table 2**). In this work, the effect of hydrodynamic dispersion is considered in addition to molecular diffusion in the liquid phase. Despite such difference, the overall diffusive force in the saturated zone is still one to two orders of magnitude less than that in the unsaturated zone away from the water table. Therefore, the McCarthy and Johnson hypothesis can be extended by stating that, even with the additional contribution from hydrodynamic dispersion, vertical mass fluxes from the groundwater will be relatively small due to limitations in aqueous phase transport. As a consequence, natural attenuation of the contaminant plume through volatilization and subsequent release into the atmosphere is a rather slow process. The above conclusion is expected to be valid in most subsurface conditions since the vertical dispersivity of 0.05 m assumed in this study is already a relatively high value in natural aquifers (Rotaru et al., 2014).

4.2 Effect of Temperature-enhanced Volatilization on TCE Transport

Figure 4 depicts the distribution of temperature and liquid saturation after 5 years of BTES operation for Scenario A1. The temperature and saturation contours from other BTES scenarios displayed very similar patterns and are thus not shown. Due to the unbalanced heat injection and extraction loads, a thermal plume has evolved downgradient of the BHEs, with the highest temperature reaching 35.4°C (**Figure 4A**). Meanwhile, changes in the liquid saturation are mostly found directly above the BHEs in the unsaturated zone. Specifically, a recondensation zone with liquid saturation up to 0.3 has developed between the BHEs and the top boundary. The increased liquid saturation in turn leads to locally higher TCE

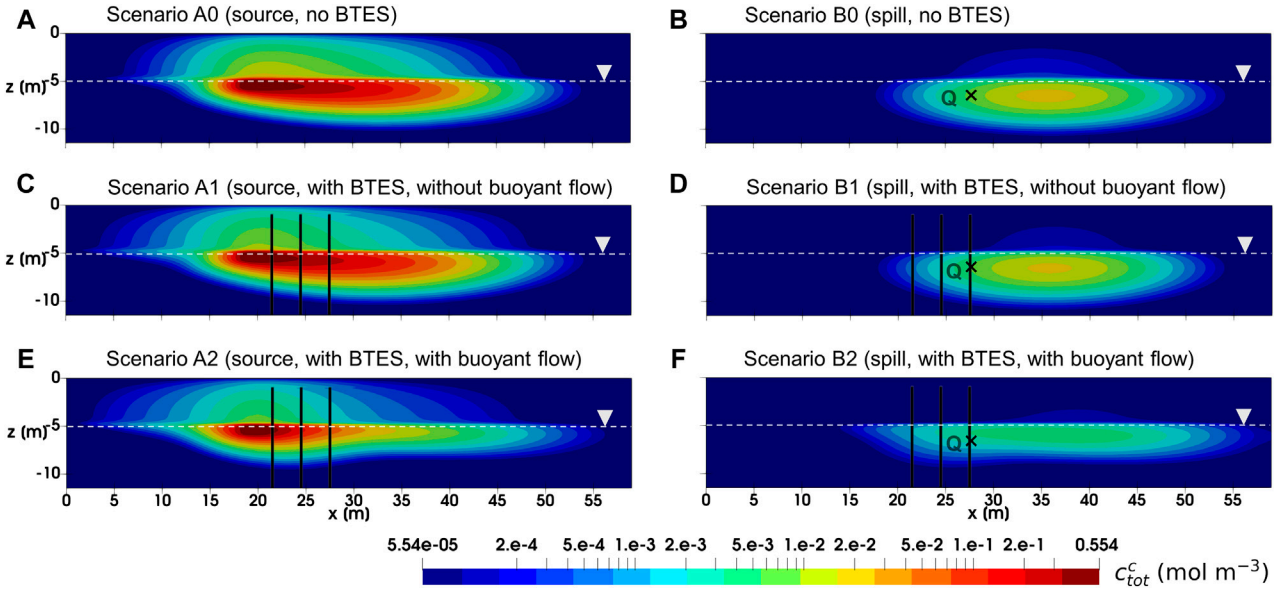

FIGURE 5 | Total TCE concentration at 5 years for all simulated scenarios. Note that the concentration contours are presented in logarithmic scale. Black cross represents the location of observation point *Q*.

molar fractions in both liquid and gas phases. Nevertheless, TCE molar fractions are already very low near the top boundary and thus the influence of saturation changes on the mass transport of TCE is expected to be negligible in the simulated scenarios.

In **Figure 5**, the simulated total TCE concentration after 5 years is illustrated for various scenarios. Here, we only focus on the comparison between baseline scenarios (A0 and B0) and BTES scenarios without buoyant flow (A1 and B1). In general, the effect of BTES operation on the development of TCE plume seems to be limited for both Scenario A1 and B1. Although the TCE concentration in the unsaturated zone has diminished to some extent compared to the baseline, only a slight mitigation of the TCE plume was found in the saturated zone.

For a quantitative evaluation of TCE fate and transport, mass balance calculations were performed and the results are shown in **Figures 6**, **7** for Group A and B scenarios respectively. Here, only the "free" TCE which is outside the source is considered for the liquid phase. In general, a very good accuracy was achieved for all conducted simulations, as mass balance errors accumulated up to 5 years and at every time step were less than 2.8 and 0.08%, respectively. For the Group A scenarios assuming constant source, a slightly faster release of TCE from the source is observed for Scenario A1 comparing to the baseline, as shown in **Figure 6A**. Such behavior is attributed to the decrease of water viscosity with temperature, leading to increased flow velocities and thus water fluxes ("flow focusing") within the heated source (Beyer et al., 2016). In **Figure 6B** where the cumulative TCE volatilization is plotted, BTES-induced temperature increase (Scenario A1) led to a 39% higher TCE mass transfer to the gas phase at the end of simulation. In particular, the increased amount of volatilized TCE (0.73 mol difference after 5 years) was able to offset the negative impact of increased TCE emission from source (0.44 mol difference after 5 years) resulting from BTES operation. As a result, a 0.29 mol decrease in the residual liquid phase TCE is obtained for Scenario A1 compared to baseline at the end of simulation (**Figure 6C**). In **Figure 6D**, the gas phase TCE of Scenario A1 shows overall higher status compared to Scenario A0, due to its higher volatilization. This is particularly evident at the beginning of heat injection phases where a sharp rise of the gas phase TCE can be noticed. Nevertheless, the above difference between Scenario A1 and A0 is diminishing at the end of each year. In **Figures 7B–D**, a similar pattern of TCE mass transfer can be observed for the instantaneous spill scenarios B0 and B1. Here, we note that an appreciable TCE volatilization only occurred after the first year in both scenarios (see **Figure 7B**). This is due to the fact the initial spill is located 1 m below the water table and that vertical transport of TCE by groundwater dispersion is rather slow.

Table 4 summarizes the reduction of total TCE mass for all simulations. Here, the residual amount of TCE includes contribution from both liquid (only "free" portion) and gas phases. As perceived from the foregoing analysis, the effect of BTES-enhanced attenuation of TCE are indeed quite limited in Scenario A1 and B1. The decrease in the residual TCE amount compared to the baseline are less than 10% in both scenarios. Although a moderate reduction rate of 44% is obtained for Scenario A1, such number is mainly attributed to the favorable location of the source (i.e. directly beneath the water table), rather than the additional benefit from BTES. This can be supported by the relatively small improvement of Scenario A1's reduction rate compared to Scenario A0s. Hence, we conclude that the limiting factor for the transfer of dissolved TCE to the unsaturated zone is still the slow dispersive transport in the aqueous phase. As a consequence, temperature-enhanced

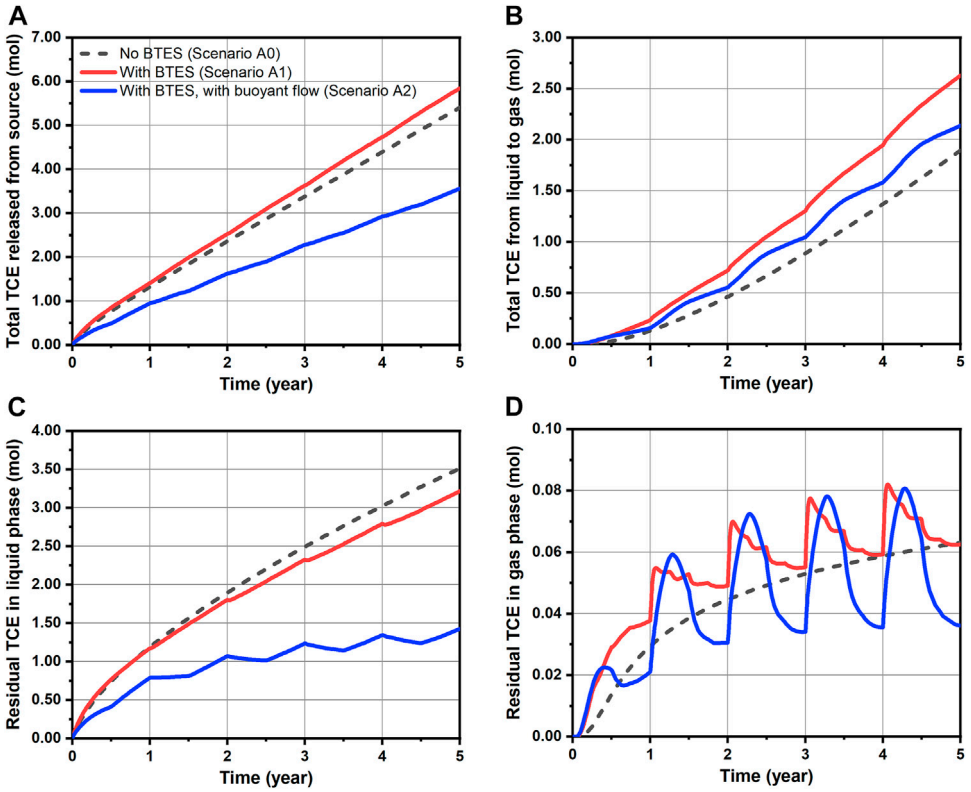

FIGURE 6 | Transport dynamics of TCE for simulated scenarios assuming constant source: **(A)** released amount from source, **(B)** total amount transferred from liquid to gas phase, **(C)** residual amount of mobile TCE in the liquid phase and **(D)** residual amount of TCE in the gas phase.

volatilization can only result in a superficial reduction of TCE mass below the water table, whereas the deeper part of the plume is largely excluded from being remediated.

4.3 Effect of Buoyant Flow on TCE Transport

In practical BTES applications, buoyant flow may be induced in medium to high permeability aquifers due to the temperature-dependent water density (Catolico et al., 2016; Boockmeyer, 2020). Since Scenario A2 and B2 are distinguished by a 100 times larger vertical permeability of the transport zone, buoyant flow is more likely to develop in these scenarios and in turn affect the mass transport of TCE.

Figures 8A,B illustrate the magnitude of vertical Darcy velocity after 1,550 days of BTES operation (i.e., after the fifth heat injection phase) for Scenario A1/B1 and Scenario A2/B2, respectively. Here, the liquid phase velocity field is identical for different contamination scenarios with the same vertical permeability, as the TCE concentration is too low to induce any changes in the liquid flow regime. In contrast to Scenario A1/B1 with virtually no buoyant flow, a moderate buoyant flow is found for Scenario A2/B2 in the vicinity of the BHEs, as evidenced by the considerably higher vertical velocities there in **Figure 8B**. In particular, the simulated maximum Darcy velocity in the z direction for Scenario A2/B2 equals to 0.6 m y^{-1}, which is in the same order of magnitude as the undisturbed groundwater flow velocity. This leads to the groundwater being directed upwards when passing through the heated zone, as marked by the arrows indicating flow direction in **Figure 8B**. As the heated water rises to the water table, it tends to spread in the left and right directions due to the much larger horizontal permeability. As a result, the horizontal flow velocity below the water table is also influenced by the buoyant flow. For example, the simulated horizontal velocity profile for Scenario A2/B2 at z = −5.5 m in **Figure 8C** shows a strong retardation in the upgradient, yet acceleration in the downgradient of the BHEs. Furthermore, a circular flow regime can even be recognized between x = 15 and 20 m in **Figure 8B**. The above flow pattern as a whole can be described as "mixed flow" (Haajizadeh and Tien, 1984), due to the fact that both buoyant flow and groundwater advection are occurring and interacting with each other.

The effect of buoyant flow on the development of TCE plume can be visualized in **Figures 5E,F**. In Scenario A2 where a constant source was assumed, the TCE concentration plot shows essentially lower concentrations in the downgradient direction along with a thinner plume below the water table. Besides, it is noted that the TCE concentration in the unsaturated zone is also reduced. On the other hand, a likewise reduction of TCE concentration is also predicted for Scenario B2 assuming initial spill. In particular, the TCE plume appears to be more "stretched out" horizontally due to the expanded advective velocity as well as hydrodynamic dispersion in the horizontal direction. To further illustrate the

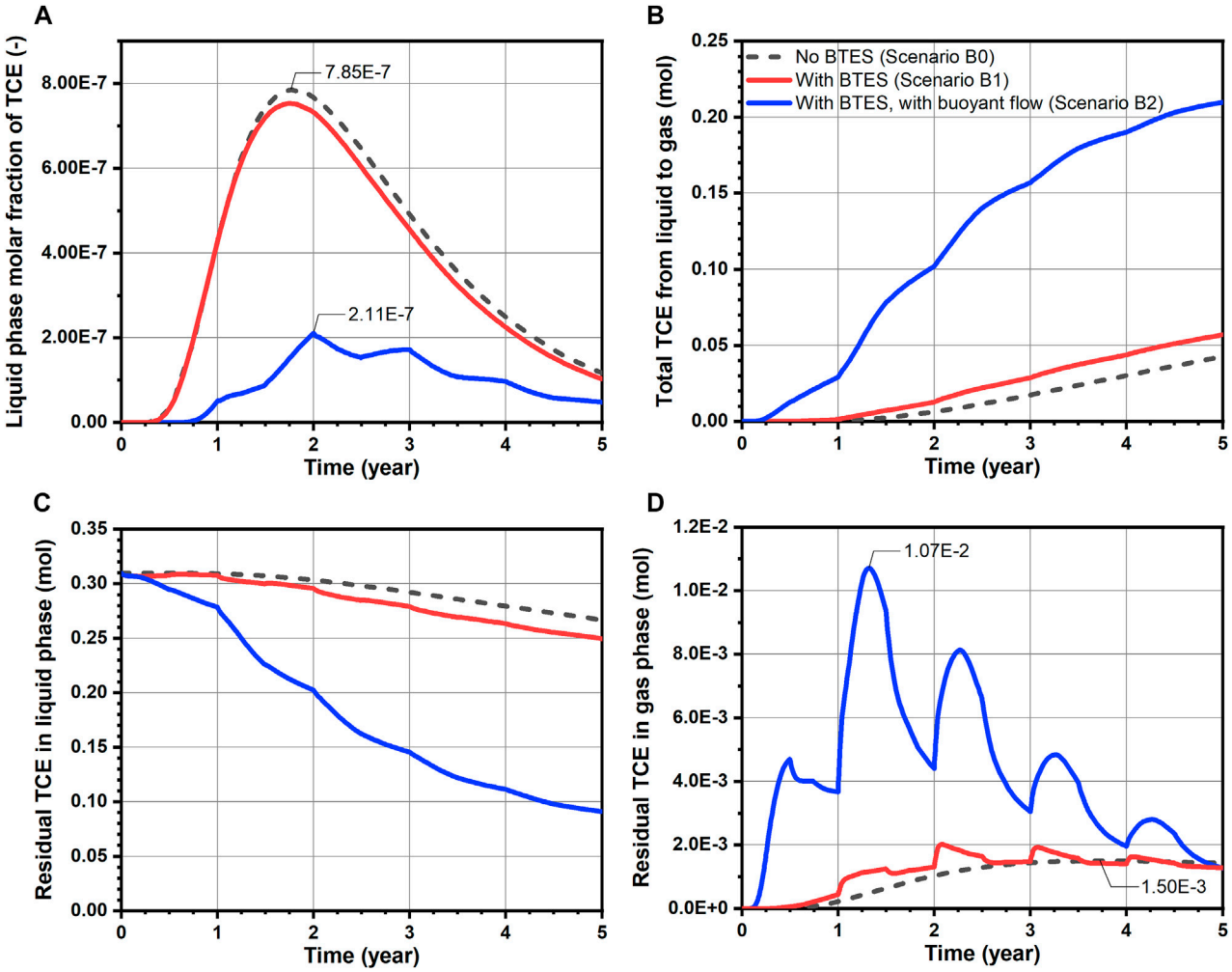

FIGURE 7 | Transport dynamics of TCE for simulated scenarios assuming instantaneous spill: **(A)** breakthrough curves of TCE molar fraction at observation point *Q* (**Figure 5B**, **(B)** total amount transferred from liquid to gas phase, **(C)** residual amount of TCE in the liquid phase and **(D)** residual amount of TCE in the gas phase.

TABLE 4 | Summary of TCE reduction after 5 years for all simulated scenarios.

Scenario #	Source emission/Initial amount (mol)	Residual amount (mol)	Reduction rate (%)	Residual amount w.r.t. baseline (% ↓)
A0 (baseline)	5.41	3.57	33.9	—
A1	5.85	3.28	43.9	8.2
A2	3.56	1.46	59.0	59.1
B0 (baseline)	0.31	0.27	13.4	—
B1	0.31	0.25	19.0	6.5
B2	0.31	0.09	70.2	65.6

effect of buoyant flow on the reduction of TCE concentration, the breakthrough curves of (liquid phase) TCE molar fraction observed at 6.14 m downgradient of the spill location (point *Q* in **Figure 5**) are illustrated in **Figure 7A**. With respect to the peak molar fraction, Scenario B2 reported a 73.1% decline compared to Scenario B0, indicating a significant reduction. Furthermore, a comparably delayed arrival of the bulk mass is observed in Scenario B2, due to the mostly reduced horizontal Darcy velocity upgradient of the observation point.

Temporal TCE mass transfer under the influence of buoyant flow is illustrated with the blue curves in **Figures 6**, **7**. For the continuous source scenario (A2), buoyant flow is recognized to contribute to the overall reduction of TCE through two distinct mechanisms. 1) In **Figure 6A**, the TCE release curve of Scenario

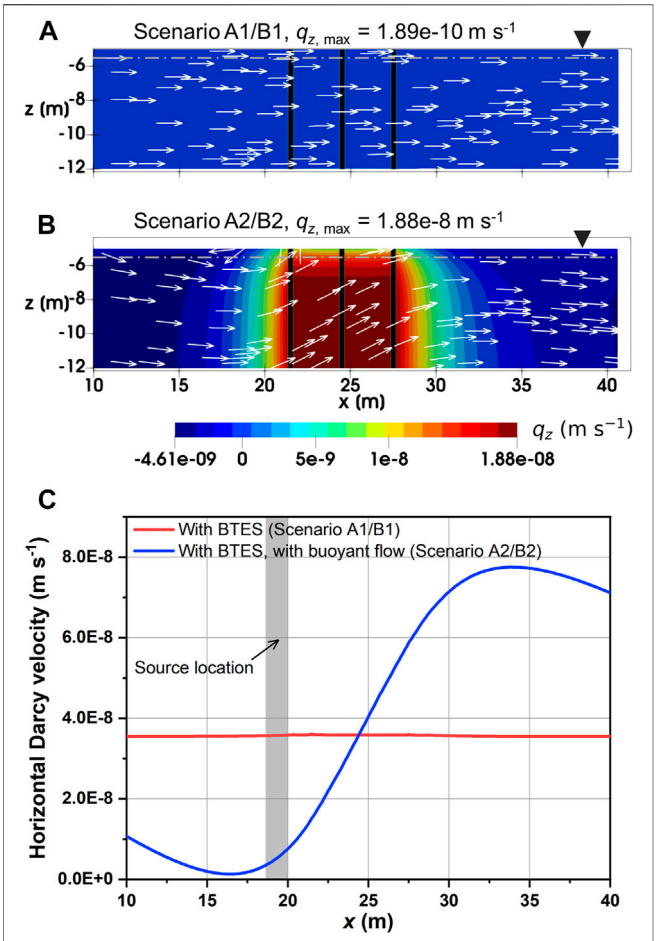

FIGURE 8 | Darcy velocity in the transport zone after 1,550 days: **(A)** magnitude of vertical velocity for Scenario A1/B1, **(B)** magnitude of vertical velocity for Scenario A2/B2 and **(C)** horizontal Darcy velocity profile at $z = -5.5$ m [dash-dotted line in **(A)** and **(B)**]. White arrows in **(A)** and **(B)** indicate the liquid phase velocity field (not to scale).

A2 is much flatter when compared to Scenario A0 and A1. This is due to the inhibited horizontal flow around the source in Scenario A2 (**Figure 8C**). As a result, up to 34% less TCE is released from the source after 5 years in Scenario A2 compared to the baseline (A0). 2) In **Figure 6B**, despite the less amount of TCE emitted from the source, a higher amount of TCE is volatilized into the gas phase in Scenario A2 than A0 (although still lower than Scenario A1). This is attributed to the induced buoyant flow in Scenario A2 which enhanced the mass transfer of aqueous TCE to the unsaturated zone by advection. Consequently, an enlarged proportion of the released TCE is volatilized in Scenario A2 (60.0%) compared to Scenario A0 (35.1%) and A1 (45.3%). The above two mechanisms led to a notable mitigation in the growth of residual TCE in both liquid and gas phases, as shown in **Figures 6C,D**. Compared to Scenario A1, the residual TCE curves of Scenario A2 exhibit larger fluctuations since the percentage of volatilized TCE is higher. Finally, we see in **Table 4** that the buoyancy effect of Scenario A2 resulted in a nearly 60% decline of the total residual TCE in comparison to Scenario A0, showing a remarkable improvement from Scenario A1 where only temperature-enhanced volatilization is considered. Again, such improvement is the combined outcome of reduced emission from the source and the stimulated mass transfer to the unsaturated zone.

In **Figures 7B–D**, a considerable improvement in TCE volatilization and reduction is also predicted for Scenario B2. Since there is no release of the contaminant from the source, the dominant mechanism to facilitate the TCE mass transfer here is obviously the heating-induced buoyant flow. This can be witnessed from the following characteristics of Scenario B2's volatilization curve in **Figure 7B**. First, an earlier TCE volatilization is observed in Scenario B2. Instead of after 1 year in scenarios without buoyant flow, the volatilized TCE is already appreciable after 0.25 years in Scenario B2. Such difference is caused by the buoyant flow driving the TCE towards the water table during the first heat injection phase. Secondly, the total volatilized TCE shows a strong increasing trend during the second and third years, whereas the growth becomes much less intense thereafter. Despite the fact that the residual TCE mass is diminishing, another important reason is that the majority of TCE at highest concentrations has escaped from the buoyancy-influenced zone (**Figure 8B**), which also tends to slow down the volatilization rate. Nevertheless, the total volatilized TCE in Scenario B2 reaches 0.21 mol after 5 years, being almost five times that of the baseline (B0). As a direct consequence of volatilization, the evolution of residual aqueous TCE in **Figure 7C** for the spill scenarios is practically a mirrored image of **Figure 7B**, indicating a major reduction in the dissolved TCE mass due to buoyant flow. Finally, in **Figure 7D**, although the gas phase TCE of Scenario B2 showed strong oscillations due to the highest volatilization rate, its final amount after 5 years is indeed similar to the baseline. Together with the flattening volatilization curve (**Figure 7B**), remediation is almost completed at this time. As a consequence of the enhanced TCE transport due to buoyant flow, the residual TCE mass in the domain is less than 0.1 mol in Scenario B2, showing a 66% reduction from the baseline (**Table 4**). Besides, the highest TCE reduction rate of over 70% is achieved in Scenario B2 among all simulated scenarios. In conclusion, in cases where the contaminant plume is well-characterized and discontinuous, a substantially enhanced volatilization can be achieved by taking advantage of the buoyant flow effect during BTES operation.

5 DISCUSSION

5.1 Effect of Buoyant Flow on Heat Storage Efficiency

The simulation results of Scenario A2 and B2 suggest that high permeability could be a positive factor by promoting thermally-induced buoyant flow and contributing to an increased volatilization of the contaminant. However, high permeability may at the same time be a negative factor for the heat storage efficiency (i.e., ratio of extracted vs. injected heat in an operating year) of BTES applications (Catolico et al., 2016; Djotsa Nguimeya Ngninjio et al., 2021). Catolico et al. (2016)

simulated the heat storage efficiencies at varying permeabilities in an unconfined aquifer without groundwater flow. Their simulation results showed that a decrease in storage efficiency occurs only at permeability values greater than 1.5×10^{-12} m^2. In our work though, the scenario setting is a bit more complicated since the permeability is assumed to be anisotropic and that a moderate groundwater flow exists. By comparing the simulated temperature distributions at the end of each heat injection and extraction period, the maximum difference between Scenario A1/B1 and A2/B2 is less than 1 K, which implies that the temperature distribution is not greatly affected by buoyant flow. However, to precisely determine whether the enhanced contaminant reduction at higher permeabilities is associated with the loss of heat storage efficiency, a detailed 3D heat transport analysis would be necessary which is beyond the scope of this study.

5.2 Implications for Combining BTES and Groundwater Remediation

In this study, we demonstrated the potential compatibility of BTES with contaminated aquifers to achieve an enhanced remediation of CHC contaminants. An important finding is that the buoyant flow induced by heat storage plays an essential role in the improvement of TCE volatilization. As our basic hypothesis, vertical mass transfer of the dissolved contaminant is limited by the slow aqueous phase dispersion. This implies that the difficulty of removing the contaminant increases dramatically when it sinks deeper into the saturated zone (Ni et al., 2015a; Janfada et al., 2020). Thus, in order to achieve significantly enhanced *in-situ* volatilization, it is important to overcome the above limitations in aqueous phase transport. Here, such principle is primarily manifested by the buoyant flow resulted from conductive heating, which enables an accelerated TCE migration to the unsaturated zone. Alternatively, a separate gas phase can be injected to facilitate the partitioning and mobilization of the contaminant, e.g. in steam injection (Hiester et al., 2013) and air sparging. Furthermore, it is worth noting that the modeled BTES system here is quite small in size. In practical BTES applications, typically large arrays of borehole are arranged in compact shapes (e.g., cylindrical) in order to increase the heat storage volume while minimizing heat losses. Therefore, real heat storage systems are expected to attain higher remediation capacities than demonstrated in this study. Considering a typical BTES lifetime of 25-30 years, complete removal of CHC plumes may appear as a feasible and attractive remediation goal even within the first few years of operation.

Besides the benefit of enhanced contaminant attenuation which occurs mainly in the saturated zone, a relocation of the volatilized contaminant into the unsaturated zone is also predicted by the numerical model. Here, the main concern from an environmental perspective is the potentially elevated contaminant concentration in the gas phase which may give rise to vapor intrusion and adversely impact the indoor air quality (Wang et al., 2012). Regarding this concern, our simulation results yield different outcomes depending on the time scale considered. In **Figures 6D**, **7D**, the gas phase TCE content of Scenario A1, A2 and B2 showed relatively large temporal fluctuations with respect to the baseline curve. Especially in Scenario B2, the maximum amount of gas phase TCE reaches 0.011 mol, which is more than seven times higher than that of the baseline (1.50×10^{-3} mol). Therefore, in short time scales (e.g., months to a few years), the significantly raised contaminant vapor concentration could possibly lead to indoor air regulations being exceeded when residential dwellings are nearby. Nevertheless, it is also observed that the gas phase contaminant retains strong "resilience" in response to subsurface temperature fluctuations—after the sharp increase due to heat injection, it was able to recover to a much lower extent at the end of each year. Furthermore, for all scenarios with BTES operation, the gas phase TCE at 5 years is either lower than or at the same level of the baseline. In other words, no significant TCE accumulation in the soil gas is predicted over the longer time scale. Such advantage is mainly attributed to the rapid diffusive transport in the gas phase, thus allowing the TCE vapor to be effectively released to the atmosphere under the high concentration gradients. Since the risk of vapor intrusion cannot be completely ruled out, long-term monitoring of the contaminant vapor concentration in the subsurface is advised to mitigate the above negative impacts of BTES operation. To fully eliminate the risk of vapor intrusion, soil vapor extraction (Baker et al., 2016) can be integrated to remove the contaminated soil gas.

5.3 Model Limitations

Although the investigated scenarios and process interactions are already quite complex, the applied numerical model still neglects several processes that may become relevant in the context of thermal energy storage in contaminated subsurface. Owing to the assumption of a two-phase (water-air) system, the model does not account for the existence of CHC contaminants as pure NAPL phase in the subsurface. When the contaminant source is present as residual NAPL phase, temperature variations may have additional impacts on NAPL solubility (Popp et al., 2016; Koproch et al., 2019), mobility (Philippe et al., 2020), etc. These effects may lead to further release and transport of the contaminant. Otherwise, when NAPL phase is present in the unsaturated zone, even in traces, the volatilization flux will be considerably higher (Ostendorf et al., 2000). Hence, the presented model is most favorably applied in areas downgradient of identified source zones, where the contaminant is already fully dissolved in the aqueous phase.

Another limitation of the numerical model is that phase transition is so far not considered. As a result of heat storage in saturated porous medium, gas phase may develop and accumulate in case of large temperature elevations at shallow groundwater depths. The formation of a gas phase can have multiple influences on heat storage and aquifer contamination, as detailed in the work of Lüders et al. (2016). One potential outcome is that the dissolved contaminant can be transported further when gas bubbles are mobilized. Since the formation of gas phase is strongly dependent on the composition of dissolved gases in groundwater (Lüders et al., 2016), simulation of such process would in general require at least four components in the model. Last but not least, many other physical and chemical

processes such as sorption and biodegradation also respond actively to temperature changes. Although the abovementioned processes are important, they are beyond the scope of this study and will be investigated in future research.

6 CONCLUSION

This study aimed at understanding the effects of high-temperature BTES on the fate and transport of CHC contaminants by simulating the coupled fluid flow, heat and mass transport in a variably-saturated aquifer using *OpenGeoSys* software. The thermal impacts on the subsurface resulting from seasonal heat storage was examined in a contaminant transport context by means of two-phase flow modeling using temperature-dependent parameters. Application of the numerical model is demonstrated for a series of scenarios of BTES operation in a shallow unconfined aquifer contaminated by TCE. The main findings of this study are hereby summarized:

1) The key mechanism limiting the transfer of the contaminant from the groundwater to the unsaturated zone is the dispersive transport process in the liquid phase.
2) Temperature increase in the subsurface can lead to an enhanced volatilization of the contaminant in groundwater. However, temperature effect alone is only able to remediate the uppermost part of the saturated zone whereas the deeper contaminated regions are practically unaffected.
3) At higher soil permeabilities, buoyant flow may be induced due to heating of the groundwater. This can change the flow dynamics and result in a significant improvement of contaminant removal.

For a constant source: Buoyant flow reduces the contaminant emission from source while at the same time drives the contaminant plume towards the water table. The combined effect led to a nearly 60% decline in residual TCE mass after 5 years of BTES operation.

For an instantaneous spill: Buoyant flow accelerates the volatilization process and increases the overall reduction of TCE from 19% to over 70%.

4) Contaminant concentration in the soil gas showed large temporal fluctuations in response to seasonal heat storage. In spite of this, seasonal heat storage was not found to further increase the soil gas content of the contaminant in the long-term.

Considering the relatively small size of the modeled BTES system, the potential of BTES in assisting the *in-situ* volatilization of CHC contaminants in groundwater looks promising. As a consequence, the combination of underground heat storage with the remediation of contaminated aquifers offers an environmentally and energetically sustainable way to foster the redevelopment of contaminated urban areas. Despite the general benefits predicted, it is important to note that many other factors for physical, chemical, biological, and geological conditions can impact the contaminant transport during heat storage in the shallow subsurface. Thus, future work should include a more comprehensive and site-specific assessment of the temperature effects to ensure that the benefits anticipated for the combination of BTES and enhanced volatilization outweigh the risk of contaminant spreading, especially when subsurface heat storage facilities are practiced near NAPL contaminated sites.

DATA AVAILABILITY STATEMENT

The original contributions presented in the study are included in the article/**Supplementary Material**, further inquiries can be directed to the corresponding authors.

AUTHOR CONTRIBUTIONS

BM: Methodology, Software, Validation, Formal analysis, Writing—Original Draft, Visualization. YY: Methodology, Investigation, Writing—Review and Editing. YH: Conceptualization, Methodology, Software, Writing—Review and Editing. OK: Writing—Review and Editing, Supervision, Project administration, Funding acquisition. HS: Conceptualization, Methodology, Software, Writing—Review and Editing, Visualization, Supervision.

FUNDING

This work was financially supported by the National Natural Science Foundation of China (Grant Number 41902311). This work was also supported by the German Federal Ministry for Economic Affairs and Energy (BMWi) for the "ANGUS II" project (Grant Number 03ET6122B).

ACKNOWLEDGMENTS

We would like to thank Christof Beyer (Kiel University) and Wenqing Wang (UFZ) for the fruitful discussions and their insightful comments. BM would also like to acknowledge the financial support from the China Scholarship Council (CSC) for his PhD study in Germany.

SUPPLEMENTARY MATERIAL

The Supplementary Material for this article can be found online at: https://www.frontiersin.org/articles/10.3389/feart.2021.790315/full#supplementary-material

REFERENCES

Atteia, O., and Höhener, P. (2010). Semianalytical Model Predicting Transfer of Volatile Pollutants from Groundwater to the Soil Surface. *Environ. Sci. Technol.* 44, 6228–6232. doi:10.1021/es903477f

Baker, R. S., Nielsen, S. G., Heron, G., and Ploug, N. (2016). How Effective Is thermal Remediation of DNAPL Source Zones in Reducing Groundwater Concentrations? *Groundwater Monit. R.* 36, 38–53. doi:10.1111/gwmr.12149

Beyer, C., Popp, S., and Bauer, S. (2016). Simulation of Temperature Effects on Groundwater Flow, Contaminant Dissolution, Transport and Biodegradation Due to Shallow Geothermal Use. *Environ. Earth Sci.* 75. doi:10.1007/s12665-016-5976-8

Boockmeyer, A. (2020). *Numerical Simulation of Borehole thermal Energy Storage in the Geological Subsurface*. Ph.D. thesis. Kiel University.

Bourgeat, A., Jurak, M., and Smaï, F. (2008). Two-phase, Partially Miscible Flow and Transport Modeling in Porous media; Application to Gas Migration in a Nuclear Waste Repository. *Comput. Geosci.* 13, 29–42. doi:10.1007/s10596-008-9102-1

Casasso, A., and Sethi, R. (2019). Groundwater-Related Issues of Ground Source Heat Pump (GSHP) Systems: Assessment, Good Practices and Proposals from the European Experience. *Water* 11, 1573. doi:10.3390/w11081573

Catolico, N., Ge, S., and McCartney, J. S. (2016). Numerical Modeling of a Soil-Borehole Thermal Energy Storage System. *Vadose zone j.* 15, 1–17. doi:10.2136/vzj2015.05.0078

Class, H., and Helmig, R. (2002). Numerical Simulation of Non-isothermal Multiphase Multicomponent Processes in Porous media. *Adv. Water Resour.* 25, 551–564. doi:10.1016/s0309-1708(02)00015-5

Cussler, E. L. (2009). *Diffusion: Mass Transfer in Fluid Systems*. Cambridgeshire: Cambridge University Press.

Datt, P. (2011). *Latent Heat of Vaporization/Condensation*. Dordrecht: Springer Netherlands, 703. doi:10.1007/978-90-481-2642-2_327

Djotsa Nguimeya Ngninjio, V., Bo, W., Beyer, C., and Bauer, S. (2021). "Experimental and Numerical Investigation of thermal Convection in a Water Saturated Porous Medium Induced by Heat Exchangers in High Temperature Borehole thermal Energy Storage," in EGU General Assembly Conference Abstracts, EGU21–8071.

Elhashmi, R., Hallinan, K. P., and Chiasson, A. D. (2020). Low-energy Opportunity for Multi-Family Residences: A Review and Simulation-Based Study of a Solar Borehole thermal Energy Storage System. *Energy* 204, 117870. doi:10.1016/j.energy.2020.117870

Fleuchaus, P., Godschalk, B., Stober, I., and Blum, P. (2018). Worldwide Application of Aquifer thermal Energy Storage - A Review. *Renew. Sust. Energ. Rev.* 94, 861–876. doi:10.1016/j.rser.2018.06.057

Grandel, S., and Dahmke, A. (2008). "Natürliche Schadstoffminderung bei LCKW-kontaminierten Standorten Methoden, Empfehlungen und Hinweise zur Untersuchung und Beurteilung," in *Christian-Albrechts-Universität zu Kiel*.

GSI Environmental (2020). Gsi Chemical Database. Available at: https://www.gsi-net.com/en/publications/gsi-chemical-database/single/547-CAS-79016.html (Accessed May 14, 2021).

Haajizadeh, M., and Tien, C. L. (1984). Combined Natural and Forced Convection in a Horizontal Porous Channel. *Int. J. Heat Mass Transfer* 27, 799–813. doi:10.1016/0017-9310(84)90001-2

Hailemariam, H., and Wuttke, F. (2020). Cyclic Mechanical Behavior of Two sandy Soils Used as Heat Storage media. *Energies* 13, 3835. doi:10.3390/en13153835

Hailemariam, H., and Wuttke, F. (2017). Temperature Dependency of the thermal Conductivity of Porous Heat Storage media. *Heat Mass. Transfer* 54, 1031–1051. doi:10.1007/s00231-017-2204-3

Heat Roadmap Europe (2017). Heating and Cooling Facts and Figures: The Transformation towards a Low-Carbon Heating & Cooling Sector. [Online], Available from: https://www.isi.fraunhofer.de/content/dam/isi/dokumente/cce/2017/29882_Brochure_Heating-and-Cooling_web.pdf (Accessed September 30, 2021).

Hiester, U., Müller, M., Koschitzky, H., Trötschler, O., Roland, U., Holzer, F., et al. (2013). *Guidelines:* In Situ *thermal Treatment (ISTT) for Source Zone Remediation of Soil and Groundwater*. Helmholtz Centre for Environmental Research.

Hilsenrath, J. (1955). *Tables of thermal Properties of Gases: Comprising Tables of Thermodynamic and Transport Properties of Air, Argon, Carbon Dioxide, Carbon Monoxide, Hydrogen, Nitrogen, Oxygen, and Steam*. Washington D.C.: US Department of Commerce, National Bureau of Standards.

Huang, Y. (2017). Heat Pipe Problem. Available at: https://www.opengeosys.org/docs/benchmarks/thermal-two-phase-flow/heat-pipe/(Accessed September 28, 2021).

Huang, Y., Kolditz, O., and Shao, H. (2015). Extending the Persistent Primary Variable Algorithm to Simulate Non-isothermal Two-phase Two-Component Flow with Phase Change Phenomena. *Geotherm Energy* 3. doi:10.1186/s40517-015-0030-8

Huang, Y., Shao, H., Wieland, E., Kolditz, O., and Kosakowski, G. (2021). Two-phase Transport in a Cemented Waste Package Considering Spatio-Temporal Evolution of Chemical Conditions. *Npj Mater. Degrad.* 5. doi:10.1038/s41529-021-00150-z

Imhoff, P. T., Frizzell, A., and Miller, C. T. (1997). Evaluation of thermal Effects on the Dissolution of a Nonaqueous Phase Liquid in Porous media. *Environ. Sci. Technol.* 31, 1615–1622. doi:10.1021/es960292x

Janfada, T. S., Class, H., Kasiri, N., and Dehghani, M. R. (2020). Comparative Experimental Study on Heat-Up Efficiencies during Injection of Superheated and Saturated Steam into Unsaturated Soil. *Int. J. Heat Mass Transfer* 158, 119235. doi:10.1016/j.ijheatmasstransfer.2019.119235

Jang, W., and Aral, M. M. (2006). Density-driven Transport of Volatile Organic Compounds and its Impact on Contaminated Groundwater Plume Evolution. *Transp Porous Med.* 67, 353–374. doi:10.1007/s11242-006-9029-8

Kolditz, O., Bauer, S., Bilke, L., Böttcher, N., Delfs, J. O., Fischer, T., et al. (2012). OpenGeoSys: an Open-Source Initiative for Numerical Simulation of Thermo-Hydro-Mechanical/chemical (THM/c) Processes in Porous media. *Environ. Earth Sci.* 67, 589–599. doi:10.1007/s12665-012-1546-x

Koproch, N., Dahmke, A., and Köber, R. (2019). The Aqueous Solubility of Common Organic Groundwater Contaminants as a Function of Temperature between 5 and 70 °C. *Chemosphere* 217, 166–175. doi:10.1016/j.chemosphere.2018.10.153

Kretzschmar, H.-J., and Wagner, W., 2019. IAPWS Industrial Formulation 1997 for the Thermodynamic Properties of Water and Steam , 7–150, doi:10.1007/978-3-662-53219-5_3

Krol, M. M., Johnson, R. L., and Sleep, B. E. (2014). An Analysis of a Mixed Convection Associated with thermal Heating in Contaminated Porous media. *Sci. Total Environ.* 499, 7–17. doi:10.1016/j.scitotenv.2014.08.028

Linstrom, P., and Mallard, W., (2001). Nist Chemistry Webbook Srd. 69. doi:10.18434/T4D303

Lüders, K., Firmbach, L., Ebert, M., Dahmke, A., Dietrich, P., and Köber, R. (2016). Gas-phase Formation during thermal Energy Storage in Near-Surface Aquifers: Experimental and Modelling Results. *Environ. Earth Sci.* 75. doi:10.1007/s12665-016-6181-5

McCarthy, K. A., and Johnson, R. L. (1993). Transport of Volatile Organic Compounds across the Capillary Fringe. *Water Resour. Res.* 29, 1675–1683. doi:10.1029/93wr00098

McNaught, A. D., and Wilkinson, A. (1997). *Compendium of Chemical Terminology*. Oxford: Blackwell Science Oxford. doi:10.1351/goldbook

Millington, R. J. (1959). Gas Diffusion in Porous media. *Science* 130, 100–102. doi:10.1126/science.130.3367.100-a

Moradi, A., M. Smits, K., and O. Sharp, J. (2018). Coupled Thermally-Enhanced Bioremediation and Renewable Energy Storage System: Conceptual Framework and Modeling Investigation. *Water* 10, 1288. doi:10.3390/w10101288

Ngueleu, S. K., Rezanezhad, F., Al-Raoush, R. I., and Van Cappellen, P. (2018). Sorption of Benzene and Naphthalene on (Semi)-arid Coastal Soil as a Function of Salinity and Temperature. *J. Contaminant Hydrol.* 219, 61–71. doi:10.1016/j.jconhyd.2018.11.001

Ni, Z., van Gaans, P., Rijnaarts, H., and Grotenhuis, T. (2018). Combination of Aquifer thermal Energy Storage and Enhanced Bioremediation: Biological and Chemical Clogging. *Sci. Total Environ.* 613-614, 707–713. doi:10.1016/j.scitotenv.2017.09.087

Ni, Z., van Gaans, P., Smit, M., Rijnaarts, H., and Grotenhuis, T. (2015a). Biodegradation of Cis-1,2-Dichloroethene in Simulated Underground thermal Energy Storage Systems. *Environ. Sci. Technol.* 49, 13519–13527. doi:10.1021/acs.est.5b03068

Ni, Z., van Gaans, P., Smit, M., Rijnaarts, H., and Grotenhuis, T. (2015b). Combination of Aquifer thermal Energy Storage and Enhanced Bioremediation: Resilience of Reductive Dechlorination to Redox Changes. *Appl. Microbiol. Biotechnol.* 100, 3767–3780. doi:10.1007/s00253-015-7241-6

Ostendorf, D. W., Hinlein, E. S., Lutenegger, A. J., and Kelley, S. P. (2000). Soil Gas Transport above a Jet Fuel/solvent Spill at plattsburgh Air Force Base. *Water Resour. Res.* 36, 2531–2547. doi:10.1029/2000wr900128

Pellegrini, M., Bloemendal, M., Hoekstra, N., Spaak, G., Andreu Gallego, A., Rodriguez Comins, J., et al. (2019). Low Carbon Heating and Cooling by Combining Various Technologies with Aquifer thermal Energy Storage. *Sci. Total Environ.* 665, 1–10. doi:10.1016/j.scitotenv.2019.01.135

Phernambucq, I. (2015). *Contaminant Spreading in Areas with a High Density of Seasonal Aquifer Thermal Energy Storage (SATES) Systems*. Master's thesis. Utrecht University.

Philippe, N., Davarzani, H., Colombano, S., Dierick, M., Klein, P.-Y., and Marcoux, M. (2020). Experimental Study of the Temperature Effect on Two-phase Flow Properties in Highly Permeable Porous media: Application to the Remediation of Dense Non-aqueous Phase Liquids (DNAPLs) in Polluted Soil. *Adv. Water Resour.* 146, 103783. doi:10.1016/j.advwatres.2020.103783

Piga, B., Casasso, A., Pace, F., Godio, A., and Sethi, R. (2017). Thermal Impact Assessment of Groundwater Heat Pumps (GWHPs): Rigorous vs. Simplified Models. *Energies* 10, 1385. doi:10.3390/en10091385

Popp, S., Beyer, C., Dahmke, A., Koproch, N., Köber, R., and Bauer, S. (2016). Temperature-dependent Dissolution of Residual Non-aqueous Phase Liquids: Model Development and Verification. *Environ. Earth Sci.* 75. doi:10.1007/s12665-016-5743-x

Roohidehkordi, I., and Krol, M. M. (2021). Applicability of Ground Source Heat Pumps as a Bioremediation-Enhancing Technology for Monoaromatic Hydrocarbon Contaminants. *Sci. Total Environ.* 778, 146235. doi:10.1016/j.scitotenv.2021.146235

Rossi, F., Cucciniello, R., Intiso, A., Proto, A., Motta, O., and Marchettini, N. (2015). Determination of the Trichloroethylene Diffusion Coefficient in Water. *Aiche J.* 61, 3511–3515. doi:10.1002/aic.14861

Rotaru, C., Ostendorf, D. W., and DeGroot, D. J. (2014). Chloride Dispersion across silt Deposits in a Glaciated Bedrock River valley. *J. Environ. Qual.* 43, 459–467. doi:10.2134/jeq2013.07.0284

Schwardt, A., Dahmke, A., and Köber, R. (2021). Henry's Law Constants of Volatile Organic Compounds between 0 and 95 °C - Data Compilation and Complementation in Context of Urban Temperature Increases of the Subsurface. *Chemosphere* 272, 129858. doi:10.1016/j.chemosphere.2021.129858

Somerton, W. H., El-Shaarani, A. H., and Mobarak, S. M., 1974. High Temperature Behavior of Rocks Associated with Geothermal Type Reservoirs, All Days, SPE, doi:10.2118/4897-ms

Sommer, W., Drijver, B., Verburg, R., Slenders, H., De Vries, E., Dinkla, I., et al. (2013). *Combining Shallow Geothermal Energy and Groundwater Remediation*.

Stroo, H. F., and Ward, C. H. (2010). In Situ *Remediation of Chlorinated Solvent Plumes*. Springer Science & Business Media. doi:10.1007/978-1-4419-1401-9

Tang, M. J., Shiraiwa, M., Pöschl, U., Cox, R. A., and Kalberer, M. (2015). Compilation and Evaluation of Gas Phase Diffusion Coefficients of Reactive Trace Gases in the Atmosphere: Volume 2. Diffusivities of Organic Compounds, Pressure-Normalised Mean Free Paths, and Average Knudsen Numbers for Gas Uptake Calculations. *Atmos. Chem. Phys.* 15, 5585–5598. doi:10.5194/acp-15-5585-2015

Touloukian, Y., Kirby, R., Taylor, R., and Lee, T. (1970). *Thermophysical Properties of Matter*. New York, 89.

van Genuchten, M. T. (1980). A Closed-form Equation for Predicting the Hydraulic Conductivity of Unsaturated Soils. *Soil Sci. Soc. America J.* 44, 892–898. doi:10.2136/sssaj1980.03615995004400050002x

Wang, X., Unger, A. J. A., and Parker, B. L. (2012). Simulating an Exclusion Zone for Vapour Intrusion of TCE from Groundwater into Indoor Air. *J. Contaminant Hydrol.* 140-141, 124–138. doi:10.1016/j.jconhyd.2012.07.004

Welsch, B., Göllner-Völker, L., Schulte, D. O., Bär, K., Sass, I., and Schebek, L. (2018). Environmental and Economic Assessment of Borehole thermal Energy Storage in District Heating Systems. *Appl. Energ.* 216, 73–90. doi:10.1016/j.apenergy.2018.02.011

Würdemann, H., Westphal, A., Lerm, S., Kleyböcker, A., Teitz, S., Kasina, M., et al. (2014). Influence of Microbial Processes on the Operational Reliability in a Geothermal Heat Store - Results of Long-Term Monitoring at a Full Scale Plant and First Studies in a Bypass System. *Energ. Proced.* 59, 412–417. doi:10.1016/j.egypro.2014.10.396

Yaws, C. L. (2014). *Transport Properties of Chemicals and Hydrocarbons*. Norwich, NY: William Andrew. doi:10.1016/c2013-0-12644-x

Yu, S., Unger, A. J. A., and Parker, B. (2009). Simulating the Fate and Transport of TCE from Groundwater to Indoor Air. *J. Contaminant Hydrol.* 107, 140–161. doi:10.1016/j.jconhyd.2009.04.009

Zuurbier, K. G., Hartog, N., Valstar, J., Post, V. E. A., and van Breukelen, B. M. (2013). The Impact of Low-Temperature Seasonal Aquifer thermal Energy Storage (SATES) Systems on Chlorinated Solvent Contaminated Groundwater: Modeling of Spreading and Degradation. *J. Contaminant Hydrol.* 147, 1–13. doi:10.1016/j.jconhyd.2013.01.002

Conflict of Interest: The authors declare that the research was conducted in the absence of any commercial or financial relationships that could be construed as a potential conflict of interest.

Publisher's Note: All claims expressed in this article are solely those of the authors and do not necessarily represent those of their affiliated organizations, or those of the publisher, the editors and the reviewers. Any product that may be evaluated in this article, or claim that may be made by its manufacturer, is not guaranteed or endorsed by the publisher.

GLOSSARY

c_p Specific heat capacity ($J\,kg^{-1}.K^{-1}$)

D_α^k Diffusion coefficient of component k in free phase α ($m^2.s^{-1}$)

F^k source or sink term of component k ($mol\,m^{-3}.s^{-1}$)

g gravitational acceleration ($m\,s^{-2}$)

H Henry's law constant ($Pa\,m^3.mol^{-1}$)

h specific enthalpy ($J\,kg^{-1}$)horizontal

$h_{\Delta e}$ latent heat of vaporization of water ($J\,kg^{-1}$)

I identity matrix

J_α^k diffusive flux of component k in phase α ($m\,s^{-1}$)

K intrinsic permeability tensor (m^2)

k any of the three chemical components

$k_{r\alpha}$ relative permeability of phase α (-)

M^k molar mass of component k ($kg\,mol^{-1}$)

N_α molar density of phase α ($mol\,m^{-3}$)

P_α pressure in phase α (Pa)

P_{cap} capillary pressure (Pa)

P_{vap} vapor pressure (Pa)

q_α Darcy velocity of phase α ($m\,s^{-1}$)

Q_T heat source or sink term ($W\,m^{-3}$)

S_α saturation of phase α (-)

S_{eL} effective liquid saturation (-)

S_{rL} residual liquid saturation (-)

T temperature (K)transpose

u specific internal energy ($J\,kg^{-1}$)

X^k overall molar fraction of component k (-)

x_α^k molar fraction of component k in phase α (-)

Greek Letters

α either of the two fluid phases

λ_{pm} effective thermal conductivity of the porous medium ($W\,m^{-1}.K^{-1}$)

μ_α dynamic viscosity of phase α ($Pa\,s$)

ϕ porosity (-)

ρ mass density ($kg\,m^{-3}$)

Operators

div divergence operator

∇ gradient operator

Superscripts

a air

c organic contaminant

T temperature (K)transpose

w water

Subscripts

G gas phase

h specific enthalpy ($J\,kg^{-1}$)horizontal

L liquid phase

l longitudinal

s soil grain

v vertical

frontiers in Earth Science

ORIGINAL RESEARCH
published: 22 December 2021
doi: 10.3389/feart.2021.786389

Performance of Multi-Well Exploitation and Reinjection in a Small-Scale Shallow Geothermal Reservoir in Huailai County

Wenzhen Yuan[1], Dailei Zhang[1], Yi Zhang[1], Jun Gao[1], Tongzhe Liu[2,3], Haizhen Zhai[4], Guangrong Jin[4]*, Guiling Wang[1,5]* and Baojian Zhang[1]*

[1]Chinese Academy of Geological Sciences, Beijing, China, [2]801 Institute of Hydrogeology and Engineering Geology, Shandong Provincial Bureau of Geology and Mineral Resources, Jinan, China, [3]Shandong Engineering Research Center for Environmental Protection and Remediation on Groundwater, Jinan, China, [4]CAS Key Laboratory of Gas Hydrate, Guangzhou Institute of Energy Conversion, Chinese Academy of Sciences, Guangzhou, China, [5]Institute of Hydrogeology and Environmental Geology, Chinese Academy of Geological Sciences, Shijiazhuang, China

The sustainable development of a shallow aquifer geothermal reservoir is strongly affected by the reinjection–production strategy. However, the reinjection–production strategy optimization of a small-scale exploitation unit with tens of meters of well spacing is site specific and has not yet been fulfilled. This study numerically investigates sustainable heat extraction based on various reinjection–production strategies which were conducted in a single-phase aquitard–aquifer geothermal system in Huailai County, Hebei Province, China. The response of the water level and production temperature is mainly discussed. The numerical results show that production without reinjection induces the highest production temperature and also the water level drawdown. Although reinjection in a single doublet well system is conducive to the control of water level drawdown, the introduction of the thermal breakthrough problem causes a decrease in the production temperature. The thermal breakthrough and sustainability of geothermal reservoirs highly depend on the well spacing between the production and reinjection wells, especially for the small-scale field. Therefore, a large well spacing is suggested. A multi-well system facilitates the control of water level drawdown while bringing intensive well interference and thermal breakthrough. Large spacing between the production and reinjection wells is also the basic principle for the design of the multi-well system. A decrease in openhole length leads to an increase in the production temperature and output thermal power. An increase in the production rate affects the thermal breakthrough highly and shortens the lifetime of the geothermal system. Furthermore, the extracted thermal energy is highly affected by the reduction in the reinjection temperature. The results in this study can provide references to achieve sustainable geothermal exploitation in small-scale geothermal reservoirs.

Keywords: geothermal energy, reinjection, production strategy, water level drawdown, sustainable development, Huailai County

OPEN ACCESS

Edited by:
Yanlong Kong,
Institute of Geology and Geophysics (CAS), China

Reviewed by:
Yuanzheng Zhai,
Beijing Normal University, China
Yonghui Huang,
Institute of Geology and Geophysics (CAS), China
Zhongfeng Duan,
China University of Petroleum(Huadong), China

****Correspondence:***
Haizhen Zhai
zhaihz@ms.giec.ac.cn
Guangrong Jin
jingr@ms.giec.ac.cn
Guiling Wang
guilingw@163.com

Specialty section:
This article was submitted to Economic Geology, a section of the journal Frontiers in Earth Science

Received: *30 September 2021*
Accepted: *15 November 2021*
Published: *22 December 2021*

Citation:
Yuan W, Zhang D, Zhang Y, Gao J, Liu T, Zhai H, Jin G, Wang G and Zhang B (2021) Performance of Multi-Well Exploitation and Reinjection in a Small-Scale Shallow Geothermal Reservoir in Huailai County. Front. Earth Sci. 9:786389. doi: 10.3389/feart.2021.786389

1 INTRODUCTION

The emission of anthropogenic greenhouse gases (GHGs) from the combustion of fossil fuels causes global climate change (Yang et al., 2018; Mallapaty, 2020), which is bad for human survival. To reduce carbon emission and dependency on fossil fuels (Cui et al., 2021), low-carbon and renewable energies are attracting extensive attention worldwide (Hu et al., 2020). Geothermal energy, which utilizes energy buried in the earth's interior, is a kind of clean and sustainable energy (Hu et al., 2020). Geothermal energy could be developed for power generation, space heating, and thermal spring, depending on the production temperature (Su et al., 2018). However, due to the intensive withdrawal of fluid or heat from the geothermal field, energy recovered naturally may not support the energy output (Rivera Diaz et al., 2016). Thus, decreases in pressure, temperature, and extracted heat are generally encountered, which runs counter to the sustainable development of a geothermal reservoir. Reinjection is generally compulsive in most of the geothermal field, and reinjection–production strategy should be carefully designed (Kamila et al., 2021).

Doublet well is widely employed to extract geothermal energy (Su et al., 2018; Markó et al., 2021) by injecting cold water in to one well while extracting hot water from another. The reinjection is expected to maintain reservoir pressure and avoid subsidence (Markó et al., 2021); however, the distance of the wells should be appropriately placed to avert thermal breakthrough (Kamila et al., 2021). Thermal breakthrough will cause the temperature to decline because the injected water may be underheated when flowing through the reservoir. Driven by the purpose of gaining the highest thermal output, a numerical simulation, based on the characterization of geological condition, fluid flow, and heat transfer, is the important tool to optimize well placement and the corresponding reinjection–production strategy (Zhang et al., 2021). The well spacing for homogenous and heterogenous reservoirs has been optimized (Willems and Nick, 2019; Liu et al., 2020). For a doublet well with lateral recharge, the reinjection well located downstream is better than it being located upstream (Kong, 2017). Anisotropic heterogeneity could lengthen or shorten the lifetime of the geothermal reservoir (Babaei and Nick, 2019), and the well spacing should be adjusted accordingly. The effect of faults (Zhang et al., 2019a), depth of production interval (Yuan et al., 2021), and permeability (Crooijmans et al., 2016; Le Lous et al., 2018) on heat production have also been discussed. Therefore, the reinjection–production strategy is affected by the characteristics of the geothermal system. Two doublet well systems (Babaei and Nick, 2019) and a well system with one production well and multiple injection wells (Zhang et al., 2019b) have also been investigated for maximum heat production.

Recently, the interest in multiple well systems in regional-scale fields has increased because of the increasing demand for low-carbon energy (Kong et al., 2020; Zhang et al., 2021). A masterplan was proposed by arranging double wells in a limited number of exploitation units (Willems and Nick, 2019; Zhang et al., 2021), which was different from previous random arrangements of doublet wells. Similar to the common practice approach in the hydrocarbon industry, the masterplan of geothermal wells focuses on optimizing heat recovery of the entire field (Willems and Nick, 2019). The distance between individual doublet wells and spacing of the injection–production wells are the main optimized options. The heat recovery efficiency was evaluated to increase by tens of percentages by the so-called "checkboard" well placements (Willems and Nick, 2019). The well configurations of the "checkboard," "lane zonation," and cluster layout (by separating the injection and production wells in to distinct injection and production zones) in a heterogenous geothermal reservoir were compared, and it was found that the heat recovery of the cluster layout was higher than the other two (Liu et al., 2020). The flow channels develop along the direction of high permeability. Geothermal production affects the regional-scale temperature and groundwater flow. Therefore, regarding the importance of natural hydrothermal flow status, Zhang et al. (2021) proposed a new method for well placement optimization. Based on the method, an intensive heat production mode using a lane pattern locally will lead to a more stable production temperature and high recoverability of the groundwater levels (Zhang et al., 2021). Therefore, the response of the natural hydrothermal process to the artificial operation affects the sustainable development of the geothermal field (Franco and Vaccaro, 2014). The reinjection–production strategy should be investigated according to the characteristics of individual reservoirs. The above studies have managed to increase heat recovery for doublet and multiple double wells in small- and regional-scale reservoirs through well spacing in an order higher than hundreds of meters, by changing the distance of the wells. However, the reinjection–production strategy optimization of a small-scale exploitation unit with tens of meters of spacing is not yet fulfilled. Changes in production–reinjection relationships between wells may induce different responses of temperature and water levels. The water transport and heat transfer under various production scenarios (well configurations) are highly related to the sustainable heat development of the geothermal reservoir. To gain a large and sustainable heat production, thermal breakthrough should be avoided as much as possible. The occurrence of thermal breakthrough may lead to the shutdown of the hydrothermal energy installation. Therefore, the reinjection–production strategy should be optimized.

This study numerically investigates the sustainability of heat production of a small-scale geothermal field based on the wells that have been drilled. The scenarios with production-only and basic doublet well systems are investigated first, and the heat production is enhanced by designing different union operations between the wells. The heat production and the response of temperature and water levels are mainly discussed. Thermal breakthrough is managed to a minimum to increase the sustainability of the geothermal site.

2 MATERIALS

2.1 Hydrogeological Setting

The research area is located in the courtyard of Aolin Spring Town, Houhaoyao Village, Huailai County, Zhangjiakou City,

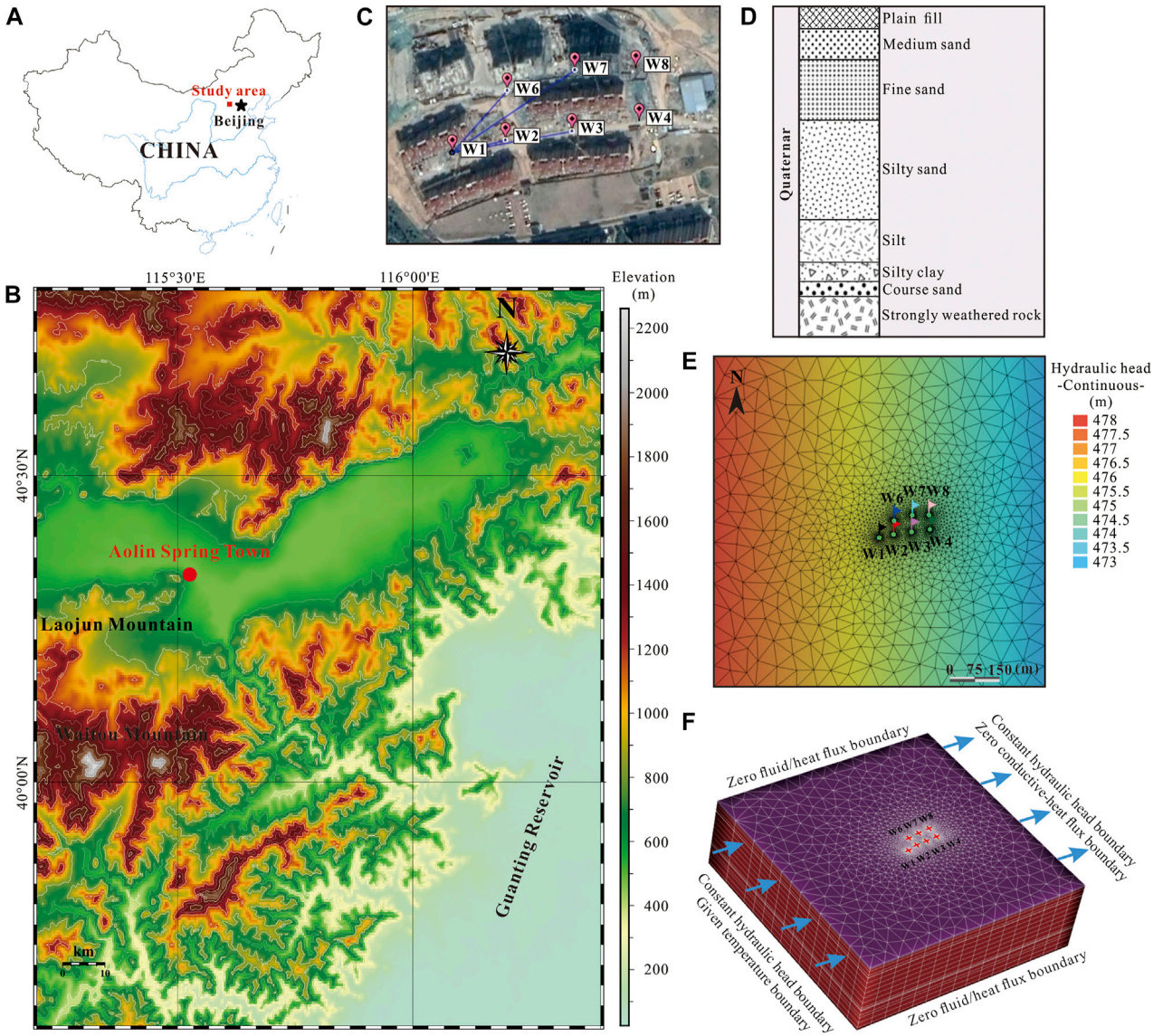

FIGURE 1 | (A) Location map of the Huailai geothermal field in northern China, **(B)** topography map of the geothermal field, **(C)** geothermal well location in Aolin Spring Town, Huailai County, **(D)** typical lithofacies revealed in W2, **(E)** domain discretization and spatial distribution of hydraulic head in the Quaternary aquifer under natural conditions without artificial heat production, and **(F)** domain discretization and boundary conditions.

Hebei Province, China (**Figure 1**). Huailai County is situated in the north of the Yanshan Mountains and the upper reaches of Yongding River and is at a distance of 120 km from Beijing. The county has an average elevation of 792 m, average annual precipitation of 413 mm, and average temperature of 10.5°C. Because of the cold weather in winters in Houhaoyao, geothermal energy is mainly exploited for heating in winter and bathing all year around.

Houhaoyao geothermal field is located in the central and southern parts of the Zhuolu–Huailai Cenozoic fault basin, the core of Laojun mountain anticline, and near the intersection of the Dahenan-Chicheng deep fault and Yuxian-Yanqing fault. The basement of the Huailai County consists of pre-Sinian schist and Archean gneiss (Wang, 2010). The Quaternary sedimentary stratum is mainly exposed in Huailai County, and its thickness can reach 2 km. The regionally developed aquifers (Fanwen et al., 2021) include 1) the Tertiary fractured pore-confined aquifer in bedrock, 2) the Quaternary pore confined aquifer of loose sediment composed of coarse sand and gravel above the bedrock, and 3) the Quaternary pore shallow phreatic aquifer composed of medium–fine sand, silt, and clay. Based on the heat transfer mode, the geothermal system in the Huailai area is classified as convective (Fanwen et al., 2021). The water temperature ranges from 40°C to 80°C and is inferred to reach 120°C in bedrock (Fanwen et al., 2021).

TABLE 1 | Basic information of geothermal wells.

Well ID	Ground elevation (m)	Depth to water table (m)	Water temperature (°C)	Well depth (m)	Utilization section (m)
W1	502.8	17.34	77.5	−172	−30 to −172
W2	508	20.35	48.4	−167	−30 to −167
W3	500.7	21.56	51.1	−172	−30 to −172
W4	496.6	20.59	52.3	−189	−30 to −189
W6	506	16.9	63.3	−160	−30 to −160
W7	500	21.34	40.7	−170.5	−30 to −170.5
W8	502.8	17.4	54.56	−172	−30 to −172

2.2 Well Placement

A total of seven geothermal wells had been drilled in the northwest of the Houhaoyao geothermal field. The wells were drilled in two northern–southern rows from the west to the east (**Figure 1**), and the wells in the southern row were designated as wells W1, W2, W3, and W4, while the wells in the northern row were wells W6, W7, and W8. The drilled depth of the geothermal wells ranged from −160 to −189 m (the surface height was zero, and locations below the surface result in a negative depth). The utilization section (openhole) was −30 to −189 m (**Table 1**). All wells had a diameter of 0.46 m. Among these wells, four production wells and three reinjection wells were initially planned, while at present, the actual strategy involved one production well of W1 and two reinjection wells of W4 and W8. All geothermal wells belonged to shallow Quaternary heat reservoirs. The buried depth of the water level ranged from −16.6 to −21.56 m, and the outlet water temperature was 40.7–77.5°C (**Table 1**). This geothermal heating system was launched in 2017 and operated for 4 years with a heating area of 80,000 m^3.

3 MODEL SETUP

3.1 Conceptual Model

The modeled sedimentary stratum was assumed to be horizontal layers. This is because the lithology changes little within a well spacing of tens of meters for drilled wells. To characterize the variation of the water table in a large domain, the modeled domain horizontally extends 1,000 m from the west to the east and 1,000 m from the north to the south. The model's top corresponds to the surface, and the model extends downward 250 m from the surface. The wells were assumed to be located at the center of the modeled domain.

The entire aquifer is mainly composed of medium sand, fine sand, and silty sand, with strongly weathered rock at the bottom. The lithologies under −5.7 m are primarily fine, medium, silty, and coarse sand, which is considered as an unconsolidated aquifer. By contrast, the surface sediment consists of a plain fill. That is, the rocks above −5.7 m could be considered as an aquitard. Therefore, two layers were characterized in the vertical direction: the aquitard with depths from 0 to −5.7 m and the shallow confined aquifer that ranged from −5.7 to −250 m. In addition, since the well screen (openhole) of the drilled wells was placed only in shallow confined aquifers beneath −30 m, the simulations mainly involved the hydraulic distribution of the confined aquifer.

TABLE 2 | Hydrogeological and operation parameters used in the model.

Parameter		Unit	Value
Aquifer			
Horizontal hydraulic conductivity		m/d	1.42
Longitudinal hydraulic conductivity		m/d	1.42
Vertical hydraulic conductivity		m/d	0.142
Porosity		1	0.3
Storage coefficient		1/m	1.5×10^{-5}
Thermal conductivity		W/(m °C)	3
Volumetric heat capacity		J/(m^3 °C)	2.5×10^6
Aquitard			
Horizontal hydraulic conductivity		m/d	0.25
Longitudinal hydraulic conductivity		m/d	0.25
Vertical hydraulic conductivity		m/d	0.025
Porosity		1	0.3
Storage coefficient		1/m	1.5×10^{-5}
Thermal conductivity		W/(m °C)	2.5
Volumetric heat capacity		J/(m^3 °C)	2×10^6
Operation			
Heating season (150 days)	Production rate	m^3/h	80
	Reinjection rate	m^3/h	80
Non-heating season (215 days)	Production rate	m^3/h	40
	Reinjection rate	m^3/h	40
Reinjection temperature		°C	40

3.2 Domain Discretization and Simulation Tool

The geometrical model consists of a square parallelepiped domain, with dimensions 1,000 m × 1,000 m × 250 m. The model was discretized vertically into 19 slices, with vertical grid sizes ranging from 1.5 to 20 m. The modeled plane domain was first discretized by two-dimensional triangulation, and discretizations around all wells were refined to characterizing the hydrothermal process around the wells. Therefore, discretization in-plane domain generated 2,913 nodes. Finally, with 19 slices and 2,913 nodes of each layer, the modeled domain was discretized into a total of 55,347 nodes and corresponding 103,734 grids.

The model of shallow geothermal exploitation and reinjection was performed using the FEFLOW code. FEFLOW is a popular three-dimensional finite-element groundwater flow, mass, and

TABLE 3 | Simulation cases.

Case ID	Production well	Production rate for each well (m^3/h)		Reinjection well	Reinjection rate for each well (m^3/h)		Distance between reinjection and production wells (m)	Well pattern
		Heating season	Non-heating season		Heating season	Non-heating season		
0	W1	80	40	—	—	—	—	Single well production without reinjection
1	W1	80	40	W2	80	40	44	Doublet well system
2	W1			W4			155	
3	W1			W7			121	
4	W1			W8			165	
5	W1, W3, W6, W8	20	10	W2, W4, W7	80/3	40/3	—	Multiple well system
6	W1, W2, W6	80/3	40/3	W4, W8	40	20	—	
7	W1	80	40	W4, W8			—	
8	W1			W4, W7			—	

Note that Case 0 corresponds to the production-only scenario. The heating season is 150 days and the non-heating season is 215 days. For production-only, doublet, and multiple well systems, the total rates of production and reinjection are kept at a constant value. The simulations are performed based on the model validated against the pumping test.

heat transport modeling software (Diersch, 2014), which has been widely used to simulate the hydrothermal behavior of the geothermal system. The detailed governing equations of water and heat transports can be found in the software manual (Diersch, 2014; Le Lous et al., 2018; Huo et al., 2019; Zhang et al., 2021). The relative error of tolerance of solutions was 0.001. The time step was auto-adjusted according to convergence.

3.3 Hydrothermal Parameters

The porosity of aquifer and aquitard were uniform 0.3. The hydraulic conductivity inferred from the pumping test was given in **Table 2**. The ratio of the vertical to the horizontal hydraulic conductivity was assumed to be 0.1. The storage coefficient was given according to the model validation against the pumping test. Other parameters such as thermal conductivity, heat capacity, and the production/reinjection rates are also listed in **Table 2**.

3.4 Initial and Boundary Conditions

Referring to the distribution of regional underground water flow field with an overall direction from the west to the east, fixed hydraulic heads of 478 and 473 m were set, respectively, to the western and eastern boundaries. The initial hydraulic head linearly decreases in the western to the eastern direction by a steady-state simulation of the natural boundary conditions based on the fixed hydraulic heads.

The initial temperature distribution was inferred using an average geothermal gradient of 0.308°C/m. The average geothermal gradient was calculated based on the measured temperature from 40 m to 120 m of well W8. The constant temperature boundary conditions of 10.5°C, equivalent to the annual mean air temperature in Huailai County, and 118.6°C were applied, respectively, to the uppermost and lowermost slices.

Geothermal water is produced, utilized, and subsequently reinjected at a specified temperature. The full reinjection of the produced water was compulsive in the geothermal site. Therefore, a constant discharge rate of water was applied at the production wells, while at the reinjection wells, cold water with constant temperature was injected at a constant reinjection rate. The production and reinjection rates differed in the heating (150 days) and non-heating (215 days) seasons. For the reference scenario, the production rate in the heating season was 80 m^3/h, while the reinjection rate was 80 m^3/h and the water temperature was 40°C. The flow and heat processes within the wellbore were not considered in the model.

3.5 Simulation Cases

To optimize heat extraction in a small-scale exploitation field, the simulation cases designed in this study are listed in **Table 3**. The simulation scenarios include a single production well without reinjection, a single doublet well system, and the multi-well system. The production-only scenario was designed to investigate the basic response of the water level and heat production capability. The scenarios of the doublet well system were designed to investigate the effect of well distance in small-scale exploitation fields on production performance. The scenarios of the multi-well system were designed for the existing seven wells to investigate the water level drawdown and heat production. Case 5 used all seven wells to extract heat, and the production and reinjection wells were arranged in a crossway. Cases 6 and 7 were designed to alleviate the thermal breakthrough effect caused by the small distance between production and reinjection wells, by separating the production wells from the reinjection wells. Case 8 corresponded to the actual running scheme at present. Sensitivity analyses were further discussed based on the best-performed Case 7.

To facilitate the analyses and discussions, three parameters, namely, water level drawdown, production temperature, and output thermal power, are defined to characterize the heat performance of different production and reinjection well systems.

The water level drawdown (ΔH) of the production/reinjection well is calculated by

TABLE 4 | Pumping test.

Well type		Pumping well	Observation well	
Well number		W1	W2	W3
Pumping rate		S1 (45.9 m^3/h, 3 h) S2 (81.3 m^3/h, 3 h) S3 (107.1 m^3/h, 13 h)	—	
Water level drawdown/m	S1	−5.24	−1.62	−0.5
	S2	−10.46	−2.86	−0.86
	S3	−17.80	−4.77	−1.72

$$\Delta H = H_{\text{fin}} - H_{\text{ini}} \tag{1}$$

where H_{ini} (m) is the initial water level and H_{fin} (m) is the final stable water level during the heating and non-heating seasons.

The production temperature (T_{pro}) of all the production wells is given by

$$T_{pro} = \frac{\sum T_i Q_i}{Q} \tag{2}$$

where Q_i (m^3/s) denotes the volumetric flow rate for production well i; T_i (°C) is the water temperature for production well i; and Q (m^3/s) is the volumetric flow rate of the working fluid.

The output thermal power (P) represents the heat extraction rate of the production and reinjection well system and is calculated by

$$P = Q\rho_f c_{pf}\left(T_{pro} - T_{reinj}\right) \tag{3}$$

where ρ_f is the water density; c_{pf} is the heat capacity of water; and T_{reinj} is the temperature of injected water. T_{reinj} is 40°C for all simulation cases and is 35, 30, and 25°C, respectively, for sensitive analysis of reinjection temperature T_{reinj} of 40, 35, and 25°C.

3.6 Model Validation

To test and verify the rationality of the model, the simulated water head and production temperature were validated with the water level and production temperature observed in the pumping test conducted in well W1 (**Table 4**). **Figure 2** shows the comparison between the simulated and measured water levels and production temperatures. By applying the pumping rates of 45.9, 81.3, and 107.1 m^3/h at the three pumping stages, the variations in the water levels of the production and reinjection wells were reproduced by the model. The drawdown of the third pumping stage of W1 was selected as the primary fitted indicator. The measured and simulated drawdowns of W1 fit well, while deviations occurred for the observation well. The relative error between the simulated and measured values of W3 was less than 0.84. For the monitoring well, the differences between the measured and simulated water levels were probably caused by the blocking around the reinjection well during the past 4 years. In the late third pumping stage, the measured and simulated production temperature of W1 fit well, while deviations occurred for the early two pumping stages. The differences between the measured and simulated production temperatures were probably caused by the difference between the original temperature field setting and the real temperature field after continuous production of the past 4 years. Because of the complex underground conditions in the field, the validated model was believed to be acceptable and could be a basis to learn the long-term heat production of the geothermal reservoir.

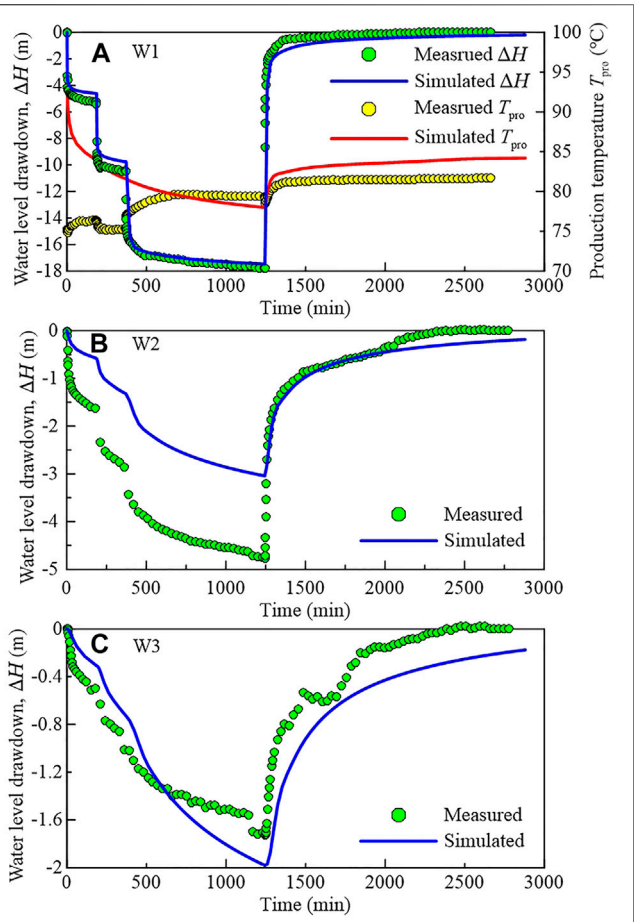

FIGURE 2 | A comparison of the measured and simulated water levels and production temperatures of the pumping test for **(A)** W1, **(B)** W2, and **(C)** W3.

4 RESULTS AND DISCUSSION

4.1 Single Production Without Reinjection

In this section, the heat production behavior of the scenario of W1 production-only without reinjection (Case 0) is investigated first. As shown in **Figure 3A**, in the heating season, the water level drawdown reached −9.85 m under a production rate of 80 m^3/h, while in the non-heating season, the water level drawdown was restored to −4.93 m, owing to the halved production rate. The periodic variations of water level drawdown occurred during the next heating season. Under the control of the water level drawdown, reinjection was conducted to find the optimized strategy to reduce the water level drawdown.

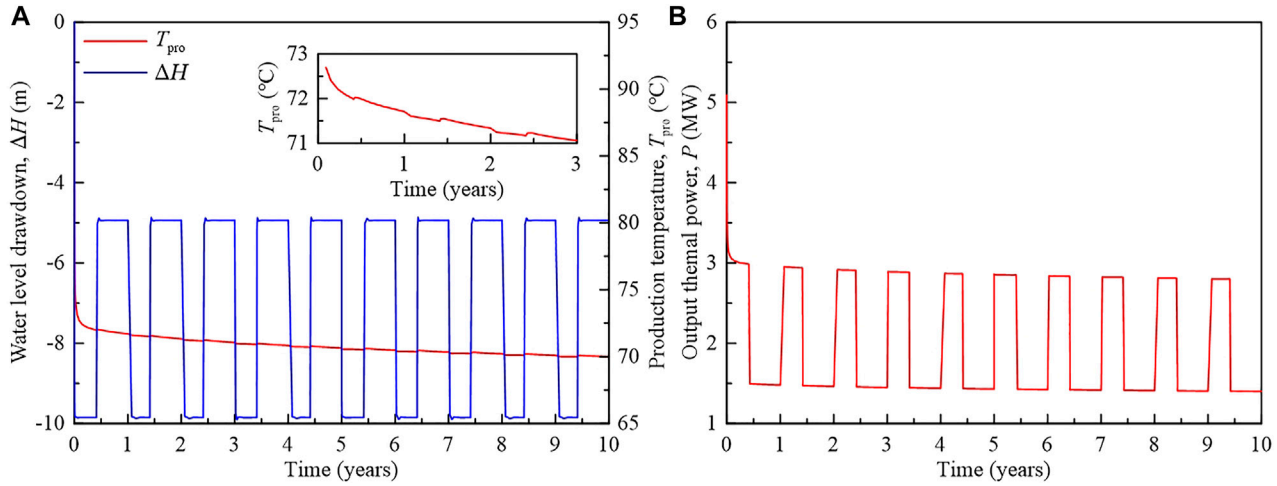

FIGURE 3 | The production performance of W1 production-only without reinjection.

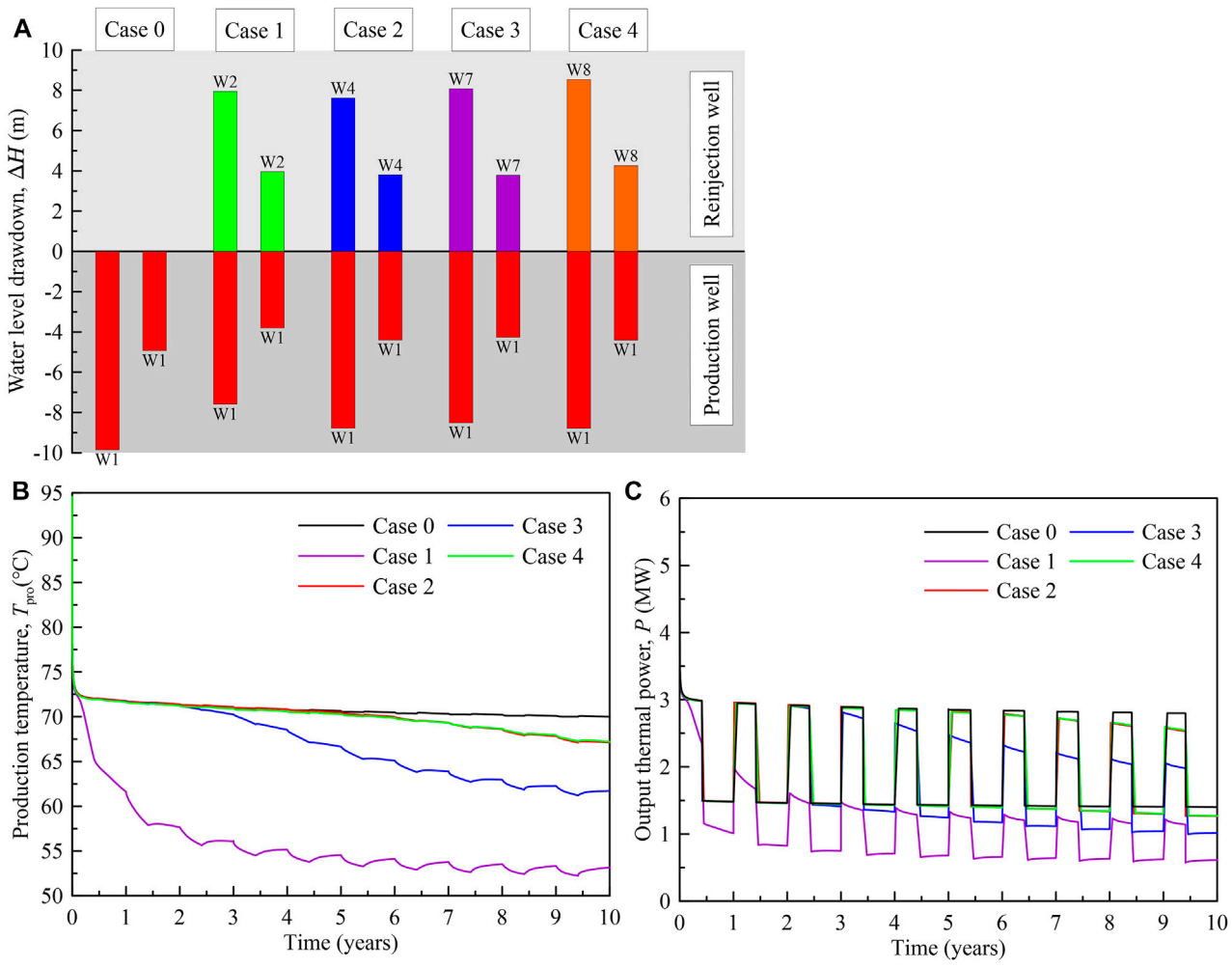

FIGURE 4 | (A) Water level drawdown of the production and reinjection wells, **(B)** the production temperature, and **(C)** the output thermal power for different well distances of the single doublet well system. The Case 0 (production-only) was added for comparison.

The production temperature rapidly decreased from 94.6°C to 73.1°C in the initial 20 days of the first heating season (**Figure 3A**). The initial rapid decrease in the production temperature is attributed to the mix of hot water from different depths around the production well. The production temperature then decreased gradually for the rest of the production period. The production temperature recovered slightly when entering the non-heating season and decreased slightly when entering the heating season. After 10 years of heat extraction, the production temperature decreased to 70°C.

The output thermal power of W1 decreased rapidly in the first 20 days of the first heating season (**Figure 3B**) from 5.1 to 3.1 MW and decreased gradually for the rest of the heating season. In the first non-heating season, the output thermal power dropped to 1.5 MW due to the halved production rate. After 10 years of heat extraction, the output thermal power dropped to 2.8 and 1.4 MW, respectively, for the heating and non-heating seasons.

4.2 Single Doublet Well System

By employing 100% reinjection, the heat production in a single doublet well system caused both a decrease in the water level in the production well and an increase in the water level in the reinjection well (**Figure 4A**). Furthermore, as supported by **Figure 4A** and **Figure 3**, the water level drawdowns of the production well for the single doublet well system were less than that for the single depressurization without reinjection. Therefore, reinjection is conducive for controlling water level drawdown due to a part of the reinjected water flowing toward the production well (**Figure 5A**) and the increased hydraulic communication between wells. Water level drawdown of production well W1 was inversely proportional to the distance of the reinjection well (**Figure 4A**). While the draw up of the water level of the reinjection well was not only related to the well distance but also to the length of the openhole. An increase in the well distance lead to a decrease in hydraulic communication; the same recharge rate in a farther reinjection well will cause a larger increment in the water level. By contrast, an increase in the openhole length meant an increase in the section area for water transport and lead to a reduction of the draw up (Case 2 in **Figure 4A**). The 100% reinjection helped counteract 10–20% water level drawdown compared with the production-only.

As shown in **Figure 4B**, the variation of the production temperature indicated that the reinjection of cold water by a single doublet well system caused the thermal breakthrough, i.e., a decrease in the production temperature (**Figure 5A**). The reinjection well location plays a significant role in controlling the critical time and the degree of thermal breakthrough at the production wells. A larger well distance significantly inhibits early thermal breakthrough at the production well, and vice versa. This is mainly affected by the heating of water flowing

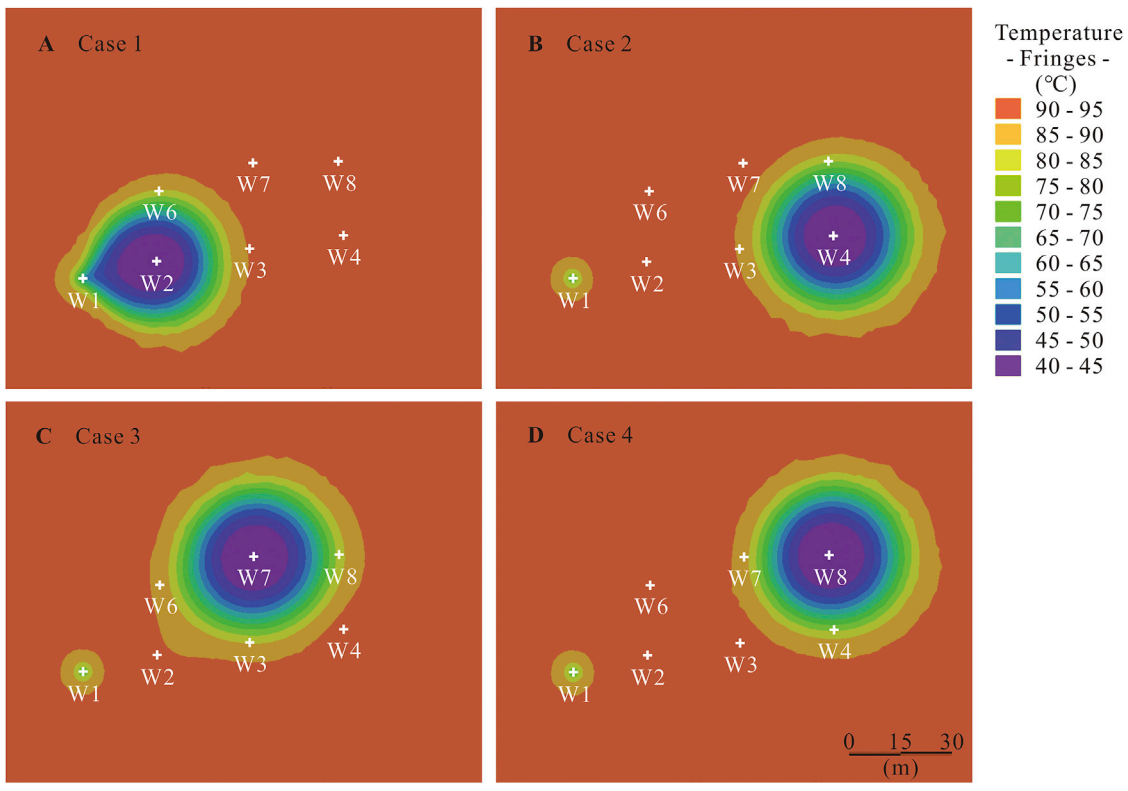

FIGURE 5 | Effect of the well distance on temperature distribution (at a depth of 160 m) for the single doublet well systems after 1 year of production. **(A)** Case 1, **(B)** Case 2, **(C)** Case 3, and **(D)** Case 4.

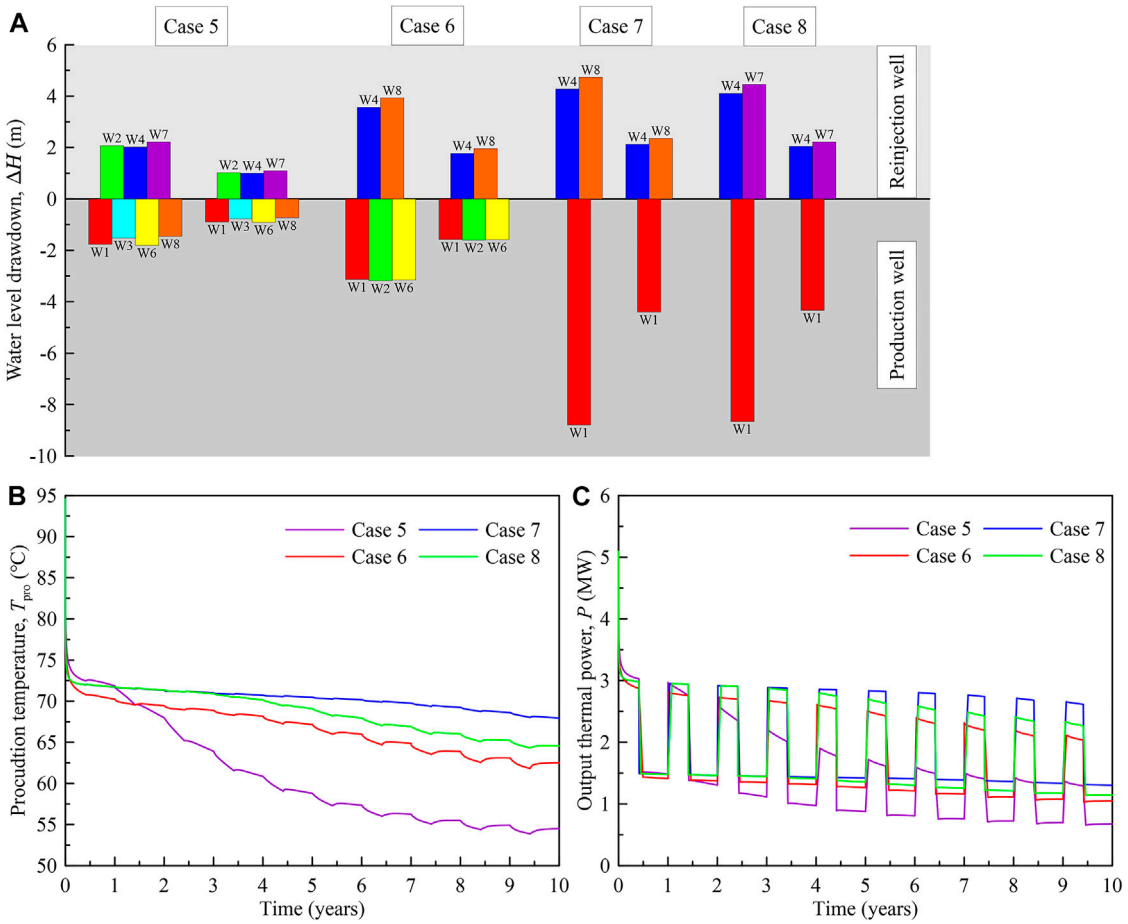

FIGURE 6 | (A) Water level drawdown, **(B)** production temperature, and **(C)** output thermal power of different multi-well systems in the heating and non-heating seasons.

through the reservoir and the mixing of cold and hot water at the production well. For Case 2, with a small well distance, cold water was quickly transported to the production well and had insufficient heating time. As a result, the production temperature highly decreased during the first heating season. Although the decrease in the production temperature was mitigated during the non-heating season, the production temperature quickly decreased again in the next heating season. The thermal breakthrough after 1 year is clearly shown in **Figure 5A**. However, 1-year reinjection with a larger well distance did not cause thermal breakthrough (**Figures 5B–D**). The production temperature of Case 2 gradually became stable as production proceeded and decreased to about 53°C (**Figure 4B**), indicating a stable hydraulic communication between wells and a mix of cold and hot water at the production well. The thermal breakthrough for Cases 2–4 occurred subsequently. The production temperature for the scenarios with similar well distances exhibited concordance. With a more significant well distance, continued reinjection would result in a longer lifetime of the geothermal reservoir but have a smaller influence on the water level. The water level drawdown and production temperature should be balanced.

The output thermal power is shown in **Figure 4C**. The output thermal power before thermal breakthrough exhibited a stable state. Once thermal breakthrough occurred, however, the thermal power generally decreased during the heating season and stabilized during the non-heating season. For the doublet well system, the performance of Case 4 was the best. After 10 years, the output thermal power of Case 4 dropped to 2.54 and 1.27 MW, respectively, for the heating and non-heating seasons (**Figure 4C**). In current drilled wells, a doublet well system with a larger well distance is favorable for sustainable heat production.

4.3 Multi-Well System

The water level drawdown of the multi-well system is shown in **Figure 6A**. Under the same total production rate, the increase in the number of production and reinjection wells, respectively, means the decrease in the individual production and reinjection rates. Therefore, the absolute water level drawdown for production and reinjection wells

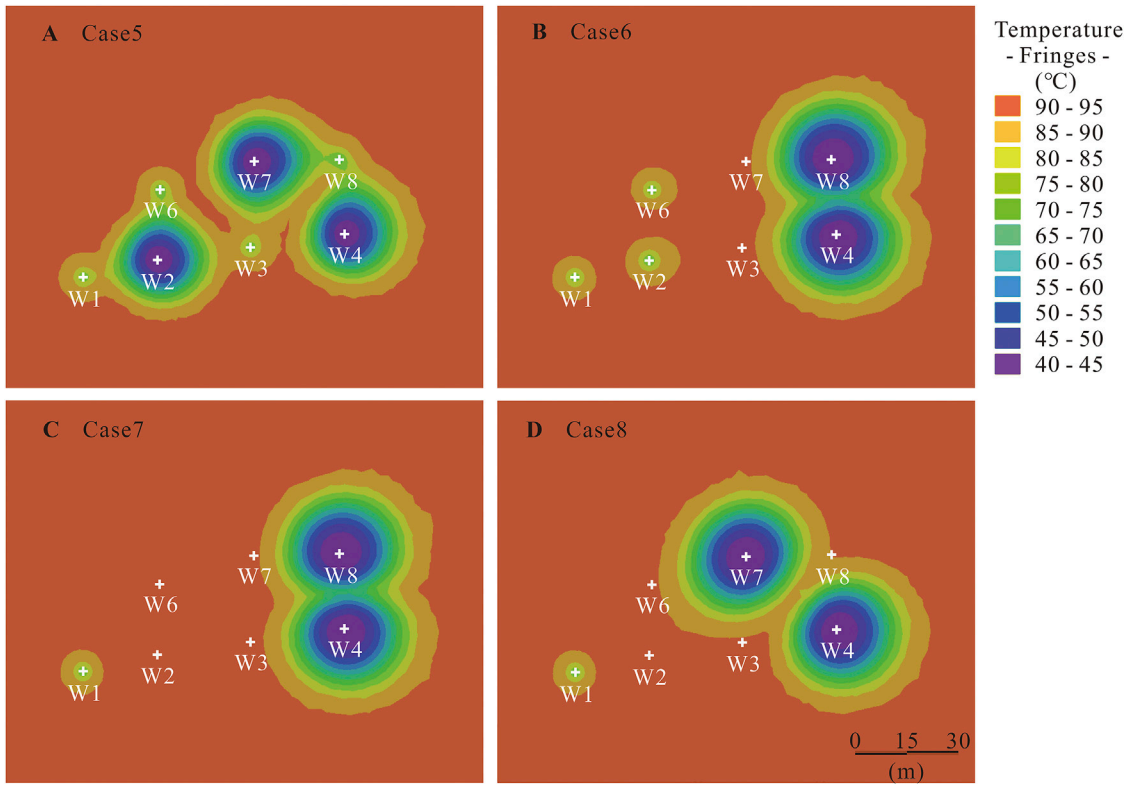

FIGURE 7 | Temperature distribution of different multi-well systems after 1 year of production (at a depth of 160 m). **(A)** Case 5, **(B)** Case 6, **(C)** Case 7, and **(D)** Case 8.

decreased. The differences in the absolute water level drawdown were attributed to the combined effect of well distance, length of openhole section, and interference between the wells. For a multi-well system with one production well (Cases 7 and 8), the water level drawdown of the production well was similar to that of Cases 3 and 4 (**Figure 4A**). Therefore, the decrease in the production rate in the production well is the main factor controlling its water level drawdown. From the viewpoint of controlling water level drawdown, the employment of a multi-well system, by employing more production and reinjection wells, actually facilitates the control of the water level. However, the investment increases with the number of wells. The heat production performance is also needed to be evaluated.

As shown in **Figure 6B**, in the first year, the production temperature and output thermal power of Case 5 were the highest, while they began to decline rapidly in the second year. This is because the four production and three reinjection wells of Case 5 were arranged in a crossway. The bottom of the openhole section of production well W3 had a deep depth, the production of high-temperature water induced the increase in the production temperature. However, due to the narrow spacing between production and reinjection wells, a thermal breakthrough occurred early in all production and reinjection wells (**Figure 7A**), resulting in unsustainable production of high-temperature water. The output thermal power of the heating season decreased over time, as a response to the decreased production temperature. The output thermal power of the early non-heating season decreased and gradually stabilized in the later non-heating season. The output thermal power decreased to half of its initial value.

During the first year of production, the production temperature of Case 6 was lower than that of the other cases. This is due to the production of low-temperature water of production well W6, which had a shallow well depth of 160 m. The mix of low-temperature water resulted in a low overall production temperature. The output thermal power was shown a decreased state in the heating season and remained stable in the non-heating season. Therefore, W6 as a production well was unsuitable for heat production.

Case 8 represents the actual operation scenario. In the first 4 years, the production temperature and output thermal power were basically stable. However, after 5 years, the production temperature and output thermal power began to decrease rapidly. The output thermal power decreased when the thermal breakthrough occurred, whereas this was constant during the non-heating season.

Among the four scenarios of a multi-well system, the performance of Case 7 was the best. The production temperature after 10 years decreased to 67.95°C, and the

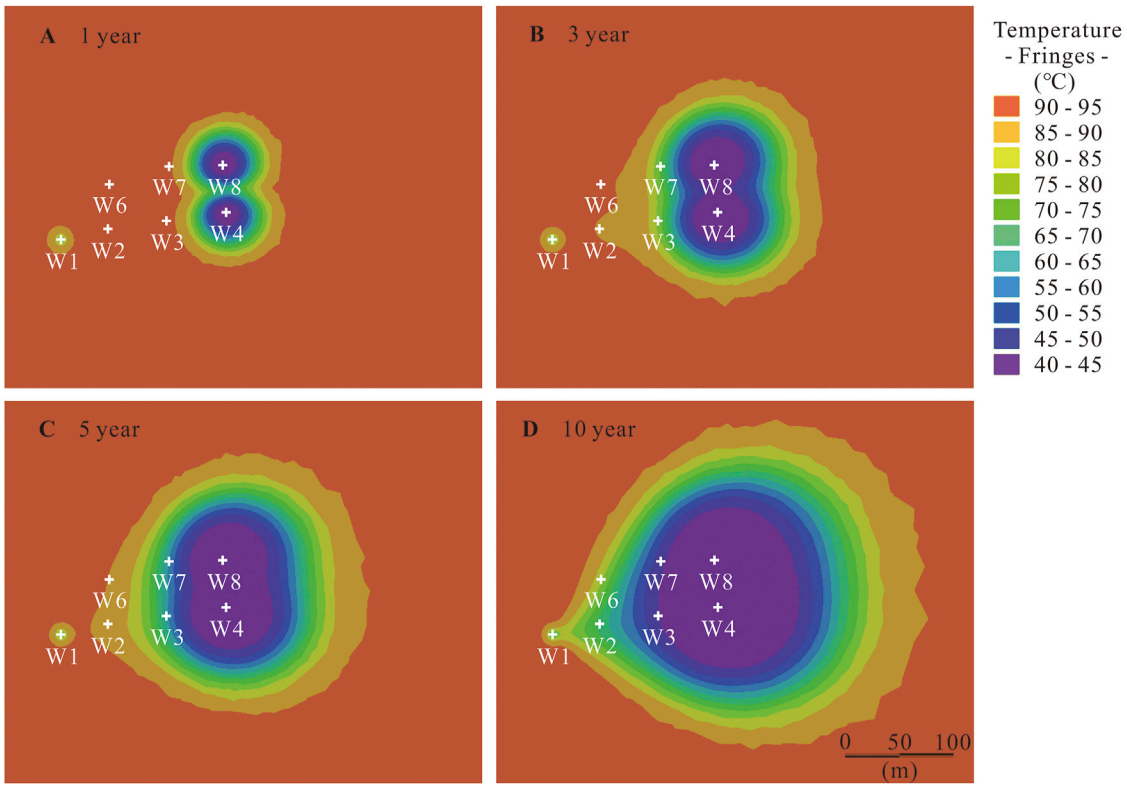

FIGURE 8 | Temperature distribution evolution of Case 7 during 10 years (at a depth of 160 m). **(A)** 1 year**, (B)** 3 years, **(C)** 5 years, and **(D)** 10 years.

output thermal power dropped to 2.6 and 1.3 MW, respectively, for the heating and non-heating seasons (**Figure 6C**).

Figure 7 shows the temperature distribution after 1 year for the multi-well system. The temperature distribution in **Figure 7A** indicated clearly that some injected cold water had been transported into the production well. The injected water in W2 tended to flow into W1, W3, and W6. The injected water in W7 tended to flow into W3 and W8. The injected water in W4 tended to flow into W8. However, for a multi-well system (Cases 6–8) with a more considerable distance between the production and reinjection wells, the temperature after 1 year indicated that there was no thermal breakthrough. A more considerable distance between the production and reinjection wells was also conducive for sustainable heat production. Furthermore, some interferences occurred between the reinjection wells; this jointly drove the cold water flow toward the production well. With continuous reinjection of cold water for Case 7, as shown in **Figure 8**, the injected cold water flowed toward both sides. A front of injected cold water began to form after 3 years. The front increased over time, and the heating effect was significant where it was close to the production well.

4.4 Sensitivity to Different Operation Strategies

The sensitivity of heat production performance to different operation strategies was further discussed based on the scenario of Case 7. The detailed parameters were openhole length, production rate, and reinjection temperature.

4.4.1 Openhole Length

The effect of the openhole length was investigated by changing the starting depth of the openhole of W1 of the reference scenario (Case 7, with openhole starting depth of −30 m). The investigated openhole lengths were 142, 132, 112, and 92 m, which corresponds, respectively, to the starting depth of −30, −40, −60, and −80 m. As shown in **Figure 9A**, the decrease in openhole length led to a decrease in the discharge area between the well and reservoir. Therefore, the pressure gradient increased in order to afford the same discharge rate. As a result, the water level dropped more with respect to the initial water level. Water level drawdown for the short openhole increased (**Figure 9A**) in both the heating and non-heating seasons.

The production temperature increased with a decrease in the openhole length of the production well (**Figure 9B**). This was because of a decrease in the openhole length in the study, meaning the starting depth of the openhole was deep. Therefore, water with high temperature easily discharged from the deep parts of the geothermal reservoir. The openhole length highly affects the production temperature, while affecting the critical time of thermal breakthrough less. A short openhole allocated in the deep parts of the reservoir

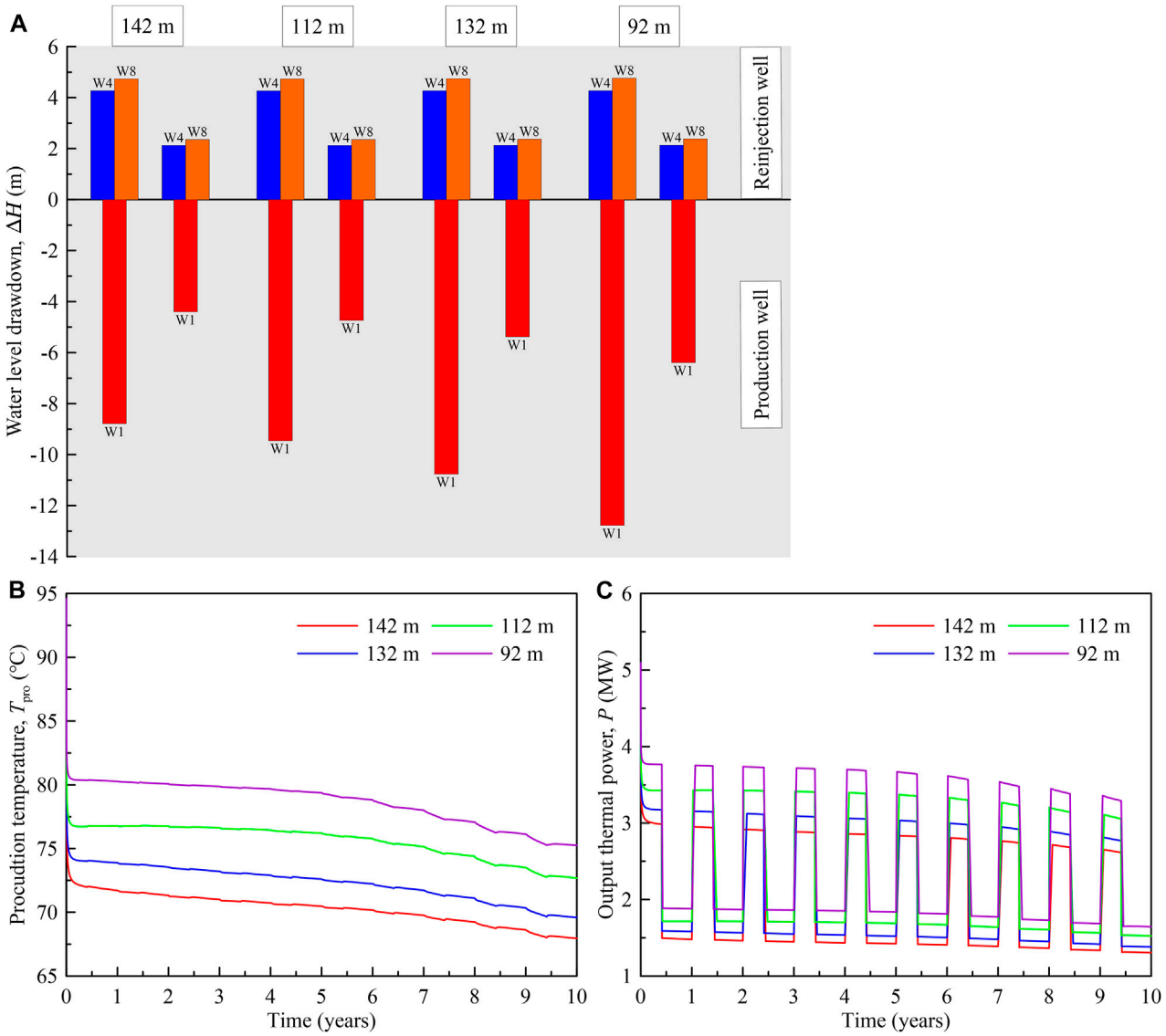

FIGURE 9 | Effect of openhole length of the production well on **(A)** water level drawdown, **(B)** the production temperature, and **(C)** the output thermal power.

facilitates the production temperature, while inducing unfavorable water level drawdown. Thus, the openhole length appears to be a key parameter in the hydraulic and thermal behaviors of the geothermal well system. The output thermal power for different openhole lengths changed similarly in both the heating and non-heating seasons. When the openhole length decreased from 142 to 92 m, the output thermal power was evaluated to increase by 23% (**Figure 9C**).

4.4.2 Production Rate

Under constant reinjection temperature, the increase in production/reinjection rates directly stimulates a more significant hydraulic gradient, which causes a decrease in the water level of the production well and an increase in the water level of the reinjection well (**Figure 10A**). By increasing the production rate from 80 to 160 m^3/h, the water level drawdown of production well W1 increased twofold from −8.8 to −17.6 m. Similar increments were also observed for the water level draw up of the reinjection wells (**Figure 10A**).

The production temperature changed similarly before the thermal breakthrough (**Figure 10B**). Naturally, the flowing time for water particles from the reinjection well to the production well is inversely proportional to the production/reinjection rates. A high production rate induced an advanced occurrence of thermal breakthrough, which is due to the increased hydraulic gradient driving a high flow rate of cold water. After thermal breakthrough, the mix of large amounts of

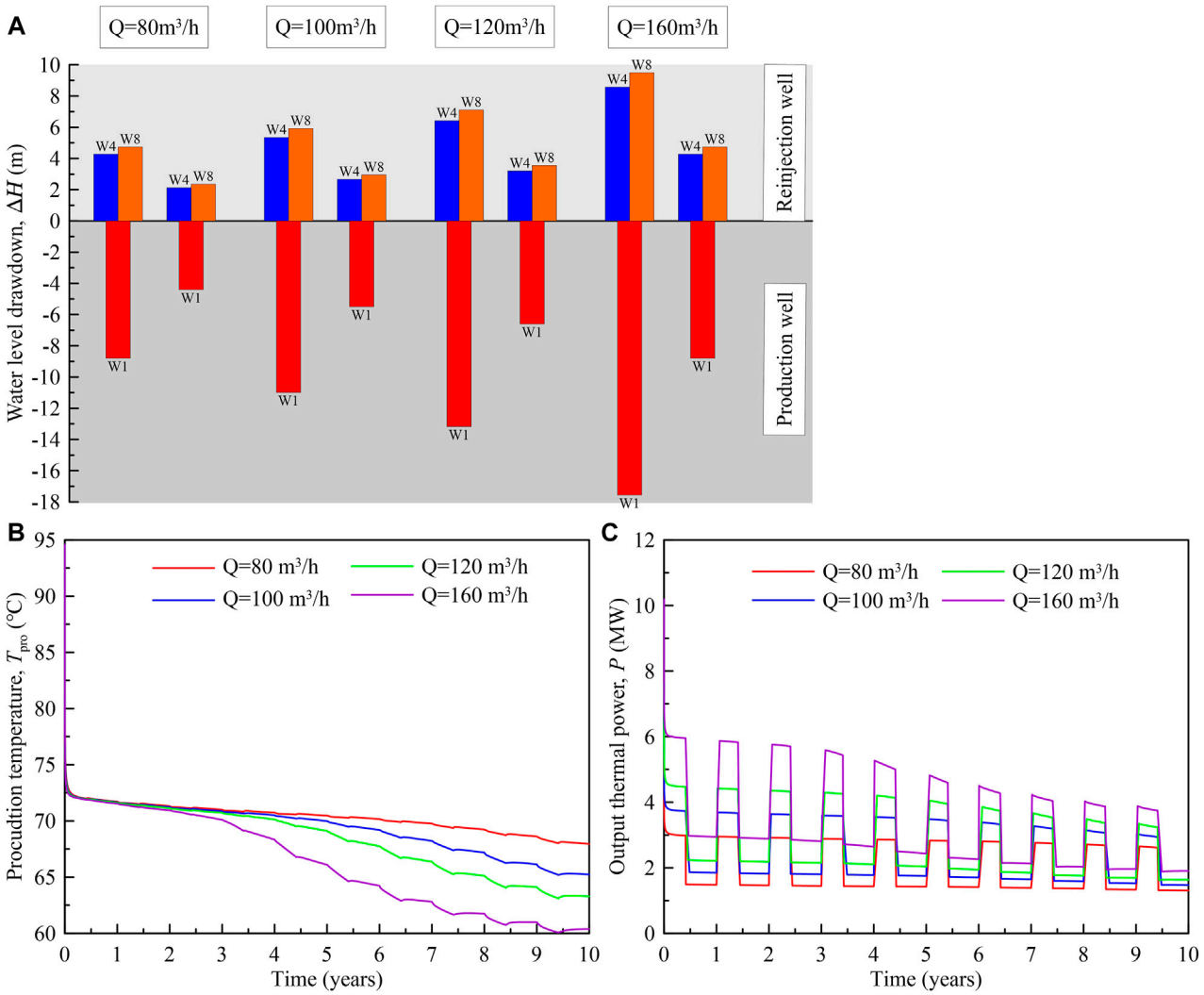

FIGURE 10 | Effect of the production rate on **(A)** water level drawdown, **(B)** the production temperature, and **(C)** the output thermal power.

insufficiently heating water induced a decrease in the production temperature. The increase in the production rate shortened the lifetime of a geothermal operation by causing early thermal breakthrough at the production well. Therefore, production temperatures after 10 years decreased with an increase in the production rate.

An increase in the production rates directly induced a high increase in output thermal power (**Figure 10C**) in the early stage. After thermal breakthrough, however, the output thermal power in the heating season decreased. The difference in output thermal power between the different production rates decreased over time, for both the heating and non-heating seasons.

4.4.3 Reinjection Temperature

By decreasing the reinjection temperature, the production temperature changed little in the early stage, while a minor difference between the different scenarios occurred in a later stage (**Figure 11**). Water level drawdowns were similar because of the unchanged production and reinjection rates and are not plotted here. Under a constant production rate, the change in reinjection temperature implied a variation of the output thermal power. The reduction in reinjection temperature from 40°C to 25°C was equivalent to the increasing line source thermal injection by 37.5%. Although a difference (<0.95°C) in the production temperatures after 10 years was observed for T_{reinj} = 40°C and 25°C, and the output thermal power in the heating season significantly increased from 3.1 MW for T_{reinj} = 40°C to 4.3 MW for T_{reinj} = 25°C.

The influence of different reinjection temperatures on the model was acceptable; the reinjection can be carried out after geothermal cascade utilization. In order to maintain sustainability of heat production and make full use of the geothermal reservoir,

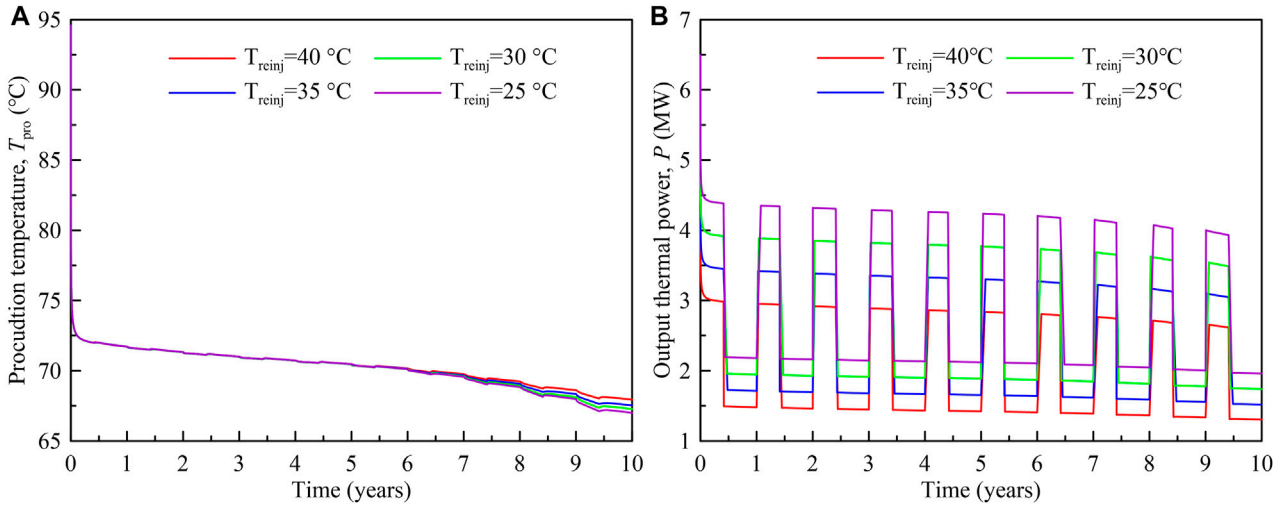

FIGURE 11 | Effect of reinjection temperature on **(A)** production temperature and **(B)** output thermal power.

the reinjection can be carried out with a water temperature between 40°C and 25°C.

5 CONCLUSION

The performance of multi-well production and reinjection strategies in a small-scale shallow geothermal reservoir was studied numerically based on the available data from the Houhaoyao geothermal field. By characterizing well placement and validating against pumping test, scenarios including single production, the single doublet system, and the multi-well system were compared. The response of the water level and production temperature was mainly discussed. The following conclusions can be drawn from this study:

1. Production without reinjection induces the highest production temperature and also the water level drawdown. The production temperature slightly decreases except for the first heating season. After 10 years, the production temperature of production-only decreased to 70°C.

2. Reinjection through the single doublet well system can alleviate drawdown of the water level while inducing a decrease of the production temperature to some extent. Well spacing significantly affects thermal breakthrough, especially for small-scale fields. Increasing the spacing between the production and reinjection wells can delay the critical time of thermal breakthrough and lengthen the lifetime of the geothermal field.

3. The employment of a multi-well system is conducive to controlling water level drawdown by designating a low rate to individual production/reinjection wells. However, interference and thermal breakthrough in the small-scale site occur quickly. Large spacing between the production and reinjection wells is also the basic principle for designing of multi-well systems.

4. A decrease in the openhole length leads to an increase in the production temperature and output thermal power. An increase in the production rate affects the thermal breakthrough highly and shortens the lifetime of the geothermal system. A reduction in the reinjection temperature affects the production temperature less, while affecting the output thermal power significantly. Reinjection can be carried out after geothermal cascade utilization at a temperature between 40°C and 25°C.

Here, we mainly discuss the possibility of the enhancement of heat exploitation by production–reinjection strategy. The feasibility of injectivity and possible land subsidence caused by water level drawdown is beyond the scope of this study. In future works, the numerical simulation will be refined by the long-term production–reinjection operation data. Meanwhile, land subsidence is needed further to analyze the effect of heat production on the stability of surface building.

DATA AVAILABILITY STATEMENT

The original contributions presented in the study are included in the article/Supplementary Material; further inquiries can be directed to the corresponding authors.

AUTHOR CONTRIBUTIONS

WY: conceptualization, methodology, data curation, and writing—original draft. DZ: investigation, resources, and formal analysis. YZ: investigation and validation. JG: investigation, data curation, and visualization. TL: investigation and validation. HZ: conceptualization, methodology, visualization, and writing—review and editing. GJ: conceptualization, supervision, and writing—review and editing. GW: supervision, investigation, and validation. BZ: investigation and validation. All authors have read and agreed to the published version of the manuscript.

FUNDING

This work was jointly supported by the National Geological Survey Project (Grant Numbers: DD20190129 and DD20190234), the National Natural Science Foundation of China (Grant Numbers: 42102289 and 42102302), the Open Foundation of Key Laboratory of Natural Gas Hydrate, CAS (Grant Number: E0290206), the Guangdong Basic and Applied Basic Research Foundation (Grant Number: 2020A1515110244), and the PetroChina Innovation Foundation (Grant Number: 2020D-5007-0212).

ACKNOWLEDGMENTS

We thank Jiwei Hou, the engineer of Aolin Spring Town, for offering the system operation information of the geothermal system.

REFERENCES

Babaei, M., and Nick, H. M. (2019). Performance of Low-Enthalpy Geothermal Systems: Interplay of Spatially Correlated Heterogeneity and Well-Doublet Spacings. *Appl. Energ.* 253, 113569. doi:10.1016/j.apenergy.2019.113569

Crooijmans, R. A., Willems, C. J. L., Nick, H. M., and Bruhn, D. F. (2016). The Influence of Facies Heterogeneity on the Doublet Performance in Low-Enthalpy Geothermal Sedimentary Reservoirs. *Geothermics* 64, 209–219. doi:10.1016/j.geothermics.2016.06.004

Cui, R. Y., Hultman, N., Cui, D., Mcjeon, H., Yu, S., Edwards, M. R., et al. (2021). A Plant-By-Plant Strategy for High-Ambition Coal Power Phaseout in China. *Nat. Commun.* 12, 1468. doi:10.1038/s41467-021-21786-0

Diersch, H.-J. (2014). *FEFLOW: Finite Element Modeling of Flow, Mass and Heat Transport in Porous and Fractured Media*. Berlin Heidelberg: Springer-Verlag.

Fanwen, M., Jiangtao, H., Wenyu, L., and Lijia, L. (2021). Magmatic Geothermal Genesis Model in the Huailai Area Based on the Constraints of the Crust-Mantle-Scale Geoelectric Structure. *Appl. Sci.* 11, 2086. doi:10.3390/app11052086

Franco, A., and Vaccaro, M. (2014). Numerical Simulation of Geothermal Reservoirs for the Sustainable Design of Energy Plants: A Review. *Renew. Sust. Energ. Rev.* 30, 987–1002. doi:10.1016/j.rser.2013.11.041

Hu, Z., Xu, T., Feng, B., Yuan, Y., Li, F., Feng, G., et al. (2020). Thermal and Fluid Processes in a Closed-Loop Geothermal System Using CO2 as a Working Fluid. *Renew. Energ.* 154, 351–367. doi:10.1016/j.renene.2020.02.096

Huo, A., Wang, X., Lyu, Y., Cheng, Y., Zheng, C., and Song, J. (2019). Simulation Research on the Reinjection Temperature fields of Deep Geothermal wells Based on Real-Scale experiment. *Energy Exploration & Exploitation* 37, 646–662. doi:10.1177/0144598718807556

Kamila, Z., Kaya, E., and Zarrouk, S. J. (2021). Reinjection in Geothermal fields: An Updated Worldwide Review 2020. *Geothermics* 89, 101970. doi:10.1016/j.geothermics.2020.101970

Kong, Y. (2017). Optimization of Well-Doublet Placement in Geothermal Reservoirs Using Numerical Simulation and Economic Analysis. *Environ. Earth Sci.* 7. doi:10.1007/s12665-017-6404-4

Kong, Y., Pang, Z., Pang, J., Li, J., Lyu, M., and Pan, S. (2020). Fault-Affected Fluid Circulation Revealed by Hydrochemistry and Isotopes in a Large-Scale Utilized Geothermal Reservoir. *Geofluids* 2020, 1–13. doi:10.1155/2020/2604025

Le Lous, M., Larroque, F., Dupuy, A., Moignard, A., and Damy, P.-C. (2018). Performance of an Open-Loop Well-Doublet Scheme Located in a Deep Aquitard-Aquifer System: Insights from a Synthetic Coupled Heat and Flow Model. *Geothermics* 74, 74–91. doi:10.1016/j.geothermics.2018.02.008

Liu, G., Wang, G., Zhao, Z., and Ma, F. (2020). A New Well Pattern of Cluster-Layout for Deep Geothermal Reservoirs: Case Study from the Dezhou Geothermal Field, China. *Renew. Energ.* 155, 484–499. doi:10.1016/j.renene.2020.03.156

Mallapaty, S. (2020). How China Could Be Carbon Neutral by Mid-century. *Nature* 586, 482–483. doi:10.1038/d41586-020-02927-9

Markó, Á., Mádl-Szőnyi, J., and Brehme, M. (2021). Injection Related Issues of a Doublet System in a sandstone Aquifer - A Generalized Concept to Understand and Avoid Problem Sources in Geothermal Systems. *Geothermics* 97, 102234.

Rivera Diaz, A., Kaya, E., and Zarrouk, S. J. (2016). Reinjection in Geothermal fields – A Worldwide Review Update. *Renew. Sust. Energ. Rev.* 53, 105–162. doi:10.1016/j.rser.2015.07.151

Su, Y., Yang, F., Wang, B., Jia, Z., and Duan, Z. (2018). Reinjection of Cooled Water into sandstone Geothermal Reservoirs in China: a Review. *Geosci. J.* 22, 199–207. doi:10.1007/s12303-017-0019-3

Wang, Y. (2010). *A Study of Characteristics and Models for Spring Discharge and Temperature of Low-To-Moderate Thermal Springs in Beijing and Northern Hebei*. Beijing: China University of Geoscience.

Willems, C. J. L., and Nick, H. M. (2019). Towards Optimisation of Geothermal Heat Recovery: An Example from the West Netherlands Basin. *Appl. Energ.* 247, 582–593. doi:10.1016/j.apenergy.2019.04.083

Yang, Z., Xu, T., Wang, F., Yang, Y., Li, X., and Zhao, N. (2018). Impact of Inner Reservoir Faults on Migration and Storage of Injected CO2. *Int. J. Greenhouse Gas Control.* 72, 14–25. doi:10.1016/j.ijggc.2018.03.006

Yuan, Y., Xu, T., Jiang, Z., and Feng, B. (2021). Prospects of Power Generation from the Deep Fractured Geothermal Reservoir Using a Novel Vertical Well System in the Yangbajing Geothermal Field, China. *Energ. Rep.* 7, 4733–4746. doi:10.1016/j.egyr.2021.07.069

Zhang, C., Jiang, G., Jia, X., Li, S., Zhang, S., Hu, D., et al. (2019a). Parametric Study of the Production Performance of an Enhanced Geothermal System: A Case Study at the Qiabuqia Geothermal Area, Northeast Tibetan Plateau. *Renew. Energ.* 132, 959–978. doi:10.1016/j.renene.2018.08.061

Zhang, S., Jiang, Z., Zhang, S., Zhang, Q., and Feng, G. (2021). Well Placement Optimization for Large-Scale Geothermal Energy Exploitation Considering Nature Hydro-thermal Processes in the Gonghe Basin, China. *J. Clean. Prod.* 317, 128391. doi:10.1016/j.jclepro.2021.128391

Zhang, W., Qu, Z., Guo, T., and Wang, Z. (2019b). Study of the Enhanced Geothermal System (EGS) Heat Mining from Variably Fractured Hot Dry Rock under thermal Stress. *Renew. Energ.* 143, 855–871. doi:10.1016/j.renene.2019.05.054

Conflict of Interest: The authors declare that the research was conducted in the absence of any commercial or financial relationships that could be construed as a potential conflict of interest.

Publisher's Note: All claims expressed in this article are solely those of the authors and do not necessarily represent those of their affiliated organizations, or those of the publisher, the editors, and the reviewers. Any product that may be evaluated in this article, or claim that may be made by its manufacturer, is not guaranteed or endorsed by the publisher.

frontiers in Earth Science

ORIGINAL RESEARCH
published: 24 December 2021
doi: 10.3389/feart.2021.782943

Genesis of the Xifeng Low-Temperature Geothermal Field, Guizhou, SW China: Constrains From Geology, Element Geochemistry, and D-O Isotopes

Yanyan Li[1,2], Ji Dor[3,4], Chengjiang Zhang[3], Guiling Wang[1,2], Baojian Zhang[1,2], Fangfang Zhang[5] and Yifei Xing[1,2]*

[1]Chinese Academy of Geological Sciences, Beijing, China, [2]MNR Laboratory of Deep Geosciences and Exploration Technology, Chinese Academy of Geological Sciences, Beijing, China, [3]College of Earth Science, Chengdu University of Technology, Chengdu, China, [4]Tibet Bureau of Geological Exploration, Lhasa, China, [5]State Key Laboratory of Geological Processes and Mineral Resources, China University of Geosciences, Beijing, China

OPEN ACCESS

Edited by:
Yinhui Zuo, Chengdu University of Technology, China

Reviewed by:
Wei Xu, Xi'an Jiaotong University, China
Xiaoyin Tang, Chinese Academy of Geologi-cal Sciences, China

***Correspondence:**
Yanyan Li
liyanyan@cags.ac.cn

Specialty section:
This article was submitted to Economic Geology, a section of the journal Frontiers in Earth Science

Received: *25 September 2021*
Accepted: *19 November 2021*
Published: *24 December 2021*

Citation:
Li Y, Dor J, Zhang C, Wang G, Zhang B, Zhang F and Xing Y (2021) Genesis of the Xifeng Low-Temperature Geothermal Field, Guizhou, SW China: Constrains From Geology, Element Geochemistry, and D-O Isotopes. Front. Earth Sci. 9:782943. doi: 10.3389/feart.2021.782943

The Xifeng geothermal field is located in the Yangtze Craton, SW China, and is one of the most representative low-temperature geothermal fields in China. Widespread thermal anomalies, hot springs, and geothermal wells have been reported by previous studies. However, the nature and forming mechanisms of the field remain poorly understood. Element geochemical (ions, rare earth elements) and stable isotopic (D, O) composition of hot springs, geothermal fluids, rivers, and cold springs from different locations of the Xifeng geothermal field were analyzed in this study. The ions studies revealed that most samples featured the Ca-Mg-HCO_3 type, except Xifeng hot springs, and which were characterized by the Ca-Mg-HCO_3-SO_4 type. Based on quartz geothermometers, the estimated reservoir temperature was 77°C. The results of stable isotopes (D, O) manifest that the Xifeng geothermal system was recharged by meteoric water at an elevation of 1,583 m from SW to NE. The research of rare earth elements (REE) revealed that their accumulation characteristics and obvious positive Eu anomaly were inherited from host feldspar-bearing reservoir dolomites through water-rock interactions. Combined with these observations, geological setting, and previous studies, it was concluded that the formation of the Xifeng geothermal field resulted from recharge, deep circulation, and secondary rising of the meteoric water along the faults. First, meteoric water infiltrated to depth through faults and crack zones. Second, the deep-infiltrated water was heated by radioactive heat, deep heat, and tectonic frictional heat. Finally, as the warmed-up waters underwent considerable deep circulation in the reservoir, it rose again along the main faults, and mixed with groundwater near the surface. Taken together, we suggest that the Xifeng geothermal system should be assigned as a faults-controlling, and deeply circulating meteoric water of low-temperature category.

Keywords: geology, element geochemistry, D-O isotopes, xifeng, SW China

INTRODUCTION

Geothermal resources are well developed in China and contribute significantly to the global supply of total resources (7.9%; Wang G. L. et al., 2017), while they are mainly produced as widespread medium-low temperature types (Wang G. L. et al., 2017; Li and Wang 2015). The occurrence of high-temperature types is limited and mainly formed in South China, e.g., southern Tibet, western Sichuan and Yunnan, as well as the south-east coastal area (Duo, 2003; Guo et al., 2007; Zhang et al., 2016; Guo et al., 2017a, b; Tian et al., 2018; Cheng et al., 2021; Zheng et al., 2021). These distribution characteristics mean that research on geothermal resources in South China mainly focuses on the high-temperature type, whereas studies on the medium-low type are limited.

South China has a significant geothermal potential and hosts many world-famous geothermal fields, including high-temperature Yangbajing, Tengchong, and Kangding, as well as low-temperature Xifeng in Guizhou Province (Guo and Wang, 2012; Guo et al., 2014; Li et al., 2018; Wang et al., 2018; Yang et al., 2018; Wang et al., 2019b; Li J. et al., 2021). There are lots of hot springs, hydrothermal manifestations, and geothermal wells located in the Xifeng geothermal field, indicating great potential for exploration, and utilized prospects (Yang et al., 2018; **Figure 1B**). Although systematic exploration and utilization of Xifeng began in the 1950s, the scientific research on the overall field is poor, and attributed to the single application mode of geothermal resources. In recent years, with the increased need for renewable energy, a new round of exploration work and scientific study has been conducted to

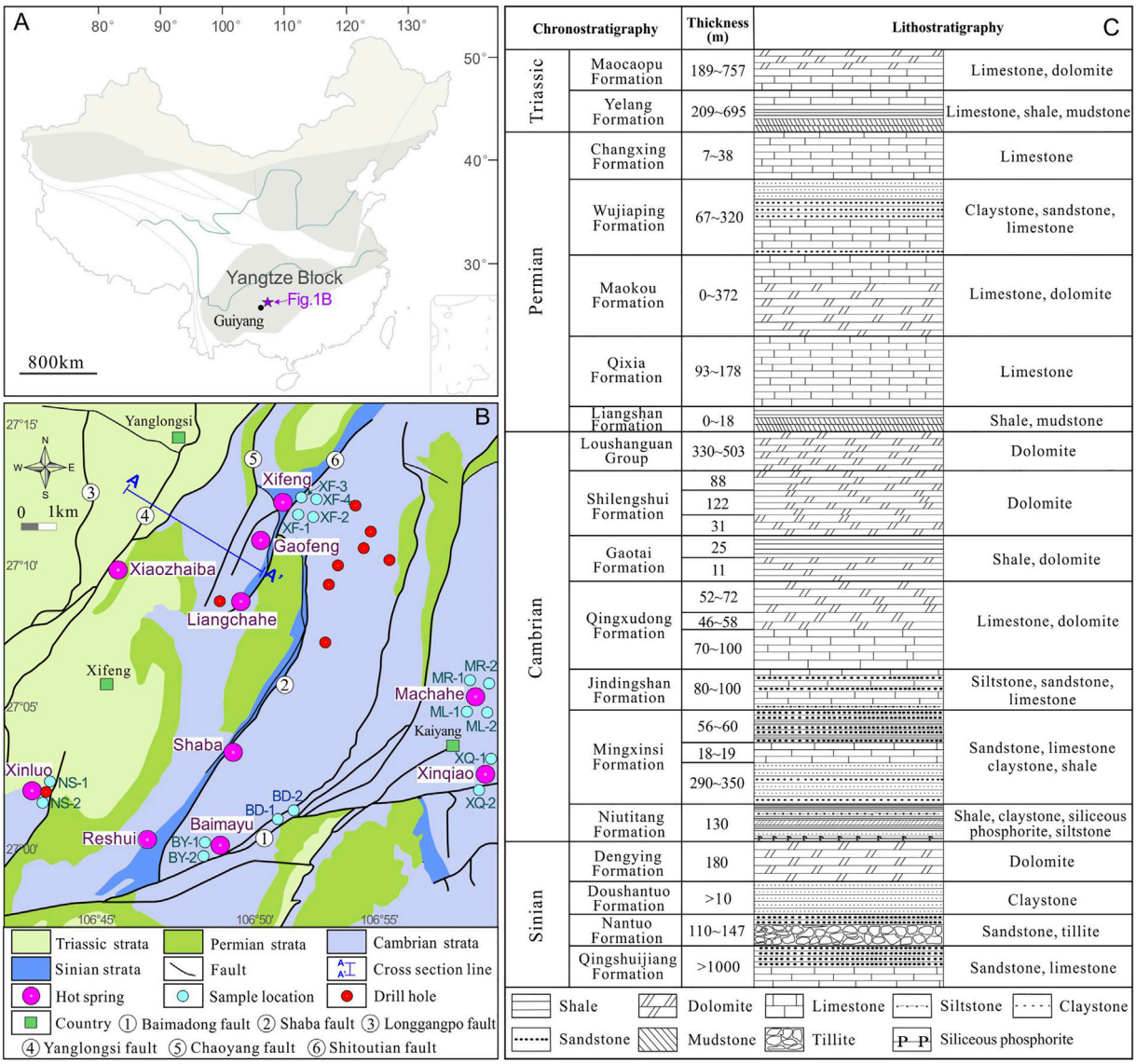

FIGURE 1 | (A) Tectonic framework of China and the location of the study area (modified from Chen et al., 2014). **(B)**. Geological map of the Xifeng geothermal field, showing major tectonic units, faults, and hot springs (modified from Song et al., 2014). **(C)** The stratigraphic column of the Xifeng geothermal field area (modified from Long et al., 2017; Li et al., 2019).

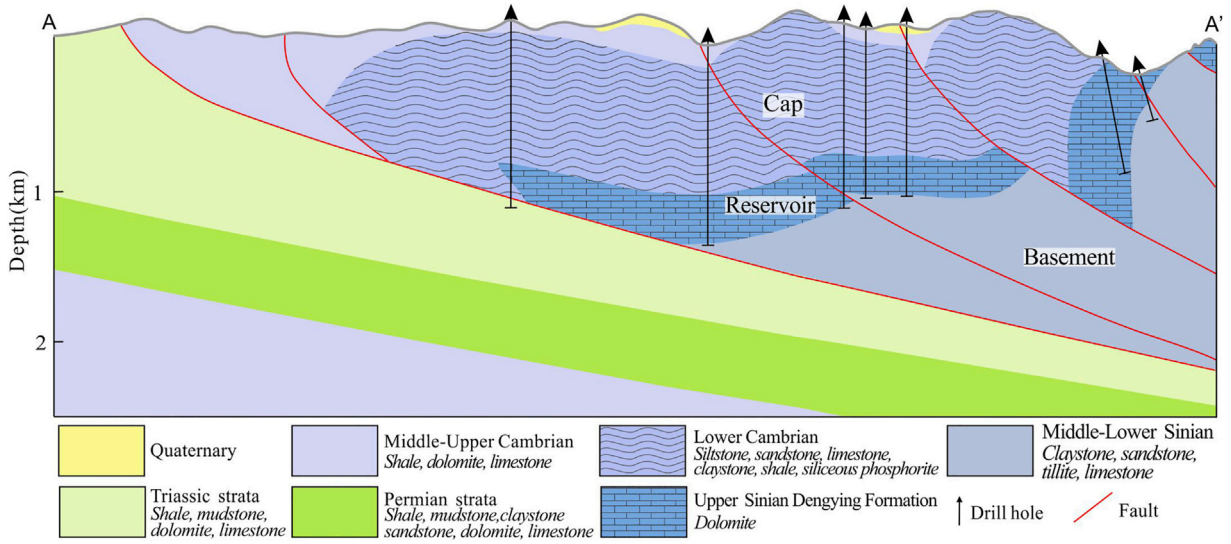

FIGURE 2 | Geological cross-section along section line A-A′ on the map in **Figure 1B** of the Xifeng geothermal field (modified from Wang H. S. et al., 2017; Cai et al., 2018).

TABLE 1 | Geothermometry equations (in°C) for the cation and silica geothermometers used in this study.

Geothermometer	Reference	Equations
Na-K	Fournier, (1979)	$T = 1{,}217/[\log(Na/K)+1.483]-273.15$
Na-K	Truesdell, (1976)	$T = 856/[\log(Na/K)+0.857]-273.15$
Na-K	Giggenbach and Goguel, (1988)	$T = 1{,}390/[\log(Na/K)+1.75]-273.15$
Na-K	Tonani, (1980)	$T = 883/[\log(Na/K)+0.78]-273.15$
Na-K	Nieva and Nieva (1987)	$T = 1{,}178/[\log(Na/K)+1.47]-273.15$
Na-K	Arnórsson, (1983)	$T = 933/[\log(Na/K)+0.993]-273.15$
Na-K	Arnórsson, (1983)	$T = 1{,}319/[\log(Na/K)+1.699]-273.15$
Na-K	Michard et al. (1979)	$T = 908/[\log(Na/K)+0.7]-273.15$
K-Mg	Giggenbach et al. (1983)	$T = 4{,}410/[14-\log(K^2/Mg)]-273.15$
Na-K-Ca	Fournier and Truesdell, (1973)	$T = 1{,}647/\{\log(Na/K)+b[\log(Ca^{1/2}/Na)+2.06]+2.47\}-273.15$, where b = 4/3, if T < 100°C; b = 1/3, if T > 100°C
Quartz, no steam loss (conductive)	Fournier, (1977)	$T = [1{,}309/(5.19-\log SiO_2)]-273.15$
Quartz, maximum steam loss at 100°C (adiabatic)	Fournier, (1977)	$T = [1{,}522/(5.75-\log SiO_2)]-273.15$
Chalcedony (no loss of steam)	Fournier, (1992)	$T = [1{,}032/(4.69-\log SiO_2)]-273.15$
Chalcedony (maximum steam loss)	Fournier, (1977)	$T = [1{,}264/(5.31-\log SiO_2]-273.15$
α-Cristobalite	Fournier, (1977)	$T = [1{,}000/(4.78-\log SiO_2)]-273.15$
β-Cristobalite	Fournier, (1977)	$T = [781/(451-\log SiO_2)]-273.15$

evaluate the potential of hydrothermal resources. Previous studies have focused on single hot springs or geothermal wells mainly based on hydrogeochemistry and geology (Li and Shen, 2014; Song et al., 2014; Cai et al., 2018). However, comprehensive comparative research on respective hot springs, geothermal wells, and related rivers from the whole geothermal field have not been conducted, meaning that the signature, evolution, and forming mechanisms of the Xifeng geothermal field remain obscure.

In this study, representative hot springs, geothermal fluids, cold springs, and related river waters were sampled for detailed element geochemistry (ions, rare earth elements) and stable isotopes (D, O) studies. This new comprehensive dataset allows us to confirm the feature, evolution, and genesis of the geothermal fluids, which will provide a favorable understanding of the forming mechanisms for the Xifeng geothermal field, and similar geothermal fields in South China and worldwide.

GEOLOGICAL TECTONIC AND HYDROGEOLOGICAL SETTINGS

Geological Setting

The Xifeng geothermal field is situated in the central Guizhou Province, southwestern China (**Figure 1A**). The geological

TABLE 2 | Measured parameters, major ion chemistry (mg/L), SiO_2 (mg/L), Rare Earth Element (μg/L), and δD-$\delta^{18}O$ composition of water samples from the Xifeng geothermal field.

Sample NO.	BY-1	BY-2	BD-1	BD-2	MR-1	MR-2	ML-1	ML-2	XQ-1	XQ-2	XF-1	XF-2	XF-3	XF-4	NS-1	NS-2
PH	8.05	7.98	8.06	8.12	8.01	7.92	7.83	7.96	8.19	8.15	8.05	8	8.08	8.05	8.06	8.19
$\delta^{18}O_{V\text{-}SMOW}$(‰)	−7.5	−8.1	−8.2	−8.1	−7.8	−8.3	−7.4	−7	−6.5	−7	−8	−8.5	−8.3	−7.9	−9.2	−8.7
$\delta D_{V\text{-}SMOW}$(‰)	−51.1	−53.7	−54.1	−55.6	−56.2	−57.4	−48.3	−47.9	−45.9	−47.7	−56.3	−59.1	−58.8	−58	−65.6	−65.6
T(°C)	12	12	13	13	43	43	14	14	14	14	56	56	56	56	48	48
K^+	1.2	1.13	2.23	2.17	1.04	1.08	7.96	7.64	2.2	2.16	3.51	3.41	3.56	3.7	3.08	2.98
Na^+	1.86	1.81	4.66	4.71	4.27	4.33	16	15.9	1.67	1.68	11.7	11.8	11.8	12.3	2.29	2.12
Ca^{2+}	34.7	35.1	47.2	49	45.1	44.6	62.1	61.2	57.2	57.3	52.7	52.5	52.8	54.3	36.9	36.9
Mg^{2+}	14.3	14.3	20.2	20.7	26.2	26	25	24.9	19.1	19.3	21.1	20.9	21.1	21.6	22.1	22.1
HCO_3^-	140	141	184	184	245	245	235	235	232	234	169	172	171	170	208	209
SO_4^{2-}	20.5	20.8	39.6	40.4	17.6	16.6	41.5	40.1	16.5	16.6	88.4	91.5	88.3	91.4	10.7	10.4
Cl^-	1.35	1.33	7.02	7.08	0.67	0.654	18.4	18	3.16	3.23	3.07	3.03	3.04	3.11	0.725	0.725
SiO_2	4.68	4.61	6.54	6.58	20.43	20.46	5.89	5.93	6.34	6.23	39.71	39.92	39.85	38.82	15.39	15.79
La	0.01	0.005	0.008	0.005	0.006	0.006	0.013	0.01	0.022	0.018	0.082	0.006	<0.002	<0.002	0.002	0.003
Ce	0.012	0.011	0.013	0.013	0.002	<0.002	0.022	0.024	0.043	0.048	0.097	0.006	0.002	0.005	0.003	0.004
Pr	0.002	0.003	<0.002	0.002	<0.002	<0.002	0.002	0.002	0.006	0.005	<0.002	<0.002	<0.002	<0.002	<0.002	0.002
Nd	0.008	0.003	0.158	0.006	0.011	0.003	0.016	0.008	0.024	0.049	0.002	0.005	0.002	0.004	0.002	0.006
Sm	<0.002	0.003	0.002	0.002	0.004	0.007	0.002	0.004	0.008	0.004	0.002	0.002	<0.002	<0.002	<0.002	0.002
Eu	0.007	0.004	0.004	0.012	0.027	0.03	0.016	0.006	0.005	0.002	<0.002	0.01	0.005	0.016	0.012	0.015
Gd	0.003	0.006	<0.002	0.004	0.002	0.005	0.011	0.013	0.005	0.005	0.003	0.005	<0.002	0.002	0.006	0.003
Tb	<0.002	<0.002	<0.002	<0.002	<0.002	0.007	<0.002	<0.002	<0.002	<0.002	<0.002	<0.002	<0.002	<0.002	<0.002	<0.002
Dy	0.003	<0.002	<0.002	0.003	<0.002	<0.002	0.004	0.002	0.007	<0.002	<0.002	<0.002	<0.002	<0.002	<0.002	0.004
Y	0.022	0.015	0.006	0.011	0.006	0.006	0.018	0.012	0.024	0.031	0.01	0.012	0.008	0.008	0.005	0.006
Ho	<0.002	<0.002	<0.002	<0.002	<0.002	<0.002	<0.002	<0.002	<0.002	0.002	<0.002	<0.002	<0.002	<0.002	<0.002	0.002
Er	0.002	0.005	<0.002	0.002	<0.002	0.002	0.005	<0.002	0.003	<0.002	<0.002	0.002	<0.002	<0.002	<0.002	0.002
Tm	0.002	<0.002	<0.002	<0.002	<0.002	<0.002	<0.002	<0.002	<0.002	<0.002	<0.002	<0.002	<0.002	<0.002	<0.002	<0.002
Yb	0.004	<0.002	0.007	0.002	<0.002	<0.002	<0.002	<0.002	0.002	0.002	<0.002	<0.002	<0.002	<0.002	0.002	0.002
Lu	0.002	<0.002	<0.002	<0.002	<0.002	<0.002	<0.002	<0.002	<0.002	<0.002	<0.002	<0.002	<0.002	<0.002	<0.002	<0.002
Total REE	<0.083	<0.067	<0.214	<0.07	<0.074	<0.08	<0.119	<0.093	<0.157	<0.176	<0.214	<0.062	<0.039	<0.055	<0.048	<0.057
δEu	>13.457	4.440	>9.418	19.978	44.950	23.878	16.063	3.918	3.723	2.106	<3.845	14.891	>11.772	>37.671	>16.312	28.836
δCe	0.619	0.655	>0.750	0.949	>0.133	0.133	0.995	1.238	0.864	1.167	>1.748	>0.400	0.231	0.577	>0.346	0.377
Sample type	River	River	River	River	Hot spring	Hot spring	River	River	Cold spring	Cold spring	Hot spring	Hot spring	Hot spring	Hot spring	Well	Well
Water type	Ca-Mg-HCO_3	Ca-Mg-HCO_3	Ca-Mg-HCO_3	Ca-Mg-HCO_3	Ca-Mg-HCO_3	Ca-Mg-HCO_3	Ca-Mg-HCO_3	Ca-Mg-HCO_3	Ca-Mg-HCO_3	Ca-Mg-HCO_3	Ca-Mg-HCO_3-SO_4	Ca-Mg-HCO_3-SO_4	Ca-Mg-HCO_3-SO_4	Ca-Mg-HCO_3-SO_4	Ca-Mg-HCO_3	Ca-Mg-HCO_3

*Notes: δEu = EuN/sqrt(SmN*GdN); δCe = CeN/sqrt(LaN*PrN); N=Post-Archean Shale normalized; LREE = La + Ce + Pr + Nd + Sm + Eu; HREE = Gd + Tb + Dy + Ho + Er + Tm + Yb + Lu.*

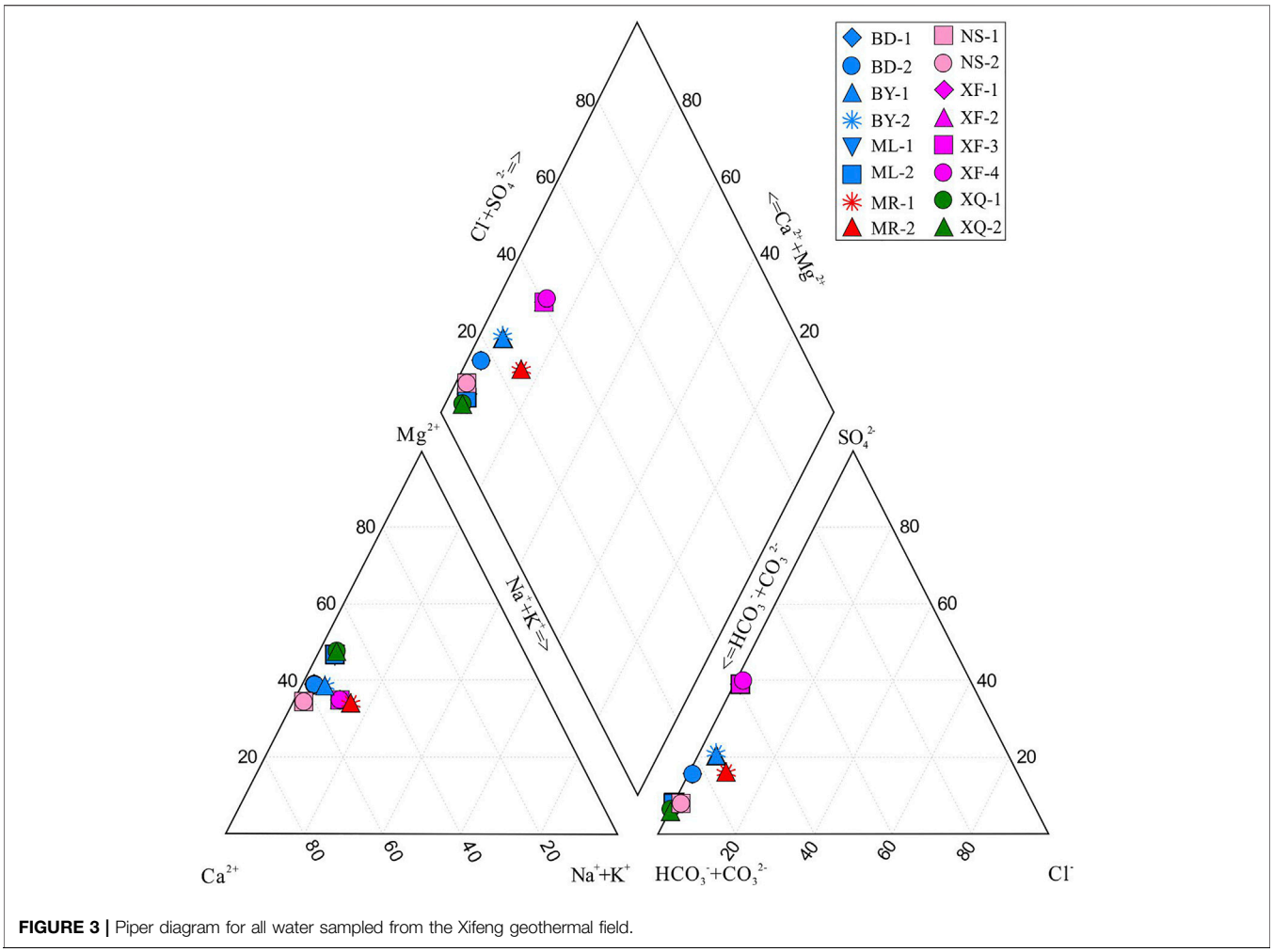

FIGURE 3 | Piper diagram for all water sampled from the Xifeng geothermal field.

location is in the Guiyang Complex Tectonic Deformation Zone related to the central Guizhou uplift within the Yangtze Craton in South China (**Figure 1A**; Ling et al., 2015, 2017; Long et al., 2017; Li et al., 2019, Li Y. Y. et al., 2021). The basement is made of Meso-to Neoproterozoic metamorphosed marine sedimentary rocks. The cover consists of Neoproterozoic (Sinian) to Triassic marine sedimentary rocks and Jurassic terrestrial sedimentary rocks, which underwent multiple Phanerozoic tectono-thermal activities (Li et al., 2019; Li J. et al., 2021).

The stratigraphic succession of the Xifeng geothermal field consists of, from bottom to top, the Sinian Qingshuijiang, Nantuo, Doushantuo, and Dengying formations, lower Cambrian Niutitang, Mingxinsi, Jindingshan, Qingxudong, Gaotai, and Shilengshui formations and Loushanguan Group, Permian Liangshan Qixia, Maokou, Wujiaping, and Changxing formations, and Triassic Yelang and Maocaopu formations (**Figure 1C**; Ling et al., 2015; Long et al., 2017; Li et al., 2019). The Dengying, Qingxudong, Gaotai, and Shilengshui formations and Loushanguan Group are made of carbonates, dominantly dolomite. The Qingshuijiang and Nantuo formations consist of sandstone intercalated with limestone and tillite, respectively. The Doushantuo Formation is made of claystone. The Niutitang Formation is comprised of shale, claystone, siliceous phosphorite, and siltstone, and the Mingxinsi Formation comprises sandstone, limestone, claystone, and shale. The Jindingshan Formation consists of siltstone, sandstone, and limestone. The Permian rocks consist of shale and mudstone (Liangshan Formation), limestone (Qixia and Changxing Formations), dolomite and limestone (Maokou Formation), and claystone, sandstone, and limestone (Wujiaping Formation). The Triassic rocks are made of limestone, shale, and mudstone (Yelang Formation), and carbonate, i.e., limestone and dolomite (Maocaopu Formation) (Ling et al., 2015; Ji, 2015; Long et al., 2018, 2019).

The central Guizhou region experienced a series of tectonic events from Sinian to late Cambrian, such as the Yunan Movement (forming the central Guizhou uplift; Mei et al., 2005; Ling et al., 2015; Long et al., 2017), Duyun and Guangxi Movements (uplifting the central Guizhou; Yu and Wang, 1995; Long et al., 2018), and Dongwu Movement as well as a late Permian Emeishan mantle-plume eruption event (Zhou et al., 2002; He et al., 2005; Jian et al., 2009). These tectonic activities resulted in widespread folding and faulting in the study area, especially the followed Indosinian orogeny, Yanshanian, and

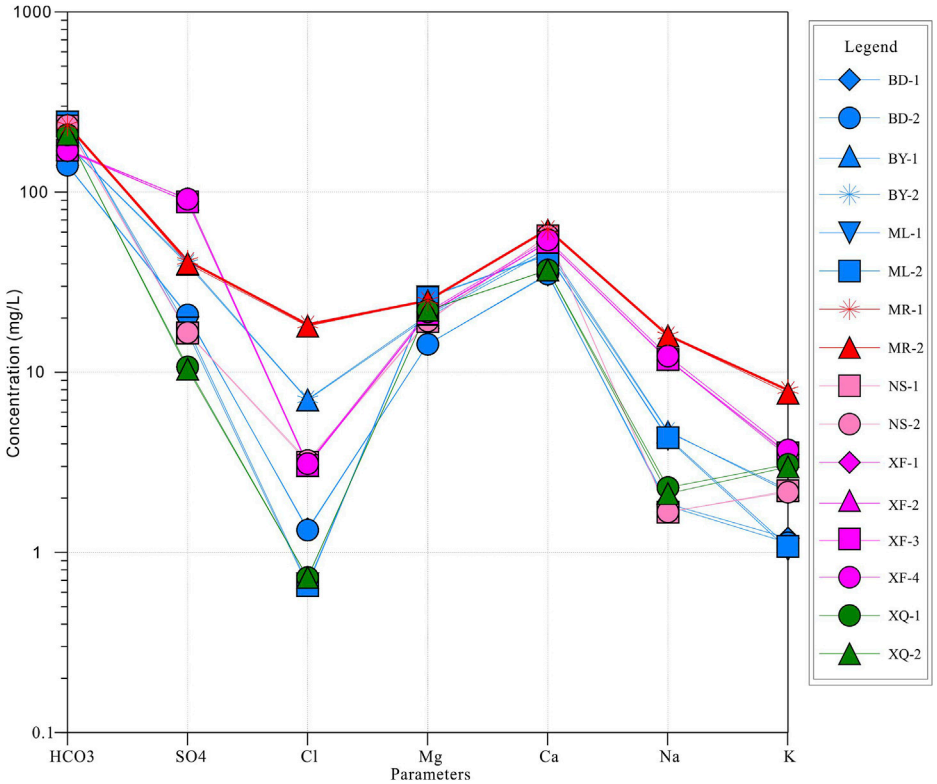

FIGURE 4 | Semi-logarithmic Schoeller diagram of all water from the Xifeng geothermal field.

Himalayan movements (Huang, 1945; Wang and Mo, 1995; Carter et al., 2001; Chen, 2005; Reid et al., 2007; Li J. et al., 2021), which controlled the distribution of geothermal resources.

Tectonic Setting

Faults are well developed in the study area due to multi-stage tectonic activities, such as the Emeishan mantle-plume eruption, Yanshanian orogeny, and Himalayan crust uplift movement (**Figure 1B**). These faults are mainly thin-skinned with high hydraulic conductivities and resulted in greater exploitation potential relative to other geothermal fields in China. One of the most important faults is the compresso-shear strike-slip Baimadong fault, which is the main conduit and connects the deep heat source (He et al., 2014; Li and Shen, 2014). The fault is around 50 km long, ENE-trending and dipping to SE at angles of 75° towards 90°, and assigned to a regional large-scale deep fault (**Figure 1B**; Zhang et al., 2017; Li et al., 2019, Li J. et al., 2021). In addition, secondary Neoid active faults such as the Shaba, Chaoyang, and Shitoutian faults are developed within the tectonic system and act as heat transporting channels (**Figure 1B**; Song et al., 2014). Among them, the Shaba fault is NE-trending and dipping to SE at angle of 70°. The Chaoyang fault is parallel to the Shaba fault with a length of ~20 km, NE-trending and dipping to SE at angles of 50° towards 70°. The Shitoutian fault with a NW orientation dips to NE at angles of 75° (Ji, 2015). The fault kinematics and orientations control the distribution of geothermal resources in the study region.

Hydrogeological Setting

The Xifeng geothermal field covers an area of 102.7 km^2 (Luo, 2020). Approximately 250 exploration and production geothermal wells have been drilled in this area since the 1950s, and the deepest depth is 2,500 m (He et al., 2014; Yang et al., 2018). Moreover, there are numerous hot springs within this area, including the famous Xifeng hot spring. The measured temperature ranges from 39 to 42°C in the Baimadong area to 53–56°C in the Xifeng area (Luo, 2020). The geothermal gradient of the study area is 2.5–3.0°C/hm with the heat flow rate varying from 50 to 75 mW/m^2 (Song et al., 2014; Wang et al., 2019a). The Dengying Formation is the main reservoir and the upper Jindingshan, Mingxinsi, and Niutitang formations form the cap of the geothermal system (**Figure 2**; He et al., 2014; Li and Shen, 2014; Song et al., 2014; Cai et al., 2018).

SAMPLING AND STUDY METHODS

Water Sample and Analyses

Fieldwork was carried out in the Xifeng area for collecting samples and obtaining relevant field data in April 2021. A total of 16 water samples (six hot spring samples, two geothermal well samples, six river samples, and two cold spring samples) at Xifeng were collected for major ions, REE, and D-O isotope analyses. Sample locations are shown in **Figure 1B**.

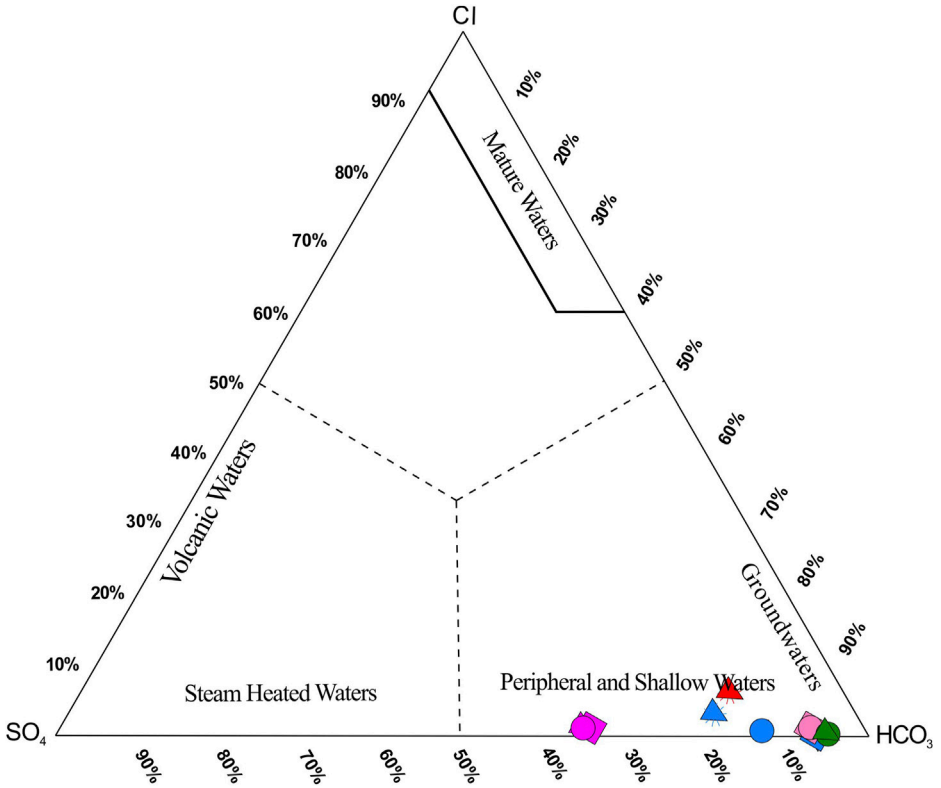

FIGURE 5 | Ternary plot of Cl-SO_4-HCO_3 for samples of the Xifeng geothermal field (after Giggenbach, 1991).

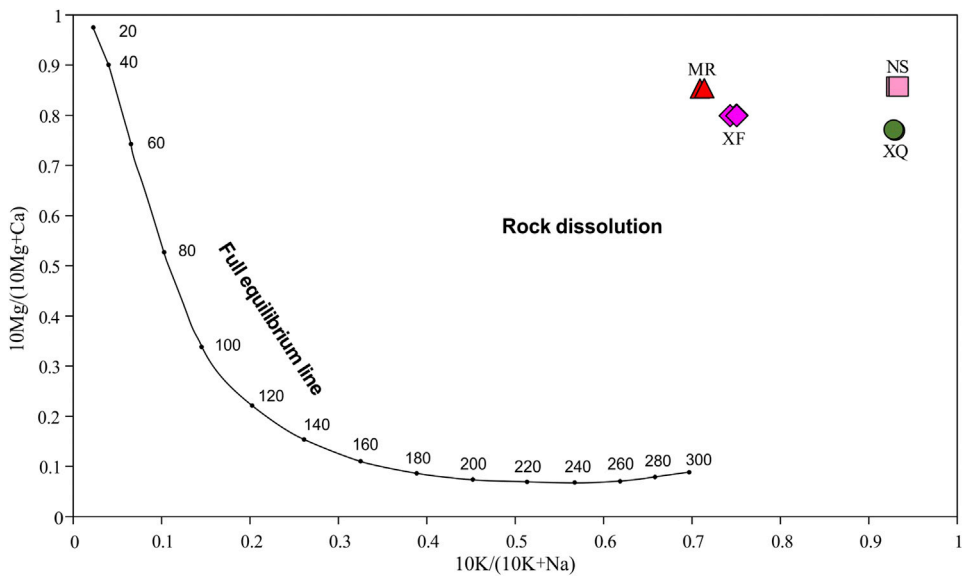

FIGURE 6 | A 10 Mg/(10 Mg + Ca) vs 10 K/(10 K + Na) plot of thermal and cold springs of the Xifeng geothermal field, using a Na/K-Mg-Ca diagram (after Giggenbach and Glover, 1992). Concentrations are in mg/L.

Time sensitive parameters were tested on site using a portable water quality analyzer. Samples were stored in new 500 ml polyethylene bottles that were rinsed with deionized water twice before sampling. All mentioned hydrochemical analyses of the water samples were performed in the Laboratory of Beijing Research Institute of Uranium Geology. Samples used for analysis

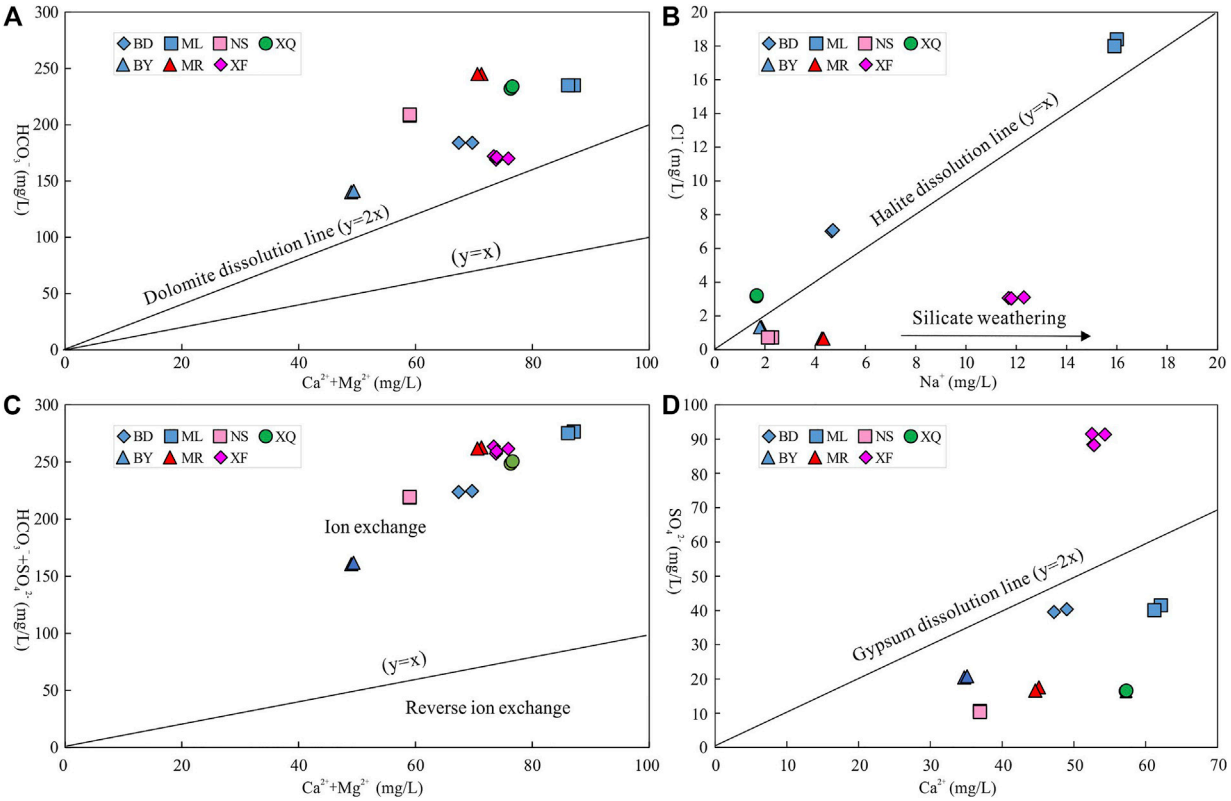

FIGURE 7 | The distribution of ionic ratios in water samples of the Xifeng geothermal field, **(A)** HCO_3^- vs Ca^{2+} + Mg^{2+}; **(B)** Cl^- vs Na+; **(C)** HCO_3^- + SO_4^{2-} vs Ca^{2+} + Mg^{2+}; and **(D)** SO_4^{2-} vs Ca^{2+}. BD represents samples labeled as BD-1 and BD-2; BY represents samples labeled as BY-1 to BY-4, ML represents samples labeled as ML-1 and ML-2; MR represents samples labeled as MR-1 and MR-2; NS represents samples labeled as NS-1 and NS-2; XF represents samples labeled as XF-1 to XF-4; and XQ represents samples labeled as XQ-1 and XQ-2.

of cations were acidified after collection through adding Suprapur HNO_3 to bring the pH to below 2. Analysis of major anions and cations was conducted by using Dionex ICS 1100 ion chromatography through Dionex ionpac AS-19HC and CS12A (4 mm × 250 mm) columns, respectively. The analysis of rare earth elements in water samples was documented using a Thermo Scientific ELEMENT XR inductively coupled plasma mass spectrometer (ICP-MS). The instrument was externally calibrated using a multielement standard solution before ICP-MS analysis. The analytical precision was better than 10% for duplicate analysis of the samples. The composition of deuterium (D) and oxygen (^{18}O) isotopes of collected water samples was analyzed by a MAT 253 mass spectrometer in a continuous flow mode using a Gas-bench II preparation and introduction system. Isotopic data are expressed in the delta (δ) notation as the per mil (‰) deviation relative to the Standard Mean Ocean Water (SMOW); the analytic precisions (1σ) are ±1.0 and ±0.1‰ for δD and $\delta^{18}O$, respectively.

Geothermometry

Chemical geothermometers are helpful to estimate the reservoir equilibrium temperature of the geothermal system by using the distribution and relative contents of various chemical indicators (i.e., dissolved silica, cation, gas, and isotopes; Das et al., 2021; Saibi et al., 2021). Among them, temperature-dependent solubility (silica) and ion-exchange reactions (i.e., Na-K, Na-K-Ca) are the most applied (Das et al., 2021).

Various geothermometers can obtain different estimated reservoir temperatures as each geothermometer documents the last equilibrium of a specific chemical element and is directly affected by processes of boiling, dilution, and precipitation. Cation geothermometers (Na-K, K-Mg, and Na-K-Ca) and silica geothermometers (quartz no steam loss, quartz maximum steam loss, chalcedony no steam loss, chalcedony maximum steam loss, α-cristobalite, and β-cristobalite) applied in this study are shown in **Table 1**.

RESULTS

Ions Characteristics

The physico-chemical compositions of samples in this study are shown in **Table 2**. All samples showed alkaline pH values. In almost all the samples, the anions were dominated by HCO_3^- and the order of abundance was: HCO_3^- > SO_4^{2-} > Cl^-. Among the cations, the main ion was Ca^{2+}, and the following order of abundance was Ca^{2+} > Mg^{2+} > Na^+ > K^+. As shown in the Piper (1944) diagram (**Figure 3**), the waters were mostly

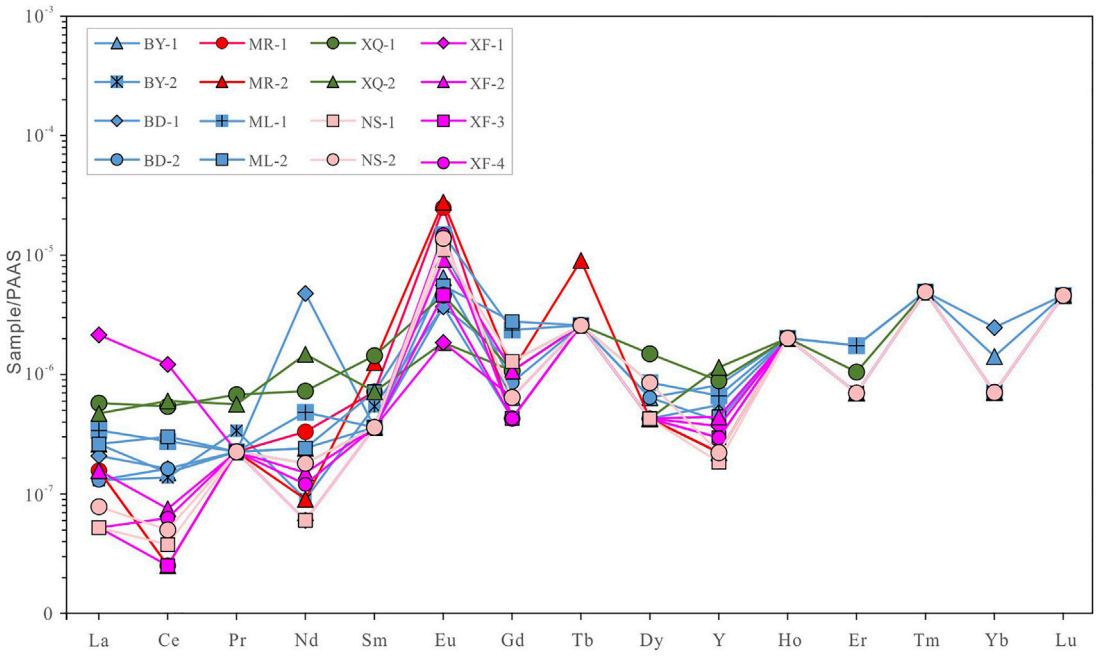

FIGURE 8 | Post-Archean Australian Average Shale (PAAS) REE diagrams for water samples from the Xifeng geothermal field. For the values shown as ranges (<0.002), the maximum values (0.002) are used for plotting.

the Ca-Mg-HCO_3 type except the Xifeng hot spring water (Ca-Mg-HCO_3-SO_4). Waters had a similar varied pattern for concentrations of the cations and anions, except the high SO_4 contents (88.3–91.5 mg/L, avg. = 89.9 mg/L) in the Xifeng hot spring as illustrated in the Schoeller (1995) semi-logarithmic diagram (**Figure 4**). The ternary plot of Cl-SO_4-HCO_3 (Giggenbach, 1991) was conducted to evaluate the type of water mixed in thermal or non-thermal fluids, notably the peripheral waters involved are shown in **Figure 5**. The groundwater reacted with host rocks though the unequilibrated state (**Figure 6**). The intercorrelation of ions during the process of the water-rock reaction is shown in **Figure 7**.

Rare Earth Elements

The REE signatures of geothermal fluids can be used to assess the influences of water-rock interaction. REE composition of sampled waters were analyzed in this study, and the results are shown in **Table 2**. Four types of water appeared to have similar PAAS-normalized REE patterns, which were featured by heavy rare earth elements (HREE) enrichment compared to light rare earth elements (LREE), and positive Eu anomalies (**Figure 8**). The total rare earth elements (REE) contents in the geothermal well fluids (~0.048 to ~ 0.057 μg/L), hot spring waters (~0.039–~0.214 μg/L), river waters (~0.067 to ~0.214 μg/L), and cold spring waters (~0.157 to 0.176 μg/L) were relatively low. The δCe values were 0.346–0.377, 0.133–0.577, 0.619–0.238, and 0.864–1.167, and δEu values were 16.312–28.836, 3.845–44.950, 3.918–19.978, and 2.106–3.723 for waters of the geothermal well, hot spring, river, and cold spring, respectively.

Hydrogen and Oxygen Isotope Compositions

Hydrogen and oxygen isotopic compositions of sampled waters in this study are shown in **Table 2**. The measured $\delta D_{v\text{-}SMOW}$ values ranged from −65.6 to −65.6‰ (avg. = −65.6‰, n = 2), −59.1 to −56.2‰ (avg. = −57.6‰, n = 6), −55.6 to −47.9‰ (avg. = −51.8‰, n = 6), and −47.7 to −45.9‰ (avg. = −46.8‰, n = 2) for the geothermal well, hot springs, river, and cold spring waters, respectively. The measured $\delta\ ^{18}O_{v\text{-}SMOW}$ values were −9.2 to −8.7 (avg. = −8.95‰, n = 2), −8.5 to −7.8‰ (avg. = −8.13‰, n = 6), −8.2 to −7‰ (avg. = −7.71‰, n = 6), and −7 to −6.5‰ (avg. = −6.75‰, n = 2) for the geothermal well, hot spring, river, and cold spring waters, respectively.

DISCUSSION

Source of Major Ions in the Geothermal Waters

Since most sampled waters were assigned to the Ca-Mg-HCO_3 type (**Figure 3**), this bicarbonate and Ca-Mg dominated feature can be attributed to the interaction with reservoir rocks, which are mainly Sinian dolomites. Ca^{2+}, Mg^{2+}, and HCO_3^- were sourced from the dissolution of dolomites following the equation of

$$CaMg(CO_3)_2(\text{dolomite}) + 2H_2CO_3 = Ca^{2+} + Mg^{2+} + 4HCO_3^- \quad (1)$$

As illustrated in **Figure 6**, the water-rock interaction is a dominant process in thermal and cold springs of the Xifeng

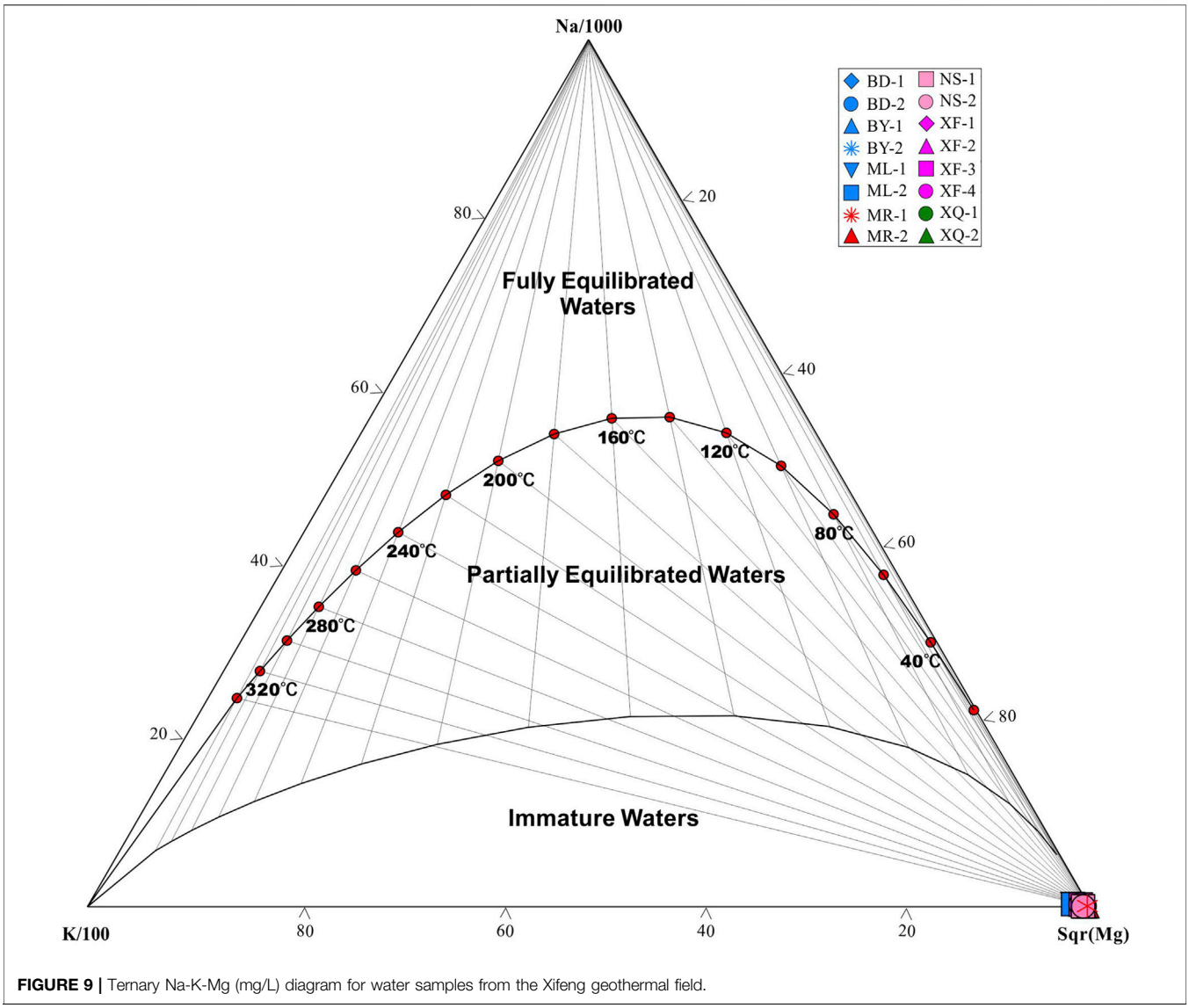

FIGURE 9 | Ternary Na-K-Mg (mg/L) diagram for water samples from the Xifeng geothermal field.

geothermal field, although water is not equalized with the host reservoir rocks. Water-rock reactions can be further evidenced by the $\delta^{18}O$ results of geothermal waters, which deviate 2‰ of units from LMWL (**Figure 11**; Taylor, 1977). Additionally, most REE concentrations of sampled waters were above the detection limits (**Table 2**), indicating that REE in the samples were not derived from meteoric waters (Lewis et al., 1994). The positive Eu anomaly (triggered by the interaction between water and feldspar-bearing rocks or the physicochemical conditions; Sverjensky, 1984; Şener et al., 2017) supports the opinion that REE in the samples were inherited from feldspar-bearing dolomites through the water-rock interaction since the temperatures of geothermal fluids were much lower than 200°C (**Figure 8**; Sverjensky, 1984).

The characteristics of major ions and their intercorrelation can be used to deduce the geochemical processes caused by the water-rock reaction that the groundwater encounters along its flow path (Adams et al., 2001). According to **Eq. 1**, the dissolution of dolomite would produce a $(Ca^{2+} + Mg^{2+})/HCO_3^-$ molar ratio of 1: 2 (Han et al., 2013; Belkhiri and Narany, 2015). However, the ratios of $(Ca^{2+} + Mg^{2+})/HCO_3^-$ were lower than 0.5 (**Figure 7A**), indicating that other sources of HCO_3^- were involved in the geothermal fluids (e.g., silicate weathering), whereas the deficit in contents of Ca^{2+} and Mg^{2+} should be influenced by other hydrochemical processes (e.g., ion-exchange reaction), rather than the sole dissolution of dolomite. The affection of silicate weathering can also be inferred from the high values of Ca^{2+}/Mg^{2+} (>1) in this study (Katz et al., 1997). Moreover, the Na^+/Cl^- molar ratios of the thermal waters were much higher than 1, further confirming the fact that the excess Na^+ was sourced from silicate weathering (**Figure 7B**; Bob et al., 2015). The plots for most samples were well above the 1:1 line of $(HCO_3^- + SO_4^{2-})/(Ca^{2+} + Mg^{2+})$ (**Figure 7C**), implying the occurrence of ion exchange. It is clear that the contents of Ca^{2+} and SO_4^{2-} in natural water commonly depended on the dissolution of gypsum and precipitated processes, as shown in the equation of $CaSO_4$

TABLE 3 | Cation and silica geothermometry of hot waters from the Xifeng geothermal field.

Sample NO.	T(Na-K)①	T(Na-K)②	T(Na-K)③	T(Na-K)④	T(Na-K)⑤	T(Na-K)⑥	T(Na-K)⑦	T(Na-K)⑧	T(K-Mg)⑨	T(Na-K-Ca)⑩	Quartz, no steam loss (conductive)⑪	Quartz, maximum steam loss at 100 °C (adiabatic)⑫	Chalcedony (no loss of steam)⑬	Chalcedony (maximum steam loss)⑭	α-Cristobalite⑮	β-Cristobalite⑯
MR-1	307.37	309.16	314.99	360.55	292.27	307.65	297.25	418.19	13.51	−2.81	64.24	69.66	32.19	42.86	15.05	−29.08
MR-2	310.25	313.28	317.57	365.29	295.09	311.41	299.81	423.67	14.18	−1.84	64.30	69.72	32.26	42.92	15.11	−29.02
XF-1	333.57	347.34	338.41	404.58	317.95	342.33	320.49	469.36	36.68	28.32	91.36	93.50	60.71	67.45	41.21	−4.87
XF-2	328.69	340.12	334.07	396.23	313.17	335.81	316.18	459.62	36.22	27.76	91.59	93.70	60.95	67.66	41.43	−4.66
XF-3	334.31	348.45	339.07	405.86	318.68	343.33	321.15	470.85	36.95	28.70	91.51	93.63	60.87	67.59	41.35	-4.73
XF-4	333.92	347.87	338.73	405.19	318.30	342.81	320.81	470.07	37.46	29.51	90.36	92.63	59.65	66.55	40.23	−5.77
NS-1	625.48	902.36	584.19	1082.63	605.11	806.36	566.83	1316.25	33.80	18.21	53.88	60.43	21.48	33.45	5.20	−38.10
NS-2	638.38	934.13	594.45	1123.74	617.84	830.84	577.20	1371.42	33.19	16.90	54.78	61.23	22.40	34.26	6.04	−37.32

Notes: T(Na-K)① (Fournier, 1979); T(Na-K)② (Truesdell, 1976); T(Na-K)③ (Giggenbach and Goguel, 1988); T(Na-K)④ (Tonani, 1980); T(Na-K)⑤ (Nieva and Nieva, 1987); T(Na-K)⑥ (Arnórsson, 1983); T(Na-K)⑦ (Michard et al., 1979); T(K-Mg)⑧ (Giggenbach et al., 1983); T(Na-K-Ca)⑨ (Fournier and Truesdell, 1973; where b = 4/3, if T < 100 °C; b = 1/3, if T > 100 °C); Quartz, no steam loss (conductive)⑩ (Fournier, 1977); Quartz, maximum steam loss at 100 °C (adiabatic)⑪ (Fournier, 1977); Chalcedony (no loss of steam)⑫ (Fournier, 1992); Chalcedony (maximum steam loss)⑬ (Fournier, 1977); α-Cristobalite⑭ (Fournier, 1977); β-Cristobalite⑮ (Fournier, 1977).

+ $2H_2O = Ca^{2+} + SO_4^{2-} + H_2O$ (Das et al., 2021). However, with influence of silicate weathering, the ratio of Ca^{2+} versus SO_4^{2-} was high than 1, except samples collected from the Xifeng hot spring ($Ca^{2+}/SO_4^{2-} < 1$; **Figure 7D**). The high SO_4^{2-} in the Xifeng hot spring may be due to the dissolution of other sulphate minerals during the deeper and long-duration circulation from high-elevation SW towards low-elevation NE in the study area (**Figure 4**; Song et al., 2014).

Geothermal Reservoir Temperature

The Giggenbach Na-K-Mg ternary diagram is used for categorizing waters as full equilibrium, partial equilibrium, or immaturity compared with reservoir rocks (Giggenbach, 1991; Giggenbach and Goguel, 1988). As shown in **Figure 9**, all the sampled waters were plotted in the field of immature waters, indicating none of them were in full or partial equilibrium with the host rocks or may have mixed with shallow groundwater. It is established that only the waters with features that were fully or partially equilibrated with the host rocks can be used to obtain reliable reservoir temperatures; immature waters produce less reliable results which are usually not regarded as the real reservoir temperatures. Hence, cation geothermometers were not appropriate for the sampled waters in this study. This can be further evidenced by geo-thermometry results obtained through different Na-K geothermometers, which showed higher estimated reservoir temperatures than that of the Na-K-Ca and K-Mg geothermometers (**Table 3**). The inconsistent results of geothermometers containing Ca and/or Mg with that of Na-K are attributed to the mix of shallow groundwaters and/or surface waters (**Figure 5**; García-Soto et al., 2016). This mix made the reliability of silica-based geo-thermometry stronger than cation geothermometers (Pandarinath, 2011; Pandarinath and Domínguez-Domínguez, 2015; Saibi et al., 2021). The reliability of silica-based geo-thermometry can be further supported by **Figure 10**, which shows that the thermal and cold springs of the Xifeng geothermal field were near to the equilibrated curve of chalcedony + quartz (Giggenbach, 1991). Given that the temperatures calculated by chalcedony and cristobalite geothermometers were much lower than the real temperatures of the hot spring and wellhead, reservoir temperatures generated though the quartz (conductive and adiabatic) geothermometers were the most reliable (García-López et al., 2014). The quartz (conductive and adiabatic) geothermometers gave the average estimated reservoir temperature of 77°C. The depth of the geothermal reservoir is around 2.57 km in the Xifeng geothermal field, assuming a temperature gradient of 3°C/100 m (Song et al., 2014).

Source and Recharge of the Geothermal Fluid

Oxygen-18 (^{18}O) and deuterium (D) contents in sampled waters from the Xifeng geothermal field were analyzed to confirm the source and circulation mechanism of geothermal fluids. On the $\delta^{18}O$-δD diagram (**Figure 11**), most samples were plotted close to

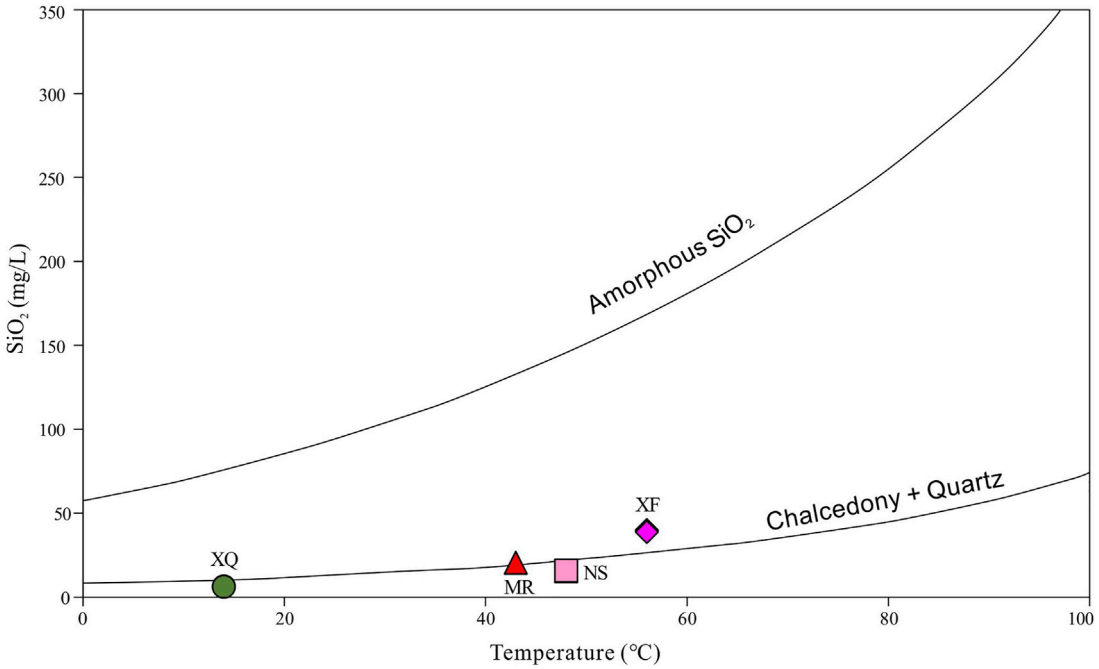

FIGURE 10 | SiO_2 concentration vs temperature plot for the samples of the Xifeng geothermal field. The amorphous SiO_2 solubility curve is from Fournier and Truesdell (1974) and chalcedony + quartz solubility is from Giggenbach (1991).

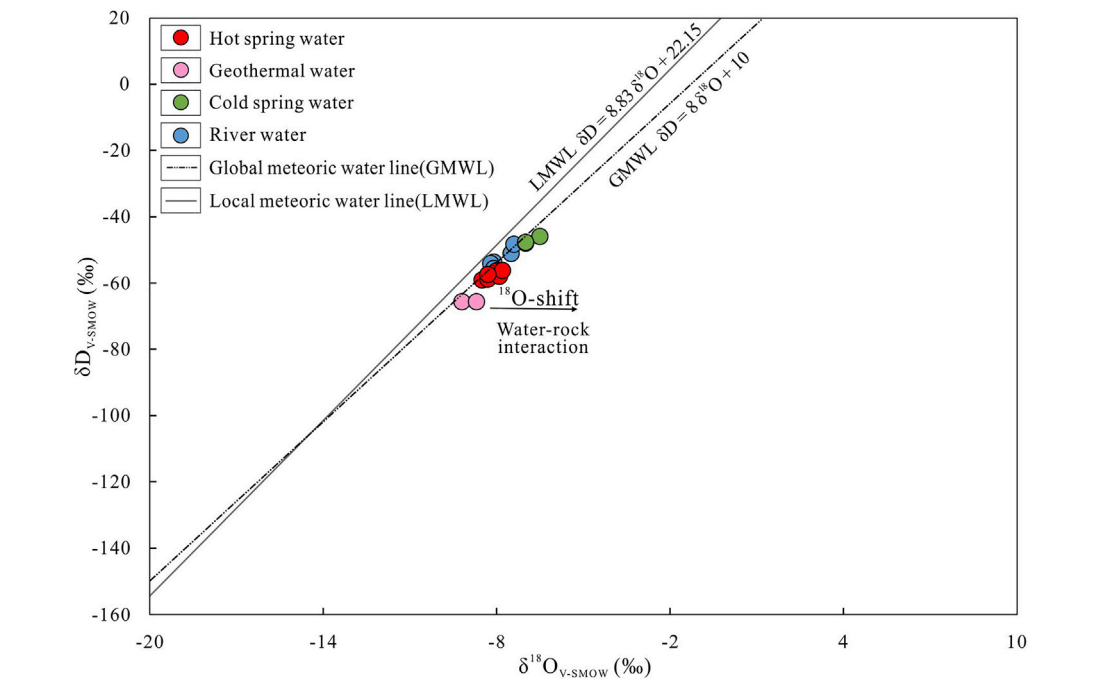

FIGURE 11 | Plot of δD vs $\delta^{18}O$ values of water samples collected from the Xifeng geothermal field.

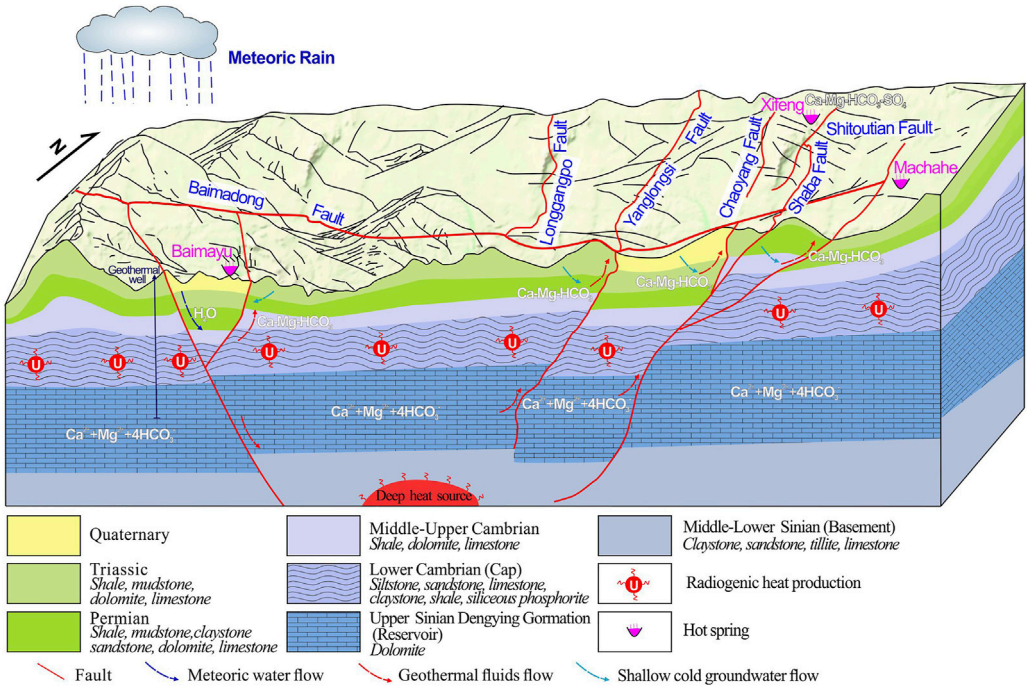

FIGURE 12 | Genetic model of the Xifeng geothermal field.

the local meteoric water line (LMWL: $\delta D = 8.83\ \delta^{18}O + 22.15$, Zhang et al., 2005) and global meteoric water line (GMWL: $\delta D = 8\ \delta^{18}O + 10$, Craig, 1961), indicating a common meteoric water origin. This is in accordance with results of the PAAS-normalized REE patterns (**Figure 8**) and variable characteristics of ions (**Figure 4**), which showed a similar source of geothermal fluids.

Craig (1961) established the δD and $\delta^{18}O$ values of precipitation relating to altitude effect, and proposed that meteoric water derived from higher elevation is gradually lighter. In **Figure 11**, the slightly depleted δD and $\delta^{18}O$ values of geothermal waters compared to those of local river waters testify that the recharge elevation of the former is higher than that of the latter. Generally, the recharge elevation of groundwater can be calculated in terms of the following formula:

$$H = \frac{\delta^{18}O_{gw} - \delta^{18}O_{1w}}{grad^{18}O} + h \qquad (2)$$

In **Eq. 2**, H (m) = recharge elevation; $\delta^{18}O_{gw}$ = oxygen isotope value of groundwater; $\delta^{18}O_{lw}$ = oxygen isotope value of local meteoric water; $grad^{18}O$ (‰/km) = isotope elevation gradient of meteoric water, and h (m) = elevation of the local meteoric sampling point. The most depleted $\delta^{18}O$ value (−9.2‰) in the geothermal samples was regarded as the $\delta^{18}O_{gw}$ to minimize the positive isotopic shift effect in this study. The average oxygen isotope value (−7.7‰) of surface meteoric water obtained in this study was used as $\delta^{18}O_{lw}$. Hence, the recharge elevation was calculated to be 1,583 m as the $\delta^{18}O$ vertical gradient in Guizhou was assumed to be −3.1‰/km (Yu et al., 1984), and with the elevation of local meteoric sampling point at 1,100 m. Combined with the geological setting, this result is reasonable as the sampling elevation is around 1,250 m for the samples collected from southwest and 750 m for those from northeast and southeast of the geothermal field.

Forming Mechanisms for the Xifeng Geothermal Field

The formation of the Xifeng geothermal field resulted from recharge, deep circulation, and secondary rising meteoric water along the faults. Based on the topographic features and geological conditions (**Figures 1**, **2**), we propose the basic conceptual model for the genesis of the Xifeng geothermal system, as illustrated in **Figure 12** and discussed.

Results of stable isotopes and geology revealed that the local meteoric water from the surrounding mountains seemed to infiltrate to depth through faults and crack zones and were the dominant recharge source for the geothermal system. Sedimentary rocks of Lower Cambrian Jindingshan, Mingxinsi, and Niutitang formations overlie the Upper Sinian Dengying reservoir units and act as cap rock (**Figure 1C**). Moreover, the black shale of the lower Cambrian Niutitang Formation in South China is well known to be enriched in radioactive heat-producing uranium elements, which are 10 and 6–20 times the content compared with that of crustal sedimentary rocks and the crust, respectively (Coveney and Nansheng, 1991; Ni et al., 2012; Pi et al., 2013; Yang et al., 2013; Pagès et al., 2018; Li et al., 2019). At Xifeng, the average U, Th, and K

contents for the black shale of the Niutitang Formation is 32.61 (μg/g), 13.25 (μg/g), and 1.86 (%), respectively (Chen 2005; Pi et al., 2013). Generally, the radioactive heat production can be calculated via the formula of $A = 0.01\rho(9.52C_U + 2.56C_{Th} + 3.48C_K)$ (Rybach, 1976). Where A (μW/m^3) refers to radioactive heat production, ρ (g/cm^3) is the rock density, C_U (μg/g), C_{Th} (μg/g), and C_K (%) are the U, Th, and K concentrations, respectively. Thereby, the heat production potential of the lower Cambrian Niutitang Formation in the study area is calculated to be 9.57 μW/m^3 with the rock density of 2.728 (Zhao et al., 1995). This value is higher than the average heat production of the continental crust (~1 μW/m^3; Waples, 2001) and can be regarded as an effective radiogenic heat source (Paternoster et al., 2017). Hence, except for the role of cap rock, the Niutitang Formation also served as a heat source due to the producing of radioactive heat (**Figure 12**). Furthermore, since the multi-period (especially in Yanshanian and Himalayan) active strike-slip of the Baimadong fault and Neoid active faults (e.g., Shaba, Chaoyang, and Shitoutian faults; **Figure 1B**) are well developed within the tectonic system of the Xifeng geothermal field, the tectonic frictional heat is speculated to act as a supplementary heat source due to the mechanical friction produced along the faults during deformation (Mase and Smith, 1987; He et al., 2014; Song et al., 2014; Zhu, 2016). Moreover, these deep large scale faults also connect to the deep earth and act as a heat transporting channel for deep heat (**Figure 12**; He et al., 2014; Li and Shen, 2014; Song et al., 2014; Li et al., 2019, Li J. et al., 2021). The existence of acid magmatic intrusion material under the central Guizhou uplift can be considered as the deep heat source, evidenced by the available geophysical information (Zhang et al., 2017).

Once the meteoric water was warmed up, it would interact with the host rocks. The interaction between water and Sinian dolomites is the dominant process for the formation of Ca-Mg-HCO_3 type waters in the Xifeng geothermal field. Moreover, the silicate weathering and ion exchange are also responsible for the formation of geothermal fluids in the Xifeng area. As to the Ca-Mg-HCO_3-SO_4 type in the Xifeng hot spring, it may be due to the dissolution of other sulphate minerals during the deeper, and long-duration circulation from high-elevation SW (i.e., 1,250 m, Baimadong area) towards low-elevation NE (i.e., 750 m, Xifeng area) in the study area (**Figure 12**; Song et al., 2014). This is consistent with the results of recharge elevation and geological setting.

Then finally, as the deep-infiltrated waters experienced considerable deep circulation, the geothermal fluids rose again along the main ENE-SE, NE-SE, and NW-NE faults. Moreover, the ascending geothermal fluids were mixed with cold groundwater in the subsidiary fractures near the surface (**Figure 5**; Giggenbach, 1991). The tectonic and stratigraphical features at the study area are favorable for the formation of abundant geothermal resources.

CONCLUSION

The geothermal fluids in the Xifeng geothermal field are hosted in dolomite from the Sinian Dengying Formation, and are capped by sedimentary rocks of the lower Cambrian Jindingshan, Mingxinsi, and Niutitang formations. Radiogenic heat, deep heat, and tectonic frictional heat serve as heat sources for the formation of the large geothermal system. The reservoir temperature is estimated to be 77°C. D-O isotopic studies indicate that the Xifeng geothermal system is recharged by meteoric water from higher elevations at 1,583 m from SW to NE. It is the water-dolomite interactions that lead to the formation of the alkaline Ca-Mg-HCO_3 type geothermal fluids. This is consistent with the research results of the REE, whose accumulation characteristics and positive Eu anomaly are inherited from host feldspar-bearing dolomites through the water-rock interaction. The high SO_4 in the Xifeng hot spring are attributed to the deeper and long-duration circulation of waters from SW towards NE. Ternary relationships among major anions indicate that a mix of cold groundwater to the ascending geothermal fluids occurred when they migrated along the main faults near the surface. Taken together, the Xifeng geothermal system should be assigned as a faults-controlling and deeply circulating meteoric water of low-temperature category.

DATA AVAILABILITY STATEMENT

The original contributions presented in the study are included in the article/Supplementary Material, further inquiries can be directed to the corresponding author.

AUTHOR CONTRIBUTIONS

YL wrote the manuscript with the support of the listed authors. All authors have made a substantial, direct, and intellectual contribution to the work and approved it for publication.

FUNDING

This study was financially supported by the National Natural Science Foundation of China (No. 42002299) and the Project of Chinese Academy of Geological Sciences (No. JKY202018).

ACKNOWLEDGMENTS

We appreciate the kind help of Professor Hansheng Long from the Guizhou Institute of Technology on the field trip. The constructive comments made by the editor and anonymous reviewers are greatly thanked.

REFERENCES

Adams, S., Titus, R., Pietersen, K., Tredoux, G., and Harris, C. (2001). Hydrochemical Characteristics of Aquifers Near Sutherland in the Western Karoo, South Africa. *J. Hydrol.* 241 (1-2), 91–103. doi:10.1016/s0022-1694(00)00370-x

Arnórsson, S. (1983). Chemical Equilibria in Icelandic Geothermal Systems. Implications for Chemical Geothermometry Investigations. *Geothermics* 12, 119–128. doi:10.1016/0375-6505(83)90022-6

Belkhiri, L., and Narany, T. S. (2015). Using Multivariate Statistical Analysis, Geostatistical Techniques and Structural Equation Modeling to Identify Spatial Variability of Groundwater Quality. *Water Resour. Manag.* 29 (6), 2073–2089. doi:10.1007/s11269-015-0929-7

Bob, M., Abd Rahman, N., Taher, S., and Elamin, A. (2015). Multi-objective Assessment of Groundwater Quality in Madinah City, Saudi Arabia. *Water Qual. Expo. Health* 7 (1), 53–66. doi:10.1007/s12403-014-0112-z

Cai, X. L., Zhang, C. J., Guo, J. B., Wu, D., Fan, X., and Yang, M. J. (2018). Geothermal Water Genetic Analysis in Kaiyang Phosphate Mine West Limb, Guizhou. *Coal Geology. China* 30 (6), 101–104. doi:10.3969/j.issn.1674-1803.2018.06.20

Carter, A., Roques, D., Bristow, C., and Kinny, P. (2001). Understanding Mesozoic Accretion in Southeast Asia: Significance of Triassic Thermotectonism (Indosinian Orogeny) in Vietnam. *Geol* 29, 211–214. doi:10.1130/0091-7613(2001)029<0211:umaisa>2.0.co;2

Chen, L. (2005). *Sedimentology and Geochemistry of the Early Cambrian Black Rock Series in the Hunan-Guizhou Area, China*. A Dissertation Submitted for the Degree of Doctor of Science of the Chinese Academy of Sciences and for the Diploma of the Institute of Geochemistry, 53–79. (in Chinese with English abstract).

Chen, Y.-J., Santosh, M., Somerville, I., and Chen, H.-Y. (2014). Indosinian Tectonics and Mineral Systems in China: An Introduction. *Geol. J.* 49, 331–337. doi:10.1002/gj.2619

Cheng, Y., Pang, Z., Di, Q., Chen, X., and Kong, Y. (2021). Three-dimensional Resistivity Structure in the Hydrothermal System beneath Ganzi Basin, Eastern Margin of Tibetan Plateau. *Geothermics* 93, 102062. doi:10.1016/j.geothermics.2021.102062

Coveney, R. M., Jr., and Nansheng, C. (1991). Ni-Mo-PGE-Au-rich Ores in Chinese Black Shales and Speculations on Possible Analogues in the United States. *Mineral. Deposita* 26, 83–88. doi:10.1007/bf00195253

Craig, H. (1961). Isotopic Variations in Meteoric Waters. *Science* 133 (3465), 1702–1703. doi:10.1126/science.133.3465.1702

Das, P., Maya, K., and Padmalal, D. (2021). Hydrochemistry, Geothermometry and Origin of the Low Temperature thermal Springs of South Konkan Region, India. *Geothermics* 90, 101997. doi:10.1016/j.geothermics.2020.101997

Duo, J. (2003). The Basic Characteristics of the Yangbajing Geothermal Field? A Typical High Temperature Geothermal System. *Eng. Sci.* 1, 42–47. doi:10.3969/j.issn.1009-1742.2003.01.008

Fournier, R. O. (1977). Chemical Geothermometers and Mixing Models for Geothermal Systems. *Geothermics* 5, 41–50. doi:10.1016/0375-6505(77)90007-4

Fournier, R. O. (1979). Geochemical and Hydrologic Considerations and the Use of Enthalpy-Chloride Diagrams in the Prediction of Underground Conditions in Hot-spring Systems. *J. Volcanology Geothermal Res.* 5, 1–16. doi:10.1016/0377-0273(79)90029-5

Fournier, R. O., and Truesdell, A. H. (1973). An Empirical Na-K-Ca Geothermometer for Natural Waters. *Geochimica et Cosmochimica Acta* 37, 1255–1275. doi:10.1016/0016-7037(73)90060-4

Fournier, R. O., and Truesdell, A. H. (1974). Geochemical Indicators of Subsurface Temperature - Part 2. *USGS J. Res.* 2, 263–270. doi:10.3133/ofr741032

Fournier, R. O. (1992). Water Geothermometers Applied to Geothermal Energy. F. D'Amore (Coordinator). *Application of Geochemistry in Geothermal Reservoir Development*. UNITAR/UNDP, Vial del Corso, Italy, 37–69.

García-López, C. G., Pandarinath, K., and Santoyo, E. (2014). Solute and Gas Geothermometry of Geothermal Wells: A Geochemometrics Study for Evaluating the Effectiveness of Geothermometers to Predict Deep Reservoir Temperatures. *Int. Geology. Rev.* 56, 2015–2049. doi:10.1080/00206814.2014.984352

García-Soto, A. Y., Pandarinath, K., Marrero-Ochoa, J. E., and Díaz-Gómez, C. (2016). Solute Geothermometry of Cerro Prieto and Los Humeros Geothermal Fields, Mexico: Considerations on Chemical Characteristics of Thermal Water. *Arab. J. Geosci.* 9, 517. doi:10.1007/s12517-016-2529-0

Giggenbach, W. F. (1991). "Chemical Techniques in Geothermal Exploration," in *Application of Geochemistry in Resources Development* (UNITAR/UNDP Guidebook), 119–144.

Giggenbach, W. F., and Glover, R. B. (1992). Tectonic Regime and Major Processes Governing the Chemistry of Water and Gas Discharges from the Rotorua Geothermal Field, New Zealand. *Geothermics* 21, 121–140. doi:10.1016/0375-6505(92)90073-i

Giggenbach, W. F., and Goguel, R. L. (1988).*Collection and Analysis of Geothermal and Volcanic Water and Gas Discharges*. Department of Scientific and Industrial Research, Chemistry Division: Petone. 4th ed. (New Zealand). Report No.: CD 2401.

Giggenbach, W. F., Gonfiantini, R., Jangi, B. L., and Truesdell, A. H. (1983). Isotopic and Chemical Composition of Parbati Valley Geothermal Discharges, North-West Himalaya, India. *Geothermics* 12 (2-3), 199–222. doi:10.1016/0375-6505(83)90030-5

Guo, Q. H., Wang, Y. X., and Liu, W. (2007). Major Hydrogeochemical Processes in the Two Reservoirs of the Yangbajing Geothermal Field, Tibet, China. *J. Volcanol. Geotherm. Res.* 166 (3–4), 255–268. doi:10.1016/j.jvolgeores.2007.08.004

Guo, Q., Kirk Nordstrom, D., and Blaine McCleskey, R. (2014). Towards Understanding the Puzzling Lack of Acid Geothermal Springs in Tibet (China): Insight from A Comparison with Yellowstone (USA) and Some Active Volcanic Hydrothermal Systems. *J. Volcanology Geothermal Res.* 288 (1), 94–104. doi:10.1016/j.jvolgeores.2014.10.005

Guo, Q., Liu, M., Li, J., Zhang, X., Guo, W., and Wang, Y. (2017a). Fluid Geochemical Constraints on the Heat Source and Reservoir Temperature of the Banglazhang Hydrothermal System, Yunnan-Tibet Geothermal Province, China. *J. Geochemical Exploration* 172, 109–119. doi:10.1016/j.gexplo.2016.10.012

Guo, Q., Planer-Friedrich, B., Liu, M., Li, J., Zhou, C., and Wang, Y. (2017b). Arsenic and Thioarsenic Species in the hot springs of the Rehai Magmatic Geothermal System, Tengchong Volcanic Region, China. *Chem. Geology.* 453, 12–20. doi:10.1016/j.chemgeo.2017.02.010

Guo, Q., and Wang, Y. (2012). Geochemistry of Hot Springs in the Tengchong Hydrothermal Areas, Southwestern China. *J. Volcanology Geothermal Res.* 215-216, 61–73. doi:10.1016/j.jvolgeores.2011.12.003

Han, Y., Wang, G., Cravotta, C. A., III, Hu, W., Bian, Y., Zhang, Z., et al. (2013). Hydrogeochemical Evolution of Ordovician Limestone Groundwater in Yanzhou, North China. *Hydrol. Process.* 27 (16), 2247–2257. doi:10.1002/hyp.9297

He, B., Xu, Y. G., and Wang, Y. M. (2005). Nature of the Dongwu Movement and its Temporal and Spatial Evolution. *J. China Univ. Geosci.* 30, 89–96. doi:10.3321/j.issn:1000-2383.2005.01.012

He, W. J., Xiang, X. L., Li, Y. G., and Wu, X. J. (2014). Genesis and Hydrochemical Characteristics of Xinluo, Guizhou Province. *Ground water* 36 (5), 39–40. doi:10.3969/j.issn.1004-1184.2014.05.013

Huang, T. K. (1945). On Major Tectonic Forms of China. *J. Geol.* 55, 59–60. doi:10.1086/625397

Ji, Q. (2015). *The Hydrogeochemical Characteristics and Genesis Research of Xifeng Hot Springs in Guizhou*. A Dissertation Submitted for the Degree of Master of Chengdu University of Technology, 1–51. (in Chinese with English abstract).

Jian, P., Liu, D., Kröner, A., Zhang, Q., Wang, Y., Sun, X., et al. (2009). Devonian to Permian Plate Tectonic Cycle of the Paleo-Tethys Orogen in Southwest China (II): Insights from Zircon Ages of Ophiolites, Arc/back-Arc Assemblages and Within-Plate Igneous Rocks and Generation of the Emeishan CFB Province. *Lithos* 113, 767–784. doi:10.1016/j.lithos.2009.04.006

Katz, B. G., Coplen, T. B., Bullen, T. D., and Davis, J. H. (1997). Use of Chemical and Isotopic Tracers to Characterize the Interactions between Ground Water and Surface Water in Mantled Karst. *Groundwater* 35 (6), 1014–1028. doi:10.1111/j.1745-6584.1997.tb00174.x

Lewis, A. J., Palmer, M. R., and Kemp, A. J. (1994). Variations of the Rare Earth Element Abundances in Hydrothermal Waters from the Yellowstone Hydrothermal System, Wyoming, USA. *Mineralogical Mag.* 58A, 525–526. doi:10.1180/minmag.1994.58a.2.11

Li, D. W., and Wang, Y. X. (2015). Major Issues of Research and Development of Hot Dry Rock Geothermal Energy. *Earth Sci.* 40 (11), 1858–1869. doi:10.3799/dqkx.2015.166

Li, J., Sagoe, G., Wang, X., and Yang, Z. (2021a). Assessing the Suitability of Lithium-Related Geothermometers for Estimating the Temperature of Felsic Rock Reservoirs. *Geothermics* 89, 101950. doi:10.1016/j.geothermics.2020.101950

Li, J., Yang, G., Sagoe, G., and Li, Y. (2018). Major Hydrogeochemical Processes Controlling the Composition of Geothermal Waters in the Kangding Geothermal Field, Western Sichuan Province. *Geothermics* 75, 154–163. doi:10.1016/j.geothermics.2018.04.008

Li, Y. Y., Zhang, C. J., Chi, G. X., Duo, J., Li, Z. H., and Song, H. (2019). Black and Red Alterations Associated with the Baimadong Uranium Deposit (Guizhou, China): Geological and Geochemical Characteristics and Genetics Relationship with Uranium Mineralization. *Ore Geol. Rev.* 111, 102981. doi:10.1016/j.oregeorev.2019.102981

Li, Y. Y., Zhang, C. J., Duo, J., Zhang, F. F., Song, H., Zhang, B. J., et al. (2021b). Genesis of the Baimadong Carbonate-Hosted Uranium Deposit, Guizhou, SW China: Constrains from Geology, Fluid Inclusions, and C-O Isotopes. *Ore Geol. Rev.* 139, 104487. doi:10.1016/j.oregeorev.2021.104487

Li, Z. S., and Shen, X. D. (2014). Genesis of the Xinluo Geothermal Well in Xifeng, Guizhou Province. *Geology. Exploration* 50 (6), 1155–1159. (in Chinese with English abstract).

Ling, K.-Y., Zhu, X.-Q., Tang, H.-S., and Li, S.-X. (2017). Importance of Hydrogeological Conditions during Formation of the Karstic Bauxite Deposits, Central Guizhou Province, Southwest China: A Case Study at Lindai Deposit. *Ore Geology. Rev.* 82, 198–216. doi:10.1016/j.oregeorev.2016.11.033

Ling, K.-Y., Zhu, X.-Q., Tang, H.-S., Wang, Z.-G., Yan, H.-W., Han, T., et al. (2015). Mineralogical Characteristics of the Karstic Bauxite Deposits in the Xiuwen Ore Belt, Central Guizhou Province, Southwest China. *Ore Geology. Rev.* 65, 84–96. doi:10.1016/j.oregeorev.2014.09.003

Liu, P. (2001). Discussion on the Metallogenic Setting of the Qianzhong-Yu'nan Bauxite in Guizhou and its Genesis. *Guizhou Geol.* 18, 238–243. doi:10.3969/j.issn.1000-5943.2001.04.006

Long, Y., Chi, G., Liu, J., Jin, Z., and Dai, T. (2017). Trace and Rare Earth Elements Constraints on the Sources of the Yunfeng Paleo-Karstic Bauxite Deposit in the Xiuwen-Qingzhen Area, Guizhou, China. *Ore Geology. Rev.* 91, 404–418. doi:10.1016/j.oregeorev.2017.09.014

Long, Y., Chi, G., Liu, J., Zhang, D., and Song, H. (2018). Uranium Enrichment in a Paleo-Karstic bauxite deposit, Yunfeng, SW China: Mineralogy, Geochemistry, Transport - Deposition Mechanisms and Significance for Uranium Exploration. *J. Geochemical Exploration* 190, 424–435. doi:10.1016/j.gexplo.2018.04.010

Long, Y., Lu, A., Gu, X., Chi, G., Ye, L., Jin, Z., et al. (2020). Cobalt Enrichment in A Paleo-Karstic Bauxite Deposit at Yunfeng, Guizhou Province, SW China. *Ore Geology. Rev.* 117, 103308. doi:10.1016/j.oregeorev.2019.103308

Luo, T. (2020). *Study on the Enrichment Mechanism of H_2SiO_3 and Sr in Xifeng Water*. A Dissertation Submitted for the Degree of Master of Guizhou University, 1–69. (in Chinese with English abstract).

Mase, C. W., and Smith, L. (1987). Effects of Frictional Heating on the Thermal, Hydrologic, and Mechanical Response of a Fault. *J. Geophys. Res.* 92 (B7), 6249–6272. doi:10.1029/jb092ib07p06249

Mei, M. X., Ma, Y. S., Deng, J., Li, H., and Zheng, K. B. (2005). Tectonic Palaeogeographic Changes Resulting from the Caledonian Movement and the Formation of the Dianqiangui Basin: Discussion on the Deep Exploration Potential of Oil and Gas in the Dianqiangui Basin. *Earth Sci. Front.* 12, 227–236. (in Chinese with English abstract).

Michard, G. (1979). Géothermomètres Chimiques. *Bull. de BRGM* 2, 183–189.

Ni, S. J., Xu, Z. Q., Zhang, C. J., Song, H., and Luo, C. (2012). Uranium Metallogenesis and Ore Genesis of the Rich-Large Black Rock Series-type Uranium Deposits in Southwest China. *Adv. Earth Sci.* 27, 1035–1042. (in Chinese with English abstract).

Nieva, D., and Nieva, R. (1987). Developments in Geothermal Energy in Mexico-part Twelve. A Cationic Geothermometer for Prospecting of Geothermal Resources. *Heat Recovery Syst. CHP* 7 (3), 243–258. doi:10.1016/0890-4332(87)90138-4

Pagès, A., Barnes, S., Schmid, S., Coveney, R. M., Jr., Schwark, L., Liu, W. H., et al. (2018). Geochemical Investigation of the Lower Cambrian Mineralised Black Shales of South China and the Late Devonian Nick Deposit, Canada. *Ore Geol. Rev.* 94, 396–413. doi:10.1016/j.oregeorev.2018.02.004

Pandarinath, K., and Domínguez-Domínguez, H. (2015). Evaluation of the Solute Geothermometry of Thermal Springs and Drilled Wells of La Primavera (Cerritos Colorados) Geothermal Field, Mexico: a Geochemometrics Approach. *J. South Am. Earth Sci.* 62, 109–124. doi:10.1016/j.jsames.2015.05.002

Pandarinath, K. (2011). Solute Geothermometry of Springs and wells of the Los Azufres and Las Tres Vírgenes Geothermal fields, Mexico. *Int. Geology. Rev.* 53 (9), 1032–1058. doi:10.1080/00206810903442014

Paternoster, M., Oggiano, G., Sinisi, R., Caracausi, A., and Mongelli, G. (2017). Geochemistry of Two Contrasting Deep Fluids in the Sardinia Microplate (Western Mediterranean): Relationships with Tectonics and Heat Sources. *J. Volcanology Geothermal Res.* 336, 108–117. doi:10.1016/j.jvolgeores.2017.02.011

Pi, D.-H., Liu, C.-Q., Shields-Zhou, G. A., and Jiang, S.-Y. (2013). Trace and Rare Earth Element Geochemistry of Black Shale and Kerogen in the Early Cambrian Niutitang Formation in Guizhou Province, South China: Constraints for Redox Environments and Origin of Metal Enrichments. *Precambrian Res.* 225, 218–229. doi:10.1016/j.precamres.2011.07.004

Piper, A. M. (1944). A Graphic Procedure in the Geochemical Interpretation of Water-Analyses. *Trans. AGU* 25 (6), 914–928. doi:10.1029/tr025i006p00914

Reid, A., Wilson, C. J. L., Shun, L., Pearson, N., and Belousova, E. (2007). Mesozoic Plutons of the Yidun Arc, SW China: U-Pb Geochronology and Hf Isotopic Signature. *Ore Geol. Rev.* 31, 88–106. doi:10.1016/j.oregeorev.2004.11.003

Saibi, H., Batir, J. F., and Pocasangre, C. (2021). Hydrochemistry and Geothermometry of thermal Waters from UAE and Their Energetic Potential Assessment. *Geothermics* 92, 102061. doi:10.1016/j.geothermics.2021.102061

Schoeller, H. (1955). Geochemie des eaux souterraines. *Revue De L'institute Francois Du Petrole* 10, 230–244.

Şener, M. F., Şener, M., and Uysal, I. T. (2017). The Evolution of the Cappadocia Geothermal Province, Anatolia (Turkey): Geochemical and Geochronological Evidence. *Hydrogeol. J.* 25, 2323–2345. doi:10.1007/s10040-017-1613-1

Song, X. Q., Duan, Q. S., Meng, F. T., and Cao, Z. D. (2014). Geological Genesis Analysis of the Xifeng Hot Spring in Guizhou. *Geol. Sci. Tech. Inf.* 33 (5), 216–220. (in Chinese with English abstract).

Sverjensky, D. A. (1984). Europium Redox Equilibria in Aqueous Solution. *Earth Planet. Sci. Lett.* 67, 70–78. doi:10.1016/0012-821X(84)90039-6

Taylor, H. P., Jr. (1977). Water/rock Interactions and the Origin of H2O in Granitic Batholiths. *J. Geol. Soc.* 133, 509–558. doi:10.1144/gsjgs.133.6.0509

Tian, J., Pang, Z., Guo, Q., Wang, Y., Li, J., Huang, T., et al. (2018). Geochemistry of Geothermal Fluids with Implications on the Sources of Water and Heat Recharge to the Rekeng High-Temperature Geothermal System in the Eastern Himalayan Syntax. *Geothermics* 74, 92–105. doi:10.1016/j.geothermics.2018.02.006

Tonani, F. B. (1980). "Some Remarks on the Application of Geochemical Techniques in Geothermal Exploration," in *Advances in European Geothermal Research*. Editors A. S. Strub and P. Ungemach (Dordrecht: Springer), 428–443. doi:10.1007/978-94-009-9059-3_38

Truesdell, A. H. (1976). "Summary of Section III: Geochemical Techniques in Exploration," in Proceedings of Second United Nations Symposium on the Development and Use of Geothermal Resources, San Francisco, May 20-29 (Lawrence Berkeley Laboratory), 53–89. U. S. Government Printing Office.

Wang, G. L., Zhang, W., Liang, J. Y., Lin, W. J., Liu, Z. M., and Wang, W. L. (2017a). Evaluation of Geothermal Resources Potential in China. *Acta Geoscientica Sinica* 38 (4), 449–459. doi:10.3975/cagsb.2017.04.02

Wang, H., and Mo, X. (1995). An Outline of the Tectonic Evolution of China. *Episodes* 18, 6–16. doi:10.18814/epiiugs/1995/v18i1.2/003

Wang, H. S., Cai, X. L., Lei, L. F., and Liu, C. B. (2017b). Analysis on Structural Characteristics in Yangshui Mining Area of Kaiyang Phosphate Mine, Central Guizhou. *Geology. Chem. Minerals* 39 (2), 90–95. (in Chinese with English abstract).

Wang, X., Wang, G., Lu, C., Gan, H., and Liu, Z. (2018). Evolution of Deep Parent Fluids of Geothermal Fields in the Nimu-Nagchu Geothermal Belt, Tibet, China. *Geothermics* 71, 118–131. doi:10.1016/j.geothermics.2017.07.010

Wang, Y., Hu, S., Wang, Z., Jiang, G., Hu, D., Zhang, K., et al. (2019a). Heat Flow, Heat Production, Thermal Structure and its Tectonic Implication of the

Southern Tan-Lu Fault Zone, East-Central China. *Geothermics* 82, 254–266. doi:10.1016/j.geothermics.2019.06.007

Wang, Y., Pang, Z., Hao, Y., Fan, Y., Tian, J., and Li, J. (2019b). A Revised Method for Heat Flux Measurement with Applications to the Fracture-Controlled Kangding Geothermal System in the Eastern Himalayan Syntaxis. *Geothermics* 77, 188–203. doi:10.1016/j.geothermics.2018.09.005

Waples, D. W. (2001). A New Model for Heat Flow in Extensional Basins: Radiogenic Heat, Asthenospheric Heat, and the McKenzie Model. *Nat. Resour. Res.* 10, 3. doi:10.1023/a:1012521309181

Yang, E. L., Lu, X. B., Bao, M., Luo, J. J., and Hu, Q. C. (2013). Enrichment and Origin of Some Trace Elements in Black Shales from the Early Cambrian in Eastern Guizhou Province. *Adv. Earth Sci.* 28, 1160–1169. doi:10.11867/j.issn.1001-8166.2013.10.1160

Yang, R. K., Luo, W., Pei, Y. W., and Wang, Q. (2018). Distribution and Fluids Hydrochemistry Characteristics of Hydrothermal Resources in Guizhou Province. *Geol. Surv. China* 5 (2), 38–44. doi:10.19388/j.zgdzdc.2018.02.06

Yu, J., Zhang, H., Yu, F., and Liu, D. (1984). Oxygen and Hydrogen Isotopic Compositions of Meteoric Waters in the Eastern Part of Xizang. *Chin. J. Geochem.* 3 (2), 93–101. doi:10.1007/BF03179285

Zhang, X. P., Sun, W. Z., and Liu, J. M. (2005). Stable Isotopes in Precipitation in the Vapor Transport Path in Kunming of Southwest China. *Resour. Environ. Yangtze Basin* 14 (5), 665–669. doi:10.1007/s11769-005-0033-7

Zhang, X. Q., Huang, K. P., Yuan, L., Shen, X. D., and Zheng, M. R. (2017). Prospecting Potential Analysis and Uranium Mineralization Control of Deep Fracture and Interlayer Detachment Structure System of Baimadong Uranium deposit in Guizhou. *Guizhou Geol.* 34, 237–243. doi:10.3969/j.issn.1000-5943.2017.04.004

Zhang, Y., Tan, H., Zhang, W., Wei, H., and Dong, T. (2016). Geochemical Constraint on Origin and Evolution of Solutes in Geothermal Springs in Western Yunnan, China. *Geochemistry* 76, 63–75. doi:10.1016/j.chemer.2015.11.002

Zhao, P., Wang, J. Y., Wang, J. A., and Luo, D. G. (1995). Characteristics of Heat Production Distribution in SE China. *Acta Petrologica Sinica* 11 (3), 292–305.

Zheng, H. R., Luo, J., Zhang, Y., Feng, J. Y., Zeng, Y., and Wang, M. C. (2021). Geological Characteristics and Distribution of Granite Geothermal Reservoir in Southeast Coastal Areas in China. *Front. Earth Sci.* 9, 683–696. doi:10.3389/feart.2021.683696

Zhou, M.-F., Yan, D.-P., Kennedy, A. K., Li, Y., and Ding, J. (2002). SHRIMP U-Pb Zircon Geochronological and Geochemical Evidence for Neoproterozoic Arc-Magmatism along the Western Margin of the Yangtze Block, South China. *Earth Planet. Sci. Lett.* 196, 51–67. doi:10.1016/s0012-821x(01)00595-7

Zhu, P. P. (2016). Frictional Strength and Heat Flow of Southern San Andreas Fault. *J. Seismol.* 20 (1), 291–304. doi:10.1007/s10950-015-9527-7

Conflict of Interest: The handling editor declared a shared affiliation with the authors JD and CZ at the time of review

The authors declare that the research was conducted in the absence of any commercial or financial relationships that could be construed as a potential conflict of interest.

Publisher's Note: All claims expressed in this article are solely those of the authors and do not necessarily represent those of their affiliated organizations, or those of the publisher, the editors and the reviewers. Any product that may be evaluated in this article, or claim that may be made by its manufacturer, is not guaranteed or endorsed by the publisher.

frontiers in Earth Science

ORIGINAL RESEARCH
published: 03 January 2022
doi: 10.3389/feart.2021.787057

Assessing the Geothermal Resource Potential of an Active Oil Field by Integrating a 3D Geological Model With the Hydro-Thermal Coupled Simulation

Yonghui Huang[1,2,3], *Yuanzhi Cheng*[1,2,3]*, *Lu Ren*[4], *Fei Tian*[1,2,3], *Sheng Pan*[5], *Ke Wang*[1,2,3], *Jianwei Wang*[4], *Yuexia Dong*[6] *and Yanlong Kong*[1,2,3]*

[1]*Key Laboratory of Shale Gas and Geoengineering, Institute of Geology and Geophysics, Chinese Academy of Sciences, Beijing, China,* [2]*Innovation Academy for Earth Science, Chinese Academy of Sciences, Beijing, China,* [3]*College of Earth and Planetary Sciences, University of Chinese Academy of Sciences, Beijing, China,* [4]*Jidong Oilfield Company of PetroChina, Tangshan, China,* [5]*Key Laboratory of Continental Collision and Plateau Uplift, Institute of Tibetan Plateau Research, Chinese Academy of Sciences, Beijing, China,* [6]*Advisory Center, China National Petroleum Corporation, Beijing, China*

OPEN ACCESS

Edited by:
Mohammad Parsa,
University of New Brunswick
Fredericton, Canada

Reviewed by:
Harish Puppala,
BML Munjal University, India
Oleg E. Melnik,
Lomonosov Moscow State University,
Russia

***Correspondence:**
Yanlong Kong
ylkong@mail.iggcas.ac.cn
Yuanzhi Cheng
chengyuanzhi@mail.iggcas.ac.cn

Specialty section:
This article was submitted to Economic Geology, a section of the journal Frontiers in Earth Science

Received: *30 September 2021*
Accepted: *15 November 2021*
Published: *03 January 2022*

Citation:
Huang Y, Cheng Y, Ren L, Tian F, Pan S, Wang K, Wang J, Dong Y and Kong Y (2022) Assessing the Geothermal Resource Potential of an Active Oil Field by Integrating a 3D Geological Model With the Hydro-Thermal Coupled Simulation. Front. Earth Sci. 9:787057. doi: 10.3389/feart.2021.787057

Assessment of available geothermal resources in the deep oil field is important to the synergy exploitation of oil and geothermal resources. A revised volumetric approach is proposed in this work for evaluating deep geothermal potential in an active oil field by integrating a 3D geological model into a hydrothermal (HT)-coupled numerical model. Based on the analysis of the geological data and geothermal conditions, a 3D geological model is established with respect to the study area, which is discretized into grids or elements represented in the geological model. An HT-coupled numerical model was applied based on the static geological model to approximate the natural-state model of the geothermal reservoir, where the thermal distribution information can be extracted. Then the geothermal resource in each small grid element is calculated using a volumetric method, and the overall geothermal resource of the reservoirs can be obtained by making an integration over each element of the geological model. A further parametric study is carried out to investigate the influence of oil and gas saturations on the overall heat resources. The 3D geological model can provide detailed information on the reservoir volume, while the HT natural-state numerical model addressed the temperature distribution in the reservoir by taking into account complex geological structures and contrast heterogeneity. Therefore, integrating the 3D geological modeling and HT numerical model into the geothermal resource assessment improved its accuracy and helped to identify the distribution map of the available geothermal resources, which indicate optimal locations for further development and utilization of the geothermal resources. The Caofeidian new town Jidong oil field serves as an example to depict the calculation workflow. The simulation results demonstrate in the Caofeidian new town geothermal reservoir that the total amount of geothermal resources, using the proposed calculation method, is found to be 1.23e+18 J, and the total geothermal fluid volume is 8.97e+8 m^3. Moreover, this approach clearly identifies the regions with the highest potential for geothermal resources. We believe this approach provides an alternative

method for geothermal potential assessment in oil fields, which can be also applied globally.

Keywords: geothermal resource, geological model, HT model, geothermal energy in oil fields, fault model

1 INTRODUCTION

Due to the increasing market demand for energy, the shortage of conventional fossil fuels, and the concerns regarding the environmental aspects, the exploitation of renewable energy has become the focus of research and keeps gaining attention in recent years. Geothermal energy is a stable, environmentally friendly, and cheap renewable energy source, showing a promising perspective as a conventional fuel substitute. Such energy transition promotes geothermal energy development in oil fields.

Developing geothermal energy in oil fields offers remarkable natural advantages: 1) producing geothermal energy from oil and gas wells is an economically efficient way since drilling costs can be significantly saved. 2) Sufficient data and geological information have been collected from the long-term oil and gas productions, which could minimize the uncertainties and risks in geothermal production.

To achieve an efficient development of geothermal energy in an oil field, a solid knowledge of the overall geothermal resources and their distribution is an indispensable factor. Geothermal resource assessment is a standard practice adopted by the geothermal industry in evaluating a geothermal system and its potential generation capacity. It plays a crucial role in quantifying the amount of available thermal energy for geothermal exploration, providing essential information for further decision making, economical evaluation, and so on. It also serves as a framework for developing a geothermal prospect in a sustainable manner. The success of a geothermal development project relies on a robust resource assessment methodology that can predict, with a lower level of uncertainty, the magnitude of energy that is stored and can be extracted and utilized from a given geothermal reservoir.

The quantification of geothermal resources in oil and gas reservoirs requires subsurface temperature and volume information, which can be a demanding task to accurately assess (Li and Sun, 2014). Common methods for assessing geothermal resource potential include the volumetric "heat in place" method (Muffler and Cataldi, 1978) (i.e., volumetric method), analytical method, and numerical modeling method (Ciriaco et al., 2020). According to Li and Sun (2014), the volumetric method is a suitable approach for the estimation of geothermal resources in oil and gas reservoirs. In the volumetric method, two major aspects must be considered to achieve an accurate assessment of the geothermal resources: first, a good understanding of the geological structure, which includes the identification of the boundaries of a geothermal reservoir, and the volume estimation of the reservoir; and second, inferring the temperature distribution of the geothermal reservoir. Recently, scholars have extended the volumetric method to improve the accuracy of geothermal potential assessment or provide the associated uncertainty estimation of individual parameters. Pocasangre and Fujimitsu (2018) presented a Python-based stochastic library for evaluating geothermal power potential using the volumetric method.

However, previous research to some extent isolated the geothermal resources with the complex geological structure interpretation. With the wide applications of geophysical methods in geothermal explorations and resource assessments, the detailed geological characteristics can be well interpreted. Carrier et al. (2019) proposed new geoelectrical methods to identify thermal groundwater at depth, and the combination of the resistivity and gravity models provides an effective and reliable method for the imaging of shallow geothermal resources. Tian et al. (2020) combined the volumetric method with a microtremor survey, which identifies the specific thickness of the layers for each junior unit. Cheng et al. (2021) constructed a 3D resistivity structure in the hydrothermal (HT) system for setting up the geothermal conceptual models.

Recently, to integrate different sources of geological data, 3D geological modeling is emerging as a comprehensive method. The combination of 3D geological modeling can be used to calculate the volume of a reservoir accurately and automatically and assign values to parameters of each element to achieve an accurate calculation of geothermal reserves. Moreover, 3D geological modeling is helpful to analyze the geothermal geological conditions and realize the visualization of geological structures, especially for regions in which complex geological settings are expected. In recent years, more and more attempts have been made to link the volumetric method to 3D geological modeling. Calcagno et al. (2014) presented an integrated 3D method to estimate the geothermal potential, by taking into account the coherent and well-constraint interpretation of the geological structure. Zhu et al. (2020) created a 3D geological model and then interpolated isothermal surfaces into the model. Finally, the geothermal resource potential can be calculated by the integration of the geological model and the isothermal surfaces.

Besides the detailed 3D geological interpretation, accurate thermal information and 3D thermal model are also of particular importance for geothermal resource assessment. Traditionally, the calculated temperature distribution is based on either the geostatistical interpolation with well-log data or a 1D analytical temperature solution along the depth profiles (Bédard et al., 2020). Although these methods offer a convenient estimation with short computation time, they might lack a physical underpinning, as the influence of comprehensive geological structures and faults and fractures on the thermal distribution cannot be well addressed, which leads to an inaccurate temperature prediction. Numerical modeling serves as an efficient and powerful tool for the computing of the temperature field in the fluid environment as well as useful tools for simulating local temperature distribution in geothermal and their surroundings. Fuchs et al. (2020) presented a 3D

numerical crustal temperature model with inverse optimization methodology and analyze the present-day conductive thermal field of the Danish onshore. Gascuel et al. (2020) presented a numerical simulation routine to analyze the information available from a small and sparse dataset to predict temperature distribution at depth for remote sedimentary basins and assess the geothermal resource potential. A novel lithospheric-scale 3D temperature model of the Hungary geothermal reservoir is proposed in Békési et al. (2020) and Békési et al. (2018), in which the observed temperature anomalies can be approximated by updating the thermal properties of the layers through the ensemble smoother with multiple data assimilation techniques.

Upon the considerations, a revised volumetric method is applied for the geothermal resource assessment in oil fields by integrating a 3D geological model with HT-coupled natural-state modeling. A Petrel–OpenGeoSys coupling routine is provided to fulfill the goals. First, a detailed 3D geological model is established via Schlumberger–Petrel, by interpreting the well-log data. A python script is used to convert the GRDECL format exported by Petrel into VTU format, which can be either imported to Paraview for a further post-process or serve as a finite element mesh input to an open-source code OpenGeoSys (OGS) (Kolditz et al., 2012) for numerical simulation. A 3D HT-coupled model is run in OGS until a quasi-equilibrium state is reached. The temperature values are thereby assigned to each grid element of the 3D mesh. Then, the total geothermal resources of the reservoir can be assessed with the revised volumetric method by integrating geothermal resource value over each grid element.

With the help of the geological model, the volume distribution can be obtained, and the thickness of the geothermal formation can also be identified accurately. The integration of 3D geological modeling into the HT numerical simulation could help to analyze the potential and distribution of geothermal resources. By this integration, the study visualizes the local geological structures and isothermal surfaces and identifies the local thermal anomalies. Based on geothermal field analysis, the distribution of resources can be analyzed comprehensively.

The proposed workflow has been applied to a geothermal reservoir in the Caofeidian new town Jidong oil field. It is currently the focus for geothermal exploration and development in the Jidong oil field.

The paper is organized as follows: first, the detailed geological setting is introduced (**Section 2**). The section is followed by a detailed description of the revised volumetric method (**Section 3**). In **Section 4**, the 3D geological model setup and the HT model simulation results in the Caofeidian new town are summarized and presented. The temperature distribution and geothermal resources in this area are characterized. A comprehensive discussion on the calculation results is made thereby. Finally, **Section 5** is dedicated to conclusions and gives some perspective outlook of this study.

2 GEOLOGICAL SETTING

Jidong oil field is located in the Nanpu Sag. The Nanpu sag is in the northern part of the North China Plain geographically and in the central north of the Bohai Bay Rift Basin tectonically. Lying against the southern margin of the Yanshan platform fold belt to the north, it is a single-faulted ridge sag with a fault in the north and overlap in the south formed by Mesozoic and Cenozoic rifts on the base of the North China platform, covering an area of 1,930 km^2 (Lai et al., 2019). The Nanpu sag and the surrounding areas include three sub-sags (i.e., Shichang sub-sag, Linque sub-sag, and Caofeidian sub-sag) and three bulges (i.e., Baigezhuang bulge, Matouying bulge, and Laowangzhuang bulge) (**Figure 1**).

During the late Yanshan Movement–Early Himalayan Movement, as the tectonic stress field in east China shifted from northwest (NW) compression to NW extension, the structural deformations in the Nanpu sag and its surrounding areas were affected by the Tanlu strike–slip fault zone and Zhangjiakou–Penglai strike–slip fault zone, where multiple periods of geological activities resulted in a series of northeast (NE)-trending faults, which imposes dominant controls on geothermal resource distribution. Moreover, the well-developed sedimentary caprock in the Tertiary of the Nanpu sag provides good conditions for the formation of geothermal resources.

Our study is focused on the Caofeidian new town, which is located in the northeast of the Nanpu Sag (as shown in **Figure 1**). Significant urban development directly forms above the reservoir, indicating large heat demands, heat can be utilized directly above the source with minimal losses in terms of heat transporting. This region is currently the focus of geothermal exploration and development in the Jidong oil field. The pilot projects of geothermal heating supply have been carried out in this area.

Caofeidian geothermal field, as part of the Gaoshangpu–Liuzan geothermal field, is located between the Shichang sub-sag and the Matouying uplift area. According to the seismic interpretation results, the geothermal reservoir of the Caofeidian new town is located in the southern part of the Gaoshangpu–Liuzan structural belt. The northern boundary of the water area is the Gaoliu fault, the east and west boundaries are controlled by the drilling wells within the Caofeidian new town area, and the southern boundary is controlled by the onshore drilling wells, with a total area of 27.85 km^2. As faults often serve as fast channels for heat convection and conduction, the geothermal anomaly zones often locate close to the faults (Kong et al., 2020). In this area, geothermal anomaly zones are found distributed on both sides of the Gaoliu fault.

2.1 Stratigraphic Characteristics

The Nanpu sag is a Tertiary sedimentary lake basin developing on the basement of the Middle Paleozoic. The sedimentary stratigraphy of the Nanpu Sag has been extensively studied mostly through drilling for hydrocarbon exploration. From the top to bottom formations, the Cenozoic sedimentary strata formed in the Nanpu Sag include Quaternary strata, the Minghuazhen (Nm) and Neogene Guantao (Ng) formations, and the Dongying (Ed) and Paleogene Shahejie (Es) formations (Guo et al., 2013). The Minghuazhen and Neogene Guantao Formations throughout the Nanpu sag are deposited in a low-sinuosity fluvial system and a braided fluvial system with well-developed sandstone.

The Nanpu Sag is characterized as the richest oil-bearing basin in northeast China. The sandstones constitute an important reservoir not only for oil and gas deposits but also for geothermal purposes. The Guantao Formation serves as the main geothermal reservoir in the Jidong oil field for bearing

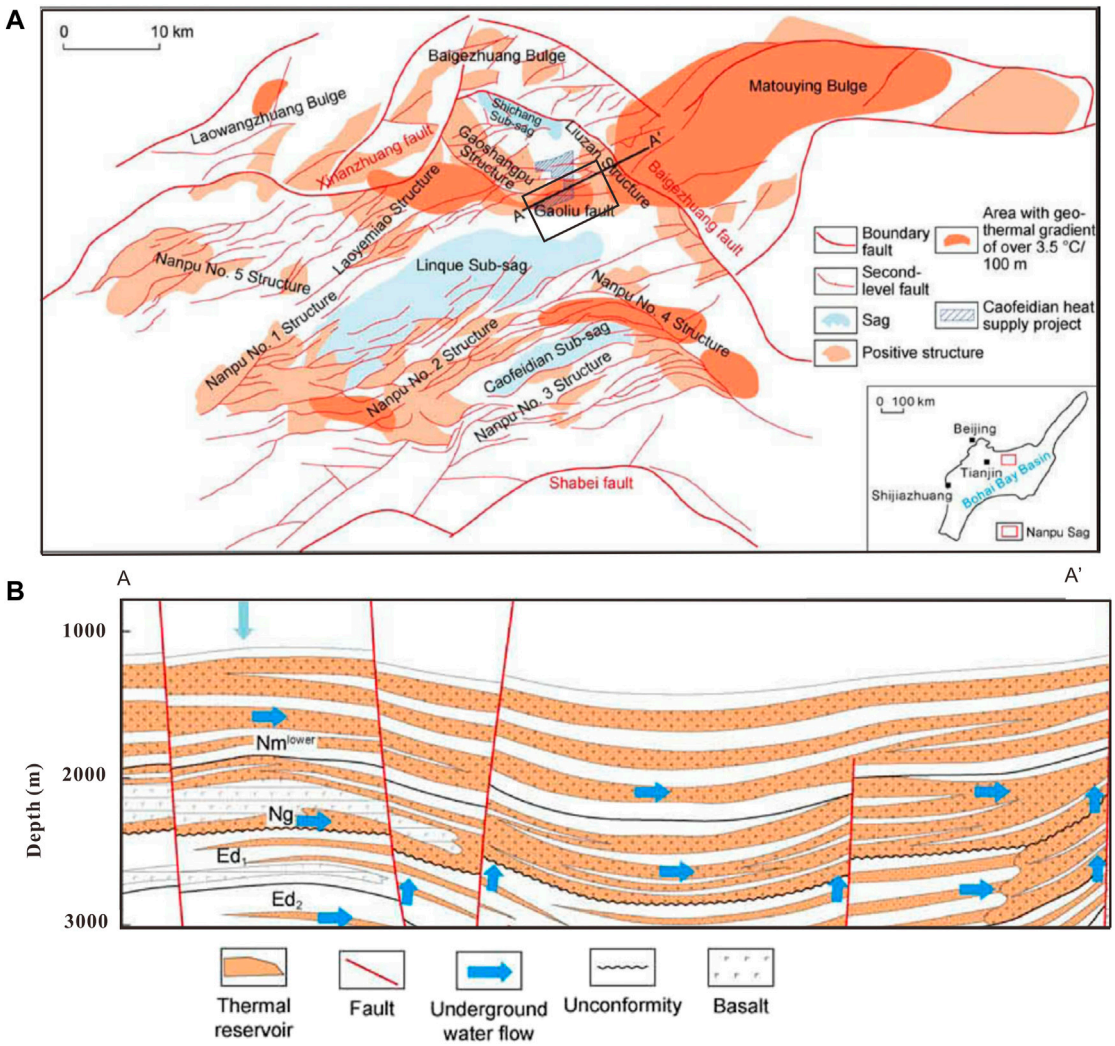

FIGURE 1 | (A) The geological map and distribution of geothermal anomalous zones in the Nanpu sag. The location of Caofeidian new town is also labeled as a black rectangle. **(B)** Cross-section profile of the Caofeidian new town geothermal field [revised from Dong et al. (2021)].

relatively high-temperature geothermal water. It also holds a relatively high thickness, which can be as large as 350–600 m. The Guantao Formation is dominated by braided river deposits and interchannel deposits, with sand contents of 60%–70%. It consists of gray-white massive sandstone, glutenite, basic volcanic rock, and thin layers of gray and variegated mudstone.

The Guantao Formation can be divided into 4 members from top to bottom, which correspond to members Ng1, Ng2, Ng3, and Ng4, wherein members Ng1–Ng3 are considered as the main formation for geothermal resource exploitation due to the large thickness and good connectivity. The averaged porosity in the Guantao Formation is approximately 25%–35%, and the permeability ranges between 600 and 2,000 mD.

2.2 Regional Thermal Background

The Nanpu sag has undergone four stages of rifting since the Cenozoic, and each stage of rifting was accompanied by a magmatic thermal event (Dong et al., 2010). Therefore, the Nanpu sag is often characterized by a relatively high thermal background.

The current heat flow in the Nanpu sag can reach 93.8–100.1 mW/m^2, basically comparable with that of Xiongxian County, Hebei (113.9 mW/m^2) and Dagang, Tianjin (105.9 mW/m^2). The Matouying bulge has a higher heat flow value of 148.9 mW/m^2. The heat flow distribution in this area exhibits "high in the bulges and low in the sub-sags." According to the data information collected from drilling wells, the geothermal gradient at the bottom of the Cenozoic caprock is over 5.0°C/100 m and 8.3°C/100 m at maximum. In the sag area, the geothermal gradient at the bottom of the Cenozoic caprock is lower (3.0–4.0°C/100 m). The geothermal fluid temperature of the Guantao Formation in the Nanpu sag is mostly below 90°C, so these geothermal fields are characterized as low-medium enthalpy geothermal fields.

Forty geothermal wells have been drilled in the Caofeidian new town area as shown in **Figure 2**. The associated bottom hole

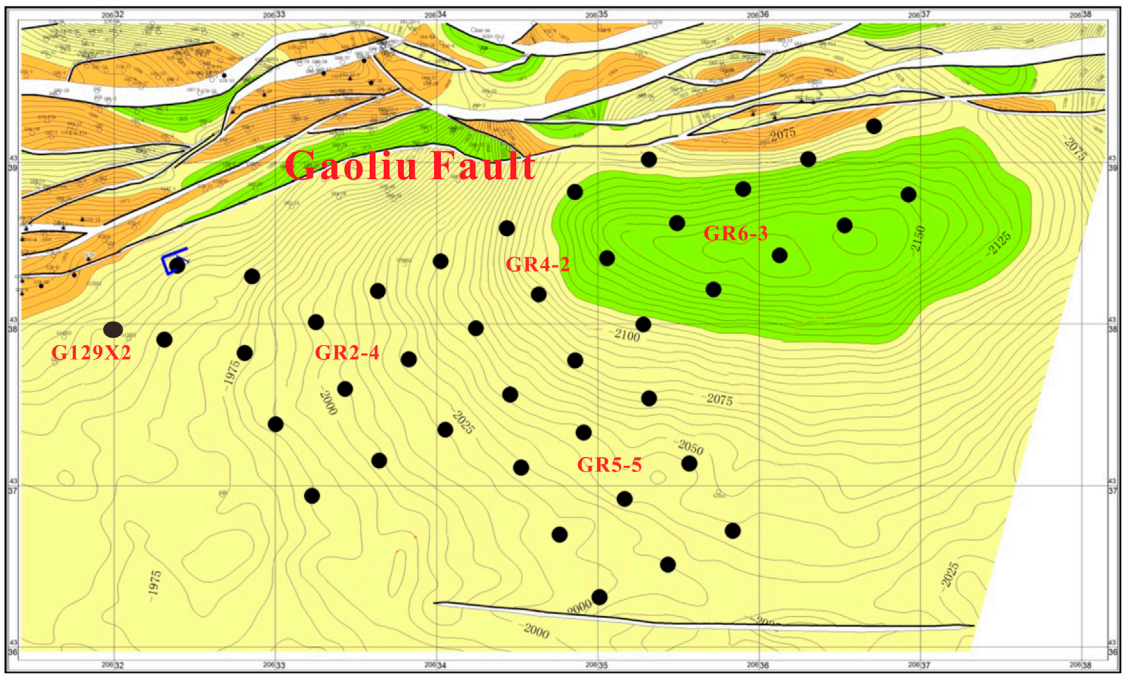

FIGURE 2 | The well locations in the study area are labeled by black circles.

pressure (BHP) and bottom hole temperature (BHT) data have been collected and corrected to minimize both drilling disturbance and paleoclimatic variations. It is important to note that the geothermal resource exploration in the Caofeidian new town area is a pilot project and is still in an early stage. Consequently, there are rare equilibrium temperature logging data available, and the measured thermal conductivity data are lacking as well. The corrected BHT data are further applied to calculate the surface heat flow and geothermal gradients. The calculated heat flow in the Caofeidian geothermal field ranges between 50 and 74 mW/m^2, while the thermal gradient ranges between 26 and 36°C/100 m. According to the report from previous literature (Jiang et al., 2019), the arithmetic mean thermal conductivity in the Nanpu sag is approximately 2 W/(mK).

3 METHODS

3.1 3D Geological Modeling

In this section, a detailed account is given of the construction of the geological model of the Caofeidian geothermal formation using available well-log data. Petrel software was used as the 3D geological modeling packages to represent the reservoir geology, structure, stratigraphic envelope, reservoir sublayers, and faults in 3D, which further result in the structural and property models. The reservoir volume is discretized into a 3D mesh with elements. For each element, lithofacies and rock properties such as porosity and permeability are assigned.

The 3D geological model can show intuitively the topography and geomorphology, stratum lithology, and spatial variation of geological structures. The relationship between them can be also addressed. In this work, the 3D geological model covers the Minghuazhen and Guantao Formations, i.e., from the top to bottom: Nm3, Ng1, Ng2, Ng3, and Ng4. And the depth of the model ranges from 1,900 to 2,800 m. As members Ng1–Ng3 are the main formations for the geothermal exploration, a special focus has been placed on members Ng1–Ng3.

The first step of the geological model construction is to model the horizon of the Caofeidian geothermal formation with the structural map and the well-log data. Reinterpreted formation tops with well logs (Bédard et al., 2020) are used in this study as the basis for the interpretation of the formation horizons in depth. The surfaces of the Minghuazhen and Guantao Formations are modeled with the formation tops in wells along the depth. The horizons are then interpolated between the wells.

By considering the regional tectonic background of the study area, the characteristics of fault systems and combination patterns of faults were sorted, to make clear the plane and vertical combinations of faults. Subsequently, a stratigraphic framework was built based on the interpreted horizon interfaces and fault model and then a 3D geological structure model in the domain. The 3D faulted model was divided by faults according to the geological structure map.

After the geological structure model is fully set up, the distribution of reservoir properties is described, and a sedimentary facies model is constructed. In this study, a dual modeling approach combining the deterministic and stochastic models is applied to establish the reservoir properties within the data-constrained modeling program.

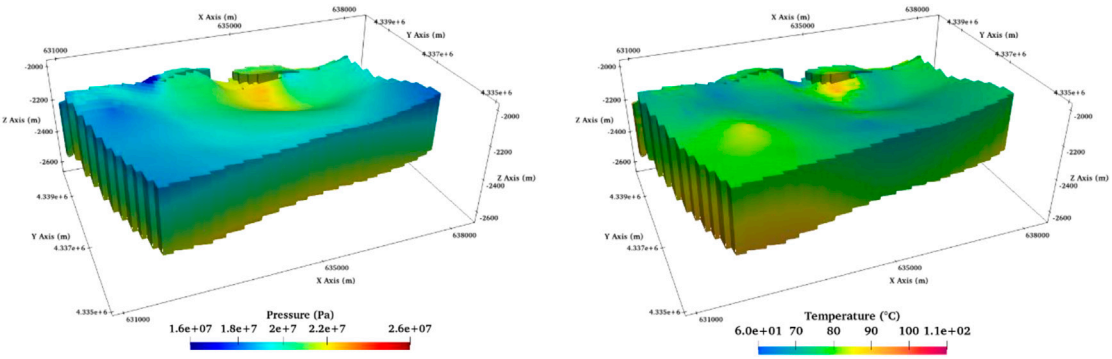

FIGURE 3 | The initial conditions of pressure (Pa) and temperature (°C). Note that the figure has been zoomed in on the *z*-axis by a factor of 4.

3.2 Hydrothermal-Coupled Natural-State Simulation

In this section, an HT-coupled numerical model is performed to characterize the temperature distribution in the Caofeidian geothermal field. The structure and petrophysical property information from the 3D geological model serve as inputs to the numerical model.

3.2.1 Governing Equation

The governing equations to describe the HT-coupled model are presented here.

According to the mass conservation of both liquid and solid phases, aqueous fluid flow in porous media can be expressed as

$$S_m \frac{\partial p}{\partial t} + \nabla \cdot \mathbf{q}_m = 0 \tag{1}$$

where S_m is the constrained specific storage (1/Pa) and $\mathbf{q}_m$ is the Darcy velocity vector (m/s). The specific storage undergoes a mechanical alteration in response to pressure and can be given as $S_m = (1 - \mathrm{n}) \times \mathrm{K}_s + \mathrm{n} \times \mathrm{K}_l$ in terms of the bulk modulus of solid K_s and that of liquid K_l (Pa). The Darcy velocity q_m is given as

$$\mathbf{q}_m = -\frac{\boldsymbol{K}}{\mu}\left(\nabla p + \rho_l(\mathrm{T})\mathbf{g}\right)$$

The temperature distribution is based on the energy conservation of the solid–fluid mixture assuming local thermal equilibrium between the two phases (Ts = Tf = T):

$$c\rho(\mathrm{T})\frac{\partial \mathrm{T}}{\partial \mathrm{t}} + \nabla\left(\mathrm{c_l}\rho_l(\mathrm{T})\mathbf{q}_m\mathrm{T}\right) - \nabla\left(\lambda_b \nabla \mathrm{T}\right) = 0 \tag{2}$$

λ_b represents the bulk thermal conductivity, which can be estimated as $\lambda_b = \mathrm{n}\lambda_f + (1 - n)\lambda_s$, with λ_f and λ_s corresponding to the fluid and solid thermal conductivities. c and $\mathrm{c_l}$ (J/kg/K) are the specific heat capacities of the porous medium and geothermal fluid, respectively, with c defined as

$$c\rho(\mathrm{T}) = (1 - \mathrm{n})\mathrm{c_s}\rho_s + \mathrm{nc_l}\rho_l(\mathrm{T})$$

In the model, faults can be idealized as a 2D parallel plate with a prescribed thickness. The fluid and heat flux should be exchanged between porous medium and faults. To numerically handle these exchanges is to impose continuity conditions of pressure and temperature along the boundary of porous media and faults. The so-called "common node approach" in the finite element method (FEM) is adopted in the model, which is essentially based on the superposition of 2D fault elements onto the elements of the rock matrix. Thus, nodes at fault locations are common nodes that receive contributions from both the rock matrix elements and the fault faces (Blessent et al., 2009). The approach is feasible when faults have higher permeability and the fluid flow within the fault mainly occurs along the fault surfaces.

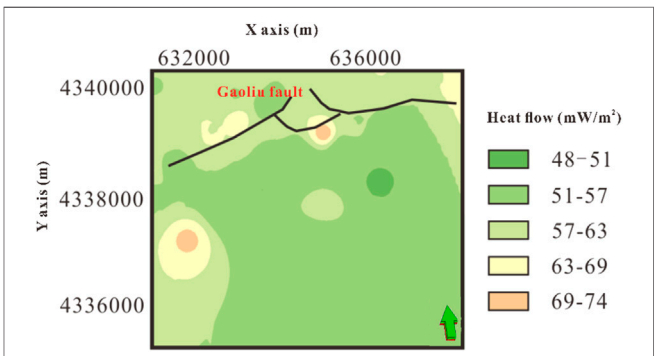

FIGURE 4 | The heat flow distribution in the study area.

The governing equations have been implemented in a flexible, object-oriented, FEM-based numerical framework OpenGeoSys-V5 (Kolditz et al., 2012). The discretized linear system is solved using a preconditioned Krylov space solver (BiCGSTAB). A Newton–Raphson iteration scheme is employed for the linearization.

3.2.2 Model Setup

3.2.1.1 Initial Conditions

The BHP in (Pa) at each well can be obtained from the well-log data. By assuming the pressure at the top surface (depth = 0 m) is identical to the atmospheric pressure, the gradient of the pressure p'_{grad} in (Pa m^{-1}) at the well can be calculated as

$$p'_{grad} = \left(\frac{\mathrm{P}_{BHP} - \mathrm{P}_{atm}}{\mathrm{z}_{BHP}}\right)$$

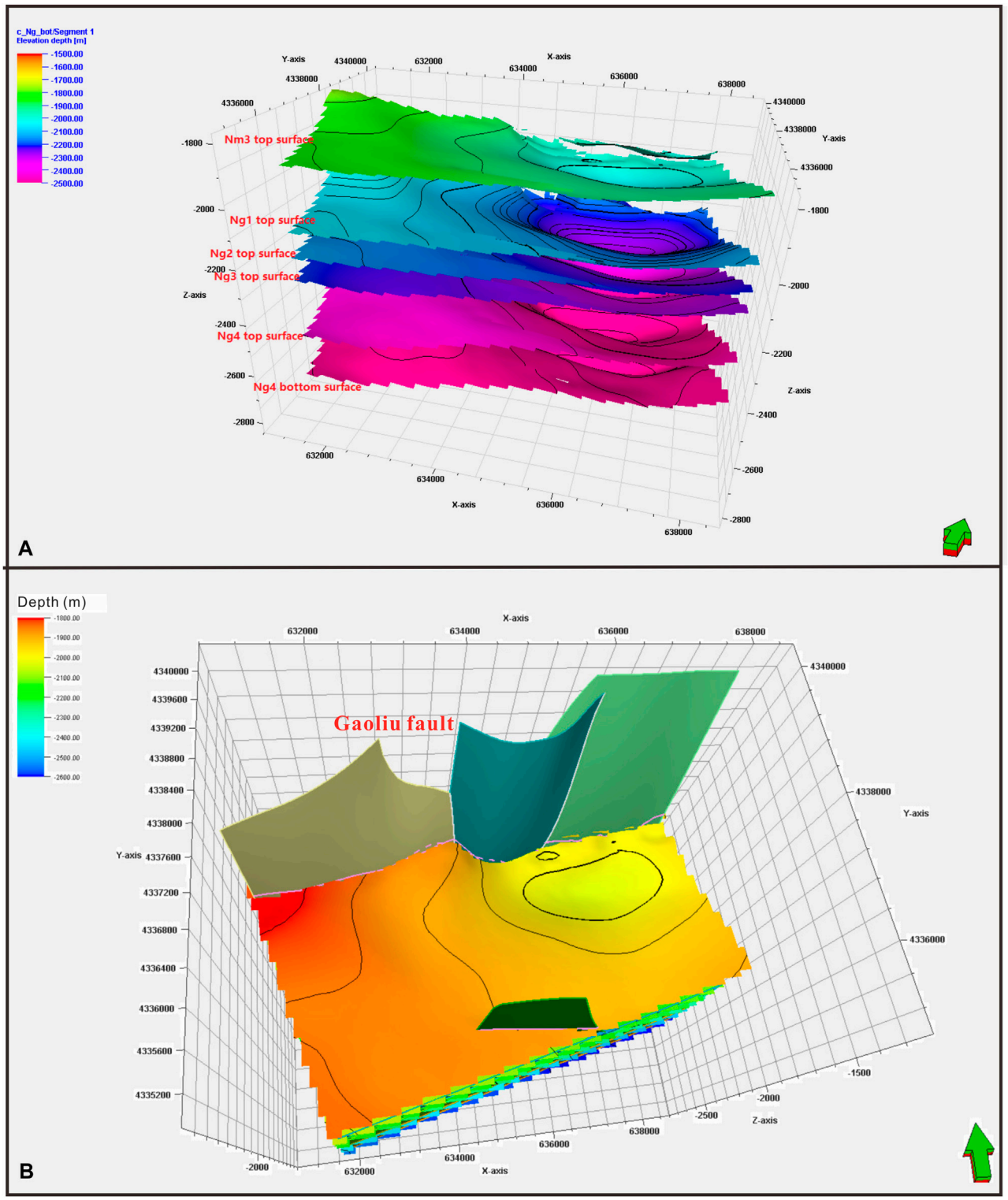

FIGURE 5 | Qualitative sketch of the 3D geological model. **(A)** The geological horizons of Minghuazhen and Guantao Formations (Nm3 and Ng1–Ng4). **(B)** The geometry of the fault developments in the 3D geological model.

where z_{BHP} (m) is the depth that corresponds to the BHP.

Then an ordinary Kriging interpolation scheme is performed to get the distribution of the pressure gradient over the entire area of the domain. The experimental variogram is calculated on 40 sampling data at each well, and the variogram was best modeled by a linear function with and a slope of 4.7e−11. Thus, the 3D pressure distribution at each grid element of the 3D geological model can be obtained according to the centroid coordinates of each element following

$$P_{z(\mathrm{Ng})} = \mathrm{P}_{atm} + p'_{grad}(x, y) * z_{\mathrm{Ng}} \tag{3}$$

where $P_{z(\mathrm{Ng})}$ (Pa) is the pressure at depth z (m) and $p'_{grad}(x, y)$ corresponds to the gradient of pressure at the (x, y) coordinates. The interpolated 3D pressure distribution serves as the initial pressure condition of the HT model.

Similarly, we get the temperature initial condition based on the BHT data. No relevant information derived from the well logging indicating the thermal convection is available in this study area. Therefore, a thermal conduction regime is assumed in the model. The temperature distribution can be calculated cell by cell directly in the 3D geological model from the top to bottom using the linear decreasing relationship theory, with the following equation (Bédard et al., 2020):

$$T_{z(\mathrm{Ng})} = T_0 + \left(\frac{Q_0 \cdot z_{\mathrm{Ng}}}{\lambda_{\mathrm{Ng}}}\right)$$

where $T_{z(\mathrm{Ng})}$ (℃) is the temperature at depth z (m) and T_0 is the annually averaged surface temperature that is assumed to be 13.5°C. Q_0 (mW/m^2) is the surface heat flow at the x–y coordinates. λ_{Ng} [W/(m K)] is the thermal conductivity at this depth.

Figure 3 visualizes the initial conditions of pressure and temperature in 3D distribution.

3.2.1.2 Boundary Conditions

For the upper model boundary, we applied a fixed temperature distribution as the Dirichlet boundary condition. For the bottom boundary surface, a Neumann boundary condition is applied to account for the heat flow at this area. The heat flow boundary values vary spatially, as shown in **Figure 4**. All the lateral boundaries are assumed thermal isolated.

3.2.1.3 Model Parameters

Variations in the fluid density and viscosity resulting from the temperature and pressure change are accounted for in the simulations with an equation of state according to the International Association for the Properties of Water and Steam (IAPWS) (Wagner and Kretzschmar, 2008).

The numerical model is run until a steady state is reached. The overall time of 10 thousand years was considered sufficiently long for the model to reach a steady state and therefore reflect the natural state of the geothermal reservoir. The varied time step size is applied in the model with the maximum time step size set to 1 thousand years.

3.3 Geothermal Resources

After the subsurface temperature was assessed, the estimation of the geothermal resources was then achieved with the 3D model calculating the thermal energy in place or heat volume.

The governing equation of the revised volumetric method on the overall geothermal resources can be written as

$$Q = \sum_{i=0}^{N} V_i (T_i - T_0)\left[\rho_r C_r (1 - \varphi_i) + \rho_w C_w \varphi_i\right] \tag{4}$$

where ρ_r and ρ_w are the density of rock and fluid, respectively, in kg/m^3; C_r and C_w are the specific heat capacity of rock and fluid, respectively, in J/kg/°C. The subscript i indicates the element index of the mesh, and N is the total number of elements of the mesh. V_i is the volume of the ith element, while T_i and φ_i are the temperature and porosity, respectively, of the ith element. T_0 is the reference temperature, which corresponds to the constant temperature of the surface.

To summarize the overall workflow, we thus propose a revised volumetric methodology for estimating the geothermal potential by coupling the 3D geological model with the HT numerical simulation.

1) A coherent 3D geological model interpreted based on the field and well data is established by Petrel.
2) The 3D geological model is converted into a mesh in Paraview format, which can be imported to OpenGeoSys software to prepare the HT-coupled numerical model. The thermal and pressure initial and boundary conditions are simultaneously included in the model.
3) The 3D HT model considering the geological structure and thermal properties of the rocks runs until a natural equilibrium state is reached. The natural-state model is validated against the measured temperature logs at different wells.
4) Finally, the geothermal resources on each grid element can be estimated by the volumetric method considering the volume and temperature data assigned to this cell. Then the total geothermal resources are further calculated by integrating each grid element over the whole domain.

4 RESULT AND DISCUSSION

4.1 3D Geological Modeling

4.1.1 Horizon

Identifying the thickness and the directions of layers among the horizons of this 3D grid was of particular importance to construct the structure framework. Moreover, identifying an estimation of the geothermal resource requires an accurate illustration of layered volumes. Therefore, each unit in the Guantao Formation had been divided into many layers based on the lithological and petrophysical properties. **Figure 5A** illustrates the layering of the geological model with respect to the Guantao model. It can be observed that Ng1 and Ng2 are relatively thin, which hold thickness at approximately 75–100 m, while Ng3 is rather thicker, which is more than 150 m thick. Ng1 and Ng2 consist of 20 layers; however, Ng3 consists of 40 layers based on the petrophysical properties.

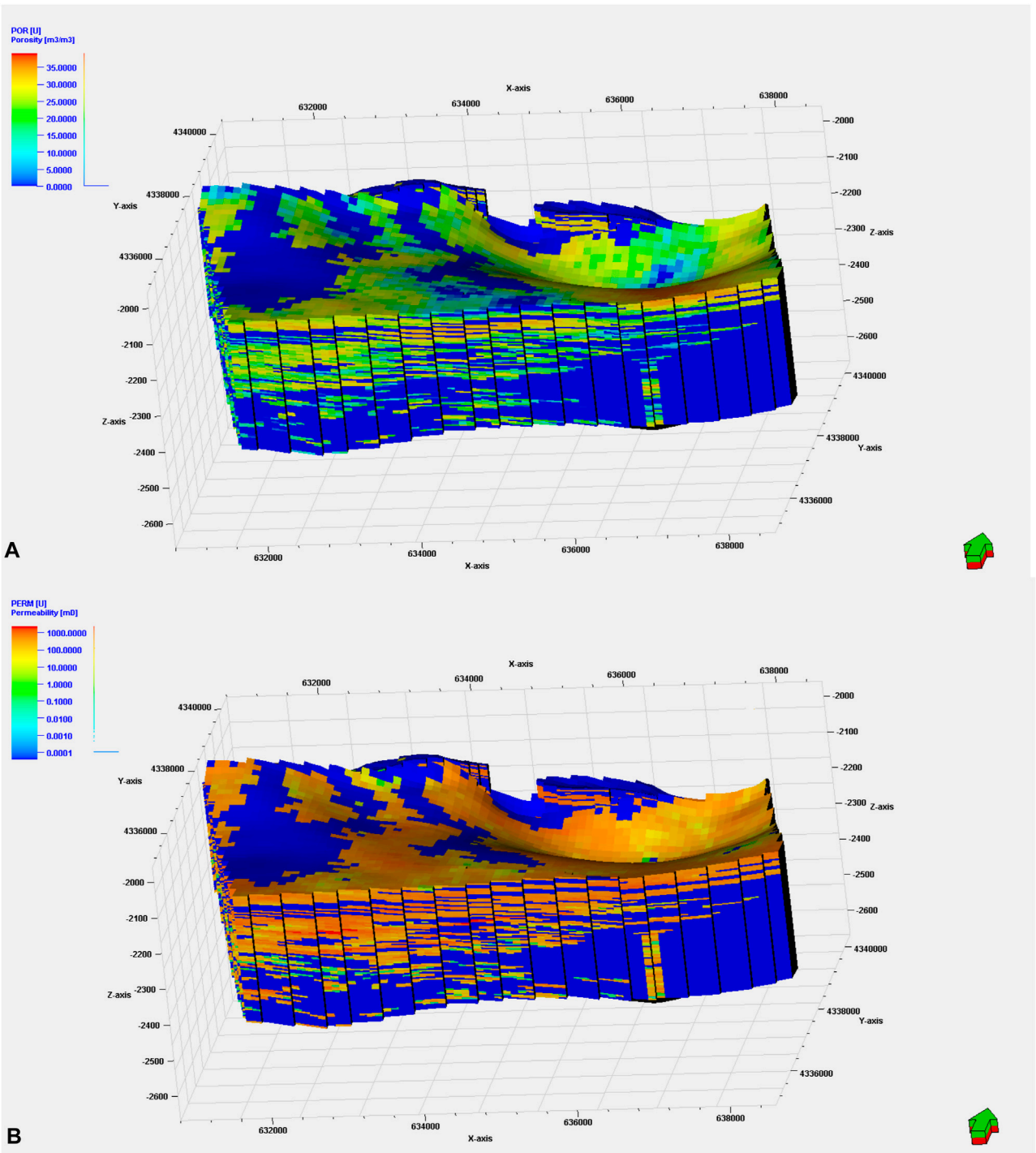

FIGURE 6 | (A) The 3D porosity (%) model and **(B)** the permeability (mD) model for members Ng1–Ng3 of the Guantao Formation. Note that permeability is presented in log scale.

4.1.2 Fault Model

The fault model was the primary step for constructing the structure model with Petrel tools. Special attention has been paid to the Gaoliu fault since it plays the dominant role in this area. The fault polygons that the Petrel software provides are applied in this fault model to characterize each type of vertical fault, diagonal fault, curve fault, and various geometry structure faults. The initial surface is established by applying fault polygon with various stratification planes. Then fault section is corrected by adjusting the fault section. By using the

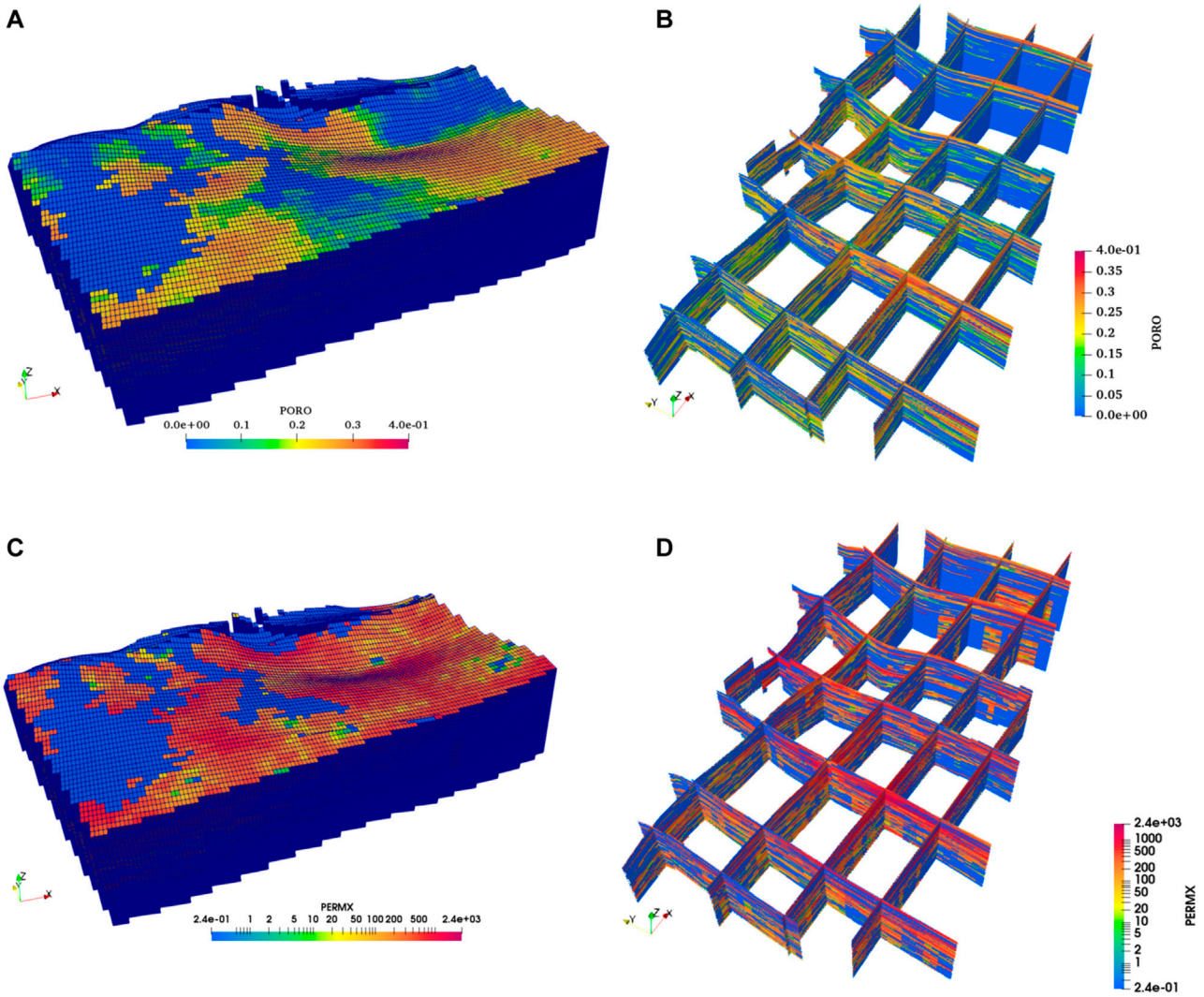

FIGURE 7 | The converted mesh with **(A)** 3D porosity (–) distribution, **(B)** the cross-section profile of porosity, **(C)** 3D permeability (mD) distribution, and **(D)** the cross-section profile of permeability, shown in Paraview. Note that the permeability is presented in log scale.

breakpoint data obtained from single well correlations, the position and shape of fault can be conveniently revised and corrected. **Figure 5B** illustrates the fault model of the study area. The vertical fault polygons lying in the north part represent the Gaoliu fault.

4.1.3 Porosity and Permeability Model

Evaluating reservoir volume and fluid volume highly relies on the determination of its porosity. The porosity model of the Guantao Formation was built based on the outcome result that has been derived from the petrophysical interpretation of wells loggings. In this model, the arithmetic average method is applied to scale up the well logs. The Sequential Gaussian Simulation method was used to distribute the porosity in the model. The porosity occurrence distribution is a concern between 0% and 34.39% of the Guantao Formation with an average porosity value of 10.5%; among these, the averaged porosity for Ng1, Ng2, and Ng3 is approximately 13.6%, 11.1%, and 7.78%, respectively. **Figure 6A** represents the established 3D porosity model of the Guantao Formation (Ng1–Ng3) in Petrel.

Permeability is an intrinsic parameter for the reservoir rock. Its measures the ease with which a fluid flows through the connecting pore space of the reservoir rock. The reservoir rock permeability is a vital property to determine the orientation movement and flow rate of the reservoir fluid in the formation. In this model, similar to the porosity model, the permeability model is built based on the permeability log generated. The harmonic average method was applied to scale up the well logs. Furthermore, Sequential Gaussian Simulation was used as the geostatistical method to create the permeability model. The permeability model shows that the permeability of the Guantao Formation ranges between 0.017 and 2,382 mD, having an average permeability of 128.37 mD. Among these, the averaged intrinsic permeability for Ng1, Ng2, and Ng3 is

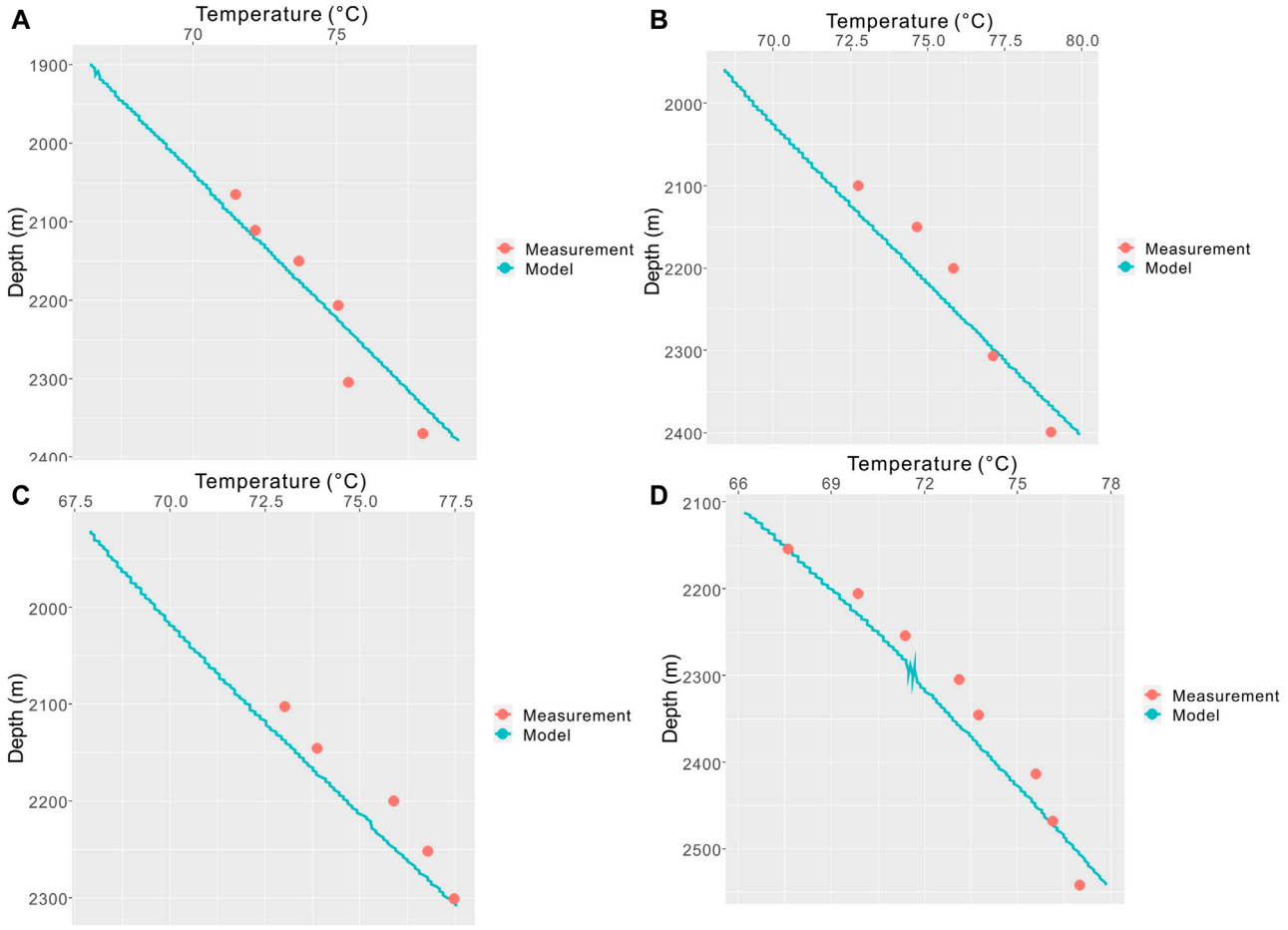

FIGURE 8 | Comparison of simulated temperature data with the measured temperature data at different wells. The well locations are shown in **Figure 2**.

approximately 281.3, 221.5, and 126.1 mD, respectively. The outcome value indicated that the Guantao Formation has relatively high permeability. **Figure 6B** represents the permeability model of the Guantao Formation (Ng1–Ng3).

4.1.4 Petrel to OpenGeoSys

Figure 7 shows the converted VTU format geological mesh demonstrated in Paraview interface with respect to the porosity and permeability distributions. The converted mesh is composed of 4,506,687 points and 564,000 elements. For each small grid element, it holds a size of 50 m * 50 m * 10 m. The faults are incorporated in the mesh and assumed as vertical. They were implemented in the mesh for modeling the sharp discontinuity in the surface.

4.2 Hydrothermal-Coupled Numerical Model

This section presents the HT simulation results of the natural state of the geothermal reservoir. The natural-state model, with defined parameters and boundary conditions described in **Section 3.2**, was run with these initial conditions of temperature and pressure for a time span of 1 Ma. The results of the natural-state model were then compared with temperature measurements from different well logs and BHT data. The model was run numerous times during calibration to provide the best match between the simulation and measured static pressure and temperature data.

4.2.1 Model Fit to Temperature Observations

Temperature observations at different logs were used to quantify the accuracy of the modeled temperatures with independently measured datasets for HT model validation. A good agreement between measured and modeled temperatures is obtained for the HT model (**Figure 8**). The comparison with both the simulation and measurement temperature datasets consistently leads to the relative temperature errors of less than approximately 2°C.

4.2.2 Simulated Subsurface Temperature Distribution

The simulated subsurface temperature field is characterized by significant lateral and vertical spatial variations across the Caofeidian area, reflecting the structural geological differences with large variations in the formation depth and heat flow. A

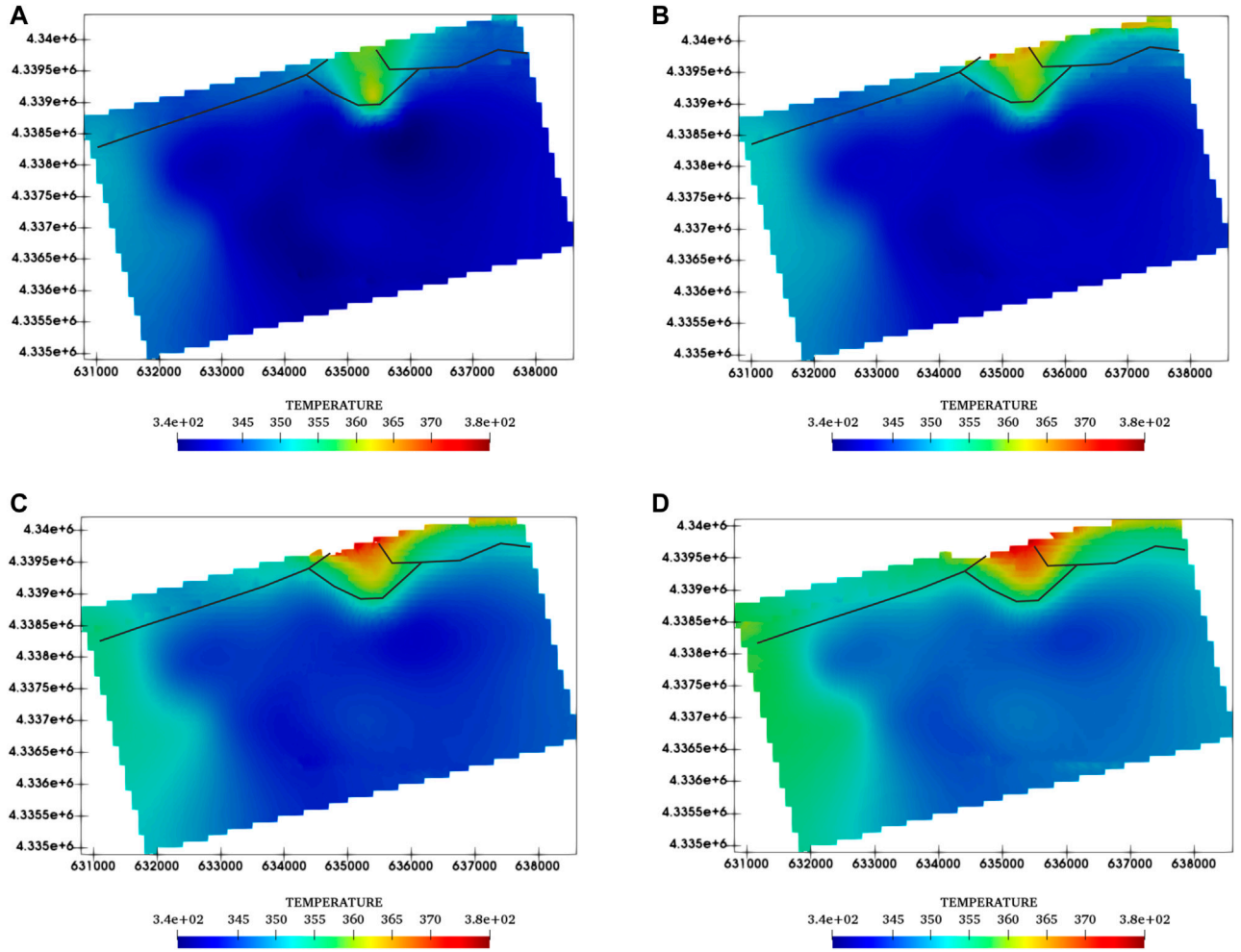

FIGURE 9 | 2D profiles of temperature (K) distribution at different depths. **(A)** 2,000 m, **(B)** 2,100 m, **(C)** 2,200 m, and **(D)** 2,300 m.

TABLE 1 | Parameters for geothermal resource calculation in the traditional volumetric method (Dong et al., 2021).

Horizon	Surface area of the calculated area/106 m^2	Thermal reservoir thickness (m)	Average temperature of rock and water (°C)	Reference temperature (°C)	Density of rock and water (kg/m^3)	Specific heat capacity of rock and water [J/kg/K]	Porosity of rock (%)
Member Ng1	27.85	81	76	13.5	2,200/990	878/4,180	27
Member Ng2	27.85	78	79	13.5	2,200/990	878/4,180	29
Member Ng3	27.85	90	83	13.5	2,200/990	878/4,180	29

significant geothermal anomaly zone can be found in the vicinity of the Gaoliu fault.

At a depth of 2,000 m (**Figure 9A**), it is largely located at the bottom formation of the Minghuazhen Formation (Nm). The temperatures range between 65°C and 85°C. Temperatures higher than 80°C can be observed at the middle margin of the Gaoliu fault. Large areas in this layer show temperatures of between 65°C and 75°C with local positive temperature anomalies usually associated with the Gaoliu fault. A higher temperature zone, higher than 75°C, is found in the southwest part.

At a depth of 2,100 m (**Figure 9B**), it is largely located in the Guantao Formation (member Ng1). The temperatures range between 70°C and 90°C. Temperatures higher than 85°C can be observed at the middle margin of the Gaoliu fault. Large

TABLE 2 | Statistics on geothermal resources of Guantao Formation (Ng1–3) in Caofeidian geothermal field.

Horizon	Geothermal resources/10^{16} J	Standard coal equivalent/10^6 t	Recoverable resources/10^{16} J	Geothermal fluid resources/108 m^3	Standard coal equivalent/10^6 t	Recoverable hot water resources/108 m^3
Member Ng1	35.63	12.13	8.91	6.09	30.20	1.22
Member Ng2	36.59	12.46	9.15	6.30	31.24	1.26
Member Ng3	42.21	14.37	10.56	7.27	36.04	1.46
Total	114.43	38.96	28.62	19.66	97.48	3.94

TABLE 3 | The geothermal resource calculation (Ng1–Ng3), compared with the traditional volumetric method results.

	Proposed method	Traditional method
Member Ng1 (J)	3.42e+17	3.56e+17
Member Ng2 (J)	2.83e+17	3.65e+17
Member Ng3 (J)	6.43e+17	4.21e+17
Total geothermal resources (J)	1.27e+18	1.14e+18
Total reservoir volume (m^3)	4.49e+9	6.934e+9
Standard coal equivalent (t)	4.32e+7	3.896e+7
Exploitable geothermal resource (total) (J)	3.08e+17	2.86 e+17

TABLE 4 | The geothermal fluid volume calculation (Ng1–Ng3), compared with the traditional volumetric method results.

	Proposed method	Traditional method
Member Ng1	3.33e+8	6.09 e+8
Member Ng2	2.20e+8	6.30e+8
Member Ng3	3.44e+8	7.27e+8
Total geothermal fluid volume (m^3)	8.97e+8	19.66e+8
Recoverable hot water resources (total) (J)	1.8 e+8	3.94e+8

areas in this layer show temperatures of between 70°C and 80°C with local positive temperature anomalies usually associated with the Gaoliu fault. A higher temperature zone, higher than 80°C, is found in the southwest part.

At a depth of 2,200 m (**Figure 9C**), it is largely located in the Guantao Formation (member Ng2). The temperatures range between 73°C and 95°C. Temperatures higher than 90°C can be observed at the middle margin of the Gaoliu fault. Large areas in this layer show temperatures of between 75 and 85°C with local positive temperature anomalies usually associated with the Gaoliu fault. A higher temperature zone, higher than 85°C, is found in the southwest part.

At a depth of 2,300 m (**Figure 9D**), it is largely located in the Guantao Formation (member Ng3). The temperatures range between 80°C and 110°C. Temperatures higher than 100°C can be observed at the middle margin of the Gaoliu fault. Large areas in this layer show temperatures of between 80°C and 90°C with local positive temperature anomalies usually associated with the Gaoliu fault. A higher temperature zone, higher than 90°C, is found in the southwest part.

4.3 Geothermal Resources

4.3.1 Traditional Volumetric Method

According to the characteristics of the thermal reservoir medium in the study area, the traditional geothermal reservoir volumetric method was used to evaluate the geothermal resources in the Guantao Formation of the Caofeidian geothermal field. The total amount of heat contained in the rock mass and water in a certain area can be determined according to the formulations.

The parameters required to calculate the geothermal resources and geothermal fluid resources are listed in **Table 1**. Thus, the total geothermal resources of the Guantao Formation (Ng1–Ng3) in the Caofeidian geothermal field are calculated and summarized in **Table 2**. The recoverable geothermal resources are calculated by considering a geothermal energy recovery rate of 25%, "Geothermal Resources Geological Prospecting Specification" GB/T 11615–2010, China. The associated geothermal fluid resources can be also obtained by considering a hot water resource recovery rate of 20%.

4.3.2 The Proposed Revised Volumetric Method

The coupling between the 3D geological model and natural-state HT numerical model allows the calculation of the total amount of geothermal energy distributed in each grid element. The 3D geological model is used for estimating the volume information of the geothermal reservoir.

Table 3 summarizes the total geothermal resources estimated by the proposed volumetric method and traditional method. The total geothermal resources estimated is 1.27e+18 J, which is 12.5% larger than the traditional method, while the total volume of member Ng1–Ng3 formations in the Caofeidian geothermal field is approximately 4.49e+9 m^3, which is 35% less than the traditional estimation.

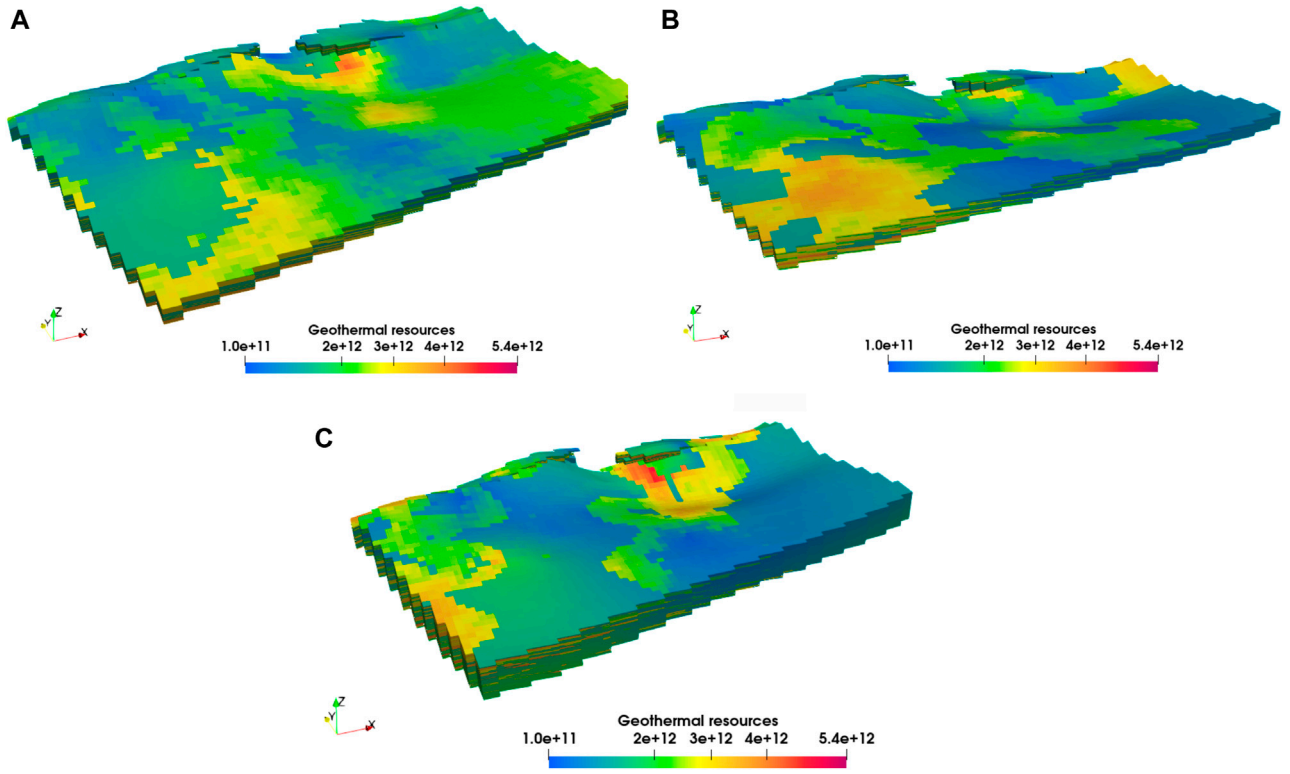

FIGURE 10 | 3D model showing the geothermal resource (J) distribution: **(A)** member Ng1, **(B)** member Ng2, and **(C)** member Ng3.

Similar to the traditional calculation, member Ng3 bears the most geothermal resources, due to high temperature and large thickness. However, member Ng2 bears fewer geothermal resources than member Ng1, although its temperature is higher, which contrasts with the traditional method calculation.

The total geothermal fluid resource calculation estimated by the proposed volumetric method is shown in **Table 4**, compared with the traditional method. The total geothermal fluid volume estimated is 8.97e+8 m^3, which is nearly half compared with the traditional methods, which can be explained by two facts: 1) the total volume of the Ng1–Ng3 formations estimated in the proposed method is 35% less than the traditional method, and 2) the porosity is overestimated in the traditional method.

The proposed method can also exhibit the spatial distribution of the geothermal resources associated with each grid element. **Figure 10** presents the local distribution of geothermal resources in members Ng1, Ng2, and Ng3.

4 DISCUSSION

This section aims to investigate the influence of saturation on geothermal resource estimation in oil fields. Fluid saturation is the crucial parameter for accurate estimation and is always assumed to be constant based on limited known data, which is obviously not true in oil and gas reservoirs, where water saturation may increase, while the oil and gas saturations decrease to some extent. The alterations of fluid saturations during hydrocarbon or geothermal productions may induce errors in geothermal resource estimation in oil fields. By courtesy of the oil field database, which could not only provide the oil/gas/water saturation but also the dynamic changes along with the production history, the operators are able to accurately evaluate the geothermal reserves at any interesting point of production history and help the decision making on the geothermal project.

The previous interpretation has only taken the saturated water into account; however, as mentioned before, the study area is located in an active oil field, which means it is very likely the geothermal fluid is mixed with oil. Such facts are also validated by the samples collected at the geothermal wells, such as GR4-1 and GR4-2. Therefore, in order to account for the influence of the oil and gas saturations on the total geothermal resources of this area, revised volumetric method calibration is carried out by assessing the geothermal resources with respect to water, oil, and gas. For this purpose, the revised volumetric method (**Eq. 1**) is extended as follows (Li and Sun, 2014):

$$Q = \sum_{i=0}^{N} V_i (T_i - T_0)\left[\rho_r C_r (1-\varphi_i) + \rho_w C_w \varphi_i \left(1 - S_{oi} - S_{gi}\right) + \rho_o C_o \varphi_i S_{oi} + \rho_g C_g \varphi_i S_{gi}\right] \quad (5)$$

where S_o and S_g are the oil saturation; and ρ_o, C_o and ρ_g, C_g are the density and specific heat capacity of oil and gas, respectively.

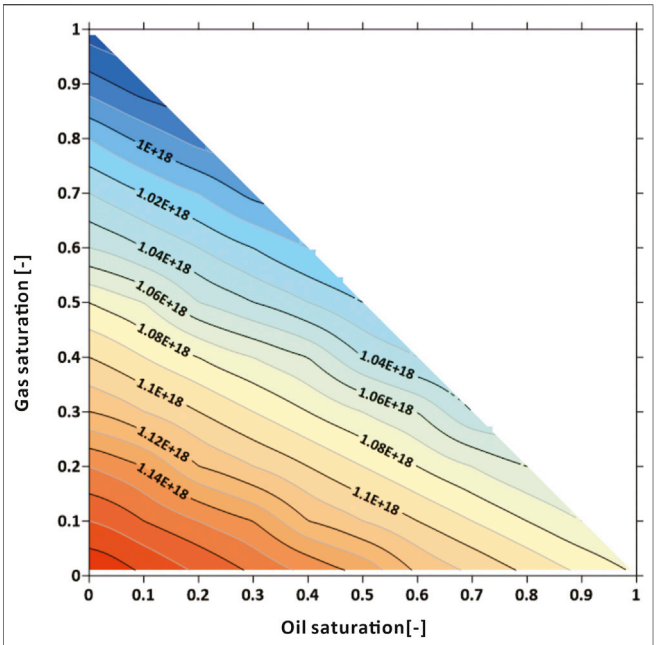

FIGURE 11 | The estimated geothermal resources varying with gas and oil saturations.

Here, due to lack of the information and measured data regarding the oil saturation distribution at the Ng formation, a simple scenario is assumed by varying the oil and gas saturations from 0 to 1 while keeping the sum of both saturations at less than 1. A preliminary analysis is made thereby on the influence of oil and gas existence on the total geothermal resource assessment. **Figure 11** depicts the estimated geothermal resource evolution with the gas and oil saturation. It can be observed that the increase of the oil and gas saturations leads to the decline of the overall geothermal energy. That can be explained by the fact that the density and specific heat capacity of oil and gas are less than those of water. The saturation of gas leads to a more significant contribution to the decline of geothermal resources, due to its density being even smaller.

5 CONCLUSION

This paper presents a comprehensive investigation of geothermal resource assessment in an active oil field. A revised volumetric method is proposed by integrating the 3D geological modeling into an HT-coupled numerical model. Special attention has been paid to account for the existence of the oil and gas phases.

In the proposed calculation method, a 3D geological model is introduced as the model basis. On the one hand, it provides detailed information on the reservoir volume; on the other hand, it serves as a basis and input geometry mesh to the HT numerical simulation. Moreover, HT natural-state numerical model addressed the temperature distribution in the reservoir by taking into account complex geological structures and highly contrasting heterogeneous distributed porosity and permeability. Therefore, the calculation results are more in line with the actual situation.

This approach improves the accuracy of the geothermal potential assessment. In the Caofeidian geothermal field, the geothermal resource is found to be 1.23e+18 J using the revised calculation method, which is 12.5% larger than those of the traditional volumetric method. The associated geothermal fluid volume is 8.97e+8 m^3, which is nearly half of those calculated from the traditional method. Also, the possible distribution of available temperature data could be plotted in 3D, which helps identify the optimal place to develop geothermal resources.

The proposed method can provide solid information to the planning and management of deep geothermal resources in the Caofeidian new town geothermal field. It also demonstrates the potential to be applied to other geothermal reservoirs, especially for those with complex geological structures and high heterogeneities.

DATA AVAILABILITY STATEMENT

The original contributions presented in the study are included in the article/Supplementary Material, further inquiries can be directed to the corresponding authors.

AUTHOR CONTRIBUTIONS

YK and YC designed the study and gave conceptual advice. YH conducted the model runs, analyzed the model results, and prepared the manuscript. LR, JW, and YD provided raw data information and model parameters. FT contributed to the geological model setup. SP and KW helped the model post-process and visualization. All authors contributed to the editing of the manuscript and gave approval of the content in its current form.

FUNDING

This work was financially supported by the National Key Research and Development Program of China (No. 2019YFB1504101). We also acknowledge the support from National Natural Science Foundation of China (41902311, 42004060) and the Youth Innovation Promotion Association of CAS (2020067).

ACKNOWLEDGMENTS

We thank the PetroChina Jidong Oilfield Company and the individuals who contributed to the raw datasets and information used in this work.

REFERENCES

Bédard, K., Comeau, F.-A., Raymond, J., Gloaguen, E., Malo, M., and Richard, M.-A. (2020). Deep Geothermal Resource Assessment of the St. Lawrence Lowlands Sedimentary basin (Québec) Based on 3D Regional Geological Modelling. *Geomech. Geophys. Geo-energ. Geo-resour.* 6 (3), 1–18. doi:10.1007/s40948-020-00170-0

Békési, E., Lenkey, L., Limberger, J., Porkoláb, K., Balázs, A., Bonté, D., et al. (2018). Subsurface Temperature Model of the Hungarian Part of the Pannonian Basin. *Glob. Planet. Change* 171, 48–64. doi:10.1016/j.gloplacha.2017.09.020

Békési, E., Struijk, M., Bonté, D., Veldkamp, H., Limberger, J., Fokker, P. A., et al. (2020). An Updated Geothermal Model of the Dutch Subsurface Based on Inversion of Temperature Data. *Geothermics* 88, 101880. doi:10.1016/j.geothermics.2020.101880

Blessent, D., Therrien, R., and MacQuarrie, K. (2009). Coupling Geological and Numerical Models to Simulate Groundwater Flow and Contaminant Transport in Fractured media. *Comput. Geosciences* 35, 1897–1906. doi:10.1016/j.cageo.2008.12.008

Calcagno, P., Baujard, C., Guillou-Frottier, L., Dagallier, A., and Genter, A. (2014). Estimation of the Deep Geothermal Potential within the Tertiary Limagne basin (French Massif Central): An Integrated 3D Geological and thermal Approach. *Geothermics* 51, 496–508. doi:10.1016/j.geothermics.2014.02.002

Carrier, A., Fischanger, F., Gance, J., Cocchiararo, G., Morelli, G., and Lupi, M. (2019). Deep Electrical Resistivity Tomography for the Prospection of Low- to Medium-Enthalpy Geothermal Resources. *Geophys. J. Int.* 219, 2056–2072. doi:10.1093/gji/ggz411

Cheng, Y., Pang, Z., Di, Q., Chen, X., and Kong, Y. (2021). Three-dimensional Resistivity Structure in the Hydrothermal System beneath Ganzi Basin, Eastern Margin of Tibetan Plateau. *Geothermics* 93, 102062. doi:10.1016/j.geothermics.2021.102062

Ciriaco, A. E., Zarrouk, S. J., and Zakeri, G. (2020). Geothermal Resource and reserve Assessment Methodology: Overview, Analysis and Future Directions. *Renew. Sustainable Energ. Rev.* 119, 109515. doi:10.1016/j.rser.2019.109515

Dong, Y., Huang, H., Ren, L., Li, H., DU, Z., E, J., et al. (2021). Geology and Development of Geothermal Field in Neogene Guantao Formation in Northern Bohai Bay Basin: A Case of the Caofeidian Geothermal Heating Project in Tangshan, China. *Pet. Exploration Development* 48, 775–786. doi:10.1016/S1876-3804(21)60063-0

Dong, Y., Xiao, L., Zhou, H., Wang, C., Zheng, J., Zhang, N., et al. (2010). The Tertiary Evolution of the Prolific Nanpu Sag of Bohai Bay Basin, China: Constraints from Volcanic Records and Tectono-Stratigraphic Sequences. *Geol. Soc. America Bull.* 122, 609–626. doi:10.1130/B30041.1

Fuchs, S., Balling, N., and Mathiesen, A. (2020). Deep basin Temperature and Heat-Flow Field in Denmark - New Insights from Borehole Analysis and 3D Geothermal Modelling. *Geothermics* 83, 101722. doi:10.1016/j.geothermics.2019.101722

Gascuel, V., Bédard, K., Comeau, F.-A., Raymond, J., and Malo, M. (2020). Geothermal Resource Assessment of Remote Sedimentary Basins with Sparse Data: Lessons Learned from Anticosti Island, Canada. *Geotherm. Energ.* 8, 1–32. doi:10.1186/s40517-020-0156-1

Guo, Y., Pang, X., Dong, Y., Jiang, Z., Chen, D., and Jiang, F. (2013). Hydrocarbon Generation and Migration in the Nanpu Sag, Bohai Bay Basin, Eastern China: Insight from basin and Petroleum System Modeling. *J. Asian Earth Sci.* 77, 140–150. doi:10.1016/j.jseaes.2013.08.033

Jiang, G., Hu, S., Shi, Y., Zhang, C., Wang, Z., and Hu, D. (2019). Terrestrial Heat Flow of continental China: Updated Dataset and Tectonic Implications. *Tectonophysics* 753, 36–48. doi:10.1016/j.tecto.2019.01.006

Kolditz, O., Bauer, S., Bilke, L., Böttcher, N., Delfs, J. O., Fischer, T., et al. (2012). OpenGeoSys: an Open-Source Initiative for Numerical Simulation of Thermo-Hydro-Mechanical/chemical (THM/C) Processes in Porous media. *Environ. Earth Sciearth Sci.* 67, 589–599. doi:10.1007/s12665-012-1546-x

Kong, Y., Pang, Z., Pang, J., Li, J., Lyu, M., and Pan, S. (2020). Fault-Affected Fluid Circulation Revealed by Hydrochemistry and Isotopes in a Large-Scale Utilized Geothermal Reservoir. *Geofluids* 2020, 1–13. doi:10.1155/2020/2604025

Lai, J., Pang, X., Xu, F., Wang, G., Fan, X., Xie, W., et al. (2019). Origin and Formation Mechanisms of Low Oil Saturation Reservoirs in Nanpu Sag, Bohai Bay Basin, China. *Mar. Pet. Geology.* 110, 317–334. doi:10.1016/j.marpetgeo.2019.07.021

Li, K., and Sun, W. (2014). Modified Method for Estimating Geothermal Resources in Oil and Gas Reservoirs. *Math. Geosci.* 47, 105–117. doi:10.1007/s11004-013-9516-8

Muffler, P., and Cataldi, R. (1978). Methods for Regional Assessment of Geothermal Resources. *Geothermics* 7, 53–89. doi:10.1016/0375-6505(78)90002-0

Pocasangre, C., and Fujimitsu, Y. (2018). A Python-Based Stochastic Library for Assessing Geothermal Power Potential Using the Volumetric Method in a Liquid-Dominated Reservoir. *Geothermics* 76, 164–176. doi:10.1016/j.geothermics.2018.07.009

Tian, B., Kong, Y., Gong, Y., Ye, C., Pang, Z., Wang, J., et al. (2020). An Improved Volumetric Method of Geothermal Resources Assessment for Shallow Ground Combining Geophysical Data. *Renew. Energ.* 145, 2306–2315. doi:10.1016/j.renene.2019.08.005

Wagner, W., and Kretzschmar, H.-J. (2008). "International Steam Tables: Properties of Water and Steam Based on the Industrial Formulation IAPWS-IF97," in *IAPWS industrial formulation 1997 for the thermodynamic properties of water and steam*, 7–150. doi:10.1007/978-3-540-74234-0_3

Zhu, Z., Lei, X., Xu, N., Shao, D., Jiang, X., and Wu, X. (2020). Integration of 3D Geological Modeling and Geothermal Field Analysis for the Evaluation of Geothermal Reserves in the Northwest of Beijing Plain, China. *Water* 12, 638. doi:10.3390/w12030638

Conflict of Interest: Authors LR and JW are employed by Jidong Oilfield Company of PetroChina. Author YD is employed by Advisory Center, China National Petroleum Corporation.

The remaining authors declare that the research was conducted in the absence of any commercial or financial relationships that could be construed as a potential conflict of interest.

frontiers in Earth Science

ORIGINAL RESEARCH
published: 10 January 2022
doi: 10.3389/feart.2021.819659

Heat Flow and Thermal Source of the Xi'an Depression, Weihe Basin, Central China

Wei Xu[1], Xiaoyin Tang[2]*, Luyao Cheng[1], Ying Dong[3], Yuping Zhang[4], Tingting Ke[1], Ruyang Yu[5] and Yi Li[6]*

[1]Institute of Global Environmental Change, Xi'an Jiaotong University, Xi'an, China, [2]Institute of Geomechanics, Chinese Academy of Geological Sciences, Beijing, China, [3]Xi'an Center of China Geological Survey, Xi'an, China, [4]Key Laboratory of Coal Resources Exploration and Comprehensive Utilization, Ministry of Land and Resources, Xi'an, China, [5]School of Earth Resources, China University of Geosciences, Wuhan, China, [6]Sichuan Institute of Geological Engineering Investigation Group Co. Ltd., Chengdu, China

The Xi'an Depression of the Weihe Basin, located in the transition zone where the North China, Qinling and Yangtze plates collide with each other, is an important area of geothermal energy utilization in China. Studies of heat flow and thermal sources are of great significance to the exploration and development of geothermal resources in this area. In this paper, six temperature logs boreholes, and 14 thermal conductivity samples have been used to study the geothermal gradient and terrestrial heat flow in the area. The results show that the geothermal gradients of Xi'an Depression range from 20.8 C/km to 49.1 C/km, with an average of 31.7 ± 5.0 C/km. The calculated heat flow is 59.4–88.6 mW/m^2, and the average value is 71.0 ± 6.3 mW/m^2, which indicates a high thermal background in the area. The high anomalous zones are near the Lintong-Chang'an Fault zone in the southeast, the Weihe Fault in the north, and the Fenghe Fault in the central Xi'an Depression. These deep and large faults not only control the formation of the Xi'an Depression but also provide an important channel for the circulation of groundwater and affect the characteristics of the shallow geothermal distribution. The temperature of the Moho in the Xi'an Depression ranges from 600 to 700°C, and the thermal lithosphere thickness is about 90–100 km. The characteristics of lithospheric thermal structure in Xi'an Depression indicate that the higher thermal background in the study area is related to lithospheric extension and thinning and asthenosphere thermal material upwelling.

Keywords: geothermal gradient, heat flow, thermal sources, xi'an depression, weihe basin

OPEN ACCESS

Edited by:
Yinhui Zuo,
Chengdu University of Technology, China

Reviewed by:
Zhanli Ren,
Northwest University, China
Shaowen Liu,
Nanjing University, China

****Correspondence:***
Wei Xu
xwswpi@xjtu.edu.cn
Xiaoyin Tang
xytang2015@sina.com

Specialty section:
This article was submitted to Economic Geology, a section of the journal Frontiers in Earth Science

Received: *22 November 2021*
Accepted: *20 December 2021*
Published: *10 January 2022*

Citation:
Xu W, Tang X, Cheng L, Dong Y, Zhang Y, Ke T, Yu R and Li Y (2022) Heat Flow and Thermal Source of the Xi'an Depression, Weihe Basin, Central China. Front. Earth Sci. 9:819659. doi: 10.3389/feart.2021.819659

INTRODUCTION

Terrestrial heat flow is the basis for the study of the regional thermal background (Jiang et al., 2019; Wang et al., 2020; Xu et al., 2021), geothermal resource evaluation (Ciriaco et al., 2020), and tectono-thermal evolution (Qiu et al., 2014; Zuo et al., 2020; Chang et al., 2021; Jiang et al., 2021).

The Weihe Basin is situated between the southwestern margin of the North China Plate and the Qinling Orogenic Belt (**Figure 1**). It is a half-graben rift basin controlled by its southern and northern bounding faults and filled with 7,000 m Cenozoic sediments (Rao et al., 2014). The Weihe Basin has a great geothermal resource exploration potential. The history of geothermal development and utilization in this area can be traced back to Huaqin Hot Springs in the Tang Dynasty (Stober and Bucher, 2013). Based on the results of geology, tectonics, geophysics, and geochemistry, etc.,

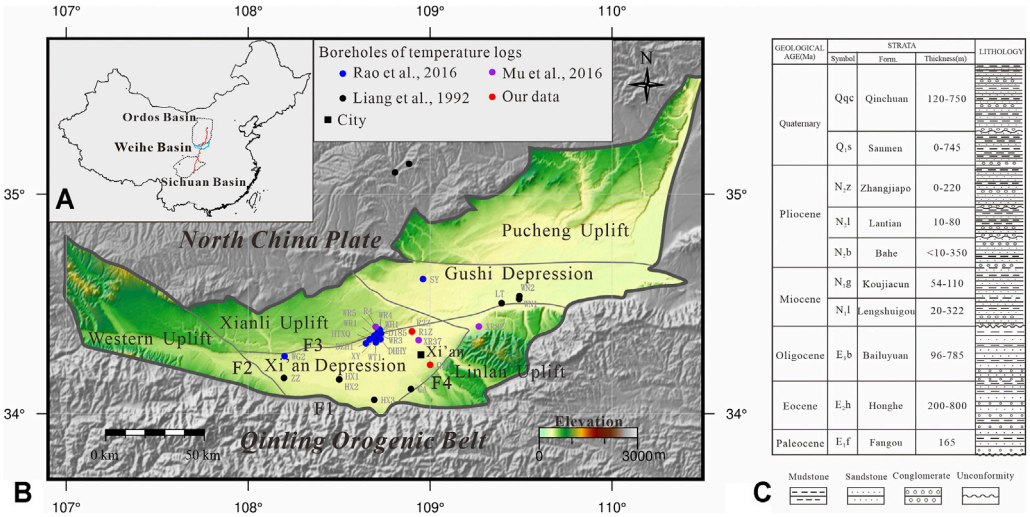

FIGURE 1 | (A) The location of the Weihe Basin [Redline is the Yuquan-Yulin geophysical transect referred to Teng et al. (2014)]; **(B)** Tectonic units of the Weihe Basin and adjacent areas (F1-North Qinling Piedmont Fault, F2-Longxian-Qishan-Yabai Fault, F3-Weihe Fault, F4-Chang'an-Lintong Fault); **(C)** Generalized stratigraphic column of the Weihe Basin (stratigraphic data from http://geocloud.cgs.gov.cn/#/portal/home).

previous studies have been conducted on the characteristics of the geothermal field (Rao et al., 2016; Ren et al., 2020), the characteristics of underground hot water (Qin et al., 2005a; Ma et al., 2008b) the evaluation of geothermal resources (Mu et al., 2016; Zhang et al., 2020), and the characteristics of the thermal structure of the lithosphere in the Weihe Basin (Rao et al., 2016; Liang et al., 1992).

The Xi'an Depression is a secondary tectonic unit of the Weihe Basin. It is the main area for the exploration and utilization of geothermal resources. However, most of the temperature log boreholes are concentrated in Xianyang City. The accurate determination of the geothermal field and the further study of controlling factors in the Xi'an Depression (such as fault structures and groundwater circulation systems) are restricted. In addition, the Xi'an Depression developed many deep faults, but different researchers have disputes over whether these deep faults control thermal anomalies (Rao et al., 2016; Deng et al., 2017). Therefore, the thermal background and the mechanism of thermal anomalies in the Xi'an Depression still need to be strengthened.

In this paper, we used temperature logs data from six boreholes and 14 thermal conductivity data and studied the geothermal gradient and heat flow of the Xi'an Depression combined with data collected from the previous studies (Liang et al., 1992; Rao et al., 2016). Then, the relationship between heat flow and faults and groundwater circulation is studied, and the mechanism of regional thermal background is discussed. The research is of great significance for understanding the distribution characteristics of geothermal resources and thermal sources in the Xi'an Depression.

GEOLOGICAL SETTING

The Xi'an Depression is the main tectonic unit of the Weihe Basin, located in the central and southern parts of the basin (**Figure 1A**). The west is bounded by the Longxian-Qishan-Yabai Fault and adjacent to the Western Uplift; the north is separated by the Weihe Fault and adjacent to the Xianli Uplift; the east is bounded by the Chang'an-Lintong Fault and adjacent to the Linlan Uplift; the south is adjacent to the Qinling Orogenetic Belt separated by the North Qinling Piedmont Fault.

The basement of the Xi'an Depression mostly consists of Proterozoic metamorphic rocks (Wang H et al., 2010). The Paleogene includes the Honghe Formation (E_2h), the Bailuyuan Formation (E_3b); the Neogene includes the Lengshuigou Formation (N_1l), the Koujiacun Formation (N_1k), the Bahe Formation (N_2b), the Lantian Formation (N_2l), the Zhangjiapo Formation (N_2z) and the Quaternary strata. These sedimentary units consisted of an alternation of sandstone and mudstone layers (**Figure 1B**) (Liu and Xue, 2004).

The Xi'an Depression is located at the intersection of China's east-west tectonic divisions and north-south tectonic divisions. It is a complex transition zone where the Qinling Orogenetic Belt, the North China Block, and the Yangtze Block collide with each other. Before the Early Cretaceous, the Xi'an Depression belonged to the southern margin of the Ordos paleo-continent and was dominated by subsidence and sedimentation. It experienced three tectonic evolutionary stages during the Late Ordovician to Early Cretaceous, including the Caledonian, the Hercynian, and the Late Indo-East Yanshanian tectonic activities (Zhao and Liu, 1990; Yang, 2002). In the Caledonian, tectonic compression occurred in the study area, resulting in the overall uplift and denudation. In the Hercynian, the study area was further compressed, and uplift occurred in the south and depression occurred in the north. During the Late Indo-East Yanshanian, the Weihe Basin was uplifted widely, and the deformation of the northern margin of the Weihe Basin was strengthened, and the compressive deformation zone was extended northward. Since the early cretaceous, the formation of the northern margin of the

TABLE 1 | Thermal conductivity for the rocks from the Xi'an Depression.

Well no	Depth (m)	Lithology	Thermal conductivity (W/(mK))		References
			measured	corrected	
XS1	113.60	Sandstone	1.92	2.17	Our data
XS2	160.60	Sandstone	1.88	2.13	
XG1	117.00	Clay	1.94	2.19	
XG2	100.00	Clay	1.67	1.92	
XG3	47.00	Clay	1.61	1.86	
XG4	67.00	Clay	1.63	1.88	
XS3	101.60	Clay	1.89	2.14	
XS4	79.40	Clay	1.84	2.09	
XS5	140.70	Clay	1.68	1.93	
XU1		Mudstone	2.11	2.32	Luo, (2015)
XU2		Mudstone	1.68	1.89	
XU3		Sandstone	2.41	2.62	
XU4		Sandstone	3.24	3.45	
XU5		Sandstone	3.03	3.25	

Qinling Orogenetic Belt caused by the northward overthrust under the control of the north-south compressive stress has become an important tectono-thermal event (Liu et al., 2006). Since the Cenozoic, the Xi'an Depression has turned into an extension environment. It can be divided into four stages: rifting stage in the Eocene-Oligocene, uplifting stage in the late Oligocene-early Miocene, subsidence stage in the middle Miocene-Pliocene and the same for the Quaternary (Han et al., 2002; Liu et al., 2006; Liu et al., 2010; Wang J et al., 2010).

TABLE 2 | Thermal conductivity of the sedimentary strata in the Xi'an Depression.

Formation	Lithology	n	Thermal conductivity [W/(m·K)]		
			Range	Harmonic mean	Mixing value
Q	Clay	7	1.86–2.19	1.99 ± 0.12	2.03 ± 0.10
	Sandstone	2	2.13–2.17	2.15 ± 0.02	
N	Mudstone	2	1.89–2.32	2.08 ± 0.22	2.29 ± 0.25
	Sandstone	3	2.62–3.45	3.07 ± 0.35	

The mixing value is the thermal conductivity calculated from different lithology and the thickness of the lithology in the stratum.

METHODS AND DATA

Thermal Conductivity

Thermal conductivity is an important parameter for studying heat flow, lithospheric thermal structure, and temperature distribution inside the Earth (Wang, 2016). In this paper, a total of nine core samples from the Quaternary strata in the Xi'an Depression were sampled for thermal conductivity testing. The samples were measured using the TCS (Thermal Conductivity Scanning) technique by LGM-Lippmann Company (Popov et al., 2016). It has a measurement range of 0.2–25.0 W/(mK) with a measurement resolution of 0.001 W/(mK). The accuracy is ±3% on individual samples. These samples were measured at room temperature conditions, and each sample was tested three times to take the average value.

Combined with the collected data (Luo, 2015), a total of 14 rock thermal conductivity data were obtained (**Table 1**). The results show that the thermal conductivity of Xi'an Depression range from 1.61 W/(mK) to 3.24 W/(mK), with an average value of 2.04 ± 0.49 W/(mK).

The factors affecting the thermal conductivity of rocks mainly include water saturation, porosity, and mineral composition (Brigaud et al., 1990; Pribnow et al., 1996; Jougnot and Revil, 2010). Since the testing data are derived from dry rock samples, it is necessary to consider the water saturation calibration. In this study, the thermal conductivity data are corrected by using the water saturation method (Yu et al., 2020).

According to the geological data of the Xi'an Depression, the average porosity of the formations of N_2l-N_2b, N_1l-N_1g, E_3b is 22.2, 20.3, and 16.5%, respectively (Huang et al., 2021). According to the trend of porosity distribution with depth, we assume that the porosity of Quaternary is about 25.0%. Then, the results of the dry rock samples measured at the laboratory are corrected (**Table 1**). The corrected thermal conductivity ranges from 1.86 W/(mK) to 3.45 W/(mK), the average value is 2.28 ± 0.48 W/(mK). The corrected value is about 12% higher than the measured value.

Combined with the lithological thickness ratios (Huang et al., 2021) and weighted harmonic mean thermal conductivity of each lithology, the thermal conductivity of different formations can be calculated. We established a thermal conductivity column for sedimentary strata in the Xi'an Depression (**Table 2**). The mean bulk thermal conductivity of the Neogene is 2.29 ± 0.25 W/(mK), and the Quaternary is 2.03 ± 0.10 W/(mK).

Temperature Logs

The temperature of the sedimentary basin is mainly based on the temperature measurement data from the drilling boreholes, which can reflect the true condition of the geothermal field in the basin. In this study, high-quality precision temperature logs of three boreholes in the Xi'an Depression were measured (**Figure 1**). These boreholes have been stopped production for

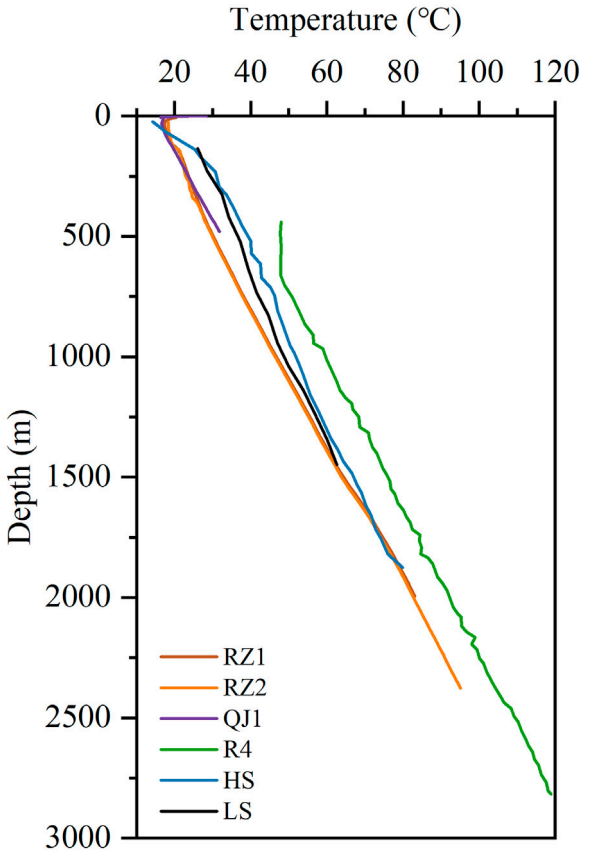

FIGURE 2 | Temperature logs of the boreholes in the Xi'an Depression [R4, HS, LS refers from Mu et al. (2016)]

more than 1 year, and the temperature has reached thermal equilibrium.

The equipment for the borehole temperature logging operation of R1Z and R2Z is made by Spartek Systems, Canada. It has a measurement sensitivity of 0.001°C, a depth interval of temperature recording of 10 cm, and a temperature measurement range from 0 to 150°C. The equipment used in QJ1 is the DEFI Series made by the JFE Advantech Co., Ltd, Japan, with a measurement resolution of 0.001°C, a temperature measurement interval of 0.15 cm, and a temperature measurement range of −3–45 °C.

Figure 2 shows the systematical temperature logging curves (temperature-depth profile) of the three boreholes. The depth section of R1Z ranges from 6 to 1996 m, corresponding to a temperature range of 20–83°C; The R2Z is measured from 25 to 2,377 m with a temperature range of 18.4–95.1°C (Zhang et al., 2019). The depth of QJ1 is 0–480 m with a temperature range of 16.3–31.8°C. The study also collected temperature logs data from three boreholes (Mu et al., 2016), with a maximum depth of 2,830 m and a maximum temperature of 119.0°C. Except that the shallow temperature is affected by climate or convection of groundwater, the temperature curve generally increases linearly with depth, indicating that the heat transfer method is conductive type, which can be used to characterize the present thermal field characteristics of the Xi'an Depression.

RESULTS

Geothermal Gradient

Geothermal gradient is the rate of temperature change with depth and is the crucial parameter for calculating the heat flow value. To obtain an accurate geothermal gradient, we have considered many factors, such as climate change, the convection of groundwater, and the effect of stratigraphic stratification. This paper selected relatively stable temperature intervals and used the least-square regression method to calculate the geothermal gradients for different layers, and the correlation coefficients are all above 99% (**Table 3**). The results show that the geothermal gradient ranges from 27.5 to 37.6 C/km, with an average value of 32.7 ± 7.0 C/km. It is lower than that of Songliao Basin in northeast China (37.0 C/km) (Wu and Xie, 1985), and consistent with that of Bohai Bay Basin in east China 32.8 C/km (Hu et al., 2001; Gong, 2003; Qiu et al., 2009), and higher than the stable basins in central and western China, Sichuan Basin 22.7 C/km (Xu et al., 2011), Tarim Basin 22.6 C/km (Feng et al., 2009), Junggar Basin 21.3 C/km (Rao et al., 2013) and Qaidam Basin 28.6 C/km (Li et al., 2015).

The spatial pattern of geothermal gradient was analyzed by considering the above data and data from previous studies (**Figure 3**; **Table 3**) (Liang et al., 1992; Rao et al., 2016). The geothermal gradient of the Xi'an Depression is about 20.8–49.1 C/km, with an average of 31.7 ± 5.0 C/km. **Figure 3** shows that most regions of the Xi'an Depression have geothermal gradients greater than 30 C/km, and the southwest and eastern parts are lower than 30 C/km. High anomalous zones occur in the northern and central-southern parts of the area with geothermal gradients of about 35–50 C/km.

Heat Flow

Terrestrial heat flow is equal to the product of the thermal conductivity and the vertical geothermal gradient. The geothermal gradient can be calculated by systematical steady-state temperature data, which are measured in the drilled borehole. The thermal conductivity of rock samples in the corresponding depth intervals can be tested in the laboratory. With these two parameters, we can obtain heat flow values. Its mathematical expression is:

$$q = K\frac{dT}{dZ} \tag{1}$$

where q is the heat flow (mW/m^2); K is the rock thermal conductivity [W/(mK)]; dT/dZ is the geothermal gradient (°C/km).

The standard deviation of heat flow depends on standard deviations of the rock thermal conductivity and geothermal gradient. The heat flow uncertainty is calculated as:

$$\sigma_q = \sqrt{G^2\sigma_K^2 + K\sigma_G^2} \tag{2}$$

TABLE 3 | Geothermal gradients and heat flow data of the Weihe Basin.

Well no	Longitude	Latitude	Form	Depth (m)	Gradient (°C/km)	K [W/(m·K)]	Heat flow (mW/m^2)		References
							section	average	
R1Z	108.90043	34.37635	Q	329–1,016	32.2 ± 0.1	2.03 ± 0.10	65.4 ± 3.2	75.7 ± 6.3	Our data
			N	1,016–1979	37.6 ± 0.1	2.29 ± 0.25	86.1 ± 9.4		
R2Z	108.90028	34.37670	Q	312–1,014	32.2 ± 0.1	2.03 ± 0.10	65.4 ± 3.2	74.0 ± 6.1	
			N	1,014–2,377	36.1 ± 0.1	2.29 ± 0.25	82.7 ± 9.0		
QJ1	108.99980	34.22450		99–480	34.8 ± 0.1	2.03 ± 0.10	70.6 ± 3.5	70.6 ± 3.5	
R4	108.70089	34.39828		703–2,816	33.0 ± 0.1	2.16 ± 0.19	71.3 ± 6.3	71.3 ± 6.3	
HS	108.93662	34.33698		335–1816	28.0 ± 0.3	2.16 ± 0.19	60.5 ± 5.3	60.5 ± 5.3	
LS	109.26804	34.39929		147–1,455	27.5 ± 0.5	2.16 ± 0.19	59.4 ± 5.3	59.4 ± 5.3	
YX1	108.80722	35.09806			20.8	3.19 ± 0.23		66.4 ± 0.5	Liang et al. (1992)
YX2	108.88417	35.13722		1,330–2089	23.4 ± 0.3	2.84 ± 0.37		66.3 ± 8.6	
ZZ	108.19667	34.16444			28.4 ± 0.5	2.43 ± 0.25		69.0 ± 7.3	
HX2	108.50028	34.15750		500–2,650	29.5 ± 0.2	2.43 ± 0.25		71.6 ± 7.5	
HX3	108.69306	34.06389		475–900	31.9 ± 0.5	2.43 ± 0.25		77.5 ± 8.2	
XY	108.69889	34.34222			49.1 ± 0.7	1.45 ± 0.20		71.2 ± 9.9	
CA	108.89472	34.11361			31.1 ± 0.7	2.43 ± 0.25		75.6 ± 8.1	
LT	109.39333	34.50583			31.0 ± 0.2	2.08 ± 0.31		64.6 ± 9.5	
WN1	109.48917	34.52472			32.0 ± 0.2	2.08 ± 0.30		66.4 ± 9.7	
WN2	109.49056	34.53778			28.5 ± 0.1	2.19 ± 0.32		62.5 ± 9.1	
WH1	108.72583	34.36972		360–1,150	34.8	2.11		73.4	Rao et al. (2016)
WR1	108.69278	34.35750		450–2,720	33.4	2.40		80.2	
WR3	108.71889	34.36500		520–2,710	29.6	2.43		71.9	
WR4	108.72361	34.38417		480–2,820	31.5	2.43		76.5	
WR5	108.71278	34.37333		530–1,600	32.6	2.21		72.0	
D185	108.73032	34.36708		510–1,390	29.4	2.18		64.1	
SY	108.96139	34.61528		180–1,140	32.3	2.08		67.2	
WT1	108.70222	34.32722		380–1740	40.1	2.21		88.6	
DHHY	108.72694	34.34167		360–1938	30.6	2.24		68.5	
HTXQ	108.66778	34.34028		520–2,700	30.4	2.43		73.9	
WG2	108.20028	34.26389		480–1,250	35.8	2.15		77.0	
DZH1	108.64722	34.32278		320–1,010	34.3	2.10		72.0	
					31.7 ± 5.0			71.0 ± 6.3	

K: Thermal conductivity.

where G is geothermal gradient; σ_K and σ_G are standard deviations of the rock thermal conductivity geothermal gradient.

In this study, based on the above temperature logs data and measured thermal conductivity data, the heat flow values of the six boreholes were calculated (**Table 3**). The results show that the maximum heat flow of the six boreholes is 75.7 ± 6.3 mW/m^2, the minimum is 59.4 ± 5.3 mW/m^2, and the average heat flow is 68.6 ± 3.6 mW/m^2. It is close to that of Songliao Basin in northeast China 70.9 mW/m^2 (Jiang et al., 2019), and slightly higher than that of Bohai Bay Basin 64.3 ± 14.7 mW/m^2 (Gong et al., 2011; Jiang et al., 2019), much higher than Tarim Basin in western China 43.0 mW/m^2 (Feng et al., 2009), Sichuan Basin 53.2 mW/m^2 (Xu et al., 2011), Junggar Basin 42.5 mW/m^2 (Rao et al., 2013) and Qaidam Basin 55.1 mW/m^2 (Li et al., 2015).

Combined with heat flow data from previous studies (**Table 3**) (Liang et al., 1992; Rao et al., 2016), the spatial pattern of heat flow was analyzed (**Figure 3**). The heat flow values in Xi'an Depression range from 59.4 to 88.6 mW/m^2, and the average heat flow is 71.0 ± 6.3 mW/m^2, which is significantly higher than the average continental heat flow of 60.4 ± 12.3 mW/m^2 in China (Jiang et al., 2016). **Figure 3** shows that the northern and central south parts are the high anomalous zones with high heat flow of 70–90 mW/m^2, and the southwest and eastern parts are low heat flow areas of 60–70 mW/m^2.

DISCUSSION

Factors Influencing the Distribution of Thermal Anomalies

Faults are the main factors affecting the distribution of geothermal anomalies in the Xi'an Depression. Many fault structures are developed in the Xi'an Depression. The fault structures can be divided into four groups according to their distribution directions, EW direction, NE direction, NW direction, and NNE direction (**Figure 4**) (Li et al., 1994; Mu et al., 2016). Among them, the faults of EW, NE, and NW trending are the most developed and constitute the basic structural framework of the study area. The southern part of the Xi'an Depression is the EW-trending North Qinling Piedmont Fault (F1) and Yuxia-Tieluzi Fault (F2), the NE-trending Weihe Fault (F3) in the north, the NW-trending Yabai Fault (F6) in the west, the NNW-trending Fenghe Fault (F7) in the central part, the NW-trending Jinghe Fault (F11) in

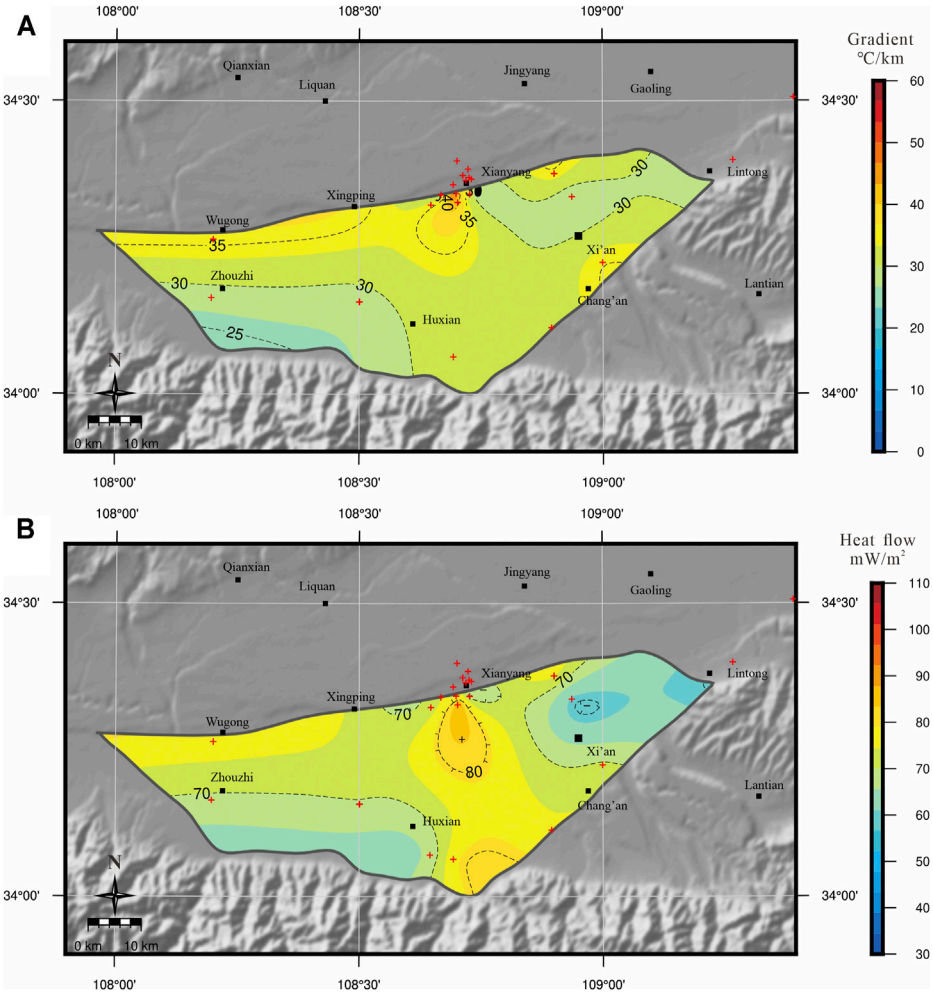

FIGURE 3 | Contour maps of the geothermal gradient **(A)** and heat flow **(B)** of the Xi'an Depression and adjacent areas. Red crosses show the locations of the geothermal measurements.

the northeast, and the NNE-trending Lintong-Changan Fault (F12) in the southeast. These deep faults not only control the formation of the Xi'an Depression but also provide an important channel for the circulation of groundwater and affect the characteristics of the geothermal distribution. **Figure 4** shows the relationship between heat flow distribution and faults. In the southern part of the Xi'an Depression, the high heat flow zone corresponds to the NNE-trending Lintong-Chang'an fault zone (F12); in the northern part, the high heat flow zone corresponds to the NE-trending Weihe fault (F3); the central high-heat flow zone corresponds to the NNW-trending Fenghe fault (F7).

Groundwater circulation is important to the distribution of geothermal anomalies in the Xi'an Depression. The geothermal reservoirs of the Weihe Basin are recharged by rain that falls on the northern slope of the Qinling Mountains, North Mountains, and the pediment surface water (Qin et al., 2005b; Ma et al., 2008b; Luo, 2015). The low heat flow of the eastern area of the depression may relate to the mix of water from the Qinling Mountains, water from Weibei, local surface water, and ground cold water (Li and Li, 2010). Two geothermal water reservoirs may be distinguished in the Weihe Basin; they are circulating (current) geothermal reservoirs and isolated (fossil) geothermal reservoirs (Ma et al., 2008a; Ma et al., 2008b). The host environments of the geothermal water of Xianyang and Xi'an are belonging to an isolated geothermal reservoir at a depth deeper than 1,500 m. Groundwater circulation depth is an important parameter in the research of the geothermal field. It is estimated that the circulation depth of geothermal water in the Xianyang geothermal system can reach 4,900 m based on the temperature of the geothermal reservoir and geothermal gradient (Luo, 2015). Hydrogen and oxygen isotope evidence show that the geothermal water in Xianyang is supplied by atmospheric precipitation in the Qinling mountains, and the noble gas isotope $^{3}He/^{4}He—^{4}He/^{20}Ne$ indicate that the fluid circulation occurs only in the crust depth and is not supplemented by mantle-derived materials (Luo et al., 2019). Therefore, we believe that the geothermal water in Xi'an Depression mainly receives the atmospheric precipitation of the Qinling Mountains, forming

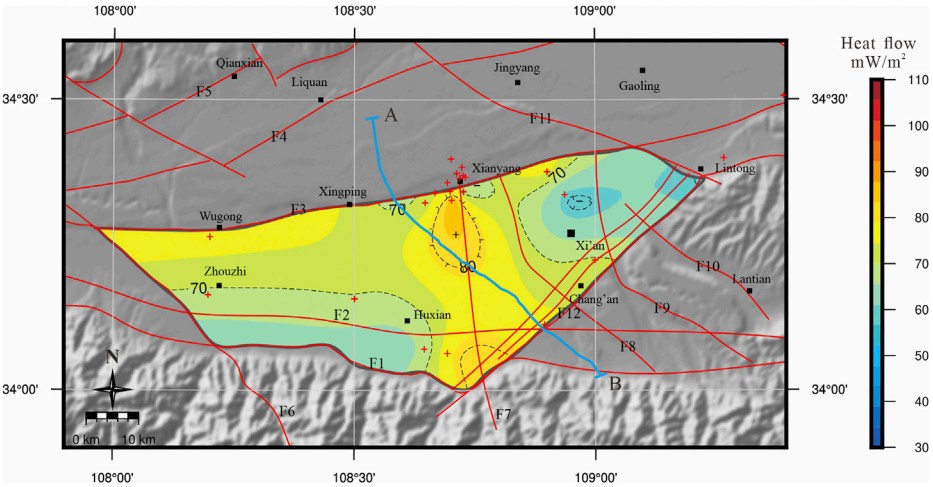

FIGURE 4 | The relationship between heat flow distribution and faults in Xi'an Depression [**(A,B)**: deep seismic reflection survey profile (Ren et al., 2013); F1-North Qinling Piedmont Fault, F2-Yuxia-Tieluzi Fault, F3-Weihe Fault, F4-Liquan-Shuangquan fault, F5-Qianxian-Fuping Fault, F6-Yabai Fault, F7-Fenghe Fault, F8-Zaohe Fault, F9-Chanhe Fault, F10-Bahe fault, F11-Jinghe Fault, F12-Lintong-Changan Fault].

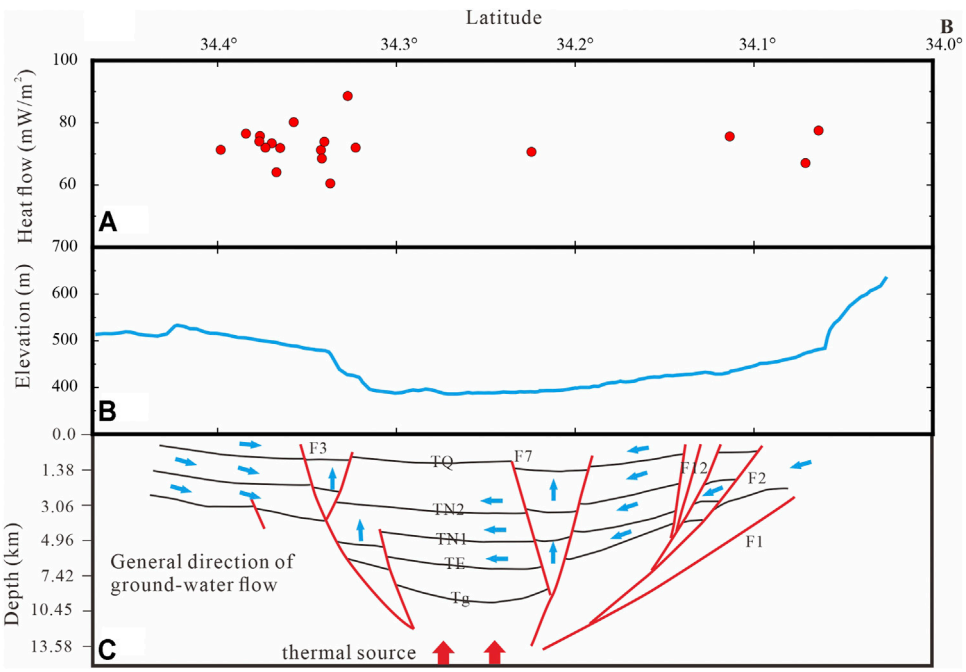

FIGURE 5 | Heat flow **(A)**, elevation **(B)** and Schematic diagram of deep structure and water flow direction **(C)** (Ma et al., 2008b; Ren, 2012; Ren et al., 2013) observed and calculated response along the geophysical transect [**(A,B)** transect can be seen in **Figure 4**] (TQ is the bottom boundary of the Quaternary Formation, TN1 and TN2 are the reflected waves of the new Tertiary Formations, TE is the bottom boundary of the old Tertiary Formation, and the reflected wave Tg may be the top boundary of the crystalline basement).

circulating geothermal reservoirs in the deep part of the Weihe fault and the Lintong-Chang'an fault zone, and forming isolated geothermal reservoir in the central part of the Xi'an Depression (**Figure 5**). The shallow area is still dominated by heat conduction. Circulating geothermal reservoirs are controlled by open fractures, the geothermal water mixes with atmospheric precipitation moving downwards during the process of moving upward along the open fractures. Isolated geothermal reservoirs are mainly characterized by high temperature and high pressure and are distributed deep in the

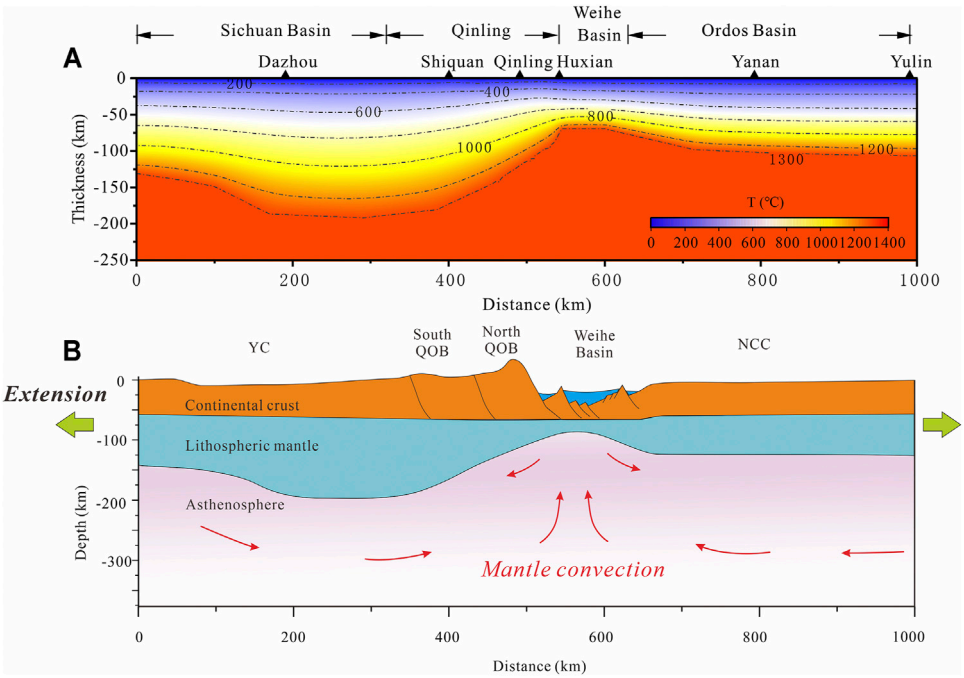

FIGURE 6 | Thermal structure of Sichuan Basin-Qinling Orogenic Belt-Weihe Basin-Ordos Basin in central China **(A)** and schematic diagram of deep dynamic mechanism **(B)** [modified from Xu et al. (2020)]

middle of the basin. The upward migration of deep geothermal water not only affects the geothermal field near the fault zone, but may also affect the formations on both sides of the fault, causing the temperature higher than normal, and forming a high heat flow anomalous zone near the deep fault.

The thickness of the sedimentary layer is also a factor affecting the geothermal anomalies. The sediment source areas of Xi'an Depression are from the Qinling and Weibei uplifts. The topographic features of this depression show an increasing trend on the whole from north to south, and the sediment filling gradually thickens to the north (**Figure 5**). According to the analysis of thermal reservoir, the thicker the reservoir rock bodies is, the more favorable it is to store hot water. Therefore, the thermal anomalies in the north are more significant than those in the south.

Thermal Source of the Xi'an Depression

Tectonic activity can change the thermal state of the crustal or lithosphere. The range and magnitude of the thermal state of the crustal or lithosphere changed by tectonic activity are mainly controlled by the combined effects of thermal relaxation, changes in the lithospheric heat generation rate, and tectonic processes (Furlong and Chapman, 2013). As the lithospheric thinning and crustal extension, affected by the equilibrium effect, the deep thermal matter rises, which increases the surface heat flow. The higher heat flow in the Weihe Basin belongs to the thermal effect of the crustal extension and thinning event (Xu et al., 2020). Based on the 2-D profile of the Yuquan-Yulin seismic reflection transect, we used the finite element method (Litmod-2D) (Afonso et al., 2008) to measure the elevation, Bouguer gravity, geoid height, heat flow, mantle composition, crustal and lithospheric structure as constraints to simulate the thermal structure of the continental lithosphere in the Sichuan Basin-Qinling Orogenic Belt-Ordos Basin (Xu et al., 2020). According to the distribution characteristics of the temperature field in the deep part of the profile, the temperature of the Moho in the Xi'an Depression ranges from 600 to 700°C, and the thermal lithosphere thickness is about 90–100 km (**Figure 6**). The results show that the Weihe Basin has a thin lithosphere and is affected by the thermal upwelling of the asthenosphere, resulting in a high thermal background in the study area.

Since the Cenozoic, the Xi'an Depression has turned into an extensional environment, beginning the development period of extensional fault basin, and it is still in the extensional stage at present (Han et al., 2002; Liu et al., 2006;Liu et al., 2010; Wang H et al., 2010). Therefore, the Xi'an Depression is in a state where the lithosphere and crust are stretched and thinned, resulting in a higher heat flow. Its deep geodynamic mechanism may be influenced by intracontinental deformation of the Yangtze and North China Plates in the Late Mesozoic, the far-field effect of the collision between the Indian Plate and the Eurasian Plate, and the eastward extrusion of the Qinghai-Tibetan Plateau (**Figure 6**). Based on the strong intracontinental deformation of the Yangtze and North China Plates in the Late Mesozoic, combined with the far-field effect of the collision between the Indian Plate and the Eurasian Plate and the eastward extrusion of Qinghai-Tibetan

Plateau, the deep part of the Qinling orogenic belt is still squeezed from north to south, and accompanying the uplift of the Qinling Mountains and the subsidence of the Weihe Basin in the north (Zhang et al., 1996; Zhang et al., 1997; Wang et al., 2003; Meng et al., 2005; Meng, 2017). As a result, the Xi'an Depression is in a continuous tensile stress field, the depression continues to subsidence, the lithosphere is thinned, and the upwelling of asthenosphere thermal materials further deepens the lithosphere thinning and leading to high heat flow.

CONCLUSION

1) The geothermal gradient of the Xi'an Depression in the Weihe Basin is 20.8–49.1 °C/km, with an average value of 31.7 ± 5.0 °C/km. The heat flow ranges from 59.4 to 88.6 mW/m^2, and the average heat flow is 71.0 ± 6.3 mW/m^2, which is significantly higher than the average continental heat flow of 60.4 ± 12.3 mW/m^2 in China.
2) The results of heat flow indicate that the Xi'an Depression belongs to a high thermal background area. The high heat flow zones are related to faults and groundwater circulation. The geothermal anomalous areas are near the Lintong-Chang'an fault zone in the south, the Weihe fault in the north, and the Fenghe fault in the central part of the depression.
3) The high thermal background in this area is related to the influence of the strong intracontinental deformation of the Yangtze and North China Plates in the Late Mesozoic, the far-field effect of the collision between the Indian Plate and the Eurasian Plate, and the eastward extrusion of Qinghai-Tibetan Plateau. The Xi'an Depression is in a continuous tensile stress field, the lithosphere is thinned, and the upwelling of thermal materials further deepens the lithosphere thinning, leading to high heat flow.

DATA AVAILABILITY STATEMENT

The original contributions presented in the study are included in the article/supplementary material, further inquiries can be directed to the corresponding authors.

AUTHOR CONTRIBUTIONS

WX: Conceptualization, Investigation, Methodology, Software, Writing—Original Draft, Writing—Review and Editing, Formal analysis, Visualization XT: Conceptualization, Writing—Review and Editing, Supervision LC: Investigation, Methodology, Software, Data Curation YD: Investigation, Resources YZ: Investigation, Resources TK: Investigation, Writing—Reviewing RY: Investigation, Methodology, Data Curation YL: Investigation, Data Curation.

FUNDING

This work is funded by the Xi'an Center of China Geological Survey (2019-060), the National Natural Science Foundation of China (Nos. 42172335, 41590855 and 41804079), and the Natural Science Foundation of Shaanxi Province (No. 2020JQ-032).

ACKNOWLEDGMENTS

We would like to thank Prof. Song Rao (Yangtze University, China) and Dr. Kai Qi (Northwest University, China) for helping with the thermal conductivity data of the Xi'an Depression. Our heartfelt gratitude is also extended to the editors and reviewers for their scientific and linguistic revisions of the manuscript.

REFERENCES

Afonso, J. C., Fernàndez, M., Ranalli, G., Griffin, W. L., and Connolly, J. A. D. (2008). Integrated Geophysical-Petrological Modeling of the Lithosphere and Sublithospheric Upper Mantle: Methodology and Applications. *Geochem. Geophys. Geosyst.* 9, a–n. doi:10.1029/2007GC001834

Brigaud, F., Chapman, D. S., and Le Douaran, S. (1990). Estimating thermal Conductivity in Sedimentary Basins Using Lithologic Data and Geophysical Well Logs (1). *AAPG Bull.* 74 (9), 1459–1477. doi:10.1306/0c9b2501-1710-11d7-8645000102c1865d

Chang, J., Glorie, S., Qiu, N., Min, K., Xiao, Y., and Xu, W. (2021). Late Miocene (10.0~6.0 Ma) Rapid Exhumation of the Chinese South Tianshan: Implications for the Timing of Aridification in the Tarim Basin. *Geophys. Res. Lett.* 48 (3), e2020G–e90623G. doi:10.1029/2020GL090623

Ciriaco, A. E., Zarrouk, S. J., and Zakeri, G. (2020). Geothermal Resource and reserve Assessment Methodology: Overview, Analysis and Future Directions. *Renew. Sust. Energ. Rev.* 119, 109515. doi:10.1016/j.rser.2019.109515

Deng, Y., Ren, Z., and Ren, W. (2017). Geothermal Distribution Control Factors and Geothermal prospect in Guanzhong Region. *Land Dev. Eng. Res.* 2 (11), 19–27.

Feng, C.-G., Liu, S.-W., Wang, L.-S., and Li, C. (2009). Present-Day Geothermal Regime in Tarim Basin, Northwest China. *Chin. J. Geophys.* 52, 1237–1250. doi:10.1002/cjg2.1450

Furlong, K. P., and Chapman, D. S. (2013). Heat Flow, Heat Generation, and the thermal State of the Lithosphere. *Annu. Rev. Earth Planet. Sci.* 41, 385–410. doi:10.1146/annurev.earth.031208.100051

Gong, Y.-l., Zhang, H., and Ye, T.-f. (2011). Heat Flow Density in Bohai bay basin: Data Set Compilation and Interpretation. *Proced. Earth Planet. Sci.* 2, 212–216. doi:10.1016/j.proeps.2011.09.034

Gong, Y. L. (2003). *The thermal Structure and thermal Evolution of Bohai Bay Basin Eastern China*.

Han, H., Zhang, Y., and Yuan, Z. (2002). The Evolution of Weihe Down-Faulted basin and the Movement of the Fault Blocks. *J. Seismological Res.* 4 (25), 362–368.

Hu, S., O'Sullivan, P. B., Raza, A., and Kohn, B. P. (2001). Thermal History and Tectonic Subsidence of the Bohai Basin, Northern China: A Cenozoic Rifted and Local Pull-Apart basin. *Phys. Earth Planet. Interiors* 126, 221–235. doi:10.1016/S0031-9201(01)00257-6

Huang, J., Zhou, Y., Teng, H., Liang, X., Gao, J., Cao, X., et al. (2021). On the Occurrence Characteristics and the Estimation of Geothermal Water in Xi'an Sag,guanzhong basin. *Northwest. Geology.* 54 (1), 196–203.

Jiang, G., Gao, P., Rao, S., Zhang, L., Tang, X., Huang, F., et al. (2016). Compilation of Heat Flow Data in the china continental Area (4rd Edition). *Chin. J. Geophys.* 44, 2892–2910.

Jiang, G., Hu, S., Shi, Y., Zhang, C., Wang, Z., and Hu, D. (2019). Terrestrial Heat Flow of continental China: Updated Dataset and Tectonic Implications. *Tectonophysics* 753, 36–48. doi:10.1016/j.tecto.2019.01.006

Jiang, S., Zuo, Y., Yang, M., and Feng, R. (2021). Reconstruction of the Cenozoic Tectono-thermal History of the Dongpu Depression, Bohai bay basin, china: Constraints from Apatite Fission Track and Vitrinite Reflectance Data. *J. Pet. Sci. Eng.* 205, 108809. doi:10.1016/j.petrol.2021.108809

Jougnot, D., and Revil, A. (2010). Thermal Conductivity of Unsaturated clay-rocks. *Hydrol. Earth Syst. Sci.* 14 (1), 91–98. doi:10.5194/hess-14-91-2010

Li, G., and Li, F. (2010). *The Circulation Law and Sustainable Utilization of Ground Hot Water in Guanzhong basin*. Beijing: China Science Publishing & Media LTD.

Li, T., Xu, J., and Ren, G. (1994). Study on Geomechanical Modelling of the Fault Activites in Xi'an Area. *J. Eng. Geology.* 2 (3), 34–42.

Li, Z., Gao, J., Zheng, C., Liu, C., Ma, Y., et al. (2015). Present-day Heat Flow and Tectonic-thermal Evolution since the Late Paleozoic Time of the Qaidam basin. *Chin. J. Geophys.* 58, 3687–3705.

Liang, S., Sun, T., Han, Y., and Shi, S. (1992). Terrestrial Heat Flow in the 4th Geoscience Transection of china. *Sci. Bull.* 37 (2), 143–146.

Liu, C., Zhao, H., Gui, X., Yue, L., Zhao, J., and Wang, J. (2006). Space-time Coordinate of the Evolution and Reformation and Mineralization Response in Ordos basin. *Acta Geologica Sinica* 80 (5), 637–646.

Liu, H., and Xue, X. (2004). Discussion on the Cenozoic and its Chronology in the Weihe River basin. *J. Earth Sci. Enivronmental* 26 (4), 1–5.

Liu, J. H., Zhang, P. Z., Zheng, D. W., Wan, J. L., and Wang, W. T. (2010). The Cooling History of Cenozoic Exhumation and Uplift of the Taibai Mountain, Qinling, china: Evidence from the Apatite Fission Track(aft) Analysis. *Chin. J. Geophys.* 53 (10), 2405–2414. doi:10.1007/s11430-010-0016-0

Luo, L. (2015). *Genesis and Reservoir Modification Analysis of Xianyang Geothermal System, Guanzhong basin*. [dissertation]. [Beijing]: University of Chinese Academy of Sciences.

Luo, L., Zhu, X., He, C., Mao, X., Xu, Z., Wang, X., et al. (2019). Study on the Genesis of Geothermal Fluid in Xianyang Geothermal Field. *Geol. Rev.* 65 (6), 1422–1430.

Ma, Z., Wang, X., Su, Y., and Yu, J. (2008b). Oxygen and Hydrogen Isotope Exchange and its Controlling Factors in Subsurface Geothermal Water S in the central Guanzhong basin, Shaanxi, china. *Geol. Bull. China* 27 (6), 888–894.

Ma, Z., Yu, J., Li, Q., Wang, X., Li, F., Mu, G., et al. (2008a). Environmental Isotope Distribution and Hydrologic Geologic Sense of Guanzhong basin Geothermal Water. *J. Earth Sci. Environ.* 30 (4), 396–401.

Meng, Q.-R., Wang, E., and Hu, J.-M. (2005). Mesozoic Sedimentary Evolution of the Northwest Sichuan basin: Implication for Continued Clockwise Rotation of the south china Block. *Geol. Soc. America Bull.* 117 (3-4), 396. doi:10.1130/B25407.1

Meng, Q. (2017). Origin of the Qinling Mountains. *Scientia Sinica Terrae* 47 (4), 412–420.

Mu, G., Li, F., Yan, W., and Li, C. (2016). *Occurrence Rules and Key Technologies of Exploitation and Utilization of Geothermal Resources in Guanzhong basin*. Beijing: Geological Publishing House.

Popov, Y., Beardsmore, G., Clauser, C., and Roy, S. (2016). Isrm Suggested Methods for Determining thermal Properties of Rocks from Laboratory Tests at Atmospheric Pressure. *Rock Mech. Rock Eng.* 49 (10), 4179–4207. doi:10.1007/s00603-016-1070-5

Pribnow, D., Williams, C. F., Sass, J. H., and Keating, R. (1996). Thermal Conductivity of Water-Saturated Rocks from the KTB Pilot Hole at Temperatures of 25 to 300°C. *Geophys. Res. Lett.* 23 (4), 391–394. doi:10.1029/95gl00253

Qin, D., Turner, J. V., and Pang, Z. (2005a). Hydrogeochemistry and Groundwater Circulation in the Xi'an Geothermal Field, China. *Geothermics* 34 (4), 471–494. doi:10.1016/j.geothermics.2005.06.004

Qin, D., Turner, J. V., and Pang, Z. (2005b). Hydrogeochemistry and Groundwater Circulation in the Xi'an Geothermal Field, china. *Geothermics* 34 (4), 471–494. doi:10.1016/j.geothermics.2005.06.004

Qiu, N., Wei, G., Li, C., Zhang, Y., and Guo, Y. (2009). Distribution Features of Current Geothermal Field in the Bohai Sea Waters. *Oil Gas Geology.* 30, 412–420.

Qiu, N., Zuo, Y., Chang, J., and Li, W. (2014). Geothermal Evidence of Meso-Cenozoic Lithosphere Thinning in the Jiyang sub-basin, Bohai bay basin, Eastern north china Craton. *Gondwana Res.* 26 (3-4), 1079–1092. doi:10.1016/j.gr.2013.08.011

Rao, G., Lin, A., Yan, B., Jia, D., and Wu, X. (2014). Tectonic Activity and Structural Features of Active Intracontinental normal Faults in the Weihe Graben, central china. *Tectonophysics* 636, 270–285. doi:10.1016/j.tecto.2014.08.019

Rao, S., Hu, S., Zhu, C., Tang, X., Li, W., et al. (2013). The Characteristics of Heat Flow and Lithospheric thermal Structure in Junggar Basin, Northwest China. *Chin. J. Geophys.* 56, 2760–2770.

Rao, S., Jiang, G. Z., Gao, Y. J., Hu, S. B., and Wang, J. Y. (2016). The thermal Structure of the Lithosphere and Heat Source Mechanism of Geothermal Field in Weihe basin. *Chin. J. Geophys.-Ch.* 59 (6), 2176–2190.

Ren, J., Feng, X., Wang, F., Peng, J., Liu, C., Dai, W., et al. (2013). Fine Crust Structures of Xi'an Sag in the Weihe basin Revealed by a Deep Seismic Reflection Profile. *Chin. J. Geophys.* 56 (2), 513–521.

Ren, J. (2012). *Probe on the Deep Crustal Structure in Weihe basin and Tectonics Research of basin*. [dissertation]. [Xi'an]. Chang'an University.

Ren, Z., Liu, R., Ren, W., Qi, K., Yang, G., Cui, J., et al. (2020). Distribution of Geothermal Field and its Controlling Factors in the Weihe basin. *Acta Geologica Sinica* 94 (7), 1938–1949. doi:10.1111/1755-6724.14458

Stober, I., and Bucher, K. (2013). History of Geothermal Energy Use from Theoretical Models to Exploration and Development. *Springer Berlin Heidelberg*, 15–24. Berlin, Heidelberg. doi:10.1007/978-3-642-13352-7_2

Teng, J. W., Li, S. L., Zhang, Y. Q., Wang, F. Y., Pi, J. L., et al. (2014). Fine Velocity Structures and Deep Processes in Crust and Mantle of the Qinling Orogenic Belt and the Adjacent North China Craton and Yangtze Craton. *Chin. J. Geophys.* 57, 3154–3175.

Wang, E., Meng, Q., Clark Burchfiel, B., and Zhang, G. (2003). Mesozoic Large-Scale Lateral Extrusion, Rotation, and Uplift of the Tongbai-Dabie Shan belt in east China. *Geol* 31 (4), 307. doi:10.1130/0091-7613(2003)031<0307:mlsler>2.0.co;2

Wang, H., Liu, B., Ma, Z., Li, Y., and Jin, W. (2010). Analysis of Distribution of Geophysical Characteristics and Reservior-Forming Conditions in the Pre-cenozoic Strata in the Weihe basin. *Prog. Geophys.* 25 (4), 1280–1287.

Wang, J. (2016). *Geothermics and its Applications*. Beijing: Science Press.

Wang, J., Liu, C., Yan, J., Zhao, H., Gao, F., and Liu, C. (2010). Development Time and Evolution Characteristics of Weibei Uplift in the South of Ordos basin. *J. Lanzhou Univ. (Natural Sciences)* 46 (4), 22–29.

Wang, Y., Wang, L., Hu, D., Guan, J., Bai, Y., Wang, Z., et al. (2020). The Present-Day Geothermal Regime of the north Jiangsu basin, east china. *Geothermics* 88, 101829. doi:10.1016/j.geothermics.2020.101829

Wu, Q., and Xie, Y. (1985). Geothermal Heat Flow in the Songhuajiang-Liaoning Basin. *Seismology Geology.* 7, 59–64.

Xu, M., Zhu, C.-Q., Tian, Y.-T., Rao, S., and Hu, S.-B. (2011). Borehole Temperature Logging and Characteristics of Subsurface Temperature in the Sichuan Basin. *Chin. J. Geophys.* 54, 224–233. doi:10.1002/cjg2.1604

Xu, W., Huang, S., Zhang, J., Zuo, Y., Zhou, Y., Ke, T., et al. (2021). Geothermal Gradient and Heat Flow of the Erlian basin and Adjacent Areas, Northern china: Geodynamic Implication. *Geothermics* 92, 102049. doi:10.1016/j.geothermics.2021.102049

Xu, W., Li, Y., Zhou, L., Ke, T., and Cheng, L. (2020). Lithospheric thermal Regime under the Qinling Orogenic belt and the Weihe basin: a Transect across the Yangtze and the north china Cratons in central china. *Tectonophysics* 789, 228514. doi:10.1016/j.tecto.2020.228514

Yang, J. (2002). *Ordos basin Tectonic Evolution and Hydrocarbon Distribution Rule*. Beijing: Petroleum Industry Press.

Yu, R., Huang, S., Zhang, J., Xu, W., Ke, T., Zuo, Y., et al. (2020). Measurement and Analysis of the thermal Conductivities of Rocks Samples from the Baiyinchagan Sag and Uliastai Sag, Erlian basin, Northern china. *Acta Petrol. Sin.* 36 (2), 621–636.

Zhang, G., Meng, Q., Liu, S., and Yao, A. (1997). Huge Intracontinental Subduction Zone at South Margin of north china Block and Present 3-d Lithospheric Framework of the Qinling Orogenic belt. *Geol. J. Univ.* 3 (2), 129–143.

Zhang, G. W., Meng, Q. G., Yu, Z. P., Sun, Y., Zhou, D. W., and Guo, A. L. (1996). Orogenesis and Dynamics of the Qinling Orogen. *Sci. China Ser. D-Earth Sci.* 39 (3), 225–234. doi:10.1360/yd1996-39-3-225

Zhang, J., Dong, M., Wang, B., Ai, Y., and Fang, G. (2020). Geophysical analysis of geothermal resources and temperature structure of crust and upper mantle beneath guanzhong basin of shaanxi,china. *Journal Earch Sci. Environ.* 43 (1), 150–163.

Zhang, Y., Huang, S., Yang, F., Wang, X., Yu, R., Li, Y., et al. (2019). Geothermal Features of Two Deep U-Shape Downhole Heat Exchangers in the Xi'an Depression,guanzhong basin. *Coal Geology. China* 31 (6), 54–61.

Zhao, Z., and Liu, C. (1990). The Formation and Evolution of the Sedimentary Basins and Their Hydrocarbon Occurrence in the north china Craton. *Xi'an: Northwest. Univ. Press* 53 (5), 2–5. (in Chinese).

Zuo, Y., Jiang, S., Wu, S., Xu, W., Zhang, J., Feng, R., et al. (2020). Terrestrial Heat Flow and Lithospheric thermal Structure in the Chagan Depression of the Yingen-Ejinaqi Basin, north central China. *Basin Res.* 32 (6), 1328–1346. doi:10.1111/bre.12430

Conflict of Interest: Author YL is employed by Sichuan Institute of Geological Engineering Investigation Group Co. Ltd.

The remaining authors declare that the research was conducted in the absence of any commercial or financial relationships that could be construed as a potential conflict of interest.

The handling Editor declared a past co-authorship with the authors TK, RY, YL.

Publisher's Note: All claims expressed in this article are solely those of the authors and do not necessarily represent those of their affiliated organizations, or those of the publisher, the editors and the reviewers. Any product that may be evaluated in this article, or claim that may be made by its manufacturer, is not guaranteed or endorsed by the publisher.

frontiers in Earth Science

ORIGINAL RESEARCH
published: 14 January 2022
doi: 10.3389/feart.2021.787133

Determining the Recoverable Geothermal Resources Using a Numerical Thermo-Hydraulic Coupled Modeling in Geothermal Reservoirs

Yifan Fan[1], Shikuan Zhang[2], Yonghui Huang[3,4,5], Zhonghe Pang[3,4,5] and Hongyan Li[6]*

[1]China Three Gorges Corporation, Beijing, China, [2]CAUPD Beijing Planning & Design Consultants Co., Ltd., Beijing, China, [3]Key Laboratory of Shale Gas and Geoengineering, Institute of Geology and Geophysics, Chinese Academy of Sciences, Beijing, China, [4]College of Earth and Planetary Sciences, University of Chinese Academy of Sciences, Beijing, China, [5]Innovation Academy for Earth Science, Chinese Academy of Sciences, Beijing, China, [6]Sinopec Green Energy Geothermal Development Co.,Ltd., Xiong'an, China

Recoverable geothermal resources are very important for geothermal development and utilization. Generally, the recovery factor is a measure of available geothermal resources in a geothermal field. However, it has been a pre-determined ratio in practice and sustainable utilization of geothermal resources was not considered in the previous calculation of recoverable resources. In this work, we have attempted to develop a method to calculate recoverable geothermal resources based on a numerical thermo-hydraulic coupled modeling of a geothermal reservoir under exploitation, with an assumption of sustainability. Taking a geothermal reservoir as an example, we demonstrate the effectiveness of the method. The recoverable geothermal resources are 6.85×10^{18} J assuming a lifetime of 100 years in a well doublet pattern for geothermal heating. We further discuss the influence of well spacing on the recoverable resources. It is found that 600 m is the optimal well spacing with maximum extracted energy that conforms to the limit of the pressure drop and no temperature drop in the production well. Under the uniform well distribution pattern for sustainable exploitation, the recovery factor is 26.2%, which is higher than the previous value of 15% when depending only on lithology. The proposed method for calculating the recoverable geothermal resources is instructive for making decisions for sustainable exploitation.

Keywords: recoverable geothermal resources, numerical model, sustainable exploitation, reinjection, well spacing

OPEN ACCESS

Edited by:
Haibing Shao, Helmholtz Association of German Research Centres (HZ), Germany

Reviewed by:
Fengtian Yang, Jilin University, China
Chaofan Chen, Helmholtz Association of German Research Centres (HZ), Germany

****Correspondence:***
Yifan Fan
fan_yifan@ctg.com.cn

Specialty section:
This article was submitted to Economic Geology, a section of the journal Frontiers in Earth Science

Received: *30 September 2021*
Accepted: *19 November 2021*
Published: *14 January 2022*

Citation:
Fan Y, Zhang S, Huang Y, Pang Z and Li H (2022) Determining the Recoverable Geothermal Resources Using a Numerical Thermo-Hydraulic Coupled Modeling in Geothermal Reservoirs. Front. Earth Sci. 9:787133. doi: 10.3389/feart.2021.787133

INTRODUCTION

Geothermal energy is a clean energy that barely pollutes the atmosphere or emits greenhouse gases (Lund et al., 2011; Pang et al., 2012). Compared with solar and wind energy, geothermal energy is continuous and stable. Geothermal energy usage has increased substantially in recent decades, and geothermal direct use is the most versatile and common form in many countries (Dickson and Fanelli, 2013; Shortall et al., 2015). In China, direct use of geothermal energy is widely distributed, and the total amount of heat has been the largest in the world (Zhu et al., 2015). Xiongxian geothermal field is currently supplying heat for 4.5 million square meters of houses, the largest district heating capacity in the world from a single geothermal field (Pang, 2018). Therefore, we have taken Xiongxian geothermal field as the example in our study of recoverable geothermal resources.

Over-exploitation of geothermal water may lead to a continuous decline in the groundwater level as well as reservoir temperature (Sanyal et al., 2000; Allis et al., 2009; Duan et al., 2011). Sustainable utilization of geothermal resources is a challenge facing the scientific community (Mongillo and Axelsson, 2010). The amount of recoverable resources is very important for sustainable geothermal resource management. There was a 30-m drop in the groundwater level from 2001 to 2009 in the majority of wells in the Xiongxian geothermal field (Kong et al., 2014). The recoverable geothermal resources in Xiongxian geothermal field are calculated by using a recovery factor of 15%, as set in the national standard (DZ40-85, 1985; Yang et al., 2015; Wang, 2009; Pang et al., 2017), which does not consider sustainability issues such as thermal breakthrough and pressure drop.

The renewability and sustainability of geothermal energy have attracted the attention of many scholars (White and Williams, 1975; Rybach et al., 1999; Stefansson, 2000; Axelsson et al., 2001; Rybach, 2003; Sanyal, 2005). Sustainability is reasonably defined as the ability to economically maintain the installed capacity over the amortized life of a power plant by taking practical steps (such as make-up well drilling) to compensate for resource degradation (pressure drawdown and/or cooling) (Sanyal, 2005). The project or amortized life is usually 20–50 years (O'Sullivan and O'Sullivan, 2016). Franco and Donatini (2017), who agree with Sanyal's (2005) opinion on sustainability, believe that the geothermal potential of a particular area is to assess the maximum water yield to keep the heat extraction energy unchanged for an amortized time considering the temperature and pressure variation in the geothermal field. Williams et al. (2008) think any estimate of reservoir production potential should evaluate longevity from the perspective of injection and eventual thermal breakthrough. However, regrettably, few people consider sustainable use of geothermal resources when calculating the recoverable geothermal resources. It is therefore crucial and urgent to determine recoverable geothermal resources under conditions where temperature drop does not occur and pressure drop is within the threshold value in the production well, keeping the energy output of the well unchanged during the project lifetime; assumed to be 100 years. The lifetime of a geothermal field is defined as the thermal breakthrough time in the well doublet, that also meets the pressure drop limit (Gringarten, 1978).

Comerford et al. (2018) estimated geothermal heat recovery from a hot sedimentary aquifer in Guardbridge, Scotland using coupled groundwater flow and heat transport numerical model combining the heterogeneity of the medium. Simulation indicated production is sustainable for over 50 years in assumed extraction scenarios. However, the maximum thermal exploitation amount that keeps sustainable and the pressure change is not taken into account. Bodvarsson and Tsang (Bödvarsson and Tsang, 1982) and Williams (2007) estimated the recoverable geothermal resources for fracture reservoirs based on analytical equation and for fracture spacing of less than 30 m, the cold sweep will not achieve the production well in 30 years. The maximum extraction rate is not given. Kong et al. (2017) has put forward an optimistic well spacing using economic analysis which does not consider the sustainable exploration of a geothermal reservoir. Williams (2007), Williams (2010) established an idealized fractural reservoir model exploited by a single production and injection well doublet to describe the cold water injection front. The temperature of the production well began to decrease at about 5 years. The annual recoverable geothermal resources and recovery factor were evaluated with the change of production years. However, due to the decrease in temperature, recoverable geothermal resources cannot be maintained in a sustainable way. Sanyal et al. (2004) summarized the results of a national assessment of hydrothermal resources undertaken by USGS and GeothermEX according to industry experience over 26 years and estimated minimum sustainable capacity of 17 fields. GeothermEX assessment considered recovery factor 0.131 according to statistical fit. He also gave a semi-empirical equation that sustainable heat production capacity is the sum of natural heat discharge rate and the maximum heat production rate and indicated the value range from 3 to 17%, with a mean of 11%. However, in the calculation, the empirical coefficient of sustainability factor ranges so widely that the error is ±70% about the median of 10% (Grant, 2015). In the national standard of China, the recovery factor (Rg for simplicity) is set as 15% to calculate recoverable resources for thermal reservoirs with fractured carbonate rock (DZ40-85, 1985). The mean recovery factor recommended by the Australian code for sedimentary reservoirs is 17.5% with a range of 10–25% with a uniform probability (Williams et al., 2008; AGRCC, 2010a; AGRCC, 2010b; O'Sullivan and O'Sullivan, 2016). However, it is very unreliable to assess recoverable resources by depending on a pre-determined Rg decided by the reservoir lithology. Simple analytical models for a homogeneous and isotropic aquifer have been adopted to assess the recoverable geothermal resources that the extraction can be economically maintained in a geothermal field for urban heating (Gringarten, 1978; AGRCC, 2010a; Ferguson and Grasby, 2014; Ufondu, 2017).

In this study, a numerical thermo-hydraulic coupled modeling based on a trial method is proposed to calculate the recoverable geothermal resources in Xiongxian geothermal field. The recoverable geothermal resources and lifetime are related to the exploitation amount that can maintain the heat extraction unchanged throughout the authorized life of the field. The numerical model is established using many parameters, such as thermal conductivity, permeability, viscosity, and others, which are more accurate than using the predetermined Rg set in the standard. Additionally, lateral water flow and seasonal district heating are also considered in the numerical model, which was not taken into account in the analytical model. Therefore, the optimal well spacing that maintains the temperature of the fluid unchanged and the drawdown in the production well within the allowed value is discussed in this study.

MODELING METHOD

The procedures include two steps. One step is the numerical simulation, which is related to the geological and physical

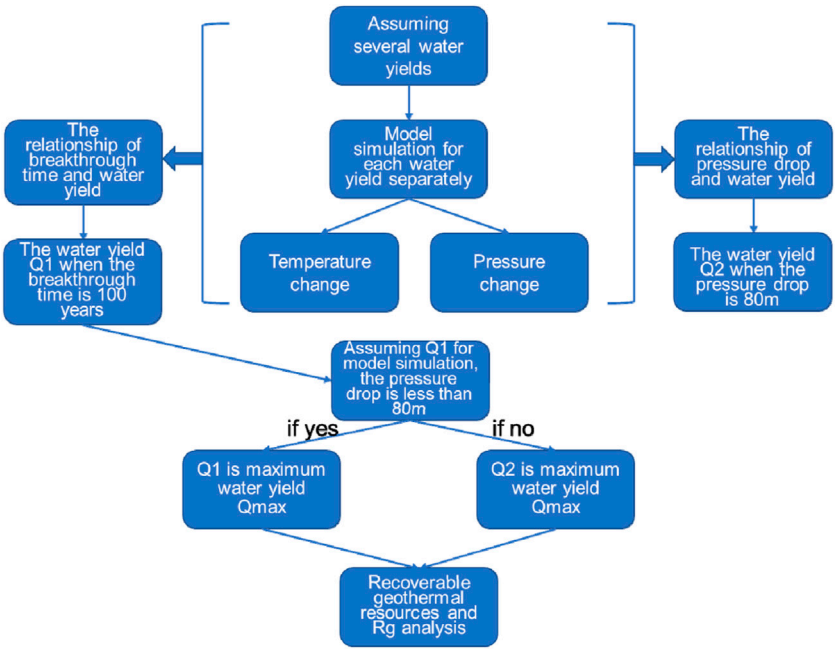

FIGURE 1 | Procedure to acquire the recoverable resources and Rg.

processes. The other step analyses the recoverable geothermal resources and recovery factors according to water pressure drop and thermal breakthrough.

Numerical Model

The present work focuses on numerical modeling for maximum heat extraction. The model in this study contains the 1D injection/production wells and 2D porous matrix of the Xiongxian Jixian system reservoir. Lateral runoff, seasonal heating, and different well spacing in well doublet patterns are considered in the model. The numerical model is based on a two-dimensional transient heat transfer model, and the following two **Equations 1**, **2** are used to realize the common simulation of the thermal front and pressure drawdown.

Mass conservation equation for control of flow in porous media is as follows:

$$S\frac{\partial P}{\partial t} - \nabla\left(\frac{k}{\mu}\left(\nabla P + \rho_l g\right)\right) = q \tag{1}$$

where S represents the specific storage of the medium (1/m), P represents the groundwater pressure (Pa), t represents time (s), k represents the permeability (m^2), μ represents the groundwater dynamic viscosity (Pas), ρ_l represents the groundwater density (kg/m^3), g represents the gravitational acceleration (m/s^2) and q is the volumetric source or sink of the groundwater ($kg/m^3/s$).

The processes of heat conduction and convection are governed by the following constitutive **Equation 2**:

$$\rho C_r\frac{\partial T_w}{\partial t} + \rho_l C_l v \cdot \nabla T_w - \nabla\left(\lambda \nabla T_w\right) = q_T \tag{2}$$

where ρ represents the density of the porous medium (kg/m^3), λ represents the heat conductivity of the porous medium (W/m/°C), C_r is the specific heat capacity of the porous medium (J/kg/°C), C_l is the specific heat capacity of the groundwater (J/kg/°C), v represents the fluid velocity (m/s), T_w is the groundwater temperature (°C), and q_T is the source/sink term of heat (W/m^2).

Recoverable Geothermal Resources Analysis

The changes in temperature and pressure at the production well can be known from the model. The following is a description of the steps taken to acquire the recoverable resources and Rg (**Figure 1**).

1) Assuming multiple mining scenarios with a series of water yields, the other conditions of the model in these scenarios, including initial conditions, boundary conditions, and grid settings are all the same;
2) Carry out numerical simulations for multiple scenarios with different water yields separately. In every scenario, temperature change and hydraulic pressure change with the mining time of the reservoir are obtained through model simulation;
3) Based on the simulation results, the temperature change curve of the production well can be obtained in every mining scenario. Reinjection of geothermal water into reservoirs could help maintain the reservoir pressure but may lead to thermal breakthrough. Therefore, each water yield corresponds to the thermal breakthrough time when the temperature of the production well drops. Therefore, the

corresponding relationship between water yield and thermal breakthrough time is obtained.

By analogy, the pressure change curve of the production well can be obtained in every mining scenario. The corresponding relationship between water yield and the maximum value of the pressure drop is obtained.

4) According to the relationship between water yield and thermal breakthrough time, assuming that the thermal breakthrough time is 100 years, the corresponding water yield Q1 in this scenario can be obtained.

Similarly, according to the relationship between water yield and the maximum value of the pressure drop, assuming that the maximum pressure drop is the pressure threshold, the corresponding water yield Q2 in this scenario can be obtained.

5) Assuming that the water yield is Q1, a numerical model simulation is performed to obtain the pressure change of the production well over time. If the maximum value of the pressure drop is less than the threshold, Q1 is the maximum water yield Q_{max} all over the multiple scenarios.

If the maximum value of the pressure drop with the water yield Q1 is more than the threshold, Q2 is the maximum water yield Q_{max} all over the multiple scenarios.

The pressure drop threshold is assumed to be 80 m. This pressure threshold can be changed according to the actual situation of the geothermal field. In order to prevent atmospheric corrosion, the pump should be about 70 m below the surface of the water. If the water pump of the production well is located at about 150 m under the water level, the maximum water level can only drop another 80 m.

6) Based on the maximum water yield Qmax, the geothermal recoverable resource for a single well doublet at the wellhead E_{single} can be calculated as follow (Williams, 2004; Williams 2010)

$$E_{single} = m_{WH}\,(h_{WH} - h_{ref}) \tag{3}$$

Where, m_{WH} is the mass of the extractable water yield, h_{WH} is the enthalpy of the extracted fluid, and h_{ref} is the enthalpy at a reference temperature.

$$m_{WH} = Q_{max}\rho_l t_{life} \tag{4}$$

$$h_{WH} = C_l T_R \tag{5}$$

$$h_{ref} = C_l T_{ref} \tag{6}$$

$$E_{single} = Q_{max}\rho_l C_l t_{life}\,(T_R - T_{ref}) \tag{7}$$

where Q_{max} is the maximum water yield per well (m^3/h); ρ_l and C_l are the density (kg/m^3) and specific heat capacity [J/(kg·°C)] of the fluid, respectively; T_R is the reservoir temperature, T_{ref} is a reference or abandonment temperature (°C) (Garg and Combs, 2015), 30°C in this study and t_{life} is the time period ahead of thermal breakthrough or the maximum pressure drawdown limit

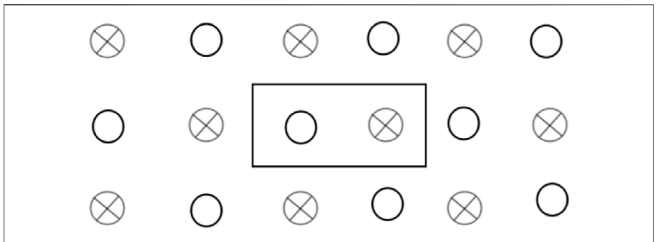

FIGURE 2 | Selected reference volume (doublet in a closed rectangle) in a multiple well doublet production pattern.

value in the production well, namely, the reservoir lifetime (year). In **Equation 7**, the unit of lifetime should be changed to hours.

7) The layout of the well doublet pattern in the geothermal field area is arranged as follows. In **Figure 2**, ⊗ represents the recharge well, and ○ represents the production well. The layout of wells shown in **Figure 2** was adopted in the large-scale exploitation condition (Gringarten, 1978). Under this kind of well doublet pattern arrangement, a constant pressure boundary can be achieved and the reservoir lifetime is longer than that of a single well doublet. It has been proved that the maximum energy can be extracted when the length of the rectangular boundary in **Figure 2** is twice that of the well spacing and the width is equal to the well spacing. Such well layout design can make sure that the thermal breakthrough influence area is between the injection and production wells.

The well spacing is D (m). The number of well doublets n in the exploitation area S (m^2) is

$$n = \frac{S}{2D^2} \tag{8}$$

Then, the total maximum water yield is as follow

$$Q_{total} = nQ_{max} \tag{9}$$

Where Q_{total} is the total maximum water yield for all production wells (m^3/h).

8) Recoverable geothermal resources can be obtained as follows:

$$E_{recovery} = \sum_{1}^{n} Q_{max}\rho_l C_l t_{life}\,(T_R - T_{ref}) \tag{10}$$

9) To calculate the recovery factor, the total geothermal resource is needed to be obtained. The volumetric method is applied to calculate the total geothermal resource. The volumetric method was originally proposed in the USGS Assessment of Geothermal Resources (Nathenson, 1975; White and Williams, 1975; Muffler and Cataldi, 1978), and the total geothermal resource in a reservoir is calculated as

$$E = \rho C V\,(T_R - T_{ref}) \tag{11}$$

Here, ρ and C are the density (kg/m^3) and heat capacity (J/(kg·°C)) in the reservoir, respectively, V is the reservoir volume

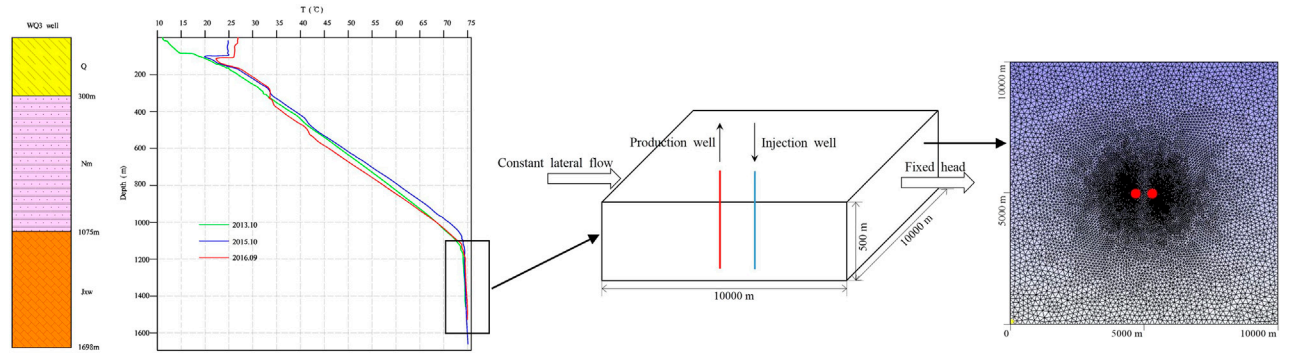

FIGURE 3 | Computational model of the deep Jixian system reservoir of the Xiongxian geothermal area.

(m^3), T_R is the reservoir temperature, and T_{ref} is a reference or abandonment temperature (°C).

The recovery factor is defined as the ratio of the extracted thermal energy (measured at the wellhead) to the total geothermal energy contained originally in a given subsurface volume of rock and water (Axelsson et al., 2001), and this factor can be deduced by **Equations 1**, **6** as follows:

$$Rg = \frac{E_{recovery}}{E} = \frac{\sum_{1}^{n} Q_{max}\rho_l C_l t_{life}\left(T_R - T_{ref}\right)}{\rho c V\left(T_R - T_{ref}\right)} = \frac{Q_{max}\rho_l C_l t_{life}}{2\rho c H D^2} \quad (12)$$

Where, H is the reservoir depth (m).

Model Configuration

In order to illustrate the sustainable recoverable resources of a geothermal reservoir, a two-dimensional hydro-thermal coupling model was established to simulate the hydro-thermal distribution in the field and the temperature and pressure change of the production well. The numerical model can be used to calculate the maximum water yield of sustainable exploitation for which the outlet temperature does not drop and the pressure does not exceed the critical value in the production well within 100 years of geothermal field life. Then, the recoverable resources can be calculated. This numerical model simulates the seasonal heating under the conditions of well doublet production patterns. The amount of recoverable resources is not fixed but varies with the production flow rate and production pattern, such as well spacing. The influence of well spacing is analyzed using the numerical model, and the optimal well spacing was found in this section.

A few assumptions are made in the model for simplicity. These are listed as follows: the reservoir is supposed to be horizontal and of uniform thickness; the model of the reservoir is a rectangle of 10 km in length and 10 km in width to ignore the boundary effects; the permeability and thermal conductivity of the reservoir rock is assumed to be isotropic; the reservoir is regarded as a homogeneous aquifer; the thermal reservoir is mined at a constant water yield; the production and reinjection rate is balanced. The model is a cross-section horizontal two-dimensional (2-D) model. Since the reservoir in Jixian system formation encountered by drilling is about 500 m, the reservoir thickness in the model is set to 500 m. The reservoir is approximately located at a depth of 1 km underground (**Figure 3**). The main parameter values are listed in **Table 1**.

Grid System

The numerical model is spatially discretized and is refined near the production well and reinjection well (**Figure 3**). The specific heat capacity and density of reservoir rocks are 920 J/kg°C and 2,700 kg/m^3 respectively. The permeability of the whole reservoir is set to be 1×10^{-13} m^2, the porosity is 0.03 (Kong et al., 2017; Pang, 2018).

Initial Condition

The temperature of the layer is set at 75°C, and its hydraulic pressure is 0 Pa in the whole model range in the beginning. A steady-state simulation was performed first with the lateral recharge, the result of which was adopted as the initial condition for the transient flow model. The details are as follows. First, run the numerical model with the consistent temperature and pressure throughout the model area with the lateral recharge. Then the initial hydraulic pressure distribution is achieved. Lastly, this new hydraulic pressure distribution is used as the initial condition for simulation.

Boundary Condition

A hydraulic fixed head is set as a constant value of 0 m on the right side, and the lateral recharge of 1.6×10^{-6} m^2/s from the left side is considered in the numerical model (Kong et al., 2017).

Source Term

Assuming that all of the water from the production well is reinjected into the recharge well, the pumping rate is equal to the quantity of water recharge. The temperature of the injection water is 30°C. Seasonal heating in 3 months of the year (from November 15th to March 15th) is considered in the numerical model.

In this work, the numerical model was developed with OpenGeoSys (OGS), which is a finite element and open-source software for solving multiple problems (Kolditz et al., 2012). A 2-D numerical model was established using OGS to simulate fluid and thermal transfer in the reservoir.

TABLE 1 | Main parameter values in the numerical model.

Reservoir rocks					Fluid		Lateral recharge (m^2/s)
Specific heat capacity (J/kg·°C)	Density (kg/m^3)	Thermal conductivity (W/m•K)	Permeability (m^2)	Porosity	Specific heat capacity (J/kg·°C)	Density (kg/m^3)	
920	2,700	2.4	1×10^{-13}	0.03	4,180	1,000	1.6×10^{-6}

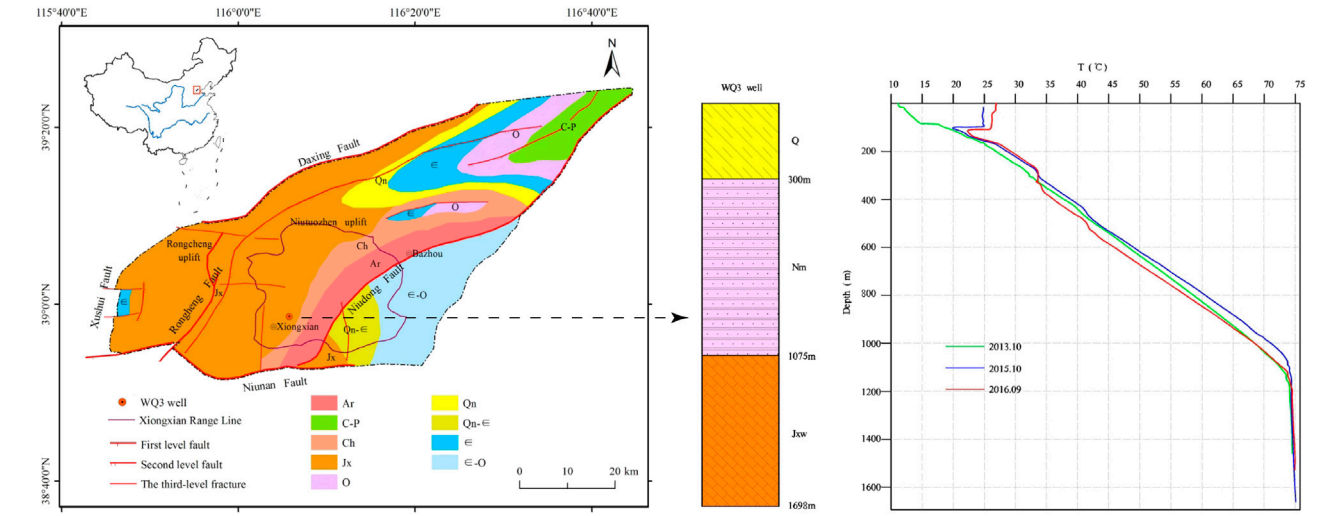

FIGURE 4 | Pre-Cenozoic geological map in the Niutuozhen uplift; the location and temperature profile of monitoring well in the Xiongxian geothermal field (C-P: Carboniferous–Permian; O: Ordovician; Ch: Changcheng system; Qn: Qingbaikou system; Jx: Jixian; ∈: Cambrian; Q-Quaternary; Nm-Neogene minghuazhen group; Jxw-Jixian wumishan group) [adapted by Pang et al. (2018)].

CASE STUDY

The numerical modeling is applied to Xiongxian in northern China as our study area, in which space heating is already on the way. The geothermal field in Xiongxian is located southwest of the Niutuozhen uplift, in the northern part of the Jizhong Depression, which is situated in the Bohai Bay Basin. The Bohai Bay Basin is a large Mesozoic-Cenozoic Cratonian sedimentary basin filled with continental Paleocene, Neogene, and Quaternary sediments. This basin was developed in the Tertiary on the basement of the North China Platform and includes many independent Paleogene fault depressions. The entire area settled into a large depression during the Neogene period (Kong et al., 2014; Kong et al., 2020).

There are four main faults forming the boundaries of the Niutuozhen uplift, including the Niudong fault, the Rongcheng fault, the Daxing fault, and the Niunan fault (**Figure 4**). These faults were formed from the Late Jurassic to the Cretaceous by folding movement. The Xiongxian geothermal field is in the southern part of the Niutuozhen uplift, the bedrock of which is consisted of middle-upper Proterozoic Jixian system dolomite and Sinian dolomite. The Niutuozhen geothermal field has excellent geological structural conditions for the formation of geothermal resources. The Middle and Upper Proterozoic basement uplift causes the distribution of terrestrial heat flow and the geothermal gradient to have the characteristics of being high at the bulge axis and gradually decreasing toward the edge of the bulge. The high value of the geothermal gradient of the Cenozoic caprock in the geothermal field spreads in the NEE direction, and the overall trend is higher in the southwest and lower in the northeast. The geothermal gradient of the Quaternary and Neogene caprocks in the Xiongxian district in the southern area of Niutuozhen geothermal field is between 4.86–7.64 °C/100 m, showing the characteristics of a conductive geothermal field. The geothermal gradient of the geothermal reservoir of the Wumishan group is much smaller than that of the upper caprock, with an average of 0.62°C/100 m, showing obvious convective heat transfer characteristics. The terrestrial heat flow in the southern area of the Niutuozhen geothermal field is between 83.13 and 119.65 mW/m^2. The terrestrial heat flow mainly comes from the heat generated by the radioactive decay of shallow rocks in the crust and the heat conducted by the upper mantle. According to the lithology and drilling information in the Xiongxian district, the lithology of geothermal reservoirs includes Neogene sandstone and lower Proterozoic Jixian system dolomite bedrock. Jixian system dolomite bedrock, especially the Wumishan group, is the main aquifer for space heating due to higher reservoir temperature, water yield, and wide distribution (Pang et al., 2018). The geothermal fluid in the bedrock thermal reservoir is mainly recharged by the lateral runoff from the

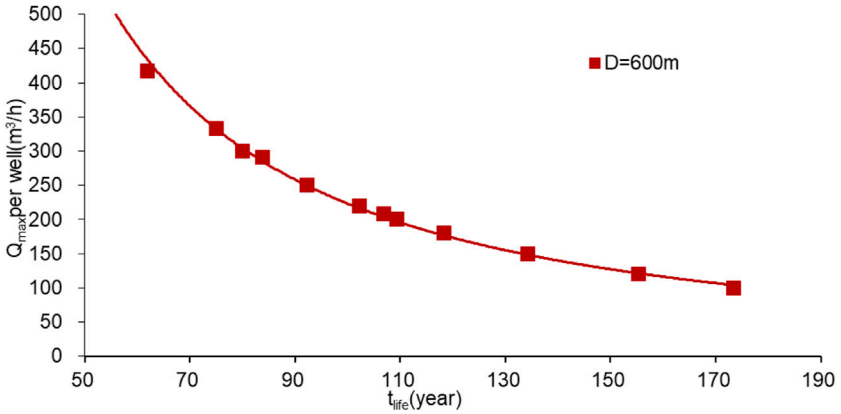

FIGURE 5 | Relationship between the time when thermal breakthrough occurred and the water yield per production well.

Taihang Mountain in the west and the Yanshan Mountain in the north. After deep circulation heating, the geothermal water is stored in the bedrock thermal reservoir. In geologic history, the degree of rock karst weathering is approximately uniform. A homogeneous isotropic aquifer in the Jixian system dolomite was assumed in this study to establish a method to calculate the recoverable resources for district heating (Kong et al., 2014). According to the work of our research group, there are six wells in Xiongxian for continuous temperature measurement in the borehole, including one mining well, one monitoring well, and four recharge wells. In this paper, since the monitoring well does not produce geothermal water, the temperature profile is less affected and more presentative (Pang, 2018). The location of the monitoring well and the measured temperature are in **Figure 4**. The temperature logging is respectively from September 2013, September 2015, and October 2016. The average temperature gradient is about 5.13°C/100 m for the Cenozoic cap and 0.16°C/100 m for bedrock, which is small. The temperature is about 75°C at the bottom of the hole.

RESULTS AND DISCUSSION

Assuming different water yields, the pressure and temperature changes should be different. A total of 12 scenarios have been simulated to have a grasp of the effect of pressure and temperature to obtain the recoverable geothermal resources. The water yields of 12 scenarios are 100, 120, 150, 180, 200, 208, 220, 250, 292, 300, 333, and 417 m^3/h respectively. In order to optimize the well spacing, the scenarios with several well spacing 300, 400, 500, 600, and 700 m are simulated respectively.

Maximum Water Yield

Assuming an arbitrary production water yield, the model simulates the temperature change of a production well with the production time. When the temperature of the production well begins to drop, this is referred to as thermal breakthrough time. Similarly, the thermal breakthrough time for each water yield can be acquired. By using the trial method and setting several water yields for the production well, the corresponding lifetime of the geothermal field can be obtained. Then, the correlation diagram between the water yield and the lifetime of the geothermal field can be established (**Figure 5**). The corresponding water yield can be acquired when the lifetime is 100 years. When the well spacing is 600 m, the fitting curvilinear equation of the correlation between the water yield and the lifetime of the geothermal field is

$$Q_{\max} = 132299 \times t_{\text{life}}\hat{}(-1.386), D = 600m \tag{13}$$

When the lifetime of the geothermal field is 100 years, the maximum water yield per well Q_{max} correspondingly is $Q_{\max} = 132299 \times 100\hat{}(-1.386) = 223.64\, m^3/h$.

When the water yield per well is 223.64 m^3/h, the model simulates the variation diagram of the temperature distribution from the recharge well to the production well with time, as shown in **Figure 6**. **Figure 7** shows that when the well spacing is 600 m and the water yield per well is 223.64 m^3/h, the temperature of the production well changes with the mining time. The temperature of the production well starts to decline when 100 years (**Figure 7**).

When Q_{max} is 223.64 m^3/h, the maximum pressure drop value is 92 m, which is bigger than the pressure drop threshold of 80 m. Then, the water yield of 223.64 m^3/h is the maximum water yield that doesn't meet the conditions of no drop in temperature and the critical values of pressure drawdown at the production well. The maximum pressure drawdowns under different water yields were simulated as **Figure 8** shows. According to the law of water yield and drawdown, the maximum water yield 198.29 m^3/h was calculated when the drawdown is 80 m.

Well Spacing Optimization

Well spacing has an impact on the recoverable resources. If the well spacing increases, the time for thermal breakthrough becomes longer, but the pressure drop of the production well increases, which may lead to exceeding the limit value. Also, the larger the well spacing is, the lower the number of wells in a geothermal field and the lower the drilling costs. The optimal well

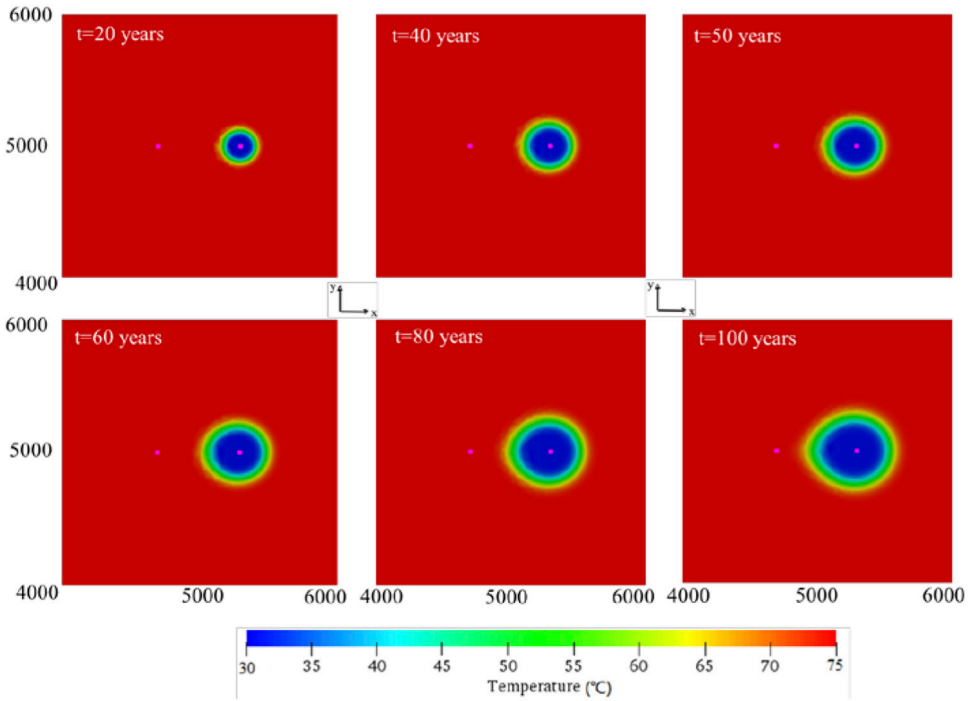

FIGURE 6 | When the well spacing is 600 m and the water yield per production well is 223.64 m^3/h, the temperature distribution displays in the geothermal field in the year 100.

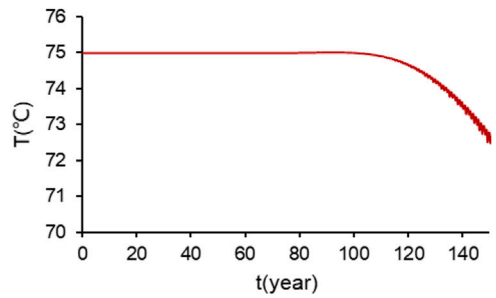

FIGURE 7 | When the well spacing is 600 m and the water yield per production well is 223.64 m^3/h, the temperature of the production well changes with the production time.

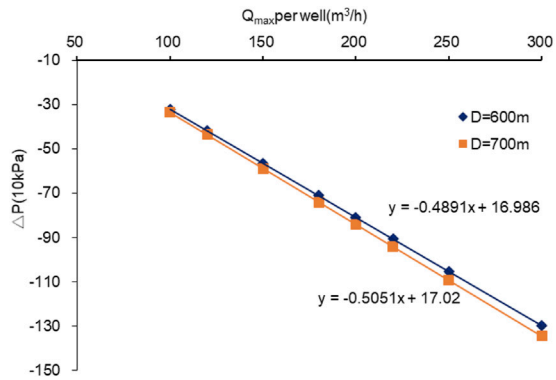

FIGURE 8 | The relationship of maximum drawdowns and different water yields when the well spacing is 600 m and 700 m.

spacing with the maximum water yield to meet the pressure drop limit can then be obtained.

In the numerical model, under different well spacing, multiple sets of thermal breakthrough times can be obtained by assuming multiple groups of water yields, as shown in **Figure 9**. The curvilinear fitting is based on the relationship between the water yield and the lifetime of the geothermal field for different well spacing. When the well spacing is 300 m, the fitting curvilinear equation is

$$Q_{\max} = 203674 \times t_{\text{life}}\hat{}(-2.041), D = 300m \quad (14)$$

Similarly,

$$Q_{\max} = 86400 \times t_{life}\hat{}(-1.553), D = 400m \quad (15)$$

$$Q_{\max} = 105027 \times t_{life}\hat{}(-1.448), D = 500m \quad (16)$$

$$Q_{\max} = 136430 \times t_{life}\hat{}(-1.31), D = 700m \quad (17)$$

When the well spacing is 300, 400, 500, and 700 m and the geothermal field lifetime is 100 years, the maximum water yield per well $Q_{\max}$ of 16.86, 67.69, 133.44, and 327.27 m^3/h, respectively, can be obtained by each individual fitting equation, and the maximum water yield per well $Q_{\max}$ is 198.29 m^3/h when the well spacing is 600 m (**Figure 8**). When the well spacing is 300, 400, and 500 m, the

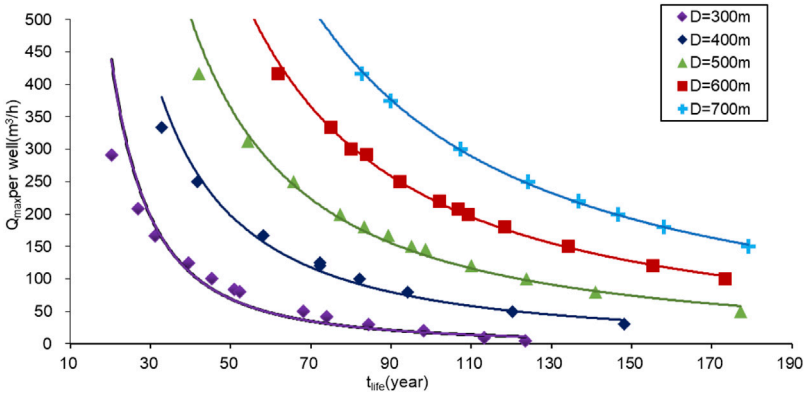

FIGURE 9 | Relationship between the time when thermal breakthrough occurred and the maximum water yield per well under different well spacing.

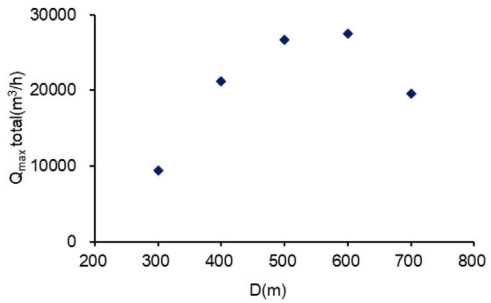

FIGURE 10 | When the lifetime of the geothermal field is 100 years, the relationship between the total maximum water yield and the well spacing.

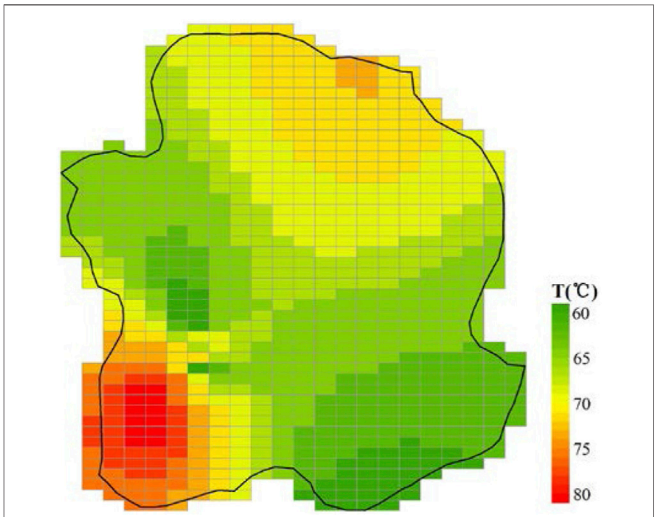

FIGURE 11 | The study area is divided into several rectangles and the reservoir temperature distribution in the Jixian reservoir is superimposed.

maximum water yield per well will not exceed the pressure limit. However, When the well spacing is 700 m, the maximum water yield exceeds the pressure limit. The maximum drawdowns under different water yields were simulated when the well spacing is 700 m as **Figure 9** shows. According to the law of water yield and drawdown, the maximum water yield of 192.08 m^3/h was calculated when the drawdown was 70 m. According to **Equations 8**, **9**, the number of well doublets and the total water yield of the wells $Q_{total} = nQ_{max}$ can be acquired. When the well spacing D is 300, 400, 500, 600, and 700 m and the number of well doublets n is 556, 313, 200, 139, and 102, the total water yield of the wells is 9,368.35, 21,152.60, 26,688.92, 27,540.95, and 19,600.08 m^3/h, respectively, on the premise of a lifetime of 100 years, as shown in **Figure 10**. Among these well spacing, the total water yield is the maximum, which is 27,540.95 m^3/h, when the well spacing is 600 m.

The pressure simulation results for each well spacing were obtained under the premise that the maximum water yield is consistent with the assumption that the temperature does not decrease during the production period of 100 years. The change in the pressure of the production well could be acquired by simulation. The maximum pressure drawdown occurred at the end of the 120-days heating season. With increasing well spacing, the pressure of the production well decreased greatly.

Owing to the drawdown value limit of 80 m, the pressure drawdown was within the acceptable limits of 80 m in the well doublet pattern. Also, at this point, the total water yield reaches the maximum. Thus, 600 m is the optimal spacing and conforms to the requirements of sustainable production with maximum water yield and therefore, maximum recoverable resource.

Geothermal Recoverable Resources

According to the drilling temperature data and the kriging interpolation algorithm in Xiongxian, the reservoir temperature distribution in the Jixian system of Xiongxian is obtained (Pang, 2018). Based on the aforementioned uniform well distribution with the optimal spacing of 600 m under the condition of sustainable assumption, Xiongxian can be divided into the well layout diagram as shown in **Figure 11**.

Maximum water yield can be extracted when the length of the rectangular boundary is twice that of the well spacing and the width is equal to the well spacing, as arranged in **Figure 11**. In each rectangular square, there is a pair of wells. According to this pattern, the number of well doublets n in the exploitation area can

TABLE 2 | Assessment of the recoverable geothermal resources in the Xiongxian geothermal field.

Items	Wang (2009)	Yang et al. (2015)	Yang et al. (2015) (Monte Carlo)	This article
Depth range (carbonate reservoir)	2000–3000 m	1618 m	Depend on temperature	500 m
T_{ref} (Reference temperature) (°C)	14.5	2.5	2.5	30
Total geothermal resource of Xiongxian (10^{16}kJ)	7.5	18.3	14.5	2.6
Converted standard coal (10^{8}t)	25.6	62.4	49.6	144
Recovery factor	15%	15%	15%	26.2%
Geothermal recoverable resource (10^{15}kJ)	11.3	27.5	21.8	6.85
Converted standard coal (10^{8}t)	3.8	9.4	7.4	2.33

be obtained as 803. Assuming that mining is carried out at the maximum water yield, the total maximum water yield is from **Equation 9** $Q_{\text{total}} = nQ_{\max} = 159230.75m^3/h$.

The recoverable geothermal resources can be calculated according to the following **Equation 10** $E_{\text{Recoverable}} = \sum_{i=1}^{i=803} Q_{\max}\rho_1 C_1 \text{t}_{\text{life}} (T - T_{\text{ref}})$. Therefore, in the Jixian system reservoir, the annual recoverable resources are 6.85×10^{16} J, and the recoverable resources in 100 years are 6.85×10^{18} J.

Based on the above-calculated results, the recovery factor can be computed according to **Equation 12**

$$Rg = \frac{E_{\text{recovery}}}{E} = \frac{\sum_{1}^{n} Q_{\max}\rho_l C_l t_{\text{life}} (T_R - T_{\text{ref}})}{\rho c V (T_R - T_{\text{ref}})} = \frac{Q_{\max}\rho_l C_l t_{\text{life}}}{2\rho c \text{H} D^2}$$

When the well spacing n is 600 m, the recovery factor is 26.2%.

In the Xiongxian geothermal field, the total geothermal resources have been estimated by the Volume method (Wang, 2009; Yang et al., 2015). In their work, the recoverable geothermal resource is calculated by multiplying the total amount of resources by 15% (DZ40-85, 1985). Their results are listed in **Table 2** to compare with our results.

It could be found that different total geothermal resources were obtained. This is attributed to the difference in the parameters including reservoir thickness and the reference temperature. Since the reference temperature used in this article is the temperature of the recharge water, and the reference temperature chosen by the others is the underground constant temperature zone or the average temperature of the atmosphere, the total amount of resources we calculated is low. However, here we insist on using the temperature of the recharge water as the reference temperature, because the heat we use for district heating is actually the heat released by the geothermal water circulation once, that is, the heat contained in the difference between the production temperature and the recharge temperature. Anyway, it can be known from the calculation formula $Rg = E_{\text{recovery}}/E = Q_{\max}\rho_l C_l t_{\text{life}}/2\rho c H D^2$ that Rg has no relationship with the reference temperature. Therefore, under the condition of uniform well distribution for sustainable exploitation, the recovery factor is 26.2%, which is much larger than the national standard of 15% (DZ40-85, 1985), which is generally an empirical parameter related to lithology. In contrast, our method presented here could be used for geothermal field exploitation in the future because it takes into account many parameters, such as thermal conductivity, permeability, viscosity, seasonal district heating, and others.

CONCLUSION

A numerical thermo-hydraulic coupled modeling in a geothermal reservoir is set up to investigate the geothermal recoverable resources during an operation time of 100 years with sustainability assumption. This work provides another way for sustainable exploitation and the calculation of recoverable resources.

The maximum water yield for per production well in well doublet pattern that keeps the heat extraction energy unchanged for an amortized time is 16.86, 67.69, 133.44, 198.29, and 192.08 m^3/h, respectively, when the well spacing is 300, 400, 500, 600, and 700 m. According to the relationships among the well spacing, the drawdown of production wells, and maximum water yield of total wells, it is found that 600 m is the optimal well spacing with maximum exploitation amount and conforming to sustainability. The optimal well spacing can guide the management of geothermal fields.

The amount of recoverable geothermal resources in the Jixian system reservoir was calculated under the optimal spacing layout. The recoverable resources in 100 years are 6.85×10^{18} J. The calculation result of the recovery factor is 26.2%, which is higher than the previous value of 15% when only depending on lithology.

DATA AVAILABILITY STATEMENT

The raw data supporting the conclusion of this article will be made available by the authors, without undue reservation.

AUTHOR CONTRIBUTIONS

YF and YH conceived and designed the numerical investigation; YF created the numerical model; YH examined the accuracy of the proposed model; YF and SZ designed the graphics and analyzed the result; YF wrote the manuscript; SZ, YF, and HL revised the manuscript; ZP proposed instructive suggestions to the manuscript.

ACKNOWLEDGMENTS

We thank Dr. Yanlong Kong for his valuable advice on the manuscript. Many thanks to Dr. Jumei Pang, Dr. Ji Luo, Dr. Chaofan Chen, Dr. Yingchun Wang, Dr. Yiman Li, and Dr. Tianming Huang for discussions and constructive comments on an earlier version of the manuscript. Appreciation goes to for their guidance.

REFERENCES

Allis, R., Bromley, C., and Currie, S. (2009). Update on Subsidence at the Wairakei-Tauhara Geothermal System, New Zealand. *Geothermics* 38, 169–180. doi:10.1016/j.geothermics.2008.12.006

Australian Geothermal Reporting Code Committee (AGRCC) (2010a). *Australian Code for Reporting of Exploration Results, Geothermal Resources and Geothermal Reserves: The Geothermal Reporting Code*. second edition. Adelaide: Australian Geothermal Energy Group AGEG and the Australian Geothermal Energy Association.

Australian Geothermal Reporting Code Committee (AGRCC) (2010b). *Geothermal Lexicon for Resources and Reserves Definition and Reporting*. second edition. Adelaide: Australian Geothermal Energy Group AGEG and the Australian Geothermal Energy Association.

Axelsson, G., Gudmundsson, A., Steingrimsson, B., Palmason, G., Armannsson, H., Tulinius, H., et al. (2001). Sustainable Production of Geothermal Energy: Suggested Definition. *IGA-News.* 43, 1–2.

Bödvarsson, G. S., and Tsang, C. F. (1982). Injection and thermal Breakthrough in Fractured Geothermal Reservoirs. *J. Geophys. Res.* 87, 1031–1048. doi:10.1029/jb087ib02p01031

Böttcher, N., Blöcher, G., Cacace, M., and Kolditz, O. (2012). "Heat Transport," in *Thermo-hydro-mechanical-chemical Processes in Porous media*. Editors O. Kolditz, and U. J. Görke (Berlin,Germany: Springer), 89–105. doi:10.1007/978-3-642-27177-9_4

Chen, C., Lin, M., and Cheng, J. (2011). *Groundwater Dynamics*. 5th ed. Beijing: Geological Publishing House.

Comerford, A., Fraser-Harris, A., Johnson, G., and McDermott, C. I. (2018). Controls on Geothermal Heat Recovery from a Hot Sedimentary Aquifer in Guardbridge, Scotland: Field Measurements, Modelling and Long Term Sustainability. *Geothermics* 76, 125–140. doi:10.1016/j.geothermics.2018.07.004

Dickson, M. H., and Fanelli, M. (2013). *Geothermal Energy: Utilization and Technology*. NewYork: Routledge Press.

Duan, Z., Pang, Z., and Wang, X. (2011). Sustainability Evaluation of limestone Geothermal Reservoirs with Extended Production Histories in Beijing and Tianjin, China. *Geothermics* 40, 125–135. doi:10.1016/j.geothermics.2011.02.001

DZ40-85 (1985). *Method for Geothermal Resource Assessment Ministry of Geology and mineral Resources of the People's Republic of China*. Beijing, China: GEOLOGICAL PUBLISHING HOUSE.

Ferguson, G., and Grasby, S. E. (2014). The Geothermal Potential of the Basal Clastics of Saskatchewan, Canada. *Hydrogeol. J.* 22, 143–150. doi:10.1007/s10040-013-1061-5

Franco, A., and Donatini, F. (2017). Methods for the Estimation of the Energy Stored in Geothermal Reservoirs. *Proc. J. Phys. Conf. Ser.* 796, 12025. doi:10.1088/1742-6596/796/1/012025

Garg, S. K., and Combs, J. (2015). A Reformulation of USGS Volumetric "Heat in Place" Resource Estimation Method. *Geothermics* 55, 150–158. doi:10.1016/j.geothermics.2015.02.004

Grant, M. A. (2015). Resource Assessment, a Review, with Reference to the Australian Code. *Resource* 19, 25.

Gringarten, A. C. (1978). Reservoir Lifetime and Heat Recovery Factor in Geothermal Aquifers Used for Urban Heating. *Pageoph* 117, 297–308. doi:10.1007/bf00879755

Gringarten, A. C., and Sauty, J. P. (1975). A Theoretical Study of Heat Extraction from Aquifers with Uniform Regional Flow. *J. Geophys. Res.* 80, 4956–4962. doi:10.1029/jb080i035p04956

Kolditz, O., Bauer, S., Bilke, L., Böttcher, N., Delfs, J. O., Fischer, T., et al. (2012). OpenGeoSys: an Open-Source Initiative for Numerical Simulation of Thermo-Hydro-Mechanical/chemical (THM/C) Processes in Porous media. *Environ. Earth Sciearth Sci.* 67, 589–599. doi:10.1007/s12665-012-1546-x

Kong, Y., Pang, Z., Shao, H., Hu, S., and Kolditz, O. (2014). Recent Studies on Hydrothermal Systems in China: a Review. *Geotherm. Energ.* 2, 19. doi:10.1186/s40517-014-0019-8

Kong, Y., Pang, Z., Shao, H., and Kolditz, O. (2017). Optimization of Well-Doublet Placement in Geothermal Reservoirs Using Numerical Simulation and Economic Analysis. *Environ. Earth Sci.* 76, 118. doi:10.1007/s12665-017-6404-4

Kong, Y., Pang, J., Pang, Z., Li, J., and Pan, S. (2020). Fault-Affected Fluid Circulation Revealed by Hydrochemistry and Isotopes in a Large-Scale Utilized Geothermal Reservoir. *Geofluids* 24, 1–13. doi:10.1155/2020/2604025

Lund, J. W., Freeston, D. H., and Boyd, T. L. (2011). Direct Utilization of Geothermal Energy 2010 Worldwide Review. *Geothermics* 40 (3), 159–180. doi:10.1016/j.geothermics.2011.07.004

Mongillo, M. A., and Axelsson, G. (2010). Preface to Geothermics Special Issue on Sustainable Geothermal Utilization. *Geothermics* 39, 279–282. doi:10.1016/j.geothermics.2010.09.011

Muffler, P., and Cataldi, R. (1978). Methods for Regional Assessment of Geothermal Resources. *Geothermics* 7, 53–89. doi:10.1016/0375-6505(78)90002-0

Nathenson, M. (1975). *Physical Factors Determining the Fraction of Stored Energy Recoverable from Hydrothermal Convection Systems and Conduction-Dominated areas[R]*. Menlo Park, Calif.(USA): Geological Survey.

O'Sullivan, M. J., and O'Sullivan, J. P. (2016). "Reservoir Modeling and Simulation for Geothermal Resource Characterization and Evaluation," in *Geothermal Power Generation*. Editor R. DiPippo (Amsterdam, Netherlands: Elsevier), 165–199. doi:10.1016/B978-0-08-100337-4.00007-3

Pang, J. (2018). "A Study on the Responsing Mechanism of Karstic Geothermal Reservoir to Large Scale Production and Reinjection in Niutuozhen Geothermal Field,". [PhD thesis] (Beijing, China: University of Chinese Academy of Sciences).

Pang, J., Pang, Z., Lv, M., Tian, J., and Kong, Y. (2018). Geochemical and Isotopic Characteristics of Fluids in the Niutuozhen Geothermal Field, North China. *Environ. Earth Sci.* 77, 1–21. doi:10.1007/s12665-017-7171-y

Pang, Z. H., Kong, Y. L., Pang, J. M., Hu, S., and Wang, J. (2017). Geothermal Resources and Development in Xiongxian New Area. *Bull. Chin. Acad. Sci.* 32, 1224–1230. doi:10.16418/j.issn.1000-3045.2017.11.007

Pang, Z., Hu, S., and Wang, J. (2012). A Roadmap to Geothermal Energy Development in China. *Keji Daobao/Sci. Technol. Rev.* 30, 18–24.

Rybach, L. (2003). Geothermal Energy: Sustainability and the Environment. *Geothermics* 32, 463–470. doi:10.1016/s0375-6505(03)00057-9

Rybach, L., Mégel, T., and Eugster, W. J. (1999). How Renewable Are Geothermal Resources? *Geotherm. Resour. Counc. Trans.* 23, 563–566.

Sanyal, S. K., Butler, S. J., Brown, P. J., Goyal, K., and Box, T. (2000). An Investigation of Productivity and Pressure Decline Trends in Geothermal Steam Reservoirs. *Trans. Resour. Counc.* 24, 325–330.

Sanyal, S. K., Klein, C. W., Lovekin, J. W., and Henneberger, R. C. (2004). *National Assessment of U.S. Geothermal Resources—A Perspective*. United States: Geothermal Resources Council Transactions.

Sanyal, S. "Sustainability and Renewability of Geothermal Power Capacity," in Proceedings of the World Geothermal Congress, Antalya, Turkey, April 2005.

Shortall, R., Davidsdottir, B., and Axelsson, G. (2015). Geothermal Energy for Sustainable Development: A Review of Sustainability Impacts and Assessment Frameworks. *Renew. Sustain. Energ. Rev.* 44 (C), 391–406. doi:10.1016/j.rser.2014.12.020

Stefansson, V. "The Renewability of Geothermal Energy," in Proceedings of the Proceedings of the World Geothermal Congress, Kyushu-Tohoku, Japan, May-June 2000, 883–888.

Ufondu, L. S. (2017). "Assessment of the Potential Heat Stored in the Deep Aquifers of the Willison basin for Geothermal Energy Production,". Doctoral dissertation (Canada: University of Saskatchewan).

Wang, S. "Geothermal Resource Assessment in Xiongxian," in Proceedings of Chinese Geophysical Society, China, July 2009, 1. Chinese geophysics.

White, D. E., and Williams, D. L. (1975). *Assessment of Geothermal Resources of the United States*. Geological Survey (Menlo Park, California (USA): US Department of the Interior).

Williams, C. F. "Development of Revised Techniques for Assessing Geothermal Resources," in Proceedings of the Proceedings, 29th Workshop on Geothermal Reservoir Engineering, Stanford University, Stanford, California, January 2004, 7.

Williams, C. F., Reed, M., and Mariner, R. H. (2008). *A Review of Methods Applied by the US Geological Survey in the Assessment if Identified Geothermal Resources*. University Park, Pennsylvania, United States: Citeseer.

Williams, C. F. "Thermal Energy Recovery from Enhanced Geothermal Systems-Evaluating the Potential from Deep, High-Temperature Resources," in Proceedings of 35th Workshop on geothermal reservoir engineering, Stanford University, U.S, February 2010.

Williams, C. F. "Updated Methods for Estimating Recovery Factors for Geothermal Resources," in Proceedings of Thirty-Second Workshop on Geothermal Reservoir Engineering, Stanford University, Stanford, California, January 2007.

Yang, F. T., Liu, S. L., Liu, J. X., Pang, Z., and Zhou, D. "Combined Monte Carlo Simulation and Geological Modeling for Geothermal Resource Assessment: a Case Study of the Xiongxian Geothermal Field, China," in Proceedings of the Proceedings of the World Geothermal Congress, Australia-Newzealand, April 2015.

Zhu, J., Hu, K., Lu, X., Huang, X., Liu, K., and Wu, X. (2015). A Review of Geothermal Energy Resources, Development, and Applications in China: Current Status and Prospects. *Energy* 93, 466–483. doi:10.1016/j.energy.2015.08.098

Conflicts of Interest: Author YF is employed by China Three Gorges Corporation. Author SZ is employed by CAUPD Beijing Planning & Design Consultants Co., Ltd. Author HL is employed by Sinopec Green Energy Geothermal Development Co.,Ltd.

The remaining authors declare that the research was conducted in the absence of any commercial or financial relationships that could be construed as a potential conflict of interest.

Publisher's Note: All claims expressed in this article are solely those of the authors and do not necessarily represent those of their affiliated organizations, or those of the publisher, the editors, and the reviewers. Any product that may be evaluated in this article, or claim that may be made by its manufacturer, is not guaranteed or endorsed by the publisher.

frontiers in Earth Science

ORIGINAL RESEARCH
published: 20 January 2022
doi: 10.3389/feart.2022.817411

Microtremor Survey Method: A New Approach for Geothermal Exploration

Tian Baoqing[1,2]*, *Ding Zhifeng*[1,2]*, *Yang Liming*[3], *Fan Yifan*[3] and *Zhang Bo*[3]

[1]Institute of Geophysics, China Earthquake Administration, Beijing, China, [2]Key Laboratory of Earthquake Source Physics, China Earthquake Administration, Beijing, China, [3]Institute of Science and Technology, China Three Gorges Corporation, Beijing, China

Geothermal resources are a type of sustainable and green energy, which can play an important role in emission peaks and carbon neutrality. Determining the best development target area is key to resource development and geophysical methods are commonly used for this purpose. Owing to serious human and industrial interference, the microtremor survey method is often adopted for geothermal exploration in urban areas. It is a passive source method, which is non-invasive and environmentally friendly. In this method, the Rayleigh wave dispersion curve is extracted using spatial autocorrelation based on the vertical component signal at the observation station. A genetic algorithm is used to invert the dispersion curve of one survey point to obtain strata parameters such as layer thickness, S-wave velocity, and density. It provides critical parameters for the cap layer and reservoirs for geothermal exploration. For a chain microtremor measurement, a two-dimensional (2D) apparent S-wave velocity section can be generated. The apparent S-wave velocity is calculated from the phase velocity using the following empirical method: the 2D apparent S-wave velocity section helps to identify the buried channel for heat flow and track the irregular shapes of the reservoirs or cap layers. It has been verified that the microtremor survey method is reliable and accurate compared with borehole materials. As a newly developed non-invasive geophysical method, it can be widely used in geothermal exploration.

Keywords: geothermal resources, exploration, microtremor survey method, strata parameters, buried channel

OPEN ACCESS

Edited by:
Haibing Shao,
Helmholtz Association of German Research Centres (HZ), Germany

Reviewed by:
José Borges,
University of Evora, Portugal
Maysam Abedi,
University of Tehran, Iran

***Correspondence:**
Tian Baoqing
tianbaoqing@cea-igp.ac.cn
Ding Zhifeng
dingzf@cea-igp.ac.cn

Specialty section:
This article was submitted to Economic Geology, a section of the journal Frontiers in Earth Science

Received: *18 November 2021*
Accepted: *03 January 2022*
Published: *20 January 2022*

Citation:
Baoqing T, Zhifeng D, Liming Y, Yifan F and Bo Z (2022) Microtremor Survey Method: A New Approach for Geothermal Exploration. Front. Earth Sci. 10:817411. doi: 10.3389/feart.2022.817411

INTRODUCTION

High-frequency climate and environmental disasters push mankind to pay more attention to protecting the environment. One of the best methods is energy conservation and emission reduction. Switching from traditional fossil fuels to renewable and green energy decreases the emission of carbon dioxide (CO_2). Renewable and green energy mainly include solar, wind, biomass, and geothermal energy.

Geothermal energy comes from the interior of the Earth, and is stable because it does not depend on the weather. It originates from the decay of radioactive elements contained in the Earth. As a result, the amount of geothermal energy is large, equal to 170 million times that of coal with a potential exploitable resource of 4,948 trillion tons of standard coal equivalent. China is located in the circum-Pacific geothermal belt and the Mediterranean–Himalayan geothermal belt, where geothermal energy is abundant. Geothermal types include shallow geothermal energy, medium-deep depth hydrothermal resources, and hot dry rock geothermal resources. It is used for various proposed, such as generating power, heating, and cooling based on the different types of geothermal resources. Identifying an excellent target for exploiting geothermal resources is the most important

factor, which typically relies on geophysical methods to ensure geothermal reservoirs and channels for heat flow (Kana et al., 2015).

Geophysical methods can be divided into invasive and non-invasive methods. Seismic methods, magnetic methods, and gravity methods are non-invasive methods. Based on the wave velocity difference of the strata, seismic methods can identify strata with different rock properties and determine the location and parameters of buried faults. Magnetic methods such as the magnetotelluric method (MT), audiomagnetotelluric method (AMT), and controlled source audio-frequency magnetotelluric method (CSAMT), can explore the distribution characteristics, properties, and geological fault occurrences and determine the thickness and depth of cap layers. Gravity methods help to depict the bedrock conditions, spreading of structures, and location of faults. For example, a 3D seismic survey was conducted in Saxony, Germany for geothermal exploration (Lüschen et al., 2015), which is an indispensable tool for geothermal exploration, even in crystalline basement rocks. To identify the geothermal potential, seismic reflection imaging can provide amplitude contrasts that may be related to volcanic rocks and possible hydrothermal alteration fronts (Sena-Lozoya et al., 2020). MT is an important method for the exploration of geothermal systems (Rosenkjaer et al., 2015). Uchida and Sasaki (2006) developed a stable inversion technique for the 3D interpretation of MT data and applied it to a large-volume MT dataset obtained in the Ogiri geothermal area, in southwestern Japan. CSAMT provides an efficient means of delineating the shallow resistivity pattern above a hydrothermal system (Sandberg and Hohmann, 1982). Di et al. (2006) successfully applied the CSAMT method to geothermal exploration in the Beijing area and accurately located geothermal reservoirs deeper than 2 km. Gravity methods can help to delineate the structural features that control the geothermal system, such as the research on the Eburru geothermal system in Kenya (Maithya et al., 2020). To understand the subsurface structure and its relation to the observed geothermal phenomenon, a land gravity survey was carried out in the Kinigi geothermal field, Northwest Rwanda (Uwiduhaye et al., 2018). In addition, joint inversion is typically adopted for geothermal exploration. Zaher et al. (2018) used airborne gravity and magnetic geophysical data to preliminarily explore the geothermal potential in the Siwa Oasis, Western Desert, Egypt. Joint inversion of gravity and surface wave data constrained by MT highlighted unconventional geothermal prospects in felsic basement (Ars et al., 2019).

Ambient noise tomography has also been adopted for geothermal exploration (Planès et al., 2020). The microtremor survey method (MSM) is a new, non-invasive geophysical method used for geothermal exploration, which also uses ambient noise as a signal. An observation array is typically adopted to collect field data. The frequency–wavenumber spectrum method F–K, (Capon, 1969), and spatial autocorrelation method SPAC, (Aki, 1957), are commonly adopted to extract the Rayleigh wave dispersion curve. Compared with F–K, SPAC has more accurate results (Ohori et al., 2002) with circular arrays. Bettig et al. (2001) presented a modified SPAC, which allows the use of irregular, almost

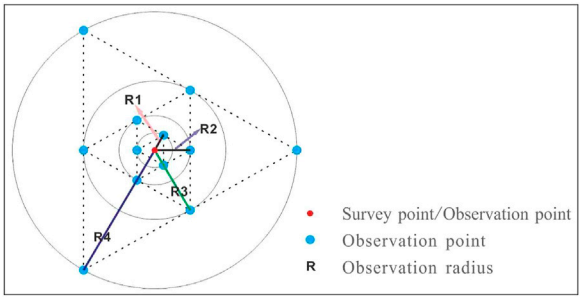

FIGURE 1 | Regular triangular array for collecting the microtremor signal.

carbitrarily shaped arrays. Okada and Ling (1994), Okada (2006) proposed an extended SPAC method with arbitrarily shaped arrays. Asten (2006) used the SPAC method to process the passive seismic data from finite circular array. Owing to the fundamental assumption of plane wave propagation of surface waves, attention must be paid to the near-source effect in array-based microtremor surveys (Roberts and Asten, 2008). Asten et al. (2019) developed a spatially averaged coherency (krSPAC), which allows spatial averaging of spectra from multiple pairs of sensors, irrespective of differences in spatial separation of the pairs. Cho and Iwata (2021) examined the limits and benefits of the SPAC microtremor array method. Microtremors have been applied to various aspects based on different processing methods. Roberts and Asten (2005) used microtremor array (SPAC) measurements to estimate the S-wave velocity profile of Quaternary silts. Chávez-García et al. (2007) adopted microtremors to achieve the S-wave velocity structure around the Teide Volcano. Stephenson and Odum (2010) applied the SPAC to characterise the S-wave velocity in the upper 300 m of Salt Lake Valley, Utah. It is also possible in SPAC observation to identify a 2D structure and interpret S-wave velocity profiles in a deep and narrow valley environment (Claprood et al., 2011). MSM has been used to determine soil characteristics (Ozer et al., 2017), estimate the near-surface S-wave velocity structure at a site exhibiting low to high impedance contrast (Setiawan et al., 2019), and identify the sediment (Raptakis and Makra, 2010; Tian et al., 2019; Tian et al., 2020a). Tian et al. (2016; 2017) applied the MSM method to identify the parameters of different strata and ensure the geothermal channel information. In addition, Tian et al. (2020b) combined MSM with geothermal assessment to improve precision. Using the regression method, the relationship between S-wave velocity, density, and thermal conductivity was identified (Tian et al., 2020c).

In this study, we investigated MSM, which can be widely applied to geothermal development and utilisation. First, we briefly introduce the observation array and the SPAC method. For different exploration targets, MSM is classified into two specific techniques: microtremor sounding and 2D microtremor profile methods. The inversion results of the dispersion curve provide layer parameters (depth, thickness, S-wave velocity, and density) for the geothermal system. To identify the geothermal channel, a 2D microtremor profiling method was adopted, which contained several survey points in a survey line. Our preliminary results appear to be useful for studying geothermal systems.

MICROTREMOR SURVEY METHOD (MSM)

MSM is a passive surface-wave geophysical method. Microtremor signals mainly contain surface waves and body waves. The low-frequency waves (<1 Hz) arise from changes in pressure, sea waves, and tides, while the high-frequency (>1 Hz) waves originate from human sources and living activities. Based on the SPAC requirements, the microtremor signal must be collected by an array. Commonly, a regular triangular array (**Figure 1**) is selected to record the microtremor signal. The Rayleigh wave dispersion curve is extracted from the vertical component signal using the SPAC method (Aki, 1957), which assumes that the signal is stationary and random. Meanwhile, the surface wave is mainly the fundamental mode (Okada, 2003; Okada, 2006).

Usually, the frequency spectrum of the microtremor signal for two observation points A (0,0) and B (r,θ) can be expressed as;

$$X(t,0,0) = \int_{-\infty}^{\infty}\int_{0}^{2\pi} \exp\{i\omega t\} d\varsigma(\omega,\phi) \tag{1}$$

$$X(t,r,\theta) = \int_{-\infty}^{\infty}\int_{0}^{2\pi} \exp\{i\omega t + irk(\omega)\cos(\theta-\phi)\} d\varsigma(\omega,\phi) \tag{2}$$

where ω is the angular frequency, θ is the azimuth angle, k is the wave number, and r is the distance (radius) between the two stations.

The SPAC function between two stations is defined as

$$\begin{aligned} S(r,\theta) &= \int_{-\infty}^{\infty}\left[\int_{0}^{2\pi} \exp\{irk\cos(\theta-\phi)\} h(\omega,\phi) d\phi\right] d\omega \\ &= \int_{-\infty}^{\infty} g(\omega,r,\theta) d\omega \end{aligned} \tag{3}$$

Here, the spatial covariance function is defined as

$$g(\omega,r,\theta) = \int_{0}^{2\pi} \exp[irk\cos(\theta-\phi)] h(\omega,\phi) d\phi \tag{4}$$

For the circular array, the azimuth average of the spatial covariance function for the SPAC function and the phase velocity can be obtained.

$$\begin{aligned} \bar{g}(\omega,r) &= \frac{1}{2\pi}\int_{0}^{2\pi} g(\omega,r,\theta) d\theta \\ &= \int_{0}^{2\pi}\left[\frac{1}{2\pi}\int_{0}^{2\pi} \exp[irk\cos(\theta-\phi)] d\phi\right] h(\omega,\phi) d\phi \\ &= J_0(rk)\int_{0}^{2\pi} h(\omega,\phi) d\phi = J_0(rk)\cdot h_0(\omega) \end{aligned} \tag{5}$$

Here, J_0 is the zero-order Bessel function and h is the average power.

Then, the SPAC coefficient $\rho(\omega,r)$ is defined in the angular frequency ω.

$$\rho(\omega,r) = \bar{g}(\omega,r)/h_0(\omega) = J_0(rk) \tag{6}$$

As a result, we can obtain

$$\rho(f,r) = J_0 2\pi f r/c(f) \tag{7}$$

Using **Eq. 7**, the phase velocity can be calculated in distance r and frequency f.

When the Rayleigh wave dispersion curve is extracted, it is used to invert the S-wave velocity structure using the Monte Carlo algorithm. In our research, a genetic algorithm was selected to invert the geological structure. During the inversion, a initial inversion model with layer's parameters is assumed to begin the inversion which is one horizontally stratified geological model. If the observation array is located at the fractured strata, the results of inversion has a relatively lower accuracy.

In some cases, it is not necessary to invert the S-wave velocity structure during the detection of geological structures. The relative change trend such as low velocity anomaly in the S-wave velocity section can reveal the location and depth of the structure accurately. The 2D microtremor profiling method is also based on the Rayleigh wave dispersion curve. It transforms the phase velocity (Vr-f) to the apparent S-wave velocity (Vx-H) using an empirical **Eq. 8** for each survey point (Tian et al., 2017; Tian et al., 2022). Then, the apparent S-wave velocity section is obtained by horizontal interpolation and smoothing between every survey point. The workflow of MSM is shown in **Figure 2**.

$$v_{x,i} = \left(\frac{t_i\cdot v_{r,i}^4 - t_{i-1}\cdot v_{r,i-1}^4}{t_i - t_{i-1}}\right)^{1/4} \tag{8}$$

Here, the Vx represents the apparent S-wave velocity of the *i*th layer, t represent the time, Vr represents the phase velocity of the *i*th layer.

DATA ACQUISITION, PROCESSING, AND DISCUSSION

According to the exploration target, different techniques were selected to determine geothermal geological parameters. This section introduces three objectives for geothermal exploration. Different observation parameters and inversion methods were presented specifically to satisfy each item.

Determining the Geothermal System Parameters

Geothermal cap layers and reservoirs are known for some geothermal fields. Therefore, it is critical to determine the corresponding parameters. Accurate parameters of all strata are important for the different stages of geothermal development. For example, during the feasibility step, the estimation of the geothermal deposit and exploitation amount depends on the reservoir thickness. In addition, the reservoir

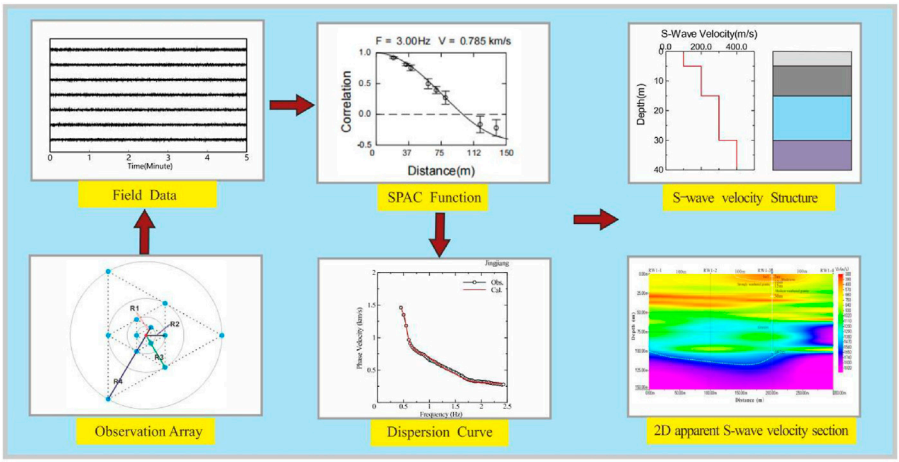

FIGURE 2 | Microtremor survey method (MSM) workflow.

depth is a vital parameter for drilling, which may decide whether the geothermal development is successful or not.

Data Acquisition

JingJiang, China is taken as an example where the geothermal reservoir is Triassic limestone. Based on the probing depth requirement, we deployed one survey point with four overlay circular observation arrays (**Figure 1**) to record the microtremor signals. The radii were 80–160–320–640 m. At every observation point, a three-component MTKV-3C seismometer and Datamark LS-8800 were used to record the microtremor signals. The main frequency of the observation seismometer was 1 Hz. At the same time, one cycle delay and amplifier circuit was adopted to achieve lower frequency signal. At each survey point, a 30 minute continuous signal was obtained.

Data Processing and Discussion

First, the original microtremor signal was processed by removing the data mean and trend, normalization and spectral whitening. Based on the original field data, the SPAC coefficients were calculated for every two stations. Then, they were fitted to the zero-order Bessel function for different frequencies and distances. After the dispersion curve was extracted, a genetic algorithm was adopted for inversion. The dispersion curve and inversion S-wave velocity structures are shown in **Figure 3**.

Simultaneously, one borehole was drilled at this microtremor survey point. A comparison between the inversion results and borehole materials is shown in **Table 1**. The MSM distinguished several subsurface layers based on the wave velocity differences. In the same geologic age, it also distinguished different layers if there was a wave velocity difference. The error was small when the wave velocity difference was large. For example, it accurately identified the interference between the Quaternary Neogene and the Zhouchongcun Formation of the Triassic. However, the probing error was slightly larger when identifying the interference between two layers with small wave velocity differences, such as the layer of cream mudstone, gypsum, and layer of gypsum, creating mudstone. In general, the MSM can provide accurate parameters for layers with different rocks.

Identifying the Buried Channel for Heat Flow

Convective geothermal resources are one resource type, which is frequently chosen for development and exploitation, which relies on channel formation for heat flow. Therefore, locating the buried channel and determining the channel parameters are the primary tasks for geothermal exploration. Faults (fracture zones) are channels for heat flow. To identify buried faults, one 2D section was the most intuitive and accurate method. In the horizontal direction of the section, the lateral position was determined. This section provided an accurate understanding of the width and depth of the channel. It also showed the fracturing degree of the fault by comparing the background values.

Data Acquisition

A research area in Zhejiang Province, China was selected to depict the ability of the MSM to identify the buried channel for heat flow. To obtain a 2D section, one microtremor survey line was deployed, including six survey points. The observation system is shown in **Figure 4**. For each observation array, the radii are 125–250–375–500 m using a 1 Hz main frequency for the observation seismometer. The time was automatically corrected using the GPS system among all seismometers. The microtremor signal was recorded for 30 min in each observation array.

Data Processing and Discussion

The field data were processed by removing the data mean and trend, normalization and spectral whitening. For every survey point, the dispersion curve was extracted using the SPAC method. All the dispersion curves are shown in **Figure 5A**. To achieve an apparent S-wave, the dispersion curve was transformed to the curve of the apparent S-wave velocity (Vx) and depth (H) using **Eq. 8**. Using the results of Vx-H, the 2D apparent S-wave velocity

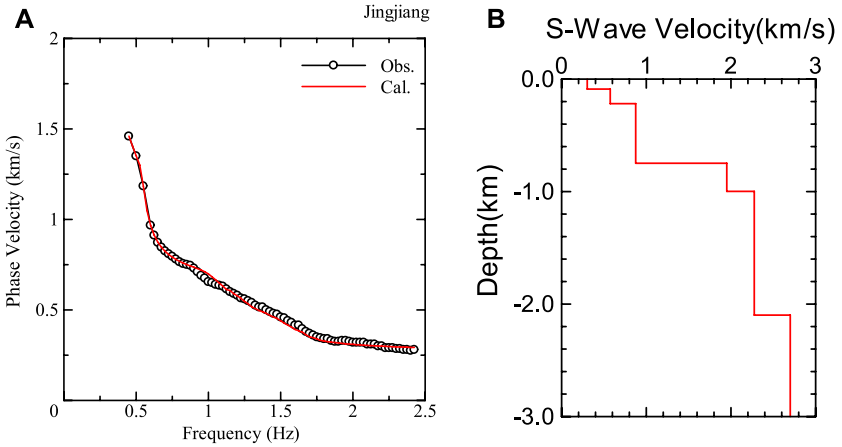

FIGURE 3 | Dispersion curve **(A)** and inversion S-wave velocity structure **(B)**.

TABLE 1 | Comparison between the inversion result and borehole materials.

Borehole			Inversion results of MSM					Error of Depth(m)
Strata	Lithology	Depth (m)	No	Vs (km/s)	Thickness (m)	Depth (m)	Density (g/cm^3)	
Quaternary -Neogene	Clay, fine sand, coarse sand, gravel	213	1	0.302	88	88	1.784	-
			2	0.574	130	218	1.909	5
Zhouchongcun Formation of Triassic	Linestone	750	3	0.874	530	748	2.029	2
	Cream mudstone and gypsum	1,026	4	1.950	250	998	2.335	28
	Gypsum and Creaming mudstone	2,101	5	2.275	1,100	2098	2.408	3

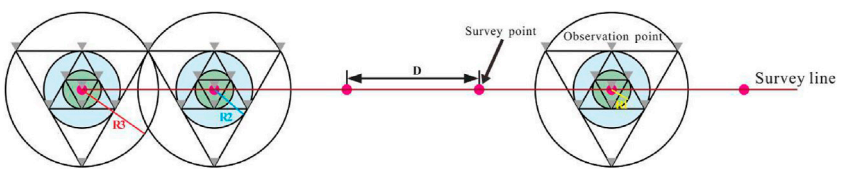

FIGURE 4 | Observation system for a microtremor survey line. In this figure, R represents the observation radii and D represents the distance between two survey points.

section (**Figure 5B**) was calculated using Kriging interpolation and smoothing among all the survey points.

At the survey point located in the fault, the dispersion curve showed a low phase velocity at a low frequency compared with other dispersion curves. The apparent S-wave velocity section clearly indicated a buried fault. The strata can be divided into several layers. The depth of the first layer was 0–100 m, with a Vx of 300–400 m/s. The Vx of the second layer varied from 600 to 900 m/s at depths of 100–350 m. The lithology barely changed in this layer, and fracture zones developed in the third layer. An obvious low-velocity anomaly was observed from 800 to 1,500 m at distance of 600–650 m. The Vx values of the low-velocity anomaly and normal layer were approximately 1,600 m/s and 3,000 m/s, respectively. This anomaly is named Fault F1, and its width is approximately 50 m. Compared with the fracture zone, the surrounding rock is intact with high wave velocity. Geothermal resources are strongly related to this fault, which breaks and cuts off the fresh bedrock, resulting in fracture zones. This provides an excellent channel for heat flow.

The 2D microtremor profiling method has relatively high precision for probing geological structures. In the section of apparent S-wave velocity, the strata that are stably deposited (uniform colour) could be continuously traced laterally. Areas with obvious lithology changes, such as fault fracture zones, showed low-velocity anomalies because of the underestimation of phase velocity using SPAC. The obvious low-velocity anomaly

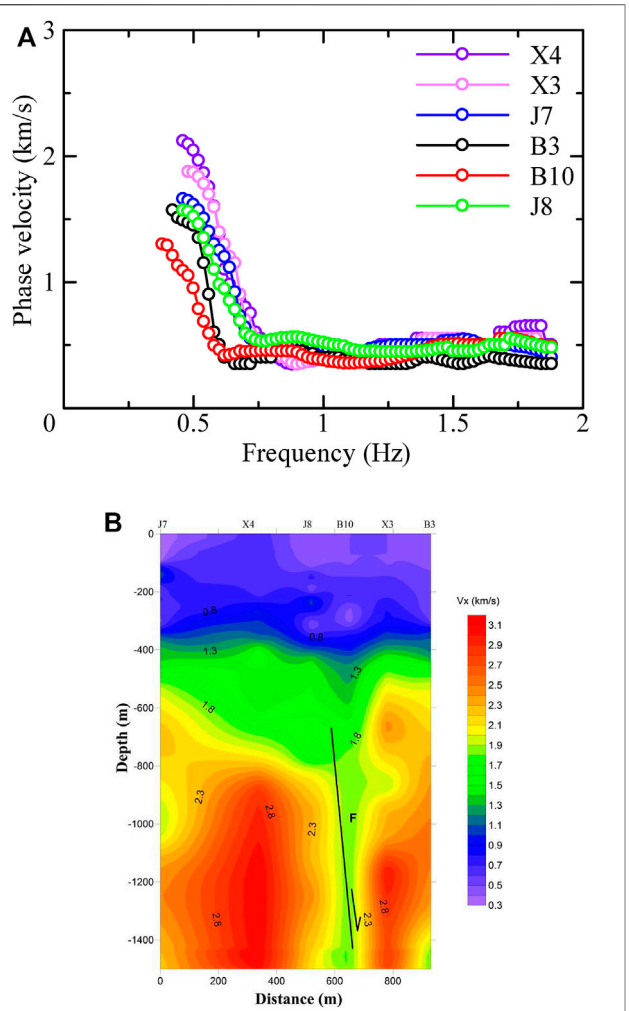

FIGURE 5 | Dispersion curve of all the survey points **(A)** and 2D apparent S-wave velocity section to identify the buried channel for heat flow **(B)**.

can be used to interpret and identify buried faults (fracture zones) and other geological structures in the apparent S-wave velocity profile.

According to the comparison study and analysis of the detection results of the 2D microtremor profiling method and drilling results, it can be seen that the buried fracture zone displayed an obvious low-velocity anomaly in the 2D apparent S-wave velocity profile, which is an important indicator explaining the buried geothermal structure. Using the 2D micromotion profiling method to detect the thermal control structure and exploit the convection-type geothermal resources, the detection accuracy was high, and the measured effect was good. There were obvious lithologic differences on both sides of the normal fault plane, and the detection effect was good.

Tracking Irregular Strata Shapes

Estimating the amount of geothermal energy and exploiting geothermal resources requires a comprehensive understanding of the upward and downward trends of strata. The diagenetic environment of different geological periods and the function of tectonic movement in the test area resulted in complex geological structures. As a result, the strata were not homogeneous. Geophysical sections imaged the subsurface to generate a prospective stratigraphic structure. For conductive geothermal resources, information on reservoirs helps to calculate the total reserves of geothermal resources and locate the best drilling position.

Data Acquisition

Here, one research area in Shandong Province, China, is taken as an example to track the shape of different layers using a 2D apparent S-wave velocity section. This research area mainly exploits shallow geothermal resources above 150 m. The microtremor survey line included four survey points. The observation radii were 5–10–20–40 m. The main frequency of the observation seismometer was 2 Hz. The microtremor signal was recorded for 50 min in each observation array.

Data Processing and Discussion

The processing workflow for extracting the Rayleigh wave dispersion curve was the same as that for the above two sections. All the dispersion curves of the survey points are shown in **Figure 6A**. In addition, the dispersion curve of every survey point was transformed into Vx-H. The section was plotted

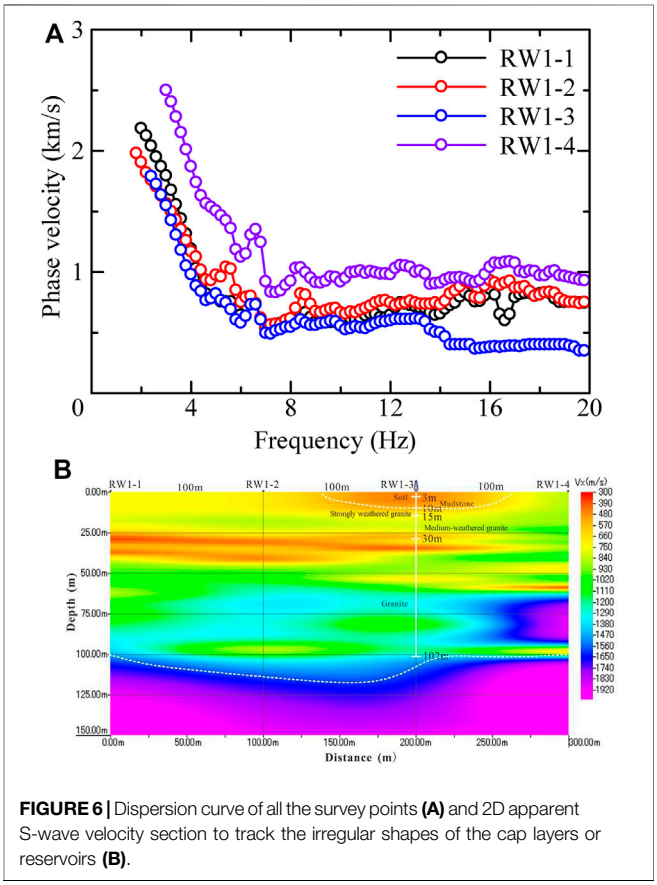

FIGURE 6 | Dispersion curve of all the survey points **(A)** and 2D apparent S-wave velocity section to track the irregular shapes of the cap layers or reservoirs **(B)**.

using lateral Kriging interpolation and smoothing of the survey points.

Figure 6A shows that the phase velocity of survey points RW1-4 is larger than that of the others. The dispersion curves of RW1-1 to RW1-3 exhibit the same spreading trend. The apparent S-wave velocity section shows that the strata are complex and variable (**Figure 6B**). Soil and mudstone develop from 0 to 10 m near survey point RW1-3. It only develops around survey point RW1-3 and stretches approximately 100 m horizontally. The Vx of the soil and mudstone was approximately 350–390 m/s. In the depth range of 25–40 m, a low-velocity layer was developed, which disappeared at a horizontal distance of 270 m with a Vx of 300–350 m/s. In this research area, weathered granite was developed to different degrees. The strongly weathered granite had a Vx of approximately 600 m/s leading to wide dispersion. Below this layer, medium-weathered granite also developed widely. Its thickness is approximately 40–50 m and the Vx is approximately 900–1,000 m/s. The Vx of the fresh granite was approximately 1,100–1,200 m/s. Below a depth of 125 m, the bedrock is intact, and the Vx was greater than 1,400 m/s.

At survey point RW1-3, drilling to a depth of 102 m was emplowed to verify the effectiveness of the MSM. The rock core of this borehole included soil, mudstone, strongly weathered granite, medium-weathered granite, and granite. Based on the correlation with these drilling materials, the 2D microtremor profile method could distinguish weathered granite with different degrees. In addition, it accurately determined the bedrock. Using the 2D apparent S-wave velocity section, we could track the developing trends of different rock layers, including geothermal reservoirs and cap layers. Meanwhile, it provided geological information on the bedrock, which plays an important role in the development of shallow geothermal resources.

CONCLUSION

Geothermal resources have received much attention because of the requirement for energy conservation and emissions reduction. As one kind of green energy that comes from the Earth's interior, it is stable and sustainable. Geothermal amounts above 3 km of, subsurface and generating power, can be widely used for geothermal resources, such as warming, cooling, and generating power. Geophysical methods are usually adopted to provide essential information to search for an excellent developing target area.

The MSM is a new approach that has been successfully applied to geothermal exploration. It adopts ambient noise as a signal to avoid the inconvenience of an artificial signal source. In addition, the observation array for recording the field data is independent. Compared with traditional geophysical methods, the MSM is flexible and economical. In particular, it can be deployed under the interference of human and industrial activities. Because most of the development and utilisation of geothermal resources is located in cities or towns, this method is regarded as one of the most effective.

According to different exploration purposes, MSMs can be classified into two types: microtremor sounding methods and 2D microtremor profiling methods. The microtremor sounding method uses a genetic algorithm for inversion. It provides the parameters of the different rock layers and the S-wave velocity, layer thickness, and density are obtained from the inversion. In some research areas, cap layers and reservoirs are known. For geothermal exploration, it is necessary to provide the depth, thickness S-wave velocity, and density. The microtremor sounding method can accurately identify the related parameters of the different layers. The 2D microtremor profiling method must deploy several survey points to achieve an apparent S-wave velocity section. It can be used to identify the location and depict the developed characteristics of the buried channel. In addition, it can track the irregular shapes of cap layers or reservoirs. Based on the comparison between the results of the MSM and borehole, it is verified that this method is accurate and reliable for geothermal exploration. The development of clean and green energy is a new approach for geothermal exploration.

DATA AVAILABILITY STATEMENT

The raw data supporting the conclusion of this article will be made available by the authors, without undue reservation.

AUTHOR CONTRIBUTIONS

TB: Methodology, writing—review and editing. DZ: Supervision. YL: Writing—review and editing, investigation FY and ZB: Investigation.

FUNDING

This work was supported by the National Natural Science Foundation of China (under grant 41941016-01) and Institute of Geophysics, China Earthquake Administration (under grant DQJB21K47).

ACKNOWLEDGMENTS

The authors would like to express deep gratitude to the editors and reviewers for their valuable comments and suggestions that greatly improved this paper.

REFERENCES

Aki, K. (1957). Space and Time Spectra of Stationary Stochastic Waves with Special Reference to Microtremors. *Bull. Earthquake Res. Inst. Tokyo Univ.* 35, 415–456.

Ars, J.-M., Tarits, P., Hautot, S., Bellanger, M., Coutant, O., and Maia, M. (2019). Joint Inversion of Gravity and Surface Wave Data Constrained by Magnetotelluric: Application to Deep Geothermal Exploration of Crustal Fault Zone in Felsic Basement. *Geothermics* 80 (7), 56–68. doi:10.1016/j.geothermics.2019.02.006

Asten, M. W. (2006). On Bias and Noise in Passive Seismic Data from Finite Circular Array Data Processed Using SPAC Methods. *Geophysics* 71, V153–V162. doi:10.1190/1.2345054

Asten, M. W., Stephenson, W. J., and Hartzell, S. (2019). Spatially Averaged Coherencies (krSPAC) and Rayleigh Effective-Mode Modeling of Microtremor Data from Asymmetric Arrays. *Geophysics* 84, EN47–EN56. doi:10.1190/geo2018-0524.1

Bettig, B., Bard, P. Y., Scherbaum, F., and Riepl, J. (2001). Analysis of Dense Array Noise Measurements Using the Modified Spatial Auto-Correlation Method (SPAC): Application to the Grenoble Area. *Bollettino di Geofisica Teorica Ed. Applicata* 42, 281–304.

Capon, J. (1969). High-resolution Frequency-Wavenumber Spectrum Analysis. *Proc. IEEE* 57 (8), 1408–1418. doi:10.1109/proc.1969.7278

Chávez-García, F. J., Luzón, F., Raptakis, D., and Fernández, J. (2007). Shear-wave Velocity Structure Around Teide Volcano: Results Using Microtremors with the SPAC Method and Implications for Interpretation of Geodetic Results. *Pure Appl. Geophys.* 164, 697–720. doi:10.1007/s00024-007-0184-9

Cho, I., and Iwata, T. (2021). Limits and Benefits of the Spatial Autocorrelation Microtremor Array Method Due to the Incoherent Noise, with Special Reference to the Analysis of Long Wavelength Ranges. *J. Geophys. Res. Solid Earth* 126 (2), e2020JB019850. doi:10.1029/2020JB019850

Claprood, M., Asten, M. W., and Kristek, J. (2011). Using the SPAC Microtremor Method to Identify 2D Effects and Evaluate 1D Shear-Wave Velocity Profile in Valleys. *Bull. Seismological Soc. America* 101 (2), 826–847. doi:10.1785/0120090232

Di, Q., Shi, K., Li, Y., Wang, R., Fu, C., and An, Z. (2006). Successful Applications of CSAMT for Deep Geothermal Exploration in Urban Areas. *SEG Tech. Program Expanded Abstr.*, 820–824. doi:10.1190/1.2370383

Domra Kana, J., Djongyang, N., Danwe Raïdandi, D., Njandjock Nouck, P., and Abdouramani Dadjé, fnm. (2015). A Review of Geophysical Methods for Geothermal Exploration. *Renew. Sustain. Energ. Rev.* 44, 87–95. doi:10.1016/j.rser.2014.12.026

Lüschen, E., Görne, S., von Hartmann, H., Thomas, R., and Schulz, R. (2015). 3D Seismic Survey for Geothermal Exploration in Crystalline Rocks in Saxony, Germany. *Geophys. Prospecting* 63 (4), 975–989. doi:10.1111/1365-2478.12249

Maithya, J., Fujimitsu, Y., and Nishijima, J. (2020). Analysis of Gravity Data to Delineate Structural Features Controlling the Eburru Geothermal System in Kenya. *Geothermics* 85 (5), 101795. doi:10.1016/j.geothermics.2019.101795

Ohori, M., Nobata, A., and Wakamatsu, K. (2002). A Comparison of ESAC and FK Methods of Estimating Phase Velocity Using Arbitrarily Shaped Microtremor Arrays. *Bull. Seismological Soc. America* 92 (6), 2323–2332. doi:10.1785/0119980109

Okada, H., and Ling, S. Q. (1994). *About a Recent Study on the Surveying Geologic Structures by Using the Microtremor Survey Method*. Sapporo, Hokkaido: Report of Hokkaido University. (in Japanese).

Okada, H., and Suto, K. (2003). *The Microtremor Survey Method. Geophysical Monograph Series No.12*. Tulsa: Society of Exploration Geophysicists. doi:10.1190/1.9781560801740

Okada, H. (2006). Theory of Efficient Array Observations of Microtremors with Special Reference to the SPAC Method. *Exploration Geophys.* 37, 73–85. doi:10.1071/EG06073

Ozer, C., Ozyalin, S., Ozel, O., and Polat, O. (2017). Determination of Soil Characteristic Using SPAC Method in Karsiyaka-Izmir, Turkey. *Iosr Jagg* 05 (2), 53–59. doi:10.9790/0990-0502015359

Planès, T., Obermann, A., Antunes, V., and Lupi, M. (2020). Ambient-noise Tomography of the Greater Geneva Basin in a Geothermal Exploration Context. *Geophys. J. Int.* 220 (1), 370–383. doi:10.1093/gji/ggz457

Raptakis, D., and Makra, K. (2010). Shear Wave Velocity Structure in Western Thessaloniki (Greece) Using Mainly Alternative SPAC Method. *Soil Dyn. Earthquake Eng.* 30, 202–214. doi:10.1016/j.soildyn.2009.10.006

Roberts, J., and Asten, M. (2008). A Study of Near Source Effects in Array-Based (SPAC) Microtremor Surveys. *Geophys. J. Int.* 174 (1), 159–177. doi:10.1111/j.1365-246X.2008.03729.x

Roberts, J., and Asten, M. (2005). Estimating the Shear Velocity Profile of Quaternary Silts Using Microtremor Array (SPAC) Measurements. *Exploration Geophys.* 36 (1), 34–40. doi:10.1071/EG05034

Rosenkjaer, G. K., Gasperikova, E., Newman, G. A., Arnason, K., and Lindsey, N. J. (2015). Comparison of 3D MT Inversions for Geothermal Exploration: Case Studies for Krafla and Hengill Geothermal Systems in Iceland. *Geothermics* 57 (9), 258–274. doi:10.1016/j.geothermics.2015.06.001

Sandberg, S. K., and Hohmann, G. W. (1982). Controlled-source Audiomagnetotellurics in Geothermal Exploration. *Geophysics* 47 (1), 100–116. doi:10.1190/1.1441272

Sena-Lozoya, E. B., González-Escobar, M., Gómez-Arias, E., González-Fernández, A., and Gómez-Ávila, M. (2020). Seismic Exploration Survey Northeast of the Tres Virgenes Geothermal Field, Baja California Sur, Mexico: A New Geothermal prospect. *Geothermics* 84 (3), 101743. doi:10.1016/j.geothermics.2019.101743

Setiawan, B., Jaksa, M., Griffith, M., and Love, D. (2019). Estimating Near Surface Shear Wave Velocity Using the SPAC Method at a Site Exhibiting Low to High Impedance Contrast. *Soil Dyn. Earthquake Eng.* 122, 16–38. doi:10.1016/j.soildyn.2019.03.036

Stephenson, W. J., and Odum, J. K. (2010). 28. Application of the Spatial-Autocorrelation Microtremor-Array Method for Characterizing S-Wave Velocity in the Upper 300 M of Salt Lake Valley, Utah. *Geophys. Dev. Ser.*, 447–460. doi:10.1190/1.9781560802259.ch28

Tian, B., Du, Y., Jiang, H., Zhang, R., and Zhang, J. (2020a). Estimating the Shear Wave Velocity Structure above the Fresh Bedrock Based on Small Scale Microtremor Observation Array. *Bull. Eng. Geol. Environ.* 79, 2997–3006. doi:10.1007/s10064-020-01761-7

Tian, B., Du, Y., You, Z., and Zhang, R. (2019). Measuring the Sediment Thickness in Urban Areas Using Revised H/V Spectral Ratio Method. *Eng. Geology.* 260, 105223. doi:10.1016/j.enggeo.2019.105223

Tian, B., Kong, Y., Gong, Y., Ye, C., Pang, Z., Wang, J., et al. (2020c). Thermal Conductivity Characterisation of Shallow Ground via Correlations with Geophysical Parameters. *Eng. Geology.* 272, 105633. doi:10.1016/j.enggeo.2020.105633

Tian, B., Kong, Y., Gong, Y., Ye, C., Pang, Z., Wang, J., et al. (2020b). An Improved Volumetric Method of Geothermal Resources Assessment for Shallow Ground Combining Geophysical Data. *Renew. Energ.* 145, 2306–2315. doi:10.1016/j.renene.2019.08.005

Tian, B., Xu, P., Ling, S., Du, J., Xu, X., and Pang, Z. (2017). Application Effectiveness of the Microtremor Survey Method in the Exploration of Geothermal Resources. *J. Geophys. Eng.* 14, 1283–1289. doi:10.1088/1742-2140/aa7f4e

Tian, B., Xu, P., Ling, S., Xu, X., Du, J., and Pang, Z. (2016). Application of the Initial Model Feature of Microtremor to Investigate a Part of the Geothermal Field of Jiangsu Region in China. *Environ. Earth Sci.* 75, 1298. doi:10.1007/s12665-016-5940-7

Tian, B., You, Z., Wang, G., and Zhang, J. (2022). Building a Geothermal Formation Model Using Microtremor Array Measurement. *Geophysics* 87 (1), B23–B30. doi:10.1190/geo2021-0014.1

Uchida, T., and Sasaki, Y. (2006). Stable 3D Inversion of MT Data and its Application to Geothermal Exploration. *Exploration Geophys.* 37 (3), 223–230. doi:10.1071/EG06223

Uwiduhaye, J. d. A., Mizunaga, H., and Saibi, H. (2018). Geophysical Investigation Using Gravity Data in Kinigi Geothermal Field, Northwest Rwanda. *J. Afr. Earth Sci.* 139 (3), 184–192. doi:10.1016/j.jafrearsci.2017.12.016

Zaher, A. M., Saibi, H., Mansour, K., Khalil, A., and Soliman, M. (2018). Geothermal Exploration Using Airborne Gravity and Magnetic Data at Siwa Oasis, Western Desert, Egypt. *Renew. Sustain. Energ. Rev.* 82 (2), 3824–3832. doi:10.1016/j.rser.2017.10.088

Conflict of Interest: YL, FY, and ZB were employed by the China Three Gorges Corporation.

The remaining authors declare that the research was conducted in the absence of any commercial or financial relationships that could be construed as a potential conflict of interest.

Publisher's Note: All claims expressed in this article are solely those of the authors and do not necessarily represent those of their affiliated organizations, or those of the publisher, the editors and the reviewers. Any product that may be evaluated in this article, or claim that may be made by its manufacturer, is not guaranteed or endorsed by the publisher.

frontiers in Earth Science

ORIGINAL RESEARCH
published: 02 February 2022
doi: 10.3389/feart.2021.787222

Study on Chemical Genesis of Deep Geothermal Fluid in Gaoyang Geothermal Field

Yifei Xing[1,2,3], Haowen Yu[4], Zhao Liu[4], Jie Li[5]*, Shaoyun Liu[4], Sihang Han[4] and Guiling Wang[1,2,3]**

[1]Chinese Academy of Geological Sciences, Beijing, China, [2]MNR Laboratory of Deep Geosciences and Exploration Technology, Ministry of Natural Resources of the People's Republic of China, Beijing, China, [3]Geothermal and Hot Dry Rock Exploration and Development Technology Innovation Center, Ministry of Natural Resources of the People's Republic of China, Beijing, China, [4]School of Water Resources and Environment, Hebei GEO University, Shijiazhuang, China, [5]Engineering Research Center of Groundwater Pollution Control and Remediation, Ministry of Education, College of Water Sciences, Beijing Normal University, Beijing, China

Geothermal resources are clean energy with a great potential for development and utilization. Gaoyang geothermal field, located in the middle of the raised area in Hebei province, China, is one of the three major geothermal fields in the Xiong'an New Area. With the development of the Xiong'an New Area, this geothermal field has become a research hotspot. According to the latest survey, the bottom-hole temperature of the D34 and D35 areas in the north of Gaoyang geothermal field is 149°C and 116°C, respectively, which indicates favorable target areas for geothermal exploitation The circulation mechanism and chemical origins of geothermal fluid are unclear in the Gaoyang geothermal field, which hinders the evaluation of geothermal resources in this region. Therefore, water chemistry and isotopic studies were performed on the Gaoyang geothermal fluid to understand the genesis of the Gaoyang geothermal field. Piper trigram and Na-K-Mg software were also used to explore the genesis of the underground hot water. Combined with stratigraphy and geothermal geology, it can be concluded that the primary hydrochemical type of the Gaoyang geothermal field is Na-HCO_3·Cl. In the process of upward migration of geothermal water, leaching and cation alternating adsorption took place, and finally, high TDS geothermal water was formed. Our results are helpful for geothermal resource evaluation and utilization and provide scientific guidance for the sustainable development of geothermal resources.

Keywords: genesis mechanism, deep geothermal fluid, gaoyang, water chemical characteristics, thermal reservoir temperature

OPEN ACCESS

Edited by:
Yinhui Zuo,
Chengdu University of Technology, China

Reviewed by:
Wei Xu,
Xi'an Jiaotong University, China
Ying Li,
China Earthquake Administration, China

***Correspondence:**
Haowen Yu
yuhaowen0688@163.com
Jie Li
lijie@bnu.edu.cn
Guiling Wang
guilingw@163.com

Specialty section:
This article was submitted to Economic Geology, a section of the journal Frontiers in Earth Science

Received: *30 September 2021*
Accepted: *08 December 2021*
Published: *02 February 2022*

Citation:
Xing Y, Yu H, Liu Z, Li J, Liu S, Han S and Wang G (2022) Study on Chemical Genesis of Deep Geothermal Fluid in Gaoyang Geothermal Field. Front. Earth Sci. 9:787222. doi: 10.3389/feart.2021.787222

INTRODUCTION

Geothermal resources are clean and efficient green energy. Studying and exploring the development and utilization of geothermal resources, which is conducive to the establishment and improvement of the energy structure of this region, can promote the development of the region's economic level. The construction of Xiong'an New Area, a millennium plan and a national event, is a significant decision made by the CPC Central Committee for the current development of the nation according to the development needs of the new era. Since North China has been plagued by fog and haze pollution for a long time, the effective utilization of geothermal resources in clean heating is one of the effective means to control fog, and haze (Pang et al., 2017; Liu et al., 2020; Wang et al., 2021a). Therefore, the investigation of geothermal resources in Xiong'an New Area and the further development and utilization are decisive measures to

solve the heating problem in winter, improve the energy structure, reduce the air pollution level, and build an environment-friendly city with green integration which can coexist harmoniously.

It is important to perfect geothermal resource exploration and evaluation in the Xiong'an New Area to investigate and study the typical geothermal resources in the Gaoyang geothermal field. In recent years, several experts and scholars have conducted extensive geothermal resources research around Xiong'an New Area. Pang et al. evaluated the geothermal resources in Xiong'an New Area, and recommended a focus on the exploration of ultra-deep carbonate thermal reservoirs (Pang et al., 2017); Wang et al. studied the characteristics and genetic mechanism of the present geothermal field in Xiong'an New Area, it was considered that the higher geothermal field characteristics was caused by the combination of stratigraphic assemblage, convection of geothermal water, and the development of faults (Wang et al., 2019); Hu et al. made a dynamic prediction of geothermal recoverable resources in the Rongcheng uplift area of Xiong'an New Area (Hu et al., 2020); Ma et al. studied the spatial structure of geothermal field in the Rongcheng area, Xiong'an New Area, constructed a 3D geological model and estimated geothermal resources (Ma et al., 2020); Wang et al. discussed and summarized the thermal reservoir characteristics and high-yield geothermal well parameters of Wumishan Formation in Gaoyang Low Uplift Area, Xiong'an New Area, and considered that the deep geothermal reservoir of Gaoyang geothermal field had good resource endowment (Wang et al., 2020); Wang et al. discussed the heat accumulation mechanism of the deep buried hill in the northeast of Gaoyang geothermal field in Xiong'an New Area, verified that the deep carbonate geothermal water in Gaoyang Geothermal Field had high temperature, large flow, and huge development potential (Wang et al., 2021b).

At present, researchers have achieved rich results around the Niutuo and Rongcheng geothermal fields. However, there are few studies on Gaoyang geothermal field, and some of those studies are limited to small areas. There is no overall understanding of the geothermal resources of this geothermal field. In particular, there is no scientific explanation for the geothermal fluid circulation mechanism and chemical genesis. It is difficult to fully guide the development of the Gaoyang geothermal field. This study aims to use hydrogeochemistry to conduct in-depth analysis and discussion on the chemical origin of Geothermal fluid in the Gaoyang geothermal field, make a preliminary evaluation of the overall situation of this geothermal field. The results will yield theoretical support for the efficient use and development of deep geothermal resources in the Xiong'an New Area, and also provide a scientific basis for relevant urban construction policies.

STUDY AREA

General Situation of Physical Geography

Gaoyang geothermal field is located in the south of Anxin County, Gaoyang County, Lixian County, Anguo City, Shenzhen City, and the west of Anping County, covering an area of about 3,000 square kilometers. The study area is located in the middle of Jizhong Plain and the triangle of Beijing, Tianjin, and Baoding and belongs to the transitional zone from Taihang piedmont plain to the alluvial plain. The terrain has a gentle slope from northwest to southeast, which is relatively flat at an altitude of 7.9–19.5 m. The water system is well developed, with Juma River in the south, Daqing River and Baiyangdian Lake in the north, east, and south, and Pinghe River in the southwest. This area belongs to the warm temperate semi-arid monsoon climate with outstanding continental climate characteristics. The annual average temperature is 12.6°C, and the annual extreme maximum temperature is 42°C while the minimum is −24.5°C. The annual average precipitation and evaporation are 464 and 1696.8 mm, respectively. The annual average relative humidity is 65%, and the frost-free period is 192 days. The Jinbao Highway, Jinbao Expressway, and Baojin Intercity Railway under construction run through the whole territory, with 16 km west of Beijing-Guangzhou Railway, 8 km west of Beijing-Hong Kong-Macao Expressway, and 30 km east of Beijing-Kowloon Railway. The geographical position is very advantageous and transportation is convenient. Detailed information is shown in **Figure 1**.

Geology

The study area is located in the Bohai Bay Basin, which is a large Mesozoic-Cenozoic intracratonic sedimentary basin filled with Paleocene, Neogene, and Quaternary continental sediments. Among them, the Cenozoic strata including Quaternary, Upper Tertiary, and Lower Tertiary were exposed at the surface. The quaternary system was composed of silt, silty clay, clay, and sand layers. Mountainous areas are mainly distributed in intermountain basins, foothills, and river valleys, with the lithology of sand, gravel, and silt. The plain area is widely distributed, and its lithology is composed of various sand layers, silt, silty clay, and clay. The tertiary system is composed of light mudstone interbedded with sandstone and gravelly sandstone with unequal thickness. The lithology of Eogene is interbedded with sandstone and mudstone of unequal thickness, which is widely distributed in the plain area.

The study area has experienced the Luliang, Caledonian, Haixi, and Indo-China tectonic movements, in which in the main the whole crust rises and falls, while folds, faults, and magmatic activities are weak. After that, the strong Yanshan movement in the Paleocene from the Mesozoic Jurassic to the Cenozoic Eogene and Himalayan movement in Late Tertiary have transformed the North China Basin from a divided uneven fault depression to a nearly unified subsidence-oriented period in the whole region, which lasted until Quaternary. The basin generally accepts Neogene and Quaternary sediments, and unconformity covers its front strata, forming a unified large-scale sedimentary basin, forming the present tectonic pattern of uneven bedrock structure and flat landform landscape under the cover of Cenozoic. The geological structure of the study area is located in the northeast of China-Korea quasi-platform (Grade I), North China fault depression (Grade II), and Jizhong platform depression (Grade III). The main faults in this area are Gaoyang fault and Xushui fault. The Gaoyang fault is located in the normal fault to the west of Gaoyang and Lixian County, striking NE and dipping NW. The throw (vertical displacement) of the fault is approximately 100–550 m, whereas the heave (horizontal

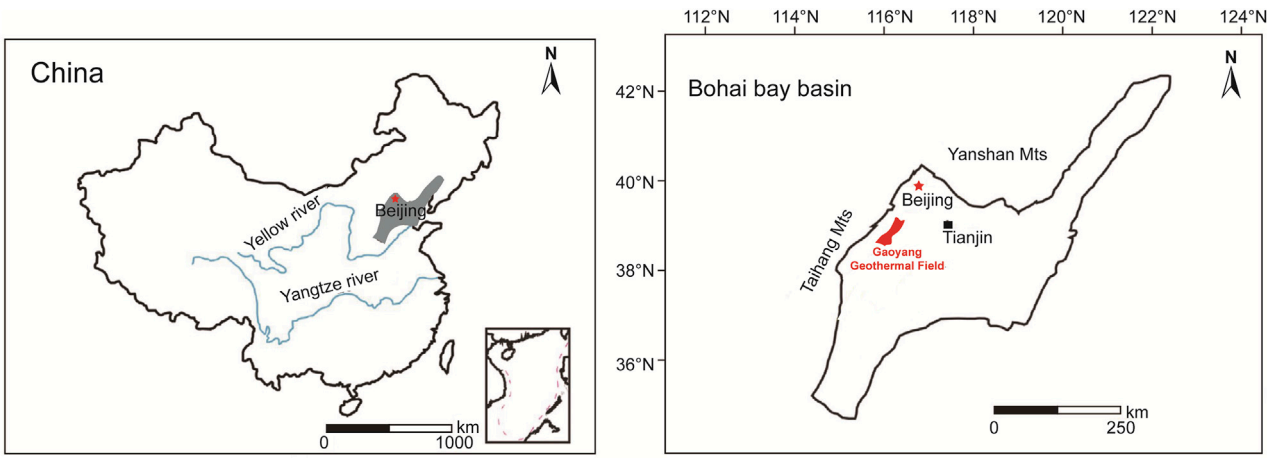

FIGURE 1 | Traffic location map of the study area [revised from (Kong et al., 2020)].

displacement) is approximately 43 km. It is a fault that controls the thickness and structure of the Tertiary. The Xushui fault, located in the line from Xu Shui and Anxin to Zhaobeikou, is a boundary between Rongcheng uplift and Baoding fault depression, with a length of about 35 km. It is a positive fault, strikes near the east-west, dips to the south, with an angle of about 45°, a vertical fault distance of 1,200–3,200 m, and a horizontal fault distance of 1,000–2,500 m. This fracture cuts through the crystalline basement and is a long-term active deep fracture.

Geothermal Geological Conditions

According to the sedimentary rhythm cycle of stratigraphic age, development degree of the thermal reservoir, distribution of stable water-resisting layer, and its hydrogeological characteristics, the thermal reservoir in this area is divided into Neogene pore thermal reservoir, and bedrock fissure karst thermal reservoir from top to bottom.

Neogene pore thermal reservoirs are widely distributed in the area, with a buried depth of 500–600 m at the top boundary and 600–950 m at the bottom, shallow in the west and deep in the east. The stratum thickness is 200–700 m, which is generally thin in the north and thick in the south. The lithology of the thermal reservoir is mainly sandstone and gravelly sandstone, mixed with siltstone, with poor diagenesis. The thickness ratio of the hot sand reservoir is in the range of 12.03 and 25.04%, and the thickness of the single sand layer is generally 3–5 m, the maximum thickness is 14 m, and the porosity is 30–33%.

The buried depth of the bedrock thermal reservoir is 3,000 m, including the Jixian, Cambrian, and Ordovician thermal reservoirs. The top buried depth is 3,000–4,500 m. The Ordovician thermal reservoir is composed of carbonate strata of Fengfeng Formation, Cixian Formation, and Majiagou Formation in the Middle Ordovician and Liangjiashan Formation and Yeli Formation in the Lower Ordovician, with a thickness of about 600–800 m, which is missing in the high part of the structure due to denudation. The karst development degree of the thermal reservoir is quite different due to the difference of its top cover, and the fracture karst rate in the area directly

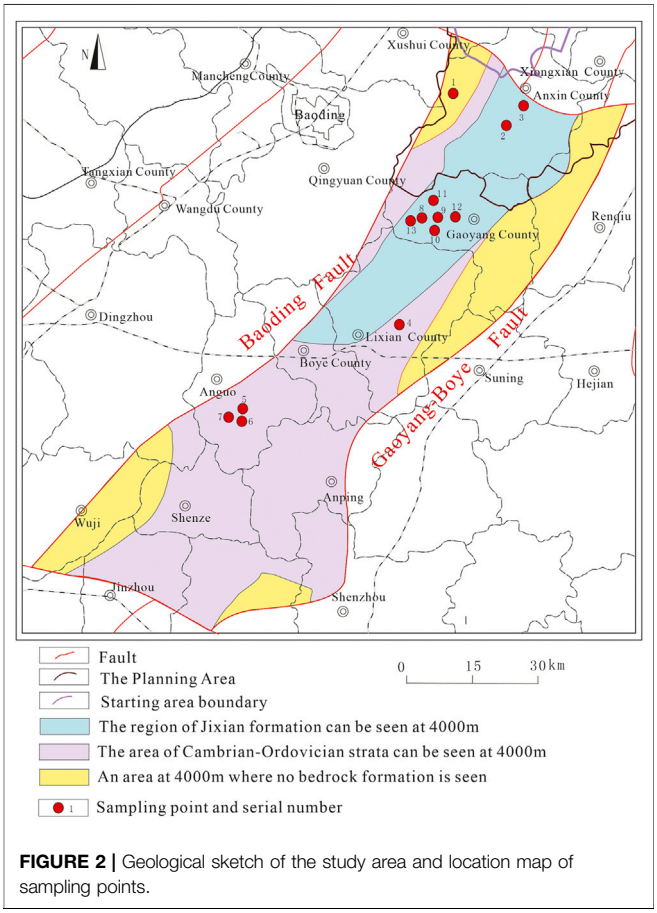

FIGURE 2 | Geological sketch of the study area and location map of sampling points.

covered by Eogene is higher than that in the area covered by Carboniferous-Permian. The average effective porosity of Ordovician thermal reservoir is 3–4%, the ratio of reservoir thickness to reservoir thickness is about 20%, the water inflow of a single well is 150–1,500 m^3/d, and the water temperature can reach 34–73°C. The Cambrian thermal reservoir is composed of

TABLE 1 | Main components of water samples in the study area.

Number	Name	Area	pH	TDS	Na^+	K^+	Mg^{2+}	Ca^{2+}	Cl^-	SO_4^{2-}	HCO_3^-	CO_3^{2-}
				mg/L								
1	AX67	Anxin	8.62	828	324	1.87	2.9	11.5	210	54.9	393	22.4
2	AX68	Anxin	8.47	1,592	598	4.02	4.28	25	728	24.4	378	16.4
3	AX3	Anxin	8.57	1,840	684	6.76	9.06	30.9	925	5.1	319	18.2
4	L73	Lixian	8.46	977	376	4.23	0.838	17.4	201	108	488	21.9
5	AG38	Anguo	8.55	618	242	2.64	0.834	10.8	94.7	67.9	360	17.7
6	AG39	Anguo	8.41	687	265	2.99	0.635	11.5	133	90.5	336	13.5
7	AG40	Anguo	8.5	686	266	2.79	0.742	11	121	86.5	358	17
8	G1	Gaoyang	8.11	2,246	738.1	7.18	1.49	12.5	840.3	44.06	542.4	0
9	G2	Gaoyang	8.37	1,434	438.2	4	0.78	6.13	272.7	85.31	557	12.17
10	G3	Gaoyang	8.45	1,352	409.2	3.51	0.52	5.27	204.3	88.1	567.5	18
11	G4	Gaoyang	8.53	1,033	294.7	1.75	0.48	3.57	85.92	86.19	500.3	18
12	G5	Gaoyang	7.89	2,323	786.1	5.81	1.12	9.78	866.6	75.93	511	0
13	G6	Gaoyang	7.95	6,360	2017.9	87.2	6.4	51.6	1599.6	1264.4	1196.5	0.9

carbonate strata of Fengshan Formation in the Upper Cambrian and Fujunshan Formation in the Lower Cambrian. The thickness revealed by drilling is 30–70 m, and the lithology is brownish-gray fine-grained dolomite and calcareous dolomite. It is mainly distributed in Baxian County of Jizhong platform depression, Ningjin of Linqing platform depression, and Matouying platform depression of Huanghua platform depression. It belongs to a karst fissure type thermal reservoir, with reservoir thickness accounting for about 10% of the reservoir thickness, average effective porosity of 3–6% and wellhead water temperature of 70–78°C. The thermal reservoir of the Wumishan Formation in the Jixian System is a set of shallow sea facies deposits, with lithology of dolomite and argillaceous dolomite in the middle, and with a total thickness of over 300–1,000 m, developed karst fissures, and good connectivity. The thickness of the thermal reservoir occupies 25–64.2% of the formation thickness, and the average effective porosity is 3–6%. The water inflow of a single well is 400–1,500 m^3/d, and the wellhead water temperature reaches 60–80°C, up to 104°C. This thermal reservoir is the best bedrock thermal reservoir in this area.

DATA ACQUISITION

A total of 13 hydrochemical samples were collected on thisoccasion, including 3 geothermal wells in Anxin, 1 geothermal well in Lixian, 3 geothermal wells in Anguo, and 6 geothermal wells in Gaoyang, all of which were carried out in strict accordance with the Code for Geological Exploration of Geothermal Resources (GB/T11615-2010) (Sun et al., 2015a). The distribution of sampling points is shown in **Figure 2**. The pH value was measured by field sampling hand-held tester, and wellhead temperature was also measured on-site. The remaining data was sent to the laboratory of Beijing Institute of Nuclear Industry Geology for water quality analysis and testing. Samples were tested according to DZ/T0064-93 underground water quality inspection method and GB/T 5750 standard test method for drinking water. Testing instruments include 883 Basic IC plus ion chromatograph, ICS-1100 ion chromatograph, AT-510 automatic titration analyzer, UV-POWER ultraviolet-visible spectrophotometer, B644237471 conductivity meter, and 785 DMP automatic potentiometric titrator, etc. Cations in water samples are mainly determined by atomic absorption spectrometry, while anions are mainly determined by turbidimetry. The balance error of anion and cation is controlled within 5%, which is in line with the error regulation (Yu et al., 2021), and is sufficient to meet the requirements of this study. Test results are shown in **Tables 1**, **2** below.

HYDROCHEMICAL CHARACTERISTICS OF GEOTHERMAL FLUIDS

Hydrochemical Characteristics

As shown in **Table 1**, the pH value of geothermal fluid in the study area is generally higher than 7, ranging from 7.9 to 8.6, with an average value of 8.4, which is characterized by weak alkalinity. TDS, i.e., total dissolved solids, refers to the total amount of all solutes in water, including the contents of inorganic substances, and organic substances. All these factors determine the conductivity of the aqueous solution. It can be seen from the table that the TDS value of geothermal water is on the high side as a whole, ranging from 618 mg/L to 6,360 mg/L, among which the TDS value of geothermal water in Gaoyang County is the highest, and the TDS of geothermal wells in other counties and areas is positively correlated with the conductivity value of water samples.

The pH value of Gaoyang geothermal well sample points is between 7.9 and 8.4, the wellhead temperature ranges from 63.1° to 105°C, and the TDS ranges from 1,033 mg/L to 6,360 mg/L, with an average value of 2,458 mg/L. The highest point of TDS is G6. The pH value of Anxin geothermal well samples is between 8.47 and 8.62, which is weakly alkaline. The wellhead temperature ranges from 42° to 45°C, and the TDS value ranges from 828 to 1840 mg/L. The wellhead temperature of the L73 water sample point of the Lixian geothermal well is 70°C, the pH value is 8.46, which is weakly alkaline water, and the TDS value is 977 mg/L. The pH value of Anguo city geothermal well sample points is 8.4–8.5, which is weakly alkaline. The wellhead temperature ranges from 65° to 70°C, and TDS ranges from 618 mg/L to

TABLE 2 | Secondary component content of water samples in the study area.

Number	Name	Water-stype	Stype	Well depth	T	F^-	NO_3^-	NH_4^+	H_2SiO_3	EC
				m	°C	mg/L	mg/L	mg/L	mg/L	μS/cm
1	AX67	Na-HCO_3-Cl	Groundwater	1503.14	44	1.82	2.12	<0.033	26.2	1,440
2	AX68	Na-Cl-HCO_3	Groundwater	1589.23	42	1.8	<0.08	<0.033	25.1	2,810
3	AX3	Na-Cl	Groundwater	1,380	45	1.32	<0.08	0.286	15.9	3,144
4	L73	Na-HCO_3-Cl	Groundwater	2005	70	2.73	<0.08	0.225	56.9	1,607
5	AG38	Na-HCO_3-Cl	Groundwater	1800	65	1.42	<0.08	<0.033	41.3	1,036
6	AG39	Na-HCO_3-Cl	Groundwater	1800	66	1.66	<0.08	<0.033	47.3	1,177
7	AG40	Na-HCO_3-Cl	Groundwater	1900	70	1.86	<0.08	<0.033	44.9	1,151
8	G1	Na-Cl-HCO_3	Groundwater	1866.23	72.9	2.44	<0.20	0.39	61.24	1,330
9	G2	Na-HCO_3-Cl	Groundwater	1814.87	76.5	2.64	<0.20	0.18	69.43	727
10	G3	Na-HCO_3-Cl	Groundwater	1882.33	71	3.06	<0.20	0.18	64.98	522
11	G4	Na-HCO_3	Groundwater	1830.63	63.1	3.57	<0.20	<0.04	47.48	463
12	G5	Na-Cl-HCO_3	Groundwater	1923.58	78.3	2.36	<0.20	0.53	69.31	782
13	G6	Na-Cl-SO_4-HCO_3	Groundwater	3,555	105	9.63	<0.20	1.96	164	—

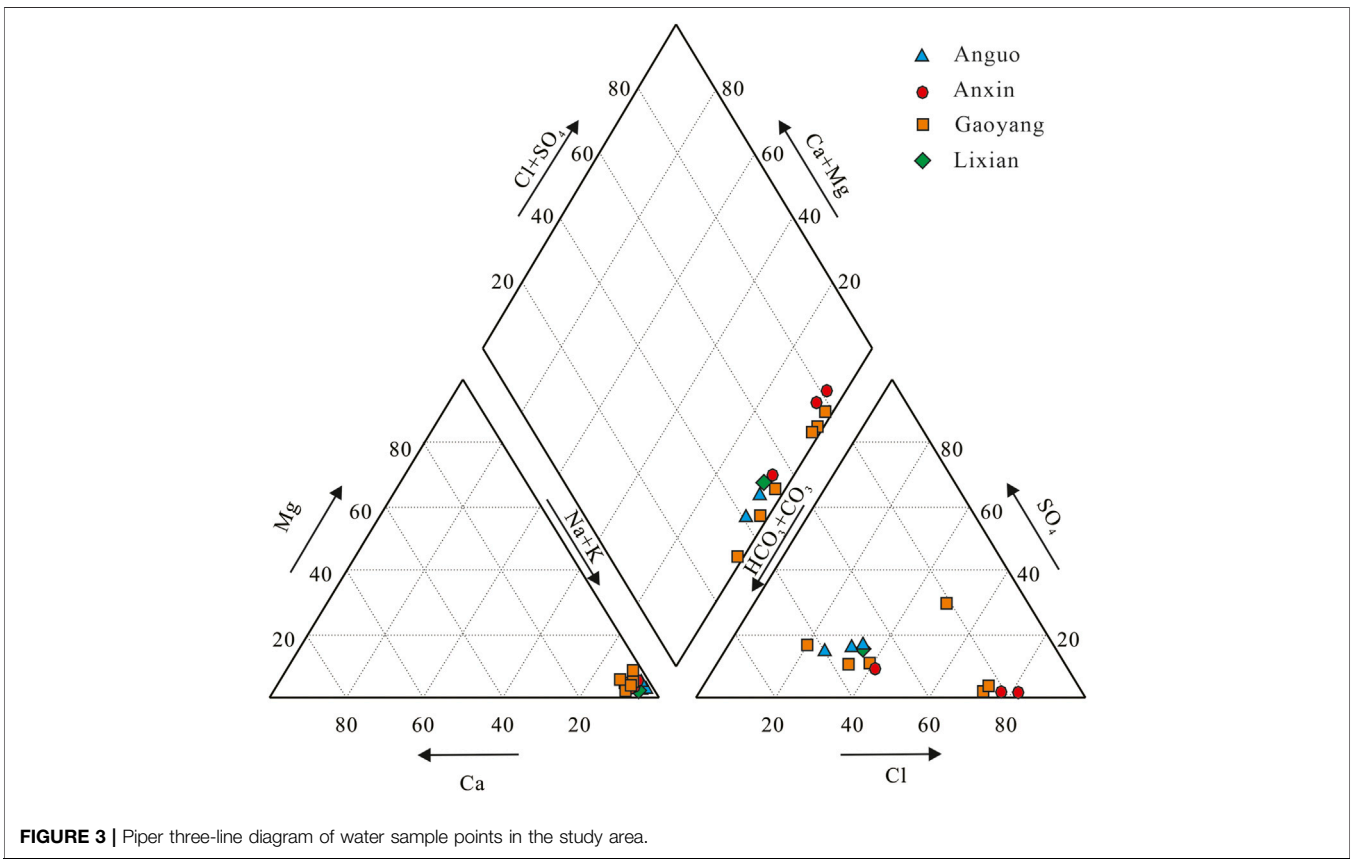

FIGURE 3 | Piper three-line diagram of water sample points in the study area.

687 mg/L. According to the national standard GB5749-2006 "Sanitary Standard for Drinking Water", the limit requirement of total dissolved solids (TDS) for drinking tap water is total dissolved solids ≤1,000 mg/L. Therefore, some water samples in the study area do not meet the standard of domestic water.

Piper's three-line diagram and Durov's diagram of hydrochemistry are often used to analyze the distribution characteristics of hydrochemistry ions, which directly reflect hydrochemistry types. The triangles at the lower left and right of the Piper three-line diagram are cation and anion regions, respectively. According to the hydrochemical data in this study area, the corresponding Piper three-line diagram and Durov diagram of hydrochemical are drawn, as shown in **Figures 3**, **4**.

It can be seen from **Figures 3**, **4** that the main hydrochemical type of geothermal well sample points in

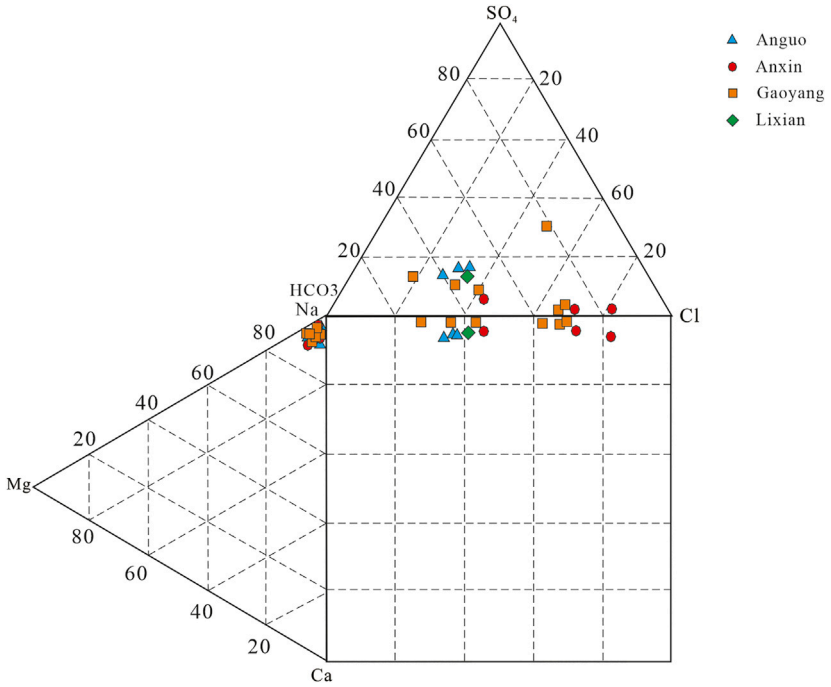

FIGURE 4 | Durov diagram of water sample points in the study area.

Gaoyang county is Na-HCO_3· Cl type. Cations in geothermal water are mainly Na^+, while anions are mainly HCO_3^- and Cl^-. The mole percentage of Na^+ is over 90%, while HCO_3^- is mostly between 20 and 60%, and Cl^- is between 40 and 80%. The chemical type of a few points such as G6 water is Na-Cl SO_4 HCO_3. The chemical types of water samples from the Anxin geothermal well are mainly Na-HCO_3·Cl and Na-Cl·HCO_3. Cations in geothermal water are mainly Na^+, while anions are mainly Cl^- and HCO_3^-. The mole percentage of Na^+ is over 90%, while Cl^- is about 80%, and HCO_3^- is about 20–50%. The hydrochemical type of Lixian geothermal water sample point is Na-HCO_3·Cl type, the main cation is Na+, and the main anions are Cl– and HCO_3^-. The hydrochemical type of geothermal well samples in Anguo City is Na-HCO_3· Cl, with Na^+ as the main cation and Cl^- and HCO_3^- as the anions, which is similar to that in Lixian County.

Generally speaking, the thermal water sampling points in the study area are in the range where alkali metal ions are larger than alkaline earth metal ions. The chemical types of water are relatively stable because the sources of Cl^- mainly include human activities, deep magma, rock leaching, etc (Brown, 2002; Sun et al., 2015b; Liu, 2018; Zhang et al., 2019; Yu et al., 2021). Combined with the actual situation of the local thermal display area, it is speculated that the groundwater may have undergone sufficient leaching, cation alternating adsorption, and concentration precipitation in the deep thermal reservoir environment at high temperature and high pressure, which finally leads to the water chemistry characteristics as analyzed above.

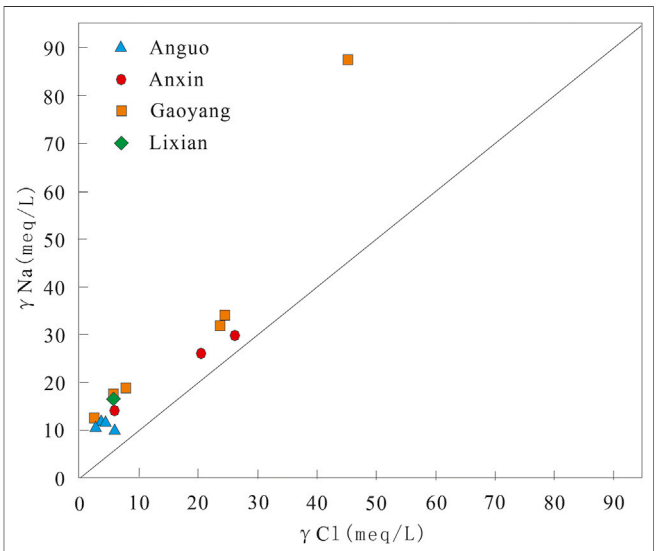

FIGURE 5 | Ion correlation diagram of water samples in the study area.

Hydrochemical Analysis

Generally speaking, by analyzing the ion proportional coefficient and Gibbs diagram of some components in groundwater, the source of hydrochemical components in groundwater and the mechanism of hydrochemical genesis can be studied. The Gibbs diagram often divides the genetic types of hydrochemical components into atmospheric precipitation, water-rock interaction, and evaporation precipitation, with TDS as the

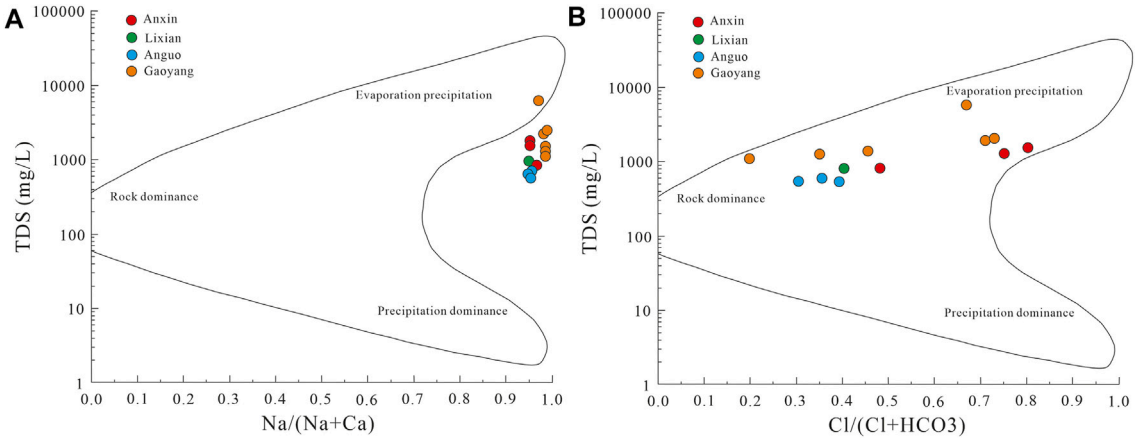

FIGURE 6 | Gibbs pattern distribution of water samples in the study area.

ordinate and $Na^+/(Na^+ + Ca^{2+})$ and $Cl^-/(Cl^- + HCO_3^-)$ as the abscissa on the semi-logarithmic coordinate axis (Gibbs, 1970). Since $\gamma Na/\gamma Cl$ coefficient is the basis for analyzing the genesis of groundwater, the author has drawn the ion correlation diagram of $\gamma Na/\gamma Cl$ coefficient and Gibbs model diagram of water samples in the study area according to the actual situation of the study area. The detailed information is shown in **Figures 5**, **6**.

The $\gamma Na/\gamma Cl$ coefficient is the basis for analyzing the genesis of groundwater. The straight line marked with 1:1 in the Figure is a curve with $\gamma Na/\gamma Cl$ value of 1, which indicates that the water source is the dissolved water of salt rock formation. If the $\gamma Na/\gamma Cl$ coefficient of the water sample is greater than 1, it means that the source of Na^+ in the water is the dissolution of silicate rocks (Sun et al., 2021). It can be seen from **Figure 5** that the water sample points in the study area are above the 1:1 curve of $\gamma Na/\gamma Cl$, and the water sample points of some geothermal wells in Gaoyang county are on the upper side, which indicates that the geothermal fluid in the study area belongs to continental sedimentary water. These water sample points are also close to this line, which indicates that the geothermal water is mainly the leaching water of salt rock formation, and there is also silicate dissolution.

According to the Gibbs model diagram in **Figure 6**, for cations, most of the water samples in the study area fall on the upper right of the diagram, and the range of $Na^+/(Na^+ + Ca^{2+})$ value is about 0.9, which indicates that underground hot water is mainly affected by evaporation and precipitation. As for anions, some water samples fall in the upper right of the figure, while the other water samples fall in the middle, and the value of $Cl^-/(Cl^- + HCO_3^-)$ ranges from 0.25 to 0.9, which indicates that the geothermal water is affected by evaporation precipitation and water-rock interaction. The reason may be that, when water samples from various areas in the study area flow upward from deep high temperature and high-pressure environment, with the decrease of pressure, deep hot water is mixed with it, and leaching and water-rock interaction occur one after another, which makes the final water hydrochemical composition of the water body form a situation in which Na-HCO_3·Cl type is the main body.

THERMAL RESERVOIR TEMPERATURE ESTIMATION

In order to evaluate the development potential of the thermal reservoir in the geothermal area, it is necessary to calculate the thermal reservoir temperature of water samples in the geothermal area. The geochemical thermometer method is the most widely used method to estimate the temperature of an underground thermal reservoir. The principle of this method is that at a specific temperature, the chemical reaction between the geothermal water, and the surrounding rock minerals generally reaches equilibrium in a certain period. In the process of reaching the surface, this equilibrium state can be maintained, so that the equilibrium state of the underground thermal reservoir can be calculated. Based on this principle, this study mainly used cation thermometer and silica thermometer for heat storage temperature calculations to estimate the temperature of an underground thermal reservoir (Xu and Guo, 2009).

Cationic Geothermal Thermometer

Nieva et al. put forward a cationic combination thermometer that uses K, Na, Ca, and Mg ions to calculate the temperature of the thermal reservoir (Nieva and Nieva, 1987). Na-K thermometer, Na-K-Ca thermometer, and K-Mg thermometer, etc. are involved with different suitable terms. The K-Na geothermal temperature is often used to estimate the temperature of the deep thermal reservoir with an applicable range of 25–350°C based on the equilibrium between geothermal water and albite/potash feldspar. It should be noted that the mixing of shallow groundwater can induce a bias to the result. Na-K-Ca thermometer is mainly aimed at the medium and low-temperature thermal water and shallow geothermal water with high calcium. The ion variable factors are increased to three types, and correction coefficients are in addition. However, the calculation results have serious deviations when the external environment changes. The K-Mg thermometer is controlled by the exchange reaction among muscovite, potash feldspar, and chlorite, and is suitable for medium and low-temperature geothermal fields distributed in

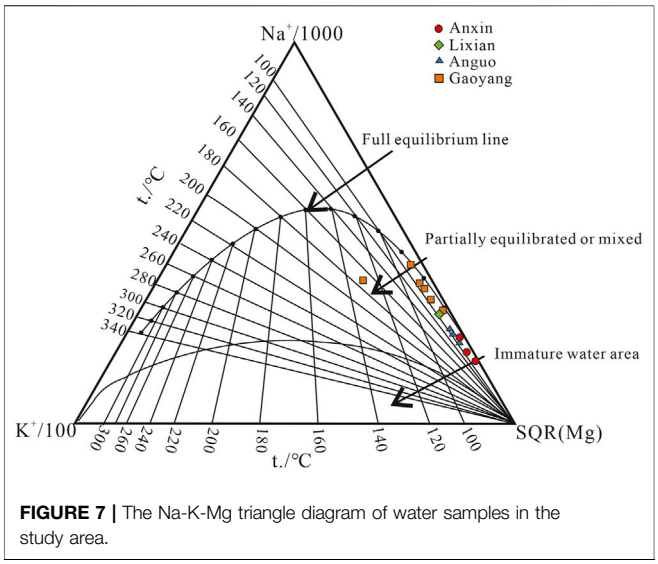

FIGURE 7 | The Na-K-Mg triangle diagram of water samples in the study area.

TABLE 3 | Estimation results of underground hot water temperature in study area by cationic thermometer.

Number	T (°C)	Na-K (°C)	K-Mg (°C)
AX67	44.00	21.01	44.83
AX68	42.00	27.29	56.62
AX3	45.00	44.40	59.75
Average		30.90	53.73
L73	70.00	50.60	76.28
AG38	65.00	49.11	65.35
AG39	66.00	50.74	71.34
AG40	70.00	47.22	67.94
Average		49.02	68.21
G1	72.90	43.66	82.18
G2	76.50	40.72	75.80
G3	71.00	37.89	77.53
G4	63.10	22.16	62.33
G5	78.30	31.32	80.47
G6	105.00	132.96	132.36
Average		51.45	85.11

shallow layers with a temperature of 0–250°C. The accuracy of the result is affected by the primary thermodynamic balance due to the change in the concentration of Mg^{2+} when shallow groundwater is mixed in (Zhao et al., 2020). Based on the cation temperature scale, The established Na-K-Mg triangle diagram can be used to determine the collected water sample type from mature water, mixed water, and immature water. Different geothermal temperature scales are selected to calculate the thermal reservoir temperature based on the water types (Giggenbach Werner, 1988; Wang et al., 2018).

The water samples in the study area all fall in the partial equilibrium region in the Na-K-Mg triangle diagram (**Figure 7**), which indicates indicate that these geothermal waters have not reached equilibrium due to the water-rock interaction or the mixing processes during up-flowing of thermal water. The Na-K thermometer is suitable to calculate the temperature of a deep high-temperature thermal reservoir but not for that of a shallow thermal reservoir. The Na-K-Ca thermometer is used to calculate medium and low-temperature thermal water and shallow geothermal water with high calcium, but the calculated value will have a large deviation when the mixing phenomenon occurs. The K-Mg thermometer is suitable for shallow geothermal fields with medium and low temperatures, but its calculated value may be affected due to the mixing effect. Therefore, the Na-K and K-Mg thermometers are mainly used within the scope of this study area, as shown in the following formula. The calculated value of the thermal reservoir temperature of the obtained water sample is shown in **Table 3**.

$$t = \frac{933}{\lg(Na/K) + 0.933} - 273.1 \quad (4.1)$$

$$t = \frac{4410}{13.95 - \lg(K^2/Mg)} - 273.15 \quad (4.2)$$

where t is the value of thermal reservoir temperature to be calculated in °C, and Na, K, and Mg are the concentration of Na^+, K^+, and Mg^{2+} in the geothermal fluid in mg/L respectively.

Silicon Dioxide Geothermal Thermometer

Silica thermometers are the first and most widely used geochemical thermometers in geothermal research; types mainly include quartz thermometers (non-vapor loss), quartz thermometers (maximum loss), chalcedony thermometers (non-vapor loss), and chalcedony thermometers (maximum loss). Silica is generally not easily affected by other ions and volatile components, and its content can remain relatively stable during the thermal fluid cooling process and is suitable for non-acidic, non-diluted geothermal fluid conditions at 20–250°C (Xu and Guo, 2009; Yu et al., 2021). The geothermal water samples in the study area are in partial equilibrium water or mixed water, which is affected by the intrusion of surface cold water.

The temperature of the other water sample points is lower than the local boiling point temperature according to the temperature measured at the sampling point of each water sample except for G6. Therefore, silica non-vapor loss thermometers including quartz non-vapor loss thermometers and chalcedony non-vapor loss thermometers are considered for use. The on-site test temperature of the water sample at G6 is higher than 100°C, so the quartz maximum loss thermometer and the chalcedony maximum loss type thermometer are selected. The calculation formula is shown below, and the calculation results are shown in **Table 4** below.

(1) quartz thermometer (non-vapor loss)

$$t = \frac{1309}{5.19 - \lg(SiO_2)} - 273.15 \quad (4.3)$$

(2) quartz thermometer (maximum loss)

$$t = \frac{1522}{5.75 - \lg(SiO_2)} - 273.15 \quad (4.4)$$

(3) chalcedony thermometer (non-vapor loss)

TABLE 4 | Estimation results of underground hot water temperature in study area by silica thermometer.

Number	T (°C)	Maximum steam loss of chalcedony (°C)	Non-steam loss of chalcedony (°C)	Maximum steam loss in quartz (°C)	Non-steam loss of quartz (°C)
AX67	44.00	42.40	31.67	69.21	63.73
AX68	42.00	40.94	30.00	67.78	62.12
AX3	45.00	26.20	13.31	53.28	45.92
Average		36.51	24.99	63.42	57.26
L73	70.00	71.37	65.34	97.27	95.70
AG38	65.00	58.78	50.56	85.14	81.79
AG39	66.00	64.00	56.66	90.18	87.55
AG40	70.00	61.98	54.29	88.22	85.31
Average		61.59	53.84	87.85	84.88
G1	72.90	74.40	68.92	100.17	99.05
G2	76.50	79.69	75.22	105.23	104.91
G3	71.00	76.88	71.87	102.54	101.80
G4	63.10	64.15	56.83	90.32	87.71
G5	78.30	79.61	75.13	105.16	104.83
G6	105.00	120.73	125.44	143.94	150.60
Average		74.94	69.59	100.69	99.66

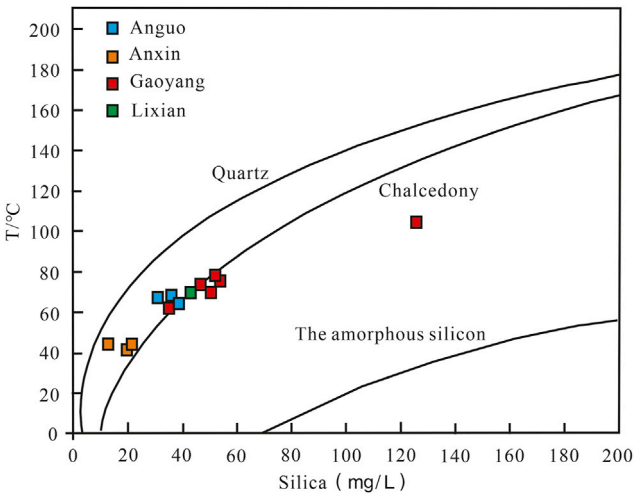

FIGURE 8 | Relationship between solubility and temperature of SiO_2 in the study area.

$$t = \frac{1032}{4.69 - \lg(SiO_2)} - 273.15 \quad (4.5)$$

(4) chalcedony thermometer (maximum loss)

$$t = \frac{1264}{5.31 - \lg(SiO_2)} - 273.15 \quad (4.6)$$

where t is the value of thermal reservoir temperature to be calculated in °C, SiO_2 is the concentration of SiO_2 in mg/L.

The curve of SiO_2 solubility and temperature (**Figure 8**) can be used to determine the mineral dissolution state and the type of minerals that control the content of SiO_2 due to the functional relationship (Lu et al., 2010; Sun et al., 2021). Most of the thermal water samples in the study area are close to the melting curve of quartz and chalcedony, that is, the geothermal water samples in Anxin, Anguo, Lixian, and Gaoyang are between the solubility curves of quartz and chalcedony. Therefore, both quartz and chalcedony thermometers are suitable.

Combined with **Table 3**, through the Na-K thermometer and K-Mg thermometer in the cation thermometer, it can be concluded that the average temperature in the Anxin area is 30.9°C and 53.73°C respectively, in the Lixian area is 50.6°C and 76.28°C respectively, the Anguo area 49.02°C and 68.21°C respectively, and the Gaoyang area is 51.45°C and 85.11°C respectively. Obviously, the temperature of the geothermal field in the Gaoyang area is relatively the highest. However, due to the large deviation of the calculation results due to the presence of the mixing of thermal and cold water, the calculated results of the K-Mg thermometer are higher for each region. The Na-K thermometer is suitable for estimating the temperature of deep thermal reservoirs, but not suitable for estimating that of a shallow one.

In combination with **Table 4**, it shows that the temperature of some water sample points obtained by using a chalcedony thermometer is lower than the temperature measured at the time of collection, which is inconsistent with the facts. Therefore, for the point where the sampling temperature is lower than 100°C, the result of the quartz non-vapor loss type thermometer is adopted; for G6, where the sampling temperature is higher than 100°C, the result of the quartz maximum loss type thermometer is adopted. Combined with the previous analysis of applicable conditions and scope, the value of the quartz thermometer is used for the shallow thermal reservoir temperature of various thermal fields, and the values of the Na-K thermometer and quartz thermometer are used for the deep thermal reservoir temperature of various thermal fields. Therefore, it can be seen that the shallow thermal reservoir temperature range is about 45–63°C in Anxin, 76–95°C in Lixian, 81–87°C in Anguo, and 87–104°C in Gaoyang. The temperature range of the deep thermal reservoir in the entire study area is about 104–150°C.

CONCLUSION

(1) The study area is located in the northeast of the China-Korea quasi-platform (Grade I), North China fault depression (Grade II), and Jizhong platform depression (Grade III). The main faults in this area are the Gaoyang fault and the Xushui fault, which provide a good migration channel for geothermal water. Neogene pore thermal reservoirs and bedrock fissure karst thermal reservoirs are widely distributed in this region, in addition, the karst fissures are well developed and have good connectivity, which is a thermal reservoir with good conditions.

(2) The main hydrochemical type of the Gaoyang geothermal field is Na-HCO_3·Cl, with high TDS contents. The Gibbs diagram and ion ratio analysis proves that when the geothermal water flows upward from the deep high temperature and high-pressure environment, as the pressure of the surrounding environment decreases and the mixing with the deep thermal water occurs, leaching and alternating cation adsorption occur. And the intense water-rock reaction leads to the high TDS values of geothermal water.

(3) The mixing of shallow cold recharge with the ascending thermal fluids through faults is confirmed by the presence of water partially in equilibrium from the Na-K-Mg triangle diagram. The shallow thermal reservoir temperature is about 45–63°C in Anxin, 76–95°C in Lixian, 81–87°C in Anguo, and 87–104°C in Gaoyang, respectively. The temperature range of the deep thermal reservoir in the entire study area is about 104–150°C.

DATA AVAILABILITY STATEMENT

The original contributions presented in the study are included in the article/Supplementary Material, further inquiries can be directed to the corresponding authors.

AUTHOR CONTRIBUTIONS

All authors listed have made a substantial, direct, and intellectual contribution to the work and approved it for publication.

FUNDING

This study was financially supported by the National Key R&D Program of China (2018YFC0604302 and 2019YFB1504102) and China Geological Survey (DD20189114).

ACKNOWLEDGMENTS

We appreciate the kind help of the editor and anonymous reviewers.

REFERENCES

Brown, G. H. (2002). Glacier Meltwater Hydrochemistry. *Appl. Geochem.* 17 (7), 855–883. doi:10.1016/s0883-2927(01)00123-8

Gibbs, R. J. (1970). Mechanisms Controlling World Water Chemistry. *Science* 170 (3962), 1088–1090. doi:10.1126/science.170.3962.1088

Giggenbach Werner, F. (1988). Geothermal Solute Equilibria. Derivation of Na-K-Mg-Ca Geoindicators[J]. *Pergamon* 52 (12), 2749–2765. doi:10.1016/0016-7037(88)90143-3

Hu, Q., Gao, J., Ma, F., Zhao, Z., Liu, G., Wang, G., et al. (2020). Dynamic Prediction of Geothermal Recoverable Resources in the Rongcheng Uplift Area of the Xiong'an New Area[J]. *Acta Geol. Sin.* 94 (7), 2013–2025. doi:10.19762/j.cnki.dizhixuebao.2020230

Kong, Y., Pang, Z., Pang, J., Li, J., Lyu, M., and Pan, S. (2020). Fault-Affected Fluid Circulation Revealed by Hydrochemistry and Isotopes in a Large-Scale Utilized Geothermal Reservoir. *Geofluids* 2020, 1–13. doi:10.1155/2020/2604025

Liu, M., He, T., Wu, Q., and Guo, Q. (2020). Hydrogeochemistry of Geothermal Waters from Xiongan New Area and its Indicating Significance[J]. *Earth Sci.* 45 (6), 2221–2233. (in Chinese).

Liu, X. (2018). *Study on Groundwater and Soil Environmental Response in Opencast Coal Mine Area [D]*. Inner Mongolia: Inner Mongolia University.

Lu, Z., Wu, L., and Luo, X. (2010). Application of Geothermometers to Calculate the Temperature of Geothermal Reservoirs in Wudang Area of Guiyang []. *Geotechn. Invest. Surv.* 45 (6), 832–836.

Ma, F., Wang, G., Zhang, W., Zhu, X., Zhang, H., and Yue, G. (2020). Structure of Geothermal Reservoirs and Resource Potential in the Rongcheng Geothermal Filed in Xiong'an New Area. *Acta Geologica Sinica* 94 (7), 1981–1990. doi:10.19762/j.cnki.dizhixuebao.2020217

Nieva, D., and Nieva, R. (1987). Developments in Geothermal Energy in Mexicoâ Part Twelve. A Cationic Geothermometer for Prospecting of Geothermal Resources[J]. *Heat Recovery Syst. CHP* 7 (3), 243–256. doi:10.1016/0890-4332(87)90138-4

Pang, Z., Kong, Y., Pang, J., Hu, S., and Wang, J. (2017). Geothermal Resources and Development in Xiongan New Area[J]. *Bull. Chin. Acad. Sci.* 32 (11), 1224–1230. doi:10.16418/j.issn.1000-3045.2017.11.007

Sun, H., Ma, F., Zhao, L., Liu, Z. M., Wang, G. L., and Nan, D. W. (2015). The Distribution and Enrichment Characteristics of Fluoride in Geothermal Active Area in Tibet[J]. *China Environ. Sci.* 35 (1), 251–259. (in Chinese).

Sun, H., Ma, F., Lin, W., Liu, Z., Wang, G., and Nan, D. (2015). Geochemical Characteristics and Geothermometer Application in High Temperature Geothermal Field in Tibet[J]. *Geol. Sci. Techn. Inf.* 34 (3), 171–177.

Sun, H., Lang, X., Nan, D., Liu, Z., Guo, N., Li, H., et al. (2021). Geothermal Water Genesis and Engineering Effect in Saga Chongqu Basin Tibet[J]. *Safety and Environmental Engineering* 28 (3), 147–155. doi:10.13578/j.cnki.issn.1671-1556.20210021

Wang, X., Wang, G., Lu, C., Gan, H., and Zhao, L. (2018). Evolution of Deep Parent Fluids of Geothermal fields in the Nimu–Nagchu Geothermal belt, Tibet, China[J]. *Geothermics* 71, 118. doi:10.1016/j.geothermics.2017.07.010

Wang, Z., Zhang, C., Jiang, G., Hu, J., Tang, X., and Hu, S. (2019). Present-day Geothermal Field of Xiongan New Area and its Heat Source Mechanism[J]. *Chin. J. Geophys.* 62 (11), 4313–4322. (in Chinese). doi:10.6038/cjg2019M0326

Wang, G., Gao, J., Zhang, B., Xing, Y., Zhang, W., and Ma, F. (2020). Study on the thermal Reservoir Characteristics of the Wumishan Formation and Huge Capacity Geothermal Well Parameters in the Gaoyang Low Uplift Area of Xiong'an New Area. *Acta Geol. Sin.* 94 (7), 1970–1980. doi:10.19762/j.cnki.dizhixuebao.2020235

Wang, G., Zhang, H., Zhang, W., and Ma, F. (2021). Development and Utilization of Geothermal Resources in Xiongan New Area [J]. *China High-Tech* 1, 46–47.

Wang, S., Zhang, B., Li, Y., Xing, Y., Yuan, W., Li, J., et al. (2021). Heat Accumulation Mechanism of Deep Ancient Buried hill in the Northeast of Gaoyang Geothermal Filed, Xiong'an New Area[J]. *Bull. Geol. Sci. Techn.* 40 (3), 12–21. (in Chinese). doi:10.19509/j.cnki.dzkq.2021.0319

Xu, S., and Guo, Y. (2009). *Fundamentals of Geothermics [M]*. Beijing: Science Press.

Yu, H., Liu, Z., Rong, F., Chen, K., Nan, D., Liu, S., et al. (2021). Characteristics and Source Mechanism of Geothermal Field in Cuona, Tibet[J]. *Bull. Geol. Sci. Techn.* 40 (3), 34–44. doi:10.19509/j.cnki.dzkq.2021.0318

Zhang, X., Hao, H., Liu, K., Mao, W., Xiao, Y., et al. (2019). Hydrogeochemical Characteristics and Formation of the Ivory Spring in Jiacha County of Tibet[J]. *Hydrogeol. Eng. Geol.* 46 (4), 1–9. doi:10.16030/j.cnki.issn.1000-3665.2019.04.01

Zhao, J., Zhang, W., Ma, F., Zhu, X., Zhang, H., and Wang, G. (2020). Geochemical Characteristics of the Geothermal Fluid in the Rongcheng Geothermal Field, Xiong'an New Area[J]. *Acta Geol. Sin.* 94 (7), 1991–2001. doi:10.19762/j.cnki.dizhixuebao.2020234

Conflict of Interest: The authors declare that the research was conducted in the absence of any commercial or financial relationships that could be construed as a potential conflict of interest.

Publisher's Note: All claims expressed in this article are solely those of the authors and do not necessarily represent those of their affiliated organizations, or those of the publisher, the editors and the reviewers. Any product that may be evaluated in this article, or claim that may be made by its manufacturer, is not guaranteed or endorsed by the publisher.

frontiers in Earth Science

ORIGINAL RESEARCH
published: 10 February 2022
doi: 10.3389/feart.2022.806416

Long-term Performance Evaluation and Economic Analysis for Deep Borehole Heat Exchanger Heating System in Weihe Basin

Wanlong Cai[1], Fenghao Wang[1], Jinghua Jiang[1], Zeyuan Wang[1], Jun Liu[2,3] and Chaofan Chen[4]**

[1]School of Human Settlements and Civil Engineering, Xi'an Jiaotong University, Xi'an, China, [2]Key Laboratory of Coal Resources Exploration and Comprehensive Utilization, Ministry of Natural Resources, Xi'an, China, [3]Shaanxi Coal Geology Group Company Limited, Xi'an, China, [4]Helmholtz Centre for Environmental Research-UFZ, Leipzig, Germany

OPEN ACCESS

Edited by:
Yanlong Kong,
Institute of Geology and Geophysics (CAS), China

Reviewed by:
Xiaoming Tian,
Delft University of Technology, Netherlands
Hirotaka Saito,
Tokyo University of Agriculture and Technology, Japan
Isa Kolo,
University of Glasgow, United Kingdom

***Correspondence:**
Fenghao Wang
fhwang@mail.xjtu.edu.cn
Chaofan Chen
chaofan.chen@ufz.de

Specialty section:
This article was submitted to Economic Geology, a section of the journal Frontiers in Earth Science

Received: 31 October 2021
Accepted: 07 January 2022
Published: 10 February 2022

Citation:
Cai W, Wang F, Jiang J, Wang Z, Liu J and Chen C (2022) Long-term Performance Evaluation and Economic Analysis for Deep Borehole Heat Exchanger Heating System in Weihe Basin. Front. Earth Sci. 10:806416. doi: 10.3389/feart.2022.806416

To reduce carbon emission and achieve carbon neutrality, deep geothermal energy has been widely extracted for building heating purpose. In recent years, deep borehole heat exchanger (DBHE) heating system has gained more attention, especially in densely populated urban areas in Weihe Basin, northern China. The long-term performance and the economic feasibility are essential for the system application. In this work, the DBHE model implemented in OpenGeoSys software is verified against an analytical solution and a comprehensive economic analysis approach is further proposed. Then the short-term thermal performance tests are conducted to obtain the tentative heat extraction capacity for long-term simulation. The long-term simulations are further performed with the heat pump unit under the adjusted tentative heat extraction rate imposed on the DBHE. Finally, a comprehensive economic analysis is applied to the DBHE heating system over 15 heating seasons. Results show that the minimum coefficient of performance value of the heat pump is 4.74 over the operation of 15 heating seasons. With the increase of depth for the DBHE, the total electricity consumption of heat pumps and circulation pumps has a prominent promotion. With the comprehensive approach of economic analysis, the depth of 2,600 m has the lowest levelized cost of total heating amount, which is the best system design for the application in Weihe Basin. The present results are specific to the conditions in Weihe Basin, but the proposed economic analysis approach is generic.

Keywords: deep borehole heat exchanger, heating system, heat extraction performance, economic analysis, Weihe Basin, OpenGeoSys

Abbreviations: BHE, borehole heat exchanger; COP, coefficient of performance; DBHE, deep borehole heat exchanger; FEM, finite element method; GSHP, ground source heat pump; HVAC, heating, ventilation, and air conditioning; LCOH, levelized cost of heating capacity; NPV, net present value.

1 INTRODUCTION

Considering the restriction of global warming imposed by The Paris Agreement 2015, countries worldwide are firmly devoted to pursuing a rapid transition toward renewable energy (De La Peña et al., 2022). In recent years, the European Union (Rodrigues et al., 2022), China (Zhao et al., 2022), and many other countries (Salvia et al., 2021) all made ambitious pledges to reach carbon neutrality by 2060 or earlier. To make sure the carbon emission target can be achieved, the environmentally friendly, highly efficient renewable energy solution will play a more crucial role in the future (Zhao and You, 2020). In view of the high proportion of building energy consumption within the whole energy usage worldwide (Ürge-Vorsatz et al., 2015), especially the huge amount of energy consumed for building heating and hot water supply (about 40% or even more in Europe) (Dias and Costa, 2018; Lin and Lin, 2019), it is of great importance to propose more renewable energy solutions for building heating, especially in cold regions. Compared with other renewable energy sources, geothermal energy gains lots of attention in serving as a building heating source for its stability, versatility, and extensive availability (Anderson and Rezaie, 2019; Lund and Toth, 2021) in the last few decades.

The history of people directly using geothermal energy could be traced back to ancient times, and the natural or artificial hot springs are usually used for baths or heating. Since the concept of ground source heat pump (GSHP) has been proposed in the last century, the shallow borehole heat exchanger (BHE) is then introduced to many projects for wide use (Ozgener et al., 2007). The shallow BHE coupled geothermal heat pump system can extract/inject energy from/to subsurface for building heating/cooling. One of the advantages of the system is that it does not rely on the local hydrothermal geothermal resource due to the closed loop in the subsurface. Thus, this shallow geothermal utilization technology has had a rapid development in the last decades. However, in densely populated regions, several hundreds of BHEs are needed to meet the large heating demand. This requires a colossal drilling area (Javadi et al., 2019) on the ground surface. Besides, due to the unbalanced heating and cooling demand in cold regions, the soil thermal balance (Soltani et al., 2019) is very difficult to maintain, making the system unsustainable in long-term operation (Chen et al., 2020b). These two aspects largely constrain the system application in a densely populated area where heating demand is larger. To efficiently utilize the geothermal energy for heating purposes in densely populated cold regions, an approach of the deep borehole heat exchanger (DBHE, see **Figure 1**) is proposed (Kohl et al., 2002), and several pioneered projects were executed (Morita et al., 1992; Kohl et al., 2000) at the end of the last century. The DBHE usually has a depth of 2,000~3,000 m and a coaxial pipe installed in the borehole (Śliwa and Kotyza, 2003; Chen et al., 2019a), leading to a large heat exchange surface area with the surrounding subsurface.

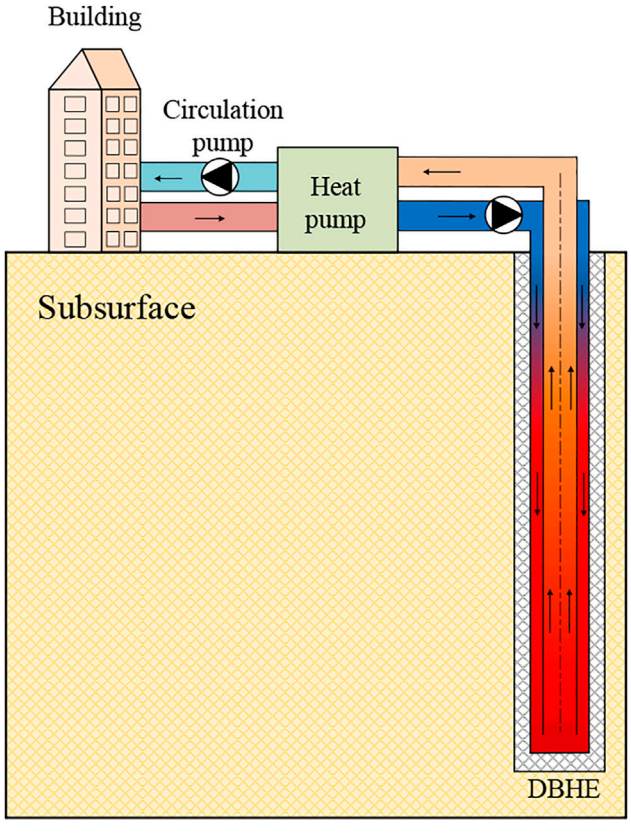

FIGURE 1 | Schematic diagram of the DBHE heating system.

The related pilot applications show that the DBHE heating system has satisfactory performance, while it has a high initial drilling cost that may lack economic potential, especially in Europe (Sapinska-Sliwa et al., 2016).

Under the constraints of large building-heating demand and limited land area in China's densely populated urban area, the DBHE heating technology has been widely applied in northern China. It has gained lots of attention from both the Chinese government and the heating market in recent years. Starting from 2017, there are a few DBHE heating pilot projects reported in northern China (Huang et al., 2020), most of which are located in Xi'an city, Weihe Basin (Wang et al., 2017; Deng et al., 2019). The related experimental field tests indicated that the average coefficient of performance (COP) of the DBHE-coupled GSHP heating system can reach 4.58 (Deng et al., 2020). Considering the concentrated heating load and low drilling cost in China heating market, the DBHE heating technology is of good feasibility to extract deep geothermal energy, serving as the primary building heating source in the future.

To further investigate the heat extraction performance of the DBHE heating system, considerable research about the DBHE system has been conducted in the last few years. With analytical (Luo et al., 2019; Pan et al., 2019) and numerical approaches (Kong et al., 2017; Fang et al., 2018; Song et al., 2018), researchers developed several simulation tools to investigate and quantify the performance of the DBHE and the response of surrounding soil/rock. Some commercial software, such as FLUENT (Li et al., 2020) and COMSOL (Hu et al., 2020), are also applied to simulate the heat transfer process of the DBHE system. Using the FEFLOW

software, Le Lous et al. (2015) performed a series of detailed numerical investigations to study the heat extraction performance of the DBHE under different design parameters and geological conditions. The results indicated that increasing the drilling depth of pipe accounts for the considerable heat extraction of the DBHE. By introducing the Laplace transformation and Stehfest inversion technology, Beier (2020) proposed a novel analytical method to simulate coupled thermal-hydraulic process of the DBHE system, in which the geothermal gradient in the subsurface can be considered. Nevertheless, the geological properties are the same along the whole DBHE length in the analytical solution. To investigate the impact of geological parameters (Liu et al., 2020) on the system's long-term sustainability, Cai et al. (2018) developed a 2D numerical model and validated the model against the field data. Xu et al. (2020) further conducted a series of scenarios, which demonstrated the impact of intermittent heating mode on the DBHE heat extraction performance. Pan et al. (2020) performed an economic analysis for the DBHE system by using an analytical solution proposed by Beier et al. (2014), while the variation of heat pump performance was not taken into account.

Due to the time-consuming simulations in the fully discretized 3D model, most related research on the DBHE system are focused on the short-term operation (e.g., one heating season or 1 year). In addition, few studies can be found on the economic analysis of the DBHE system, which actually largely affects the system applicability in the long term. Based on the related sensitivity analysis results of the DBHE, the drilling depth has been proved by researchers that a more extended depth will bring higher outlet temperature and higher heat extraction capacity. Nevertheless, the drilling depth is constrained with higher drilling costs for the deeper rock. Another critical knowledge gap in simulating the DBHE is that the simulation of the DBHE only contains the subsurface part but ignores the corresponding influence on the heat pump system. In this context, the investigations on heat extraction performance and sustainability of the DBHE-based long-term simulations, considering the interaction with heat pump system, are of great significance for its economic analysis and the selection of design parameters.

In our previous work (Chen et al., 2019a; Cai et al., 2021), a numerical model established by OpenGeoSys (OGS) software was developed for simulating the coaxial DBHE and surrounding soil. The model had been validated against experimental data measured from several pilot projects in Xi'an, Weihe Basin (Cai et al., 2021). In these studies, the accuracy of our model simulating the long-term heat extraction performance of a DBHE and the surrounding subsurface is thoroughly illustrated. In contrast, further economic analysis with the performance of the heat pump system involved has not been carried out yet. In this context, a series of scientific questions are raised for the DBHE heating system: How can a long-term performance evaluation be conducted when the heat pump characteristic in the DBHE heating system is considered? How does a comprehensive economic analysis affect the decision-making for the DBHE system in designing the optimal drilling depth? With the initial and operating costs considered, which depth of the DBHE is more economically sustainable against others in Weihe Basin?

In this paper, the aforementioned scientific questions were analyzed by a series of elaborated numerical simulations. The DBHE system model was constructed with the OpenGeoSys software (Kolditz et al., 2012) and further deployed based on the actual geological parameters in Weihe Basin. Through the constructed numerical model, thermal performance tests of the DBHE system were carried out, and the tentative heat extraction capacities of the DBHE were evaluated. After that, the long-term heat extraction performance of the DBHE system with different depths was analyzed in detail. In the next step, a comprehensive economic analysis for the DBHE was investigated during long-term operation, and the electricity consumption of the heat pump and circulation pump was also evaluated. At the end of the article, practical suggestions of drilling depth are made for the design of the DBHE heating systems.

2 METHODOLOGY

2.1 Dual Continuum FEM Method in OpenGeoSys

In the present model framework for DBHE simulation, many researchers tend to select numerical approaches since they are more capable of handling the flexible initial and boundary conditions that emerge from the field study. The numerical DBHE model used in this study is implemented by using Dual Continuum Finite Element Method (DC-FEM) (Al-Khoury et al., 2010; Shao et al., 2016) in the open-source software OpenGeoSys (OGS) (Kolditz et al., 2012). In the field of deep coaxial borehole heat exchanger simulation, the coaxial pipe with an annular inlet (CXA) is recommended for heat extraction (Chen et al., 2019a). The governing equations for the fluid inside the centered and annular borehole read:

$$\rho_f c_f \frac{\partial T_i}{\partial t} + \rho_f c_f \mathbf{v}_i \cdot \nabla T_i = \nabla \cdot (\Lambda_i \cdot \nabla T_i) + H_i \tag{1}$$

Boundary condition (Robin Type):

$$q_{nT_i} = -\Phi_{io}(T_o - T_i) \text{ on } \Gamma_i \tag{2}$$

$$\rho_f c_f \frac{\partial T_o}{\partial t} + \rho_f c_f \mathbf{v}_o \cdot \nabla T_o = \nabla \cdot (\Lambda_o \cdot \nabla T_o) + H_o \tag{3}$$

Boundary condition (Robin Type):

$$q_{nT_o} = -\Phi_{io}(T_i - T_o) - \Phi_{og}\left(T_g - T_o\right) \text{ on } \Gamma_o \tag{4}$$

where ρ_f and c_f refer to the density and specific heat capacity of the circulation fluid, respectively. The H and Γ are the heat sink/source term and heat transfer boundary. The $\mathbf{v_i}$ and $\mathbf{v_o}$ denote the flow velocity of fluid in the inner and outer pipes, respectively. Φ_{io} refers to the heat transfer coefficient between inner and outer pipes while Φ_{og} denotes the heat transfer coefficient between the outer pipe and grout (Diersch et al. 2011).

The term of hydrodynamic thermal dispersion tensor Λ reads:

$$\Lambda_f = \left(\lambda_f + \rho_f c_f \beta_L \|\mathbf{v}_f\|\right)\mathbf{I} \tag{5}$$

where β_L denotes the longitudinal heat dispersivity and $\mathbf{I}$ refers to the identity matrix. The $\mathbf{v_f}$ is the Darcy velocity of groundwater flow in the subsurface.

The governing equations for the grout surrounding the outer pipe and the soil surrounding the borehole are given as follows:

$$\rho_g c_g \frac{\partial T_g}{\partial t} = \nabla \cdot \left(\lambda_g \cdot \nabla T_g\right) + H_g \quad (6)$$

Boundary condition (Robin Type):

$$q_{nT_g} = -\Phi_{og}\left(T_o - T_g\right) - \Phi_{gs}\left(T_s - T_g\right) \text{ on } \Gamma_g \quad (7)$$

$$\rho_s c_s \frac{\partial T_s}{\partial t} = \nabla \cdot \left(\Lambda_s \cdot \nabla T_s\right) + H_s \quad (8)$$

Boundary condition (Robin Type):

$$q_{nT_s} = -\Phi_{gs}\left(T_g - T_s\right) \text{ on } \Gamma_s \quad (9)$$

in which the detailed calculation of heat transfer coefficient Φ between soil and borehole can be found in Diersch et al. (2011).

Following the DC-FEM approach, the simulation domain is divided into two compartments, including the line elements representing boreholes and the 3D prism elements standing for the surrounding subsurface. All the governing equations inside the borehole (**Eqs. 1**, **3**, **6**) are solved on 1D line elements and the surrounding subsurface equation (**Eq. 8**) is solved in 3D prism elements. The heat flux between each component inside the borehole and between the surrounding subsurface is calculated by the temperature difference and the corresponding heat transfer coefficient. They are explicitly linked and solved together with the governing equations in the numerical model. Compared with the fully discretized 3D model, the number of elements can be significantly reduced through the model implementation with DC-FEM technology (Al-Khoury et al., 2010). More detailed documentation on benchmarks and tutorials of DBHE modeling features can be found on the official website of OpenGeoSys (Bilke et al., 2020).

2.2 Model Verification

The BHE model implemented in OpenGeoSys software has previously been verified against analytical solution by Chen et al. (2020b, 2021) and monitoring data from actual projects in Europe (Meng et al., 2019; Chen et al., 2020a). The related calculation model is proved to be of the capability to reproduce the variation of long-term heat extracting performance for the DBHE system. As for the DBHE model, a thorough model validation has been conducted based on a multi-DBHE pilot project in Xi'an (Cai et al., 2021). In this study, the DBHE model established in OpenGeoSys considering the geothermal gradient is also verified based on the analytical DBHE solution proposed by Beier (2020). The setting of related parameters can be found in **Table 1** and the operation time is set as one entire heating season.

The verification results (see **Figure 2**) show that the circulation temperatures calculated by the OpenGeoSys match well against Beier's model. At the end of the heating season, the maximum difference between the results calculated by two models is no more than 0.57°C (less than 2.2%). Throughout the simulation, the inlet and outlet temperatures calculated by the OpenGeoSys are slightly higher than Beier's model, which can be explained by the different calculation method in non-dimensional number within the DBHE between the OpenGeoSys and Beier's model. This verification ensures that our model has enough accuracy and can be used in investigating the long-term performance of the DBHE.

2.3 Model Configuration

Based on the parameter settings in **Table 1**, the models in this study are then further extended for several different drilling depths from approximately 2,000 to 3,000 m to meet our purpose in solving the scientific questions proposed in **Section 1**. According to the published geological data (Ren et al., 2020) and *in situ* test results from realistic projects (Cai et al., 2021), the scenarios are configured based on the geological conditions and geothermal features in Weihe Basin (see **Table 2**).

For the boundary conditions of the model, the average ambient air temperature of 14.8°C (Dirichlet type) and typical geothermal heat flux 65 mW/m^2 (Neumann type) are imposed at the top and bottom surface of the domain, respectively. Moreover, based on the assumption of homogeneous media in the subsurface, the typical linear geothermal gradient in Xi'an is set as 35.0°C/km (Ren et al., 2020), serving as the initial condition of the model. To prevent the thermal plume from interfering with the domain boundary, the domain size is set to be 300 × 300 × (depth + 200) m. The mesh density and time step size of the simulation are chosen based on our previous work (Cai et al., 2021), in which the time step size of the simulation is first chosen to be 1 h in the heating season and later increased to 6 h during the recovery period. Furthermore, the heat pump and water pump units are introduced to our model. The performance curve of the heat pump is selected from a reference sample of heat pump manufacturer (Hein et al., 2016), which will be explained in detail in the next section. All the aforementioned simulation scenarios are all run for 15 years, which is the typical life-cycle span of an HVAC (heating, ventilation, and air conditioning) system in China (Chen S. et al., 2019).

3 LONG-TERM ECONOMIC EVALUATION APPROACH

In this section, a comprehensive approach for the long-term economic evaluation of the DBHE heating system (see **Figure 1**) is proposed, in which the heat extraction performance, electricity consumption of heat pump and circulation pump, and initial costs are all taken into account.

To facilitate the economic analysis and not hinder the correctness of the main conclusion, several assumptions made in this study are listed as follows:

- The economic analysis of the DBHE heating system will just focus on the variation of performance of heat source side, which contains the DBHE, circulation pump of heat source, and heat pump. The range of drilling depth is set from 2,000 to 3,000 m in corroding to the technical regulation for DBHE heating system in Shaanxi Province (DBJ61/T166, 2020). Also, the prescriptive heating season for Weihe Basin, Shaanxi, lasts 4 months, from November 15 to the next March 15.
- The circulation temperatures for user side and building heating load are supposed to be constant so that the performance

TABLE 1 | Detailed parameters of the simulated DBHE for both OpenGeoSys and Beier's model

Item	Parameter	Value	Unit
Borehole	Borehole depth	2,500	m
	Borehole diameter	0.2413	m
	Outer diameter of inner tube	0.1100	m
	Wall thickness of inner tube	0.0100	m
	Thermal conductivity of inner tube wall	0.42	W m^{-1} K^{-1}
	Outer diameter of outer pipe	0.1778	m
	Wall thickness of outer pipe	0.0092	m
	Thermal conductivity of outer pipe wall	40	W m^{-1} K^{-1}
	Heat extraction capacity	250	kW
Soil	Density	1.76×10^3	kg m^{-3}
	Specific heat capacity	1.43×10^3	J kg^{-1} K^{-1}
	Thermal conductivity	2.2	W m^{-1} K^{-1}
Grout	Density	2.19×10^3	kg m^{-3}
	Specific heat capacity	1.73×10^3	J kg^{-1} K^{-1}
	Thermal conductivity	1.4	W m^{-1} K^{-1}
Circulating fluid	Thermal conductivity	0.6	W m^{-1} K^{-1}
	Specific heat capacity	4.19×10^3	J kg^{-1} K^{-1}
	Density	998	kg m^{-3}
	Dynamic viscosity	9.31×10^{-4}	kg m^{-1} s^{-1}

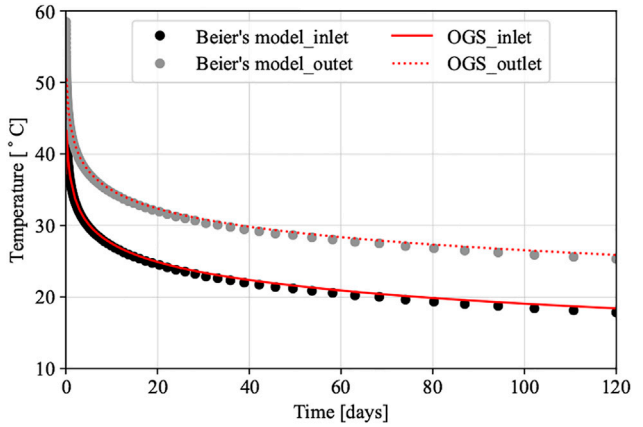

FIGURE 2 | Verification of the proposed DBHE model based on OpenGeoSys against Beier's analytical solution.

TABLE 2 | Detailed geophysical parameters of Weihe Basin, China

Geological formation	Depth (m)	Geophysical parameters[1]		
		λ	ρC_p	α
Clay	0~500	1.6	2.52×10^6	2.85×10^{-3}
Gravel	500~1,300	1.8	1.91×10^6	3.39×10^{-3}
Mudstone	1,300~2,000	2.0	1.88×10^6	3.84×10^{-3}
Sandstone	> 2,000	2.5	1.96×10^6	4.59×10^{-3}

λ denotes the thermal conductivity (W m^{-1} K^{-1}); ρC_p is the volumetric heat capacity (J m^{-3} K^{-1}); α is the thermal diffusivity (m^2/h).

of heat pump will be just in correlation to the inlet temperature of heat pump on the source side. According to the reference sample (Hein et al., 2016), the COP of heat pump is defined as

$$COP_{hp} = a_1 + b_1 \times T_{in,hp} \tag{10}$$

where a_1 and b_1 are the coefficients, which are 3.925 and .083, respectively.

Based on the definition of COP, the hourly electricity cost of heat pump is calculated as

$$C_{hp,h} = \frac{Q_{DBHE}}{COP_{hp} - 1} \times \Delta t \times E_p \tag{11}$$

where Q_{DBHE} is the heat extraction rate of the DBHE (kW). Δt is the operation time, and the interval used in this work is 1 h. E_p is the electricity price, which is set to 0.7669 Yuan/kWh (Shaanxi, 2018).

- The DBHE will suffer a performance attenuation during long-term operation. Therefore, for the DBHE heating system equipped with different depths of boreholes, the index used in this study is to let the COP of the heat pump be at the same level at the end of the running period. Also, to prevent pollution on deep groundwater resources, the anti-freeze solution is not allowed to add to the DBHE system (DBJ61/T166, 2020). Thus, the inlet temperature of the DBHE should not fall below 0°C to prevent freeze in pipes. With these assumptions, the maximum heat extraction capacity will be obtained for the convenience of further economic analysis.
- The geological conditions for simulation are set as the typical values of Weihe Basin. Based on our previous work (Chen C. et al., 2019), the existence of groundwater flow does not provide a notable increase of heat extraction for the DBHE so that the groundwater flow is not introduced. The drilling cost data are acquired from a local drilling company in Xi'an and summarized to a quadratic polynomial form according to the suggestions from Lukawski et al. (2014). The estimation of drilling cost (unit: Yuan) reads:

$$C_{drilling} = a_2 + b_2 \times D + c_2 \times D^2 \quad (12)$$

where D is the drilling depth (m). a_2, b_2, and c_2 are the coefficients, which are 850,909, −890, and 0.536, respectively.

- The electricity consumption of circulation pump is calculated based on the flow friction of the DBHE, which is determined by the Darcy–Weishbach equation. The pump efficiency is set as 85%.

$$F_{DBHE} = f \times \frac{D}{d_e} \times \frac{\rho v^2}{2} \quad (13)$$

in which d_e is the equivalent diameter of pipe.

Based on the classic calculation method in hydrology, the equivalent diameter of pipe is determined by

$$d_e = \frac{4A}{X} \quad (14)$$

where A and X are the flow cross-sectional area and perimeter of the flow area, respectively.

The Darcy friction factor f is calculated by Churchill correlation (Churchill, 1977):

$$f^{-1} = \left(\frac{1}{\left[\left(\left(\frac{8}{\mathrm{Re}}\right)^{10} + \left(\frac{\mathrm{Re}}{36\,500}\right)^{20} \right) \right]^{1/2}} + \left[2.21 \left(\ln \frac{\mathrm{Re}}{7} \right) \right]^{10} \right)^{1/5} \quad (15)$$

Based on the similar concept of levelized cost of energy and evaluation criterion in shallow GSHP system (Cui et al., 2019), a novel index of levelized cost of heating capacity (LCOH) is proposed for the DBHE heating system in this study. The heat extraction capacity of the DBHE and electricity consumption of corresponding heat pumps and water pumps are all involved in this index, in which the dynamic COP of heat pump and circulation resistance are considered. The definition of LCOH index for the DBHE heating system reads:

$$LCOH = \frac{C_{ini.} + \sum_{i=1}^{N} \frac{C_{ann.}}{(1+r)^i}}{\sum_{i=1}^{N} \frac{Q_{tot.}}{(1+r)^i}} \quad (16)$$

where $C_{ini.}$ and $C_{ann.}$ are initial cost and annual cost of the DBHE heating system, respectively. N is the typical operation period of HVAC system, which is set to 15 years (Chen S. et al., 2019). r is the discount rate, which is 6% for typical HVAC system (Khadra et al., 2020). $Q_{tot.}$ is the total heating amount supplied from the DBHE heating system to the building sector, including the heat extraction of the DBHE, and the power consumed by heat pumps and circulation pumps. Based on this economic evaluation approach and related index, the economic analysis for the DBHE heating system in Weihe Basin will be carried out in the next section.

4 RESULTS

In this section, the long-term heat extraction performance of the DBHE with different depths will be assessed and thorough economic analysis for the DBHE heating system will be executed following the approach proposed in **Section 3**.

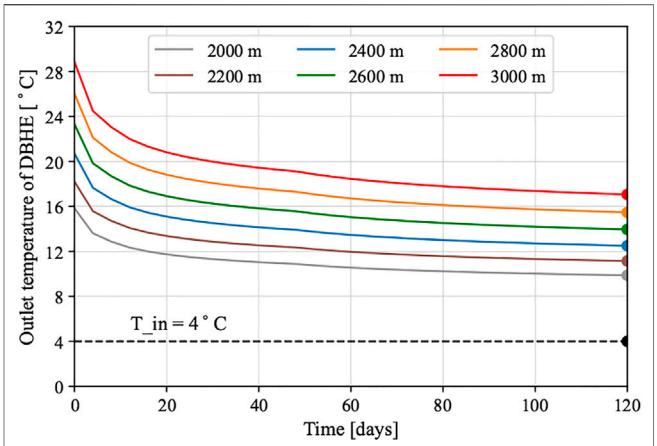

FIGURE 3 | Thermal performance test of heat extraction capacity for the DBHE with different drilling depths.

4.1 Determination of Tentative Heat Extraction Capacity for Different Depths

Generally, there are two types of boundary conditions imposing on the DBHE, including fixed inlet temperature and fixed heat extraction rate, which correspond to the so-called thermal performance test and thermal response test (Choi et al., 2019). For a certain depth of the DBHE, to quantify its tentative heat extraction capacity, the boundary condition of fixed inlet temperature is chosen for the DBHE in this section. All inlet temperatures are fixed at 4°C, which is the threshold of circulation temperature in the heat pump unit (Cai et al., 2021). The flow rate of circulation fluid is 0.01 m^3/s for different depths of the DBHE, including 2,000, 2,200, 2,400, 2,600, 2,800, and 3,000 m. The other DBHE parameter setting and subsurface properties are listed in **Table 1** and **Table 2**.

The outlet temperature evolution of six DBHEs with different depths over the first heating season is presented in **Figure 3**. For all the tentative tests with the chosen parameters for the DBHE with different depths, the outlet temperatures tend to have a rapid dropdown at the first couple of days. For example, the outlet temperature of the DBHE with 3,000 m decreases by 10.85°C in the first 60 days, while the temperature drop is only 0.95°C in the next 60 days. The trend of outlet temperature variation indicates that the heat extraction rate of the DBHE after 60 days does not change too much, from 587.02 to 548.45 kW for the DBHE with 3,000 m depth.

When looking into the outlet temperatures among DBHEs with different depths, it has a higher value with deeper depth. While reaching the end of the heating season (marked in **Figure 3**), the outlet temperatures for six different depths are 9.87, 11.15, 12.51, 13.95, 15.47, and 17.06°C, respectively. In a conservative way of calculating tentative heat extraction capacity, the corresponding values are calculated according to the temperature difference at the end of heating season in

Figure 3. It is found that the calculated tentative heat extraction capacity increases with the increment of drilling depth of the DBHE. From the depth of 2,000–3,000 m, the tentative heat performance capacity (black numbers above the bar) increases by 122.3%, from 246.72 to 548.45 kW. This implies that a deeper DBHE has a more considerable heat extraction potential.

4.2 Long-Term Heat Extraction Performance of the DBHE With Different Depths

In a more practical case, the inlet temperature of DBHE cannot be fixed in long-term operation, while the heating demand is usually kept fixed. Therefore, for long-term simulation of the DBHE, the fixed heat extraction rate is imposed to mimic real-world projects. In this section, the fixed heat extraction rate is imposed according to the calculated tentative heat extraction capacities from short-term thermal performance tests in the previous section. If the temperature drop of circulation temperature after the long-term operation is too large (below 0°C and have a risk of freeze) or too small (the DBHE can provide higher heating capacity), the heat extraction capacity will be adjusted until a proper value is obtained. It also needs to be mentioned that the flow rate for each DBHE with different depths is not the same. It is designed based on both the heat extraction rate and the typical temperature difference consumed by evaporator in heat pump. By adopting the official engineering standard in China (GB50189, 2015), the typical temperature difference of heat exchanger (evaporator) equipped in the heat pump unit is set to 10°C.

The variation of circulation temperature of the DBHE with different depth under 15-year operation is presented in **Figure 4**. It is worth noting that the temperature dropdown of several scenarios in **Figure 4A** is too large (below 0°C) to maintain the system operation, which means the tentative heat extraction capacities are slightly overestimated by the short-term thermal performance test. Therefore, the heat extraction rates used in long-term simulation for the DBHE with shallower depths are conducted with a slight reduction (no more than 5%; see the red values in **Figure 6**) of original tentative values. The evolution of circulation temperature with the adjusted heat extraction capacity is depicted in **Figure 4B**.

In **Figure 4A**, the inlet temperatures for scenarios with the depth from 2,000 to 2,800 m have a quick drop-down to under zero and the system will not work anymore due to the freezing of circulation fluid. As for the scenario with 3,000 m depth of the borehole, the long-term performance of the DBHE system under its corresponding tentative heat extraction capacity just reached 0°C inlet temperature threshold at the end of the 15th heating season. This indicates that the corresponding heat extraction rate has reached the upper limit of heat extraction potential. However, for the other five scenarios, this tentative heat extraction rate is beyond these upper potentials and is unsustainable in 15 years.

To make all the scenarios fully conform to the inlet temperature and COP index, **Figure 4B** presents the circulation fluid temperature evolution with adjusted heat extraction rate. Under the adjusted heat extraction rate, the inlet temperatures at the end of the last heating season are higher than 0°C for all six scenarios.

Furthermore, **Figure 5** illustrates the soil temperature profiles at the depth of 200 m above each DBHE bottom for all the six scenarios at the first and 15th year. As shown in **Figure 5A,B**, the soil temperature in the subsurface surrounded the DBHE suffers severe drop-down compared with the initial value, which is caused by the heat extraction of the DBHE. After 15-year operation, the thermally affected radius of every DBHE is about 60 m. In every year, the heating season lasts 4 months, then another 8 months to recovery. **Figure 5C,D** shows the temperature distribution after the first and last year. It can be seen that the soil temperature around each DBHE has a recovery effect. For example, for the 2,000 m DBHE, the soil temperature at the end of the last recovery season is 69.8°C, which is 51.9°C higher than the temperature value at the end of the last heating season.

For the six scenarios, the adjusted heat extraction rates presented in **Figure 6** can be regarded as the upper limit of the heat extraction capacity. For the DBHE with depth of 2,000 m, the adjusted heat extraction rate is 5% lower than the tentative value predicted by the short-term thermal performance test. With the increased depth, the tentative heat extraction rate is more close to the upper limit of heat extraction potential. The reduction proportion of tentative heat extraction rate is gradually decreased from 4 to 1% for the depth varied from 2,200 to 2,800 m. Finally, by applying this adjusted heat extraction rate, all the circulation temperatures under different drilling depths of DBHE are at the same level, which is of an excellent agreement to the inlet temperature and COP criterion.

4.3 Variation of COP in Long-Term Operation

To conduct a comprehensive economic analysis for the DBHE heating system, the variation of performance of heat pump is of significance to be evaluated. Based on the assumption in **Section 3**, the COP of heat pump is only changed according to the outlet temperature of DBHE.

With the adjusted heat extraction rate imposed on the DBHE, the heat pump COP values over 15 heating seasons are presented in **Figure 7** for the six different DBHE depths. In the first year of operation, the DBHE heating system with a deeper drilling borehole has a higher COP value of the heat pump. The COP for the scenario with 3,000 m depth of DBHE is 5.95, while the COP for the system with 2,000 m depth of DBHE is just 5.59. As the operation goes on, the COP values among the DBHE heating system with different drilling depths tend to be identical. The DBHE heating system with a deeper drilling depth maintains a larger COP in a couple of days at the beginning of every heating season. At the last heating season, the COP value for DBHE depth from 2,000 to 3,000 m increases from 5.56 to 5.87. Over the operation of 15 heating seasons, the minimum COP value of the heat pump is 4.74 for all six scenarios. It proved that using the DBHE heating system can have very high efficiency. Nevertheless, the applicability of the DBHE heating system in Weihe Basin is

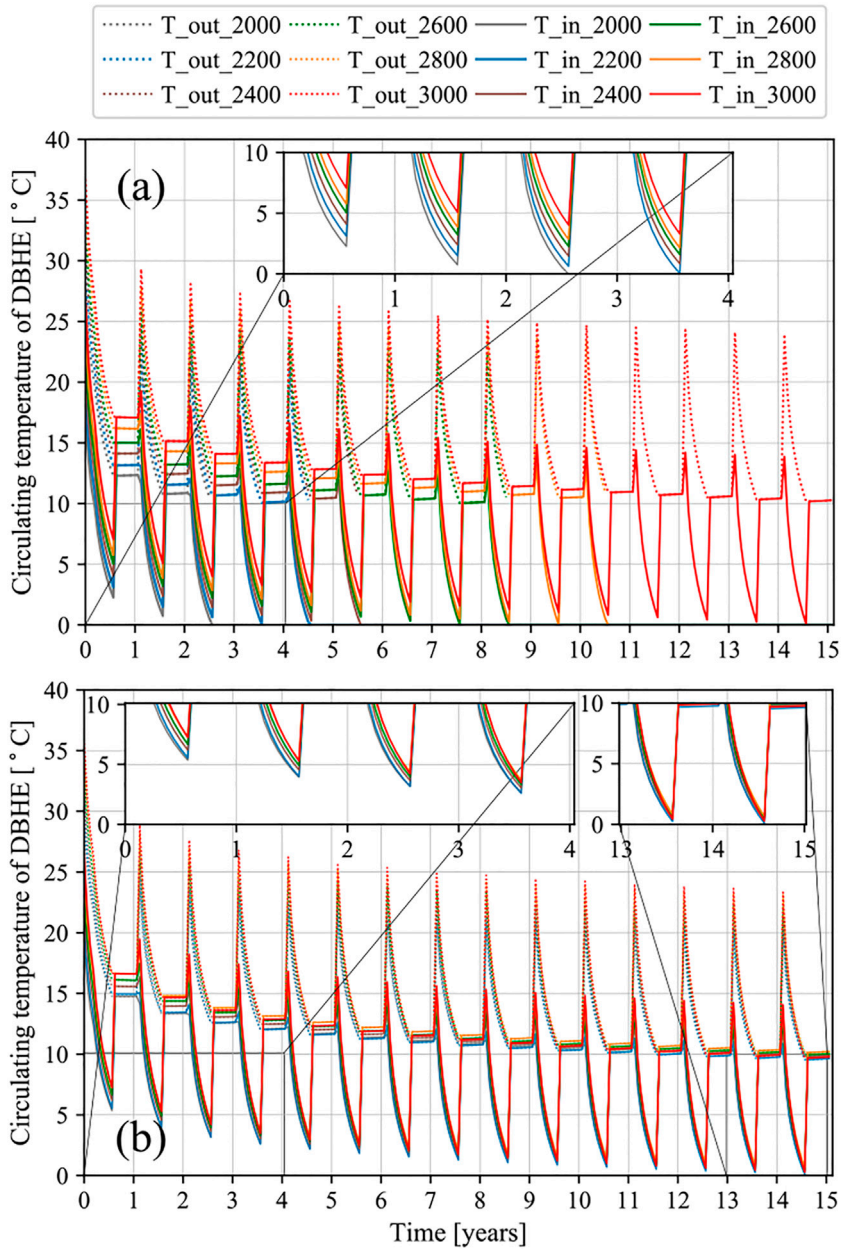

FIGURE 4 | Long-term heat extraction performance of the DBHE **(A)** with the tentative heat extraction capacity **(B)** with the adjusted heat extraction capacity.

not only determined by the high efficiency of the system but also the sustainable economic feasibility.

4.4 Variation of Operational Costs and Overall Economic Analysis for the DBHE Heating System

Based on the long-term heat extraction capacity determined in **Section 4.2**, economic analyses for the DBHE heating system are performed over long-term operation. In this section, according to the calculation method stated in 3, the consumption of heat pump and circulation pump can be addressed based on the circulation temperature variation of the DBHE and electricity price. The corresponding parameters of Weihe Basin in 3 are used for the calculation of consumption. The total accumulated electricity consumption of heat pump and circulation pump during 15 heating seasons and also the average COP of heat pump are presented in **Figure 8**.

It can be seen in **Figure 8** that the total electricity consumption of the circulation pump considerably rises with a deeper drilling depth of the DBHE. For the DBHE heating system with depth of 2,000 m, the total electricity consumption of heat pump and circulation pump is 2.40×10^6 kWh and 1.35×10^5 kWh, while for the 3,000 m DBHE, it was 5.48×10^6 kWh for the electricity

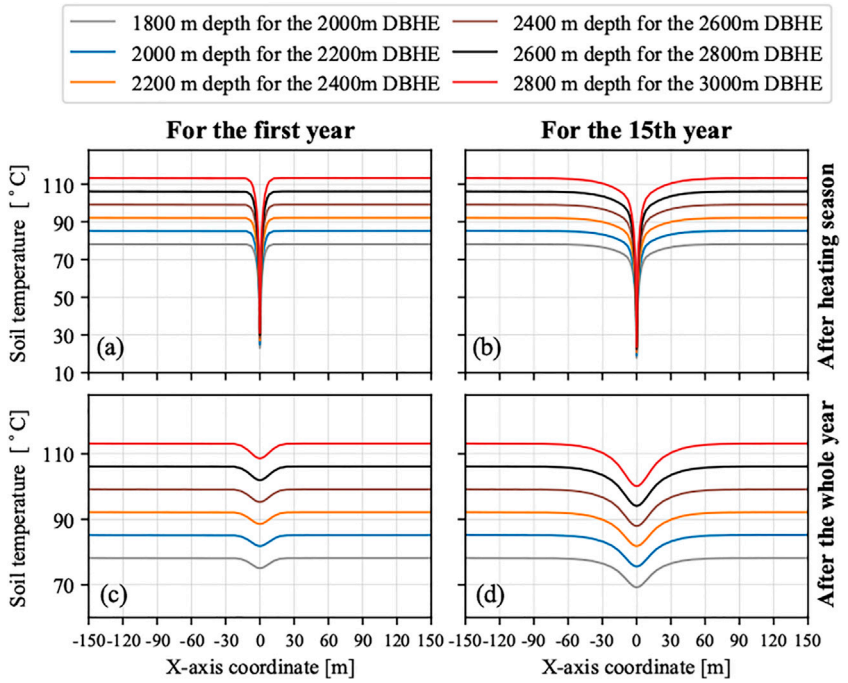

FIGURE 5 | Soil temperature distribution for the DBHE with different drilling depths **(A)** at the end of the first heating season; **(B)** at the end of the last heating season; **(C)** at the end of first year; **(D)** at the end of last year.

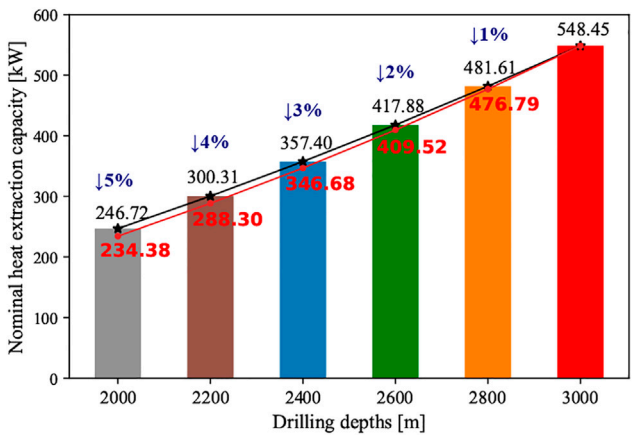

FIGURE 6 | Determination of tentative heat extraction capacity for the DBHE with different drilling depths.

consumption of heat pump and 2.09 × 10^6 kWh for the circulation pump. The total electricity consumption by heat pump and circulation pump increases by 2.28 and 15.5 times, respectively. The significant increment of electricity consumed by circulation pump can be explained by the higher circulation flow rate (0.013 m^3/s) for the 3,000 m DBHE, compared with flow rate (0.0056 m^3/s) of 2,000 m DBHE. In addition, the reason for higher total electricity consumption by heat pump is the outlet temperature from the DBHE. As indicated by **Figure 4B**, after operation of 15 heating seasons, the average outlet temperature of 3,000 m DBHE is a little higher than the others, leading to about one times increase based on the 2,000 m DBHE. Also, the black line gives the variation of COP of the DBHE heating system with different drilling depths. The DBHE system with deeper depth produces a higher heat extraction amount and has a similar variation trend of circulation temperature. The slight increment of outlet temperature will result in higher COP for the heat pump and less power consumed. This phenomenon can also explain the slow increase in the total electricity consumption of heat pumps from the aspects of COP. In total, the consumption of heat pumps and circulation pumps has a prominent promotion with a deeper drilling depth of the DBHE.

From the aforementioned investigation, it is clearly known that the DBHE heating system with deeper drilling depth has higher considerable heat extraction rate while it assumes more electricity on heat pump and circulation pump. Therefore, a combined economic analysis for the DBHE heating system during long-term operation is necessary to illustrate the system applicability. **Figure 9A** depicts the LCOH and net present value (NPV) for the DBHE heating system with different depths. With deeper depth of the DBHE, the LCOH of the DBHE heating system tends to decrease from 0.594 Yuan (2,000 m) to 0.568 Yuan (2,600 m). Then the LCOH shows a slow increase to 0.573 Yuan (3,000 m), which means that the DBHE heating system with a drilling depth of 2,600 m has the slowest LCOH. For the DBHE heating system with depth of 2,600 m, its levelized cost of total heating amount is lower than other systems with shallower or deeper depths, which can give reference to

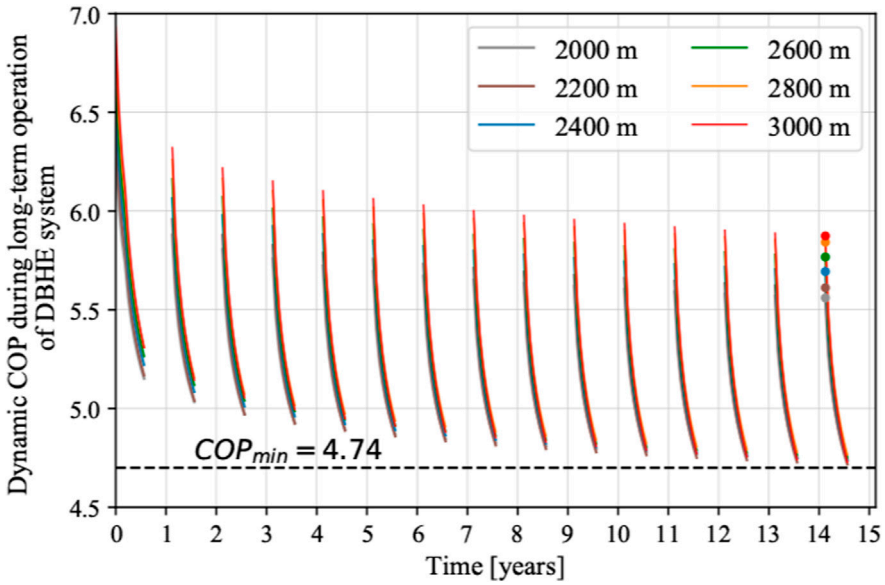

FIGURE 7 | Variation of COP for the DBHE heating system with different drilling depths.

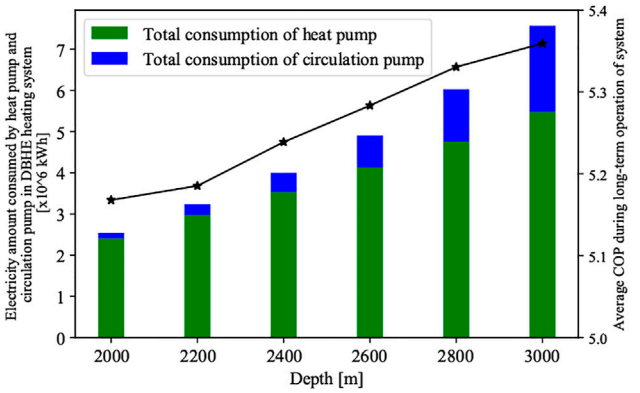

FIGURE 8 | Electricity amount consumed by heat pump and circulation pump in the DBHE heating system.

parameter design in applying the DBHE heating system in Weihe Basin. **Figure 9B** illustrates the NPV variation over long-term operation of the DBHE with the depth of 2,600 m. It can be seen that the NPV value shows an approximate-linear increase over the operation of 15 years. After 10-year operation, the NPV turns to be higher than zero, which illustrates that the pay-off time of the 2,600 m DBHE is around 10 years.

5 DISCUSSION

5.1 Comparison With Other Published DBHE Models

In comparison with other two-dimensional DBHE models (Nian et al., 2019; Brown et al., 2021), the 3D DBHE model presented in this work is also well applicable in modeling the heat extraction performance of the DBHE (Kong et al., 2017), especially for the flexible boundary conditions and segmented soil properties. Furthermore, the proposed model has been validated by several experimental data, including northwestern and northeastern China (Huang et al., 2020; Cai et al., 2021), and other regions (Chen et al., 2020a).

It is worth noting that there are no hydraulic governing equations in the current DBHE model, which means the thermal properties of the circulation fluid cannot be changed according to the pressure values. This assumption is reasonable for a DBHE system with a depth shallower than 3 km under a normal geothermal gradient as concluded by Chen et al. (2019). For a DBHE system with a depth more than 3 km and a very high geothermal gradient (Doran et al., 2021), the pressure- and temperature-dependent heat transfer coefficients have to be taken into account in the DBHE simulation. However, this is not the case discussed in this work in Weihe Basin. In Weihe Basin, the average geothermal gradient is lower than 0.04°C/m (Ren et al., 2020). For a specific case with a very higher geothermal gradient, e.g., in Tibet, China, the system utilized for geothermal heat extraction could be hydrothermal system or enhanced geothermal system instead of a closed-loop system to have better performance and efficiency.

5.2 Replicability and Applicability of the Proposed Evaluation Method

Although this study presents a thorough and comprehensive approach to evaluate the economic feasibility for the DBHE heating system, the related conclusion is very site specific, totally based on the local parameters in Weihe Basin. For

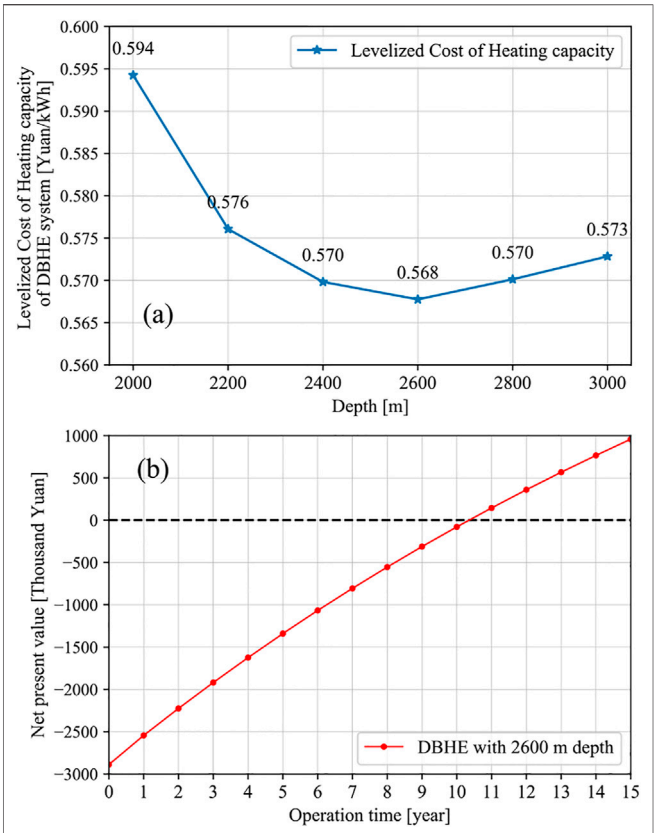

FIGURE 9 | The LCOH **(A)** and NPV **(B)** value for the DBHE heating system with different drilling depths.

other regions, a similar approach should be performed according to the local conditions, most notably the drilling cost, geological properties, and operation period. In addition, with the urgent need for the reduction of carbon emission, the carbon trade market will make a difference in evaluating the economic feasibility of renewable energy technology. Using geothermal energy as its energy source will profit more because it can earn an extra carbon index sold in the carbon trade market.

6 CONCLUSION

In this study, a series of numerical models based on the typical geological conditions in Weihe Basin, China, have been carried out to simulate the long-term heat extraction performance. The economic feasibility of the DBHE heating systems with different drilling depths has been evaluated as well. Short-term thermal performance tests have been conducted to get the tentative heat extraction capacity and the adjusted heat extraction rates used for long-term performance simulation of the DBHE. Then, according to the local electricity price and calculation of power assumed by the heat pump and circulation pump, a combined economic analysis for the DBHE heating system is performed based on the long-term simulation results. To be more specific:

- For a deeper DBHE, the calculated tentative heat extraction rate by thermal performance test is much higher. The tentative heat performance capacity increases from 246.72 kW of 2,000 m DBHE to 548.45 kW of 3,000 m DBHE.
- The tentative heat extraction slightly overestimates the upper limit of heat extraction potential of the DBHE. A slight reduction (no more than 5%) gives a more reasonable heat extraction rate for the long-term operation of the DBHE.
- With the adjusted heat extraction rate imposed on the DBHE, the DBHE heating system with a deeper drilling borehole has a higher COP value of the heat pump in the first year of operation. Over the operation of 15 heating seasons, the minimum COP value of the heat pump is 4.74 for all six scenarios.
- The total electricity consumption of heat pumps and circulation pumps have a prominent promotion with a deeper drilling depth of the DBHE. For the depth of 2,600 m, its LCOH is lower than other systems with other depths, so that it is the better choice for application in Weihe Basin.

DATA AVAILABILITY STATEMENT

The raw data supporting the conclusion of this article will be made available by the authors, without undue reservation.

AUTHOR CONTRIBUTIONS

WC: conceptualization, methodology, software, validation, writing—original draft, visualization. FW: conceptualization, formal analysis, project administration, funding acquisition, supervision. JJ: methodology, investigation, validation. ZW: methodology, visualization. JL: formal analysis, investigation. CC: methodology, software, validation, writing—review and editing.

FUNDING

This research is financially supported by the Key Research and Development Project of Shaanxi Province (2020ZDLSF06-08), as well as the Open Project of Key Laboratory of Coal Resources Exploration and Comprehensive Utilization (KF 2021-1), which is funded by the Chinese Ministry of Natural Resources.

ACKNOWLEDGMENTS

The authors would like to thank Prof. Zhanli Ren for his helpful advice on selecting geological parameters of Weihe Basin and Prof. Beier for his public MATLAB program on the analytical solutions. Also, the authors would like to thank all the reviewers and editors for their constructive comments on this paper.

REFERENCES

Al-Khoury, R., Kölbel, T., and Schramedei, R. (2010). Efficient Numerical Modeling of Borehole Heat Exchangers. *Comput. Geosciences* 36, 1301–1315. doi:10.1016/j.cageo.2009.12.010

Anderson, A., and Rezaie, B. (2019). Geothermal Technology: Trends and Potential Role in a Sustainable Future. *Appl. Energ.* 248, 18–34. doi:10.1016/j.apenergy.2019.04.102

Beier, R. A., Acuña, J., Mogensen, P., and Palm, B. (2014). Transient Heat Transfer in a Coaxial Borehole Heat Exchanger. *Geothermics* 51, 470–482. doi:10.1016/j.geothermics.2014.02.006

Beier, R. A. (2020). Thermal Response Tests on Deep Borehole Heat Exchangers with Geothermal Gradient. *Appl. Therm. Eng.* 178, 115447. doi:10.1016/j.applthermaleng.2020.115447

Bilke, L., Shao, H., Chen, S., and Cai, W. (2020). OpenGeoSys Tutorial. Available at: https://www.opengeosys.org/docs/userguide/basics/introduction/.

Brown, C. S., Cassidy, N. J., Egan, S. S., and Griffiths, D. (2021). Numerical Modelling of Deep Coaxial Borehole Heat Exchangers in the Cheshire basin, UK. *Comput. Geosciences* 152, 104752. doi:10.1016/j.cageo.2021.104752

Cai, W., Wang, F., Chen, S., Chen, C., Liu, J., Deng, J., et al. (2021). Analysis of Heat Extraction Performance and Long-Term Sustainability for Multiple Deep Borehole Heat Exchanger Array: A Project-Based Study. *Appl. Energ.* 289, 116590. doi:10.1016/j.apenergy.2021.116590

Cai, W., Wang, F., Liu, J., Wang, Z., and Ma, Z. (2019). Experimental and Numerical Investigation of Heat Transfer Performance and Sustainability of Deep Borehole Heat Exchangers Coupled with Ground Source Heat Pump Systems. *Appl. Therm. Eng.* 149, 975–986. doi:10.1016/j.applthermaleng.2018.12.094

Chen, C., Cai, W., Naumov, D., Tu, K., Zhou, H., Zhang, Y., et al. (2021). Numerical Investigation on the Capacity and Efficiency of a Deep Enhanced U-Tube Borehole Heat Exchanger System for Building Heating. *Renew. Energ.* 169, 557–572. doi:10.1016/j.renene.2021.01.033

Chen, C., Shao, H., Naumov, D., Kong, Y., Tu, K., and Kolditz, O. (2019a). Numerical Investigation on the Performance, Sustainability, and Efficiency of the Deep Borehole Heat Exchanger System for Building Heating. *Geothermal Energy* 7, 18. doi:10.1186/s40517-019-0133-8

Chen, S., Cai, W., Witte, F., Wang, X., Wang, F., Kolditz, O., et al. (2020a). Long-term thermal Imbalance in Large Borehole Heat Exchangers Array-A Numerical Study Based on the Leicester Project. *Energy and Buildings* 231, 110518. doi:10.1016/j.enbuild.2020.110518

Chen, S., Witte, F., Kolditz, O., and Shao, H. (2020b). Shifted thermal Extraction Rates in Large Borehole Heat Exchanger Array–A Numerical experiment. *Appl. Therm. Eng.* 167, 114750. doi:10.1016/j.applthermaleng.2019.114750

Chen, S., Zhang, Q., Li, H., Mclellan, B., Zhang, T., and Tan, Z. (2019b). Investment Decision on Shallow Geothermal Heating & Cooling Based on Compound Options Model: A Case Study of china. *Appl. Energ.* 254, 113655. doi:10.1016/j.apenergy.2019.113655

Choi, W., Kikumoto, H., and Ooka, R. (2019). Critical Comparison between thermal Performance Test (Tpt) and thermal Response Test (Trt): Differences in Heat Transfer Process and Extractable Information. *Energ. Convers. Management* 199, 111967. doi:10.1016/j.enconman.2019.111967

Churchill, S. W. (1977). Comprehensive Correlating Equations for Heat, Mass and Momentum Transfer in Fully Developed Flow in Smooth Tubes. *Ind. Eng. Chem. Fundamentals* 16, 109–116. doi:10.1021/i160061a021

Cui, Y., Zhu, J., Twaha, S., Chu, J., Bai, H., Huang, K., et al. (2019). Techno-economic Assessment of the Horizontal Geothermal Heat Pump Systems: A Comprehensive Review. *Energ. Convers. Management* 191, 208–236. doi:10.1016/j.enconman.2019.04.018

DBJ61/T166 (2020). *Technical Regulation for Medium Deep Geothermal Buried Pipe Heating System*. Shaanxi Province: Department of Housing and Urban-Rural Development. [Dataset].

De La Peña, L., Guo, R., Cao, X., Ni, X., and Zhang, W. (2022). Accelerating the Energy Transition to Achieve Carbon Neutrality. *Resour. Conservation Recycling* 177, 105957.

Deng, J., He, S., Wei, Q., Li, J., Liu, H., Zhang, Z., et al. (2020). Field Test and Optimization of Heat Pumps and Water Distribution Systems in Medium-Depth Geothermal Heat Pump Systems. *Energy and Buildings* 209, 109724. doi:10.1016/j.enbuild.2019.109724

Deng, J., Wei, Q., Liang, M., He, S., and Zhang, H. (2019). Field Test on Energy Performance of Medium-Depth Geothermal Heat Pump Systems (Md-ghps). *Energy and Buildings* 184, 289–299. doi:10.1016/j.enbuild.2018.12.006

Dias, J. M., and Costa, V. A. (2018). Adsorption Heat Pumps for Heating Applications: A Review of Current State, Literature Gaps and Development Challenges. *Renew. Sustainable Energ. Rev.* 98, 317–327. doi:10.1016/j.rser.2018.09.026

Diersch, H.-J., Bauer, D., Heidemann, W., Rühaak, W., and Schätzl, P. (2011). Finite Element Modeling of Borehole Heat Exchanger Systems: Part 1. Fundamentals. *Comput. Geosciences* 37, 1122–1135. doi:10.1016/j.cageo.2010.08.003

Doran, H. R., Renaud, T., Falcone, G., Pan, L., and Verdin, P. G. (2021). Modelling an Unconventional Closed-Loop Deep Borehole Heat Exchanger (Dbhe): Sensitivity Analysis on the Newberry Volcanic Setting. *Geothermal Energy* 9, 1–24. doi:10.1186/s40517-021-00185-0

Fang, L., Diao, N., Shao, Z., Zhu, K., and Fang, Z. (2018). A Computationally Efficient Numerical Model for Heat Transfer Simulation of Deep Borehole Heat Exchangers. *Energy and Buildings* 167, 79–88. doi:10.1016/j.enbuild.2018.02.013

Gb50189 (2015). *Design Standard for Energy Efficiency of Public Buildings*. PR China: Ministry of Housing and Urban-Rural Development. [Dataset].

Hein, P., Kolditz, O., Görke, U.-J., Bucher, A., and Shao, H. (2016). A Numerical Study on the Sustainability and Efficiency of Borehole Heat Exchanger Coupled Ground Source Heat Pump Systems. *Appl. Therm. Eng.* 100, 421–433. doi:10.1016/j.applthermaleng.2016.02.039

Hu, X., Banks, J., Wu, L., and Liu, W. V. (2020). Numerical Modeling of a Coaxial Borehole Heat Exchanger to Exploit Geothermal Energy from Abandoned Petroleum wells in Hinton, Alberta. *Renew. Energ.* 148, 1110–1123. doi:10.1016/j.renene.2019.09.141

Huang, Y., Zhang, Y., Xie, Y., Zhang, Y., Gao, X., and Ma, J. (2020). Field Test and Numerical Investigation on Deep Coaxial Borehole Heat Exchanger Based on Distributed Optical Fiber Temperature Sensor. *Energy* 210, 118643. doi:10.1016/j.energy.2020.118643

Javadi, H., Ajarostaghi, S. S. M., Rosen, M. A., and Pourfallah, M. (2019). Performance of Ground Heat Exchangers: A Comprehensive Review of Recent Advances. *Energy* 178, 207–233. doi:10.1016/j.energy.2019.04.094

Khadra, A., Hugosson, M., Akander, J., and Myhren, J. A. (2020). Economic Performance Assessment of Three Renovated Multi-Family Buildings with Different HVAC Systems. *Energy and Buildings* 224, 110275. doi:10.1016/j.enbuild.2020.110275

Kohl, T., Brenni, R., and Eugster, W. (2002). System Performance of a Deep Borehole Heat Exchanger. *Geothermics* 31, 687–708. doi:10.1016/s0375-6505(02)00031-7

Kohl, T., Salton, M., and Rybach, L. (2000). "Data Analysis of the Deep Borehole Heat Exchanger Plant Weissbad (Switzerland)," in *Proceedings World Geothermal congress*. Kyushu-Tohoku, Japan, 3459–3464.

Kolditz, O., Bauer, S., Bilke, L., Böttcher, N., Delfs, J.-O., Fischer, T., et al. (2012). Opengeosys: an Open-Source Initiative for Numerical Simulation of Thermo-Hydro-Mechanical/chemical (Thm/c) Processes in Porous media. *Environ. Earth Sci.* 67, 589–599. doi:10.1007/s12665-012-1546-x

Kong, Y., Chen, C., Shao, H., Zhonghe, P., Liangping, X., and Jiyang, W. (2017). Principle and Capacity Quantification of Deep-Borehole Heat Exchangers. *Chin. J. Geophys.* 60, 4741–4752. doi:10.6038/cjg20171216

Le Lous, M., Larroque, F., Dupuy, A., and Moignard, A. (2015). Thermal Performance of a Deep Borehole Heat Exchanger: Insights from a Synthetic Coupled Heat and Flow Model. *Geothermics* 57, 157–172. doi:10.1016/j.geothermics.2015.06.014

Li, C., Guan, Y., Liu, J., Jiang, C., Yang, R., and Hou, X. (2020). Heat Transfer Performance of a Deep Ground Heat Exchanger for Building Heating in Long-Term Service. *Renew. Energ.* 166, 20–34. doi:10.1016/j.renene.2020.11.111

Lin, J., and Lin, B. (2019). The Actual Heating Energy Conservation in china: Evidence and Policy Implications. *Energy and Buildings* 190, 195–201. doi:10.1016/j.enbuild.2019.03.004

Liu, J., Wang, F., Cai, W., Wang, Z., and Li, C. (2020). Numerical Investigation on the Effects of Geological Parameters and Layered Subsurface on the thermal

Performance of Medium-Deep Borehole Heat Exchanger. *Renew. Energ.* 149, 384–399. doi:10.1016/j.renene.2019.11.158

Lukawski, M. Z., Anderson, B. J., Augustine, C., Capuano, L. E., Jr, Beckers, K. F., Livesay, B., et al. (2014). Cost Analysis of Oil, Gas, and Geothermal Well Drilling. *J. Pet. Sci. Eng.* 118, 1–14. doi:10.1016/j.petrol.2014.03.012

Lund, J. W., and Toth, A. N. (2021). Direct Utilization of Geothermal Energy 2020 Worldwide Review. *Geothermics* 90, 101915. doi:10.1016/j.geothermics.2020.101915

Luo, Y., Guo, H., Meggers, F., and Zhang, L. (2019). Deep Coaxial Borehole Heat Exchanger: Analytical Modeling and thermal Analysis. *Energy* 185, 1298–1313. doi:10.1016/j.energy.2019.05.228

Meng, B., Vienken, T., Kolditz, O., and Shao, H. (2019). Evaluating the thermal Impacts and Sustainability of Intensive Shallow Geothermal Utilization on a Neighborhood Scale: Lessons Learned from a Case Study. *Energ. Convers. Management* 199, 111913. doi:10.1016/j.enconman.2019.111913

Morita, K., Bollmeier, W. S., and Mizogami, H. (1992). *An experiment to Prove the Concept of the Downhole Coaxial Heat Exchanger (DCHE) in Hawaii*. Los Angeles, United States: Geothermal Resources Council.

Nian, Y.-L., Cheng, W.-L., Yang, X.-Y., and Xie, K. (2019). Simulation of a Novel Deep Ground Source Heat Pump System Using Abandoned Oil wells with Coaxial Bhe. *Int. J. Heat Mass Transfer* 137, 400–412. doi:10.1016/j.ijheatmasstransfer.2019.03.136

Ozgener, L., Hepbasli, A., and Dincer, I. (2007). A Key Review on Performance Improvement Aspects of Geothermal District Heating Systems and Applications. *Renew. Sustainable Energ. Rev.* 11, 1675–1697. doi:10.1016/j.rser.2006.03.006

Pan, A., Lu, L., Cui, P., and Jia, L. (2019). A New Analytical Heat Transfer Model for Deep Borehole Heat Exchangers with Coaxial Tubes. *Int. J. Heat Mass Transfer* 141, 1056–1065. doi:10.1016/j.ijheatmasstransfer.2019.07.041

Pan, S., Kong, Y., Chen, C., Pang, Z., and Wang, J. (2020). Optimization of the Utilization of Deep Borehole Heat Exchangers. *Geothermal Energy* 8, 1–20. doi:10.1186/s40517-020-0161-4

Ren, Z., Liu, R., Ren, W., Qi, K., Yang, G., Cui, J., et al. (2020). Distribution of Geothermal Field and its Controlling Factors in the Weihe basin. *ACTA GEOLOGICA SINICA* 94, 1938–1949. doi:10.1111/1755-6724.14458

Rodrigues, R., Pietzcker, R., Fragkos, P., Price, J., McDowall, W., Siskos, P., et al. (2022). Narrative-driven Alternative Roads to Achieve Mid-century Co2 Net Neutrality in Europe. *Energy* 239, 121908. doi:10.1016/j.energy.2021.121908

Salvia, M., Reckien, D., Pietrapertosa, F., Eckersley, P., Spyridaki, N.-A., Krook-Riekkola, A., et al. (2021). Will Climate Mitigation Ambitions lead to Carbon Neutrality? An Analysis of the Local-Level Plans of 327 Cities in the EU. *Renew. Sustainable Energ. Rev.* 135, 110253. doi:10.1016/j.rser.2020.110253

Sapinska-Sliwa, A., Rosen, M. A., Gonet, A., and Sliwa, T. (2016). Deep Borehole Heat Exchangers—A Conceptual and Comparative Review. *Int. J. Air-Conditioning Refrigeration* 24, 1630001. doi:10.1142/s2010132516300019

Shaanxi, P. G. (2018). Notice of Shaanxi Provincial price bureau on Adjusting Shaanxi Power Grid Electricity price. Available at: http://sndrc.shaanxi.gov.cn/zjww/jgcs/jgc/lsxx/jgysbbz/zyspjg/dl/aAj2Yj.htm.

Shao, H., Hein, P., Sachse, A., and Kolditz, O. (2016). *Geoenergy Modeling II: Shallow Geothermal Systems*. Berlin, Germany: Springer.

Śliwa, T., and Kotyza, J. (2003). Application of Existing wells as Ground Heat Source for Heat Pumps in Poland. *Appl. Energ.* 74, 3–8. doi:10.1016/S0306-2619(02)00125-3

Soltani, M., Kashkooli, F. M., Dehghani-Sanij, A., Kazemi, A., Bordbar, N., Farshchi, M., et al. (2019). A Comprehensive Study of Geothermal Heating and Cooling Systems. *Sustainable Cities Soc.* 44, 793–818. doi:10.1016/j.scs.2018.09.036

Song, X., Wang, G., Shi, Y., Li, R., Xu, Z., Zheng, R., et al. (2018). Numerical Analysis of Heat Extraction Performance of a Deep Coaxial Borehole Heat Exchanger Geothermal System. *Energy* 164, 1298–1310. doi:10.1016/j.energy.2018.08.056

Ürge-Vorsatz, D., Cabeza, L. F., Serrano, S., Barreneche, C., and Petrichenko, K. (2015). Heating and Cooling Energy Trends and Drivers in Buildings. *Renew. Sustainable Energ. Rev.* 41, 85–98.

Wang, Z., Wang, F., Liu, J., Ma, Z., Han, E., and Song, M. (2017). Field Test and Numerical Investigation on the Heat Transfer Characteristics and Optimal Design of the Heat Exchangers of a Deep Borehole Ground Source Heat Pump System. *Energ. Convers. Management* 153, 603–615. doi:10.1016/j.enconman.2017.10.038

Xu, T., Hu, Z., Feng, B., Feng, G., Li, F., and Jiang, Z. (2020). Numerical Evaluation of Building Heating Potential from a Co-axial Closed-Loop Geothermal System Using Wellbore–Reservoir Coupling Numerical Model. *Energy Exploration & Exploitation* 38, 733–754. doi:10.1177/0144598719889799

Zhao, N., and You, F. (2020). Can Renewable Generation, Energy Storage and Energy Efficient Technologies Enable Carbon Neutral Energy Transition? *Appl. Energ.* 279, 115889. doi:10.1016/j.apenergy.2020.115889

Zhao, X., Ma, X., Chen, B., Shang, Y., and Song, M. (2022). Challenges toward Carbon Neutrality in china: Strategies and Countermeasures. *Resour. Conservation Recycling* 176, 105959. doi:10.1016/j.resconrec.2021.105959

Conflict of Interest: Author JL was employed by the company Shaanxi Coal Geology Group Company Limited.

The remaining authors declare that the research was conducted in the absence of any commercial or financial relationships that could be construed as a potential conflict of interest.

The handling editor declared a past co-authorship with one of the authors CC.

NOMENCLATURE

$\boldsymbol{A}$ flow cross-sectional area (m^2)

$\boldsymbol{C}$ economic cost (Yuan)

$\boldsymbol{c}$ specific heat capacity ($J\,kg^{-1}\,K^{-1}$)

$\boldsymbol{D}$ drilling depth (m)

$\boldsymbol{d_e}$ equivalent diameter of the pipe (m)

$\boldsymbol{E_q}$ electricity price (Yuan/kWh)

$\boldsymbol{F}$ flow friction (Pa)

$\boldsymbol{f}$ Darcy friction factor

$\boldsymbol{H}$ heat sink/source term ($W\,m^{-3}$)

$\mathbf{I}$ identity matrix (–)

$\boldsymbol{K}$ roughness of pipe (mm)

$\boldsymbol{L}$ length of pipe (m)

$\boldsymbol{N}$ integer (–)

$\boldsymbol{P}$ power (kW)

$\boldsymbol{Q}$ heat extraction amount (kW)

$\boldsymbol{q_n}$ heat flux ($W\,m^{-2}$)

$\boldsymbol{r}$ discount rate

$\boldsymbol{Re}$ Reynolds number (–)

$\boldsymbol{T}$ temperature (°C)

$\boldsymbol{t}$ time (h)

$\mathbf{v}$ vector of flow velocity ($m\,s^{-1}$)

$\boldsymbol{X}$ perimeter of the flow area (m)

$\boldsymbol{\alpha}$ thermal diffusivity ($m^2\,h^{-1}$)

$\boldsymbol{\beta_L}$ longitudinal heat dispersivity (m)

$\boldsymbol{\Gamma}$ boundary

$\boldsymbol{\lambda}$ thermal conductivity ($W\,m^{-1}\,K^{-1}$)

$\boldsymbol{\Lambda}$ thermal hydrodynamic dispersion tensor ($W\,m^{-1}\,K^{-1}$)

$\boldsymbol{\Phi}$ heat transfer coefficient ($W\,m^{-1}\,K^{-1}$)

$\boldsymbol{\rho}$ density ($kg\,m^{-3}$)

$\boldsymbol{\Theta}$ Darcy friction factor (–)

$\boldsymbol{\Delta}$ difference operator

$\boldsymbol{\nabla}$ nabla vector operator

$\sum$ integral operator

$\boldsymbol{f}$ circulation fluid in borehole

$\boldsymbol{g}$ grout

$\boldsymbol{hp}$ heat pump

$\boldsymbol{i}$ inner pipe (outflow)

$\boldsymbol{in}$ inlet

$\mathbf{max}$ maximum

$\boldsymbol{o}$ outer pipe (inflow)

$\boldsymbol{out}$ outlet

$\boldsymbol{s}$ soil/rock

frontiers in Earth Science

ORIGINAL RESEARCH
published: 10 February 2022
doi: 10.3389/feart.2021.786849

Tectono-Thermal Evolution and its Significance of Hydrocarbon Exploration in the Fuyang Sag, Southern North China Basin: A Case Study of Well WFD-1

Peng Gao[1,2]*, *Zhao Li*[1], *Miao Miao*[1,3], *Shizhen Li*[1,2] *and Hongda Zhang*[1]

[1]Oil and Gas Survey, China Geological Survey, Beijing, China, [2]The Key Laboratory of Unconventional Petroleum Geology, China Geological Survey, Beijing, China, [3]School of the Earth Sciences and Resources, China University of Geosciences, Beijing, China

The study of tectono-thermal evolution of sedimentary basins reveals both geothermal field characteristics and hydrocarbon generation and expulsion in the basin. However, there are only a few studies on the tectono-thermal evolution of the Fuyang Sag. This means the hydrocarbon exploration in the study area is restricted and unable to be effectively supported. Based on the geophysical exploration and drilling results, the tectono-thermal evolution of the Fuyang Sag has been studied for the first time in this paper. Using the organic geochemical data of the source rocks, the influence of tectono-thermal evolution on hydrocarbon exploration in the Fuyang Sag was discussed. The burial history of the Fuyang Sag since the late Paleozoic falls into four stages: stable sedimentation, rapid subsidence and deposition, long-term continuous uplift and denudation, and sedimentation. The heat flow evolution history of the Fuyang Sag since the late Paleozoic is characterized by ascending first and descending afterward. The main source rocks in the sag increased rapidly during the Permian and was gradually finalized in the Yanshanian period. The Fuyang Sag was reformed after the early hydrocarbon generation. The main source rocks with deeper burial depth, weaker uplift, and denudation reformation have greater potential for hydrocarbon exploration in the sag. The results of this study provide not only a scientific basis and important guidance for hydrocarbon exploration in the Fuyang Sag, and but also effective geothermal constraints for further geodynamics research in the Southern North China Basin.

Keywords: tectono-thermal evolution, hydrocarbon generation, Carboniferous-Permian source rocks, oil and gas exploration, Fuyang Sag

OPEN ACCESS

Edited by:
Yanlong Kong,
Institute of Geology and Geophysics (CAS), China

Reviewed by:
Chuanqing Zhu,
China University of Petroleum, China
Shijun Jiang,
Jinan University, China

***Correspondence:**
Peng Gao
ps1_gao@163.com

Specialty section:
This article was submitted to Economic Geology, a section of the journal Frontiers in Earth Science

Received: *30 September 2021*
Accepted: *28 December 2021*
Published: *10 February 2022*

Citation:
Gao P, Li Z, Miao M, Li S and Zhang H (2022) Tectono-Thermal Evolution and its Significance of Hydrocarbon Exploration in the Fuyang Sag, Southern North China Basin: A Case Study of Well WFD-1. Front. Earth Sci. 9:786849. doi: 10.3389/feart.2021.786849

INTRODUCTION

As a driving force of various geodynamic processes (Morgan, 1984; Wang, 1996), heat is also an important influencing factor of oil and gas accumulation (Welte and Tissot, 1984; Tissot et al., 1987; Qiu et al., 2004). In the geological history, the thermal state of sedimentary basin changed dynamically with tectonic evolution, including the evolution of formation temperature, geothermal gradient, and heat flow (Qiu et al., 2005). Therefore, it is of significance to study the tectono-thermal evolution of sedimentary basin. On the one hand, the research reveals the

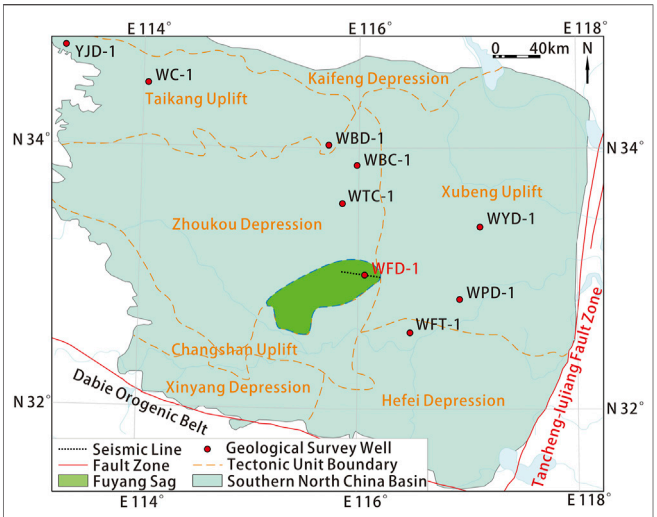

FIGURE 1 | Map showing the location of the Fuyang Sag and the main structural subdivisions of the Southern North China Basin.

characteristics of the geothermal field in different evolution stages of the basin and illustrates effective constraints for the analysis of dynamic mechanism and tectonic attributes of the basin in a specific period of geological evolution (Hanks et al., 2006; Hu et al., 2007; Qiu et al., 2014; Liu et al., 2016; Gao et al., 2018). On the other hand, the research restores the thermal maturity process and hydrocarbon generation and expulsion stages of organic matter in source rocks, to provide a scientific basis for oil and gas exploration in the basin (Zhu et al., 2010; Zuo et al., 2011; Li et al., 2013; Zuo et al., 2013; Tang et al., 2014).

For a long time, many structural units in the Southern North China Basin (SNCB) have been studied, including oil and gas exploration potential (Wu et al., 1992; Wang et al., 1999; Zhao et al., 2001; Xu et al., 2003; Xu et al., 2004; Yu et al., 2005; Xie et al., 2006; Xie and Zhou, 2006; Liu et al., 2009; Zhao et al., 2010; Xu et al., 2011), but the relevant research on the Fuyang Sag, one of its structural units, was relatively scarce. The burial history, organic matter maturity evolution history, and hydrocarbon generation history of source rocks in the Fuyang Sag have not been studied yet, which are vital to oil and gas exploration. The oil and gas exploration in the Fuyang area was therefore restricted and ineffectively supported. Furthermore, the SNCB is located at the tectonic junction of the Dabie Orogenic Belt and the Tancheng-lujiang Fault Zone. Its tectonic evolution history is vital to understanding the basin-orogene coupling process in eastern China. The Fuyang Sag is located in the middle of the SNCB, which is a critical position for basin research. The lack of tectono-thermal evolution of such a position cannot support the geodynamics research of the basin-orogene coupling.

In recent years, based on the drilling and geophysical exploration carried out by the Oil and Gas Survey, China Geological Survey in the Fuyang Sag, the stratigraphic development in the sag was revealed (Gao et al., 2021), and many types of geological data in the sag were obtained. Based on these basic geological data, the tectono-thermal evolution of the Fuyang Sag is studied for the first time. Combined with regional geological background, two-dimensional seismic survey, and drilling data, this study reconstructed the stratigraphic burial history of the Fuyang Sag, restored heat flow and formation temperature evolution history of the Fuyang Sag by using vitrinite reflectance measured from drilling cores and cuttings as paleo-geothermometers. Furthermore, the maturity evolution and hydrocarbon generation history of the main source rocks in the Fuyang Sag was reconstructed. Combined with source rock organic geochemical data, this study discusses the influence of tectono-thermal evolution of the Fuyang Sag on oil and gas exploration in the study area. The results of this study are significant for guiding the hydrocarbon exploration in the Fuyang Sag and can also provide effective constraints for further geodynamics research in the SNCB.

GEOLOGICAL SETTING

The Fuyang Sag belongs to the SNCB tectonically (**Figure 1**). It is regionally controlled by the Dabie Orogenic Belt in the south and the Tancheng-lujiang Fault Zone in the east. It is a secondary tectonic unit developed and formed on the basement of the North China Craton, with an area of about 10,000 km^2 (Lu et al., 2011). The regional geological background shows that the Fuyang Sag is located at the junction of the North China Block and the Dabie Orogenic Belt, and the basin evolution since the Paleozoic has different features, which can mainly be divided into two stages: Paleozoic stable subsidence and Mesozoic-Cenozoic deformation and transformation (Xu et al., 2003; Sun et al., 2004; Huang et al., 2005; Yu et al., 2005; Kuang et al., 2009; Yang et al., 2012).

According to the drilling strata of WFD-1 (**Figure 2**), the only geological survey well in the Fuyang Sag, the strata developed from the top to bottom are Quaternary, Neogene, Paleogene, Permian Shangshihezi Formation, Permian Xiashihezi Formation, Permian Shanxi Formation, Carboniferous Taiyuan Formation, Carboniferous Benxi Formation, and Ordovician Majiagou Formation, respectively. The Permian Shangshihezi Formation (P_{2s}) is dominated by mudstone and sandstone, with coal seams concentrated in the middle, and its sedimentary environment is dominated by the delta sedimentary system, interspersed with the coastal system. The Permian Xiashihezi Formation (P_{2x}) is characterized by the interbedding of sandstone, mudstone, and coal seams, which belongs to the distributary channel deposition of the delta plain. The Permian Shanxi Formation (P_{1s}) is interbedded with sandstone and dark mudstone and intercalated with several thin coal seams, which is a delta sedimentary environment formed during regression. The Carboniferous Taiyuan Formation (C_{2t}) is composed of epicontinental sea carbonate rocks and coastal clastic rocks, and the main sedimentary environment is lagoon facies and marsh facies. The Carboniferous Benxi Formation (C_{2b}) is a set of purplish-red ferric aluminum mudstone, and its sedimentary environment is the lagoon and epicontinental sea. Ordovician Majiagou Formation (O_{2m}) mainly developed limestone formed in an epicontinental sea sedimentary environment (Gao et al., 2021).

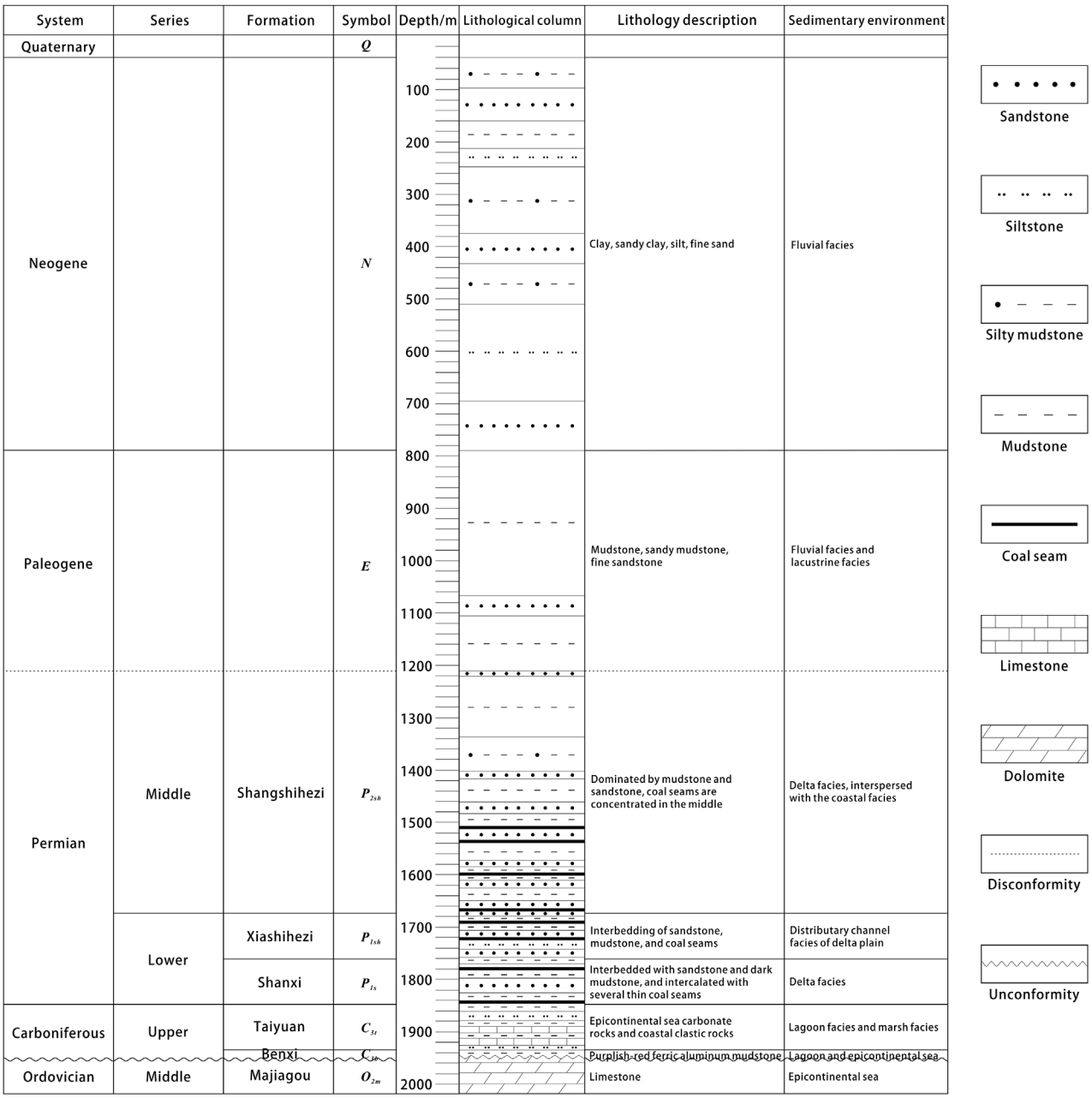

FIGURE 2 | Carboniferous-Permian stratigraphic column revealed by WFD-1.

The 2D seismic profile (**Figure 3**) across the Fuyang Sag depicts the east-west structural pattern, fault characteristics, and stratigraphic distribution of the Fuyang Sag. The Fuyang Sag is a dustpan-shaped fault depression with east-west distribution formed by the influence of the Cenozoic regional extensional tectonic environment. The sag presents a structural form of steep in the west and gentle in the east. A series of normal faults dipping eastward are developed on the west side of the sag, while a series of normal faults dipping westward are developed on the east side of the sag. All faults in the sag developed before the Neogene and ended up below the Neogene. The Carboniferous-Permian strata in the sag are continuously deposited, the Permian Shangshihezi Formation is in unconformable contact with the overlying Paleogene, and the strata inbetween are missing due to structural denudation (Liang and Liu, 2014). There is little difference in thickness between the Carboniferous-Permian and the Neogene in the east and west of the sag. The Paleogene is thinner in the east and thicker in the west of the sag.

There were oil and gas displays shown in the structural units in the adjacent area of the Fuyang Sag, and in different strata such as Paleogene, Lower Cretaceous, Permian, Upper Carboniferous, Ordovician, and Cambrian (Wu et al., 1992; Xu et al., 2004; Xie

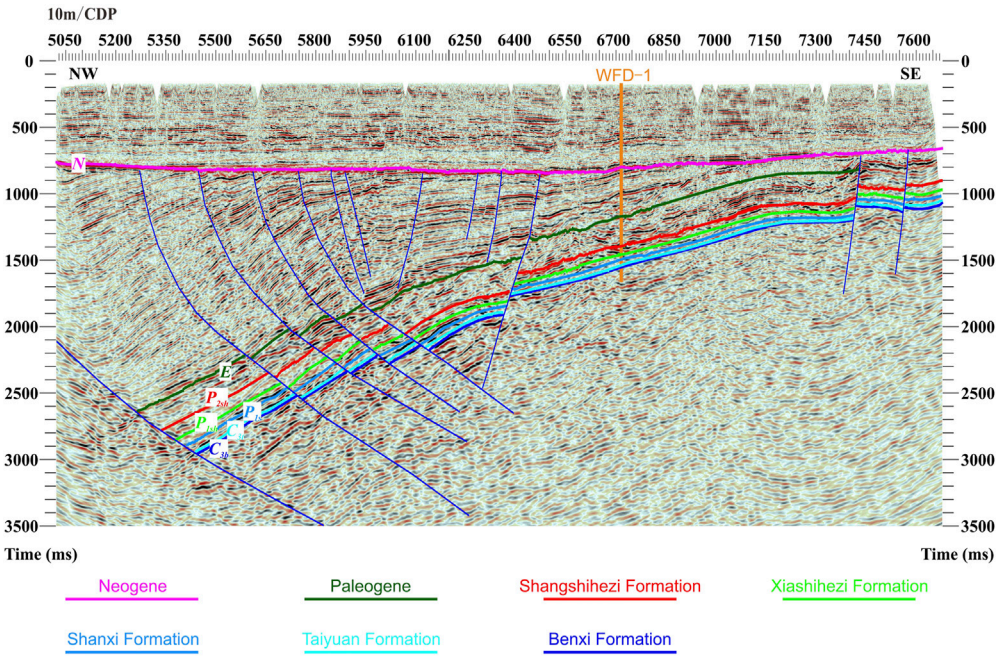

FIGURE 3 | 2D seismic profile across the Fuyang Sag. Its location is shown in **Figure 1**. Different color lines refer to different formation bottom interfaces. The blue curves represent faults. The yellow straight line shows the location and depth of well WFD-1 on this seismic profile.

et al., 2006; Xie and Zhou, 2006; Zhang, 2016). The geochemical analysis shows that all the liquid hydrocarbons have the characteristics of high saturation hydrocarbon and low asphaltene and belong to coal-derived oils from the Carboniferous-Permian system. Previous studies on reservoir forming conditions and geochemical characteristics of source rocks suggested that the main source rocks in this area are the Carboniferous-Permian coal-measure source rocks, with source-reservoir-cap assemblage, but the reservoir physical property is poor (Ma, 2006; Zhu et al., 2006).

PALEO-GEOTHERMOMETERS AND THERMAL HISTORY RECONSTRUCTION

The research of basin-scale tectono-thermal evolution is to use the paleo-geothermometers that record paleo-temperature information in the basin to inverse the thermal history of sedimentary strata (Price, 1983; Hu et al., 2001). There are many types of paleo-geothermometers, among which the vitrinite reflectance (Ro) is a well-developed paleo-geothermometer recording the highest paleo-temperature. In addition, a variety of dynamic models have been established for using vitrinite reflectance to reconstruct thermal history (Waples, 1980; Lerche et al., 1984; Tissot et al., 1987). In this study, "EASY%Ro" model, a widely used and simplified model (Burnham and Sweeney, 1989; Sweeney and Burnham, 1990), was adopted as the dynamic model of vitrinite reflectance.

The 40 vitrinite reflectance data of the Fuyang Sag were obtained from the test results of cores and cuttings drilled by

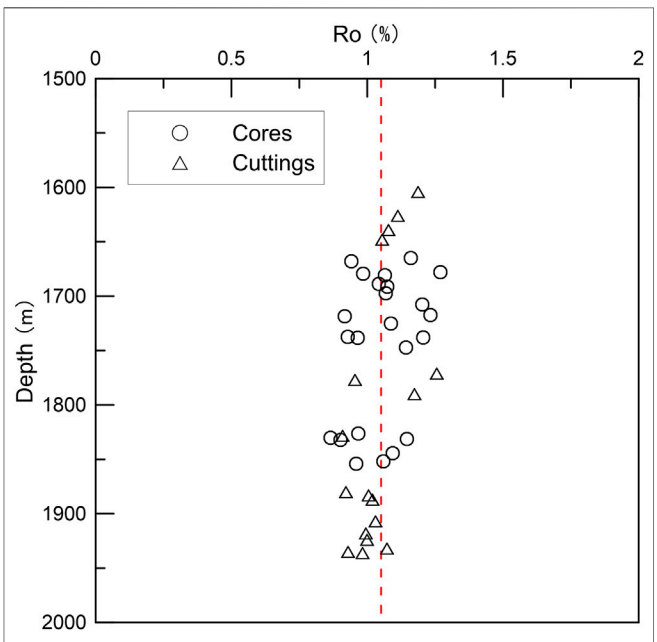

FIGURE 4 | Plot of measured vitrinite reflectance (Ro data) vs. depth from WFD-1. The circles represent core samples, and the triangles represent cutting samples. The red dashed line refers to the average Ro value of 1.05%.

WFD-1. The tested samples were all from the Carboniferous-Permian strata, with depths ranging from 1500–2000 m and Ro ranging from 0.86 to 1.27%, with an average of 1.05% (including 23 core samples with an average Ro of 1.06%, and 17 cutting

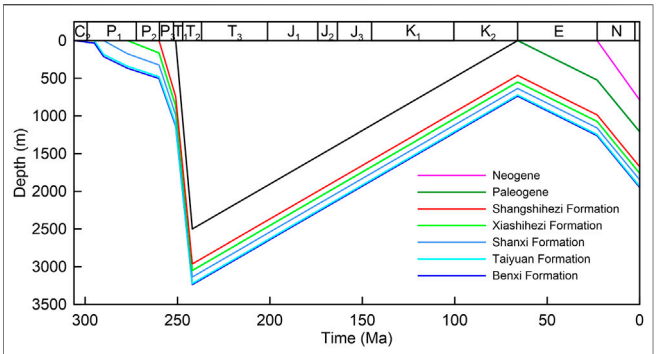

FIGURE 5 | Burial history of the Fuyang Sag. Different color lines refer to the modeling results of burial depth evolution path of different formations with geological time.

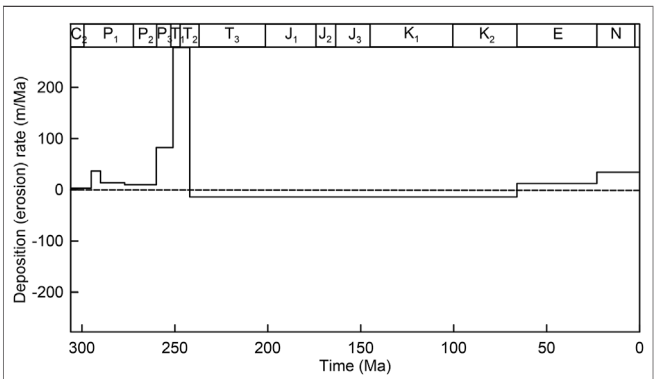

FIGURE 6 | Deposition (erosion) rate of the Fuyang Sag. The broken line represents the deposition (erosion) rate of the Fuyang Sag in each geological time. The dashed line refers to the deposition (erosion) rate of 0 m/Ma. It means deposition when the rate is greater than 0 m/Ma, and it means erosion when the rate is less than 0 m/Ma.

samples with an average Ro of 1.04%). The Ro values both from cores and cuttings show no significant change with the increase of depth (**Figure 4**). This indicates that the Carboniferous and Permian vitrinite reflectance data were generally more consistent and had experienced the same thermal evolution history. Combined with the current geothermal gradient of 25°C/km in the Fuyang Sag, the measured Ro values of the Carboniferous-Permian were higher than that of the formation temperature at the current buried depth, indicating that the formation had experienced higher paleo-temperature. This situation may be caused by early geothermal events or later uplift and denudation.

The software used in this thermal history modeling was the Thermodel for Windows. Default parameters in the Thermodel for Windows were used for the initial porosity, matrix density, and heat capacity. The paleo-surface temperature was set as 10°C during the geological evolution. Mechanic compaction coupled with the reciprocal porosity-depth relationship (Falvey and Middleton, 2005) was used to model the burial history. The effect of compaction was accounted for using Sclater and

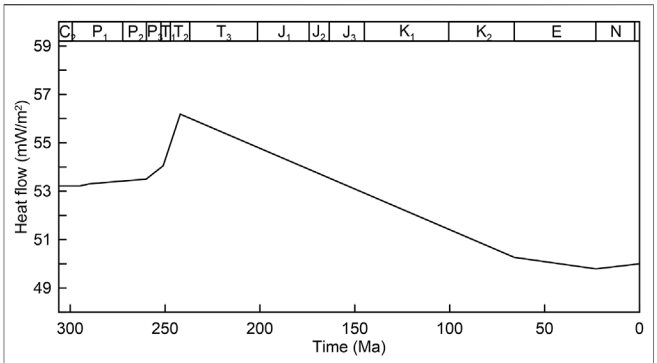

FIGURE 7 | Heat flow history of the Fuyang Sag. The line shows the modeling result of heat flow evolution path in the Fuyang Sag since 306 Ma.

Christie's model (Sclater and Christie, 1980). According to previous studies on denudation in the Fuyang area (He, 2009; Yang, 2017), the amount of denudation between the Permian and Paleogene in the Fuyang Sag was about 2500 m. Based on regional geological and geophysical data, drilling results, and previous research, the burial history of the Fuyang Sag was reconstructed. With vitrinite reflectance as paleo-geothermometer, the thermal history of the Fuyang Sag was studied using the paleo heat flow method. Based on the above study, the maturity evolution history of the Carboniferous-Permian source rock in the Fuyang Sag was modeled by the "EASY%Ro" dynamic model.

TECTONO-THERMAL EVOLUTION MODELING RESULT

Tectonic Subsidence Analysis

The reconstructed burial history and deposition (erosion) rate of the Fuyang Sag are shown in **Figures 5**, **6** respectively. The burial history of the Fuyang Sag from the Late Paleozoic to the present day can be divided into four stages. Before the Middle Permian, the Fuyang Sag was in a stable sedimentation stage, with a deposition rate of about 3–36 m/Ma. After the late Permian, the Fuyang area experienced the peak of the Indosinian movement. Influenced by the convergence and collage of the North China Block and the Yangtze Block, rapid sedimentation occurred, with a deposition rate of about 82–277 m/Ma. This rapid sedimentation lasted for a short period, only about 18 Ma. Subsequently, the Fuyang Sag entered the Yanshan Movement, with a long-term continuous uplift and denudation until the Cenozoic, and the erosion rate was about 14 m/Ma. In the Cenozoic, the Fuyang Sag turned into a sedimentation stage. The Paleogene deposition rate was about 12 m/Ma, and the Neogene deposition rate was about 34 m/Ma.

Thermal History Reconstruction Result

Based on the present-day geothermal field and paleo-geothermometer data in the study area, the heat flow evolution history of WFD-1 since the late Paleozoic was systematically reconstructed (**Figure 7**). The evolution history of heat flow in

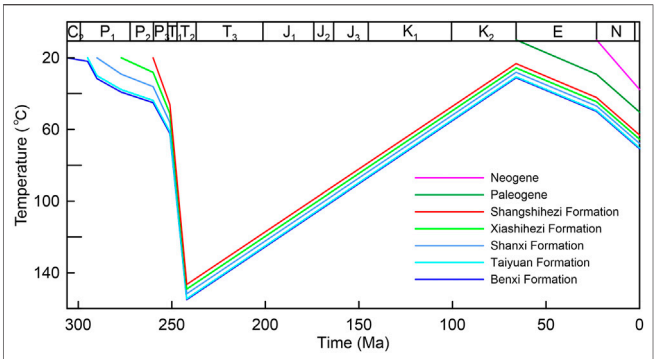

FIGURE 8 | Formation temperature history of the Fuyang Sag. Different color lines refer to the modeling results of temperature evolution path of different formations with geological time.

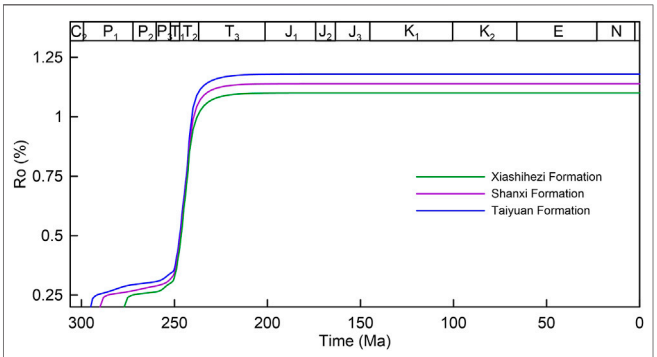

FIGURE 9 | The three color lines refer to the maturity evolution modeling results of the three main source rock formations with geological time in the Fuyang Sag.

the Fuyang Sag since the late Paleozoic was characterized by rising first and falling afterward. The terrestrial heat flow in the Fuyang Sag was about 53 mW/m^2 in the late Paleozoic. At the end of the Indosinian period, due to the tectonic background of the collision and compression of the North China Block and the Yangtze Block, the terrestrial heat flow rose slightly to about 56 mW/m^2. Since then, the Fuyang Sag continued to be in the uplifting and cooling stage, and the terrestrial heat flow slowly dropped to about 50 mW/m^2. In the Cenozoic era, the terrestrial heat flow in the Fuyang Sag tended to be stable and maintained at about 50 mW/m^2. The temperature evolution of strata in the Fuyang Sag is influenced by tectonic subsidence and terrestrial heat flow simultaneously. There was no significant thermal event disturbance, and the change of heat flow was relatively moderate in the Fuyang Sag, making the burial and denudation of the formation the main controlling factors of the formation temperature evolution. The formation temperature history (**Figure 8**) shows the same trend as the burial history.

Source Rock Maturity Modeling Result

According to the research results of the thermal history of WFD-1, the maturity evolution histories of the main source

TABLE 1 | Carboniferous-Permian hydrocarbon organic geochemical test results of WFD-1.

Formation	Lithology	TOC(%)			Chloroform asphalt "A" (%)			S1+S2(mg/g)			Ro/(%)		
		Range	Average	Amount	Range	Average	Amount	Range	Average	Amount	Range	Average	Amount
Shangshihezi	Organic-rich mudstone	1.3~7.4	2.69	17	0.0435~0.2558	0.1497	2	0.95~13.33	3.1	17	0.942~1.187	1.089	6
	Coal	23.1~40.4	31.75	2	—	—	—	55.98~132.87	97.14	2	—	—	—
Xiashihezi	Organic-rich mudstone	0.8~9.2	3.4	7	0.0101~0.1474	0.0658	3	1.69~124.54	59.26	7	0.928~1.269	1.085	14
	Coal	16.9~76.8	54.3	26	0.0363 ~2.2810	0.9374	9	109.38~245.73	180.22	26	—	—	—
Shanxi	Organic-rich mudstone	1.16~5.14	2.74	14	0.0259 ~0.4726	0.2422	2	0.56~203.19	68.99	14	0.865~1.256	1.047	9
	Coal	33.2~70.9	64.13	13	0.9211 ~1.5271	1.1999	4	96.31~214.21	171.09	13	—	—	—
Taiyuan	Organic-rich mudstone	1.55~6.15	3.52	15	0.0736 ~0.1183	0.0959	2	1.69~177.92	34.36	15	0.921~1.072	1.007	9
	Coal	45.0~60.6	52.98	5	1.5661 ~2.1942	1.7531	4	200.28~220.85	210.57	5	—	—	—

TABLE 2 | Kerogen types of Carboniferous-Permian source rocks in the Fuyang Sag.

Formation	Lithology	Sapropelite + exinite (%)	Vitrinite (%)	Inertinite (%)	Index of type (%)	Kerogen type
Shangshihezi	Mudstone	10	90	0	–57.5	III
	Carbonaceous mudstone	5	95	0	–67.75	III
Xiashihezi	Mudstone	20	70	10	–50	III
	Coal	20	60	20	–55	III
Shanxi	Mudstone	60	30	10	2.5	II_2
	Coal	5	80	15	–72.5	III
Taiyuan	Mudstone	40	40	20	–10	III
	Carbonaceous mudstone	50	40	10	–15	III

rocks (P_{2x}, P_{1s}, C_{2t}) in the Fuyang Sag were simulated (**Figure 9**). Before the Middle Permian, the three sets of main source rocks in the Fuyang Sag were buried and matured slowly under the influence of stable subsidence and sedimentation of the regional tectonic environment. After entering the Late Permian, due to the convergence and compression of the North China Block and the Yangtze Block by the Indosinian movement, each set of strata in the Fuyang Sag began to settle and bury rapidly. With the slight increase of heat flow and geothermal gradient, the maturity of the three sets of source rocks increased rapidly. Ro reached low maturity stage (0.5%) at 247–246 Ma, early maturity stage (0.7%) at 244–243 Ma, and late maturity stage (1.0%) at 240–236 Ma. During the Yanshanian period, the Fuyang Sag continued to uplift and cool, and the formation temperature continued to decrease. Under this influence, the maturity of each set of source rocks gradually finalized. In the Himalayan period, although the Fuyang Sag was deposited and buried again, the maturity degree did not increase again because the formation temperature experienced by each set of source rocks did not exceed the previous maximum formation temperature.

DISCUSSION

The Influence of Tectono-Thermal Evolution of the Fuyang Sag on Oil and Gas Exploration in Terms of Hydrocarbon Generation

The Fuyang Sag experienced rapid subsidence and deposition during the Indosinian tectonic period, which provided a favorable structural environment for the development and maturity of source rocks. According to the formation drilled by WFD-1, the thickness of the Carboniferous-Permian in the Fuyang Sag is about 737.6 m, of which the thickness of organic-rich mudstone (TOC > 1%) is about 101.25 m. The Carboniferous-Permian hydrocarbon organic geochemical experimental test results of WFD-1 is shown in **Table 1**. The experimental test results reveal that the maturity of the Carboniferous-Permian source rocks in the Fuyang Sag was relatively consistent, which generally reached the late maturity stage (1.0%). The organic kerogen types of the Carboniferous-Permian source rocks in the Fuyang Sag are type III or type II_2 (**Table 2**).

The source rocks of the Carboniferous-Permian marine-continental transitional facies are mainly type III kerogen in coal measure organic matter. The hydrocarbon generation mechanism of this kerogen type is mainly the thermal degradation of organic matter under the action of temperature. The main products are small molecular hydrocarbons (such as methane and its homologs) (Fu et al., 1992). Therefore, the hydrocarbon products of the Carboniferous-Permian marine-continental transitional shale are mainly gaseous hydrocarbons, and the yield of liquid hydrocarbons is relatively low. As a result, the marine-continental transitional source rocks of coal measures do not show an obvious gas generation peak of liquid hydrocarbon cracking to generate gaseous hydrocarbon, but a long-term continuous generation of gaseous hydrocarbon (organic matter directly generates small molecule group gaseous hydrocarbon) (Cao et al., 2014). Type III kerogen enters the gas generation window earlier than type I and type II_2 kerogen. With the increase of thermal evolution of source rocks, gaseous hydrocarbons are generated continuously, and the range of the gas generation window is larger (**Figure 10**).

According to the gas generation efficiency of type III kerogen, the total gas generation is less at a relatively low maturity of source rock (about 1.0%). The total gas generation of marine-continental transitional coal measure source rock continues to increase when the thermal evolution degree rises, which is favorable for type III kerogen to directly generate gaseous hydrocarbons. In addition, high maturity organic matter forms abundant organic dissolution pores in the thermal evolution process, which improves the porosity and provides space for a hydrocarbon reservoir. Therefore, the higher the maturity of the Carboniferous-Permian source rocks with high TOC in the Fuyang Sag, the stronger the adsorption capacity of shale gas, so that the high maturity source rocks have higher shale gas accumulation capacity (Bowker, 2007; Robert and Stephen, 2007).

According to the thermal history modeling result, the main hydrocarbon generation period of the Fuyang Sag is the Indosinian-early Yanshanian. The hydrocarbon accumulated before the tectonic events, which indicates that the Fuyang Sag is an early hydrocarbon generation sag. The present-day average

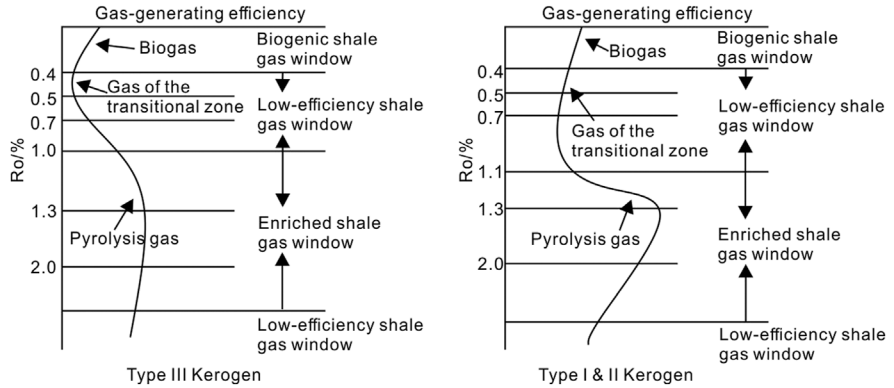

FIGURE 10 | Comparison of hydrocarbon generation features of different kerogen. The curve represents the change of gas-generating efficiency with the increase of maturity (Ro value). Modified from Cao et al., 2014.

geothermal gradient in the Fuyang Sag is about 25°C/km, and the average heat flow is about 50 mW/m^2 (Zhang et al., 2007; He et al., 2009). Both of them are lower than the average geothermal values of eastern China (Hu et al., 2000; Jiang et al., 2019). Under this influence, the Carboniferous-Permian hydrocarbon source rocks with higher maturity in the Fuyang Sag are now buried at a large depth. Therefore, hydrocarbon exploration in the Fuyang Sag should target the Carboniferous-Permian with a buried depth of more than 3500 m to the west of the sag (with higher Ro values).

The Influence of Tectono-Thermal Evolution of the Fuyang Sag on Hydrocarbon Exploration in Terms of Hydrocarbon Preservation

The Fuyang Sag is a reformed sag after the early hydrocarbon generation. The Carboniferous-Permian formations in the Fuyang Sag experienced the influence of Yanshanian and Himalayan tectonic movements, and the main source rocks experienced the process of sedimentary-uplift and denudation-rebury (Yu et al., 2005; Lin et al., 2011). During the Indosinian period, the Carboniferous-Permian source rocks experienced rapid burial heating, and the maturity of organic matter increased rapidly. When the Ro exceeded 0.5%, source rocks entered the hydrocarbon generation threshold and began to generate hydrocarbon. Then the source rocks reached the late maturity stage (1.0%). During the Yanshanian period, the maturity evolution stagnated, and hydrocarbon generation ceased after regional uplift and denudation. During the Himalayan period, the whole area was deposited and buried again, but the burial depth of the Carboniferous-Permian source rocks did not exceed the maximum burial depth in the previous period, the formation temperature did not reach the highest paleo-temperature. Therefore, the maturity of organic matter could not increase again to form secondary hydrocarbon generation (Lin et al., 2011).

From the late Jurassic to the early Cretaceous, the tectonic environment of the Fuyang Sag was in a stage of compression thrust-strike slip pull basin evolution (Xu et al., 2004) under the background of compression torsion. The fault-folding reformation and uplift denudation in this period may have a certain destructive effect on the hydrocarbon reservoirs formed in the earlier and the same period. Therefore, hydrocarbon exploration in the Fuyang Sag should be based on preservation conditions (Zhao et al., 2011), and the areas with weaker uplift and denudation reconstruction in the later stage, that is, the favorable areas of residual Mesozoic strata, should be optimized.

First, the area with the remaining Mesozoic strata indicates that the area experienced weak tectonic events during the Yanshanian period. Since the upper Paleozoic formation was not exposed, the marine-continental transitional shale itself is a barrier for the preservation of self-generating and self-storing shale oil and gas reservoirs. The upper Paleozoic strata have not been damaged by tectonic events, which is conducive to the formation of large area, widely and continuously distributed unconventional oil and gas reservoirs, and it is favorable for the preservation of oil and gas resources generated in the early stage. Second, the lower porosity, permeability, and other physical properties of the overlying Mesozoic strata can form favorable caps for Paleozoic hydrocarbon accumulation and become good caprocks for the Carboniferous-Permian shale oil and gas reservoirs. Third, in the later re-burial process, the overlying strata may have a certain hydrocarbon-generating capacity due to the effect of burial maturation, which can not only seal the Paleozoic oil and gas reservoir by the poor physical properties but also produce the hydrocarbon concentration sealing effect (Fu et al., 2008) due to hydrocarbon generation and expulsion. In addition, the overpressure source rock even has the pressure sealing effect, which is more conducive to the sealing and preservation of the lower oil and gas reservoir. Fourth, the thick overlying strata of shale oil and gas reservoirs are also conducive to hydrocarbon accumulation and preservation.

Although no magmatic activity was identified in the drilling and geophysical exploration in the Fuyang Sag, igneous rocks

were encountered in several drilling wells in the surrounding tectonic units. Therefore, the impact of magmatism on oil and gas reservoirs should be considered in hydrocarbon exploration in the study area. On the one hand, the magmatic activity prior to the mass generation of hydrocarbon is conductive to the process. The high temperature, high pressure, and active chemical properties of magma can promote hydrocarbon generation, improve the reservoir property of surrounding rock, and form abnormal high-pressure fields and various types of traps, which are conducive to oil and gas accumulation (Wan et al., 2014). On the other hand, magmatic activity after the mass generation of hydrocarbon is destructive to the process. The newly formed high-temperature geothermal field may destroy the reservoir and its structure, causing oil and gas to escape upward. After the high-temperature magma intrudes into the source rock, it will bake the surrounding source material and generate hydrocarbon to carbonize it (Zhang et al., 2016). The Yanshanian movement peaked from the late Jurassic to the early Cretaceous, with regional high geothermal anomalies caused by intense magmatic and volcanic activities. Hydrocarbon had been generated before the Yanshanian movement in the Fuyang Sag, so the late magmatic activities are destructive to the early oil and gas reservoirs. Therefore, in the hydrocarbon exploration in the Fuyang Sag, the igneous rock development area should be kept off to avoid the influence of magmatic activities on the Carboniferous-Permian oil and gas reservoirs.

CONCLUSION

1) The burial history of the Fuyang Sag since the Late Paleozoic can be divided into four stages. Before the Middle Permian, the Fuyang Sag was in a stable sedimentation stage. After the Late Permian, the study area experienced rapid subsidence and deposition. Long-term continuous uplift and denudation occurred in the Fuyang Sag during the Yanshanian tectonic period. The sedimentation in the Fuyang Sag was recovered in the Cenozoic era.
2) The heat flow evolution history of the Fuyang Sag since the Late Paleozoic can be characterized by ascending first and descending afterward. The terrestrial heat flow of the Fuyang Sag in the late Paleozoic was about 53 mW/m^2. At the end of the Indosinian period, the terrestrial heat flow increased slightly to about 56 mW/m^2. After that, the terrestrial heat flow slowly decreased to about 50 mW/m^2. The terrestrial heat flow tends to be stable in the Cenozoic era. The formation temperature history of the Fuyang Sag shows the same trend as the burial history.
3) The three sets of main source rocks in the Fuyang Sag were slowly buried and matured before the Middle Permian. During the Permian, the maturity of the three sets of source rocks increased rapidly, with Ro reaching the late maturity stage of 1.0%. The maturity of each set of source rocks was gradually finalized in the Yanshanian period. During the Himalayan period, the thermal evolution degree of each set of source rocks did not increase again.
4) The organic matter type of the Carboniferous-Permian source rocks of marine-continental transitional facies in the Fuyang Sag is mainly type III kerogen. This kerogen type generates and expels more hydrocarbon at high maturity. Influenced by the thermal history of the Fuyang Sag, the source rocks with deeper burial depth have greater potential for oil and gas exploration. The Fuyang Sag is a reformed sag after the early hydrocarbon generation. The areas in the sag with weaker uplift and denudation reformation in the later period are favorable areas for hydrocarbon exploration.

DATA AVAILABILITY STATEMENT

The raw data supporting the conclusion of this article will be made available by the authors, without undue reservation.

AUTHOR CONTRIBUTIONS

The first author PG completed most of the work of the article, the second author ZL analyzed the Well WFD-1 and the seismic profile, the third author MM revised the manuscript and polished the language, the fourth author SL designed the experimental tests and revised the manuscript, and the fifth author HZ analyzed the vitrinite reflectance data. All authors listed have made a substantial, direct, and intellectual contribution to the work and approved it for publication.

FUNDING

This study is financially supported by China Geological Survey Project (No. DD20190088, No. DD20190561, No. DD20190725), the Project for high-level-innovation Talents in Science and Technology (No. 12110600000018003918) and Guangxi Government Procurement Project (No. (2021)-3421-001-012). All funds received were for experimental fees and open access publication fees.

ACKNOWLEDGMENTS

We sincerely thank two reviewers for their valuable comments and suggestions, which significantly improved the manuscript.

REFERENCES

Bowker, K. A. (2007). Barnett Shale Gas Production, Fort Worth basin: Issues and Discussion. *Bulletin* 91, 523–533. doi:10.1306/06190606018

Burnham, A. K., and Sweeney, J. J. (1989). A Chemical Kinetic Model of Vitrinite Maturation and Reflectance. *Geochimica Et Cosmochimica Acta* 53, 2649–2657. doi:10.1016/0016-7037(89)90136-1

Cao, D., Wang, C., Li, J., Qin, R., Yang, G., and Zhou, J. (2014). Basic Characteristics and Accumulation Rules of Shale Gas in Coal Measures (In

Chinese with English Abstract). *Coal Geology. Exploration* 42, 25–30. doi:10.3969/j.issn.1001-1986.2014.04.006

Falvey, D. A., and Middleton, M. F. (2005). Passive continental Margins: Evidence for a Prebreakup Deep Crustal Metamorphic Subsidence Mechanism. *Oceanologica Acta* 4, 103–114.

Fu, G., Liu, B., and Lv, Y. (2008). Comprehensive Evaluation Method for Sealing Ability of Mudstone Caprock to Gas in Each Phase. *Lithologic Reservoirs* 20, 16–20. doi:10.3969/j.issn.1673-8926.2008.01.004

Fu, J., Liu, D., and Cheng, G. (1992). *Coal Hydrocarbon Geochemistry*. Beijing: Science Press. (in Chinese).

Gao, P., Li, Z., Li, S., Zhou, Z., Wei, S., and Zhang, H. (2021). An Important Discovery of High-Quality Source Rocks of marine-continental Transitional Facies, Obtained by Borehole WFD-1, Fuyang Area, Anhui Province (In Chinese). *China Geology.* 48, 1659–1660. doi:10.12029/gc20210527

Gao, P., Qiu, Q., Jiang, G., Zhang, C., Hu, S., Lei, Y., et al. (2018). Present-day Geothermal Characteristics of the Ordos Basin, Western North China Craton: New Findings from Deep Borehole Steady-State Temperature Measurements. *Geophys. J. Int.* 214, 254–264. doi:10.1093/gji/ggy127

Hanks, C. L., Parris, T. M., and Wallace, W. K. (2006). Fracture Paragenesis and Microthermometry in Lisburne Group Detachment Folds: Implications for the thermal and Structural Evolution of the Northeastern Brooks Range, Alaska. *Bulletin* 90, 1–20. doi:10.1306/08090504134

He, Z., Liu, C., Zhao, J., and Liu, Y. (2009). A Study on Geothermal Field and its Geological Significance in Southern Area of the North China Craton. *Geol. Rev.* 55, 428–434. doi:10.16509/j.georeview.2009.03.012

He, Z. (2009). *The Research of Palaeozoic thermal History and its Oil-Gas Geological Significance in Zhoukou Depression*. Xi'an: Northwest University. Master Master.

Hu, S., Fu, M., Yang, S., Yuan, Y., and Wang, J. (2007). Palaeogeothermal Response and Record of Late Mesozoic Lithospheric Thinning in the Eastern North China Craton. *Geol. Soc. Lond. Spec. Publications* 280, 267–280. doi:10.1144/sp280.13

Hu, S., He, L., and Wang, J. (2000). Heat Flow in the continental Area of China: a New Data Set. *Earth Planet. Sci. Lett.* 179, 407–419. doi:10.1016/s0012-821x(00)00126-6

Hu, S., O'Sullivan, P. B., Raza, A., and Kohn, B. P. (2001). Thermal History and Tectonic Subsidence of the Bohai Basin, Northern China: a Cenozoic Rifted and Local Pull-Apart basin. *Phys. Earth Planet. Interiors* 126, 221–235. doi:10.1016/s0031-9201(01)00257-6

Huang, Z., Gao, C., and Ji, R. (2005). Analysis of Evolution of Meso-Cenozoic Basins in Southern North China (In Chinese with English Abstract). *Oil Gas Geology.* 26, 252–256. doi:10.11743/ogg20050220

Jiang, G., Hu, S., Shi, Y., Zhang, C., Wang, Z., and Hu, D. (2019). Terrestrial Heat Flow of continental China: Updated Dataset and Tectonic Implications. *Tectonophysics* 753, 36–48. doi:10.1016/j.tecto.2019.01.006

Kuang, H., Liu, Y., Peng, X., Yang, F., Chen, M., Cen, C., et al. (2009). Sedimentary and Tectonic Features and Proto-basin of Early Cretaceous Tanzhuang—Shenqiu Sag, Zhoukou Depression, in Southern Area of North China Craton (In Chinese with English Abstract). *Geol. Rev.* 55, 804–815. doi:10.16509/j.georeview.2009.06.005

Lerche, I., Yarzab, R., and Kendall, C. S. C. (1984). Determination of Paleoheat Flux from Vitrinite Reflectance Data. *AAPG Bull.* 68, 1704–1717. doi:10.1306/ad461980-16f7-11d7-8645000102c1865d

Li, Z., Xu, M., Zhao, P., Sun, Z., and Zhu, C. (2013). Geothermal Regime and Hydrocarbon Kitchen Evolution in the Jianghan Basin. *Sci. China Earth Sci.* 56, 240–257. doi:10.1007/s11430-012-4462-8

Liang, B., and Liu, H. (2014). Sedimentary basin Evolution and Geological Elements of Unconventional Oil and Gas Reservoirs in Fuyang Area, Anhui Province (In Chinese with English Abstract). *J. Palaeogeogr.* 16, 179–192. doi:10.7605/gdlxb.2014.02.017

Lin, X., Chen, Q., and Li, J. (2011). Distribution and Geochemical Characteristics of Permian Source Rocks in the Southern North-China (In Chinese with English Abstract). *Mar. Geology. Front.* 27, 21–26. doi:10.16028/j.1009-2722.2011.04.004

Liu, G., Sun, B., Huang, C., Luo, X., Zhang, L., Zhou, X., et al. (2009). Potential of the Deep Oil-Gas Reservior-Forming and Direction of the Deep Oil-Gas Exploitation in Southern North China Basin (In Chinese with English Abstract). *J. Graduates* 30, 113–123. doi:10.13471/j.cnki.acta.snus.2009D113

Liu, Q., He, L., Huang, F., and Zhang, L. (2016). Cenozoic Lithospheric Evolution of the Bohai Bay Basin, Eastern North China Craton: Constraint from Tectono-thermal Modeling. *J. Asian Earth Sci.* 115, 368–382. doi:10.1016/j.jseaes.2015.10.013

Lu, Y., Ding, H., Shi, Y., and Chen, C. (2011). Exploration prospect of Unconventional Natuaral Gas in Fuyang Area (In Chinese with English Abstract). *Complex Hydrocarbon Reservoirs* 4, 5–9. doi:10.16181/j.cnki.fzyqc.2011.04.002

Ma, B. (2006). Study on the Condition of Oil and Gas Reservoir in the Fuyang Region (In Chinese with English Abstract). *Geology. Anhui* 16, 31–35. doi:10.3969/j.issn.1005-6157.2006.01.031

Morgan, P. (1984). The thermal Structure and thermal Evolution of the continental Lithosphere. *Phys. Chem. Earth* 15, 107–193. doi:10.1016/0079-1946(84)90006-5

Price, L. C. (1983). Geologic Time as a Parameter in Organic Metamorphism and Vitrinite Reflectance as an Absolute Paleogeothermometer. *J. Pet. Geol* 6, 5–37. doi:10.1111/j.1747-5457.1983.tb00260.x

Qiu, N., Hu, S., and He, L. (2004). *Theory and Application of Thermal Regime in Sedimentary Basin (In Chinese)*. Beijing: Petroleum Industry Press.

Qiu, N., Li, H., and Jin, Z. (2005). Study of the thermal History Reconstruction for Lower Paleozoic Carbonate Succession (In Chinese with English Abstract). *Earth Sci. Front.* 12, 561–567. doi:10.13745/j.esf.sf.2005.4.561

Qiu, N., Zuo, Y., Chang, J., and Li, W. (2014). Geothermal Evidence of Meso-Cenozoic Lithosphere Thinning in the Jiyang sub-basin, Bohai Bay Basin, Eastern North China Craton. *Gondwana Res.* 26, 1079–1092. doi:10.1016/j.gr.2013.08.011

Robert, G. L., and Stephen, C. R. (2007). Mississippian Barnett Shale: Lithofacies and Depositional Setting of a Deep–Water Shale–Gas Succession in the Fort Worth basin, Texas. *AAPG Bull.* 91, 579–601. doi:10.1306/11020606059

Sclater, J. G., and Christie, P. A. F. (1980). Continental Stretching: An Explanation of the Post-Mid-Cretaceous Subsidence of the central North Sea Basin. *J. Geophys. Res.* 85, 3711–3739. doi:10.1029/jb085ib07p03711

Sun, X., Zhang, M., Long, S., Hao, F., Liu, P., and Liu, C. (2004). Overthrust Tectonic in Northern Qinling-Dabie Orogenic belt and basin-controlling Faults in Zhoukou Depression and Hefei basin (In Chinese with English Abstract). *OIL GAS GEOLOGY.* 25, 191–198. doi:10.11743/ogg20040213

Sweeney, J. J., and Burnham, A. K. (1990). Evaluation of a Simple Model of Vitrinite Reflectance Based on Chemical Kinetics. *AAPG Bull.* 74, 1559–1570. doi:10.1306/0c9b251f-1710-11d7-8645000102c1865d

Tang, X., Yang, S., and Hu, S. (2014). Thermal and Maturation History of Jurassic Source Rocks in the Kuqa Foreland Depression of Tarim Basin, NW China. *J. Asian Earth Sci.* 89, 1–9. doi:10.1016/j.jseaes.2014.03.023

Tissot, B., Pelet, R., and Ungerer, P. (1987). Thermal History of Sedimentary Basins, Maturation Indices, and Kinetics of Oil and Gas Generation. *AAPG Bull.* 71, 1445–1466. doi:10.1306/703c80e7-1707-11d7-8645000102c1865d

Wan, C., Jin, Q., Li, J., and Miu, J. (2014). Outline on Magmatic Activities Controlling Oil-Gas Theory in Rift Basins. *Pet. Geology. Recovery Efficiency* 21, 1–5. doi:10.13673/j.cnki.cn37-1359/te.2014.01.001

Wang, J. (1996). *Geothermics in China*. Beijing: Seismological Press.

Wang, Z., He, H., and Cheng, K. (1999). Exploration prospect of Paleozoic Primary Oil and Gas Reservoirs in North China (In Chinese). *ACTA PETROLEI SINICA* 20, 1–6. doi:10.7623/syxb199902001

Waples, D. W. (1980). Time and Temperature in Petroleum Formation: Application of Lopatin's Method to Petroleum Exploration. *AAPG Bull.* 64, 916–926. doi:10.1306/2f9193d2-16ce-11d7-8645000102c1865d

Welte, D., and Tissot, P. (1984). *Petroleum Formation and Occurrence*. Berlin: Springer.

Wu, F., Chen, Z., and Zhang, N. (1992). Sedimentary Types and Organic Characteristics of Hydrocarbon Source Rocks of Carboniferous-Permian, South Part of Huabei (In Chinese with English Abstract). *Earth Sci.* 17, 687–698. doi:10.3799/dqkx.1992.689

Xie, D., He, M., Zhou, L., and Xie, Q. (2006). Characteristics of Overthrust Structures on Northern Edge of East Qinling - Dabie Orogenic belt and Hydrocarbon Potentials (In Chinese with English Abstract). *OIL GAS GEOLOGY.* 27, 48–55. doi:10.11743/ogg20060109

Xie, D., and Zhou, L. (2006). Discussion on Hydrocarbon Generation Potential and Secondary Hydrocarbon Generation of Organic Matter from Permo-Carboniferous Coal Measures in the Southern North China (In Chinese

with English Abstract). *Coal Geology. Exploration* 34, 30–34. doi:10.3969/j.issn.1001-1986.2006.01.030

Xu, H., Zhao, Z., Lu, F., Yang, Y., Tang, Z., Sun, G., et al. (2004). Tectonic Evolution of the Nanhuabei Area and Analysis about its Petroleum Potential (In Chinese with English Abstract). *Geolecloni ca el Metallogenia* 28, 450–463. doi:10.16539/j.ddgzyckx.2004.04.450

Xu, H., Zhao, Z., Yang, Y., and Tang, Z. (2003). Structural Pattern and Structural Style of the Southern North China Basin (In Chinese with English Abstract). *ACTA GEOSCIENTIA SINICA* 24, 27–33. doi:10.3321/j.issn:1006-3021.2003.01.005

Xu, X., Chen, X., Lei, M., Li, S., Zhou, X., and Wu, M. (2011). Exploration Prospects of the Carboniferous and Permian in the Southern North China (In Chinese with English Abstract). *Pet. Geology. Experiment* 33, 148–154. doi:10.11781/sysydz201102148

Yang, M., Liu, C., Zeng, P., Bai, H., and Zhou, J. (2012). Prototypes of Late Triassic Sedimentary Basins of North China Craton (NCC) and Deformation Pattern of its Early Destruction (In Chinese with English Abstract). *Geol. Rev.* 58, 1–18. doi:10.16509/j.georeview.2012.01.011

Yang, P. (2017). Carboniferous-Triassic Erosion Recovery in Fuyang Area (In Chinese). *Inner Mongolia Petrochemical Industry* 2017 (7), 38–41. doi:10.3969/j.issn.1006-7981.2017.07.038

Yu, H., Lu, F., Guo, Q., Lu, W., Wu, J., and Han, S. (2005). Proto-sediment basin Types and Tectonic Evolution in the Southern Edge of North China Plate (In Chinese with English Abstract). *Pet. Geology. Experiment* 27, 111–117. doi:10.11781/sysydz200502111

Zhang, J. (2016). Analysis on Hydrocarbon Generation Characteristics of Carboniferous-Permian Source Rocks in Fuyang Exploration Area (In Chinese). *J. Yangtze Univ. (Natural Sci. Edition)* 13, 18–23. doi:10.3969/j.issn.1673-1409.2016.35.018

Zhang, P., Wang, L., Liu, S., Li, C., and Ding, Z. (2007). Geothermal Field in the South Huabei Basins (In Chinese with English Abstract). *Prog. Geophys.* 22, 604–608. doi:10.6038/pg2007EE0604

Zhang, Q., Jin, W., Wang, J., Chen, W., Li, C., Jiao, S., et al. (2016). Relationship between Magma-thermal Field and Hydrocarbon Accumulation (In Chinese with English Abstract). *Prog. Geophys.* 31, 1525–1541. doi:10.6038/pg20160416

Zhao, J., Liu, C., He, Z., and Liu, Y. (2010). Thermal Evolution Degree and its Hydrocarbon Geological Implications of the Main Strata Series in the Southern North China Craton (In Chinese with English Abstract). *Pet. Geology. Experiment* 32, 101–107. doi:10.11781/sysydz201002101

Zhao, J., Liu, C., Liu, Y., He, Z., Mao, W., and Zhu, B. (2011). Reconstruction of thermal Evolutionary History of the Upper Paleozoic in the Southern North China (In Chinese with English Abstract). *Oil Gas Geology*. 32, 64–74. doi:10.11743/ogg20110108

Zhao, Z., Li, D., Zhu, Y., Zhou, J., and Feng, J. (2001). Structural Evolution and Oil and Gas System Analysis of Hefei Basin (In Chinese). *Pet. Exploration Development* 28, 8–13. doi:10.3321/j.issn:1000-0747.2001.04.008

Zhu, C., Xu, M., Yuan, Y., Zhao, Y., Shan, J., He, Z., et al. (2010). Palaeogeothermal Response and Record of the Effusing of Emeishan Basalts in the Sichuan basin. *Chin. Sci. Bull.* 55, 949–956. doi:10.1007/s11434-009-0490-y

Zhu, H., Pang, X., and Wang, Y. (2006). Characteristics of Source Rocks in Permo-Carboniferous Coal Measure Formations in Fuyang Area (In Chinese with English Abstract). *Nat. Gas Industry* 26, 18–20. doi:10.3787/j.issn.1000-0976.2006.11.018

Zuo, Y., Qiu, N., Pang, X., Chang, J., Hao, Q., and Gao, X. (2013). Geothermal Evidence of the Mesozoic and Cenozoic Lithospheric Thinning in the Liaohe Depression. *J. Earth Sci.* 24, 529–540. doi:10.1007/s12583-013-0347-9

Zuo, Y., Qiu, N., Zhang, Y., Li, C., Li, J., Guo, Y., et al. (2011). Geothermal Regime and Hydrocarbon Kitchen Evolution of the Offshore Bohai Bay Basin, North China. *Bulletin* 95, 749–769. doi:10.1306/09271010079

Conflict of Interest: The authors declare that the research was conducted in the absence of any commercial or financial relationships that could be construed as a potential conflict of interest.

Publisher's Note: All claims expressed in this article are solely those of the authors and do not necessarily represent those of their affiliated organizations, or those of the publisher, the editors, and the reviewers. Any product that may be evaluated in this article, or claim that may be made by its manufacturer, is not guaranteed or endorsed by the publisher.

frontiers in Earth Science

OPINION
published: 17 February 2022
doi: 10.3389/feart.2022.805129

Sustainability Utilization of the Fault-Controlled Wentang Geothermal Field With Hydrogeological Numerical Model at Site Scale

Wenjie Sun[1]*, *Kai Liu*[2]*, *Junjie Bai*[1] and *Yaoyao Zhang*[2]

[1]National Engineering Research Center of Coal Mine Water Hazard Controlling, China University of Mining and Technology, Beijing, China, [2]Chinese Academy of Geological Sciences, Beijing, China

Keywords: geothermal, sustainability utilization, numerical simulation, Wentang, hot spring

INTRODUCTION

Geothermal energy is a renewable geological resource with the potential to provide a reasonable amount of electricity, heating/cooling, and balneology (Anderson and Rezaie, 2019; Soltani et al., 2021). If only 1% of the total estimated available geothermal energy could be utilized by humanity, it could provide almost 2,800 years of power at a constant rate (around 500 EJ per annum) (Olasolo et al., 2016).

The availability, including renewability and sustainability of energy, is one of the most critical aspects of social development (Anderson and Rezaie, 2019; Neves et al., 2021; Palomo-Torrejón et al., 2021). Renewability describes the property of the resource, the ability of a system to replace an amount of removed resource on a fixed time scale, and it depends mainly on the geological and hydrogeological features of the regional system. In contrast, the term sustainability refers to how the resource is utilized. Sustainability refers to the development of a resource in such a way that meets the needs of the present without compromising the ability of future generations to meet their own needs (Fabbri et al., 2017). Sustainable exploitation is crucial to guarantee their long-term utilization, future maintenance, and environmental protection (Eyerer et al., 2020; Torresan et al., 2020). To achieve sustainable utilization, the flow rate of exploited water (and thermal), which mainly depends on the local hydraulic properties of the reservoir and the model of utilization, must be lower or equal to the renewable recharge of the system (Kaczmarczyk et al., 2020).

The Wentang hot spring is a well-known geothermal field in Jiangxi Province, which is called the homeland of hot springs in China (He and Zhu, 2021). Wentang hot spring has been used for 2,000 years, and the outflow amount could be up to 13,000 tons daily with a temperature range of 50°C–72°C. Due to the development of local tourism and health industries, the demand for hot water is increasing, which is met by drilling wellbores that exploited the thermal groundwater. The ongoing exploitation seems renewable for the utilization of the WGF geothermal resource.

Even though rigorous management policies have been established in WGF for energy production, the literature is lacking detailed information on the sustainable utilization of thermal water for tourism purposes. For now, the daily recharge water amount depends on the outflow. As we know, the cold water needs time to flow the warm rock and turn into geothermal water (De Simone et al., 2013). A large amount of hot water needed cannot be extracted immediately. This phenomenon is more obvious in winter with large consumption demand. During the recharge pumping test in 2012, the temperature decreased from 64°C to 58°C under the injection water amount of 20,181 m^3/day, and the temperature has a five drop under the continuous pumping period with increasing consumption demand. A considerable increase in the flow rate could cause a higher drawdown depleting the resource for future generations. The sustainable use of a site-specific management plan

OPEN ACCESS

Edited by:
Yanlong Kong,
Institute of Geology and Geophysics (CAS), China

Reviewed by:
Gang Lin,
China University of Mining and Technology, China
Shufang Wang,
Beijing Institute of Hydrogeology and Engineering Geology, China

***Correspondence:**
Wenjie Sun
swj@cumtb.edu.cn
Kai Liu
acancer@163.com

Specialty section:
This article was submitted to Economic Geology, a section of the journal Frontiers in Earth Science

Received: *29 October 2021*
Accepted: *11 January 2022*
Published: *17 February 2022*

Citation:
Sun W, Liu K, Bai J and Zhang Y (2022) Sustainability Utilization of the Fault-Controlled Wentang Geothermal Field With Hydrogeological Numerical Model at Site Scale. Front. Earth Sci. 10:805129. doi: 10.3389/feart.2022.805129

FIGURE 1 | The location of Wentang geothermal field in Wentang Town, Jiangxi Province of China.

accounts for the local hydrogeological characteristics of the system, the energy demand, and the long-term exploitation. For both high- and low-enthalpy geothermal systems, integration with other renewable sources, such as biomass and solar energy, can be an interesting way to upgrade, as well (Amoresano et al., 2013).

The question on how long would the water flow from the recharge area to the outflow wellbore need to be answered to make the fine management policy (Kiryukhin et al., 2018; Wang et al., 2020). The long-lasting utilization of the thermal resource, as well as the huge amount of data (i.e., hydrogeological data, flow rates, information about the utilization of the thermal resource, and tourism data), represent a probable unique case study. A numerical study dedicated to the prediction of the long-term sustainability of geothermal heat extraction in a fault-control geological setting while integrating site-specific information and monitoring data is of great value to both academia and industry (Meng et al., 2019). Hence, a proper site-wise parameterized model for geothermal use on a neighborhood scale is of great importance for sustainability utilization. Comprehensive analysis with operation data, preliminary 2D model, hydraulic connection test, and 3D hydrogeological reconstruction model, rather than a simplified conceptualization of the geological setting, can increase the consistency of the modeling results (Blöcher et al., 2010; Mottaghy et al., 2011; Zhao et al., 2015).

In the *Geological and hydrogeological setting* section, the geological setting of WGF is presented, and the main parameters are analyzed. In the *Data analysis and model result discussion* section, operation data and preliminary 2D model results are first introduced, and the results of hydraulic connection tests with 3D hydrological models are shown for quantitative analyses. The conclusions are presented and discussed in the *Conclusion* section.

GEOLOGICAL AND HYDROGEOLOGICAL SETTING

Geological Setting

The Wentang geothermal field (WGF) is located in the northwest wing of the Wugong Mountain anticline in Yichun City, Jiangxi Province, as shown in **Figure 1**. The strata and rocks in the Wentang area mainly include Quaternary, metamorphic rock series of Laohutang formation in Sinian Songshan group, migmatite, granite, and dyke of Yanshanian. The Wugongshan compound anticline, belonging to the Paleo-Cathaysian system, suffered severe damage and transformation due to late structural variation, especially the Caledonian mixed petrification and Yanshanian tectonic–magmatic activity, and became more fragmented and extremely fragmented.

There are two main fault groups that are closely related to the recharge and outflow of WGF: NNE- and NW-trending faults, as shown in **Figure 2**. The F_1 fault system consists of F_1^1, F_1^2, F_1^3, F_1^4, and some associated structures, with F_1^1 as the main fault. The F_1^1 is a large-scale compression torsion fault, with a strike of 55°–60°. The F_2 fault system consists of a compression torsion fault (F_2^1) and a tension torsion branch fault (F_2^2), which is almost covered by Quaternary. As the main fault, F_2^1 has a strike of 55°–60° and a dip angle of 55°–60°, in general, as shown in **Figure 3**.

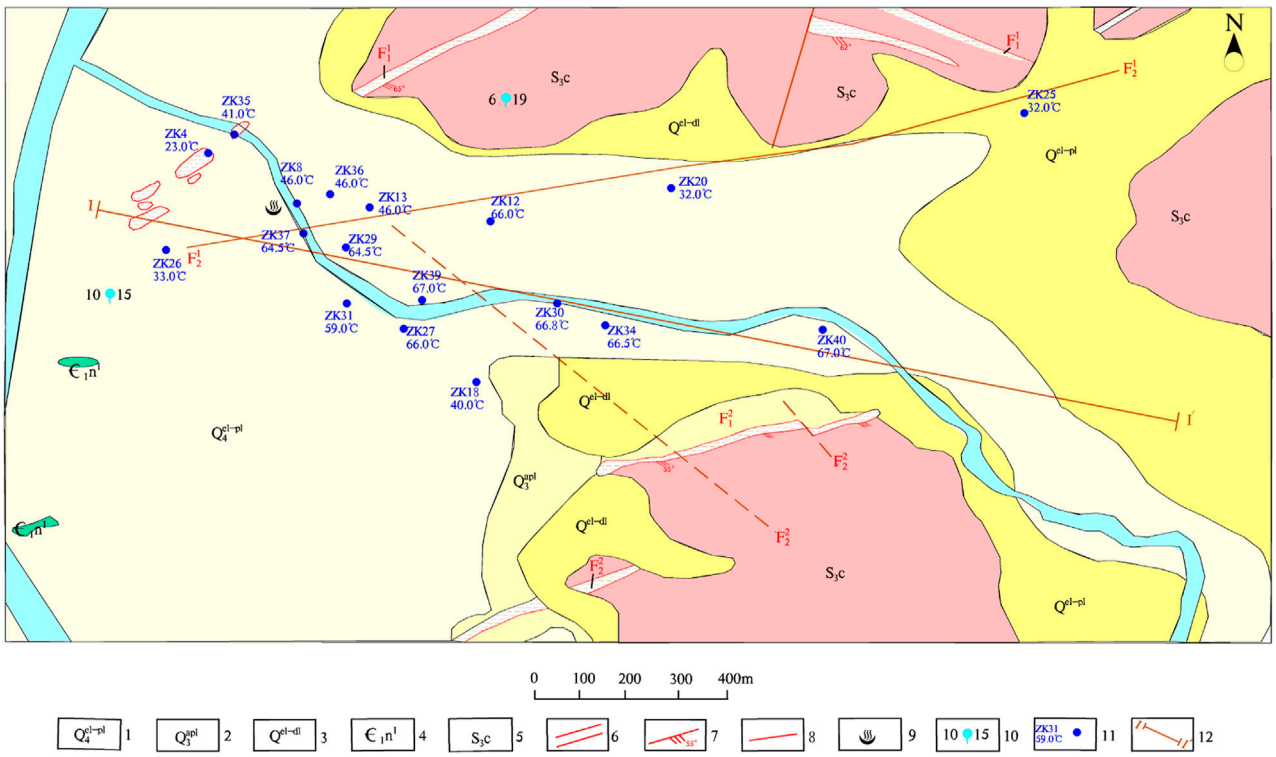

FIGURE 2 | Geological map of Wentang geothermal field. 1 Quaternary Holocene flood alluvial layer. 2 Quaternary upper Pleistocene glacial deposit. 3 Quaternary eluvial layer. 4 Lower Cambrian Niujiaohe Formation. 5 Late Silurian Chouping Unit. 6 Silicified fracture zone. 7 Measured and speculated hidden compression-torsion fault. 8 Measured and speculated compression-torsion fault. 9 Hot spring. 10 Spring. 11 Borehole. 12 Cross section.

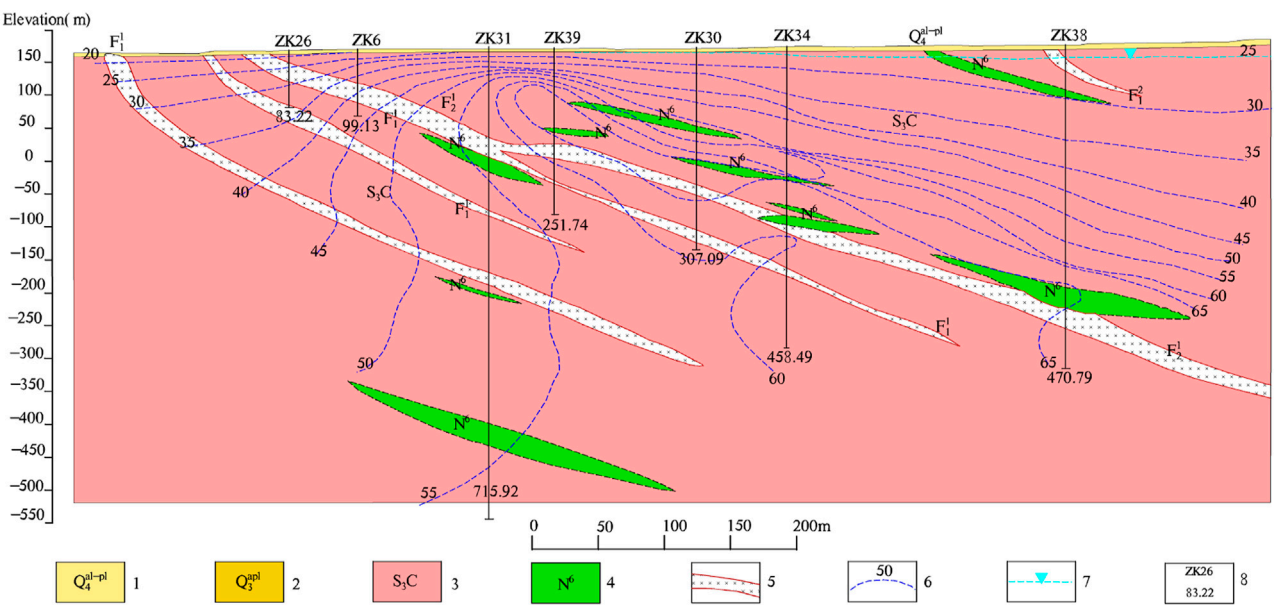

FIGURE 3 | Structure profile of cross section I–I′ that is plotted in **Figure 2**. 1 and 2 are the same as in **Figure 2**. 3 Late Silurian Chouping Unit. 4 Himalayan period diabase. 5 Transtensional Fault (Silicified fracture zone). 6 Isotherm. 7 Geothermal water level. 8 Borehole number and depth.

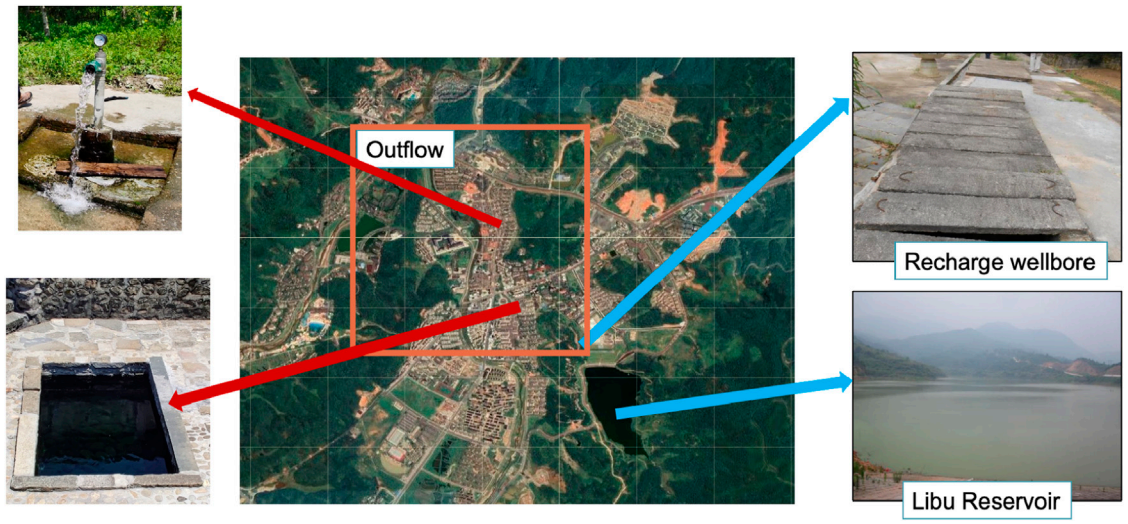

FIGURE 4 | Recharge (the blue arrow line) and outflow (the orange square area and typical representative listed by the red arrow line) area of the Wentang geothermal field.

TABLE 1 | Key results of the pumping test that was carried out in the Wentang geothermal field (WGF) over the years.

Time	Recharge quantity (m^3/day)	Outflow quantity (m^3/day)
1973	-	1,300
1982	6,200	3,500
2005	10,805	7,097
2008	23,366	10,239
2011	20,181	13,053

TABLE 2 | Statistical table of thermal reservoir thickness in main movement zones of geothermal water.

Borehole no	Elevation range (m)	Thickness (m)	Temperature (°C)
ZK27	163.70–180.32	16.60	66.0
ZK29	29.56–50.00	20.44	64.5°C
ZK33	28.00–47.12	19.12	64.5°C
ZK30	162.00–176.20	14.20	66.8°C
	205.00–225.00	20.00	
ZK34	186.83–208.00	21.97	66.5°C
ZK38	336.40–340.00	3.60	66.0°C
	370.00–403.50	33.40	
ZK39	72–120	48.00	65.5°C
ZK40	312.75–324.06	29.31	67.0°C

Hydrogeological Conditions

In the process of infiltration, runoff, and storage, the geothermal water continuously dissolves the soluble substances in the rocks, forming the unique water chemical composition of WGF. The main characteristics of WGF geothermal water are as follows: the highest water temperature is 72°C, pH value is 7.1–7.8 (weakly alkaline), salinity is 0.08–0.263 g/L (freshwater), and the hydrochemical type is sodium bicarbonate–calcium water containing metasilicic acid and selenium.

The cold groundwater there mainly consists of Quaternary pore water and bedrock fissure water. Quaternary pore water is mainly distributed in intermountain valleys, which is composed of sandy soil and gravel layer. The aquifer is 2- to 5-m thick, and it is mainly supplied by atmospheric precipitation and bedrock fissure water and discharged into rivers and valleys. Only a small amount of spring water is exposed. Bedrock fissure water is mainly distributed in the middle and low mountain areas and slopes and occurs in the weathering fissures and structural fissures of metamorphic rock, migmatite, and granite. The runoff modulus is 3–6 L/s·km^2, and the spring discharge is 0.1–1 L/s. The water temperature of bedrock fissure water is generally 13°C–19°C, the hydrochemical type is HCO_3–Na or Na, Ca, and the salinity is 0.04–0.18 g/L. The recharge source of bedrock fissure water in the area is mainly meteoric water, which flows along the slope to the lower part, and then discharges into gullies in the form of down springs or scattered streams.

According to the groundwater head measurements, the groundwater flow direction was predominantly southeastward (**Figure 4**) toward the northwestward about 1.0 km away.

Pumping Test

The recharge and pumping test of WGF was carried out during the first exploration from 1971 to 1973. After the continuous exploration and development in 1982, 2005, 2008, and 2011, the recharge and outflow quantity has been greatly improved (see **Table 1** for detailed data).

The results of the pumping test show that the distribution and movement of geothermal water are strictly controlled by the tension torsion fault (F_2[2]), which is manifested in water temperature, water level, and hydrochemistry. There is a great difference between the permeability and water abundance of rocks inside and outside the tension torsion zone. The tension torsion zone is the main channel of geothermal water, which has good water permeability and water abundance. During the

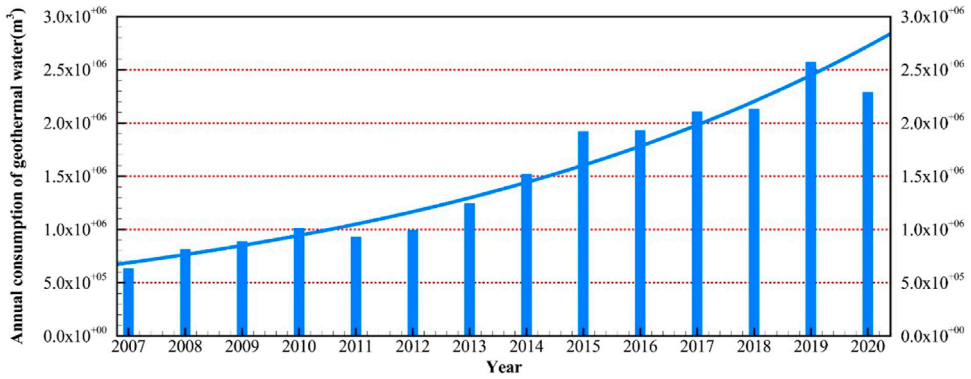

FIGURE 5 | Annually increasing consumption of geothermal water in the last 14 years.

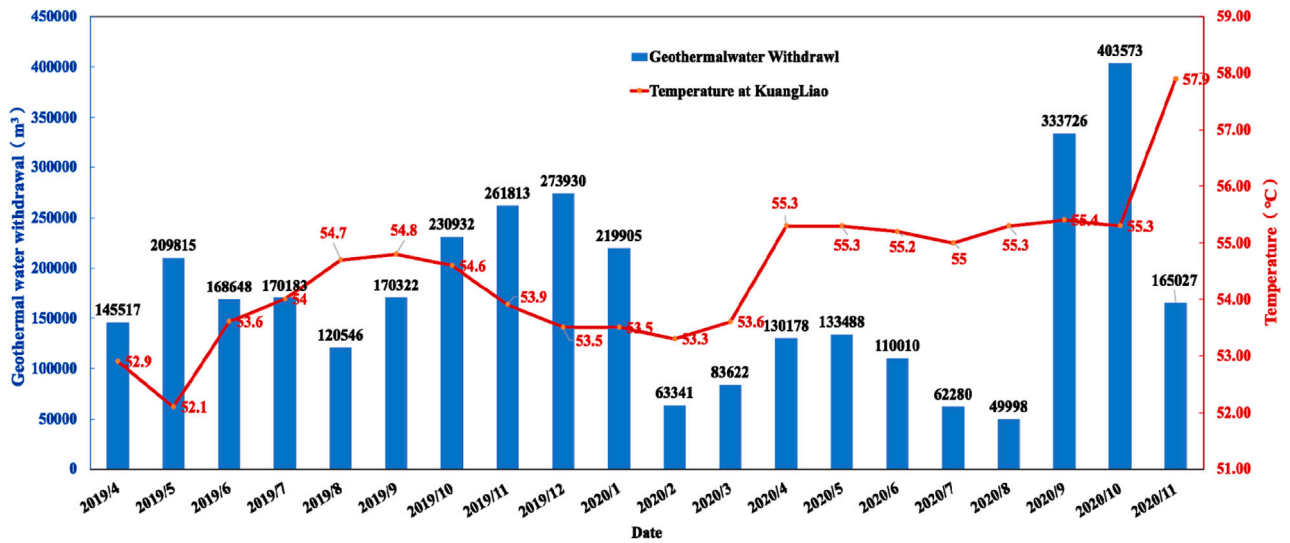

FIGURE 6 | The monthly monitoring data of geothermal water withdrawn and temperature of Kuangliao from April 2019 to November 2020.

pumping test, the water level in the borehole located inside the tension torsion zone has a small drawdown with a large discharge, and the temperature of pumping water is close to the highest water temperature before the pumping test. On the contrary, the water level draw-down of the borehole outside the tension torsion band is large with a small flow rate, which is 10 times smaller than that inside the tension torsion band, and the pumping temperature is 3°C–5.5°C lower than that before pumping. In addition, the pumping test indicates that there is a relatively impermeable boundary on the west side of the tension torsion zone.

Generally, the groundwater is recharged by the atmospheric precipitation infiltrated through rock fissures, joints, and structural fracture zones in the southern Wugong Mountain. Through the complex deep circulation, the cold groundwater absorbs the heat energy in the rock by the way of heat conduction and convection. The geothermal water gathers at a certain place in the deep and flows northward along the faulted channel including the torsional structural fissures and pores. The geothermal water flow is blocked by the fault structure near WGF and is discharged to the surface in the form of ascending hot spring.

DATA ANALYSIS AND MODEL RESULT DISCUSSION

Operation and Monitoring Data

The first systematic survey was conducted in 1971, and some wellbores located close to the thermal spring were drilled. After that, 56 wellbores were drilled, and only 16 of them were preserved until now. With the logging data, the main reservoir thickness of each wellbore is listed in **Table 2**.

The annual consumption of geothermal water increased gradually in the last 14 years, and the amount in 2019 is five times that in 2007, as shown in **Figure 5**. Due to the impact of

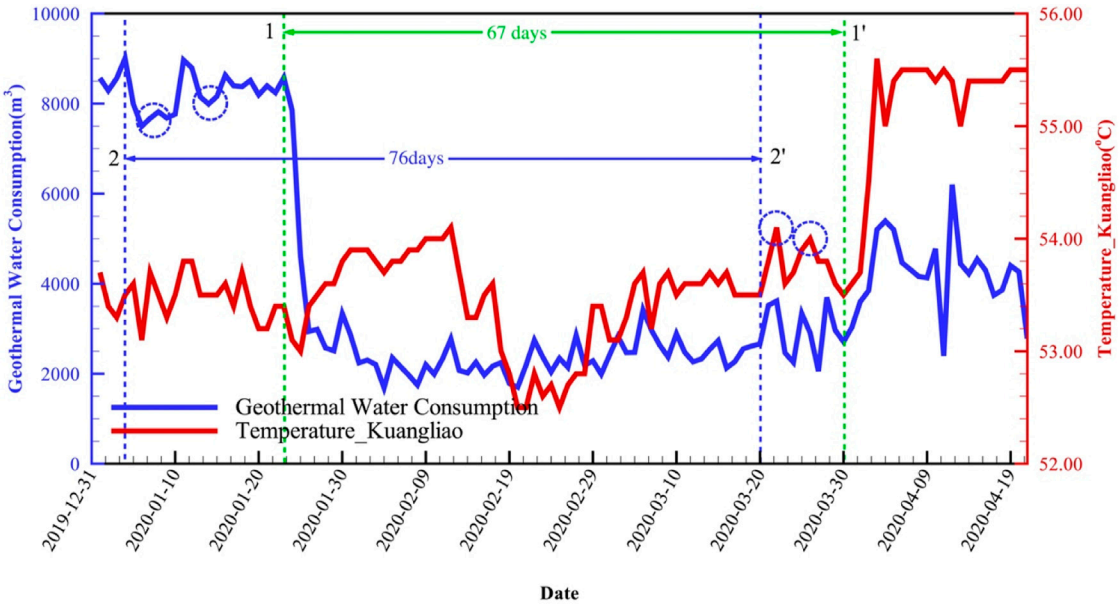

FIGURE 7 | The daily monitoring data, which show the relation between geothermal water consumption and temperature variation of Kuangliao.

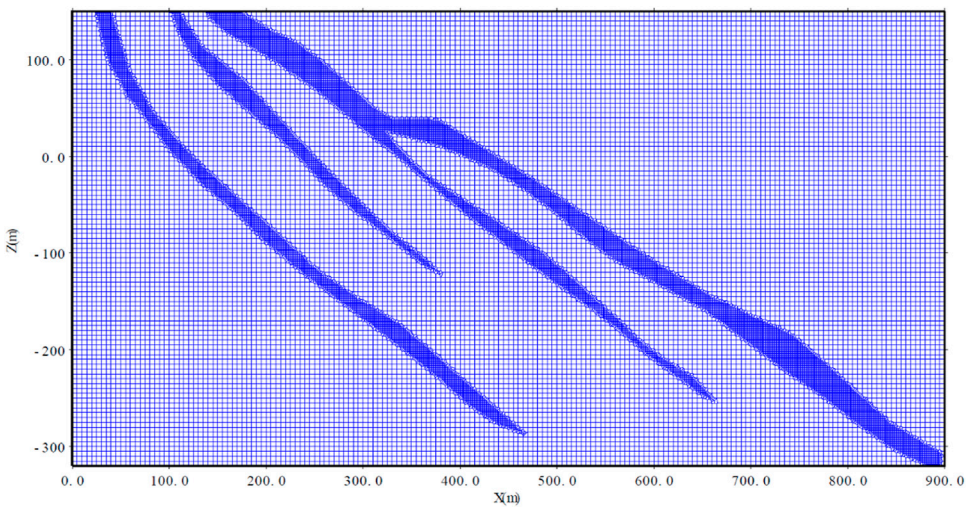

FIGURE 8 | The 2D model discretization (the mesh around the fault has been refined, as shown in the dark blue area).

COVID19, the consumption in 2020 was a little decreased. More detail can be seen from the monthly consumption data in **Figure 6**, and the results indicate that peak usage occurs during the winter. As the monthly consumption change, the temperature also fluctuates with a range of about 5°C. Specifically, when the consumption increases, the temperature decreases, but there is a certain delay. **Figure 7** shows the daily monitoring data, which show the relation between geothermal water consumption and temperature variation.

At point 1, the geothermal water consumption suddenly drops down due to the beginning of COVID-19, the temperature increases at point 1′ after a delay of 67 days. Following this clue, another changing trend is identified at point 2 to point 2′ with a delay of 76 days. Based on these two sets of data, it might take 2 months for the geothermal water to flow from the recharge area to the production well (named KL).

Preliminary Study With 2D Model

A 2D homogeneous model is built using the TOUGH3 simulator to preliminarily depict the geothermal water flow in the subsurface (Jung et al., 2017). The cross-section I–I′, which is shown in **Figure 3**, is selected as the model domain. The domain is discretized using the integral finite difference method

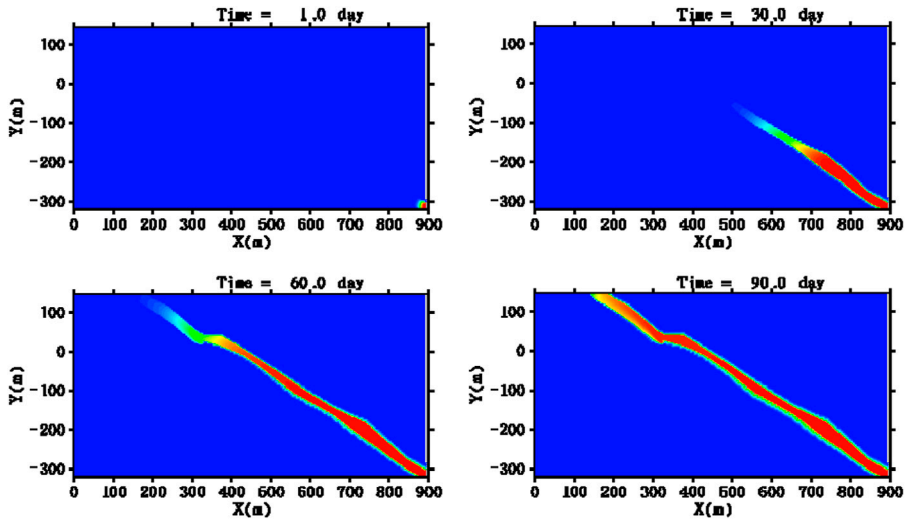

FIGURE 9 | Geothermal water migration plume (the red color in the figure represents the geothermal water saturation).

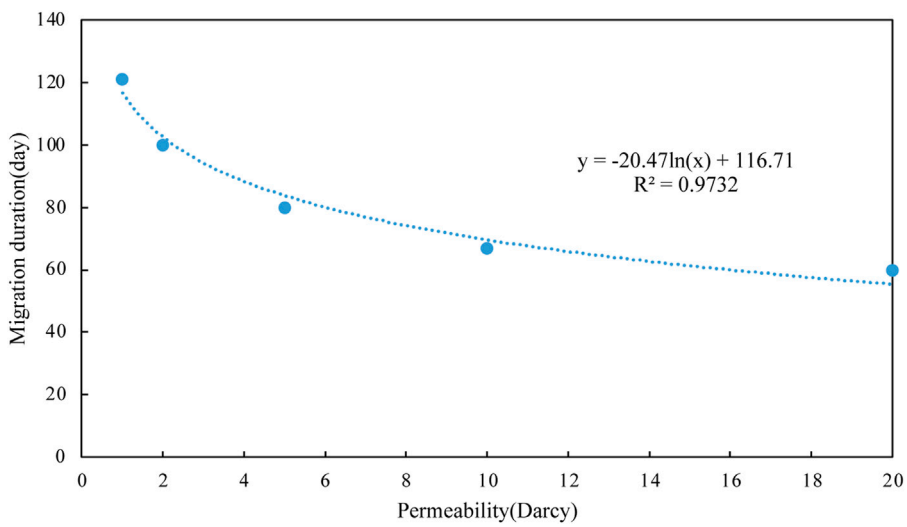

FIGURE 10 | Migration duration under different representative permeabilities of fracture zone.

(Narasimhan and Witherspoon, 1976), with mesh refinement in the fault zone, as shown in **Figure 8**. Focusing on the saturated section of the unconfined aquifer, the applied 2D model is idealized as a homogeneous layer with the fully saturated flow and heat transport properties. As for the boundary conditions, a fixed hydraulic head difference is assigned between the recharge and outflow boundaries.

As shown in **Figure 9**, it takes about 90 days for the geothermal water to migrate from the bottom to the ground. The fracture zone in the model is represented by the so-called high-speed channel within a certain width by the large permeability. Several permeability schemes (1Darcy, 2Darcy, 5Darcy, 10Darcy, 20Darcy) are designed to conduct the sensitivity analysis (**Figure 10**). The results indicate the decline of migration time duration as the representative permeability of the fracture zone in the 2D model.

Hydraulic Connection Test and 3D Hydrological Model

The initial model results indicate a 60- to 100-day migration time duration. However, in realistic geological conditions, the time duration might differ. Therefore, a hydraulic connection test and a comprehensive 3D model are conducted to gain the time duration from the recharge area to the outflow area. The test started on August 15 and ended on November 15.

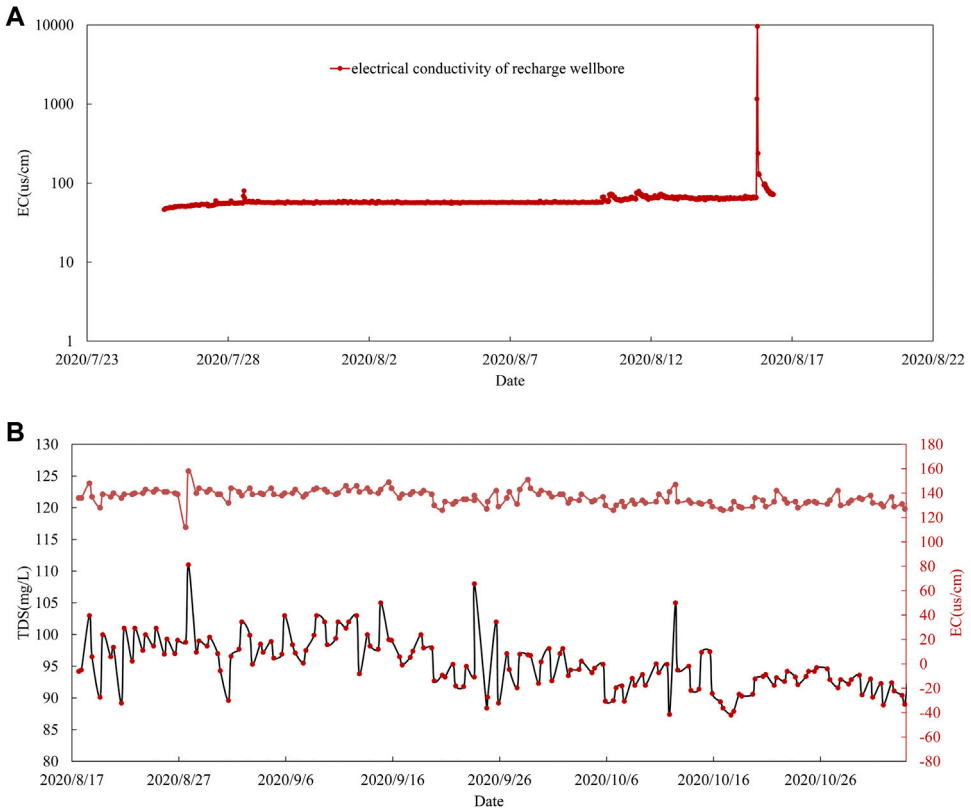

FIGURE 11 | The monitoring data of the KL exploitation wellbore in the hydraulic connection test. **(A)** Electrical conductivity variation of the recharge area before and right after the hydraulic connection test; **(B)** the TDS and electrical conductivity (EC) during the later 3 months.

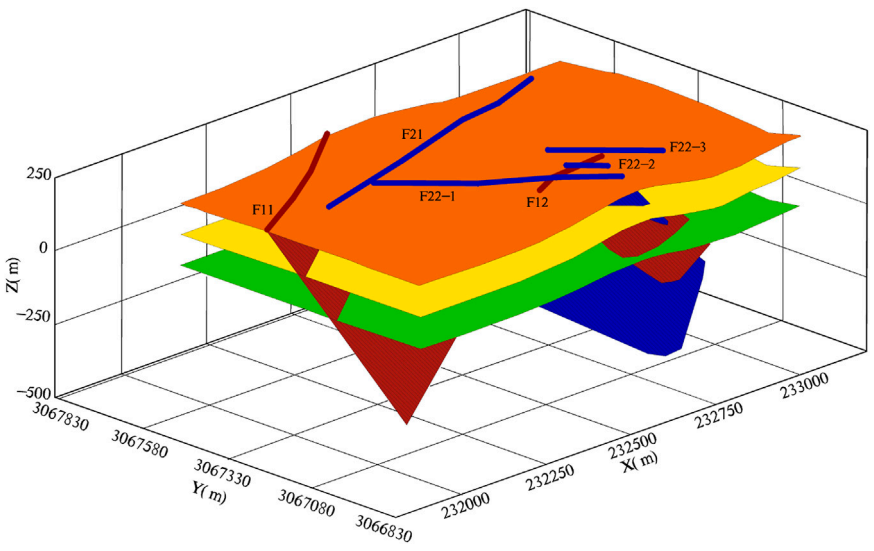

FIGURE 12 | The 3D model with multifaults (the different colors represent the geological domain depicted in **Figure 2**, in which the blue color represents the focused fault area in the numerical model).

A certain amount of salt (60 kg NaCl) is injected into the recharge area within an hour, and the electrical conductivity (EC) and TDS of the nearest exploitation wellbore (named KL) are monitored with the automatic checkout equipment. **Figure 11A** shows that the EC is captured in the recharge area with a sudden increase. The monitoring data of KL, as shown in **Figure 11B**, indicate that there are multipeak of EC and TDS variations. The first fluctuation arrived on August 27, which is just 12 days after the injection. The second fluctuation is 38 days later on September 23. The third fluctuation happened on October 12, which is about 2 months after the injection.

In order to avoid the indeterminacy of the 2D model, a comprehensive 3D model with multifaults is built based on the more detailed geological conditions, as shown in **Figure 12**. With limited parameters of the fault and fracture zone, it takes about 90 days for the geothermal water migration from the recharge area to the outflow wellbore (KL in this model). The 3D model results still differ from the hydraulic connection test result in which the numerical model only represented the third peak electrical conductivity captured. There are several reasons for the differences between the model and observation. One of the most important reasons is that there are several hydraulic tunnels between neighborhood wells. Some other methods, such as the lumped model, might be considered to further refine the model based on some generalized parameters.

CONCLUSION

Sustainability utilization of the fault-controlled neighborhood-scale Wentang Geothermal Field is one of the most critical aspects of the local social development. The comprehensive analysis of operation data analysis, preliminary study with 2D model, and hydraulic connection test with 3D hydrological model indicate that the migration time duration for the geothermal water is within the range of 1–3 months. According to this conclusion, a dynamic management policy that recharges the groundwater 2 months earlier before a large amount of geothermal utilization is suggested to the local geothermal regulatory agency. It is beneficial to reduce possible hot water temperature fluctuations and to balance the water table. For more sustainable development, the use of geothermal water should be more strictly controlled.

In addition, more aspects should be given importance in future studies: 1. Detailed parameters of the fracture zone should be gained to get a better understanding of the geothermal flow migration. 2. A high efficiency parallel computing method should be involved to enhance the model simulation process; otherwise, the simulation will be inefficient, which leads to time-consuming work.

AUTHOR CONTRIBUTIONS

WS, KL, JB, and YZ contributed to the conception and design of the study. WS wrote sections of the manuscript. KL organized the database. JB was in charge of the figures. YZ performed the statistical analysis. All authors contributed to the manuscript revision, and read and approved the submitted version.

FUNDING

This study is funded by the China Geological Survey (No. DD20201165, No. DD20221819), CGS Research Fund (No. JKY202004), National Natural Science Foundation of China (42172282, 42002255), Shanxi Key Laboratory of Coalmine Water Hazard Control (2021SKMS01), Fundamental Research Funds for the Central Universities (2021YJSDC06), and State Key Laboratory of Coal Resources and Safe Mining (SKLCRSM20DC02).

REFERENCES

Amoresano, A., De Sio, P., Langella, G., and Meo, S. (2013). Biomass and Solar Integration in Low Enthalpy Geothermal Plants. *Int. Rev. Model. Simul.* 6 (3), 981–987.

Anderson, A., and Rezaie, B. (2019). Geothermal Technology: Trends and Potential Role in a Sustainable Future. *Appl. Energ.* 248, 18–34. doi:10.1016/j.apenergy.2019.04.102

Blöcher, M., Zimmermann, G., Moeck, I., Brandt, W., Hassanzadegan, A., and Magri, F. (2010). 3D Numerical Modeling of Hydrothermal Processes during the Lifetime of a Deep Geothermal Reservoir. *Geofluids* 10, 406–421. doi:10.1111/j.1468-8123.2010.00284.x

De Simone, S., Vilarrasa, V., Carrera, J., Alcolea, A., and Meier, P. (2013). Thermal Coupling May Control Mechanical Stability of Geothermal Reservoirs during Cold Water Injection. *Phys. Chem. Earth, Parts A/B/C* 64, 117–126. doi:10.1016/j.pce.2013.01.001

Eyerer, S., Schifflechner, C., Hofbauer, S., Bauer, W., Wieland, C., and Spliethoff, H. (2020). Combined Heat and Power from Hydrothermal Geothermal Resources in Germany: An Assessment of the Potential. *Renew. Sustainable Energ. Rev.* 120, 109661. doi:10.1016/j.rser.2019.109661

Fabbri, P., Pola, M., Piccinini, L., Zampieri, D., Roghel, A., and Libera, N. D. (2017). Monitoring, Utilization and Sustainable Development of a Low-Temperature Geothermal Resource: A Case Study of the Euganean Geothermal Field (NE, Italy). *Geothermics* 70, 281–294. doi:10.1016/j.geothermics.2017.07.002

He, J., and Zhu, Z. a. (2021). Research on Sustainable Utilization of Rural Resources in Tourism Development in Mountain Area. *IOP Conf. Ser. Earth Environ. Sci.* 632 (2), 022083. doi:10.1088/1755-1315/632/2/022083

Jung, Y., Pau, G. S. H., Finsterle, S., and Pollyea, R. M. (2017). TOUGH3: A New Efficient Version of the TOUGH Suite of Multiphase Flow and Transport Simulators. *Comput. Geosciences* 108, 2–7. doi:10.1016/j.cageo.2016.09.009

Kaczmarczyk, M., Tomaszewska, B., and Operacz, A. (2020). Sustainable Utilization of Low Enthalpy Geothermal Resources to Electricity Generation through a cascade System. *Energies* 13 (10), 2495. doi:10.3390/en13102495

Kiryukhin, A. V., Polyakov, A. Y., Usacheva, O. O., and Kiryukhin, P. A. (2018). Thermal-permeability Structure and Recharge Conditions of the Mutnovsky High-Temperature Geothermal Field (Kamchatka, Russia). *J. Volcanology Geothermal Res.* 356, 36–55. doi:10.1016/j.jvolgeores.2018.02.010

Meng, B., Vienken, T., Kolditz, O., and Shao, H. (2019). Evaluating the thermal Impacts and Sustainability of Intensive Shallow Geothermal Utilization on a Neighborhood Scale: Lessons Learned from a Case Study. *Energ. Convers. Management* 199, 111913. doi:10.1016/j.enconman.2019.111913

Mottaghy, D., Pechnig, R., and Vogt, C. (2011). The Geothermal Project Den Haag: 3D Numerical Models for Temperature Prediction and Reservoir Simulation. *Geothermics* 40, 199–210. doi:10.1016/j.geothermics.2011.07.001

Narasimhan, T. N., and Witherspoon, P. A. (1976). An Integrated Finite Difference Method for Analyzing Fluid Flow in Porous media. *Water Resour. Res.* 12, 57–64. doi:10.1029/wr012i001p00057

Neves, R., Cho, H., and Zhang, J. (2021). Pairing Geothermal Technology and Solar Photovoltaics for Net-Zero Energy Homes. *Renew. Sustainable Energ. Rev.* 140, 110749. doi:10.1016/j.rser.2021.110749

Olasolo, P., Juárez, M. C., Morales, M. P., D´Amico, S., and Liarte, I. A. (2016). Enhanced Geothermal Systems (EGS): A Review. *Renew. Sustainable Energ. Rev.* 56, 133–144. doi:10.1016/j.rser.2015.11.031

Palomo-Torrejón, E., Colmenar-Santos, A., Rosales-Asensio, E., and Mur-Pérez, F. (2021). Economic and Environmental Benefits of Geo-thermal Energy in Industrial Processes. *Renew. Energ.* 174, 134–146. doi:10.1016/j.renene.2021.04.074

Soltani, M., Moradi Kashkooli, F., Souri, M., Rafiei, B., Jabarifar, M., Gharali, K., et al. (2021). Environmental, Economic, and Social Impacts of Geothermal Energy Systems. *Renew. Sustainable Energ. Rev.* 140, 110750. doi:10.1016/j.rser.2021.110750

Torresan, F., Piccinini, L., Pola, M., Zampieri, D., and Fabbri, P. (2020). 3D Hydrogeological Reconstruction of the Fault-Controlled Euganean Geothermal System (NE Italy). *Eng. Geology.* 274, 105740. doi:10.1016/j.enggeo.2020.105740

Wang, Y., Liu, Y., Dou, J., Li, M., and Zeng, M. (2020). Geothermal Energy in China: Status, Challenges, and Policy Recommendations. *Utilities Policy* 64, 101020. doi:10.1016/j.jup.2020.101020

Zhao, Y., Feng, Z., Feng, Z., Yang, D., and Liang, W. (2015). THM (Thermo-Hydro-Mechanical) Coupled Mathematical Model of Fractured media and Numerical Simulation of a 3D Enhanced Geothermal System at 573 K and Buried Depth 6000-7000 M. *Energy* 82, 193–205. doi:10.1016/j.energy.2015.01.030

Conflict of Interest: The authors declare that the research was conducted in the absence of any commercial or financial relationships that could be construed as a potential conflict of interest.

Publisher's Note: All claims expressed in this article are solely those of the authors and do not necessarily represent those of their affiliated organizations, or those of the publisher, the editors, and the reviewers. Any product that may be evaluated in this article, or claim that may be made by its manufacturer, is not guaranteed nor endorsed by the publisher.

frontiers in Earth Science

ORIGINAL RESEARCH
published: 18 February 2022
doi: 10.3389/feart.2022.819778

Performance Comparison of H_2O and CO_2 as the Working Fluid in Coupled Wellbore/Reservoir Systems for Geothermal Heat Extraction

*Hongwu Lei**

State Key Laboratory of Geomechanics and Geotechnical Engineering, Institute of Rock and Soil Mechanics, Chinese Academy of Sciences, Wuhan, China

CO_2 is considered as a novel heat-transmission fluid for extracting geothermal energy from enhanced geothermal systems (EGS), attributed to its high compressibility, expansivity and low viscosity in comparison to water. In order to compare the performance of CO_2 and H_2O as the working fluid in EGS, a classical five-spot model based on the geologic and geothermal conditions at the Songliao Basin, China, was constructed. Results obtained from the coupled wellbore/reservoir model revealed that the net heat extraction and flow rate are greater for CO_2 than for H_2O at a fixed operation pressure difference between the injection and production wellheads. However, the wellhead temperature is far lower for CO_2 than for H_2O due to the strong Joule–Thomson effect of CO_2 in the wellbore. Moreover, a stronger pressure change in the wellbore is observed by using CO_2, attributed to the gravity and high flow velocity of CO_2; this pressure change induces a drop in the frictional pressure. For CO_2, the enthalpy change in the wellbore is mainly contributed by the gravitational potential, while for H_2O, it is contributed by the gravitational potential and lateral heat exchange. The heat extraction performance depends on the operation pressure difference and injection temperature for H_2O-based EGS, while it depends on the wellhead pressures of both the injection and production wells as well as the injection temperature for CO_2-based EGS. A high operation pressure is favorable for improving the heat extraction performance (especially the production temperature) for CO_2. With the temperature drop limitation at the downhole of the production well, the heat extraction performance is better by using H_2O than that by using CO_2 as the working fluid. However, the low-power consumption for maintaining fluid circulation demonstrates the application potential of CO_2-based EGS.

Keywords: enhanced geothermal systems, coupled wellbore/reservoir systems, performance comparison, numerical simulation, carbon dioxide, water

OPEN ACCESS

Edited by:
Yanlong Kong,
Institute of Geology and Geophysics (CAS), China

Reviewed by:
Micol Todesco,
Istituto Nazionale di Geofisica e Vulcanologia (INGV), Italy
Guodong Cui,
China University of Geosciences Wuhan, China

***Correspondence:**
Hongwu Lei
hongwulei2008@aliyun.com

Specialty section:
This article was submitted to Economic Geology, a section of the journal Frontiers in Earth Science

Received: *22 November 2021*
Accepted: *19 January 2022*
Published: *18 February 2022*

Citation:
Lei H (2022) Performance Comparison of H_2O and CO_2 as the Working Fluid in Coupled Wellbore/Reservoir Systems for Geothermal Heat Extraction. Front. Earth Sci. 10:819778. doi: 10.3389/feart.2022.819778

1 INTRODUCTION

Geological sequestration of carbon dioxide (CO_2) in geological formations has been recognized as a technically feasible method to control or slow down the climate change trend (White et al., 2003; Orr, 2004; Metz et al., 2005; Goodman et al., 2013; IPCC 2014). It is recently considered as a novel heat-transmission fluid instead of H_2O for extracting geothermal energy from EGS, which can

simultaneously achieve energy extraction and CO_2 geological sequestration (Brown D., 2000; Mohan et al., 2013; Xu R. et al., 2015; Pan F. et al., 2017; Wang et al., 2018; Shi et al., 2018; Bongole et al., 2019; Singh et al., 2020; Cui et al., 2021). CO_2 could perform better than H_2O, because of 1) large buoyancy force caused by a density difference between cold and hot CO_2, leading to the natural thermosiphon; 2) strong mobility, which can yield large flow velocities for a given pressure gradient; 3) low reactivity, which reduces or eliminates scaling problems caused by the water-rock geochemical reaction (Brown, 2000).

Although there is no commercial project with CO_2 as the working fluid for extracting deep geothermal energy, a number of numerical simulations were conducted to examine the feasibility and heat mining performance. Pruess (2006) used TOUGH2 to simulate the heat extraction performance of CO_2-based EGS and demonstrated that the mass flows and net heat extraction rate generated by CO_2 are higher than that generated by H_2O, by four times and 50%, respectively. Furthermore, Pruess (2008) conducted three-dimensional simulations to investigate the production behavior and revealed that production wells should be open only in a limited vertical interval near the reservoir top to avoid thermal breakthrough due to the large contrast in the CO_2 density. To consider fluid flow and heat transfer in wellbores, Atrens et al. (2010) conducted a simple calculation with pipe flow and the first law of thermodynamics for wellbores and a lumped-parameters model for reservoirs and showed that compared to water, CO_2 is less effective for extracting energy under conditions similar to those utilized for past EGS trials (Murphy et al., 1999). Following the same calculation method, Zhang et al. (2013) compared the thermodynamic performance for CO_2-based EGS and H_2O-based EGS systems, indicating that CO_2-based EGS produces more power in reservoirs with a low recoverable thermal energy, and operation parameters should be optimized to match the actual CO_2-based EGS condition. Recently, the calculation for the effect of impurities on CO_2-based EGS revealed that the system efficiency decreases with the increase in the impurity fractions (Zhang et al., 2016).

To simultaneously consider fluid flow and heat transfer in wellbores and reservoirs, T2Well (Pan et al., 2011; Pan and Oldenburg 2014) was developed and used to evaluate the heat and flow in wells for CO_2-based EGS; the results revealed that an appropriate CO_2 flow rate is required to generate a positive electric power output for a fixed flow-rate production. Xu et al., 2015b used T2Well to numerically identify advantages and disadvantages of using CO_2 as the working fluid and revealed that a very low-temperature fluid was obtained by CO_2, which is major disadvantage for CO_2-based EGS. Luo et al. (2014) investigated dramatic variations in the supercritical CO_2 properties and thermal-hydraulic turbulence features of CO_2 in the wellbores in a doublet CO_2-EGS system based on conditions at the European EGS site at Groβ Schönebeck using the CFD code FLUENT 6.3. The result demonstrated that a CO_2 injection rate of 10 kg/s is apparently favorable for an expected geothermal utilization lifetime of 20 years Huang et al. (2014) coupled the reservoir simulator TOUGH2 (Pruess et al., 1999) with the wellbore simulator HOLA (Aunzo et al., 2011) to evaluate the potential heat extraction using H_2O in the Songliao Basin.

In this study, a classical five-spot model based on the geological and geothermal conditions of the Songliao Basin is constructed. The coupled wellbore/reservoir simulator T2Well (Pan et al., 2011; Pan and Oldenburg 2014) is employed to simulate the fully coupled thermal and hydrodynamic (TH) processes. The comparison of the performance, including net heat extraction, flow rate, and production temperature as well as the TH processes in the wellbores and reservoir between H_2O-based and CO_2-based EGS is performed. Then, sensitivity analysis to the operation parameters, including pressures of injection and production wellheads and injection temperature, is examined. Finally, the optimum results for both H_2O-based and CO_2-based EGS with the temperature drop limitation at the downhole of production well for the project lifetime are compared. The novelty of this

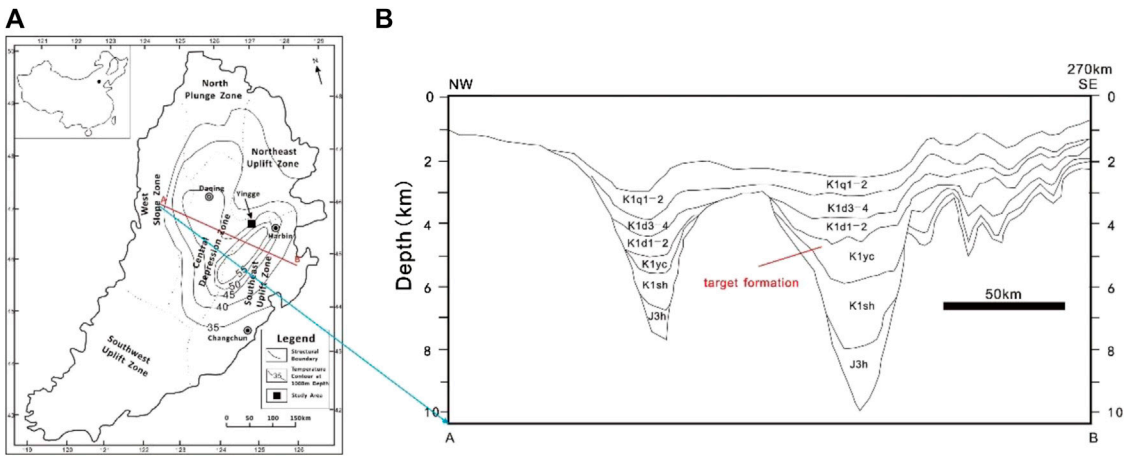

FIGURE 1 | (A) Location map of the potential EGS site in the Songliao Basin (China) and **(B)** Stratigraphic profiles near the study area.

TABLE 1 | The governing equations solved in T2Well (Pan and Oldenburg, 2014).

Description	Equation
Mass and Energy Conservation	$\frac{d}{dt}\int_{V_n} M^\kappa dV_n = \int_{\Gamma_n} F^\kappa \cdot n d\Gamma_n + \int_{V_n} q^\kappa dV_n$
For Mass	$M^\kappa = \phi \sum_\beta S_\beta \rho_\beta X_\beta^\kappa,\ F^\kappa = \sum_\beta u_\beta \rho_\beta X_\beta^\kappa$
For Energy (Reservoir)	$M^\kappa = (1-\phi)\rho_R C_R T + \phi \sum_\beta S_\beta \rho_\beta U_\beta,\ F^\kappa = -\lambda \nabla T + \sum_\beta u_\beta \rho_\beta h_\beta$
For Energy (Wellbore)	$M^\kappa = \sum_\beta S_\beta \rho_\beta \left(U_\beta + \frac{u_\beta^2}{2} + gz\cos\theta\right)$
	$F^\kappa = -\lambda \frac{\partial T}{\partial z} - \frac{1}{A}\sum_\beta [A S_\beta u_\beta \rho_\beta (h_\beta + \frac{u_\beta^2}{2} + gz\cos\theta)] - q'$
Darcy's law	$u_\beta = -k\frac{k_{r\beta}}{\mu_\beta}(\nabla P_\beta - \rho_\beta g)$
Momentum Conservation Equation	$\frac{\partial}{\partial t}(\rho_m u_m) + \frac{1}{A}\frac{\partial}{\partial z}[A(\rho_m u_m^2 + \gamma)] = -\frac{\partial P}{\partial z} - \frac{\Gamma f \rho_m \lvert u_m \rvert u_m}{2A} - \rho_m g\cos\theta$
Drift-Flux Model	$u_G = C_0 \frac{\rho_m}{\rho_m^*} u_m + \frac{\rho_L}{\rho_m^*} u_d,\ u_L = \frac{(1-S_G C_0)\rho_m}{(1-S_G)\rho_m^*} u_m - \frac{S_G \rho_G}{(1-S_G)\rho_m^*} u_d$

study lies in that 1) the coupling TH processes in wellbore/reservoir system is considered and 2) the performance from the optimum results for both H_2O-based and CO_2-based EGS is compared.

2 MODEL SETUP

2.1 Geological Setting of the Songliao Basin

The Songliao Basin, located in northeastern China, is a Mesozoic to Cenozoic continental sedimentary rhombic basin, with a length of 750 km and a width of 330–370 km. The total area of the basin is 260,000 km^2, comprising six primary structural units including the north plunge zone, west slope zone, northeast uplift zone, central depression zone, southeast uplift zone, and southeast uplift zone, respectively (**Figure 1A**). The basin was formed by rifting during the late Jurassic, and it was filled by 10-km-thick sediments. The stratigraphic sequence of the basin is dominated by Mesozoic and Cenozoic strata from the Late Jurassic to the Quaternary. The deep formations (buried depth > 2 km) of the basin include the Quantou Formation (K1q), the Denglouku Formation (K1d), the Yingcheng Formation (K1yc), the Shahezi Formation (K1sh), and the Huoshiling Formation (J3h) (**Figure 1B**). These deep formations are generally composed of sandstone, shale, siltstone, and volcanic and volcaniclastic rocks. The Songliao Basin is regarded as one of the most potential sites for EGS resource exploration,

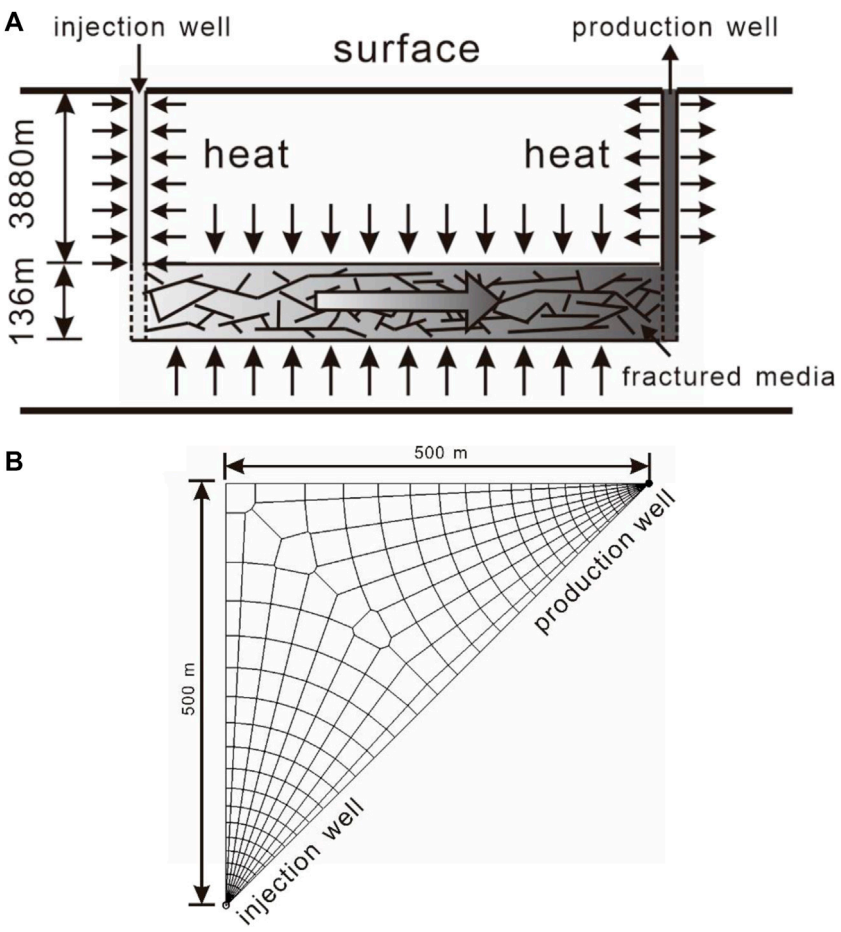

FIGURE 2 | (A) Conceptual model for the heat extraction from EGS and **(B)** grid partition of the reservoir.

according to the heat flow and depth–temperature datasets (Jiang et al., 2016).

The average geothermal gradient of the basin is ~3.7°C/100 m, which is one of the highest geothermal gradients among the Chinese basins. According to the MIT report on the definition of an enhanced geothermal system (EGS) (MIT, 2006), the potential depth for geothermal exploitation is between 3 and 6 km, and the acceptable temperature for EGS development is greater than 150°C. Therefore, the formations of K1yc, K1sh, and J3h are the potential candidates for EGS. The formation of K1yc in Shuangcheng Fault Depression, northeast of the central depression zone as the target formation, was selected; it is considered as the most potential site for EGS previously (Huang et al., 2014).

2.2 Simulation Tool

The injection and production wells play key roles in the transportation of the fluid and heat in the reservoir. Temperature and pressure would drastically vary in the wellbores, especially by using CO_2 as the working fluid (Atrens et al., 2010). In this study, the integrated wellbore-reservoir simulator T2Well (Pan et al., 2011; Pan and Oldenburg 2014) is employed to compare the fluid flow and heat transfer in the coupled wellbore/reservoir system with CO_2 and H_2O as working fluids. The governing equations are listed in **Table 1**. T2Well introduces a special wellbore sub-domain into the numerical grid, thereby extending the current numerical reservoir simulator TOUGH2 to simultaneously and efficiently calculate the flow in the wellbore and reservoir (Pan and Oldenburg 2014). This software is successfully employed to simulate the non-isothermal multiphase, multicomponent flow process in coupled wellbore/reservoir systems for CO_2 geological sequestration and geothermal extraction (Hu et al., 2012; Li et al., 2015; Pan et al., 2015; Rasmusson et al., 2015). The module ECO2N V2.0 (Pan L. et al., 2017) that can describe fluid property of CO_2-H_2O-NaCl systems within temperatures of up to 300°C is incorporated into T2Well for this study.

2.3 Model Description

The target reservoir is located at a depth of 3800 m with a thickness of 136 m. To improve heat production, hydro-fracturing is implemented to enhance permeability in this deep granite reservoir. Therefore, the target reservoir is considered as fractured media. A model composed by the target reservoir and injection and production wellbores (**Figure 2A**) is employed to capture the fluid flow and heat-transfer process in the entire wellbore/reservoir system. For comparing the heat-extraction capability of two heat-transmission fluids, the classic "five-spot" well pattern is employed. The reservoir model can be simplified to a 1/8 symmetry domain due to the symmetry, which can significantly reduce the computational burden. The wells are located at two vertices of the triangle simulation zone, with a distance of 707 m (**Figure 2B**).

To simulate fluid flow and heat transfer in fractures and in the matrix pores, the dual-porosity multiple interacting continua (MINC) (Pruess and Narasimhan, 1982; Pruess and Narasimhan, 1985) model is employed. First, one-layer 2D irregular grids are created to represent the reservoir (**Figure 2B**). The grid size increases from 0.1 m near the well to 50 m outside. Second, the primary grids are partitioned into five sub-grids by using a set of volume fractions. The injection and production wells fully perforate the reservoir and extend 3,880 m up to the surface. Two 1D vertical grids comprising seventy-eight 50-m grid blocks are created for the wellbores, which are attached to the 2D reservoir grids to represent the injection and production wells.

The reservoir is assumed to be initially saturated with CO_2 or H_2O. The reservoir temperature is set to 150°C, and its pressure is ~37.5 MPa according to the calculation with a geothermal gradient of 37°C/km and a hydrostatic pressure distribution. The model also considers the heat exchange between the fluid and the surrounding rock in the wellbore. **Table 2** lists the parameters used in the model.

TABLE 2 | Parameters for the five-spot heat extraction problem in enhanced geothermal systems.

Parameters	Values
Reservoir	
Thickness	136 m (depth 3,880–4,016)
Fracture volume fraction	2%
Fracture space	50 m
Porosity	Fracture domain: 0.50 Matrix domain: 0.08
Permeability	Fracture domain: 3.2×10^{-14} m^2 Matrix domain: 3.2×10^{-16} m^2
Rock grain density Rock thermal conductivity Rock specific heat	2440 kg/m^3 2.1 W/m°C 1000 J/kg°C
Wellbore	
Diameter	0.2 m
Well roughness	4.53×10^{-5}
Injection/Production strategy	
Injection pressure (wellhead[a])	Initial[b]+2 MPa CO_2:10.7 + 2 = 12.7 MPa H_2O: 0.35 + 2 = 2.35
Injection temperature (wellhead) Production pressure (wellhead)	20°C Initial CO_2: 10.7 MPa H_2O: 0.35 MPa
Duration of heat extraction	30 years

[a]*The condition in the first grid denotes the wellhead condition.*
[b]*The initial pressure distribution in the wellbore is different between CO_2 and H_2O because of their density difference.*

3 RESULTS AND DISCUSSION

3.1 Base Case

Figure 3 shows the temperature, flow rate and net heat extraction rate in the H_2O-based and CO_2-based EGS, respectively. In the H_2O-based EGS, the fluid production rate and temperature are maintained at ~20 kg/s and 135°C, respectively (**Figure 3A**). The net heat extraction rate (calculated by $G = R_{pro}h_{pro} - R_{inj}h_{inj}$,

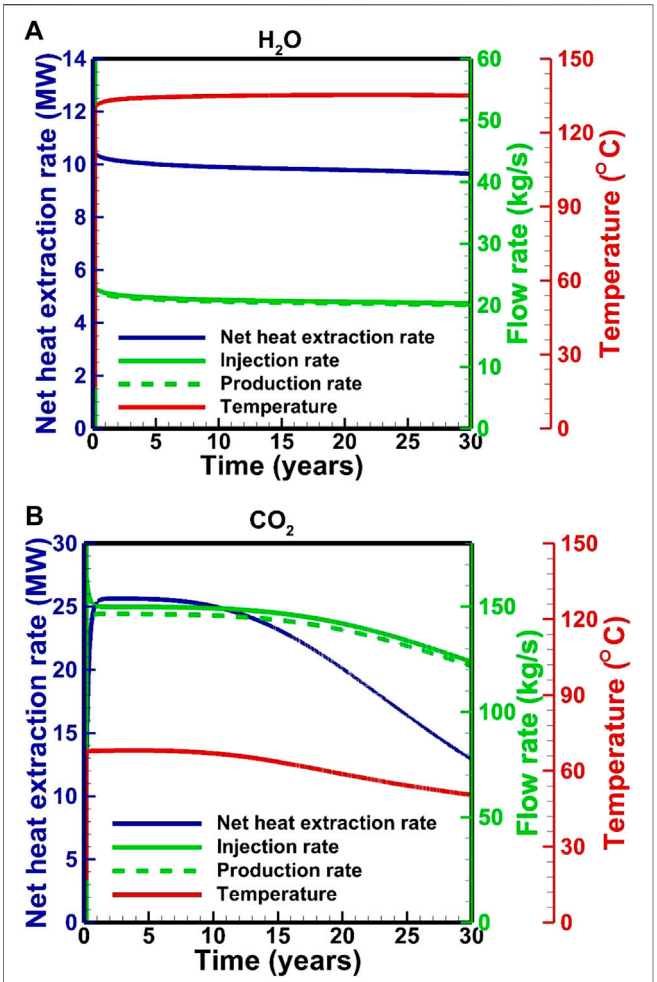

FIGURE 3 | Key performance parameters for **(A)** the H_2O-based and **(B)** CO_2-based EGS from simulations.

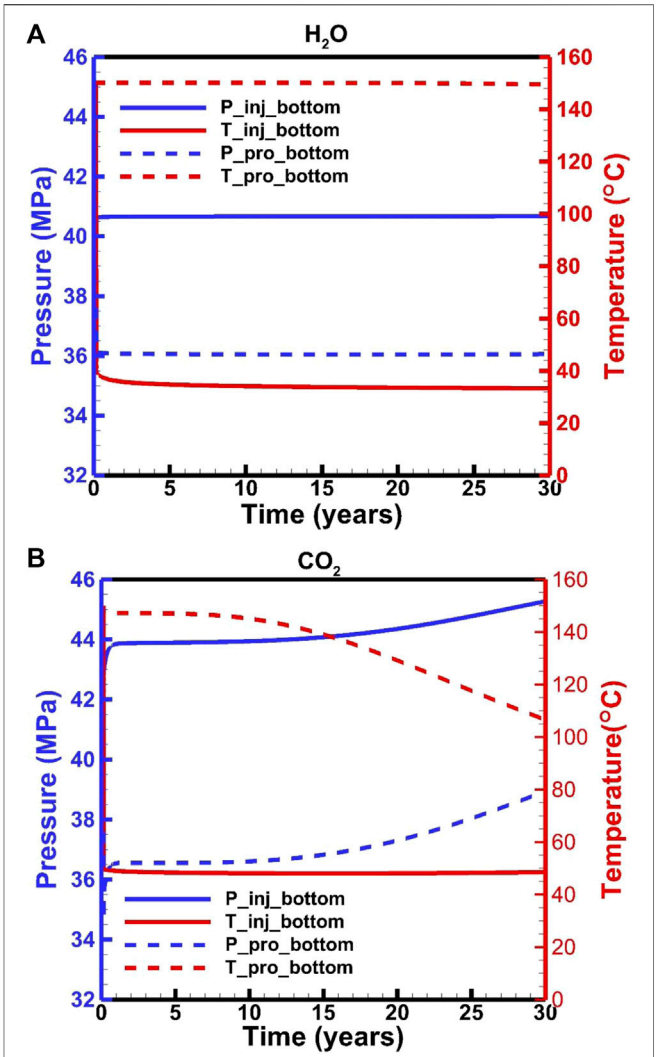

FIGURE 4 | Downhole pressure and temperature for **(A)** the H_2O-based and **(B)** CO_2-based EGS.

where R is rate, and h is enthalpy) is ~10 MW. In the CO_2-based EGS, the stable heat extraction lasts for ~10 years, and then the fluid production rate and temperature decrease from ~146 kg/s to 120 kg/s and from 67 to 50°C, respectively (**Figure 3B**). The net heat extraction rate decreases from ~25 to 13 MW. The H_2O-based EGS operation is more stable than that of the CO_2-based EGS. However, the net heat extraction rate for the CO_2-based EGS is 1.3–2.5 times greater than that for the H_2O-based EGS, indicating that the CO_2-based EGS can accelerate heat recovery. Compared with that of H_2O-based EGS, the high production rate due to the high CO_2 mobility (indicated by ρ/μ, where ρ and μ are density and viscosity, respectively) offsets the disadvantage of the low heat capacity for CO_2-based EGS.

In the H_2O-based EGS, downhole pressures are maintained at 40.6 and 36.0 MPa in the injection and production wells, respectively (**Figure 4A**). The downhole temperatures are maintained at 33 and 150°C in the injection and production wells, respectively (**Figure 4A**). On the other hand, in CO_2-based EGS, the downhole pressures and temperatures in the production well are stable for the first 10 years, followed by an increase from 36.6 to 38.9 MPa and a decrease from ~150 to 106°C, respectively. The downhole temperature in the injection well is stabilized at 48°C, but the pressure increases from 44.0 to 45.3 MPa. These fluctuations correspond to the change in flow rate. The downhole pressure in the injection well is determined by the flow process in the wellbore under a fixed wellhead pressure. The decrease in the flow rate results in a pressure loss related to the wellbore roughness. Pressure and temperature distributions satisfy the relative stable condition after a fluid injection of 0.03–0.04 years (**Figure 5**). In this short period, the downhole pressure in the injection well for the H_2O-based EGS increases from 37.5 to 40.6 MPa, while the pressure increases to 44.0 MPa for the CO_2-based EGS. There are about 1.1 and 4.5 MPa contributed by the change in density from the wellbore for the H_2O-based and CO_2-based EGS, respectively. This result is related to the fact that the density of CO_2 is more sensitive to temperature. In the production well, the average fluid temperature generally increases due to the

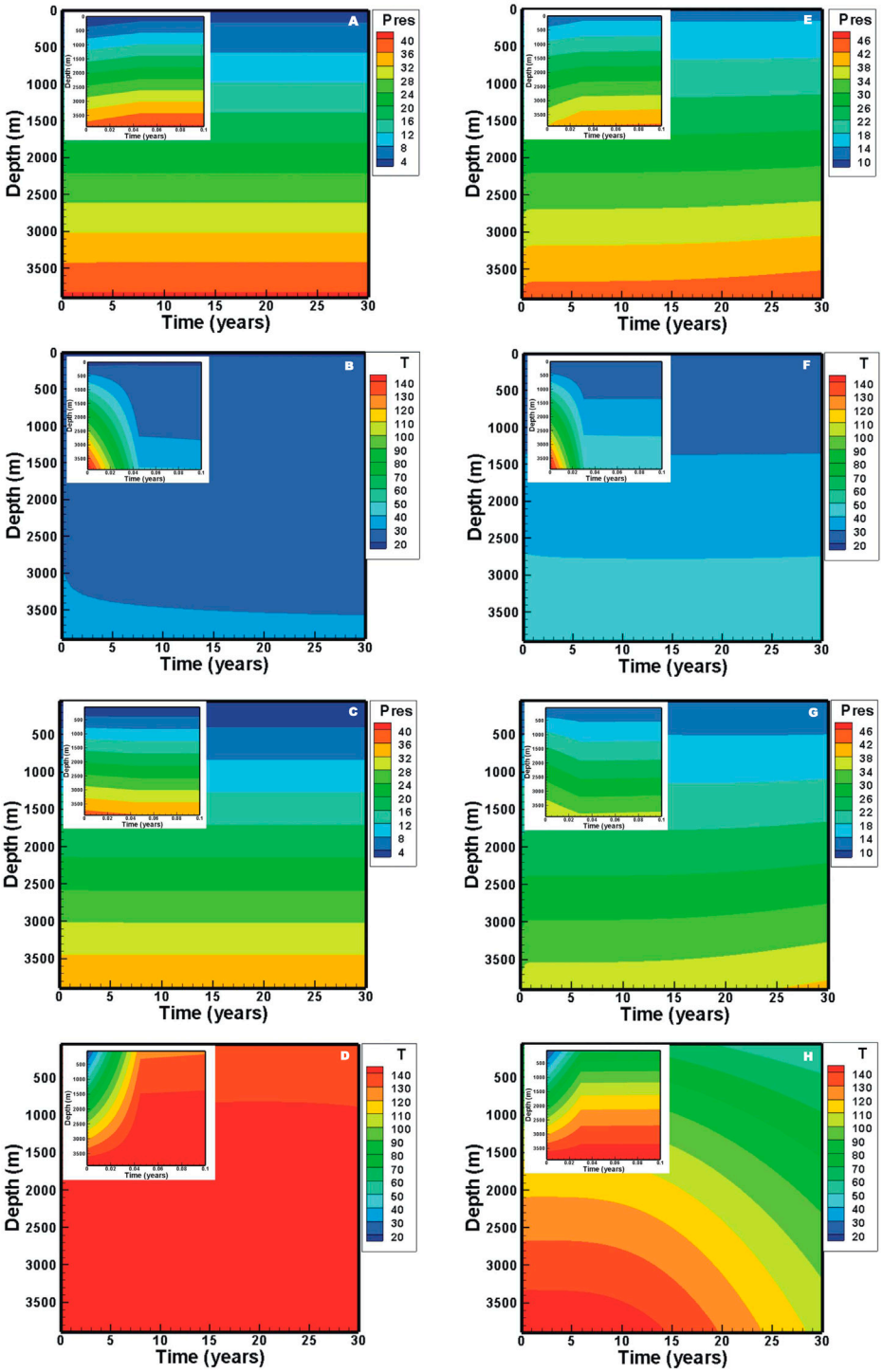

FIGURE 5 | Evolution of pressure and temperature distributions in the wellbore: **(A)** pressure and **(B)** temperature for H_2O in the injection well, **(C)** pressure and **(D)** temperature for H_2O in the production well, **(E)** pressure and **(F)** temperature for CO_2 in the injection well, **(G)** pressure and **(H)** temperature for CO_2 in the production well.

upward flow of the hot fluid from the reservoir. The downhole pressures decrease by 1.5 and 0.9 MPa at the start of production for the H_2O-based and CO_2-based EGS, respectively. This is because that the temperature redistribution in the production well results in a decrease in density. With the heat in the reservoir is gradually extracted, and the fluid temperature in the production wellbore decreases for the CO_2-based EGS, thereby increasing the pressure (**Figure 5**).

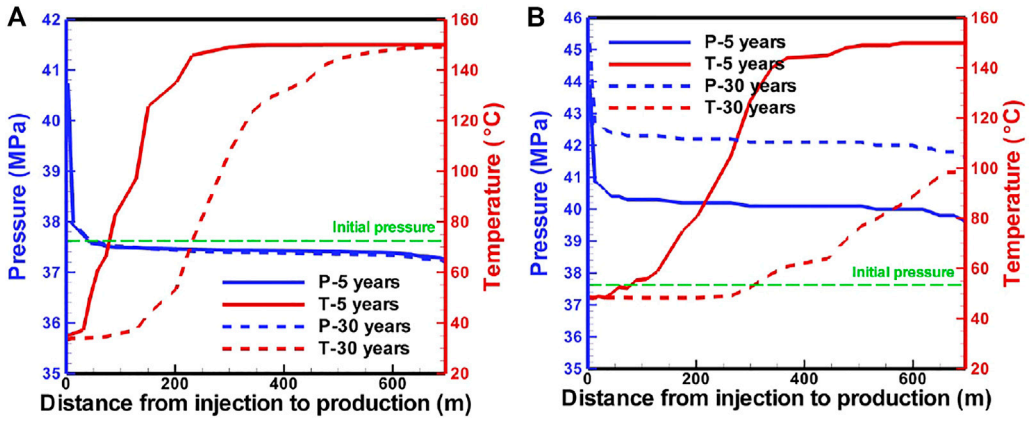

FIGURE 6 | Pressure and temperature profiles along a line from the injection well to the production well in the reservoir for **(A)** H_2O-based and **(B)** CO_2-based EGS.

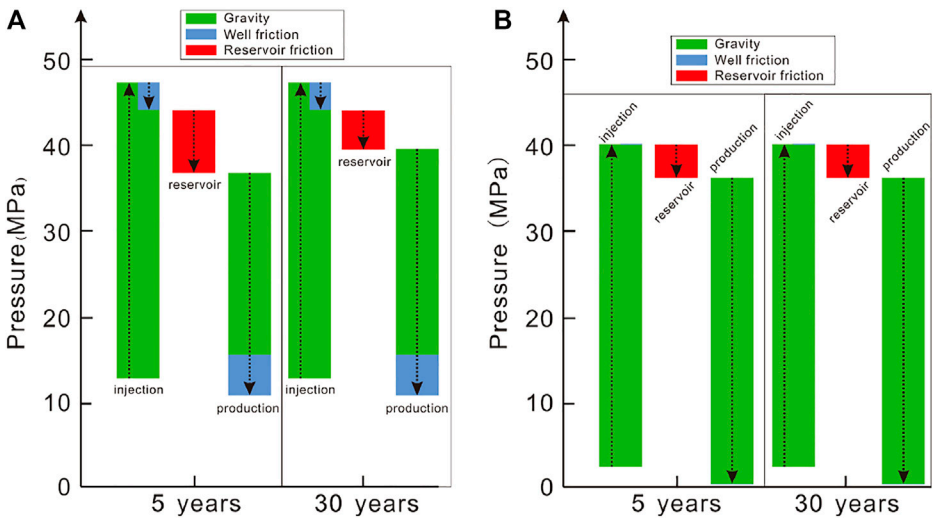

FIGURE 7 | Pressure changes along the flow path for **(A)** the CO_2-based and **(B)** H_2O-based EGS based on simulations. Arrow upward denotes an increase, otherwise it denotes a decrease.

Fluid pressure profiles (**Figure 6**) reveal that strong pressure gradients are observed near the injection well. The pressure in the reservoir for the CO_2-based EGS increases with the production due to the decrease in temperature, thereby increasing the pressure at the downhole of the production well. Finally, the decrease in temperature and increase in pressure lead to a decrease in the flow rate and net heat extraction rate (**Figure 3B**). The temperature-decrease zone extends to ~230 m after the production of 5 years for the H_2O-based EGS (**Figure 6A**), while it extends to ~300 m for the CO_2-based EGS (**Figure 6B**). After the production of 30 years, they extend to 660 m (**Figure 6A**) for H_2O and the production well for CO_2 (**Figure 6B**), and the downhole temperature in the production well decreases to 100°C for CO_2 (**Figure 6B**). Heat extraction within a zone of 180 m away from the injection well is completed after the production of 30 years for the H_2O-based EGS (**Figure 6A**), while the zone reaches to ~260 m for the CO_2-based EGS (**Figure 6B**).

Based the governing equations in **Table 1**, the change in the pressure along the wellbore is contributed by the gravity and well frictional term, while it is contributed by the frictional term in the reservoir. The gravitational contribution to the pressure gradient is dominant. In the CO_2-based EGS, the gravitational contribution accounts for 91 and 82%–89% in the injection and production wells, respectively (**Figure 7A**). The proportion of the well frictional term in the production well is greater than that in the injection well, attributed to the small density under the conditions of a high temperature and a high flow velocity in the production well. In the H_2O-based EGS, the well frictional term is neglected due to a small value resulting from a low flow velocity. (**Figure 7B**). The reservoir frictional term is greater for the CO_2-based EGS than for the

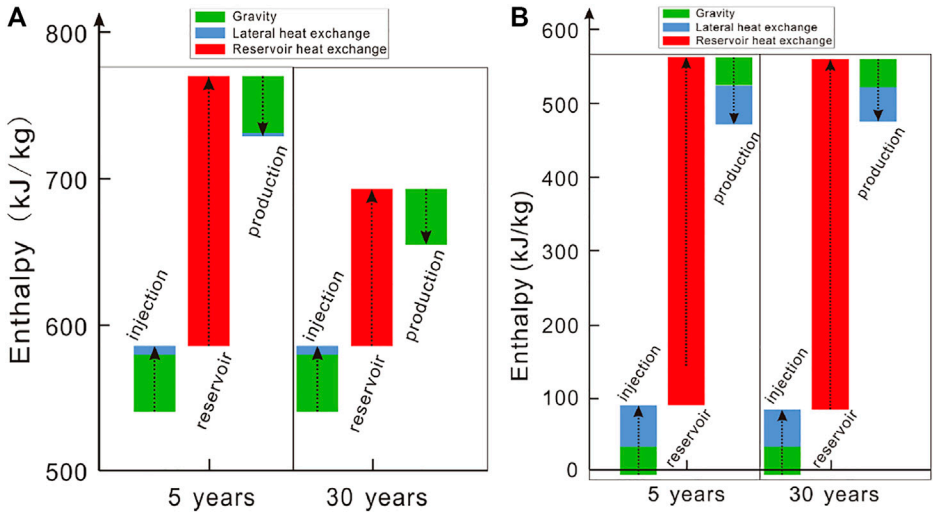

FIGURE 8 | Enthalpy changes along the flow path for **(A)** the CO_2-based and **(B)** H_2O-based EGS based on simulations. In both cases, the reference state (zero enthalpy) is chosen as (*T, P*) = (20°C, 10 MPa). Arrow upward denotes an increase, otherwise it denotes a decrease.

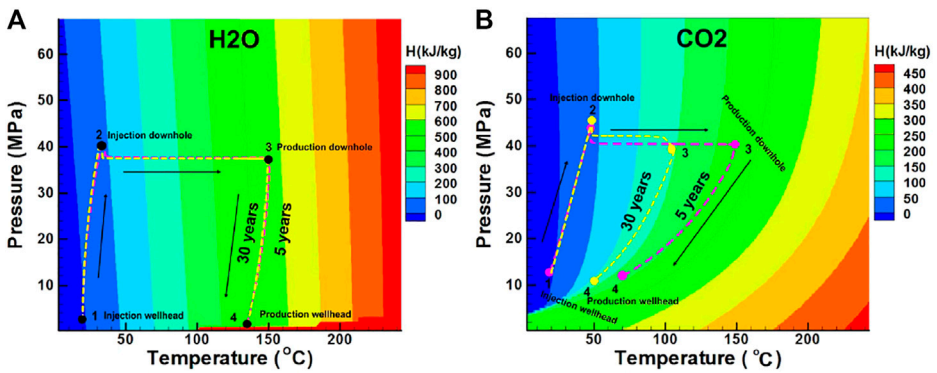

FIGURE 9 | State (*P, T, E*) change along the flow path for **(A)** the H_2O-based and **(B)** CO_2-based EGS.

TABLE 3 | Parameters used in sensitivity analysis based on the base case.

Case	Parameters	Description
Case 1	Pinj[a] = 4 MPa, Ppro[b] = 2 MPa	Increase operation pressure
Case 2	Pinj = 6 MPa, Ppro = 4 MPa	Increase operation pressure
Case 3	Pinj = 4 MPa, Ppro = 0 MPa	Increase operation pressure difference
Case 4	Pinj = 6 MPa, Ppro = 0 MPa	Increase operation pressure difference
Case 5	Pinj = 6 MPa, Ppro = 6 MPa	Increase operation pressure and reduce operation pressure difference
Case 6	Pinj = 6 MPa, Ppro = 7 MPa	Increase operation pressure and set negative operation pressure difference
Case 7	Tinj[c] = 30°C	Increase injection temperature
Case 8	Tinj = 40°C	Increase injection temperature

[a]*Pinj denotes the increased pressure compared to the initial pressure at the injection wellhead.*
[b]*Ppro denotes the increased pressure compared to the initial pressure at the production wellhead.*
[c]*Tinj denotes the injection temperature at the wellhead.*

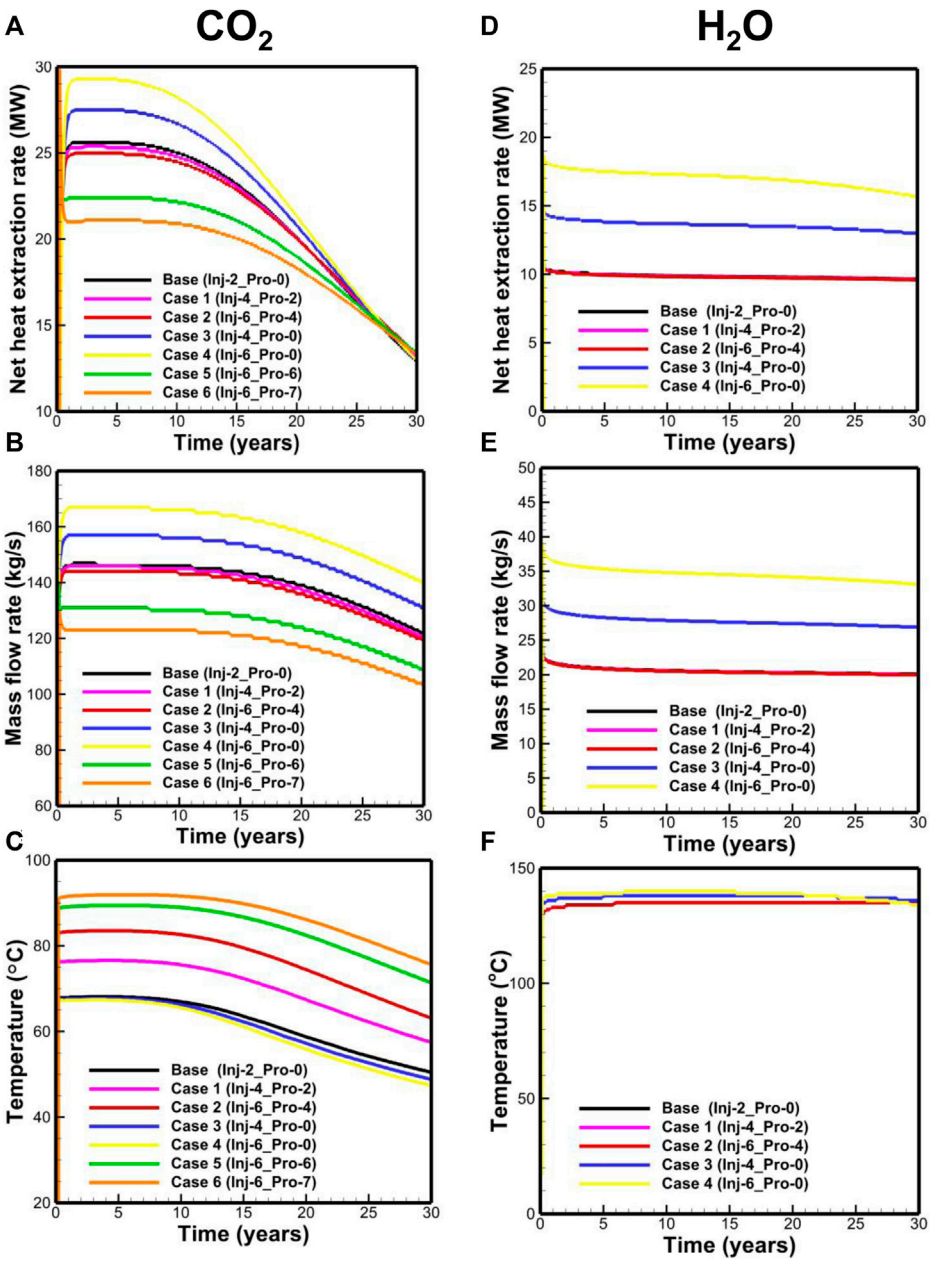

FIGURE 10 | Performance of **(A)** net heat extraction rate, **(B)** mass-flow rate, **(C)** temperature for the CO_2-based EGS, **(D)** net heat extraction rate, **(E)** mass-flow rate, and **(F)** temperature for the H_2O-based EGS.

H_2O-based EGS, because the pressure gradient in the reservoir only depends on the downhole pressure difference between injection and production wells determined by the flow process in the wellbores.

The enthalpy change along the flow path is mainly contributed by the gravitational potential energy, lateral heat exchange with the surroundings in the wellbores, and heat exchange with the reservoir. The enthalpy change contributed by the gravitational potential energy is dominant in the wells for the CO_2-based EGS (**Figure 8A**). In the early stage, a heat of ~184 kJ per kilogram CO_2 is extracted by CO_2 from the reservoir, which decreases to 108 kJ in the late stage due to the decrease in the reservoir temperature. For the H_2O-based EGS, the contributions to the enthalpy change by the gravitational potential and lateral heat exchange are similar in the wells (**Figure 8B**). A heat of 490 kJ per kilogram H_2O is extracted by H_2O (**Figure 8B**). Hence, H_2O exhibits a high heat-carrying capacity due to its high heat capacity. To obtain the same heat extraction rate as H_2O, the CO_2 mass rate should be 2.6 times of that of H_2O.

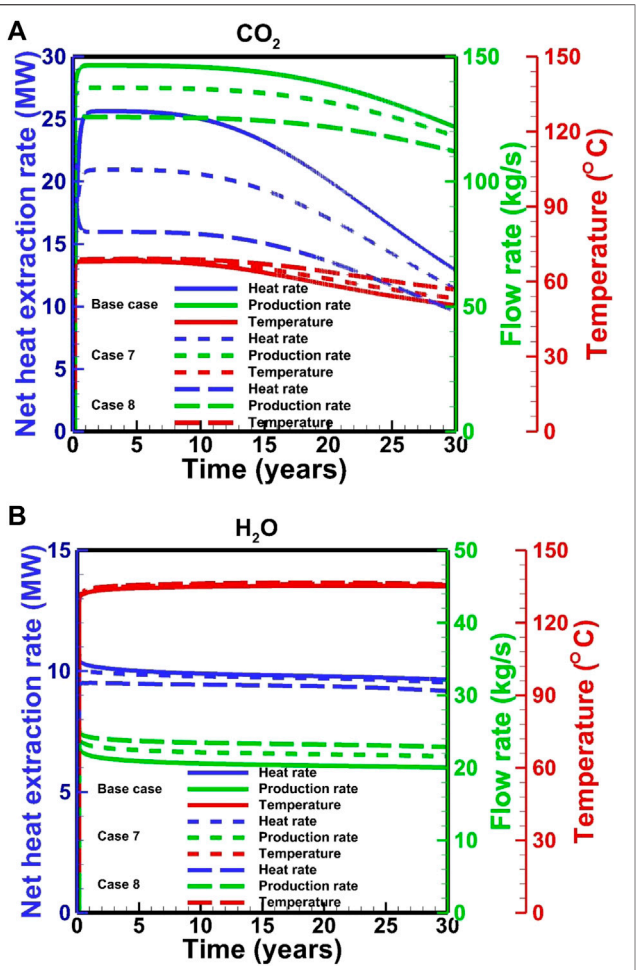

FIGURE 11 | Effect of injection temperature on the performance for **(A)** the CO_2-based and **(B)** H_2O-based EGS.

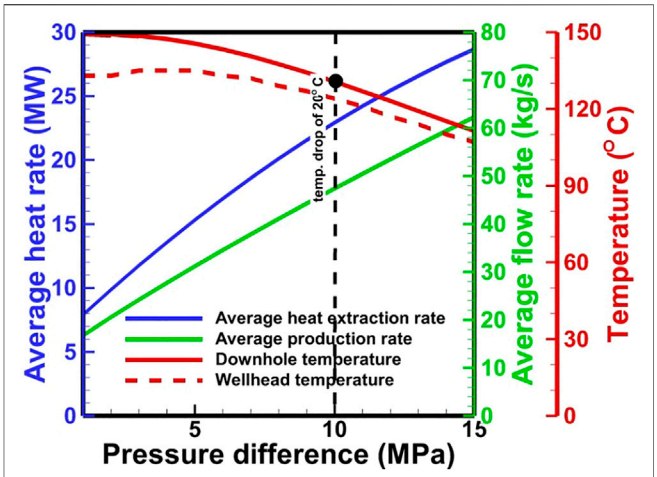

FIGURE 12 | Effect of pressure difference on performance for the H_2O-based EGS.

Figure 9 shows the state change of pressure–temperature–enthalpy diagram along the flow path. The CO_2-based EGS is significantly affected by the Joule–Thomson effect of CO_2, which reduce the temperature in the production well (**Figure 9B**). The disadvantage can be weakened in the CO_2-based EGS under high-pressure conditions.

3.2 Sensitivity Analysis to Operation Conditions

Operation conditions (i.e., injection pressure and temperature as well as production pressure) exhibit a key effect on the EGS performance. To examine the effect, sensitivity analysis to these key parameters (**Table 2**) is performed. The parameters that are not listed in **Table 3** are the same as the base case.

3.2.1 Effect of the Injection and Production Pressures

Compared to the base case, the results of Case 1 and Case 2 (**Figures 10A–C**) reveal that the increase in the operation pressure for the CO_2-based EGS leads to a slight decrease in the net heat extraction rate and mass-flow rate, albeit clearly increase of the production temperature. This is related to the fact that the increase in the operation pressure would shift the curve upward in **Figure 9B**, indicative of the decreased Joule–Thomson effect. The comparison of the base case, Case 3, and Case 4 ((**Figures 10A–C**) reveals that the increase in the operation pressure difference leads to the increase in the net heat extraction rate and mass-flow rate and weakly decreases the wellhead temperature. The results of Case 5 and Case 6 demonstrate that the CO_2-based EGS can run under a negative pressure difference (Pinj − Ppro < 0), indicating that CO_2 can circulate without the need for external pumping. The phenomenon is attributed to the high compressibility and expansivity of CO_2. The simulated results for the H_2O-based EGS (**Figures 10D–F**) reveal that the net heat extraction rate and mass-flow rate are only related to the operation pressure difference.

3.2.2 Effect of Injection Temperature

Effects of the injection temperature on the performance of CO_2-based and H_2O-based EGS are different. For the CO_2-based EGS, the high injection temperature leads to the low downhole pressure in the injection well, thereby decreases the pressure gradient in the reservoir and ultimately reduces the mass-flow rate and net heat extraction (**Figure 11A**). The slight temperature difference is observed in the late stage of heat extraction, which is related to the different temperature decrease rates in the reservoir. For the H_2O-based EGS, the effect of injection temperature on the flow viscosity is superior to the effect of pressure gradient. Therefore, a high injection temperature leads to a high mass-flow rate (**Figure 11B**). However, the net heat extraction rate is inverse because the additional heat from the production is less than that from the injection.

3.3 System Optimization for Heat Extraction

EGS stable operation requires a minimal temperature drop and the maximal net heat extraction during the development period. For the comparison of CO_2 with H_2O, a target temperature drop

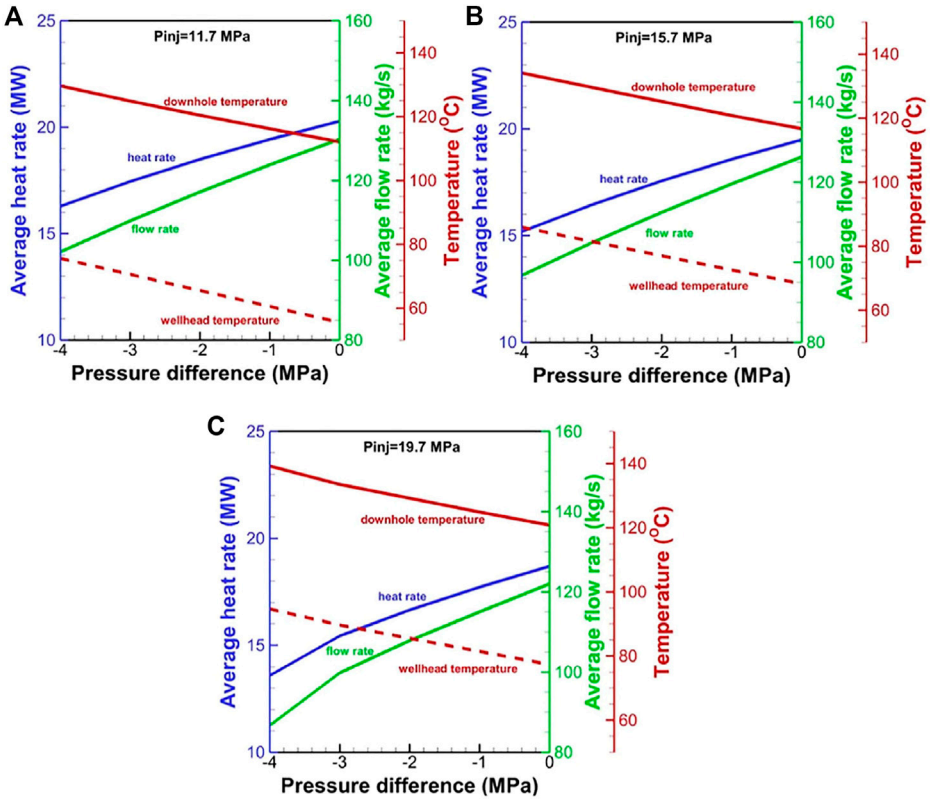

FIGURE 13 | Effect of pressure difference on performance for the CO_2-based EGS at the wellhead pressure of **(A)** 11.7 MPa, **(B)** 15.7 MPa, and **(C)** 19.7 MPa in the injection well.

is set as 20°C at the bottom of the production well after 30 years. For a specific EGS site, the most easily optimized parameter is the wellhead pressure. To prevent the damage of the reservoir by high pressure, the maximal pressure in the reservoir is limited to the value of 1.5 times of the initial pressure (56.25 MPa). Considering the strong Joule–Thomson effect of CO_2 in the wellbore, the wellhead pressure in the production well should be as high as possible to obtain the maximal temperature in the CO_2-based EGS. Based on a simple calculation method for the pressure and temperature distribution proposed by Atrens et al. (2010), the estimated maximal allowed wellhead pressures in the production and injection wells for the CO_2-based EGS are ~25 and 20 MPa, respectively. The pressure differences from 1 to 15 MPa with an interval of 1 MPa are used in the simulation for the system optimization of the H_2O-based EGS. For CO_2, the negative pressure differences (e.g., $P_{inj} - P_{pro} \leq 0$) are only considered based on the previous simulated results. The injection pressures ranging from 11.7 to 19.7 MPa with an interval of 2 MPa and the negative pressure differences ranging from -5 to 0 MPa with an interval of 1 MPa. A total of 30 models are operated for the system optimization of the CO_2-based EGS.

The optimal pressure difference is ~10 MPa for a temperature drop limitation of 20°C for the H_2O-based EGS (**Figure 12**). The corresponding net heat extraction rate, flow rate, and production temperature are 22.9 MW, 47.4 kg/s, and 124°C, respectively. For CO_2, the numerical result reveals that the negative pressure difference should not be greater than 5.0 MPa. Otherwise, the driving force is not always sufficient to drive CO_2 to the wellhead. The net heat extraction and flow rate at the low operation pressure are greater than that at the high operation pressure, but the wellhead temperature exhibits an inverse relationship (**Figure 13**). Under the temperature drop limitation, when the injection pressure increases from 11.7 to 19.7 MPa, the production wellhead temperature increases from 76 to 86°C (**Figure 14**). The corresponding flow rate and net heat extraction slightly increase. The negative pressure differences change from −4.1 MPa to −2.1 MPa, indicating that a large driving force is required at the high operation pressure. The optimal pressures for the CO_2-based EGS are the maximal limited pressure of 19.7 MPa (implying that the operation pressure is as high as possible) at the injection well and 21.8 MPa at the production well. The corresponding net heat extraction rate, flow rate, and production temperature are 16.3 MW, 105.4 kg/s, and 86°C, respectively. Clearly, the heat extraction performance using CO_2 is worse than that using H_2O under the temperature drop limitation. However, the negative pressure difference for CO_2 may lead to lower power consumption to maintain fluid circulation. Moreover, the low reactivity between CO_2 and formation can prevent scaling and formation plugging, and large amounts of CO_2 could be

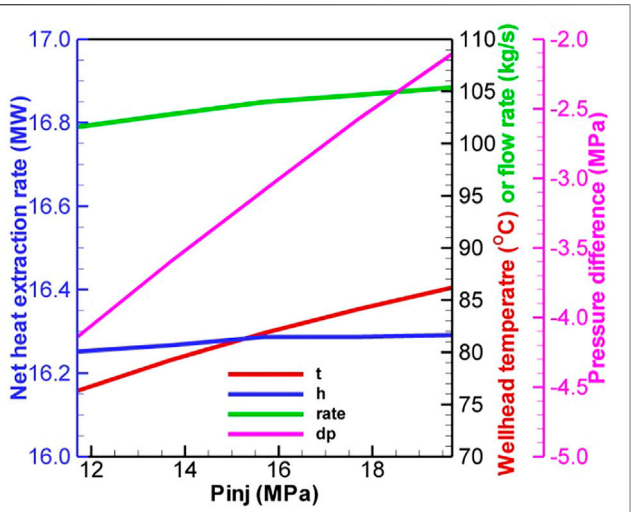

FIGURE 14 | Effect of injection pressure on performance with the temperature drop limitation for the CO_2-based EGS.

stored by heat extraction. These features make CO_2 competitive with H_2O for heat extraction.

4 CONCLUDING REMARKS

CO_2 is recently considered as a competitive working fluid in comparison to H_2O for extracting heat from hot dry rocks. A coupled wellbore/reservoir simulation is conducted to comprehensively compare the performance of both fluids. The following major conclusions are drawn:

(1) At a fixed wellhead pressure difference, the net heat extraction and flow rate are greater for CO_2 than those for H_2O due to a large pressure gradient in the reservoir and high density gradient within CO_2-base system, but the wellhead temperature is far lower in CO_2-base system than that in H_2O-base system due to the strong Joule–Thomson effect of CO_2 in the wellbore.
(2) In the wellbore, the pressure change is mainly affected by gravity. For CO_2, the frictional pressure drop accounts for 9–18% due to the high flow velocity. The enthalpy change is mainly contributed by the gravitational potential for CO_2, while it is mainly contributed by the gravitational potential and lateral heat exchange for H_2O.
(3) The heat extraction performance for H_2O depends on the pressure difference at the wellheads and injection temperature, while the performance of CO_2-based system depends on the pressure and temperature at the wellhead of injection well and production well. A high running pressure is favorable for improving the heat extraction performance (especially the production temperature) for CO_2. A high injection temperature cannot increase the net heat extraction.
(4) With the constraint of temperature drop of 20°C at the bottom of the production well, the heat extraction performance by using H_2O as the working fluid is better than that by using CO_2. The optimal pressure difference is ~10 MPa for H_2O. The corresponding net heat extraction rate, flow rate, and production temperature are 22.9 MW, 47.4 kg/s, and 124°C, respectively. The optimal pressures for the CO_2-based EGS are the maximal limited pressure of 19.7 MPa (implying that the operation pressure is as large as possible) at the injection wellhead and 21.8 MPa at the production wellhead. The corresponding net heat extraction rate, flow rate, and production temperature are 16.3 MW, 105.4 kg/s, and 86°C, respectively.

The present results are limited to the given conditions and parameters. However, the numerical experiments provide a critical insight into the hydrodynamic and heat-transfer processes for the H_2O-based and CO_2-based EGS considering the coupled wellbore/reservoir systems. The critical evaluation of modeling results can provide a reference to design the H_2O-based and CO_2-based EGS. In future studies, the realistic fracture network after fracturing should be considered in the model.

DATA AVAILABILITY STATEMENT

The original contributions presented in the study are included in the article/supplementary material, further inquiries can be directed to the corresponding author.

AUTHOR CONTRIBUTIONS

HL contributed to all of the study.

FUNDING

This study was supported by the National Natural Science Foundation of China (Grant Nos. 41602255 and 51809259).

REFERENCES

Atrens, A. D., Gurgenci, H., and Rudolph, V. (2010). Electricity Generation Using a Carbon-Dioxide Thermosiphon. *Geothermics* 39, 161–169. doi:10.1016/j.geothermics.2010.03.001

Aunzo, Z. P., Bjornsson, G., and Bodvarsson, G. S. (2011). *Wellbore Models GWELL, GWNACL, and HOLA User's Guide*. USA: Caliornia.

Bongole, K., Sun, Z., Yao, J., Mehmood, A., Yueying, W., Mboje, J., et al. (2019). Multifracture Response to Supercritical CO 2 -EGS and water-EGS Based on Thermo-hydro-mechanical Coupling Method. *Int. J. Energ. Res* 43 (13), 7173–7196. doi:10.1002/er.4743

Brown, D. (2000). "A Hot Dry Rock Geothermal Energy Concept Utilizing Supercritical CO2 Instead of Water," in Proceedings of the Twenty-Fifth Workshop on Geothermal Reservoir Engineering, Stanford University, January 24-26, 2000, 233–238.

Cui, G., Ren, S., Dou, B., and Ning, F. (2021). Geothermal Energy Exploitation from Depleted High-Temperature Gas Reservoirs by Recycling CO2: The Superiority and Existing Problems. *Geosci. Front.* 12 (6), 101078. doi:10.1016/j.gsf.2020.08.014

Goodman, A., Bromhal, G., Strazisar, B., Rodosta, T., Guthrie, W. F., Allen, D., et al. (2013). Comparison of Methods for Geologic Storage of Carbon Dioxide in saline Formations. *Int. J. Greenhouse Gas Control.* 18, 329–342. doi:10.1016/j.ijggc.2013.07.016

Hu, L., Pan, L., and Zhang, K. (2012). Modeling Brine Leakage to Shallow Aquifer through an Open Wellbore Using T2WELL/ECO2N. *Int. J. Greenhouse Gas Control.* 9, 393–401. doi:10.1016/j.ijggc.2012.05.010

Huang, X., Zhu, J., Niu, C., Li, J., Hu, X., and Jin, X. (2014). Heat Extraction and Power Production Forecast of a Prospective Enhanced Geothermal System Site in Songliao Basin, China. *Energy* 75, 360–370. doi:10.1016/j.energy.2014.07.085

Jiang, G. Z., Li, W. W., Rao, S., Shi, Y. Z., Tang, X. Y., Zhu, C. Q., et al. (2016). Heat Flow, Depth-Temperature, and Assessment of the Enhanced Geothermal System (EGS) Resource Base of continental China. *Environ. Earth Sci.* 75 (22). doi:10.1007/s12665-016-6238-5

Li, M., Gou, Y., Hou, Z., and Were, P. (2015). Investigation of a New HDR System with Horizontal wells and Multiple Fractures Using the Coupled Wellbore-Reservoir Simulator TOUGH2MP-WELL/EOS3. *Environ. Earth Sci.* 73 (10), 6047–6058. doi:10.1007/s12665-015-4242-9

Luo, F., Xu, R.-N., and Jiang, P.-X. (2014). Numerical Investigation of Fluid Flow and Heat Transfer in a Doublet Enhanced Geothermal System with CO 2 as the Working Fluid (CO 2 -EGS). *Energy* 64, 307–322. doi:10.1016/j.energy.2013.10.048

Metz, B., Davidson, O., Coninck, H. D., Loos, M., and Meyer, L. (2005). *Carbon Dioxide Capture and Storage-Special Report of the Intergovernmental Panel on Climate Change*. Cambridge: Cambridge University Press.

MIT (2006). *The Future of Geothermal Energy—Impact of Enhanced Geothermal Systems (EGS) on the United States in the 21st Century. An Assessment by an MIT-Led Interdisciplinary Panel*. Boston, MA, USA: Massachusetts Institute of Technology, 372.

Murphy, H., Brown, D., Jung, R., Matsunaga, I., and Parker, R. (1999). Hydraulics and Well Testing of Engineered Geothermal Reservoirs. *Geothermics* 28 (4-5), 491–506. doi:10.1016/s0375-6505(99)00025-5

Orr, F. M. (2004). Storage of Carbon Dioxide in Geologic Formations. *J. Pet. Techn.* 56 (9), 90–97. doi:10.2118/88842-jpt

Pan, F., McPherson, B. J., and Kaszuba, J. (2017a). Evaluation of CO2-Fluid-Rock Interaction in Enhanced Geothermal Systems: Field-Scale Geochemical Simulations. *Geofluids* 2017, 1–11. doi:10.1155/2017/5675370

Pan, L., Freifeld, B., Doughty, C., Zakem, S., Sheu, M., Cutright, B., et al. (2015). Fully Coupled Wellbore-Reservoir Modeling of Geothermal Heat Extraction Using CO 2 as the Working Fluid. *Geothermics* 53, 100–113. doi:10.1016/j.geothermics.2014.05.005

Pan, L. H., Oldenburg, C. M., Wu, Y. S., and Pruess, K. (2011). *T2Well/ECO2N Vession 1.0: Multiphase and Non-isothermal Model for Coupled Wellbore-Reservoir Flow of Carbon Dioxide and Variable Salinity Water. Earth Science Division*. Berkeley: Lawrence Berkeley National Laboratory, University of California.

Pan, L., and Oldenburg, C. M. (2014). T2Well-An Integrated Wellbore-Reservoir Simulator. *Comput. Geosciences* 65, 46–55. doi:10.1016/j.cageo.2013.06.005

Pan, L., Spycher, N., Doughty, C., and Pruess, K. (2017b). ECO2N V2.0: A TOUGH2 Fluid Property Module for Modeling CO2-H2O-NACL Systems to Elevated Temperatures of up to 300°C. *Greenhouse Gas Sci. Technol.* 7 (2), 313–327. doi:10.1002/ghg.1617

Pruess, K. (2006). Enhanced Geothermal Systems (EGS) Using CO2 as Working Fluid-A Novel Approach for Generating Renewable Energy with Simultaneous Sequestration of Carbon. *Geothermics* 35 (4), 351–367. doi:10.1016/j.geothermics.2006.08.002

Pruess, K., and Narasimhan, T. N. (1985). A Practical Method for Modeling Fluid and Heat Flow in Fractured Porous media. *Soc. Pet. Eng. J.* 25 (6), 14–26. doi:10.2118/10509-pa

Pruess, K., and Narasimhan, T. N. (1982). On Fluid Reserves and the Production of Superheated Steam from Fractured, Vapor-Dominated Geothermal Reservoirs. *J. Geophys. Res.* 87 (B11), 9329–9339. doi:10.1029/jb087ib11p09329

Pruess, K., Oldenburg, C., and Moridis, G. (1999). *TOUGH2 User's Guide, Version 2.0*. Berkeley: Earth Science Division, Lawrence Berkeley National Laboratory, University of California.

Pruess, K. (2008). On Production Behavior of Enhanced Geothermal Systems with CO2 as Working Fluid. *Energ. Convers. Manag.* 49 (6), 1446–1454. doi:10.1016/j.enconman.2007.12.029

Ram Mohan, A., Turaga, U., Shembekar, V., Elsworth, D., and Pisupati, S. V. (2013). Utilization of Carbon Dioxide from Coal-Based Power Plants as a Heat Transfer Fluid for Electricity Generation in Enhanced Geothermal Systems (EGS). *Energy* 57, 505–512. doi:10.1016/j.energy.2013.05.047

Rasmusson, K., Tsang, C.-F., Tsang, Y., Rasmusson, M., Pan, L., Fagerlund, F., et al. (2015). Distribution of Injected CO2in a Stratified saline Reservoir Accounting for Coupled Wellbore-Reservoir Flow. *Greenhouse Gas Sci. Technol.* 5 (4), 419–436. doi:10.1002/ghg.1477

IPCC (2014). "Climate Change 2014: Synthesis Report," in *Contribution of Working Groups I, II and III to the Fifth Assessment Report of the Intergovernmental Panel on Climate Change*. Editors R K Pachauri and L A Meyer (Geneva, Switzerland: IPCC), 151.

Shi, Y., Song, X., Shen, Z., Wang, G., Li, X., Zheng, R., et al. (2018). Numerical Investigation on Heat Extraction Performance of a CO2 Enhanced Geothermal System with Multilateral wells. *Energy* 163, 38–51. doi:10.1016/j.energy.2018.08.060

Singh, M., Tangirala, S. K., and Chaudhuri, A. (2020). Potential of $$\hbox {CO}_{2}$$ Based Geothermal Energy Extraction from Hot Sedimentary and Dry Rock Reservoirs, and Enabling Carbon Geo-Sequestration. *Geomech. Geophys. Geo-energ. Geo-resour.* 6 (1), 32. doi:10.1007/s40948-019-00139-8

Wang, C.-L., Cheng, W.-L., Nian, Y.-L., Yang, L., Han, B.-B., and Liu, M.-H. (2018). Simulation of Heat Extraction from CO2-based Enhanced Geothermal Systems Considering CO2 Sequestration. *Energy* 142, 157–167. doi:10.1016/j.energy.2017.09.139

White, C. M., Strazisar, B. R., Granite, E. J., Hoffman, J. S., and Pennline, H. W. (2003). Separation and Capture of CO2from Large Stationary Sources and Sequestration in Geological Formations-Coalbeds and Deep Saline Aquifers. *J. Air Waste Manag. Assoc.* 53 (6), 645–715. doi:10.1080/10473289.2003.10466206

Xu, R., Zhang, L., Zhang, F., and Jiang, P. (2015a). A Review on Heat Transfer and Energy Conversion in the Enhanced Geothermal Systems with water/CO2as Working Fluid. *Int. J. Energ. Res.* 39 (13), 1722–1741. doi:10.1002/er.3352

Xu, T., Feng, G., Hou, Z., Tian, H., Shi, Y., and Lei, H. (2015b). Wellbore-reservoir Coupled Simulation to Study thermal and Fluid Processes in a CO2-based Geothermal System: Identifying Favorable and Unfavorable Conditions in Comparison with Water. *Environ. Earth Sci.* 73 (11), 6797–6813. doi:10.1007/s12665-015-4293-y

Zhang, F.-Z., Jiang, P.-X., and Xu, R.-N. (2013). System Thermodynamic Performance Comparison of CO2-EGS and Water-EGS Systems. *Appl. Therm. Eng.* 61 (2), 236–244. doi:10.1016/j.applthermaleng.2013.08.007

Zhang, F.-Z., Xu, R.-N., and Jiang, P.-X. (2016). Thermodynamic Analysis of Enhanced Geothermal Systems Using Impure CO 2 as the Geofluid. *Appl. Therm. Eng.* 99, 1277–1285. doi:10.1016/j.applthermaleng.2016.01.126

Conflict of Interest: The author declares that the research was conducted in the absence of any commercial or financial relationships that could be construed as a potential conflict of interest.

NOMENCLATURE

A wellbore cross-sectional area

C_R specific heat of the rock

C_0 profile parameter account for the effect of local gas saturation and velocity profile over the pipe cross-section

F^κ mass or heat flux of component κ

f apparent friction coefficient

g or g gravitational acceleration

h_β specific enthalpy of phase β

k absolute permeability

$k_{r\beta}$ relative permeability of phase β

M^κ mass or energy per volume of component κ

P pressure

P_β fluid pressure in phase β

q^κ sinks and sources of component κ

$\dot{q}$ wellbore heat loss/gain per unit length of wellbore

S_G gas phase saturation

S_β saturation of phase β

t time

T temperature

u_d drift velocity of gas

u_G gas phase velocity

u_L liquid phase velocity

u_m mixture velocity (velocity of mass center)

u_β or u_β velocity of phase β

U_β specific internal energy of phase β

V_n subdomain of the flow system

X_β^κ mass fraction of component κ present in phase β

z one-dimensional coordinate along the length of the wellbore

Γ perimeter of the wellbore cross-section

Γ_n closed boundary surface of V_n

γ a quantity caused by slip between the two phases

θ incline angle of the wellbore

λ thermal conductivity

μ_β viscosity of phase β

ρ_G gas phase density

ρ_m mixture density

ρ_m^* profile-adjusted average density

ρ_R grain density of the rock

ρ_β density of phase β

ϕ porosity

frontiers in Earth Science

ORIGINAL RESEARCH
published: 22 February 2022
doi: 10.3389/feart.2022.784245

Study on Thermal Conductivity of Thermal Insulation Cement in Geothermal Well

Fengyan Zhang and Lixin Li*

Chinese Academy of Geological Sciences, Beijing, China

When geothermal fluid flows to the wellhead along the wellbore, there is a thermal transfer from the high-temperature geothermal fluid to the low-temperature formation. This process can directly lead to the decrease of wellhead temperature and loss of geothermal energy. Even though previous studies have confirmed that reducing the thermal conductivity of cement could validly cut down the heat loss of geothermal fluid, the influence factors of thermal conductivity are limited. In this research, we conducted detailed studies of the influence factors of thermal conductivity and compressive strength for cement. The results show that with the increase of water-cement ratio and thermal insulation materials, thermal conductivity and compressive strength decline. Furthermore, curing temperature is another important factor to improve the thermal preservation effect, but the testing temperature has the opposite influence. Based on these results, the present study concluded that porosity, Skeleton ingredients, curing temperature, and test temperature are vital factors for thermal conductivity. This research provides theoretical guidance for increasing the wellhead temperature of geothermal fluid and enhancing the efficiency of geothermal energy.

Keywords: insulation cement, thermal conductivity, geothermal well, insulation material, compressive strength

OPEN ACCESS

Edited by:
Yinhui Zuo,
Chengdu University of Technology, China

Reviewed by:
Wei Xu,
Xi'an Jiaotong University, China
Jie Hu,
Chengdu University of Technology, China

****Correspondence:***
Fengyan Zhang
zhangfy18@cags.ac.cn

Specialty section:
This article was submitted to Economic Geology, a section of the journal Frontiers in Earth Science

Received: *27 September 2021*
Accepted: *20 January 2022*
Published: *22 February 2022*

Citation:
Zhang F and Li L (2022) Study on Thermal Conductivity of Thermal Insulation Cement in Geothermal Well. Front. Earth Sci. 10:784245. doi: 10.3389/feart.2022.784245

1 INTRODUCTION

Geothermal energy is clean and sustainable and has been widely used for power generation, heating, and farming (Bildirici and Gökmenoğlu, 2017; Wang et al., 2017; Hamm and Metcalfe, 2019; Yang et al., 2021). In recent years, with the increased need for renewable energy, the exploration and utilization of medium-low temperature geothermal resources have been widely developed in China (Ma et al., 2016; Zhao and Fu, 2019). However, the temperature difference between high-temperature geothermal fluid and low-temperature formations results in the temperature in the wellhead being lower than that in the actual reservoir (Hasan and Kabir, 2002). This is unfavorable to the application of geothermal energy, especially for geothermal wells featured by high bottom temperature or lower fluid-production rate (Kanev et al., 1997; Tóth, 2006).

The wellhead temperature of the geothermal fluid is one of the most important parameters to determine the usage modes and applied efficiency for geothermal energy (Kanev et al., 1997; Tekin and Akin, 2011; Zhou and Zhang, 2013; Gorman et al., 2014). Hence, elevating this temperature is vital for the exploration and utilization of geothermal energy. Recently, more and more research has focused on cement sheath, as its great contribution to heat transfer (Yang et al., 2013; Won et al., 2015). Meanwhile, the theory that decreasing cement thermal conductivity can prominently reduce heat loss has been proposed (Ichim et al., 2016,

TABLE 1 | Composition of Class G cement.

Chemical composition	MgO	SO_3	Maximum of total alkalinity	C_3S	C_2S	C_3A	Maximum value of C_4AF+2C_3A
Content (%)	2.99	1.94	0.6	58.65	16.25	1.12	16.64

Ichim et al., 2018; Li et al., 2017; Zhao, 2020). Based on this theory, calculation method and influence factors (e.g., water-cement ratio, testing temperature, and additives) of cement thermal conductivity have been confirmed (Ichim et al., 2018; Won et al., 2015; Fang et al., 2020). These results revealed the change laws of thermal conductivity from macroscopical sight. The study of influencing factors is not comprehensive and the microcosmic mechanisms remain obscure.

This paper aims to confirm the change laws and corresponding microcosmic mechanisms of thermal conductivity for cement. A precisely designed steady-state method was used at the selected representative thermal insulation materials. Based on this research, thermal conductivity, and compressive strength were affected by different influence factors (i.e., water-cement ratio, thermal insulation materials content, curing, and testing temperature) are documented. Combined with the results of microcosmic analysis (Porosity test and scanning electron microscope), a method of interpreting changes in thermal conductivity and compressive strength from microcosmic sights is proposed. The research results could provide a theoretical basis for the effective utilization of geothermal energy.

2 MATERIAL AND METHODS

2.1 Material

In this study, class G cement was used as the basic material as it has been commonly used in geothermal wells. Simultaneously, floating beads with a hollow structure and expanded perlite with a honeycomb-like structure were selected as insulation materials. Results of chemical composition and physical properties of Class G cement are shown in **Tables 1**, **2**. The properties of these two thermal insulation materials are shown in **Table 3**.

2.2 Methods

In this research, four different (0.5, 0.55, 0.6, and 0.7) water-cement ratios (w/c ratio) were chosen for pure cement slurry. The mass ratio of thermal insulation materials to Class G cement is 5%, 10%, 15%, and 20% respectively. Besides, a fixed w/c ratio (0.7) was selected for thermal insulation cement slurry, and water-reducing agents were used in maintaining its rheological properties. The comparison between pure cement with a w/c ratio of 0.7 (w/c = 0.7) and thermal insulation cement with different contents of thermal insulation materials was conducted. Meanwhile, the steady-state method was used to accurately calculate the thermal conductivity of cement. The tools designed for making cement samples in this study are shown in **Figure 1**. During the design process, the ratio between sample diameter and thickness was greater than 8.

Cement powder and thermal insulation materials were mixed before the thermal insulation cement was made. Then the mixture was poured into a water-bearing agitator with low stirring speed. Meanwhile, the pouring process was completed in 15 s. The slurry was then cured in a curing chamber with curing temperatures of 60°C, 90°C, and 120°C for 24 h, and the curing pressure was set at 10 MPa.

After curing, the thermal conductivity of the cement sample was tested by DRPL-III high precision thermal conductivity tester (measuring range 0.001–3 W/(m.K), and the measurement accuracy was 1%. In this study, we use "hot plate temperature—cold plate temperature" to represent the test temperature combination. When the hot plate temperature is 70°C and the cold plate temperature is 30°C, it is expressed as "70–30°C." Two conditions were set for analyzing pure cement thermal conductivity. One set the hot plate temperature at 70°C with different w/c ratios (i.e., 0.5, 0.55, 0.6, and 0.7) and curing temperature (i.e., 60°C, 90°C, and 120°C). The other set the curing temperature at 60°C with varied w/c ratios (i.e., 0.5, 0.55, 0.6, and 0.7) and hot plate temperatures (i.e., 50°C, 70°C, and 90°C). Moreover, the analysis of the thermal conductivity of thermal insulation cement was also conducted under two different conditions. One was set the hot plate temperature at 70 °C with varied content of thermal insulation materials (i.e., 5%, 10%, 15%, and 20%) and curing temperatures (i.e., 60°C, 90°C, and 120°C). The other was set the curing temperature at 60 °C with different w/c ratios (i.e., 5%, 10%, 15%, and 20%) and hot plate temperatures (i.e., 50°C, 70°C, and 90°C).

The microstructures of pure cement and thermal insulation cement were observed by using Nova NanoSEM 450 and AxioCam MRc5. YAW-300B automatic pressure testing machine was used to test compressive strength. The maximum test value of this device is 300 kN, and the test error is within 1%. During the test, the loading speed was kept at 71.7 ± 7.2 kN/min. Dry density and the median pore throat size of cement were achieved through AutoPore IV 9505. Test pressure was set at 1.0 MPa, and the chosen test temperature was 20°C. Rigaku Ultima IV was used to test changes in mineral types and the content of cement. All the equipment was calibrated before use.

TABLE 2 | Physical properties of Class G cement.

Inspection item	Density (g/cm^3)	Specific surface area (m^2/kg)	Water-cement ratio	Thicking time (min)	Compressive strength (MPa)8 h		Thermal conductivity (W·(m·K)$^{-1}$)
				52°C, 20 MPa	38°C, 20 MPa	60°C, 20 MPa	70°C, 20 MPa
Measured valne	3.14	622	0.5	110	2.5	12	0.896

TABLE 3 | Properties of thermal insulation materials.

Serial number	Properties	Density (g/cm^3)	Type	Size (mesh)	Particle structure	Thermal conductivity ($W·(m·K)^{-1}$)	SiO_2 (%)	Al_2O_3 (%)
a	Floating beads	0.48	powder	40–100	hollow	0.065	56	32.7
b	Expanded perlite	0.43	powder	40–100	honeycomb	0.037	70	15

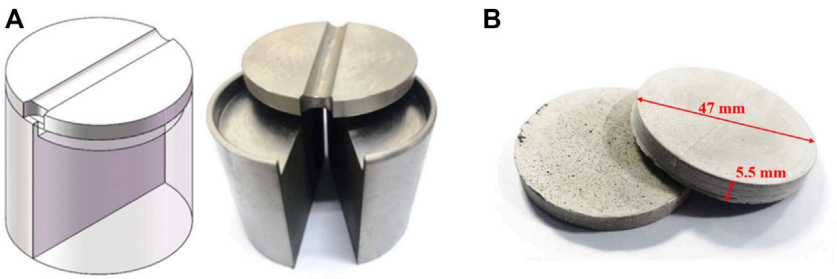

FIGURE 1 | Curing molds and test samples. **(A)** Curing mold assembly drawing. **(B)** Thermal conductivity test sample.

3 RESULTS AND DISCUSSION

3.1 Pure Cement

3.1.1 Microstructure and Related Parameters

The microstructure of pure cement under a microscope and scanning electron microscope (SEM) is shown in **Figures 2A–D**. As the w/c ratio increases from 0.5 to 0.7, the number and size of primary macropores and micropores in pure cement increases significantly, whereas the per unit volume of small cracks was reduced (**Figures 2A–D**).

The test results of dry density and the median pore throat radius of pure cement under different w/c ratios are shown in **Figure 2E**. With the increase of w/c ratio, the dry density gradually decreases, whereas the median pore throat radius gradually increased (**Figure 2E**). In a word, the change rates of dry density and median pore throat radius were gradually reduced. That is when the w/c ratio is 0.6, the dry density and median pore throat radius are 1.37 g/cm^3 and 53 μm respectively, accounting for 67.9 and 61.3% of the total decrease. The increase in the number and size of the primary macropores is the main reason for the changes in dry density and median pore throat radius.

The XRD results of pure cement with different w/c ratios (0.5 and 0.7) are shown in **Figure 3**. As shown in the figure, the increase of w/c ratio or curing temperature can effectively improve the hydration degree of C_3S, C_2S, and C_4AF, which will result in an obvious increase of CH and CSH content (**Figures 3A–D**).

3.1.2 Thermal Conductivity

The thermal conductivity obtained under different curing and hot plate temperatures is shown in **Table 4** and plotted in **Figures 4A,B**. Notably, as the content of floating beads increases, the thermal conductivity decreases rapidly at first and then the reduction rate becomes relatively slow **(Figures 4A,B)**. The thermal conductivity of pure cement (w/c = 0.7) is 21.2%, 25.0%, and 25.6% respectively lower than that of pure cement (w/c = 0.5) under three different curing temperatures (i.e., 60°C, 90°C, 120°C) (**Figure 4A**). In the same case, the decrease percentage is higher than 20.1% under three different hot plate temperatures (**Figure 4B**). It is believed that the improvement of the degree of hydration of cement particles and cement porosity are two major factors that lead to the decrease of thermal conductivity. Moreover, as the w/c ratio is lower than 0.55, most of the added water is involved in the hydration of the cement particles, and a small number of them are used to form pores. In this process, the increased hydration degree of cement particles will convert more C_3S and C_3A into CSH with relatively weak heat conduction capacity, which is the main reason for the reduction of heat transfer capacity of cement skeleton (Qomi et al., 2014; Kumar and Mitra, 2021). When the w/c ratio is between 0.55 and 0.6, the increase rate of cement particle hydration degree gradually decreases, and the increased pores become the main result of the w/c ratio increase. In this case, the thermal conduction capacity of air is much lower than that of cement skeleton. Therefore, the increased pores can effectively reduce the cross-sectional area and prolong the path of heat transfer in cement. The above three results are the main way to reduce the pure cement thermal conductivity. When the w/c ratio is higher than 0.6, the free water required for cement particle hydration reaches saturation, and the main function of increased free water is to improve porosity. However, as the ratio between the subsequently added free water and total volume of cement slurry continues to decrease, the free water that can be distributed per unit volume slurry also continues to decrease. This leads to a slower change rate in porosity and thermal conductivity.

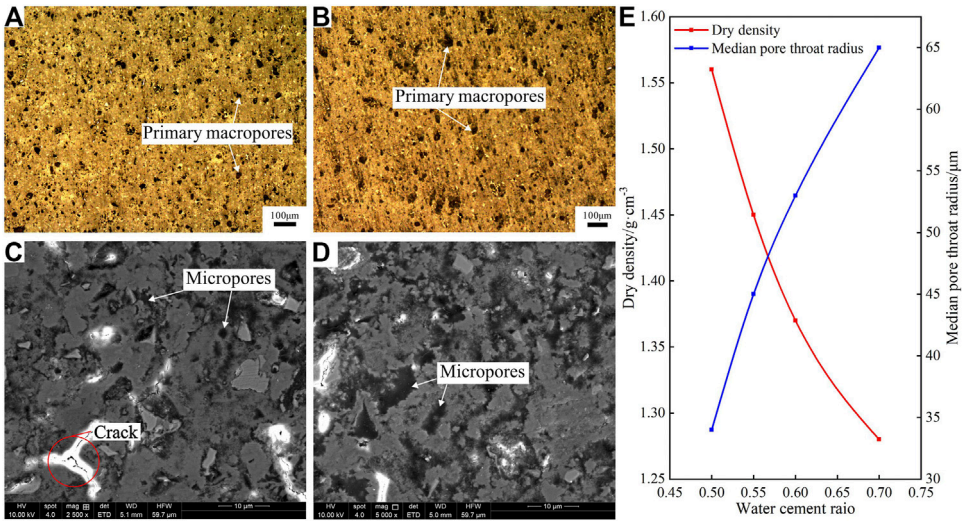

FIGURE 2 | Microstructure and related parameters of pure cement. **(A)** Microstructure of pure cement (w/c = 0.5) under the microscope. **(B)** Microstructure of pure cement (w/c = 0.7) under the microscope. **(C)** Microstructure of pure cement (w/c = 0.5) under SEM. **(D)** Microstructure of pure cement (w/c = 0.7) under SEM. (E) Dry density and median pore throat radius of pure cement.

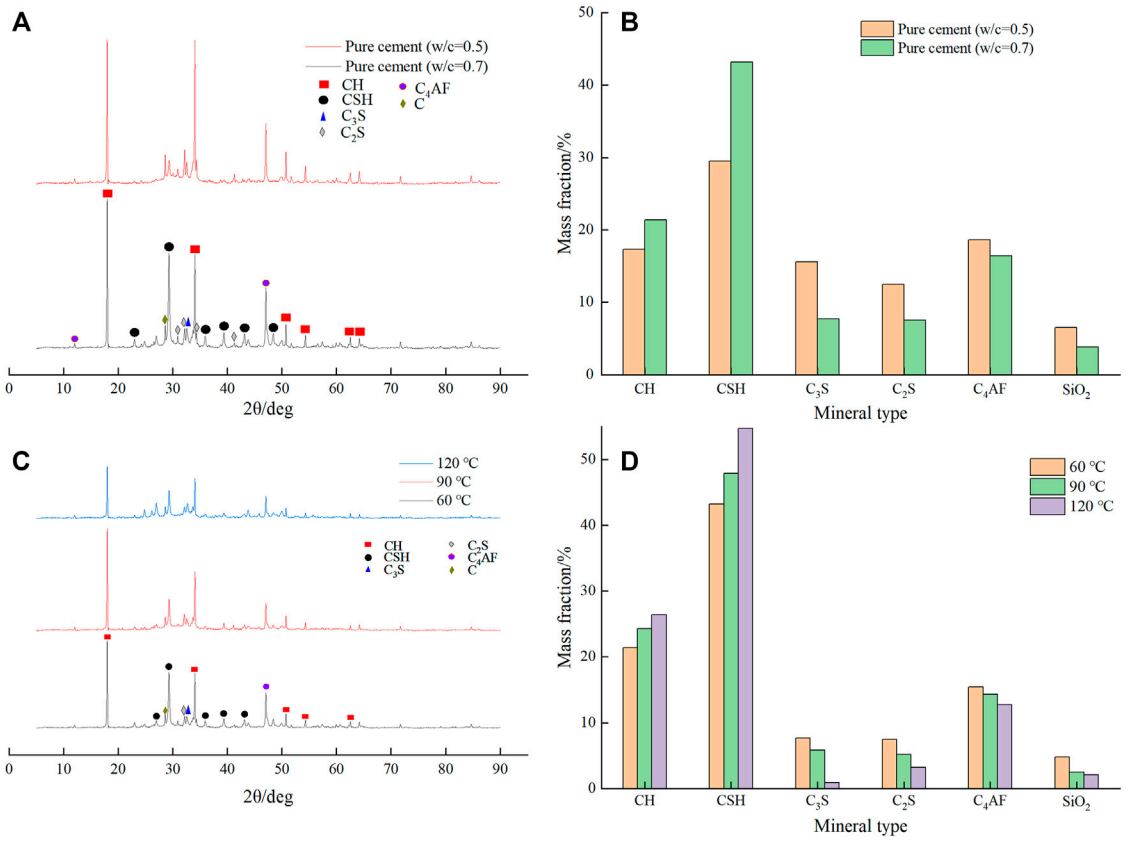

FIGURE 3 | XRD test results of pure cement with w/c ratio of 0.5 and 0.7. **(A)** XRD results of pure cement with w/c ratio of 0.5 and 0.7. The curing temperature is 60°C. **(B)** Mineral content statistics of Panel **(A)** results. **(C)** XRD results of pure cement (w/c = 0.7) under different curing temperatures. **(D)** Mineral content statistics of Panel **(C)** results.

TABLE 4 | Thermal conductivity and compressive strength of cement.

Insulation material content (%)	Thermal conductivity (W·(m·K)$^{-1}$)						Compressive strength (MPa)		
	Curing temperature (°C)			Hot plate temperature (°C)			Curing temperature (°C)		
	60	90	120	50	70	90	60	90	120
w/c = 0.5	0.909	0.880	0.863	0.872	0.909	0.948	63.9	84.3	108.8
w/c = 0.55	0.847	0.816	0.783	0.825	0.847	0.866	58.8	66.1	95.4
w/c = 0.6	0.777	0.734	0.698	0.752	0.777	0.816	45.3	60.8	87.8
w/c = 0.7	0.716	0.66	0.6423	0.696	0.716	0.757	39.2	45.0	63.9
5% floating beads	0.689	0.646	0.626	0.653	0.689	0.724	29.5	45.6	45.5
10% floating beads	0.652	0.622	0.612	0.597	0.652	0.673	27.4	48.6	42.6
15% floating beads	0.611	0.585	0.571	0.557	0.611	0.636	24.7	41.2	43.6
20% floating beads	0.592	0.571	0.559	0.533	0.592	0.610	22.5	38.4	45.4
5% expanded perlite	0.693	0.625	0.611	0.642	0.693	0.712	40.5	43.8	50.8
10% expanded perlite	0.622	0.576	0.563	0.569	0.622	0.636	39.1	42.4	48.4
15% expanded perlite	0.578	0.548	0.542	0.523	0.578	0.598	36.7	42.3	46.2
20% expanded perlite	0.565	0.534	0.532	0.503	0.565	0.575	32.9	40.0	45.5

According to **Figure 4A**, thermal conductivity significantly reduces as the curing temperature increases. Under the condition of w/c = 0.5 and three different curing temperatures (i.e., 60°C, 90°C, 120°C), the thermal conductivity is 0.909 W/(mK), 0.880 W/(mK), and 0.863 W/(mK) respectively. However, as the w/c ratio changes to 0.7, the thermal conductivity decreases to 0.716 W/(mK), 0.660 W/(mK), and 0.642 W/(mK) respectively. Therefore, when the curing temperature increases from 60 to 120°C, the decrease of thermal conductivity is 5% (w/c = 0.5) and 10.3% (w/c = 0.7) respectively. In summary, it can be determined that the increase in the hydration degree of cement particles and the content of substances with low thermal conductivity, caused by the increase of curing temperature, are the main reasons for the decrease in thermal conductivity.

As shown in **Figure 4B**, as the hot plate temperatures elevate, the thermal conductivity increases obviously. When the hot plate temperature is increased to 90°C, the thermal conductivity is 0.948 W/(mK), 0.816 W/(mK), and 0.757 W/(mK), which correspond with a w/c ratio is 0.5, 0.6 and 0.7, respectively. These values are 8.6% higher than that of the hot plate temperature set at 50°C. The results are mainly attributed to the fact that the improvement of hot plate temperature can enhance the vibration intensity of the heated skeleton. Meanwhile, the convective heat transfer of gas in connecting pores of cement has also been strengthened.

3.1.3 Compressive Strength

Compressive strength test results are shown in **Table 3** and plotted in **Figure 4C**. With the increase of w/c ratio, the cement compressive strength decreases apparently. However, it shows an opposite trend to the ascending curing temperature (**Figure 4C**). As the curing temperature increases gradually, the compressive strength of cement (w/c = 0.7) is 39.2, 45.0, and 63.9 MPa respectively, which is 38.6%, 46.6%, and 41.3% lower

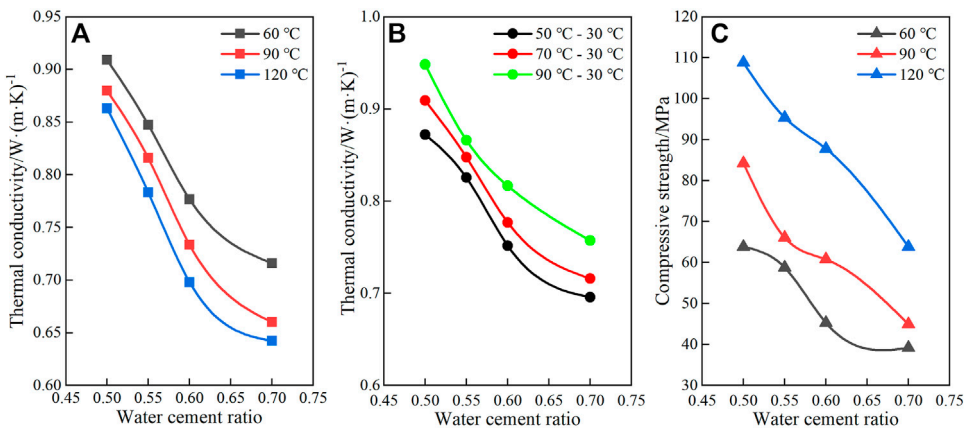

FIGURE 4 | Thermal conductivity and compressive strength test results of pure cement under different conditions. **(A)** Test results of thermal conductivity at different curing temperatures. The test temperature combination is 70–30°C. **(B)** Test results of thermal conductivity at different hot plate temperatures. The curing temperature is 60°C. **(C)** Test results of compressive strength at different curing temperatures.

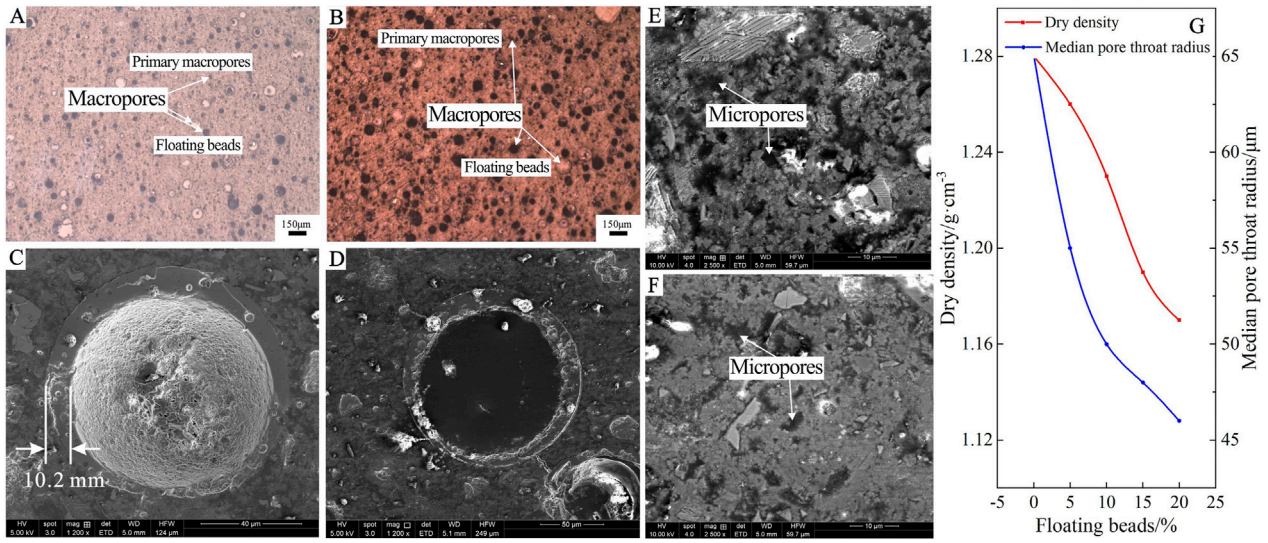

FIGURE 5 | Microstructure and related parameters of thermal insulation cement with floating beads. **(A)** Microstructure of thermal insulation cement with 10% floating beads under the microscope. **(B)** Microstructure of thermal insulation cement with 20% floating beads under the microscope. **(C, D)** Microstructure of floating beads under SEM. **(E)** Microstructure of thermal insulation cement with 10% floating beads under SEM. **(F)** Microstructure of thermal insulation cement with 20% floating beads under SEM. **(G)** Dry density and median pore throat radius of thermal insulation cement with floating beads.

than that of cement (w/c = 0.5). Similarly, the compressive strength is 108.8, 87.8, and 63.9 MPa, which correspond with w/c ratio is 0.5, 0.6, and 0.7 respectively under curing temperature set at 120°C. These results show that the compressive strength increased 70.3%, 93.8%, and 63.0% compared with the curing temperature set at 60°C. Analysis shows that the increase in the number and size of primary macropores and micropores is the main reason for the reduction of compressive strength (**Figure 2**). The increase of curing temperature contributes to the ascending CSH content. The enhancement of CSH content is the primary factor leading to the improvement of compressive strength.

The increase of the w/c ratio can effectively improve the size and number of primary macropores and micropores, as well as the hydration degree of cement particles. This can result in the reduction of the heat transfer capacity of the cement skeleton and heat transfer area. However, the heat transfer path appears to have an opposite trend. Similarly, the increase of curing and hot plate temperature can also change the thermal conductivity. Furthermore, the increase in the number and size of primary macropores and micropores is the main reason for the significant decrease in compressive strength.

3.2 Thermal Insulation Cement With Floating Beads

3.2.1 Microstructure and Related Parameters

The macropores and micropores of the thermal insulation cement are shown in **Figures 5A,B,E,F**. The microstructure of the floating beads in the cement is shown in **Figures 5C,D**. Dry density and median pore throat radius are shown in **Table 5** and plotted in **Figure 5G**.

Floating beads distribute evenly in the cement (**Figures 5A,B**). The surface can be closely combined with the cement skeleton, and its hollow structure can effectively replace the skeleton (**Figures 5C,D**). Increasing the content of floating beads can not only significantly increase the number and size of macropores, but also effectively reduce the number of micropores and increase the density of skeleton (Tylor, 1997; **Figures 5A,B,E,F**).

The dry density and median pore throat radius decrease as the increase of floating beads. Besides, the reduction rate gradually slows down (**Figure 5G**). At the same time, most floating beads can stay closed, so there is no effect on the distribution of internal communicating pore in cement. Therefore, the reduction of dry density is mainly attributed to the increase of floating beads. However, the decrease in the size of primary macropores and micropores in the cement leads to a decrease in the median pore throat radius. In addition, the analysis shows that when the content of floating beads is 0–5%, its main function is to replace the primary macropores and compress the micropores. Therefore, the dry density changes are relatively small, whereas the median pore throat radius varies greatly. When the dosage of floating beads changes to 5%, the decreased value of dry density and median pore throat radius accounts for 18.2 and 52.6% of the total decrease, respectively. As the dosage varies from 5 to 15%, the main function of floating beads further replaces the cement skeleton and compresses the original pores. This will make the reduction rate of dry density changed larger than the median pore throat radius. When the dosage of floating beads reaches 15%, a decrease in dry density and median pore throat particle size account for 81.8 and 89.5% of the total decrease, respectively. In addition, as the dosage is 15–20%, the ratio of the floating beads to

TABLE 5 | Dry density and median pore throat radius of cement.

	Dry density (g/cm^3)	Median pore throat radius (μm)
w/c = 0.5	1.56	34
w/c = 0.55	1.45	45
w/c = 0.6	1.37	53
w/c = 0.7	1.28	65
5% floating beads	1.26	55
10% floating beads	1.23	50
15% floating beads	1.19	48
20% floating beads	1.17	46
5% expanded perlite	1.25	57
10% expanded perlite	1.19	48
15% expanded perlite	1.14	45
20% expanded perlite	1.11	43

the total volume of cement slurry is greatly reduced, so the decrease in dry density is also significantly reduced.

The SEM results of floating beads and skeleton in thermal insulation cement are shown in **Figures 6A,B**. Among them, points of spectrogram 1 and spectrogram 2 are selected from the surface of floating beads, and spectrogram 3 is from the cement skeleton. The XRD results of pure cement (w/c = 0.7) and thermal insulation cement with 20% floating beads are shown in **Figures 6C,D**.

The result of spectrogram 1 can further confirm that mainly two types of oxides i.e., SiO_2 and Al_2O_3, exist on the surface of float beads. Comparing spectrogram 2 with 3, it can be found that the calcium content has increased in some areas of the surface of the floating bead. It may be generated by the reaction between oxides and calcium-containing substances in cement slurry (**Figures 6A,B**). In addition, the research of XRD shows that the addition of floating beads will reduce the content of $Ca(OH)_2$ and increase the content of CSH in cement (**Figures 6C,D**). This can further support the opinion that the oxides that existed on the surface of the floating beads can react with $Ca(OH)_2$ and form CSH at the end (**Equation 1**, **2**).

$$xCa(OH)_2 + SiO_2 + mH_2O \rightarrow xCaO \cdot SiO_2 \cdot mH_2O \quad (1)$$

$$yCa(OH)_2 + Al_2O_3 + mH_2O \rightarrow yCaO \cdot SiO_2 \cdot mH_2O \quad (2)$$

3.2.2 Thermal Conductivity

The test results of thermal conductivity for thermal insulation cement with floating beads are shown in **Table 4** and plotted in **Figures 7A,B**. The thermal conductivity gradually decreases with the increase of floating beads. Specifically, the reduction rate of thermal conductivity gradually increases at first, and then gradually decreases (**Figures 7A,B**). This is similar to the change rule of dry density, as the effect of the floating beads varies under different dosages.

The increased curing temperature can effectively reduce thermal conductivity (**Figure 7A**). When the curing temperature is 60°C, 90°C, and 120°C, the thermal conductivity of thermal insulation cement with 20% float beads is 0.5922 W/(mK), 0.5713 W/(mK), and 0.5591 W/(mK) respectively.

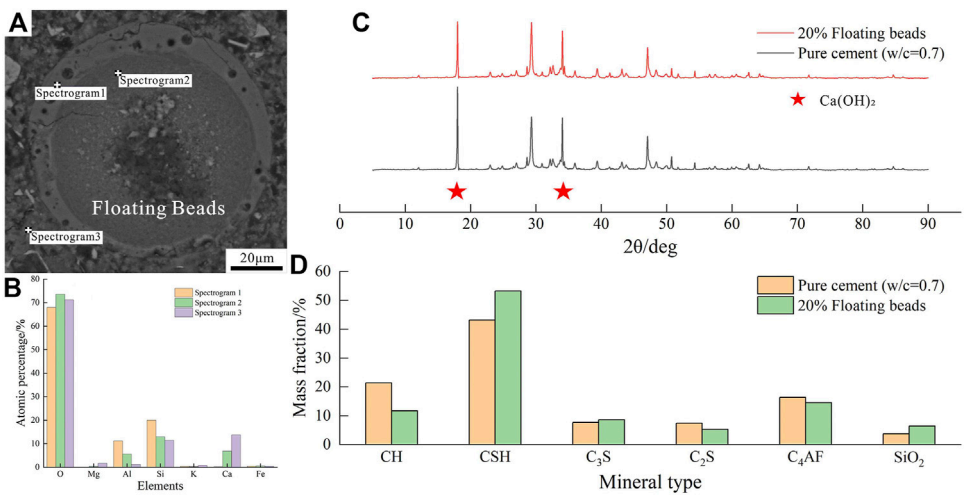

FIGURE 6 | Energy spectrum analysis and XRD results of thermal insulation cement with floating beads. **(A)** The selected points of spectrograms. **(B)** Atomic number statistics from energy spectrum analysis results. **(C)** XRD test results of pure cement (w/c = 0.7) and thermal insulation cement with 20% floating beads. **(D)** Mineral content statistics of XRD test results.

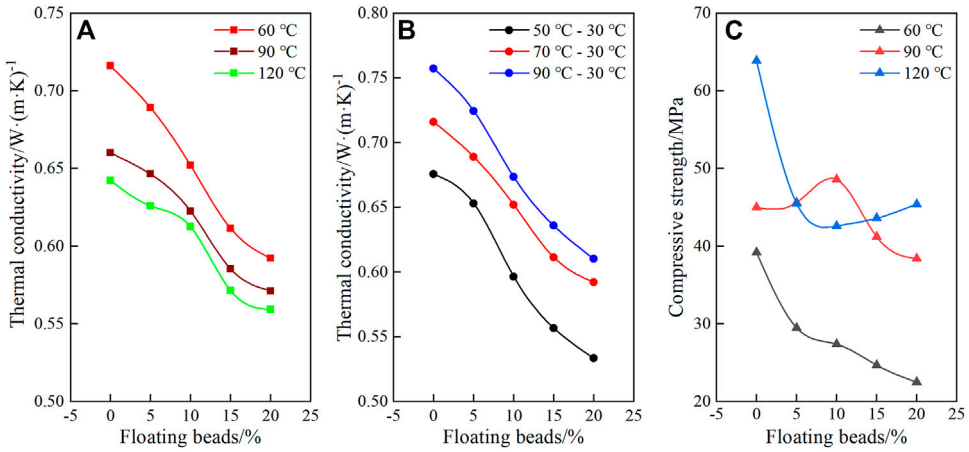

FIGURE 7 | Thermal conductivity and compressive strength test results of thermal insulation cement with floating beads under different conditions. **(A)** Test results of thermal conductivity at different curing temperatures. The test temperature combination is 70–30°C. **(B)** Test results of thermal conductivity at different hot plate temperatures. The curing temperature is 60°C. **(C)** Test results of compressive strength at different curing temperatures.

Compared with pure cement (w/c = 0.7), the thermal conductivity decreases by 17.3%, 13.4%, and 12.9%. In addition, for heat insulation cement with 20% floating beads, the thermal conductivity reduction rate is 4.5 and 6.1%, respectively, which corresponds with the curing temperatures of 60–90 and 120°C. For the thermal insulation cement with 10% floating beads, as the curing temperature is increased, the thermal conductivity reduction rate is 3.5 and 5.6%. The test results clearly show that the reduction rate of thermal conductivity gradually decreases, which is caused by the increase of curing temperature. The increase of porosity and hydration degree of cement particles are the main factors for the decrease in thermal conductivity.

The thermal conductivity increases with the improvement of the hot plate temperature (**Figure 7B**). Moreover, the change rules of thermal conductivity at three different hot plate temperatures are the same. The thermal conductivity of thermal insulation cement with 10 and 20% floating beads is 0.5966 W/(mK) and 0.5335 W/(mK) respectively, with the hot plate temperature is set at 50°C. When the hot plate temperature is increased to 70°C, the thermal conductivity increase rate is 9.3 and 11.0%, respectively. The increased rate of thermal conductivity is 12.9 and 14.4% respectively, with the hot plate temperature is set at 90°C. As the hot plate temperature increases, the increase rate of the thermal conductivity decreases. Based on these results, we can conclude that the increase of hot plate temperature can enhance the convective strength of gas inside the floating beads. This is different from the enhancement of gas flow in the connected pores of pure cement.

3.2.3 Compressive Strength

The compressive strength of thermal insulation cement with floating beads is shown in **Table 4** and plotted in **Figure 7C**. An increase in the content of floating beads will reduce thermal conductivity, but the effect of increasing curing temperature is the opposite (**Figure 7C**). The compressive strength of thermal insulation cement with 20% floating beads at different curing temperatures (i.e., 60°C, 90°C, and 120°C) are 22.5, 38.4, and 45.4 MPa, respectively, which are 42.6%, 14.7%, and 28.9% lower than pure cement under the same w/c ratio. Furthermore, when the curing temperature is increased to 90 and 120°C, the increased rate of compressive strength for thermal insulation cement with 20% float beads is 70.7 and 101.8%. Generally, the compressive strength of thermal insulation cement can be maintained at a relatively high level. Research on the microstructure of cement shows that although the addition of floating beads can effectively reduce the number and size of primary pores, the hollow structure of the floating beads can significantly increase the porosity of the cement. This is the main reason for the decrease in compressive strength. In addition, the strength of floating beads derived from the thicker shell (**Figure 5C**), and hydration of active substances can effectively enhance the strength of the surrounding cement skeleton. This is an important factor for maintaining high compressive strength.

In summary, the addition of floating beads can effectively reduce the thermal conductivity of cement and maintain its compressive strength. Specifically, the increase in porosity is the main reason for the decrease in thermal conductivity. However, the extension of the heat conduction path and hydration of active substances on the surface of the floating beads are other reasons. Moreover, the increase in hydration degree of cement particles, the thicker shell of floating beads, as well as the increase in strength of the surrounding cement skeleton, are important factors for maintaining the cement compressive strength.

3.3 Thermal Insulation Cement With Expanded Perlite

3.3.1 Microstructure and Related Parameters

The analyzed results of macropores and micropores for thermal insulation cement with expanded perlite are shown in **Figures 8A,B,E,F**. The microstructure of the expanded perlite in the

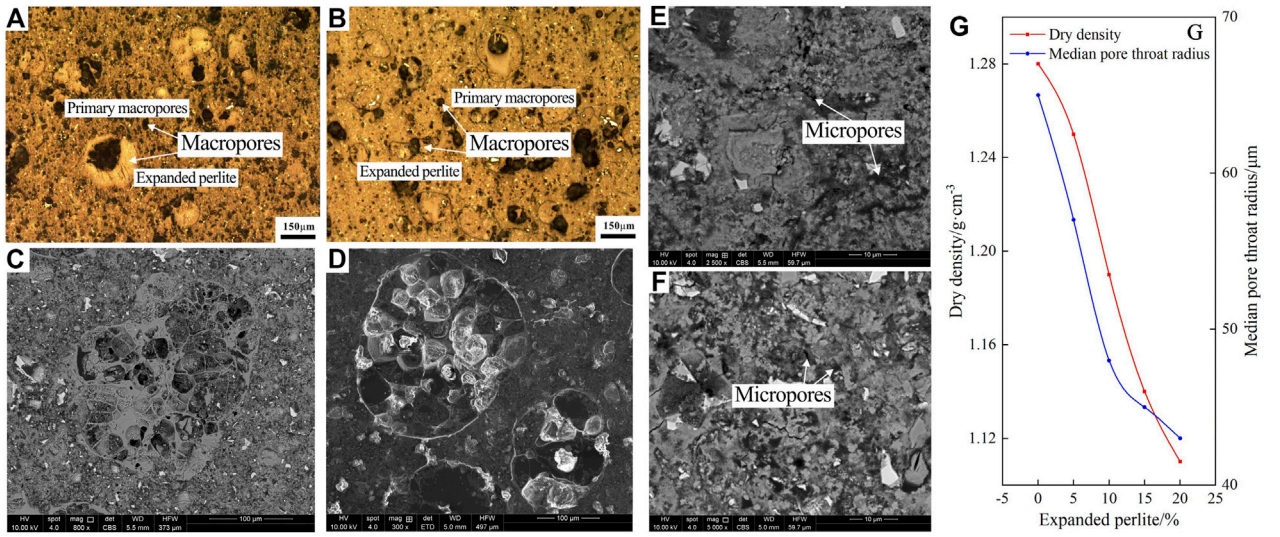

FIGURE 8 | Microstructure and related parameters of thermal insulation cement with expanded perlite. **(A)** Microstructure of thermal insulation cement with 10% expanded perlite under the microscope. **(B)** Microstructure of thermal insulation cement with 20% expanded perlite under the microscope. **(C,D)** Microstructure of expanded perlite under SEM. **(E)** Microstructure of thermal insulation cement with 10% expanded perlite under SEM. **(F)** Microstructure of thermal insulation cement with 20% expanded perlite under SEM. **(G)** Dry density and median pore throat radius of thermal insulation cement with expanded perlite.

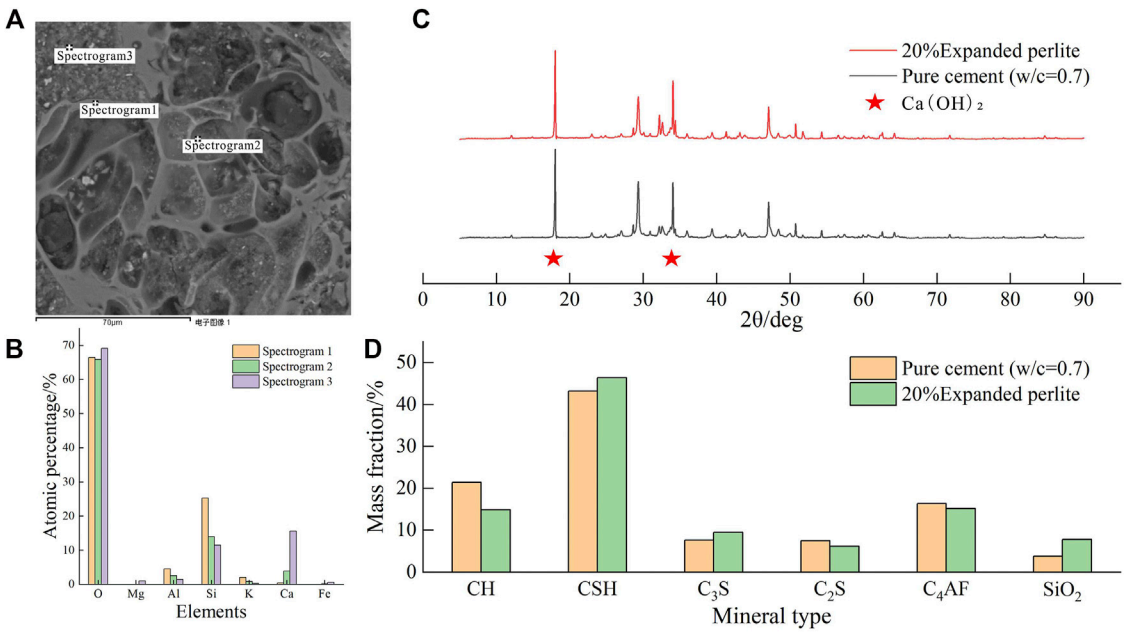

FIGURE 9 | Energy spectrum analysis and XRD test results of thermal insulation cement with expanded perlite. **(A)** The selected points of spectrograms. **(B)** Atomic number statistics from energy spectrum analysis results. **(C)** XRD test results of pure cement (w/c = 0.7) and thermal insulation cement with 20% expanded perlite. **(D)** Mineral content statistics of XRD test results.

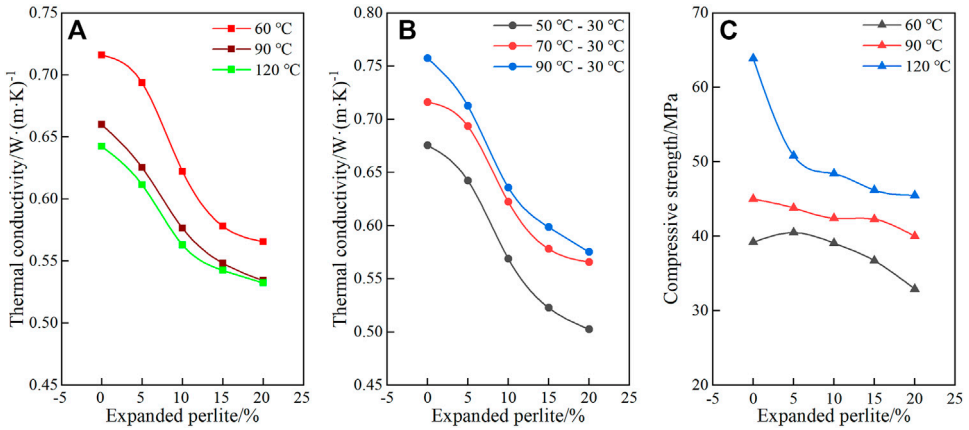

FIGURE 10 | Test results of thermal conductivity and compressive strength of thermal insulation cement with expanded perlite under different conditions. **(A)** Test results of thermal conductivity at different curing temperatures. The test temperature combination is 70–30°C. **(B)** Test results of thermal conductivity at different hot plate temperatures. The curing temperature is 60°C. **(C)** Test results of compressive strength at different curing temperatures.

cement under the SEM is shown in **Figures 8C,D**. Dry density and median pore throat radius are shown in **Table 5** and plotted in **Figure 8G**.

The addition of expanded perlite can notably replace the primary macropores and compress micropores. As a result, with the addition of expanded perlite, the number and size of primary macropores and micropores are gradually reduced (**Figures 8A,B,E,F**). This ultimately leads to the continuous decrease of the median pore throat radius (**Figure 8G**). Simultaneously, an increase in the expanded perlite content will also significantly reduce the dry density because of its internal honeycomb-like structure (**Figures 8C,D,G**). When the content of expanded perlite is 10%, the dry density and median pore throat radius is 1.23 g/cm^3 and 50 μm, and the decreased value under this amount accounts for 45.4 and 78.9% of the total decrease value. Compared with the thermal insulation cement with floating beads, the cement with expanded perlite has significant advantages for reducing the dry density, and the effect on reducing the median pore throat radius is equivalent.

The SEM results of expanded perlite and skeleton in thermal insulation cement are shown in **Figures 9A,B**. Among them, points of spectrogram 1 and spectrogram 2 are selected from the surface of expanded perlite, and spectrogram 3 is from the cement skeleton. The XRD results of pure cement (w/c = 0.7) and thermal insulation cement with 20% expanded perlite are shown in **Figures 9C,D**.

Comparing the results of spectrogram 1, spectrogram 2, and spectrogram 3, it can be deduced that the main substances that existed on the surface of expanded perlite are SiO_2 and Al_2O_3, which are similar to floating beads. These oxides can react with $Ca(OH)_2$ in the slurry to form CSH (**Figures 9A,B**). Eventually, the content of $Ca(OH)_2$ is reduced, and the content of CSH is increased (**Figures 9C,D**).

3.3.2 Thermal Conductivity

The test results of thermal conductivity for thermal insulation cement with expanded perlite at different curing and hot plate temperatures are shown in **Table 4** and plotted in **Figures 10A,B**.

In addition to expanded perlite, the thermal conductivity gradually decreases, and the reduction rate increased first and then decreased (**Figures 10A,B**). This change rule and reasons are identical to that of cement with floating beads. The thermal conductivity of thermal insulation cement with 20% expanded perlite at a curing temperature of 60°C, 90°C, and 120°C are 0.5656 W/(mK), 0.5343 W/(mK) and 0.5436 W/(mK), respectively, which are 21.0%, 19.0%, and 17.1% lower than that of pure cement with a w/c ratio of 0.7 (**Figure 10A**). Similarly, under three different hot plate temperatures, the thermal conductivity of thermal insulation cement with 20% expanded perlite has a reduced rate of larger than 21%. Combined with the analyzed data, the thermal conductivity of thermal insulation cement with expanded perlite is generally lower than that of cement with floating beads. This may be caused by the relatively small density of expanded perlite. Therefore, with the same mass fraction addition, the amount of expanded perlite that can be added to the cement slurry is much more. Furthermore, the honeycomb-like structure in the expanded perlite is another factor. This structure is more effective in reducing fluid convection in the insulation material (**Table 3** and **Figure 8C**).

The thermal conductivity decreases with the increase of curing temperature (**Figure 10A**). This can be attributed to an increase in the hydration degree of cement particles and surface oxides of expanded perlite. The thermal conductivity of thermal insulation cement with 10% expanded perlite can be reduced by 7.3 and 9.5% when the curing temperature is 60–90°C and 120°C, respectively. Under the situation with the expanded perlite content is 20%, the reduction rate is 5.5 and 5.9%.

Similarly, the thermal conductivity increases with the increase of the hot plate temperature. The higher the temperature, the lower the growth rate. The thermal conductivity of thermal insulation cement with 20% expanded perlite can be increased by 12.5 and 14.4% when the hot plate temperature is 50–70°C and 90°C, respectively.

3.3.3 Compressive Strength

The test results of compressive strength for thermal insulation cement with expanded perlite are shown in **Table 4** and plotted in **Figure 10C**. With the addition of expanded perlite, the compressive strength gradually decreases. The results indicate that the increase of curing temperature can significantly enhance the cement compressive strength (**Figure 10C**). When the content of expanded perlite is 20%, the compressive strength at different curing temperatures (i.e., 60°C, 90°C, and 120°C) are 32.9, 40.0, and 45.5 MPa, respectively. In general, the compressive strength of thermal insulation cement with expanded perlite can maintain a high value under the above test conditions, especially higher than that of cement with floating beads. This may be caused by the relatively higher SiO_2 content on the surface of the expanded perlite. It can effectively increase the skeleton strength around the expanded perlite and reduce the possibility of stress concentration. Moreover, the existence of the honeycomb-like structure can greatly improve the plasticity of the cement skeleton, and finally improve the compressive capacity (**Figures 8C,D**).

In a word, with the addition of expanded perlite and floating beads, thermal conductivity and compressive strength have similar varied trends and mechanisms. However, the honeycomb-like structure inside the expanded perlite is favorable to obtain lower thermal conductivity and maintain the higher compressive strength of cement.

4 CONCLUSION

This paper has introduced a steady-state test method. The thermal conductivity and compressive strength of cement under different conditions were tested. The microscopic mechanism of the thermal conductivity and compressive strength change were also explained. The conclusions are as follows:

1) The use of thermal insulation materials can effectively reduce the thermal conductivity of cement and maintain its compressive strength. Specifically, the increase of w/c ratio, thermal insulation material, and curing temperature can significantly reduce cement thermal conductivity. However, the first two factors and the last factor have opposite effects on the compressive strength. Furthermore, the increase in hot plate temperature will increase thermal conductivity. In comparison, the effect of expanded perlite is better than that of floating beads.
2) The increase of porosity and hydration degree of cement particles can effectively reduce the heat transfer area and heat transfer capacity of the skeleton. They are the main reasons for the decrease in thermal conductivity. The extension of the heat transfer path and hydration of active substances on the insulation material surface can effectively reduce the thermal transfer efficiency of the skeleton, which are other reasons for the decrease of thermal conductivity. In addition, the hydration of cement particles is the basis for cement to maintain the necessary compressive strength. The strength of the insulation material, the hydration of the surface-active substance, and the internal honeycomb-like structure are important factors to maintain the compressive strength at a high level.
3) Combined with the actual conditions of the formations and engineering, the lower formation temperature of the upper well section will result in a relatively low curing temperature and a relatively large temperature difference (between the hot water and formations) during the pumping process. This will result in a relatively high thermal transfer capacity of cement in the upper well section, and thus this area is the main thermal loss area.

DATA AVAILABILITY STATEMENT

The original contributions presented in the study are included in the article/supplementary material, further inquiries can be directed to the corresponding author.

AUTHOR CONTRIBUTIONS

FZ wrote the manuscript and is responsible for providing overall idea, experimental design, and data analysis, LL is responsible for instrument operation. All authors approve the article for publication.

FUNDING

This work was financially supported by the National Key Research and Development Program of China (Grant No. 2019YFB1504102) and a project of the Chinese Academy of Geological Sciences (Grant No. JKY202008).

ACKNOWLEDGMENTS

We thank the editor, associate editor, and reviewers for their constructive comments, which helped greatly improve the paper.

REFERENCES

Bildirici, M. E., and Gökmenoğlu, S. M. (2017). Environmental Pollution, Hydropower Energy Consumption and Economic Growth: Evidence from G7 Countries, Hydropower Energy Consumption and Economic Growth: Evidence from G7 Countries. *Renew. Sust. Energ. Rev.* 75 (C), 68–85. doi:10.1016/j.rser.2016.10.052

Fang, Y., Zhang, Y., and Ran, Z. Z. (2020). Thermal Conductivity of Cementing Conductive Cement in Medium and Deep Geothermal Well. *Mater. Rep.* 34 (20), 32–37+56. doi:10.11896/cldb.19030004

Gorman, J. M., Abraham, J. P., and Sparrow, E. M. (2014). A Novel, Comprehensive Numerical Simulation for Predicting Temperatures within Boreholes and the Adjoining Rock Bed. *Geothermics* 50, 213–219. doi:10.1016/j.geothermics.2013.10.001

Hamm, S., and Metcalfe, E. (2019). Harnessing the Heat beneath Our Feet: Geothermal Energy. *Front. Young Minds* 7, 105. doi:10.3389/frym.2019.00105

Hasan, A. R., and Kabir, C. S. (2002). *Fluid Flow and Heat Transfer in Wellbores*. Texas: Society of Petroleum Engineers, 64–73.

Ichim, A., Teodoriu, C., and Falcone, G. (2016). "Influence of Cement Thermal Properties on Wellbore Heat Exchange," in Proceeding of the 41st Workshop on Geothermal Reservoir Engineering Stanford University, Stanford, California, Feb 2016.

Ichim, A., Teodoriu, C., and Falcone, G. (2018). Estimation of Cement Thermal Properties through the Three-phase Model with Application to Geothermal Wells. *Energies* 11 (10), 2839. doi:10.3390/en11102839

Kanev, K., Ikeuchi, J., Kimurat, S., and Okajima, A. (1997). Heat Loss to the Surrounding Rock Formation from a Geothermal Wellbore. *Geothermics* 26, 329–349. doi:10.1016/S0375-6505(96)00046-6

Li, X. Y., He, H. P., Duan, Y. Z., and Li, Y. F. (2017). Analysis on the Thermal Efficiency Improvement Process for Geothermal Well in Porous Sandstone. *Oil Drilling Prod. Tech.* 39 (4), 484–490. doi:10.13639/j.odpt.2017.04.016

Ma, B., Cao, Y., Wang, Y., Jia, Y., Qin, H. S., and Chen, Y. (2016). Origin of Carbonate Cements with Implications for Petroleum Reservoir in Eocene Sandstones, Northern Dongying Depression, Bohai Bay basin, China. *Energy Exploration & Exploitation* 34 (2), 199–216. doi:10.1177/0144598716629871

Qomi, M. J. A., Bauchy, M., Ulm, F.-J., and Pellenq, R. J.-M. (2014). Anomalous Composition-dependent Dynamics of Nanoconfined Water in the Interlayer of Disordered Calcium-Silicates. *J. Chem. Phys.* 140 (5), 054515. doi:10.1063/1.4864118

Sarkar, P. K., and Mitra, N. (2021). Thermal Conductivity of Cement Paste: Influence of Macro-Porosity. *Cement Concrete Res.* 143, 106385. doi:10.1016/j.cemconres.2021.106385

Tekin, S., and Akin, S. (2011). "Estimation of the Formation Temperature from the Inlet and Outlet Mud Temperatures while Drilling Geothermal Formations," in Proceedings of 36th Workshop on Geothermal Reservoir Engineering, Stanford (Stanford University).

Tóth, A. (2006). "Heat Losses in a Planned Hungarian Geothermal Power Plant," in Proceedings of the Thirsty-First Workshop on Geothermal Reservoir Engineering, Stanford, Feb 2016 (Stanford University).

Tylor, H. F. W. (1997). *Cement Chemistry*. London: Thomson Telford Publishers. doi:10.1680/cc.25929

Wang, G. L., Zhang, W., Liang, J. Y., Lin, W. J., and Wang, W. L. (2017). Evaluation of Geothermal Resources Potential in China. *Acta Geoscientica* 38 (04), 449–450+134+451. doi:10.3975/cagsb.2017.04.02

Won, J., Lee, D., Na, K., Lee, I.-M., and Choi, H. (2015). Physical Properties of G-Class Cement for Geothermal Well Cementing in South Korea. *Renew. Energ.* 80, 123–131. doi:10.1016/j.renene.2015.01.067

Yang, M., Meng, Y. F., Li, G., Deng, J. M., and Zhao, X. M. (2013). A Transient Heat Transfer Model of Wellbore and Formation during the Whole Drilling Process. *Acta Petrolei Sinica* 34 (2), 366–371. doi:10.7623/syxb201302021

Yang, T., Zhao, P., Li, Q., Zhao, Y., and Yu, T. (2021). Study on Thermophysical Properties of a Lead-Bismuth-Based Graphene Nanofluid. *Front. Energ. Res.* 9, 727447. doi:10.3389/fenrg.2021.727447

Zhao, J. (2020). Discussion on Technical Feasibility of Thermal Insulation Cement in Jiangsu Oilfield. *Inner Mongolia Petrochemical Industry* 3, 86–88. doi:10.3969/j.issn.1006-7981.2020.11.032

Zhao, X. T., and Fu, H. Y. (2019). Analysis of Current Status and Prospects of Geothermal Energy Development and Utilization. *Environ. Dev.* 31 (5), 233. doi:10.16647/j.cnki.cn15-1369/X.2019.05.139

Zhou, F., and Zhang, X. (2013). Assessment of Heat Transfer in an Aquifer Utilizing Fractal Theory. *Appl. Therm. Eng.* 59 (1-2), 445–453. doi:10.1016/j.applthermaleng.2013.06.013

Conflict of Interest: The authors declare that the research was conducted in the absence of any commercial or financial relationships that could be construed as a potential conflict of interest.

Publisher's Note: All claims expressed in this article are solely those of the authors and do not necessarily represent those of their affiliated organizations, or those of the publisher, the editors, and the reviewers. Any product that may be evaluated in this article, or claim that may be made by its manufacturer, is not guaranteed or endorsed by the publisher.

frontiers in Earth Science

ORIGINAL RESEARCH
published: 01 March 2022
doi: 10.3389/feart.2022.818129

The Heat Source Origin of Geothermal Resources in Xiong'an New Area, North China, in View of the Influence of Igneous Rocks

Yue Cui[1,2], Chuanqing Zhu[1], Nansheng Qiu[1], Boning Tang[1], Sasa Guo[1] and Zhiwei Lu[3]*

[1]State Key Laboratory of Petroleum Resources and Prospecting, China University of Petroleum, Beijing, China, [2]Institute of Porous Flow and Fluid Mechanics, Chinese Academy of Sciences, Langfang, China, [3]Viterbi School of Engineering, University of Southern California, Los Angeles, CA, United States

The Xiong'an new area has abundant geothermal resources, and heat source research plays an important role in the geothermal system. Using the logging curve, we calculated the radioactive heat production of sedimentary layers and igneous rocks in non-sample wells; analyzed the influence of igneous rock distribution, residual heat, and its thermal increment on crust; and clarified the heat source origin of hydrothermal geothermal resources in Xiong'an new area. Sedimentary layers data (5,504) of 20 wells were converted to determine the applicable GR-A empirical relationship, and the radioactive heat production of igneous rocks with different lithologies was estimated. Finite element simulations show that igneous rock intrusions in the study area reach thermal equilibrium with the surrounding rock after 0.5 Ma at most. Upon cooling, the difference in thermal physical properties to the surrounding rock only leads to a higher heat flow of about 3.55 mW/m^2 in the partial of the Niutuozhen salient. It is known that the development of igneous facies impacts the heat source. Under the geothermal background of "cold crust-hot mantle," the mantel heat was the primary source, which the Yanshanian intrusions injected into the central salient, increasing the crustal heat by about 12% and the heat source by about 6%. The measured heat flow becomes higher in the salient (raised about 12.04 mW/m^2–29.25 mW/m^2) where the deep faults developed due to the groundwater convection. Heat conduction from crust-mantle heat flow and heat convection caused by deep faults are responsible for the current geothermal state in Xiong'an new area.

Keywords: Xiong'an new area, igneous rock heat production, GR-A empirical relationship, finite element simulation, heat source origin

OPEN ACCESS

Edited by:
Yanlong Kong,
Institute of Geology and Geophysics (CAS), China

Reviewed by:
Song Rao,
Yangtze University, China
Jiao Tian,
China Earthquake Administration, China

***Correspondence:**
Chuanqing Zhu
zhucq@cup.edu.cn

Specialty section:
This article was submitted to Economic Geology, a section of the journal Frontiers in Earth Science

Received: *19 November 2021*
Accepted: *11 January 2022*
Published: *01 March 2022*

Citation:
Cui Y, Zhu C, Qiu N, Tang B, Guo S and Lu Z (2022) The Heat Source Origin of Geothermal Resources in Xiong'an New Area, North China, in View of the Influence of Igneous Rocks. Front. Earth Sci. 10:818129. doi: 10.3389/feart.2022.818129

INTRODUCTION

Magmatic activity is closely related to tectonic activity, which is the basis for the study of basin formation, thermal evolution, and present thermal state (Rosa et al., 2015; Liu et al., 2018; Alain et al., 2020). In areas where volcanoes are developed, the temperature field is not only affected by the steady-state temperature field but also related to the heat carried by high-temperature magma. The steady geothermal field mainly occurs in the lithosphere without a high-temperature abnormal body, which is related to mantle heat, the heat produced by radioactive elements, and stratigraphic thermal conductivity (Mundry, 1970; Liu et al., 2018).

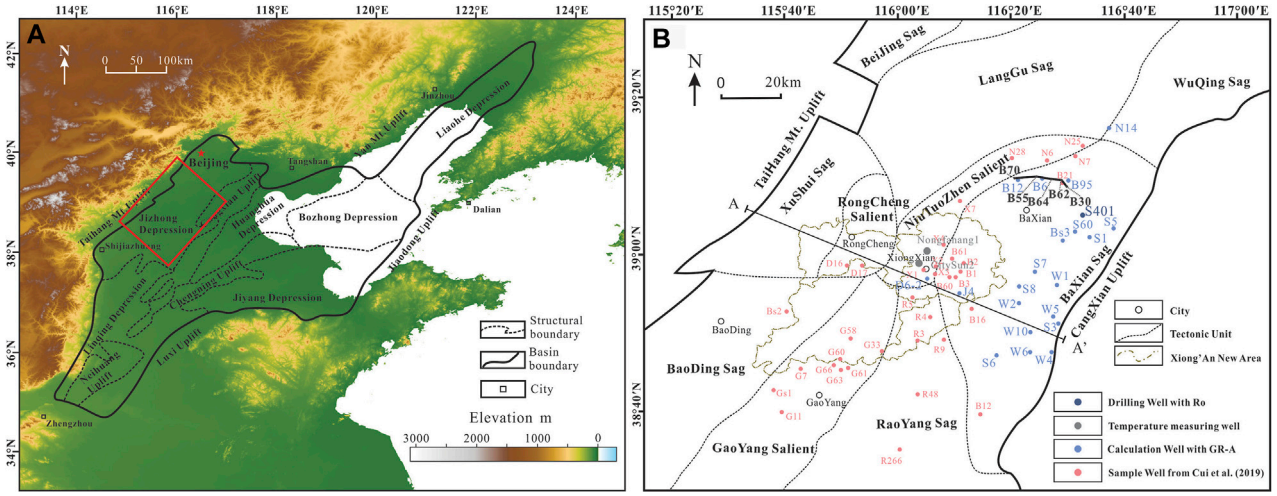

FIGURE 1 | Structural location map of **(A)** Bohai Bay Basin and **(B)** Xiong'an new area.

The Xiong'an new area is located in the Bohai Bay Basin, which has similar geothermal characteristics and heat flow background. The average geothermal gradient in the Bohai Bay Basin is 34.7°C/km, while that in the Jizhong depression, where the study area is located, is relatively low (32.4°C/km). The average heat flow in the Bohai Bay Basin is 64.4 ± 8.1 mW/m^2, which is 2.5 mW/m^2 higher than that of Chinese basins (61 mW/m^2), where that of Jizhong depression is 61.1 ± 9.4 mW/m^2 (Hu et al., 2001; Gong, 2003; Gong et al., 2011; Qiu et al., 2014; Chang et al., 2016). Archaeozoic, multi-stage magmatic activities have developed in the Bohai Bay Basin, and large areas of magmatic rocks were formed during late Mesozoic and Cenozoic mantle-derived volcanism due to the reduction of the lithosphere caused by the subduction of the western Pacific plate. Previous studies on the eruption period and scale of volcanic have been carried out (Zhang and Shi, 1997; Wu et al., 2005; Tang et al., 2013; Gong, 2014), but the residual heat effects of volcanic intrusion in the region have not been studied enough. Although the contribution of igneous rocks to the thermal anomalies in Xiong'an new area is considered to be insufficient, and a "binary heat accumulation" model of crust-mantle production has been proposed, there are insufficient opportunities for quantitative studies (Pang et al., 2015).

Therefore, this paper determined the spatiotemporal distribution of Mesozoic and Cenozoic igneous rocks, simulated the influence of magmatic intrusions on the geothermal field, quantitatively calculated the influence of igneous rocks on current thermal anomalies, and analyzed the heat source origin in a deep stratum of the study area to provide a reference for understanding the mechanism of geothermal resources in Xiong'an new area.

GEOLOGICAL SETTING AND GEOTHERMAL BACKGROUND

The Xiong'an new area is located in the north of the Jizhong depression in the Bohai Bay Basin of the North China Craton (NCC), containing Rongcheng salient, Niutuozhen salient, Gaoyang low salient, etc., surrounded by Langgu sag, Xushui sag, Baxian sag, Baoding sag, and Raoyang sag (**Figure 1**). Most of the area is covered by three geothermal fields of Niutuozhen, Rongcheng, and Gaoyang, where there are abundant geothermal resources, most of which are exposed on the surface in the form of hot springs, and underground hot water is also found in drilling wells.

The Xiong'an new area is in the Bohai Bay Basin, a Meso-Cenozoic superficial rift basin in the eastern of the NCC which has undergone several tectonic movements since the Archean. From the extension and rift structure formed in the middle and late Proterozoic, the platform was uplifted and eroded as a whole, and a stable marine craton was formed in the early Paleozoic. In the Middle Carboniferous, the plate descended and developed marine continents with alternate deposits. Hercynian movement at the end of the Permian caused the disappearance of the Triassic in the basin. During the Mesozoic Yanshanian movement, strong intracontinental orogeny, basin formation, and magmatic-thermal processes developed, in addition to a series of large faults developed in NE, NNE, and EW directions. Taihang, Yanshan, and Jiaoliao mountains rose and exposed a lot of metamorphism bedrock. The magmatic activity in Mesozoic Yanshanian was the strongest sign of tectonic movement in the Jizhong depression (Li et al., 2017). The Niutuozhen salient in the study area began to develop and continued to uplift during the late Yanshanian movement, exposing the Mesoproterozoic strata, of which the Jurassic was completely denuded. Affected by the Paleogene Himalayan movement, strong fault tectonic movement occurred in the basin, forming a series of faults and uplifts (He and Zheng, 2016; Liang et al., 2016). Meanwhile, the Cenozoic Himalayan period was characterized by extremely extensive basalt eruption (Liu, 1992; Wang et al., 2012). The basin entered the depression stage, changing from stretching to compression and weaking fault activity during the Neogene.

Gravity and magnetic anomalies area combined at different depths, densities, and magnetic geological bodies, including local gravity and magnetic variations caused by deep faults and igneous rocks. Bouguer gravity with high anomaly reflects basement uplift, while low anomaly reflects basin and depression (Li et al., 2017). Magnetic exploration can determine the boundaries of magnetic geological bodies and structures, while local gravity and magnetic anomalies can usually be used to identify deep faults and igneous rock (Wu and Pan, 2005; Pamukcu et al., 2007). According to the statistics of Bouguer gravity anomaly and regional rock magnetism in Hebei Province (Li, 1999; Guo et al., 2001; Li et al., 2017; Yu et al., 2017; Shan, 2018), the positive and negative gravity anomalies correspond well with the shapes of the salient and sag and the orientation of the large faults, and the Archean-Paleoproterozoic deep metamorphic rocks in North China constitute the magnetic basement of this area, along with carbonate rocks and sand-mudstone which are generally non-magnetic and weak magnetism, respectively. The Quaternary strata, on the other hand, are more magnetic due to the local development of clays. And the Yanshanian igneous rock also has strong magnetism. It was found that there are two gently and moniliform rising positive magnetic anomalies in Xiongxian and on the east and west sides of Rongcheng (Yu et al., 2017), respectively, which indicates that igneous rocks are developed here.

Thus, the study area has developed metamorphic rocks of the Archean, marine carbonate rocks of the middle and late Proterozoic (Ch and Jx), to marine carbonate rocks of the middle Ordovician of Paleozoic (Pz), marine continent alternate facies clastic rocks intercalated with carbonate rocks of the Permian of Pz. Mesozoic (Mz) strata are locally developed, mainly mudstone and volcanic eruptive rocks, and Paleogene (E), Neogene (N), and Quaternary (Q) lacustrine and fluvial facies sandstone and mudstone from bottom to top. Among them, the sandstone of Minghuazhen formation and Guantao formation (N), the carbonate rock of the Gaoyuzhuang formation, and Wumishan formation (Jx) are favorable geothermal reservoirs. The karst heat storage in Wumishan formation has the characteristics of wide distribution, shallow burial, high temperature, large reserves, high water quality, and ease to recharge, which is the key development reservoir currently (Kong et al., 2015).

The thermal evolution of the NCC remained stable from the early Paleozoic to Mesozoic which has experienced two heat flow peaks since the Mesozoic (85 mW/m^2–88 mW/m^2), while the current heat flow is 60 mW/m^2–68 mW/m^2 (Qiu et al., 2016). The current geothermal gradient at a uniform depth of 0–3000 m is between 20.8°C/km–41.0°C/km, with an average of 31.6°C/km (Chang et al., 2016). The current heat flow is between 48.7–79.7 mW/m^2, and the geothermal gradient and heat flow gradually increase from west to east, with a good correspondence between their planar distribution (Qiu et al., 2016).

ANALYTICAL METHODS

Well Selection

Up to now, there have been few studies on the heat production of the sedimentary layers in the Jizhong depression of Bohai Bay Basin. Mostly, the heat production of 38 samples from 25 wells measured by Gong (2003) was used. Based on this, the measured heat production of 83 samples from 32 wells was added in a previous study (Cui et al., 2019). However, for the unsampled area, the relationship between natural gamma-ray logging and heat production still needs to be investigated to determine the heat production of the sedimentary layers in the whole study area. In this paper, the logging curves were collected from 20 representative wells in the central of the Jizhong depression, where the Xiong'an new area is located. The measurement interval is 0.125 m.

Calculation Principle of GR-A Empirical Relationship

Natural gamma-ray logging (GR) is one of the common radioactive geophysical logging methods, which records the intensity of the natural gamma-rays along the stratigraphy of the borehole wall. Rocks generally contain different amounts of radioactive elements and release radiation constantly. The principle of natural gamma-ray logging is to place a detector instrument into the well to receive the gamma-ray produced by the decay of radioactive elements (Brich, 1954; Rao et al., 2014). The detector can convert the gamma-ray into an electric pulse signal, and then the electric pulse signal is amplified by the amplifier and transmitted to the ground by a cable. The surface instrument converts the number of electric pulses formed per minute into a proportional potential difference for recording, which usually needs to be shaped by a discriminator to eliminate interference and distortion signals, and then to integrate them. Finally, natural gamma-ray logging data are obtained. The standard unit of natural gamma-ray logging well is API, and the curve is represented by GR. Because the sensitivity of the natural gamma-ray logging tool to U, Th, and K have a similar proportion to heat production coefficient, there must be a simple linear relationship between natural gamma-ray logging count and heat production within a specific borehole depth interval, which constitutes the theoretical basis for directly calculating rock heat production by using natural gamma-ray logging (Li, 2015). The measurement interval of natural gamma-ray logging is only 0.125 m, and the accuracy is guaranteed by the dense measuring points. The conversion accuracy of heat production is also higher, which can be on a decimeter level.

Rybach (1986) first proposed the linear relationship of GR-A based on the comparison between the measured heat production and the natural gamma-ray count, and the calculated equation is as follows:

$$A = 0.0145[GR(API) - 0.5] \quad (1)$$

Bucker and Rybach (1996) made further corrections to the linear relationship of GR-A based on a large number of measured data of borehole cores and fitting by the least square's method. This is also the most widely used empirical relationship at present (Bucker et al., 2001; Norden and Forster, 2006), and the calculated equation is as follows:

$$A = 0.0158[GR(API) - 0.8] \quad (2)$$

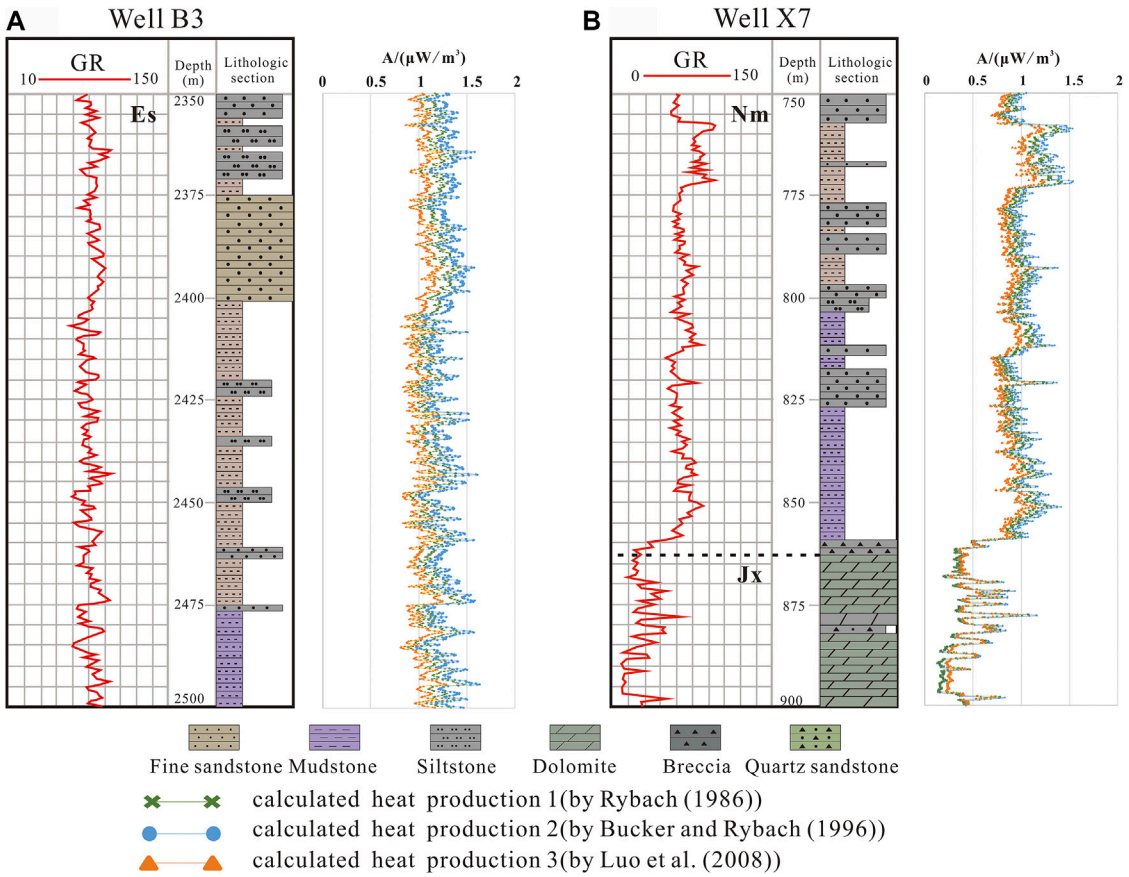

FIGURE 2 | The curves of GR logging and calculated heat production of **(A)** Wells B3 and **(B)** Well X7. The green line in **Figure 2** is the heat production of the sedimentary layer calculated according to **Eq. 1** by Rybach (1986); the blue line is the heat production of sedimentary layer calculated according to **Eq. 2** by Bucker and Rybach (1996); the orange line is the heat production of sedimentary layer calculated according to **Eq. 3** by Luo et al. (2008).

Luo et al. (2008) established a new linear relationship of GR-A based on the correlation analysis of natural radioactivity logging (natural gamma-ray and natural gamma spectroscopy) and measured heat production from the main borehole of China Continental Scientific Drilling (CCSD) at 100–5000 m, and the calculated equation is as following:

$$A = 0.0115[GR(API)+9.1] \quad (3)$$

RESULT

GR-A Calculation Results

Three empirical equations were used to calculate the heat production of these 18 wells. **Figure 2** shows the heat production curves of wells B3 and X7 calculated by three methods. It can be seen that the trends of the three calculation results are consistent; the heat production calculated by Bucker and Rybach is higher, and the differences in heat production obtained by the three calculation methods are greater in the stratum with higher GR values. The dolomite stratum with lower GR values and the sandstone and mudstone stratum with higher GR value in well X7 are in good agreement with the calculation results.

The author extracted 1/40 of the logging curves of these typical wells, that is, one natural gamma-ray logging value was taken every 5 m and recorded as a sedimentary layer. The above empirical relationships were used to calculate, respectively, the heat production of 5,504 sedimentary layers in 20 wells was calculated, and classified according to lithology (**Table 1** and **Figure 3**). It can be seen from the statistical results in **Table 1** that the heat production calculated by **Eq. 2** is the highest, followed by **Eqs. 1** and **3**. The heat production of sandstone is generally slightly lower than that of mudstone, and that of dolomite is generally lower than that of limestone. In **Eq. 1**, mudstone and sandstone are mainly distributed in 0.5–1.5 $\mu W/m^3$, respectively; limestone and dolomite are mainly distributed in 0–1 $\mu W/m^3$ and 0–0.5 $\mu W/m^3$, respectively. In **Eq. 2**, mudstone and sandstone are mainly distributed in 1–2 $\mu W/m^3$ and 0.5–1.5 $\mu W/m^3$, respectively; limestone and dolomite are mainly distributed in 0–1 $\mu W/m^3$ and 0–0.5 $\mu W/m^3$, respectively. In **Eq. 3**, mudstone and sandstone are mainly distributed in 0.5–1.5 $\mu W/m^3$, respectively; limestone and dolomite are mainly distributed in 0–1 $\mu W/m^3$ and 0–0.5 $\mu W/m^3$, respectively.

TABLE 1 | Comparison and statistics of calculated radioactive heat production of different lithologies using different empirical relationships and measured heat production.

Lithology		A (μM/m^3) by Rybach (1986)	A (μM/m^3) by Bucker and Rybach (1996)	A (μM/m^3) by Luo et al. (2008)	A (μM/m^3) test by Cui et al. (2019)	A (μM/m^3) test by Gong (2003)
Mudstone	Distribution	0.393–2.58	0.423–2.807	0.422–2.157	0.573–2.863	0.890–1.980
	mean (N)	1.241 (3,629)	1.348 (3,629)	1.095 (3,629)	1.586 (6)	1.491 (29)
	standard deviation	0.303	0.330	0.240	0.922	0.249
Sandstone	Distribution	0.246–2.615	0.263–2.845	0.306–2.184	0.822–2.106	0.980–1.580
	mean (N)	1.07 (1,453)	1.162 (1,453)	0.959 (1,453)	1.401 (15)	1.268 (8)
	standard deviation	0.334	0.364	0.265	0.348	0.175
Limestone	Distribution	0.078–1.951	0.079–2.121	0.172–1.658	— —	— —
	mean (N)	0.467 (248)	0.504 (248)	0.481 (248)		1.090 (1)
	standard deviation	0.352	0.383	0.279		— —
Dolomite	distribution	0.057–1.704	0.058–1.852	0.156–1.462	0.043–2.724	— —
	mean (N)	0.307 (174)	0.330 (174)	0.354 (174)	0.321 (42)	
	standard deviation	0.321	0.349	0.254	0.460	

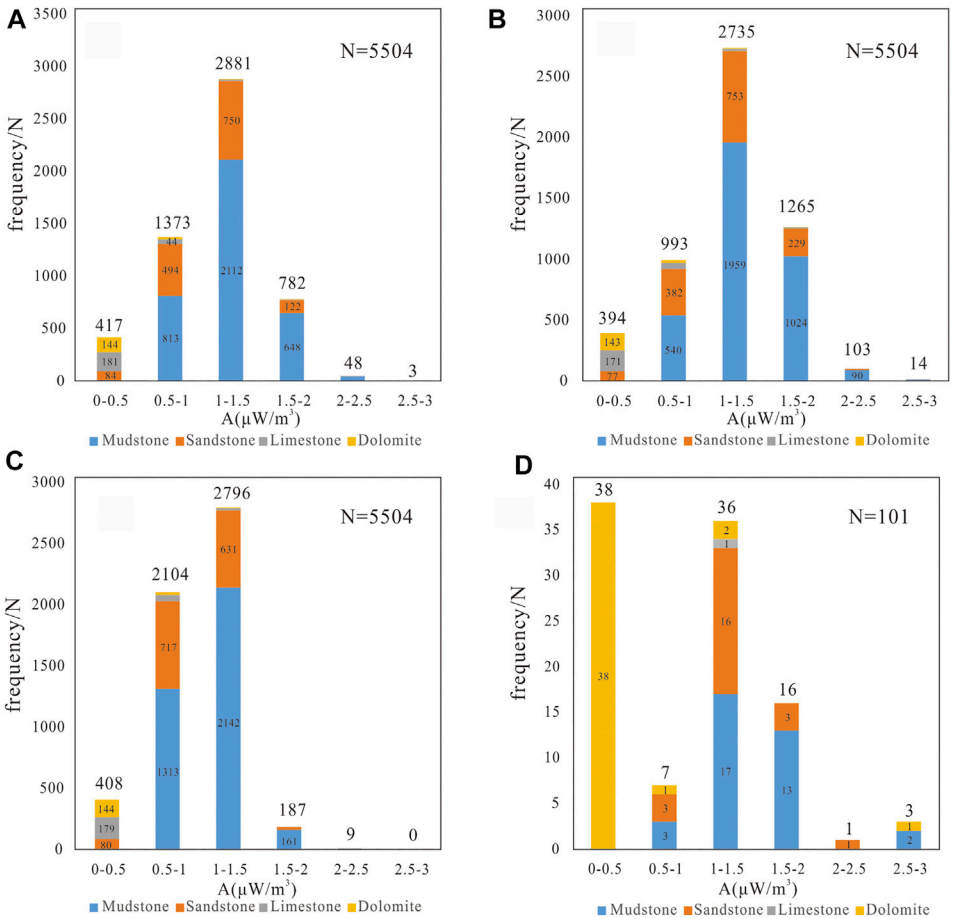

FIGURE 3 | Statistic frequency histogram of sedimentary calculated heat production using GR-A empirical relationships and measured heat production in Xiong'an new area. **(A)** is calculated heat production using empirical relationship by Rybach (1986); **(B)** is calculated heat production using empirical relationship by Bucker and Rybach (1996); **(C)** is calculated heat production using empirical relationship by Luo et al. (2008); **(D)** was measured heat production by Gong (2003) and Cui et al. (2019).

In order to establish a framework for heat production in the sedimentary layers of Xiong'an new area, the GR-A empirical relationship should be used for conversion and statistics for areas and layers with no or less sampling. Comparing the average heat production of different lithology obtained from these three empirical relationships with the measured average value

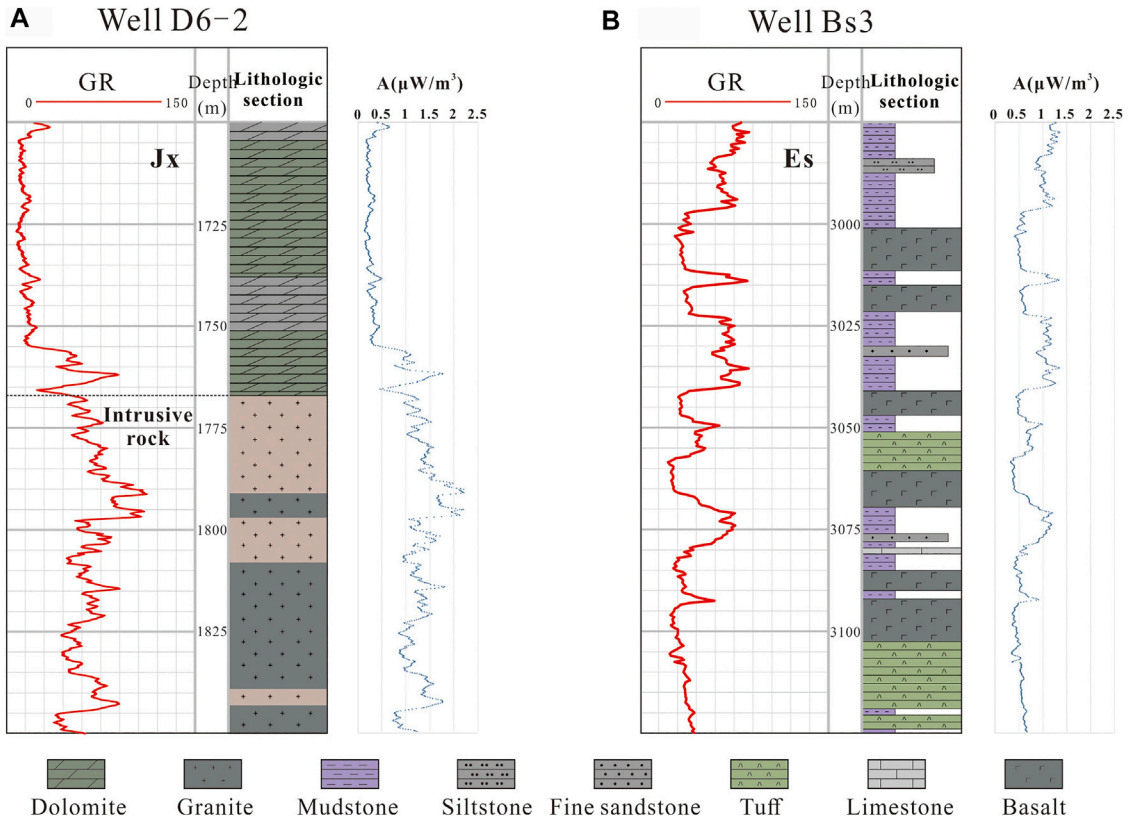

FIGURE 4 | The curves of GR logging and calculated heat production rate of **(A)** Wells D6-2 and **(B)** Well Bs3.

(**Table 1**) (Gong, 2003; Cui et al., 2019), it is found that the result calculated by **Eq. 2** is more consistent with the measured value.

At the same time, these two wells are also the locations where the previously measured heat production samples are. Among them, mudstone samples were taken at 2415 m depth of well B3, and the measured heat production is 1.42 μW/m^3, the calculated heat production is 1.25, 1.36, and 1.10 μW/m^3 by using the three equations, respectively; mudstone and siltstone samples were taken from 778 to 806 m depths of X7 well, and the measured heat production is 0.65, and 1.32 μW/m^3, respectively, the calculated heat production of the two places are 0.62, 0.67, 0.61 μW/m^3 and 1.15, 1.24, 1.02 μW/m^3, respectively, according to the three equations. It can be seen that **Eq. 2** is most suitable for the calculated heat production in Xiong'an new area, and the deviation is also within a reasonable range.

The Heat Production of Igneous Rock

Therefore, for the unsampled igneous rocks, 20 wells that encountered igneous rocks in Langgu sag Baxian sag were selected in this study, and the most applicable **Eq. 2** was used to calculate the heat production. Well D6-2, which encountered Yanshanian granite, and Well Bs3, which encountered Cenozoic diabase and basalt, were chosen to plot the natural gamma-ray logging and calculated heat production curves (**Figure 4**). Also, heat production value was taken at 2 m intervals and heat production scatter plots were drawn for the igneous rocks encountered in these 20 wells (**Figure 5**). The results showed that the heat production of basalt is between 0.3 and 0.7 μW/m^3, the tuff heat production is between 0.3 and 0.6 μW/m^3, the diabase heat production is between 0.4 and 0.6 μW/m^3, and the granite heat production is between 0.6 and 1.5 μW/m^3.

According to the analysis and calculation of the composition of igneous rock in different periods, it is found that the Cenozoic igneous rocks are mainly basic eruption rocks and shallow intrusion rocks. The heat production ranges from to 0.88 μW/m^3, with an average value of 0.55 μW/m^3. The Yanshanian igneous rocks are mainly intermediate-acid plutonic intrusion rocks, with a heat production ranging from 1.08 to 2.21 μW/m^3, with an average value of 1.64 μW/m^3. The basalt and orbit samples measured in the previous are inferred to be igneous rock samples developed in the late Lvliang period (during 1.65 to 1.8 Ga) based on previous studies (Cui et al., 2019), with heat production of 0.94 and 1.17 μW/m^3, respectively.

Distribution of Igneous Rocks

Combined with drilling data, it is found that the Mesozoic igneous rocks are mainly developed on Niutuozhen and Rongcheng salients which are mainly moniliform distribution along deep and large faults in this area, which is one of the signs of active movement in Yanshanian. This means that acid intrusive rock granodiorite developed in the south of Niutuozhen salient with a length of 3–13 km and a buried depth of 2.2–3.5 km,

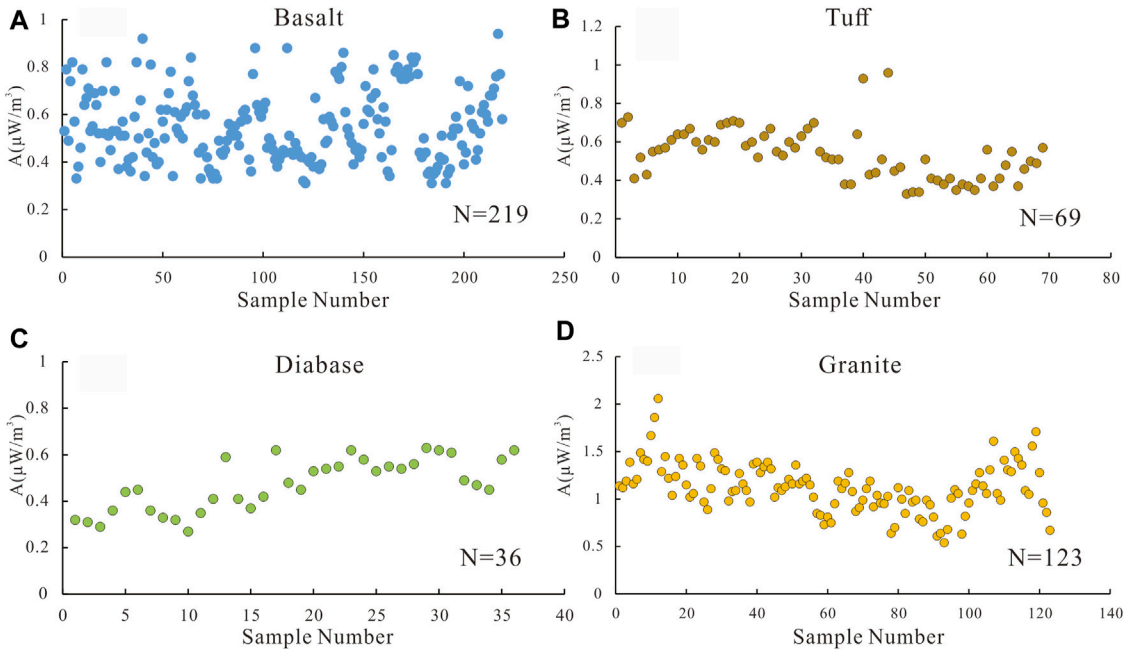

FIGURE 5 | Scatter plot of calculated heat production of different kinds of igneous rocks. **(A)** Basalt; **(B)** Tuff; **(C)** Diabase; **(D)** Granite.

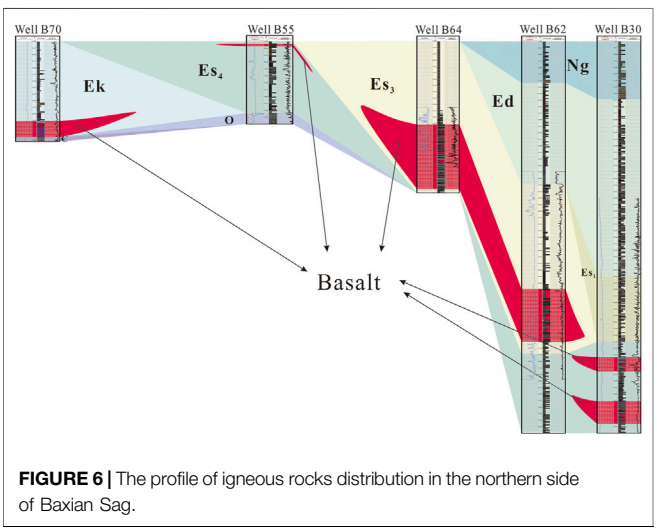

FIGURE 6 | The profile of igneous rocks distribution in the northern side of Baxian Sag.

moniliform intermediate-acid intrusive rock diorite developed on the west side of Rongcheng salient, and moniliform acid intrusive rock granite developed on the northeast side of Niutuozhen salient and its middle part between Rongcheng salient with all a length of 3–6 km and a buried depth of 3–6 km (**Figure 7**) (Li et al., 2017).

Cenozoic igneous rocks are mainly distributed in Baxian and Langgu sags. At the beginning of sag formation, the fault activity was strong, and the magmatic activity was roughly dominated by large-scale intrusion along the beds and underwater eruption along the fault. In the profile of northern Baxian sag (well B70, B55, B64, B62, and B30, the profile position shown in **Figure 1**), it is found that basalt is mainly developed in the lower part of the third stage of Shahejie formation, the upper part of the fourth stage of Shahejie formation, and the bottom of Kongdian formation (**Figure 6**). The sedimentary rocks contacting the overlying and underlying stratum are mainly mudstone and siltstone. In the connecting well profile, the thickness of basalt in the fourth stage of Shahejie formation is nonuniform, and the thickness is only 13 m in well B55 but 51 m in well B30.

According to the statistics of igneous rock data of 97 wells in Baxian sag, it is found that several stages of magmatic activity occurred in the Cenozoic Paleogene, and the lithologies are mainly basalt, diabase, and tuff, mainly developed in Es_3 and Es_4. The distribution of igneous rocks is relatively continuous, while the thickness is uneven, and the thickest can be as high as 490 m (**Figure 7**).

DISCUSSION

Influence of Igneous Intrusions on Surrounding Rocks

Magmatic activity is closely related to tectonic activity and is controlled by deep faults. It is of great significance to study the formation, thermal evolution, and current geothermal state of the basin (Jin et al., 2012; Chang and Liu, 2018). In a volcanically active tectonic area, we need to consider the influence of magma pocket on stratigraphy before the onset of the magmatic activity, the influence of magma eruption on the overlying stratum, the influence of magmatic intrusion on the surrounding rock, and the influence of magma cooling on the stratum. The thermal effects of magma intrusion have been studied by different scholars at home

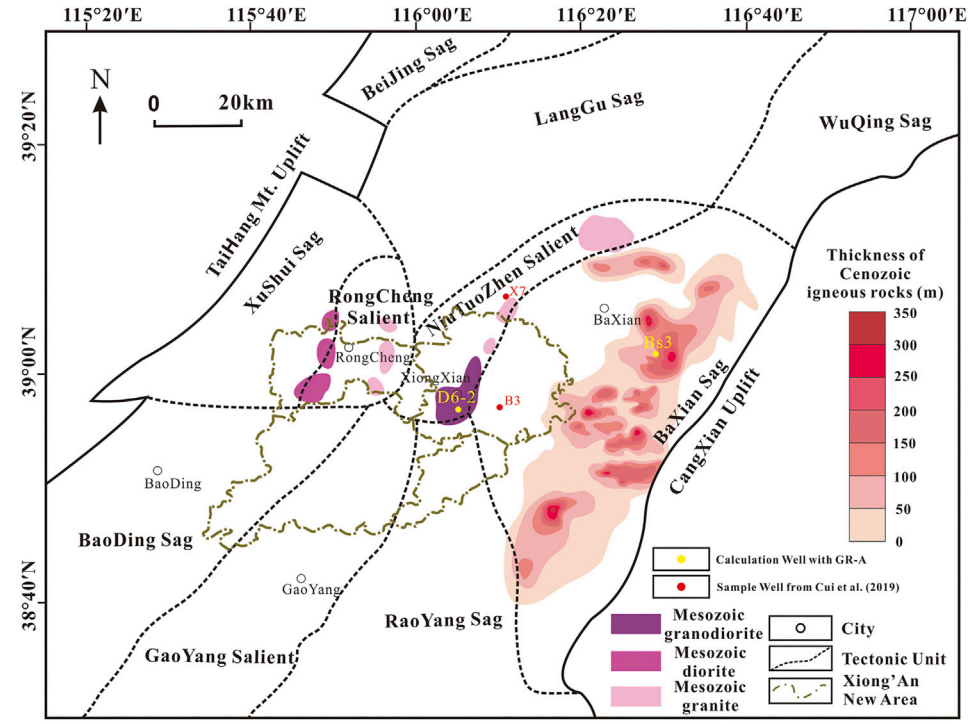

FIGURE 7 | Spatiotemporal distribution of igneous rocks in Xiong'an new area and the thickness of igneous rock in Baxian sag.

and abroad (Mundry, 1970; Liu et al., 2018). It is shown that the degree of influence of magmatic intrusions depends on the time of intrusion, the size and geometry, and the lithology of intrusive bodies. Also, it is related to the physical properties of surrounding rocks.

Basic Equation, Model, and Parameter Selection of Heat Conduction

The high-temperature deep subsurface molten material rises along structurally vulnerable zones to the upper crust or the surface, forming magmatic activity which will provide a local heat source to the sedimentary basin. After magmatic intrusion, the heat transfer mode is mainly heat conduction. The finite element method is one of the commonly used numerical simulation methods to solve the heat conduction equation, and it can be used to evaluate the influence of high-temperature magmatic intrusion on the surface temperature field (Zhang et al., 1982; Bonneville and Capolsini, 1999; Tang et al., 2013). Its essence is to discretize the continuous temperature field in the calculation area into a finite number of temperature points and then solve the value of these temperature points through a given series of conditions to approximate the actual temperature field changes.

Since the actual magmatic intrusion and surrounding rock changes after the intrusion are a series of complex geological processes, this study assumes that the magmatic intrusion occurs instantaneously and the heat transfer method is heat conduction. The heat conduction equation for calculating the influence of the magma intrusion is as follows:

$$\rho C_p \frac{\partial T}{\partial t} + \nabla(-K\nabla T) = Q \tag{4}$$

where ρ is rock density kg/m^3, C_p is the specific heat capacity of rock under normal pressure J/(kgK), T is temperature ˚C, t is time s, K is rock thermal conductivity W/(mK), and Q is rock heat production μW/m^3.

The upper boundary temperature of this study is the surface temperature of 15˚C; the bottom boundary temperature only considers the influence of the intrusive body, ignoring the local high thermal background when the intrusion body is formed; the left and right boundaries are set as adiabatic boundaries.

The establishment of the model is based on the distribution of igneous rocks in different periods as previously mentioned, with a certain degree of simplification. The Yanshanian intrusion rock was mainly distributed in the Niutuozhen and Rongcheng alient in the form of moniliform. The Cenozoic intrusion rock was mainly distributed in the Langgu and Baxian sags in the form of rock covers. And these simplified models were shown in **Figure 8**.

The profile of the Mesozoic late Yanshanian intrusion (model a) simplifies the stratigraphic style of Langgu sag, Niutuozhen salient, and Baxian sag, with Cenozoic sandstone strata at the top and middle and upper Proterozoic carbonate stratum at the bottom. The length of the profile is 50 km, with the total stratigraphic thickness of 10 km, the thickness of the Cenozoic stratum in the two sags of 6 km, and the thickness of the Cenozoic stratum in the salient of 1.5 km. The intrusions are defined as granite, which is elliptical in profile, with a major axis length of

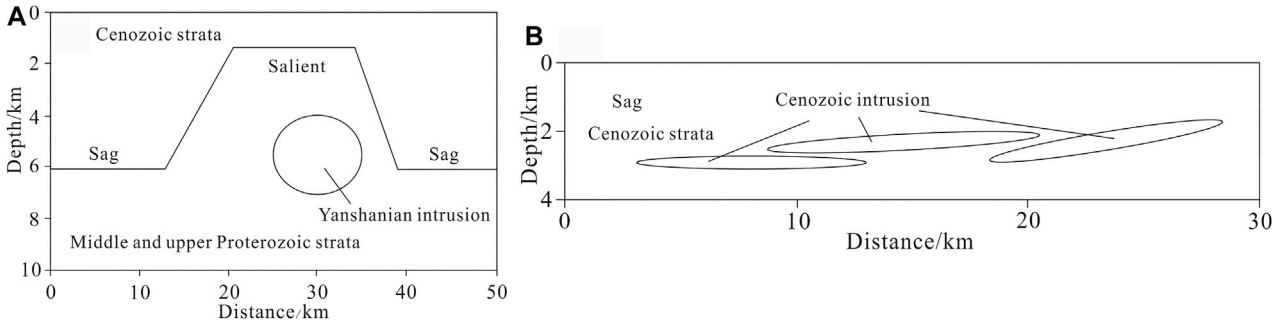

FIGURE 8 | Simplified intrusions and strata of **(A)** Yanshanian and **(B)** Cenozoic.

TABLE 2 | Simulation parameters.

Model (a)	Parameter	Value	Model (b)	Parameter	Value
Yanshanian intrusions	Initial temperature	900 °C	Cenozoic intrusions	Initial temperature	1,000 °C
	Density	2,800 kg/m^3		Density	3,000 kg/m^3
	Thermal conductivity	2.6 W/(m·K)		Thermal conductivity	2.5 W/(m·K)
	Specific heat capacity	787.1 J/(kg·K)		Specific heat capacity	787.1 J/(kg·K)
	Heat production	3 μW/m^3		Heat production	0.5 μW/m^3
Cenozoic stratum	Density	2,650 kg/m^3	Cenozoic stratum	Density	2,650 kg/m^3
	Thermal conductivity	2.01 W/(m·K)		Thermal conductivity	2.01 W/(m·K)
	Specific heat capacity	787.1 J/(kg·K)		Specific heat capacity	787.1 J/(kg·K)
Middle-Upper Proterozoic Stratum	Density	2,840 kg/m^3	-		
	Thermal conductivity	5.16 W/(m·K)			
	Specific heat capacity	787.1 J/(kg·K)			
Top boundary temperature		14°C	Top boundary temperature		14°C
Bottom boundary temperature		200°C	Bottom boundary temperature		120°C

5 km and a minor axis length of 1.5 km, that is, the intrusion is 10 km long and 3 km thick (**Figure 8A**). The profile of the Cenozoic intrusion (model b) simplifies the stratigraphic style of Baxian sag, and the simplified models are all Cenozoic sandstone stratum due to most of the Cenozoic intrusions being bedding intrusion with a large intrusion area but small thickness, and the surrounding rocks being Paleogene sandstone and mudstone. The profile length is 30 km with a total stratigraphic thickness of 4 km. The intrusions are defined as diabase, with lengths of 10, 12, and 10 km on the profile, and thicknesses of 0.4, 0.4, and 0.5 km, respectively (**Figure 8B**).

Because the temperature of magma varies with its composition, the Yanshanian mainly occurred in granite intrusion, and the Cenozoic mainly occurred in diabase. The parameter settings are shown in **Table 2**, and some of the parameters are based on previous research (Zhang and Shi, 1997; Gong, 2014).

Two-Stage Intrusions Influence on Surrounding Rocks

After the magmatic intrusion, its temperature decreases rapidly without the influence of external heat sources, and the temperature of its surrounding rock changes. At 0.01 Ma after the magmatic intrusion, the temperature of the surrounding rock rises rapidly due to the high-temperature baking effect of magma. With time, by 0.02, 0.05, or even 0.1 Ma, the temperature of the magma decreases rapidly, and the surrounding rock affected by the temperature of the magma also starts to decrease slowly. And the temperature of the surrounding rocks farther away from the intrusion rise and decrease more slowly than that of the surrounding rock closer to the intrusion (**Figure 9A**). At the time of 0.2 Ma, the residual heat of the intrusion gradually dissipated, and it gradually reaches a state of thermal equilibrium with the surrounding rock, until the 0.5 Ma temperature field finally reached equilibrium. After equilibrium, the temperature of the stratum is affected by various aspects such as structural configuration, thermal conductivity, and the ratio of the different stratum. The thermal conductivity of Cenozoic sandstone stratum is low with a thinner thickness in salient and thicker in sag. The thermal conductivity of the middle and upper Proterozoic carbonate stratum is relatively high with obviously thicker thickness in the salient. Therefore, under this influence, the temperature converges to the high thermal conductivity at the same depth, that is, in the upper part of salient the isotherm is a convex curve, consistent with the base undulation, while the lower part of the salient is a concave curve, opposite to the basement undulation. In the vicinity of the intrusion, the temperature profile changes slightly due to the influence of the intrusion shape and thermophysical properties, and there is a small bump in the temperature profile near the intruder.

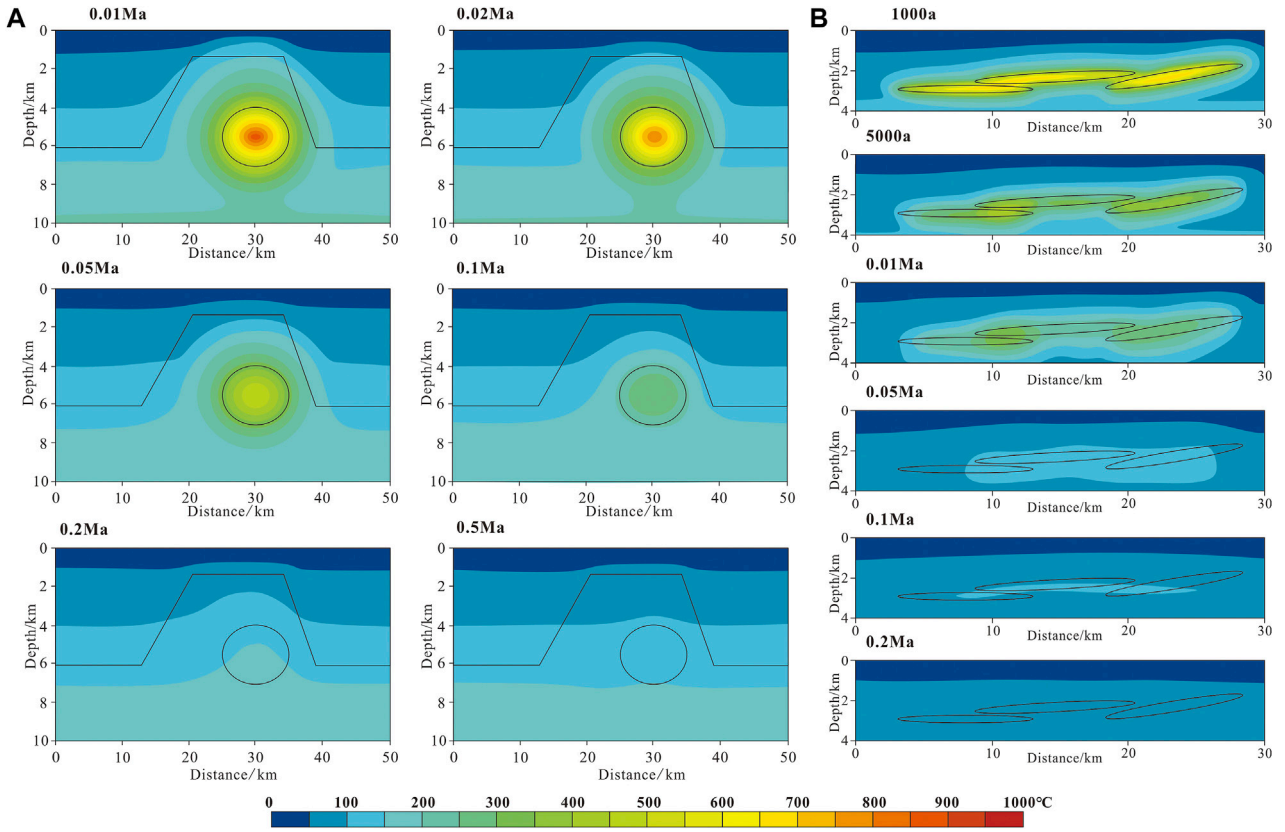

FIGURE 9 | Thermal effects of **(A)** Yanshanian intrusions and **(B)** Cenozoic intrusions on surrounding rocks.

Compared with Yanshanian, the temperature of the Cenozoic magmatic intrusion drops more rapidly after intruding into the stratum. It reaches the same temperature at 0.1 Ma and reaches a steady-state at 0.2 Ma. The range of temperature change of the surrounding rock is also smaller due to magmatic intrusion (**Figure 9B**). After reaching the steady-state, the isotherm will also change due to the difference in thermophysical properties between the intrusion and the strata. However, the thickness of the intrusion body is too small, so there is almost no change in the temperature profile.

Summarizing the previous research and combining the experimental results of the thermal simulation, it can be found that the larger the intrusion, the larger the influence range of the residual heat and the longer the time; the closer the intrusion is, the more likely the residual heat effect is on the current temperature field (Mundry, 1970). Based on the results of this paper, it can be concluded that the thermal effect of residual heat on the current temperature is not obvious for either the large granite intrusion in late Yanshanian or a recent Cenozoic diabase intrusion. It is negligible that the residual heat produced by tectonic thermal movement, i.e., magmatism, does not have a significant effect on the current temperature field when discussing the subsequent heat source mechanism.

In addition, the organic maturity Ro is mainly controlled by temperature. According to the collected Ro data, the Ro and depth distribution of Wells C5 and S401 were drawn (**Figure 10**). The locations of these two wells are shown in **Figure 1**. It can be seen that after the intrusion of the igneous rock, a peak of Ro appears, which shows that after the intrusion intrudes into the stratum, the scope of the residual thermal influence is relatively small. Combined with the results of the thermal simulation, it can be seen that after Mesozoic and Cenozoic igneous rocks intrude into the stratum, the residual heat is lost extremely quickly, and the influence range is small; the residual heat effect hardly affects the current geothermal field.

The Influence of Igneous Rock Facies on Current Heat Flow

Due to the intrusion and eruption of magma, the stratum thermophysical properties will change in the local area. The influence of the igneous rock on the thermal conductivity after cooling has been discussed earlier, and it has been found that its influence is almost negligible. The influence of rock radioactive heat production is related to the shape and size of the igneous rock and the heat production of the surrounding rock.

The heat production contribution of the sedimentary layer can be obtained according to the following equation:

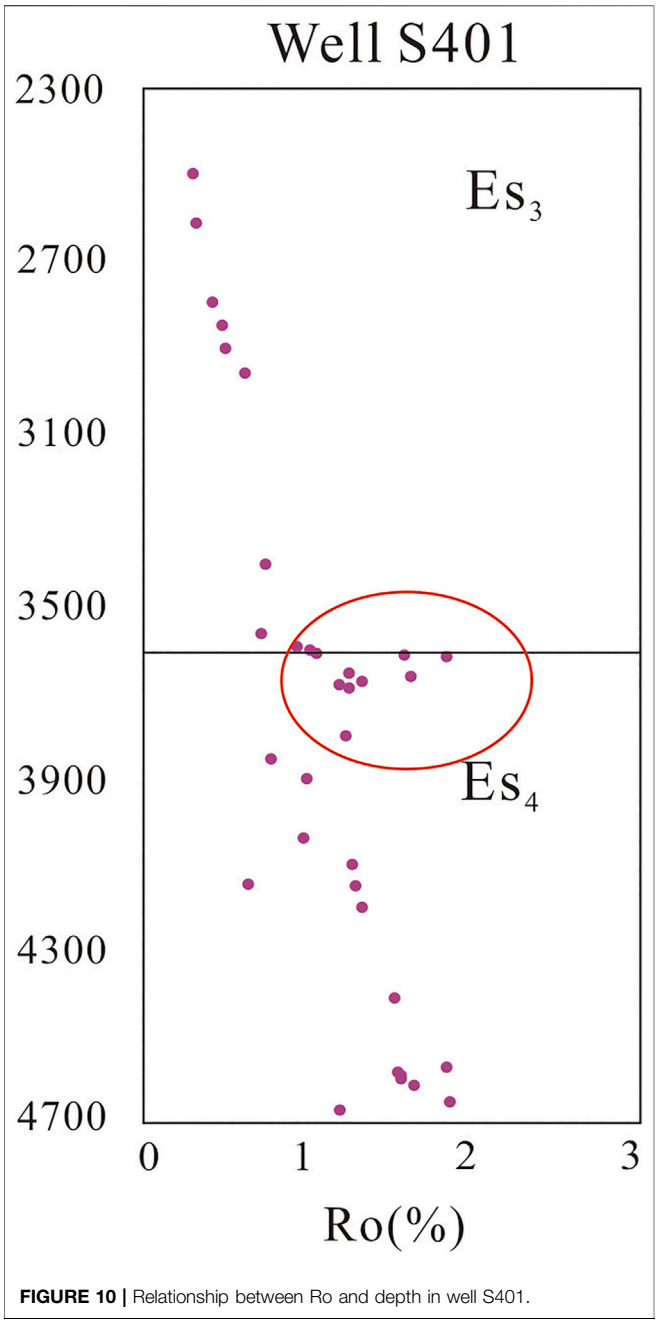

FIGURE 10 | Relationship between Ro and depth in well S401.

$$q_c = \sum A_i \times D_i \quad (5)$$

where q_c is crust heat flow, mW/m^2; A_i is the radioactive heat production of layer i, μW/m^3; and D_i is the thickness of layer i, km.

To calculate the thermal effect of igneous facies, we only need to get the difference of thermal contribution between igneous facies and sedimentary layer with the same thickness.

The Yanshanian igneous rocks are mainly distributed in the Niutuozhen and Rongcheng salients, and the intruded stratum are middle and upper Proterozoic carbonate stratum. With a thickness of 3 km, its heat production contribution is about 4.92 mW/m^2, while the middle and upper Proterozoic stratum with the same thickness contributes 1.38 mW/m^2. It can be seen that the Yanshanian igneous rock intrusions increased the heat flow value of Niutuozhen and Rongcheng salients to a certain extent, about 3.55 mW/m^2, which is difficult to ignore (**Figure 11A**).

The Cenozoic igneous rocks are dominated by large area bedding intrusions and overflow eruptions, which are relatively thin and were developed in the Shahejie formation. With a thickness of 0.5 km, its heat production contribution is about 0.275 mW/m^2, while that of the Shahejie formation of the same thickness is 0.58 mW/m^2. It can be inferred that the Cenozoic igneous rock has reduced the heat flow in the sag to a certain extent by about 0.225 mW/m^2, but most of the igneous rocks have a thickness of fewer than 0.5 km, which has a smaller difference in heat production of the Shahejie formation of the same thickness, where the difference is almost negligible (**Figure 11B**).

The difference in heat production affects the terrestrial heat flow to some extent, while thermal conductivity has almost no effect. Corresponding the distribution of igneous rock to the heat flow, it can be found that the terrestrial heat flow is higher in the areas where Mesozoic igneous rocks are developed, i.e., the southern of Niutuozhen salient and the Rongcheng salient, while the Langgu and Baxian sags in areas where Cenozoic igneous rocks are developed are not caused by igneous rocks, although the values tend to be low.

The Genetic Model of Heat Source

Previous studies believe that the Bohai Bay Basin experienced five thermal evolution stages during the Mesozoic-Cenozoic, with differences in the thermal evolution of each tectonic unit (Zuo et al., 2013). The thermal evolution history of the Jizhong depression from the Triassic to Jurassic is a stable stage of heat flow upward, starting from 43 to 60 mW/m^2, influenced by the subduction of the Pacific plate to the NCC starting at 200 Ma (Windley et al., 2011; Kusky et al., 2014), with convection in the mantle, upwelling of asthenosphere material, and a slow rise in heat flow. From the Early Cretaceous to the Late Cretaceous, the first phase of heat flow peaked at 87 mW/m^2, during which strong tectonic deformation movements occurred, the eastern part of the NCC was damaged, the asthenosphere was upwelled, and magmatic activity was significantly enhanced. From the late Cretaceous to the end of Cretaceous, the heat flow declined rapidly to 68 mW/m^2, and the basin transitioned from a compressive stress environment to a Paleogene tensile stress environment. Until the Eocene to Oligocene, the heat flow increased again and reached the peak of the second phase of heat flow (80 mW/m^2). Under the influence of tension, the lithosphere thinned again and magma erupted upwelling. Since the Neogene, tectonic activities gradually disappeared, the contribution of deep heat sources has decreased, and the paleo heat flow has declined to about 60 mW/m^2.

According to previous studies (Hyndman et al., 1968; Lachenbruch, 1970; Lachenbruch and Sass, 1977), the Moho surface temperature of the Australian shield is 420°C and that of the stable area in the eastern United States is 660°C, while the

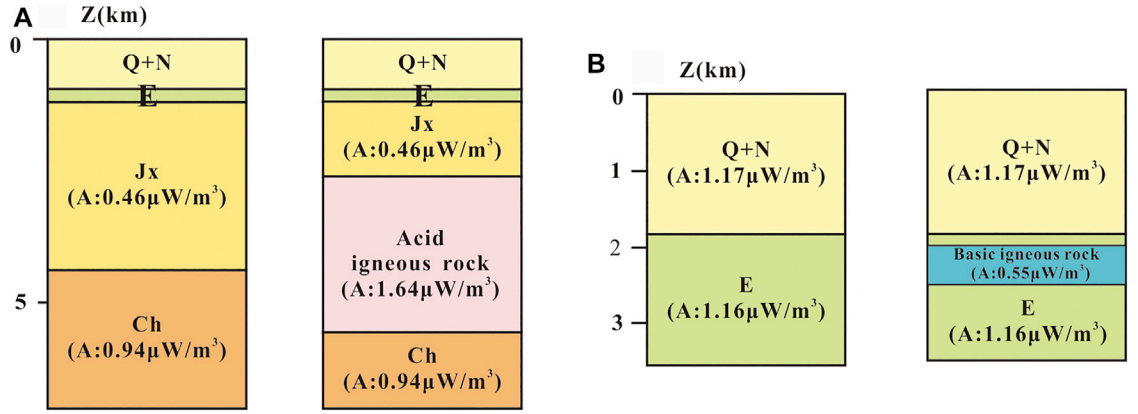

FIGURE 11 | Schematic diagram of heat production difference under the influence of igneous facies, the heat production data was after by Cui et al. (2019). **(A)** Yanshanian intrusions; **(B)** Cenozoic intrusions.

Moho surface temperature in the tectonically active zone of the Cenozoic mountains in the western United States can be as high as 1,000°C or more, and the Moho surface temperature in the Xiongan New Area is 500–600°C (Cui et al., 2020). It can be found that after the Neogene, the Jizhong depression gradually transformed into a tectonic stable area, in which the thermal state also declined from the peak state in the Paleogene, and the paleo heat flow has little impact on the temperature field of the current study area. However, due to the deposition of huge and thick Neogene and Quaternary deposited with low thermal conductivity, the study area is subject to a certain degree of thermal insulation. Since the previous lithosphere thinning, the heat flow can be more easily conducted to the shallow crust, which is also the background of the formation of obvious geothermal anomalies in the study area.

The main contents of heat source origin include the radioactive heat production by the decay of U, Th, ^{40}K, and other radioactive elements in crustal rocks (i.e., crustal heat flow), the heat from the mantle (i.e., mantle heat flow), and the heat generated by tectonic thermal movement cooling (magmatism). The heat generated by tectonic thermal movement cooling has been discussed previously. The contribution of crustal heat flow and mantle heat flow is still the main contributor of terrestrial heat flow in the study area and even the Bohai Bay Basin.

The crustal heat flow is generated by the accumulation of heat production in the sedimentary layer and the upper, middle, and lower crust, the surface of that determined by the distribution of seismic wave velocity. According to the crust-mantle velocity structure diagram of the Jizhong depression (**Figure 12A**) (Ma et al., 1991), the thickness distribution is found to be different in the horizontal direction, and the range of seismic wave velocity varies in different tectonic zones. The author corresponds the profile to the terrestrial and mantle heat flow in the Bohai Bay Basin calculated previously (Cui et al., 2019) and finds that the heat flow provided by the mantle accounts for a relatively large portion of the terrestrial heat flow (**Figure 12A**). According to the distribution of the crust-mantle heat flow, Wang et al. (1996) proposed the concepts of "cold crust-hot mantle" and "hot crust-cold mantle" to explain the thermal structure of the basin. When the heat flow in the crust exceeds 50%, the crust is considered to be relatively "hot," while the mantle is relatively "cold," which is the "hot crust-cold mantle." On the contrary, it is a "cold crust-hot mantle." It is a typical "cold crust-thermal mantle" geothermal background in Bohai Bay Basin, in which the more eastward to Jiyang depression, the more obvious this thermal structure is.

The seismic wave velocity of the upper crust, middle crust, and lower crust in the Jizhong depression ranges from 2.0 to 6.1 km/s, 6.1 to 6.3 km/s, and 6.5 to 7.2 km/s, respectively. The differences in the thickness of the upper, middle, and lower crust in Jizhong depression, laterally, correspond well to the salient and sag in the depression. In the case of small differences in mantle heat flow variation, the terrestrial heat flow in salient is significantly higher than that in sag. **Figure 12B** shows a schematic diagram of the geothermal resource genesis in the AA section within the Jizhong depression, and the location of that was shown in **Figure 1**. The gray line indicates the geothermal heat flow collected by literature (Gong, 2003; Jiang et al., 2019), and the red one indicates the simulated geothermal heat flow (Cui et al., 2019), while the remaining two blue lines are the temperature profiles at a depth of 1 and 3 km underground, respectively. The good correspondence between geothermal heat flow and basement relief illustrates the difference in geothermal heat flow caused by the rationing of sediment layer and crustal thickness. The mantle heat flow ranges from 30 to 35 mW/m^2, and the terrestrial heat flow ranges from 56 to 60.1 mW/m^2, with a calculated crust-mantle heat flow ratio ranging from 0.6 to 0.88, which is a typical "cold crust-hot mantle" type thermal structure. In addition, several deep and large fractures developed in the study area not only control the deposition of the strata but also provide good channels for groundwater transport. Cold piedmont water from Taihang and Yanshan Mountains infiltrates through the surface and migrates along with the pores and fractures in the sedimentary layer, and is gradually heated by the stratum during this process. Heated by the heat from the deep crust rapidly, as the heat carrier, there is groundwater convection with the shallow

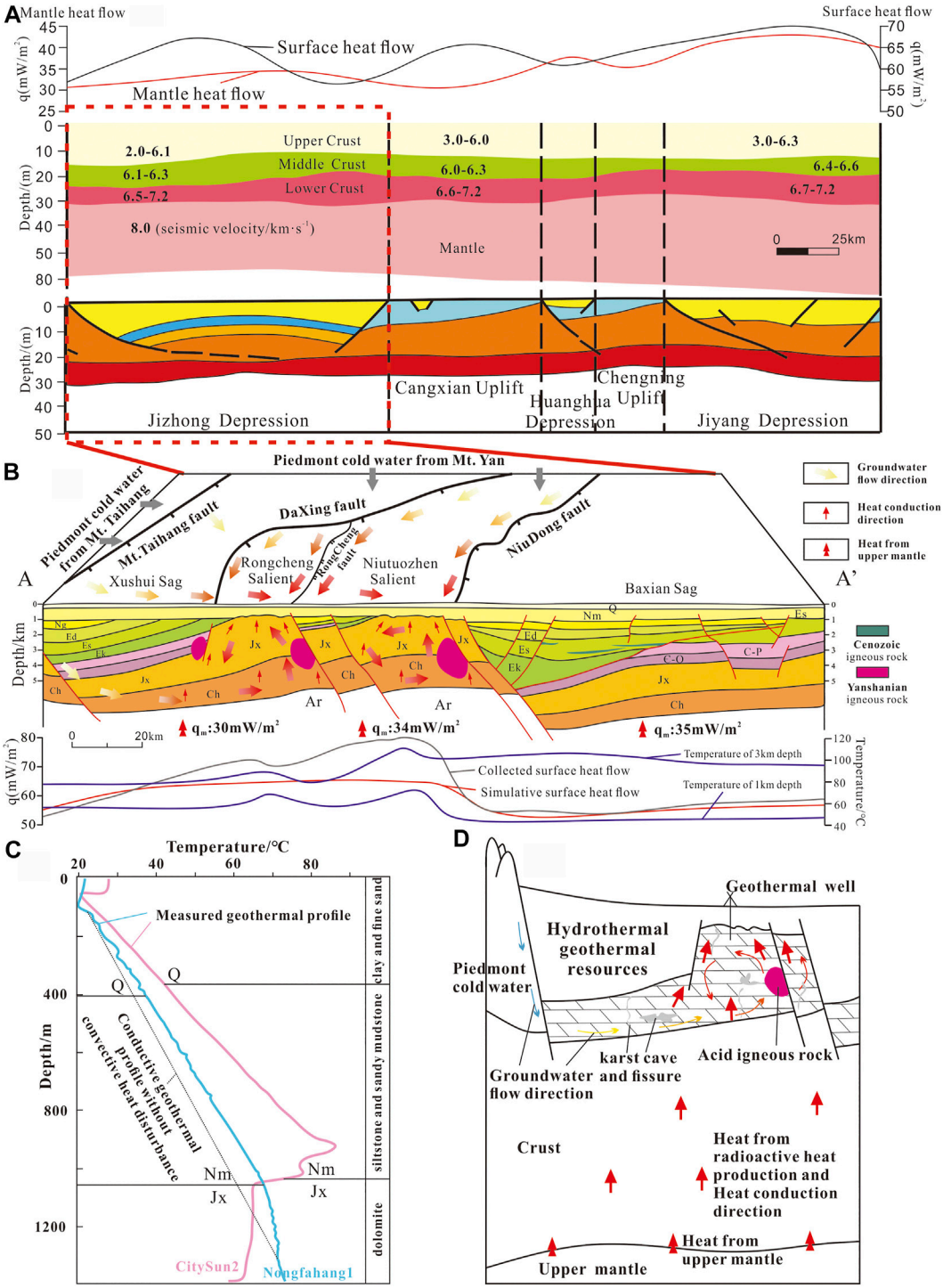

FIGURE 12 | Aggregative model of the heat source genesis in Xiong'an new area. **(A)** Crust mantle velocity structure and mantle terrestrial heat flow through Jizhong depression after Ma et al. (1991) and Xu (2017); **(B)** Genesis of conduction-convection geothermal resources of AA′ section in Jizhong depression; **(C)** Well temperature diagram affected by heat convection after by Wang et al. (2019); **(D)** Genetic model of geothermal resources in Xiong'an new area.

stratum groundwater along the fracture zone under the influence of deep faults, and is stored in the sandstone reservoir of Paleogene and the carbonate reservoir of Wumishan formation, forming a thermal anomaly area, namely a geothermal field. The difference between the simulated calculation (the red line) and the measured value (the grey line) confirms the influence of groundwater activities on the geothermal field. The influence degree of groundwater activities is

consistent with research results from Chen (1998), which aligns well with the fluctuation of 1 and 3 km isotherms groundwater activities (**Figure 12B**). The change of temperature measurement curves in two geothermal wells (well citysun2 and well nongfahang1) in Niutuozhen salient also confirms the influence of geothermal water disturbance (**Figure 12C**) (Wang et al., 2019).

Combined with the previous study and **Figure 12B** (Cui et al., 2019), the study area can be simply divided into western sag, central salient, and eastern sag. And thermal convection mainly affects the western sag and central salient. The measured heat flow from west to east in these three areas ranges from 48.7 to 60.4 mW/m^2, with the average of 52.9 mW/m^2, 65.7 mW/m^2 to 90 mW/m^2, with the average of 69.2 mW/m^2, 50.6 mW/m^2 to 66.2 mW/m^2, with the average of 57.9 mW/m^2, respectively. The mantel heat flow is 30, 34, and 35 mW/m^2, respectively, from west to east, and the crustal heat flow is 26.3, 26.1, and 21 mW/m^2, respectively, from west to east. Thermal convection makes it reduced in western sag (reduced about 6.88–7.8 mW/m^2) and raised in central salient (raised about 12.04–29.25 mW/m^2), with nearly no influence in eastern sag. In addition, the crustal heat flow was refined, and the heat flow contribution of each stratum is 1.1–2 mW/m^2, 0.1–2.4 mW/m^2, 0–0.6 mW/m^2, 0.9–1.2 mW/m^2, and 1.9–2.4 mW/m^2 in Q + N, E, Mz + Pz, Jx, Ch, respectively. In conclusion, under the background of the extension and thinning of the geothermal lithosphere in the Bohai Bay Basin, the "cold crust-hot mantle" thermal structure has been formed in Xiong'an new area. About 53–62% of heat is produced by mantle and 38–47% of heat is produced by crustal heat flow, which means mantle heat flow is the main source of heat source in the study area. Among them, about 12% heat increment to the crustal heat production is provided by the Yanshanian igneous rocks in the area where it develops, and about 6% to the heat source. The groundwater supplied by the piedmont is gradually heated by the stratum in the process of migration, and convection occurs with the shallow groundwater in the salient, resulting in the high measured terrestrial heat flow. A large number of holes and fractures developed in the carbonate stratum provide good storage space for hot groundwater. The Great Basin in the western United States and the soultz geothermal field in France are similar; faults and inclined sedimentary layers control the circulation of fluid and thus the distribution of heat flow (Kohl et al., 2000; Genter et al., 2010).

The sand mud interbeds developed in the shallow stratum have low thermal conductivity and provide a water barrier, causing less heat dissipation, which together form the genetic model of geothermal resources in Xiong'an new area (**Figure 12D**).

CONCLUSION

Calculated by GR-A optimal empirical formula, the radioactive heat production of mudstone ranges from 0.423 to 2.807 $\mu W/m^3$ (avg. 1.348 $\mu W/m^3$); that of sandstone ranges from 0.263 to 2.845 $\mu W/m^3$ (avg. 1.162 $\mu W/m^3$); that of limestone ranges from 0.079 to 2.121 $\mu W/m^3$ (avg. 0.504 $\mu W/m^3$); and that of dolomite ranges from 0.058 to 1.852 $\mu W/m^3$ (avg. 0.33 $\mu W/m^3$). Meanwhile, those of basalt, tuff, diabase, and granite are 0.3–0.7 $\mu W/m^3$, 0.3–0.6 $\mu W/m^3$, 0.4–0.6 $\mu W/m^3$, and 0.6–1.5 $\mu W/m^3$, respectively. All in all, the average radioactive heat production of intermediate-acid plutonic intrusive rock developed in Yanshanian and basic extrusive rock and hypabyssal intrusive rock developed in Cenozoic are 1.64 and 0.55 $\mu W/m^3$, respectively.

In the late Mesozoic Yanshannian, moniliform intermediate and acid intrusion rock was mainly developed in the salients. In the Cenozoic Paleogene, basalt and diabase were mainly developed along with the bedding in the sags. Thermal simulation results show that the igneous rock intrusion and surrounding rock can reach thermal equilibrium after 0.5 Ma at most, indicating that the residual heat does not affect the current temperature field. After balance, the difference in thermal properties between the intrusion body and the surrounding rock has a limited impact on the distribution of the surface heat flow, which only increases the heat flow in a local area of the salient about 3.55 mW/m^2.

Under the thermal background of the typical "cold crust–hot mantle" thermal structure, the mantel heat is the main source, where the Yanshanian igneous rocks developed in the central salient contribute about 12% of the heat increment to the heat generation of the crust and 6% of that to the heat source. And thermal convection makes it improved in the central salient (raised about 12.04–29.25mW/m^2). Together with the crust and mantle heat production, they constitute the heat source genesis of the geothermal resources in Xiong'an new area. Under this heat flow background, large-scale carbonate thermal reservoirs, sufficient lateral fluid supply, and certain circulation depth together constitute the hydrothermal geothermal resources in the study area.

DATA AVAILABILITY STATEMENT

The original contributions presented in the study are included in the article/Supplementary Material, and further inquiries can be directed to the corresponding author.

AUTHOR CONTRIBUTIONS

YC was the primary finisher of this paper, CZ provided the source of the sample and funding, NQ provided the funding of this paper, too. And BT, SG, and ZL completed part of data processing work for this paper.

FUNDING

The study was supported by the National Natural Science Foundation of China (Grant Nos. 42172334) and the National Key Research and Development Program of China (Grant Nos. 2021YFA0716003 and Grant Nos. 2018YFC0604302).

REFERENCES

Alain, B., Alexandre, C., and Catherine, A. (2020). Numerical Simulations of Magmatic Enclave Deformation. *J. Volcanol. Geotherm. Res.*, 392. doi:10.1016/j.jvolgeores.2020.106790

Bonneville, A., and Capolsini, P. (1999). THERMIC: A 2-D Finite-Element Tool to Solve Conductive and Advective Heat Transfer Problems in Earth Sciences. *Comput. Geosciences* 25 (10), 1137–1148. doi:10.1016/s0098-3004(99)00075-8

Brich, F. (1954). *Heat from Radioactivity*. New York: Wiley. Nuclear Geology.

Bucker, C., Jarrard, R. D., and Wunik, T. (2001). Downhole Temperature, Radiogenic Heat Production, and Heat Flow from the CRP-3 Drillinghole, Victoria Land Basin, Antarctica. *Terra Antartica* 8 (3), 151–160.

Bücker, C., and Rybach, L. (1996). A Simple Method to Determine Heat Production from Gamma-ray Logs. *Mar. Pet. Geology.* 13 (4), 373–375. doi:10.1016/0264-8172(95)00089-5

Chang, J., Qiu, N. S., Zhao, X. Z., Xu, W., Xu, Q. C., Jin, F. M., et al. (2016). Present-day Geothermal Regime of the Jizhong Depression in Bohai Bay Basin, East China. *Chin. J. Geophysics* 59 (3), 1003–1016. (in Chinese with English abstract). doi:10.6038/cjg20160322

Chang, Y. Q., and Liu, J. (2018). Research on Development Characteristics of Magmatic Rock in Qianjiaying Mining Area and Their Influence on Geothermal Anomaly. *China Coal* 44 (9), 38–42+70. (in Chinese with English abstract). doi:10.19880/j.cnki.ccm.2018.09.007

Chen, M, X. (1988). *The Geothermal in North China*. Beijing, China: Science Press.

Cui, Y., Zhu, C., Qiu, N., Tang, B., and Guo, S. (2019). Radioactive Heat Production and Terrestrial Heat Flow in the Xiong'an Area, North China. *Energies* 12 (24), 4608. doi:10.3390/en12244608

Cui, Y., Zhu, C. Q., Qiu, N. S., Tang, B. N., and Guo, S. S. (2020). Geothermal Lithospheric Thickness in the central Jizhong Depression and its Geothermal Significance. *Acta Geologica Sinica* 94 (7), 1960–1969. (in Chinese with English abstract). doi:10.19762/j.cnki.dizhixuebao.2020213

Genter, A., Evans, K., Cuenot, N., Fritsch, D., and Sanjuan, B. (2010). Contribution of the Exploration of Deep Crystalline Fractured Reservoir of Soultz to the Knowledge of Enhanced Geothermal Systems(egs). *Comptes Rendus Geosciences* 342 (7), 502–516. doi:10.1016/j.crte.2010.01.006

Gong, L. (2014). *2D Numerical Simulation of Geothermal Field with Finite Element Method*. Hunan: Central South University, 21–27. (in Chinese with English abstract).

Gong, Y.-l., Zhang, H., and Ye, T.-f. (2011). Heat Flow Density in Bohai Bay Basin: Data Set Compilation and Interpretation. *Proced. Earth Planet. Sci.* 2, 212–216. doi:10.1016/j.proeps.2011.09.034

Gong, Y. L. (2003). *Thermal Structure and thermal Evolution of the Bohai Bay Basin in Eastern China*. Nanjing: Najing University, 79–100. (in Chinese with English abstract).

Guo, Y. Z., Dong, J., Chen, D., and Lv, S. Y. (2001). Statistical Characteristics of Regional Rock Electrical Properties in Hebei Province. *Geophys. Geochemical Exploration* 5, 328–336. (in Chinese with English abstract). doi:10.3969/j.issn.1000-8918.2001.05.002

He, B. Z., and Zheng, M. L. (2016). Structural Characteristics and Formation Dynamics: A Review of the Main Sedimentary Basins in the Continent of China. *Acta Geologica Sinica* 90 (4), 1156–1194. (in Chinese with English abstract). doi:10.1111/1755-6724.13037

Hu, S. B., Sullivan, P. B., Raza, A., and Kohn, B. P. (2001). Thermal History and Tectonic Subsidence of the Bohai Basin, Northern China: a Cenozoic Rifted and Local Pull-Apart basin. *Phys. Earth Planet. Interiors* 126 (3-4), 221–235. doi:10.1016/s0031-9201(01)00257-6

Hyndman, R. D., Lambert, I. B., Heier, K. S., Jaeger, J. C., and Ringwood, A. E. (1968). Heat Flow and Surface Radioactivity Measurements in the Precambrian Shield of Western Australia. *Phys. Earth Planet. Interiors* 1 (2), 129–135. doi:10.1016/0031-9201(68)90057-5

Jiang, G., Hu, S., Shi, Y., Zhang, C., Wang, Z., and Hu, D. (2019). Terrestrial Heat Flow of continental China: Updated Dataset and Tectonic Implications. *Tectonophysics* 753, 36–48. doi:10.1016/j.tecto.2019.01.006

Jin, C. S., Qiao, D. W., and Dan, W. N. (2012). Meso-Cenozoic Volcanic Rock Distribution and Reservoir Characteristics in the Bohai Bay Basin. *Oil &Gas Geology.* 33 (1), 19–29+36. (in Chinese with English abstract). doi:10.11743/ogg20120103

Kohl, T., Bächler, D., and Rybach, L. (2000). "Steps towards a Comprehensive Thermo-Hydraulic Analysis of the HDR Test Site Soultz-Sous-Forets," in Proceedings, World Geothermal Congress 2000, Japan, May28–June10, 2000 (Japan: Kyushu-Tohoku).

Kong, Y. L., Pang, Z. H., Wu, C. Y., and Miao, J. (2015). A Comparative Study of Single Factor and Multivariate Statistical Methods for Surface Water Quality Assessment. *Water Policy* 16 (1), 157–167. doi:10.2166/wp.2013.042

Kusky, T. M., Windley, B. F., Wang, L., Wang, Z., Li, X., and Zhu, P. (2014). Flat Slab Subduction, Trench Suction, and Craton Destruction: Comparison of the North China, Wyoming, and Brazilian Cratons. *Tectonophysics* 630, 208–221. doi:10.1016/j.tecto.2014.05.028

Lachenbruch, A. H. (1970). Crustal Temperature and Heat Production: Implications of the Linear Heat-Flow Relation. *J. Geophys. Res.* 75 (17), 3291–3300. doi:10.1029/jb075i017p03291

Lachenbruch, A. H., and Sass, J. H. (1977). "Heat Flow in the United States and the Thermal Regime of the Crust," in *The Earth's Crust. Its Nature and Physical Properties*. Editors A. F. Spilhaus and J. Managing (Washington DC: American Geophysical Union Geophysical Monograph Series), 20, 332–359.

Li, H., Yu, J. B., Lv, H., and Xiao, P. F. (2017). Gravity and Aeromagnetic Responses and Heat-Controlling Structures of Xiongxian Geothermal Area. *Geophys. Geochemical Exploration* 41 (2), 242–248. (in Chinese with English abstract). doi:10.11720/wtyht.2017.2.08

Li, W. Q. (2015). *The Influence of Geothermal Features and Radioactive Heat Production of Rocks to Potential of Geothermal Resources in Eastern Area of Liaoning Province*. Ph. D thesis of Jilin University. (in Chinese with English abstract).

Li, Z. C. (1999). Seismic and Geological Interpretation of Magma Intrusions. *Coal Geology. China* 4, 59–60+65. (in Chinese).

Liang, J., Wang, H., Bai, Y., Ji, X., and Duo, X. (2016). Cenozoic Tectonic Evolution of the Bohai Bay Basin and its Coupling Relationship with Pacific Plate Subduction. *J. Asian Earth Sci.* 127, 257–266. doi:10.1016/j.jseaes.2016.06.012

Liu, Q. Z. (1992). Distribution and Gas-Bearing Characteristics of the Cenozoic Igneous Rocks in the Jizhong Depression. *Exp. Pet. Geology.* 2, 188–194. (in Chinese with English abstract).

Liu, Z., Dai, L.-m., Li, S., Guo, L.-l., Hu, M.-y., Ma, F.-f., et al. (2018). Mesozoic Magmatic Activity and Tectonic Evolution in the Southern East China Sea Continental Shelf Basin: Thermo-Mechanical Modelling. *Geol. J.* 53, 240–251. doi:10.1002/gj.3021

Luo, M., Pan, H. P., Zhao, Y. G., Zhang, H. J., and Zhou, F. (2008). Natural Radioactivity Logs and Interpretation from the CCSD Main Hole. *Earth Science-Journal China Univ. Geosciences* 5, 661–671. (in Chinese with English abstract). doi:10.3321/j.issn:1000-2383.2008.05.009

Ma, X. Y., Liu, C. Q., and Liu, G. D. (1991). Xiangshui (Jiangsu Province) to Mandal (Nei Monggol) Geoscience Transect. *Acta Geologica Sinica* 3, 199–215.

Mundry, E. (1970). Mathematical Estimation Concerning the Cooling of a Magnetic Intrusion. *Geothermics* 2, 662–668. doi:10.1016/0375-6505(70)90067-2

Norden, B., and Forster, A. (2006). Thermal Conductivity and Radiogenic Heat Production of Sedimentary and Magmatic Rocks in the Northeast German Basin. *AAPG Bull.* 90 (6), 936–962. doi:10.1306/01250605100

Pamukçu, O. A., Akçığ, Z., Demirbaş, Ş., and Zor, E. (2007). Investigation of Crustal Thickness in Eastern Anatolia Using Gravity, Magnetic and Topographic Data. *Pure Appl. Geophys.* 164, 2345–2358. doi:10.1007/s00024-007-0267-7

Pang, Z. H., Pang, J. M., Kong, Y. L., Luo, L., and Wang, S. F. (2015). *Large Karstic Geothermal Reservoirs in Sedimentary Basins in China: Genesis, Energy Potential and Optimal Exploitation*. Melbourne, Australia: World Geothermal Congress.

Qiu, N. S., Zuo, Y. H., Chang, J., and Li, W, Z. (2014). Geothermal Evidence of Meso-Cenozoic Lithosphere Thinning in the Jiyang sub-basin, Bohai Bay Basin, Eastern North China Craton. *Gondwana Res.* 26 (3-4), 1079–1092. doi:10.1016/j.gr.2013.08.011

Qiu, N., Zuo, Y., Xu, W., and Chang, J. (2016). Meso-Cenozoic thermal Structure of the Lithosphere in the Bohai Bay Basin, Eastern North China Craton. *Geol. J.* 51 (5), 794–804. doi:10.1002/gj.2693

Rao, S., Zhu, C. Q., Liao, Z. B., Jiang, G. Z., Hu, S. B., and Wang, J. Y. (2014). Heat Production Rate and Heat Flow Contribution of the Sedimentary Formation in

Junggar Basin, Northwest China. *Chin. J. Geophys.* 57 (5), 1554–1567. (in Chinese with English abstract). doi:10.6038/cjg20140519

Rosa, D. M., Ester, P., Cecilia, M., and Scandone, R. (2015). Numerical Study of Conductive Heat Losses from a Magmatic Source at Phlegraean Fields. *J. Volcanology Geothermal Res.* 290, 75–81. doi:10.1016/j.jvolgeores.2014.12.007

Rybach, L. (1986). Amount and Significance of Radioactive Heat Sources in Sediments. *Collection Colloques et Seminares* 44, 311–322.

Shan, S. Q. (2018). *Structural Geometry and Kinematics of the Taihang Mountain piedmont Fault and its Controlling on the Development of the Bohai Bay Basin*. Beijing: China University of Geosciences, Beijing, 21–25. (in Chinese with English abstract).

Tang, X. Y., Zhang, G. C., Liang, J. S., Yang, S. C., Rao, S., and Hu, S. B. (2013). Influence of Igneous Intrusions on the Temperature Field and Organic Maturity of the Changchang Sag, Qiongdongnan Basin, south China Sea. *Chin. J. Geophys.* 56 (1), 159–169. (in Chinese with English abstract). doi:10.6038/cjg20130116

Wang, J. Y., Xiong, L. P., and Huang, S. P. (1996). Heat Transfer and Groundwater Activity in Sedimentary Basins. *Quat. Sci.* 2, 147–158. (in Chinese with English abstract).

Wang, P. X., Yang, X., and Bian, X. D. (2012). Petrologic and Geochemical Characteristics of Igneous Rock in Jizhong Depression. *Geol. Sci. Techn. Inf.* 31 (4), 1–10. (in Chinese with English abstract).

Wang, Z., Jiang, G., Zhang, C., Hu, J., Shi, Y., Wang, Y., et al. (2019). Thermal Regime of the Lithosphere and Geothermal Potential in Xiong'an New Area. *Energy Exploration & Exploitation* 37, 787–810. doi:10.1177/0144598718778163

Windley, B. F., Maruyama, S., and Xiao, W. J. (2011). Delamination/thinning of Sub-continental Lithospheric Mantle under Eastern China: The Role of Water and Multiple Subduction. *Am. J. Sci.* 310 (10), 1250–1293. doi:10.2475/10.2010.03

Wu, F. Y., Lin, J. Q., Wilde, S. A., Zhang, X. O., and Yang, J. H. (2005). Nature and Significance of the Early Cretaceous Giant Igneous Event in Eastern China. *Earth Planet. Sci. Lett.* 233 (1-2), 103–119. doi:10.1016/j.epsl.2005.02.019

Wu, X. Y., and Pan, J. T. (2005). Fractal Dimension Calculation of Aeromagnetic Data and its Application to the Deduction of Igneous Rock Distribution. *Geophys. Geochemical Exploration* 29 (4), 291–294. (in Chinese with English abstract). doi:10.3969/j.issn.1000-8918.2005.04.003

Xu, W. (2017). *Meso-Cenozoic thermal Regime and Lithospheric Thinning in the Bohai Bay Basin*. Beijing: Ph. D thesis of China University of Petroleum, 49. (in Chinese with English abstract).

Yu, C. C., Qiao, R. X., and Zhang, D. S. (2017). The Basement Tectonic Characteristics from Interpretation of Aeromagnetic Data in Xiong'an Region. *Geophys. Geochemical Exploration* 41 (3), 385–391. (in Chinese with English abstract). doi:10.11720/wtyht.2017.3.01

Zhang, J. M., Sun, H. W., and Xiong, L. P. (1982). Mathematical Simulating of Regional Geothermal Field and Case Analysis. *Chin. J. Geology.* 3 (3), 315–321.

Zhang, J., and Shi, Y. L. (1997). The thermal Modeling of Magma Intrusion in Sedimentary Basins. *Prog. Geophys.* 3, 55–64. (in Chinese with English abstract).

Zuo, Y. H., Qiu, N. S., Chang, J., Hao, Q. Q., Li, Z. X., Li, J. W., et al. (2013). Meso-Cenozoic Lithospheric Thermal Structure in the Bohai Bay Basin. *Acta Geologica Sinica* 87 (02), 145–153. doi:10.1016/j.gsf.2016.09.003

Conflict of Interest: The authors declare that the research was conducted in the absence of any commercial or financial relationships that could be construed as a potential conflict of interest.

frontiers in Earth Science

ORIGINAL RESEARCH
published: 02 March 2022
doi: 10.3389/feart.2022.783556

Characteristics of Porosity and Permeability of Ultra-High Temperature Perforated Damage Zone in Sandstone Targets

Changgui Xu[1], *Hao Liang*[2]* *and Shusheng Guo*[2]

[1]Exploration Department of CNOOC Ltd., Beijing, China, [2]CNOOC (China) Co., Ltd., Haikou, China

Perforating as a widely-applied stimulation technology is becoming incrementally important in unconventional oil/gas development. It can effectively improve deep-lying high-temperature, high-pressure (HTHP), low-porosity, low-permeability reservoirs, eliminate near-wellbore surface pollution, and increase drainage area. Characteristics of damage zone porosity directly reflect perforating performance. To study porosity and permeability of damage zone in sandstone targets, the paper collected sandstone cores from the 3rd section of the Zhuhai Formation to conduct a simulation experiment for HTHP perforation of large-size targets. After the simulation experiment, an automatic scanner was used to find the planar distribution of the porosity and permeability parameters of the 150°C perforation holes in the cores. The study led to two findings. First, the temperature has a minor effect on the hole depth and diameter in a specified scope. The hole depth decreases as the negative pressure increases and the depth decreases as the effective stress increases. Second, a UHP perforated sandstone target is remarkably zone-specific in planar distribution of the hole porosity and permeability. The damage zone can be divided into the fracture zone, the transition zone, the compaction zone and the undisturbed zone. Besides, the zone permeability damage was quantified. These findings can effectively support research on numerical value simulation for HTHP perforation holes. Besides, they can support HTHP well perforating design and improve near-wellbore permeability enhancement and plug removal.

Keywords: perforation hole, damage zone, sandstone target, porosity and permeability characteristic, UHT reservoir

OPEN ACCESS

Edited by:
Haiyan Zhu,
Chengdu University of Technology, China

Reviewed by:
Yongcun Feng,
China University of Petroleum, Beijing, China
Fanhui Zeng,
Southwest Petroleum University, China

***Correspondence:**
Hao Liang
lianghao8@cnooc.com.cn

Specialty section:
This article was submitted to Economic Geology, a section of the journal Frontiers in Earth Science

Received: *26 September 2021*
Accepted: *07 February 2022*
Published: *02 March 2022*

Citation:
Xu C, Liang H and Guo S (2022) Characteristics of Porosity and Permeability of Ultra-High Temperature Perforated Damage Zone in Sandstone Targets. Front. Earth Sci. 10:783556. doi: 10.3389/feart.2022.783556

1 INTRODUCTION

Over the years, quite a few perforated completion techniques have been developed for reservoir development (Zhu, et al., 2015) in China and beyond. These techniques include mainly deep-penetrating shaped charge perforating, underbalanced perforating, fracture perforating, ultrahigh pressure (UHP) perforating, sand jet perforating, oriented perforating, full-bore perforating and perforating processes, and auxiliary processes (Zhu, et al., 2013). The generalization of these applications is very effective in enhancing the efficiency of perforated completion and reservoir development (Zhu, et al., 2014). Using the concrete target to check the perforating and safety performance of the perforator is the most common practice under surface condition in China and beyond. Cement/sand performance, maintenance process and time length have a major effect on the

concrete leading to poor internal homogeneity. In other words, different and individual test targets tend to have very heterogeneous internal structures. Judging from the current studies, concrete strength is an important factor affecting perforating performance. For example, every 6.9 MPa increase in compressive strength causes a 5–7% decrease in the average hole depth. This suggests that characteristics of different concrete targets have a major effect on the test results. What make the steel target a better solution than the concrete target are good homogeneity, preparation simplicity/speed, and low cost. However, the physical properties of the steel target are drastically different from those of real reservoirs, unable to reflect the actual perforating process.

Berea sandstone in North America is the most used nature rock target in perforating simulation. Besides, rock outcrops in the Sichuan Basin and the Erdos Basin are also used for various tests and studies.

As early as 1952, Henry, 1952 perforated tight dolomitic sandstone specimens measuring 3 3/4inches in diameter and 10–12 inches in length with the common bullet and the shaped charge bullet for a comparative analysis of performance differences. In 1978, Saucier and Lands, 1978 evaluated the effect of crustal stress on the perforating parameters and flow efficiency according to API RP-43 standards. Halleck et al. systematically summarized the effects of the effective stress based on the findings of around 300 perforating operations in 120 tests. When a 3,000 psi effective stress was applied to the test target, the penetration effect of the bullet on the rock (not including casing and cement) fell by 10–14%. The flow efficiency of the rock specimens decreased as the effective stress rose. In 2003, Karacan and Halleck, 2003 perforated Berea sandstone specimens with saturated gas (nitrogen) and liquid (silicone oil) respectively to analyze the differences of the porosity and permeability of compaction zones. The saturated nitrogen-perforated specimens had a hole diameter of 0.5–0.7 cm and a hole depth of around 14 cm, while the silicone oil-perforated specimens had a diameter of 1.2–1.4 cm and a hole depth of 16 cm. In the saturated nitrogen-perforated specimens, the compression band thickness was around 6 mm at the opening and decreased incrementally as the hole depth increased, Meantime, compression band porosity was 6–8% lower than those of original rock specimens. By contrast, compression bands were not found in saturated silicone oil-perforated specimens. Besides, perforating caused diagenetic particles to fracture. In the saturated nitrogen-perforated specimens, these particles were more seriously fractured. In 2008, Snider et al., 2008 used three different types of bullets to perforate 30 coal specimens, finding the hole depth to be far smaller than the predicted value of the existing sand rock hole models. Moreover, the hole diameter (0.07–0.32 in) was significantly smaller than that of common sandstone. In 2011, Grove et al., 2011 first summarized the inadequacies of the existing test and analysis methods in regard of CFE (Core Flow Efficiency) computation, concluding that the original methods generated greater errors. Therefore, they developed more reliable test methods and data processing methods to compute the flow efficiency, the effective permeability and

FIGURE 1 | Final experimental sandstone targets (Φ400 mm).

thickness of the compression band. In 2012, Huang, 2012 worked with the Schlumberger Well Completion Center to conduct perforating test on Indiana limestone and analyzed the effect of rock strength on the penetration depth (or hole depth). They measured rock strength and hole depth under different confining pressures. By predicting the hole depth with the analytical method developed by Alekseevskii, they prepared graphs for the bullet speed and the penetration depth. In 2019, Brenden Grove et al., 2019 analyzed and evaluated the effect of the high-temperature, high-pressure (HTHP) reservoir condition of offshore oil fields on UHP pressure perforating.

Perforating simulation test is becoming incrementally complex. Homogeneous small-size steel targets and cement targets were used but were gradually replaced by large-size sandstone targets. Initially, single factors were the variables in perforating test and gradually multiple factors were used instead. Initially, perforating test was conducted under normal temperature and pressure (NTP) surface condition. Gradually more perforating tests were conducted under HTHP condition, a condition closer to oil and gas reservoir condition and it turned out that test results were more correct and reliable. Perforating simulation test has been broadly applied in perforating parameters acquisition, reservoir damage mechanism research, penetration depth-affecting factor evaluation, perforation hole geometry research, hole flow efficiency evaluation, bullet performance analysis, and evaluation of the effect of perforating on sand production.

At present, from the research on perforation by domestic and foreign scholars, it can be seen that the experimental research objects of perforation simulation are mainly concentrated on concrete, and the temperature is less considered. Therefore, the test results are difficult to reflect the real underground perforation situation. In view of the existing problems, the author uses the third-segment sandstone core of Zhuhai Formation to carry out physical simulation of large-size perforation under high temperature and high pressure, to study the characteristics of perforation

TABLE 1 | Experimental plan investigating the effect of temperature on perforating.

Experiment S/N	Bullet type	Target strength (MPa)	Temperature (°C)	Confining pressure (MPa)	Negative pressure (MPa)	Remarks
1	CN-127-40 RT-25-5 (25°C)	400	25	25	5	Different temperatures
2	CN-127-40 HT-25-5 (50°C)		50			
3	CN-127-40 HT-25-5 (100°C)		100			
4	CN-127-40 UHT-25-5 (150°C)		150			

TABLE 2 | Experimental plan investigating the effect of negative pressure on perforating.

Experiment S/N	Bullet type	Target strength (MPa)	Temperature (°C)	Confining pressure (MPa)	Negative pressure (MPa)	Effective stress (MPa)	Remarks
5	CN-127-40-HT-25-5	40	Room temperature	25	5	20	Different negative pressures under the same effective stress
6	CN-127-40-HT-30-10			30	10		
7	CN-127-40-HT-35-15			35	15		

TABLE 3 | Experimental plan investigating the effect of effective stress on perforating.

Experiment S/N	Bullet type	Target strength (MPa)	Temperature (°C)	Confining pressure (MPa)	Negative pressure (MPa)	Effective stress (MPa)	Remarks
8	CN-127-40-HT-20-10	40	Room temperature	20	10	10	Different effective stresses under the same negative pressure
9	CN-127-40-HT-25-10			25		15	
10	CN-127-40-HT-30-10			30		20	
11	CN-127-40-HT-35-10			35		25	

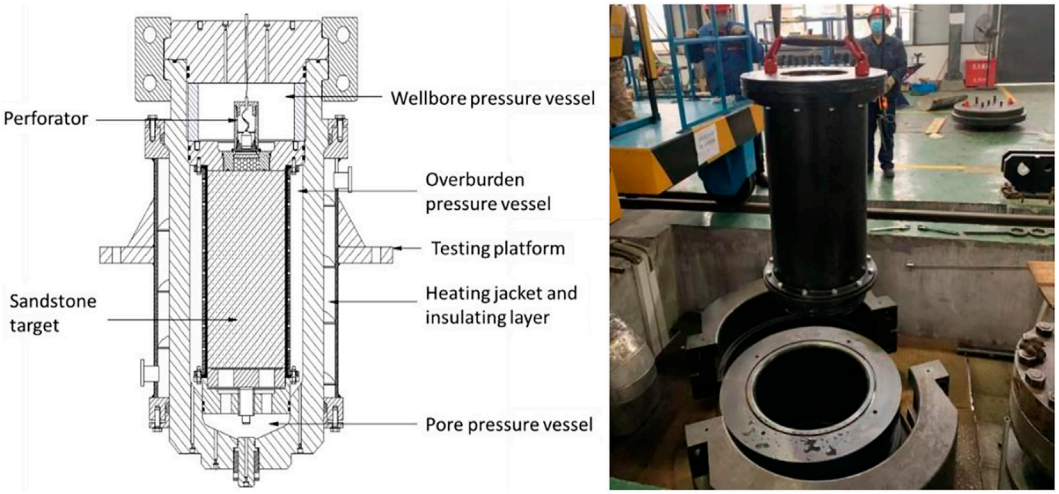

FIGURE 2 | Structural representation of the perforating performance experimental unit.

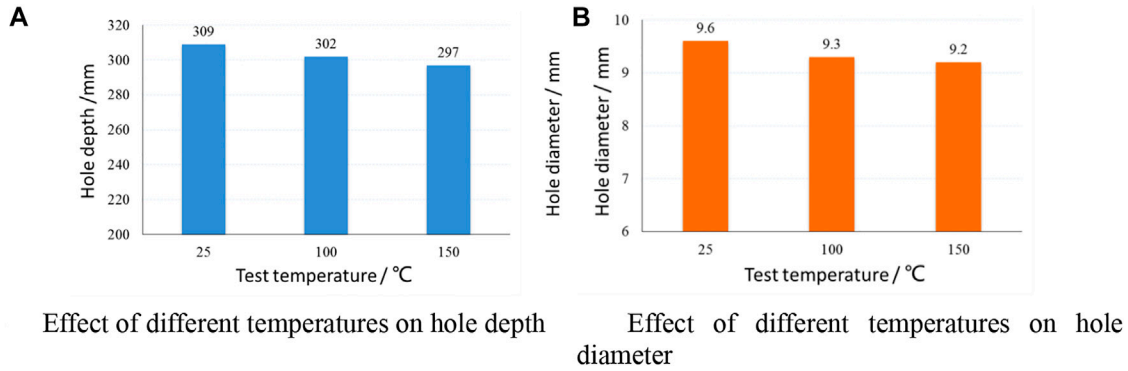

FIGURE 3 | Effect of different temperatures on hole size (depth and diameter). **(A)** Effect of different temperatures on hole depth **(B)** Effect of different temperatures on hole diameter.

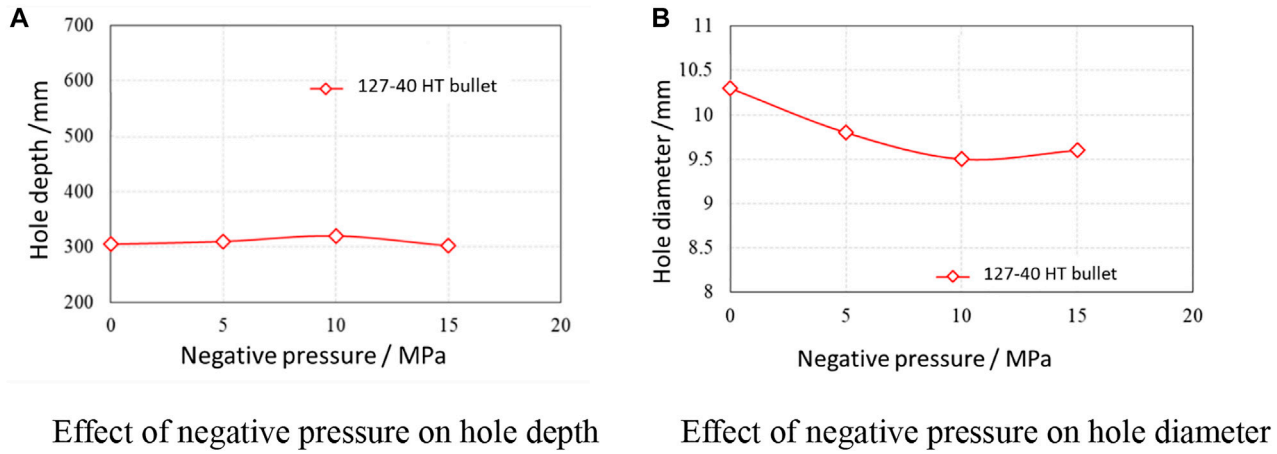

FIGURE 4 | Effect of negative pressure on hole size (depth and diameter) (Effective Stress: 20 MPa). **(A)** Effect of negative pressure on hole depth **(B)** Effect of negative pressure on hole diameter.

channel loss and permeability, and to provide a theoretical basis for on-site construction.

2 EXPERIMENTAL SPECIMENS, MATERIALS, METHODS AND EQUIPMENT

2.1 Sandstone Target Characteristics

For this paper, rock specimens extracted from the 2nd section of the Zhuhai Formation were used for experimentation. According to log interpretation, the 2nd section has a 8–11% rock porosity. The test has determined the permeability to be 2–5 mD and the uni-axial compressive strength to be around 45 MPa. **Figure 1** shows the final experimental sandstone specimens.

2.2 Experimental Plan

For this paper, sandstone cores were extracted from the 3rd section of the Zhuhai Formation to physically simulate a large-size hole experiment which primarily studies the effect of three reservoir characteristics, such as temperature, negative pressure condition and effective formation stress, on the result of the perforating experiment.

2.2.1 Effect of Different Temperatures

CN-127 bullets were used for sandstone cores with a 40 MPa target strength. The hole density was 40 m. Four temperature variables (25°C, 50°C, 100°C and 150°C) were set under the same confining pressure of 25 MPa and the same negative pressure of 5 MPa **Table 1**.

2.2.2 Effect of Negative Pressure

CN-127 bullets were used for sandstone cores with a 40 MPa target strength. Three negative pressure variables (5, 10 and 15 MPa) were set under the same effective stress of 20 MPa **Table 2**.

2.2.3 Effect of Negative Pressure

CN-127 bullets were used for sandstone cores with a 40 MPa target strength. Four negative pressure variables (10, 15, 20 and

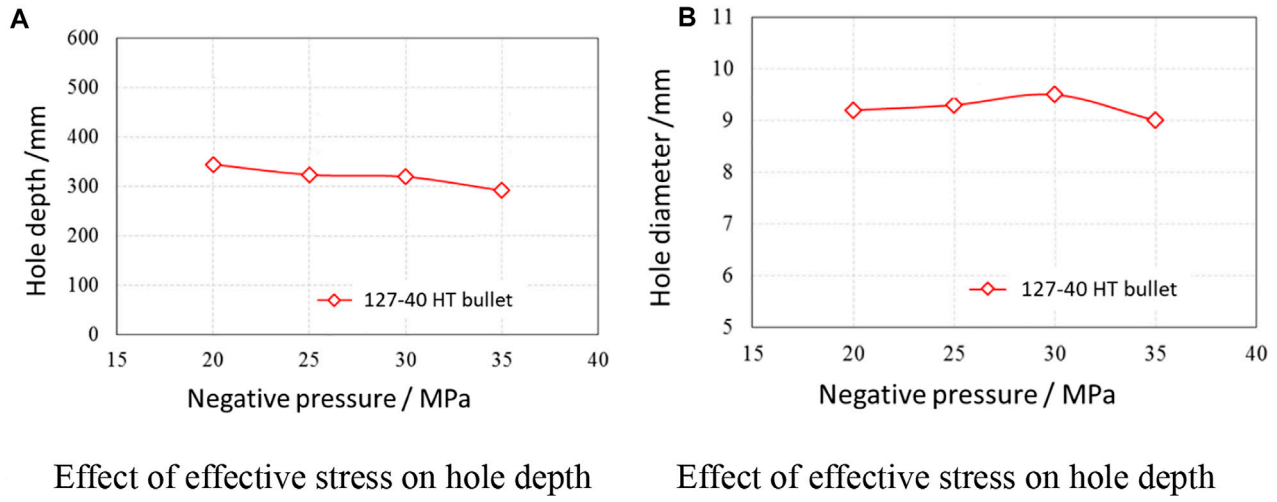

FIGURE 5 | Effect of effective stress on hole size (Negative Pressure: 10 MPa). **(A)** Effect of effective stress on hole depth **(B)** Effect of effective stress on hole depth.

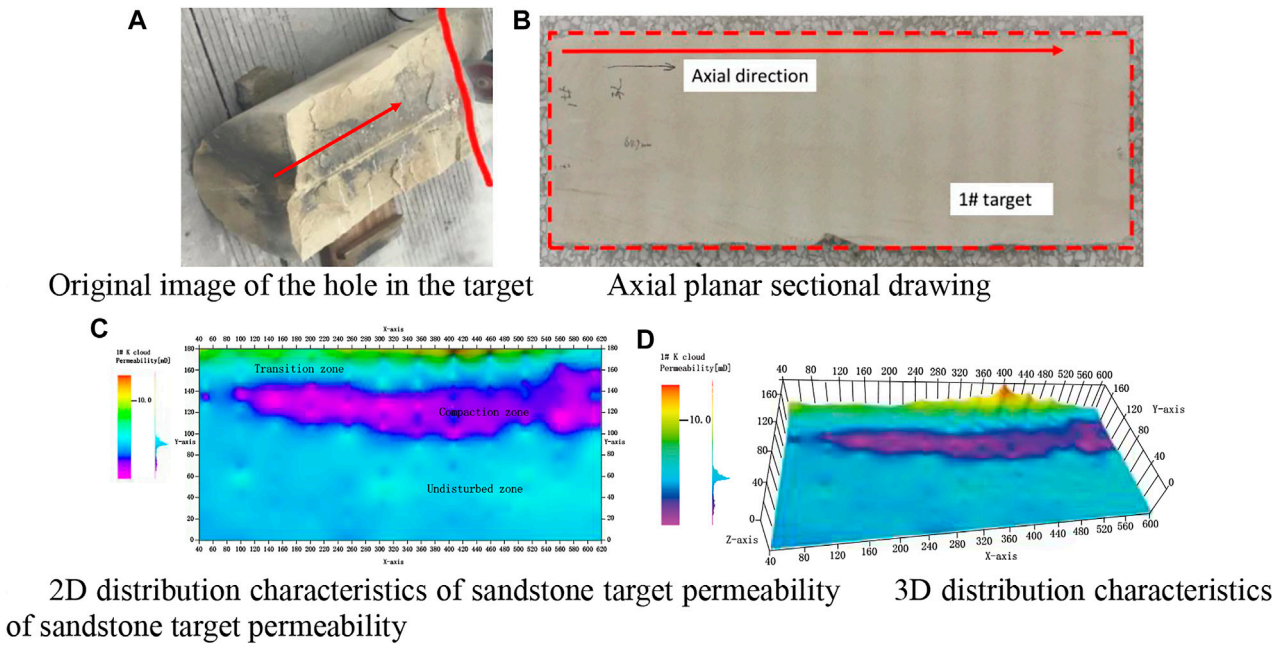

FIGURE 6 | Sandstone target specimens and respective permeability values [CN-127-40-HT-25-5 (100°C)]. **(A)** Original image of the hole in the target **(B)** Axial planar sectional drawing **(C)** 2D distribution characteristics of sandstone target permeability **(D)** 3D distribution characteristics of sandstone target permeability.

25 MPa) were set up under the same negative pressure of 10 MPa **Table 3**.

2.2 Perforating Simulation System for the Large-Size Hole

The perforating simulation system, or perforating simulator, consists primarily of a perforating performance experimental unit, a nitrogen compressor system, a hydraulic pressure system, a heating and cooling system, and a central control and monitoring system. The perforating simulator can perform HT perforating test and pre-perforating and post-perforating fluidity test for the sandstone target under three-phase pressurization condition (wellbore pressure, overburden formation stress, and pore pressure). As indicated in **Figure 2**, the main features of the unit are a wellbore pressure vessel, a perforator, an overburden pressure vessel, a wellbore, and a pore pressure dampener. The unit can meet the requirements

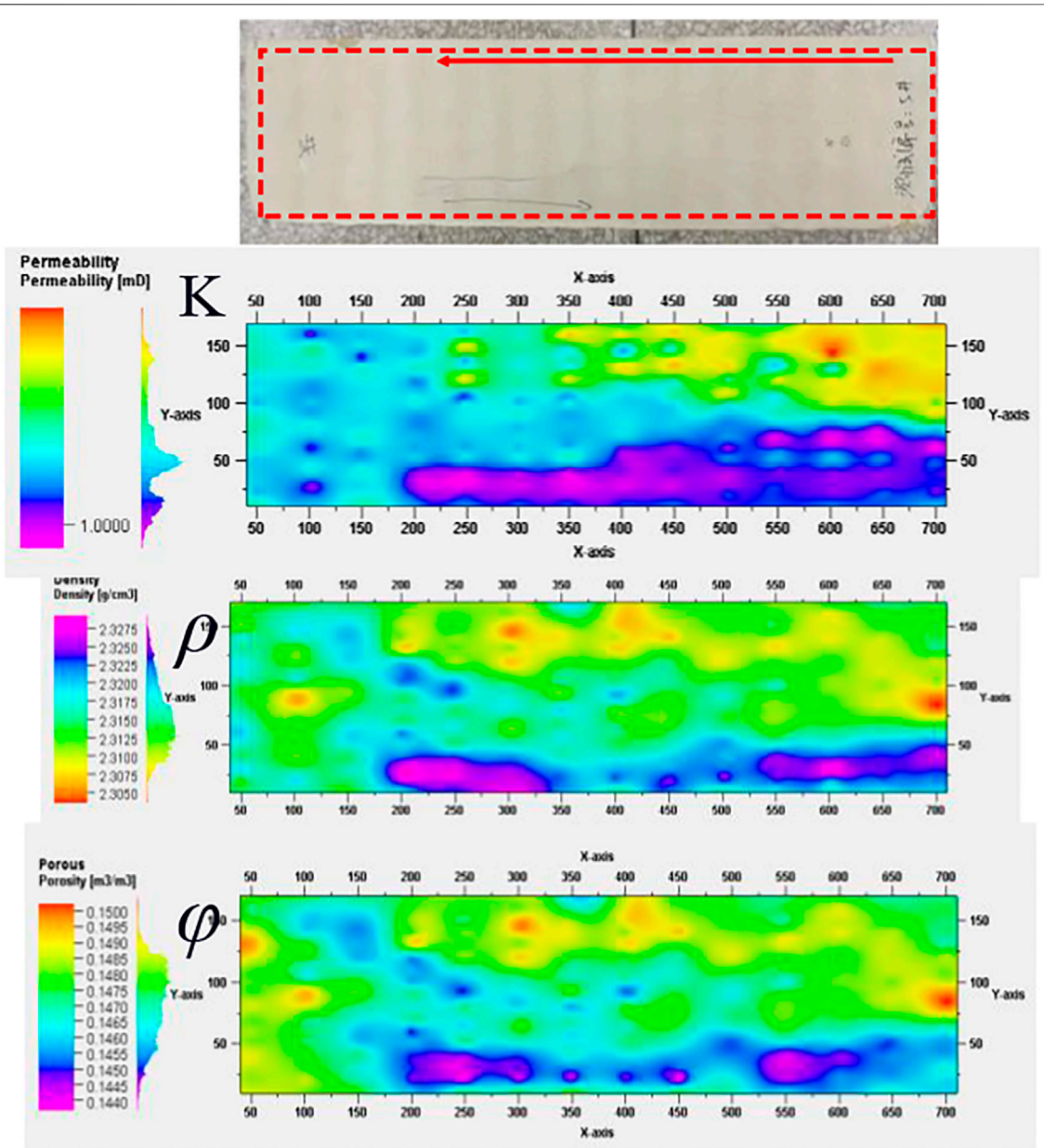

FIGURE 7 | Permeability-density-porosity axial planar distribution diagram [CN-127-40 HT-25-5 (100°C)].

for φ400 mm × 800 mm sandstone targets at a maximum as well as an experimental pressure up to 100 MPa and an experimental temperature up to 200°C. The unit comprises primarily three main vessels (i.e., a wellbore pressure vessel, a confining pressure vessel and a pore pressure vessel), a perforator, a pressure separator, and a sandstone target.

The nitrogen compressor system consists of a set of high-pressure nitrogen cylinders, a nitrogen compression and pressure experimental cabinet, and a high pressure valve. The rated pressure is 70 MPa. It works mainly to increase gas pressure inside the pore pressure vessel of the perforating performance experimental unit so as to simulate downhole reservoir pressure.

The hydraulic pressure system has a rated pressure of 100 MPa, consisting of a hydraulic pressure experimental cabinet, a high-pressure valve and others. The cabinet has three outlets, connected to the wellbore pressure vessel, the overburden pressure vessel and the pore pressure vessel, respectively. The pipe connected to the pore pressure vessel, arranged in parallel to the nitrogen compression pipe, can achieve gas/liquid conversion. The pressure pipes, all fitted with safety relief valves, has a 105 MPa safety pressure setting. The booster pump system includes a high-pressure pump and a LP pump. In low pressure (LP) condition (lower than 18 MPa), the heavy duty LP pump is used to boost pressure, while in high-pressure condition, light duty LP

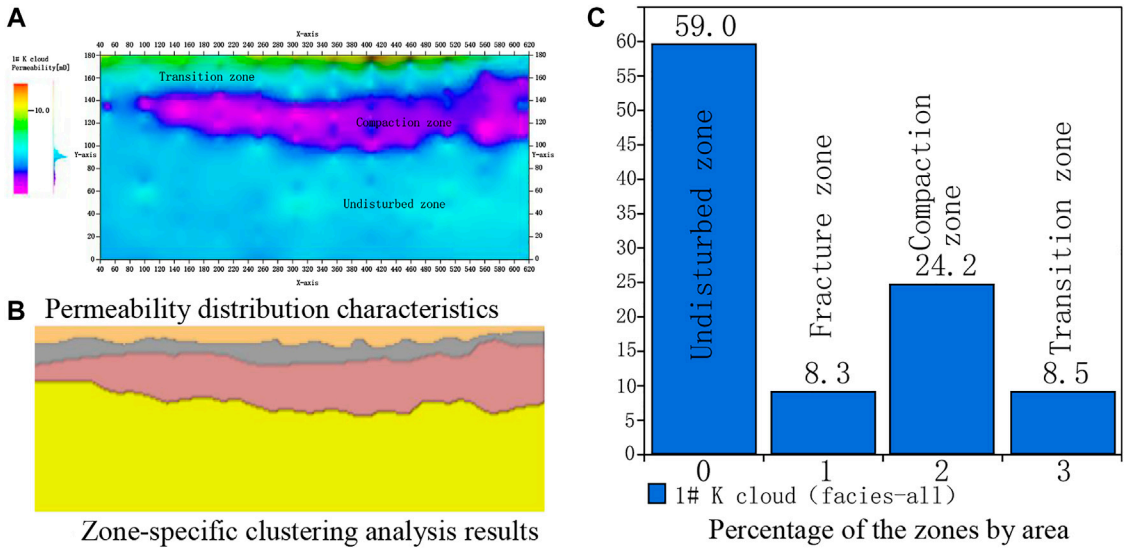

FIGURE 8 | Hole damage area analysis [CN-127-40 HT-25-5 (150°C)]. **(A)** Permeability distribution characteristics **(B)** Zone-specific clustering analysis results **(C)** Percentage of the zones by area.

pump is used to boost pressure. This is intended to coordinate safety with time efficiency.

The heating and cooling system consists of a heater-cooler, HT steel pipes and accessories. The heater-cooler can heat the air and transfers it to the heating jacket to boost the temperature of the perforating performance experimental unit. At the same time, it transfers room-temperature air to the jacket for convective heat transfer and perforator cooling.

The central control and monitoring system consists of a microcomputer, a central control cubicle, a manual console, a PLC and electronic components, testing software, a temperature/pressure transducer and an electrical control cubicle. The microcomputer and the control cabinet are used mainly to supply or cut off electricity to the various electrical devices; gather, show and record the values of various parameters (e.g., temperature, pressure and flow); conduct temperature and pressure control for the major media inside the system; and set up safety voltage drop and alarm values.

2.3 Automatic Core Porosity and Permeability Scanner

Core porosity and permeability scanning is conducted following the perforating experiment. For different formations from which cores were extracted, porosity and permeability parameters were therefore obtained, to study characteristics of porosity and permeability of the damage zone.

A core porosity and permeability scanner includes a measuring probe which is pressed onto the surface of a specimen and injects compressed gas (normally nitrogen) through a hole. As the core is a homogeneous material, nitrogen will enter the limited specimen volume before being released hemispherically into the ambient air. The probe tip, made of soft silicone, can prevent nitrogen leaking from the specimen. The scanner injects steady-state nitrogen into the core specimen to find the permeability at any place. It can also find rock density and porosity by measuring P-wave velocity (V_p) and S-wave velocity (V_s). With steady-state air injection, the scanner can determine the permeability of any part of the specimen. It also allows for automatic continuous scanning of multiple parameters (e.g., permeability, resistivity, and wave velocity) of the core and slab. Besides, the scanner also realize convergence and analysis of multi-parameter scanning data as well as logging curve correction.

The scanner is capable of permeability and P-wave and S-wave velocity scanning for the planar points, lines and planes of the sandstone target in an axial/radial direction. It can determine the target permeability, porosity, and rock density distribution changes of the target. Therefore, parameters of the perforating damage (e.g., shape, area and thickness) are determined macroscopically as a basis for subsequent CT/SEM scan of experimental specimens.

3 LAW OF THE EFFECT OF DIFFERENT RESERVOIR CONDITIONS ON HOLE DIAMETER AND DEPTH

3.1 Effect of Temperature on Hole Diameter and Depth

The CN_127-40 HT bullet perforating experiment was performed on sandstone targets with identical physical properties at different temperatures (50, 100 and 150°C), under the confining pressure of 25 MPa and the negative pressure of 5 MPa. In **Figure 3**, the bar charts of temperature, hole depth and dimensions of casing simulators (secondary target) were given according to the perforating experiment results. The bullet withstood a temperature of 160°C/48 h. When limited within the range of temperature tolerance, such

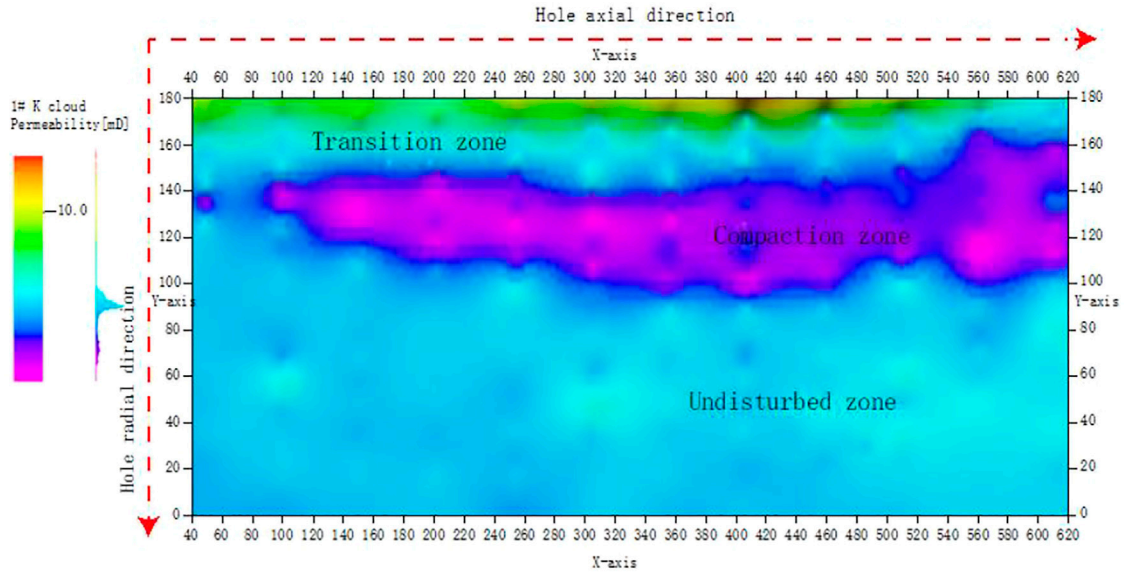

FIGURE 9 | Hole permeability distribution and radial direction analysis diagram [CN-127-40-UHT-25-5 (150°C)] (The black line represents the sampling position).

temperature had a small effect on both the depth and diameter of deep holes. When the temperature rose from 25 to 150°C, the hole depth only decreased from 309 to 297 mm and the hole diameter only dropped by 0.4 mm. This indicated a less-than-5% change in hole depth and diameter.

3.2 Effect of Decompression Condition on Hole Diameter and Depth

The experiment gave the hole depth data at different negative pressures, finding that the negative pressure didn't have a significant effect on the depth of deep holes **Figure 4A**. Besides, **Figure 4B** shows the effect of the negative pressure on the sandstone target on the hole diameter. Regardless of the rise in negative pressure, the hole diameter didn't change significantly.

3.3 Effect of Effective Formation Stress on Hole Diameter and Depth

As shown in **Figure 5A**, the hole depth decreased with the increase in the effective stress. With the effective stress on the sandstone target increasing from 20 to 35 MPa, the hole depth reduced by 53 mm (or 15.36%). However, seen from the effective stress-hole diameter correlation curve in **Figure 5B**, the effective stress had a minor effect on the overall hole diameter. An increase in the effective stress caused no significant changes to such diameter.

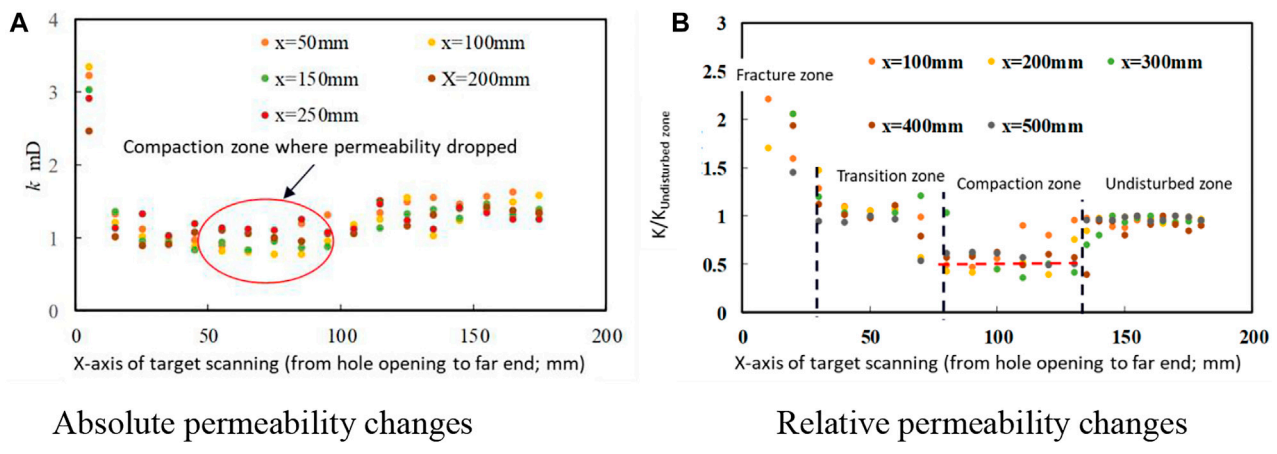

FIGURE 10 | Curve of the directionless axial permeability changes in the radial direction [CN-127-40-UHT-25-5 (150°C)]. **(A)** Absolute permeability changes **(B)** Relative permeability changes

4 POROSITY AND PERMEABILITY DISTRIBUTION CHARACTERISTICS OF THE DAMAGE ZONE IN THE ULTRAHIGH PRESSURE TARGET PERFORATION HOLE

4.1 Acquisition of Rock Porosity and Permeability Planar Distribution Data in Different Parts of the Damage Zone

A core scanner was used to obtain the characteristics of post-perforating changes in target porosity, permeability, sound wave and density. The compaction zones were accurately classified and quantitatively evaluated. Since the different experimental groups have similar permeability distribution, the sandstone targets extracted using the CN-127-40 HT bullet were the case under discussion.

Figure 6 shows the permeability of the sandstone specimen. For the purpose of scanning, a longitudinal section was cut off manually from the specimen. The permeability distribution was obviously zone-specific. To put it alternatively, there is an obvious high-permeability zone (fracture zone) and an obvious low-permeability zone (compaction zone) along the axis of the hole. By permeability distribution characteristics, the sandstone target was divided into the fracture zone, the transition zone, the compaction zone, and the undisturbed zone.

Core scanning returned the permeability values of the points, lines and planes as well as P-wave and S-wave velocity. Based on rock density and porosity, the P-wave and S-wave velocity measurements found the rock density and porosity typical of four bullet types. Then the density, porosity and permeability of the sandstone target were derived in the cloud diagram (**Figure 7**).

4.2 Planar Distribution Characteristics of Rock Porosity and Permeability in the Damage Zone of the UHT Target Hole

A cluster analysis of the planar distribution characteristics and sandstone target permeability test data found results of the target, perforating process and zone-specific cluster analysis. A column chart showing zone area percentages was also obtained.

4.2.1 Planar Distribution Characteristics of UHT Target Porosity

The cluster analysis was successfully made to automatically classify the target, perforated with the CN-127-40-HT-25-5 (150°C) bullet, into zones based on permeability. Such parameters served to obtain the transverse wave and lengths of the zones, from which the thicknesses were obtained. The analytical findings show that the fracture zone accounts for 8.3% of the scanned area of the target, the transition zone accounts for 8.5% of the scanned area, and the compaction zone accounts for 24.2% of the scanned area. As shown in **Figure 8**, the average thickness of the fracture zone is 15.27 mm and the average thickness of the compaction zone is 44.53 mm.

4.2.2 Planar Permeability Distribution Characteristics of UHT and HT Targets

Based on the studies of the target's planar characteristics, this paper further analyzed the target's changes in the radial/dimensionless permeability along the hole at different positions (**Figures 9**, **10**). According to the figures, the radial/dimensionless permeability dropped from high (in the fracture zone) to low (in the compaction zone), and then rose to flat (in the undisturbed zone). Based on permeability change characteristics, the permeability values of different zones were determined. Then the average permeability was used to determine the permeability damage rate of the holes to be 44%.

5 CONCLUSION

This paper involves sandstone cores extracted from the 3rd section of the Zhuhai Formation to study the multidimensional porosity characteristics of the damage zone in sandstone target holes in different reservoir conditions. A physical simulation experiment with large-size perforation holes was conducted using various variables, such as temperature, negative pressure and effective formation stress. Then a core porosity and permeation analysis was conducted to find the planar distribution characteristics of porosity and permeation of the cores.

The study has led to the following conclusion.

Judging from the macroscopic parameters of the perforated sandstone targets, temperature has a minor effect on the hole depth and diameter, with only a change of. The negative pressure also has a small effect on the hole depth and diameter. As the effective stress increases, the depth of the hole made by CN_127-40- HT bullet reduced by 15.36% (equal to 53 mm). Overall, the effective formation stress has a small effect on hole diameter.

Microscopically, the planar distribution of the hole porosity and permeation demonstrates is obviously zone-specific. There are four zones: the fracture zone, the transition zone, the compaction zone and the undisturbed zone.

Along the radial direction of the holes, the radial/dimensionless permeability drops from high (in the fracture zone) to low (in the compaction zone), and then rose to even (in the undisturbed zone). Calculations find that permeability damage rate of the holes is 44%.

DATA AVAILABILITY STATEMENT

The original contributions presented in the study are included in the article/Supplementary Material, further inquiries can be directed to the corresponding author.

AUTHOR CONTRIBUTIONS

HL has completed the ideas and research goals and aims, as well as conduct the data curation and the original Draft. CX has done the validation of experiments and the review and editing or the draft. SG has done the formal analysis and the supervision of experiments.

REFERENCES

Grove, B., DeHart, R., McGregor, J., Dennis, H., and Christopher, C. (2019). "Operators Optimize High-Pressure/High-Temperature and Ultrahigh-Pressure Perforation Strategies Using Laboratory Testing," in Offshore Technology Conference, Houston, Texas, May 2019.

Grove, B., Harvey, J., Zhan, L., and Atwood, D. (2011). "Translating Perforating Laboratory Results to the Downhole Environment," in SPE European Formation Damage Conference, Noordwijk, The Netherlands, June 2011.

Henry, L. (1952). Experimental Evaluation of Well Perforation Methods as Applied to Hard limestone. *Pet. Trans.* 4, 163–168.

Huang, H. (2012). Effects of High Pressure Strength of Rock Material on Penetration by Shaped Charge Jet. *AIP Conf. Proc.* 1426, 1153. doi:10.1063/1.3686484

Karacan, C. Ö., and Halleck, P. M. (2003). Comparison of Shaped-Charge Perforating Induced Formation Damage to Gas- and Liquid-Saturated sandstone Samples. *J. Pet. Sci. Eng.* 40, 61–75. doi:10.1016/s0920-4105(03)00084-6

Saucier, R. J., and Lands, J. F. (1978). A Laboratory Study of Perforations in Stressed Formation Rocks. *J. Pet. Technol.* 30, 1347–1353.

Snider, P. M., Walton, I. C., Skinner, T. K., and Atwood, D. C. (2008). First Laboratory Perforating Tests in Coal Show lower-Than-expected Penetration. *SPE Drilling & Completion* 23, 93–99. doi:10.2118/102309-MS

Zhu, H. Y., Deng, J., Jin, X., Hu, L., and Luo, B. (2015). Hydraulic Fracture Initiation and Propagation from Wellbore with Oriented Perforation. *Rock Mech. Rock Eng.* 48 (2), 585–601. doi:10.1007/s00603-014-0608-7

Zhu, H. Y., Deng, J. G., Chen, Z. J., An, F. C., Liu, S. J., Peng, C. Y., et al. (2013). Perforation Optimization of Hydraulic Fracturing of Oil and Gas Well. *Geomech. Eng.* 5 (5), 463–483. doi:10.12989/gae.2013.5.5.463

Zhu, H. Y., Deng, J. G., Liu, S. J., Wen, M., Peng, C. Y., Li, J. R., et al. (2014). Hydraulic Fracturing Experiments of Highly Deviated Well with Oriented Perforation Technique. *Geomech. Eng.* 6 (2), 153–172. doi:10.12989/gae.2014.6.2.153

Conflict of Interest: Author HL and SG are employed by CNOOC (China) Co. Ltd.

The remaining authors declare that the research was conducted in the absence of any commercial or financial relationships that could be construed as a potential conflict of interest.

frontiers in Earth Science

ORIGINAL RESEARCH
published: 04 March 2022
doi: 10.3389/feart.2022.786290

A Fractal Model for Effective Thermal Conductivity in Complex Geothermal Media

Yan Zeng, Bingyu Ji, Ying Zhang, Jianyun Feng, Jun Luo and Mingchuan Wang*

Sinopec Petroleum Exploration and Production Research Institute, Beijing, China

Thermal conductivity is an important macroscopic thermo-physical parameter due to its significant effects on the temperature field distribution and heat flow magnitude in the material at heat conduction equilibrium. However, because of the extremely complex pore structure and disordered pore distribution, a well-accepted relationship between effective thermal conductivity (ETC) and geometric structural parameters is still lack. In this study, a novel fractal model with variation pore diameter is established systematically based on the assumption that the rough elements of wall surface, pore size distribution and capillary tortuosity follow the fractal scaling law. Thermal-electrical analogy is introduced to predict the ETC of unsaturated geothermal media. The proposed model explicitly relates the ETC to the microstructural parameters (relative roughness, porosity, fractal dimensions and radius fluctuation amplitude) and fluid properties. The proposed model is validated by comparing with existing experimental data. A parametric analysis is performed for presenting the effects of the structural parameters and fluid properties on the ETC. The results show that pore structure has significant effect on ETC of unsaturated porous media. ETC gradually decreases with the increment of porosity, relative roughness, and fractal dimensions. The present study improves the accuracy in predicting ETC and sheds light on the heat transfer mechanisms of geothermal media.

Keywords: effective thermal conductivity, fractal analysis, capillary bundle model, roughness, mixing law

OPEN ACCESS

Edited by:
Shu Jiang,
The University of Utah, United States

Reviewed by:
Benedikt Ahrens,
Fraunhofer IEG—Fraunhofer Research Institution for Energy Infrastructures and Geothermal Systems, Germany
Yang Zhiqiang,
Harbin Institute of Technology, China
Zilong Deng,
Southeast University, China
Ruyue Wang,
SINOPEC Petroleum Exploration and Production Research Institute, China

****Correspondence:***
Yan Zeng
zengyan.syky@sinopec.com

Specialty section:
This article was submitted to Economic Geology, a section of the journal Frontiers in Earth Science

Received: *30 September 2021*
Accepted: *07 February 2022*
Published: *04 March 2022*

Citation:
Zeng Y, Ji B, Zhang Y, Feng J, Luo J and Wang M (2022) A Fractal Model for Effective Thermal Conductivity in Complex Geothermal Media. Front. Earth Sci. 10:786290. doi: 10.3389/feart.2022.786290

1 INTRODUCTION

Geothermal energy is a non-carbon source of renewable energy based on heat flux from the subsurface of the earth, a reliable and abundant energy source with great potential (Manzella et al., 2018; Noorollahi et al., 2019; Soltani et al., 2021). The heat produced in the earth's mantle is transferred via convection and conduction, of which conduction is the most important process, with an average global output of 1.4×10^{21} J/a (100 times the volcanic eruption, earthquake and hydrothermal activity) (Clauser and Huenges, 1995; Mostafa et al., 2004). The heat conduction process in rock depends on its fabric and can be estimated by the physical mechanisms of the basic transport procedures within the distinct phases of rock media and thermal exchange in an interface (Miao T. et al., 2016; Jia et al., 2019). The defining equation for effective thermal conductivity (ETC) is $\boldsymbol{q} = -k\boldsymbol{\nabla}T$, where $\boldsymbol{q}$ is the heat flux, k is the effective thermal conductivity, and $\boldsymbol{\nabla}T$ is the temperature gradient. This is known as Fourier's Law for heat conduction (e.g., Cahill, 1990). As ETC is a dominant parameter among all the thermal properties of rock, its accurate and efficient prediction is essential. Therefore, it is very meaningful to conduct some in-depth studies to reveal its essential features.

Previous research demonstrated that ETC of heterogeneous rock medium is not only affected by the intrinsic thermal properties of each fluid phase, but also the complicated relationship between the topology and geometry of pore spaces and solid matrix (Ghanbarian and Daigle, 2016). Extensive research has been conducted on ETC of porous media to characterized heat transport through rock and many predictive methods for ETC have been proposed. The ETC models can be categorized into three groups according to the principles and methods employed: 1) theoretical models, 2) empirical models by experimental measurement, and 3) mathematical models via numerical simulation. The theoretical models have been developed via reasonable simplifications for geometrical structures and transfer mechanisms. Various analytical models have been proposed based on classical mixing laws (Tong et al., 2009; Xia et al., 2019a; Lin et al., 2021). Yang et al. (2016) developed a statistical second-order two-scale method to predict heat transfer properties of inhomogeneous random structures. Whereafter, they established a novel three-scale homogenization algorithm to predict heat transfer performance of porous media with periodic configurations (Yang et al., 2018). However, the existing theoretical models have the problem of low accuracy because the complex pore and solid structures have been ignored. *In-situ* testing is the most common method to characterized ETC for shallow rocks and many empirical equations for predicting ETC are obtained by regression analysis of experimental data. Gao and Yu (2007) simplified the G-function of the ground source heat pump and calculated the ETC of surrounding ground. Kwon et al. (2011) investigated the influence of mineral composition, porosity, and saturation on the ETC using the transient flat surface source method. Although a large amount of experimental data may be available, the reported results from different experimental approached often differ significantly and cannot reflect the transmission mechanism (Xia et al., 2019b). With the development of computer technology, many numerical methods have been proposed, such as finite element method (Li et al., 2020), Monte Carlo method (Belova and Murch, 2004), and lattice Boltzmann method (Gupta et al., 2006) to evaluate ETC of porous media. However, these empirical ETC models composed of experimental data and mathematical models usually contain one or more empirical constants, sometimes lacking a clear physical meaning.

It has been experimentally shown that porous media have fractal scale characteristics such as random, scale invariance, and self-affine. First proposed by Mandelbrot (1982), fractal geometry exhibits evident advantages for addressing the complexity structure of porous media, compared with Euclidean geometry (Yu, 2008). Therefore, fractal theory has been successfully used to study the ETC of porous media to account for the effect of microstructure. Yu and Cheng (2002a) proposed a fractal particle chain model for ETC of double dispersion porous media by fractal and thermal-electrical analogy theory. However, scale length of the porous media should be estimated, which can cause inaccuracy. Jin et al. (2016) utilized the self-similar Sierpinski carpet to model the pore structure of autoclaved aerated concrete and built a two-phase fractal model to predict ETC. Miao T. J. et al. (2016) derived an analytical expression for ETC of dual-porosity media. The expression is found to be a function of the fractal dimensions and the microstructural parameters. Xu et al. (2019) determined the relation between ETC and geometric structures of the fractal tree-like branched model and the accuracy of the relationship was evaluated using the experimental data and those calculated by former models. Nevertheless, the effect of roughened surfaces on ETC has not been incorporated by mentioned above models.

In recent years, many researchers began to investigate the effects of rough morphology and wall-fluid interaction on thermal characteristics (Cao et al., 2006; Chakraborty et al., 2019; Qin et al., 2019; Motlagh and Kalteh, 2020). Chen and Zhang (2014) conducted a molecular dynamics simulation of ETC in rough nanochannels to investigate how surface topography, which characterized by the fractal Cantor structure, affects the thermal conductance at liquid-solid interfaces. A novel and effective Gauss model was built to characterize microchannels with roughness was proposed by Guo et al. (2015), and the feasibility of the model was evaluated using other typical models of both 2D and 3D proposed in literature. Askari et al. (2017) incorporated thermal contact resistance between a packing of grains with rough surface into numerical simulation of heat conduction under compressive pressure. The simulation results showed that ETC is enhanced more in the grains with smoother surfaces and lower Young's modulus.

To the best of our knowledge, although there is considerable research has been conducted on the ETC of porous media with either numerical simulations or experiments, these existing models usually contain empirical constants and cannot account for microscopic mechanism. ETC of porous media is strongly influenced by the heterogeneity and randomness of the internal structure. In this study, a new generalized ETC model is proposed based on fractal theory for porous media with self-similar pore size and roughness surface. The proposed fractal model is then validated by published experimental data, and the effect of various geometrical parameters and intrinsic thermal properties are discussed in detail.

2 FRACTAL CHARACTERISTICS OF THERMAL CONDUCTIVITY MODEL FOR POROUS MEDIA

2.1 Fractal Characteristics for Rough Surface

As is reported by Mandelbrot (1982), the cumulative size distribution of the surfaces of porous media have the characteristics of the fractal geometry with the self-similarity and fractional dimensions, and follows the fractal scaling law (Majumdar and Bhushan, 1991):

$$N(\varepsilon \geq \delta) = (\delta_{\max}/\delta)^{D}, \tag{1}$$

where D is the fractal dimension for particles, δ is diameter, N is the cumulative number of particles of size equal to and greater

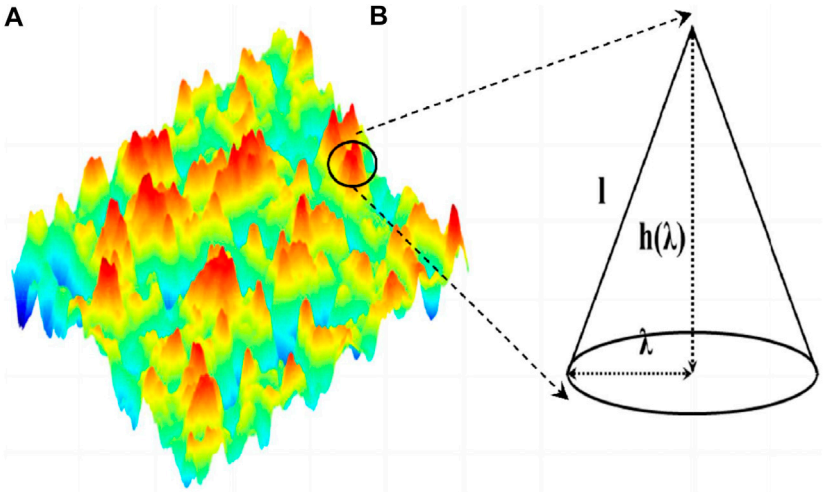

FIGURE 1 | Schematic illustrations of the rough surface. **(A)** A real surface with random character; **(B)** A representative cone-like rough element.

than δ, ε is the length scale. The number of particles whose sizes lying in an infinitesimal range of δ and $\delta + d\delta$ is

$$-dN = D\delta_{max}^{D}\delta^{-(D+1)}d\delta, \tag{2}$$

and the probability density function for particles is (Yu and Li, 2001)

$$f(\lambda) = D\delta_{min}^{D}\delta^{-(D+1)}. \tag{3}$$

In general, many researchers considered the rough elements as cones and each cone has a constant ration ξ of height h to base diameter d (Cai et al., 2010; Yang et al., 2014; Guo et al., 2015). In this study, we assume that every cone does not overlap each other (**Figure 1**). Moreover, the height of cones is also assumed to follow the fractal scaling law **Eq. 4**. The relevant equations are also applicable as long as the relevant symbols are properly replaced by cone parameters (e.g. δ_{min} and δ_{max} are changed by the minimum cone base diameter d_{min} and the max cone base diameter d_{max}, respectively).

The base area fractal dimension, which is similar to that for particles, and the same symbol D is used, can be expressed as (Yu et al., 2009)

$$D = D_E - \ln\varphi/\ln\alpha, \tag{4}$$

where D_E is the Euclidean dimension ($D_E = 2$ in 2D and $D_E = 3$ in 3D), φ is the ratio of the total base area of rough elements to the pore surface area. For the sake of simplicity, we define $\alpha = d_{min}/d_{max}$. Due to the normalization condition, Yu and Li (2001) argued the fractal criterion holds approximately, when $\alpha \le 10^{-2}$. The fractal dimension D lies within the range $0 \le D \le 2$, as $D = 0$ means that there is no rough elements on a surface, and $D = 2$ corresponds to an extremely rough surface, which rough elements covers the whole surface.

As shown in **Figure 1**, total base area of rough elements A_r and the total volume of all rough elements V_r can be obtained by an integration of all diameters from d_{min} to d_{max}:

$$A_r = -\int_{d_{min}}^{d_{max}} A_i dN = -\int_{d_{min}}^{d_{max}} \frac{\pi d_i^2}{4} dN = \frac{\pi D d_{max}^2 (1-\varphi)}{4(2-D)}, \tag{5}$$

$$V_r = -\int_{d_{min}}^{d_{max}} V_i dN = -\int_{d_{min}}^{d_{max}} \frac{\pi d_i^3}{12}\xi dN = \frac{\pi\xi d_{max}^3 (1-\alpha^{3-D})}{12(3-D)}. \tag{6}$$

Based on **Eq. 5**, the surface area of a capillary A_{cs} can be given as

$$A_{cs} = \frac{A_r}{\varphi} = \frac{\pi D d_{max}^2 (1-\varphi)}{4(2-D)\varphi}. \tag{7}$$

Combing **Eqs 7**, **8**, the average height of rough elements $\bar{h}$ is calculated by

$$\bar{h} = \frac{V_r}{A_{cs}} = \frac{\xi\varphi d_{max}(2-D)(1-\alpha^{3-D})}{3(3-D)(1-\varphi)}. \tag{8}$$

The porous media can be considered as a bundle of tortuous capillaries with variable cross-section area (see **Figure 2**). Consistent with the former derivation, the mean diameter λ distribution for a capillary channel has a similar form with **Eq. 2**,

$$-dN = D_f\lambda_{max}^{D_f}\lambda^{-(D_f+1)}d\lambda, \tag{9}$$

where λ_{max} is the maximum mean capillary diameter, D_f is the capillary fractal dimension, which can be expressed as

$$D_f = D_E - \frac{\ln\phi}{\beta}, \tag{10}$$

where ϕ is the porosity, $\beta = \lambda_{min}/\lambda_{max}$ and λ_{min} is the minimum mean capillary diameter. Hence, the relative roughness γ in a single capillary can be written as

$$\gamma = \frac{2\bar{h}}{\lambda}. \tag{11}$$

It is assumed that each capillary in porous media has identical relative roughness. Thus, **Eq. 11** can be rewritten as

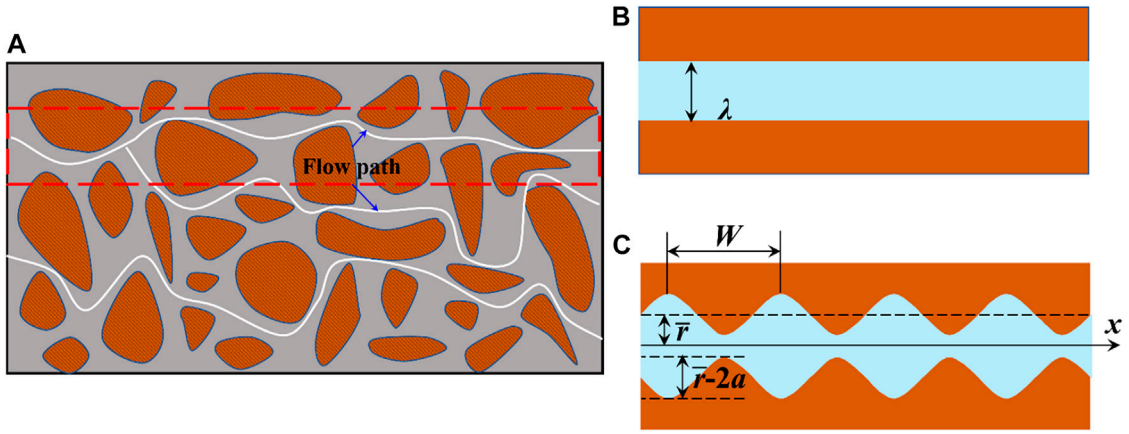

FIGURE 2 | Schematic diagram of porous media. **(A)** 2D structure of porous media; **(B)** Cross-section of the capillary with a constant diameter; **(C)** Cross-section of the capillary with sinusoidal periodically constricted boundary.

$$\frac{(h_{\max})_{\lambda_{\min}}}{(h_{\max})_{\lambda}} = \frac{\lambda_{\min}}{\lambda}, \tag{12}$$

where $(h_{\max})_{\lambda\min}$ is the maximum height of rough element in the minimum capillary and $(h_{\max})_{\lambda}$ is the maximum height of rough element in a capillary which the diameter is λ. Combining **Eqs 8**, **11**, **12**, the relative roughness can be given as follows:

$$\gamma = \frac{2\varphi (h_{\max})_{\lambda_{\min}} (2-D)\left(1-\alpha^{3-D}\right)}{3\lambda_{\min}(3-D)(1-\varphi)}. \tag{13}$$

In **Eq. 13**, the relative roughness is described as an expression of geometrical parameters and each parameter has a physical meaning. The effective capillary diameter λ_e, which fluid can occupy, is expressed as $\lambda_e = (1 - \gamma)\,\lambda$.

Fractal Model for Porous Media

Although porous media model has been studied extensively, the complex geometric structure has been always simplified as capillaries with a constant diameter (Liu et al., 2018; Xiao et al., 2020), as shown in **Figure 2B**. However, the actual porous structure has different pore size, including pores with large diameter and throat with small diameter (Wang et al., 2019; Chen et al., 2020). Therefore, we proposed a porous media model with varying diameters (**Figure 2C**). In this paper, the uniform capillary is improved into a capillary with parallel, curved, and sinusoidal periodically constricted boundary. The profile of the capillary can be represented by **Eq. 14**

$$r(x) = \bar{r}\left(1 + a\sin\frac{2\pi}{W}x\right), \tag{14}$$

where $\bar{r} = \lambda_e/2$ denotes the mean radius. Due to the tortuous nature of actual porous media, the capillary length is not less than L_0 and can be obtained according to the capillary tortuosity (Yu and Ping, 2002; Yu and Li, 2004),

$$L_t(\lambda) = \lambda^{1-D_T} L_0^{D_T}, \tag{15}$$

where $L_t(\lambda)$ is the actual length of capillary, D_T is the tortuosity fractal dimension for capillary, which can describe the tortuous degree of the capillary quantitatively. The value of D_T is in the scope $1 < D_T < 2$ and $1 < D_T < 3$ in 2D and 3D space, respectively. When $D_T = 1$, it means a straight capillary, while it corresponds to a highly tortuous capillary that complete fills the space for $D_T = 2$ (or 3). As the tortuosity fractal is difficult to determine by experiment, the following approximate formula is used in this paper (Wei et al., 2015).

$$D_T \approx (D_E - D_f + 1) + (D_E - D_f)\frac{\log D_f - \log(D_f - 1)}{\log\phi}. \tag{16}$$

Similarly with **Eq. 5**, integrate λ from $\lambda_{\min}$ to $\lambda_{\max}$, the cross-section area of porous media A_p can be obtained by

$$A_p = \frac{\pi D_f (1-\phi)}{4\phi(2-D_f)}\lambda_{\max}^2. \tag{17}$$

Assume the porous media is cylinder-shaped, the fractal dimension characteristic length L_0 is given as

$$L_0 = \sqrt{\frac{4A_p}{\pi}} = \sqrt{\frac{D_f(1-\phi)}{\phi(2-D_f)}}\lambda_{\max}. \tag{18}$$

On the other hand, according to the periodicity of sinusoidal profile, the volume V_{sc} of the single constricted capillary is approximately expressed as

$$V_{sc} = \int_0^{L_t} \pi r^2(x)dx = \frac{L_t}{W}\int_0^W \pi\left[\bar{r}\left(1 + a\sin\frac{2\pi}{W}x\right)^2\right]dx$$

$$= \frac{\pi(1-\gamma)^2}{8} L_0^{D_T}\lambda^{3-D_T}(2+a^2). \tag{19}$$

Fractal Model for Saturation

As we all know, the geothermal system may be two-phase before production or may evolve into a two-phase system because of fluid production. The fluid tends to flow without lateral mixing, and there are no cross-currents perpendicular to the direction of flows, nor

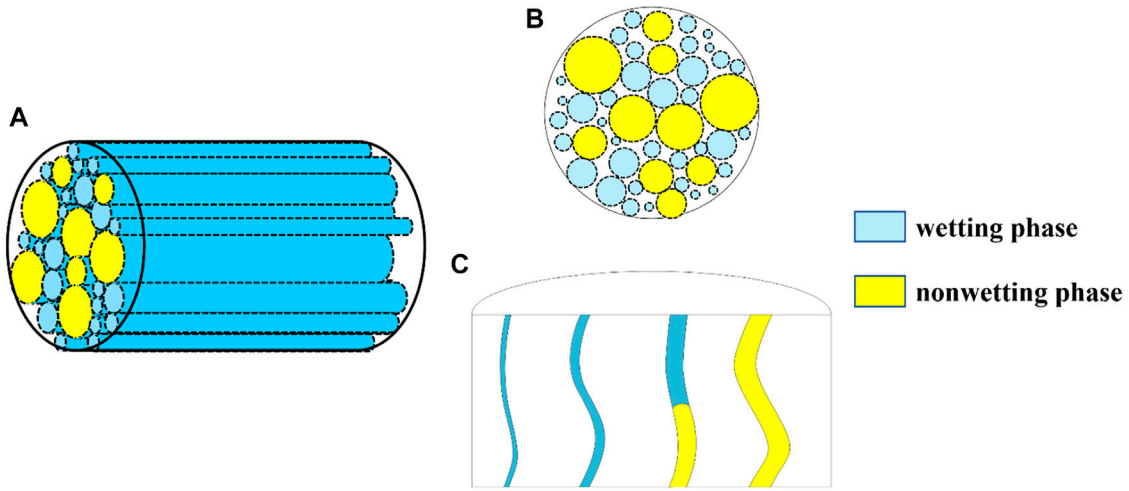

FIGURE 3 | A schematic diagram of fractal capillary bundle model of porous media. **(A)** 3D structure; **(B)** transverse view; **(C)** longitudinal view.

eddies or swirls of fluid (Geankoplis et al., 2018). To force the nonwetting phase to displace the wetting phase in capillary, the extra pressure required to be greater than the capillary pressure. Based on the Young-Laplace equation, the capillary pressure can be estimated by $p_c = 4\sigma\cos\theta/\lambda$, where σ is the interfacial tension, θ is the wetting angle of the liquid on the surface of the capillary. The equation shows that the smaller the capillary diameter, the greater the pressure. Thus, there is a critical capillary diameter λ_c, at which leads the capillary pressure equals to the extra pressure, for porous media (**Figure 3**). The critical capillary diameter can be estimated by $\lambda_c = 4\sigma\cos\theta/\Delta p$, where Δp is the extra pressure. When $\lambda < \lambda_c$, it means that the capillary pressure is greater than the total extra pressure, and all the capillaries that meet the condition are fully saturated with the wetting fluid. Contrarily, the extra pressure breaks through the capillary pressure, allowing the nonwetting phase to enter the capillary, the capillary diameter will be $\lambda \geq \lambda_c$. At this situation, all corresponding capillaries are occupied by the nonwetting phase.

Based on the above analysis, we assume that the orientation of capillaries was approximately taken to be perpendicular to the cross section of the porous media, and the capillary pressure is dependent on the mean diameter, regardless of the varying radius. Then, the wetting fluid saturation on the cross section of the porous media can be gotten as

$$Sw = \frac{\int_{\lambda_{min}}^{\lambda_c} V_{sc} dN}{\int_{\lambda_{min}}^{\lambda_{max}} V_{sc} dN} = \frac{\lambda_c^{3-D_T-D_f} - \lambda_{min}^{3-D_T-D_f}}{\lambda_{max}^{3-D_T-D_f} - \lambda_{min}^{3-D_T-D_f}}. \quad (20)$$

The Critical Capillary Diameter λ_c Is Determined by

$$\lambda_c = \left[\left(1 - \phi^{(3-D_T-D_f)/(2-D_f)}\right)Sw + \phi^{(3-D_T-D_f)/(2-D_f)}\right]^{\frac{1}{3-D_T-D_f}}\lambda_{max}. \quad (21)$$

Fractal Model for Effective Thermal Conductivity

The heat flow can be modelled by analogy to an electrical circuit where heat flow is represented by current, temperatures are represented by voltages, and thermal resistances are represented by resistors (Swift et al., 2001). According to the Fourier's law (e.g., Nunziato, 1971; Cahill, 1990), the thermal conductivity can be obtained (Fraisse et al., 2002)

$$dR = \frac{dx}{A_c k} = \frac{L_t}{\pi \bar{r}^2 \left(1 + a\sin\frac{2\pi}{W}x\right)^2 k}, \quad (22)$$

where k is the thermal conductivity, A_c is the cross-section area of a single capillary. Since the actual length of a single capillary satisfies $L_t(\lambda) \gg W$, the thermal resistance can be obtained by directly integrating **Eq. 22**

$$R(\lambda) = \frac{L_t}{W}\int_0^W \frac{dx}{\pi \bar{r}^2 \left(1 + a\sin\frac{2\pi}{W}x\right)^2 k} = \frac{2L_t}{k\pi^2(1-\gamma)^2\lambda^2}\int_0^{2\pi}\frac{dx}{(1+a\sin x)^2}. \quad (23)$$

According to table of integrals (Gradshteyn and Ryzhik, 2014), the definite integrals on the right-hand side of **Eq. 23** can be calculated as

$$\int_0^\pi \frac{dx}{(a+b\cos x)^{n+1}} = \sum_{k=0}^{n}\frac{(2n-2k-1)!!\,(2k-1)!!}{(n-k)!k!}\left(\frac{a+b}{a-b}\right)^k. \quad (24)$$

Then the thermal resistance of a single channel filled with nonwetting, and wetting phase can be respectively expressed as

$$R_{nw}(\lambda) = \frac{4L_0^{D_T}}{k_{nw}\pi(1-\gamma)^2(1-a^2)^{3/2}\lambda^{D_T+1}}, \quad (25)$$

$$R_w(\lambda) = \frac{4L_0^{D_T}}{k_w\pi(1-\gamma)^2(1-a^2)^{3/2}\lambda^{D_T+1}}, \quad (26)$$

TABLE 1 | Properties of rock-forming minerals.

	Albite	Orthoclase	Calcite	Quartz	Anhydrite
Thermal conductivity (W/m·K)	2.14	2.31	3.59	7.69	4.76
Density (kg/m^3)	2.62	2.57	2.70	2.65	2.96

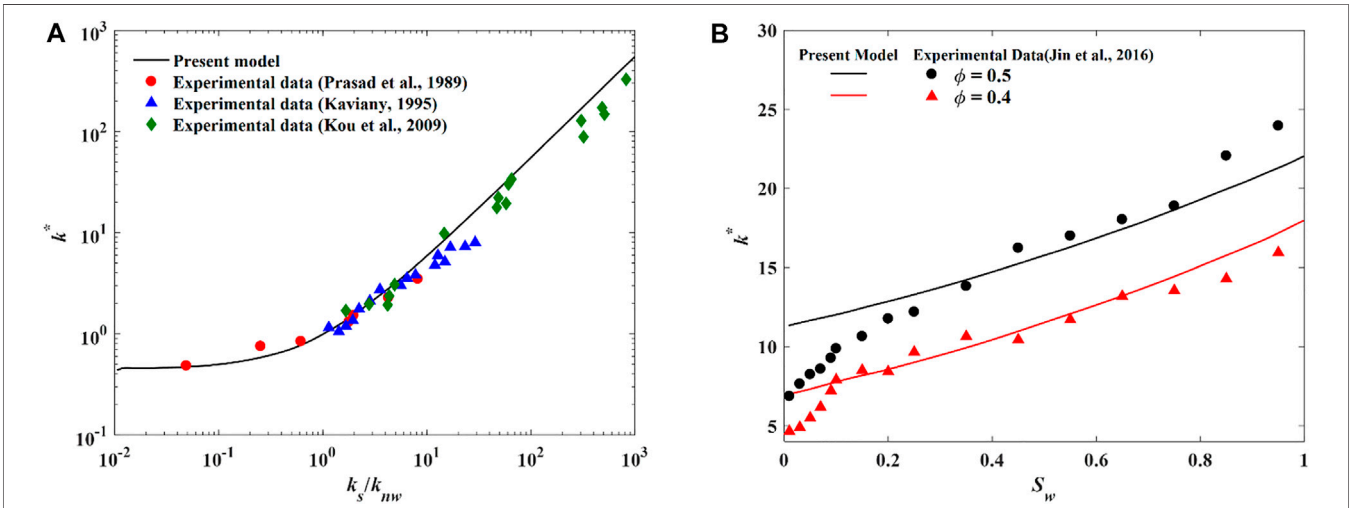

FIGURE 4 | The comparison between proposed model prediction and experimental data. **(A)** k_s/k_{nw} vs. k^*; **(B)** S_w vs. k^*.

where k_{nw} and k_w are the thermal conductivity of nonwetting and wetting phase, respectively. The total thermal conductivity for each phase can be given as

$$\frac{1}{R_{nwt}} = -\int_{\lambda_c}^{\lambda_{max}} \frac{1}{R_{nw}(\lambda)} dN, \tag{27}$$

$$\frac{1}{R_{wt}} = -\int_{\lambda_{min}}^{\lambda_c} \frac{1}{R_w(\lambda)} dN. \tag{28}$$

Combining **Eqs 9**, **25–28**, the total thermal resistance for nonwetting R_{nwt} and wetting R_{wt} in capillary can be written as

$$R_{nwt} = \frac{4L_0^{D_T}(1+D_T-D_f)}{k_{nw}\pi(1-\gamma)^2(1-a^2)^{3/2}D_f\lambda_{max}^{1+D_T}\left[1-(\lambda_c/\lambda_{max})^{1+D_T-D_f}\right]}, \tag{29}$$

$$R_{wt} = \frac{4L_0^{D_T}(1+D_T-D_f)}{k_w\pi(1-\gamma)^2(1-a^2)^{3/2}D_f\lambda_{max}^{1+D_T}\left[(\lambda_c/\lambda_{max})^{1+D_T-D_f}-(\lambda_{min}/\lambda_{max})^{1+D_T-D_f}\right]}. \tag{30}$$

The solid phase thermal resistance of porous media can be obtained as

$$R_s = \frac{L_0}{(1-\phi)Ak_s}, \tag{31}$$

where k_s is the thermal conductivity of solid phase. The total ETC of porous media can be calculated as

$$k_e = \frac{L_0}{A_p}\frac{1}{R_t} + k_s = \frac{L_0}{A_p}\left(\frac{1}{R_{nwt}} + \frac{1}{R_{wt}} + \frac{1}{R_s}\right), \tag{32}$$

where R_t is the total thermal resistance.

Substitution of **Eqs 17**, **29** and **Eq. 33** into **Eq. 32** obtains the ETC of porous media,

$$k_e = (1-\phi)k_s + \frac{(1-a^2)^{3/2}(1-\gamma)^2(2-D_f)\phi\lambda_{max}^{D_T-1}}{(1+D_T-D_f)(1-\phi)L_0^{D_T-1}}\left[k_{nw} - (k_{nw}-k_w)\left(\frac{\lambda_c}{\lambda_{max}}\right)^{1+D_T-D_f} - k_w\phi^{\frac{1+D_T-D_f}{2-D_f}}\right] \tag{33}$$

It can be seen from **Eq. 33** that the ETC is a function of porosity, fractal dimensions for capillary and tortuosity, relative roughness, characteristic length, maximum capillary diameter, radius amplitude, and wetting phase saturation. Each parameter in the proposed theoretical model has a specific physical meaning and can by determined by experiments. Consequently, it is conveniently to estimate ETC of porous media with this model.

3 MODEL VALIDATION AND COMPARISON

Method to Establish Parameters

In order to validate the proposed model, the parameters involved in **Eq. 33** should be obtained at first. In this study, they are established as follows.

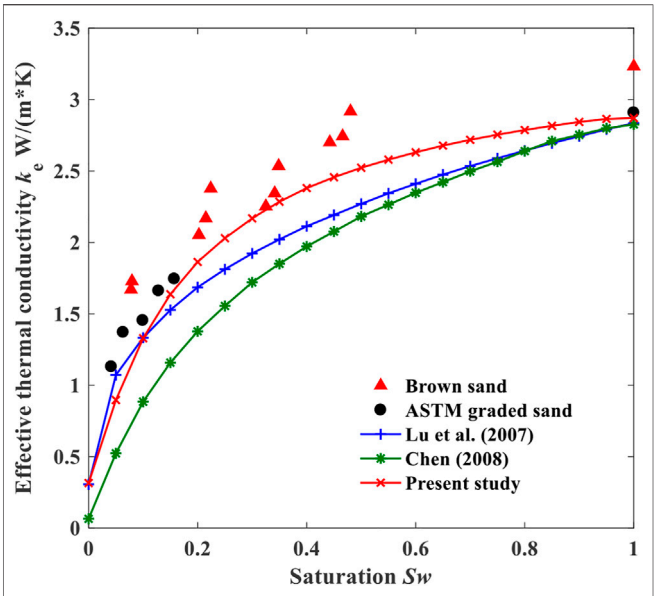

FIGURE 5 | Comparison of the present model with other models.

3.1.1 The Thermal Conductivity

The thermal conductivity of fluid can be calculated by several comprehensive equations, which is mainly influenced by many factors such as the density, temperature, pressure, and viscosity (Tsilingiris, 2008; Zhou et al., 2016). Here, we adopted constant nominal values to simplify the calculation: k_w = 0.607 W/(mK) and k_{nw} = 0.026 W/(mK) (Giraud et al., 2015).

The thermal conductivity of solid is dependent on mineral particles of rocks and can be calculated using the following expression (Tang et al., 2008):

$$k_s = \prod_{i=1}^{n} k_i^{\varsigma_i}, \tag{34}$$

where k_i and ς_i are the thermal conductivity and volume fraction of i'th mineral. To obtain ς_i, the following transform expression is applied:

$$\varsigma_i = \frac{m_i}{\rho_i \sum_1^n m_i/\rho_i}, \tag{35}$$

where, m_i is the mass fraction of i'th mineral, which can be get from X-ray diffraction (XRD) analysis, ρ_i is the density of i'th mineral. Besides, the properties of rock-forming minerals is also presented in **Table 1** according to Tang et al. (2008). In this study, the thermal conductivity k_s is calculated as: k_s = 1.322 W/(mK).

3.1.2 The Pore Structure Parameter

Because the maximum height of the rough element to the base diameter should approximately satisfy $0.12 < \xi < 0.17$ (Li, 2003), a value of ξ = 0.15 is adopted in the following analysis, and $(h_{max})_{\lambda min}/\lambda_{min}$ = 0.05 is set. The ratio of the total base area of rough elements to the surface area of capillary φ = 0.2 is suggested for simplification by Cai et al. (2014). In fractal geometry, box-counting dimension is a way of determining the fractal dimension of a set S in a Euclidean space $\mathbf{R}^n$ (Li et al., 2009). Based on cross-section photograph imaged by scanning electron microscope, box-counting dimension and real streamline through samples are obtained to calculate capillary fractal dimension and tortuosity fractal dimension (Yu, 2008; Xu, 2015). In this paper, we estimate fractal dimensions using **Eqs 4**, **10**, **16** for simplification. As a statistically self-similar fractal object, the minimum size is much less than the maximum size. According to the criterion for fractal analysis, the scale ratio (α and β) is set to 10^{-3} by Yu and Cheng (2002b). Furthermore, the relative roughness can be predicted by geometric parameters according to **Eq. 13**.

Model Validation

Inserting geometric parameters, fractal dimensions, relative roughness, saturation, and thermal conductivity of each phase into **Eq. 33**, the ETC of samples can be obtained accordingly. **Figure 4A** presents the comparison between the predicted ETC (Sw = 1 in **Eq. 33**) and experimental data for two-phase saturated porous media at the porosity of 0.4 (Prasad et al., 1989; Kooi, 2008; Kaviany, 2012). In order to eliminate the dimensional effect, the dimensionless ETC is defined by $k^* = k_e/k_{nw}$. From **Figure 4A**, it is clear that the proposed model prediction is in good agreement with the experimental data, especially when the dimensionless of thermal conductivity for solid is between 1 and 10.

Another comparison of dimensionless ETC between the proposed model and experimental results of unsaturated porous media by Jin et al. (2016) is shown in **Figure 4B**. It must be pointed out that there is slightly overprediction at low saturation and shows acceptable prediction at high saturation. The experimental results have a critical saturation, which is around 0.15 for this case. Under the critical saturation, the dimensionless ETC increases rapidly with the increase of Sw. However, the increase rate decreases significantly when Sw is bigger than the critical saturation. We speculate that this might be due to the connectivity of the wetting phase. At low saturation, the wetting phase tends to be absorbed on the surface of pores and cannot lead to a continuous path from the inlet to outlet. Thus, as the increase of Sw, the wetting phase occupies more pores space and creates conducting bridges between the pores, which can enhance heat transfer sharply. However, a path of least resistance for heat transfer is formed at relatively high Sw, wetting phase becomes the main heat conduction medium. At this situation Sw shows marginal effect. The proposed model fails out to catch this phenomenon due to the capillary bundle model cannot represent connectivity. Nonetheless, it is apparent that our model shows reasonable prediction for ETC of saturated and unsaturated porous media.

Comparison With Other Models

On the basis of the previous validation, we adopt the proposed model and other models to calculated ETC for quartz sand and also conducted a comparison of the predicted results with experimental data in literature. Considering the large amount of quartz existing in sand samples, k_s = 7.5 W/(mK), as suggested by Chen (2008). The average porosity of 0.4 is used in all the models. **Figure 5** plots the variations of the ETC with saturation

TABLE 2 | Default values of the parameters.

Parameters	k_s (W/m·K)	k_w (W/m·K)	k_{nw} (W/m·K)	γ	a	ϕ
Values	3.78	0.63	0.08	0.036	0.1	0.1

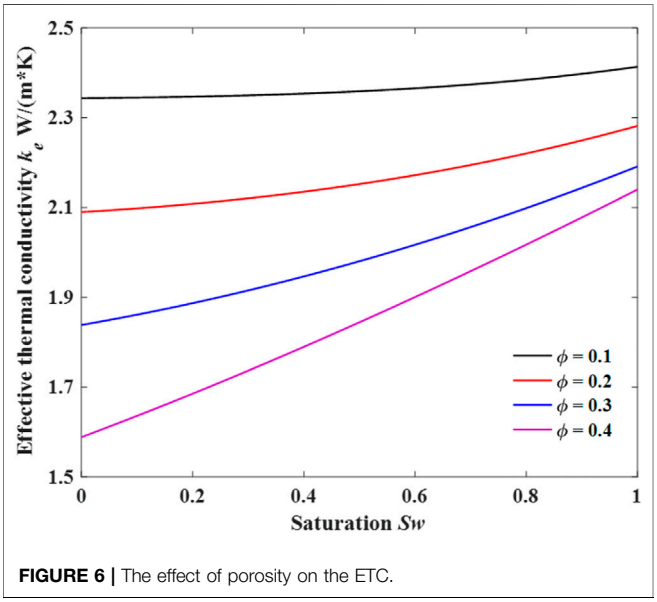

FIGURE 6 | The effect of porosity on the ETC.

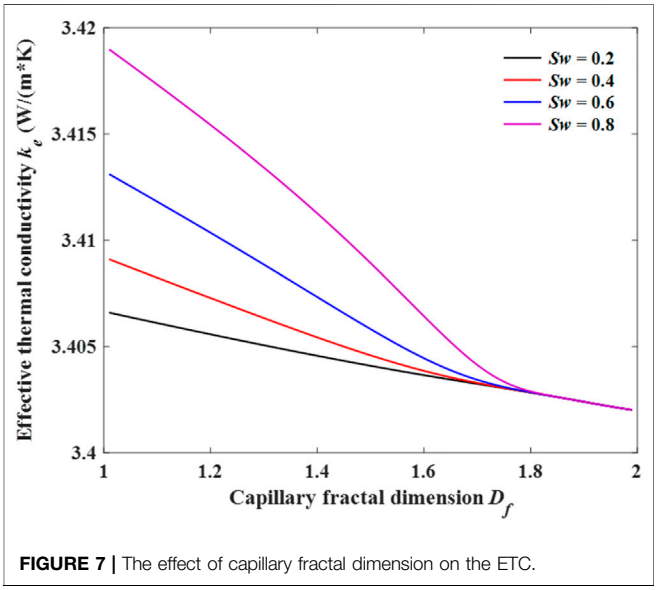

FIGURE 7 | The effect of capillary fractal dimension on the ETC.

under constant porosity value. Also plotted in the figure are the predictions by Chen's series-parallel model (Chen, 2008) and Lu's medium theory model (Lu et al., 2007). It is obvious that the Chen's model and Lu's model estimates almost evolve in the same manner with saturation, and the present model mostly predicting slightly larger values. When compared with the experimental data, all of the other models underestimated the ETC. The proposed model can certainly show better agreement than other models.

4 SENSITIVITY ANALYSIS AND DISCUSSION

The effect of some key parameters in the proposed ETC model are discussed and, in this way, the understanding of the proposed model can be improved. The default values of the parameters in the following analysis are shown in **Table 2**.

Effects of Saturation

Figure 6 shows the relationship between the ETC and porosity under different water saturation. The results confirm that the ETC decreases significantly with increasing porosity. This is attributed to the decrease of solid phase. Additionally, the ETC will increase as *Sw* increases under large porosity. It is important to note, that the evidence relies on the thermal conductivity of wetting phase is much larger than that of the nonwetting phase. However, the ETC at different saturations is almost equal when the porosity is low (<~0.10). For deep geothermal resources, even after a special reservoir rock simulation process, the porosity is still very low. So geothermal fluid has little effect on ETC at this situation.

Effects of Fractal Dimension

The effect of capillary fractal dimension D_f on ETC under difference water saturation at constant tortuosity fractal dimension (D_T = 1.5) is shown in **Figure 6**. As can be seen from **Figure 6**, the ETC decreases obviously with the increment of fractal dimension D_f. The capillary fractal dimension describes the complexity of pore structure, and it increases continuously as the complicacy of pore increases. According to **Eq. 10**, a higher fractal dimension means a higher pore size range. A widely pore size distribution increases the contact area between geothermal fluid and pore surface, which can weaken the thermal resistance and according lower ETC. Although, the ETC decreases faster under a higher saturation, the difference of ETC caused by saturation disappears with the increase of fractal dimension. The present results are consistent with the work by Shen et al. (2020). They also demonstrate a lower ETC by increase of pore fractal dimension.

Figure 8 shows the effect of tortuosity fractal dimension on the ETC. Tortuosity fractal dimension has been used to quantify tortuosity. The value of tortuosity fractal dimension in 2D for a straight line is 1 and ranges up to 2 for a plane-filling curve. From the figure we can see that the tortuosity fractal dimension can lower the ETC. A possible explanation for this might be that a higher tortuosity fractal dimension means higher tortuosity, which directly increases the flow path of geothermal fluids in porous media and reduces the

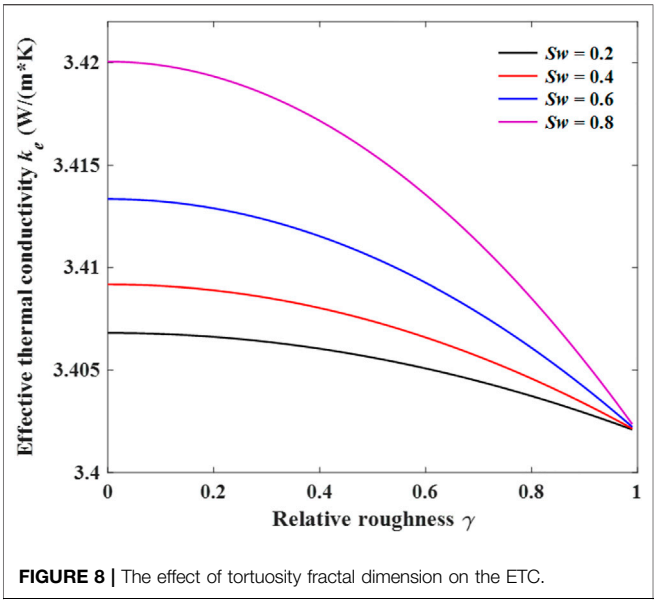

FIGURE 8 | The effect of tortuosity fractal dimension on the ETC.

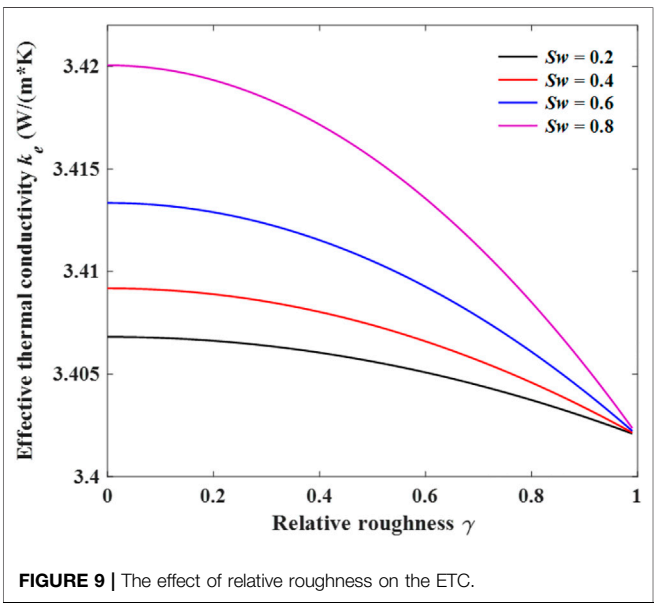

FIGURE 9 | The effect of relative roughness on the ETC.

distance of heat transport through tortuous capillaries, thus leading to a decrease of ETC for porous media.

Effects of Structural Parameters

Figure 9 illustrates the influence of relative roughness on ETC at a different saturation when the porosity equals 0.1. In **Figure 8** there is a clear trend of decreasing ETC of porous media with the increase of relative roughness. This relationship may partly be explained by the increase of heat transfer in capillaries as the decrease of surface area. In addition, the figure also shows that the ETC increases with an increase in saturation, since higher saturation indicates higher wetting volume fraction of higher thermal conductivity, leading to a decrease in thermal resistance.

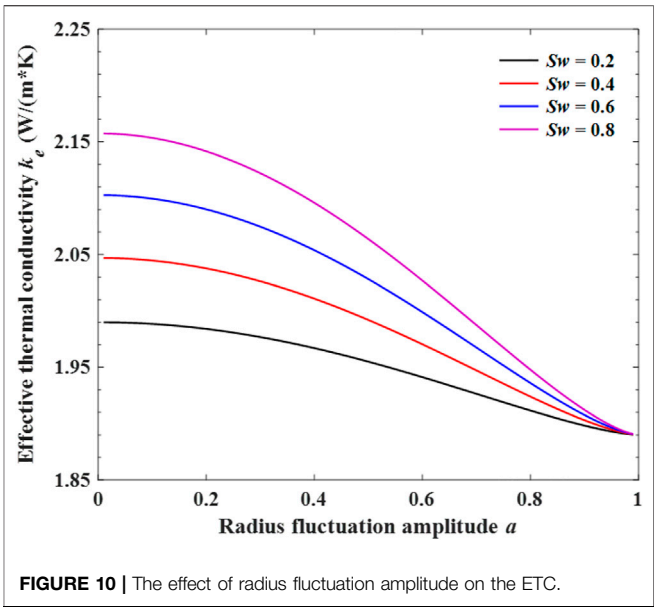

FIGURE 10 | The effect of radius fluctuation amplitude on the ETC.

Figure 10 shows the effect of radius fluctuation amplitude on the ECT, when capillary fractal dimension is D_f = 1.8 and tortuosity fractal dimension is D_T = 1.2. Closer inspection of the figure shows radius fluctuation amplitude has a significant influence on the ETC. With the increase of radius fluctuation amplitude, the ETC decreases slowly at the beginning. However, when the radius fluctuation amplitude is large, the ETC decreases rapidly and reaches the valley value. The capillary has a strong contraction as radius fluctuation amplitude becomes larger, leading to an increase of flow resistance for geothermal fluids to pass through the solid region. As the fluid flow is obstructed by solid phase, the heat transfer is also affected by the reduction of fluid-solid contact area.

5 CONCLUSION

This paper presents a generalized fractal model for effective thermal conductivity of porous media based on the fractal geometry theory and thermal-electrical analogy method. Through solving equations and quantitative calculation, the analytical expression of ETC is expressed as a function of porosity, relative roughness, radius fluctuation amplitude, fractal dimensions for pore and tortuosity, wetting phase saturation, and intrinsic thermal conductivities for solid, wetting and nonwetting phase. Meanwhile, the analytical expression for ETC is calculated and compared with experimental data to prove the applicability of the theoretical model, and the proposed model indicates a good agreement. It has found that the relationship between ETC and relative roughness as well as radius fluctuation amplitude depends on the saturation. Different saturation results in a different variation rate. The results show that pore structure has significant influence on ETC. The ETC of porous media can decrease by the increase of porosity and fractal dimensions.

It should be noted that the present generalized model for ETC only focused on the effect of pore structure, such as rough surface, nonuniform pores and pore size distribution on the heat conduction

in porous media. The model can be improved by considering pore network connectivity and wettability. As in two-phase flow, connectivity, and wettability lead to extremely uneven spatial distribution of wetting and nonwetting phases, which can impact ETC heavily. Overall, the proposed model consists of geometric parameters have specific physical meanings, which and sheds light on the heat conduction mechanisms and provides guidelines for geothermal exploitation and thermal storage engineering construction.

DATA AVAILABILITY STATEMENT

The raw data supporting the conclusion of this article will be made available by the authors, without undue reservation.

AUTHOR CONTRIBUTIONS

YZ is responsible for formula derivation, BJ and YZ are responsible for literature research, JF and JL are responsible for collecting experimental data, MW is responsible for sensitivity analysis.

FUNDING

This study was financially supported by National Key Research and Development Project (No. 2019YFC0604903, No. 2021YFA0716004) and Joint Funds of the National Natural Science Foundation of China (Grant No.U20B6001).

REFERENCES

Askari, R., Hejazi, S. H., and Sahimi, M. (2017). Effect of Deformation on the thermal Conductivity of Granular Porous media with Rough Grain Surface. *Geophys. Res. Lett.* 44 (16), 8285–8293. doi:10.1002/2017gl074651

Baotian, P., Qingyang, L., Xiaofei, H., Haopeng, G., Zibian, L., Shaofei, J., et al. (2011). Initial thermal Conditions Around an Underground Research Tunnel at Shallow Depth. *Int. J. Rock Mech. Mining Sci.* 48 (1), 86–94. doi:10.1111/ter.12052

Belova, I. V., and Murch, G. E. (2004). Monte Carlo Simulation of the Effective thermal Conductivity in Two-phase Material. *J. Mater. Process. Technol.* 153-154, 741–745. doi:10.1016/j.jmatprotec.2004.04.191

Cahill, D. G. (1990). Thermal Conductivity Measurement from 30 to 750 K: the 3ω Method. *Rev. scientific Instr.* 61 (2), 802–808. doi:10.1063/1.1141498

Cai, J. C., Perfect, E., Cheng, C. L., and Hu, X. Y. (2014). Generalized Modeling of Spontaneous Imbibition Based on Hagen–Poiseuille Flow in Tortuous Capillaries with Variably Shaped Apertures. *Langmuir* 30 (18), 5142–5151. doi:10.1029/2001tc001336

Cai, J. C., Yu, B. M., Zou, M. Q., Mei, M. F., and Guo, Z. (2010). Fractal Analysis of Surface Roughness of Particles in Porous Media. *Gondwana Res.* 27 (2), 157–160. doi:10.1016/j.gr.2018.08.009

Cao, B. Y., Chen, M., and Guo, Z. Y. (2006). Effect of Surface Roughness on Gas Flow in Microchannels by Molecular Dynamics Simulation. *Int. J. Eng. Sci.* 44 (13), 927–937. doi:10.1111/ter.12173

Chakraborty, P., Ma, T. F., Cao, L., Wang, Y., Zhang, D., Zhang, C., et al. (2019). Jurassic-Early Cenozoic Tectonic Inversion in the Qilian Shan and Qaidam Basin, North Tibet: New Insight from Seismic Reflection, Isopach Mapping, and Drill Core Data. *J. Geophys. Res. Solid Earth* 136, 702–708. doi:10.1029/2019jb018086

Chen, H., Yang, M., Chen, K., and Zhang, C. (2020). Relative Permeability of Porous Media with Nonuniform Pores. *Geofluids* 2020, 1–14. doi:10.1016/j.earscirev.2021.103730

Chen, S. X. (2008). Early Cenozoic Faulting of the Northern Tibetan Plateau Margin from Apatite (U-Th)/He Ages. *Earth Planet. Sci. Lett.* 44 (10), 1241–1246. doi:10.1016/j.epsl.2010.04.051

Chen, Y. P., and Zhang, C. B. (2014). Role of Surface Roughness on thermal Conductance at Liquid–Solid Interfaces. *Int. J. Heat Mass Transfer* 78, 624–629. doi:10.1029/2005jb004187

Clauser, C., and Huenges, E. (1995). Thermal Conductivity of Rocks and Minerals. *Rock Phys. phase relations: a handbook Phys. constants* 3, 105–126. doi:10.1130/0091-7613(1998)026<0043:teyfat>2.3.co;2

Fraisse, G., Viardot, C., Lafabrie, O., and Achard, G. (2002). Development of a Simplified and Accurate Building Model Based on Electrical Analogy. *Energy and buildings* 34 (10), 1017–1031. doi:10.1029/2008tc002344

Gao, Q., and Yu, C. (2007). The Simplified Cylindrical Source Model for Determining the Thermal Conductivity Underground Soil. *J. Struct. Geology.* 28 (12), 1402–1406. doi:10.1016/0191-8141(83)90035-4

Geankoplis, C. J., Hersel, A. A., Lepek, D. H., Li, W., Zhao, S., and Li, X. (2018). *Transport Processes and Separation Process Principles*. MA: Prentice hall Boston. doi:10.1016/j.epsl.2016.05.045

Ghanbarian, B., Daigle, H., and Fang, X. (2016). Early Cenozoic Activated Deformation in the Qilian Shan, Northeastern Tibetan Plateau: Insights from Detrital Apatite Fission-Track Analysis. *Water Resour. Res.* 52 (1), 295–314. doi:10.1111/bre.12533

Giraud, A., Sevostianov, I., Chen, F., and Grgic, D. (2015). Direct Stratigraphic Dating of India-Asia Collision Onset at the Selandian (Middle Paleocene, 59 ± 1 Ma). *Int. J. Rock Mech. Mining Sci.* 80, 379–387. doi:10.1130/g36872.1

Gradshteyn, I., and Ryzhik, I. M. (2014). Sedimentary Characteristics of Cenozoic Strata in central-southern Ningxia, NW China: Implications for the Evolution of the NE Qinghai-Tibetan Plateau. *J. Asian Earth Sci.* 39, 740–759 doi:10.1016/j.jseaes.2010.05.008

Guo, L., Xu, H. J., Gong, L., Tapponnier, P., Malavieille, J., Arnaud, N., et al. (2015). Influence of wall Roughness Models on Fluid Flow and Heat Transfer in Microchannels. *Appl. Therm. Eng.* 84, 399–408. doi:10.1016/s0040-1951(01)00196-2

Gupta, N., Chaitanya, G. R., and Mishra, S. C. (2006). Lattice Boltzmann Method Applied to Variable thermal Conductivity Conduction and Radiation Problems. *J. Thermophys. Heat Transfer* 20 (4), 895–902. doi:10.1002/2016tc004187

Jia, G. S., Tao, Z. Y., Meng, X. Z., Ma, C. F., Chai, J. C., and Jin, L. W. (2019). Review of Effective thermal Conductivity Models of Rock-Soil for Geothermal Energy Applications. *Geothermics* 77, 1–11. doi:10.1016/j.palaeo.2021.110416

Jin, H. Q., Yao, X. L., Fan, L. W., Xu, X., and Yu, Z. T. (2016). Experimental Determination and Fractal Modeling of the Effective thermal Conductivity of Autoclaved Aerated concrete: Effects of Moisture Content. *Int. J. Heat mass transfer* 92, 589–602. doi:10.1130/l1037.1

Li, J., Du, Q., Sun, C. X., Wang, G., Shi, X., and Liang, X. (2009). Block Rotation: Tectonic Response of the Sichuan basin to the Southeastward Growth of the Tibetan Plateau along the Xianshuihe-Xiaojiang Fault. *Pattern Recognition* 42 (11), 2460–2469. doi:10.1002/2013tc003337

Li, K.-Q., Li, D.-Q., and Liu, Y. (2020). Meso-scale Investigations on the Effective thermal Conductivity of Multi-phase Materials Using the Finite Element Method. *Int. J. Heat Mass Transfer* 151, 119383. doi:10.1016/j.ijheatmasstransfer.2020.119383

Li, Z. X., Peizhen, Z., Dewen, Z., Guangliang, Z., Huiping, Z., Wenjun, Z., et al. (2003). Experimental Study on Flow Characteristics of Liquid in Circular Microtubes. *Geol. Soc. America Bull.* 7 (3), 253–265. doi:10.1130/b30611.1

Lin, W.-t., Liu, P.-Z., Liu, J., Geng, L.-H., Ren, G.-L., Zheng, D.-W., et al. (2021). Numerical Model for Geothermal Energy Utilization from Double Pipe Heat Exchanger in Abandoned Oil wells. *Adv. Geo-Energy Res.* 5 (2), 212–221. doi:10.1016/j.tecto.2011.04.006

Liu, R., Bo, L., Jiang, Y., Jing, H., and Yu, L. (2018). On the Relationship between Equivalent Permeability and Fractal Dimension of Dual-Porosity media. *Fractals* 26, doi:10.1142/S0218348X1850072X

Lu, S., Ren, T. S., Gong, Y. S., Horton, R., Zheng, D., Liu, C., et al. (2007). An Improved Model for Predicting Soil Thermal Conductivity from Water Content

at Room Temperature. *Soil Sci. Soc. America J.* 71 (1). doi:10.1038/ncomms15887

Majumdar, A., and Bhushan, B. (1991). *Fractal Model of Elastic-Plastic Contact between Rough Surfaces*. doi:10.1016/j.jseaes.2017.07.020

Mandelbrot, B. B., Wang, Y., Ding, W., Xu, S., Zhang, Y., Li, B., et al. (1982). *The Fractal Geometry of Nature*. New York: W. H. Freeman. doi:10.1130/b35944.1

Manzella, A., Bonciani, R., Allansdottir, A., Botteghi, S., Donato, A., Giamberini, S., et al. (2018). Environmental and Social Aspects of Geothermal Energy in Italy. *J. Asian Earth Sci.* 72, 232–248. doi:10.1016/j.jseaes.2008.10.001

Miao, T., Chen, A., Xu, Y., Yang, S., and Yu, B. (2016a). Optimal Structure of Damaged Tree-like Branching Networks for the Equivalent thermal Conductivity. *Int. J. Therm. Sci.* 102, 89–99. doi:10.1016/j.ijthermalsci.2015.10.040

Miao, T. J., Cheng, S. J., Chen, A. M., and Yu, B. M. (2016b). Mode of Cenozoic East-West Extension in Tibet Suggesting a Common Origin of Rifts in Asia during the Indo-Asian Collision. *Int. J. Heat Mass Transfer* 102, 884–890. doi:10.1029/2000jb900168

Mostafa, M., Afify, N., Gaber, A., and Abu Zaid, E. (2004). Investigation of thermal Properties of Some basalt Samples in Egypt. *J. Therm. Anal. Calorim.* 75 (1), 179–188. doi:10.1016/j.earscirev.2005.05.004

Motlagh, M. B., Kalteh, Y.-Q., au, L.-C., au, W.-M., au, S.-P., au, X.-H., et al. (2020). Cenozoic Tectonic Evolution of Qaidam basin and its Surrounding Regions (Part 1): The Southern Qilian Shan-Nan Shan Thrust belt and Northern Qaidam basin. *J. Mol. Liquids* 318, 114028. doi:10.1130/b26180.1

Noorollahi, Y., Shabbir, M. S., Siddiqi, A. F., Ilyashenko, L. K., and Ahmadi, E. (2019). Review of Two Decade Geothermal Energy Development in Iran, Benefits, Challenges, and Future Policy. *Geothermics* 77, 257–266. doi:10.1130/b26232.1

Nunziato, J. W. (1971). On Heat Conduction in Materials with Memory. *Q. Appl. Maths.* 29 (2), 187–204. doi:10.1146/annurev.earth.28.1.211

Qin, X., Zhou, Y., Sasmito, A. P., Li, Y., Li, C., and Xiao, L. (2019). An Effective thermal Conductivity Model for Fractal Porous media with Rough Surfaces. *Adv. Geo-Energy Res.* 3 (2), 149–155. doi:10.1130/ges01520.1

Shen, Y. Q., Xu, P., Qiu, S. X., Rao, B. Q., Yu, B. M., Zhang, P. Z., et al. (2020). The Growth of Northeastern Tibet and its Relevance to Large-Scale continental Geodynamics: A Review of Recent Studies. *Int. J. Heat Mass Transfer* 152, 119540. doi:10.1002/tect.20081

Soltani, P.-Z., Farzanehkhameneh, P., Kashkooli, F. M., Al-Haq, A., Nathwani, J., Wang, Q., et al. (2021). Optimization and Energy Assessment of Geothermal Heat Exchangers for Different Circulating Fluids. *Geol* 228, 113733. doi:10.1130/g20554.1

Swift, G., Molinski, T. S., and Lehn, W. (2001). A Fundamental Approach to Transformer thermal Modeling. I. Theory and Equivalent Circuit. *IEEE Trans. Power Deliv.* 16 (2), 171–175. doi:10.1130/ges00523.1

Tang, W.-J., Cui, P.-Z., Le, W.-P., au, H.-P., au, D.-Y., and Liu, J.-H. (2008). A Study on the thermal Conductivity of Compacted Bentonites. *Appl. Clay Sci.* 41 (3-4), 181–189. doi:10.1002/tect.20022

Tong, F., Jing, L., and Zimmerman, R. W. (2009). An Effective thermal Conductivity Model of Geological Porous media for Coupled Thermo-Hydro-Mechanical Systems with Multiphase Flow. *Int. J. Rock Mech. Mining Sci.* 46 (8), 1358–1369. doi:10.1016/j.ijrmms.2009.04.010

Tsilingiris, P. T. (2008). Thermophysical and Transport Properties of Humid Air at Temperature Range between 0 and 100°C. *Energ. Convers. Manage.* 49 (5), 1098–1110. doi:10.1016/j.enconman.2007.09.015

Wang, H., Su, Y., Wang, W., and Sheng, G. (2019). Testing Models of Tibetan Plateau Formation with Cenozoic Shortening Estimates across the Qilian Shan-Nan Shan Thrust belt. *Chem. Eng. Sci.* 209, 115166. doi:10.1130/ges01254.1

Wei, W., Cai, J., Hu, X., and Han, Q. (2015). An Electrical Conductivity Model for Fractal Porous media. *Geophys. Res. Lett.* 42 (12), 4833–4840. doi:10.1016/j.tecto.2020.228642

Xia, B. Q., Pan, Z. H., Yan, J., Zhao, C. Y., and Chen, X. (2019b). Mesoscopic Exploration on Mass Transfer in Porous Thermochemical Heat Storage Materials. *Int. J. Heat Mass Transfer* 135, 52–61. doi:10.1130/l1042.1

Xia, B. Q., Pan, Z., Yan, J., Zhao, C. Y., Zhang, Y., Wu, L., et al. (2019a). Mesoscopic Exploration on Mass Transfer in Porous Thermochemical Heat Storage Materials. *Int. J. Heat Mass Transfer* 135, 52–61. doi:10.1130/b31721.1

Xiao, B., Zhang, Y., Wang, Y., Wang, W., and Long, G. (2020). An Investigation on Effective Thermal Conductivity of Unsaturated Fractal Porous Media with Roughened Surfaces. *Fractals* 28 (5). doi:10.1142/s0218348x20500802

Xu, H., Xing, Z., and Vafai, K. (2019). Analytical Considerations of Flow/thermal Coupling of Nanofluids in Foam Metals with Local thermal Non-equilibrium (LTNE) Phenomena and Inhomogeneous Nanoparticle Distribution. *Int. J. Heat Fluid Flow* 77, 242–255. doi:10.1016/j.ijheatfluidflow.2019.04.009

Xu, P. (2015). A Discussion on Fractal Models for Transport Physics of Porous media. *Fractals* 23 (03), 1530001. doi:10.1142/s0218348x15300019

Yang, S., Yu, B., Zou, M., and Liang, M. (2014). A Fractal Analysis of Laminar Flow Resistance in Roughened Microchannels. *Int. J. Heat Mass Transfer* 77, 208–217. doi:10.1016/j.ijheatmasstransfer.2014.05.016

Yang, Z., Cui, J., and Sun, Y. (2016). Transient Heat Conduction Problem with Radiation Boundary Condition of Statistically Inhomogeneous Materials by Second-Order Two-Scale Method. *Int. J. Heat Mass Transfer* 100, 362–377. doi:10.1016/j.ijheatmasstransfer.2016.04.093

Yang, Z., Sun, Y., Cui, J., Yang, Z., and Guan, T. (2018). A Three-Scale Homogenization Algorithm for Coupled Conduction-Radiation Problems in Porous Materials with Multiple Configurations. *Int. J. Heat Mass Transfer* 125, 1196–1211. doi:10.1016/j.ijheatmasstransfer.2018.05.024

Yu, B., Cai, J., and Zou, M. (2009). On the Physical Properties of Apparent Two-phase Fractal Porous media. *Vadose Zone J.* 8 (1), 177–186. doi:10.2136/vzj2008.0015

Yu, B., and Cheng, P. (2002b). A Fractal Permeability Model for Bi-dispersed Porous media. *Int. J. Heat mass transfer* 45 (14), 2983–2993. doi:10.1016/s0017-9310(02)00014-5

Yu, B., and Cheng, P. (2002). A Fractal Permeability Model for Bi-dispersed Porous media. *Int. J. Heat Mass Transfer* 45 (14), 2983–2993. doi:10.1016/s0017-9310(02)00014-5

Yu, B., and Cheng, P. (2002a). Fractal Models for the Effective thermal Conductivity of Bidispersed Porous media. *J. Thermophys. Heat transfer* 16 (1), 22–29. doi:10.2514/2.6669

Yu, B., and Li, J. (2001). Some Fractal Characters of Porous Media. *Fractals* 09 (03), 365–372. doi:10.1142/s0218348x01000804

Yu, B. M. (2008). Analysis of Flow in Fractal Porous media. *Appl. Mech. Rev.* 61 (5). doi:10.1115/1.2955849

Yu, B. M., and Li, J. H. (2004). A Geometry Model for Tortuosity of Flow Path in Porous Media. *Chin. Phys. Lett.* 21 (008), 1569–1571.

Zhou, H., Liu, H., Hu, D., Yang, F., Lu, J., and Zhang, F. (2016). Anisotropies in Mechanical Behaviour, thermal Expansion and P-Wave Velocity of sandstone with Bedding Planes. *Rock Mech. Rock Eng.* 49 (11), 4497–4504. doi:10.1007/s00603-016-1016-y

Conflict of Interest: All authors are employed by the company SINOPEC.

The reviewer RW declared a shared affiliation with the authors to the handling editor at time of review.

Publisher's Note: All claims expressed in this article are solely those of the authors and do not necessarily represent those of their affiliated organizations, or those of the publisher, the editors and the reviewers. Any product that may be evaluated in this article, or claim that may be made by its manufacturer, is not guaranteed or endorsed by the publisher.

GLOSSARY

a radius fluctuation amplitude

A area, m^2

D fractal dimension

k Thermal conductivity, W/(m*K)

L length, m

N pore number

p capillary pressure, Pa

r radius of sinusoidal capillary, m

R thermal resistance, K/W

S saturation

V volume, m^3

W wavelength of along the axis, m

Greek letters

α ratio of minimum to maximum base diameter

β ratio of minimum to maximum pore size

γ relative roughness

δ base diameter, m

ε length scale

σ surface tension, N/m

θ contact angle

φ ratio of base area of rough element to surface area of capillary

φ porosity

λ pore size

ξ ratio of height to base diameter

τ tortuosity

Subscripts

ave Averaged

c critical

cs capillary surface

e effective

E Euclidean

f fractal

min minimum

max maximum

nw nonwetting phase

p pore

s solid

sc single capillary

t total

T tortuosity

w wetting phase.

frontiers in Earth Science

ORIGINAL RESEARCH
published: 22 March 2022
doi: 10.3389/feart.2022.844605

Geochemical and Isotopic Characteristics of Two Geothermal Systems at the Nanpu Sag, Northern Bohai Bay Basin

Ke Wang[1,2,3], Cong Hua[4], Lu Ren[5], Yanlong Kong[1,2,3], Wenjie Sun[6]*, Sheng Pan[7], Yuanzhi Cheng[1,2,3], Yonghui Huang[1,2,3], Fei Tian[1,2,3], Weizun Zhang[1,6], Dajun Qin[1,2,3], Feng Ma[8,9], Jianwei Wang[5] and Yuexia Dong[10]*

[1]Key Laboratory of Shale Gas and Geoengineering, Institute of Geology and Geophysics, Chinese Academy of Sciences, Beijing, China, [2]Innovation Academy for Earth Science, Chinese Academy of Sciences, Beijing, China, [3]College of Earth and Planetary Sciences, University of Chinese Academy of Sciences, Beijing, China, [4]Key Laboratory of Groundwater Resources and Environment, Ministry of Education, College of Environment and Resources, Jilin University, Changchun, China, [5]Jidong Oilfield Company of PetroChina, Tangshan, China, [6]College of Geoscience and Surveying Engineering, China University of Mining and Technology (Beijing), Beijing, China, [7]Key Laboratory of Continental Collision and Plateau Uplift, Institute of Tibetan Plateau Research, Chinese Academy of Sciences, Beijing, China, [8]The Institute of Hydrogeology and Environmental Geology, Chinese Academy of Geological Sciences, Shijiazhuang, China, [9]Technology Innovation Center for Geothermal and Hot Dry Rock Exploration and Development, Ministry of Natural Resources, Shijiazhuang, China, [10]Advisory Center, China National Petroleum Corporation, Shijiazhuang, China

OPEN ACCESS

Edited by:
Ryan Mathur,
Juniata College, United States

Reviewed by:
Ying Li,
China Earthquake Administration, China
Aisha Al Suwaidi,
Khalifa University, United Arab Emirates

***Correspondence:**
Yanlong Kong
ylkong@mail.iggcas.ac.cn
Wenjie Sun
swj@cumtb.edu.cn

Specialty section:
This article was submitted to Economic Geology, a section of the journal Frontiers in Earth Science

Received: *28 December 2021*
Accepted: *23 February 2022*
Published: *22 March 2022*

Citation:
Wang K, Hua C, Ren L, Kong Y, Sun W, Pan S, Cheng Y, Huang Y, Tian F, Zhang W, Qin D, Ma F, Wang J and Dong Y (2022) Geochemical and Isotopic Characteristics of Two Geothermal Systems at the Nanpu Sag, Northern Bohai Bay Basin. Front. Earth Sci. 10:844605. doi: 10.3389/feart.2022.844605

The utilization of geothermal energy has gradually increased in northern China because of its unique advantages as a heating supply. However, the sustainable exploitation of geothermal energy usually requires a comprehensive investigation of the geothermal water circulation pattern prevailing at a proposed site. During the exploitation of geothermal energy resources at Nanpu Sag in northern China, thermal anomalies were found to exist in two adjacent regions: the Caofeidian and the Matouying. To reconcile the anomalies and to examine both the source of recharge water and the geothermal systems' circulation dynamics, a comprehensive investigation was performed using multiple chemical and isotopic tracers (δ^2H, δ^{18}O, ^{87}Sr/^{86}Sr, δ^{13}C, and ^{14}C). The total dissolved solids (TDS) of the geothermal water are approximately 750 mg/L and 1,250 mg/L, respectively. The geothermal water isotopes at the two sites are also different, with average values of -9.3‰ and -8.2‰ for δ^{18}O and -73.4‰ and -71‰ for δ^2H, respectively. Moreover, the ^{87}Sr/^{86}Sr ratio of geothermal water at Matouying is 0.7185, which is much greater than that of Caofeidian, with an average value of 0.7088. All the results confirm the difference between the two geothermal systems and may explain the two circulation patterns of deep groundwater at Caofeidian and Matouying. The reservoir temperature obtained from theoretical chemical geothermometers is estimated to be 83–92°C at the Caofeidian and 107–137°C at the Matouying, respectively. The corrected ^{14}C age implies a low circulation rate that would allow sufficient time to heat the water at Caofeidian. In addition, we propose a geothermal conceptual model in our study area. This model could provide key information regarding the geothermal sustainable exploitation and the effective management of geothermal resources.

Keywords: hydrothermal energy, geochemical characteristic, isotopic characteristic, two geothermal systems, conceptual model, nanpu sag

INTRODUCTION

Hydrothermal energy is obtained by utilizing the heat or energy from the groundwater within the geothermal systems (Byrappa & Yoshimura, 2012). It is recognized that hydrothermal energy is clean, environmentally friendly, stable, and reliable when people use the heat or energy from hydrothermal water (Rybach, 2003; Marrasso et al., 2018). Besides, hydrothermal energy demonstrates the characteristic of large reservoirs and wide distribution (Wang, 2015a; Shortall et al., 2015; Moya et al., 2018; Lund & Toth, 2021). In northern China, hydrothermal energy is widely used because of its unique advantages as a heating supply (Wang, 2009; Duan et al., 2011; Kong et al., 2014; An et al., 2016; Wang et al., 2018). However, to realize the rational exploitation and utilization of hydrothermal geothermal resources, it is necessary to consider the sustainability of long-term exploitation as well as the environmental and geological consequences of exploitation (Hahnlein, Bayer, Ferguson, & Blum, 2013). To determine the exploitation potential of a hydrothermal system, it is imperative to document the water and heat sources, the thermal reservoir, the water transporting channels, and the thermal caprock of the geothermal field (Pang et al., 2018; Huang et al., 2021a). Although one can easily monitor the temperature and thermal reservoir characteristics of hydrothermal systems, it is difficult to determine the water sources, water flow paths, and heat sources for complicated geochemical processes. Precipitation generally recharges into hydrothermal reservoirs through deep, subsurface circulations. Within the circulation period, the geothermal water is heated from the comparative hot surrounding rocks with which it interacts (Lister, 1980; Le Gal et al., 2018). Therefore, the geochemical characteristics and isotopic composition of geothermal water will change accordingly (Yang et al., 2017). Thus, the combination of geochemical and isotopic characteristics in hydrothermal systems is of great value for determining the origin of the hydrothermal water and characterizing the water-rock-gas interaction process.

In northern China, a typical hydrothermal system known as the Caofeidian has been developed and utilized for many years as a heating supply (Chang et al., 2016; Dong et al., 2021; Wang et al., 2021). However, temperature anomalies have been detected in the geothermal development process at the Matouying, located less than 20 km east of the Caofeidian. The temperature of the geothermal boreholes at the Matouying was found to be much higher than those of the Caofeidian. To distinguish the temperature anomalies and realize the sustainable utilization of hydrothermal energy, it is necessary to investigate the patterns of deep groundwater circulation and geothermal reservoir conditions. Although some geophysical studies have been conducted to investigate the causes of the temperature anomalies within this area, no research has been conducted to compare the hydrothermal waters at the Caofeidian and the Matouying from the geochemical and isotopic information.

In this study, we conducted detailed geochemical and isotopic analyses of geothermal waters at the Caofeidian and the Matouying to distinguish the differences between the two sites and investigate the hydrothermal system characteristics. ^{14}C dating was used to assess the age of deep geothermal groundwater. We also determined the heat source and circulation patterns of different geothermal waters based on their geochemical and isotopic characteristics. The principal research objectives of this study are: 1) to investigate the geochemical and isotopic characteristics of the geothermal groundwater at the Caofeidian and the Matouying; 2) to determine the causes of geothermal water differences between the two areas; and 3) to propose a conceptual model of geothermal water circulation in the research areas.

GEOLOGICAL AND HYDROGEOLOGICAL SETTINGS

Caofeidian is located 80 km south of Tangshan and 120 km east of Tianjin in the north-central part of the Bohai Bay Basin which locates in the northern China (**Figure 1A** and **Figure 2**). In terms of geological structure, the Caofeidian is located in the north of the Nanpu Sag, one of the major oil and gas fields in China (**Figure 2**). The Nanpu depression is located in the north of the Huanghua Depression, and its northwest boundary is the Xinanzhuang fault, separated from the Xinanzhuang Uplift and Laowangzhuang Uplift (**Figure 2**) (Dong et al., 2021). The northeast boundary is the Baigezhuang fault, which is adjacent to the Baigezhuang Uplift and the Matouying Uplift (**Figure 2**). The southern Nanpu depression is in a fault-superposition relationship with the Shaleitian Uplift. Geothermal anomaly zones were found in the Matouying Uplift area near the Baigezhuang fault. The Caofeidian and Matouying areas are located on the west and east sides of the Baigezhuang fault, respectively (**Figure 2**).

In general, Nanpu Sag is a Tertiary sedimentary lake basin (Wang et al., 2022). From the surface downwards, the Nanpu Sag and its surrounding areas are characterized by Cenozoic, Mesozoic, Paleozoic, Neoproterozoic, and Archean strata (Zhu et al., 2014; Wang et al., 2020). The stratigraphic distribution and thickness of different structural units of the Nanpu Sag vary greatly (Wang et al., 2021). Baigezhuang Fault is a border fracture separating Matouying and Nanpu, which has controlling effect on the formation and evolution of Nanpu Sag. Because of the movement of Baigezhaung Fault, the Archean granite was uplifted at Matouying. Besides, the destruction of the eastern North China Craton and the thinning of the regional lithosphere also contributed to the shallow depth of granite at Matouying (Qiu et al., 2014; Qiu et al., 2016; Zhang et al., 2020b; Dong et al., 2021). According to the geophysical work by Dong et al. (2008), the depth of Baigezhuang Fault was estimated to be more than 5 km downwards, which reached the basement of Archean granite. The main heat reservoirs in the Nanpu Sag are the Neogene Guantao Formation and the Neogene Minghuazhen

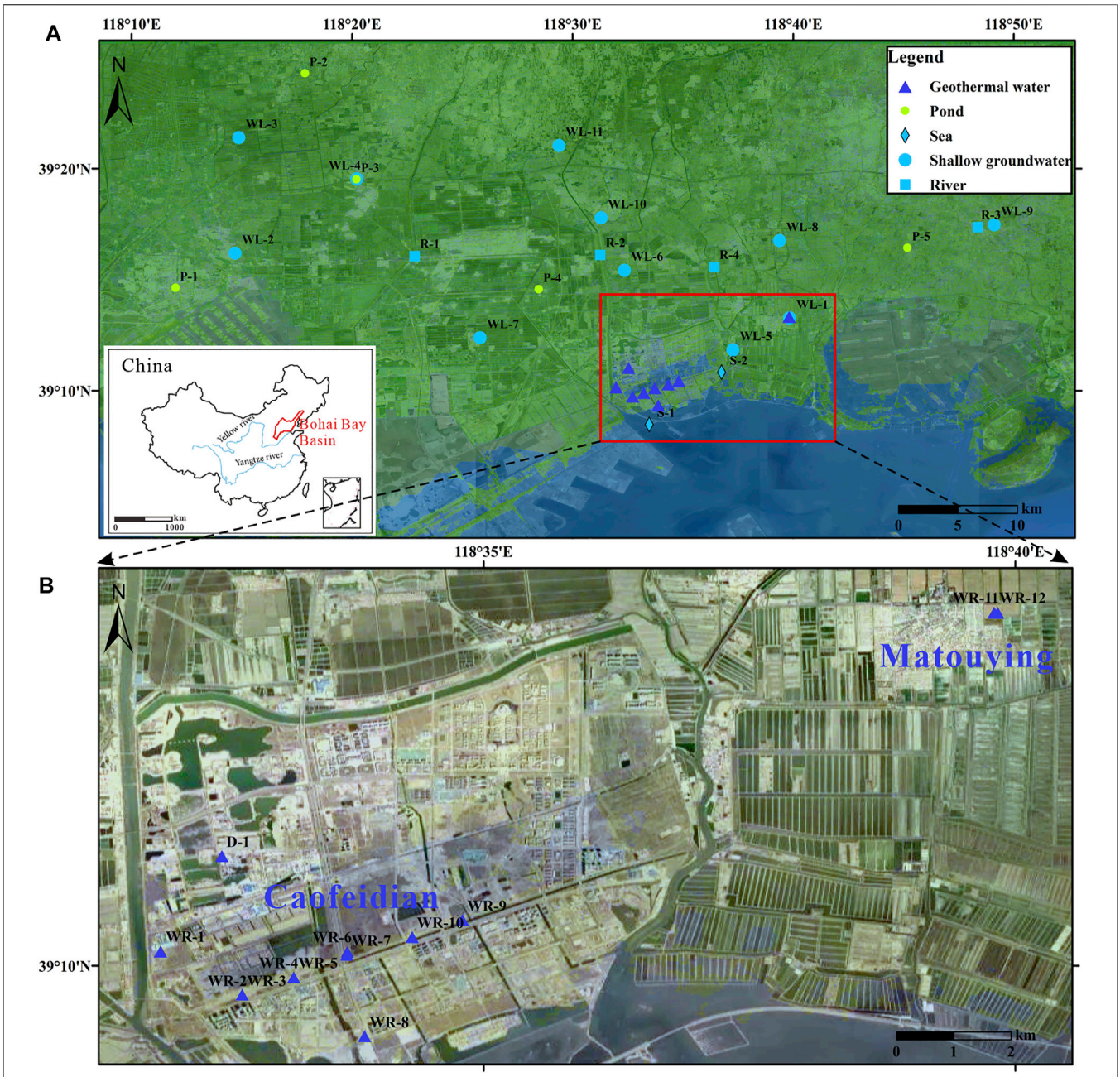

FIGURE 1 | (A): Location of Bohai Bay Basin in China and all the sampling sites in the study area, the red rectangle represents the area where the geothermal water were sampled; **(B)**: The sampling locations of geothermal water in the two regions Caofeidian and Matouying.

Formation (**Figure 3**), followed by the Cambrian and the Ordovician. The Neogene strata is principally driven by the uplift and sag of the Paleogene. Except for the absence of the Laowangzhuang uplift, the Guantao Formation contains a thickness of 300–900 m in our study area except for the Laowangzhuang Uplift. The thermal reservoirs of the Guantao Formation are mainly fine sandstone and gravel sandstone with an average porosity of 30–35%. The bottom boundary of the Guantao Formation thermal reservoir is 2,100–2,600 m deep, gradually increasing in depth from north to south. The Minghuazhen Formation has a thickness of 1,000–2000 m throughout the study region. The bottom boundary of the Minghuazhen Formation's thermal reservoir is 1700–2,200 m deep, gradually deepening from north to south. The Quaternary in this region belongs to the Pleistocene-Holocene strata, which are not integrated with the underlying Minghuazhen Formation. Quaternary in this area is a set of undiagenetic interbedded yellow glutenite and clay,

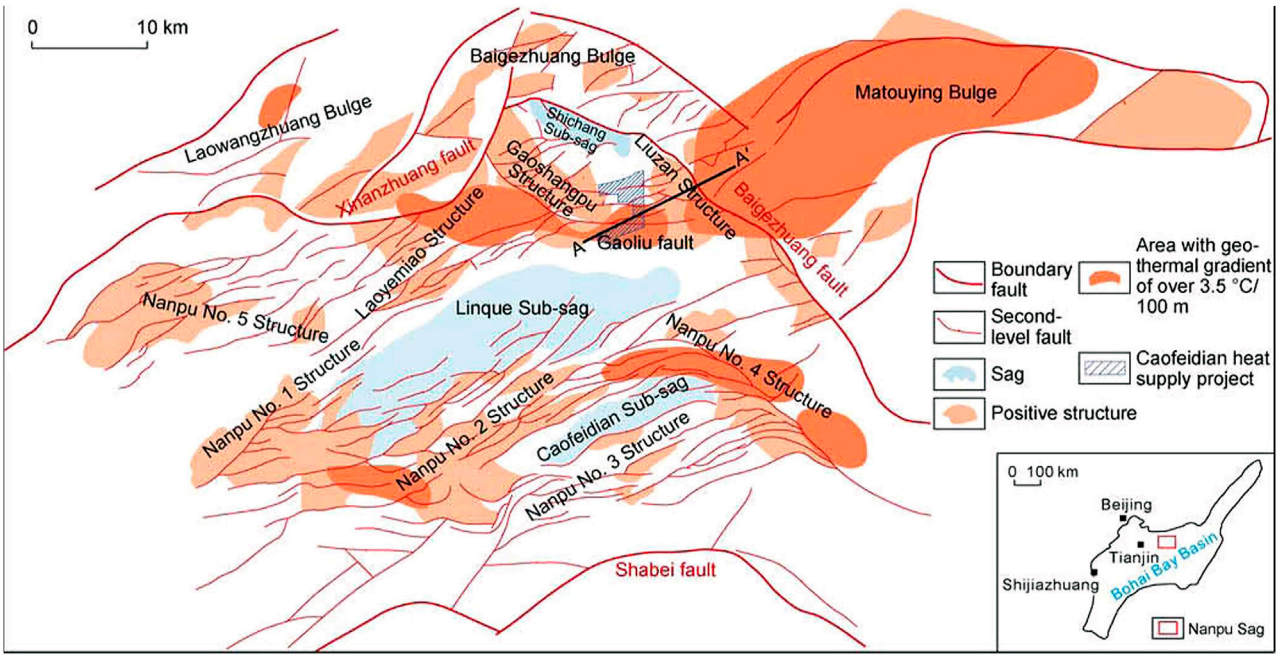

FIGURE 2 | Geological map of the Nanpu Sag and its locations in Bohai Bay Basin (cited from Dong et al., 2021).

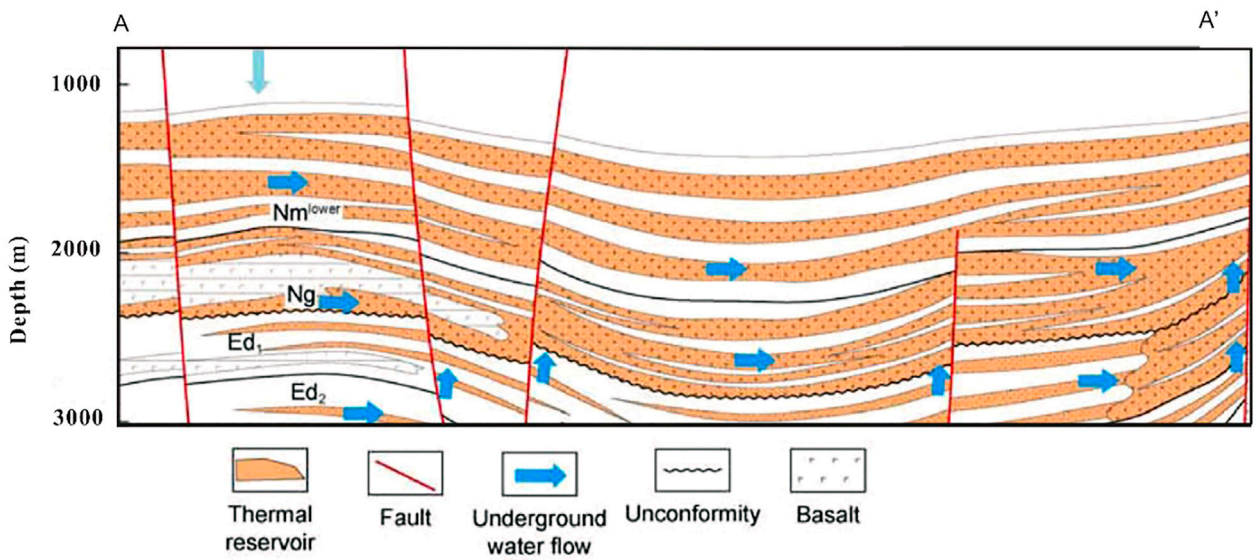

FIGURE 3 | Cross section **(A,A')** of the Nanpu Sag (cited from Huang et al., 2021b).

the bottom of which are alluvial and alluvial glutenite layers. In this study, we focus on the Neogene sandstone aquifer because it is the principal geological formation exploited for geothermal energy production in the Caofeidian and the Matouying. Our study objective is the Neogene heat reservoir. The Neogene strata in the Caofeidian, and the Matouying is mainly porous sandstone, which has the characteristics of high porosity and permeability.

SAMPLING AND ANALYSIS

Field sampling was performed at the Nanpu Sag in December and November 2019. A total of 35 water samples were collected, including 12 from geothermal wells, 11 from shallow wells, and one from deep wells in the Dongying Formation. To compare the hydrochemistry and isotopic characteristics of groundwater and surface water, we also collected four river samples, five pond

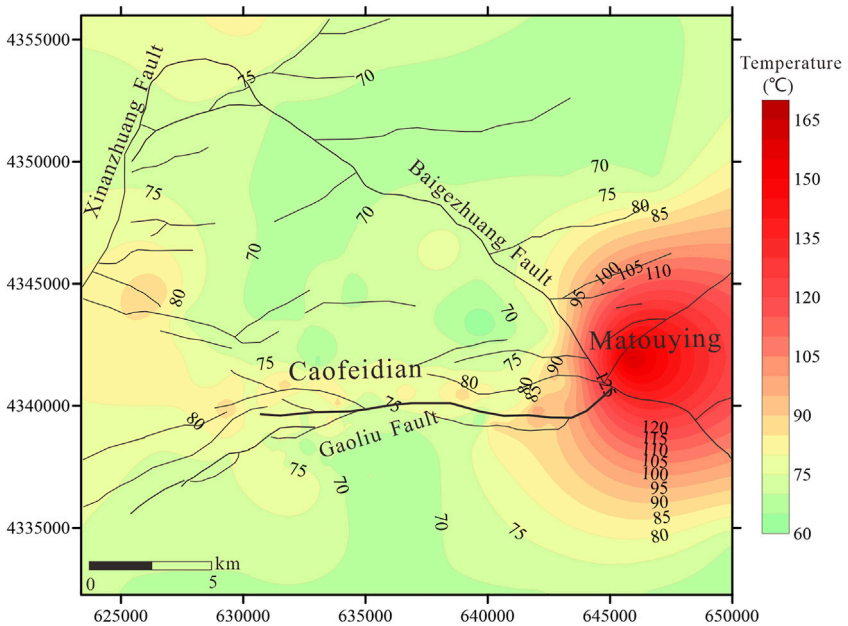

FIGURE 4 | Temperature gradient of the geothermal wells at the depth of 2120m in the study area.

samples, and 2 seawater sample in different directions of the geothermal wells. All sampling locations are shown in **Figure 1A**. The sampling time was within the heat supply period, consequently, the water samples from the geothermal boreholes are representative of the water within the aquifer. All the samples were filtered *in situ* with a 0.23 μm membrane prior to bottling and sealing with Parafilm. Samples for cation and trace element analysis were acidified with ultra-purified HNO_3 to adjust the pH of each sample to less than 2. The acidified process was not added to the samples for anion and water isotope analyses.

Temperature, pH, electrical conductivity (EC), and total dissolved solids (TDS) were measured in the field using a multi-parameter device (Hach HQ40D). HCO_3^- and CO_3^{2-} were measured in the field using a digital titrator (16,900 Digital Titrator, Hach) with indicators including phenolphthalein and methyl orange colorants. The samples were sent for analysis at the Water Isotopes and Water–Rock Interaction Laboratory, Institute of Geology and Geophysics, Chinese Academy of Sciences.

Cations and anions were identified according to the National Analysis standard DZ/T0064.28–93 and DZ/T0064.51–93, respectively. The detection limit was 0.1 mg/L. The trace elements were determined using ICP-MS (7500C, Agilent) with an analytical precision of less than 0.5%. Stable isotopes (δ^2H and $\delta^{18}O$) were measured using a laser absorption water isotope spectrometer analyzer (Picarro L2120-i). All δ^2H and $\delta^{18}O$ values are expressed in δ notation per mil relative to the Vienna Standard Mean Ocean Water (V-SMOW). The measurement precisions of δ^2H and $\delta^{18}O$ were ±0.5‰ and ±0.1‰, respectively. The trace elements were determined using ICP-MS (7500C, Agilent) at the Analytical Laboratory of Beijing Research Institute of Uranium Geology with an analytical precision of less than 0.5%. The carbon isotopic compositions (i.e., ^{14}C and ^{13}C) were determined by Beta Analytic, Inc. using accelerator mass spectrometry (AMS) and isotope ratio mass spectrometry (IR-MS), respectively. The analytical precision of the AMS ^{14}C results was ±0.1%. The ^{14}C ages were corrected using the $\delta^{13}C$ mixing model (Clark and Fritz, 2013):

$$t = -8267\ln\left(\frac{C_t}{qC_0}\right) \quad (1)$$

$$q = \frac{\delta^{13}C_t - \delta^{13}C_d}{\delta^{13}C_s - \delta^{13}C_d} \quad (2)$$

where t is the groundwater age, C_t is the measured ^{14}C activity, q is the correction factor, and $\delta^{13}C_t$, $\delta^{13}C_d$, and $\delta^{13}C_s$ represent the measured $\delta^{13}C$ values for the groundwater, the dissolved calcite (0‰), and soil (-23‰), respectively.

RESULTS

Local Hydrothermal Pattern

The temperature gradient of the geothermal wells is shown in **Figure 4**. By comparing the geothermal water temperature at the Caofeidian and the Matouying, we found significant differences between the two locations. The temperature of the geothermal water sampled at the Matouying has a maximum of 117°C, which is much greater than that of the Caofeidian, 70–80°C. In addition, the geothermal gradient for the Neogene Guantao Formation at Matouying is also much greater than that observed at the Caofeidian, which is about 4.0–7.0 and 2.3–3.9°C/100 m, respectively. Although the distance between the two geothermal

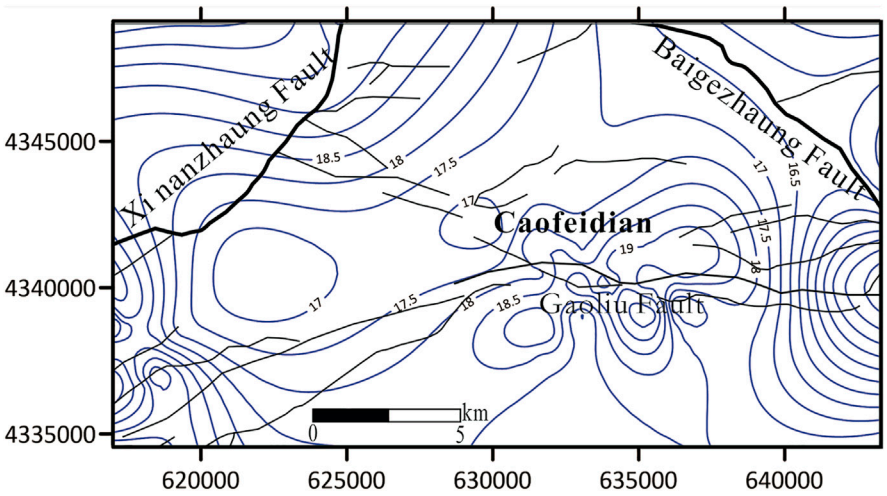

FIGURE 5 | Contours of hydrostatic pressure of the geothermal wells at the depth of 2000m at Caofeidian.

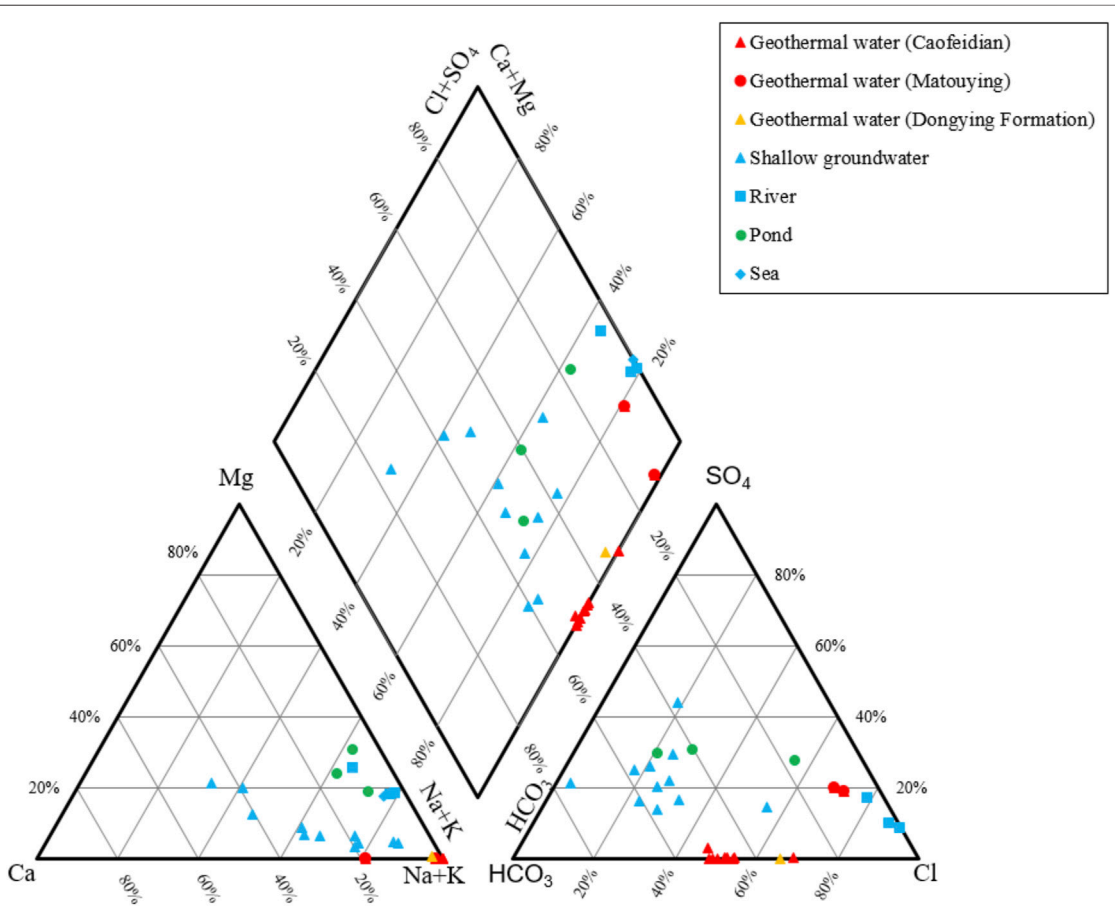

FIGURE 6 | Piper diagram of different water bodies around geothermal sites.

TABLE 1 | Chemical and isotope composition of water samples at Nanpu Sag.

Sample label	Type	Date	Depth(m)	pH	T (°C)	EC (μs/cm)	TDS (mg/L)	Na^+ (mg/L)	K^+ (mg/L)	Mg^{2+} (mg/L)	Ca^{2+}(mg/L)	F^- (mg/L)	Cl^- (mg/L)	NO_3^- (mg/L)	SO_4^{2-} (mg/L)	CO_3^{2-} (mg/L)	HCO_3^- (mg/L)	Water types	$\delta^{18}O$ (‰)	δ^2H (‰)
P-1	Pond	1-Dec-2019	—	8.23	0	1,194	531	97.4	6.27	20.73	20.13	0.84	71.81	3.01	103.84	0	174.12	HCO_3-Cl-SO_4-Na-Mg-Ca	−2.61	−31.87
P-2		1-Dec-2019	—	8.46	4.4	3,581	1789	461.36	27.37	65.4	50.69	1.75	85.44	0	166.6	0	354.51	HCO_3-SO_4-Cl-Na-Ca	−1.82	−26.79
P-3		1-Dec-2019	—	9.25	0	1,647	834	171.97	8.01	45.66	16.43	0.76	223.85	0	151.52	19.71	116.5	Cl-SO_4-HCO_3-Na-Mg-Ca	−1.93	−30.5
P-4		4-Dec-2019	—	8.56	2.6	2,900	2,600	590.27	41.44	154.85	31.52	1.67	1,053.62	0	289.28	30.8	299.39	Cl-SO_4-HCO_3-Na-Mg	1.29	-7.56
P-5		6-Dec-2019	—	9.33	3.5	2,810	2,460	828.44	27.6	77.44	22.44	1.54	1,027.26	0	86.17	67.76	388.33	Cl-HCO_3 -Na	−0.74	−23.37
R-1	River	1-Dec-2019	—	8.86	0	3,780	2,138	1,175.3	55.57	254.58	152.04	30.07	2,139.52	0	637.39	27.1	190.41	Cl-SO_4 -Na	−0.83	−18.68
R-2		4-Dec-2019	—	7.78	1.7	9,390	9,280	1,310.82	50.69	167.66	57.99	2.28	2,473.26	0	388.31	0	124.02	Cl -Na	−4.11	−37.96
R-3		6-Dec-2019	—	8.79	2.2	1,155	11,230	2,243.91	67.58	301.14	81.9	5.95	4,218.2	0	582.56	24.64	206.69	Cl -Na	−4.82	−42.52
R-4		6-Dec-2019	—	8.66	4.2	498	399	42.05	5.23	24.12	60.52	0.55	53.91	11.99	121.66	2.46	120.26	HCO_3-SO_4-Cl -Na-Ca-Mg	−7.4	−55.8
S-1	Sea	4-Dec-2019	—	8.05	2.6	2,770	2,910	9,186.84	374.69	1,149.19	609.47	5.2	18,249.49	0	2,386.67	0	97.71	Cl -Na	−0.96	−9.65
S-2		4-Dec-2019	—	7.93	2.8	2,530	2,610	8,720.65	349.9	1,112.36	244.37	9.98	16,804.85	0	2,237.45	0	102.72	Cl -Na	−1.41	−12.93
WL-1	Shallow groundwater	30-Nov-2019	200	8.2	28	561	280	83.75	1.07	2.52	17.67	0.78	29.88	0	32.15	11.09	108.98	HCO_3-Na-Ca	−10.08	−76.02
WL-2		1-Dec-2019	300–400	8.19	14	652	327	74.39	0.59	3.31	15.98	0.86	33.5	0	53.84	12.32	106.48	HCO_3-SO_4-Cl-Na-Ca	−10.19	−77.07
WL-3		1-Dec-2019	200	7.9	13.5	608	305	37.99	0.45	9.96	32.05	0.51	22.17	0	43.55	0	126.52	HCO_3-SO_4-Cl-Na-Ca	−9.73	−74.89
WL-4		1-Dec-2019	470	8.27	9	593	294	82.93	0.83	1.98	18.7	1.07	27.34	8.23	87.57	0	95.2	Cl-HCO_3-SO_4-Na-Ca	−9.97	−76.44
WL-5		2-Dec-2019	100	7.67	—	568	300	115.2	1.08	3.12	10.18	0.81	38.9	0.77	25.78	0	134.04	HCO_3-Na	−10.02	−75.34
WL-6		4-Dec-2019	280	7.9	13.3	441	273	69.01	0	5.22	29.84	0.28	43.62	0.59	29.92	0	116.5	HCO_3-Cl-SO_4-Na-Ca	−9.96	−77.44
WL-7		4-Dec-2019	300	8.33	16.8	470	283	101.53	0.7	2.96	10.21	0.93	28.94	0.25	27.79	4.93	131.53	HCO_3-Cl-SO_4 -Na	−10	−74.61
WL-8		6-Dec-2019	230	7.8	15.3	393	237	72.61	0.73	3.66	25.83	0.3	22.99	0	39.37	0	101.47	HCO_3-Cl-SO_4-Na-Ca	−10.2	−75.97
WL-9		6-Dec-2019	280	8	16	705	437	104.27	0.92	5.85	44.87	0.52	120.66	0	42.83	0	113.99	Cl-HCO_3-SO_4 -Na-Ca	−10.07	−74.97
WL-10		6-Dec-2019	230	7.97	13.6	475	303	64.02	0.76	8.97	48.62	0.23	42.07	0	45.29	0	131.53	HCO_3-Cl-SO_4 - Na-Ca	-9.67	-76.11
WL-11		6-Dec-2019	230	7.84	13.5	369	233	36.35	0.46	12.58	45.43	0.26	3.77	0	31.23	0	140.3	HCO_3-SO_4-Cl -Na-Ca	-9.85	-71.45
WR-1	Geothermal water (Caofeidian)	28-Nov-2019	2,422	8.2	77.7	1,635	833	229.29	3.38	0	0	6.03	145.8	0	0.81	33.26	207.94	Cl-HCO_3-Na	−9.23	−73.19
WR-2		29-Nov-2019	2,332	8.37	79.4	1,484	733	231.95	3.83	0	0	5.17	140.42	0	0.42	19.71	107.73	Cl-HCO_3-Na	−9.44	−73.51
WR-3		29-Nov-2019	2,497	8.49	77.4	1,379	691	220.62	3.18	0	0	5.8	135.34	0	0	11.09	229.24	Cl-HCO_3-Na	−9.27	−72.79
WR-4		29-Nov-2019	2,388	8.46	78.2	1,390	703	219.13	3.45	0	0	5.69	147.05	0	1.14	7.39	226.73	Cl-HCO_3-Na	−9.35	−73.06
WR-5		29-Nov-2019	2,442	8.47	79.2	1,510	752	225.36	3.65	0	0	5.8	146.79	0	1.7	14.78	231.75	Cl-HCO_3-Na	−9.26	−73.13
WR-6		29-Nov-2019	2,476	8.42	78	1,433	704	216.34	3.15	0	0	5.52	143.42	0	0	13.55	209.2	Cl-HCO_3-Na	-9.32	-73.22
WR-7		29-Nov-2019	2,475	8.37	70	1,539	767	247.27	4.33	0	0	6.13	153.6	0	0	13.55	271.83	Cl-HCO_3-Na	−9.27	−73.01
WR-8		29-Nov-2019	2,500	8.4	76.3	1,524	762	235.8	3.49	0	3.09	6.35	136.86	0	12.42	13.55	255.55	Cl-HCO_3-Na	−9.28	−76.11
WR-9		29-Nov-2019	2,534	8.43	80	1,475	740	233.51	3.7	0	0	5.89	150.25	0	0	17.25	234.25	Cl-HCO_3-Na	−9.27	−73.2
WR-10		30-Nov-2019	—	8.42	81	1,673	831	279.5	4.72	0	0	6.36	162	1.84	0.47	12.32	296.88	Cl-HCO_3-Na	−9.18	−72.83
WR-11	Geothermal water (Matouying)	30-Nov-2019	—	8.52	117	2,794	1,408	346.33	13.63	0	71.24	16.04	433	0	155.19	11.09	91.45	Cl-SO_4-HCO_3-Na	−8.18	−70.73
WR-12		30-Nov-2019	—	7.27	—	2,239	1,111	306.67	7.26	0	4.41	12.21	370.99	0	144.38	0	100.21	Cl-SO_4-HCO_3-Na	−8.28	−71.37
D-1	Geothermal water (Dongying Formation)	3-Dec-2019	2,161–2,492	8.15	8	3,990	2,260	774.01	16.79	2.67	16.88	3.5	735.3	0	0	0	652.65	Cl-HCO_3-Na	−8.25	−69.31

fields was less than 20 km, a significant difference was observed in the temperature patterns at the two sites. **Figure 4** also illustrates that there are significant thermal disturbances near the Gaoliu Fault, indicating that the Gaoliu and Xinanzhuang faults are important channels for the migration of geothermal water. The rapid changes in temperature near the Baigezhuang Fault suggest the presence of a barrier dividing Caofeidian and Matouying into two geothermal systems. The Xinanzhuang, Baigezhuang, and Gaoliu faults in the study area are the main heat-controlling and water-controlling structures. From the contour of hydrostatic pressure of geothermal water at the depth of 2000m (**Figure 5**), it can be concluded that the flow direction of geothermal water is from northwest to southeast at Caofeidian, which keeps in accordance with the modeling results by Huang et al. (2021b).

Hydrochemistry Characteristic

All water samples are plotted in **Figure 6** and shown in **Table 1**. The results show that the chemical characteristics of geothermal water at Caofeidian and Matouying are distinct. For geothermal water at the Caofeidian, the TDS ranges from 691 mg/L to 833 mg/L, with an average value of approximately 750 mg/L. In addition, the water type was characterized by the presence of Cl·HCO_3-Na. The pH was between 8.2 and 8.49. The principal cation was Na^+ (219–279.0 mg/L) and the concentration of K^+ was low, ranging from 3.1 to 4.7 mg/L. Ca^{2+} and Mg^{2+} were not detected in any of the 10 geothermal boreholes. For geothermal water at the Matouying, the TDS values were 1,111 mg/L and 1,408 mg/L, which were greater than those observed at the Matouying. The principal cations were also Na^+ (306 mg/L and 346 mg/L), and the principal anions were Cl^-, SO_4^{2-}, and HCO_{3-}. The geothermal water at Matouying was Cl·SO_4·HCO_3-Na, with pH was 7.27 and 8.52.

The TDS of the shallow groundwater ranged from 233 mg/L to 437 mg/L. The pH range of the shallow groundwater was 7.67–8.33. The principal cation was Na^+(36–104 mg/L), which was found in greater concentrations than K^+ (0–1.08 mg/L), Ca^{2+}(10.2–48.6 mg/L), and Mg^{2+}(2.0–12.58 mg/L). The principal anions were Cl^-, HCO_3^-, and SO_4^{2-}. The shallow groundwater water types were HCO_3-Na·Ca and HCO_3·SO_4·Cl-Na·Ca. The TDS of surface water, including river water, pond water, and sea water, was much higher than that of groundwater.

Water Isotopic Composition

The stable isotope compositions of the water samples are shown in **Figure 7** and **Table 1**, which indicate that stable isotopes of shallow groundwater are located in relatively centralized region with a range of -9.7‰ to -10.2‰ for $\delta^{18}O$ and a range of -77.4‰ to -71.5‰ for δ^2H. We can easily distinguish between the two groups of geothermal water at the Caofeidian and the Matouying. For geothermal water at the Caofeidian, stable isotopes ranged from -9.4‰ to -9.2‰ for $\delta^{18}O$ and from -76.1‰ to –72.8‰ for δ^2H, respectively. The stable isotopes of geothermal water at Matouying are more enriched than other groundwater samples with $\delta^{18}O$ values of -8.2‰ and -8.3‰ and δ^2H values of -70.7‰ and -71.4‰, respectively. The stable isotopes of rivers, ponds, and seas are much more enriched than those of the sampled groundwater. In addition, the local meteoric line (LMWL) presented in previous studies by Fang et al. (2014), and the equation is $\delta^2H = 6.61\delta^{18}O+0.69$. We found that shallow groundwater was distributed along the LMWL, whereas the sampling geothermal waters were all located below the LMWL.

Groundwater Dating

Based on the hypothesis that dissolved inorganic carbon (DIC) is derived from soil CO_2 and carbonate dissolution, the $\delta^{13}C$ mixing model was used to calculate and correct the groundwater ^{14}C age based on the significant difference in $\delta^{13}C$ values between soil CO_2 and carbonate minerals (Huang and Pang, 2011; Kong et al., 2020). The groundwater ages of the geothermal water samples are shown in **Table 2**.

As can be seen from **Table 2**, the geothermal water ^{14}C at Caofeidian is 1.01–1.98 PMC, and the estimated age is 27-32 ka. The geothermal water ^{14}C at Matouying is 3.16 PMC, and the estimated age is about 21 ka. In general, the geothermal water at Matouying formed more recently than that of the Caofeidian, which indicates a different circulation pattern at the two sites.

DISCUSSION

Recharge Source of Geothermal Water

Comparing the hydrochemical composition of geothermal water with shallow groundwater, the water types were different, and the concentrations of K^+ and Cl^- were significantly greater in geothermal water (**Figure 6** and **Table 1**). The greater TDS value of geothermal water indicates the geological process by which precipitation infiltrates into the ground and then interacts with the minerals through which it flows (Domenico and Schwartz, 1998; Ma et al., 2011). The isotope composition of geothermal water at both sites deviated from the LMWL and was more enriched in ^2H and ^{18}O than in shallow groundwater (**Figure 7**). For the isotope enrichment of geothermal water, we propose some hypothesis to address the $\delta^{18}O$-δ^2H pattern of geothermal water in **Figure 7**, including evaporation process, water-rock interaction, mixing process and bacterial SO_4^{2-} reduction process (BSR). First, the evaporation process is usually expressed by evaporation line of surface water like ponds and lakes within a study area. However, the geothermal water isotopes is located far below the water line of ponds water isotope (**Figure 7**), which could provide robust evidence to exclude the hypothesis of evaporation. Considering the different isotopic signature of geothermal water, geological settings and hydrothermal patterns at Caofeidian and Matouying, the $\delta^{18}O$-δ^2H pattern as well as the recharge source of geothermal water at the two places are investigated respectively. For the geothermal water at Caofeidian, the ^{18}O enrichment of geothermal water may be due to the water-rock interaction with surrounding minerals at certain pressures and temperatures (Pang et al., 2017). For the ^2H enrichment of geothermal water at Caofeidian, we attribute it to the process of bacterial SO_4^{2-} reduction (BSR), which converts SO_4^{2-} to H_2S and accompanies the enrichment for ^2H. The low concentration of SO_4^{2-} in geothermal water provides evidence for the occurrence of the BSR process (Matray et al., 1994). Such phenomenon has also been detected in the geothermal water of Niutuizhen reservoir, northern China (Kong et al., 2020). However, the reduction of

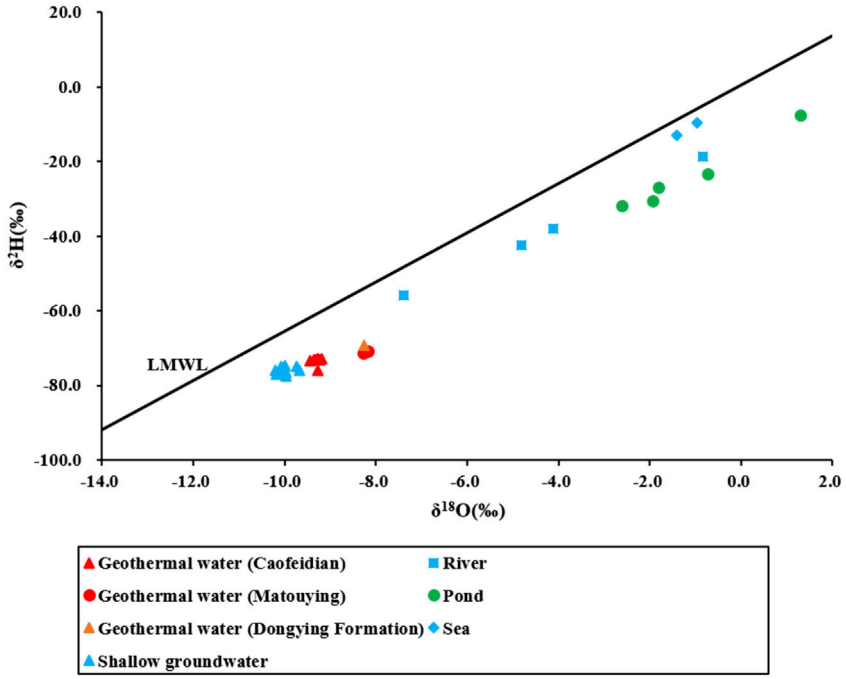

FIGURE 7 | Isotopes of all the water samples at the Caofeidian and the Matouying.

TABLE 2 | Groundwater age of geothermal water at the Caofeidian and the Matouying.

Sample Label	Region	^{14}C (pmc)	$\delta^{13}C$ (‰)	Age
WR-8	Caofeidian	1.01	−11.5	32,258
WR-9	Caofeidian	1.98	−11.7	26,836
WR-11	Matouying	3.16	−9.1	20,894

SO_4^{2-} (approximately 0.05 g) was not sufficient to increase ^2H by 0.5‰. There are other reasons for the enrichment of ^2H. We attribute this to the mixing process with groundwater from the underlying Dongying Formation, which may recharge the upper Guantao Formation with more enriched isotopes through the faults connecting the two formations (**Figure 3**). As for the Matouying geothermal water, the even more enriched isotopes can be attributed to the water-rock interaction under higher temperature conditions. The high value of $^{87}Sr/^{86}Sr$ for geothermal water at the Matouying also suggests that the geothermal water has experienced deep circulation into the granite strata at higher temperatures (Barbieri & Morotti, 2003; Guo et al., 2009; Khaska et al., 2015). Besides, the much higher concentration of Li and B of geothermal water than that in the shallow groundwater can also be a good indicator for the deep circulation of geothermal water (Giggenbach et al., 1995).

Reservoir Temperature Calculation

Considering the low concentrations of Ca^{2+} and Mg^{2+} in the geothermal water in the study area, Na-K geothermometers were employed for the calculation of the reservoir temperature (Fournier, 1979; Arnorsson et al., 1983; Pang & Reed, 1998). According to the calculation results of the Na-K geothermometers, the estimated reservoir temperature is completely different between the geothermal water at Caofeidian and Matouying (**Table 3**). The reservoir temperature at the Caofeidian is 83–92°C while the reservoir temperature at the Matouying is 107–137°C, which also indicates the different geothermal systems at the two sites.

Heat Sources

The reservoir temperature of the geothermal water at the Matouying is much greater than that at Caofeidian (**Table 2**). We attribute the thermal anomalies at the Matouyong to the normal thermal conductivity as well as the radioactive heat generated by the granite (Wang, 2015b; Zhang et al., 2020a). The much greater concentration of radioactive heat-generating elements including uranium (U), thorium (Th), and potassium (K) observed in geothermal water at the Matouying suggests the existence of additional radioactive heat (**Table 4**). In addition, the higher concentration of Sr and $^{87}Sr/^{86}Sr$ of geothermal water at Matouying transports the signal from potassium-rich rocks, which also indicates the additional radioactive heat generated from granite (Faure & Powell, 2012; Capo et al., 1998). And the radioactive heat from granite has also been illustrated in the granite of the Bohai Bay Basin (Jiang et al., 2016; Li et al., 2017; Qiu et al., 2015). Thus, it can be concluded that part of the heat source of the geothermal water at Matouying originates from the heat generated by granite radioactive elements, which is different from the heat source of the geothermal water at the Caofeidian, which originates from the natural geothermal heating of the earth's crust.

TABLE 3 | Estimated reservoir temperature at the Caofeidian and the Matouying.

Sampling Lable	WR-1	WR-2	WR-3	WR-4	WR-5	WR-6	WR-7	WR-8	WR-9	WR-10	WR-11	WR-12
	Caofeidian										Matouying	
T (°C)	83.6	89.7	82.6	86.8	88.1	83.1	92	83.9	87.1	90.2	136.6	107.4

TABLE 4 | Trace elements (Li, B, U, Th, Sr) and $^{87}Sr/^{86}Sr$ characteristic of geothermal water at the Caofeidian and the Matouying.

Sample lable	Type	Li (μg/L)	B (μg/L)	Sr (μg/L)	U (μg/L)	Th (μg/L)	$^{87}Sr/^{86}Sr$
WL-1	Shallow groundwater	9.53	6	401	0.044	<0.002	0.708,895
WL-3		6.69	<0.002	870	0.045	<0.002	0.709,043
WL-6		6.41	1	674	0.036	<0.002	0.70894
WL-9		5.4	<0.002	845	0.048	<0.002	0.708,938
WL-11		4.9	3	764	0.05	<0.002	0.709,244
WR-1	Caofeidian geothermal water	38.4	311	69.6	0.002	0.02	0.708,236
WR-8		35.9	284	92.8	0.003	0.005	0.70998
WR-9		31.2	343	106	<0.002	0.003	0.708,136
WR-11	Matouying geothermal water	657	739	591	0.012	0.008	0.718,459

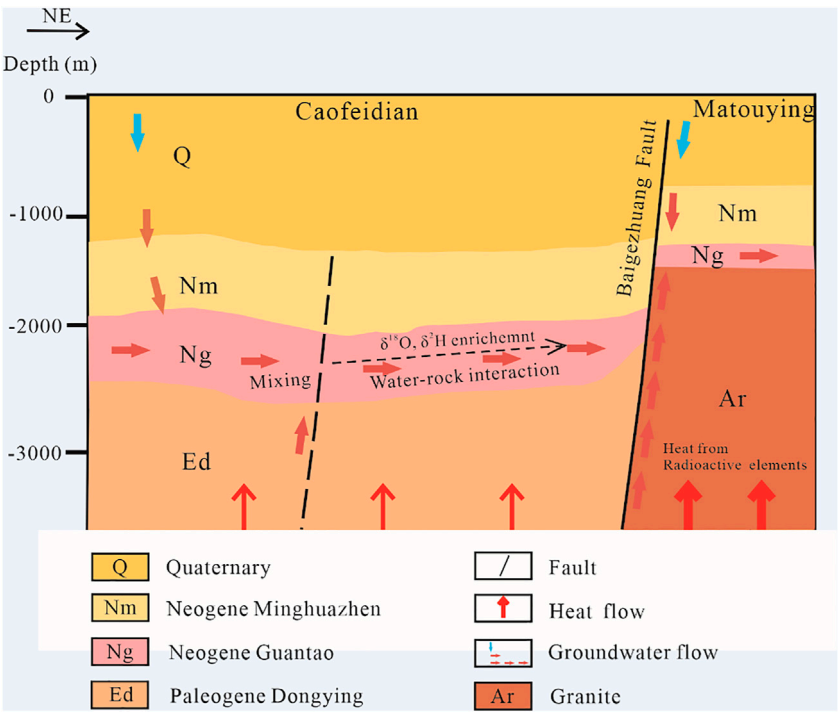

FIGURE 8 | Conceptual model of hydrothermal genesis of the Caofeidian and the Matouying geothermal reservoirs.

Conceptual Genetic Model

Based on the above analysis with regard to the geological setting, hydrothermal pattern, geochemical, and isotopic data, a conceptual genetic model of the geothermal water in our study area is proposed in **Figure 8**. Generally, all geothermal water originates from local precipitation. Then, the different infiltrated water flow pathways would result in distinct geothermal water at the two observation sites. The geothermal water rises upward through deep faults and fractures, which can be regarded as hydrothermal channels. Quaternary deposits comprising immature yellow gravel and clay interbeds serve as cap rocks for geothermal systems. The

geochemical and isotopic composition of geothermal water at the Caofeidian indicate that the infiltrated water would experience the water-rock reaction with the sandstone along its pathways, the BSR process, and the mixing process from deeper Ed geothermal water. The Geothermal water flow direction is from the northwest to the southeast. The geothermal water heating source at the Caofeidian is thermal conductivity and fluid convection. The Baigezhuang fault functions as a barrier to divide the two geothermal systems. Geothermal water at the Matouying would infiltrate deep into the granite and ascend at higher temperatures. Thus, the heat generated from radioactive elements within the granite is an additional heat source for geothermal water in the Matouying.

CONCLUSION

We found different hydrothermal patterns at the Caofeidian and the Matouying geothermal systems through water temperature and pressure monitoring. By conducting detailed geochemical and isotopic analyses of the geothermal water, we investigated the hydrothermal system characteristics of the two geothermal systems and distinguished the recharge source and circulation pattern of geothermal water at the two sites. Although geothermal water originates from precipitation at both systems, the circulation pattern of groundwater is distinct for tthem. The geothermal water at Caofeidian has experienced the process of infiltration, interaction with sandstone, BSR, and mixing with geothermal water from the underlying Dongying Formation. The infiltrated water is able to circulate deeply into the granite underlying the Matouying system. Application of Na-K geothermometers indicated reservoir temperatures to be in the interval of 83–92°C at the Caofeidian and 107–137°C at the Matouying, respectively. The corrected ^{14}C age of geothermal water indicates a lower circulation rate and rare renewability for geothermal water at the Caofeidian system. This study provides multiple information on the geothermal systems in our study area, and the results are instructive and significant with respect to the sustainable exploitation of geothermal resources in the Caofeidian and the Matouying geothermal systems.

DATA AVAILABILITY STATEMENT

The original contributions presented in the study are included in the article/Supplementary Material, further inquiries can be directed to the corresponding authors.

AUTHOR CONTRIBUTIONS

YK and WS designed the study and gave conceptual advice. KW, CH, and SP conducted field work, analyzed the laboratory results, and prepared the manuscript. LR, JW, and YD provided row data information and basic information about the geothermal wells. YC, YH, and FT contributed to the geological settings section. DQ, WZ, and FM conducted laboratory analysis of the samples. All authors contributed to the editing of the manuscript, and approval of the content in its current form.

FUNDING

This work was financially supported by the National Key Research and Development Program of China (Grant no. 2019YFB1504101). We also acknowledge the financial support from National Natural Science Foundation of China (Grant no. 52192623), the Youth Innovation Promotion Association of Chinese Academy of Sciences (Grant no. 2020067) and the PetroChina Jidong Oilfield Company.

ACKNOWLEDGMENTS

We thank the PetroChina Jidong Oilfield Company for providing the data used in this work and the staff like Liping Yuan, Chaoqun Liu and other individuals who helped the field sampling work.

REFERENCES

An, Q., Wang, Y., Zhao, J., Luo, C., and Wang, Y. (2016). Direct Utilization Status and Power Generation Potential of Low-Medium Temperature Hydrothermal Geothermal Resources in Tianjin, China: A Review. *Geothermics* 64, 426–438. doi:10.1016/j.geothermics.2016.06.005

Arnórsson, S., Gunnlaugsson, E., and Svavarsson, H. (1983). The Chemistry of Geothermal Waters in Iceland. III. Chemical Geothermometry in Geothermal Investigations. *Geochimica et Cosmochimica Acta*, 47(3), 567–577. doi:10.1016/0016-7037(83)90278-8

Barbieri, M., and Morotti, M. (2003). Hydrogeochemistry and Strontium Isotopes of spring and mineral Waters from Monte Vulture Volcano, Italy. *Appl. Geochem.* 18 (1), 117–125. doi:10.1016/S0883-2927(02)00069-0

Byrappa, K., and Yoshimura, M. (2012). *Handbook of Hydrothermal Technology*. New York: William Andrew.

Capo, R. C., Stewart, B. W., and Chadwick, O. A. (1998). Strontium Isotopes as Tracers of Ecosystem Processes: Theory and Methods. *Geoderma*, 82(1-3), 197–225. doi:10.1016/S0016-7061(97)00102-X

Chang, J., Qiu, N. S., Zhao, X. Z., Xu, W., Xu, Q. C., Jin, F. M., et al. (2016). Present-day Geothermal Regime of the Jizhong Depression in Bohai Bay basin, East China. *Chin. J. Geophysics-Chinese Edition* 59 (3), 1003–1016. doi:10.6038/cjg20160322

Clark, I. D., and Fritz, P. (2013). *Environmental Isotopes in Hydrogeology*. Boca Raton: CRC Press. doi:10.1201/9781482242911

Domenico, P. A., and Schwartz, F. W. (1998). *Physical and Chemical Hydrogeology*. New York: Wiley, (Vol. 506).

Dong, Y., Wang, Z., Zheng, H., and Xu, A. (2008). Control of Strike-Slip Faulting on Reservoir Formation of Oil and Gas in Nanpu Sag. *Pet. Exploration Dev.* 35 (4), 424–430. doi:10.1016/s1876-3804(08)60090-7

Dong, Y., Huang, H., Ren, L., Li, H., Du, Z., E, J., et al. (2021). Geology and Development of Geothermal Field in Neogene Guantao Formation in Northern Bohai Bay Basin: A Case of the Caofeidian Geothermal Heating Project in Tangshan, China. *Pet. Exploration Dev.* 48 (3), 775–786. doi:10.1016/S1876-3804(21)60063-0

Duan, Z., Pang, Z., and Wang, X. (2011). Sustainability Evaluation of limestone Geothermal Reservoirs with Extended Production Histories in Beijing and Tianjin, China. *Geothermics* 40 (2), 125–135. doi:10.1016/j.geothermics.2011.02.001

Fang, C., Liu, F. T., Meng, L. S., Liu, H. W., Qin, Y. F., and Zheng, J. N. (2014). Application of Hydrogen and Oxygen Isotopes to Study Hydrologic Cycle in the Caofeidian Area. *North. China Geology.* (2), 102–107.

Faure, G., and Powell, J. L. (2012). *Strontium Isotope Geology*, 5. Springer Science & Business Media.

Fournier, R. O. (1979). A Revised Equation for Na/K Geothermometers. *Geoth Res. Counc. Trans.* 3, 221–224. doi:10.1016/0016-7037(73)90060-4

Giggenbach, W. F., Stewart, M. K., Lyon, G. L., Sano, Y., and Goguel, R. L. (1995). *Isotopic and Chemical Composition of Waters and Gases from the East Coast Accretionary Prism*. New Zealand.

Guo, Q., Wang, Y., and Liu, W. (2009). O, H, and Sr Isotope Evidences of Mixing Processes in Two Geothermal Fluid Reservoirs at Yangbajing, Tibet, China. *Environ. Earth Sci.* 59 (7), 1589–1597. doi:10.1007/s12665-009-0145-y

Hähnlein, S., Bayer, P., Ferguson, G., and Blum, P. (2013). Sustainability and Policy for the thermal Use of Shallow Geothermal Energy. *Energy Policy* 59, 914–925. doi:10.1016/j.enpol.2013.04.040

Huang, T., and Pang, Z. (2011). "*Combined Conceptual Model (V& P Model) to Correct* Groundwater Radiocarbon Age," in Paper presented at the 2011 International Symposium on Water Resource and Environmental Protection, 20–22.

Huang, Y., Pang, Z., Kong, Y., and Watanabe, N. (2021a). Assessment of the High-Temperature Aquifer Thermal Energy Storage (HT-ATES) Potential in Naturally Fractured Geothermal Reservoirs With a Stochastic Discrete Fracture Network Model. *J. Hydrol.* 603, 127188. doi:10.1016/j.jhydrol.2021.127188

Huang, Y., Cheng, Y., Ren, L., Tian, F., Pan, S., Wang, K., et al. (2021b). Assess the Geothermal Resource Potential of an Active Oil Field by Integrating a 3D Geological Model with the Hydro-thermal Coupled Simulation. *Front. Earth Sci.* 1178. doi:10.3389/feart.2021.787057

Jiang, G., Gao, P., Rao, S., Zhang, L., Tang, X., Huang, F., et al. (2016). Compilation of Heat Flow Data in the Continental Area of China. *Chin. J. Geophys.* 59 (8), 2892–2910.

Khaska, M., Le Gal La Salle, C., Videau, G., Flinois, J.-S., Frape, S., Team, A., et al. (2015). Deep Water Circulation at the Northern Pyrenean Thrust: Implication of High Temperature Water-Rock Interaction Process on the Mineralization of Major spring Water in an Overthrust Area. *Chem. Geology.* 419, 114–131. doi:10.1016/j.chemgeo.2015.10.028

Kong, Y., Pang, Z., Pang, J., Li, J., Lyu, M., and Pan, S. (2020). Fault-Affected Fluid Circulation Revealed by Hydrochemistry and Isotopes in a Large-Scale Utilized Geothermal Reservoir. *Geofluids* 2020, 1–13. doi:10.1155/2020/2604025

Kong, Y., Pang, Z., Shao, H., Hu, S., and Kolditz, O. (2014). Recent Studies on Hydrothermal Systems in China: a Review. *Geothermal Energy* 2 (19). doi:10.1186/s40517-014-0019-8

Le Gal, V., Lucazeau, F., Cannat, M., Poort, J., Monnin, C., Battani, A., et al. (2018). Heat Flow, Morphology, Pore Fluids and Hydrothermal Circulation in a Typical Mid-Atlantic Ridge Flank Near Oceanographer Fracture Zone. *Earth Planet. Sci. Lett.* 482, 423–433. doi:10.1016/j.epsl.2017.11.035

Li, Z., Zuo, Y., Qiu, N., and Gao, J. (2017). Meso-Cenozoic Lithospheric thermal Structure in the Bohai Bay Basin, Eastern North China Craton. *Geosci. Front.* 8 (5), 977–987. doi:10.1016/j.gsf.2016.09.003

Lister, C. R. B. (1980). Heat Flow and Hydrothermal Circulation. *Annu. Rev. Earth Planet. Sci.*, 8, 95–117. doi:10.1146/annurev.ea.08.050180.000523

Lund, J. W., and Toth, A. N. (2021). Direct Utilization of Geothermal Energy 2020 Worldwide Review. *Geothermics* 90, 101915. doi:10.1016/j.geothermics.2020.101915

Ma, R., Wang, Y., Sun, Z., Zheng, C., Ma, T., and Prommer, H. (2011). Geochemical Evolution of Groundwater in Carbonate Aquifers in Taiyuan, Northern China. *Appl. Geochem.* 26 (5), 884–897. doi:10.1016/j.apgeochem.2011.02.008

Marrasso, E., Roselli, C., Sasso, M., and Tariello, F. (2018). Global and Local Environmental and Energy Advantages of a Geothermal Heat Pump Interacting with a Low Temperature thermal Micro Grid. *Energ. Convers. Manag.* 172, 540–553. doi:10.1016/j.enconman.2018.07.028

Matray, J. M., Lambert, M., and Fontes, J. C. (1994). Stable Isotope Conservation and Origin of saline Waters from the Middle Jurassic Aquifer of the Paris Basin, France. *Appl. Geochem.*, 9(3), 297–309. doi:10.1016/0883-2927(94)90040-X

Moya, D., Aldás, C., and Kaparaju, P. (2018). Geothermal Energy: Power Plant Technology and Direct Heat Applications. *Renew. Sust. Energ. Rev.* 94, 889–901. doi:10.1016/j.rser.2018.06.047

Pang, Z.-H., and Reed, M. (1998). Theoretical Chemical Thermometry on Geothermal Waters: Problems and Methods. *Geochimica et Cosmochimica Acta*, 62(6), 1083–1091. doi:10.1016/S0016-7037(98)00037-4

Pang, Z., Kong, Y., Li, J., and Tian, J. (2017). An Isotopic Geoindicator in the Hydrological Cycle. *Proced. Earth Planet. Sci.* 1517, 534–537. doi:10.1016/j.proeps.2016.12.135

Pang, Z., Kong, Y., Shao, H., and Kolditz, O. (2018). Progress and Perspectives of Geothermal Energy Studies in China: from Shallow to Deep Systems. *Environ. Earth Sci.* 77 (16). doi:10.1007/s12665-018-7757-z

Qiu, N., Xu, W., Zuo, Y., and Chang, J. (2015). Meso-Cenozoic thermal Regime in the Bohai Bay Basin, Eastern North China Craton. *Int. Geology. Rev.* 57 (3), 271–289. doi:10.1080/00206814.2014.1002818

Qiu, N., Zuo, Y., Chang, J., and Li, W. (2014). Geothermal Evidence of Meso-Cenozoic Lithosphere Thinning in the Jiyang sub-basin, Bohai Bay Basin, Eastern North China Craton. *Gondwana Res.* 26 (3-4), 1079–1092. doi:10.1016/j.gr.2013.08.011

Qiu, N., Zuo, Y., Xu, W., Li, W., Chang, J., and Zhu, C. (2016). Meso-Cenozoic Lithosphere Thinning in the Eastern North China Craton: Evidence from thermal History of the Bohai Bay Basin, North China. *J. Geology.* 124 (2), 195–219. doi:10.1086/684830

Rybach, L. (2003). Geothermal Energy: Sustainability and the Environment. *Geothermics* 32 (4-6), 463–470. doi:10.1016/S0375-6505(03)00057-9

Shortall, R., Davidsdottir, B., and Axelsson, G. (2015). Geothermal Energy for Sustainable Development: A Review of Sustainability Impacts and Assessment Frameworks. *Renew. Sust. Energ. Rev.* 44, 391–406. doi:10.1016/j.rser.2014.12.020

Wang, E., Feng, Y., Liu, G., Chen, S., Wu, Z., and Li, C. (2021). Hydrocarbon Source Potential Evaluation Insight into Source Rocks-A Case Study of the First Member of the Paleogene Shahejie Formation, Nanpu Sag, NE China. *Energ. Rep.* 7, 32–42. doi:10.1016/j.egyr.2020.11.099

Wang, E., Li, C., Feng, Y., Song, Y., Guo, T., Li, M., et al. (2022). Novel Method for Determining the Oil Moveable Threshold and an Innovative Model for Evaluating the Oil Content in Shales. *Energy* 239, 121848. doi:10.1016/j.energy.2021.121848

Wang, E., Liu, G., Pang, X., Li, C., Zhao, Z., Feng, Y., et al. (2020). An Improved Hydrocarbon Generation Potential Method for Quantifying Hydrocarbon Generation and Expulsion Characteristics with Application Example of Paleogene Shahejie Formation, Nanpu Sag, Bohai Bay Basin. *Mar. Pet. Geology.* 112, 104106. doi:10.1016/j.marpetgeo.2019.104106

Wang, G.-l., Zhang, W., Zhang, W., Ma, F., Lin, W.-j., Liang, J.-y., et al. (2018). Overview on Hydrothermal and Hot Dry Rock Researches in China. *China Geology.* 1 (2), 273–285. doi:10.31035/cg2018021

Wang, J. (2009). "Discussions on Geothermal Energy Exploration and Utilization of China, from the point of World Geothermal Energy," in Proceedings of workshop on Chinese scientific geothermal energy exploration (Beijing: Geology Press).

Wang, J. (2015a). Geothermal Energy Should Play a More Important Role in the Smog Control and Space Heating/Refrigeration in China. *Scientific Tech. Rev.* 33 (24), 1.

Wang, J. (2015b). *Geothermics and its Application*. Beijing: Science press.

Wang, Z. T., Rao, S., Xiao, H. P., Wang, Y. B., Jiang, G. Z., Hu, S. B., et al. (2021). Terrestrial Heat Flow of Jizhong Depression, China, Western Bohai Bay basin and its Influencing Factors. *Geothermics* 96. doi:10.1016/j.geothermics.2021.102210

Yang, P., Cheng, Q., Xie, S., Wang, J., Chang, L., Yu, Q., et al. (2017). Hydrogeochemistry and Geothermometry of Deep thermal Water in the Carbonate Formation in the Main Urban Area of Chongqing, China. *J. Hydrol.* 549, 50–61. doi:10.1016/j.jhydrol.2017.03.054

Zhang, B., Li, Y., Gao, J., Wang, G., Li, J., Xing, Y., et al. (2020a). Genesis and Indicative Significance of Hot Dry Rock in Matouying, Hebei Province. *Acta Geologica Sinica* 94 (7), 2036–2051.

Zhang, C., Hu, S., Song, R., Zuo, Y., Jiang, G., Lei, Y., et al. (2020b). Genesis of the Hot Dry Rock Geothermal Resources in the Gonghe basin: Constraints from the Radiogenic Heat Production Rate of Rocks. *Chin. J. Geophys.* 63 (7), 2697–2709.

Zhu, G., Wang, Z., and Cao, Z. (2014). Origin and Source of the Cenozoic Gas in the Beach Area of the Nanpu Sag, Bohai Bay Basin, China. *Energy Exploration & Exploitation*, 32(1), 93–111. doi:10.1260/0144-5987.32.1.93

Conflict of Interest: Authors LR and JW are employed by Jidong Oilfield Company of PetroChina. Author YD is employed by Advisory Center, China National Petroleum Corporation.

The remaining authors declare that the research was conducted in the absence of any commercial or financial relationships that could be construed as a potential conflict of interest.

Publisher's Note: All claims expressed in this article are solely those of the authors and do not necessarily represent those of their affiliated organizations, or those of the publisher, the editors and the reviewers. Any product that may be evaluated in this article, or claim that may be made by its manufacturer, is not guaranteed or endorsed by the publisher.

frontiers in Earth Science

ORIGINAL RESEARCH
published: 24 March 2022
doi: 10.3389/feart.2022.824056

Distribution Characteristics of the Deep Geothermal Field in the Sichuan Basin and its Main Controlling Factors

Chuanqing Zhu[1,2]*, *Tong Xu*[1,2], *Nansheng Qiu*[1,2], *Tiange Chen*[3], *Ming Xu*[4] and *Rui Ding*[1,2]

[1]State Key Laboratory of Petroleum Resources and Prospecting, China University of Petroleum (Beijing), Beijing, China, [2]College of Geosciences, China University of Petroleum (Beijing), Beijing, China, [3]Research Institute of Petroleum Exploration Development, Beijing, China, [4]Tianjin Geothermal Exploration and Development-Design Institute, Tianjin, China

Geothermal energy and petroleum are two resources that coexist in sedimentary basins, and both of them are closely related to temperature. Based on the surface heat flow and the rock thermophysical properties, the deep geothermal field was calculated, then temperature distribution characteristics and the primary influencing factors on the geothermal state were discussed. The temperature distribution map of the Sichuan Basin for depths of 3,000–9,000 m presented the central and southern areas are characterized by relatively higher temperatures while the northwestern and northeastern areas are characterized by lower temperatures. Strata temperature in the central and southern areas exceeded 150°C as the burial depth reached 5,000 m. At the depth of 7,000 m, the temperatures in the central and southern areas were above 180°C, which is the threshold temperature for hot dry rock (HDR), while the temperatures in the northwestern and northeastern areas were below 160°C, which is close to the lower limit for oil crude oil cracking. The central and southern areas are favorite zones for the exploration of geothermal energy, conversely, the relatively lower temperatures in the northern, northwestern, and eastern areas are conducive to the presence of oil and gas. The unevenly distribution of geothermal field were controlled by the thicknesses of sedimentary layer and the crust, which indicates the lithosphere flexure and thickening caused by compression and depression, rapid deposition in the foreland depressions. The results can provide geothermal understandings for the exploration and development of the petroleum and geothermal resources and could serve as a reference for geodynamic studies in the Sichuan Basin.

Keywords: geothermal field, thermal conductivity, radioactive heat production, heat flow, Sichuan Basin

OPEN ACCESS

Edited by:
Yanlong Kong,
Institute of Geology and Geophysics (CAS), China

Reviewed by:
Yingchun Wang,
Chengdu University of Technology, China
Yiquan Li,
Nanjing University, China
Yiman Li,
Institute of Geology and Geophysics (CAS), China

***Correspondence:**
Chuanqing Zhu
zhucq@cup.edu.cn

Specialty section:
This article was submitted to Economic Geology, a section of the journal Frontiers in Earth Science

Received: *28 November 2021*
Accepted: *21 February 2022*
Published: *24 March 2022*

Citation:
Zhu C, Xu T, Qiu N, Chen T, Xu M and Ding R (2022) Distribution Characteristics of the Deep Geothermal Field in the Sichuan Basin and its Main Controlling Factors. Front. Earth Sci. 10:824056. doi: 10.3389/feart.2022.824056

INTRODUCTION

Geothermal resources utilization can not only save non-renewable energy but also reduce carbon emissions and pollution to mitigate smog. Therefore, geothermal resources have become a topic of interest in research on the development and exploitation of new energy. Geothermal energy and petroleum are two resources that coexist in sedimentary basins. Oilfields are rich not only in oil and gas but also often in geothermal resources. Thus, geothermal energy is rapidly developed and exploited in oil and gas exploration areas (Wang et al., 2016; Shah et al., 2017). The knowledge and experience gained from oil and gas development is often transferable to the exploitation of geothermal energy. Furthermore, a considerable number of abandoned boreholes are available

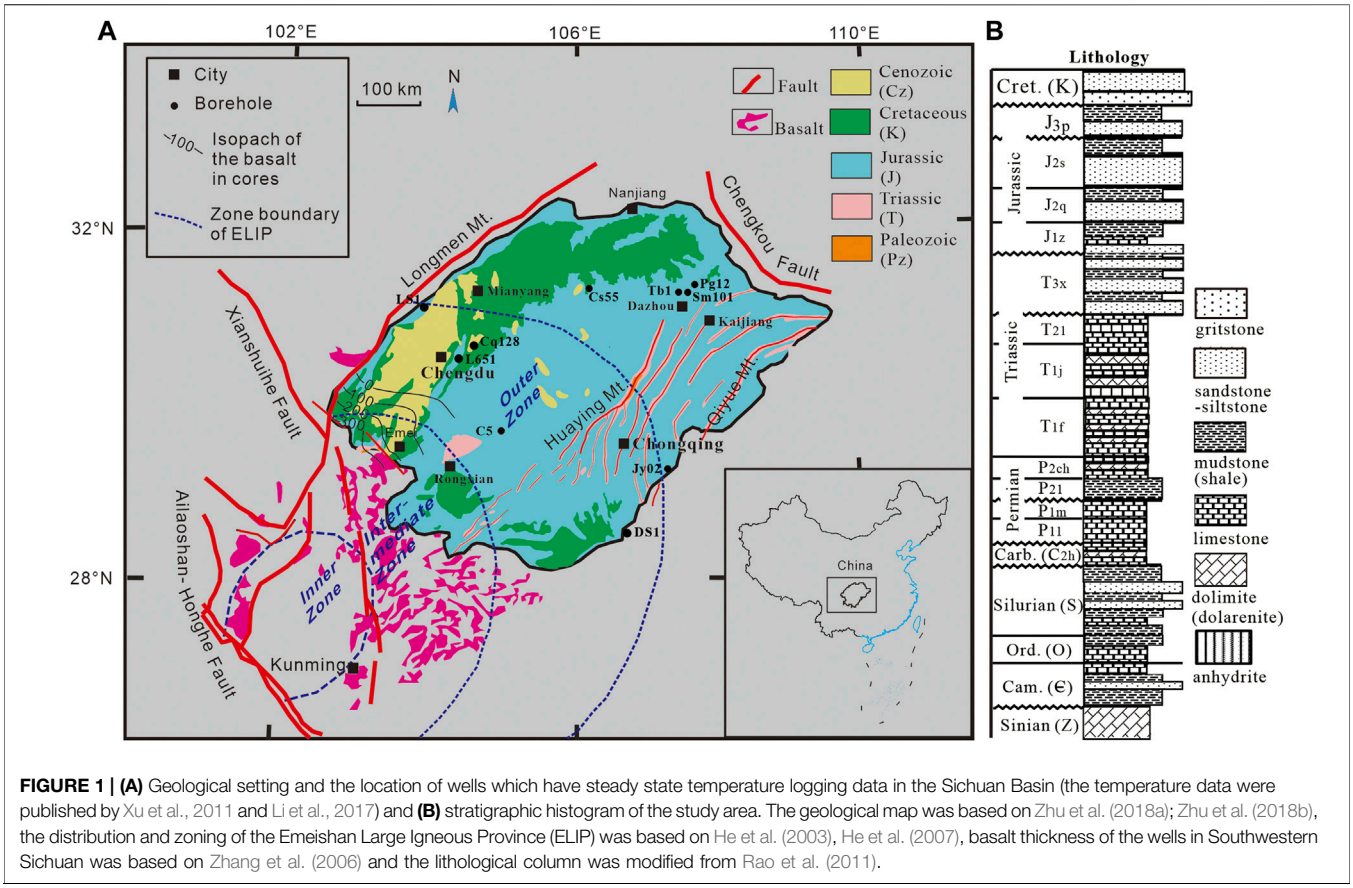

FIGURE 1 | (A) Geological setting and the location of wells which have steady state temperature logging data in the Sichuan Basin (the temperature data were published by Xu et al., 2011 and Li et al., 2017) and **(B)** stratigraphic histogram of the study area. The geological map was based on Zhu et al. (2018a); Zhu et al. (2018b), the distribution and zoning of the Emeishan Large Igneous Province (ELIP) was based on He et al. (2003), He et al. (2007), basalt thickness of the wells in Southwestern Sichuan was based on Zhang et al. (2006) and the lithological column was modified from Rao et al. (2011).

for re-exploitation of geothermal resources instead of oil and gas. With the valuable technical expertise gained from previous drilling and oil production processes, scientists can use exploratory boreholes to exploit geothermal resources with minor modifications. This reduces the development costs and risks, which has created a booming market for geothermal energy exploitation in oil and gas fields (Li et al., 2016).

The Sichuan Basin is a petroliferous basin in Southwest China. The Puguang and Yuanba gas fields in the basin are important for natural gas production. The Sichuan Basin is also rich in geothermal resources with approximately 300 hot springs distributed in the peripheral mountains (Wang, 2005). Numerous medium- and low-temperature geothermal areas near Chongqing have been developed for domestic heating and industrial and agricultural production (Lv et al., 2010). However, the exploitation of geothermal resources in the research area mainly are hot springs or shallow geothermal wells in the mountain areas, the exploitation of deep geothermal energy has not yet developed in the hinterland of the basin. The Sichuan Basin is densely populated, and its agricultural and industrial sectors are well developed. Its high-temperature (≥150°C) geothermal resources should also be developed to supply clean energy. Research on the geothermal fields and terrestrial heat flow in the Sichuan Basin began in the 1980s. Over the past 4 decades, numerous studies have been conducted on the basin and the surrounding areas, including temperature measurements from hundreds of wells, the thermal physical properties of the rocks, and various terrestrial heat flow data (Yuan et al., 2006; Xu et al., 2011; Li et al., 2020). These studies have provided basic knowledge on the thermal state of the Sichuan Basin. For example, higher heat flow has been observed in the central and southern areas of the basin, while lower heat flow has been identified in the northeastern, northwestern, and southeastern areas. Scientists have enriched their knowledge of the stratigraphy through oil and gas exploration to augment their data on the thermal and physical properties of the rock.

Deep geothermal field is the most basic parameter to evaluate geothermal resources, and also affect hydrocarbon generation, migration, and accumulation processes. However, the deep temperature fields had not been stated over all, limited to the distribution and depth of the drilling and logging of boreholes. Further investigation on the geothermal fields of the basin is necessary. In this study, data collected from previous studies were used to calculate the deep geothermal fields in the basin and evaluate its distribution characteristics and primary influencing factors. The results should benefit the exploration and development of the petroleum and geothermal resources in the basin and could serve as a reference for geodynamic studies.

GEOLOGICAL BACKGROUND

The Sichuan Basin is located in the western margin of the Upper Yangtze Plate and is a marine and continental superimposed basin, in which the foreland basins developed on a cratonic platform (Guo et al., 1996, Meng et al., 2005; Liu et al., 2006) (**Figure 1A**). It is characterized by a distinctive rhombic rim that reflects the evolution of deep fractures in the Upper Yangtze and the development of thrust–fold structures. The central part of the Sichuan Basin is a rigid basement that formed in the Neoproterozoic–Mesoproterozoic era; it is uplifted with thin sedimentary layers. The northwestern and southeastern parts of the basin are a ductile basement that is covered with thick sedimentary layers (Wang et al., 2002). The Sichuan Basin has deposits of sedimentary rocks that are up to 10,000 m thick that can be dated to the Sinian Period (Guo et al., 1996; Wang et al., 2002; Liu et al., 2006), with diverse rock types and depositional systems. The Sinian–Middle Triassic strata are characterized by marine facies that are dominated by carbonate rocks such as limestone and dolomite and that contain mudstone and sandstone. From the Middle–Late Triassic Period onwards, a thick set of foreland basin deposition had formed, contains sandstone, mudstone, and other terrestrial clastic deposits (**Figure 1B**).

The tectono-thermal evolution of the Sichuan Basin can be divided into four stages. The first stage was the formation of the cratonic basin in the Early Paleozoic. A relatively low background heat flow was recorded despite the ongoing weak lithospheric tension (He et al., 2014; Zhu et al., 2016). The second stage occurred during the Early Permian–Middle Triassic, which was controlled by two events: the lithospheric re-extension and the Emeishan mantle plume. In particular, the Emeishan mantle plume increased the heat flow to its peak value in the southwestern part of the basin, which was at the intermediate zone of the mantle plume (Zhu et al., 2016; Zhu et al., 2018a, Zhu et al., 2018b). The third stage occurred during the Late Triassic–Early Cretaceous when the Sichuan Basin and surrounding orogenic belt started to evolve into an inland basin because of the closure of the Paleo-Tethys Ocean. As the lithosphere and sedimentary layers thickened, the heat flow continued to decrease (He et al., 2011; He, 2014). The fourth stage reflects the tectono-thermal evolution since the Cretaceous when uplift and exhumation started in the Sichuan Basin (Zhu et al., 2016). Currently, the terrestrial heat flow in the Sichuan Basin is unevenly distributed. A higher heat flow can be observed at the central area, while lower heat flows have been observed in other areas, and the Sichuan Basin can be regarded as a "cold basin" due to the low mean heat flow (Xu et al., 2011).

TABLE 1 | The lithology composition and the thermal conductivity (K) and heat production rate (A) of sedimentary layers in the Sichuan Basin[a].

Strata	Lithology	K (μW/m^3)	A (μW/m^3)
K-C_Z	60% Sandstone 30% Siltstone 10% Mudstone	2.31	0.93
J	25% Sandstone 20% Siltstone 50% Mudstone 5% Limestone	2.52	1.02
T_3	60% Sandstone 30% Siltstone 10% Mudstone	3.31	0.93
T_{1-2}	50% Limestone 20% Anhydrite 30% Dolomite	3.26	0.42
P	85% Limestone 10% Mudstone, Shale 5% Dolomite	2.75	0.48
D- C	50% Limestone 45% Dolomite 5% Sandstone	3.63	0.51
S	60% Shale, Mudstone 20% Siltstone 20% Sandstone	2.89	1.09
O	50% Shale, Mudstone 35% Limestone 15% Dolomite	2.82	0.77
Cam	70% Limestone 20% Shale, Mudstone 10% Siltstone	2.89	0.61
Z	80% Dolomite 10% Limestone 5% Sandstone 5% Mudstone	3.86	0.62

[a]*Note:Lithology of the strata and the heat production rate (A) sourced from Zhu et al. (2018a).*

TABLE 2 | Crustal structure and heat generation rate in the Sichuan Basin[a].

Crust	v_p (km/s)	v_s (km/s)	H (km)	Heat generation rate (μW/m^3)
Upper crust	6	3.5	33	0.657
Lower crust	6.7	3.9	54	0.144

[a]V_p *values are taken from Wang et al. (2019).*

CALCULATION OF THE DEEP TEMPERATURES

Methods

Boreholes can be used to measure the temperature at different depths directly. In contrast, temperatures of undrilled strata cannot be directly measured but can only be obtained by calculation. The main mode of heat transfer in the crust is conduction, thus, the temperature of stratum i deep in a sedimentary basin can be calculated by using the one-dimensional heat conduction equation (Qiu et al., 2004):

$$\mathbf{T_z = T_{i0} + q_{i0} \times \frac{d}{K_i} - \frac{A_i \times d^2}{(2K_i)}} \quad (1)$$

where T_{i0} is the temperature for the top surface of the stratum, q_{i0} is the heat flow for the top surface of the stratum, K_i is the thermal conductivity of the stratum, A_i is the heat generation rate of the stratum, and d is the thickness of the stratum. If the heat generation rate of the stratum decreases exponentially with the depth, this results in the following equation:

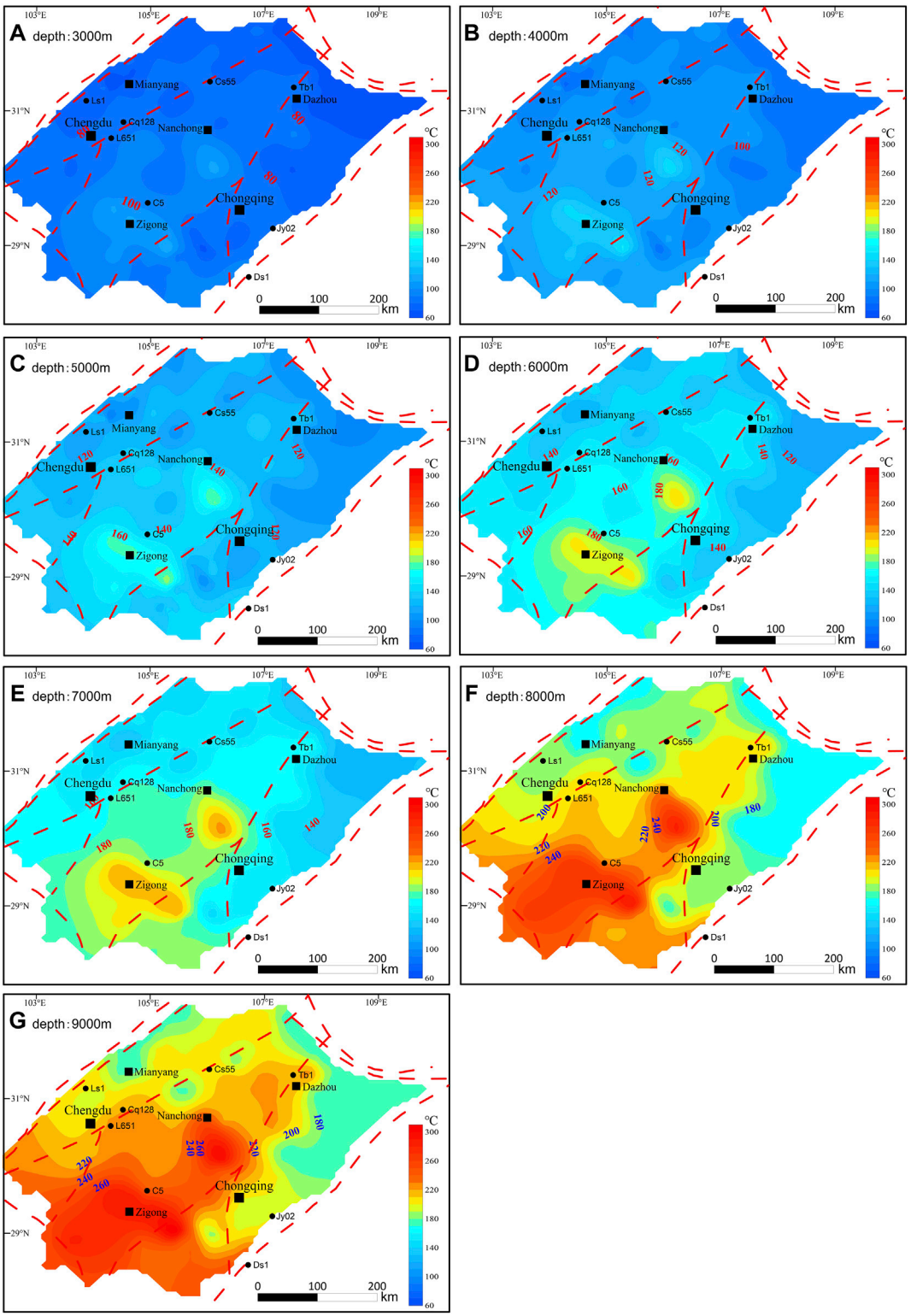

FIGURE 2 | Temperature distribution at the depth of 3,000–9000 m **(A–G)** in the Sichuan Basin. The red dash lines indicate the main faults which controlled the boundary of the basin and its surrounding mountains or divide the tectonic units inside the basin.

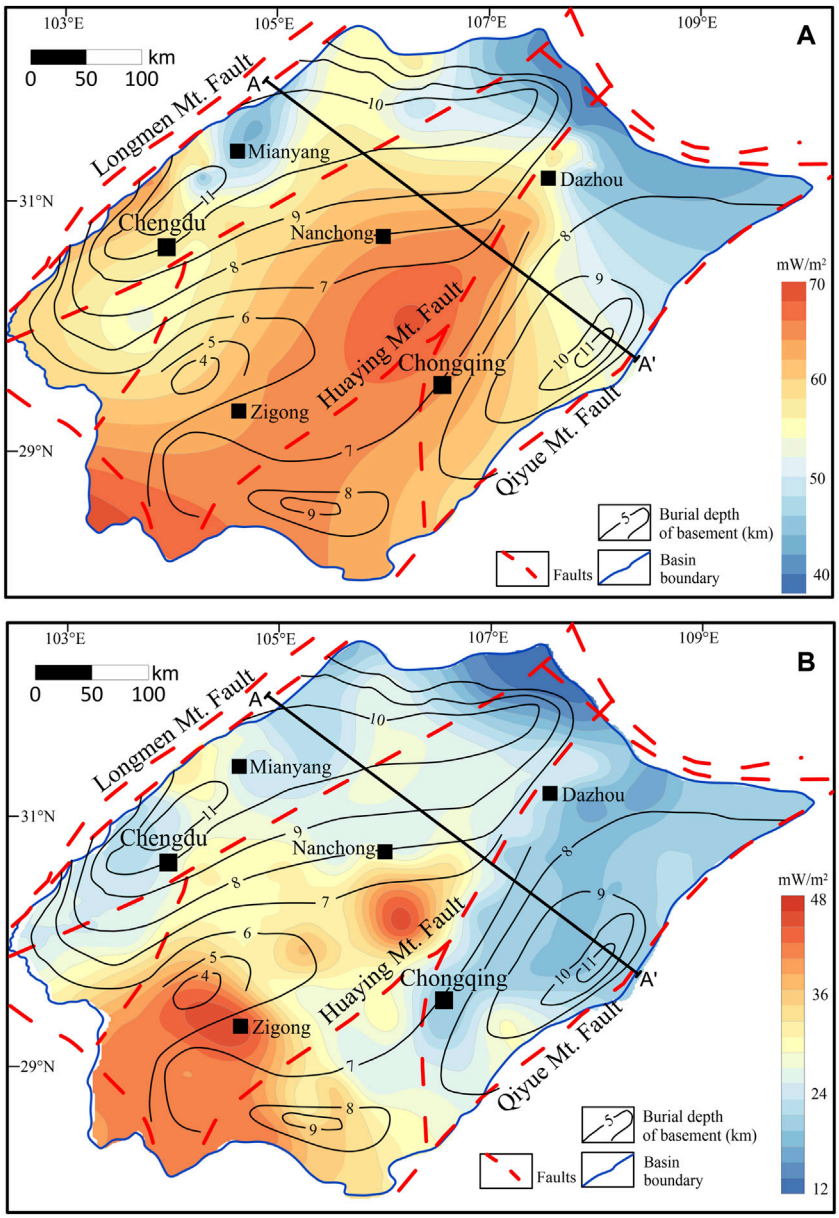

FIGURE 3 | distribution **(A)** (edited after Xu et al., 2011; Zhu et al., 2018a and Qiu et al., 2022), the mantle heat flow distribution **(B)** and the burial depth of the folded basement (edited after Luo, 1998) of the Sichuan Basin. The mantle heat flow was calculated based on the surface heat flow, the heat production rate in the sedimentary layers, the basement and the other parts of the crust. An obvious correlation can be found from both of the surface heat flow, mantle heat flow and the basement burial depth.

$$\mathbf{Tz} = \mathbf{T_0} + \frac{\mathbf{q_0 Z}}{\mathbf{K}} - \frac{\mathbf{A' D^2}\left(\mathbf{1} - \mathbf{e}^{-\frac{\mathbf{Z}}{\mathbf{D}}}\right)}{\mathbf{K}} \quad (2)$$

where q_0 is the heat flow of the top surface of the stratum (mW/m^2), K is the rock thermal conductivity of the stratum (W/(mK)), A' is the heat generation rate of the stratum (μW/m^3), and D is the thickness of a stratum containing radioactive elements.

Eq. 1 is mostly used to calculate deep temperatures in sedimentary strata, and **Eq. 2** is mostly used to calculate temperatures below the basement. Note that these equations do not apply below the upper mantle. There are two reasons: strata are rich with radioactive elements in the crust within about 10–20 km above the upper mantle, and heat conduction at that depth is no longer a decisive influencing factor for the temperature.

Parameters and Boundary Conditions

According to **Eqs 1**, **2**, the boundary conditions for calculating the temperature of deep strata include the heat flow and temperature of the top surface. For the surface heat flow, data from Xu et al.

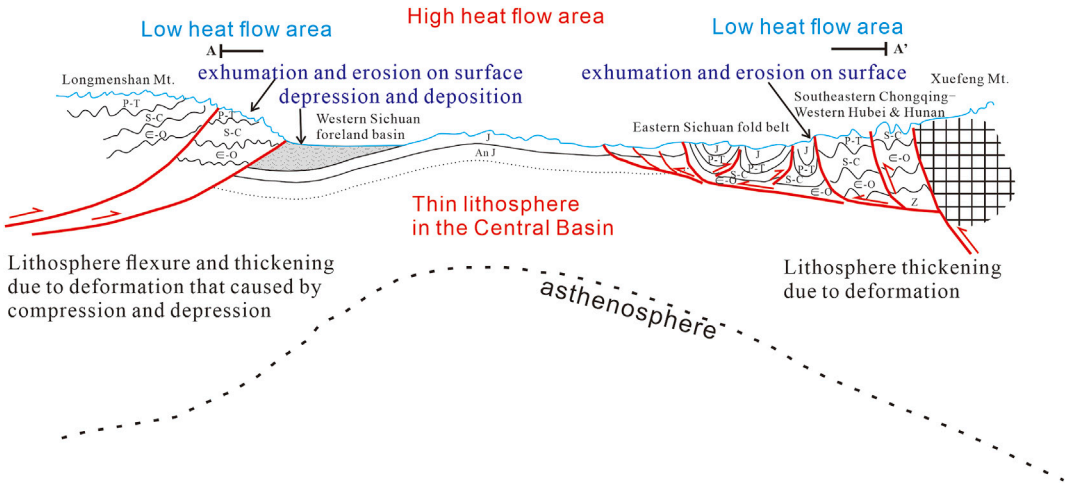

FIGURE 4 | Cartoon shows the main controlling factors on the unevenly distribution of geothermal field in the Sichuan Basin and its surrounding mountains (the geological model was modified after Zhu et al., 2019).

(2011) were adopted. For the surface temperature, the Sichuan Basin thermostatic zone temperature of 16°C was adopted (according to Wang et al., 2017). The thermal physical parameters of the rock required for calculation included the rock thermal conductivity and radiogenic heat generation rate of the strata.

In the Sichuan Basin, numerous studies have been conducted to test thermal conductivity. In this study, more than 1,300 thermal conductivity measurements from previous research (Li, 1990; Han and Wu, 1993; Wang et al., 1995; Xu et al., 2011; Li et al., 2017; Tang et al., 2019; Li et al., 2020) were collected. These were then used to calculate the weighted average of the thermal conductivity of different lithologies tested by different researchers (**Supplementary Appendix S1**). The thermal conductivity of each sedimentary formation was established based on the lithological composition of the main strata (**Table 1**). The thermal conductivity of the Cretaceous and Jurassic strata was relatively low at 2.5 W/(m·K), while that of the Permian, Ordovician, and Cambrian was approximately 3.0 W/(m·K). The thermal conductivity of the Triassic, Devonian, Carboniferous, and Sinian strata was greater than 3.0 W/(m·K).

The heat generation rate of the sedimentary layers was measured (**Table 1**, Zhu et al., 2018a). Among sedimentary rocks, mud shale generally has a relatively high heat generation rate, followed by carbonate rocks of terrestrial origin or those that contain clastic materials from a terrestrial margin. Marine carbonate rocks have a relatively low heat generation rate. The heat generation rate of terrestrial strata in the Sichuan Basin was approximately 1.0 μW/m^3, and that of the marine strata was lower at around 0.6 μW/m^3. The heat generation rate of the Silurian system can be as high as 1.09 μW/m^3 because of the high proportion of sandy mudstone. The heat generation rate of rocks below the basement was estimated by using the seismic wave velocity (v_p) (Rybach and Buntebarth, 1984):

$$\mathbf{In\ A = 12.6 - 2.17 v_p} \quad (3)$$

where A is the rock heat generation rate (μW/m^3) and v_p is the seismic wave velocity (km/s) at a pressure of 100 MPa. **Table 2** presents the estimated heat generation rates of rocks in the upper and lower crust beneath the sedimentary layers of the Sichuan Basin.

RESULTS: THE DEEP GEOTHERMAL TEMPERATURE FIELD OF THE SICHUAN BASIN

Figure 2 showed the temperature distribution map of the Sichuan Basin for depths of 3,000–9,000 m, which calculated by one-dimensional heat conduction equation, taking the surface heat flow, the thermostatic zone temperature, the thermal conductivity and heat production rate of different formations and the formation depths as parameters and boundary conditions. The central and southern areas are characterized by relatively high temperatures at all depths, while the northwestern and northeastern areas are characterized by low temperatures. It is obviously that the strata temperature is lower than 100°C at the depth of 3000 m excluding some high temperatures in central and southern areas (**Figure 2A**). At the depth of 4000 m (**Figure 2B**), the maximum temperature in the central and southern areas reach 150°C, which is the threshold of high-temperature geothermal resources, while the temperatures in other areas are below 120°C. Strata temperature in the central and southern areas exceed 150°C as the burial depth reach 5,000 m (**Figure 2C**), while it is lower than 140°C in most other areas. At the depth of 6,000 m (**Figure 2D**), the temperature is above 150°C for large parts of the central and southern areas, and the maximum temperature reach 185°C, while the temperature is below 120°C for most parts of the northwestern and northeastern

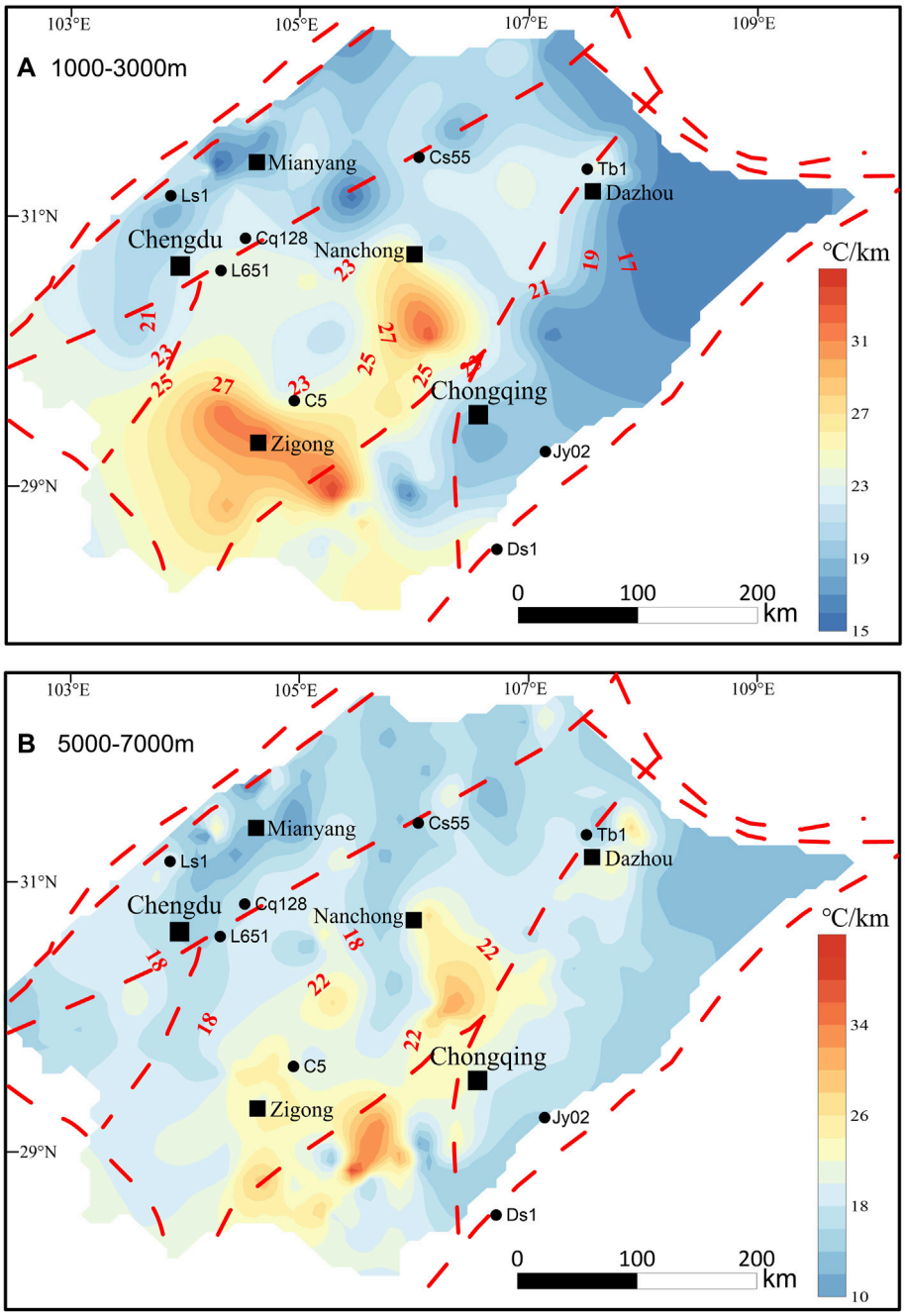

FIGURE 5 | Temperature gradient distribution within the depth of 1,000m–3000 m **(A)** and 5,000m–7000 m **(B)** in the Sichuan Basin.

areas. Similar temperature distribution patterns were observed at the depth of 7,000–9,000 m (**Figure 2E–2G**). At the depth of 7,000 m (**Figure 2E**), the temperatures in the central and southern areas are above 180°C, which is the threshold temperature for hot dry rock (HDR). The temperatures in the northwestern and northeastern areas are below 160°C, which is close to the lower limit for crude oil cracking. The relatively low temperatures in the northern, northwestern, and eastern areas of the Sichuan Basin are conducive to the presence of oil and gas. Given an economic depth should be considered regarding its cost for the exploitation of geothermal energy and also the petroleum resources, it is suggested that the temperature distributions of the depth within 4–6 km are applicable for geothermal resources evaluation and these of the depth within 7–9 km are referential for oil and gas.

Note that the strata temperature is influenced not only by the heat flow and thermal physical properties but also by the burial depth of a formation. Therefore, for specific formations (e.g., oil

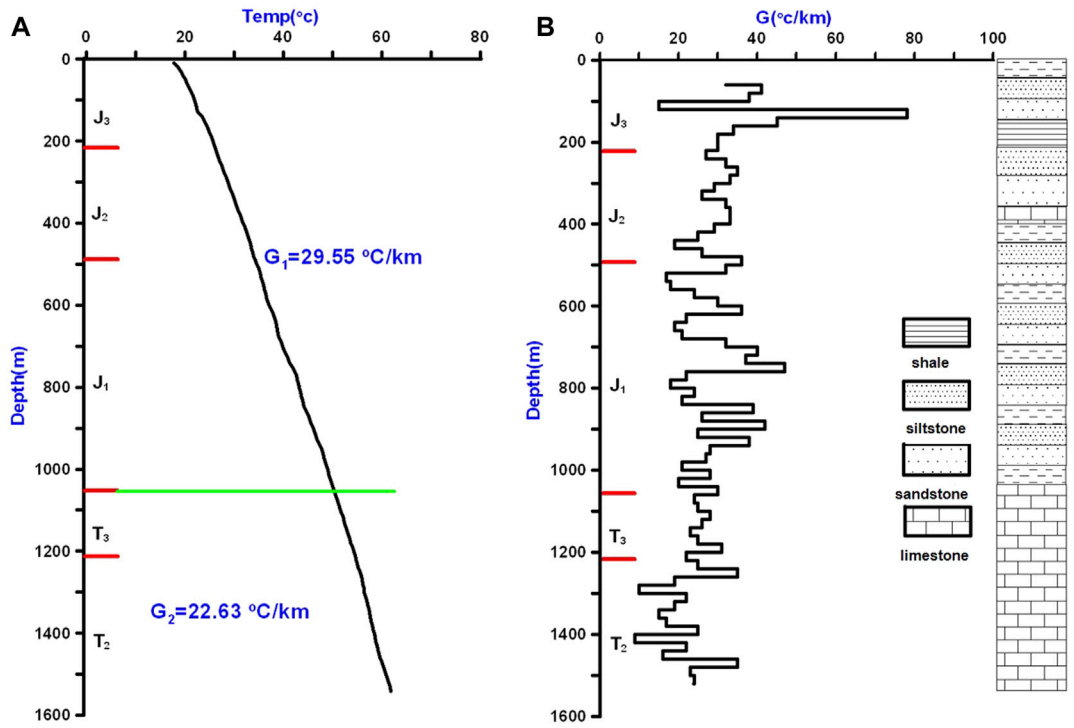

FIGURE 6 | Temperature logging curve **(A)** and the temperature gradient **(B)** of borehole C5.

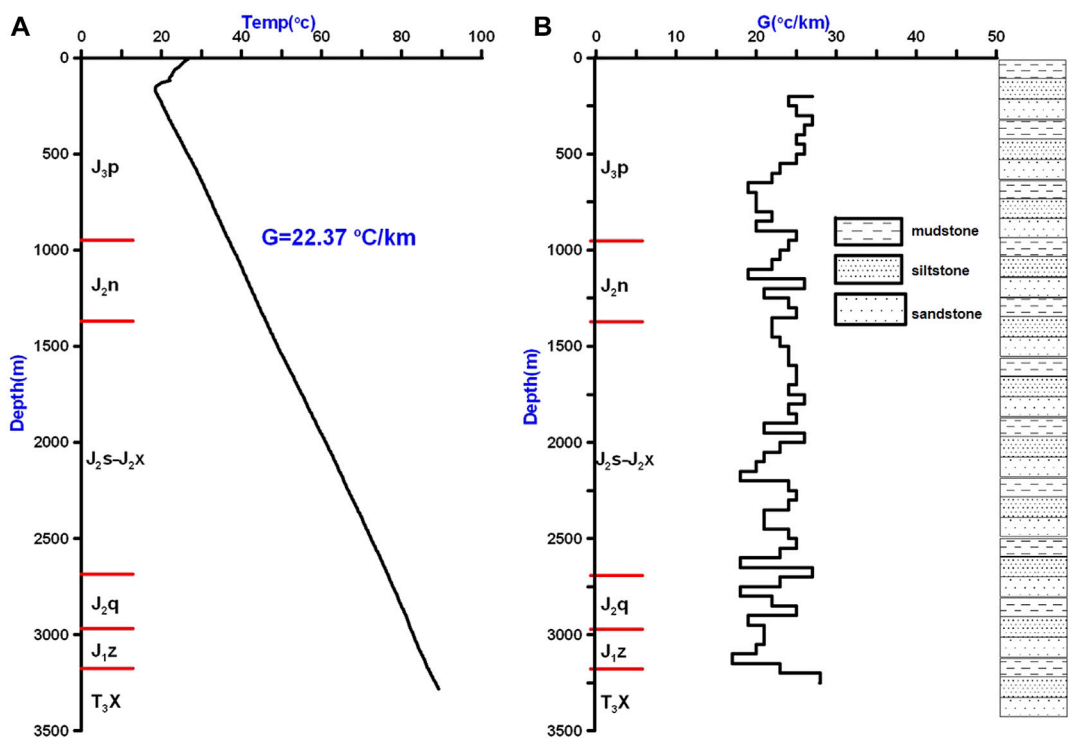

FIGURE 7 | Temperature logging curve **(A)** and the temperature gradient **(B)** of borehole Cq128.

and gas reservoirs), the highest temperatures are more likely to be observed in areas with greater burial depths. In this case, this would correspond with the northwestern and northeastern areas of the Sichuan Basin, which characterized by lower heat flow and temperature gradient but have a thick sediment layer.

DISCUSSIONS: THE PRIMARY CONTROLLING FACTORS OF THE GEOTHERMAL FIELD IN THE SICHUAN BASIN

Terrestrial heat flow directly reflects the geothermal and geological background of a region. The terrestrial heat flow in the Sichuan Basin is 35.4–68.8 mW/m^2 with an average of 53.2 mW/m^2. This is below the average of 60 mW/m^2 in the Lower Yangtze region and 63 mW/m^2 for mainland China (Xu et al., 2011; Yuan et al., 2006). Regarding the distribution, the terrestrial heat flow was greater in the uplifted area and lower in the depressed area. The terrestrial heat flow is above 60 mW/m^2 in the central and southwestern areas of the Sichuan Basin and is 50–60 W/m^2 in the northwestern area (**Figure 3A**). The terrestrial heat flow is lower in the eastern area, particularly in the northeast where it is approximately 40 mW/m^2 at the front edge of the Dabashan fold belt. The deep temperature distribution in the Sichuan Basin shows a good correlation with the terrestrial heat flow, which is primarily influenced by the geotectonics and lithospheric thermal structure. The mantle heat flow in the Sichuan Basin is 12–49 mW/m^2 with higher values in the southwestern and central areas and lower values in the northeastern area (**Figure 3B**). This is similar to the surface heat flow distribution. The intense magma activities and eruptions mainly took placed in Permian (the Emeishan mantle plume and basalt eruption) and raised the heat flow to its peak value (Zhu et al., 2016). There was no obvious magma activity after Jurassic in the basin, thus the surface heat flow can be considered an stable conductive heat flow.

At the basin scale, the average mantle heat flow is approximately 30 mW/m^2, while the average crustal heat flow is 32 mW/m^2. The ratio of the crustal heat flow to the mantle heat flow is close to 1:1, which indicates that the Sichuan Basin has a cold mantle and cold crust. In the basin, the surface and mantle heat flow distributions show negative correlations with the thicknesses of the sedimentary layers and crust. This is indicative of the thermal effects of tectonics and sedimentation during the development of foreland basins. The heat flow in the Sichuan Basin slowly decreased during the Late Triassic–Early Cretaceous, and its tectono-thermal evolution was primarily controlled by two factors. First, the thermal perturbation caused by the lithospheric thinning during the Late Permian–Early Middle Triassic began to decrease (Zhu et al., 2016), which gradual decreased the heat flow of the basin basement. Second, the formation and evolution of the foreland basin and its later uplifting and exhumation reduced the heat flow (Huang et al., 2012). The reduced heat flow caused by foreland basin evolution and uplift and exhumation is primarily controlled by the following factors. First, lithosphere flexure and thickening, as well as gradual cooling, which were caused by compression and depression. Second, the surface heat flow was affected by the deposition in the foreland depressions. Third, exhumation caused by the compressional deformation can also reduce the surface heat flow in the mountain areas (**Figure 4**).

The difference in thermal conductivity among different sedimentary layers and crystalline rocks also affects the deep temperature fields and the redistribution of the heat flow. The temperature gradient negatively correlates with the strata thermal conductivity under a constant heat flow. In fact, thermal conductivity has a more significant impact than the heat production of strata in sedimentary basins, unless ultra-high radioactivity layers exist. Various temperature gradients were vertically revealed by the deep geothermal fields (**Figure 5**) and some temperature logging data of boreholes (**Figure 6**). Two different average temperature gradients in clastic formations and limestone formations were obtained in borehole C5: it is lower in the latter formations which has a relative higher thermal conductivity. As a contrast, the temperature gradient is relative steady in borehole Cq128, for only clastic formations revealed (**Figure 7**).

Furthermore, non-uniform temperature and the difference in thermal conductivity causes thermal refraction, which leads heat to converge to the uplifted basement area with high thermal conductivity. The upper sedimentary layers form an insulating cover, make these uplifts into favorable geothermal targets.

CONCLUSION

Controlled by the thicknesses of sedimentary layer and the crust, the heat flow and deep temperature distributed unevenly in the Sichuan Basin. The central and southern areas have higher temperatures than northeastern and northwestern areas in the same depth, due to the high heat flow.

Lithosphere flexure and thickening caused by compression and depression, rapid deposition in the foreland basin, the exhumation in the surrounding mountains reduce the surface heat flow in foreland depressions in the northwestern and northeastern basin and their surrounding mountains.

Different thermal conductivities of strata affect the deep temperature fields and lead to thermal refraction. Uplifts in sedimentary basins characterized by higher heat flow and covered by relative insulating layers form the geothermal favorable targets.

The central and southern areas characterized by higher heat flow and temperatures are advantageous for geothermal energy exploitation. The relatively low temperatures in the northern, northwestern, and eastern areas of the Sichuan Basin are conducive to the presence of oil and gas.

DATA AVAILABILITY STATEMENT

The original contributions presented in the study are included in the article/**Supplementary Material**, further inquiries can be directed to the corresponding author.

AUTHOR CONTRIBUTIONS

CZ was the primary finisher of this paper, NQ provided the funding of this paper. TX, TC, and RD completed part of data processing work for this paper.

FUNDING

This study was supported by the National Natural Science Foundation of China (Grant No. 41830424 and 41772248).

SUPPLEMENTARY MATERIAL

The Supplementary Material for this article can be found online at: https://www.frontiersin.org/articles/10.3389/feart.2022.824056/full#supplementary-material

REFERENCES

Guo, Z. W., Deng, K. L., Han, Y. H., Liu, Y. K., Yin, J. T., Wang, Q. G., et al. (1996). *The Formation and Development of Sichuan Basin*. Beijing: Geological Publishing House.

Han, Y. H., and Wu, C. S. (1993). Geothermal Gradient and Heat Flow Values of Some Deep wells in Sichuan Basin. *Oil Gas Geology.* 14 (1), 80–84. doi:10.11743/ogg19930111

He, L. (2014). Permian to Late Triassic Evolution of the Longmen Shan Foreland Basin (Western Sichuan): Model Results from Both the Lithospheric Extension and Flexure. *J. Asian Earth Sci.* 93 (oct. 05), 49–59. doi:10.1016/j.jseaes.2014.07.007

He, B., Xu, Y.-G., Chung, S.-L., Xiao, L., and Wang, Y. (2003). Sedimentary Evidence for a Rapid, Kilometer-Scale Crustal Doming Prior to the Eruption of the Emeishan Flood Basalts. *Earth Planet. Sci. Lett.* 213, 391–405. doi:10.1016/s0012-821x(03)00323-6

He, B., Xu, Y.-G., Huang, X.-L., Luo, Z.-Y., Shi, Y.-R., Yang, Q.-J., et al. (2007). Age and Duration of the Emeishan Flood Volcanism, SW China: Geochemistry and SHRIMP Zircon U-Pb Dating of Silicic Ignimbrites, post-volcanic Xuanwei Formation and clay Tuff at the Chaotian Section. *Earth Planet. Sci. Lett.* 255, 306–323. doi:10.1016/j.epsl.2006.12.021

He, L., Xu, H., and Wang, J. (2011). Thermal Evolution and Dynamic Mechanism of the Sichuan Basin during the Early Permian-Middle Triassic. *Sci. China Earth Sci.* 54 (12), 1948–1954. doi:10.1007/s11430-011-4240-z

He, L. J., Huang, F., Liu, Q. Y., Li, C. R., and Wang, J. Y. (2014). Tectono-thermal Evolution of Sichuan Basin in Early Paleozoic. *J. Earth Sci. Env* 36 (2), 10–17.

Huang, F., Liu, Q. Y., and He, L. J. (2012). Tectono-thermal Modeling of the Sichuan Basin since the Late Himalayan Period. *Chin. J. Geophys.* 55 (11), 3742–3753. doi:10.6038/j.issn.0001-5733.2012.11.021

Li, Q. Y. (1990). *Study on Deep thermal Characteristics of the Sichuan Basin*. Chengdu University of Technology.

Li, H. T., Li, J. Y., and Zhang, G. Y. (2016). *Research and Comprehensive Development and Utilization of Buried hill Geothermal Resources in Huabei Oilfield*. Beijing: Petroleum Industry Press.

Li, C. R., Rao, S., Hu, S. B., Wang, J. Y., Wei, Z. H., Huang, Q. Q., et al. (2017). Present-day Geothermal Field of the Jiaoshiba Shale Gas Area in Southeast of the Sichuan Basin, SW China. *Chin. J. Geophys.* 60 (2), 617–627. doi:10.6038/cjg20170216

Li, X. L., Liu, S. W., Xu, M., Li, X. D., and Hao, C. Y. (2020). Estimation of Subsurface Formation Temperature and its Implications for Hydrocarbon Generation and Preservation in the Upper Yangtze Area, south China. *Acta Geologica Sinica* 94 (6), 1896–1910. doi:10.1111/1755-6724.13809

Liu, H. P., Li, J. M., Li, X. Q., Liu, L. Q., Li, X. J., and Hu, S. H. (2006). Evolution of Cratonic Basins and Carbonate-Evaporite Sedimentary Sequence Hydrocarbon Systems in China. *Geoscience* 20 (1), 1–18. doi:10.3969/j.issn.1000-8527.2006.01.001

Luo, Z. (1998). New Recognition of Basement in Sichuan Basin. *J. Chengdu Univ. Technol.* 25, 191–200.

Lv, Y. X., Hu, W., Du, C. L., and Yang, Z. G. (2010). Review on the Progress of Geothermal Water Exploration Research in Chongqing. *Chin. J. Underground Space Eng.* 6 (s2), 1544–1547. doi:10.3969/j.issn.1673-0836.2010.z2.005

Meng, Q.-R., Wang, E., and Hu, J.-M. (2005). Mesozoic Sedimentary Evolution of the Northwest Sichuan Basin: Implication for Continued Clockwise Rotation of the South China Block. *Geol. Soc. America Bull.* 117 (3), 396–410. doi:10.1130/b25407.1

Qiu, N. S., Hu, S. B., and He, L. J. (2004). *Theory and Application of thermal Regime Study in Sedimentary Basins*. Beijing: Petroleum Industry Press.

Qiu, N., Chang, J., Zhu, C., Liu, W., Zuo, Y., Xu, W., et al. (2022). Thermal Regime of Sedimentary Basins in the Tarim, Upper Yangtze and North China Cratons, China. *Earth-Science Rev.* 224, 103884. doi:10.1016/j.earscirev.2021.103884

Rao, S., Tang, X. Y., Zhu, C. Q., Hu, S. B., and Wang, J. Y. (2011). The Application of Sensitivity Analysis in the Source Rock Maturity History simulation:An Example from Palaeozoic marine Source Rock of Puguang-5 Well in the Northeast of Sichuan Basin. *Chin. J. Geology.* 46 (1), 213–225. doi:10.3969/j.issn.0563-5020.2011.01.017

Rybach, L., and Buntebarth, G. (1984). The variation of heat generation, density and seismic velocity with rock type in the continental lithosphere. *Tectonophysics* 103(1-4), 335–344. doi:10.1016/0040-1951(84)90095-7

Shah, M., Vaidya, D., Dhale, S., Sircar, A., Sahajpal, S., and Yadav, K. (2017). "Exploitation and Utilization of Oilfield Geothermal Resources in INDIA," in *Nanotechnology for Energy and Water*. Editors G. Anand, J. K. Pandey, and S. Rana (Switzerland AG: Springer Nature), 47–52. doi:10.1007/978-3-319-63085-4_7

Tang, B., Zhu, C., Xu, M., Chen, T., and Hu, S. (2019). Thermal Conductivity of Sedimentary Rocks in the Sichuan Basin, Southwest China. *Energy Exploration & Exploitation* 37 (2), 691–720. doi:10.1177/0144598718804902

Wang, D. Y. (2005). Geological Genesis Analysis of the Niangchunchi Hot spring in Mianzhu, Sichuan, China. *J. Chengdu Univ. Tech. (Nat. Sci. Ed.* 32 (5), 479–485. doi:10.1360/gs050303

Wang, L. S., Li, C., Shi, Y. S., and Wang, Y. H. (1995). Distributions of Geotemperature and Terrestrial Heat Flow Density in Lower Yangtze Area. *Chin. J. Geophys.* 38 (4), 469–476.

Wang, Z. C., Zhao, W. Z., Zhang, L., and Wu, S. X. (2002). *Tectonic Sequences and Natral Gas Prospecting in the Sichuan basin*. Beijing: Geological Press House.

Wang, S., Yan, J., Li, F., Hu, J., and Li, K. (2016). Exploitation and Utilization of Oilfield Geothermal Resources in China. *Energies* 9 (10), 798. doi:10.3390/en9100798

Wang, W. L., Wang, G. L., Zhu, X., and Liu, Z. M. (2017). Characteristics and Potential of Shallow Geothermal Resources in Provincial Capital Cities of China. *Geology. China* 44 (6), 1062–1073. doi:10.12029/gc20170602

Wang, Y. H., Tang, L., Huang, C. M., Fu, Y., Jiang, B., and Guan, Y. (2019). Study on One Dimensional Velocity Model of Sichuan Area. *Earthquake Res. Sichuan* 2019(3), 8–12. doi:10.13716/j.cnki.1001-8115.2019.03.003

Xu, M., Zhu, C. Q., Tian, Y. T., Rao, S., and Hu, S. B. (2011). Borehole Temperature Logging and Characteristics of Subsurface Temperature in Sichuan Basin. *Chin. J. Geophys.* 54 (4), 224–233. doi:10.1002/cjg2.1604

Yuan, Y.-S., Ma, Y.-S., Hu, S.-B., Guo, T.-L., and Fu, X.-Y. (2006). Present-day Geothermal Characteristics in South China. *Chin. J. Geophys.* 49 (4), 1005–1014. doi:10.1002/cjg2.922

Zhang, R. X., Wang, X. Z., Lan, Q., and Kang, B. P. (2006). Reservoir Evaluation of Emeishan Basalts in Southwest Sichuan. *Nat. Gas Explor Dev.* 29, 17–20. doi:10.3969/j.issn.1673-3177.2006.01.004

Zhu, C., Hu, S., Qiu, N., Rao, S., and Yuan, Y. (2016). The thermal History of the Sichuan Basin, SW China: Evidence from the Deep Boreholes. *Sci. China Earth Sci.* 59 (1), 70–82. doi:10.1007/s11430-015-5116-4

Zhu, C., Xu, M., Qiu, N., and Hu, S. (2018a). Heat Production of Sedimentary Rocks in the Sichuan Basin, Southwest China. *Geochem. J.* 52 (5), 401–413. doi:10.2343/geochemj.2.0530

Zhu, C., Hu, S., Qiu, N., Jiang, Q., Rao, S., and Liu, S. (2018b). Geothermal Constraints on Emeishan Mantle Plume Magmatism: Paleotemperature Reconstruction of the Sichuan Basin, SW China. *Int. J. Earth Sci. (Geol Rundsch)* 107 (1), 71–88. doi:10.1007/s00531-016-1404-2

Zhu, C., Qiu, N., Liu, Y., Xiao, Y., and Hu, S. (2019). Constraining the Denudation Process in the Eastern Sichuan Basin, China Using Low-Temperature Thermochronology and Vitrinite Reflectance Data. *Geol. J.* 54, 426–437. doi:10.1002/gj.3191

Conflict of Interest: The authors declare that the research was conducted in the absence of any commercial or financial relationships that could be construed as a potential conflict of interest.

frontiers | Frontiers in Earth Science

ORIGINAL RESEARCH
published: 08 April 2022
doi: 10.3389/feart.2022.782273

Flow Path of the Carbonate Geothermal Water in Xiong'an New Area, North China: Constraints From ^{14}C Dating and H-O Isotopes

Baojian Zhang[1,2]*, *Siqi Wang*[1,2]*, *Fengxin Kang*[3], *Yanyan Li*[1,2], *Linyang Zhuo*[4], *Jun Gao*[1,2], *Wenzhen Yuan*[1,2] *and Yifei Xing*[1,2]

[1]*Chinese Academy of Geological Sciences, Beijing, China,* [2]*Technology Innovation Center of Geothermal and Hot Dry Rock Exploration and Development, Ministry of Natural Resources, Beijing, China,* [3]*Shandong Provincial Bureau of Geology and Mineral Resources, Jinan, China,* [4]*School of Water Resources and Environment, China University of Geosciences (Beijing), Beijing, China*

OPEN ACCESS

Edited by:
Yinhui Zuo,
Chengdu University of Technology, China

Reviewed by:
Yingchun Wang,
Chengdu University of Technology, China
Yiman Li,
Institute of Geology and Geophysics (CAS), China

***Correspondence:**
Baojian Zhang
zbjsddk@126.com
Siqi Wang
wsiqi17@163.com

Specialty section:
This article was submitted to Economic Geology, a section of the journal Frontiers in Earth Science

Received: *24 September 2021*
Accepted: *28 February 2022*
Published: *08 April 2022*

Citation:
Zhang B, Wang S, Kang F, Li Y, Zhuo L, Gao J, Yuan W and Xing Y (2022) Flow Path of the Carbonate Geothermal Water in Xiong'an New Area, North China: Constraints From ^{14}C Dating and H-O Isotopes. Front. Earth Sci. 10:782273. doi: 10.3389/feart.2022.782273

Studying the flow path of geothermal water in geothermal fields is an important basis for the scientific development and management of geothermal resources. However, due to the influence of engineering volume, economic benefits and demand, it is very difficult to fully grasp the flow path of deep geothermal water in large areas. The use of hydrogeochemical tracers to determine the flow path of geothermal water is a scientific and effective research method. In order to accurately describe the flow path of carbonate geothermal water in the Xiong'an New Area and its surrounding areas, this study systematically analyzed the ^{14}C, ^{18}O, and ^{2}H data of carbonate and Cenozoic sandstone geothermal water, Quaternary groundwater, as well as mountain spring water of the study area. Based on these results, we can conclude that 1) The ^{14}C, *d*, and ^{18}O values are favourable clues for indicating the circulating runoff conditions and runoff paths of geothermal water. 2) The salinity of the Xushui-Wenan and Lilan transfer zone are <3 g/l, the ^{14}C values are lower than 25000 years, the *d* value is higher, and the phenomenon of "^{18}O drift" is weak, all these indicating the dominant flow path of carbonate geothermal water, featured by relative lower temperature. 3) The salinity of karst geothermal water in the southwest of Gaoyang low uplift, Rongcheng uplift and Niutuozhen uplift is > 3 g/l, the ^{14}C values are higher than 40,000 years, the *d* value is lower, and the phenomenon of "^{18}O drift" is obvious, all these indicating that the tectonic sites are the convergence areas of regional karst geothermal water, featured by relative high temperature. 4) The hydrochemical indicators combined with previous carbonate groundwater flow field indicate that the recharge of carbonate geothermal water in the Xiong'an New Area may not only drive from the western Taihang Mountains, but also along the Xushui-Wenan transfer zone and the Lilan fault, with the recharge of carbonate groundwater from the Cangxian uplift from east to west. By further identifying and defining the dominant flow path and supply direction of carbonate geothermal water in the Xiong'an New Area and surrounding areas, it provides strong support for the scientific development of regional carbonate geothermal water.

Keywords: Xiong'an New Area, carbonate thermal reservoir, ^{14}C dating, D-O isotope, geothermal water flow path, development and utilization

INTRODUCTION

At present, the studies on flow path of underground water are mainly focused on shallow depth by tracer agent and/or hydrogeochemistry (Hu et al., 2019; Wang et al., 2020). Based on these methods, the recharge, runoff, and discharge of underground water are revealed (Solder et al., 2020; Smerdon and Gardner 2022). Meanwhile, determining the flow path of geothermal water is also important for revealing the genesis of geothermal fields. It is a prerequisite for the scientific development and management of geothermal resources. However, it is difficult for a deep thermal reservoir to establish a large-scale systematic pressure monitoring network to obtained the flow path. Carbonate geothermal reservoir is a main type for that of North China (Chen, 1988). The geothermal water in the carbonate reservoir of North China are charactered by obvious hydrogeochemical zoning, which has positive response characteristics and important indicators for the dynamic zoning of geothermal water (Zhang et al., 2015). Hence, it is reasonable to use the difference in hydrogeochemical characteristics of geothermal water with the help of geological conditions such as the documented flow field of geothermal water and geotectonics to accurately determine the flow path of geothermal water. This helps to clarify the origin and formation mechanism of groundwater. Since Craig (1961) first determined the hydrogen and oxygen isotope standard and proposed the δD-^{18}O linear equation for atmospheric precipitation to study the origin and formation of groundwater, researchers have used hydrogen and oxygen isotopes to study groundwater (Rets et al., 2017), the origin of geothermal water and the influencing factors of its formation (Ma et al., 2008; Zhang et al., 2010; Chatterjee et al., 2019). Great progress has been made using the main ions and stable isotopes of geothermal water to evaluate its flow path (Sun et al., 2016; Avşar and Altuntaş, 2017; Mcgibbon et al., 2018) and the potential of geothermal resources (Luo et al., 2017). ^{14}C is suitable for studying the migration mechanism of deep geothermal water as it has a half-life of 5730 ± 40 a (Wang and Zhu, 2001). It has provided great application effects in terms of age, composition, and flow direction of geothermal water (Wang et al., 2013; Hao et al., 2020).

The Niutuozhen and Rongcheng large-scale geothermal fields in Xiong'an New Area have a long history of development due to the shallow thermal reservoir depth of carbonate rocks (Chen et al., 1982). These are well-known carbonate geothermal fields in China. Previous studies on the detection of deep bedrock thermal reservoirs and new formations in this area have made great progress (Wang et al., 2018; Wu et al., 2018). In particular, the Chinese Academy of Geological Sciences has made progress in exploration of deep carbonate geothermal resources in the Gaoyang low uplift of Xiong'an New Area. In 2020, it discovered the highest temperature geothermal well in the North China Basin with a wellhead temperature of 123.4°C (Wang et al., 2021). With regard to the mechanism of the bedrock uplift (buried hill type) geothermal field in the North China Basin, it is thought that the geothermal anomaly is a result of the redistribution of the relatively uniform heat flow from the deep crust to the surface during the upward conduction process (Chen, 1988; Chen, 1992). Pang et al. (2017) established a "dual heat accumulation" model of the Niutuozhen geothermal field, and noted that the abundant geothermal resources in Xiong'an New Area are formed under the dual mechanism of "rock thermal conductivity" and "basin-scale groundwater circulation." Wang et al. (2021) found that the carbonate geothermal water flow field influences the buried hill geothermal field in the Xiong'an New Area. Previous studies have concluded that carbonate geothermal water in Xiongan New Area drives from the western Taihang Mountains. After infiltration of these water, it migrated from west to east along the deep carbonate strata. Then after heated by deep circulation, the water upwelled along the deep and large faults and discharged into the Niutuozhen uplift and Rongcheng uplift in Xiong'an New Area. For areas besides the Taihang Mountains, there is no clear understanding of whether the carbonate geothermal water in the Xiong'an New Area comes from other sources. This need established through the research on the flow path of the carbonate geothermal water in the Xiongan New Area and surrounding areas.

In this study, we tested and collected ^{14}C dating and δD-$\delta^{18}O$ isotopic data in and around Xiong'an New Area. We also acquired other data such as the regional geological structure and carbonate geothermal water flow field. These data allowed us to clarify the Xiong'an New Area and its surrounding carbonate geothermal water flow path. This research provides geological support for the scientific and rational development and utilization of regional carbonate geothermal water.

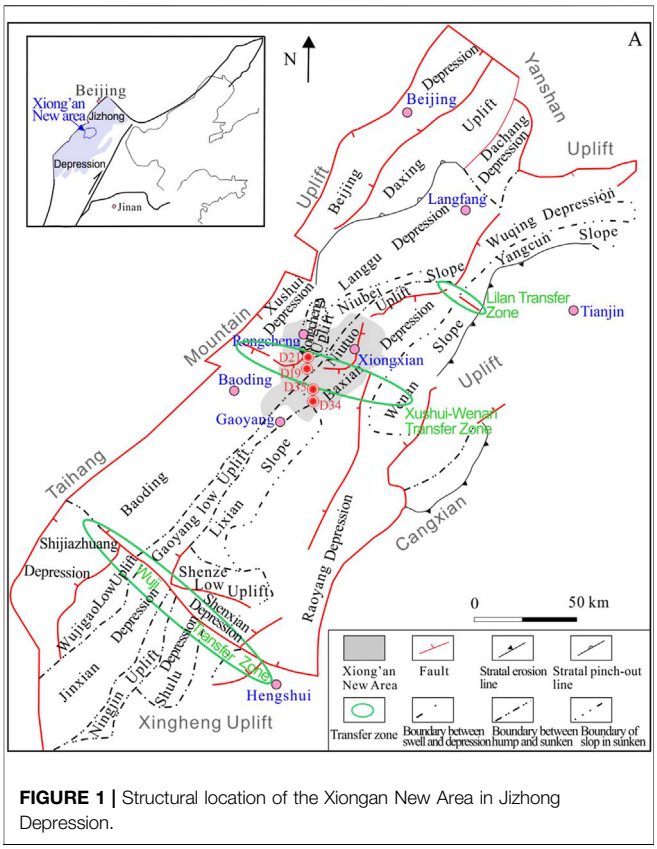

FIGURE 1 | Structural location of the Xiongan New Area in Jizhong Depression.

GEOTHERMAL GEOLOGICAL BACKGROUND

Geological Structure

The Xiong'an New Area is located in the central and western part of the Jizhong Depression in the Bohai Bay Basin. The Jizhong Depression is mainly composed of secondary tilting blocks, skip-shaped depressions, and buried hill structural units formed by a series of normal faults or reverse normal faults under Mesozoic extrusion and Cenozoic extension. The Rongcheng Uplift, Niutuozhen Uplift, Gaoyang Low Uplift, and Lixian Slope involved in Xiong'an New Area are located in the central uplift belt of the Jizhong Depression, while the Xushui Depression and Baoding Depression are located in the western depression belt, and the Bazhou Depression and Raoyang Depression are located in the eastern depression belt (**Figure 1**). In addition, there is the NWW-SEE-trending Xushui-Wenan structural transformation belt in the middle of the Jizhong Depression, which is the first-level structural transformation belt in the Jizhong Depression. This structural transformation belt divides the Jizhong Depression into a southern area and a northern area, and hence, the adjacent depressions on both sides are different in structural style and deformation strength.

Stratum and Major Thermal Reservoir

From bottom to top, the main strata in the study area are Archean, Great Wall System, Jixian System, Neogene, Quaternary, and Paleogene in depressions and low uplifts. The main thermal reservoir in the study area is the Wumishan Formation of the Jixian System, followed by the Gaozhuang Formation, and between them is a thin layer of Yangzhuang Formation.

(1) Geothermal resources in the Wumishan formation of Jixian system

The geothermal resources of the Wuzhishan Formation are mainly composed of dolomite and are widely distributed in Xiong'an New Area. The buried depth of the Wuzhishan Formation in the Rongcheng Uplift ranges from 600 to 2400 m, and from 530 to 2400 m in the Niutuozhen Uplift ranges. At the top of the Gaoyang Low Uplift and along the Yanling Buried Hills in the northern part of the Lixian Slope, the top buried depth ranges from 3000 to 3500 m and the deep top buried depth ranges from 3500 to 4000 m or deeper. The thickness of the geothermal resources of the Wuzhishan Formation is approximately 1000–1400 m. That is slightly thinner at the axis of the Rongcheng Uplift and relatively thicker around it, with an overall relatively uniform distribution and an average value of 19% for the reservoir-thickness ratio. The porosity of the rocks is generally less than 6.0%, with a maximum porosity of 22.4% and an average porosity of 3.39%. The permeability distribution ranges from 0.01 to 1000 mD and above, is mainly between 0.01 and 100 mD (87.8%) (Dai et al., 2019).

(2) The geothermal resources in the Gaoyuzhuang formation of Jixian system

Surrounding the study area, a few wells have been drilled into the Gaoyuzhuang Formation of the Jixian System. The top depth of the exposed geothermal resources of the Gaoxiangzhuang Formation ranges from 1425 to 3600 m, with a thickness generally greater than 1000 m. The lithology consists mainly of grey dolomite intercalated with muddy dolomite and siliceous dolomite, containing flint agglomerates or bands. The porosity is 2–6% and the permeability is 0.1–160 mD. The formation temperature is generally 75–95°C. The water yield is approximately 45–80 m^3/h and TDS is approximately 3000 mg/L.

The burial depth of the Jixian System in the subduction zone of the Xushui-Wenan tectonic transformation belt in the study area is 2500–3500 m. The burial depth of the bedrock in the depressions is mostly above 4000 m and can reach approximately 5000 m outside the study area. The maximum burial depth of the bedrock in the Raoyang Depression is over 6500 m, and the maximum burial depth of the bedrock in the Baxian Depression is over 10000 m. The Xushui-Wen'an tectonic transformation belt is an indicator of fluid (oil and gas) transport in the Raoyang and Baxian Depressions on both sides and contributes to fluid (hydrocarbon) accumulation.

SAMPLE COLLECTION AND TESTING

Sample Collection

In this study, 92 samples of ^{14}C, D (deuterium), and ^{18}O isotopes were taken in and around Xiong'an New Area (**Figure 2**), including 33 carbonate geothermal waters in the Jixian System, 52 sandstone geothermal waters in the Neogene, 3 bedrock spring waters in Taihang Mountain, and 4 samples of Quaternary shallow groundwater. In addition, 30 previous test results of ^{14}C, D, and ^{18}O isotopes were collected, including 6 geothermal waters from Neogene sandstone and 24 geothermal waters from carbonate rock.

Test Method for Samples

The isotope test analysis was done by Beta Analytic Inc. of the United States, and the results were obtained on Dissolved Inorganic Carbon (DIC). The DIC extraction process was to inject sample water into an acid bath attached to the evacuated collection line. This procedure reduced the pH to <1, and the evolved CO_2 was dried with methanol slush and collected in liquid nitrogen. CO_2 was then graphitized on the cobalt as a target for Accelerator Mass Spectrometry (AMS) manufacturing in a hydrogen atmosphere. The results were obtained on the DIC and are reported both as a fraction of modern ($F^{14}C$). Reported radiocarbon results are relative to NIST SRM-4990C. Reported deuterium and oxygen isotopes (δD and $\delta^{18}O$) are reported relative to V_{SMOW}. Measurements were performed using gas-bench Isotope Ratio Mass Spectrometry (IRMS).

Correction of ^{14}C Age for Geothermal Water

^{14}C dating is one of the most important and reliable methods for groundwater dating, and is widely used for groundwater with age changed from 1 to 35 ka. Since geothermal water contain dissolved inorganic carbon and deep inorganic "dead carbon", showing totally different features with groundwater. It is necessary to correct the apparent ^{14}C age obtained by test. Based on previous experience in ^{14}C age correction of groundwater in North China, methods of chemical dilution correction model based on chemical balance (Tarmers model) and an isotope mixing model based on ^{14}C

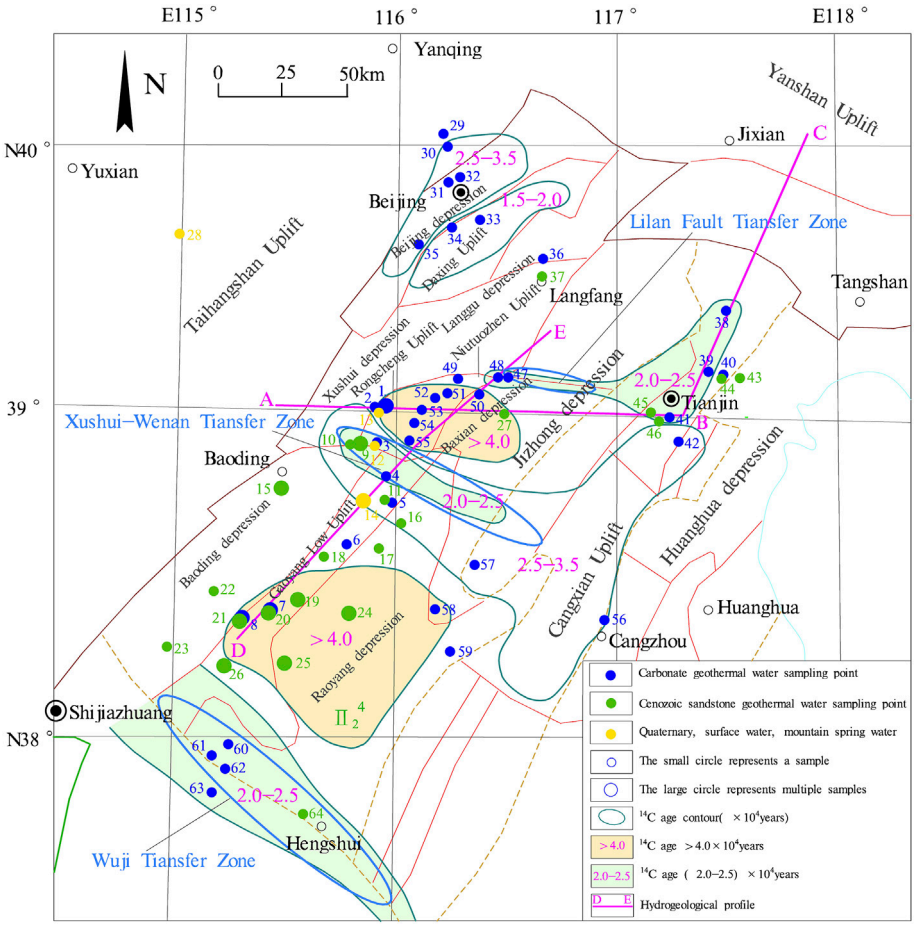

FIGURE 2 | Samples of geothermal water isotopes and isotope dating contours of carbonate geothermal water in the study area.

mass balance (Pearson model) were applied in this study (Ingerson and Person, 1964; Tarmers, 1967). According to the corrected results, the result of "Pearson model" has a larger error, while that of the "Tarmers model" is close to the apparent age of ^{14}C. Therefore, the ^{14}C age calculated by the "Tarmers model" are adopted (**Supplementary Table S1**). The ^{14}C apparent age is directly used for the mountain spring water and shallow groundwater. As previous geothermal water, if there are measured data of $\delta^{13}C$ and ^{14}C, use the "Pearson model" to recalibrate, and then use statistical methods, and use the original "Pearson model" to correct the results without measured data. The average proportional relationship between the results of geothermal water "Tarmers model" and "Pearson model" of Niutuozhen geothermal water, divided by "Pearson model" correction result by 0.77 as "Pearson model" correction age; if it cannot be corrected, ^{14}C apparent age is directly used.

RESULT

Flow Conditions of Geothermal Water

Figure 2 and **Supplementary Table S1** show that the area of the carbonate geothermal water with great ^{14}C age in the Jizhong Depression and its surroundings is located in the center of Gaoyang Low Uplift, Rongcheng Uplift, and segment of Niutuozhen uplift. There areas are featured with the ^{14}C age>40000 years. This may be caused by the relatively closed hydrodynamic conditions insides the bugle as the Rongcheng uplift and the Niutuozhen uplift are surrounded by the thicker depressions in the Cenozoic, while the long Gaoyang and low uplifts are bounded by the Baoding and Raoyang depressions. The ^{14}C age of carbonate geothermal water in Cangxian uplift is mostly lower than 25000 years, and as the distance from the Yanshan Uplift increases from north to south, the ^{14}C age of carbonate geothermal water gradually increases. This is because although the Cangxian uplift is closer to the interior of the Bohai Bay Basin, there is no deep Cenozoic sag between the north of the Cangxian uplift and the Yanshan groundwater recharge area, so that the groundwater in the Yanshan recharge area can follow the karst-developed Cangxian uplift. The long drive from north to south makes the ^{14}C age of carbonate geothermal water in the Cangxian uplift at a relatively low level as a whole. Although the Daxing Uplift in Beijing is farther from the mountainous area than the Beijing Depression, its ^{14}C age of carbonate geothermal water (approximately 20000 years) is smaller than that of the

Beijing Depression (>30000 years). This shows that the recharge conditions of carbonate geothermal water in the uplift area are better than those in the depression area. The ^{14}C age of the carbonate geothermal water in the Fengheying Low Uplift in Beijing is 33300 years (sample No. 36), indicating that the low uplift carbonate geothermal water with a relatively sealed hydrogeological environment is also poorly recharged.

Regarding the uplift area, the geothermal water age of carbonate rocks near the deep and large faults of the edge of the uplift is generally younger than that of the interior segment. For example, the ^{14}C age of the carbonate geothermal water at point 40 near the fault on the eastern margin of the Cangxian uplift is 8000 years, which is much less than the ^{14}C age (24000 years) at point 39, that is farther from the marginal fault. The geothermal water circular and alternate conditions in the deep fault belt appear to be better than those in the inner part of the uplift where faults are not developed.

As showed in **Figure 2**, the ^{14}C values of carbonate geothermal water in Xushui-wenan, Lilan, and Wuji transfer zones are relatively lower (20000–25000 years). The ^{14}C ages of the carbonate geothermal water at point 47 and 48 near the Lilan transfer zone in the northeastern edge of Niutuozhen Uplift range from 16200 to 22400 years, which is significantly less than that of the carbonate geothermal water in the southwestern Niutuozhen Uplift and Rongcheng Uplift (>40000 years). The ^{14}C age of geothermal water from northeast to southwest increases gradually, indicating that carbonate geothermal water may flow from northeast to southwest. The ^{14}C age of carbonate geothermal water in the Xushui-Wenan structural transformation belt between the Rongcheng Uplift-Niutuozhen Uplift and the Gaoyang Low Uplift is relatively low (23800–24800), obvious lower than the uplift segment of north and south, indicating that the circular and alternate conditions of geothermal water in the Wenan structural transformation belt with developed faulted structures are relatively great. It also shows that it may be the dominant flow channel for regional karst geothermal water. The ^{14}C age of carbonate geothermal water in the Wuji structural transformation zone is 15700–22900 years, which is significantly lower than the that in the northern Gaoyang low uplift. This shows that the fault structure in the structural transformation zone in the region is dense, the fractured karst is relatively developed, and the circulation and alternating conditions of geothermal water are relatively good, which is the dominant channel for the flow of regional karst geothermal water, so the groundwater age is relatively low. Compared with the age of the geothermal water in the upper Cenozoic, carbonate geothermal water presents, different characteristics are showed in different structural parts. For example, the Neogene Guantao Formation geothermal water in the Xushui-Anxin structural belt is generally 30000–40000 years old, which is 0.5–15000 years older than the carbonate geothermal water in the lower part. The carbonate rock geothermal water at point 41, located in the southwest of Tianjin, is 6000 to 15000 years younger than the Neogene Guantao Formation geothermal water above it. The carbonate rock geothermal water in the Gaoyang low uplift and the Neogene Guantao Formation geothermal water in the upper part are featured by the same age, about 40000 years old. This is also in the area with relatively good circulation conditions, which is the dominant channel for the flow of regional karst geothermal water.

D-^{18}O Isotopic Characteristics and Indication for Geothermal Water Flow Conditions

Figure 3 shows the δD and $\delta^{18}O$ plots of regional surface water, Quaternary shallow groundwater, and Taihang Mountain spring water. Obviously, all points located near the global meteoric water line ($\delta D = 8\delta^{18}O + 10$; Craig, 1961), Tianjin meteoric water line ($\delta D = 7.7\delta^{18}O + 8.7$; Deng et al., 2012), and northern Shandong meteoric water line ($\delta D = 7.5\delta^{18}O + 5.4$; Yang et al., 2009), and slightly drifting to the right. This indicates that the recharge source of regional shallow groundwater is meteoric water and is affected by evaporation to a certain extent.

The Cenozoic geothermal water in the Gaoyang Low Uplift is relatively close to the meteoric water line because its thermal reservoir is mainly the shallow buried Neogene Guantao Formation. The Cenozoic geothermal water in the Baoding Depression, which close to the Taihang Mountain recharge area, is farther away from the meteoric water line. This is because the thermal reservoir temperature of the Guantao Formation in Baoding Depression is relatively low, and part of the deep thermal reservoir of Paleogene Dongying Formation and Shahejie Formation is used. This also indicates that the deeper the geothermal water is, the older it is.

As a result of water–rock interaction, the values of ^{18}O in water often increases, which is called "^{18}O drift" The degree of ^{18}O drift can reflect the residence time and metamorphic degree of water in the aquifer. As shown in **Figure 3**, compared with Cenozoic geothermal water, the "^{18}O drift" phenomenon of carbonate geothermal water is more obvious. The temperature of carbonate rock geothermal reservoir in the study area is lower than 200°C, and no obvious oxygen isotope fractionation can be produced. This may be caused by isotopic exchange between carbonate geothermal water and oxygen-bearing host rocks (carbonate or silicate) over a long geological history. The ^{18}O drift phenomenon of carbonate geothermal water in Rongcheng, Niutuozhen, and Gaoyang Uplift is more obvious than that in Cangxian Uplift, while the ^{18}O drift phenomenon of carbonate geothermal water in the northern Cangxian Uplift is more obvious than that in the southern Cangxian Uplift. This indicates that the farther away from the recharge area, the worse the circular and alternate conditions and the more obvious the ^{18}O drift phenomenon. There is no deep depression in the northern Cangxian Uplift, which can directly receive the mountainous recharge, and the circular and alternate conditions are great. Therefore, the phenomenon of ^{18}O drift of the carbonate geothermal water in the northern Cangxian Uplift is not obvious. Similarly, the "^{18}O drift" phenomenon of carbonate geothermal water in the Xushui-Wenan transfer zone is obviously weaker than that in the Niutuozhen uplift and the Gaoyang low uplift, indicating that the carbonate thermal storage occurs in this structural transformation zone. The

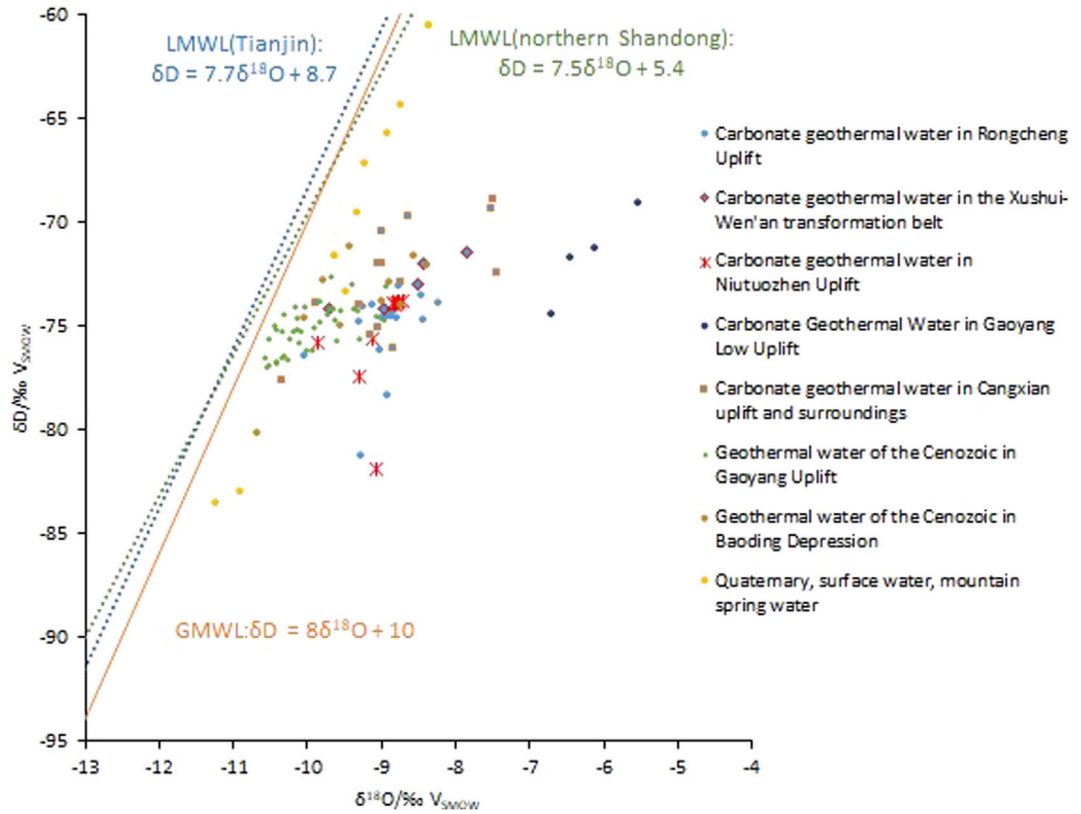

FIGURE 3 | Characteristics and relationship of δD-$\delta^{18}O$ of geothermal water in Xiong'an New Area and its surroundings.

circulation and alternating conditions of geothermal water are better.

To facilitate the comparison of the difference in meteoric water in different regions, Dansgaard (1964) proposed the concept of the deuterium excess parameter (*d*) and defined it as $d = \delta D - 8\delta^{18}O$. The *d* values are equivalent to the intercept values when the slope of meteoric water ($\delta D/\delta^{18}O$) in the area is 8. An important feature of the *d* parameter is that it is not affected by seasons, altitudes, and other factors in the same area, and is only directly related to the length of its residence time in the aquifer (Yin et al., 2001). It is therefore suitable for studying the circular and alternate conditions and deterioration degree of geothermal water. Parameter *d* can be used as a measure of the degree of ^{18}O isotope exchange in the water-rock interactions. The smaller the values of *d*, the more sealed the hydrogeological environment, the slower the groundwater runoff speed, the longer the water residence time in the aquifer, and the higher the degree of water metamorphism.

The *d* values of carbonate geothermal water in the southern Cangxian Uplift and Xushui-wenan transfer zone are higher, whereas those of Rongcheng and Niutuozhen Uplift are relatively low (0 to -10), except the higher *d* values of carbonate geothermal water in the northern part of Cangxian uplift (**Figure 4**). In addition, the phenomenon of ^{18}O drift is relatively apparent, indicating that the carbonate geothermal water in these areas has poor circular and alternate conditions, long residence time in the aquifer, and a strong metamorphic degree. The parameter *d* of the Gaoyang Uplift is the smallest and the ^{18}O drift is the most distinct, indicating that the geothermal water in the Gaoyang

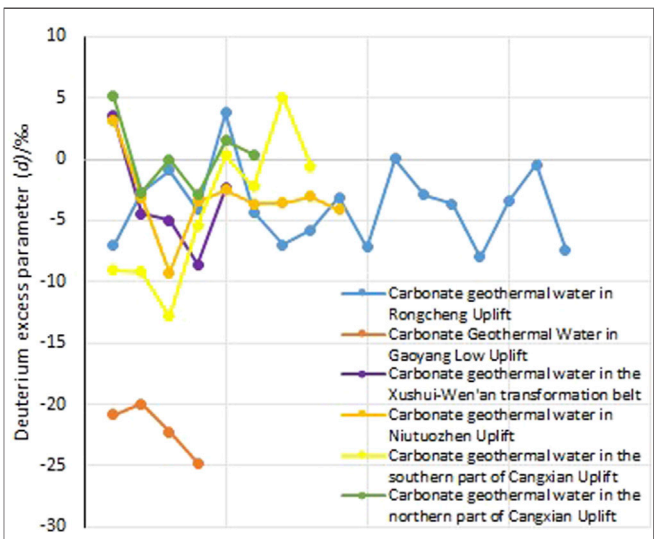

FIGURE 4 | Characteristics of deuterium excess parameter (*d*) in Xiong'an New Area and surrounding carbonate geothermal water.

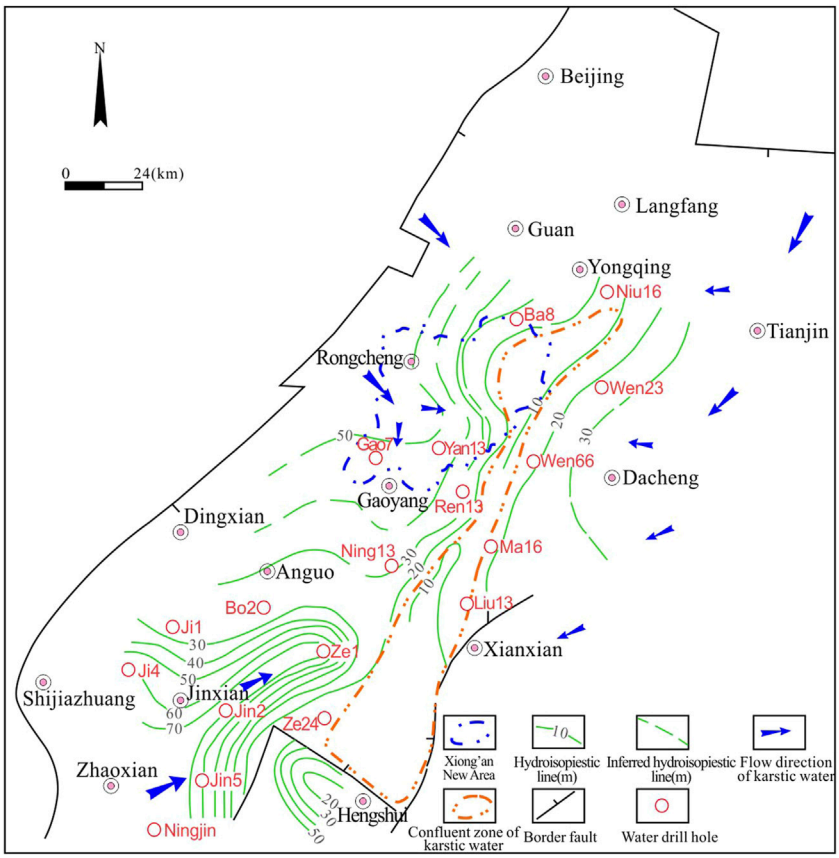

FIGURE 5 | Contour map of piezometric level of buried hill in the Jizhong Depression [according to Yan and Yu (2000)].

Uplift has circular and alternate conditions, long residence time in the aquifer, and a strong metamorphic degree. At the same time, the ^{18}O drift is distinct due to the large buried depth of the carbonate reservoir, high temperature of the water, and obvious ^{18}O exchange between water and rock under the high-temperature conditions in the Gaoyang Uplift (Craig, 1966). This is consistent with the occurrence of geothermal water indicated by the ^{14}C age and the δD-$\delta^{18}O$ characteristics of geothermal water. That is the high d values of geothermal water in the northern Cangxian uplift and the Xushui-Wenan transition zone are the structural parts with better conditions for the alternation of regional carbonate geothermal water circulation.

DISCUSSION

Decades of geothermal water exploitation history and the influence of oilfield fluid exploitation as well as injection activities have caused significant changes in the basement geothermal water hydrodynamic field of the Xiong'an New Area. The current geothermal water hydrodynamic field no longer reflects the bedrock geothermal water recharge, runoff, and drainage conditions present in the natural state. Therefore, this study used the earlier bedrock geothermal water hydrodynamic field characteristics (Yan and Yu, 2000) to illustrate the bedrock geothermal water recharge, runoff, and drainage conditions in the study area.

The bedrock geothermal water in the Jizhong Depression is mainly recharged by Taihang Mountains in the west and Yanshan Mountains in the north (**Figure 5**). The groundwater level of the bedrock in the Xushui-Wenan structural transformation belt is slightly higher than that of the uplift areas on both of the north and south sides. This may be due to a series of NWW-SEE faults in the Xushui-Wenan structural transformation belt connecting the piedmont faults in the eastern foothills of the Taihang Mountains, making it easier to recharge groundwater from the piedmont of the Taihang Mountains along the Xushui-Wenan structural transformation belt. The Cangxian Uplift is connected to the Yanshan Mountain towards the northeast. The relatively shallow buried carbonate thermal reservoir developed many karst fissures and the recharge conditions are better. As a result, the groundwater level of the bedrock of the Cangxian Uplift is significantly higher than that of the Jizhong Depression on the west, which enables the bedrock groundwater of the Cangxian Uplift to flow westward.

A large number of ^{14}C, D (deuterium), and ^{18}O isotopes of carbonate geothermal water around Xiong'an New Area were tested. This compensated for the lack of distribution and quantity of carbonate geothermal wells and the unclear groundwater flow

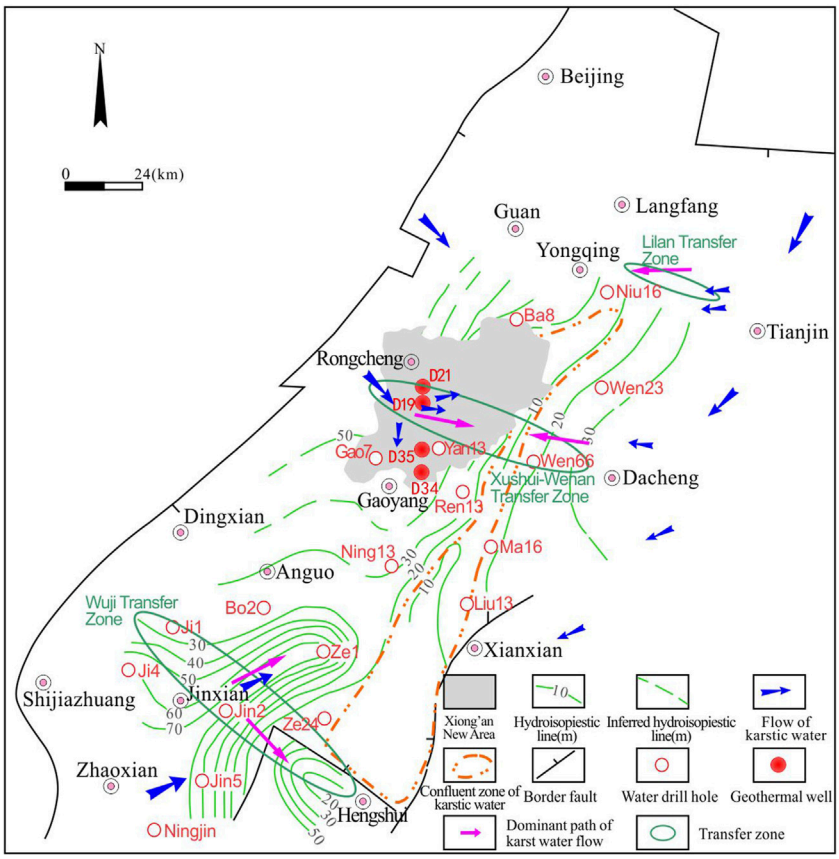

FIGURE 6 | The flow path identification diagram of karst geothermal water in Xiong'an New Area and its surroundings.

field modified by the disturbances caused by human exploitation. However, there are rare understand on the flow path of geothermal water. Local artificial exploitation definitely has not fundamentally changed the flow field morphology of regional karst geothermal water. Using the good indicators of ^{14}C, D, and ^{18}O isotopes, the flow path of karst geothermal water in Xiong'an New Area and its surroundings can be accurately inferred.

The karst geothermal water in Xiong'an New Area and its surroundings is mainly recharged by the Taihang Mountains in the west and the Yanshan Mountains in the north. **Figure 5** shows that the recharge mainly comes from the northwest, west, southwest, and northeast. However, since the maximum thickness of the Cenozoic in the Baxian Depression, Raoyang Depression, and Baoding Depression on both sides of the uplift of Niutuozhen, Rongcheng, and Gaoyang can reach 6000–10000 m, it is difficult to charge karst geothermal water in shallow buried uplift areas for carbonate groundwater deeply buried under the great thickness of the Cenozoic. The most likely recharge path is the relatively shallow buried area of the bedrock at the edge of the depression. The Xushui-Wenan structural transformation belt, which is located between The Xushui Depression-Rongcheng Uplift-Niutuozhen Uplift-Baxian Depression-Wen'an Slope and Baoding Depression-Gaoyang Uplift-Raoyang Depression, is characterized by dense structural development and a relatively shallow bedrock burial depth (approximately 4000–5000 m). The buried depth of bedrock is 1000–3000 m, which is shallower than that of the depression on both sides. Karst is still relatively developed in the carbonate strata at this depth, which can form the dominant flow channel of karst geothermal water. The karst hydraulic pressure and deuterium excess parameter *d* values in the Xushui-Wenan structural transformation belt between Rongcheng and Gaoyang is significantly higher than that of the uplift areas on both sides (**Figures 6**, **7**, **Supplementary Table S1**). The ^{14}C age and salinity of geothermal water are significantly lower than those of the bulge areas on both sides. According to the carbonate geothermal wells constructed in the past 2 years, the water temperature of the D19 and D21 geothermal wells located in the Xushui-Wenan structural transformation belt is significantly lower than that of the D34 and D35 geothermal wells with similar well depths outside the Xushui-Wenan structural transformation belt (about 30–40°C lower). This indicates that the Xushui-Wenan structural transformation belt is the dominant flow channel of regional karst geothermal water, which is conducive to the recharge of karst water from the Taihang mountains in the west and can receive the recharge from the Cangxian uplift in the east. Therefore, geothermal water has a low degree of

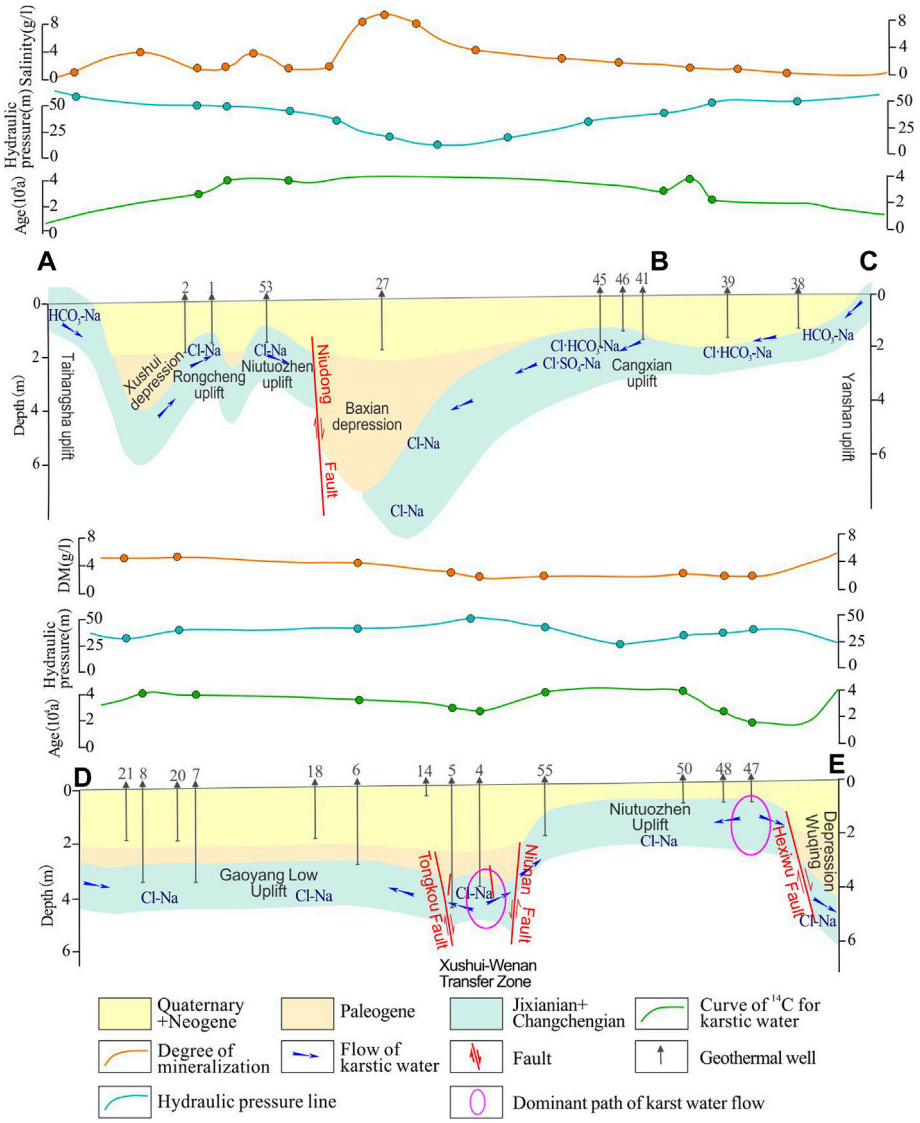

FIGURE 7 | Geological cross-section along section line **(A–E)** on the map of **Figure 2** of the study area.

metamorphism, low ^{14}C age and salinity, and relatively low temperature.

In addition, a small structural transformation belt also developed between the Wuqing Depression-Yangcun Slope and Baxian Depression-Wenan Slope. This structural transformation belt is distributed along the NWW-trending Lilan fault (Yao, 2014), and the bedrock burial depth is relatively shallow (approximately 4000–5000 m) (Wang, 2020). Karst is well developed in the carbonate strata, and it has conditions allowing it to form the dominant flow channel of karst geothermal water. The ^{14}C ages of the carbonate geothermal water at point 47 and 48 in the northeast of Niutuozhen uplift are 16200–22400 years old, which is significantly younger than the ^{14}C ages of the carbonate geothermal water in the southwest of the Niutuozhen Uplift and Rongcheng Uplift (>40000 years). However, the *d* values are significantly higher than the latter. This indicates that the karst geothermal water may flow from northeast to southwest. The Lilan transfer zone between Wuqing Depression-Yangcun Slope and Baxian Depression-Wenan Slope may be the dominant flow channel of another regional karst geothermal water recharge from Cangxian uplift to the west. The ^{14}C age of carbonate geothermal water in the northern Cangxian uplift is relatively low, the hydrochemical type is Cl·HCO_3-Na or Cl·SO_4-Na type, and the salinity is low, appearing characteristics of closer to the recharge area (**Figure 7**).

CONCLUSION

The ^{14}C age, deuterium excess parameter (*d*), and the ^{18}O drift phenomenon are good indicators of the circulating runoff conditions and runoff path of geothermal water. Geothermal

water flow conditions are good in sections with low ^{14}C age and salinity, high *d* values, and weak ^{18}O drift phenomenon, corresponding to the dominant recharge channel for carbonate geothermal water.

The ^{14}C dating, ^{18}O, and ^{2}H data of carbonate geothermal water, Cenozoic sandstone geothermal water, quaternary groundwater, and mountain springs in Xiongan New Area and surroundings and the analysis of regional carbonate groundwater flow field and structural conditions, indicated that the dominant flow paths and main recharge channels of regional carbonate geothermal water are as follows. 1) The karst geothermal water in the Xiong'an New Area and its surroundings is mainly recharged by the Taihang Mountains in the west and the Yanshan Mountains in the north. The Xushui-Wenan structural transformation belt is the dominant flow channel for the regional karst geothermal water, which is conducive to the recharge of karst water from the Taihang Mountains in the west and also receives recharge from the Cangxian uplift in the east. 2) The northeastern part of the Niutuozhen Uplift may receive the recharge of carbonate geothermal water from Cangxian uplift in the east through the Lilan transfer zone. 3) For the southwest of Gaoyang low Uplift, Rongcheng and Niutuozhen Uplift, the ^{14}C age >40000, the *d* is low, and the phenomenon of "^{18}O drift" is obvious, indicating that these structural parts are the convergence areas of regional karst geothermal water.

Through the identification and definition of the dominant flow path and recharge direction of carbonate geothermal water in Xiong'an New Area and its surrounding areas, a clearer basis for discriminating the flow field and temperature of carbonate geothermal water is obtained. All these studies provide geothermal geology for scientific development carbonate geothermal energy.

The ^{14}C values of carbonate geothermal water in the southwest of Gaoyang low uplift, Rongcheng uplift, and Niutuozhen uplift is lower than 0.44 pmc, and the ^{14}C age of carbonate rock geothermal water can only be determined to be > 40000 years old, which cannot be accurately determined. Therefore, when estimating the age of groundwater >40000 years, groundwater dating methods with a large dating range such as ^{36}Cl and ^{3}He-^{4}He should be used.

DATA AVAILABILITY STATEMENT

The original contributions presented in the study are included in the article/**Supplementary Material**, further inquiries can be directed to the corresponding authors.

AUTHOR CONTRIBUTIONS

BZ wrote the manuscript with the support of the list authors. All authors have made a substantial, direct, and intellectual contribution to the manuscript.

FUNDING

This research was financially supported by National Natural Science Foundation of China (Nos 41902310, U1906209, and 42072331), National Key Research and Development Projects of China (2019YFB1504102) and Project of China Geological Survey (Nos DD20189114 and DD20190129).

ACKNOWLEDGMENTS

The editor, associate editor, and reviewers are thanked for their constructive comments that greatly improved the paper.

SUPPLEMENTARY MATERIAL

The Supplementary Material for this article can be found online at: https://www.frontiersin.org/articles/10.3389/feart.2022.782273/full#supplementary-material

REFERENCES

Avşar, Ö., and Altuntaş, G. (2017). Hydrogeochemical Evaluation of Umut Geothermal Field (SW Turkey). *Environ. Earth Sci.* 76, 582. doi:10.1007/s12665-017-6929-6

Chatterjee, S., Sinha, U. K., Biswal, B. P., Jaryal, A., Jain, P. K., Patbhaje, S., et al. (2019). An Integrated Isotope-Geochemical Approach to Characterize a Medium Enthalpy Geothermal System in India. *Aquat. Geochem.* 25, 63–89. doi:10.1007/s10498-019-09352-z

Chen, M. X. (1992). Advances of Studies of Geothermal Resources in China. *Adv. Earth Sci.* 7 (3), 9–14. CNKI:SUN:DXJZ.0.1992-03-001

Chen, M. X. (1988). *Geothermal in North China*. Beijing: Science Press.

Chen, M. X., Huang, G. S., Zhang, W. R., Zhang, R. Y., and Liu, B. Y. (1982). The Temperature Distributibution Pattern and the Utilization of Geothermalwater at Niutuozhen Basement Protrusion of Central Hebei Province. *Scientia Geologica Sinica* 3, 239–252. doi:10.1007/BF01033890

Craig, H. (1966). Isotopic Composition and Origin of the Red Sea and Salton Sea Geothermal Brines. *Science* 154, 1544–1548. doi:10.1126/science.154.3756.1544

Craig, H. (1961). Isotopic Variations in Meteoric Waters. *Science* 133, 1702–1703. doi:10.1126/science.133.3465.1702

Dai, M. G., Lei, H. F., Hu, J. G., Guo, X. F., Ma, P. P., and Zhang, J. Y. (2019). Evaluation of Recoverable Geothermal Resources and Development Parameters of Mesoproterozoic thermal Reservoir with the Top Surface Depth of 3500 M and Shallow in Xiong'an New Area. *Acta Geologica Sinica* 93, 2874–2888. 10.1111/1755-6724.13979. doi:10.3969/j.issn.0001-5717.2019.11.012

Dansgaard, W. (1964). Stable Isotopes in Precipitation. *Tellus* 16, 436–468. doi:10.3402/tellusa.v16i4.8993

Deng, W. P., Yu, X. X., and Jia, G. D. (2012). Sources and Stable Isotope Characteristics of Precipitation in North China. *Bull. Mineralogy, Petrology Geochem.* 31 (5), 489–493. doi:10.3969/j.issn.1007-2802.2012.05.007

Hao, Y., Pang, Z., Kong, Y., Tian, J., Wang, Y., Liao, D., et al. (2020). Chemical and Isotopic Constraints on the Origin of saline Waters from a Hot spring in the Eastern Coastal Area of China. *Hydrogeol J.* 28, 2457–2475. doi:10.1007/s10040-020-02199-7

Hu, Y., Ma, R., Wang, Y., Chang, Q., Wang, S., Ge, M., et al. (2019). Using Hydrogeochemical Data to Trace Groundwater Flow Paths in a Cold alpine Catchment. *Hydrological Process.* 33 (14), 1942–1960. doi:10.1002/hyp.13440

Ingerson, E., and Person, F. J. (1964). "Estimation of Age and Rate of Motion of the Groundwater by the C Method," in *Proceedings of Sugawara Festival on Recentresearches in the fields of Atmosphere, Hydrosphere, and Nuclear Geochemisrtry* (Tokyo: Maruzen), 237–266.

Ke, B. L. (2009). Characteristics of Geothermal Geology in the Northwestern Part of the Urban Beijing Geothermal Field. *Geoscience* 23, 49–56. doi:10.3969/j.issn.1000-8527.2009.01.008

Liu, K., Liu, Y. C., Sun, Y., Liu, J. R., and Wang, S. F. (2015a). Characteristics of Deuterium Excess Parameters of Geothermal Water in Beijing. *Geology. China* 42, 2029–2035. CNKI:SUN:DIZI.0.2015-06-029

Liu, Y. C., Liu, K., Sun, Y., Liu, J. R., and Guo, G. X. (2015b). Hydrochemical Characteristics and Isotopic Analysis of Geothermal Water in Liangxiang Geothermal Field. *South-to-North Water Transfers Water Sci. Technology* 13, 963–967. doi:10.13476/j.cnki.nsbdqk.2015.05.030

Luo, J., Pang, Z., Kong, Y., and Wang, Y. (2017). Geothermal Potential Evaluation and Development Prioritization Based on Geochemistry of Geothermal Waters from Kangding Area, Western Sichuan, China. *Environ. Earth Sci.* 76, 343. doi:10.1007/s12665-017-6659-9

Lv, J. B. (2004). *Characteristics of the Geothermal Field in Northern Beijing and the Influence of its Exploitation on Seismic Ground Fluid Behavior*. China Earthquake Administration: Doctor's thesis of Institute of Geology.

Ma, Z. Y., Wang, X. G., Su, Y., and Yu, J. (2008). Oxygen and Hydrogen Isotope Exchange and its Controlling Factors in Subsurface Geothermal Waters in the central Guanzhong basin, Shaanxi, China. *Geol. Bull. China* 27, 888–894. doi:10.1016/S1872-5791(08)60056-1

Mcgibbon, C., Crossey, L. J., Karlstrom, K. E., and Grulke, T. (2018). Carbonic Springs as Distal Manifestations of Geothermal Systems, Highlighting the Importance of Fault Pathways and Hydrochemical Mixing: Example from the Jemez Mountains, New Mexico. *Appl. Geochem.* 98, 45–57. doi:10.1016/j.apgeochem.2018.08.015

Pang, Z. H., Kong, Y. L., Pang, J. M., Hu, S. B., and Wang, J. Y. (2017). Geothermal Resources and Development in Xiongan New Area. *Bull. Chin. Acad. Sci.* 32 (11), 1224–1230. doi:10.16418/j.issn.1000-3045.2017.11.007

Rets, E., Chizhova, J., Loshakova, N., Tokarev, I., Kireeva, M., Budantseva, N., et al. (2017). Erratum to: Using Isotope Methods to Study alpine Headwater Regions in the Northern Caucasus and Tien Shan. *Front. Earth Sci.* 11, 702. doi:10.1007/s11707-017-0674-8

Smerdon, B. D., and Gardner, W. P. (2022). Characterizing Groundwater Flow Paths in an Undeveloped Region through Synoptic River Sampling for Environmental Tracers. *Hydrological Process.* 36 (1), e14464. doi:10.1002/hyp.14464

Solder, J. E., Beisner, K. R., Anderson, J., and Bills, D. J. (2020). Rethinking Groundwater Flow on the South Rim of the Grand Canyon, USA: Characterizing Recharge Sources and Flow Paths with Environmental Tracers. *Hydrogeol J.* 28 (5), 1593–1613. doi:10.1007/s10040-020-02193-z

Sun, Z., Ma, R., Wang, Y., Ma, T., and Liu, Y. (2016). Using Isotopic, Hydrogeochemical-Tracer and Temperature Data to Characterize Recharge and Flow Paths in a Complex Karst Groundwater Flow System in Northern China. *Hydrogeol J.* 24, 1393–1412. doi:10.1007/s10040-016-1390-2

Tarmers, M. A. (1967). "Radiocarbon Ages of Groundwater in an Arid Zone Unconfined Aquifer," in *Stout G E Isotope Techniques in the Hydrologic Cycle, Geophysics* (Washington D C: AGU), 143–152.

Wang, G. L., Li, J., Wu, A. M., Zhang, W., and Hu, Q. Y. (2018). A Study of the Thermal Storage Characteristics of Gaoyuzhuang Formation, A New Layer System of Thermal Reservoir in Rongcheng Uplift Area, Hebei Province. *Acta Geoscientica Sinica* 39, 533–541. doi:10.3975/cagsb.2018.071901

Wang, K., and Zhu, J. (2001). A Conceptual Model of the Tianjin Geothermal System Based on Isotopic Studies. *Sci. China Ser. E-technol. Sci.* 44, 160–164. doi:10.1007/bf02916809

Wang, P., Zhang, F., and Chen, Z. (2020). Characterization of Recharge Processes and Groundwater Flow Paths Using Isotopes in the Arid Santanghu basin, Northwest China. *Hydrogeology J.* 28 (3), 1–15. doi:10.1007/s10040-020-02119-9

Wang, S., Pang, Z., Liu, J., Lin, P., Liu, S., and Yin, M. (2013). Origin and Evolution Characteristics of Geothermal Water in the Niutuozhen Geothermal Field, North China Plain. *J. Earth Sci.* 24, 891–902. doi:10.1007/s12583-013-0390-6

Wang, S. Q., Zhang, B. J., Li, Y. Y., Xing, Y. F., Yuan, W. Z., Li, J., et al. (2021). Heat Accumulation Mechanism of Deep Ancient Buried hill in the Northeast of Gaoyang Geothermal Field, Xiong'an New Area. *Bull. Geol. Sci. Technology* 40, 533–541. doi:10.19509/j.cnki.dzkq.2021.0319

Wang, Y. Z. (2020). *Carboniferous-Permian Coal-Derived Gas Resource Potential Analysis and Favorable Area Prediction in the Northeast of Jizhong Depression*. Beijing: Doctoral Dissertation of China University of Geosciences.

Wu, A. M., Ma, F., Wang, G. L., Liu, J. X., Hu, Q. Y., and Miao, Q. Z. (2018). A Study of Deep-Seated Karst Geothermal Reservoir Exploration and Huge Capacity Geothermal Well Parameters in Xiongan New Area. *Acta Geoscientica Sinica* 39, 523–532. doi:10.3975/cagsb.2018.071104

Yan, D. S., and Yu, Y. T. (2000). *Evaluation and Utilization of Geothermal Resources in Beijing Tianjin Hebei Oil Region.* Wuhan: China University of Geosciences Press, 58–59.

Yang, L. Z., Zhang, G. H., Hu, N. S., Liu, C. H., and Liu, Z. Y. (2009). Recognition of Ground Water Supplying Features for Northern Shandong plain;China Using Environmental Isotope Information. *Geol. Bull. China* 28, 515–522. doi:10.3969/j.issn.1671-2552.2009.04.013

Yao, J. L. (2014). *Analysis of Carboniferous-Permian Tectonic Control of Oil and Gas in the Northeast of Jizhong Depression*. Beijing): Master's thesis of China University of Geosciences.

Yao, Z. J. (1995). Paleoclimate Record of Geothermal Water for Last 0.03 Ma in North China. *Earth Sci.* 20 (4), 383–388. CNKI:SUN:DQKX.0.1995-04-005

Yin, G., Ni, S. J., and Zhang, Q. C. (2001). Euterium Excess Parameter and Geohydrology Significance-Taiking the Geohydrology Researches in Jiuzhaigou and Yele, Sichuan for Example. *J. Chengdu Univ. Technology* 7 (3), 251–254. doi:10.3969/j.issn.1671-9727.2001.03.006

Zhang, B. J., Gao, Z. J., Zhang, F. Y., Hao, S. H., Liu, F. Y., and Zang, J. J. (2015). Hydrodynamic Condition and Response of Formation Water Chemical fields of Geothermal Water in North China Basin. *Earth Sci. Front.* 22 (06), 217–226. doi:10.13745/j.esf.2015.06.017

Zhang, B. J., Xu, J. X., Ma, Z. M., Shen, Z. L., and Qi, L. (2010). Analysis on Groundwater Supply Sources Using Hydrogen and Oxygen Isotope Data-A Case Study of Yanggu-Qihe Salient, Northwestern Shandong, China. *Geol. Bull. China* 29, 603–609. doi:10.3969/j.issn.1671-2552.2010.04.016

Zhang, D. Z., Liu, Z. G., Lu, H. L., Su, Y. Q., Kou, Q. H., Feng, L. Q., et al. (2014). *Hebei Geothermal*. Beijing: Geological Publishing Press.

Conflict of Interest: The authors declare that the research was conducted in the absence of any commercial or financial relationships that could be construed as a potential conflict of interest.

frontiers | Frontiers in Earth Science

ORIGINAL RESEARCH
published: 08 April 2022
doi: 10.3389/feart.2022.787156

Mechanism and Prediction of Geothermal Resources Controlled by Neotectonics in Mountainous Areas: A Case Study of Southeastern Zhangjiakou City, China

Wenzhen Yuan[1], Xiaodong Lei[2], Tongzhe Liu[3], Siqi Wang[1], Yifei Xing[1], Ruijie Zhu[4], Fengtian Yang[4], Dailei Zhang[1]*, Jun Gao[1] and Baojian Zhang[1]*

[1]Chinese Academy of Geological Sciences, Beijing, China, [2]Beijing Institute of Geologic Survey Technology, Beijing, China, [3]Institute of Hydrogeology and Engineering Geology, Shandong Provincial Bureau of Geology and Mineral Resources, Jinan, China, [4]Key Laboratory of Groundwater Resources and Environment (Jilin University), Ministry of Education, Changchun, China

OPEN ACCESS

Edited by:
Yanlong Kong,
Institute of Geology and Geophysics (CAS), China

Reviewed by:
Yonghui Huang,
Institute of Geology and Geophysics (CAS), China
Chuanqing Zhu,
China University of Petroleum, China

***Correspondence:**
Dailei Zhang
zhangdailei89@163.com
Fengtian Yang
yangfengtian@jlu.edu.cn

Specialty section:
This article was submitted to Economic Geology, a section of the journal Frontiers in Earth Science

Received: *30 September 2021*
Accepted: *21 February 2022*
Published: *08 April 2022*

Citation:
Yuan W, Lei X, Liu T, Wang S, Xing Y, Zhu R, Yang F, Zhang D, Gao J and Zhang B (2022) Mechanism and Prediction of Geothermal Resources Controlled by Neotectonics in Mountainous Areas: A Case Study of Southeastern Zhangjiakou City, China. Front. Earth Sci. 10:787156. doi: 10.3389/feart.2022.787156

The geothermal resources in mountainous areas are usually controlled by neotectonic faults. To minimize the risk in site selection for geothermal drilling, the controlling mechanism must be identified. Based on the neotectonic control theory for geothermal resources, the occurrence of the geothermal resources in the mountainous area in southeastern Zhangjiakou city was investigated. The investigation was divided into three stages. Firstly, field investigation for neotectonics was carried out to characterize the kinematics and the stress state of the faults, including fault occurrences, tectonic stages, and paleostress analysis, and in total 19 neotectonic faults were confirmed. Based on Riedel shear model and present stress field, their conductivity for geothermal water was inferred; secondly, geophysical and geochemical surveys were applied to identify the stress state and characterize the occurrence of the potential water conductive faults. The results showed that the combined use of magnetotelluric sounding (MT), controllable source audio magnetotelluric sounding (CSAMT), and 2D seismologic survey is effective in delineating fault occurrence, strata distribution, and water conductivity within 1,000 m depth, while measurement of ^{222}Rn activity in soil gas across the neotectonic faults is effective to investigate the groundwater conductivity of the faults, and all the neotectonic faults in the study area striking clockwise from N5°E to N25°W are considered to be water conductive; thus, the areas at the intersection zones of neotectonic faults in the basin in groundwater runoff and discharge regions are promising targets for geothermal exploration. This conceptual model was verified by the geothermal fields already discovered in the study area and proved to be reasonable, and then a potential drilling site was predicted and proved to be successful. It is suggested that this workflow for geothermal exploration is suitable for Zhangjiakou city and may also be applied to other mountainous areas.

Keywords: neotectonic faults, geothermal resources, mountainous areas, conceptual model, drilling site prediction

INTRODUCTION

Hydrothermal resources are the main geothermal resources being used (Kong, 2017; Wang et al., 2017); accurate positioning of the resources is essential to reduce the overall development cost. Structurally, hydrothermal resources are distributed in large sedimentary basins and mountainous areas. Geothermal resources in sedimentary basins mainly occur in layered reservoirs and are easy to explore, whereas in mountainous areas are mainly controlled by open faults, and more investigation works are needed. Due to multi-stage structural evolution and complex structural features, it is often difficult to determine their mechanical properties through field observation. In addition, mechanical properties of faults are often segmented. These factors bring great risks to the prediction of geothermal resources targets. At present, the combination of geophysical and geochemical surveys is frequently applied to geothermal exploration in mountainous areas (Moghaddam et al., 2016). The geophysical methods adopted mainly include gravity, seismic and magnetotelluric surveys, etc. (Peng et al., 2019; Foley et al., 2020; Sena-Lozoya et al., 2020), while geochemical methods usually include soil gas (radon, CO_2, etc.) measurement, soil element geochemistry and hydrogeochemistry, etc. (Gang et al., 2012; Vaselli et al., 2013; Chang et al., 2014; Hanson et al., 2014; Pinti et al., 2017; Kong et al., 2020; Rodriguez et al., 2021). However, the application of these methods, such as survey line layout and data interpretation, must be based on the study of geological structures, especially on the understanding of how fault systems control the flow pathway of the thermal water; otherwise, it may result in blindness or great uncertainty in geothermal exploration. In the practice of geothermal exploration, there are many failed cases which resulted from ignoring the fact that the occurrence of thermal water in mountainous areas is controlled by open faults. Thus, it is key to identify the mechanical properties of the faults. In China, a theory named "Neotectonic control theory for geothermal resources" was proposed for convective hydrothermal resources (Xiao, 1986; Wang et al., 1993). The theory holds that whether a fault is open or closed depends on two most vital factors, i.e., its age and stress state. Generally, faults active in the Cenozoic are young enough and can hardly be infilled or cemented completely; thus, if the faults are tensile in the present stress field, they have the potential to act as a flow pathway for thermal water, and the area around the intersection zone of the tensile faults with other tensile or compressive shear faults in the regional groundwater discharge area would be the most promising area of hydrothermal resources. In this sense, faults active in the Cenozoic are regarded as neotectonic faults. Therefore, in the exploration of geothermal resources in the mountainous area, investigation and analysis of neotectonic faults should be firstly conducted to preliminarily infer their mechanical properties, followed by geophysical and geochemical surveys to identify if the faults are open, and then confirmed by drilling. Finally, the conceptual model of the thermal water controlled by neotectonic fault systems can be established, which would guide geothermal exploration.

Neotectonic faults have some distinctive characteristics; e.g., they are active in the Cenozoic, deep cutting, poorly infilled and cemented, and tensile (with high permeability) and thus control the formation of low to medium temperature convective type geothermal systems (Wang et al., 1993). Xiao (1986) summarized the characteristics of Cenozoic tectonic movement in China and proposed that neotectonic activities can be divided into four stages, namely, Paleogene, Neogene to the beginning of Quaternary, middle and late Quaternary, and Holocene. Here, according to the new tectonic stage division in China (Wan, 2011), the four stages are adjusted: the first stage is Paleocene (65–52 Ma), belonging to Sichuan Period; the second stage is Eocene to Oligocene, i.e., Huabei Period (52–23.5 Ma); the third period is Neogene to Early Pleistocene, i.e., Himalayan Period (23.5–0.78 Ma); and the fourth stage is the Middle Pleistocene to Holocene, that is, the Neotectonic Period (since 0.78 Ma). As tectonic stress fields in each period is different, the mechanical properties of the Neotectonic faults also change through the geological history. In field investigations, the mechanical properties and degree of openness of neotectonic faults can be preliminarily judged according to the characteristics of the pre-Cenozoic old structures and Neotectonic stress fields, the strike direction and mechanical properties of the faults formed under the Cenozoic tectonic stress fields, the history of neotectonic activities can be restored in combination with fault dating, and the openness of Neotectonic faults can be verified by means of geophysical and geochemical surveys. The Neotectonic control theory for geothermal resources has been widely applied in geothermal exploration practices to both low to medium and high temperature systems in China for approximately 30 years and has been verified to be effective (Yang et al., 2012; Lang et al., 2016; Kang et al., 2020). Zhangjiakou city is located in the northwest of Hebei Province, to the northwest of Beijing. It is an important node on the economic corridor between China, Mongolia, and Russia and is one of the new energy bases in national planning. In total, more than 20 geothermal fields have been found in this area, indicating a promising reserve of geothermal resources. In the mountainous region adjacent to Beijing in southeastern Zhangjiakou City, two large geothermal fields, i.e., Houhaoyao and Xijiabao, and one geothermal anomaly area, i.e., Nuanquan, have been found in recent years (**Figure 1**), but the genesis mechanism of the geothermal systems in this area is still not fully studied. Researchers believe that the geothermal anomaly in this area is related to the fracture network of deep faults but did not determine the mechanical properties of the faults due to limited field data and exploration depth (Wei, 2006; Li et al., 2020).

Based on previous researches and guided by the neotectonic control theory for geothermal resources, combined with geophysical and geochemical exploration methods, this research investigated and analyzed the mechanical properties of the neotectonic controlling faults, obtained the conceptual genesis model of the geothermal systems, then predicted the promising targets, and finally verified the geothermal potential by geothermal drilling. This study provides a reference for geothermal exploration in mountainous areas.

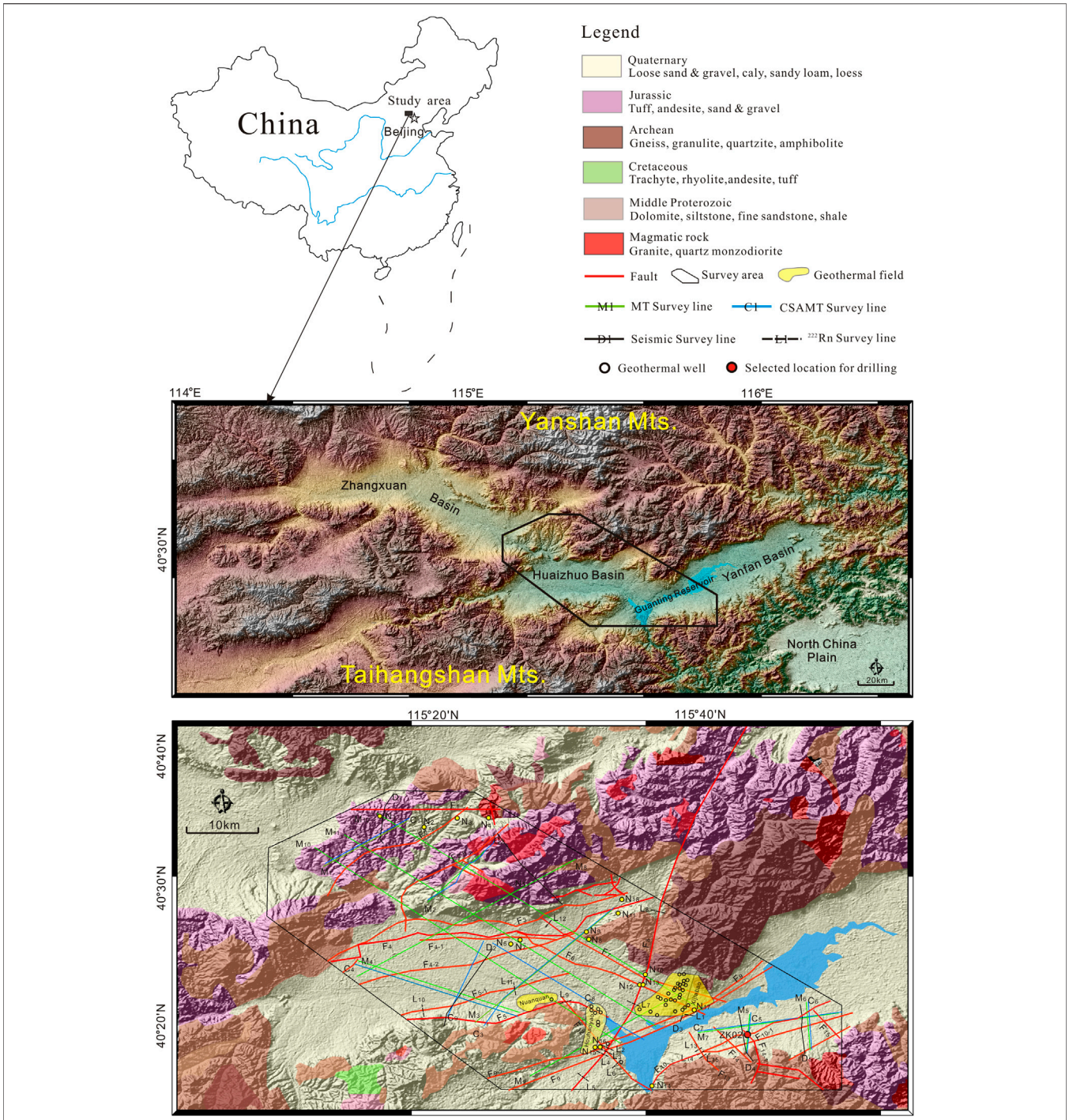

FIGURE 1 | Schematic geological map and location of field survey lines of the study area.

STUDY AREA

Local Geology

The study area is in the mountainous area in Northwest Hebei, to the northwest of Beijing. Tectonically, it includes the east of Zhangxuan Basin, the west of Huaizhuo Basin, and Yanfan Basin (**Figure 1**). The geomorphic units mainly include river plains, hills, and mountains. The middle and low mountain areas are mostly tectonic erosion landforms dominated by carbonate rocks or igneous rocks. The terrain in the area fluctuates greatly; it is generally high in the northwest and low in the southeast. The altitude is between approximately 900 and 1,700 m, and the relative height difference is approximately 500–1,000 m.

The study area is a semi-arid area and has a temperate continental monsoon climate with four distinct seasons. The annual average temperature is 8°C. In hottest July, the average temperature is 24°C. The coldest month is January, and the average temperature is −9°C. The average annual precipitation is 360 mm, whereas the evaporation is 1,900 mm. The main rivers in the area belong to Yongdinghe River system of Haihe River Basin, which flows into the Guanting Reservoir, which is an important drinking water source for Beijing.

The strata in the study area comprise Archaean to Cenozoic except for the Lower Paleozoic, Upper Ordovician, Upper Paleozoic Silurian, Devonian, Carboniferous, and Permian. The Archean constitutes the regional basement, which is a set of metamorphic rock series formed under middle to deep regional metamorphism. The lithology is anorthosite, anorthosite amphibolite, and anorthosite gneiss. The Middle Proterozoic includes three systems, the Lower mainly consists of quartz sandstone, siltstone, sandy shale, etc., with carbonate lens at the bottom, and the strata thickness is 300–810 m. The Middle is dominated by carbonate rocks. The lithology is mainly dolomite and chert banded dolomite layered by quartz sandstone, siltstone, and shale. It outcrops in the northern mountainous areas north to the HuaiZhuo Basin, the thickness of dolomite is 370–1800 m, and the Upper system mainly comprises dolomite and quartz sandstone. The Paleozoic in the study area lacks Permian, Carboniferous, Devonian, Silurian, and Ordovician, and only the Cambrian outcrops sporadically. The Cambrian lithology is mainly Oolitic limestone, shale, argillaceous banded limestone, and marl. The formation thickness in this area is 230–400 m. The Triassic system is limited in distribution with a small thickness (approximately 70 m), which is mainly fluvial lacustrine sandy shale. The Jurassic is widely distributed throughout the region, which is composed of a set of complex continental volcanic sedimentary rock series. The main lithology is sandstone, conglomerate, tuff and andesite, etc. The Cretaceous comprises a set of river-lake facies, including terrigenous clastic rock and neutral volcanic rock strata distributed sporadically. The total thickness of the stratum reaches up to tens of thousands of meters. The Cenozoic includes Paleogene, Neogene, and Quaternary. The Paleogene includes Oligocene and Eocene, and the main lithology is basalt, interlayered with clay rock. The Neogene system in this area includes the Miocene and Pliocene. It is a set of river-lake facies and basic volcanic facies; the main lithology is interbedded sandy conglomerate and clay, which is not outcropped. Most of the study area is covered by the Quaternary, including Holocene (Q_4), Upper Pleistocene (Q_3), Middle Pleistocene (Q_2), and Lower Pleistocene (Q_1), and is mainly distributed in intermountain valleys and piedmont edges. It is a set of loose sand gravel, sandy soil, clay, and loess, with a general thickness of tens of meters, and reaches up to150–700 m. At present, the distribution of strata in the area is mainly investigated based on the outcrops in surrounding mountainous areas. The detailed lithology and thickness of the formations in the study area are characterized by geophysical survey and drilling in this work.

The magmatism in the study area was intensive. It is a part of the Daxing'anling Mountain and Taihangshan Mountain tectonic magmatic belt. The major magmatic episodes occurred in the Mesozoic and reached the peak in the Middle and Late Mesozoic. The magmatic rock body formed is characterized by large scale, wide distribution and strong mineralization. It mainly occurs in the form of rock foundation, stock, wall, and branch in different scales. Magmatic intrusion and volcanic eruption are controlled by the Dahenan-Chicheng Fault (F_8), which strikes NE-NNE (**Figure 1**).

According to previous investigations, faults in the study area can be roughly divided into five groups, i.e., NW-, NWW-, ENE-, NNE-, and WE-striking faults, which are strike-slip faults. Some faults outcrop as normal or reverse faults at different segments, which is typical for wrench faults or a result of multi-stage activities. These faults have been described geometrically in previous studies, but the mechanical properties and permeability of the faults are still not fully studied, which is the focus of the present work.

Paleostress Regime

The study area has been folded and uplifted since the Jurassic and has experienced five main tectonic stages, accompanied by changes of stress fields, as a result of the tectonic regime transformation due to plate movement, i.e., the subduction of the North America Plate and Izanagi Plate to the west and northwest, respectively, in the Jurassic to Early Cretaceous, the fast northward movement of the Indian Plate and collision with the Eurasian Plate in the Middle Cretaceous-Paleogene, and the pushing against the Indian Plate and the Pacific Plate in the Eocene to Neotectonic. The principal stress of each tectonic stage is listed in **Table 1**. The faults in the study area generally show multi-stage activities in the Cenozoic under the paleostress regimes.

METHODOLOGY

The mechanical properties and water conductivity of the main faults in the study area are comprehensively investigated by 1) field investigation—according to the distribution of the main faults in the area, 10 routes are arranged for neotectonic investigation. The investigations include fault occurrences, tectonic stages, and paleostress analysis; 2) geophysical survey—three geophysical exploration methods were adopted, including magnetotelluric sounding (MT), controllable source audio magnetotelluric sounding (CSAMT), and two-dimensional (2D) seismology. The application of MT is to preliminarily find out the occurrence of faults and stratigraphic structure within 4,000 m depth, providing basis for further study on water conductivity of faults and reservoir structure. CSAMT is further applied to exploring the occurrence of the main faults within 1,500 m depth, inferring water conductivity of the faults, and lithology, burial depth, and thickness of reservoir and caprock in combination with geological and other geophysical data. Moreover, 2D seismology is applied to prospecting the occurrence of main faults and strata within 4,000 m depth in key

TABLE 1 | Tectonic stages and orientation of principal stress of the study area since Jurassic.

Geologic time	Tectonic periods	Orientation of principal stress
Jurassic to Early Cretaceous	Yanshan	NW-NNW (Wan, 2011)
Middle Cretaceous to Paleogene	Sichuan	NNE (Wan, 2003)
Eocene to Oligocene	Huabei	NWW (Wan, 2003)
Neogene to Early Pleistocene	Himalayan	NNW (Wan, 2003)
Middle Pleistocene to Holocene	Neotectonic	NEE (80° ± 10°) (He, 1989)

TABLE 2 | Summary of field characteristics of the main faults in the study area.

Fault	Segment	Average strike	Stress state	Age	Type	^{222}Rn	MT and CSAMT	MT and 2D seismology
F1		WE	High tension	Q	Reverse		Impermeable	>1,000
F2–5	1	N40°E	Moderate tension	J	Normal		ND	>1,500
	2	N78°E	High tension	J	Normal		ND	>1,500
	3	N56°E	Moderate tension	J	Normal		ND	>1,500
F2–6	1	N6°W	Compression/shear	J	Normal		ND	>1,500
	2	N32°E	Low tension/weak shear	J	Normal		ND	>1,500
	3	N63°E	Moderate tension	J	Normal		ND	>1,500
	4	N48°E	Moderate tension	J	Normal		ND	>1,500
F3	1	N62°E	Moderate tension	Q	Reverse		Low conductive	2,000
	2	N87°W	High tension	Q	Reverse		Conductive	2,000–4,000
	3	N75°E	High tension	Q	Reverse		Conductive	4,000
F4		N84°E	High tension	Q	Normal		Conductive	>3,500
F4–1		WE	High tension	Q	Normal		Conductive	>3,500
F4–2		N78°E	High tension	Q	Normal		Conductive	>3,500
F5	1	N87°E	High tension	Q3	Normal		Conductive	1,300–5,000
	2	N82°W	Moderate tension	Q3	Normal		Conductive	1,300–5,000
	3	N71°E	High tension	Q3	Normal		Conductive	1,300–5,000
	4	N85°W	High tension	Q3	Normal		Conductive	1,300–5,000
	5	N75°W	Moderate tension	Q3	Normal		Conductive	1,300–5,000
F5–1		N76°E	High tension	Q3	Normal	Conductive	Conductive	1,300–5,000
F6		N67°W	Moderate tension	Q4	Normal		Conductive	4,000
F7	1	N60°W	Moderate tension	Q2	Normal	Conductive	Conductive	3,000
	2	N74°W	High tension	Q2	Normal	Conductive	Conductive	3,000
F8	1	N15°E	Low tension/weak shear	Q	Normal	Conductive	Conductive	>4,000
	2	N38°E	Moderate tension	Q	Normal	Conductive	Conductive	>4,000
	3	N26°E	Low tension/weak shear	Q	Normal	Conductive	Conductive	>4,000
F9		N65°E	High tension	Q2	Normal	Conductive	Conductive	>2,000
F9–1	1	N68°E	High tension	Q2	Normal	Conductive	Conductive	>2,000
	2	N55°E	Moderate tension	Q2	Normal	Conductive	Conductive	>2,000
F9–2		N75°E	High tension	Q2	Normal	Conductive	Conductive	>2,000
F10	1	N36°E	Moderate tension	Q3	Normal		Conductive	4,000
	2	N68°E	High tension	Q3	Normal		Conductive	4,000
F12		N40°W	Low tension/weak shear	Q	Normal	Conductive	Conductive	>3,000
F13	1	N31°W	Low tension/weak shear	Q	Normal	Conductive	Conductive	>3,000
	2	N50°W	Low tension/weak shear	Q	Normal	Low conductive	Conductive	>3,000
F14		N45°W	Low tension/weak shear	Q	Normal			
F15		N43°W	Low tension/weak shear	Q	Normal			

zones based on MT and CSAMT and conducting comprehensive interpretation of water conductivity of the main faults; and 3) soil gas survey—^{222}Rn in soil gas is sensitive to water conductive faults and thus is a good indicator for the location of opened fault segments, where ^{222}Rn activity in soil gas would be much higher than further away from the faults. In this study, ^{222}Rn activity in soil gas was measured across the main fault segments along 15 profiles (**Figure 1**). ^{222}Rn activity was measured with a DURRIDGE RAD7 Radon Detector, with a precision of 10%. The distance between two survey points is 50–200 m, and the measured depth is 0.8–1.1 m.

RESULTS AND DISCUSSION

Mapped Structures

Structural characteristics of the main faults were observed in the field at 18 outcrops; the field characteristics are summarized in

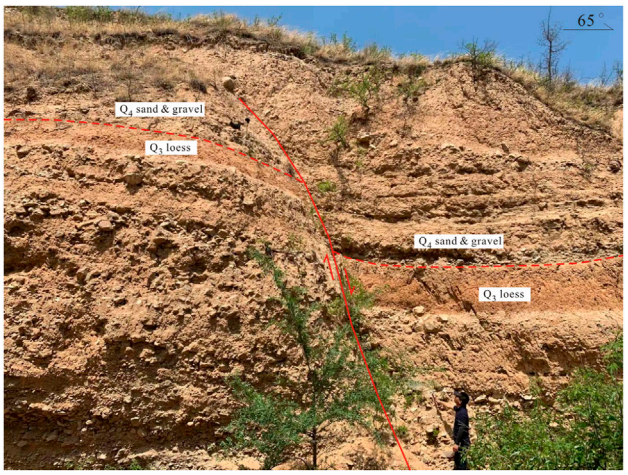

FIGURE 2 | ENE-striking normal fault (F_{10}, refer to **Figure 1**, N_{14}, for the location). The Late Pleistocene (Q_3) loess was cut by the fault, indicating the latest active age.

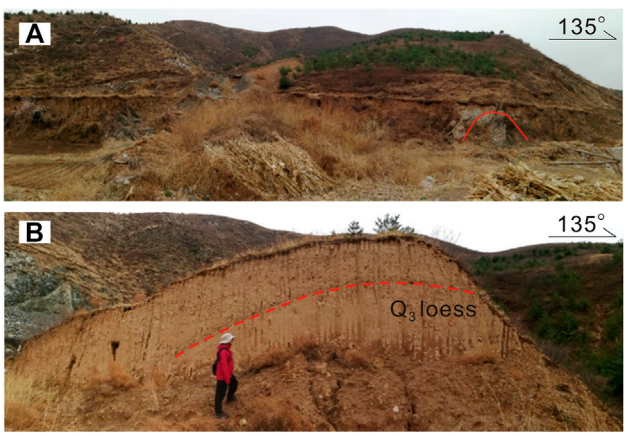

FIGURE 3 | NNE-striking normal fault and NW-striking fault (refer to **Figure 1**, N_{10}, for the location). **(A)** Panorama of the entire outcrop and an anticline developed in pre-Cenozoic formations. **(B)** Folded loess profile along the NW-striking fault, indicating the axis of compression in NW direction.

Table 2. The faults observed are mainly normal faults, and only a few ENE-striking (F_3) and WE-striking (F_1) faults are reverse faults. The latest active time of the faults found through field investigation is in Quaternary; thus, the main faults in the study area are neotectonic faults (**Figures 2**, **3**) (Qi and Feng, 2019), except for $F_{2\text{-}5}$ and $F_{2\text{-}6}$, which were developed in Jurassic, and no obvious signs of neotectonic activities were found. In total, 19 neotectonic faults were identified (**Table 2**).

Stress State of the Neotectonic Faults Under Present Stress

The regime of a stress field determines the type and orientation of faults generated, and subsequent changes of the stress field affect

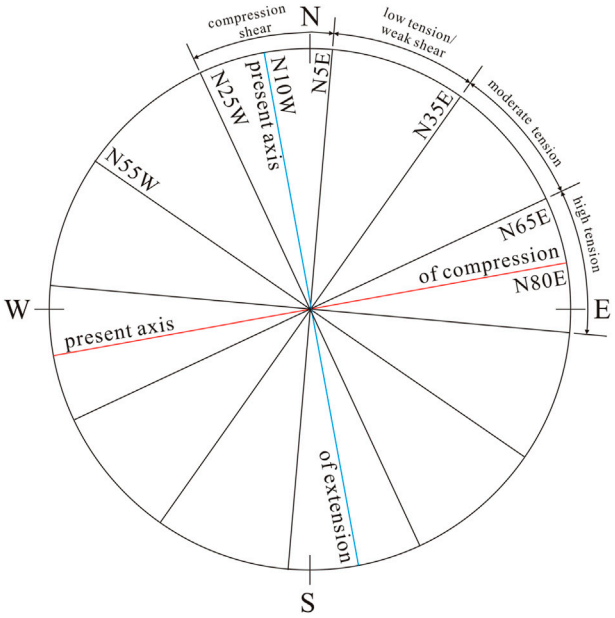

FIGURE 4 | Strike state of the neotectonics faults in the present stress filed in the study area. The current axis of compression orients N80°E.

the mechanical and hydrologic characteristics of the faults; thus, pre-existing faults may exhibit different hydrologic characteristics in the present stress field. The neotectonic faults would have developed heterogeneous hydrologic characteristics along strike due to local transtension or transpression (Dickerson and Fryer, 2009; Moore and Walsh, 2020). Therefore, the stress state of the neotectonic faults can be inferred by comparing the strike of the neotectonic faults and the orientation of the present stress field.

According to He (1989), the current axis of compression (greatest compressive stress) orients N80° ± 10°E; thus, N80°E is adopted as the compromise value for all the data. According to Riedel shear model, assuming a typical angle of internal friction of 30° (Keaton, 2017), the maximum tension is interpreted to exist along any fault plane that is within 15° of N80°E, which is normal to the axis of extension (N5°E to N25°W), while the moderate tension is oriented within 15–45° of the axis of compression (N35°E to N65°E); the low tension with a component of weak shear stress is oriented within 15–45° or parallel to the axis of extension (least compressive stress) (N5°E to N25°W) and compression/shear within 15° or being parallel to the axis of extension (N5°E to N25°W) (**Figure 4**) (Qi and Feng, 2019). Based on this model, the stress state of each fault segment was estimated (**Table 2**).

From the hydrogeologic point of view, the entire or certain segment of neotectonic faults could act as either pathways or barriers for groundwater flow depending upon their stress state. Neotectonic faults in tension would provide pathways, whereas faults in compression would act as planar barriers for groundwater flow (Xiao, 1986; Faunt, 1997). According to the stress state of the neotectonic faults, water conductivity of the main faults in the area could be preliminarily judged. Except for the near NS-striking segment 1 of fault $F_{2\text{-}6}$, whose stress state is

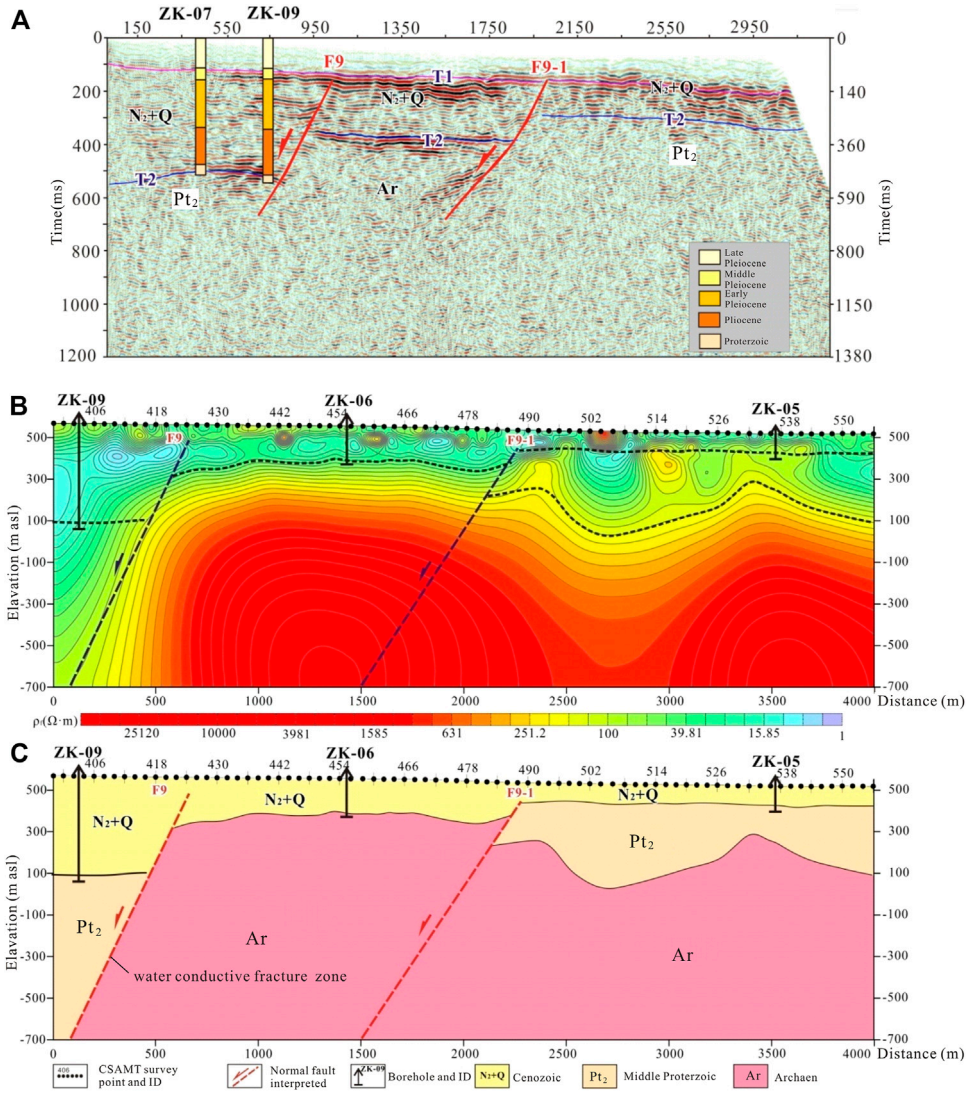

FIGURE 5 | Interpretation of faults from geophysical data (F_9, refer to **Figure 1** for the location). **(A)** 2D seismic time section. **(B)** CSAMT inversion section and geologic interpretation map. **(C)** Comprehensive geologic interpretation based on 2D seismology and CSAMT.

compression/shear, and fault F1, which is a pre-Cenozoic fault and probably had been healed, the other faults are all neotectonic faults and in tension, having the potential to be pathways for thermal water. However, there are other factors affecting the potential, such as the intensity of current stress and paleostress, the scale of faults, etc. Therefore, water conductivity of the neotectonic faults should be further identified by both the geophysical and geochemical surveys.

Identification of Water Conductivity of Neotectonic Faults

Geophysical Survey

Integral interpretation of geophysical data was conducted to delineate the occurrence of the neotectonic faults and evaluate their potential of being pathways for thermal water (**Figure 5**). For MT and CSAMT data, faults were interpreted based on electrical discontinuity, which may result from displacement of strata on both sides of faults or accompanying fracture zone near faults, which facilitate the storage and flow of groundwater. As seismic reflection interface is a physical interface with different rock wave impedance, phase axis generally reflects underground lithologic interface. The main discrimination signs for faults are 1) reflected wave in-phase axis dislocation—due to different scale of faults, it may manifest as the dislocation of wave group and wave system of reflected waves. However, the wave group relationship on both sides of the fault is relatively stable, and the characteristics are clear, which is generally the reflection of medium and small-scale faults; 2) bifurcation, merging, distortion, and strong phase conversion occur in the standard reflection phase axis, which is generally a reflection of small-scale faults; 3) sudden increase/decrease or disappearance of reflection

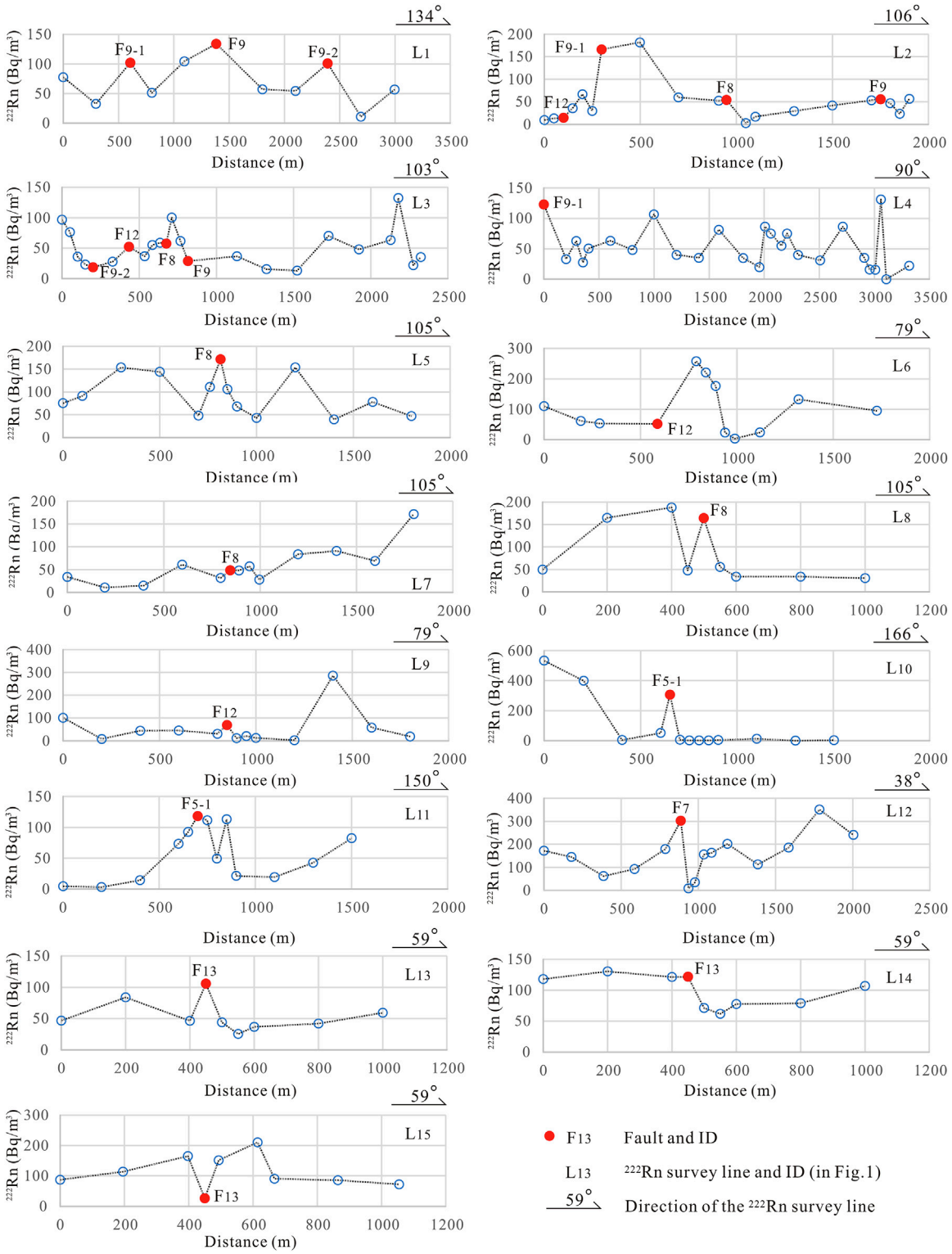

FIGURE 6 | ^{222}Rn activity in soil gas across main fault segments.

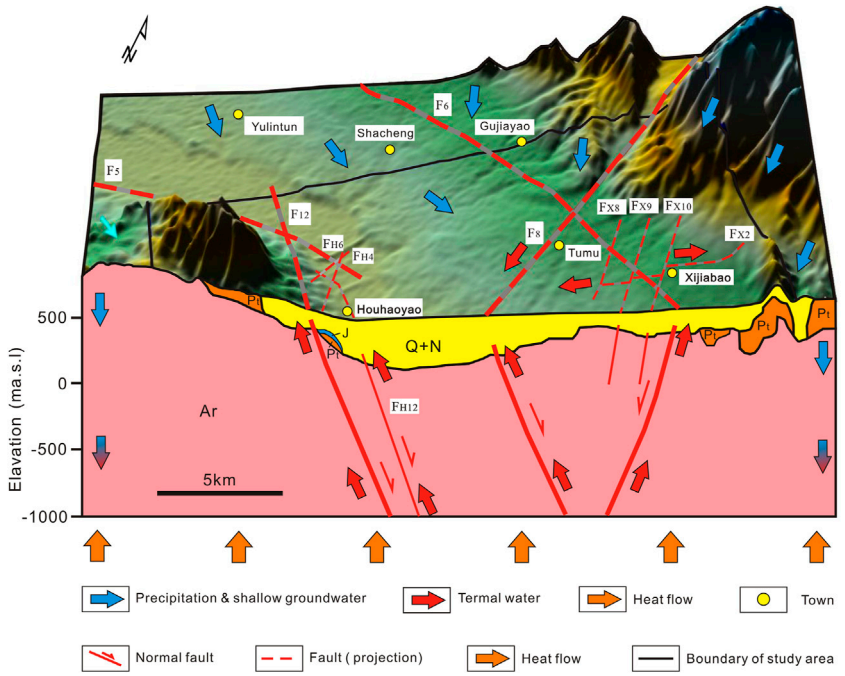

FIGURE 7 | Schematic diagram of genesis model of Houhaoyao and Xijiabao geothermal fields.

phase axis or sudden change in wave group interval, which is often a reflection of large-scale faults; 4) abrupt changes in reflection phase axis, and the reflection is disordered or blank. This can be caused by strata displacement, sudden change of stratum occurrence on both sides, and distortion of reflected wave ray under fault plane due to shielding effect of fault; and 5) appearance of special waves, which is an important sign to identify faults, such as cross section wave and diffracted wave at the dislocation of reflection layer.

According to the interpretations based on geophysical surveys, most of the neotectonic faults have potential to be water conductive, except for fault F_1, which is pre-Cenozoic and the water conductivity has probably diminished due to infill and cementation, and faults $F_{2\text{-}5}$ and $F_{2\text{-}6}$, in which no significant large-scale continuous low resistance was found along the faults (**Table 2**). Some faults show heterogeneity in water conductivity in different segments, such as fault F_3, in which the MT images (M_{10}, M_{11}, and M_{12}; refer to **Figure 1** for the location) show that low resistance in the southern segment of the fault is significant and extends to more than 4,000 m depth (segments 2 and 3), while in the northern segment (segment 1), the low resistance is weak and extends to only 2,000 m depth, indicating a lower permeability. This is consistent with the stress state of each segment of the fault; i.e., segment 1 is in moderate tension, whereas segments 2 and 3 are in high tension (**Table 2**).

Geochemical Survey

The water conductivity of the neotectonic faults is further reflected by ^{222}Rn activity in soil gas across main fault segments. ^{222}Rn activity in soil gas is influenced mainly by faults permeability, groundwater table depth, lithology and physical properties of soil, and meteorological conditions including air moisture content, temperature, atmospheric pressure, and precipitation (Künze et al., 2012; Zarroca et al., 2012). Higher ^{222}Rn activity at the damage zone of the faults is interpreted as an indicator of good water conductivity. Results show that along the 15 survey lines, ^{222}Rn activities show significant heterogeneity across the faults (**Figure 6**). ^{222}Rn activities are usually higher at the fault zones than further from them, indicating that the faults are conductive for groundwater. The activities are above 50–100 Bq/m^3, whereas further from the damage zone activities are lower. However, the ^{222}Rn activities also show significant differences for different faults or different segments of the same faults. For example, ^{222}Rn in soil gas is lower than 60 Bq/m^3 at F_{12} and lower than 125 Bq/m^3 at F_{13} but higher than 100 Bq/m^3 at F_9 and up to 306 Bq/m^3 at $F_{5\text{-}1}$. This could result from the difference in permeability of the faults due to different stress states; e.g., F_{12} and F_{13} are in low tension with weak shear, while F_9 and $F_{5\text{-}1}$ are in high tension. For a certain fault, the ^{222}Rn along the fault also changes significantly, such as F_8, where ^{222}Rn ranges from 48.5 to 171.6 Bq/m^3 within the fault zone from survey lines L_7, L_2, L_3, and L_8 to L_5; F_9, where ^{222}Rn activities range from 23.2 to 134.3 Bq/m^3 from survey lines L_3 and L_2 to L_1; F_{12}, where ^{222}Rn activities range from 14.7 to 69.1 Bq/m^3 from survey lines L_2, L_3, and L_6 to L_9; and F_{13}, where ^{222}Rn activities range from 26.4 to 121.7 Bq/m^3 from survey lines L_{15} and L_{13} to L_{14}. The heterogeneity in ^{222}Rn activities could result from differences in stress states of the fault segments, groundwater table depth, and permeability. For F_8, the north part (segment 1) is in moderate tension and shows

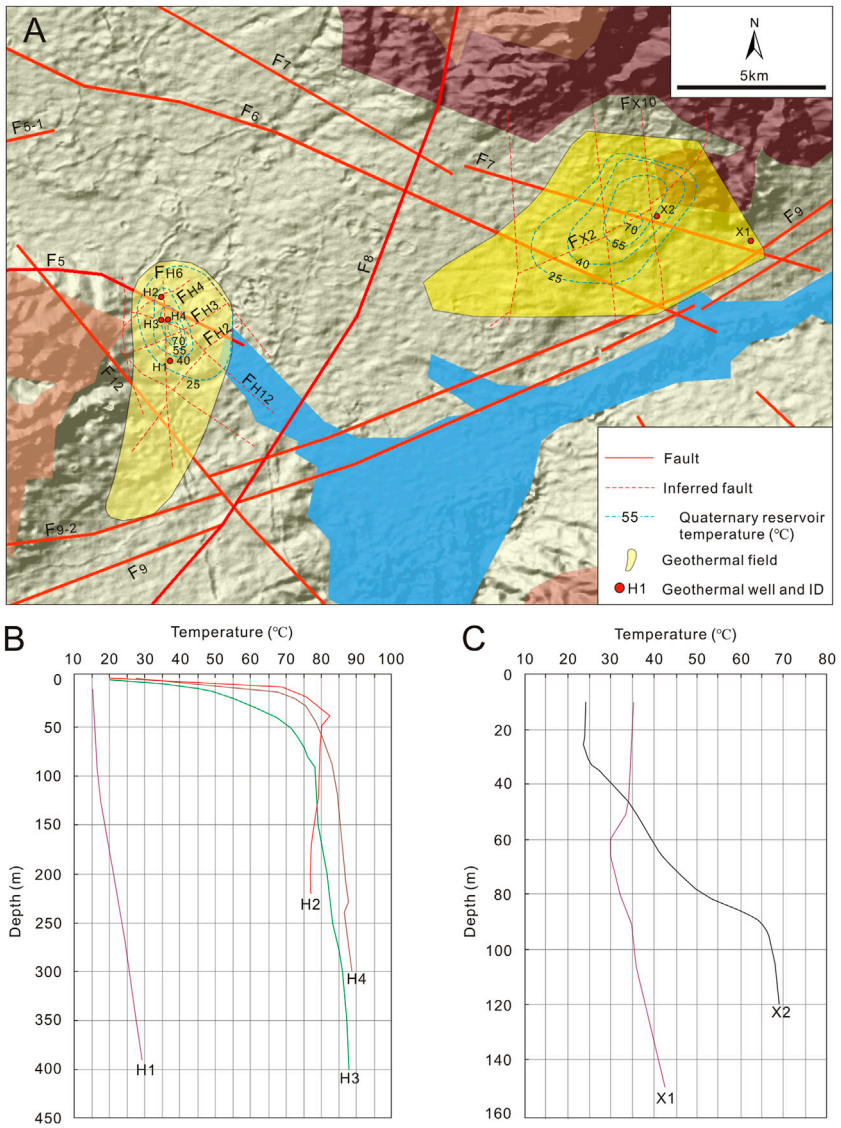

FIGURE 8 | (A) Location of Houhaoyao and Xijiabao geothermal fields. **(B, C)** Temperature–depth curve of geothermal wells in Houhaoyao and Xijiabao geothermal fields, respectively.

the highest ^{222}Rn activities (L_5), while the middle (segment 2) and south (segment 3) parts are in low tension with weak shear (**Table 2**), showing lower ^{222}Rn activities. Along these two parts, it is groundwater table depth which influences ^{222}Rn activities. In the mountainous area (L_8) with deeper groundwater table depth, ^{222}Rn activities are higher, whereas in the basin where groundwater table depth is shallower, the ^{222}Rn activities are lower (L_7, L_2, and L_3) (**Figure 1**). For F_9, from L_1 to L_2 and L_3 along the groundwater flow direction, the ^{222}Rn activities decrease gradually as the groundwater table rises (**Figure 1**). For F_{12}, the ^{222}Rn activities also show a decreasing trend along the groundwater flow (from L_9, L_6, and L_3 to L_9). For F_{13}, the ^{222}Rn activities in the southeast segment (L_{15}) is significantly lower than that in the northwest segment (L_{13} and L_{14}) (**Figure 1**), indicating higher conductivity in the northwest segment. The highest ^{222}Rn activities are at survey line L_{14}, where F_{10} and F_{13} intersect each other and the rocks are highly broken (**Figure 1**), resulting in a high permeability around the intersection zone. The ^{222}Rn activities are lower at L_{13}, reflecting the shallow depth of the groundwater table.

Case Study of Discovered Geothermal Fields

In order to check the water conductivity of the neotectonics faults, two discovered geothermal fields in the study area, i.e., Houhaoyao and Xijiapu geothermal fields, were chosen as study cases. These geothermal fields are located on the piedmonts of Huanzhuo Basin, where five regional faults, including F_5, F_6, F_7, F_8, F_9, and F_{12} cross the region. The strata mainly comprise the Archean basement, Neogene and Quaternary, with limited distribution of the Jurassic and Middle Proterozoic. The

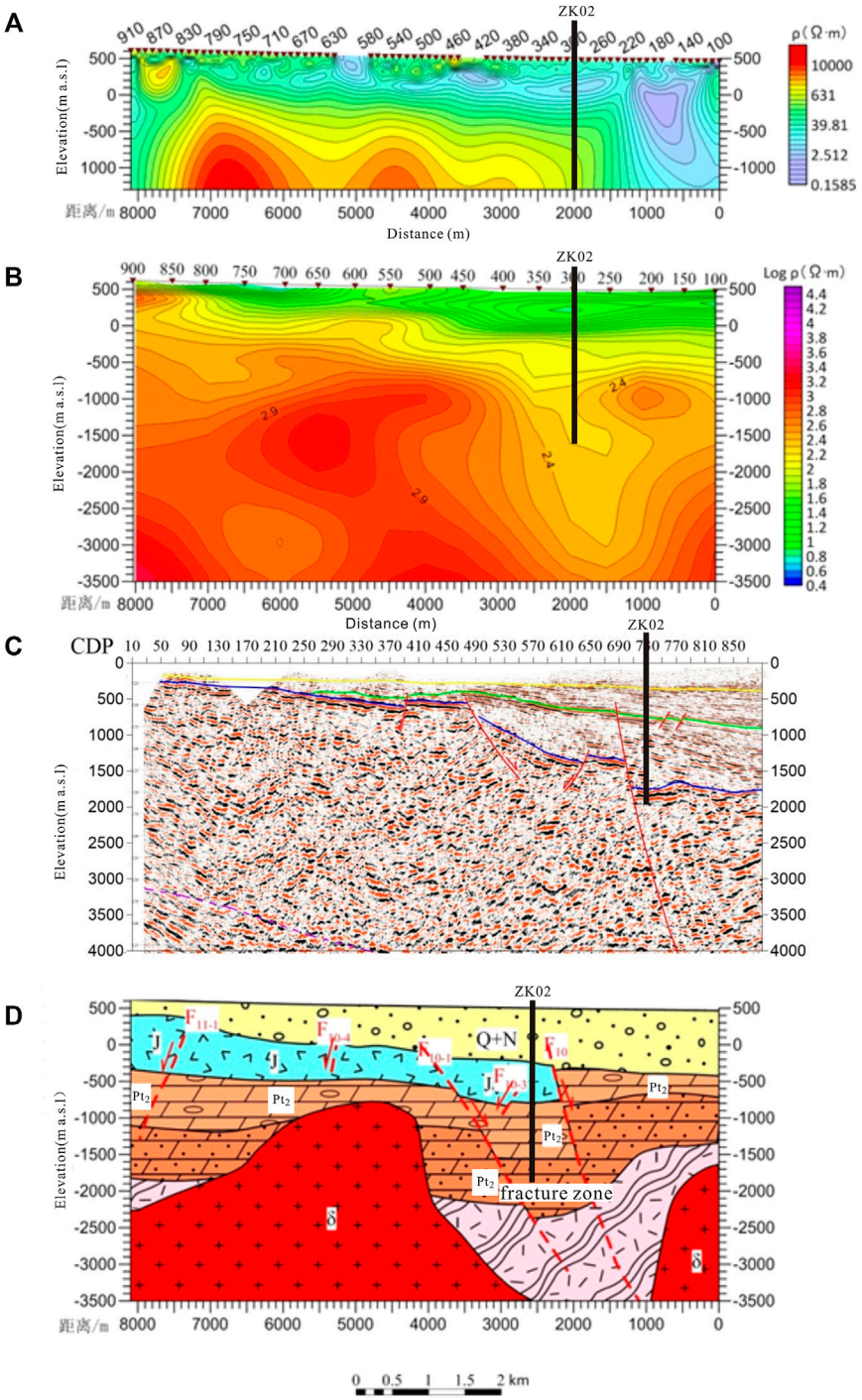

FIGURE 9 | Interpreted geologic profile of target Well ZK02. **(A)** Resistance inversion profile of C_5 survey line (refer to **Figure 1** for the location). **(B)** Resistance inversion profile of M_5 survey line (refer to **Figure 1** for the location). **(C)** Depth converted 2D seismic section of D_4 survey line (refer to **Figure 1** for the location). **(D)** Geologic interpretation map.

thickness of the Neogene and Quaternary is approximately120–600 m and overlays the Archean directly (**Figure 7**). The Archean and the Neogene and Quaternary form a two-layer geothermal reservoir. The open neotectonic faults in the Archean constitutes the bedrock geothermal reservoir, and as the thermal water flows up into the Neogene and Quaternary, the shallow sandstone reservoir forms. The temperature of the regional shallow groundwater is 10–15°C, while the well head temperature of the thermal water in these geothermal fields are usually 44.5–68.5°C, with the highest

temperature of 88.6°C. Assuming the 25°C-isothermal line of groundwater as the boundary of the geothermal reservoirs, the distribution of the reservoirs was determined (**Figure 8A**).

Geophysical surveys showed that there are many secondary or small-scale faults in the geothermal fields. According to MT and CSAMT, in Houhaoyao geothermal field, NE-striking faults F_{H2}, F_{H3}, and F_{H4} and NW-striking fault F_{H12} are normal faults and show low resistance in the deep, indicating that they are water conductive. The low resistance zones of F_{H2}, F_{H3}, and F_{H4} were found to be connected below approximately 3,000 m depth and were inferred to be secondary faults of F_8. Fault F_{H6} has higher resistance in the deep, indicating a lower water conductivity. Well temperature loggings show that wells in the intersection zones of the F_5, F_{H3}, F_{H4}, and F_{H6} show significant temperature anomaly; e.g., the temperature in Wells H_2, H_3, and H_4 increases sharply to 75–89°C from 30 m–400 m depth, whereas temperature anomalies in wells further from the intersection zones are weak; e.g., in Well H_1 near Fault F_{H6}, the well temperature increases slowly from 10°C to 29°C between 10 and 400 m depth (**Figure 8B**). In Xijiabao geothermal field, Fault F_{X2} shows low resistance from 400 m depth in the Quaternary; the fault is a normal fault with an offset of 200–300 m, indicating it is a water conductive neotectonics fault, while the NNW-striking faults F_{X8}, F_{X9}, and F_{X10} show no significant low resistance in the deep and were inferred as groundwater barriers. Groundwater in wells near the intersection zone of F_{X10} and F_{X2} shows the highest temperature; e.g., the well head temperature of Well X_2 increased quickly from 24°C to 70°C between 10 and 120 m depth, whereas the temperature in Well X_1 near the intersection zone of F_9 and F_7 increases slower from 35°C to 43°C between 10 and 150 m depth (**Figure 8C**), indicating the thermal water mainly flows up from F_{X2}. The water conductivity of the faults can also be reflected by the geometry of the isothermals of the groundwater; in the two geothermal fields, the long axis of the isothermals is controlled by the intersection zones of the NE-striking faults and the other faults, indicating the NE-striking faults are water conductive.

Thus, the circulation of the thermal water in these geothermal fields is controlled by open neotectonics faults striking NE and NW; where they are intersected by NNW-striking faults which are water barriers, or other water conductive faults, the stratum is broken, facilitating the upflow of thermal water (**Figure 7**).

PREDICTION AND VERIFICATION OF TARGET AREA

According to the analysis above, all the neotectonic faults in the study area striking clockwise from N5°E to N25°W are likely to be water conductive; the areas at the intersection zones of neotectonic faults in the basin in groundwater runoff and discharge regions are promising targets for geothermal exploration. Based on this conceptual model, a potential site for geothermal drilling was selected in Donghuanyuan Town, located southeast of the study area (**Figure 1**). Geophysical exploration revealed that the geothermal reservoir is a fracture zone in dolomite of the Middle Proterozoic; the burial depth of the reservoir is approximately 1,000 m, with a thickness of approximately 1,000 m. The caprock is Quaternary, Neogene, and Jurassic. There are several groups of intersecting faults and fracture zones in the area, which is favorable for enrichment of thermal water.

The proposed Well ZK02 is located at point 290 along C_5 survey line (**Figure 1**). The location was selected based on the following reasons: 1) the target area is located at the intersection of two groups of neotectonic faults striking NEE (F_{10}) and NNW ($F_{14\text{-}1}$); 2) on the gravity anomaly and aeromagnetic anomaly map (Yuan et al., 2021), the target area is located in the northwest of the northeast gradient zone; 3) the inverted resistance of C_5 survey line and M_5 survey line (**Figure 1**) changes greatly in the transverse direction, and there is an obvious low resistance zone which extends to approximately 3,000 m depth, indicating that the water yield of deep karst affected by the faults is excellent; and 4) the phase axis of D_4 survey line (**Figure 1**) is obviously broken at this point, indicating that layer T_2 is disconnected from the Middle Proterozoic, with an offset of approximately 500 m (**Figure 9**).

The strata encountered by drilling include the Quaternary and Neogene, with a bottom depth of 1,327.9 m, and the lithology is clay, sand, gravel. and glutenite; the Middle Proterozoic has a bottom depth of 2,960 m and a thickness of 1,632 m, and the lithology is mainly dolomite, shale, glutenite, and mudstone, containing diorite porphyrite veins; the bottom depth of the Archean is 3,006.9 m, the drilled thickness is 46.9 m, and the lithology is mainly granite gneiss.

The well is artesian after completion, with a static water level of 9.8 m above the ground. The well temperature measured 72 h after drilling at the depth of 3,000 m was 69.0°C. Results from three drawdown pumping tests show that when the drawdown is 34 m, the water yield reaches up to 160.4 m^3/h, proven to be a high-quality geothermal well.

CONCLUSION

In total, 19 neotectonic faults were identified in a field neotectonic investigation in Yanfan and Xuanhuai Basins, among which the faults striking clockwise from N5°E to N25°W are tensile faults under the present stress filed. The combined use of MT, CSAMT, and 2D seismologic survey was proved to be effective in delineating fault occurrence, strata distribution, and water conductivity.

Measurement of ^{222}Rn activity in soil gas across neotectonic faults is useful to investigate the groundwater conductivity of the faults. The ^{222}Rn activity is mainly influenced by stress state of the fault, groundwater table depth, and the rock broken degree.

The areas at the intersection of water conductive neotectonic faults located in groundwater runoff or discharge area are most promising for geothermal exploration. Based on the neotectonic control theory for geothermal resources and geophysical exploration, the location of geothermal Well ZK02 in Donghuanyuan Town is successfully selected, which is proved to be a high-quality geothermal well by drilling.

This study shows that the application of neotectonic control theory for geothermal water in geothermal resource exploration in Zhangjiakou mountainous area is effective and has the potential to be extended to other mountainous regions (Wang et al., 2015).

DATA AVAILABILITY STATEMENT

The original contributions presented in the study are included in the article; further inquiries can be directed to the corresponding authors.

AUTHOR CONTRIBUTIONS

WY: Conceptualization, Methodology, Investigation, Data curation, Writing–original draft. XL: Investigation, Data curation, Visualization. TL: Investigation, Resources, Conceptualization. SW: Investigation, Resources, Data curation. YX: Investigation, Validation. BZ: Investigation, Validation. RZ: investigation. FY: Conceptualization, Supervision, Writing–review and editing. DZ: Investigation, Resources, Formal analysis. JG: Investigation, Data curation, Visualization. All authors have read and agreed to the published version of the manuscript.

FUNDING

This work was jointly supported by the National Natural Science Foundation of China (Grant Numbers: 42102289 and 4210020524) and the National Geological Survey Project (Grant Numbers: DD20190129 and DD20221677).

REFERENCES

Chang, Z. Y., Shi, J., Li, Q. H., Zhao, H. B., and Zhou, X. Y. (2014). The Application of Soil Radon Measurement Technology to Geothermal Exploration in Taxkorgan County, Xinjiang. *Geophys. geochemical exploration* 38 (4), 654–659. doi:10.11720/wtyht.2014.4.05

Dickerson, R., and Fryer, W. (2009). "Potential Effects of Faults on Groundwater Flow for the Yucca Flat Basin, Nevada Test Site," in *American Geophysical Union, Fall Meeting 2009, Abstract ID*, H33B–H0874.

Foley, N., Tulaczyk, S., Auken, E., Grombacher, D., Mikucki, J., Foged, N., et al. (2020). Mapping Geothermal Heat Flux Using Permafrost Thickness Constrained by Airborne Electromagnetic Surveys on the Western Coast of Ross Island, Antarctica. *Exploration Geophys.* 51 (1), 84–93. doi:10.1080/08123985.2019.1651618

Gang, F. P., Lyv, Y., Yu, L. P., and Chen, Y. X. (2012). The Utilization of Combined Radon and CSAMT Methods to Detect Underground Geological Structures: a Case Study of Detection in Palian and Fapa Profiles, Luxi Area, Western Yunnan Province. *Geol. Bull. China* 31 (Z1), 389–395. doi:10.3969/j.issn.1671-2552.2012.02.024

Hanson, M. C., Oze, C., and Horton, T. W. (2014). Identifying Blind Geothermal Systems with Soil CO 2 Surveys. *Appl. Geochem.* 50, 106–114. doi:10.1016/j.apgeochem.2014.08.009

He, S. H. (1989). Calculation of the Affections of the Principal Stress Direction and Magnitude on the Fault Reactivation. *Crustal Deformation and Earthquake* 9 (3), 44–52.

Kang, F. X., Sui, H. B., and Zheng, T. T. (2020). Heat Accumulation and Water Enrichment Mechanics of piedmont Karstic Geothermal Reservoirs: a Case Study of Northern Jinan. *Acta Geologica Sinica* 94 (5), 1606–1624. doi:10.19762/j.cnki.dizhixuebao.2020150

Keaton, J. R. (2017). "Angle of Internal Friction," in *Encyclopedia of Engineering Geology. Encyclopedia of Earth Sciences Series*. Editors P. Bobrowsky, and B. Marker (Cham: Springer). doi:10.1007/978-3-319-12127-7_16-1

Kong, Y., Pang, Z., Pang, J., Li, J., Lyu, M., and Pan, S. (2020). Fault-Affected Fluid Circulation Revealed by Hydrochemistry and Isotopes in a Large-Scale Utilized Geothermal Reservoir. *Geofluids* 2020, 1–13. doi:10.1155/2020/2604025

Kong, Y., Pang, Z., Shao, H., and Kolditz, O. (2017). Optimization of Well-Doublet Placement in Geothermal Reservoirs Using Numerical Simulation and Economic Analysis. *Environ. Earth Sci.* 76, 118. doi:10.1007/s12665-017-6404-4

Künze, N., Koroleva, M., and Reuther, C. D. (2012). 222Rn Activity in Soil Gas across Selected Fault Segments in the Cantabrian Mountains, NW Spain. *Radiat. Measurements* 47 (5), 389–399. doi:10.1016/j.radmeas.2012.02.013

Lang, X. Y., Lin, W. J., Liu, Z. M., Xing, L. X., and Wang, G. L. (2016). Hydrochemical Characteristics of Geothermal Water in the Guide Basin. *Earth Sci.* 41 (10), 1723–1734. doi:10.3799/dqkx.2016.509

Li, H. Q., Zhang, S. S., Xie, M. Z., Ren, J. S., and Zhou, J. F. (2020). Tectonic System and its Geothermal Water Controlling in Zhangjiakou Area. *Coal Geology. China* 32 (05), 74–82.

Moghaddam, M. M., Mirzaei, S., Nouraliee, J., and Porkhial, S. (2016). Integrated magnetic and gravity surveys for geothermal exploration in Central Iran. *Arabian J Geosci.* 9, 506.

Moore, J. P., and Walsh, J. J. (2021). Quantitative Analysis of Cenozoic Faults and Fractures and Their Impact on Groundwater Flow in the Bedrock Aquifers of Ireland. *Hydrogeol J.* 29, 2613–2632. doi:10.1007/s10040-021-02395-z

Peng, C., Pan, B., Xue, L., and Liu, H. (2019). Geophysical Survey of Geothermal Energy Potential in the Liaoji Belt, Northeastern China. *Geotherm Energy* 7 (1), 14. doi:10.1186/s40517-019-0130-y

Pinti, D. L., Castro, M. C., Lopez-Hernandez, A., Han, G., Shouakar- Stash, O., Hall, C. M., et al. (2017). Fluid Circulation and Reservoir Conditions of the Los Humeros Geothermal Field (LHGF), Mexico, as Revealed by a noble Gas Survey. *J. Volcanology Geothermal Res.* 333-334 (334), 104–115. doi:10.1016/j.jvolgeores.2017.01.015

Qi, B. S., Feng, C. J., Tan, C. X., Zhang, P., and Meng, J. (2019). Application of comprehensive geophysical-drilling exploration to detect the buried North Boundary active Fault Belt of Yanqing-Fanshan Basin in Sangyuan Town, Beijing-Zhangjiakou area. *Geol. China.* 46 (3), 468–481. doi:10.12029/gc20190303

Rodriguez, F., Perez, N. M., and Melian, G. V. (2021). Exploration of Deep-Seated Geothermal Reservoirs in the Canary Islands by Means of Soil CO_2 Degassing Surveys. *Renew. Energ.* 164, þ1017–1028. doi:10.1016/j.renene.2020.09.065

Sena-Lozoya, E. B., González-Escobar, M., Gómez-Arias, E., González-Fernández, A., and Gómez-Ávila, M. (2020). Seismic Exploration Survey Northeast of the Tres Virgenes Geothermal Field, Baja California Sur, Mexico: A New Geothermal prospect. *Geothermics* 84, 101743. doi:10.1016/j.geothermics.2019.101743

Vaselli, O., Higueras, P., Nisi, B., María Esbrí, J., Cabassi, J., Martínez-Coronado, A., et al. (2013). Distribution of Gaseous Hg in the Mercury Mining District of Mt. Amiata (Central Italy): A Geochemical Survey Prior the Reclamation Project. *Environ. Res.* 125, 179–187. doi:10.1016/j.envres.2012.12.010

Wan, T. F. (2011). *The Tectonics of China*. Beijing: Geology Press.

Wang, J. Y., Xiong, L. P., and Pang, Z. H. (1993). *Low to Medium Convective Type Geothermal Systems*. Beijing: Scientific press.

Wang, W. X., Zhao, N., Zhang, Y. N., Cao, S. P., and Li, G. K. (2015). Geochemical Anomalies of Soil Elements and Their Implications for Geothermal fields in the Tianjin Area. *Geology. Exploration* 51 (5), 932–938. doi:10.13712/j.cnki.dzykt.2015.05.013

Wang, G. L., Zhang, W., Liang, J. Y., Lin, W. J., Liu, Z. M., and Wang, W. L. (2017). Evaluation of Geothermal Resources Potential in China. *Acta Geoscientica Sinica* 38 (4), 449–459. doi:10.3975/cagsb.2017.04.02

Wei, H. Z. (2006). A Discussion on Geothermal Resources in Zhangjiakou. *Coal Geology. China* 4, 38–41. doi:10.3969/j.issn.1674-1803.2006.04.015

Xiao, N. S. (1986). *Analysis of Neotectonics and its Application in Groundwater Exploration*. Beijing: Geology Press.

Yang, F. T., Pang, Z. H., Wang, C. H., Duan, Z. F., Luo, L., and Li, Y. M. (2012). Genesis Model of Laozishan Geothermal Field in the Subei Basin. *J. Jilin Univ. (Earth Sci. Edition)* 42 (2), 468–475. doi:10.3969/j.issn.1671-5888.2012.02.022

Yuan, W. Z., Zhang, D. L., Xing, Y. F., Gao, J., Zhang, B. J., Li, Y. Y., et al. (2021). *Investigation and Evaluation Report of Geothermal Resources in Zhangjiakou Area*. Beijing: CGS.

Zarroca, M., Linares, R., Bach, J., Roqué, C., Moreno, V., Font, L., et al. (2012). Integrated Geophysics and Soil Gas Profiles as a Tool to Characterize Active Faults: the Amer Fault Example (Pyrenees, NE Spain). *Environ. Earth Sci.* 67 (3), 889–910. doi:10.1007/s12665-012-1537-y

Conflict of Interest: The authors declare that the research was conducted in the absence of any commercial or financial relationships that could be construed as a potential conflict of interest.

frontiers | Frontiers in Earth Science

ORIGINAL RESEARCH
published: 08 April 2022
doi: 10.3389/feart.2022.785900

Detecting Geothermal Resources in a Plateau Area: Constraints From Land Surface Temperature Characteristics Using Landsat 8 Data

Ben Dong[1,2], *Shuyi Dong*[1,2]*, *Yingchun Wang*[1,3], *Fayang Wen*[1,2], *Chunmei Yu*[1,2], *Jinlin Zhou*[1,3] *and Rongcai Song*[3]

[1]State Key Laboratory of Oil and Gas Reservoir Geology and Exploitation, Chengdu University of Technology, Chengdu, China, [2]College of Earth Sciences, Chengdu University of Technology, Chengdu, China, [3]College of Energy Resources, Chengdu University of Technology, Chengdu, China

Geothermal energy is a kind of clean energy, which attracts more attention. The detection of geothermal resources is inseparable from regional geothermal prospects. Land surface temperature (LST) is an indispensable parameter for geothermal exploration, but the retrieval accuracy of LST for complex and remote areas is currently a major challenge. In this article, based on Landsat 8 remote sensing data, the characteristics of surface temperature retrieval methods are systematically reviewed, and the differences among these three algorithms are researched by using them to detect the surface temperature in the study area, which is Kangding County, Sichuan Province, China. Then the experimental results of the three algorithms are verified by using long-time (more than 1 year) measured data from the two monitoring sites, and the monitoring sites are situated in Zhonggu and Lao Yulin area of Kangding County. The results show that the radiative transfer equation (RTE) has the highest accuracy, and the mean error is 0.372°C; mono-window algorithm (MW) has a mean error of –0.606°C; and the split-window (SW) algorithm has the lowest accuracy, with a mean error of –2.07°C. The experimental results were used to select an algorithm with relatively high accuracy and low sensitivity. At the same time, a time series was used to perform temperature retrieval for this study area from November 2016 to December 2017 to evaluate the applicability of the method. The result shows that the RTE has the highest accuracy in mid-winter and a relatively low accuracy in summer in Kangding County. The purpose of this article is to establish a suitable method for high-precision surface temperature retrieval in plateau areas and to provide technical support for exploring geothermal resources or evaluating geothermal potential in these areas.

Keywords: land surface temperature, algorithm comparison, time series, Landsat 8, Kangding geothermal area

OPEN ACCESS

Edited by:
Shu Jiang,
The University of Utah, United States

Reviewed by:
Zheming Shi,
China University of Geosciences, China
Carolina Pagli,
University of Pisa, Italy

***Correspondence:**
Shuyi Dong
32678751@qq.com

Specialty section:
This article was submitted to Economic Geology, a section of the journal Frontiers in Earth Science

Received: *29 September 2021*
Accepted: *24 January 2022*
Published: *08 April 2022*

Citation:
Dong B, Dong S, Wang Y, Wen F, Yu C, Zhou J and Song R (2022) Detecting Geothermal Resources in a Plateau Area: Constraints From Land Surface Temperature Characteristics Using Landsat 8 Data. Front. Earth Sci. 10:785900. doi: 10.3389/feart.2022.785900

1 INTRODUCTION

At present, it is common to apply satellite remote sensing data for surface temperature retrieval characteristics. Because of medium spatial and temporal resolution, free continuous observation data, systematic scientific data archiving, *etc*., MODIS, Landsat series remote sensing images, and other remote sensing data are widely used (Duan et al., 2021). Using remote sensing image data information to delineate geothermal anomaly zones has attracted a lot of research work in recent

years, which shows the growing interest in clean energy. The estimates of the prospects of geothermal rely on field exploration, which is expensive and subjective to the constraints of remote areas. Through the use of remote sensing thermal infrared data, it has been able to accurately obtain and highlight geothermal anomaly areas in the study area (Qin et al., 2011; van der Meer et al., 2014). This technology has been studied by scholars, who have reached a good conclusion on this issue. Previous studies are as follows:

As early as 1961, the Geothermal survey of Yellowstone National Park in the United States applied infrared remote sensing in geothermal exploration and successfully identified hot springs and other near-surface geothermal anomalies. At the beginning of the 21st century, the use of remote sensing hyperspectral data to analyze and detect geothermal anomalies began to enter the picture. By using hyperspectral data analysis, Nash et al. (2003) explored spectral anomalies of vegetation caused by geothermal gases, and by obtaining and analyzing the spectral anomalies, they completed research works related to geothermal exploration. Reath and Ramsey (2013) proposed a method to search for geothermal resources by using the spectrum of special minerals in geothermal active areas; moreover, they used hyperspectral thermal infrared data to conduct geothermal exploration research.

The use of remote sensing LST data combined with other data models to analyze and detect geothermal anomalies has become an indispensable technical tool in the geothermal industry today. Qin et al. (2011) demonstrated the use of Landsat ETM + thermal infrared (TIR) data to detect possible geothermal sites in Zhangzhou, China. They concluded that TIR data are an effective technique for detecting thermal anomalies. They found that the distribution of geothermal regions is consistent with the development of faults in the study area, which form thermal pathways for heat transfer from magma bodies in the region. Romaguera et al. (2018) mapped geothermal anomalies in the Kenya Rift Valley in the form of a 45-day time series during the winter of 2012 by combining ground-based models with remote sensing LST data. He further proposed that the areas of strong topography lead to anomalously high LST values (false positives). The conclusion showed that spatial averages are generally high in geothermal active areas, and the relative frequency of high LST is also high. Chan et al. (2018) indicated that the occurrence of hot springs and geothermal drilling has good spatial consistency with abnormal areas by using multi-temporal luminance temperature images to verify LST anomaly results and verified selected geothermal anomaly areas in detail through field investigations of hot springs and geothermal drilling. Alexandra et al. (2021) showed that an area with geothermal potential displays LST anomalies, and they extracted a 7-year LST time series of the study area, defined LST thresholds for different land covers, and used a set of logical manipulation algorithms to confirm the possibility of geothermal activity in the study area.

So far, there are still problems to be solved by researchers using LST data to detect geothermal areas. Eneva et al. (2009) pointed out the importance of obtaining nighttime surface temperatures when conducting geothermal soundings. However, it is still hard to eliminate relative hot and cold temperature anomalies caused by differences in the specific heat capacities of different surface objects. Falalakis and Gemitzi (2020) pointed out that the need for spatially and temporally consistent LST datasets cannot be met with existing techniques for estimating LST under cloudy skies.

When performing LST calculations on remote sensing data, researchers have proposed a variety of algorithms. Among these algorithms, there are many representative algorithms, including atmospheric correction method (also called radiative transfer equation method), split-window algorithm, and single-window algorithm. Yu et al. (2014) studied and compared the accuracy of these three algorithms, and finally showed that the radiative transfer equation method had the highest accuracy, followed by the split-window algorithm and the single-window algorithm (Hu et al., 2017). This experiment was proposed by quantitative comparative analysis, which has both accuracy and persuasiveness. Xiao et al. (2021) proposed that mountainous terrain is highly undulating and spatially heterogeneous, and the surface temperature inversion exhibits modeling hard, long time-series data acquisition, and validation. Nowadays, most surface temperature inversion algorithms are based on a flat surface and homogeneous ground area. It seems that no scholars have put forward an appropriate surface temperature inversion algorithm in the plateau region. The high altitude, low atmospheric water vapor content, and other points of the plateau region influence the results calculated by the algorithm.

In this paper, the authors used the atmospheric correction method, split-window algorithm, and single-window algorithm to calculate the surface temperature in Kangding County, and compare and verify the experimental results with the measured data from real-time monitoring stations in Zhonggu and Lao Yulin area. Then in this article, we will analyze the accuracy and sensitivity of the three algorithms in detail, the algorithm relatively suitable for the study area will be derived, and the applicability of the algorithm in the highland region will be comprehensively evaluated by using a time-series format. One of the purposes of this article is to provide a reference for the scholars who will apply surface temperature retrieval algorithms to highland areas.

2 STUDY AREA

2.1 Geographical Location

Kangding County is located in the west of Sichuan Province and the east of Ganzi Tibetan Autonomous Prefecture, spanning 29°08′–30°46′ north latitude and 101°02′–102°30′ east longitude, covering an area of 11,600 square kilometers. National Highway 318 is the main route connecting the outside and Kangding, and Provincial Highway 211 connects Aba and Liangshan autonomous prefectures. **Figure 1** shows the geographical scope of Kangding County.

2.2 Geological Background

The study area is located on the eastern edge of the Qinghai–Tibet Plateau—the border between the western Sichuan Plateau and the

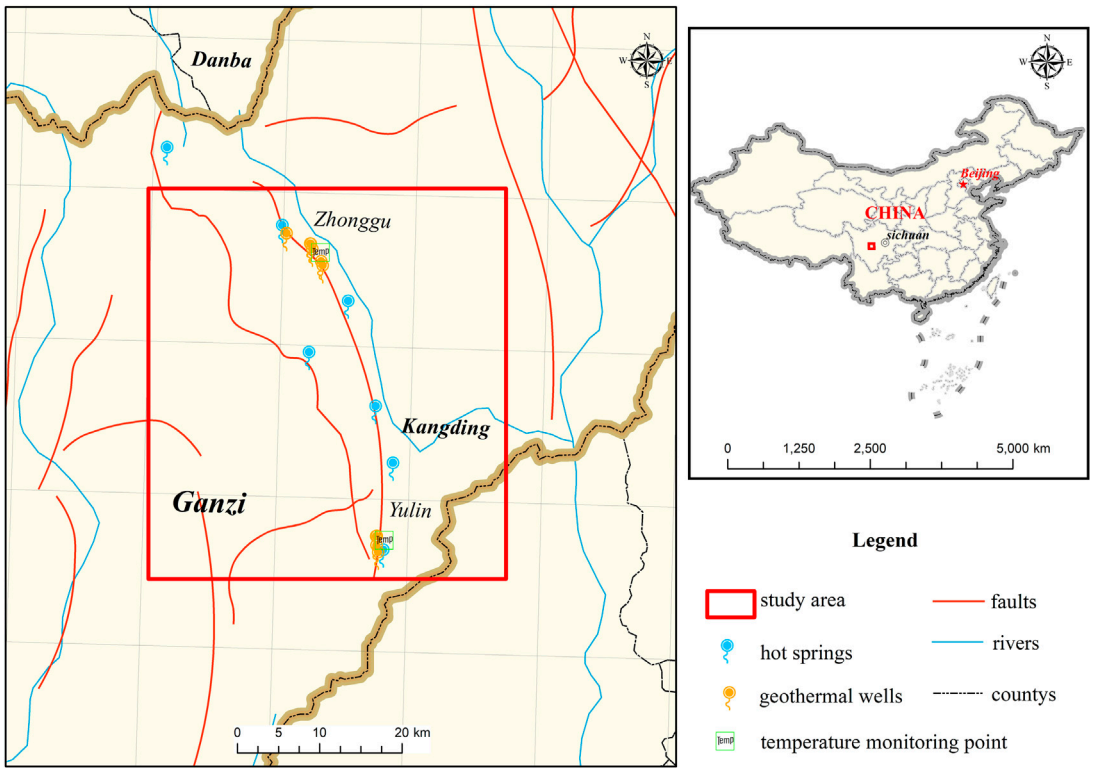

FIGURE 1 | Geographical location and tectonic map of the study area.

Sichuan Basin, and has long been subjected to cold physical and chemical weathering, and tectonic uplift erosion, forming a typical deep-cut alpine landform. Haizi Mountain, Zanduashan Mountain, and Gongga Mountain in the middle of the Big Snow Mountain run from north to south across the whole territory; these mountains divide the Big Snow Mountain into two parts, east and west parts. In the east, there are high mountains and valleys, and in the west and northwest, there are hilly plateaus, high mountains, and deep valleys. The highest point is 7,556 m above sea level, and the lowest point is only 1,390 m.

Kangding County is located in the transition zone between the western edge of the Sichuan Basin and the Qinghai–Tibetan Plateau, and the terrain slopes from west to east. According to the geographical latitude, Kangding should have a subtropical climate; because of the complex topography, there are significant vertical differences, forming a unique plateau-type continental monsoon climate. There is a large temperature difference between morning and evening, and the weather ranges from rainy and foggy to humid. The average annual temperature is 7.1°C, the average summer temperature is 15.7°C, and the lowest temperature is −14.9°C (January). The frost-free period is about 150–250 days, and the snow and ice period is from November to April every year. The multi-year average annual precipitation is 815.7 mm, mainly concentrated in May to September (multi-year average precipitation of 625.6 mm), accounting for 76.7% of the total annual precipitation. The multi-year average number of precipitation days is 178.7 days, and the average evaporation is 1,285.5 mm. The multi-year average relative humidity is 73%, with a higher humidity from June to October, averaging 80.8%, and the lowest from December to March, averaging 65%. In view of the potential geothermal resources, local characteristics, and unique tourism resources in Kangding, it is of great significance for surface temperature monitoring in Kangding County.

3 STUDY DATA AND PREPROCESSING

3.1 Data Source

On 11 February 2013, NASA successfully launched the Landsat 8 satellite, which carries two sensors, the OLI Land Imager and the thermal infrared sensor (TIRS). Landsat 8 maintains basic consistency with Landsat 1–7 in terms of spatial resolution and spectral characteristics. The satellite has a total of 11 bands, bands 1–7 and 9–11 have a spatial resolution of 30 m, band 8 is a 15-m resolution panchromatic band, and the satellite can achieve global coverage once every 16 days.

Landsat 8 remote sensing image data were download from USGS (https://earthexplorer.usgs.gov/) on 20 November 2016. The image was collected at 3:48 p.m. with a resolution of 30 m. Due to the topographic factors of Kangding County, the remote sensing image covering to this area has a long-time distribution and poor image quality, and its annual amount of cloud cover is bigger. After selection, the remote sensing image of 20 November

2016 was chosen as the experimental data, which has moderate/good image quality, and the cloud cover is less than 5%. In conclusion, it is relatively suitable for temperature retrieval.

Our temperature measuring equipment is the American HOBO thermometer. The collected temperature can be approximated as the surface temperature data, and the data can be collected every 30 min on average. The collection period is from October 2016 to December 2017. In the image, we selected the average temperature of the region pixel 10 × 10 of the coordinate point of the equipment as the final experimental result (The pixel range was selected through experiments; i.e., the average regional temperature of different pixel ranges was selected as the experimental results and compared with the measured values, and the pixel range with high accuracy was selected, including 5 × 5, 10 × 10, 20 × 20, 25 × 25; refer to **Supplementary Table S1** for details).

3.2 Preprocessing

Due to limitations of space, spectrum, time, and radiation resolution of remote sensing system, it is difficult to accurately record the information of complex land surface, which will cause errors in the process of data acquisition. These errors degrade the quality of remote sensing data and affect the accuracy of experimental results, so preprocessing of the acquired remote sensing images is required. The preprocessing process includes radiometric calibration, atmospheric correction, image fusion, image stitching, and geometric alignment.

4 COMPARISON OF ALGORITHMS AND CALCULATION OF PARAMETERS

4.1 Atmospheric Correction Method

The atmospheric correction method is also known as the radiative transfer equation (RTE) algorithm. The basic principles of the atmospheric correction method are as follows: first, to estimate the atmospheric influence on the surface thermal radiation, then subtract this atmospheric effect from the total amount of thermal radiation observed by the satellite sensor to obtain the surface thermal radiation intensity, and then convert this thermal radiation intensity into the corresponding surface temperature. The calculation formulas are

$$T_{surface} = \frac{K_2}{ln\left(\frac{K_1}{B(T_s)+1}\right)}, \tag{1}$$

$$B(T_s) = \frac{\left[L_\lambda - L_\uparrow - \tau \times (1-\tau) \times L_\downarrow\right]}{\varepsilon\tau}, \tag{2}$$

$$L_\lambda = gain \times DN + offset, \tag{3}$$

where K_1 (W/m^2/sr/μm) and K_2 (K) are sensor-specific calibration constants; for Landsat 8: Band 10: K_1 = 774.89, K_2 = 1,321.08; Band 11: K_1 = 480.89, K_2 = 1,201.14; $T_{surface}$ is the surface temperature (K), B (T_s) is the radiation brightness received by the sensor for a blackbody with temperature T_s (K); Lλ (W/m^2/sr/μm) is the satellite sensor converting its image element gray value DN to the received radiation brightness value using the radiation calibration factor; gian (W/m^2/sr/μm) and offset (W/m^2/sr/μm) are the slope and the intercept of the response functions for Band 10 and 11, respectively. DN is the original pixel value of the image; τ and ε are the atmospheric transmittance and surface specific emissivity, respectively; L↑(W/m^2/sr/μm), L↓(W/m^2/sr/μm), and τ can be obtained through the NASA query website (https://atmcorr.gsfc.nasa.gov/). The calculation of surface-specific emissivity using the NDVI threshold method was proposed by Sobrino et al. (2003). Pv is the vegetation cover, which can be calculated from the normalized vegetation index NDVI according to the like dichotomous model.

$$\varepsilon = 0.004Pv + 0.986. \tag{4}$$

4.2 Mono-Window Algorithm

The Mono-window algorithm (MW) is an algorithm derived by Qin et al. (2003) based on the surface thermal radiation induction equation. They deduced an algorithm for land surface temperature retrieval using Landsat TM Band 6 data, which is applicable to deduce land surface temperature from remote sensing data of a hot band. It is a linearized first-order Taylor series expansion of the Planck function based on the thermal radiation transfer equation. They simplified the computational models of atmospheric upward radiative brightness and atmospheric downward radiative brightness. The calculation formula is

$$T_s = \frac{[a_6(1-C_6-D_6)] + [b_6(1-C_6-D_6)+C_6+D_6]T_{sen} - D_6T_a}{C_6}, \tag{5}$$

where T_S is the surface temperature (K); T_{sen} is the brightness temperature on the sensor (K); T_a is the average atmospheric temperature (K); a and b are the reference coefficients, when the surface temperature is 0–70°C, a = 67.355,351 and b = 0.458,606; C and D are the intermediate variables, and the calculation formula is

$$C = \varepsilon\tau, \tag{6}$$

$$D = (1-\tau)[1 + (1-\varepsilon)\tau]. \tag{7}$$

The key to the surface temperature retrieval by the single-window algorithm is to calculate the brightness temperature T_{sensor}, the surface specific emissivity ε, the atmospheric transmittance, and the average atmospheric action temperature T_a. Among them, the calculation of the atmospheric transmittance can be referred to **Table 1**. In the table, ω is the atmospheric moisture content (g/cm^2) and is calculated as follows:

$$\omega = 0.0981 \times 6.1078 \times 10^{\frac{7.5t}{t+273.15}} RH + 0.1697, \tag{8}$$

where t is the average atmospheric temperature (°C), RH is the relative humidity, and the data can be obtained through the website of China Meteorological Administration. For the mean atmospheric temperature, Qin et al. (2004) also provided an empirical formula that was derived from the standard atmosphere provided by the Modtran model. As for the article, the authors use the mid-latitude winter mean atmosphere, on account of the location of the study area, as shown in **Equation 9**, where it is the near-surface temperature (K).

TABLE 1 | Atmospheric transmittance estimation equation.

Atmospheric profile	Moisture content w/(g·cm^{-2})	Atmospheric transmittance estimation equation	Correlation coefficient squared (R^2)	Standard error (SEE)
High temperature	0.4–1.6	τ6 = 0.974,290–0.08007ω	0.99611	0.002368
	1.6–3.0	τ6 = 1.031412–0.11536ω	0.99827	0.002539
Low temperature	0.4–1.6	τ6 = 0.982,007–0.09611ω	0.99463	0.003340
	1.6–3.0	τ6 = 1.053710–0.14142ω	0.99899	0.002375

$$T_a = 16.0110 + 0.92621\,(t + 273.15). \quad (9)$$

4.3 Split-Window Algorithm

The split-window algorithm was originally developed for sea surface temperature retrieval, specifically for NOAA/AVHRR channels 4 and 5, and was later also used for surface temperature retrieval, which is more mature and has higher accuracy. Based on the surface heat radiation conduction equation, the split-window algorithm takes into account the difference of atmospheric absorption between two adjacent thermal infrared channels (generally 10.5–11.5 μm and 11.5–12.5 μm) in a 10–13 μm atmospheric window, and eliminates the influence of atmosphere through various combinations of the measured values of the two channels, then the atmospheric and surface emissivity revisions are made. Its calculation formulas is

$$T_s = A_0 + A_1 T_i + A_2 T_j. \quad (10)$$

T_s is the surface temperature (K); T_i and T_j are the brightness temperatures (K) corresponding to i and j bands, in K. Combining with the characteristics of Landsat 8, i = 10 and j = 11; A_0, A_1, and A_2 are the conversion parameters of TIRS10,11 bands, which are determined by the factors of atmospheric transmittance and surface specific emissivity, and for different algorithms, their values vary. The inverse regression coefficients of TIRS in different temperature ranges derived by Qin et al. (2004) were selected for this algorithm, taking a10 = −62.8065 and b10 = 0.4338; a11 = −67.1728 and b11 = 0.4694. Combined with the characteristics of Landsat 8, each parameter is calculated as

$$A_0 = E_1 a_{10} - E_2 a_{11}, \quad (11)$$

$$A_1 = 1 + A + E_1 b_{10}, \quad (12)$$

$$A_2 = -A - E_1 b_{11}, \quad (13)$$

$$A = \frac{D_{10}}{E_0}, \quad (14)$$

$$E_1 = \frac{D_{11}\,(1 - C_{10} - D_{10})}{E_0}, \quad (15)$$

$$E_2 = \frac{D_{10}\,(1 - C_{11} - D_{11})}{E_0}, \quad (16)$$

$$E_0 = D_{11} C_{10} - D_{10} C_{11}, \quad (17)$$

$$C_i = \varepsilon_i \tau_i(\theta), \quad (18)$$

$$D_i = (1 - \tau_i(\theta))\,(1 + (1 - \varepsilon_i)\tau_i(\theta)), \quad (19)$$

$$L_i = a_i + b_i \tau_i. \quad (20)$$

4.4 Time Series

After a series of accuracy and sensitivity analyses, it was initially concluded that RTE has the highest applicability in this study area, followed by MW, and SW has some limitations for this study area due to its excessive sensitivity to atmospheric transmittance and surface specific emissivity. To better highlight the applicability of RTE, the method was used to make the corresponding temperature retrieval for the study area from November 2016 to December 2017, presented as a time series, and then compared and analyzed with the measured data to discuss and evaluate the applicability of RTE in the highland region.

Landsat 8 image data were still downloaded from USGS (https://earthexplorer.usgs.gov/), and the time series distribution was from November 2016 to December 2017. Due to the influence of high cloud coverage on experimental results, images with cloud coverage less than 15% were selected as experimental objects; 11 selected image data could fully represent temperature changes in the study area for 1 year. The data selection process is shown in **Table 2**.

5 RESULTS

5.1 Experimental Results of the Three Algorithms

Based on real-time monitoring instruments in two areas, Zhonggu and Lao Yulin, surface temperature was calculated using RTE, MW, and SW, and the results were compared with the measured data. **Figure 2A**, **Figure 2B**, and **Figure 2C** show the results of RTE, MW, and SW retrieval, respectively. Referring to the LST results obtained from the retrieval of the three algorithms, the overall temperature distribution trend is roughly the same, with high correlation. The areas with higher temperatures are mainly located in the western mountainous areas; the northeastern and southeastern areas have lower temperatures; the northern and central areas have moderate temperatures. Combined with the surrounding terrain factors of Kangding County, it is concluded that the high temperature area is relatively concentrated in the west and northwest, while the eastern area is mainly bare soil and trees, and there are more low temperature areas.

From **Table 3**, the temperature values derived from the retrieval of the three algorithms are Zhonggu: 16.314, 16.027, and 14.928°C, and the measured temperature is 16.034°C, while the temperature values in the Lao Yulin were 16.317, 14.654, and 12.819°C, and the measured temperature was 15.843°C. The

TABLE 2 | Selection of image data.

Time	Note	Choose
2016.11.04	Large cloud cover in the Nakatani Village area (it will affect the results of the Nakatani Village area experiment)	√
2016.11.20	—	√
2016.12.06	—	√
2016.12.22	Overall image cloud coverage is too high (it seriously affects experimental results)	×
2017.1.07	—	√
2017.1.23	Trace clouds in the Lao Yulin area (it does not affect the experimental results in the Lao Yulin area)	√
2017.2.08	Trace of cloud cover in Kangding City (it does not affect the experimental results)	√
2017.3.28	—	√
2017.4.13	—	√
2017.4.29	High cloud coverage in Kangding City (it seriously affects the experiment results)	×
2017.7.11	Part of the study area is not in the image map	×
2017.10.06	—	√
2017.11.07	—	√
2017.12.25	—	√

statistics of surface temperature retrieval results are shown in **Table 3**, △ indicates the absolute error of retrieval results, and △R indicates the mean error.

5.2 Experimental Results of the Time Series

After the screening of the 11 image data, RTE was used to conduct temperature retrieval for the 11 images. The statistics of the experimental results are shown in **Figure 3** and **Table 4**.

6 DISCUSSION

6.1 Precision Analysis of the Three Algorithms

According to the results in **Table 3**, the mean error of RTE is 0.372°C, the mean error of MW is −0.606°C, and the mean error of SW is −2.07°C. Among them, the RTE retrieval results are all higher than the measured results, while the retrieval results of the two other algorithms are lower than the measured results; in terms of accuracy, it is obvious that RTE has the lowest temperature deviation, higher accuracy, and more credibility, followed by MW, while SW has a lower accuracy.

The analysis results show that the temperature retrieval results of RTE in this study area are higher than the measured data, while MW and SW are generally lower than the measured data. The preliminary judgment is that due to the complex topography of the Kangding area, the observation angle and the topographic features, slope, and slope direction in the study area will affect the accuracy of the algorithm, the sensitivity of various algorithms is different, and the degree of influence by atmospheric water vapor content and surface specific emissivity are different.

6.2 Sensitivity Analysis

6.2.1 Atmospheric Transmittance Sensitivity Analysis

Atmospheric transmittance has a very important effect on the conduction of surface heat radiation in the atmosphere and is the basic of surface temperature retrieval. Accurate acquisition of atmospheric transmittance is beneficial to access performance of surface temperature with high accuracy. There are many factors affecting the atmospheric transmittance, such as air pressure, air temperature, aerosol content, and atmospheric water vapor content; all have different degrees of effect on the conduction of thermal radiation, thus making the surface thermal radiation conduction in the atmosphere produce attenuation parameters.

Based on the remote sensing data of the study area in Kangding County on 20 November 2016, sensitivity analysis was performed on the atmospheric transmittance. The retrieval results of the three algorithms were observed and then compared with the measured data for analysis. △m indicates the average rate of change of surface temperature due to the effect of atmospheric transmittance. The results of the sensitivity analysis are shown in **Table 5** and **Figure 4**.

According to **Table 5** and **Figure 4**, when atmospheric transmittance increases or decreases by 0.1, the average change rate of atmospheric transmittance obtained by RTE, MW, and SW is 4.17, 0.51, and 9.08% respectively, and the average change of surface temperature is 0.667°C, 0.086 2°C, and 1.299°C, respectively. The results show that MW is less sensitive to atmospheric transmittance and less affected by atmospheric transmittance; RTE has moderate influence and sensitivity to it; SW is greatly influenced and sensitive to it.

6.2.2 Sensitivity Analysis of Surface Specific Emissivity

Surface specific emissivity is another key parameter for surface temperature retrieval. In the analysis of surface specific emissivity sensitivity, three algorithms are modeled separately, and the relevant parameters mentioned above are pre-input as constant values when applying these models to surface temperature retrieval. Based on the remote sensing data of the study area in Kangding County on 20 November 2016, a sensitivity analysis of the surface specific emissivity was performed, taking a step size of 0.01, observing the retrieval results of the three algorithms, and then comparing the analysis with the actual measured data. △1 indicates the average rate of change of surface temperature due to the effect of atmospheric transmittance, and the results of sensitivity analysis are shown in **Table 6** and **Figure 5**.

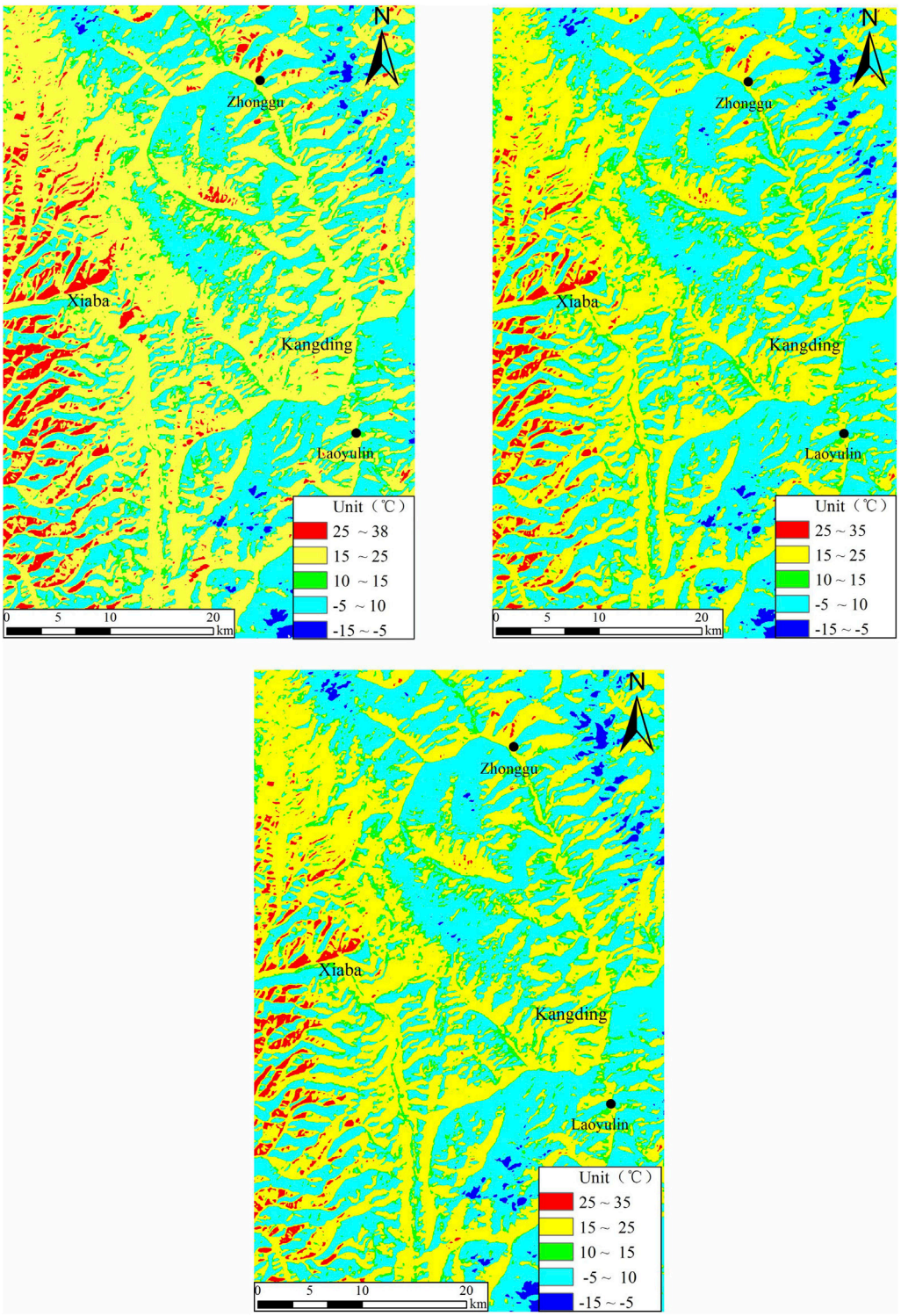

FIGURE 2 | Plot of LST retrieval results of three algorithms. From left to right:**(A)** RTE; **(B)** MW; and **(C)** SW.

According to **Table 6** and **Figure 5**, as the surface specific emissivity increases by 0.01, the average rate of change of RTE retrieval results by surface specific emissivity is 0.36% and the average change of surface temperature value is 0.06°C; the average rate of change of MW by surface specific emissivity is 0.49% and the average change of surface temperature value is 0.08°C; the

TABLE 3 | Statistics of LST retrieval results (unit: °C).

Retrieval algorithm	Lao Yulin	△	Zhong Gu	△	$\triangle_R$
RTE	16.317	0.474	16.314	0.271	0.372
MW	14.654	−1.189	16.027	−0.024	−0.606
SW	12.818	−3.025	14.928	−1.115	−2.07
Real	15.843	—	16.043	—	—

average rate of change of SW by surface specific emissivity is 5.88% and the average change of surface temperature value was 0.8°C. The results show that RTE and MW are less influenced by surface specific emissivity and both have less sensitivity to surface specific emissivity; SW is more affected by surface emissivity and sensitive to atmospheric transmittance.

6.2.3 Near-Surface Temperature Sensitivity Analysis

The influence of near-surface temperature on the temperature retrieval results is mainly reflected in the fact that the change of near-surface temperature directly affects the average atmospheric temperature, while it indirectly has a significant effect on the change of atmospheric transmittance. For the mean atmospheric temperature, Qin et al. (2003) provided an empirical formula, which was derived from the standard atmosphere provided by the Modtran model. The study area of Kangding County was determined to be a mid-latitude winter mean atmosphere, corresponding to **Eq. 9**.

Based on the remote sensing data of the study area in Kangding County on 20 November 2016, the sensitivity analysis of near-surface temperature is carried out with an increase of 1°C, and the retrieval results of the three algorithms were observed and then compared with the actual measured data for analysis. △1 indicates the average rate of change of surface temperature due to the effect of near-surface temperature, and the results of sensitivity analysis are shown in **Table 7** and **Figure 6**.

According to **Table 7** and **Figure 6**, the average rate of change of RTE retrieval results by near-surface temperature is 1.64% for every 1°C increase in near-surface temperature, and the average change of surface temperature value is 0.27°C. However, when the temperature increases by 3°C, the temperature changes from a decreasing trend to an increasing trend, and the preliminary judgment is that because the near-surface temperature will indirectly affect the atmospheric transmittance when the atmospheric correction model is established, when the value-added reaches a certain limit, it will change the atmospheric transmittance and thus affect the retrieval results. The average rate of change of MW by near-surface temperature is 0.43%, and the average change of surface temperature value is 0.07°C; the average rate of change of SW by near-surface temperature is 2.69%, and the average change of surface temperature value is 0.42°C. The results show that MW is less affected by near-surface temperature and less sensitive to near-surface temperature; RTE is affected by near-surface temperature and will become larger with the gradual increase of temperature and more sensitive to near-surface temperature; SW is more affected by near-surface temperature and more sensitive to near-surface temperature.

6.3 Precision Analysis of the Time Series

In order to more intuitively compare the retrieval accuracy of RTE in this study area for 1 year, the measured data and experimental results of each station were drawn into a line graph for comparison. The measured data were not collected up to 25 December 2017, because the monitoring site stopped operating on 10 November 2017. The applicability of RTE in the study area can still be evaluated by comparing the overall experimental results with the measured data trends (for details, see **Figure 7** and **Figure 8**). Detailed data are shown in the attached **Supplementary Table S2**.

According to **Table 7**, and **Figure 7** and **Figure 8**, the trend of RTE retrieval is basically the same with the measured data, and the time series were divided into winter and summer with February 8 as the node. The overall accuracy of the results is about 0–4°C, and the highest retrieval accuracy in winter with an error of 0–1°C; the retrieval accuracy in summer is lower with an error of 1–4°C. By comparison, it is found that the error results of the 3 days of 4 November 2016, 8 February 2017, and 6 October 2017 are significantly different between the two monitoring stations. The overall experiment accuracy is higher in the Laoyulin area, and the accuracy is higher in Zhonggu Village in different time periods. Preliminary judgment might be because the terrain of Kangding urban area is obvious. The altitudes of Zhonggu Village and Laoyulin area are different, and the atmospheric water vapor content and near-surface temperature in the high-altitude area are relatively low. In addition, they are affected by topography, slope aspect, cloud cover, and vegetation coverage, so the experimental errors of the same method in the two places are completely different.

We found that from July to mid-September, the experimental results in the Zhonggu Village area were lower than the measured value, while the experimental results in the Laoyulin area were higher than the measured value. Preliminary judgment cloud cover is one of the reasons; as the result of the Kangding area for performance is often cloudy in the summer, there are thick clouds and the characteristics of dispersion may directly affect the study area, and we did not choose this period of remote sensing images, so if the actual situation in the clouds covered the study area, deviation will directly lead to the result of the experiment. In the location of this study area, winter and summer are predominant throughout the year, and in the peak of summer, cloudy or scattered thick clouds often appear. We did not select remote sensing images from July to September, when cloudiness is most pronounced, but simulated the surface temperature during this period by using experimental results from images with low cloudiness in other months. However, we can judge the possible factors for the anomalous deviations in the two plots: 1. caused by cloud cover and 2. differences in the sensitivity of the algorithm in different seasons. Finally, we conclude that the accuracy of RTE is higher in winter and lower in summer in the study area of Kangding County. The above sensitivity and accuracy analyses shows that the surface temperature retrieval results of RTE are more reliable than the other two algorithms in the Kangding study area and are suitable for highland areas.

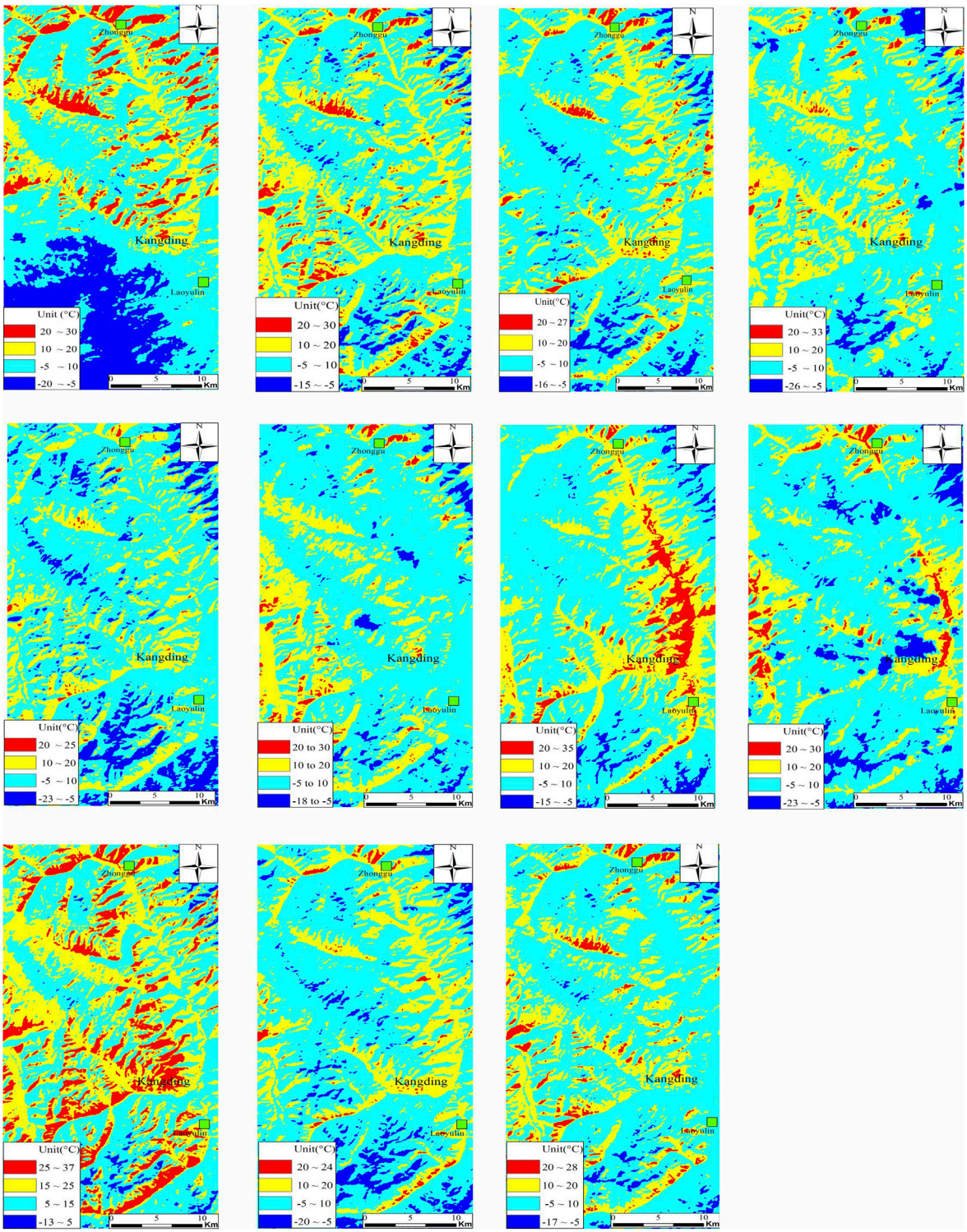

FIGURE 3 | RTE LST retrieval results. In the order of 11.04.2016–12.12.2017.

TABLE 4 | Statistics of RTE LST retrieval results.

Time	Region	T (°C)	Real (°C)	Region	T (°C)	Real (°C)
2016.11.04	Zhonggu	19.463	17.001	Lao Yulin	16.112	16.868
2016.11.20	Zhonggu	16.314	16.043	Lao Yulin	16.317	15.843
2016.12.06	Zhonggu	8.432	8.519	Lao Yulin	9.478	10.185
2017.1.07	Zhonggu	7.76	7.496	Lao Yulin	10.387	11.313
2017.1.23	Zhonggu	5.28	6.13	Lao Yulin	9.056	9.979
2017.2.08	Zhonggu	4.69	6.67	Lao Yulin	10.227	10.495
2017.3.28	Zhonggu	15.357	19.79	Lao Yulin	20.589	23.615
2017.4.13	Zhonggu	14.697	15.625	Lao Yulin	20.152	19.439
2017.10.06	Zhonggu	21.975	20.979	Lao Yulin	22.822	24.795
2017.11.07	Zhonggu	13.89	14.19	Lao Yulin	17.434	18.015
2017.12.25	Zhonggu	12.61	—	Lao Yulin	11.439	—

TABLE 5 | Variation in surface temperature due to atmospheric transmittance errors (unit: °C).

Change in atmospheric transmittance/°C	−0.1	0	0.1	0.2	$\triangle_m$ (%)
RTE	16.981	16.314	15.658	15.011	4.17
MW	16.119	16.027	15.938	15.850	0.51
SW	16.224	14.928	13.631	12.335	9.08
Real	16.304	—	—	—	—

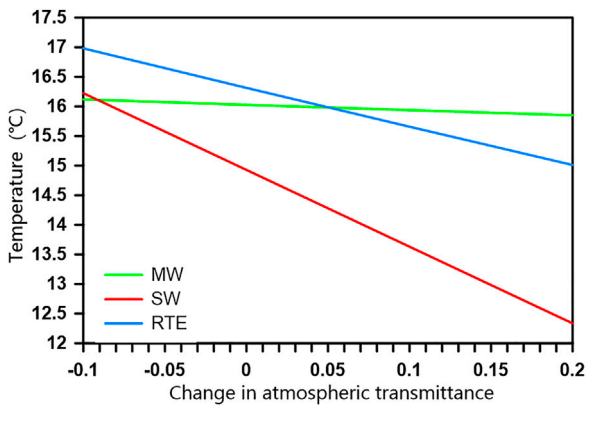

FIGURE 4 | Variation in surface temperature due to atmospheric transmittance errors.

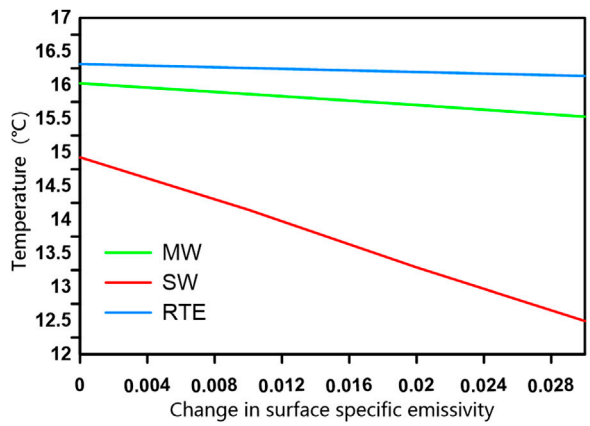

FIGURE 5 | Surface temperature change due to surface specific emissivity error.

TABLE 6 | Surface temperature change due to surface specific emissivity error (unit: °C).

Change in surface specific emissivity/°C	0	0.01	0.02	0.03	$\triangle_1$ (%)
RTE	16.314	16.254	16.195	16.136	0.36
MW	16.027	15.867	15.7038	15.530	0.49
SW	14.928	14.148	13.291	12.495	5.88
Real	16.304	—	—	—	—

TABLE 7 | Changes in surface temperature due to near-surface temperature errors (unit: °C).

Near-surface temperature change/°C	0	1	2	3	$\triangle_1$ (%)
RTE	16.314	16.232	16.065	16.645	1.64
MW	16.027	16.134	16.069	16.003	0.43
SW	14.928	15.416	15.802	16.224	2.69
Real	16.304	—	—	—	—

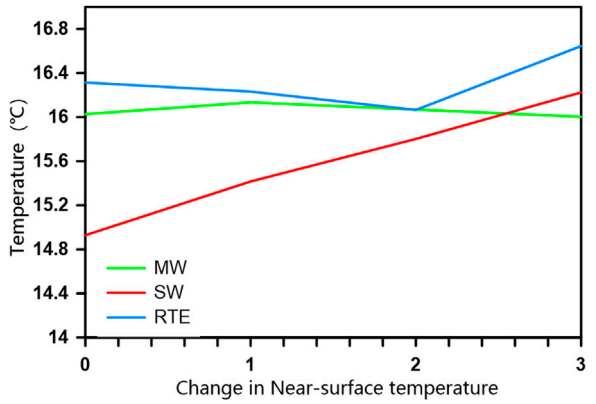

FIGURE 6 | Variation of surface temperature due to near-surface temperature error.

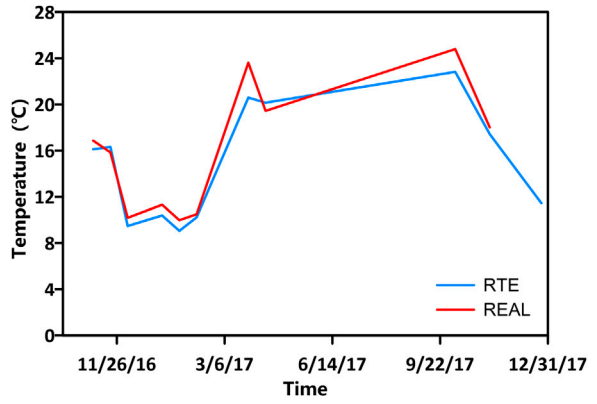

FIGURE 7 | Comparison of experimental results and actual measurement data in Zhonggu.

7 GEOTHERMAL ANOMALY DETECTION USING LST

Local and regional geothermal energy prospects are a prerequisite for geothermal energy development. However, due to operational costs and site accessibility, existing geophysical methods for estimating geothermal potential are usually limited to the exploration scale. Therefore, exploration of large-scale areas such as surface temperature and thermal anomalies mainly relies on thermal infrared images from remote sensing satellite (Chan et al., 2018). Although IR remote sensing is currently limited to detecting supersurface and shallow buried geothermal resources, it is a valuable tool that provides an effective mapping and quantification method that can greatly facilitate the assessment of local geothermal potential and the development of geothermal resources.

7.1 Method

Usually, scholars use high-resolution time series data, together with two LST datasets (one for remotely sensed data and the other for land surface empirical data) to discuss the thermal anomaly area. Some scholars have also adopted a deviation bias approach in which the differences between the two LST datasets in a non-geothermal region are analyzed, the region is clustered based on hydrometeorological and surface properties, and a spatially averaged LST deviation is assigned to each cluster, and then the LST is calculated for the entire region. It is then assumed that these differences are partly due to the geothermal component being represented in the remote sensing data only, which allows the geothermal area to be determined and the results to be compared with the given geothermal area map. However, it is not always possible to choose a specific time and date for analysis due to the constraints of the acquisition time in a given region.

7.2 Geological Influences in Geothermal Area

Due to the large number of geothermal fields in the geothermal active area, rift zones occur when tectonic extension and convection in the area of upwelling thermal material thins the lithospheric plates. The continuous supply of heat sources increases the heat flow and thermal energy at shallow depths compared to other tectonic environments, leading to anomalies in the land surface LST. Using remote sensing image data LST to detect geothermal fields leads to more dispersed geothermal anomalies. Several other areas are highlighted, which form potential geothermal zones, and the highlighted points are often associated with thermally active tectonic zones, that is, basement faults in the basement or rising angular structures.

7.3 Identification of Geothermal Anomaly Area

The two temperature monitoring sites selected for this study—the Laoyulin and the Zhonggu area—have hot spring. In the northern part of the study area, the hot spring in the Zhonggu area is called Xikang Hot spring, and the temperature of the hot spring reaches 76°C. In the southern part, the hot spring in the Laoyulin area is called Guanding Hot spring, and the temperature reaches 77.6°C. Xikang Hot spring has become one of the local tourist attractions, featuring its spa and wellness. After exploration of these two areas, boiling hot springs and geysers were found in two areas. By investigating the hot springs and the field, the selected area was preliminarily judged as the geothermal anomaly area. It also shows that there is a good spatial consistency between hot spring occurrence and thermal anomaly areas.

7.4 Status of Kangding Geothermal Area

Through the previous research results, the geotectonic and background of the Kangding geothermal activity area in the study area of this article are analyzed. First, due to the special geological and tectonic background of the Kangding geothermal anomaly area, the hydrothermal activity in the study area is intense. The geothermal system belongs to the convective conduction type, so the traditional method of analyzing geothermal gradient by testing the geothermal heat flow value is not precise enough [even though geodetic heat flow values for the region have been discussed by researchers in the region, they are still imperfect (Guo et al., 2017). In addition, the tectonic activity in the Kangding area is

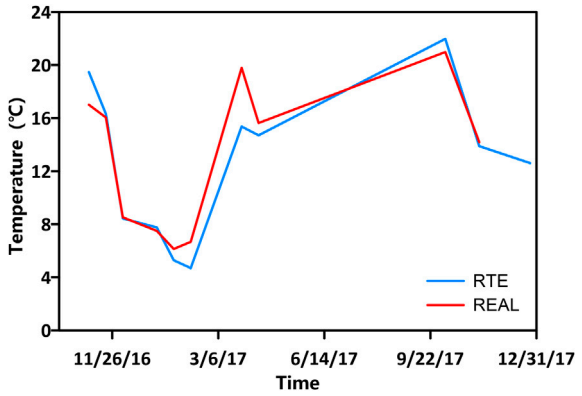

FIGURE 8 | Comparison of experimental results and measured data in the Lao Yulin.

intense, the heat flow component consisting of shear friction heat generation and plastic deformation heat generation in the crust should not be negligible, and the proportion of the heat contribution to the lithosphere from the radiogenic heat flow component in the crust and the conduction heat flow component in the mantle is unknown, so it is an effective means to detect the geothermal field by LST using remote sensing thermal infrared data for the area.

However, only preliminary work has been done in this paper, that is, a comparative analysis of three surface temperature retrieval algorithms and a comprehensive evaluation of the applicability of RTE in highland areas, aiming to provide a relatively reliable basis for geothermal resource for the future development or excavation of geothermal prospective areas.

8 CONCLUSION

Based on Landsat 8 remote sensing imagery of 20 November 2016 in the Kangding County study area, three algorithms are adopted in this study: the atmospheric correction method (radiative transfer equation, RTE), split-window algorithm (SW algorithm), and mono-window algorithm (MW algorithm) were used to retrieval the surface temperature of the study area. Based on the measured data of two real-time monitoring stations located in Zhonggu and Laoyulin area, Kangding county, comparative analysis and accuracy verification of retrieval results are made, and the following conclusions are preliminarily drawn:

1) In the study area with complex topographic features—Kangding County as an example, RTE has the highest accuracy with a mean error of 0.372°C, followed by MW with an accuracy of −0.606°C, which is slightly higher than that of SW, −2.07°C.
2) In the study area, the temperature values using RTE retrieval are higher than the measured values, while the temperature values of MW and SW retrieval are lower than the measured values. It is preliminarily judged that the accuracy of the algorithm is affected by the observation angle, the topographic features, slope, and slope direction in the study area.
3) For the two monitoring stations, Zhonggu and Laoyulin area, the regional temperature difference values of the three algorithms are also different. The regional temperature difference value of RTE is the smallest, only 0.01°C, followed by MW with a regional temperature difference value of 1.373°C, and SW with the largest regional temperature difference value of 2.11°C. The influence of regional factors also causes different effects on the retrieval results of each algorithm, among which RTE has the smallest influence and SW has the largest influence.
4) High emissivity and low water vapor content exist in the high-altitude study area like Kangding. After comprehensive comparison analysis, it is concluded that MW has the lowest comprehensive sensitivity; RTE has higher sensitivity to atmospheric transmittance and moderate comprehensive sensitivity. However, SW is too sensitive to surface specific emissivity and atmospheric transmittance, which has some limitations for temperature retrieval in this area.
5) Through in-depth analysis of the temperature retrieval results of RTE in the study area of Kangding County by using time series, it can be seen that the experimental accuracy of RTE in Kangding County is higher in winter and relatively lower in summer, and affected by altitude and other factors, the performance effects in different regions are different.
6) The use of thermal infrared remote sensing can produce spatially representative experimental results over a much larger area than traditional geothermal exploration methods. However, this method is also only applicable to the exploration of shallow geothermal resources, so in the future, we need to discover new means of exploring and monitoring geothermal resources. This requires not only further mastery of the mechanistic analysis of geothermal anomalies but also a thorough analysis of the geological structure of the study area. This approach of combining geothermal mechanistic analysis with geological structures will greatly improve the effectiveness of geothermal exploration and monitoring.

In this article, by comparing the results of temperature retrieval of the three algorithms in the study area of Kangding County and systematically evaluating the RTE in the form of time series, the results show that the algorithm has certain applicability for LST retrieval in the study area and can provide some references for surface temperature retrieval in highland areas. However, due to the insufficient number of monitoring stations, the accuracy of the three algorithms could not be verified and evaluated more systematically and comprehensively.

DATA AVAILABILITY STATEMENT

The original contributions presented in the study are included in the article/**Supplementary Material**; further inquiries can be directed to the corresponding author.

AUTHOR CONTRIBUTIONS

DB: algorithm analysis, methodology, and writing—original draft. SD: writing—review, algorithm analysis, methodology. WY: writing—review and editing, and methodology. WF: mapping and analysis of results. YC: algorithm analysis and mapping. ZJ: writing—original draft, and analysis of results. SR: writing—review and editing, and methodology.

FUNDING

This study was supported by the Natural Science Foundation of China's project: No. 42002300.

ACKNOWLEDGMENTS

The editors and the two reviewers are also thanked for their comments on the improvement of the manuscript.

SUPPLEMENTARY MATERIAL

The Supplementary Material for this article can be found online at: https://www.frontiersin.org/articles/10.3389/feart.2022.785900/full#supplementary-material

REFERENCES

Alexandra, G., Paschalis, D., and George, F. (2021). Detecting Geothermal Anomalies Using Landsat 8 thermal Infrared Remotely Sensed Data International Journal of Applied Earth Observations and Geoinformation. *Int. J. Appl. Earth Obs. Geoinf.* Available at: www.elsevier.com/locate/jag.

Chan, H. P., Chang, C. P., and Dao, P. D. (2018). Geothermal Anomaly Mapping Using Landsat ETM+ Data in Ilan Plain, Northeastern Taiwan. *Pure Appl. Geophys.* 175 (1), 303–323. doi:10.1007/s00024-017-1690-z

Duan, S. B., Ru, C., Li, Z., Wang, M. M., Xu, H. Q., Li, H., et al. (2021). Progress of Remote Sensing Inversion of Surface Temperature from Landsat thermal Infrared Data. *J. Remote Sensing* 08, 1591–1617.

Eneva, M., and Coolbaugh, M. F. (2009). Importance of Elevation and Temperature Inversions for the Interpretation of thermal Infrared Satellite Images Used in Geothermal Exploration. *Trans. - Geothermal Resour. Counc.* 33, 415–418.

Falalakis, G., and Gemitzi, A. (2020). A Simple Method for Water Balance Estimation Based on the Empirical Method and Remotely Sensed Evapotranspiration Estimates. *J. Hydroinformatics* 22, 440–451. doi:10.2166/hydro.2020.182

Guo, Q., Pang, Z., Wang, Y., and Tian, J. (2017). Fluid Geochemistry and Geothermometry Applications of the Kangding High-Temperature Geothermal System in Eastern Himalayas. *Appl. Geochem.* 81, 63–75. doi:10.1016/j.apgeochem.2017.03.0070883-2927

Hu, D., Qiao, K., Wang, X., Zhao, L., and Guohua, J. (2017). Inversion Using Single Window Algorithm Landsat 8 TIRS Data Surface Temperature [J]. *J. Wuhan Univ. (Information Sci. Edition)* 42 (07), 869–876. doi:10.13203/j.whugis20150164

Nash, G. D., Moore, J. N., and Sperry, T. (2003). Vegetal-spectral Anomaly Detection at the Cove Fort-Sulphurdale thermal Anomaly, Utah, USA: Implications for Use in Geothermal Exploration: Implications for Use in Geothermal Exploration. *Geothermics* 32 (2), 109–130. doi:10.1016/s0375-6505(03)00012-9

Qin, Q., Zhang, N., Nan, P., and Chai, L. (2011). Geothermal Area Detection Using Landsat ETM+ thermal Infrared Data and its Mechanistic Analysis-A Case Study in Tengchong, China. *Int. J. Appl. Earth Obs. Geoinf.* 13 (4), 552–559. doi:10.1016/j.jag.2011.02.005

Qin, Z., Li, W., Zhang, M., Karnieli, A., and Berliner, P. (2003). Atmospheric Parameter Estimation Method by Single Window Algorithm[J]. *Remote Sensing Land Resour.* 02, 37–43.

Qin, Z., Mao, K., and Liu, W. (2004). Inversion of Surface Temperature in the Bohai Rim Using MODIS Imagery and Single Window Algorithm. *Mapp. Spat. Geogr. Inf.* 06, 23–25.

Reath, K. A., and Ramsey, M. S. (2013). Exploration of Geothermal Systems Using Hyperspectral thermal Infrared Remote Sensing. *J. Volcanol. Geotherm. Res.* 265, 27–38. doi:10.1016/j.jvolgeores.2013.08.007

Romaguera, M., Vaughan, R. G., Ettema, J., Izquierdo, V. E., Hecker, C. A., and van der Meer, F. D. (2018). Detecting Geothermal Anomalies and Evaluating LST Geothermal Component by Combining thermal Remote Sensing Time Series and Land Surface Model Data. *Remote Sensing Environ.* 204, 534–552. doi:10.1016/j.rse.2017.10.003

Sobrino, J. A., and Jimnez-Muoz, J. C. (2003). A Generalized Single-Channel Method for Retrieving Land Surface Temperature from Remote Sensing Data. *J. Geophys. Res.* 108 (D22), 4688. doi:10.1029/2003JD003480

Van der Meer, F., Hecker, C., van Ruitenbeek, F., van der Werff, H., de Wijkerslooth, C., and Wechsler, C. (2014). Geologic Remote Sensing for Geothermal Exploration: A Review. *Int. J. Appl. Earth Obs. Geoinf.* 33, 255–269. doi:10.1016/j.jag.2014.05.007

Xiao, Y., Ma, M., and Wen, J. (2021). Progress in Land Surface Temperature Retrieval over Complex Surface. *Remote Sens. Technol. Appl.* 36 (1), 33–43.

Yu, X., Guo, X., and Wu, Z. (2014). Land Surface Temperature Retrieval from Landsat 8 TIRS-Comparison between Radiative Transfer Equation-Based Method, Split Window Algorithm and Single Channel Method. *Remote Sens.* 6 (10), 9829–9852. doi:10.3390/rs6109829

Conflict of Interest: The authors declare that the research was conducted in the absence of any commercial or financial relationships that could be construed as a potential conflict of interest.

Publisher's Note: All claims expressed in this article are solely those of the authors and do not necessarily represent those of their affiliated organizations, or those of the publisher, the editors, and the reviewers. Any product that may be evaluated in this article, or claim that may be made by its manufacturer, is not guaranteed or endorsed by the publisher.

Advantages of publishing in Frontiers

OPEN ACCESS
Articles are free to read for greatest visibility and readership

FAST PUBLICATION
Around 90 days from submission to decision

HIGH QUALITY PEER-REVIEW
Rigorous, collaborative, and constructive peer-review

TRANSPARENT PEER-REVIEW
Editors and reviewers acknowledged by name on published articles

Frontiers
Avenue du Tribunal-Fédéral 34
1005 Lausanne | Switzerland

Visit us: www.frontiersin.org
Contact us: frontiersin.org/about/contact

REPRODUCIBILITY OF RESEARCH
Support open data and methods to enhance research reproducibility

DIGITAL PUBLISHING
Articles designed for optimal readership across devices

FOLLOW US
@frontiersin

IMPACT METRICS
Advanced article metrics track visibility across digital media

EXTENSIVE PROMOTION
Marketing and promotion of impactful research

LOOP RESEARCH NETWORK
Our network increases your article's readership